

DOCTORAL THESIS

Oil Shale Oxyfuel CFB Combustion

Mais Hanna Suleiman Baqain

TALLINN UNIVERSITY OF TECHNOLOGY
DOCTORAL THESIS
26/2024

Oil Shale Oxyfuel CFB Combustion

MAIS HANNA SULEIMAN BAQAIN



TALLINN UNIVERSITY OF TECHNOLOGY

School of Engineering

Department of Energy Technology

This dissertation was accepted for the defence of the degree 29/04/2024

Supervisor: Prof. Dr. Alar Konist
School of engineering
Tallinn University of Technology
Tallinn, Estonia

Co-supervisor: Dr. Dmitri Nešumajev
School of engineering
Tallinn University of Technology
Tallinn, Estonia

Opponents: Prof. Dr. Bo Leckner
Department of Energy and Environment
Chalmers University of Technology
Gothenburg, Sweden

Dr. Lauri Loo
Energy modeler
R8 Technologies OÜ
Tallinn, Estonia

Defence of the thesis: 10/06/2024, Tallinn

Declaration:

Hereby I declare that this doctoral thesis, my original investigation and achievement, submitted for the doctoral degree at Tallinn University of Technology has not been submitted for doctoral or equivalent academic degree.

Mais Baqain

Signature



European Union
European Regional
Development Fund



Investing
in your future

Copyright: Mais Baqain, 2024

ISSN 2585-6898 (publication)

ISBN 978-9916-80-148-2 (publication)

ISSN 2585-6901 (PDF)

ISBN 978-9916-80-149-9 (PDF)

DOI <https://doi.org/10.23658/taltech.26/2024>

Printed by Koopia Niini & Rauam

Baqain, M. (2024). *Oil Shale Oxyfuel CFB Combustion* [TalTech Press].
<https://doi.org/10.23658/taltech.26/2024>

TALLINNA TEHNIKAÜLIKOOL
DOKTORITÖÖ
26/2024

Oxyfuel tehnoloogia rakendamine põlevkivi CFB põletamisele

MAIS HANNA SULEIMAN BAQAIN



Contents

| | |
|--|----|
| List of Publications | 7 |
| List of Conference Contributions | 7 |
| Author’s Contribution to the Publications | 9 |
| Introduction | 10 |
| Research Objectives and Novelty..... | 11 |
| Research Methodology | 13 |
| Research Contribution and Dissemination | 13 |
| Research Outline..... | 14 |
| Abbreviations..... | 16 |
| 1 LITERATURE REVIEW | 17 |
| 1.1 CO ₂ Capture Technologies..... | 17 |
| 1.1.1 Pre-combustion..... | 17 |
| 1.1.2 Post-Combustion..... | 17 |
| 1.1.3 Oxyfuel Combustion..... | 18 |
| 1.2 Solid Fuel Oxy-Combustion | 19 |
| 1.2.1 Ash Behaviour | 21 |
| 1.2.2 Emissions of Nitrogen Oxides..... | 22 |
| 1.2.3 Emissions of Sulfur Oxides | 23 |
| 1.3 Oxygen Production Technologies (OPTs) | 24 |
| 1.4 Negative CO ₂ Emissions..... | 25 |
| 2 EXPERIMENTAL METHODS | 27 |
| 2.1 Materials | 27 |
| 2.1.1 Oil shale..... | 27 |
| 2.1.2 Biomass | 28 |
| 2.1.3 Semicoke | 29 |
| 2.2 Equipment and Methods | 30 |
| 2.2.1 60 kWth Circulating Fluidized Bed (CFB) Pilot Facility..... | 30 |
| 2.2.2 TG–MS Analyses | 32 |
| 3 RESULTS AND DISCUSSION..... | 33 |
| 3.1 Air and Oxyfuel Overall Combustion Process..... | 33 |
| 3.2 Ash Behaviour | 34 |
| 3.2.1 Physical Properties | 34 |
| 3.2.2 Chemical Composition | 35 |
| 3.2.3 Mineral Composition..... | 36 |
| 3.2.4 Trace Elements and Heavy Metals..... | 37 |
| 3.2.5 Extent of Carbonate Decomposition (ECD) | 38 |
| 3.3 Emissions..... | 39 |
| 3.3.1 NO _x and N ₂ O..... | 39 |
| 3.3.2 SO ₂ | 42 |
| 3.3.3 CO..... | 43 |
| 3.4 Oil shale and Biomass Oxyfuel Combustion like Conditions | 45 |
| 4 CONCLUSIONS AND FUTURE WORK..... | 50 |
| List of Figures | 52 |
| List of Tables | 54 |

| | |
|-------------------------------|-----|
| References | 55 |
| Acknowledgements..... | 66 |
| Abstract..... | 67 |
| Lühikokkuvõte..... | 69 |
| Appendix (Publications) | 71 |
| Curriculum vitae..... | 339 |
| Elulookirjeldus..... | 340 |

List of Publications

The list of author's publications, on the basis of which the thesis has been prepared:

- I **Baqain, M.**; Rüstü Yörük, C.; Nešumajev, D.; Järvik, O.; Konist, A. (2023). Ash characterisation formed under different oxy-fuel circulating fluidized bed conditions. *Fuel*, 338, #127244. DOI: 10.1016/j.fuel.2022.127244.
- II **Baqain, Mais**; Neshumayev, Dmitri; Konist, Alar (2023). NO_x and N₂O Emissions from Ca-rich Fuel Conversion in Oxyfuel Circulating Fluidized Bed Combustion. *Thermal Science and Engineering Progress*, 42, #101938. DOI: 10.1016/j.tsep.2023.101938.
- III **Baqain, M.**; Neshumayev, D.; Konist, A. (2022). Oxyfuel Conversion of Ca-rich fuel in a 60 kW_{th} Circulating Fluidized Bed. *Proceedings of the 16th Greenhouse Gas Control Technologies Conference (GHGT-16)* 23-24 Oct 2022. GHGT. DOI: 10.2139/ssrn.4276982.
- IV **Baqain, Mais**; Neshumayev, Dmitri; Konist, Alar (2024). TG-MS analysis and kinetic study of co-combustion of ca-rich oil shale with biomass in air and oxy-like conditions. *Carbon Capture Science & Technology*, 10, #100162. DOI: 10.1016/j.ccst.2023.100162.
- V Neshumayev, Dmitri; **Baqain, Mais**; Konist, Alar. The emissions of NO_x, SO₂, CO and decomposition of carbonates during oxyfuel combustion of low heating value semicoke in CFB pilot facility. [submitted to Fuel Journal-under review].
- VI Chunfei Wu, Qi Huang, Zhicheng Xu, Ayesha Tariq Sipra, Ningbo Gao, Luciana Porto de Souza Vandenberghec, Sabrina Vieira, Carlos Ricardo Soccol, Ruikai Zhao, Shuai Deng, Sandra K.S. Boetcher, Shijian Lu, Huancong Shi, Dongya Zhao, Yupeng Xing, Yongdong Chen, Jiamei Zhu, Dongdong Feng, Yu Zhang, Lihua Deng, Guoping Hu, Paul A. Webley, Daxin Lian, Zhichen Ba, Agata Mlonka-Mędrala, Aneta Magdziarz, Norbert Miskolczi, Szabina Tomasek, Su Shiung Lamq, Shin Ying Foong, Hui Suan Ng, Long Jiangs, Xinlong Yan, Yongzhuo Liu, Ying Ji, Hongman Sunv, Yu Zhang, Haiping Yang w, Xiong Zhang, Mingzhe Sun, Daniel C.W. Tsang, Jin Shan, Christoph Muller, Margarita Rekhina, Maximilian Krödel, Alexander H. Bork, Felix Donat, Lina Liua, Xin Jin h, Wen Liub, Syed Saqline, Xianyue Wub, Yongqing Xu, Asim Laeeq Khand, Zakawat Ali, Haiqing Line, Leiqing Hue, Jun Huang, Rasmeet Singh, Kaifang Wan, Xuezhong He, Zhongde Dai, Shouliang Yi, Alar Konist, **Mais Hanna Suleiman Baqain**, Yijun Zhao, Shaozeng Sun, Guoxing Chen, Xin Tu, Anke Weidenka, Sibudjing Kawi, Kang Hui Limo, Chunfeng Song, Qing Yang, Zhenyu Zhaor, Xin Gao, Xia Jiang, Haiyan Ji, Toluleke E. Akinola, Adekola Law, Olajide S. Otitoju, Meihong Wang, Guojun Zhang, Lin Ma, Baraka C. Sempuga, Xinying Liu, Eni Oko, Michael Daramola, Zewei Yu, Siming Chen, Guojun Kang, Qingfang Li a, Li Gao, Ling Liu, Hui Zhou. (2023). A comprehensive review of carbon capture science and technologies. *Carbon Capture Science & Technology*, #100178. DOI: 10.1016/j.ccst.2023.100178.

List of Conference Contributions

- I. Baqain, M.; Yörük, C. R.; Nešumajev, D.; Järvik, O.; Konist, A. (2022). Characterisation of Ashes Formed at CFB Oxy-fuel Combustion of Ca-rich Fuel. Fluidized Bed Conversion Conference, 8-11 May 2022. Gothenburg, Sweden: Chalmers University of Technology.

- II. Baqain, M.; Neshumayev, Dmitri; Konist, Alar (2022). NO_x Emissions from Ca-rich Fuel Conversion in Oxy-fuel Circulating Fluidized Bed Combustion. 25th Conference on Process Integration, Modelling and Optimisation for Energy Saving and Pollution Reduction PRES22, 5 – 8 September 2022. Bol, Croatia: De Gruyter.
- III. Baqain, M.; Neshumayev, D.; Konist, A. (2023). SO₂ Emissions from Oxyfuel Combustion of Ca-rich fuel in a 60 kWth Circulating Fluidized Bed. Carbon Capture Science and Technology conference-online (CCST 2023) 20-23 Jul 2023. Tsinghua University, China.
- IV. Konist, A.; Baqain, M.; Neshumayev, D. (2023). Experimental study of semicoke combustion in oxyfuel circulating fluidized bed pilot facility. The 5th International Conference on Circulating Fluidized Bed Boom, (CFBB05) 26-29 Jul 2023. Kunming, China: Kunming University of Science and Technology.

Author's Contribution to the Publications

Contribution to the papers in this thesis are:

- I Conceptualizing the study in cooperation with all the co-authors; developing the methodology with all co-authors; processing the data; conducting the analysis and validation of the results and drafting the manuscript in cooperation with all the co-authors; visualizing the manuscript and writing and revision.
- II Conceptualizing the study in cooperation with all the co-authors; developing the methodology with all co-authors; processing the data; conducting the analysis and validation of the results and writing and revision of manuscript.
- III Conceptualizing the study in cooperation with all the co-authors; developing the methodology with all co-authors; processing the data; conducting the analysis and validation of the results and writing of manuscript.
- IV Conceptualizing the study, design of the experiment, setting up experimental apparatus, sample preparation, conducting the experimental work, data collection and analysis, and writing and revision of manuscript.
- V Partially developing the methodology with all co-authors; partially processing the data; partially conducting the analysis and validation of the results, writing of the manuscript.
- VI Performing a literature search, identifying research gaps, organizing information, writing and revision of manuscript.

Introduction

The EU climate action plan set an interim target of reducing greenhouse gas (GHG) emissions to at least 55% below 1990 levels by 2030 [1]. Renewables and the enhancement of energy efficiency are crucial for establishing a low-carbon economy, and these approaches are expected to play an important role in the future. Despite the rapid growth of renewable energy is growing, it is not sufficiently fast enough to fulfil the mounting global electricity demand [2]. Consequently, the combustion of fossil fuels remains a major means of satisfying the world's rising energy needs. The fossil fuel combustion process is associated with the release of GHG and air pollutants (such as CO₂, SO₂, NO_x, etc.). However, compared to the direct replacement of fossil fuels, strategies to reduce the emitted CO₂ are in high demand. This has facilitated the research and implementation of carbon capture utilisation and storage (CCUS) [3], which is the only technology that allows the continued use of fossil fuels, while also substantially reducing GHG emissions. Oxyfuel circulating fluidised bed (CFB) combustion is among the most promising CO₂ abatement technologies for cleaner combustion [4]–[8]. By replacing air with a mixture of high-purity oxygen and flue gas, the overall process becomes nitrogen-lean and can generate flue gas that is rich in CO₂ and ready for carbon capture and storage.

Estonia has a long history of using oil shale, and its energy supply is dominated by domestically produced oil shale, which provides the country a high degree of energy independence and high carbon intensity.

Estonian oil shale is a low-grade Ca-rich fuel with high volatile organic compound and ash content, primarily carbonate minerals [9], [10]. Oil shale can be burned to generate heat and power or used to produce liquid fuel [11]. The combustion of a low-rank fuel such as oil shale results in considerably higher rate of CO₂ combustion. The pyrolysis of oil shale results in the ex situ process producing a solid organic-containing residue waste called semicoke. Waste products from the two aforementioned technologies are the core interests of current research.

Semicoke is a potentially harmful solid material with a low energy content (low heating value of 1–4 MJ/kg), the value of which depends on the type of technology used, and this generally limits the possibilities of its further efficient utilisation. Currently, there no study has presented suitable and efficient semicoke utilisation at the industrial level. Semicoke is used as a solid heat carrier and burned, and hot ash is formed during the combustion of semicoke, which serves as a source of energy for the pyrolysis of oil shale in retorts [12], [13].

The widespread utilisation of Estonian oil shale necessitates the exploration of techniques to mitigate CO₂ emissions. A notable achievement in this regard was the substantial reduction in CO₂ emissions achieved through the decommissioning and retrofitting of pulverised combustion (PC) boilers with CFB technology [14]. Special attention was given to the co-combustion of oil shale with CO₂-neutral fuel biomass for further CO₂ reduction. It has been shown that the co-utilisation of biomass with oil shale enhances the combustion performance and reduces pollutant emissions, solid waste, and ash formation [15]–[17].

In the context of the European green deal, the outcomes from COP27 and COP28 highlighted discussions on CCS as a crucial tool in the transition to a carbon-neutral economy [3], [18]. Estonia's commitment to reach carbon neutrality by 2050, along with significant reductions in greenhouse gas emissions by 2030, underscores the importance

of exploring all available avenues for emission reduction, including CCUS, which announced a government plan of 80% decrease in GHG emissions by that date, including 70% by 2030 [19]. Thus, the reduction of GHGs can be accomplished in several ways as follows. 1) Improving the efficiency of combustion systems owing to calcite decomposition reduction, as mentioned earlier, using oil shale in CFB boilers. 2) Utilising alternative fuels, such as biomass, to achieve negative CO₂ emissions, or co-firing blended fuels, such as biomass with oil shale, for better GHGs emission reduction, and 3) Implementing CO₂ capture technologies, such as pre-combustion, post-combustion, and oxyfuel combustion capture. The efficiency of these capture technologies is dependent on the CO₂ concentration in the flue gas stream. Increased concentrations of CO₂ in the exhaust gas stream facilitates a capture process that requires less complicated chemical treatments and energy [20]. Therefore, CO₂ capture and sequestration is more convenient and cost-effective. Overall, it can be expected that among all the available options, oxyfuel CFB combustion for the Estonian power sector represents the most promising carbon capture technology in terms of techno-economic feasibility [21], reduction potential of emissions, energy efficiency, and ease of retrofitting into currently operated power plants. Consequently, the scope of the ClimMit project [22] facilitated the development of advanced experimental progress in investigating the combustion of kukersite oil shale for both air and different oxyfuel combustion regimes in a 60 kWth CFB pilot facility in the Energy Technology Department at Tallinn University of Technology.

Research Objectives and Novelty

Oil shale plays a significant role in Estonia's energy landscape, with approximately 40% of its electricity demand being met by this resource and approximately 2% only of the generated ash being recovered [19]. This reliance has resulted in increased interest in and several studies on various aspects for Estonian oil shale oxyfuel combustion. These include thermogravimetric analysis experiments to investigate the kinetics of oil shale combustion in a CO₂ environment [23]–[25], small-scale batch laboratory reactor experiments [26], process simulator-based modelling of the oxyfuel combustion process with oil shale [25], [27], [28], and basic pilot scale experiments under O₂/CO₂ combustion atmosphere of a maximum 30% inlet O₂ [29], [30]. These studies laid the groundwork for pilot-scale oxyfuel combustion applications. Prior to full-scale implementation, pilot-scale projects are crucial for the development and validation of new technologies. Researchers and engineers can assess feasibility, performance, and potential challenges in real-world conditions.

This ultimate goal of this study is to provide the first experimental tests of oil shale oxyfuel combustion in a 60 kWth CFB pilot facility under multiple O₂/CO₂ combustion environments and high inlet O₂% with the application of recycled flue gas (RFG).

The first research objective was to focus on the effects of oxyfuel on the combustion of organic matter and reactions of mineral matter and compare them with air-based combustion. More precisely, this study aimed to answer the following questions **[Paper I]**:

- How does the transition from air to oxyfuel combustion under O₂/CO₂ and O₂/RFG with extremely high inlet O₂% affect heat distribution and the combustion process of particles?
- What will be the mineral matter behaviour under elevated CO₂ partial pressure?

What is the chemical and mineral characterisation of oil shale ash under oxyfuel regimes for further ash handling and utilisation?

The second research objective was to evaluate the emissions produced under different O_2/CO_2 and O_2/RFG regimes by understanding the following phenomena [Papers II and III]:

- NO_x and N_2O formation pathways for oil shale oxyfuel CFB combustion and control measures.
- Direct and indirect sulfation behaviour and sulfur capture efficiency.
- Specific carbon emission, and the extent of carbonate decomposition on the total CO_2 reduction

The third research objective was to maximise the CO_2 capture process through the partial replacement of oil shale with biomass for negative CO_2 emissions, the theoretical study was conducted using TG–MS analysis under air and different oxy-like conditions. This study addressed the following questions [Paper IV]:

- What is the effect of the oil shale biomass ratio on combustion characteristics and evolved emissions?
- What are the synergistic effects of different fuel ratios under several combustion regimes and heating rates?
- What is the kinetics of oil shale, biomass, and their blends under different oxy-conditions?

The fourth research objective was to integrate oxyfuel combustion into the shale oil industry for the first time by implementing the following items [Paper V]:

- Use of extremely low-heating-value waste (semicoke) in the oxyfuel combustion process.
- Performing pilot scale combustion process successfully under different regimes.
- Evaluation of mineral matter behaviour and the main pollutant emissions.

Ultimately, and for future consideration, the objectives were extended to include a literature review investigating recent oxygen production technologies and the most efficient technology with the lowest energy penalty [Paper VI].

Consequently, this thesis classifies the removal of atmospheric CO_2 produced by the oil shale industry employing the oxyfuel process among other competitive technologies. A process evaluation was achieved through an extensive experimental investigation of an oxyfuel combustion series in a 60 kWth pilot facility utilising oil shale fuel.

The novelty of the present research is based on a detailed experimental investigation, which served as a technical reference model for the industrial application of oxyfuel combustion technology in oil shale power plants for the first time.

The primary focus of this dissertation was the characterisation of the ash produced by the oxyfuel combustion of oil shale. The chemical and mineral compositions of the produced ash were comprehensively investigated, with particular emphasis on Ca-Mg silicates, clay minerals, free lime, and anhydrite. These compounds have significant implications for the potential utilisation routes of ash and for understanding their formation mechanisms under a broader range of oxyfuel conditions. These are expected to facilitate appropriate strategies for ash management and utilisation.

To the best of our knowledge, this study is the first to report NO_x and N_2O emissions during oil shale combustion under O_2/CO_2 and O_2/RFG environments under the influence of various factors, including the effects of different combustion atmospheres, excess oxygen volumetric ratios in the primary oxidiser, and dense bed temperatures on total

NO_x and N₂O formation. The identification of these optimal operating conditions during oil shale oxyfuel CFB combustion can aid in lowering the cost of CO₂ impurity removal.

The co-combustion study of oil shale and spruce biomass illustrates a novelty in the research on the synergistic effects of oil shale and biomass under air and oxyfuel combustion for different fuel ratios and multiple combustion heating rates.

In the course of providing the first experimental study on the potential transition to cleaner and more sustainable energy generation in the shale oil industry, the novelty of the research work was reiterated by understanding the semicoke oxy-combustion behaviour, temperature control and distribution along the riser, evolved emissions, and carbonate decomposition.

Research Methodology

The methodology employed in this thesis was based on earlier research questions and objectives as follows:

Experimental tests at the 60 kWth CFB pilot facility:

- A comprehensive literature review was conducted to understand coal and oil shale CFB and oxyfuel combustion processes. The literature was divided based on solid fuel, experiment scale, combustion regime, addressed related issues (ash, particle distribution, NO_x, N₂O, SO_x, oxy-combustion process, etc.), and the primary study findings were defined.
- Data analysis began by identifying the steady-state regime under each combustion experiment, filtering the data, collecting main process measurements, analysing solid and ash samples, collecting emission measurement data, and heat and mass calculations. The interpretation of the results was mainly based on an in-depth understanding and evaluation of the obtained outcome and research correlation with other literature that helped validate the results and provide context for understanding the significance of the findings.

Instrumental tests using TG-MS

- The co-combustion of oil shale and biomass tests were established based on a thorough literature review that filled the critical gaps required to conduct this research. The co-combustion ratios, heating rates, and combustion atmospheres were defined based on the literature. Following the experiments, the characteristics of co-combustion were identified with the evolved emissions at different heating rates, and theoretical and experimental results were calculated to identify the synergistic effects. Finally, the kinetic parameters were calculated and verified by employing multiple methods using free code available in the literature.

Research contribution and dissemination

The contributions presented in this thesis comprised three main parts:

1. **Technical feasibility of oil shale oxyfuel combustion process:** This section evaluates the viability of implementing oxyfuel combustion technology in oil shale industrial power plants. This study investigated the compatibility of oil shale with oxyfuel combustion, assessed the performance under extremely high inlet O₂%

with flue gas recirculation, analysed solid fuel combustion and ash formation, evaluated emissions and with total CO₂ in the flue gas stream (CO₂ purity), and addressed nitrogen oxide process control mechanisms. These findings contribute to the understanding of the technical feasibility and potential hurdles of adopting oxyfuel combustion for oil shale power generation. By advancing the understanding and implementation of oxyfuel combustion technology in the oil shale industry, Estonia can potentially reduce its carbon footprint while sustainably meeting its energy needs. Moreover, this study may contribute to the broader adoption of oxyfuel combustion as a cleaner alternative for power generation in other regions with similar energy-resource profiles.

2. **Application of oxyfuel combustion in shale oil industry:** This section explores the utilisation of oxyfuel combustion technology using semicoke, a substantially harmful organic waste with extremely low heating value. The combustion characteristics, performance, and emission profiles of semicoke under oxyfuel combustion conditions were investigated. By extending oxyfuel combustion to semicoke, this thesis expanded the understanding of its applicability to a wider range of solid waste utilisation and provided insights into the potential integration of the oxyfuel combustion process in the shale oil industry.
3. **Partial replacement of oil shale oxyfuel combustion with biomass for negative CO₂ emissions:** This section explores the synergistic effects of combining biomass with oil shale in oxyfuel combustion and assesses the technical potential for negative CO₂ emissions. By proposing theoretical guidelines for reducing CO₂ emissions in oil shale power generation, this study advanced sustainable energy practices in the oil shale industry.

Research Outline

This thesis 'Oil Shale Oxyfuel CFB Combustion' is the culmination of the author's research conducted at the Energy Technology Department at Tallinn University of Technology. The remainder of this paper is structured as follows.

Chapter 1 offers a literature overview describing the theoretical fundamentals, whereas the primary sections of the literature reflect the core tasks conducted in this thesis. This includes basic capture principles, oxyfuel combustion, nature of solid fuel combustion, ash behaviour [Papers I, V], and primary emissions generated from solid fuel combustion [Papers II–III and V]. Further, recent oxygen production technologies are discussed [Paper VI]. Thereafter, the bio-CCU process allowed negative CO₂ emissions [Paper IV].

Chapter 2 presents the fuels used in the experimental tests: oil shale [Papers I–IV], biomass [Paper IV], semicoke [Paper V], the experimental setup for pilot-scale tests in the 60 kWth facility [Papers I–III and V], and the experimental method for the instrumental test using TG–MS [Paper IV].

Chapter 3 includes the results and discussion of a series of experimental test operations on a 60 kWth scale. It focuses on the primary outcomes of the air and oxy-combustion process approach at steady-state operation utilising oil shale and semicoke, the analyses of ash samples from different separation ports, and flue gas measurements [Papers I–III, V].

The TG–MS experimental results indicated the primary co-combustion characteristics of oil shale and biomass, and the focus was drawn towards the synergistic effects and the main generated emissions [**Paper IV**].

Chapter 4 concludes the results of the research and presents suggestions for future work.

Abbreviations

| | |
|--------------------|---|
| ASU | Air separation unit |
| BA | Bottom ash |
| C1 | Cooler 1 |
| C2 | Cooler 2 |
| CCUS | Carbon capture utilization and storage |
| CCS | Carbon capture and storage |
| CFB | Circulating fluidized bed |
| CPU | CO ₂ compression and purification unit |
| ECD | Extent of carbonate decomposition |
| EHE | External heat exchanger |
| FTIR | Fourier transform infrared |
| GHG | Greenhouse gas |
| LOI | Loss of ignition |
| LHV | Net heating value |
| MS | Mass spectrometer |
| OPTs | Oxygen production technologies |
| PC | Pulverized combustion |
| PSD | Particle size distribution |
| RFG | Recycled flue gas |
| SHC | Solid heat carrier |
| SSA | Specific surface area |
| XRD | X-ray diffraction |
| XRF | X-ray fluorescence |
| TG | Thermogravimetric analysis |
| T _{DB} | Temperature of dense bed |
| T _{EHE} | Temperature of external heat exchanger |
| T _{Riser} | Maximum riser temperature |

1 LITERATURE REVIEW

1.1 CO₂ Capture Technologies

Carbon capture technologies can be broadly categorised into three main processes based on the stage at which CO₂ is captured: upstream, downstream, and fuel combustion. Therefore, a particular process is classified as a pre-combustion, post-combustion, or oxy-combustion technology [31], [32]. Figures 1–3 show the three approaches for CO₂ capture applied to the delivery of heat and/or power.

1.1.1 Pre-combustion

The precombustion process involves the capture of CO₂ upstream of the combustion process. In the case of solid fuel, the first step includes the gasification of the fuel to produce syngas containing primarily H₂, CO, and CO₂. For gaseous fuels, syngas is produced through reforming. Thereafter, the syngas undergoes several cleaning and CO₂ separation steps to achieve an almost pure H₂-stream that is subsequently oxidised in a dedicated gas turbine. A simplified diagram of this process is shown in Figure 1. An example of a pre-combustion approach is the integrated gasification combined cycle (IGCC) with CO₂ capture [33], [34].

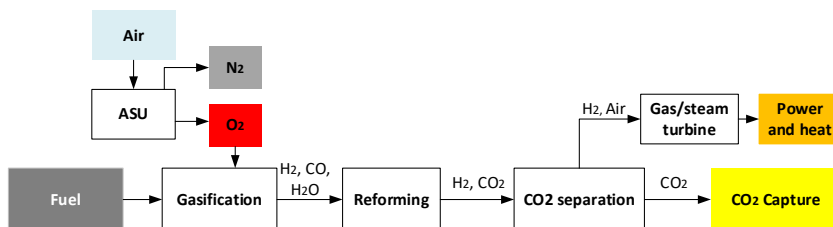


Figure 1. Pre-combustion capture process.

1.1.2 Post-Combustion

The post-combustion approach involves capturing CO₂ downstream of the combustion process. Post-combustion CO₂ capture processes are characterised by their ability to retrofit existing emission sources such as power and industrial plants. Flue gas comes from the combustion of fossil fuels and air, and is used for heat and power production, Figure 2. The flue gas flows into a downstream capture plant, where CO₂ is separated from the flue gas stream. The separated CO₂ can then be processed, stored, or utilised, depending on the application.

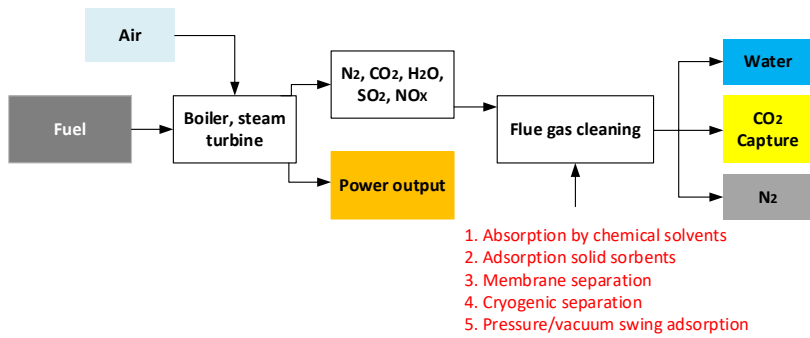


Figure 2. Post-combustion capture process.

Processes for post-combustion CO₂ capture are based on chemical or physical absorption. Chemical absorption by aqueous monoethanolamine (MEA) solvents has already been employed on a large-scale [35], [36]. Other processes include the chilled ammonia process [37], [38] and CO₂ capture using membranes [39], [40]. The calcium looping process is also categorised as a post-combustion CO₂ capture process [41].

1.1.3 Oxyfuel Combustion

Oxyfuel combustion refers to fuel oxidation in the absence of air-nitrogen. CO₂ concentrations exceeding 90% can be achieved using a mixture of pure oxygen and recycled flue gas (RFG) as the reactants for fuel combustion [4]–[7]. The oxygen used in oxyfuel combustion is separated from the air, whereas CO₂ is separated from the exhaust gas, which consists primarily of CO₂ and water vapour, by lowering the temperature and cooling the flue gas such that the vapour condenses, as shown in Figure 3. Oxyfuel combustion is a promising option for use in CFB boilers. Oxyfuel combustion ensures a high concentration of CO₂ in the flue gas, rendering carbon capture more economical than in conventional plants [42].

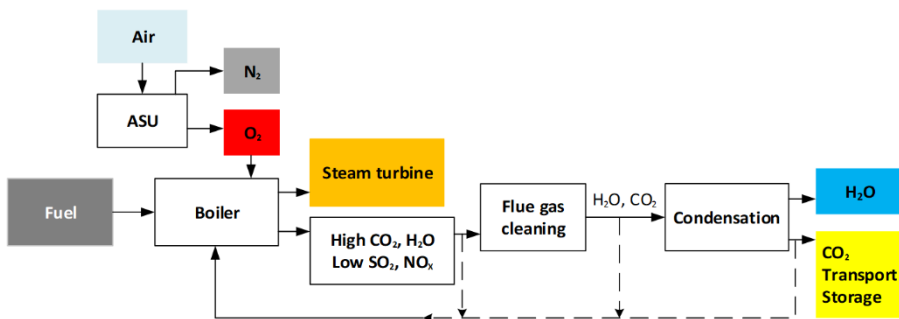


Figure 3. Oxyfuel combustion process [from paper 1]

Currently, oxyfuel combustion has a TRL > 7 [43], [44], with particular advantages, such as good environmental performance and fuel flexibility. Combustion with pure oxygen generates very high temperatures and facilitates the possibility of addition of an external heat exchanger to a solid recirculation system to control the combustion

temperatures [45]. Oxyfuel combustion with RFG can be retrofitted into existing conventional coal-or natural gas-fired power facilities [4] or implemented using a smaller boiler design. By increasing the oxygen concentration, the volume of gases flowing through the furnace was significantly reduced, thereby reducing the combustor size and capital expenses [46]. However, a primary drawback of oxyfuel combustion is the energy requirements of the air separation unit (ASU) and the cost of O₂ production, which reduces the total efficiency of the power plant [7]. The production of O₂ exceeding 95% purity is considered the primary challenge for this technology, followed by energy demands of the CO₂ compression and purification unit (CPU).

Variations in oxyfuel combustion arise from the different methods used to provide oxygen. In the most mature oxyfuel combustion process layout, oxygen in the oxidation agent is provided directly by an onsite cryogenic ASU [4], [47].

Alternative methods for supplying oxygen, such as chemical looping, are currently under investigation to mitigate the efficiency drawbacks associated with operating an ASU. In this approach, a solid oxygen carrier circulates between air and fuel reactors. Within the fuel reactor, the oxygen carrier released oxygen during fuel combustion. Subsequently, it is transferred to an air reactor, where the oxygen carrier undergoes oxidation again [48], [49].

1.2 Solid Fuel Oxy-Combustion

Oxyfuel gas turbines, with specifically designed oxyfuel burners, are used in industrial combustion processes [50]. In these industries, this technology aims to improve productivity, decrease energy consumption, and reduce NO_x emissions. However, the combustion of solid fuels is considerably more challenging. When a fuel particle is delivered to a CFB combustor, it undergoes several stages, including heating and drying, devolatilisation, volatile combustion, and char combustion.

In oxyfuel conditions, the environment wherein the fuel burns differs from that of air combustion owing to the replacement of air nitrogen with RFG and higher O₂ concentration. This affects the rate of combustion, combustion of organic matter, reactions of mineral matter, heat transfer, boiler hydrodynamics, and the behaviour of ash (i.e., CaCO₃-CaO decomposition ratios [4]). These differences are primarily caused by the dissimilar properties of CO₂ and N₂, which are the primary diluting gases in the furnace during oxyfuel and air combustion, respectively. For example, the molecular weight of CO₂ (44 g/mol) is higher than that of N₂ (28 g/mol); consequently, the density of CO₂ is higher. In addition, CO₂ exhibits a higher heat capacity compared to N₂ and possesses a lower O₂ diffusivity than N₂; consequently, an elevated O₂ concentration in the combustion atmosphere is required to maintain the same combustion characteristics as in air firing.

When compared with air combustion in CFB, the emission levels from oxyfuel combustion were found to be different. According to the pilot tests performed by Jia et al. [51], NO_x emissions were reduced.

The findings related to sulfur capture are variable. In oxyfuel combustion, the capture of SO₂ does not always proceed as in the case of conventional combustion [52], [53]. SO₂ capture may occur via direct sulfation; that is, CaCO₃ reacts directly with SO₂ [51]. The phenomena of hindered calcination and SO₂ capture efficiency in oxy-combustion has been studied by CanmetENERGY with 0.1 and 0.8 MWth CFB pilots [51], [54].

In an oxyfuel CFB boiler, limestone reactions do not proceed as in the case of conventional combustion. The partial pressure of CO₂ is high during oxyfuel combustion,

indicating that limestone calcination may be hindered [55]. In addition, if CaO particles are present in a boiler, under certain conditions, they re-carbonate to CaCO₃, which is normally an unwanted reaction in a CFB boiler.

Table 1 provides a concise summary of thesis core literature of key experimental studies investigating oxyfuel combustion using coal as a solid fuel.

Table 1. Literature studies on coal oxyfuel combustion experimental tests.

| Author | Fuel | Type | Size [MWth] | O ₂ % | Ca/S | Fuel particle size (mm) |
|--------------------------|----------------------------|---------|-------------|------------------|-------|-------------------------|
| Czakiert T. [56] | Brown coal | Oxy-CFB | Lab scale | 21-60 | - | - |
| L. Jia [57] | Bit Coal | Oxy-CFB | Lab scale | 28-30 | - | < 5 |
| K. Myöhänen [58] | Bit Coal | Oxy-CFB | 0.047-0.09 | 21-39 | 1-2.4 | - |
| L. Jia [51] | Petcoke, Bit Coal | Oxy-CFB | 0.1 | 44-60 | 2.3 | 4, 6 |
| Czakiert T. [59], [60] | Bit Coal | Oxy-CFB | 0.1 | 21-35 | - | - |
| Wu Y. [55] | Bit Coal, Coal, Petcoke | Oxy-CFB | 0.1 | 28-30 | 2-3 | - |
| Duan L. [52], [61]–[63] | Bit Coal | Oxy-CFB | 0.05 | 21-40 | 2-3 | < 6 |
| Y. Tan [64] | Petcoke, Bit Coal | Oxy-CFB | 0.8 | 23 | 3.0 | < 6 |
| L. Jia [54] | Pine bend coke, Anthracite | Oxy-CFB | 0.8 | 29 | 1-3 | - |
| De las Obras. [53], [65] | Anthracite | Oxy-BFB | 0.003 | 27-45 | 3.0 | 0.2-1.2 |
| De Diego [66], [67] | Anthracite Lignite | Oxy-BFB | 0.003 | 27-35 | 0-3 | 0.2–1.2 |
| Lupiáñez C. [68], [69] | Anthracite and lignite | Oxy-BFB | 0.9 | 28-45 | - | 0.7–1.2 |
| Lupion M. [70] | Coal | Oxy-CFB | 30 | 21 | - | - |
| M. Gómez [71] | Anthracite | Oxy-CFB | 30 | 25 | 2.5,4 | < 6 |
| Pikkarainen T. [72] | Bit coal | Oxy-CFB | 0.1 | 28-42 | 4 | 0.5-4 |
| Haoyu Li [73] | Coal | Oxy-CFB | 1 | 50 | - | 1-8 |
| Hofbauer G. [74] | Bit Coal | Oxy-CFB | 0.15 | 22-36 | - | - |
| Bithi Roy [75] | Brown coal | Oxy-CFB | Bench scale | 30-40 | - | 0.106-0.152 |
| Li Tan [76] | Coal | Oxy-CFB | 0.1 | 50 | 2.5 | 0-4 |
| Shiyuan Li [77], [78] | Coal | Oxy-CFB | 1 | 30-50 | - | - |
| Wei Li [79]–[81] | Coal | Oxy-CFB | 0.05-1 | 21-50 | 2.5-4 | 0.1-1 |
| Ji-Hong Moon [82] | Sub-bit coal, lignite | Oxy-CFB | 0.1 | 24 | - | < 10 |

Oil shale fuel combustion differs from conventional fuel owing to the use of oil shale. Moreover, no additional sorbent material is required for feeding to the CFB boiler to facilitate SO₂ capture because carbonate minerals act as sorbents for controlling SO₂ emissions. During the combustion of oil shale, the decomposition of carbonate minerals may negatively affect the amount of heat released because the evolution of mineral CO₂ is accompanied by an endothermic effect, amount of ash produced, and amount of CO₂ emitted. The share of CO₂ emissions from the mineral portion of the fuel is dependent on the content of mineral CO₂, the fuel, and the extent of carbonate mineral decomposition during the processes occurring in the combustor [83].

The ash content of Estonian oil shale can reach up to 50% without considering the amount of CO₂ present in the ash. Further, it can reach up to 70% if 100% of CO₂ remains in the ash; consequently, a large amount of solid waste is produced upon combustion.

Table 2 lists the main oil shale and semicoke combustion test studies under air and oxyfuel regimes. Air combustion is presented here and used in the research as the baseline. However, literature on oil shale oxyfuel combustion is very limited, as indicated in Table 2, and conducting original research in this area will fill important knowledge gaps and contribute to the advancement of the field.

Table 2. Literature study on oil shale combustion experimental tests.

| Author | Fuel | Type | Size [MWth] | Air/O ₂ % | Ca/S | Fuel particle size (mm) |
|---------------------------|-------------------|---------|-------------|----------------------|------|-------------------------|
| Neshumayev D. [84] | Oil shale-Estonia | CFB | 250 | Air | 8-10 | 0-15 |
| Konist A. [26] | Oil shale-Estonia | Oxy-FB | Bench scale | 21% | 8 | < 3 |
| Loo L. [29] | Oil shale-Estonia | Oxy-CFB | 0.06 | Air, 21%, 30% | 8 | < 3 |
| Khraisha Y. [85] | Oil shale-Jordan | FB | Bench scale | Air | – | 0.85-6 |
| Al-Makhadmeh L. [86]–[88] | Oil shale-Jordan | Oxy-CFB | 0.02 | Air, 27%, 35% | 0-3 | 0.035 |
| J. Xiumin [89] | Oil shale-China | CFB | Bench scale | Air | 4-8 | 0-1.2 |
| Trikkel A. [90] | Semicoke-Estonia | CFB | 0.05 | Air | – | 0-5 |
| Yu Yang [91] | Semicoke-China | BFB | Pilot scale | Air | – | < 3 |

1.2.1 Ash Behaviour

Burning of solid fuel in boilers in thermal power plants for energy use yields a residue called ash. The ash behaviour from the combustion of solid fuels such as coal, oil shale, and even low ash content in biomass must be studied for a better understanding of the combustion process and ash disposal issues. Coal oxyfuel combustion ash has been investigated in several studies [55], [77], [80], [92], [93]. It has been reported that oxyfuel combustion under an O₂/CO₂ atmosphere does not significantly change the types of minerals produced in particles. However, it affects the relative content of these minerals [77], [94]. Oxyfuel combustion can also affect the distribution of fine submicron particles [95]. Wider particle size distributions (PSDs) of fly ash were observed under 30% O₂/70% CO₂ with an elevated concentration of fine particles [96].

Oil shale combustion produces large amounts of solid waste. The influence of fluidised bed oxyfuel combustion on the formation of oil shale ash is very limited [26], [29], [30], [87]. From the perspective of power generation, the produced ash is a waste material because it has been considered hazardous waste for a long time and is mainly landfilled [97], which will soon become excessively costly. Recently, oil shale ash was removed from the list of hazardous substances, opening more opportunities for ash reuse [98].

The thermal decomposition of dolomite should be considered during the combustion of oil shale. The calculation methodology for the extent of carbonate decomposition ECD (k_{CO_2}), has been described thoroughly by Arro et al. [83].

The utilisation of solid waste from oil shale processing is difficult, and ash valorisation remains one of the most contentious issues in Estonia's energy sector. The oil shale industry accounts for more than 70% of the Estonian energy sector and approximately 40% of planned oil shale is consumed by direct combustion in thermal power plants.

The recovery of ash is extremely limited, and in the current economic situation, approximately 2% of the generated ash is only recovered [19].

1.2.2 Emissions of Nitrogen Oxides

Nitrogen oxides from fossil fuel combustion yields mainly of nitric oxide (NO), nitrogen dioxide (NO₂), and nitrous oxide (N₂O). NO_x is a generic term for nitrogen oxides (NO and NO₂), which are considered very toxic at high concentrations, are responsible for acid rain, and participate in the formation of photochemical smog [99]. Nitrous oxide (N₂O) is a greenhouse gas and the primary contributor to stratospheric ozone layer depletion [100].

In combustion processes, nitrogen oxides (NO_x) are formed by the partial oxidation of fuel-N entering the combustor and/or by the oxidant (mainly air) used for combustion. The formation of nitrogen oxides can occur primarily by three mechanisms [101] (Figure 4): (1) Thermal-NO_x, which forms because of the direct oxidation reaction between atmospheric nitrogen and oxygen; (2) Prompt-NO_x, which forms owing to the reactions between atmospheric nitrogen and hydrocarbon radicals from the fuel; and (3) Fuel-NO_x, which forms because of the oxidation of the nitrogen present in the organic matter of the fuel. The thermal and prompt nitrogen oxides mainly occur at combustion temperatures exceeding 1,100 °C, which is inherent in the fossil fuel pulverised combustion technology.

In CFB combustion technology, the operating temperatures are typically in the range of 800–900 °C, and the formation of nitrogen oxides is mainly attributable to the fuel nitrogen conversion [68]. In solid-fuel combustion, the formation of nitrogen oxides from fuel N results in a relatively large number of homogeneous and heterogeneous complex reactions, as shown in Figure 4 [102].

The formation of NO_x is not only determined by the nitrogen content of the fuel or the phase; it is also a function of multiple factors, such as the volatility of the nitrogen present in the fuel, excess air, air staging, residence time, fixed carbon in the bed, and the presence of S adsorbent catalysts [59], [68], [103]–[105]. Nitrogen oxides are reduced from volatile N and char-N through a homogeneous reaction with CO and H₂, and a heterogeneous reaction with soot, char, and adsorbent additives. Under these conditions, the formation of N₂O from the CFB system has been significant, primarily because of the oxidation of HCN in the gas phase, with a lower contribution from char-N oxidation [106]. Several studies have shown that oxyfuels inhibit NO_x formation [107]–[109]. Oxyfuel combustion has a positive effect on N₂O emissions, which are higher than those from air combustion [77], [110]. However, these emissions were reduced at higher inlet O₂% [110]–[112].

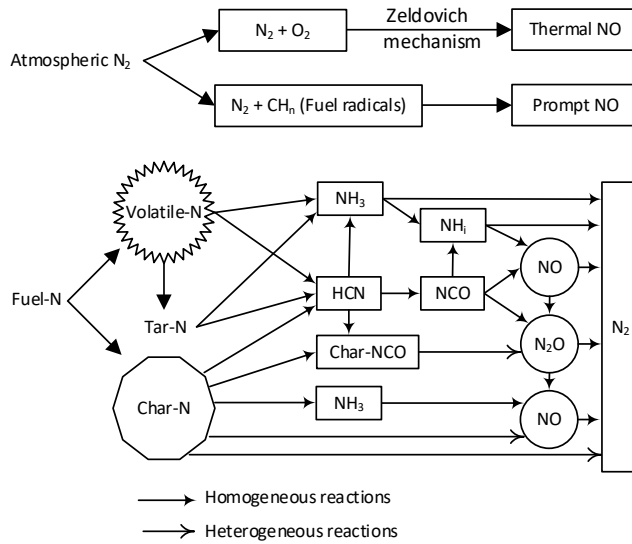


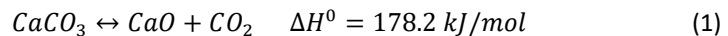
Figure 4. Pathways of nitrogen oxide formation at pulverized and CFB combustions [from paper II]

1.2.3 Emissions of Sulfur Oxides

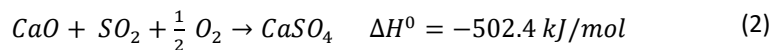
In CFB, the combustion process occurs largely in an excess of oxygen (excess air factor >1). Consequently, combustible sulfur compounds are practically completely oxidised to sulfur dioxide (SO_2). The transformation of sulfur compounds during combustion involves a complex series of reactions wherein different gaseous components simultaneously participate: SO_2 , H_2S , COS , CS_2 , O_2 , CO , H_2 , H_2O , and CO_2 [113]. In the presence of a sufficient concentration of oxygen (greater than the stoichiometric amount), the sulfur compounds formed are completely oxidised to SO_2 .

Combustion in a CFB boiler offers an additional advantage; that is, sulfur can be captured inside the combustor using a calcium-based sorbent (limestone). In oxyfuel combustion, the environment wherein the fuel burns differs from that in air combustion owing to the replacement of air-nitrogen with O_2/CO_2 or O_2/RFG . The control of SO_2 emissions is achieved because SO_2 is captured through both indirect and direct sulfation routes, which differ from conventional air combustion [114].

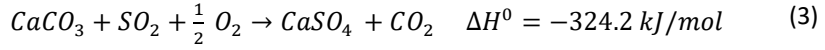
In the air-firing environment, the CFB combustor, in most cases, operates in the region below the equilibrium curve wherein limestone calcination occurs. Owing to the furnace temperature being higher than the decomposition temperature of calcite (CaCO_3), calcite dissociation occurs.



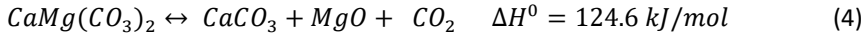
Following dissociation, indirect sulfation occurred in the CFB combustor as the limestone (CaO) reacted with sulfur dioxide (SO_2):



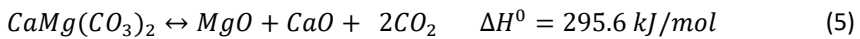
The rate of indirect sulfation can be slow or fast depending on many factors [115]. In oxyfuel combustion mode, the CFB combustor operates in the region above the CaCO_3 - CaO equilibrium curve at temperatures of 800–900 °C, hence, direct sulfation occurs:



The CFB combustor temperature and CO_2 partial pressure primarily determine direct and indirect sulfation routes [116]. It is generally believed that under oxyfuel combustion, owing to the relatively high CO_2 partial pressure, the binding of SO_2 to calcite occurs mainly via a direct reaction [4], [63]. The degree of limestone sulfation is controlled by chemical reactions and solid-state diffusion [117], and the rate of limestone sulfation decreases rapidly during the reaction process. This is because the molar volume of CaSO_4 is considerably higher than that of CaO . Thus, the small pores in CaO are plugged by a layer of CaSO_4 [118], necessitating the addition of a stoichiometric sorbent to remove sufficient SO_2 . This eventually increases solid waste generation. In general, sulfur conversion ratios exceeding 85% are achieved regardless of the combustion atmosphere; however, with oxyfuel combustion, higher conversion ratios have been reported owing to SO_2 recirculation with RFG. Moreover, the accumulated recycled SO_2 in the combustor enhances sulfur capture efficiency [59]. Notably, in case of oil shale combustion, the thermal decomposition of dolomite should also be considered for sulfur capture. The sequence of reactions of dolomite decomposition under equilibrium conditions are follow Eqs (4 and 1) [119]:



Other studies have reported that at CO_2 partial pressures below (20 kPa), dolomite decomposition into CaO and MgO is observed to occur via a single-stage reaction [120] [121]:



1.3 Oxygen Production Technologies (OPTs)

The mini-review section presented in [Paper VI] discusses the most widely used technologies for oxygen production. These technologies are divided based on conventional oxygen production: cryogenic distillation and pressure swing adsorption, and novel technologies: membranes, chemical looping, air separation, and electrochemical water-splitting technologies (Figure 5).

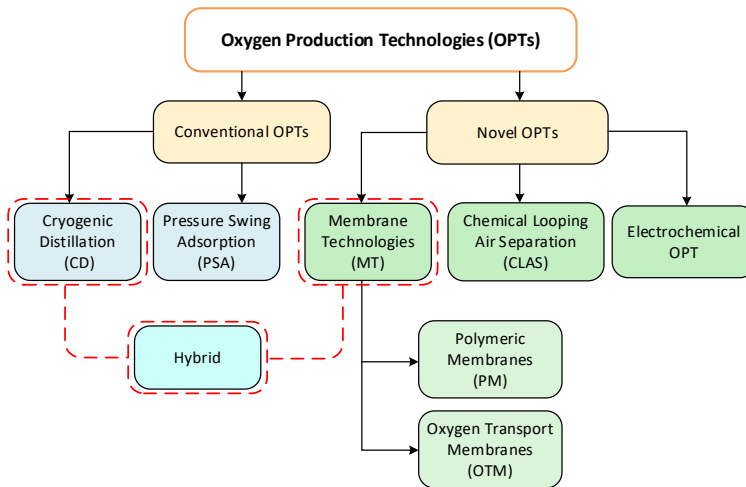


Figure 5. Main oxygen production technologies for oxyfuel combustion process [from paper VI]

An example of these technologies is the cryogenic ASU which is among the most developed technologies [122] and the most feasible method for the high-volume oxygen production required for the oxyfuel combustion process [7]. For instance, a 500 MWe coal-fired oxy-combustion power plant requires 9000–10,000 tO₂/d [123], [124]. The power consumption of the ASU unit to produce O₂ with 95% purity varies between 184 and 260 kWh/tO₂ [123], [125], [126]. For a small unit using vacuum pressure–temperature swing adsorption technology is 500–888 kWh/tO₂ [127], [128]. With oxygen transport membranes, the conventional process normally has an associated consumption of 201.38 kWh/tO₂ [129], whereas the literature estimates a decrease in power consumption ranging between 85–362 kWh/tO₂ [130].

Another example is the integration of membrane and cryogenic technologies which has recently attracted attention for further power reduction [131], [132]. It was demonstrated that a cryogenic ASU reduced power usage for 99.8% oxygen purity to 179 kWh/tO₂ [50]. In addition, the hybrid membrane cryogenic oxygen separation method exhibits a 1.1% higher net efficiency than the conventional cryogenic ASU [126].

Oxyfuel combustion requires reliable and efficient technology for oxygen production. The most feasible technology for oxygen production is dependent on several factors such as energy efficiency, scalability, cost-effectiveness, and compatibility with oxyfuel combustion systems. Apart from the cryogenic process, there are a few other promising technologies, such as chemical looping air separation and renewable base air separation.

1.4 Negative CO₂ Emissions

The removal of atmospheric CO₂ is feasible through the implementation of negative-emission technologies. Bioenergy with CCS (bio-CCS) and direct air-capture systems are the technical approaches. Bio-CCS involves the utilisation of bioenergy in a power or industrial plant combined with a CCS system [133]. Figure 6 shows a carbon balance comparison for different energy systems, which generally results in net negative emissions; whereas, fossil-CCSs usually result in near-zero emissions at best [134], [135].

The partial replacement of fossil fuels and the reduction of CO₂ emissions through the co-combustion of carbon-neutral fuels, such as biomass have garnered significant attention. The need for more aggressive action to combat climate change has become evident, as we are no longer on track to achieve the necessary 1.5-degree reduction in global temperatures. Instead, there is a growing urgency for negative carbon capture technologies. In the case of biomass co-combustion with different fuels under oxyfuel conditions, if the CO₂ produced is captured, the resulting emissions from the combustion can be considered negative carbon emissions, as explained earlier.

Recently there have been multiple studies on the co-firing of biomass and coal under oxy conditions [136]–[139]. The primary findings were a synergistic effect in the devolatilisation region during oxyfuel co-combustion and an improvement in the combustion conditions depending on the biomass-to-coal blend ratio.

The application of co-utilisation has also been extended to the use of unconventional fuels such as oil shale. Oil shale contains higher quantities of minerals than biomass, which contains only a small percentage of ash. Consequently, the combustion performance of the OS can be greatly improved to maximise the process efficiency. Several studies have investigated the interaction between OS and biomass for better design and operation of combustion facilities [15]–[17], [140], [141]. In [16], the ignition temperatures decreased towards lower temperatures. The results of biomass and oil shale co-combustion in a CFB test facility have shown that 15% of biomass thermal contribution reduces CO₂ emissions by 14.6% and ash formation by 16% compared to conventional oil shale CFB combustion [15].

Studies on the oxyfuel co-combustion of oil shale and biomass are scarce [24], [28], and further in-depth theoretical and experimental studies are required. As motivation of the research presented in [Paper IV], in a previous study [21] it was found that based on the biomass share of the fuel blend, the negative CO₂ emission can be as low as -40% (an average of -0.7 Mt CO₂/y) of the initial level when the biomass is at 50% of the fuel blend under oxyfuel CFB combustion.

There is a knowledge gap around biomass fuels, which vary widely in composition and sulphur and nitrogen contents, which can render oxyfuel utilisation of these fuels with an unconventional fuel such as oil shale more challenging. Moreover, there is a critical need to study the fundamental mechanisms associated with the oxyfuel co-combustion of oil shale and biomass. Further research is required to improve the blending and cofiring of fuel mixtures and to reduce emissions and solid waste in the oil shale industry.

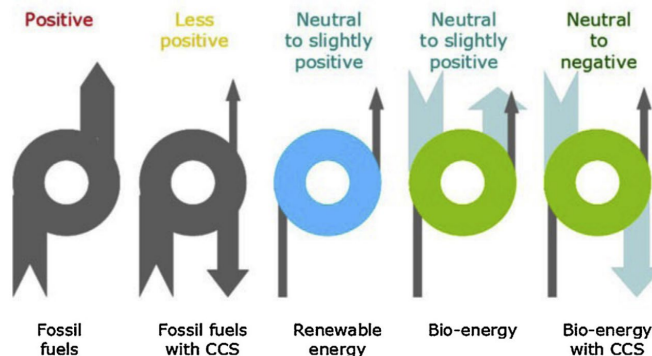


Figure 6. Carbon balance for different energy systems. ([135], adapted from *ecofriendlymag.com*; grey denotes carbon of fossil origin, blue denotes carbon of biogenic origin).

2 EXPERIMENTAL METHODS

This dissertation was based on five studies. The fuel used, experimental work, and calculation methodologies are described in detail in these papers; however, an overview of the materials, experimental devices, and methods applied is provided here.

The first section includes a short description of the materials used for Estonian oil shale [Papers I–III], biomass [Paper IV], and semicoke [Paper V]. This was followed by oxyfuel experimental tests conducted using the CFB pilot facility [Papers I–III and V] and research on oxyfuel co-combustion of oil shale and biomass using a thermogravimetric analyser coupled with a mass spectrometer TG-MS [Paper IV].

2.1 Materials

2.1.1 Oil Shale

Estonian oil shale is a low-grade Ca-rich fuel with high volatile organic compound and ash content, primarily carbonate minerals [9], [10]. Energy-rich sedimentary rocks can be burned for heat and power generation or used to produce liquid fuels [11]. Oil shale reserves in many regions exceed crude oil reserves [142], which is an important alternative to fossil fuels. Because oil shale contains higher quantities of minerals, the combustion performance can be greatly improved to maximise the process efficiency.

Estonia has a long history of using oil shale, and its energy supply is dominated by domestically produced oil shale, which provides the country a high degree of energy independence and high carbon intensity. The fuel used in this research was kukersite-type Estonian oil shale [143], which mainly comprises carbonates and sandy clay parts; therefore, the molar ratio of Ca/S in the fuel used was higher than 8. By using Ca-rich oil shale fuel, no additional sorbent material is required to be fed into the CFB boiler for SO₂ capture because carbonate minerals (calcite and dolomite greater than 60%) act as sorbents for controlling SO₂ emissions. However, the decomposition of carbonate minerals negatively affected the amount of CO₂ emitted. This implies that the application of oxyfuel combustion provides several advantages.

Kukersite-type oil shale samples, provided by the Viru Keemia Grupp, were used for the 60 kWth CFB pilot tests [Papers I–III and IV], and the fuel was sieved to pass through 3 mm openings. Table 3 presents the ultimate and proximate analyses of the oil shale fuel. Tables 4 and 5 list the chemical and mineralogical compositions of the mineral components of the oil shale, respectively. The oil shale PSD, shown in Figure 7, was determined using a laser scattering particle size distribution analyser LA-950 (HORIBA).

Table 3. Proximate and ultimate analysis of the oil shale [from paper I and IV]

| Fuel | Proximate analysis ^d (wt.%) | | | | | Ultimate analysis ^d (wt.%) | | | | | |
|-----------------|--|-------|-------|------|----------------|---------------------------------------|------|------|------|------|-------|
| | Moisture | Ash | V | FC | LHV (MJ/kg) | C | H | °O | N | S | Cl |
| OS ^b | 0.18 | 52.05 | 46.36 | 1.59 | 9.76 | 27.38 | 2.68 | 0.36 | 0.07 | 1.57 | 0.076 |

^aO% = 100-(W+A+CO₂+S+TOC+H+N) %

^bOS: Oil shale

Table 4. Chemical composition of the mineral part of the oil shale [from paper I and IV]

| Components | SiO ₂ | Al ₂ O ₃ | Fe ₂ O ₃ | CaO | MgO | Na ₂ O | K ₂ O | SO ₃ | LOI _{950 °C} |
|---------------|------------------|--------------------------------|--------------------------------|-------|-----|-------------------|------------------|-----------------|-----------------------|
| Content, wt.% | 15.39 | 3.64 | 2.03 | 22.52 | 3 | 0.09 | 1.6 | 3.91 | 47.12 |

LOI_{950 °C} = Loss of ignition at 950 °C

Table 5. Mineralogical composition of the mineral part of the oil shale [from paper I and IV]

| Components | Quartz SiO ₂ | K-feldspar KAlSi ₃ O ₈ | Calcite CaCO ₃ | Dolomite CaMg(CO ₃) ₂ | Chlorite ClO ₂ | Pyrite FeS ₂ | Illite |
|---------------|----------------------------|---|------------------------------|---|------------------------------|----------------------------|--------|
| Content, wt.% | 11.6 | 6.5 | 43.1 | 20.3 | 3.5 | 1.9 | 13 |

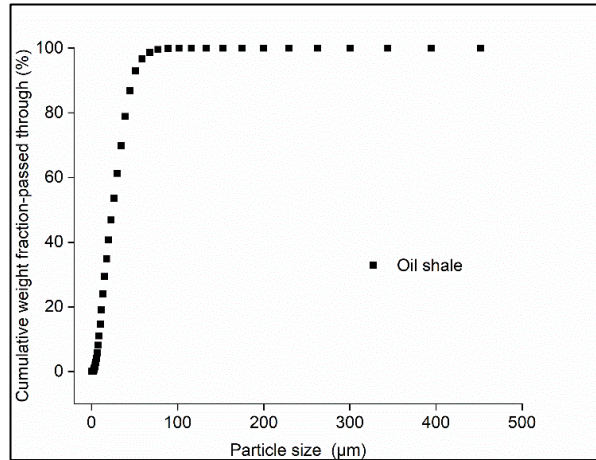


Figure 7. Particle size distribution of oil shale [from paper I]

2.1.2 Biomass

Biomass is a CO₂-neutral fuel that can be blended with different fossil fuels and burned in conventional power plants, resulting in CO₂ reduction [144]. The direct combustion of biomass as an individual fuel in boilers is plagued by several operational problems, including agglomeration, deposit formation, and corrosion, owing to its high alkali content, which can be avoided by co-combustion [15], [145].

Woody biomass comprises several complex high molecular weight compounds; the main components are hemicellulose, cellulose, and lignin, which decompose at the temperature range of 225–325 °C, 305–375 °C, and 250–500 °C, respectively [17], [146], [147]. In general, hemicellulose has a higher calorific value than other lignocellulose components [146].

In this study, common spruce biomass samples were mixed with oil shale for the TG–MS experiments [Paper IV]. Table 6 presents the proximate and ultimate analyses of the biomass used in this study. The oil shale ash and S contents were significantly higher than those in the biomass, whereas the moisture, volatiles (V), fixed carbon (FC), LHV, C, H, O, and N contents in the biomass were usually higher than those in the oil shale.

Table 6: Proximate and ultimate analysis of the spruce biomass [from paper IV]

| Fuel | Proximate analysis ^d (wt.%) | | | | LHV (MJ/kg) | Ultimate analysis ^d (wt.%) | | | | | |
|-----------------|--|------|-------|-------|----------------|---------------------------------------|------|----------------|-------|------------------|-------|
| | Moisture | Ash | V | FC | | C | H | ^a O | N | S | Cl |
| BM ^e | 6.00 | 0.27 | 84.67 | 15.06 | 20.21 | 50.04 | 6.35 | 37.24 | 0.103 | ^b n.d | 0.004 |

^aO% = 100-(W+A+CO₂+S+TOC+H+N) %

^bn.d: No detection

^eBM: Biomass

2.1.3 Semicoke

Semicoke is a solid organic residue formed during aboveground thermal shale oil production. Semicoke is a potentially harmful solid material whose properties are highly dependent on the thermal processing technology used [148]. One of its peculiar characteristics is its low energy content (low heating value of 1–4 MJ/kg). This value depends on the type of technology used, and generally limits the possibilities of its further efficient utilisation. Currently, there is no suitable and efficient utilisation of semicoke at the industrial level owing to various technical and non-technical obstacles. Therefore, its combustion for energy purposes to generate steam and electricity is considered a primary direction for its further processing. CFB are primarily used for semicoke combustion [91], [149], [150]. In the process of solid heat carrier (SHC) technology, semicoke is burned to generate a solid heat carrier, which is hot ash formed during the combustion of semicoke, which further serves as a source of energy for the pyrolysis of oil shale in retorts [151].

The proximate and ultimate analyses of a representative semicoke sample used in [Paper V] are summarised in Table 7. The chemical composition of the semicoke ash is presented in Table 8. It was prepared and tested using a Rigaku Primus II XRF spectrometer. Table 9 presents the semicoke quantitative X-ray diffraction (XRD) results. XRD experiments were performed using Cu K α radiation in the 2 θ range of 3–72° with a step size of 0.02° 2 θ and a counting time of 0.1 s/step. The X-ray tube operated at 40 kV and 40-mA.

Table 7. Proximate and ultimate analysis of the semicoke [from paper V]

| Fuel | Proximate analysis | | Ultimate analysis ^d (wt.%) | | | | | |
|-----------------|--------------------------|-------------|---------------------------------------|-------------|------|----------------|-------|------|
| | Ash ^a (wt. %) | LHV (MJ/kg) | C (total) | C (organic) | H | O ^b | N | S |
| SC ^c | 68.18 | < 1 | 10.81 | 2.90 | 0.24 | 18.49 | 0.035 | 2.24 |

^aAsh at 815 °C

^bO% = 100-(W+A+CO₂+S+TOC+H+N) %

^cSC: Semicoke

Table 8. Chemical composition of the semicoke [from paper V]

| Components | Content, wt.% |
|--------------------------------|---------------|
| SiO ₂ | 6.92 |
| Al ₂ O ₃ | 1.66 |
| Fe ₂ O ₃ | 2.48 |
| CaO | 45.1 |
| MgO | 3.58 |
| Na ₂ O | n.d. |
| K ₂ O | 0.51 |
| SO ₃ | 5.72 |
| P ₂ O ₅ | 0.13 |
| TiO ₂ | 0.101 |
| ZnO | 0.019 |
| SrO | 0.036 |

Table 9. Mineralogical composition of the semicoke [from paper V]

| Components | Content, wt.% |
|---|---------------|
| Quartz (SiO_2) | 4 |
| K-feldspar (KAlSi_3O_8) | 2.4 |
| K-mica ($\text{Al}_2\text{K}_2\text{O}_6\text{Si}$) | 0.4 |
| Calcite (CaCO_3) | 67.9 |
| Portlandite (Ca(OH)_2) | 1.8 |
| Dolomite ($\text{CaMg(CO}_3)_2$) | 1.2 |
| Periclase (MgO) | 3.8 |
| Anhydrite (CaSO_4) | 7.5 |
| Belite (C_2S) | 4.8 |
| Akermanite ($\text{Ca}_2\text{Mg(Si}_2\text{O}_7)$) | 3.9 |
| Merwinite ($\text{Ca}_3\text{Mg(SiO}_4)_2$) | 0.5 |
| Hematite (Fe_2O_3) | 1.4 |

2.2 Equipment and Methods

2.2.1 60 kWth Circulating Fluidized Bed (CFB) Pilot Facility

Oil shale, semicoke air, and oxyfuel combustion tests [Papers I–III and V] were conducted in a 60 kWth CFB pilot facility. A schematic of the pilot is shown in Figure 8, which comprised a furnace with a height of 4.90 m and an inner diameter of 0.12 m. A screw conveyor was used for fuel feeding at a height of 1.17 m, and the recirculated solids were fed back at a height of 1.5 m with secondary air. The CFB test facility can be operated using regular air, preset gas mixtures, or RFG. The combustion process was monitored at 16 points using thermal sensors, and the data controller of the test unit was fully automated using LabVIEW. The temperature measurement tap was located along the riser and heat exchanger.

The collected ash sample points are shown in Figure 8, and the bottom ash (BA), external heat exchanger (EHE), cooler 1 (C1), cooler 2 (C2), and filter ash (filter) are indicated.

The flue gas composition was measured simultaneously using a Fourier transform infrared (FTIR) analyser. The FTIR was located between coolers 1 and 2 for (CO_2 , O_2 , CO , H_2O , NO_x , N_2O , and SO_2) emission measurements.

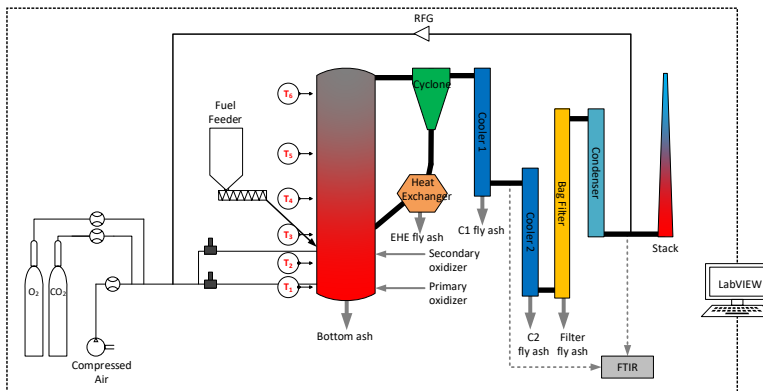


Figure 8. Circulating Fluidized Bed facility with 60 kWth capacity [from paper II]

The experiments were conducted in air, O₂/CO₂, and O₂/RFG combustion atmospheres.

Table 10 shows the different combustion modes and multiple inlet O₂% where the numbers represent the inlet oxygen concentration in volumetric percentage and the utilised fuel in the experimental test using the CFB pilot facility. The table also describes the study areas for the specified fuels (oil shale and semicoke).

The CFB pilot facility always started in the air combustion mode. When the combustion process reached the desired experimental temperature, an air-combustion baseline test was conducted. Following the completion of the air test under stable conditions, the switch from air to O₂/CO₂ (OXY21-OXY40) and O₂/RFG (OXY50 and OXY75) combustion began. The transition was accomplished smoothly, and a steady oxyfuel combustion regime was achieved in a short time. The solid particles are separated from the flue gas in the cyclone and returned to the bottom of the fluidised bed through a return leg and an external heat exchanger.

Table 10. List of experimental tests, samplings and data analyses of oil shale and semicoke CFB oxyfuel combustion.

| | | Inlet O ₂ % | OS ^a | SC ^b |
|-----------------|---------------------------------|------------------------|-----------------|-----------------|
| Combustion mode | Air | 21 | ✓ | ✓ |
| | O ₂ /CO ₂ | 21 | ✓ | ✓ |
| | | 25 | ✓ | |
| | | 30 | ✓ | ✓ |
| | | 40 | ✓ | |
| | O ₂ /RFG | 50 | ✓ | |
| | | 75 | ✓ | |
| 90 | | ✓ | | |
| Emissions | NO _x | | ✓ | ✓ |
| | N ₂ O | | ✓ | |
| | SO ₂ | | ✓ | ✓ |
| | CO | | ✓ | ✓ |
| Ash sampling | BA | | ✓ | ✓ |
| | EHE | | ✓ | ✓ |
| | C1&C2 | | ✓ | |
| | Filter | | ✓ | |
| Ash analysis | Physical properties | | ✓ | |
| | Chemical composition | | ✓ | ✓ |
| | Mineral composition | | ✓ | |
| | Carbonate decomposition | | ✓ | ✓ |
| | Trace elements and heavy metals | | ✓ | |

^aOS: Oil shale

^bSC: Semicoke

The differences between the experimental tests using oil shale or semicoke are presented in Tables 11 and 12. The study with oil shale oxyfuel combustion covered a wider range of experiments at higher inlet O₂ and with the application of RFG. Oil shale fuel was the focal point of this research. In addition, ash data sampling and analyses were performed using multiple and duplicate tests to ensure optimal quality of the results.

Table 11. List of oil shale CFB combustion experimental tests.

| Combustion Mode | No. of tests | Flue gas emissions | Ash Sampling |
|-----------------|--------------|---|-------------------------|
| Air | 25 | O ₂ , CO ₂ , H ₂ O, SO ₂ , NO _x , N ₂ O | BA, EHE, C1, C2, Filter |
| OXY21 | 7 | O ₂ , CO ₂ , H ₂ O, SO ₂ , NO _x , N ₂ O | BA, EHE, C1, C2, Filter |
| OXY25 | 1 | O ₂ , CO ₂ , H ₂ O, SO ₂ , NO _x , N ₂ O | BA, EHE, C1, C2, Filter |
| OXY30 | 17 | O ₂ , CO ₂ , H ₂ O, SO ₂ , NO _x , N ₂ O | BA, EHE, C1, C2, Filter |
| OXY40 | 3 | O ₂ , CO ₂ , H ₂ O, SO ₂ , NO _x , N ₂ O | BA, EHE, C1, C2, Filter |
| OXY50+RFG | 3 | O ₂ , CO ₂ , H ₂ O, SO ₂ , NO _x , N ₂ O | EHE |
| OXY75+RFG | 2 | – | BA, EHE, Filter |
| OXY90+RFG | 4 | O ₂ , CO ₂ , H ₂ O, SO ₂ , NO _x , N ₂ O | – |

Table 12. List of semicoke CFB combustion experimental tests.

| Combustion Mode | No. of tests | Flue gas emissions | Ash Sampling |
|-----------------|--------------|--|--------------|
| Air | 6 | O ₂ , CO ₂ , H ₂ O, SO ₂ , NO _x | BA, EHE |
| OXY21 | 2 | O ₂ , CO ₂ , H ₂ O, SO ₂ , NO _x | BA, EHE |
| OXY30 | 2 | O ₂ , CO ₂ , H ₂ O, SO ₂ , NO _x | BA, EHE |

2.2.2 TG–MS Analyses

Paper IV studied the co-combustion of oil shale and spruce biomass using a NETZSCH STA 449 F3 Jupiter thermogravimetric analyser coupled with a Netzsch quadrupole mass spectrometer (MS) 403D Aeolos (mass 1– 300 amu). This study investigated the influence of air and oxyfuel environments on the combustion of oil shale, biomass, and their blends at 1:0, 4:1, 3:2, 2:3, 1:4, and 0:1 (0, 20, 40, 60, 80, and 100 wt. % Biomass), in three different combustion modes, as presented in Table 13. The standard Al₂O₃ crucibles with 5±0.01 mg sample weight was used for the combustion analysis. The gas flow rate was 60 ml/min for a gas mixture of 21%/79% O₂/N₂ for air-based combustion, and 21/79% (OXY21) and 30%/70% (OXY30) of O₂/CO₂ for oxyfuel combustion. OXY30 mode was selected to study the effect of higher inlet O₂% on the combustion process. The non-isothermal TG was performed at a heating rates of 10, 30, and 50 °C/min from 40°C up to a final combustion temperature of 1000 °C. MS was used to investigate the dynamics of gaseous emissions (H₂O, CO₂, and SO₂).

Table 13. List of oil shale and biomass co-combustion experiments.

| Combustion Mode | No. of tests | Mixing ratio OS:BM* | Heat rate k/min | Data study |
|---|--------------|------------------------------|-----------------|--------------------------------|
| 21/79% (O ₂ /N ₂) | 18x2 | 1:0, 4:1, 3:2, 2:3, 1:4, 0:1 | 10, 30, 50 | TGA, DTG, MS, Synergy, kinetic |
| 21/79% (O ₂ /CO ₂) | 18x2 | 1:0, 4:1, 3:2, 2:3, 1:4, 0:1 | 10, 30, 50 | TGA, DTG, MS, Synergy, kinetic |
| 30/70% (O ₂ /CO ₂) | 18x2 | 1:0, 4:1, 3:2, 2:3, 1:4, 0:1 | 10, 30, 50 | TGA, DTG, MS, Synergy, kinetic |

*OS: Oil shale; BM: Biomass

3 RESULTS AND DISCUSSION

3.1 Air and Oxyfuel Overall Combustion Process

The CFB pilot facility always began in air combustion mode. When the combustion process reached the desired experimental temperature, an air combustion baseline test was conducted. Following the completion of the air test under stable conditions, the switch from air to O₂/CO₂ [Papers I–III and V] or O₂/RFG [Papers I–III] combustion began. An example of this transition is shown in Figure 9, as illustrated in Paper III, shows that the transition was accomplished smoothly within a short period. Under oil shale oxy-firing conditions, as the combustion process proceeded, the increasing temperature promoted fuel combustion in the oxygen-rich environments (O₂/CO₂) with the CO₂ concentration in the flue gas exceeding 90% (Figure 10).

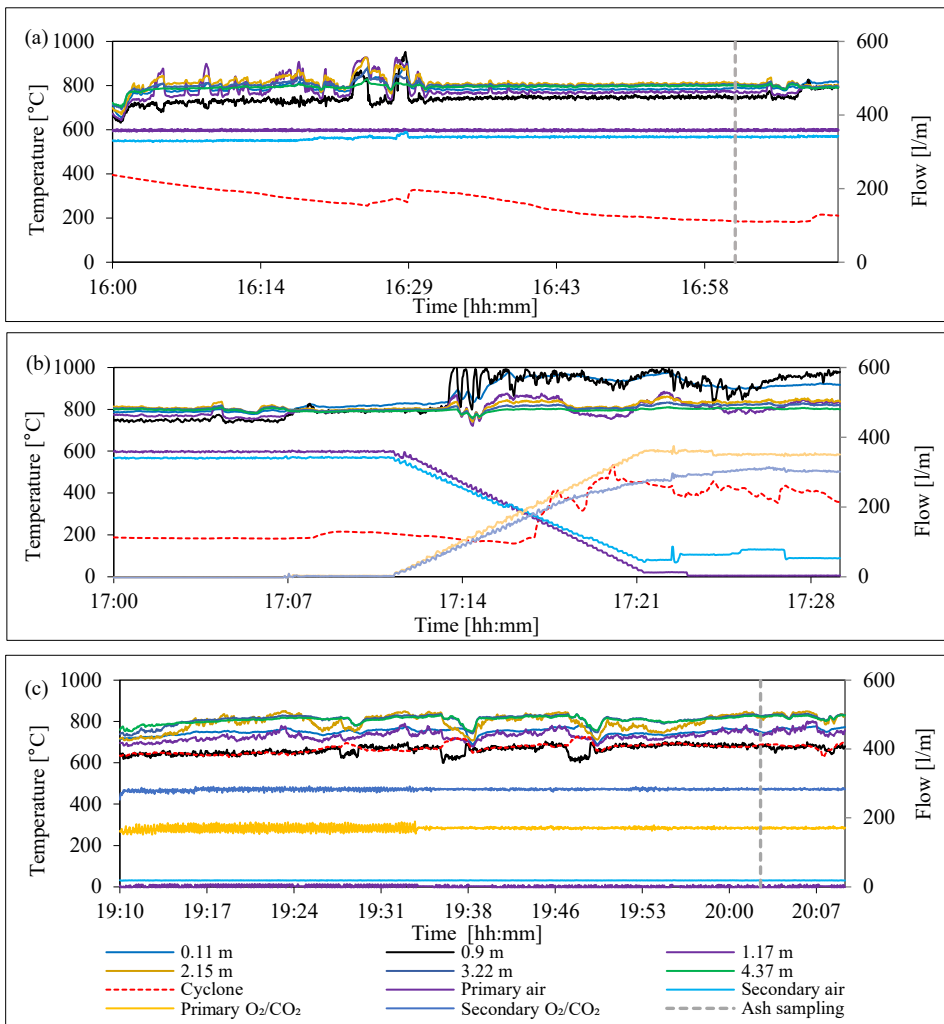


Figure 9. Operating conditions of the CFB boiler at: (a) Stable air condition; (b) Trans; and (c) Stable oxy condition [from paper III]

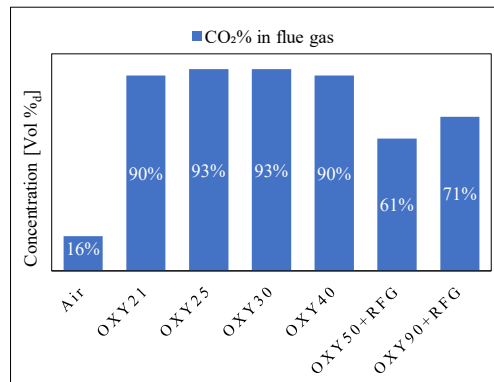


Figure 10. Oil shale CFB combustion tests and their CO₂ concentrations in the flue gas [from paper III]

In the oil shale combustion experiments, the temperatures in the CFB riser during stable regimes of air and oxyfuel combustion in the dense zone (T_{DB}) were significantly affected by the recirculation mass flow rate and temperature of the solid. This is attributed to the natural cooling of the recycled ash. A higher temperature generally indicates a higher ash recirculation rate and vice versa. The rate of solid ash recirculation is determined by the temperature of the external heat exchanger (T_{EHE}). The temperature deviation along the riser increased with the oxygen concentration in the combustion environment.

During combustion tests with semicoke, the fuel was heated to a temperature of 100–200°C before being fed into the riser. To compensate for the physical heat content of the semicoke, the combustion air supplied to the CFB riser was preheated to 500–550 °C. The axial temperature change in the combustion chamber dependent on the atmosphere are qualitatively similar when burning in air and O₂/CO₂ (21/80%) environments. Under these conditions, the temperature distribution was characterised by a temperature increase in the upper part of the riser. When burning in an oxygen-rich environment, upon increasing the oxygen content in the supplied O₂/CO₂ mixture to 30%, the heat release was redistributed relative to the riser axis. Consequently, the temperature in the lower part of the CFB combustion chamber increased. More thorough analyses of the temperature profiles can be found in Papers I and V.

3.2 Ash Behaviour

3.2.1 Physical Properties

To understand the effect of oxyfuel combustion on the particle distribution, the BA and EHE PSDs from Paper I are shown in Figure 11. The BA-PSDs shifted rightward toward larger particle sizes. Compared to air combustion, larger particles were formed under both O₂/CO₂ and O₂/RFG conditions. The EHE-PSDs exhibited finer particle formation under all oxy-combustion modes. Eventually, in oxyfuel CFB combustion, the ash distribution was related to a strong grain size separation in comparison with the air combustion atmosphere. This facilitated the production of finer particles with increasing O₂% because the oxygen concentration enhanced the mineral vaporisation and nucleation [96].

The difference between the specific surface area (SSA) in the BA and EHE ashes was significantly higher in air mode than in oxyfuel combustion, indicating larger particle size formation under oxyfuel conditions in the bed and heat exchanger of the pilot facility. The SSA of the Filter ash decreased with increase in the inlet O₂% because high temperature promoted the coalescence of minerals. This explained why the filter ash under higher inlet O₂% was larger in particle size.

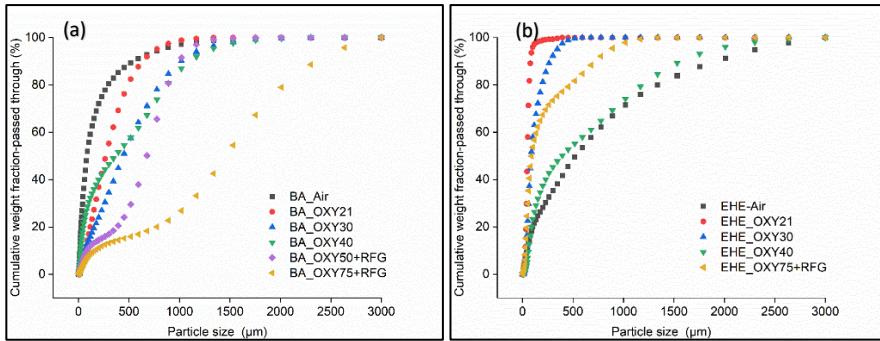


Figure 11. Comparison of particle size distribution under air and oxyfuel combustion experiments of; (a) BA and (b) EHE [from paper I]

3.2.2 Chemical Composition

In the oil shale CFB oxyfuel combustion tests, the largest ash mass fraction obtained during the combustion process was from the BA and EHE ash. Calcium oxide (CaO) was the most abundant oxide, followed by silica (SiO₂), magnesium (MgO), aluminium (Al₂O₃), and iron (Fe₂O₃) oxides, while the rest of the oxides formed during the different experiments were at lower concentrations.

The ratios of Ca:Mg oxides in the oxy-firing BAs decreased by 24% compared to those air-combustion mode. However, the same ratio for EHE ash from air to oxyfuel combustion decreased by 40%, indicating that oxy-firing BAs have a higher content of CaO. Ash alkaline earth elements CaO and MgO were relatively high in bottom ash and decreased in filter ash (down 50%) in air combustion and at low O₂ inlets under O₂/CO₂ combustion. However, at higher O₂ concentrations and with RFG, these values decreased by 30% and 20% for CaO and MgO, respectively, as the bed temperature was higher, and the residence time of the particles increased at the low solid recirculation rates.

For K₂O, SiO₂, Al₂O₃, and Fe₂O₃, these values increased in correlation with ash location. This indicated the separation of the fine sandy clay component and concentration into finer particles, where the vaporisation of SiO₂ was higher in oxy-firing than in air-firing, resulting in more submicron particles [152]. SiO₂, Na₂O, and K₂O values under oxyfuel mode decreased with increasing inlet O₂% in the combustion atmosphere and obtained the lowest value under 75%O₂/RFG (OXY75+RFG).

A higher evaporation rate of the BA-Cl content was noticed under the O₂/CO₂ mode than in air, and higher Cl condensation occurred at the low-temperature separation port (filter).

3.2.3 Mineral Composition

The dissociation of calcite was limited owing to the increased partial pressure of CO₂ even though the operating temperature increased owing to the elevated O₂ concentration. Consequently, the composition of BAs was strongly dominated by calcite; thus, the reduction in total CO₂ emissions in the flue gas from air to oxyfuel combustion exceeded (15%). However, dolomite decomposition is dependent primarily on the combustion temperature. In addition, elevated CO₂ partial pressure did not affect dolomite dissociation, were these concentrations in BA and EHE ashes reduced significantly under inlet O₂% by 25–40%, and increased with 21O₂/79CO₂% (OXY21) and OXY75+RFG at low operating temperature of approximately 744 °C. Therefore, the dolomite content varied depending on the bed/riser temperature between the different oxyfuel regimes.

The anhydrite concentrations were not affected by switching from air to the oxyfuel combustion environment (the highest in RFG). Under the O₂/RFG, higher anhydrite formation resulted from the enhanced sulfation reaction owing to the increased particle reaction time when recycling SO₂ back to the combustor. A higher SO₂ partial pressure in the combustion atmosphere eventually resulted in a higher sulphur capture efficiency [59]. Table 14 summarises the ash mineral compositions under different combustion regimes.

The limited decomposition of calcite in oxyfuel modes decreased the amount of free lime, which can react with quartz. This lowered the amount of akermanite and belite formed in BAs compared with air-firing BAs. RFG, which improved the contact and gas residence time with particles, exerted a clear effect on the increased formation of akermanite, merwinite, and belite, and the decreased amount of quartz in both BA and EHE ashes obtained from the oxyfuel modes.

The oxidising environment in O₂/CO₂ combustion slightly increased the concentration of haematite with increasing inlet O₂% (OXY21–OXY30) mainly in case of the BA and EHE ashes. Lower concentrations occurred at OXY40 and OXY75+RFG because the formation of haematite was dependent on the temperature and reaction time.

Table 14. Mineral composition of ashes during different combustion modes [from paper I]

| Component | Separation port | Air | OXY21 | OXY25 | OXY30 | OXY40 | OXY50 +RFG | OXY75 +RFG |
|---|-----------------|-------|-------|-------|-------|-------|------------|------------|
| Quartz (SiO ₂) | BA | 5.20 | 9.31 | 7.41 | 7.32 | 3.51 | 4.85 | 2.61 |
| | EHE | 5.07 | 14.31 | 15.16 | 14.10 | 7.41 | 20.82 | 11.01 |
| | Cooler | 22.08 | 22.36 | 22.81 | 22.65 | 21.18 | - | - |
| | Filter | 21.90 | 20.65 | 19.23 | 20.72 | 20.64 | - | 16.05 |
| K-feldspar (KAlSi ₃ O ₈) | BA | 1.99 | 5.11 | 3.40 | 3.91 | 3.01 | 1.31 | 0.55 |
| | EHE | 2.07 | 8.11 | 9.33 | 9.87 | 6.29 | 16.81 | 4.65 |
| | Cooler | 15.50 | 15.99 | 17.49 | 18.39 | 16.92 | - | - |
| | Filter | 17.48 | 17.34 | 17.33 | 19.01 | 17.93 | - | 9.93 |
| K-mica (Al ₂ K ₂ O ₆ Si) | BA | 6.08 | 2.50 | 0.50 | -- | -- | 1.21 | 0.15 |
| | EHE | 1.14 | 4.70 | 1.41 | 2.62 | 0.71 | 12.51 | 2.83 |
| | Cooler | 10.25 | 12.43 | 15.64 | 9.82 | 7.93 | - | - |
| | Filter | 17.68 | 20.95 | 19.03 | 16.51 | 8.12 | - | 4.21 |
| Calcite (CaCO ₃) | BA | 11.17 | 55.17 | 57.17 | 52.95 | 56.02 | 31.61 | 55.77 |
| | EHE | 44.36 | 28.62 | 33.52 | 29.51 | 33.90 | 12.21 | 19.29 |
| | Cooler | 13.53 | 14.49 | 16.64 | 16.29 | 13.25 | - | - |
| | Filter | 15.37 | 16.34 | 14.83 | 19.61 | 18.04 | - | 17.05 |

| | | | | | | | | |
|--|---------------|-------|-------|------|------|------|-------|-------|
| Dolomite (CaMg(CO ₃) ₂) | BA | 3.21 | 4.61 | 0.90 | 0.90 | 1.70 | 1.51 | 4.36 |
| | EHE | 6.51 | 5.20 | 2.11 | 1.81 | 1.93 | 1.70 | 4.24 |
| | Cooler | 1.76 | 1.65 | 1.90 | 1.00 | 1.15 | - | - |
| | Filter | 2.11 | 1.90 | 1.40 | 0.80 | 1.10 | - | 0.70 |
| Lime (CaO) | BA | 38.62 | 0.68 | -- | 1.81 | 2.59 | 16.89 | 4.48 |
| | EHE | 13.75 | 3.43 | 3.95 | 6.14 | 7.93 | 5.23 | 16.77 |
| | Cooler | 4.93 | 5.04 | 1.85 | 2.93 | 5.08 | - | - |
| | Filter | 2.87 | 1.89 | 2.93 | -- | 1.91 | - | 9.82 |
| Periclase (MgO) | BA | 6.41 | 4.71 | 6.11 | 5.82 | 8.22 | 8.79 | 6.84 |
| | EHE | 5.07 | 4.80 | 6.52 | 6.34 | 9.74 | 4.30 | 9.19 |
| | Cooler | 4.43 | 3.91 | 2.56 | 3.46 | 5.47 | - | - |
| | Filter | 3.11 | 2.41 | 2.20 | 2.70 | 5.41 | - | 5.62 |
| Anhydrite (CaSO ₄) | BA | 7.41 | 11.11 | 7.21 | 5.92 | 7.32 | 13.53 | 11.61 |
| | EHE | 7.86 | 14.31 | 8.53 | 8.26 | 8.22 | 8.11 | 12.53 |
| | Cooler | 8.15 | 6.92 | 6.62 | 8.02 | 6.68 | - | - |
| | Filter | 6.43 | 6.61 | 8.01 | 8.31 | 4.41 | - | 9.63 |
| Belite (C ₂ S) | BA | 6.75 | 1.20 | 2.30 | 3.01 | 2.41 | 8.58 | 4.68 |
| | EHE | 4.14 | 5.00 | 4.12 | 5.34 | 2.23 | 7.81 | 8.38 |
| | Cooler | 7.45 | 7.62 | 4.06 | 5.96 | 7.38 | - | - |
| | Filter | 5.83 | 5.71 | 4.61 | 2.90 | 7.21 | - | 12.94 |
| Akermanite (Ca ₂ Mg(Si ₂ O ₇)) | BA | 1.00 | 1.70 | 2.40 | 3.11 | 1.30 | 5.96 | 4.17 |
| | EHE | 1.76 | 4.00 | 3.71 | 4.23 | 5.08 | 4.90 | 5.05 |
| | Cooler | 4.68 | 3.31 | 2.91 | 4.76 | 5.47 | - | - |
| | Filter | 2.01 | 1.50 | 2.50 | 3.30 | 5.51 | - | 7.72 |
| Merwinite (Ca ₃ Mg(SiO ₄) ₂) | BA | 4.64 | -- | 0.90 | 0.80 | 0.90 | 4.14 | 3.22 |
| | EHE | 2.17 | 0.30 | 0.80 | 1.11 | 2.33 | 1.20 | 4.14 |
| | Cooler | 1.31 | 0.65 | 0.65 | 0.50 | 0.85 | - | - |
| | Filter | 0.60 | 0.60 | 0.30 | 0.70 | 1.20 | - | 3.61 |
| Sylvite (KCl) | BA | 1.44 | -- | -- | -- | -- | 1.21 | 0.15 |
| | EHE | 0.52 | -- | -- | -- | 0.30 | 0.70 | 0.00 |
| | Cooler | -- | 0.30 | -- | -- | 0.60 | - | - |
| Hematite (Fe ₂ O ₃) | BA | 0.66 | 1.40 | 2.00 | 2.61 | 1.80 | -- | 1.16 |
| | EHE | 1.03 | 1.80 | 2.61 | 2.42 | 1.62 | 3.70 | 1.72 |
| | Cooler | 2.47 | 2.16 | 3.46 | 3.26 | 2.11 | - | - |
| | Filter | 2.61 | 2.71 | 3.31 | 3.90 | 2.30 | - | 2.21 |

Overall, in the oxyfuel CFB combustion, the chemical and mineral compositions of the ash samples varied throughout the flow path of the CFB test facility, suggesting that particles of different compositions were separated. The separation appeared to be larger for coarse calcite and sulfated particles than in an air combustion atmosphere. The fine-grained sandy-clay components in the overhead ash contained a higher secondary silicate phase content, as they initiated binding with free lime, which resulted in the formation of clinker minerals.

3.2.4 Trace Elements and Heavy Metals

Most elements (As, Cu, V, Ni, Cr, Pb, Rb, Ba, Sr, and Ti) increased along the ash flow path during the oxyfuel combustion tests. These elements were depleted in the BA and condensed in the bag filter because of the low-gas-temperature regions. The condensation and adsorption processes after combustion in boilers and the accumulation of particles with decreasing temperature are considered the primary mechanisms that increased the concentrations of heavy metals in the finest particles of the overhead zones. Moreover, trace elements increased with an increase in specific elements, such as Fe, Si, and Al,

along the flow path and further from the boiler. Oxyfuel combustion exhibited a strong separation of fine ash; coarse calcite and sulphated particles were present in BA ashes, whereas sandy clay elements were concentrated more in cooler and filter ashes. For this reason, trace elements and heavy metals were mainly present in the finer particles of the overhead zones.

3.2.5 Extent of Carbonate Decomposition (ECD)

Figure 12 show the effect of dense bed (T_{DB}) and riser (T_{Riser}) temperatures on the extent of decomposition owing to the calcite ($k_{CO_2, Calcite}$) and dolomite ($k_{CO_2, Dolomite}$) decomposition of the studied BA and EHE ashes in [paper I]. As T_{DB} increased in the riser, the extent of decomposition increased in the air and O_2/CO_2 modes. BA- $k_{CO_2, Dolomite}$ is shifted slightly to a higher temperature under O_2/CO_2 compared to air combustion and reached maximum decomposition at T_{DB} 770 °C. The EHE ashes exhibited higher calcite decomposition than the BA. Hence, EHE- $k_{CO_2, Calcite}$ values were more affected by T_{Riser} . Under O_2/RFG (particularly OXY50+RFG), higher carbonate decomposition for BA and EHE ashes occurred at lower temperatures. Decomposition was mainly dependent on other operating parameters during the combustion process, including particle residence time, low CO_2 partial pressure at OXY50+RFG, and higher T_{EHE} temperature.

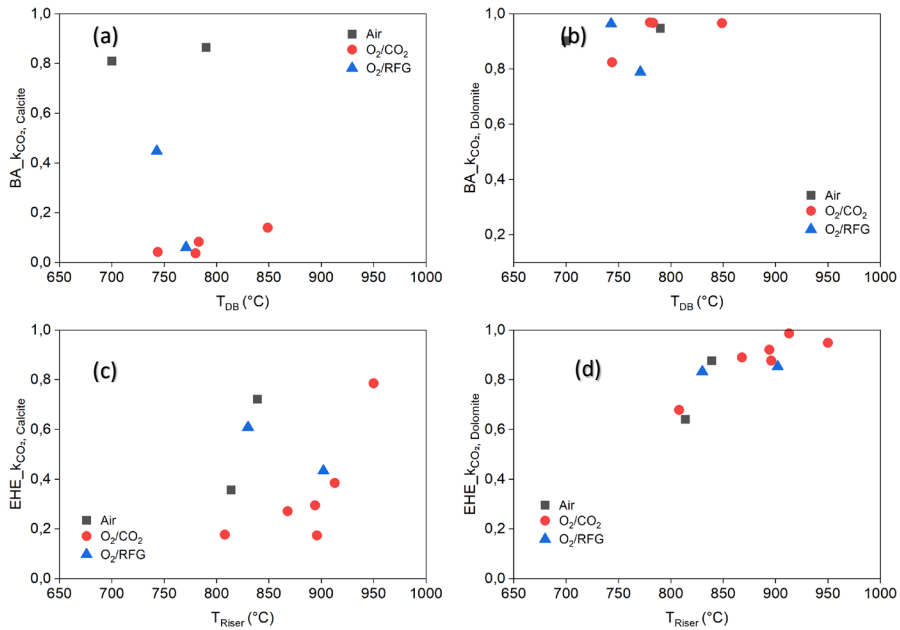


Figure 12. Effect of dense bed (T_{DB}) and riser (T_{Riser}) temperatures under air and oxyfuel experiments on: (a) BA- $k_{CO_2, Calcite}$, (b) BA- $k_{CO_2, Dolomite}$, (c) EHE- $k_{CO_2, Calcite}$, (d) EHE- $k_{CO_2, Dolomite}$ [from paper I]

Similar behaviour was observed for semicoke oxy-combustion, with slightly lower calcite decomposition because of the lower operation temperature in the dense bed region of the riser. The bottom ash circulated owing to its particle sizes and hydrodynamic conditions, and from where the particle size and residence time were later collected, as presented in Figure 13. In addition, carbonates (mainly calcite) did not thermally decompose when switched to burning in oxygen. This situation continued even at higher operating temperatures.

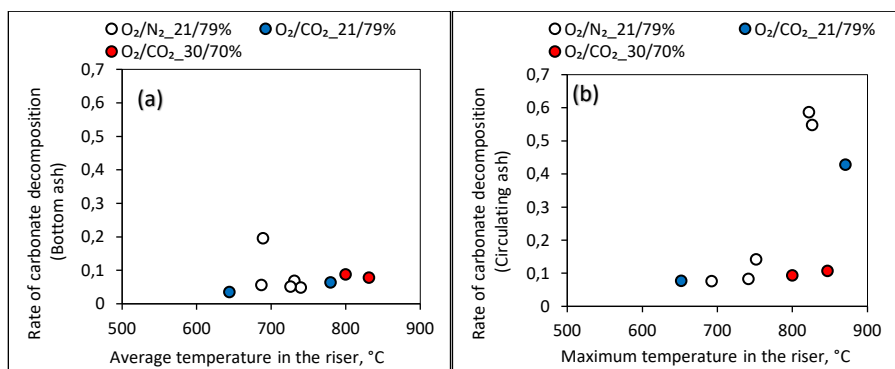


Figure 13. (a) The dependence of bottom ash carbonate decomposition on the average temperature in the riser and (b) the dependence of circulating ash carbonate decomposition on the maximum temperature in the riser [from paper V]

3.3 Emissions

The emission values are usually normalised as mass pollutants emitted per primary energy input (mg (NO_x, N₂O, SO₂, CO) /MJ) to enable a comparison between the air- and oxy-firing regimes, avoiding the effects of varying fuel loads or flue gas flow rates. The emission results from the oil shale and semicoke combustion tests under air and different oxyfuel pilot combustion conditions are presented. More detailed analyses are presented in Papers II, III, and V.

3.3.1 NO_x and N₂O

Figure 14 shows the effects of different oil shale oxyfuel combustion tests [Paper II] on nitrogen oxide emissions. The emission results clearly demonstrated that the change in the combustion atmosphere from air to O₂/CO₂ and O₂/RFG did not influence the formation of NO_x emissions despite the increase in bed temperature. Compared to air combustion, the average NO_x emissions were reduced from 120 to 105 mg/MJ under O₂/CO₂ and 98 mg/MJ under O₂/RFG. NO_x emissions were lowered significantly by 45% with increasing inlet O₂% under O₂/CO₂ mode from (21–52) vol.%. The results were aligned with those of other studies [70], [107]–[109]. With the application of RFG, NO_x formation in the dense bed zone was attributed to two sources: fuel-N conversion to NO_x, and NO_x recycling back to the combustor. The chemical reaction between fuel-N and recycled NO_x and the reduction of recycled NO_x from NO_x to N₂ reduced the NO emissions under the O₂/RFG firing mode; these results were also in line with those reported in the literature [54], [82].

N₂O concentrations were enhanced under O₂/CO₂ compared to air and decreased with increasing inlet O₂% from (21–52) vol.% from 20 mg/MJ to 4 mg/MJ. Moreover, these emissions were almost negligible under O₂/RFG mode. The enhanced oxidation of NCO to NO_x reduced the amount of available NCO required for N₂O formation [77]. These results were consistent with those of previous studies [153], [154].

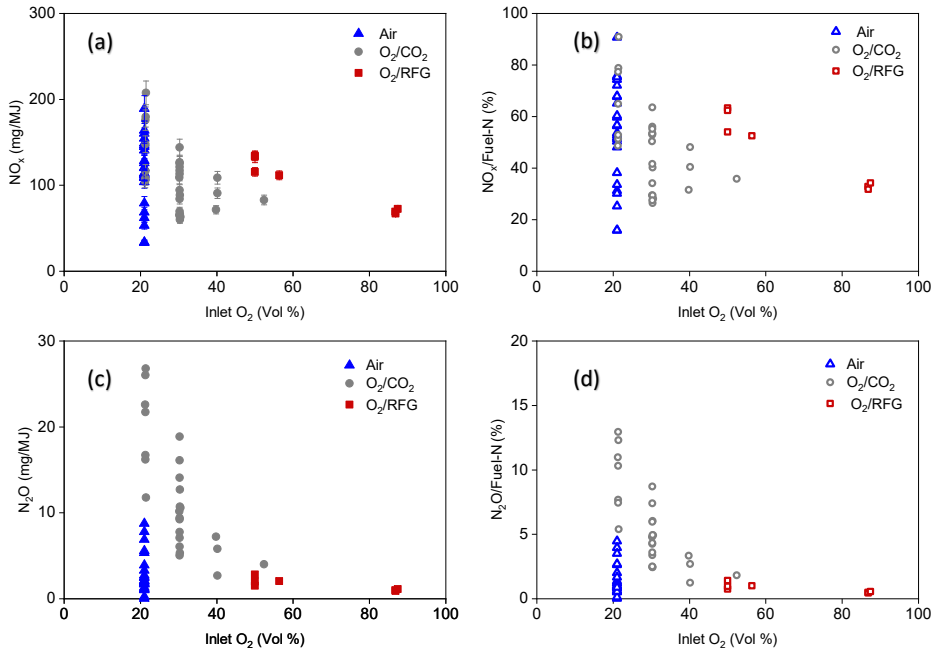


Figure 14. Effect of combustion atmosphere on; (a) Normalised NO_x emission (mg/MJ), (b) Fuel-N to NO_x conversion (%), (c) Normalised N₂O emission (mg/MJ), and (d) Fuel-N to N₂O conversion (%) [from paper II]

Figure 15 presents a comparison of the NO_x and N₂O emissions and fuel-N to NO_x and N₂O conversions in the air, O₂/CO₂, and O₂/RFG combustion modes. The emissions were compared at constant T_{DB} for each combustion environment. These tests were conducted for T_{DB} at 766°C in air, 743°C in OXY21, 793°C in OXY30, 850°C in OXY40, and 710°C under the OXY50+RFG and OXY87+RFG combustion modes. The results were similar for all tests under air and oxy-combustion. The NO_x emission increased by increasing λ_{Pr} and fuel-N mass conversions to NO_x were more favoured at higher excess oxygen ratios [54], [68], [82], [112]. The increase in NO_x emission can be explained by the fact that at oxygen-deficient conditions with lower excess oxygen ratios, higher N retention was obtained in the unburnt char. Moreover, the reduction of λ_{Pr} reduced the NO_x emissions as well. CO was produced during combustion and NO reacted with CO to form N₂ [109], [155]. By increasing the oxygen concentration, the combustion of volatile matter and char was enhanced, resulting in higher NO_x formation.

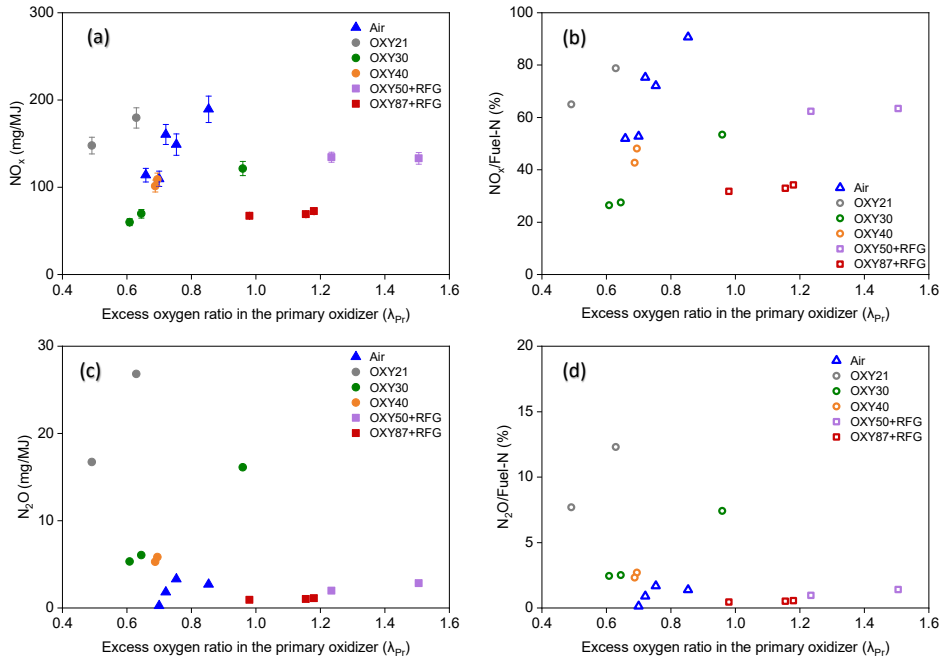


Figure 15. Effect of excess oxygen ratio in the primary oxidizer (λ_{Pr}) on; (a) Normalised NO_x emission (mg/MJ), (b) Fuel-N to NO_x conversion (%), (c) Normalised N_2O emission (mg/MJ) and (d) Fuel-N to N_2O conversion (%) [from paper II]

In the case of semicoke fuel combustion [Paper V], the general principles derived from oil shale and other fuels can be used. The amount of nitrogen in the semicoke, O_2 concentration in the riser, temperature, and degree of ash recirculation significantly affected the NO_x concentration produced during the tests under CFB conditions. The NO_x emissions (mass of NO_x to semicoke mass consumption) obtained in the experiments under different combustion modes, depending on the average temperature in the CFB riser and oxygen in the primary oxidiser (PA), are shown in Figure 16. For comparison, the NO_x emissions measured in the combustion gases generated by the Enefit-280 CFB riser are also included in the same figure. As evident, the NO_x emissions were lower when burning in oxygen compared to burning in air. This result is consistent with previous studies using oil shale or other solid fuels [63], [70], [156]. The experiments also showed that NO_x formation during semicoke combustion was generally consistent with the mechanism described above; NO_x emissions were reduced by creating a reduction zone.

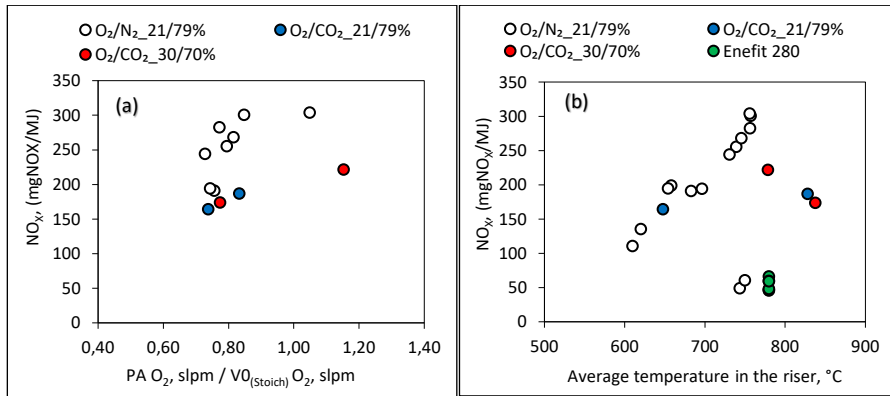


Figure 16. The dependence of normalised NO_x emissions under different combustion modes on (a) Excess O_2 supplied in the primary oxidizer (PA O_2 , slpm / $V_{O_2(Stoich)}$ O_2 , slpm); and (b) Average temperature in the riser [from paper V]

3.3.2 SO_2

The tests conducted in the CFB pilot facility utilised oil shale with a high molar ratio of Ca/S, exceeding 10, and a higher possibility of S bonding with the Ca and Mg contained in the fuel ash was obtained by increasing the Ca/S ratio. Therefore, the SO_2 emissions produced in the flue gas streams are extremely low, as shown in Figure 17 [Paper III].

Under oxy-firing conditions, as the combustion process proceeded, the elevated partial pressure of CO_2 that causes the oxy-firing atmosphere differed from that in air mode. The sulphur capture mechanisms may change from the normal sulfation path ($CaCO_3 \rightarrow CaO \rightarrow CaSO_4$) to the direct sulfation ($CaCO_3 \rightarrow CaSO_4$). Studies have shown that the behaviour of sulphur when burned in an oxygen-rich environment is analogous to that when burned in air [157]. The change in combustion atmosphere did not affect the release of SO_2 emissions in oxyfuel combustion environment, and the sulphur capture efficiency reached 99% for all combustion modes. The reason for the high Ca/S molar ratio in the oil shale fuel was the availability of a sufficient amount of excess calcium to bind with SO_2 .

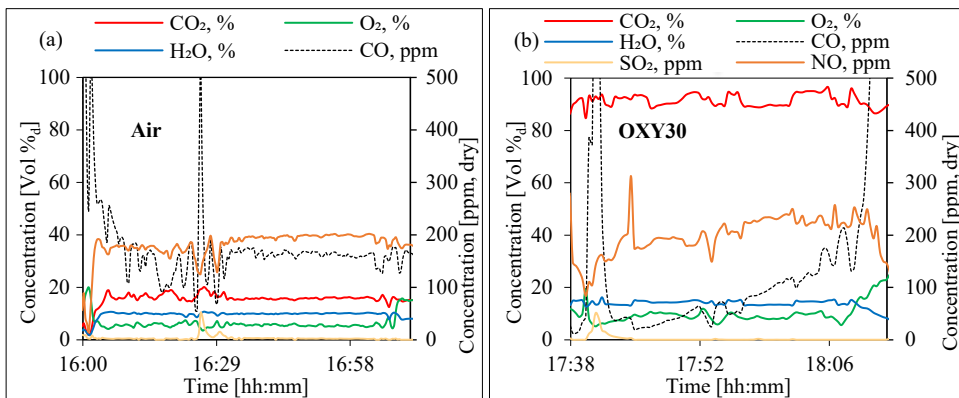


Figure 17. Pollutant emissions during stable conditions under: (a) Air; (b) Oxyfuel combustion [from paper III]

Figure 18 from [Paper V] shows the SO₂ emissions and their normalised values as mass pollutants emitted per primary (semicoke) energy input (mg (SO₂) /MJ) [65]. The maximum SO₂ capture efficiency shifted to higher temperatures (approximately 900 °C). Experiments with different types of fuels have shown that SO₂ emissions (mg/MJ) in an oxygen-rich environment are lower or at the same level as those when burning in air [4], [29].

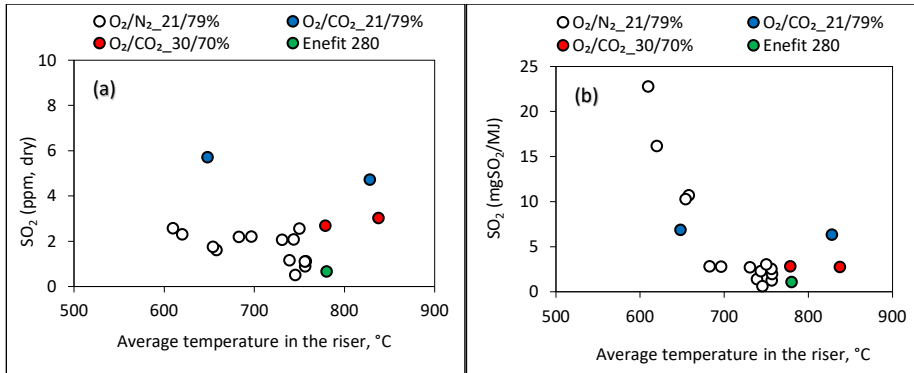


Figure 18. The dependence of SO₂ emissions on the riser average temperature under different combustion modes: (a) SO₂ emissions in ppm (b) Normalised SO₂ emissions (mgSO₂/MJ) [from paper V]

3.3.3 CO

The oxidation of CO to CO₂ is greatly influenced by the residence time of CO at the corresponding temperature and the efficiency of oxygen (combustion air) mixing with CO and fuel. Figure 19 presents CO concentrations obtained during the experimental tests of semicoke [Paper V]; in the same figure, the CO concentrations generated in the Enefit-280 CFB is shown. The CO emissions were generally higher than those of the Enefit-280 CFB. This can be explained primarily by the scale effect, that is, the shorter residence time of the gas. Further adjustment of the combustion parameters (increasing the primary air share to stoichiometry) would facilitate a reduction in the concentration of CO in the exhaust gas (Figure 19b). however, certain limits were applied to avoid an increase in the formation of nitrogen oxides. When burning in oxygen, the concentration of CO is generally lower in the oxyfuel combustion modes.

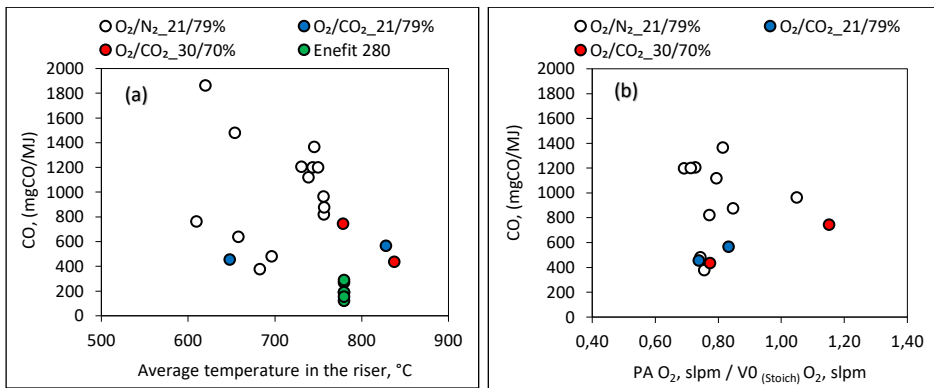


Figure 19. (a) The dependence of normalised CO emissions in (mgCO/MJ) on the average temperature in the riser, and (b) the dependence of normalised CO emissions in (mgCO/MJ) on the excess O₂ supplied in the primary oxidizer (PA O₂, slpm / VO_(Stoich) O₂, slpm) [from paper V]

For oil shale combustion in CFB [Paper II], the concentration of CO was relatively low, as the combustion temperature exceeded 800 °C. By increasing inlet O₂%, CO concentrations decreased under O₂/CO₂ mode, which indicates that higher inlet O₂% can improve combustion efficiency [78] (Figure 20). The lowest combustion efficiencies occurred under OXY21 and OXY87 + RFG, primarily because of the incomplete combustion of oil shale in an oxygen-deficient environment and low combustion temperature.

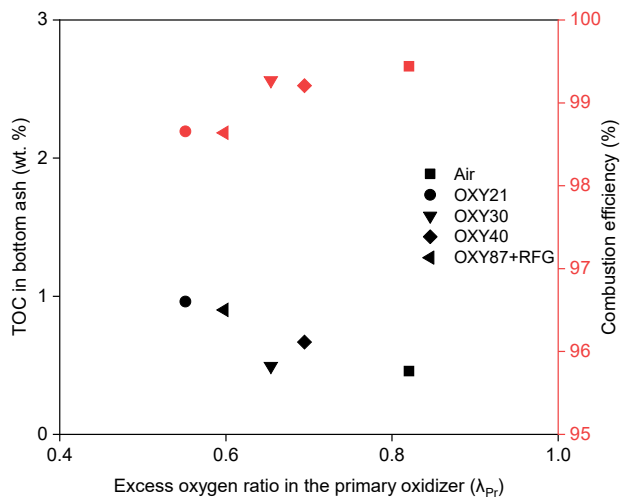


Figure 20. Effect of excess oxygen in the primary oxidizer on total organic carbon content in bottom ash and combustion efficiency [from paper II]

3.4 Oil shale and Biomass Oxyfuel Combustion like Conditions

The TG and DTG curves for oil shale, biomass, and their blends (4:1, 3:2, 2:3, and 1:4) under air and oxyfuel combustion conditions are presented in Figure 21. A more thorough description and analysis of the measurements are presented in Paper IV. The primary objective of this study was to provide theoretical guidance for the partial replacement of OS fuel and the combined application of biomass in industrial oil shale combustion boilers to achieve negative CO₂ emissions. As shown in Figure 21, the weight loss trend was similar to that of the individual fuels. The DTG curves in Figure 21(b) exhibited three main distinct peaks during air combustion, which corresponded to the weight losses of both oil shale and biomass. As the biomass ratio in the blends increased, the DTG curve intensity increased and the combustion intervals shifted toward lower temperatures. Moreover, the co-combustion profiles exhibited a reduction in mineral decomposition peak intensities at temperatures > 600°C with the increase of the biomass ratio, and T_d shifted to a lower temperature. This was owing to the presence of lower ash/mineral contents for decomposition in biomass compared to oil shale. Consequently, the addition of biomass enhanced the combustion performance of the blends and increased the reaction rate intensity identified with the higher release of volatile and improved char combustion. The effect of blends under oxyfuel combustion exhibited 4 distinct peaks, and the intensity of combustion peaks increased with the increment of the biomass blending ratio. However, the combustion intervals were similar to air combustion. These intervals shifted to a lower temperature region while the two decomposition stages' temperatures were the same as in the oil shale under oxy condition.

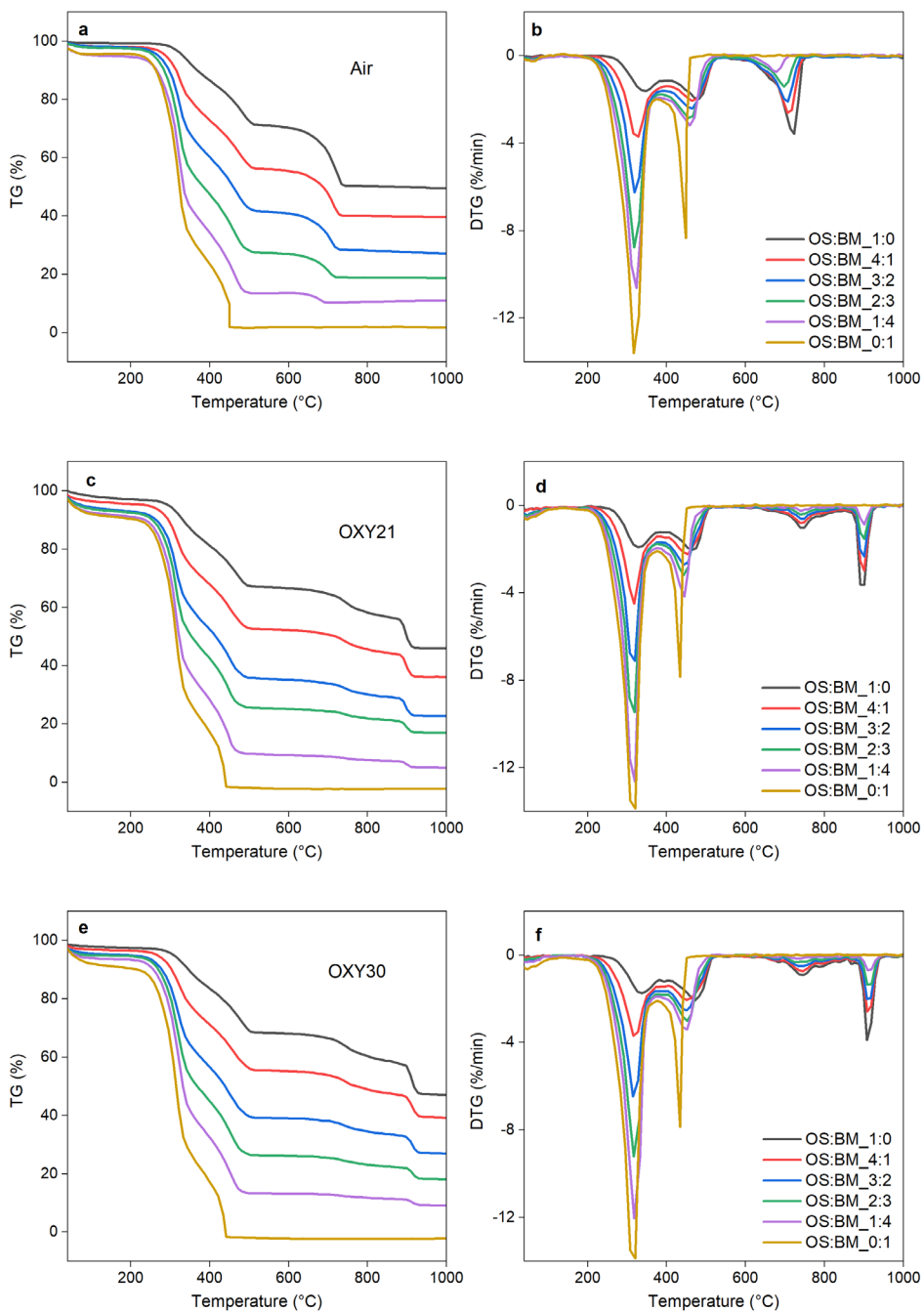


Figure 21. TG-DTG Curves under; N_2/O_2 (air) (a) and (b), OXY21 (c) and (d), and OXY30 (e) and (f) [from paper IV]

The MS results presented in Figure 22 are for a of 350 °C. The release of light hydrocarbons from oil shale to biomass OS:BM_1:0 is represented by the breakdown of organic matter with the release of CO₂ in the first peak, and the second peak at 490 °C represents char oxidation. With an increasing biomass mixing ratio, the two peaks shifted to a lower temperature, and the higher intensity indicated more volatile emissions from biomass addition. For the OS:BM_0:1, the second peak of biomass at 450°C exhibited an intense and sharp increase in CO₂ within the char oxidation region. However, the CO₂ peaks of the OS:BM_1:4 blend sample were considerably lower than those of OS:BM_0:1 in the combustion region. A possible explanation for this is the inhibitory effect of the oil shale addition in the light hydrocarbon combustion region. Under oxyfuel combustion, the H₂O and light hydrocarbon peaks correspond to fast devolatilisation, accelerating the release of gas emissions. Under oxygen conditions, the release of H₂O from OS:BM_1:0 was higher, and the observed differences between oil shale and other mixing ratios or biomass were smaller. Under oxy conditions, the SO₂ emissions from oil shale increased noticeably, and higher peaks were observed for OXY21 and OXY30 than for air combustion.

This blending method contributed significantly to improving the combustion of oil shale. When switching from air to oxyfuel combustion, the mineral decomposition behaviour was not affected by the addition of biomass.

This study investigated the synergistic effects observed in the co-combustion of different mixing ratios of oil shale and spruce biomass and showed that in air combustion, a negative effect was observed in the volatile/light hydrocarbon and char oxidation regions, indicating an inhibitory reaction (Figure 23). However, a positive synergistic effect was observed in the decomposition region at higher temperatures. Under oxygen-enriched conditions (OXY21 and OXY30 modes), positive synergistic effects were observed in the devolatilisation and combustion regions, particularly at higher biomass ratios and heating rates. This is a result of enhanced combustion under higher oxygen concentrations. A comparison with other studies [139], [158] suggests that hydrogen released during biomass devolatilisation can promote oil shale volatile release. Furthermore, under oxy conditions, a negative effect was observed in the carbonate decomposition region, indicating inhibitory decomposition of the ash mineral material.

The synergistic effects were stronger at higher heating rates, particularly in air. Overall, increasing the biomass ratio, heating rate, and oxygen concentration in the combustion atmosphere enhanced the positive synergistic effects during the co-combustion of oil shale and biomass. Further studies must be conducted to fully understand these underlying mechanisms.

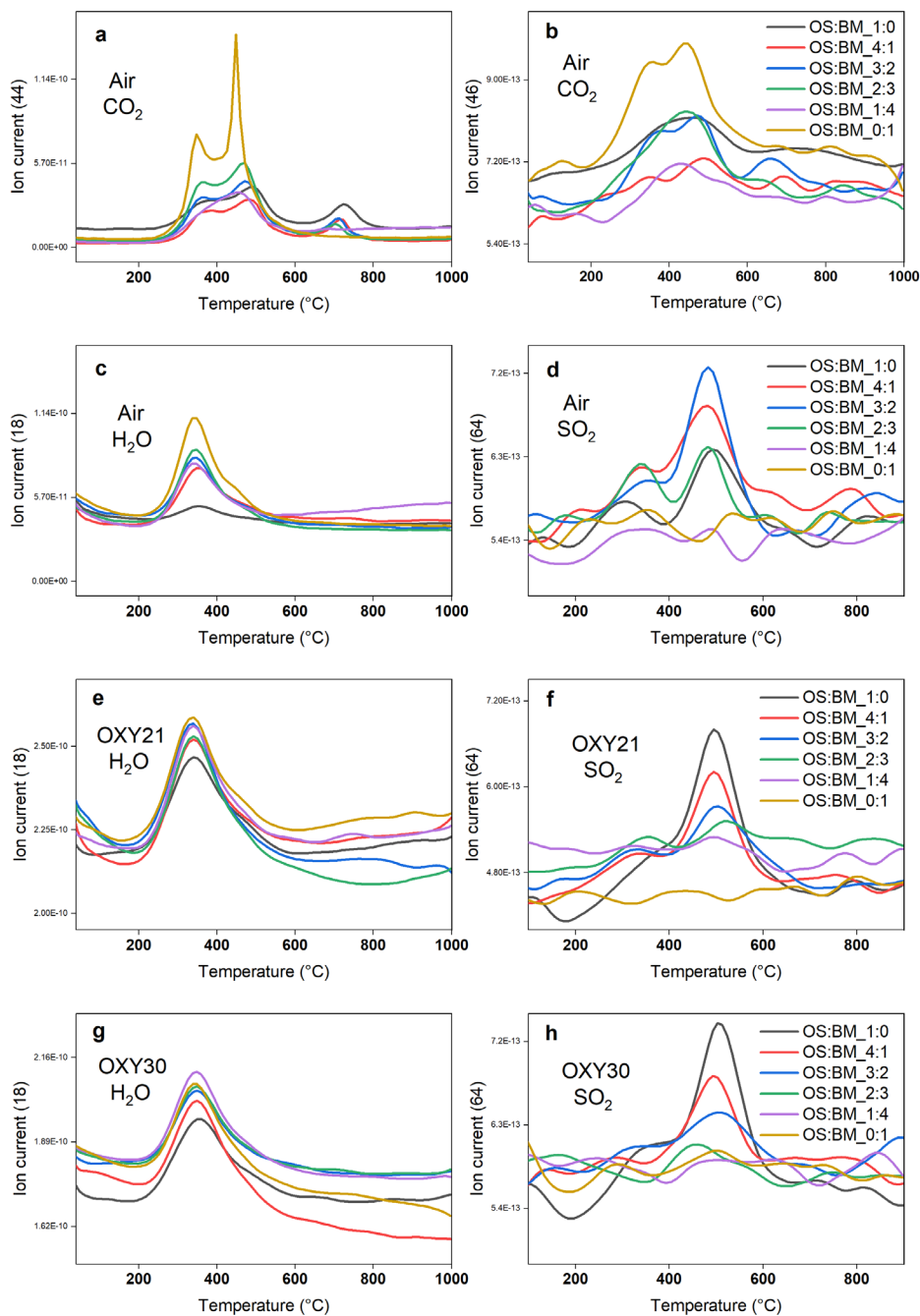


Figure 22. Comparison between CO_2 , H_2O , and SO_2 MS profiles of oil shale (OS), biomass (BM), and their blends under; N_2/O_2 (air) (a)-(d), OXY21 (e), and (f), and OXY30 (g) and (h) [from paper IV]

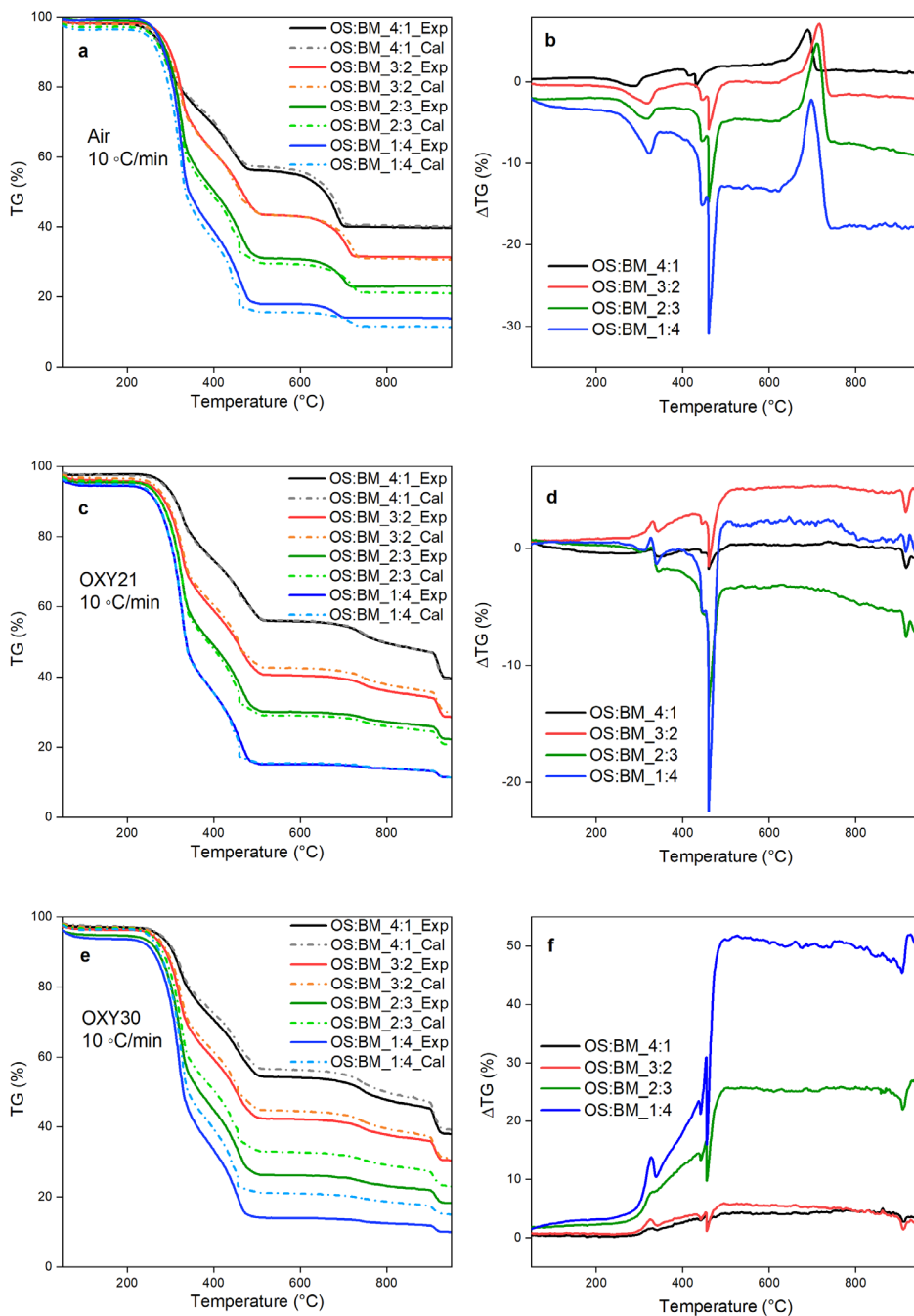


Figure 23. TG curves comparison between the experimental and calculated value from the mixtures and the differences values ΔTG curves under; N_2/O_2 (air) (a) and (b), OXY21 (c) and (d), and OXY30 (e) and (f) [from paper IV]

4 CONCLUSIONS AND FUTURE WORK

The oil shale industry is important to Estonia's economy. Oil shale is the primary resource for ensuring energy independence and constitutes a significant portion of the gross domestic product. Simultaneously, the oil shale industry is also the largest source of CO₂ emissions in Estonia. The CO₂ capture from power or industrial plants is an important contribution to satisfying the ambitious climate goals of the Paris Agreement. Therefore, if Estonia decides to continue with its oil shale industry, CO₂ capture technology must be implemented to ensure that its climate goals are achieved. In other words, to operate in a climate-neutral economy, the oil shale industry must begin to capture CO₂.

In this thesis, the utilisation of the oil shale oxyfuel combustion process is successfully demonstrated. This study investigated for the first-time, worldwide oil shale oxyfuel combustion at higher inlet O₂% and with the application of RFG. Several air and oxyfuel combustion experiments were conducted in a 60 kWth CFB pilot facility at the Energy Technology Department.

This study focused on the characterisation and mineral composition of the produced ash obtained from several separation ports under different combustion regimes. Throughout the comprehensive ash analysis study, the results indicated that under oxyfuel CFB combustion, the ash distribution exhibited a strong grain size separation compared with air firing. Thus, in real power plant applications, additional particulate filtering may be required before the preheater (if present) and at the electrostatic precipitator (ESP). The SSA results indicated that the difference between the surface areas of the BA and EHE ashes was significantly higher in air mode than in oxy-combustion. The decomposition of Ca carbonates was limited during oxyfuel combustion because of the high CO₂ partial pressure, which increased the carbonate content of the oxy-firing ashes. Thus, the total CO₂ emission reduction from air to oxyfuel combustion exceeded 15%. Consequently, the total heat gain is expected to increase, eventually leading to a lower reduction in power plant efficiency. However, a larger amount of solid waste is produced during oxyfuel combustion than during air firing. In this case, ash handling and disposal must be considered, particularly for dense-bed ash. Oxyfuel combustion exerted no noticeable impact on the concentrations of trace elements and heavy metals in the ash. These elements exhibited a larger depletion in BAs and a higher deposition in filter ashes under the oxy mode than in air. This indicated the effect of different PSDs obtained from oxy combustion than from air combustion.

With regard to gaseous emission pollutants, the influences of key operating factors, including the combustion atmosphere, excess oxygen ratio in the primary oxidiser, bed temperature, and CO concentration, were investigated in detail for NO_x and N₂O formation. By switching from air to oxyfuel combustion, the specific NO_x reduction increased from 120 mg/MJ in air to 105 mg/MJ in O₂/CO₂ mode and 98 mg/MJ in O₂/RFG. N₂O emissions reduced significantly, from 20 to 4 mg/MJ, with increase in inlet O₂% to 52% in O₂/CO₂ mode. The NO_x and N₂O emissions were the lowest of all combustion experiments at high inlet O₂% with RFG. These emissions are highly dependent on the combustion parameters in both air and oxyfuel combustion environments. The SO₂ emissions were approximately zero and sulphur capture efficiency reached more than 99%.

In the course of work on the potential for transitioning to cleaner and more sustainable energy generation in the shale oil industry, successful experimental tests were conducted using an extremely low-heating-value fuel. Semicoke air and oxyfuel

combustion tests were conducted in a 60 kWth CFB pilot facility. The combustion test temperature distributions were similar when burning in air and O₂/CO₂ (21/79%) environments. When increasing the oxygen content in the supplied O₂/CO₂ mixture to 30%, the heat release was redistributed, and the temperature in the lower part of the riser increased. The SO₂ emissions slightly increased in the air combustion mode at lower operating temperatures, and oxyfuel combustion did not influence SO₂ release. The actual NO_x emissions (per MJ) were reduced in an oxygen-enriched environment compared with air combustion. Under air combustion modes, at temperatures below 800 °C, the thermal decomposition of carbonates did not occur. At higher temperatures > 800 °C, most of the carbonates decomposed thermally and when switching from air to oxyfuel combustion, the temperature of the thermal decomposition of carbonates shifted to a higher value.

To maximise the CO₂ capture process by the partial replacement of oil shale with biomass for negative CO₂ emissions, a theoretical study was conducted using TG–MS analysis under air and different oxy-like conditions. This study was conducted to perform pilot-scale tests, thereby laying the groundwork for future considerations and potential implementation. The focal point of this research was the focus on the synergy of the effect resulting from the co-utilisation of oil shale and biomass, exemplary of a positive synergistic effect occurring in the devolatilisation and combustion of light hydrocarbons. The intensity of the peaks increased towards higher biomass ratios. At the higher heating rate of 50 °C/min, the oil shale and biomass co-combustion synergistic effects were enhanced. Overall, the test results may differ from the actual situation considering the scale effect, and oil shale is a complex fuel because several reactions can overlap during the combustion process. However, the present study provides theoretical guidance for the partial replacement of oil shale fuel and the combined application of biomass in industrial oil shale combustion boilers to achieve negative CO₂ emissions.

In conclusion, advancing oxyfuel combustion in the oil shale industry holds great promise for reducing Estonia's carbon footprint. However, the selection of the most suitable oxygen production technology depends on factors such as energy efficiency, scalability, cost-effectiveness, and compatibility with oxyfuel systems. Alongside the cryogenic process, other promising options include chemical looping air separation and renewable-based air separation technologies.

Further research should be conducted to reduce the CO₂ footprint of electricity production by reusing the ash produced during combustion. The behaviour and decomposition of dolomite under oxyfuel combustion regimes and their effects on sulphur capture routes should be investigated when utilising oil shale fuel.

Another aspect is related to experimental pilot tests on the co-combustion of wood chips and oil shale to achieve negative CO₂ emissions, assuming that the CO₂ produced from burning wood chips is not counted as CO₂ emissions.

A comprehensive life cycle assessment (LCA) study of oil shale oxyfuel combustion provides valuable insights into the environmental implications of this energy-generation technology.

Considering other integrated technologies by utilising oil shale, that is, chemical looping is another research direction.

List of Figures

| | |
|---|----|
| Figure 1. Pre-combustion capture process. | 17 |
| Figure 2. Post-combustion capture process..... | 18 |
| Figure 3. Oxyfuel combustion process [from paper I] | 18 |
| Figure 4. Pathways of nitrogen oxide formation at pulverized and CFB combustions [from paper II] | 23 |
| Figure 5. Main oxygen production technologies for oxyfuel combustion process [from paper VI] | 25 |
| Figure 6. Carbon balance for different energy systems. ([135], adapted from ecofriendlymag.com; grey denotes carbon of fossil origin, blue denotes carbon of biogenic origin). | 26 |
| Figure 7. Particle size distribution of oil shale [from paper I] | 28 |
| Figure 8. Circulating Fluidized Bed facility with 60 kWth capacity [from paper II] | 30 |
| Figure 9. Operating conditions of the CFB boiler at: (a) Stable air condition; (b) Trans; and (c) Stable oxy condition [from paper III] | 33 |
| Figure 10. Oil shale CFB combustion tests and their CO ₂ concentrations in the flue gas [from paper III] | 34 |
| Figure 11. Comparison of particle size distribution under air and oxyfuel combustion experiments of; (a) BA and (b) EHE [from paper I] | 35 |
| Figure 12. Effect of dense bed (T _{DB}) and riser (T _{Riser}) temperatures under air and oxyfuel experiments on: (a) BA-KCO ₂ , Calcite, (b) BA-KCO ₂ , Dolomite, (c) EHE-KCO ₂ , Calcite, (d) EHE-KCO ₂ , Dolomite [from paper I] | 38 |
| Figure 13. (a)The dependence of bottom ash carbonate decomposition on the average temperature in the riser and (b) the dependence of circulating ash carbonate decomposition on the maximum temperature in the riser [from paper V] | 39 |
| Figure 14. Effect of combustion atmosphere on; (a) Normalised NO _x emission (mg/MJ), (b) Fuel-N to NO _x conversion (%), (c) Normalised N ₂ O emission (mg/MJ), and (d) Fuel-N to N ₂ O conversion (%) [from paper II] | 40 |
| Figure 15. Effect of excess oxygen ratio in the primary oxidizer (λ_{Pr}) on; (a) Normalised NO _x emission (mg/MJ), (b) Fuel-N to NO _x conversion (%), (c) Normalised N ₂ O emission (mg/MJ) and (d) Fuel-N to N ₂ O conversion (%) [from paper II] | 41 |
| Figure 16. The dependence of normalised NO _x emissions under different combustion modes on (a) Excess O ₂ supplied in the primary oxidizer (PA O ₂ , slpm / V _{O(Stoich)} O ₂ , slpm); and (b) Average temperature in the riser [from paper V] | 42 |
| Figure 17. Pollutant emissions during stable conditions under: (a) Air; (b) Oxyfuel combustion [from paper III] | 42 |
| Figure 18. The dependence of SO ₂ emissions on the riser average temperature under different combustion modes: (a) SO ₂ emissions in ppm (b) Normalised SO ₂ emissions (mgSO ₂ /MJ) [from paper V] | 43 |
| Figure 19. (a) The dependence of normalised CO emissions in (mgCO/MJ) on the average temperature in the riser, and (b) the dependence of normalised CO emissions in (mgCO/MJ) on the excess O ₂ supplied in the primary oxidizer (PA O ₂ , slpm / V _{O(Stoich)} O ₂ , slpm) [from paper V] | 44 |
| Figure 20. Effect of excess oxygen in the primary oxidizer on total organic carbon content in bottom ash and combustion efficiency [from paper II] | 44 |
| Figure 21. TG-DTG Curves under; N ₂ /O ₂ (air) (a) and (b), OXY21 (c) and (d), and OXY30 (e) and (f) [from paper IV] | 46 |

Figure 22. Comparison between CO₂, H₂O, and SO₂ MS profiles of oil shale (OS), biomass (BM), and their blends under; N₂/O₂ (air) (a)-(d), OXY21 (e), and (f), and OXY30 (g) and (h) **[from paper IV]**..... 48

Figure 23. TG curves comparison between the experimental and calculated value from the mixtures and the differences values ΔTG curves under; N₂/O₂ (air) (a) and (b), OXY21 (c) and (d), and OXY30 (e) and (f) **[from paper IV]** 49

List of Tables

| | |
|---|----|
| Table 1. Literature studies on coal oxyfuel combustion experimental tests. | 20 |
| Table 2. Literature study on oil shale combustion experimental tests. | 21 |
| Table 3. Proximate and ultimate analysis of the oil shale [from paper I and IV] | 27 |
| Table 4. Chemical composition of the mineral part of the oil shale [from paper I and IV] . 27 | |
| Table 5. Mineralogical composition of the mineral part of the oil shale [from paper I and IV] | 28 |
| Table 6: Proximate and ultimate analysis of the spruce biomass [from paper IV] | 28 |
| Table 7. Proximate and ultimate analysis of the semicoke [from paper V] | 29 |
| Table 8. Chemical composition of the semicoke [from paper V] | 29 |
| Table 9. Mineralogical composition of the semicoke [from paper V] | 30 |
| Table 10. List of experimental tests, samplings and data analyses of oil shale and semicoke CFB oxyfuel combustion..... | 31 |
| Table 11. List of oil shale CFB combustion experimental tests. | 32 |
| Table 12. List of semicoke CFB combustion experimental tests. | 32 |
| Table 13. List of oil shale and biomass co-combustion experiments. | 32 |
| Table 14. Mineral composition of ashes during different combustion modes [from paper I] | 36 |

References

- [1] EU climate policy, "2030 climate & energy framework," *Ministry of Environment*, 2022. https://climate.ec.europa.eu/eu-action/climate-strategies-targets/2030-climate-energy-framework_en (accessed Mar. 25, 2023).
- [2] British Petroleum Company BP, "Statistical Review of World Energy," London, 2020. Accessed: Apr. 01, 2022. [Online]. Available: <https://www.bp.com/en/global/corporate/energy-economics/statistical-review-of-world-energy>.
- [3] C. Carbon, "COP27 carbon capture and storage," 2023. <https://www.carbonclean.com/carbon-capture-cop27> (accessed Jun. 26, 2023).
- [4] R. Stanger *et al.*, "Oxyfuel combustion for CO₂ capture in power plants," *Int. J. Greenh. Gas Control*, vol. 40, pp. 55–125, Sep. 2015, doi: 10.1016/j.ijggc.2015.06.010.
- [5] C. Yang *et al.*, "Oxy-CFB combustion technology for use in power-generation applications," *Fuel*, vol. 267, no. February, p. 117206, 2020, doi: 10.1016/j.fuel.2020.117206.
- [6] S. Seddighi, "Design of large scale oxy-fuel fluidized bed boilers: Constant thermal power and constant furnace size scenarios," *Energy*, vol. 118, pp. 1286–1294, 2017, doi: 10.1016/j.energy.2016.11.004.
- [7] S. Yadav and S. S. Mondal, "A review on the progress and prospects of oxy-fuel carbon capture and sequestration (CCS) technology," *Fuel*, vol. 308, p. 122057, Jan. 2022, doi: 10.1016/J.FUEL.2021.122057.
- [8] G. Chen, L. Shiyuan, and W. Linwei, "Current investigation status of oxy-fuel circulating fluidized bed combustion," *Fuel*, vol. 342, no. December 2022, p. 127699, 2023, doi: 10.1016/j.fuel.2023.127699.
- [9] A. Ots, *Oil shale fuel combustion*. Tallinn, Estonia: Tallinn University of Technology, 2006.
- [10] R. Kuusik, M. Uibu, K. Kirsimäe, R. Mõtlep, and T. Meriste, "Open-air deposition of Estonian oil shale ash: Formation, state of art, problems and prospects for the abatement of environmental impact," *Oil Shale*, vol. 29, no. 4, pp. 376–403, 2012, doi: 10.3176/oil.2012.4.08.
- [11] A. Konist, O. Järvi, H. Pikkor, D. Neshumayev, and T. Pihu, "Utilization of pyrolytic wastewater in oil shale fired CFBC boiler," *J. Clean. Prod.*, vol. 234, no. x, pp. 487–493, 2019, doi: 10.1016/j.jclepro.2019.06.213.
- [12] D. Neshumayev, T. Pihu, A. Siirde, O. Järvi, and A. Konist, "Solid heat carrier oil shale retorting technology with integrated CFB technology," *Oil Shale*, vol. 36, no. 2S, pp. 99–113, 2019, doi: 10.3176/OIL.2019.2S.02.
- [13] N. Golubev, "Solid oil shale heat carrier technology for oil shale retorting," *Oil Shale*, vol. 20, no. 3, 2003.
- [14] K. Plamus, A. Ots, T. Pihu, and D. Neshumayev, "Firing Estonian oil shale in CFB boilers -ASH balance and behaviour of carbonate minerals," *Oil Shale*, vol. 28, no. 1, pp. 58–67, 2011, doi: 10.3176/oil.2011.1.07.
- [15] A. Konist, T. Pihu, D. Neshumayev, and I. Külaots, "Low grade fuel - oil shale and biomass co-combustion in CFB boiler," *Oil Shale*, vol. 30, no. 2 SUPPL., pp. 294–304, 2013, doi: 10.3176/oil.2013.2S.09.

- [16] B. Maaten, A. Konist, and A. Siirde, "High-speed thermogravimetric analysis of the combustion of wood and Ca-rich fuel," *J. Therm. Anal. Calorim.*, vol. 138, no. 4, pp. 2807–2811, 2019, doi: 10.1007/s10973-019-08785-6.
- [17] E. Özgür, S. F. Miller, B. G. Miller, and M. V. Kök, "Thermal analysis of co-firing of oil shale and biomass fuels," *Oil Shale*, vol. 29, no. 2, pp. 190–201, 2012, doi: 10.3176/OIL.2012.2.07.
- [18] A. A. Noora, "Six Key Cop28 Outcomes for Ccs," no. December, 2023.
- [19] Ministry of the Environment of Estonia, "National Development Plan for the Use of Oil Shale 2016-2030," p. 75, 2016, [Online]. Available: https://www.envir.ee/sites/default/files/2016_2030ak_ingl.pdf.
- [20] A. Murugan *et al.*, "Purity requirements of carbon dioxide for carbon capture and storage," London, UK, 2019.
- [21] A. Saia, D. Neshumayev, A. Hazak, P. Sander, O. Järvik, and A. Konist, "Techno-economic assessment of CO₂ capture possibilities for oil shale power plants," *Renew. Sustain. Energy Rev.*, vol. 169, no. February, 2022, doi: 10.1016/j.rser.2022.112938.
- [22] M. Uibu *et al.*, "ClimMIT - Climate change mitigation with CCS and CCU technologies," *SSRN Electron. J.*, no. March, 2021, doi: 10.2139/ssrn.3812288.
- [23] L. Loo, B. Maaten, A. Siirde, T. Pihu, and A. Konist, "Experimental analysis of the combustion characteristics of Estonian oil shale in air and oxy-fuel atmospheres," *Fuel Process. Technol.*, vol. 134, pp. 317–324, 2015, doi: 10.1016/j.fuproc.2014.12.051.
- [24] T. Meriste, C. R. Yörük, A. Trikkel, T. Kaljuvee, and R. Kuusik, "TG-FTIR analysis of oxidation kinetics of some solid fuels under oxy-fuel conditions," *J. Therm. Anal. Calorim.*, vol. 114, no. 2, pp. 483–489, Nov. 2013, doi: 10.1007/S10973-013-3063-X/FIGURES/5.
- [25] C. R. Yörük, T. Meriste, A. Trikkel, and R. Kuusik, "Thermo-oxidation characteristics of oil shale and oil shale char under oxy-fuel combustion conditions," *J. Therm. Anal. Calorim.*, vol. 121, no. 1, pp. 509–516, 2015, doi: 10.1007/s10973-015-4484-5.
- [26] A. Konist, A. Valtsev, L. Loo, T. Pihu, M. Liira, and K. Kirsimäe, "Influence of oxy-fuel combustion of Ca-rich oil shale fuel on carbonate stability and ash composition," *Fuel*, vol. 139, pp. 671–677, 2015, doi: 10.1016/j.fuel.2014.09.050.
- [27] C. R. Yörük, A. Trikkel, and R. Kuusik, "Prediction of Flue Gas Composition and Comparative Overall Process Evaluation for Air and Oxyfuel Combustion of Estonian Oil Shale, Using Aspen Plus Process Simulation," *Energy and Fuels*, vol. 30, no. 7, pp. 5893–5900, 2016, doi: 10.1021/acs.energyfuels.6b00022.
- [28] C. R. Yörük, T. Meriste, S. Sener, R. Kuusik, and A. Trikkel, "Thermogravimetric analysis and process simulation of oxy-fuel combustion of blended fuels including oil shale, semicoke, and biomass," *Int. J. Energy Res.*, vol. 42, no. 6, pp. 2213–2224, 2018, doi: 10.1002/er.4011.
- [29] L. Loo, A. Konist, D. Neshumayev, T. Pihu, B. Maaten, and A. Siirde, "Ash and flue gas from oil shale oxy-fuel circulating fluidized bed combustion," *Energies*, vol. 11, no. 5, 2018, doi: 10.3390/en11051218.
- [30] A. Konist, E. J. Anthony, D. Neshumayev, Z. S. Baird, M. Maasikmets, and O. Järvik, "Mineral and heavy metal composition of oil shale ash from oxyfuel combustion," *ACS Omega*, vol. 5, no. 50, pp. 32498–32506, 2020, doi: 10.1021/acsomega.0c04466.

- [31] R. M. Cuéllar-Franca and A. Azapagic, "Carbon capture, storage and utilisation technologies: A critical analysis and comparison of their life cycle environmental impacts," *Journal of CO₂ Utilization*, vol. 9. Elsevier Ltd, pp. 82–102, 2015, doi: 10.1016/j.jcou.2014.12.001.
- [32] M. Bui *et al.*, "Carbon capture and storage (CCS): The way forward," *Energy and Environmental Science*, vol. 11, no. 5. Royal Society of Chemistry, pp. 1062–1176, May 01, 2018, doi: 10.1039/c7ee02342a.
- [33] C. Kunze and H. Spliethoff, "Modelling of an IGCC plant with carbon capture for 2020," *Fuel Process. Technol.*, vol. 91, no. 8, pp. 934–941, Aug. 2010, doi: 10.1016/J.FUPROC.2010.02.017.
- [34] C. Descamps, C. Bouallou, and M. Kanniche, "Efficiency of an Integrated Gasification Combined Cycle (IGCC) power plant including CO₂ removal," *Energy*, vol. 33, no. 6, pp. 874–881, Jun. 2008, doi: 10.1016/J.ENERGY.2007.07.013.
- [35] K. Stéphenne, "Start-up of World's First Commercial Post-combustion Coal Fired CCS Project: Contribution of Shell Cansolv to SaskPower Boundary Dam ICCS Project," *Energy Procedia*, vol. 63, pp. 6106–6110, Jan. 2014, doi: 10.1016/J.EGYPRO.2014.11.642.
- [36] H. C. Mantripragada, H. Zhai, and E. S. Rubin, "Boundary Dam or Petra Nova – Which is a better model for CCS energy supply?," *Int. J. Greenh. Gas Control*, vol. 82, pp. 59–68, Mar. 2019, doi: 10.1016/J.IJGGC.2019.01.004.
- [37] V. Darde, K. Thomsen, W. J. M. van Well, and E. H. Stenby, "Chilled ammonia process for CO₂ capture," *Int. J. Greenh. Gas Control*, vol. 4, no. 2, pp. 131–136, Mar. 2010, doi: 10.1016/J.IJGGC.2009.10.005.
- [38] D. P. Hanak, C. Biliyok, and V. Manovic, "Efficiency improvements for the coal-fired power plant retrofit with CO₂ capture plant using chilled ammonia process," *Appl. Energy*, vol. 151, pp. 258–272, Aug. 2015, doi: 10.1016/J.APENERGY.2015.04.059.
- [39] M. Jabłońska, A. E. Palomares Gimeno, A. Wegrzyn, and L. Chmielarz, "A short review about NO_x storage/reduction catalysts based on metal oxides and hydrotalcite-type anionic clays," *Acta Geodyn. Geomater.*, vol. 11, no. 2, pp. 175–186, 2014, doi: 10.13168/AGG.2013.0063.
- [40] R. Bredesen, K. Jordal, and O. Bolland, "High-temperature membranes in power generation with CO₂ capture," *Chem. Eng. Process. Process Intensif.*, vol. 43, no. 9, pp. 1129–1158, Sep. 2004, doi: 10.1016/J.CEP.2003.11.011.
- [41] B. Arias *et al.*, "Demonstration of steady state CO₂ capture in a 1.7 MWth calcium looping pilot," *Int. J. Greenh. Gas Control*, vol. 18, pp. 237–245, Oct. 2013, doi: 10.1016/J.IJGGC.2013.07.014.
- [42] R. I. Singh and R. Kumar, "Current status and experimental investigation of oxy-fired fluidized bed," *Renew. Sustain. Energy Rev.*, vol. 61, pp. 398–420, 2016, doi: 10.1016/j.rser.2016.04.021.
- [43] M. A. Nemitallah *et al.*, "Oxy-fuel combustion technology: current status, applications, and trends," *Int. J. Energy Res.*, vol. 41, no. 12, pp. 1670–1708, Oct. 2017, doi: 10.1002/ER.3722.
- [44] M. Bui *et al.*, "Carbon capture and storage (CCS): the way forward," *Energy Environ. Sci.*, vol. 11, no. 5, pp. 1062–1176, May 2018, doi: 10.1039/C7EE02342A.
- [45] G. Scheffknecht, L. Al-Makhadmeh, U. Schnell, and J. Maier, "Oxy-fuel coal combustion-A review of the current state-of-the-art," *Int. J. Greenh. Gas Control*, vol. 5, no. SUPPL. 1, pp. 16–35, 2011, doi: 10.1016/j.ijggc.2011.05.020.

- [46] C. Scheuer *et al.*, "Fluidized bed combustion in high concentrations of O₂ and CO₂," *Phys. Educ. Sport Child. Youth with Spec. Needs Res. – Best Pract. – Situat.*, pp. 343–354, 2006, doi: 10.2/JQUERY.MIN.JS.
- [47] T. Fujimori and T. Yamada, "Realization of oxyfuel combustion for near zero emission power generation," *Proc. Combust. Inst.*, vol. 34, no. 2, pp. 2111–2130, Jan. 2013, doi: 10.1016/J.PROCI.2012.10.004.
- [48] A. Lyngfelt and B. Leckner, "A 1000 MWth boiler for chemical-looping combustion of solid fuels – Discussion of design and costs," *Appl. Energy*, vol. 157, pp. 475–487, Nov. 2015, doi: 10.1016/J.APENERGY.2015.04.057.
- [49] T. Mattisson *et al.*, "Chemical-looping technologies using circulating fluidized bed systems: Status of development," *Fuel Process. Technol.*, vol. 172, pp. 1–12, Apr. 2018, doi: 10.1016/J.FUPROC.2017.11.016.
- [50] N. Krishnamurthy, W. Blasiak, and A. Lugnet, "Development of High Temperature Air and Oxy-Fuel combustion technologies for minimized CO₂ and NO_x emissions in Industrial Heating," *Jt. Int. Conf. Sustain. Energy Environ.*, no. December, pp. 1–6, 2004.
- [51] L. Jia, Y. Tan., and E. J. Anthony, "Emissions of SO₂ and NO_x during Oxy-Fuel CFB combustion tests in a mini-circulating fluidized bed combustion reactor," *Energy and Fuels*, vol. 24, no. 2, pp. 910–915, 2010, doi: 10.1021/ef901076g.
- [52] L. Duan, W. Zhou, H. Li, X. Chen, and C. Zhao, "Sulfur fate during bituminous coal combustion in an oxy-fired circulating fluidized bed combustor," *Korean J. Chem. Eng.*, vol. 28, no. 9, pp. 1952–1955, 2011, doi: 10.1007/s11814-011-0057-x.
- [53] M. De Las Obras-Loscertales *et al.*, "Effects of temperature and flue gas recycle on the SO₂ and NO_x emissions in an oxy-fuel fluidized bed combustor," *Energy Procedia*, vol. 37, pp. 1275–1282, 2013, doi: 10.1016/j.egypro.2013.06.002.
- [54] L. Jia *et al.*, "Commissioning of a 0.8 MWth CFBC for oxy-fuel combustion," *Int. J. Greenh. Gas Control*, vol. 7, pp. 240–243, 2012, doi: 10.1016/j.ijggc.2011.10.009.
- [55] Y. Wu, C. Wang, Y. Tan, L. Jia, and E. J. Anthony, "Characterization of ashes from a 100kWth pilot-scale circulating fluidized bed with oxy-fuel combustion," *Appl. Energy*, vol. 88, no. 9, pp. 2940–2948, 2011, doi: 10.1016/j.apenergy.2011.03.007.
- [56] T. Czakiert, Z. Bis, W. Muskala, and W. Nowak, "Fuel conversion from oxy-fuel combustion in a circulating fluidized bed," *Fuel Process. Technol.*, vol. 87, no. 6, pp. 531–538, 2006, doi: 10.1016/j.fuproc.2005.12.003.
- [57] L. Jia, Y. Tan, C. Wang, and E. J. Anthony, "Experimental study of oxy-fuel combustion and sulfur capture in mini-CFBC," *Energy and Fuels*, vol. 21, no. 6, pp. 3160–3164, 2007, doi: 10.1021/ef7002359.
- [58] K. Myöhänen, T. Hyppänen, T. Pikkarainen, T. Eriksson, and A. Hotta, "Near zero CO₂ emissions in coal firing with oxy-fuel circulating fluidized bed boiler," *Chem. Eng. Technol.*, vol. 32, no. 3, pp. 355–363, 2009, doi: 10.1002/ceat.200800566.
- [59] T. Czakiert, K. Sztékler, S. Karski, D. Markiewicz, and W. Nowak, "Oxy-fuel circulating fluidized bed combustion in a small pilot-scale test rig," *Fuel Process. Technol.*, vol. 91, no. 11, pp. 1617–1623, 2010, doi: 10.1016/j.fuproc.2010.06.010.
- [60] T. Czakiert *et al.*, "Combustible matter conversion in an oxy-fuel circulating fluidized-bed (CFB) environment," *Energy and Fuels*, vol. 26, no. 9, pp. 5437–5445, 2012, doi: 10.1021/ef3011838.

- [61] L. Duan, C. Zhao, W. Zhou, C. Qu, and X. Chen, "O₂/CO₂ coal combustion characteristics in a 50kWth circulating fluidized bed," *Int. J. Greenh. Gas Control*, vol. 5, no. 4, pp. 770–776, 2011, doi: 10.1016/j.ijggc.2011.01.007.
- [62] L. Duan, C. Zhao, W. Zhou, C. Qu, and X. Chen, "Effects of operation parameters on NO emission in an oxy-fired CFB combustor," *Fuel Process. Technol.*, vol. 92, no. 3, pp. 379–384, 2011, doi: 10.1016/j.fuproc.2010.09.031.
- [63] L. Duan, H. Sun, C. Zhao, W. Zhou, and X. Chen, "Coal combustion characteristics on an oxy-fuel circulating fluidized bed combustor with warm flue gas recycle," *Fuel*, vol. 127, pp. 47–51, 2014, doi: 10.1016/j.fuel.2013.06.016.
- [64] Y. Tan, L. Jia, Y. Wu, and E. J. Anthony, "Experiences and results on a 0.8MWth oxy-fuel operation pilot-scale circulating fluidized bed," *Appl. Energy*, vol. 92, pp. 343–347, 2012, doi: 10.1016/j.apenergy.2011.11.037.
- [65] M. De Las Obras-Loscertales *et al.*, "NO and N₂O emissions in oxy-fuel combustion of coal in a bubbling fluidized bed combustor," *Fuel*, vol. 150, pp. 146–153, 2015, doi: 10.1016/j.fuel.2015.02.023.
- [66] L. F. De Diego *et al.*, "Optimum temperature for sulphur retention in fluidised beds working under oxy-fuel combustion conditions," *Fuel*, vol. 114, pp. 106–113, 2013, doi: 10.1016/j.fuel.2012.02.064.
- [67] L. F. de Diego *et al.*, "Pollutant emissions in a bubbling fluidized bed combustor working in oxy-fuel operating conditions: Effect of flue gas recirculation," *Appl. Energy*, vol. 102, no. x, pp. 860–867, 2013, doi: 10.1016/j.apenergy.2012.08.053.
- [68] C. Lupiáñez, L. I. Díez, and L. M. Romeo, "NO emissions from anthracite oxy-firing in a fluidized-bed combustor: Effect of the temperature, limestone, and O₂," *Energy and Fuels*, vol. 27, no. 12, pp. 7619–7627, 2013, doi: 10.1021/ef4019228.
- [69] C. Lupiáñez, I. Guedea, I. Bolea, L. I. Díez, and L. M. Romeo, "Experimental study of SO₂ and NO_x emissions in fluidized bed oxy-fuel combustion," *Fuel Process. Technol.*, vol. 106, no. x, pp. 587–594, 2013, doi: 10.1016/j.fuproc.2012.09.030.
- [70] M. Lupion *et al.*, "30 MWth CIUDEN Oxy-CFB boiler - First experiences," *Energy Procedia*, vol. 37, pp. 6179–6188, 2013, doi: 10.1016/J.EGYPRO.2013.06.547.
- [71] M. Gómez, A. Fernández, I. Llavona, and R. Kuivalainen, "Experiences in sulphur capture in a 30 MWth Circulating Fluidized Bed boiler under oxy-combustion conditions," *Appl. Therm. Eng.*, vol. 65, no. 1–2, pp. 617–622, 2014, doi: 10.1016/j.applthermaleng.2014.01.012.
- [72] T. Pikkarainen, J. Saastamoinen, H. Saastamoinen, T. Leino, and A. Tourunen, "Development of 2nd generation oxyfuel CFB technology - small scale combustion experiments and model development under high oxygen concentrations," *Energy Procedia*, vol. 63, pp. 372–385, 2014, doi: 10.1016/j.egypro.2014.11.040.
- [73] H. Li *et al.*, "Experimental results for oxy-fuel combustion with high oxygen concentration in a 1MWth pilot-scale circulating fluidized bed," *Energy Procedia*, vol. 63, pp. 362–371, 2014, doi: 10.1016/j.egypro.2014.11.039.
- [74] G. Hofbauer, T. Beisheim, H. Dieter, and G. Scheffknecht, "Experiences from oxy-fuel combustion of bituminous coal in a 150 kWth circulating fluidized bed pilot facility," *Energy Procedia*, vol. 51, pp. 24–30, 2014, doi: 10.1016/j.egypro.2014.07.003.
- [75] B. Roy and S. Bhattacharya, "Oxy-fuel fluidized bed combustion using Victorian brown coal: An experimental investigation," *Fuel Process. Technol.*, vol. 117, pp. 23–29, 2014, doi: 10.1016/j.fuproc.2013.02.019.

- [76] L. Tan, S. Li, W. Li, E. Shou, and Q. Lu, "Effects of Oxygen Staging and Excess Oxygen on O₂/CO₂ Combustion with a High Oxygen Concentration in a Circulating Fluidized Bed," *Energy and Fuels*, vol. 28, no. 3, pp. 2069–2075, Mar. 2014, doi: 10.1021/EF500051C.
- [77] S. Li *et al.*, "Coal combustion emission and ash formation characteristics at high oxygen concentration in a 1 MWth pilot-scale oxy-fuel circulating fluidized bed," *Appl. Energy*, vol. 197, pp. 203–211, 2017, doi: 10.1016/j.apenergy.2017.03.028.
- [78] S. Li, M. Xu, L. Jia, L. Tan, and Q. Lu, "Influence of operating parameters on N₂O emission in O₂/CO₂ combustion with high oxygen concentration in circulating fluidized bed," *Appl. Energy*, vol. 173, pp. 197–209, Jul. 2016, doi: 10.1016/J.APENERGY.2016.02.054.
- [79] W. Li, M. Xu, and S. Li, "Calcium sulfation characteristics at high oxygen concentration in a 1MWth pilot scale oxy-fuel circulating fluidized bed," *Fuel Process. Technol.*, vol. 171, no. November 2017, pp. 192–197, 2018, doi: 10.1016/j.fuproc.2017.11.005.
- [80] W. Li, D. Liu, and S. Li, "Characteristics of Fly Ash under Oxy-Fuel Circulating Fluidized Bed Combustion," *Energy and Fuels*, vol. 32, no. 9, pp. 9666–9671, 2018, doi: 10.1021/acs.energyfuels.8b00934.
- [81] W. Li, S. Li, M. Xu, and X. Wang, "Study on the limestone sulfation behavior under oxy-fuel circulating fluidized bed combustion condition," *J. Energy Inst.*, vol. 91, no. 3, pp. 358–368, 2018, doi: 10.1016/j.joei.2017.02.005.
- [82] J. H. Moon *et al.*, "Carbon dioxide purity and combustion characteristics of oxy firing compared to air firing in a pilot-scale circulating fluidized bed," *Energy*, vol. 166, pp. 183–192, 2019, doi: 10.1016/j.energy.2018.10.045.
- [83] H. Arro, A. Prikk, and T. Pihu, "Calculation of CO₂ emission from CFB boilers of oil shale power plants," *Oil Shale*, vol. 23, no. 4, pp. 356–365, 2006.
- [84] D. Neshumayev, A. Ots, T. Parve, T. Pihu, K. Plamus, and A. Prikk, "Combustion of Baltic oil shales in boilers with fluidized bed combustion," *Power Technol. Eng.*, vol. 44, no. 5, pp. 382–385, 2011, doi: 10.1007/s10749-011-0195-7.
- [85] Y. H. Khraisha, "Batch combustion of oil shale particles in a fluidized bed reactor," *Fuel Process. Technol.*, vol. 86, no. 6, pp. 691–706, 2005, doi: 10.1016/j.fuproc.2004.07.002.
- [86] L. A. Al-makhadmeh, J. Maier, M. A. Batiha, and G. Scheffknecht, "Oxyfuel technology: Oil shale desulfurization behavior during staged combustion," *Fuel*, vol. 190, pp. 229–236, 2017, doi: 10.1016/j.fuel.2016.11.022.
- [87] L. A. Al-Makhadmeh, M. A. Batiha, J. Maier, S. E. Rawadieh, I. S. Altarawneh, and G. Scheffknecht, "Effect of air and oxyfuel staged combustion on oil shale fly ash formation with direct in-furnace limestone addition for sulphur retention," *Fuel*, vol. 220, no. November 2017, pp. 192–199, 2018, doi: 10.1016/j.fuel.2018.01.057.
- [88] L. Al-Makhadmeh, J. Maier, M. Al-Harashsheh, and G. Scheffknecht, "Oxy-fuel technology: An experimental investigations into oil shale combustion under oxy-fuel conditions," *Fuel*, vol. 103, pp. 421–429, 2013, doi: 10.1016/j.fuel.2012.05.054.
- [89] J. Xiumin, Y. Lijun, Y. Che, H. Xiangxin, and Y. Hailong, "Experimental investigation of SO₂ and NO_x emissions from Huadian oil shale during circulating fluidized-bed combustion," *Oil Shale*, vol. 21, no. 3, pp. 249–257, 2004.

- [90] A. Trikkel, R. Kuusik, A. Martins, T. Pihu, and J. M. Stencil, "Utilization of Estonian oil shale semicoke," *Fuel Process. Technol.*, vol. 89, no. 8, pp. 756–763, 2008, doi: 10.1016/j.fuproc.2008.01.010.
- [91] Y. Yang, X. Lu, Q. Wang, L. Mei, D. Song, and Y. Hong, "Experimental Study on Combustion of Low Calorific Oil Shale Semicoke in Fluidized Bed System," *Energy and Fuels*, vol. 30, no. 11, pp. 9882–9890, Nov. 2016, doi: 10.1021/ACS.ENERGYFUELS.6B01870.
- [92] T. Han, C. Wang, R. Sun, C. Zhu, Y. Liu, and D. Che, "Experimental study on ash deposition of Zhundong coal in oxy-fuel combustion," *J. Energy Inst.*, vol. 92, no. 6, pp. 1697–1709, 2019, doi: 10.1016/j.joei.2019.01.004.
- [93] H. Wu *et al.*, "Experimental research on the characteristics of ash in oxy-fuel combustion," *Fuel*, vol. 263, no. November 2019, 2020, doi: 10.1016/j.fuel.2019.116799.
- [94] S. L. Niu, K. H. Han, and C. M. Lu, "Characteristic of coal combustion in oxygen/carbon dioxide atmosphere and nitric oxide release during this process," *Energy Convers. Manag.*, vol. 52, no. 1, pp. 532–537, 2011, doi: 10.1016/j.enconman.2010.07.028.
- [95] A. Suriyawong, M. Gamble, M. H. Lee, R. Axelbaum, and P. Biswas, "Submicrometer particle formation and mercury speciation under O₂-CO₂ coal combustion," *Energy and Fuels*, vol. 20, no. 6, pp. 2357–2363, Nov. 2006, doi: 10.1021/EF060178S/ASSET/IMAGES/MEDIUM/EF060178SE00005.GIF.
- [96] Z. Zheng, H. Wang, S. Guo, Y. Luo, Q. Du, and S. Wu, "Fly Ash Deposition during Oxy-fuel Combustion in a Bench-Scale Fluidized-Bed Combustor," *Energy and Fuels*, vol. 27, no. 8, pp. 4609–4616, Aug. 2013, doi: 10.1021/EF400774B.
- [97] K. Leben *et al.*, "Long-term mineral transformation of Ca-rich oil shale ash waste," *Sci. Total Environ.*, vol. 658, pp. 1404–1415, Mar. 2019, doi: 10.1016/J.SCITOTENV.2018.12.326.
- [98] H. Lees, O. Järvik, A. Konist, A. Siirde, and B. Maaten, "Comparison of the ecotoxic properties of oil shale industry by-products to those of coal ash," *Oil Shale*, vol. 39, no. 1, pp. 1–19, 2022, doi: 10.3176/oil.2022.1.01.
- [99] J.-P. Hettelingh and L. Hordijk, "Environmental conflicts: the case of acid rain in Europe," Laxenburg, Austria, 1987.
- [100] L. L. Sloss, "NO_x emissions from coal combustion," IEA Coal Research., Ed. London, UK: IEA Coal Research, 1991, p. 62.
- [101] J. A. Miller and C. T. Bowman, "Mechanism and modeling of nitrogen chemistry in combustion," *Prog. Energy Combust. Sci.*, vol. 15, no. 4, pp. 287–338, Jan. 1989, doi: 10.1016/0360-1285(89)90017-8.
- [102] J. Konttinen, S. Kallio, M. Hupa, and F. Winter, "NO formation tendency characterization for solid fuels in fluidized beds," *Fuel*, vol. 108, pp. 238–246, Jun. 2013, doi: 10.1016/J.FUEL.2013.02.011.
- [103] L. Duan, C. Zhao, Q. Ren, Z. Wu, and X. Chen, "NO_x precursors evolution during coal heating process in CO₂ atmosphere," *Fuel*, vol. 90, no. 4, pp. 1668–1673, Apr. 2011, doi: 10.1016/J.FUEL.2010.12.014.
- [104] L. F. De Diego, C. A. Londono, X. S. Wang, and B. M. Gibbs, "Influence of operating parameters on NO_x and N₂O axial profiles in a circulating fluidized bed combustor," *Fuel*, vol. 75, no. 8, pp. 971–978, 1996, doi: 10.1016/0016-2361(96)00045-2.

- [105] F. Normann, K. Andersson, B. Leckner, and F. Johnsson, "Emission control of nitrogen oxides in the oxy-fuel process," *Prog. Energy Combust. Sci.*, vol. 35, no. 5, pp. 385–397, 2009, doi: 10.1016/j.pecs.2009.04.002.
- [106] L. E. Amand and B. Leckner, "Formation of N₂O in a Circulating Fluidized Bed Combustor," *Energy and Fuels*, no. 15, pp. 1097–1107, 1993.
- [107] K. El Sheikh *et al.*, "Advances in reduction of NO_x and N₂O emission formation in an oxy-fired fluidized bed boiler," *Chinese J. Chem. Eng.*, vol. 27, no. 2, pp. 426–443, 2019, doi: 10.1016/j.cjche.2018.06.033.
- [108] T. Wall *et al.*, "An overview on oxyfuel coal combustion-State of the art research and technology development," *Chem. Eng. Res. Des.*, vol. 87, no. 8, pp. 1003–1016, Aug. 2009, doi: 10.1016/J.CHERD.2009.02.005.
- [109] B. Engin, U. Kayahan, and H. Atakül, "A comparative study on the air, the oxygen-enriched air and the oxy-fuel combustion of lignites in CFB," *Energy*, vol. 196, p. 117021, 2020, doi: 10.1016/j.energy.2020.117021.
- [110] M. Xu and S. Li, "Experimental study on N₂O emission in O₂/CO₂ combustion with high oxygen concentration in circulating fluidized bed," *J. Energy Inst.*, vol. 92, no. 1, pp. 128–135, 2019, doi: 10.1016/j.joei.2017.10.016.
- [111] H. Zhou, Y. Li, N. Li, R. Qiu, and K. Cen, "Conversions of fuel-N to NO and N₂O during devolatilization and char combustion stages of a single coal particle under oxy-fuel fluidized bed conditions," *J. Energy Inst.*, vol. 92, no. 2, pp. 351–363, 2019, doi: 10.1016/j.joei.2018.01.001.
- [112] D. G. Raheem, B. Yilmaz, U. Kayahan, and S. Özdoğan, "Effect of Recycled Flue Gas Ratio on Combustion Characteristics of Lignite Oxy-Combustion in a Circulating Fluidized Bed," *Energy and Fuels*, vol. 34, no. 11, pp. 14786–14795, 2020, doi: 10.1021/acs.energyfuels.0c02464.
- [113] H. Ma, L. Zhou, S. Lv, J. W. Chew, and Z. Wang, "Review on Reaction Mechanisms of Sulfur Species During Coal Combustion," *J. Energy Resour. Technol.*, vol. 141, no. 10, May 2019, doi: 10.1115/1.4043554.
- [114] F. García-Labiano *et al.*, "Calcium-based sorbents behaviour during sulphation at oxy-fuel fluidised bed combustion conditions," *Fuel*, vol. 90, no. 10, pp. 3100–3108, 2011, doi: 10.1016/j.fuel.2011.05.001.
- [115] L. Chen, C. Wang, G. Yan, F. Zhao, and E. J. Anthony, "The simultaneous calcination/sulfation reaction of limestone under oxy-fuel CFB conditions," *Fuel*, vol. 237, no. March 2018, pp. 812–822, 2019, doi: 10.1016/j.fuel.2018.10.060.
- [116] Y. Bin Kim, Y. R. Gwak, S. I. Keel, J. H. Yun, and S. H. Lee, "Direct desulfurization of limestones under oxy-circulating fluidized bed combustion conditions," *Chem. Eng. J.*, vol. 377, no. June 2018, p. 119650, 2019, doi: 10.1016/j.cej.2018.08.036.
- [117] E. J. Anthony and D. L. Granatstein, "Sulfation phenomena in fluidized bed combustion systems," *Prog. Energy Combust. Sci.*, vol. 27, no. 2, pp. 215–236, 2001, doi: 10.1016/S0360-1285(00)00021-6.
- [118] F. Scala *et al.*, "Fluidized bed desulfurization using lime obtained after slow calcination of limestone particles," *Fuel*, vol. 114, pp. 99–105, 2013, doi: 10.1016/j.fuel.2012.11.072.
- [119] M. Olszak-Humienik and M. Jablonski, "Thermal behavior of natural dolomite," *J. Therm. Anal. Calorim.*, vol. 119, no. 3, pp. 2239–2248, Dec. 2015, doi: 10.1007/S10973-014-4301-6/FIGURES/7.

- [120] J. M. Valverde, A. Perejon, S. Medina, and L. A. Perez-Maqueda, "Thermal decomposition of dolomite under CO₂: insights from TGA and in situ XRD analysis," *Phys. Chem. Chem. Phys.*, vol. 17, no. 44, pp. 30162–30176, Nov. 2015, doi: 10.1039/C5CP05596B.
- [121] B. V L'vov, "Mechanism and kinetics of thermal decomposition of carbonates," *Thermochim. Acta*, vol. 386, no. 1, pp. 1–16, 2002, doi: [https://doi.org/10.1016/S0040-6031\(01\)00757-2](https://doi.org/10.1016/S0040-6031(01)00757-2).
- [122] F. Wu, M. D. Argyle, P. A. Dellenback, and M. Fan, "Progress in O₂ separation for oxy-fuel combustion—A promising way for cost-effective CO₂ capture: A review," *Prog. Energy Combust. Sci.*, vol. 67, pp. 188–205, 2018, doi: 10.1016/j.pecs.2018.01.004.
- [123] M. Chorowski and W. Gizicki, "Technical and economic aspects of oxygen separation for oxy-fuel purposes," *Arch. Thermodyn.*, vol. 36, no. 1, pp. 157–170, 2015, doi: 10.1515/aoter-2015-0011.
- [124] P. Higginbotham, V. White, K. Fogash, and G. Guvelioglu, "Oxygen supply for oxyfuel CO₂ capture," *Int. J. Greenh. Gas Control*, vol. 5, no. SUPPL. 1, pp. S194–S203, Jul. 2011, doi: 10.1016/J.IJGGC.2011.03.007.
- [125] J. Ströhle, A. Lasheras, A. Galloy, and B. Epple, "Simulation of the Carbonate Looping Process for Post-Combustion CO₂ Capture from a Coal-Fired Power Plant," *Chem. Eng. Technol.*, vol. 32, no. 3, pp. 435–442, Mar. 2009, doi: 10.1002/CEAT.200800569.
- [126] A. Skorek-Osikowska, Ł. Bartela, and J. Kotowicz, "A comparative thermodynamic, economic and risk analysis concerning implementation of oxy-combustion power plants integrated with cryogenic and hybrid air separation units," *Energy Convers. Manag.*, vol. 92, pp. 421–430, Mar. 2015, doi: 10.1016/J.ENCONMAN.2014.12.079.
- [127] E. Kianfar and V. Cao, "Polymeric membranes on base of PolyMethyl methacrylate for air separation: a review," *J. Mater. Res. Technol.*, vol. 10, pp. 1437–1461, Jan. 2021, doi: 10.1016/J.JMRT.2020.12.061.
- [128] T. Banaszekiewicz, M. Chorowski, and W. Gizicki, "Comparative analysis of oxygen production for oxy-combustion application," *Energy Procedia*, vol. 51, pp. 127–134, 2014, doi: 10.1016/j.egypro.2014.07.014.
- [129] D. J. Dillon *et al.*, "Oxy-combustion processes for CO₂ capture from advanced supercritical PF and NGCC power plant," *Greenh. Gas Control Technol.*, pp. 211–220, Jan. 2005, doi: 10.1016/B978-008044704-9/50022-7.
- [130] D. Shin and S. Kang, "Numerical analysis of an ion transport membrane system for oxy-fuel combustion," *Appl. Energy*, vol. 230, pp. 875–888, Nov. 2018, doi: 10.1016/J.APENERGY.2018.09.016.
- [131] S. J. Chen and B. Y. Yu, "Rigorous simulation and techno-economic evaluation on the hybrid membrane/cryogenic distillation processes for air separation," *J. Taiwan Inst. Chem. Eng.*, vol. 127, pp. 56–68, Oct. 2021, doi: 10.1016/J.JTICE.2021.08.001.
- [132] K. Janusz-Szymańska and A. Dryjańska, "Possibilities for improving the thermodynamic and economic characteristics of an oxy-type power plant with a cryogenic air separation unit," *Energy*, vol. 85, pp. 45–61, Jun. 2015, doi: 10.1016/J.ENERGY.2015.03.049.
- [133] J. Kemper, "Biomass and carbon dioxide capture and storage: A review," *Int. J. Greenh. Gas Control*, vol. 40, pp. 401–430, Sep. 2015, doi: 10.1016/J.IJGGC.2015.06.012.

- [134] IEA, "Combining Bioenergy with CCS. Reporting and Accounting for Negative Emissions under UNFCCC and the Kyoto Protocol," PARIS, FRANCE, 2011. Accessed: Mar. 26, 2024. [Online]. Available: <https://www.iea.org/reports/combining-bioenergy-with-ccs>.
- [135] IEAGHG, "Potential for Biomass and Carbon Dioxide Capture and Storage," cheltenham, UK, 2011. Accessed: Mar. 26, 2024. [Online]. Available: <https://ieaghg.org/publications/technical-reports/reports-list/9-technical-reports/1033-2011-06-potential-for-biomass-and-carbon-dioxide-capture-and-storage>.
- [136] U. Kayahan and S. Özdoğan, "Oxygen enriched combustion and co-combustion of lignites and biomass in a 30 kWth circulating fluidized bed," *Energy*, vol. 116, pp. 317–328, Dec. 2016, doi: 10.1016/J.ENERGY.2016.09.117.
- [137] Q. Liu *et al.*, "Experimental tests on co-firing coal and biomass waste fuels in a fluidised bed under oxy-fuel combustion," *Fuel*, vol. 286, p. 119312, Feb. 2021, doi: 10.1016/J.FUEL.2020.119312.
- [138] Y. Tan, L. Jia, and Y. Wu, "Some combustion characteristics of biomass and coal cofiring under oxy-fuel conditions in a pilot-scale circulating fluidized combustor," *Energy and Fuels*, vol. 27, no. 11, pp. 7000–7007, 2013, doi: 10.1021/ef4011109.
- [139] Z. Xiao, S. Wang, M. Luo, and J. Cai, "Combustion characteristics and synergistic effects during co-combustion of lignite and lignocellulosic components under oxy-fuel condition," *Fuel*, vol. 310, p. 122399, Feb. 2022, doi: 10.1016/J.FUEL.2021.122399.
- [140] M. Torres, P. Portugau, J. Castiglioni, A. Cuña, and L. Yermán, "Co-combustion behaviours of a low calorific Uruguayan Oil Shale with biomass wastes," *Fuel*, vol. 266, p. 117118, Apr. 2020, doi: 10.1016/J.FUEL.2020.117118.
- [141] H. Wang, Z. M. Zheng, L. Yang, X. L. Liu, S. Guo, and S. H. Wu, "Experimental investigation on ash deposition of a bituminous coal during oxy-fuel combustion in a bench-scale fluidized bed," *Fuel Process. Technol.*, vol. 132, pp. 24–30, 2015, doi: 10.1016/j.fuproc.2014.12.021.
- [142] N. E. Altun, C. Hiçyılmaz, J.-Y. Hwang, A. Suat Bağcı, and M. V Kök, "Oil shales in the world and turkey; reserves, current situation and future prospects: a review," *Oil Shale*, vol. 23, no. 3, 2006.
- [143] V. Kattai and U. Lökk, "Historical review of the Kukersite oil shale exploration in Estonia," *Oil Shale*, vol. 15, no. 2, pp. 102–110, 1998, doi: 10.3176/oil.1998.2S.02.
- [144] R. Chirone, P. Salatino, F. Scala, R. Solimene, and M. Urciuolo, "Fluidized bed combustion of pelletized biomass and waste-derived fuels," *Combust. Flame*, vol. 155(1/2), no. 1–2, pp. 21–36, Oct. 2008, doi: 10.1016/J.COMBUSTFLAME.2008.05.013.
- [145] L. Deng, J. Ye, X. Jin, T. Zhu, and D. Che, "Release and Transformation of Potassium during Combustion of Biomass," *Energy Procedia*, vol. 142, pp. 401–406, 2017, doi: 10.1016/j.egypro.2017.12.063.
- [146] N. Giummarella, G. Henriksson, L. Salmén, and M. Lawoko, "On the effect of hemicellulose removal on cellulose-lignin interactions," *Nord. Pulp Pap. Res. J.*, vol. 32, no. 4, pp. 542–549, 2017, doi: 10.3183/NPPRJ-2017-32-04-p542-549.
- [147] M. J. Prins, K. J. Ptasinski, and F. J. J. G. Janssen, "Torrefaction of wood: Part 2. Analysis of products," *J. Anal. Appl. Pyrolysis*, vol. 77, no. 1, pp. 35–40, Aug. 2006, doi: 10.1016/J.JAAP.2006.01.001.

- [148] X. Han, I. Kulaots, X. Jiang, and E. M. Suuberg, "Review of oil shale semicoke and its combustion utilization," *Fuel*, vol. 126, pp. 143–161, Jun. 2014, doi: 10.1016/J.FUEL.2014.02.045.
- [149] R. Kuusik *et al.*, "Fluidized-bed combustion of oil shale retorting solid waste *1," *Oil Shale*, vol. 21, no. 3, 2004.
- [150] H. Arro, A. Prikk, T. Pihu, and I. Öpik, "Utilization of semi-coke of estonian shale oil industry," *Oil Shale*, vol. 19, no. 2, 2002.
- [151] D. Neshumayev, T. Pihu, A. Siirde, O. Järvik, and A. Konist, "Solid heat carrier oil shale retorting technology with integrated CFB technology," *Oil Shale*, vol. 36, no. 2S, 2019, doi: 10.3176/oil.2019.2S.02.
- [152] T. Pihu *et al.*, "Oil shale CFBC ash cementation properties in ash fields," *Fuel*, vol. 93, pp. 172–180, 2012, doi: 10.1016/j.fuel.2011.08.050.
- [153] B. Roy, L. Chen, and S. Bhattacharya, "Nitrogen oxides, sulfur trioxide, and mercury emissions during oxy-fuel fluidized bed combustion of victorian brown coal," *Environ. Sci. Technol.*, vol. 48, no. 24, pp. 14844–14850, 2014, doi: 10.1021/es504667r.
- [154] R. Yoshiie, T. Kawamoto, D. Hasegawa, Y. Ueki, and I. Naruse, "Gas-Phase Reaction of NO_x Formation in Oxyfuel Coal Combustion at Low Temperature," *Energy and Fuels*, vol. 25, no. 6, pp. 2481–2486, Jun. 2011, doi: 10.1021/EF200277Q.
- [155] J. A. Lasek, M. Janusz, J. Zuwała, K. Głód, and A. Iluk, "Oxy-fuel combustion of selected solid fuels under atmospheric and elevated pressures," *Energy*, vol. 62, pp. 105–112, Dec. 2013, doi: 10.1016/J.ENERGY.2013.04.079.
- [156] J. E. Johnsson, "Formation and reduction of nitrogen oxides in fluidized-bed combustion," *Fuel*, vol. 73, no. 9, pp. 1398–1415, Sep. 1994, doi: 10.1016/0016-2361(94)90055-8.
- [157] J. Reinik *et al.*, "Changes in trace element contents in ashes of oil shale fueled PF and CFB boilers during operation," *Fuel Process. Technol.*, vol. 115, pp. 174–181, Nov. 2013, doi: 10.1016/J.FUPROC.2013.06.001.
- [158] H. Li *et al.*, "Comprehensive study on co-combustion behavior of pelletized coal-biomass mixtures in a concentrating photothermal reactor," *Fuel Process. Technol.*, vol. 211, p. 106596, Jan. 2021, doi: 10.1016/J.FUPROC.2020.106596.

Acknowledgements

The author would like to express sincere gratitude to her supervisor, Professor Alar Konist, and co-supervisor Dr. Dmitri Nešumajev, for their invaluable guidance, mentorship, and support throughout the duration of this PhD study. Special thanks are extended to Professor Oliver Järvik for his insightful contributions and expertise in the field.

The author also wishes to acknowledge and thank all the members and colleagues of the Department of Energy Technology at Tallinn University of Technology for their collaboration and assistance.

Furthermore, the author extends appreciation to her family for their unwavering support, encouragement, and understanding during the research process.

This work was supported by the European Regional Development Fund and the Estonian Research Council Grant (PSG266),

Abstract

Oil Shale Oxyfuel CFB Combustion

The EU's climate action Plan has established an interim goal of reducing greenhouse gas emissions to at least 55% below 1990 levels by 2030. Although renewable energy and improvements in energy efficiency are vital for transitioning to a low-carbon economy, they may not be sufficient to keep pace with the escalating global demand for electricity. Fossil fuel combustion remains the primary method for meeting the world's increasing energy requirements despite its inherent association with the release of GHGs and air pollutants such as CO₂, SO₂, and NO_x. Carbon capture, utilisation, and storage have emerged as pivotal technologies for curtailing emissions while maintaining fossil fuel utilisation. Among the CO₂ capture approaches, oxyfuel circulating fluidized bed (CFB) combustion exhibits potential for cleaner combustion. Estonia's heavy reliance on oil shale for energy presents a unique challenge owing to its high carbon intensity. This has necessitated the exploration of techniques to mitigate CO₂ emissions. In this context, this study was conducted within the scope of the ClimMit project, which developed advanced experimental progress for investigating the combustion of kukersite oil shale for both air and different oxyfuel combustion regimes in a 60 kWth CFB pilot facility in the Energy Technology Department. The research objective was to focus on the effects of oxyfuel on the combustion of organic matter and reactions of mineral matter through its comparisons with air-based combustion and to study ash chemical and mineral characterisation. The emissions produced under different O₂/CO₂ and O₂ with recycled flue gas (RFG) regimes were evaluated by understanding the NO_x and N₂O formation pathways for oil shale oxyfuel CFB combustion and their control measures, direct and indirect sulfation behaviours, and sulphur capture efficiency. Specific carbon emissions and the effect of carbonate decomposition on total CO₂ reduction were examined. This study aimed to maximise the CO₂ capture process by partially replacing oil shale with biomass for negative CO₂ emissions. In addition, the utilisation of semicoke, a waste product with a low heating value, in oxyfuel combustion was examined, thereby expanding the application of oxyfuel technology in the shale oil industry. This study provides novel insights into advancing oxyfuel combustion technology, offering a pathway towards a cleaner and more sustainable energy future for Estonia's oil shale industry. This thesis will serve, for the first time, as a technical reference model for the chemical and mineral compositions of the produced ash, formation of NO_x and N₂O emissions under oxyfuel combustion, and synergistic effects of oil shale and biomass oxyfuel co-combustion. Further, it presents experimental studies of semicoke combustion behaviour, temperature control and distribution, and evolved emissions under air- and oxy-fired regimes. The ash distribution exhibited a strong grain size separation compared with air firing, which suggests potential challenges in ash handling and disposal, particularly for dense-bed ashes. The limited decomposition of Ca-carbonates under oxyfuel conditions resulted in increased carbonate content in ashes. Consequently, a total CO₂ emission reduction exceeding 15% was achieved. However, oxyfuel combustion produces a larger amount of solid waste than air-firing. Further, NO_x reduction was observed in the oxyfuel mode, from 120 mg/MJ in air to 105 mg/MJ in O₂/CO₂ mode, and 98 mg/MJ in O₂/RFG. N₂O emissions decreased significantly with increasing inlet O₂%, and SO₂ emissions were nearly zero, with sulphur capture efficiency exceeding 99%. Moreover, experimental tests on semicoke combustion exhibited temperature distribution similarities between air and oxyfuel environments,

with reduced NO_x emissions under oxygen-enriched conditions. Oil shale and biomass co-combustion via TG–MS tests demonstrated positive synergistic effects in the devolatilisation and combustion of light hydrocarbons, and the synergy increased towards higher biomass ratios. At a higher heating rate of 50 °C/min, synergistic effects were enhanced. Advancing oxyfuel combustion in the oil shale industry holds great promise for the reduction of Estonia’s carbon footprint. However, the selection of the most suitable oxygen production technology depends on factors such as energy efficiency, scalability, cost-effectiveness, and compatibility with oxyfuel systems. Alongside the cryogenic process, other promising options include chemical looping and renewable-based air separation technologies.

Lühikokkuvõte

Põlevkivi oxyfuel CFB põlemine

Euroopa Liidu kliimameetmete kavas on seatud eesmärgiks vähendada 2030. aastaks kasvahoonegaaside heitkoguseid vähemalt 55% võrreldes 1990. aasta tasemega. Kuigi taastuenergia, tuumaenergia ja energiatõhususe parendamine on olulised vähese CO₂-heitega majandusele üleminekuks, ei pruugi need lahendused olla piisava kasvava ülemaailmse elektrinõudluse rahuldamiseks. Fossiilkütuste põletamine jääb peamiseks energia tootmise meetodiks, vaatamata sellele, et see on seatud kasvahoonegaaside ja õhusaasteainete, nagu SO₂ ja NO_x, emissioonidega. Selles valguses on CO₂ püüdmine ja ladustamine keske tähtsusega tehnoloogiad, mis võimaldavad vähendada fossiilkütuste kasutamise jätkamisel CO₂ heitkoguseid.

CO₂ püüdmise tehnoloogiatega paistab oma potentsiaali poolest silma tsirkuleerivas keevkihis (CFB) hapniku ja CO₂ keskkonnas põletamine ehk lühidalt hapnikus põletamine. Eesti energiatootmise suur sõltuvus põlevkivist tingib, tulenevalt põlevkivi põletamise suurest CO₂-intensiivsusest, vajaduse uurida CO₂-heitme vähendamise tehnoloogiaid. Sellest lähtuvalt on energiatehnoloogia instituudis 60 kWth CFB pilootseadmes viidud ClimMit projekti raames läbi kukersiitpõlevkivi põletamise uuringud nii õhukeskkonnas kui ka erinevate hapnikus põletamise režiimidel. Doktoritöö eesmärk oli katseliselt uurida hapnikus põletamise mõju põlevkivi põlemisele ja mineraalosalale, võrreldes neid tulemusi õhukeskkonnas (O₂/N₂) põletamisel saadud tulemustega. Samuti, hinnata erinevatel O₂/CO₂ ja O₂/RFG (hapnikus põletamine koos põlemisgaaside retsirkulatsiooniga) režiimidel tekkivaid heitkoguseid, mõista NO_x ja N₂O moodustumist põlevkivi hapnikus põletamisel ja nende kontrollimeetmeid, otsesest ja kaudset sulfaatustumist ja väävli sidumise tõhusust, süsiniku eriheitmeid ja karbonaatide lagunemise ulatuse mõju CO₂ emissioonide vähenemisele. Töö üheks eesmärgiks oli käsitleda ka põlevkivi osalise biomassiga asendamise võimalikkust hapnikus põletamisel negatiivsete CO₂ emissioonide saavutamiseks. Lisaks käsitletakse doktoritöös madala kütteväärtusega poolkoksi kasutamist hapnikus põletamisel, laiendades sellega antud tehnoloogia rakendatavust põlevkiviõlitööstusele. See töö annab uusi teadmisi hapnikus põletamise tehnoloogia arendamiseks, pakkudes võimalusi Eesti põlevkivitööstusele puhtama ja säästvama energia tuleviku suunas liikumiseks. Töö tulemused annavad esmakordselt võimaluse hinnata hapnikus põletamisel tekkiva tuha keemilist ja mineraalset koostist, NO_x ja N₂O emissioone hapnikus põletamisel, põlevkivi ja biomassi koospõletamise sünergilisi mõjusid, poolkoksi käitumist põlemisel ja temperatuuri kontrolli ning jaotust erinevatel õhukeskkonnas ja hapnikus põletamise režiimidel ja informatsiooni tekkivate heitkoguste kohta. Olulisi muutuseid täheldati tuhaosakeste suuruse jaotuses võrreldes õhukeskkonnas põletamisega, mis viitab eriti koldetuha puhul potentsiaalsetele väljakutsetele tuha käitlemisel hapnikus põletamise rakendamisel. Karbonaatide piiratud lagunemine hapnikus põletamise tingimustes tõi kaasa karbonaatide sisalduse suurenemise tuhas, mille tulemusena vähenes CO₂ koguheidete üle 15%. See omakorda aga tähendab suurema koguse tahkete jäätmete tekkimist võrreldes õhukeskkonnas põletamisega. Kui NO_x eriheide õhukeskkonnas põletamisel oli keskmiselt 120 mg/MJ, siis hapnikus põletamisel saadi vastavaks väärtuseks kuni 105 mg/MJ O₂/CO₂ režiimis ja 98 mg/MJ O₂/RFG režiimi korral. N₂O emissioon vähenes oluliselt siseneva O₂ osakaalu suurenemisel. SO₂ emissioon oli nullilähedane ehk väävli sidumise efektiivsus ületas 99%. Lisaks näitasid poolkoksi põletamise eksperimentaalsed katsed, et õhukeskkonnas ja hapnikus põletamisel on temperatuurijaotused sarnased, samas NO_x heitkogused on

hapnikus põletamisel madalamad. Põlevkivi ja biomassi koospõletamine TG-MS seadmes näitas positiivseid sünergilisi mõjusid kergete süsivesinike lagunemisel ja põlemisel ning sünergia ulatus suurenes biomassi suurema suhte suunas. Suurema kuumutamiskiiruse (50 °C/min) korral sünergilised efektid suurenesid.

Hapnikus põletamise rakendamine põlevkivitööstuses omaks Eesti süsinikujalajälje vähendamisel suurt mõju. Sobivaima põletamiseks vajaliku hapniku tootmise tehnoloogia valik sõltub aga sellistest teguritest nagu energiatõhusus, mastaapsus, kulutõhusus ja ühilduvus hapnikus põletamise süsteemidega. Lisaks krüogeensele protsessile on paljulubavateks variantideks hapnikukandja ringlusel ja taastuenergiat põhinevad õhu separeerimistehnoloogiad.

Appendix (Publications)

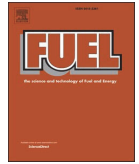
Publication I

Baqain, M.; Rüstü Yörük, C.; Nešumajev, D.; Järvik, O.; Konist, A. (2023). **Ash characterisation formed under different oxy-fuel circulating fluidized bed conditions.** Fuel, 338. DOI: 10.1016/j.fuel.2022.127244.



Contents lists available at ScienceDirect

Fuel

journal homepage: www.elsevier.com/locate/fuel

Ash characterisation formed under different oxy-fuel circulating fluidized bed conditions

Mais Baqain^a, Can Rüstü Yörük^b, Dmitri Nešumajev^a, Oliver Järvik^a, Alar Konist^{a,*}

^a Department of Energy Technology, Tallinn University of Technology, 19086 Tallinn, Estonia

^b Department of Materials and Environmental Technology, Tallinn University of Technology, 19086 Tallinn, Estonia

ARTICLE INFO

Keywords:

Ca-rich fuel
Oil shale
Circulating fluidized bed combustion
Oxy-fuel
Ash characterization

ABSTRACT

The CO₂-intensive oil shale power industry accounts for more than 70% of the Estonian energy sector, producing large amounts of ash that are mainly landfilled. Adopting oxy-fuel technology in the Estonian energy sector, in conjunction with CO₂ storage, can be a critical tool for reducing carbon footprint. Nevertheless, several differences in ash formation under oxy-fuel conditions can be expected, which can lead to additional ash handling/utilization and related environmental concerns. In this context, the composition of oil shale ash was obtained from a series of combustion experiments in a 60 kWth circulating fluidized bed (CFB) test unit under both air and oxy-fuel combustion regimes studied by means of physical, chemical analysis as quantitative X-ray diffraction and element analysis for ashes from different separation ports. During the experimental work, special attention was given to understanding the impacts of the boiler temperature, recycled flue gas (RFG), and elevated oxygen concentration. As a result, the primary goal of this research is to characterise the ash produced by oxy-fuel combustion of oil shale in order to gain a better understanding of its chemical and mineral compositions, including Ca-Mg silicates and clay minerals, as well as to investigate the behaviour of the formation of free lime and anhydrite, which are the major compounds influencing potential ash utilisation routes. The results show that although the decomposition of calcium carbonates was limited during oxy-fuel combustion because of the high CO₂ partial pressure, the contents of secondary silicates and anhydrite were slightly higher. The increased particle temperature and the higher SO₂ partial pressure (with RFG) can explain this. The particle size distributions (PSDs) were wider under oxy combustion, and the specific surface area (SSA) in Filter ashes were much higher under elevated inlet O₂% atmosphere. Oxy-fuel combustion had no significant impact on the concentration of elements in the ash. Overall, the mineralogy of the ashes formed in air and oxy-fuel combustion environments is similar, yet slight differences exist in the formation of clay minerals in the case of increased oxygen concentrations and with the application of RFG as a result of the increased residence time of the particles.

1. Introduction

Oxy-fuel combustion is one of the processes for capturing CO₂ from power plants, a technology that appears to be a promising option for using circulating fluidised bed (CFB) boilers [1–3]. Oxy-fuel combustion ensures a high concentration of CO₂ in the flue gas, making carbon capture more economical than in conventional plants [4]. CO₂ concentrations exceeding 90 % can be achieved using a mixture of pure oxygen and recycled flue gas (RFG) as the reactant for fuel combustion [5]. The oxygen used in oxy-fuel combustion is separated from the air, whereas CO₂ is separated from the exhaust gas, which consists primarily of CO₂ and water vapour, by lowering the temperature and cooling the flue gas

so that the vapour condenses [6], as shown in Fig. 1.

Oxygen in CFB boilers is used in industrial gas combustion, in which specifically designed oxy-fuel burners are utilised [7]. The purpose of this technology in these industries is to improve productivity, decrease energy consumption, and reduce NO_x emissions. In general, oxy-fuel has particular advantages, such as good environmental performance and fuel flexibility, and combustion with pure oxygen generates very high temperatures and offers the possibility of adding an external heat exchanger in a solid recirculation system to control combustion temperatures [8]. Oxy-fuel combustion with RFG can be retrofitted into existing conventional coal or natural gas-fired power facilities [1] or implemented with a smaller boiler design. By increasing the oxygen concentration, the volume of gases flowing through the furnace is

* Corresponding author.

E-mail address: alar.konist@taltech.ee (A. Konist).

<https://doi.org/10.1016/j.fuel.2022.127244>

Received 26 September 2022; Received in revised form 26 November 2022; Accepted 20 December 2022

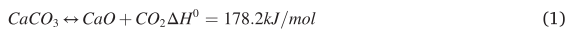
Available online 29 December 2022

0016-2361/© 2022 Elsevier Ltd. All rights reserved.

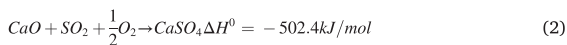
Nomenclature

| | |
|-------------|--|
| BA | Bottom ash |
| C1 | Cooler 1 |
| C2 | Cooler 2 |
| CFB | Circulating fluidized bed |
| ECD | Extent of carbonate decomposition |
| EHE | External heat exchanger |
| LOI | Loss of ignition |
| PC | Pulverized combustion |
| PSD | Particle size distribution |
| RFG | Recycled flue gas |
| SSA | Specific surface area |
| T_{DB} | Temperature of dense bed |
| T_{EHE} | Temperature of external heat exchanger |
| T_{Riser} | Maximum riser temperature |

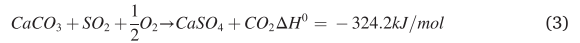
largely reduced, leading to a reduction in the combustor size and capital expenses [9]. Combustion of solid fuels, on the other hand, is much more challenging. The CFB boiler offers an additional advantage because sulfur can be captured inside the combustor using a calcium-based sorbent (limestone). In oxy-fuel combustion, the environment in which the fuel burns differs from that of air combustion owing to the replacement of air-nitrogen with RFG and higher O_2 concentration, which affect the rate of combustion, heat transfer, boiler hydrodynamics, as well as the behaviour of ashes (i.e. $CaCO_3$ -CaO decomposition ratios [1]). Another example is the control of SO_2 emissions, as SO_2 capture is achieved through both indirect and direct sulfation routes that differ from conventional air combustion [10]. In air-firing environment, the CFB combustor is operating in the region below the equilibrium curve where the limestone calcination occurred, and because the furnace temperature is higher than the decomposition temperature of calcite ($CaCO_3$), the dissociation of calcite will take place:



Following dissociation, indirect sulfation occurs in the CFB combustor as limestone (CaO) reacts with sulfur dioxide (SO_2):



The rate of indirect sulfation can be slow or fast, depending on many factors [11]. In oxy-fuel combustion mode, the CFB combustor is operating in the region above the $CaCO_3$ -CaO equilibrium curve at temperatures of 800 to 900 °C, hence direct sulfation occurs:



The CFB combustor temperature and CO_2 partial pressure primarily determine the direct and indirect sulfation routes [12], whereas some authors have generally found that indirect sulfation is slower [10], and increased CO_2 partial pressure may reduce desulfurisation efficiency by transitioning from indirect to direct sulfation [13]. In limestone sulfation, the degree of sulfation is found to be controlled by chemical reactions and solid-state diffusion [14], and the rate of limestone sulfation decreases rapidly during the reaction process, as the molar volume of $CaSO_4$ is much higher than that of CaO. Hence, the small pores in CaO are plugged by a layer of $CaSO_4$ [15], necessitating the addition of a stoichiometric sorbent to remove sufficient SO_2 . Eventually, this leads to an increase in solid waste generation. Usually, sulfur conversion ratios exceeding 85 % are achieved regardless of the combustion atmosphere; however, with oxy-fuel combustion, higher conversion ratios are reported owing to SO_2 recirculation with RFG, and accumulated recycled SO_2 in the combustor enhances sulfur capture efficiency [16]. Oxy-fuel CFB combustion provides the possibility of using different types and blends of fuels, including low-rank fuels with high sulfur content. Earlier researchers have studied different aspects of oxyfuel combustion with oil shale [17–19], while others studied the possibility of co-firing blended fuels with oil shale [20] or biomass with coal [21,22] to achieve negative CO_2 emissions.

The influence of fluidized bed oxy-fuel combustion on the formation of oil shale ash is limited [19,23–25]. Coal ash has been studied previously [26–30] for a better understanding of the combustion process and ash disposal issues. However, most of the studies on oxy-fuel combustion are at inlet oxygen concentrations below 40 %, and only a few surpass this value. Wu et al. [27] studied the physical and chemical properties of fly ash and bed ash at 100 kWth in a 30 % oxygen combustion mode. Li et al. [28] studied the mineral composition of coal fly ash for different combustion modes up to 50 % O_2 concentration, Shiyuan Li [29] compared the chemical composition of fly ash between air and 30–50 % O_2 concentrations and reported that the fly ash generated under different combustion modes had almost the same mass fractions of SiO_2 , Al_2O_3 , CaO, MgO, Fe_2O_3 , and TiO_2 , but variations were indeed observed in the levels of K_2O , Na_2O , and SO_3 . Specifically, in the O_2 /RFG modes, the percentage of alkali oxides in the fly ash, such as K_2O and Na_2O , was lower than that in the air mode and decreased significantly with an increase in O_2 concentration. Sheng et al. [31] reported that oxy-fuel combustion under an O_2/CO_2 atmosphere does not significantly change the types of minerals produced in particles, but affects the relative content of these minerals. Wang et al. [32] studied fly ash carbonation through a series of tests using a thermogravimetric analyser (TGA) under oxy-fuel combustion conditions and found that an increase

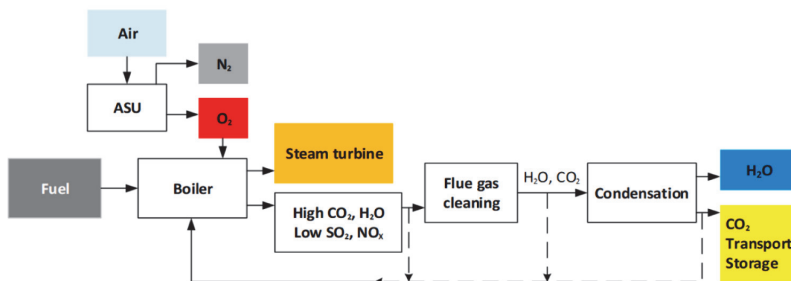
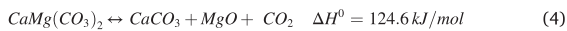


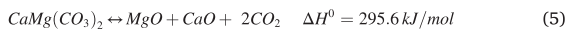
Fig. 1. Oxy-fuel combustion process.

in both CO₂ concentration and temperature significantly increases the carbonation ratio. Wall et al. [33] suggested that recarbonation could create serious problems in the back pass of the boiler, particularly when using rich Ca-coal content or by adding limestone for SO₂ emission control. Oxy-fuel combustion can also affect the distribution of sub-micron fine particles [34]. It was observed that the quantity and average particle size of submicron particles decreased under oxy-fuel combustion [35]. While Yu et al. [36] conducted an oxy-fuel combustion experiment in a 100 kW pilot facility and reported that the oxy-fuel atmosphere had no significant impact on the ash PSD and chemical composition, with the exception of ash sulfur content, because of the higher SO_x in the O₂/RFG environment. Zheng et al. [37] reported that wider PSDs of fly ash were found under 30 % O₂/70 % CO₂ with an elevated concentration of fine particles, which negatively affected the ash deposition propensity of anthracite fuel. The same results were reported by Li et al. [28] who found that the particle sizes of the oxy-fired ash in (30–50 % O₂) environment were larger than those of the air-fired ash and increased with the inlet oxygen concentration.

The fuel used in this study was kukersite-type Estonian oil shale [38,39], which is a low-grade Ca-rich fuel with high volatile organic compounds and ash content, including mainly carbonate minerals (calcite and dolomite greater than 60 %). By using Ca-rich oil shale fuel, no additional sorbent material is required to be fed to the CFB boiler for SO₂ capture, as carbonate minerals act as sorbents for controlling SO₂ emissions, and a sufficient Ca/S ratio (ca 8). During the combustion of oil shale, the thermal decomposition of dolomite should be considered as well. The sequence of reactions of dolomite decomposition under equilibrium conditions are following (Eq. (4) and (1)) [40]:



Other studies [41,42] reported that at CO₂ partial pressures below (20 kPa), the decomposition of dolomite into CaO and MgO is observed to occur via a single stage reaction (Eq. (5)).



As a result, depending on the extent of these decomposition reactions (Eq. (1), 4 and 5), the decomposition of carbonate minerals may negatively affect the amount of heat released because the evolution of mineral CO₂ is accompanied by an endothermic effect, the amount of ash produced, and the amount of CO₂ emissions emitted. The share of CO₂ emissions from the mineral part of the fuel depends on the content of mineral CO₂ in the fuel and the extent of decomposition of carbonate minerals during the processes occurring in the combustor. The calculation methodology for the extent of carbonate decomposition ECD (k_{CO_2}) has been described more thoroughly by Arro et al. [43]. The value of k_{CO_2} measured for Estonian oil shale for pulverised combustion (PC) can be as high as ($k_{\text{CO}_2} \sim 0.97$), due to the high combustion temperature (1400–1500 °C), and for CFB boilers ($k_{\text{CO}_2} \sim 0.6$ –0.8), where the operating temperature is around 800 °C [43]. The ash content of Estonian oil shale can reach up to 50 % without considering the amount of CO₂ present in the ash, and it can reach up to 70 % if 100 % of CO₂ remains in the ash; consequently, a large amount of solid waste is produced upon combustion. From the perspective of power generation, the produced ash is a waste material because it has been considered hazardous waste for a long time and is mainly landfilled [44], which will soon be too costly. In addition, Estonian kukersite oil shale contains various trace elements [45]. Aqueous eluates of fly ash can have potentially toxic effects on any aquatic species because of the high free lime concentration and high alkalinity, as noted by [45]. Z, As, Be, B, Cd, Cr, Co, Pb, Hg, Mn, and Ni are considered the most harmful elements for both human health [46] and the environment [47], and can differ between fly ash types and combustion technology. For example, CFB combustion oil shale ash has lower concentrations of heavy metals and is considered less toxic than PC [48,49]. And compared to coal, oil shale ash found to have lower hazardous conditions. A recent study [50], based on

computational methods proposed by the European Union to investigate hazardous materials in oil shale, removed oil shale ash from the list of hazardous substances and opened up more opportunities for ash reuse. The geotechnical properties of oil shale ash make it suitable for use in the production of building materials [51]. The physicochemical characteristics of fly ash, such as porosity, particle size, and surface area, enabled the oil shale fly ash to be used as an adsorbent material [52] and as a sorbent because of its high reactivity towards gaseous substances (such as SO₂) as mentioned earlier. In addition, because of its alkalinity, ash can be used to reduce soil acidity [53].

The utilisation of solid wastes from oil shale processing is difficult, and ash valorization remains one of the most contentious issues in Estonia's energy sector. Oil shale industry accounts for more than 70 % of the Estonian energy sector, and approximately 41 % of planned oil shale is consumed by direct combustion in thermal power plants. The recovery of ash is extremely limited, and in the current economic situation, approximately 2 % of the generated ash is recovered [54]. More differences in ash formation can be expected when using non-conventional fuels, such as oil shale. Data on oil shale ash formation under oxy-fuel CFB combustion conditions are very limited and no systematic study has been carried out to evaluate the influence of oxy-fuel combustion conditions on the ash composition. If oxyfuel combustion affects the composition of the ash, the resulting environmental impacts will influence the implementation of oxy-fuel technology and the proper utilisation of the oil shale ash. Adopting carbon capture technologies, such as oxy-fuel in the Estonian energy sector, together with CO₂ storage, can appear to be a key tool for providing a low carbon footprint.

The objective of the present study was to characterise the ash from the oxy-fuel combustion of oil shale to obtain a better understanding of the formation of chemical and mineral compounds. Accordingly, the behaviour of the oil shale ash was investigated for the first time under elevated O₂ concentrations, together with RFG. This study is a part of the long-term experimental work carried out in a 60 kWth CFB combustor under air, O₂/CO₂ and O₂/RFG which is of crucial importance as it can serve as a reference model for the industrial application of oxy-fuel combustion technology in oil shale power plants.

2. Experimental work

2.1. Fuel characteristic

Estonian kukersite-type oil shale samples (provided by Viru Keemia Grupp (VKG)) were used in this study. Detailed proximate and ultimate analyses of the representative oil shale samples are summarised in Table 1. Fuel sample characterisation included proximate analysis (ash, moisture, and net heating value or Lower Heating Value (LHV)), including elemental analysis using Elementar Vario MACRO CHNS and TIC to measure (C, H, N, S) and total inorganic carbon as (CO₂)_{mineral} respectively. The LHV was determined by calorimetric measurements using a bomb calorimeter (IKA2000C). The ash chemical and mineral compositions are listed in Table 2 and Table 3, and the results were obtained using X-ray fluorescence (XRF) and X-ray diffraction (XRD) analyses. Ash samples were prepared and tested using a Rigaku Primus II XRF spectrometer following ISO 29581–2:2010(E), for XRF analysis, and loss of ignition (LOI) refers to sample weight loss at 950 °C. For the XRD analyses, a Bruker D8 diffractometer fitted with a Lynx-Eye linear detector was used. XRD experiments were performed using Cu K α radiation in the 2 θ range of 3 – 72° with a step size of 0.02° 2 θ and a counting time of 0.1 s per step, and the X-ray tube operated at 40 kV and 40-mA. For the analysis, the Siroquant 3.0 code was used, which is based on the Rietveld algorithm [55]. The majority of the ash samples reflected the presence of secondary portlandite, resulting from direct contact with atmospheric moisture and partial hydration of the original lime. Consequently, the compositions were corrected to include portlandite in the lime concentration. Determination of trace element contents was

Table 1

Proximate and ultimate analysis of the fuel.

| Proximate analysis/wt _{dry} % | | | Ultimate analysis/wt _{dry} % | | | | | |
|--|------|----------------------------------|---------------------------------------|-------|------|------|------|------|
| Moisture (W) | Ash | Lower Heating Value (LHV), MJ/kg | (CO ₂) _{Mineral} | C | H | O* | N | S |
| 0.18 | 52.6 | 10.12 | 18.90 | 27.76 | 2.95 | 0.63 | 0.06 | 2.07 |

*O % = 100 - (W + Ash + CO₂ + S + TOC + H + N) %.**Table 2**

Chemical composition of the mineral part of the fuel.

| Component | SiO ₂ | Al ₂ O ₃ | Fe ₂ O ₃ | CaO | MgO | Na ₂ O | K ₂ O | SO ₃ | LOI _{950 °C} * |
|--------------|------------------|--------------------------------|--------------------------------|-------|-----|-------------------|------------------|-----------------|-------------------------|
| Content, wt% | 15.39 | 3.64 | 2.03 | 22.52 | 3 | 0.09 | 1.6 | 3.91 | 47.12 |

*LOI_{950 °C} = Loss of ignition at 950 °C.**Table 3**

Mineralogical composition of the mineral part of the fuel.

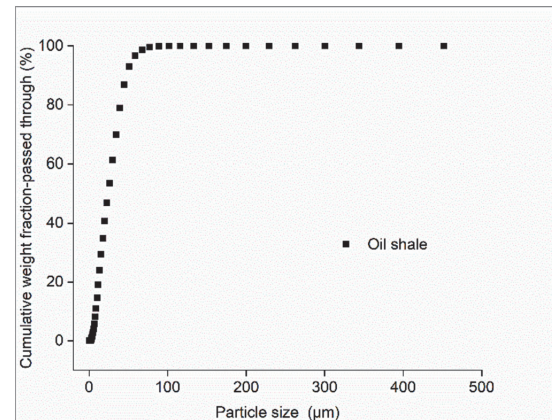
| Phase | Quartz SiO ₂ | K-feldspar KAlSi ₃ O ₈ | Calcite CaCO ₃ | Dolomite CaMg(CO ₃) ₂ | Chlorite ClO ₂ | Pyrite FeS ₂ | Illite* |
|--------------|-------------------------|--|---------------------------|--|---------------------------|-------------------------|---------|
| Content, wt% | 11.6 | 6.5 | 43.1 | 20.3 | 3.5 | 1.9 | 13 |

*illite as muscovite with Mg, Ca, and Fe.

performed using an inductive coupled plasma mass spectrometer (ICP-MS) Agilent 8800x. ICP-MS has three-stage filtering system: quadrupole mass filter, reaction cell and quadrupole mass filter allows determination of chemical elements and their isotopes with atomic mass 5–250 amu (Li–Pu). Fuel and ash physical properties characterization include particle size distribution (PSD) and specific surface area (SSA). Fig. 2 shows PSD of oil shale, the PSD analysis was carried out using laser scattering particle size distribution analyser LA-950 (HORIBA). The BET-N₂ sorption method used to measure the SSA with Kelvin 1042 sorptometer.

The chemical composition of Estonian oil shale is determined by the content of three main parts: organic, sandy-clay and carbonaceous [38]. The contents of CaO and MgO are determined by the content of sandy clay and carbonaceous part in oil shale. An average of 99.2 % of CaO and 96.7 % of MgO are bound in the carbonaceous part (typically oil shale with LHV at 8.0–8.6 MJ/kg). Based on this, it is possible to proceed from the content of CaO and MgO in the ash to determine the maximum shared CO₂ emissions were generated from the dissociation of calcite and dolomite (Eq. (1), 4 and 5) [43]:

$$CO_{2,CaO} = \frac{M_{CO_2}}{M_{CaO}} \times CaO_i \quad (6)$$

**Fig. 2.** Particle size distribution of oil shale.

$$CO_{2,MgO} = \frac{M_{CO_2}}{M_{MgO}} \times MgO_i \quad (7)$$

$$CO_{2,i} = CO_{2,CaO} + CO_{2,MgO} \quad (8)$$

Under oxy-fuel combustion conditions, the shared CO₂ produced from anhydrite formation via direct sulfation (Eq. (3)) is as follow:

$$CO_{2,CaSO_4} = \frac{M_{CO_2}}{M_{CaSO_4}} \times CaSO_{4i} \quad (9)$$

$$CO_{2,i} = CO_{2,CaO} + CO_{2,MgO} + CO_{2,CaSO_4} \quad (10)$$

where $CO_{2,CaO}$, $CO_{2,MgO}$ and $CO_{2,CaSO_4}$ are calculated for each ash fraction (i) based on the CaO_i , MgO_i and $CaSO_{4i}$ measured in the ash sample.

M_{CO_2} , M_{CaO} , M_{MgO} and M_{CaSO_4} are the molecular weights for CO₂, CaO, MgO and CaSO₄ respectively.

By determining the mineral CO₂ of ash, the total extent of carbonate decomposition ECD (k_{CO_2}) resulted from calcite and dolomite decomposition was calculated as follow:

$$k_{CO_2,i} = 1 - (CO_{2,ash,i} / CO_{2,i}) \quad (11)$$

2.2. 60 kWth circulating fluidized bed pilot facility

A schematic of the 60 kWth CFB facility is shown in Fig. 3. The pilot facility consisted of a furnace at a height of 4.90 m and an inner diameter of 0.12 m. A screw conveyor was used for fuel feeding with a height of 1.17 m, and recirculated solids were fed back at a height of 1.5 m with secondary air. The CFB test facility can be operated with regular air, preset gas mixtures, and an RFG. The combustion process was monitored at 16 points using thermal sensors, and the data controller of the test unit was fully automated using the LabVIEW system. The temperature measurement tap located along the riser and heat exchanger as well termed as (T_{DB}) represents the dense bed temperature, (T_{Riser}) the maximum temperature of the riser, and (T_{EHE}) the temperature measurement at the heat exchanger. The collected ash sample points are identified in Fig. 3, including the bottom ash (BA), external heat exchanger (EHE), cooler 1 (C1), cooler 2 (C2), and filter ash (filter).

2.3. Experimental parameters and ash sampling

The experiments were conducted under air, O₂/CO₂, and O₂/RFG

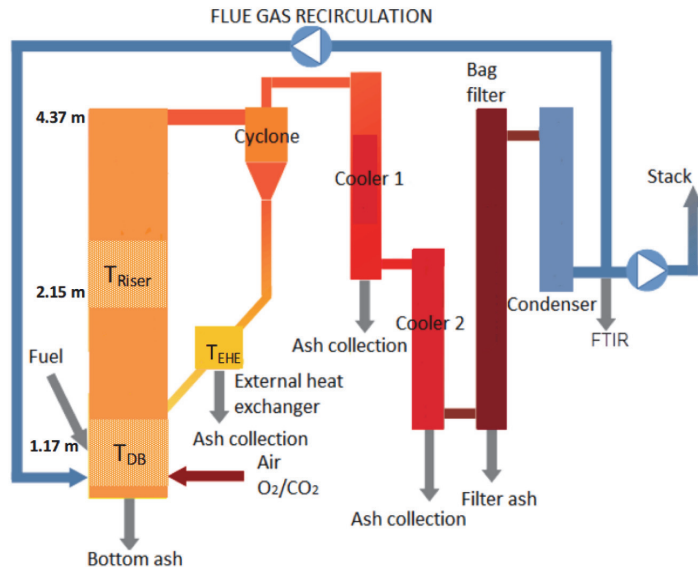


Fig. 3. Circulating fluidized bed facility with 60 kWth capacity.

combustion atmospheres. Table 4 shows the average working parameters of the CFB unit under air and different oxy-fuel conditions (OXY21, OXY25, etc.), where the numbers represent the inlet oxygen concentration in volumetric percentage.

The CFB pilot facility always started in air combustion mode. When the combustion process reached the desired experimental temperature, an air combustion baseline test was conducted. Following the completion of the air test, under stable conditions, the switch from air to O₂/CO₂ (OXY21–OXY40) or O₂/RFG (OXY50 and OXY75) combustion started. The transition was accomplished smoothly, and a steady oxy-fuel combustion regime was achieved in a short time. In our oxy-fuel tests, the inlet O₂ concentration ranged from 21 to 75 % (vol. %).

The oil shale was continuously fed into the CFB boiler at a full load. The solid particles were separated from the flue gas in the cyclone and returned to the bottom of the fluidised bed through a return leg and an external heat exchanger. As the oil shale combustion proceeds in the test unit, the CO₂ concentration in the flue gas reaches 90 % without flue gas recycling, which is a reason for the enhanced combustion in oxygen-rich environments. In this study, the collected ash samples in the CFB test unit from different ash streams represent the same ash streams produced in the Estonian oil shale industry [56], where BA, EHE, cooler (average

values of coolers 1 and 2), and filter ashes are studied in more detail.

3. Results and discussion

3.1. Temperature distribution

The temperature profiles along the CFB riser during stable regimes of air and oxy-fuel combustion are shown in Fig. 4. The bed temperatures of the riser in the dense zone (T_{DB}) are significantly affected by the recirculation mass flow rate and temperature of the solid. Because of the natural cooling of recycled ash, the graphs are slightly shifted as the temperature decreases, as shown in Fig. 4(a), (b), (c), and (d). A higher temperature generally indicates a higher ash recirculation rate, and vice versa. The rate of solid ash recirculation is determined by the temperature of the external heat exchanger (T_{EHE}). In air firing, the temperatures were similar to the values used in oil shale industrial CFB boilers [57]. Fig. 4(a) shows the effect of recirculation rate at the same combustion mode, where the higher the T_{EHE} , the higher the recirculation rate of the recycled ash; hence, the solid ash particles were used as a heat carrier agent, and the more entered the bottom end of the bed, the more heat was absorbed in the riser. In addition, the same effect was observed

Table 4
Average working parameters of 60 kWth CFB unit during different combustion modes.

| Combustion Mode | T_{DB} , °C | T_{Riser} , °C | T_{EHE} , °C | O ₂ % inlet | CO ₂ % in flue gas | RFG *(PA:SA) | Ash Sampling |
|-----------------|---------------|------------------|----------------|------------------------|-------------------------------|--------------|-------------------------|
| Air | 700 | 814 | 270 | – | 16 | No | BA, EHE, C1, C2, Filter |
| OXY21 | 744 | 808 | 666 | 21 | 90 | No | BA, EHE, C1, C2, Filter |
| OXY25 | 779 | 896 | 519 | 25 | 93 | No | BA, EHE, C1, C2, Filter |
| OXY30 | 783 | 868 | 564 | 30 | 93 | No | BA, EHE, C1, C2, Filter |
| OXY40 | 849 | 886 | 751 | 43 | 90 | No | BA, EHE, C1, C2, Filter |
| OXY50 + RFG | 771 | 813 | 709 | 52 | 61 | 1:1 | BA, EHE |
| OXY75 + RFG | 743 | 807 | 329 | 74 | 71 | 1:3 | BA, EHE, Filter |

Bottom ash (BA), external heat exchanger ash (EHE), cooler 1 ash (C1), cooler 2 ash (C2), filter ash (filter).

*PA = Primary air, SA = Secondary air.

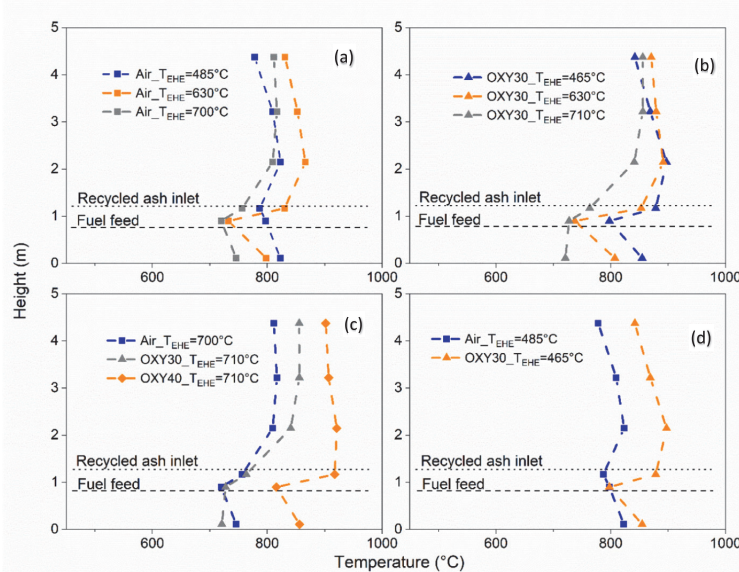


Fig. 4. Temperature distribution along riser; (a) Air-firing at different solid recirculation rates, (b) OXY30 at different solid recirculation rates, (c) Air and OXY30 at high solid recirculation rates, and (d) Air and OXY30 at low low recirculation rates.

in OXY30 Fig. 4(b). Increasing T_{EHE} through the recycled ash resulted in a more uniform temperature distribution in the overhead zones, and the latter was slightly decreased by decreasing the ash recirculation rate. Fig. 4(c) compares air and oxy-firing at high ash recirculation rates; the temperature distribution along the riser and in the overhead zone for OXY30 is almost similar to that of the air combustion mode, despite the increase in bed temperature caused by the increased oxygen concentration owing to the higher combustion rate [58]. In contrast, Fig. 4(d) shows that at a lower ash recirculation rate, the bed temperature differences between the air and OXY30 combustion modes increased. Overall, the current experiments show that by increasing the oxygen concentration in the combustion environment, the temperature deviation along the riser increased; however, some studies found that during the oxy-combustion experiments, the temperature in the riser decreased as a result of substituting the O_2/N_2 environment with O_2/CO_2 [19,59]. Consequently, the obtained results indirectly indicate a stable process inside the CFB combustor in both air and oxy-fuel combustion environments.

3.2. Physical properties

3.2.1. Particle size distribution (PSD)

Fig. 5(a) and (b) show the PSDs of BA and EHE ashes respectively under different combustion conditions. In Fig. 5(a) with increasing inlet $O_2\%$ in the combustion atmosphere, BA-PSDs were shifted rightward to a higher particle size. And compared to air combustion, larger particles were formed under both O_2/CO_2 and O_2/RFG . EHE-PSDs in Fig. 5(b) displays the same behaviour with increasing $O_2\%$ (with a slight difference under O_2/RFG). Nevertheless, compared to air combustion, EHE-PSDs show finer particle formations under all oxy combustion modes. During combustion process, oil shale particles form a porous mineral structure with a low mechanical strength. Fragmentation phenomena increase the proportion of finer fraction [38]. Depending on the size of the particles formed and the hydrodynamic resistance, a flow of ash from the bottom to the bag filter occurred along the test facility path. In oxy-fuel CFB combustion, the ash distribution is related to a strong-grained size separation in comparison to the air-combustion

atmosphere. Resulting in produce finer particles with increasing $O_2\%$, because the oxygen concentration enhances the mineral vaporization and nucleation [37]. The coarse mode in BA under oxy-fuel experiments were obtained because the composition of BA is strongly dominated by the undecomposed large particles of calcite ($CaCO_3$) and formation of anhydrite ($CaSO_4$) that are mostly derived from the bed of the riser and the heat exchanger as well. This effect will be discussed in more detail in the next section.

3.2.2. Specific surface area (SSA)

Fig. 6 presents the surface analysis results of the ash samples (BA, EHE and Filter) produced from air and oxy-fuel combustion experiments. In air combustion the surface area is between $3.4\text{--}7.9\text{ m}^2/\text{g}$. The Brunauer–Emmett–Teller (BET) surface area of the obtained ashes are within specific surface area of oil shale CFB combustion ashes that can reach $8.68\text{ m}^2/\text{g}$ under conventional air-firing mode [56]. The difference between the BET surface area in the BA and EHE ashes is significantly higher in air mode, compared to oxy-fuel combustion, indicating larger particle size formation under oxy conditions in the bed and heat exchanger of the pilot facility. The BET surface area in the BA and EHE ashes is up to 4 times is smaller than that in the Filter under OXY21. While the surface area of the Filter ash decreased with the increment of inlet $O_2\%$ from $7.7\text{ m}^2/\text{g}$ in OXY21 to $2.6\text{ m}^2/\text{g}$ in OXY75 + RFG. The results are in line with other literatures [28]. One of the possible reasons for the larger surface area observed in the Filter ash under higher $O_2\%$ atmosphere is the effect of the high carbon content residue in the Filter ash. Because high temperature promotes the coalescence of minerals, which explain why the Filter ash under higher inlet $O_2\%$ were larger in particle size.

3.3. Chemical composition

The chemical compositions of BA, EHE, cooler, and filter ash in air and different oxy-fuel combustion environments are presented in Table 5. The larger ash mass fraction obtained during the combustion process was from the BA and EHE ash. As can be seen from Table 5, calcium oxide (CaO) is the most abundant oxide, followed by silica

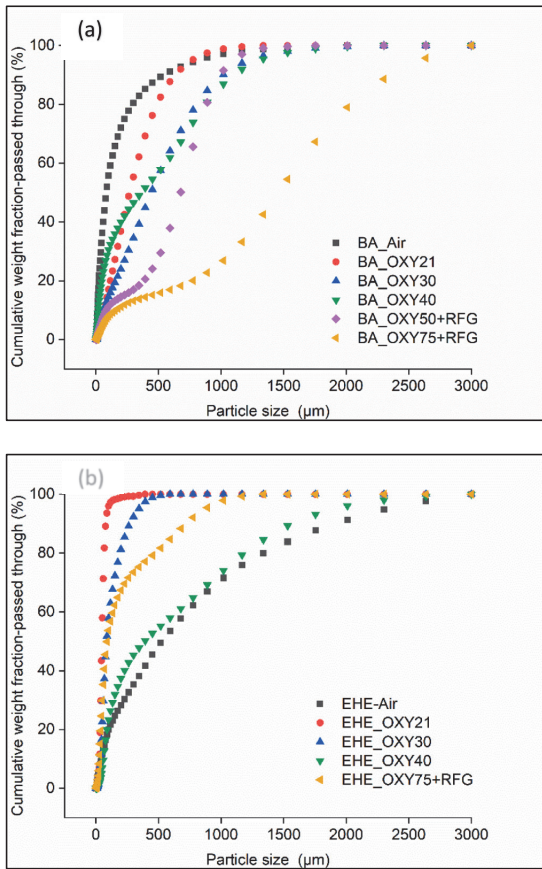


Fig. 5. Comparison of particle size distribution under air and oxy-fuel combustion experiments of; (a) BA and (b) EHE.

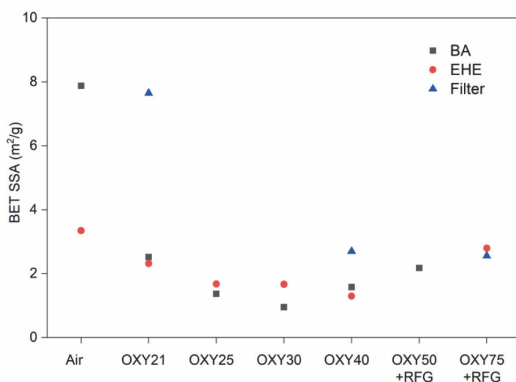
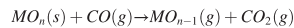


Fig. 6. Comparison of ash surface area under air and oxy-fuel combustion experiments.

(SiO₂), magnesium (MgO), aluminium (Al₂O₃), and iron (Fe₂O₃) oxides, while the rest of the oxides formed during the different experiments were in lower concentrations. The ratios of Ca:Mg oxides in the oxy-firing BAs decreased by 24 % compared with the air-combustion mode. However, the same ratios for EHE ashes from air to oxy-fuel combustion decreased by 40 %, indicating that oxy-firing BAs have a higher content of CaO. Ashes alkaline earth elements: CaO and MgO are relatively high in bottom ash and decreased in filter ashes (down 50 %) in air combustion and at low O₂ inlets during O₂/CO₂ combustion. However, at higher O₂ concentrations and with RFG, these values decreased by 30 % for CaO and 20 % for MgO, as the bed temperature was higher, and the residence time of the particles increased during the low solid recirculation rate. For K₂O, SiO₂, Al₂O₃ and Fe₂O₃ we found that these values increased in correlation with ash location, indicating the separation of the fine sandy clay component and concentration into finer particles, where the vaporisation of SiO₂ was higher in oxy-firing than in air-firing, leading to more submicron particles, which has been demonstrated previously in a conventional CFB combustion environment [38,60]. SiO₂, Na₂O and K₂O values under oxy-fuel mode decreased with increasing inlet O₂% in the combustion atmosphere and obtained the lowest value under OXY75 + RFG. As a result of fast combustion rate and a reduction atmosphere on char particle surface leading to a higher vaporization degree and more submicron particles [61]. Oxy conditions had much smaller effects on the release behaviour of Al. The mineral-bound element (Si, Ca, Mg and Al) may vaporize according to [62]:



where M represents refractory elements, such as Si, Al, Ca, and Mg, and the CO/CO₂ ratio inside the char determines the extent of vaporization.

The level of SO₃ in BA and EHE ashes is enhanced under oxy-fuel combustion compared to air. SO₃ values increased with increasing inlet O₂% under both O₂/CO₂ and O₂/RFG. As a result of the improved sulfation reaction under oxy mode with the increase of SO₂ concentrations in the combustion atmosphere. Higher evaporation rate of BA-Cl content can be noticed under O₂/CO₂ mode than in air, and higher Cl condensation occurred at low temperature separation port (Filter). Filter-Cl content under O₂/RFG did not change, and these values were still low compared to BA. RFG is expected to facilitate element release in the forms of chlorides and reduce Cl content in the ash residue. An increase in chlorine content begins at a particle size of 10 to 20 μm for CFB combustion, hence chlorine content is the highest in ash particles caught in the bag filter [38].

The LOI results of oxy-firing BAs are the highest, as they depend mainly on the ash carbonate content and strong-grained size separation for particles during the oxy-firing CFB process, as mentioned earlier. Based on previously reported studies [19,23], the results show that the difference between air and oxy-fuel combustion in terms of ash chemical composition is very close to the currently obtained results. Overall, the thermal decomposition of the Ca- and Ca-Mg-carbonate phases in the oil shale liberates large amounts of CO₂. Because the decomposition of Ca carbonates is hindered, oxy-fuel technology is particularly suitable for oil shale combustion.

3.4. Mineral composition

The mineral composition of the raw oil shale sample is reported in Table 3, and it corresponds to the typical kundersite oil shale [39]. The oil shale ash sample is characterised mainly by calcite and dolomite, exceeding 60 %, and silicate and clay minerals exceeding 30 % including silica oxide (SiO₂), k-feldspar (KAlSi₃O₈), and illite. For phase composition determination, the ash minerals for BA, EHE, cooler, and filter ash are given in Table 6. These results were obtained by analysing the ash samples using XRD and were consistent with the chemical composition results. In conventional air combustion, the CFB unit operates at a dense

Table 5
Chemical composition of ashes during different combustion modes.

| Component | Separation port | Air | OXY21 | OXY25 | OXY30 | OXY40 | OXY50 +RFG | OXY75 +RFG |
|--------------------------------|-----------------|-------|-------|-------|-------|-------|---------------|---------------|
| SiO ₂ | BA | 10.51 | 13.02 | 12.17 | 14.92 | 8.39 | 9.77 | 6.61 |
| | EHE | 8.44 | 22.68 | 24.32 | 24.00 | 16.25 | 39.25 | 20.53 |
| | Cooler | 36.47 | 36.95 | 39.24 | 37.58 | 36.88 | – | – |
| | Filter | 39.01 | 41.45 | 38.45 | 36.76 | 37.07 | – | 31.10 |
| Al ₂ O ₃ | BA | 2.26 | 2.90 | 2.69 | 3.33 | 1.74 | 2.02 | 1.35 |
| | EHE | 1.78 | 4.87 | 5.17 | 5.23 | 3.44 | 10.08 | 4.28 |
| | Cooler | 8.14 | 8.23 | 9.66 | 8.95 | 8.47 | – | – |
| | Filter | 10.63 | 11.51 | 10.48 | 9.64 | 8.66 | – | 6.99 |
| Fe ₂ O ₃ | BA | 2.25 | 2.36 | 2.28 | 2.65 | 2.36 | 2.55 | 2.22 |
| | EHE | 2.51 | 3.18 | 3.22 | 3.23 | 3.07 | 4.94 | 3.49 |
| | Cooler | 4.38 | 4.38 | 5.08 | 4.62 | 4.42 | – | – |
| | Filter | 4.70 | 5.46 | 4.99 | 4.71 | 4.31 | – | 3.58 |
| CaO | BA | 54.68 | 41.90 | 44.37 | 43.22 | 47.77 | 51.51 | 49.18 |
| | EHE | 49.91 | 35.88 | 35.38 | 36.67 | 41.45 | 23.27 | 42.82 |
| | Cooler | 26.48 | 26.88 | 22.46 | 24.59 | 27.13 | – | – |
| | Filter | 23.73 | 17.81 | 22.19 | 21.87 | 26.01 | – | 34.86 |
| MgO | BA | 5.30 | 4.67 | 4.65 | 4.60 | 6.55 | 7.94 | 6.37 |
| | EHE | 4.80 | 5.61 | 5.10 | 5.15 | 7.62 | 4.73 | 8.01 |
| | Cooler | 4.91 | 4.71 | 3.65 | 3.87 | 5.54 | – | – |
| | Filter | 3.49 | 2.97 | 3.46 | 3.72 | 5.35 | – | 5.00 |
| Na ₂ O | BA | 0.06 | 0.12 | 0.10 | 0.14 | 0.06 | 0.06 | 0.06 |
| | EHE | 0.08 | 0.19 | 0.15 | 0.18 | 0.13 | 0.40 | 0.15 |
| | Cooler | 0.22 | 0.21 | 0.29 | 0.23 | 0.26 | – | – |
| | Filter | 0.30 | 0.37 | 0.35 | 0.27 | 0.20 | – | 0.13 |
| K ₂ O | BA | 0.79 | 1.18 | 1.00 | 1.30 | 0.55 | 0.57 | 0.30 |
| | EHE | 0.62 | 2.02 | 2.31 | 2.30 | 1.34 | 4.49 | 1.68 |
| | Cooler | 3.77 | 3.78 | 4.52 | 4.19 | 3.87 | – | – |
| | Filter | 4.90 | 5.39 | 4.81 | 4.53 | 4.16 | – | 2.94 |
| P ₂ O ₅ | BA | 0.13 | 0.11 | 0.11 | 0.12 | 0.09 | 0.11 | 0.09 |
| | EHE | 0.12 | 0.13 | 0.13 | 0.13 | 0.12 | 0.17 | 0.14 |
| | Cooler | 0.14 | 0.14 | 0.14 | 0.14 | 0.15 | – | – |
| | Filter | 0.16 | 0.16 | 0.16 | 0.15 | 0.14 | – | 0.14 |
| SO ₃ | BA | 5.74 | 5.88 | 6.12 | 6.21 | 7.42 | 7.86 | 6.77 |
| | EHE | 4.79 | 7.55 | 6.12 | 6.27 | 7.27 | 3.93 | 6.43 |
| | Cooler | 4.63 | 4.27 | 3.79 | 4.36 | 4.16 | – | – |
| | Filter | 3.91 | 2.54 | 4.19 | 4.25 | 3.31 | – | 5.00 |
| Cl | BA | 0.25 | 0.13 | 0.15 | 0.12 | 0.22 | 0.19 | 0.19 |
| | EHE | 0.22 | 0.18 | 0.12 | 0.16 | 0.17 | – | 0.20 |
| | Cooler | 0.37 | 0.40 | 0.56 | 0.43 | 0.53 | – | – |
| | Filter | 0.47 | 0.48 | 0.51 | 0.52 | 0.34 | – | 0.18 |
| LOI _{950 °C} * | BA | 16.72 | 26.38 | 25.24 | 22.15 | 23.97 | 16.05 | 26.84 |
| | EHE | 26.57 | 14.92 | 15.27 | 14.20 | 16.13 | 6.73 | 10.41 |
| | Cooler | 7.68 | 8.24 | 9.05 | 8.66 | 7.28 | – | – |
| | Filter | 6.96 | 9.33 | 8.82 | 11.44 | 8.25 | – | 8.14 |

*LOI_{950 °C} = Loss of ignition at 950 °C.

- No ash sampling.

- No analytical results.

bed temperature of (T_{DB}) ~ 700 °C and a low CO₂ partial pressure. The operating conditions led to the formation of a bottom ash porous mineral structure with low mechanical strength where calcination occurred (Eq. (1)); thus, the lime concentration increased mainly in the BA and EHE ashes, as indicated in Table 6. In all oxy-fuel combustion conditions, there were higher dense bed and riser temperatures, together with higher CO₂ concentrations, compared to the air mode. The dissociation of calcite was limited owing to the increased partial pressure of CO₂ even

though the operating temperatures were increased because of the elevated O₂ concentration. As a result, the composition of BAs was strongly dominated by calcite; thus, the reduction in total CO₂ emissions in the flue gas from air to oxy-fuel combustion exceeded (15 %). On the other hand, dolomite decomposition depends mainly on the combustion temperature, following (Eq. (4) and (1)). And elevated CO₂ partial pressure didn't affect dolomite dissociation, were these concentrations in BA and EHE ashes reduced significantly under inlet O₂% from 25 to

Table 6
Mineral composition of ashes during different combustion modes.

| Component | Separation port | Air | OXY21 | OXY25 | OXY30 | OXY40 | OXY50 +RFG | OXY75 +RFG |
|--|-----------------|-------|-------|-------|-------|-------|---------------|---------------|
| Quartz (SiO ₂) | BA | 5.20 | 9.31 | 7.41 | 7.32 | 3.51 | 4.85 | 2.61 |
| | EHE | 5.07 | 14.31 | 15.16 | 14.10 | 7.41 | 20.82 | 11.01 |
| | Cooler | 22.08 | 22.36 | 22.81 | 22.65 | 21.18 | – | – |
| | Filter | 21.90 | 20.65 | 19.23 | 20.72 | 20.64 | – | 16.05 |
| K-feldspar (KAlSi ₃ O ₈) | BA | 1.99 | 5.11 | 3.40 | 3.91 | 3.01 | 1.31 | 0.55 |
| | EHE | 2.07 | 8.11 | 9.33 | 9.87 | 6.29 | 16.81 | 4.65 |
| | Cooler | 15.50 | 15.99 | 17.49 | 18.39 | 16.92 | – | – |
| | Filter | 17.48 | 17.34 | 17.33 | 19.01 | 17.93 | – | 9.93 |
| K-mica (Al ₂ K ₂ O ₆ Si) | BA | 6.08 | 2.50 | 0.50 | – | – | 1.21 | 0.15 |
| | EHE | 1.14 | 4.70 | 1.41 | 2.62 | 0.71 | 12.51 | 2.83 |
| | Cooler | 10.25 | 12.43 | 15.64 | 9.82 | 7.93 | – | – |
| | Filter | 17.68 | 20.95 | 19.03 | 16.51 | 8.12 | – | 4.21 |
| Calcite (CaCO ₃) | BA | 11.17 | 55.17 | 57.17 | 52.95 | 56.02 | 31.61 | 55.77 |
| | EHE | 44.36 | 28.62 | 33.52 | 29.51 | 33.90 | 12.21 | 19.29 |
| | Cooler | 13.53 | 14.49 | 16.64 | 16.29 | 13.25 | – | – |
| | Filter | 15.37 | 16.34 | 14.83 | 19.61 | 18.04 | – | 17.05 |
| Dolomite (CaMg(CO ₃) ₂) | BA | 3.21 | 4.61 | 0.90 | 0.90 | 1.70 | 1.51 | 4.36 |
| | EHE | 6.51 | 5.20 | 2.11 | 1.81 | 1.93 | 1.70 | 4.24 |
| | Cooler | 1.76 | 1.65 | 1.90 | 1.00 | 1.15 | – | – |
| | Filter | 2.11 | 1.90 | 1.40 | 0.80 | 1.10 | – | 0.70 |
| Lime (CaO) | BA | 38.62 | 0.68 | – | 1.81 | 2.59 | 16.89 | 4.48 |
| | EHE | 13.75 | 3.43 | 3.95 | 6.14 | 7.93 | 5.23 | 16.77 |
| | Cooler | 4.93 | 5.04 | 1.85 | 2.93 | 5.08 | – | – |
| | Filter | 2.87 | 1.89 | 2.93 | – | 1.91 | – | 9.82 |
| Periclase (MgO) | BA | 6.41 | 4.71 | 6.11 | 5.82 | 8.22 | 8.79 | 6.84 |
| | EHE | 5.07 | 4.80 | 6.52 | 6.34 | 9.74 | 4.30 | 9.19 |
| | Cooler | 4.43 | 3.91 | 2.56 | 3.46 | 5.47 | – | – |
| | Filter | 3.11 | 2.41 | 2.20 | 2.70 | 5.41 | – | 5.62 |
| Anhydrite (CaSO ₄) | BA | 7.41 | 11.11 | 7.21 | 5.92 | 7.32 | 13.53 | 11.61 |
| | EHE | 7.86 | 14.31 | 8.53 | 8.26 | 8.22 | 8.11 | 12.53 |
| | Cooler | 8.15 | 6.92 | 6.62 | 8.02 | 6.68 | – | – |
| | Filter | 6.43 | 6.61 | 8.01 | 8.31 | 4.41 | – | 9.63 |
| Belite (C ₂ S) | BA | 6.75 | 1.20 | 2.30 | 3.01 | 2.41 | 8.58 | 4.68 |
| | EHE | 4.14 | 5.00 | 4.12 | 5.34 | 2.23 | 7.81 | 8.38 |
| | Cooler | 7.45 | 7.62 | 4.06 | 5.96 | 7.38 | – | – |
| | Filter | 5.83 | 5.71 | 4.61 | 2.90 | 7.21 | – | 12.94 |
| Akermanite (Ca ₂ Mg(Si ₂ O ₇)) | BA | 1.00 | 1.70 | 2.40 | 3.11 | 1.30 | 5.96 | 4.17 |
| | EHE | 1.76 | 4.00 | 3.71 | 4.23 | 5.08 | 4.90 | 5.05 |
| | Cooler | 4.68 | 3.31 | 2.91 | 4.76 | 5.47 | – | – |
| | Filter | 2.01 | 1.50 | 2.50 | 3.30 | 5.51 | – | 7.72 |
| Merwinite (Ca ₃ Mg(SiO ₄) ₂) | BA | 4.64 | – | 0.90 | 0.80 | 0.90 | 4.14 | 3.22 |
| | EHE | 2.17 | 0.30 | 0.80 | 1.11 | 2.33 | 1.20 | 4.14 |
| | Cooler | 1.31 | 0.65 | 0.65 | 0.50 | 0.85 | – | – |
| | Filter | 0.60 | 0.60 | 0.30 | 0.70 | 1.20 | – | 3.61 |
| Sylvite (KCl) | BA | 1.44 | – | – | – | – | 1.21 | 0.15 |
| | EHE | 0.52 | – | – | – | 0.30 | 0.70 | 0.00 |
| | Cooler | – | 0.30 | – | – | 0.60 | – | – |
| Hematite (Fe ₂ O ₃) | BA | 0.66 | 1.40 | 2.00 | 2.61 | 1.80 | – | 1.16 |
| | EHE | 1.03 | 1.80 | 2.61 | 2.42 | 1.62 | 3.70 | 1.72 |
| | Cooler | 2.47 | 2.16 | 3.46 | 3.26 | 2.11 | – | – |
| | Filter | 2.61 | 2.71 | 3.31 | 3.90 | 2.30 | – | 2.21 |

- No ash sampling.

- No analytical results.

40 %, and increased with OXY21 and OXY75 + RFG at low operating temperatures ~ 744 °C. Therefore, dolomite content varies depending on the bed/riser temperatures between different oxy-fuel regimes. Almost all BAs and EHE ashes contain dolomite in both air and oxy-firing regimes which can be considered an unusual finding. The toxicity of ash leachate increases with increasing alkalinity and PH in ash landfills [63]. Oxy-fuel combustion reduces the free lime content in all ash locations, resulting in a total reduction in ash leachate behaviour in landfills.

The formation of anhydrite (CaSO_4) is mainly a result of reactions between available reactive CaCO_3 or CaO , SO_2 , and O_2 (Eqs. (2) and (3)), and the presence of anhydrite in ash samples indicate ash sulfur retention. The high concentration of calcite content in oxy-fuel combustion and the limited decomposition of it had no effect on the formation of anhydrite (CaSO_4). And anhydrite concentrations were not affected by switching from air to oxy-fuel combustion environment (being highest in RFG). Under O_2 /RFG higher anhydrite formation resulted from the enhanced sulfation reaction due to the increased particle reaction time with recycling SO_2 back to the combustor. And higher SO_2 partial pressure in the combustion atmosphere will eventually lead to higher sulfur capture efficiency [16]. The small variations in anhydrite concentrations that occurred between different oxy-fuel experiments can also be explained by the different thermal loads fed into the combustor. The sulfur capture efficiency of oil shale air combustion reached more than 90 %, and it mainly depends on the availability of alkaline minerals, particularly CaO in the case of air-firing. In oil shale oxy-fuel combustion sulfur capture efficiency reached 99 % in all oxygen combustion modes because the used molar ratio of Ca/S in oil shale is high (ca. 8), which may suggest that there was a lot of calcium in the CFB boiler, even though the sulfur retention was hindered.

Quartz (SiO_2) can be found as primary phase in the ashes of oil shale, reacting with the free available.

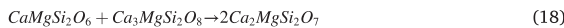
CaO/MgO phase forming secondary silicate phase as belite [64]:



Akermanite ($\text{Ca}_2\text{Mg}(\text{Si}_2\text{O}_7)$) and merwinite ($\text{Ca}_3\text{Mg}(\text{SiO}_4)_2$) are formed through a gradual phase development with the increase in temperature. At a temperature below 700 °C, merwinite phase occur, with the reduction of other silicates phases formed at lower temperature (such as wollastonite and monticellite) [65]:



And at higher temperatures, by 800 °C, the new phase akermanite begins to form:

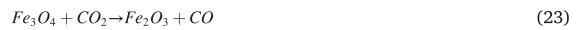
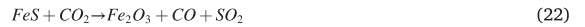


The free CaO can also react with other sandy-clay components like Al_2O_3 forming CaAl_2O_6 . Moreover, magnesium was found free as periclase (MgO) without participating in sulfation reaction, and also partially stayed bounded to carbonates as dolomite ($\text{CaMg}(\text{CO}_3)_2$). CaO/MgO phases and the formations of secondary silicate phases as belite (C_2S) and merwinite ($\text{Ca}_3\text{Mg}(\text{SiO}_4)_2$) are strongly dependent on the boiler temperatures. The limited decomposition of calcite in oxy-fuel modes decreases the amount of free lime which can react with quartz thus lowering the amount of akermanite and belite formations in BAs compared to air-firing BAs. The RFG which improves the contact and gas residence time with particles has a clear effect on the increased formations of akermanite, merwinite, belite and the decreased amount of quartz in both BA and EHE ashes obtained from oxy-fuel modes. Fe-oxide mineral in ash samples was identified as hematite (Fe_2O_3).

Hematite mineral is produced from the availability of Fe in oil shale sample. Fe-bearing mineral in origin feed oil shale sample presents as pyrite, Table 3. Pyrite starts to decompose at around 400–500 °C, and produces products of iron oxide minerals such as hematite [66]:



In the work presented by Fegley et al. [67], showed that pyrrhotite generated from pyrite decomposition was oxidized by CO_2 to form magnetite and hematite. Another work presented by Bhargava et al. [68] concluded that CO_2 participated in both pyrite decomposition and oxidation at temperature < 900 °C. Compared with N_2 , CO_2 facilitated pyrite decomposition and the release of sulfur, as the following [69].



In the presented results, the oxidizing environment in O_2/CO_2 combustion increases slightly concentrations of hematite with increasing inlet $\text{O}_2\%$ (OXY21–OXY30) mainly for BA and EHE ashes. And lower concentrations occurred at OXY40 and OXY75 + RFG as the formation of hematite was found to be dependent on the temperature and reaction time also. For the current presented results, the effect of CO_2 on pyrite decomposition needs to be studied further.

Fig. 7 provides a visual comparison between the air and oxy-fuel combustion experiments of ash mineralogical composition include (carbonates, silicates, sulfates, and oxides) and identified concentrations as wt% based on the ash sample location in the different CFB separation ports. For the carbonate group, the effect of oxy-fuel combustion can be clearly seen on both calcite (CaCO_3) and lime (CaO) in BA and EHE ashes respectively. The decomposition of BA-calcite into lime in air combustion is significantly higher than in EHE ashes, as an effect of the high bed temperature and residence particle time compared to in EHE location. These results are in correlation with SAA results. The high partial pressure of CO_2 under oxy-combustion modes inhibited BA-calcite decomposition, while the effect of elevated riser temperature T_{Riser} under oxy conditions is more dominant on EHE ashes resulting in slight increase in decomposition of EHE-calcite and eventually increasing lime concentrations. Moreover, PSD under oxy-fuel combustion shows a strong particle separation of undecomposed calcite in the bed and EHE locations. Anhydrite is mostly present in the coarser fractions of the bed ash stream, increasing in EHE ash and a slight decrease in the overhead finer ash streams. Large, sulfated particles are mostly derived from BA and EHE ashes, because coarse particles are typically produced from a layer of CaSO_4 that contains a core of unreacted CaO . For the silicates group (including quartz, k-feldspar, akermanite, merwinite, k-mica) they increase considerably in overhead ashes for all combustion modes, these sandy clay minerals increase along the flow path towards the end of the CFB unit channel. This increase indicates the separation of the fine sandy clay component and concentrated into finer particles. The specific area of the reactive surfaces of ashes is generally higher in low-particle-size ashes. For this reason, the effect of RFG and increased boiler temperatures owing to the elevated oxygen concentration has a more visible impact on the content of secondary silicates in EHE ashes which have a smaller particle size than BAs. Overall, in oxy-fuel CFB combustion, the chemical and mineral composition of the ash samples varies throughout the flow path of the CFB test facility, suggest that particles of different compositions are separated. And the separation appears to be larger for coarse calcite and sulfated particles, than in air combustion atmosphere. The fine-grained sandy-clay components in overhead ash contains higher content of secondary silicate phase, as they initiate binding with free lime which leads to the formation of clinker minerals. In conclusion, the mineralogy of the ashes formed in the air and oxy-fuel combustion

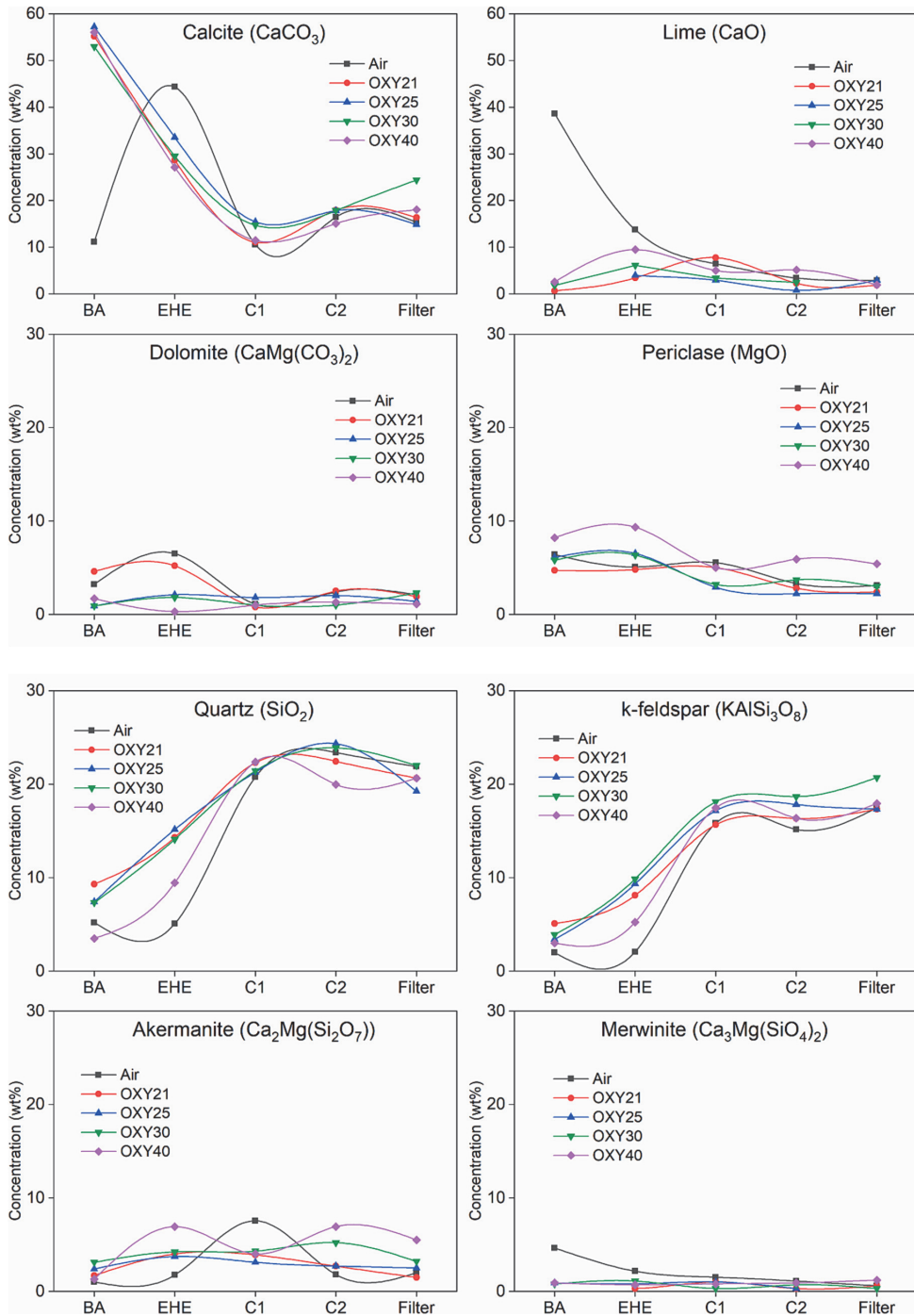


Fig. 7. Comparison of the composition of ash components under air and oxy-fuel combustion experiments at different separation ports.

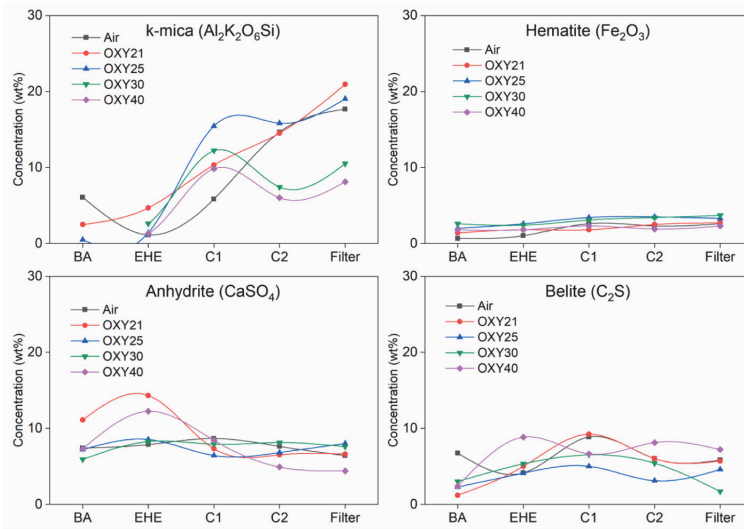


Fig. 7. (continued).

regimes are similar, yet slight differences exist in the case of increased oxygen concentrations and with the application of RFG.

3.5. Extent of carbonate decomposition ECD (k_{CO_2})

The ECD (k_{CO_2}) results of 60 kWth were calculated based on the methodology described in the experimental work. The ECD data of PC and CFB boilers presented in Table 7 are based on the results of the ash sample analyses taken from Eesti Thermal Power Plant and Balti Power Plant, respectively [56,70]. The fuel is Estonian oil shale and the k_{CO_2} of the CFB results show fuel classes of LHV at 8.2–11.5 MJ/kg, in the presented study the fuel LHV is 10.12 MJ/kg and k_{CO_2} results represent the average values taken at different experiments for each combustion mode. By comparing the results with the industrial CFB unit, under air combustion, the 60 kWth pilot facility tends to have a slightly higher BA- k_{CO_2} , while k_{CO_2} values are lower in the other separation ports when compared with both high- and low-grade oil shale results. Under the oxy-fuel combustion mode, the effect on BA can be seen more clearly, where the values are reduced under both O₂/CO₂ and O₂/RFG. Table 8 compares the total k_{CO_2} and the extent of decomposition as a result of calcite ($k_{CO_2, Calcite}$) and dolomite ($k_{CO_2, Dolomite}$) separately for BA, EHE, cooler, and filter ashes under both air and oxy-fuel combustion environments. When air firing proceeds, BA ash sulfation likely occurs via an

indirect reaction where $k_{CO_2, Calcite}$ are the highest (0.79). In oxy-fuel combustion, the high concentration of CO₂ in the combustion environment inhibited carbonate decomposition; hence, BA- $k_{CO_2, Calcite}$ dropped to levels between 0.04 and 0.17 under O₂/CO₂ environment. However, $k_{CO_2, Dolomite}$ reaches under oxy-fuel combustion to between 0.7 and 0.94, and sulfation likely occurred via the direct sulfation route (Eq. (3)), in addition to the SO₂ reaction with dolomitic calcite/lime formed based on Eq. (4) and (5). Some studies found that direct sulfation of CaCO₃ (in the case of low ECD) produced a higher conversion rate [71,72]. Contrary to other researchers, it was proposed that the surface of CaO particles is much more porous than that of CaCO₃ and diffusion resistance through the CaSO₄ product layer was significantly smaller than that encountered in the usual sulfation of CaO, which increases the sulfur capture efficiency [73]. As similar amounts of CaSO₄ were formed in both air and oxy-fuel cases, as shown in Fig. 5-anhydrite, the results suggested that the sulfation reaction was not affected by switching from air to the oxy-fuel combustion environment.

EHE ashes show a partial decomposition of calcite with increasing inlet O₂% under oxy combustion mode as a reason of the elevated T_{Riser} temperature compared to T_{DB} that has a higher effect on EHE ashes than on BA. For a better explanation Fig. 8 (a-d) show the effect of dense bed (T_{DB}) and riser (T_{Riser}) temperatures on ($k_{CO_2, Calcite}$) and ($k_{CO_2, Dolomite}$) of both BA and EHE ashes. As T_{DB} increases in the riser, the extent

Table 7
Comparison of industrial ECD (k_{CO_2}) from oil shale combustion and 60 kWth pilot facility.

| PC [56] | | CFB [70] | | 60 kWth | | | | |
|-----------------|------------|-----------------|---------------------------|---------------|-----------------|------------|---------------------------------|---------------------|
| Separation port | k_{CO_2} | Separation port | Low grade OS ^a | High grade OS | Separation port | Air | O ₂ /CO ₂ | O ₂ /RFG |
| | | | k_{CO_2} | k_{CO_2} | | k_{CO_2} | k_{CO_2} | k_{CO_2} |
| BA | 0.91 | Bottom | 0.47 | 0.68 | BA | 0.79 | 0.26 | 0.42 |
| SHA | 0.97 | INTREX | 0.97 | 0.97 | EHE | 0.54 | 0.52 | 0.45 |
| | | SH-RH | 0.79 | 0.82 | Cooler | 0.48 | 0.41 | – |
| ECO | 0.91 | ECO | 0.80 | 0.83 | Filter | 0.36 | 0.31 | 0.56 |
| CA | 0.98 | APH | 0.85 | 0.88 | | | | |
| ESP1 | 0.96 | ESP1 | 0.82 | 0.82 | | | | |
| ESP2 | 0.97 | ESP2 | 0.83 | 0.83 | | | | |
| ESP3 | 0.97 | ESP3 | 0.84 | 0.85 | | | | |
| | | ESP4 | 0.81 | | | | | |

^aOS = Oil shale.

– No ash sampling.

Table 8
Comparison of ECD (k_{CO_2}) from air and oxy-fuel experiments at different separation ports.

| Combustion mode | ECD | BA | EHE | C1 | C2 | Filter |
|-----------------|----------------------|------|------|------|------|--------|
| Air | k_{CO_2} | 0.79 | 0.54 | 0.58 | 0.37 | 0.36 |
| | $k_{CO_2, Calcite}$ | 0.76 | 0.54 | 0.52 | 0.27 | 0.25 |
| | $k_{CO_2, Dolomite}$ | 0.87 | 0.76 | 0.92 | 0.76 | 0.77 |
| OXY21 | k_{CO_2} | 0.17 | 0.29 | 0.60 | 0.30 | 0.29 |
| | $k_{CO_2, Calcite}$ | 0.04 | 0.18 | 0.56 | 0.19 | 0.17 |
| | $k_{CO_2, Dolomite}$ | 0.70 | 0.68 | 0.93 | 0.72 | 0.74 |
| OXY25 | k_{CO_2} | 0.22 | 0.36 | 0.36 | 0.21 | 0.33 |
| | $k_{CO_2, Calcite}$ | 0.04 | 0.17 | 0.25 | 0.07 | 0.26 |
| | $k_{CO_2, Dolomite}$ | 0.94 | 0.88 | 0.79 | 0.72 | 0.78 |
| OXY30 | k_{CO_2} | 0.34 | 0.57 | 0.39 | 0.35 | 0.20 |
| | $k_{CO_2, Calcite}$ | 0.17 | 0.49 | 0.29 | 0.20 | – |
| | $k_{CO_2, Dolomite}$ | 0.83 | 0.95 | 0.88 | 0.89 | 0.89 |
| OXY40 | k_{CO_2} | 0.32 | 0.57 | 0.53 | 0.54 | 0.43 |
| | $k_{CO_2, Calcite}$ | 0.13 | 0.46 | 0.44 | 0.38 | 0.16 |
| | $k_{CO_2, Dolomite}$ | 0.93 | 0.97 | 0.92 | 0.91 | 0.95 |
| OXY50 + RFG | k_{CO_2} | 0.56 | 0.41 | – | – | – |
| | $k_{CO_2, Calcite}$ | 0.45 | 0.38 | – | – | – |
| | $k_{CO_2, Dolomite}$ | 0.93 | 0.68 | – | – | – |
| OXY75 + RFG | k_{CO_2} | 0.27 | 0.48 | – | – | 0.56 |
| | $k_{CO_2, Calcite}$ | 0.12 | 0.49 | – | – | 0.51 |
| | $k_{CO_2, Dolomite}$ | 0.80 | 0.66 | – | – | 0.95 |

- No ash sampling.
- No analytical results.

decomposition of calcite and dolomite increases in air and O_2/CO_2 modes. BA- $k_{CO_2, Dolomite}$ is shifted slightly to a higher temperature under O_2/CO_2 compared to air combustion and reached maximum decomposition at T_{DB} 770 °C. EHE ashes show a higher calcite decomposition compared to BA. Hence, EHE- $k_{CO_2, Calcite}$ values are affected more by

T_{Riser} . In addition, CO_2 % might differ in bed and EHE locations, however the actual CO_2 concentration in different CFB riser were not measured during the experiment. Under O_2/RFG (particularly OXY50 + RFG), higher carbonates decompositions for BA and EHE ashes occurred at lower temperature. Whereas the decomposition is mainly dependent on other operating parameters during the combustion process include particle residence time, low CO_2 partial pressure at OXY50 + RFG, and higher T_{EHE} temperature compared to OXY75 + RFG (see Table 4).

3.6. Trace elements and heavy metals

The elements data of BA, EHE, and Filter ashes for air and oxy-fuel combustion experiments presented in Fig. 9(a–c) in increasing order are: As, Cu, V, Ni, Zn, Cr, Pb, Rb, Ba, Sr, Mn, and Ti. These elements represents the typical ash residue content of kundersite oil shale as reported in [23]. Most of the elements (As, Cu, V, Ni, Cr, Pb, Rb, Ba, Sr and Ti) increases along the ash flow path, they depleted in BA and condensed in the bag filter due to low gas temperature regions. The condensation and adsorption processes after combustion in boilers, and accumulation of particles with decreasing temperature are considered as the main mechanisms causing to increase concentrations of heavy metals in the finest particles of overhead zones. Moreover, trace elements increase with the increase of specific elements such as iron, silicon, and aluminium along the flow path and further from the boiler. Oxy-fuel combustion shows a strong separation of fine ash, the coarse calcite and sulphated particles are presented in BA ashes, while sandy clay elements concentrated more in cooler and filter ashes. For this reason, trace elements and heavy metals concentrations are mainly presented in the finer particles of overhead zones. One exception for Mn, for which the concentration was lower in the Filter than in BA, and similar results were reported in [45]. The concentration of oxygen in the entering gas also affected the content of elements in the BA. It could be seen that by increasing inlet O_2 %, the concentration of all of elements (except for Zn) decreased. And compared to air-combustion, these concentrations were lower with RFG application. Literature studies [74] reported that variations in volatilization of trace metals are enhanced under oxy-fuel combustion, due to CO_2 interaction with ash compounds. For other

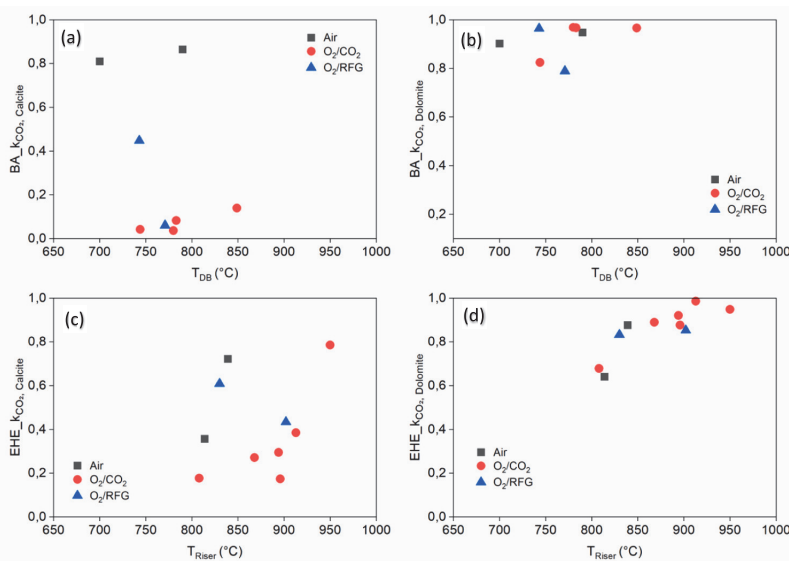


Fig. 8. Effect of dense bed (T_{DB}) and riser (T_{Riser}) temperatures under air and oxy-fuel experiments on: (a) BA- $k_{CO_2, Calcite}$, (b) BA- $k_{CO_2, Dolomite}$, (c) EHE- $k_{CO_2, Calcite}$ (d) EHE- $k_{CO_2, Dolomite}$.

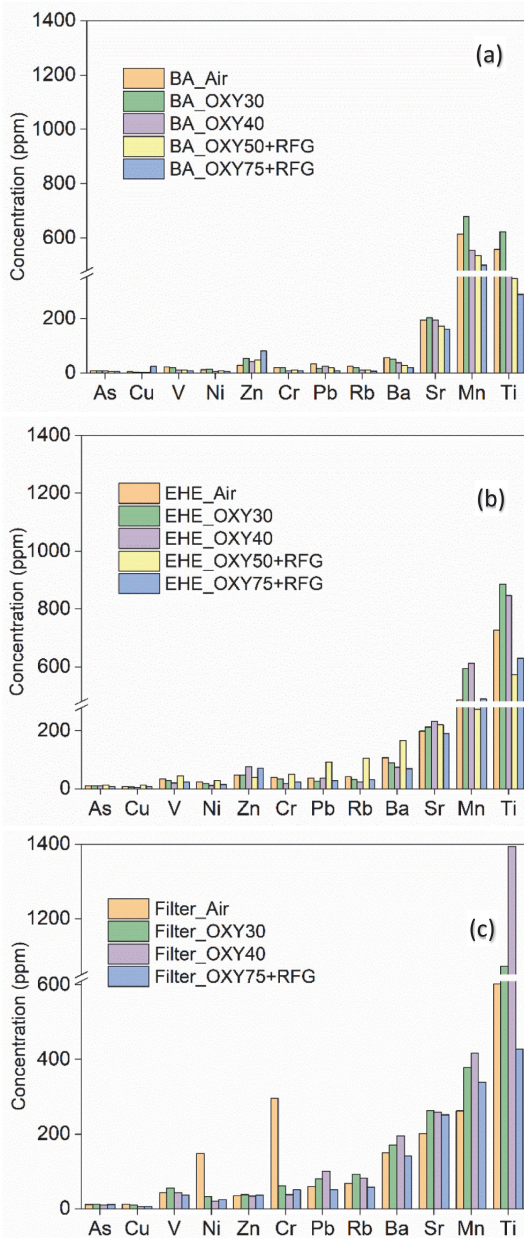


Fig. 9. Comparison of ash composition under air and oxy-fuel combustion experiments; (a) BA, (b) EHE, and (c) Filter.

ash flux, EHE ashes have slight differences in elements behaviour at higher $O_2\%$. While Filter ash elements increased with higher $O_2\%$ under O_2/CO_2 mode, and these concentrations were dropped in OXY75 + RFG combustion environment. RFG has different effect on EHE ashes as some elements (As, Cu, V, Ni, Zn, Cr, Pb, Rb and Ba) increased noticeably in OXY50 + RFG and reduced under OXY75 + RFG. Therefore, the variation must be related to differences in operating conditions of the CFB combustion experiment such as the combustion temperature in that

boiler, the time of combustion (vaporization), and the particle size distribution [75]. In conclusion, oxy-fuel combustion had no noticeable impact on the concentrations of elements in the ash. Oxy-firing effects the distribution of trace elements and heavy metals because of the different PSDs obtained from oxy combustion than in air. These elements show a larger depletion in BA and a higher deposition in filter ashes under O_2/CO_2 compared to air. However, the fuel utilized in this study is oil shale, and the element concentrations are highly dependent on the type of the fuel used in the process. That's why additional research is needed to investigate the effect of oxy-fuel and RFG application on elements behaviour. Moreover oxy-firing ashes have higher carbonate content, and oxy environment tends to lower calcite decompositions with low lime content, therefore there are potentials to reduce ash leachability of trace elements.

4. Conclusions

A series of air and oxy-fuel combustion experiments were conducted in a 60 kWth CFB pilot facility to study ash characterisation and mineral composition at different separation ports. This study represents the first investigation of oil shale oxy-combustion at higher inlet $O_2\%$ and with using RFG.

The results indicate that under oxy-fuel CFB combustion, the ash distribution shows a strong-grained size separation compared to air firing. SSA results show the difference between the surface area in the BA and EHE ashes is significantly higher in air mode, compared to oxy combustion, and higher surface area observed in the Filter ash under high $O_2\%$ atmosphere.

The decomposition of Ca-carbonates was limited during oxy-fuel combustion because of the high CO_2 partial pressure, resulting in an increase in carbonate content in the oxy-firing ashes. Thus, the total CO_2 emission reduction from air to oxyfuel combustion exceeded 15 %. The limited decomposition of calcite in oxy-fuel modes decreases the amount of free lime which can react with quartz thus lowering the amount of akermanite and belite formations in BAs compared to air-firing BAs. RFG application improves the contact and gas residence time with particles resulting in the increase formations of akermanite, merwinite, belite and decrease amount of quartz in both BA and EHE. The content of secondary silicates is higher in ashes obtained from oxy-fuel combustion because of the increased particle temperature and higher SO_2 partial pressure. Similar amounts of $CaSO_4$ were formed in both air and oxy-fuel cases, suggested that the sulfation reaction was not affected by switching from air to the oxy environment.

Oxy-fuel combustion had no noticeable impact on the concentration of elements in the ash. These elements show a larger depletion in BAs and a higher deposition in Filter ashes under oxy mode compared to air indicating the effect of different PSDs obtained from oxy combustion than in air combustion.

CRedit authorship contribution statement

Mais Baqain: Writing – original draft, Writing – review & editing. **Can Rüstü Yörük:** Writing – original draft, Writing – review & editing. **Dmitri Nešumajev:** Conceptualization, Data curation, Writing – review & editing. **Oliver Järvik:** Writing – review & editing. **Alar Konist:** Funding acquisition, Project administration, Conceptualization, Supervision, Writing – review & editing.

Declaration of Competing Interest

The authors declare that they have no known competing financial interests or personal relationships that could have appeared to influence the work reported in this paper.

Data availability

Data will be made available on request.

Acknowledgements

This research was funded by the Estonian Research Council from the National Programme for Addressing Socio-Economic Challenges through R&D (RITA), which is supported by the Estonian Government and the European Regional Development Fund.

References

- Stanger R, Wall T, Spörl R, Paneru M, Grathwohl S, Weidmann M, et al. Oxyfuel combustion for CO₂ capture in power plants. *Int J Greenh Gas Control* 2015;40: 55–125. <https://doi.org/10.1016/j.jggc.2015.06.010>.
- Yang C, Kim Y, Bang B, Jeong S, Moon J, Mun TY, et al. Oxy-CFB combustion technology for use in power-generation applications. *Fuel* 2020;267:117206. <https://doi.org/10.1016/j.fuel.2020.117206>.
- Seddighi S. Design of large scale oxy-fuel fluidized bed boilers: Constant thermal power and constant furnace size scenarios. *Energy* 2017;118:1286–94. <https://doi.org/10.1016/j.energy.2016.11.004>.
- Singh RI, Kumar R. Current status and experimental investigation of oxy-fired fluidized bed. *Renew Sustain Energy Rev* 2016;61:398–420. <https://doi.org/10.1016/j.rser.2016.04.021>.
- Cuellar-Franca RM, Azapagic A. Carbon capture, storage and utilisation technologies: A critical analysis and comparison of their life cycle environmental impacts. *J CO₂ Util* 2015;9:82–102. <https://doi.org/10.1016/j.jcou.2014.12.001>.
- Smit B. Carbon Capture and Storage: Introductory lecture. *Faraday Discuss* 2016; 192:9–25. <https://doi.org/10.1039/C6FD00148C>.
- Krishnamurthy N, Blasiak W, Lugnet A. Development of High Temperature Air and Oxy-Fuel combustion technologies for minimized CO₂ and NO_x emissions in Industrial Heating. *Jt Int Conf Sustain Energy Environ* 2004:1–6.
- Scheffknecht G, Al-Makhadmeh L, Schnell U, Maier J. Oxy-fuel coal combustion-A review of the current state-of-the-art. *Int J Greenh Gas Control* 2011;5:16–35. <https://doi.org/10.1016/j.jggc.2011.05.020>.
- Scheuer C, Boot E, Carse N, Clardy A, Gallagher J, Heck S, et al. Fluidized bed combustion in high concentrations of O₂ and CO₂. *Phys Educ Sport Child Youth with Spec Needs Res – Best Pract – Situat* 2006;343–54. <https://doi.org/10.2/JQUERY.MIN.JS>.
- García-Labiano F, Rufas A, De Diego LF, Las O-L, Gayán P, Abad A, et al. Calcium-based sorbents behaviour during sulphation at oxy-fuel fluidised bed combustion conditions. *Fuel* 2011;90:3100–8. <https://doi.org/10.1016/j.fuel.2011.05.001>.
- Chen L, Wang C, Yan G, Zhao F, Anthony EJ. The simultaneous calcination/sulfation reaction of limestone under oxy-fuel CFB conditions. *Fuel* 2019;237: 812–22. <https://doi.org/10.1016/j.fuel.2018.10.060>.
- Kim Y Bin, Gwak YR, Keel SI, Yun JH, Lee SH. Direct desulfurization of limestones under oxy-circulating fluidized bed combustion conditions. *Chem Eng J* 2019;377: 119650. <https://doi.org/10.1016/j.cej.2018.08.036>.
- Jia L, Tan Y, Anthony EJ. Emissions of SO₂ and NO_x during Oxy-Fuel CFB combustion tests in a mini-circulating fluidized bed combustion reactor. *Energy Fuel* 2010;24:910–5. <https://doi.org/10.1021/ef91076g>.
- Anthony EJ, Granatstein DL. Sulfation phenomena in fluidized bed combustion systems. *Prog Energy Combust Sci* 2001;27:215–36. [https://doi.org/10.1016/S0360-1285\(00\)00021-6](https://doi.org/10.1016/S0360-1285(00)00021-6).
- Scala F, Chironne R, Meloni P, Carcangiu G, Manca M, Mulas G, et al. Fluidized bed desulfurization using lime obtained after slow calcination of limestone particles. *Fuel* 2013;114:99–105. <https://doi.org/10.1016/j.fuel.2012.11.072>.
- Czakiert T, Sztetler K, Karski S, Markiewicz D, Nowak W. Oxy-fuel circulating fluidized bed combustion in a small pilot-scale test rig. *Fuel Process Technol* 2010; 91:1617–23. <https://doi.org/10.1016/j.fuproc.2010.06.010>.
- Konist A, Loo L, Valtsev A, Maaten B, Siirde A, Neshumayev D, et al. Calculation of the amount of Estonian oil shale products from combustion in regular and oxy-fuel mode in a CFB boiler. *Oil Shale* 2014;31:211–24. <https://doi.org/10.3176/oil.2014.3.02>.
- Al-Makhadmeh L, Maier J, Al-Harashsh M, Scheffknecht G. Oxy-fuel technology: An experimental investigations into oil shale combustion under oxy-fuel conditions. *Fuel* 2013;103:421–9. <https://doi.org/10.1016/j.fuel.2012.05.054>.
- Loo L, Konist A, Neshumayev D, Pihu T, Maaten B, Siirde A. Ash and flue gas from oil shale oxy-fuel circulating fluidized bed combustion. *Energies* 2018;11. <https://doi.org/10.3390/en11051218>.
- Yörük CR, Meriste T, Sener S, Kuuksik R, Trikkel A. Thermogravimetric analysis and process simulation of oxy-fuel combustion of blended fuels including oil shale, semicoke, and biomass. *Int J Energy Res* 2018;42:2213–24. <https://doi.org/10.1002/er.4011>.
- Tan Y, Jia L, Wu Y. Some combustion characteristics of biomass and coal cofiring under oxy-fuel conditions in a pilot-scale circulating fluidized combustor. *Energy Fuel* 2013;27:7000–7. <https://doi.org/10.1021/ef4011109>.
- Kosowska-Golachowska M, Luckos A, Kijo-Kleczkowska A. Pollutant Emissions during Oxy-Fuel Combustion of Biomass in a Bench Scale CFB Combustor. *Energies* 2022;15:1–23. <https://doi.org/10.3390/en15030706>.
- Konist A, Anthony EJ, Neshumayev D, Baird ZS, Maasikmets M, Järvi O. Mineral and heavy metal composition of oil shale ash from oxyfuel combustion. *ACS Omega* 2020;5:32498–506. <https://doi.org/10.1021/acsomega.0c04466>.
- Konist A, Valtsev A, Loo L, Pihu T, Liira M, Kirsimäe K. Influence of oxy-fuel combustion of Ca-rich oil shale fuel on carbonate stability and ash composition. *Fuel* 2015;139:671–7. <https://doi.org/10.1016/j.fuel.2014.09.050>.
- Al-Makhadmeh LA, Bathia MA, Maier J, Rawadieh SE, Altarawneh IS, Scheffknecht G. Effect of air and oxyfuel staged combustion on oil shale fly ash formation with direct in-furnace limestone addition for sulphur retention. *Fuel* 2018;220:192–9. <https://doi.org/10.1016/j.fuel.2018.01.057>.
- Wu H, Zhang Y, Chen W, Liu Z, Zhang T, Sun Q, et al. Experimental research on the characteristics of ash in oxy-fuel combustion. *Fuel* 2020;263. <https://doi.org/10.1016/j.fuel.2019.116799>.
- Wu Y, Wang C, Tan Y, Jia L, Anthony EJ. Characterization of ashes from a 100kWth pilot-scale circulating fluidized bed with oxy-fuel combustion. *Appl Energy* 2011; 88:2940–8. <https://doi.org/10.1016/j.apenergy.2011.03.007>.
- Li W, Liu D, Li S. Characteristics of Fly Ash under Oxy-Fuel Circulating Fluidized Bed Combustion. *Energy Fuel* 2018;32:9666–71. <https://doi.org/10.1021/acs.energyfuels.8b00934>.
- Li S, Li H, Li W, Xu M, Eddings EG, Ren Q, et al. Coal combustion emission and ash formation characteristics at high oxygen concentration in a 1 MWth pilot-scale oxy-fuel circulating fluidized bed. *Appl Energy* 2017;197:203–11. <https://doi.org/10.1016/j.apenergy.2017.03.028>.
- Han T, Wang C, Sun R, Zhu C, Liu Y, Che D. Experimental study on ash deposition of Zhundong coal in oxy-fuel combustion. *J Energy Inst* 2019;92:1697–709. <https://doi.org/10.1016/j.joei.2019.01.004>.
- Sheng C, Li Y. Experimental study of ash formation during pulverized coal combustion in O₂/CO₂ mixtures. *Fuel* 2008;87:1297–305. <https://doi.org/10.1016/j.fuel.2007.07.023>.
- Wang C, Jia L, Tan Y, Anthony EJ. Carbonation of fly ash in oxy-fuel CFB combustion. *Fuel* 2008;87:1108–14. <https://doi.org/10.1016/j.fuel.2007.06.024>.
- Wall T, Liu Y, R&D SB-A, University M. A scoping study on Oxy-CFB technology as an alternative carbon capture option for Australian black and brown coals. 2012. Teramae T, Takarada T. Fine ash formation during pulverized coal combustion. *Energy Fuel* 2009;23:2018–24. https://doi.org/10.1021/EF800658W/ASSET/IMAGES/LARGE/EF-2008-00658W_0001.JPG.
- Suriyawong A, Gamble M, Lee MH, Axelbaum R, Biswas P. Submicrometer particle formation and mercury speciation under O₂-CO₂ coal combustion. *Energy Fuel* 2006;20:2357–63. <https://doi.org/10.1021/EF060178S/ASSET/IMAGES/MEDIUM/EF060178SE000005.GIF>.
- Yu D, Morris WJ, Erickson R, Wendt JOL, Fry A, Senior CL. Ash and deposit formation from oxy-coal combustion in a 100 kW test furnace. *Int J Greenh Gas Control* 2011;5:S159–67. <https://doi.org/10.1016/j.jggc.2011.04.003>.
- Zheng Z, Wang H, Guo S, Luo Y, Du Q, Wu S. Fly ash deposition during oxy-fuel combustion in a bench-scale fluidized-bed combustor. *Energy Fuel* 2013;27: 4609–16. <https://doi.org/10.1021/EF400774B>.
- Ots A. Oil shale fuel combustion 2006:833.
- Kuusik R, Uibu M, Kirsimäe K, Mõtle P, Meriste T. Open-air deposition of Estonian oil shale ash: Formation, state of art, problems and prospects for the abatement of environmental impact. *Oil Shale* 2012;29:376–403. <https://doi.org/10.3176/oil.2012.4.08>.
- Olszak-Humienik M, Jablonski M. Thermal behavior of natural dolomite. *J Therm Anal Calorim* 2015;119:2239–48. <https://doi.org/10.1007/S10973-014-4301-6/FIGURES/7>.
- Valverde JM, Perejon A, Medina S, Perez-Maqueda LA. Thermal decomposition of dolomite under CO₂: insights from TGA and in situ XRD analysis. *Phys Chem Chem Phys* 2015;17:30162–76. <https://doi.org/10.1039/C5CP05596B>.
- V L'vov B. Mechanism and kinetics of thermal decomposition of carbonates. *Thermochim Acta* 386 2002 1–16 [https://doi.org/https://doi.org/10.1016/S0040-6031\(01\)00757-2](https://doi.org/https://doi.org/10.1016/S0040-6031(01)00757-2).
- Arro H, Prikka A, Pihu T. Calculation of CO₂ emission from CFB boilers of oil shale power plants. *Oil Shale* 2006;23:356–65.
- Leben K, Mõtle P, Paaver P, Konist A, Pihu T, Paiste P, et al. Long-term mineral transformation of Ca-rich oil shale ash waste. *Sci Total Environ* 2019;658:1404–15. <https://doi.org/10.1016/j.scitotenv.2018.12.326>.
- Aunela-Tapola LA, Frandsen FJ, Hänsäen EK. Trace metal emissions from the Estonian oil shale fired power plant. *Fuel Process Technol* 1998;57:1–24. [https://doi.org/10.1016/S0378-3820\(98\)00069-1](https://doi.org/10.1016/S0378-3820(98)00069-1).
- Borm PJA. Toxicity and occupational health hazards of coal fly ash (CFA). A review of data and comparison to coal mine dust. *Ann Occup Hyg* 1997;41:659–76. [https://doi.org/10.1016/S0003-4878\(97\)00026-4](https://doi.org/10.1016/S0003-4878(97)00026-4).
- Tsiridis V, Petala M, Samaras P, Kungolos A, Sakellaropoulos GP. Environmental hazard assessment of coal fly ashes using leaching and ecotoxicity tests. *Ecotoxicol Environ Saf* 2012;84:212–20. <https://doi.org/10.1016/j.ecoenv.2012.07.011>.
- Reinik J, Irha N, Steinnes E, Urb G, Jefimova J, Piirisalu E, et al. Changes in trace element contents in ashes of oil shale fueled PF and CFB boilers during operation. *Fuel Process Technol* 2013;115:174–81. <https://doi.org/10.1016/j.fuproc.2013.06.001>.
- Blinova I, Bityukova L, Kasemets K, Ivask A, Käikinen A, Kurvet I, et al. Environmental hazard of oil shale combustion fly ash. *J Hazard Mater* 2012; 229–230:192–200. <https://doi.org/10.1016/j.jhazmat.2012.05.095>.
- Lees H, Järvi O, Konist A, Siirde A, Maaten B. Comparison of the ecotoxic properties of oil shale industry by-products to those of coal ash. *Oil Shale* 2022;39: 1–19. <https://doi.org/10.3176/oil.2022.1.01>.

- [51] Usta MC, Yörük CR, Hain T, Paaver P, Snellings R, Rozov E, et al. Evaluation of New Applications of Oil Shale Ashes in Building Materials. *Miner* 2020, Vol 10, Page 765 2020;10:765. <https://doi.org/10.3390/MIN10090765>.
- [52] Pikkor H, Jarvik O, Lees H, Konist A, Siirde A, Maaten B. Characterization and enhancement of oil shale fly ash from CFB boiler. 2021 6th Int Conf Smart Sustain Technol Split 2021 2021. <https://doi.org/10.23919/SPLITECH52315.2021.9566470>.
- [53] Pihu T, Konist A, Puura E, Liira M, Kirsimäe K. Properties and environmental impact of oil shale ash landfills. *Oil Shale* 2019;36:257–70. <https://doi.org/10.3176/oil.2019.2.01>.
- [54] Ministry of the Environment of Estonia. National Development Plan for the Use of Oil Shale 2016;2016–2030:75.
- [55] Taylor JC. Computer programs for standardless quantitative analysis of minerals using the full powder diffraction profile. *Powder Diffr* 1991;6:2–9. <https://doi.org/10.1017/S0885715600016778>.
- [56] Kuusik R, Uibu M, Kirsimäe K. Characterization of oil shale ashes formed at industrial-scale CFBC boilers. *Oil Shale* 2006;22:407–19.
- [57] Hotta A, Parkkonen R, Hiltunen M, Arro H, Loosaar J, Parve T, et al. Experience of estonian oil shale combustion based on CFB technology at narva power plants. *Oil Shale* 2006;22:381–97.
- [58] Li H, Li S, Ren Q, Li W, Xu M, Liu JZ, et al. Experimental results for oxy-fuel combustion with high oxygen concentration in a 1MWth pilot-scale circulating fluidized bed. *Energy Procedia* 2014;63:362–71. <https://doi.org/10.1016/j.egypro.2014.11.039>.
- [59] Duan L, Sun H, Zhao C, Zhou W, Chen X. Coal combustion characteristics on an oxy-fuel circulating fluidized bed combustor with warm flue gas recycle. *Fuel* 2014;127:47–51. <https://doi.org/10.1016/j.fuel.2013.06.016>.
- [60] Pihu T, Arro H, Prikki A, Rootamm R, Konist A, Kirsimäe K, et al. Oil shale CFBC ash cementation properties in ash fields. *Fuel* 2012;93:172–80. <https://doi.org/10.1016/j.fuel.2011.08.050>.
- [61] Li W, Wang L, Qiao Y, Lin JY, Wang M, Chang L. Effect of atmosphere on the release behavior of alkali and alkaline earth metals during coal oxy-fuel combustion. *Fuel* 2015;139:164–70. <https://doi.org/10.1016/j.fuel.2014.08.056>.
- [62] Quann RJ, Sarofim AF. Vaporization of refractory oxides during pulverized coal combustion. *Symp Combust* 1982;19:1429–40. [https://doi.org/10.1016/S0082-0784\(82\)80320-2](https://doi.org/10.1016/S0082-0784(82)80320-2).
- [63] Kahru A, Põllumaa L. Environmental hazard of the waste streams of Estonian oil shale industry: An ecotoxicological review. *Oil Shale* 2006;23:53–93.
- [64] Vassilev SV, Baxter D, Vassileva CG. An overview of the behaviour of biomass during combustion: Part I. Phase-mineral transformations of organic and inorganic matter. *Fuel* 2013;112:391–449. <https://doi.org/10.1016/j.fuel.2013.05.043>.
- [65] Myat-Htun M, Mohammadi H, Noor AFM, Kawashita M, Ismail YMB. Comprehensive investigation of phase formation mechanism and physico-mechanical properties of ca-mg-silicate. *ASEAN Eng J* 2021;11:37–50. <https://doi.org/10.11113/AEJ.V11.16676>.
- [66] Yörük CR, Meriste T, Trikkel A, Kuusik R. Thermo-oxidation characteristics of oil shale and oil shale char under oxy-fuel combustion conditions. *J Therm Anal Calorim* 2015;121:509–16. <https://doi.org/10.1007/s10973-015-4484-5>.
- [67] Fegley B, Lidders K, Treiman AH, Klingelhöfer G. The rate of pyrite decomposition on the surface of venus. *Icarus* 1995;115:159–80. <https://doi.org/10.1006/ICAR.1995.1086>.
- [68] Bhargava SK, Garg A, Subasinghe ND. In situ high-temperature phase transformation studies on pyrite. *Fuel* 2009;88:988–93. <https://doi.org/10.1016/j.fuel.2008.12.005>.
- [69] Lv W, Yu D, Wu J, Yu X, Du Y, Xu M. A mechanistic study of the effects of CO2 on pyrrhotite oxidation. *Proc Combust Inst* 2017;36:3925–31. <https://doi.org/10.1016/j.proci.2016.06.147>.
- [70] Plamus K, Ots A, Pihu T, Neshumayev D. Firing Estonian oil shale in CFB boilers -ASH balance and behaviour of carbonate minerals. *Oil Shale* 2011;28:58–67. <https://doi.org/10.3176/oil.2011.1.07>.
- [71] Hajaligol MR, Longwell JP, Sarofim AF. Analysis and modeling of the direct sulfation of CaCO₃. *Ind Eng Chem Res* 1988;27:2203–10. <https://doi.org/10.1021/ie00084a002>.
- [72] Snow MJH, Longwell JP, Sarofim AF. Direct sulfation of calcium carbonate. *Ind Eng Chem Res* 1988;27:268–73. <https://doi.org/10.1021/ie00074a011>.
- [73] De Las O-L, Rufas A, De Diego LF, García-Labiano F, Gayán P, Abad A, et al. Morphological analysis of sulfated Ca-based sorbents under conditions corresponding to oxy-fuel fluidized bed combustion. *Fuel* 2015;162:264–70. <https://doi.org/10.1016/j.fuel.2015.09.016>.
- [74] Contreras ML, García-Frutos FJ, Bahillo A. Oxy-fuel combustion effects on trace metals behaviour by equilibrium calculations. *Fuel* 2013;108:474–83. <https://doi.org/10.1016/j.fuel.2013.02.029>.
- [75] Xu M, Yan R, Zheng C, Qiao Y, Han J, Sheng C. Status of trace element emission in a coal combustion process: a review. *Fuel Process Technol* 2004;85:215–37. [https://doi.org/10.1016/S0378-3820\(03\)00174-7](https://doi.org/10.1016/S0378-3820(03)00174-7).

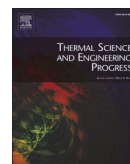
Publication II

Baqain, Mais; Neshumayev, Dmitri; Konist, Alar (2023). **NO_x and N₂O Emissions from Ca-rich Fuel Conversion in Oxyfuel Circulating Fluidized Bed Combustion**. Thermal Science and Engineering Progress, 42. DOI: 10.1016/j.tsep.2023.101938.



Contents lists available at ScienceDirect

Thermal Science and Engineering Progress

journal homepage: www.sciencedirect.com/journal/thermal-science-and-engineering-progress

NO_x and N₂O emissions from Ca-rich fuel conversion in oxyfuel circulating fluidized bed combustion

Mais Baqain^{*}, Dmitri Neshumayev, Alar Konist

Department of Energy Technology, Tallinn University of Technology, 19086 Tallinn, Estonia

ARTICLE INFO

Keywords:

NO_x
N₂O
Oxyfuel combustion
Circulated fluidized bed
Ca-rich fuel
Oil shale

ABSTRACT

A part of Estonia's power generation is based on oil shale combustion in thermal power plants, resulting in high CO₂ and pollutant emissions. The presented paper is a part of long-term experimental work to investigate the combustion of Ca-rich oil shale for air and oxyfuel combustion environments. The experiments were performed in a 60 kWth circulating fluidized bed (CFB) test facility under air, O₂/CO₂, and O₂ with the recycled flue gas (RFG) modes of inlet O₂ as vol.% ranging from 21% to 52%, and with RFG of 50% and 87%. The influence of different combustion atmospheres, excess oxygen volumetric ratios in the primary oxidizer (λ_{p1}), and dense bed temperatures (T_{DB}), on the total NO_x and N₂O formations, have been studied in detail.

The results show that specific concentrations of NO_x (per MJ) were reduced by 14% in O₂/CO₂ mode, and 22% in O₂/RFG compared to air combustion. N₂O emissions were increased in OXY21 mode and reduced significantly from 20 mg/MJ to 4 mg/MJ with increasing inlet O₂% to 52% under O₂/CO₂. NO_x and N₂O emissions were the lowest of all combustion experiments at high inlet O₂% with RFG application (OXY87 + RFG). Under all tested atmospheres, NO_x emissions were increasing with increasing excess oxygen in the primary oxidizer. N₂O enhanced with excess oxygen, accounted for the homogenous gas-phase reaction of volatile-N and the heterogeneous reaction of char-N. NO_x emissions at low operating T_{DB} were decreasing with increasing bed temperatures and increased at higher $T_{DB} > 770$ °C in air combustion and $T_{DB} > 850$ °C in OXY30. N₂O emissions were slightly decreased at higher bed temperatures under air and O₂/CO₂ modes. Combustion efficiency enhanced at higher inlet O₂% resulting in lower CO concentrations with reduced fuel burnout, and increased NO_x and N₂O emissions.

Overall, NO_x and N₂O formations were more affected by the condition of operating parameters under both air and oxyfuel combustion experiments, and the obtained results are giving confidence that oxyfuel technology does not influence the release of nitrogen emissions from oil shale combustion. To lower the cost of CO₂ impurities removal, the optimal operating conditions during oil shale CFB combustion can be confirmed after considering the discussed parameters. However, further CO₂ purification resulting from oil shale oxyfuel flue gas stream is possibly required.

Introduction

Combustion of fossil fuels is one of the major ways to meet the world's rising energy needs. Renewable energy is growing rapidly, but not fast enough to fulfil the mounting global electricity demand [1]. However, the fossil fuel combustion process is always associated with the release of greenhouse gas and air pollutants (CO₂, SO₂, NO_x). The published "Greenhouse Gas Bulletin" by the World Meteorological Organization indicates that the average CO₂ concentration in the atmosphere was considerably higher than the value before the industrial

revolution [2]. The gradual increase in earth's temperature resulting from the accumulated greenhouse gases indicates the urgent need to reduce CO₂ by adopting different low carbon footprint technologies, such as flue gas CO₂ capture [3], and oxyfuel combustion process [4].

Nitrogen oxides from fossil fuel combustion consist of mainly nitric oxide (NO), nitrogen dioxide (NO₂), and nitrous oxide (N₂O). NO_x is a generic term for nitrogen oxides (NO, NO₂), considered to be very toxic at high concentrations, responsible for acid rain, and participate in the formation of photochemical smog [5]. Nitrous oxide (N₂O) is a greenhouse gas and the main contributor to the depletion of the stratospheric ozone layer [6]. Considering their harmful effects, the standards for

^{*} Corresponding author.

E-mail address: Mais.baqain@taltech.ee (M. Baqain).

<https://doi.org/10.1016/j.tsep.2023.101938>

Received 26 January 2023; Received in revised form 3 April 2023; Accepted 1 June 2023

Available online 7 June 2023

2451-9049/© 2023 Elsevier Ltd. All rights reserved.

Abbreviations

| | |
|----------------|---|
| CFB | Circulating fluidized bed |
| FTIR | Fourier transform infrared |
| LOI | Loss of ignition |
| RFG | Recycled flue gas |
| T_{DB} | Temperature of dense bed |
| TOC | Total organic carbon |
| λ_{Pr} | Excess oxygen ratio in the primary oxidizer |

regulations on nitrogen pollutant emission levels from combustion power plants have been defined worldwide [7]. In combustion processes, nitrogen oxides (NO_x), are formed from the partial oxidation of the fuel-N entering the combustor or /and with the oxidant (mainly air) used for combustion. The formation of nitrogen oxides can occur primarily by three mechanisms [8], as shown in Fig. 1: (1) Thermal- NO_x , which forms because of the direct oxidation reaction between atmospheric nitrogen and oxygen, (2) Prompt- NO_x , which forms as a result of the reactions between atmospheric nitrogen and hydrocarbon radicals from the fuel, and (3) Fuel- NO_x , which forms because of the oxidation of the nitrogen present in the organic matter of fuel. The thermal and prompt nitrogen oxides mainly occur at combustion temperatures exceeding 1,100 °C, which is inherent in the fossil fuel pulverized combustion technology.

In circulating fluidized bed (CFB) combustion technology, operating temperatures are usually in the range of 800–900 °C, and the formation of nitrogen oxides is mainly considered to be the result of the fuel nitrogen conversion [9]. For solid fuel combustion, the formation of nitrogen oxides from the fuel-N results in a relatively large number of homogeneous and heterogeneous complex reactions, Fig. 1. These reactions are divided into two parts, the volatile phase (HCN, NH_3 , and tars-N), and the solid phase (char-N) [10]. The distribution of nitrogen between volatile and char is influenced mainly by fuel structure and combustion temperature [11]. Yet, the formation of NO_x is not only determined by the nitrogen content of the fuel or the phase, it is a function of multiple factors such as volatility of the nitrogen present in the fuel, excess air, air staging, residence time, the fixed carbon in the bed and the presence of S adsorbents catalysts [12]. At low temperatures as in fluidized bed combustion and during the decomposition of the

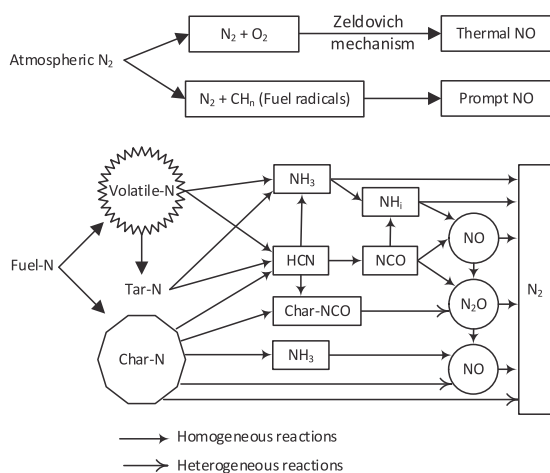


Fig. 1. Pathways of nitrogen oxide formation at pulverized and CFB combustions.

volatile-N, the formation of intermediate nitrogen compounds occurs such as HCN and ammonia (NH_3), which are subsequently oxidized to NO and N_2O and can be reduced to N_2 . During combustion, the N-char is partially oxidized to NO and N_2O and can simultaneously be reduced to N_2 . Nitrogen oxides are reduced from volatile-N and char-N through a homogeneous reaction with CO and H_2 , and a heterogeneous reaction with particles of soot, char, and adsorbent additives. Under these conditions also the formation of N_2O from the CFB system can be significant, primarily due to the oxidation of HCN in the gas phase, with a lesser contribution from char-N oxidation as well [13].

Oxyfuel combustion, a promising technology for carbon capture [14], is a process of combusting fuel in a mixture stream of pure oxygen and recycled flue gas (RFG) as the reactant of fuel combustion instead of using air [15,16].

Under oxy-fired conditions, N_2 is only present because of air in leakages, and the operating temperature (in CFB case) is less than the temperature required for the formation of thermal NO_x as well as prompt NO_x , their contributions are negligible. Thus, the nitrogen content in fuel organic matter is considered the main source of NO_x and N_2O emissions and it can vary between 0.2% and 2.5%, depending on the fuel type. The amount of NO_x emission is relatively low in CFB combustion; however, the emissions standards will tighten in the near future, and NO_x control technologies are required to meet the imposed standards. The NO_x reduction techniques are (a) primary measures applied during the combustion process and (b) secondary measures referred to as post-combustion and flue gas treatment methods. Currently, the NO_x removal efficiency exceeds 90% by adopting several secondary measures including (1) selective catalytic reduction, (2) selective non-catalytic reduction, (3) non-selective catalytic reduction, (4) pulsed corona discharge, and (5) electron beam flue gas treatments [17–21]. Multiple post-combustion methods have been discussed [15,22,23], and all the mentioned techniques can be integrated into the power unit after the combustion process. Compared to post-treatment, for example as amine absorption, oxyfuel combustion technology has a higher potential to be more energy and cost efficient [24]. However, based on the requirements of CO_2 transportation, injection, and storage, the influence of non-condensable gases, such as O_2 and NO need to be considered from the thermodynamic and hydraulic aspects. Whereas these impurities need to be removed from the CO_2 stream captured from an oxyfuel combustion process [25].

Primary measures seek to adjust the combustion parameters and modification of combustion technology to reduce NO_x formation. Many scholars have reported that the formation of NO_x from oxyfuel CFB combustion is highly affected by several parameters and they vary with the process conditions [9,26,27]. As an example, Lupiáñez et al. [9] studied the effect of O_2 concentration in the fluidized bed, bed temperature, and sorbent addition on NO emissions. Evaluating the effect of the combustion atmosphere on NO_x and N_2O emissions, several studies approved that oxyfuel can inhibit NO_x formation [28–30]. As in oxyfuel combustion atmosphere, by increasing O_2 concentration and under high CO_2 partial pressure, oxidation of HCN decreases [31]. Char gasification reactions are enhanced and the CO concentration increases, leading to NO reduction [32,33]. Moreover, the substitution of N_2 with CO_2 , in oxyfuel combustion, can lower the flame temperature, reducing NO_x formation from fuel-N [26]. Only a few studies reported the formation of N_2O emissions under oxyfuel combustion and shows that oxyfuel combustion has a positive effect on N_2O emissions, and these emissions are higher than that in air combustion [34,35]. However, these emissions were reduced at higher inlet $\text{O}_2\%$ [35–37]. Zhou et al. [36] explained the reason for high N_2O emissions under 21%/79% O_2/CO_2 than in air combustion by the inhibition of N_2O destruction due to the high CO_2 environment, and with increasing $\text{O}_2\%$, the destruction of N_2O is enhanced by increasing O radicals.

Excess oxygen is another important parameter that is positively affecting the formation of NO_x and N_2O emissions [27,38,39]. Authors reported that compared to the bed temperature, excess oxygen was

found to be the dominant variable influencing NO_x emissions [40]. Several studies have proven that gas staging is an efficient technique to reduce NO formation inside the boiler [39,41], by increasing the secondary oxidizer ratio over the primary oxidizer, and N₂O emission is reduced as well [42].

Bed temperature significantly influences the formation of NO_x and N₂O under oxyfuel CFB combustion. Generally, studies found that higher combustion temperatures enhance nitrogen release from fuel and promote their conversion to NO [26]. Zhou et al. [43], and Gong et al. [44] on the contrary, found that NO_x emissions decrease with an increase in the combustion temperature. While Tarelho et al. [45] reported that under specific combustion conditions, the effect of increasing temperature can be the opposite, and the total NO emitted is reduced. Higher temperature reduces N₂O formation, as it leads to accelerated N₂O decomposition [42]. However, there are conflicting studies about N₂O emissions, whether these emissions increase with bed temperature [46] or decrease [38]. With the application of RFG, NO_x emissions were found to be decreased, because most of the recycled NO_x and N₂O would be reduced to N₂ and N₂O in the bed combustion zone, by reacting with the amine radicals, NH and NH₂, and HCN, which reduce the volatile-N oxidized to NO [34,47,48].

Oil shale has one specific feature, its low nitrogen content, generally below 1% (wt.%, as received). Therefore, oil shale CFB combustion has low NO_x and N₂O concentrations in the flue gas [49]. The amount of NO_x and N₂O formations from fuel-N is usually proportional to fuel nitrogen content as mentioned earlier. NO_x emissions from the Estonian oil shale combustion in the industrial CFB boilers at Narva power plants are in the range of 130–160 mg/m³ (as NO₂, dry, 6% O₂) [50]. However, to meet environmental standards limits, and to achieve high CO₂ stream purity, NO_x reduction technologies are still required. For oil shale CFB combustion, limited literature can be found regarding the formation of NO_x emissions in air combustion [51–54], and oxyfuel combustion [55]. The effect of O₂/RFG on oil shale nitrogen oxide emissions has not been investigated yet. Under a 30%/70% O₂/CO₂ combustion atmosphere, it was found that the nitrogen conversion ratio to NO_x was similar to bituminous coal [56]. However, variation of NO_x formation and reduction is still a challenge in the application of oxyfuel combustion as it largely depends on the process conditions. Nevertheless, several differences in NO_x formations under oxyfuel conditions can also be expected by using Ca-rich oil shale.

This investigation is a part of the long-term experimental work carried out in a 60 kWth CFB combustor under air, O₂/CO₂, and O₂/RFG. The paper reports the result first of its kind which handles a systematic experimental study of NO_x and N₂O formations from kokersite type Estonian oil shale at a pilot scale. The combustion under oxyfuel environment with a wide variation of different parameters was carried out, and the application of RFG with high inlet O₂% has not been studied previously for the specified fuel. The paper also serves as the reference model for the industrial application of oxyfuel combustion technology in oil shale power plants.

Material

In this study oil shale fuel was used, Table 1 shows the detailed proximate analysis that includes (ash, moisture, and lower heating value (LHV)), and ultimate analyses include elemental analysis (C, H, N, S),

and TIC (total inorganic carbon) as (CO₂mineral), total organic carbon (TOC) is measured by the difference between total carbon (TC) and TIC. Ash chemical composition is presented in Table 2, ash was tested using a Rigaku Primus II X-ray fluorescence (XRF) spectrometer following ISO 29581–2:2010(E), and loss of ignition (LOI) refers to sample weight loss at 950 °C. Oil shale ash oxides are mainly composed of calcium (23%) and followed by silica (15%). Table 3 shows oil shale quantitative X-ray diffraction (XRD) results, Bruker D8 diffractometer was used, which was fitted with a Lynx-Eye linear detector, and analysis was performed using Cu Kα radiation in the 2θ range of 3 – 72°, with a step size of 0.02° 2θ and a counting time of 0.1 s per step, and the X-ray tube operated at 40 kV and 40-mA.

Test facility and operating conditions

The experiments were conducted in a 60 kWth CFB apparatus, as shown in Fig. 2. Details of the pilot facility were previously described [57]. The total height of the riser is 4.90 m, and its inner diameter is 0.12 m. The unit is fully equipped with monitoring and thermal sensors and is controlled with a LabVIEW system. The temperature measurement points are distributed along the riser in six different locations. The flue gas composition is simultaneously measured using a Fourier transform infrared (FTIR) analyser. FTIR is located between cooler 1 and cooler 2 for (CO₂, O₂, CO, H₂O, NO_x, and SO₂) emission measurements, while N₂O was measured after the condenser.

Experimental conditions in O₂/CO₂ combustion modes with inlet O₂ as vol.% of (21–52)%, and with RFG application of 50% and 87% are given in Table 4. The numbers (OXY21, OXY30, ...etc.) express the inlet oxygen concentration in volumetric percent, whereas air combustion was performed as a base case. As the air combustion process proceeds, and reached a stable condition, a transition from air to oxyfuel combustion experiment is started.

The concentration of NO_x (NO, NO₂) and the rest of the emissions (CO₂, CO, O₂, H₂O, and SO₂) in the flue gas, are monitored online by an FTIR analyser (GASMET DX4000) at stable air and oxy conditions. The optimum flue gas recycling ratio is 70% for oil shale oxyfuel combustion [58], and this ratio was decreased with increasing oxygen concentrations in the inlet gas from (50–87) vol.%. T_{DB} represents dense bed temperature and increases by increasing the inlet O₂ ratio under O₂/CO₂ mode to reach a maximum value of 866 °C. λ_{pr} represents the excess oxygen ratio in the primary oxidizer that plays an important role in the char combustion and CO concentration in the combustion bed. The combined uncertainty (U_c) measurements [59] for NO_x emissions as mg/MJ of oil shale, increase with respect to NO_x concentration. For N₂O emissions, U_c was almost negligible since these emissions were below 30 mg/MJ for all combustion experiments.

Calculations of normalised NO_x and N₂O

Since oxyfuel combustion experiments were conducted under different inlet oxygen concentrations there are differences in the oil shale feeding rates. In order to enable the comparison between air and oxy-firing, avoiding the effects of varying different fuel loads or flue gas flow rates, the (NO_x and N₂O) concentration values are normalised as mass pollutant emitted per primary (oil shale) energy input (mg (NO_x/N₂O)/MJ) [60], and is calculated by using the following equation:

Table 1
Proximate and ultimate analysis of the fuel.

| Proximate analysis ^d (wt.%) | | | Ultimate analysis ^d (wt.%) | | | | | |
|--|-------|-------------|---------------------------------------|------------------|------|----------------|------|------|
| Moisture | Ash | LHV (MJ/kg) | CO ₂ (Mineral) | ^a TOC | H | ^b O | N | S |
| 0.18 | 52.60 | 10.12 | 18.90 | 22.61 | 2.95 | 0.63 | 0.06 | 2.07 |

^a TOC% = (TC-TIC) %.

^b O% =100-(W + A + CO₂ + S + TOC + H + N) %.

Table 2
Chemical composition of the fuel ash.

| Components | SiO ₂ | Al ₂ O ₃ | Fe ₂ O ₃ | CaO | MgO | Na ₂ O | K ₂ O | SO ₃ | LOI _{950 °C} |
|---------------|------------------|--------------------------------|--------------------------------|-------|------|-------------------|------------------|-----------------|-----------------------|
| Content, wt.% | 15.39 | 3.64 | 2.03 | 22.52 | 3.00 | 0.09 | 1.60 | 3.91 | 47.12 |

Table 3
Mineral composition of the fuel ash.

| Phase | Quartz SiO ₂ | K-feldspar KAlSi ₃ O ₈ | Calcite CaCO ₃ | Dolomite CaMg(CO ₃) ₂ | Chlorite ClO ₂ | Pyrite FeS ₂ | Illite ^a |
|---------------|-------------------------|--|---------------------------|--|---------------------------|-------------------------|---------------------|
| Content, wt.% | 11.6 | 6.5 | 43.1 | 20.3 | 3.5 | 1.9 | 13.0 |

^a illite as muscovite with Mg, Ca, and Fe.

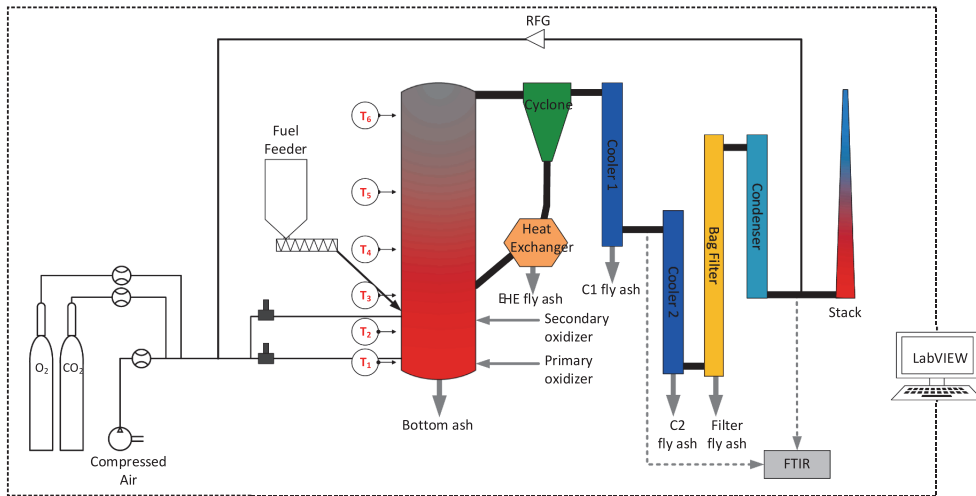


Fig. 2. Circulating Fluidized Bed facility with 60 kW capacity.

Table 4
Average working parameters of 60 kWth CFB unit during different combustion modes.

| Combustion Mode | No. of tests | T _{DB} (°C) | λ _{Pr} ^a | CO ₂ % in flue gas | NO _x U _c ^b (±) |
|-----------------|--------------|----------------------|------------------------------|-------------------------------|---|
| Air | 25 | 692–820 | 0.42–0.92 | | 3–15 |
| OXY21 | 7 | 670–757 | 0.47–0.79 | 90 | 7–14 |
| OXY30 | 17 | 666–866 | 0.61–0.96 | 93 | 4–14 |
| OXY40 | 3 | 842–856 | 0.69–0.91 | 90 | 5–7 |
| OXY52 | 1 | 866 | 0.62 | 81 | 6 |
| OXY50 + RFG | 3 | 709–723 | 0.56–0.76 | 61 | 5–7 |
| OXY87 + RFG | 4 | 697–784 | 0.60–0.83 | 50 | 3–4 |

^a λ_{Pr} is excess oxygen ratio in the primary oxidizer.

^b U_c is combined uncertainty of NO_x emissions as mg (NO_x)/MJ of oil shale.

$$\frac{\text{mg}((NO_x, N_2O)_{(fg)})}{\text{MJ}} = \frac{Y_{(NO_x, N_2O)} \dot{V}_{fg}}{\dot{m}_F \text{LHV}} \frac{M_{(NO_x, N_2O)}}{V_{mn}(NO_x, N_2O)} \quad (1)$$

Where; $Y_{(NO_x, N_2O)}$ – the measured volume fraction of NO_x or N₂O in the flue gas, (wet) in ppm,

\dot{V}_{fg} – the total flue gas volumetric flow rate, (wet) in m³/s,

\dot{m}_F – the calculated oil shale feed rate in kg/s,

LHV – the lower heating value of the oil shale fuel in MJ/kg,

$M_{(NO_x, N_2O)}$ – the molar mass of NO_x or N₂O, kg/kmol,

$V_{mn}(NO_x, N_2O)$ – the molar volume of NO_x or N₂O in m³/kmol.

Oil shale feed rate (\dot{m}_F) is obtained based on the supplied, to the furnace, air or O₂/CO₂ mixture flow rate and excess O₂ content in flue

measurements by solving the following Eq.'s (2–4):

$$O_{2(fg)} \% = \left(\frac{\dot{V}_{O_2}}{\dot{V}_{fg}} \right) \times 100\% \quad (2)$$

Where; $O_{2(fg)}$ – the measured O₂ in the flue gas, (wet) in volume.

\dot{V}_{O_2} – the excess O₂ flow rate in flue gas, Nm³/s,

\dot{V}_{fg} – the flue gas flow rate, Nm³/s.

\dot{V}_{O_2} can be determined by applying an O₂ balance around the furnace.

\dot{V}_{O_2} and \dot{V}_{fg} can be substituted by (Eq.'s 3 and 4):

$$\dot{V}_{O_2} = \dot{V}_{(in)}^{O_2} - V_{consumed}^{O_2} \cdot \dot{m}_F + \dot{V}_{(airingress)}^{O_2} \quad (3)$$

Where; $\dot{V}_{(in)}^{O_2}$ – the O₂ feeding rate to the furnace, Nm³/s,

$V_{consumed}^{O_2}$ – the specific stoichiometric oxygen demand considering oxygen available in the fuel of the 1 kg fuel fed, Nm³/kg,

$\dot{V}_{(airingress)}^{O_2}$ – the O₂ inflow due to air in-leakages, Nm³/s.

The flue gas flow rate \dot{V}_{fg} can be obtained through the gas species balance around the furnace:

$$\dot{V}_{fg} = \dot{V}_{(in)}^{(CO_2, N_2, H_2O, Ar, O_2)} + V_{comb} \cdot \dot{m}_F + \dot{V}_{(airingress)}^{O_2} - V_{consumed}^{O_2} \cdot \dot{m}_F \quad (4)$$

Where; $\dot{V}_{(in)}^{(CO_2, N_2, H_2O, Ar, O_2)}$ – the measured feeding rate of different gas species with air leakage, Nm³/s,

V_{comb} – the combustion products including CO₂ released during

carbonates decomposition from a unit mass of fuel, Nm^3/kg .

Calculations of fuel-N mass conversion ratios to NO_x and N_2O

The mass conversion (%) of nitrogen bound in the fuel to NO_x ($\text{NO}_x/\text{Fuel-N}$) and to N_2O ($\text{N}_2\text{O}/\text{Fuel-N}$) is used to conveniently compare oxyfuel NO_x and N_2O emissions to air-fired emissions. The mass balance of nitrogen is used to obtain the conversion ratio as the following equation:

$$N_F \dot{m}_F = y_{(\text{NO}_x, \text{N}_2\text{O})} \dot{V}_{\text{fg}} \frac{M_N}{M_{(\text{NO}_x, \text{N}_2\text{O})}} \quad (5)$$

Where; N_F – the nitrogen content in fuel, wt.%,

M_N – the molar mass of N, kg/kmol .

Results and discussion

Effect of combustion atmosphere

Normalised mass emissions of NO_x and N_2O and the fuel-N to NO_x and N_2O conversion rates are shown in Fig. 3. Under enriched oxyfuel combustion mode (O_2/CO_2), the inlet O_2 % feedings are 21%, 30%, 40%, and 52% vol.%. And in oxyfuel mode (O_2/RFG), the inlet O_2 % feedings are 50% and 87% vol.%. The range of operating parameters for each combustion mode is presented in Table 4. The change of combustion atmosphere from air to O_2/CO_2 and O_2/RFG does not influence the formation of NO_x emissions, despite the increase in bed temperature. Compared to air combustion, the average NO_x emissions were reduced from 120 mg/MJ to 105 mg/MJ under O_2/CO_2 , and to 98 mg/MJ under O_2/RFG . NO_x emissions were lowered significantly by 45% with increasing inlet O_2 % under O_2/CO_2 mode from (21–52) vol.%. Oxyfuel combustion has been approved in several studies, by using different types of fuels, it can reduce NO_x emissions [28–30,33], but reported results for not as high O_2 concentrations in the combustion atmosphere. For comparison purposes, oil shale flue gas composition is the closest to typical coal or the subbituminous and lignite coal flue gas compositions. The current results show a total reduction in fuel-N conversions to NO_x

with increasing inlet O_2 % in the combustion atmosphere. Generally, the higher O_2 concentration in the combustor usually promotes fuel burning by increasing the temperature as shown in Table 4. Zhou et al. [36] reported that NO formation during devolatilization and char combustion reached its maximum values at 30% O_2 concentration. As the combustion conditions tend to be more oxidative and higher O_2 concentration results in a higher combustion rate, and more free radicals promote NO formation. Typically, OH radicals are produced in oxyfuel combustion [61], and the OH radicals could lead to more H and O radicals in the bed region. These radicals can promote the oxidation of nitrogen-containing intermediates, such as HCN and NH_3 , into NO_x in the primary combustion zone, in the meantime, NO_x is more easily converted to N_2 owing to the oxygen-deficient atmosphere. Therefore, fuel-N conversions to NO_x under oxyfuel combustion atmosphere are much smaller than that in an air atmosphere. Under $\text{OXY50} + \text{RFG}$, NO_x emissions were slightly increased, hence recycled NO_x accumulated in the boiler [37], and no further reduction of NO_x to N_2O and N_2 is occurring. At higher inlet O_2 %, under $\text{OXY87} + \text{RFG}$, NO_x emissions were the lowest among the average NO_x emissions under all tested atmospheres. Reduction of NO_x emissions under RFG have also been reported previously, and these results are in line with other literatures [62,63]. With the application of RFG , NO_x formation in the dense bed zone is due to two sources: Fuel-N conversion to NO_x , and NO_x that is recycled back to the combustor. The chemical reaction between fuel-N and recycled NO_x and the reduction of recycled NO_x from NO_x to N_2 contribute to lower NO emissions under O_2/RFG firing mode. Li et al. [34] studied the combustion of Chinese bituminous coal in O_2/RFG and proposed that the intermediate radicals (NH and NCO) are important for the reaction processes for the NH_3 and HCN , they can react with the recycled NO to produce N_2 or N_2O through reactions (Eq.'s 6–9):

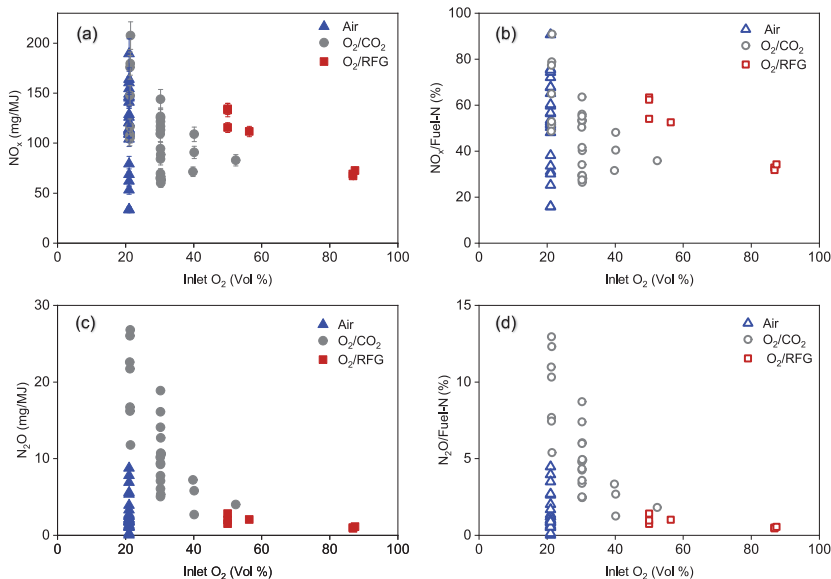


Fig. 3. Effect of combustion atmosphere on; (a) Normalised NO_x emission (mg/MJ), (b) Fuel-N to NO_x conversion (%), (c) Normalised N_2O emission (mg/MJ), and (d) Fuel-N to N_2O conversion (%).

CFB combustion with RFG is considered an effective way to reduce nitrogen oxide emissions. By recycling the emissions back to the combustor, flame temperature, and excess oxygen are reduced in the combustion zone, with the elevated CO₂ concentration, the combustion process is hindered, and bed temperature is decreased resulting in lower NO_x emissions.

N₂O concentrations were enhanced under O₂/CO₂ compared to air and decreased with increasing inlet O₂% from (21–52) vol.% from 20 mg/MJ to 4 mg/MJ, and these emissions were almost negligible under O₂/RFG mode. As a result of enhanced NCO oxidation to NO_x, and reduce the available NCO amount that is required for N₂O formation [34] Eq. (9). These results are consistent with other literatures [64,65], yet N₂O emissions with RFG were higher, as Yoshiie et al. [65] reported that N₂O was further increased owing to the accumulation of additional recirculated N₂O. While, Zhou et al. [36] found that N₂O emissions in 21%/79% O₂/CO₂ atmosphere are higher than that in air, and decreased at higher O₂ concentrations. The destruction of N₂O by O radicals is enhanced with increasing O₂ concentration as the following [36]:



In conclusion, the results illustrate that the effect of the combustion atmosphere on kukersite oil shale oxyfuel combustion does not influence the release of NO_x emissions. And the concentration of NO_x and N₂O emissions are considerably reduced when higher inlet O₂ concentration is used and with RFG application. Moreover, during the combustion experiments, the variations in O₂% in the primary gas excess oxygen ratio, and the increase of CO concentration in the CFB combustor, led to

further NO_x reduction [32]. This effect will be explained in more detail in the next section.

Effect of excess oxygen ratio in the primary oxidizer (λ_{pr})

The oxygen concentration in the flue gas is one of the most important parameters during the combustion process that affects oxides formations. The excess oxygen ratio in the dense bed region (λ_{pr}) is defined as the volumetric ratio of the oxygen supplied with the primary oxidizer that is used in the combustion, to the amount of stoichiometric oxygen demand, and calculated as the following equation:

$$\lambda_{pr} = \frac{\text{Oxygen flowrate in the primary oxidizer } \dot{V}_{(in)}^{O_2} \left(\frac{Nm^3}{s} \right)}{\text{Specific stoichiometric oxygen demand } V_{consumed}^{O_2} \left(\frac{Nm^3}{kg} \right) \times \dot{m}_F \left(\frac{kg}{s} \right)} \quad (12)$$

In oxyfuel combustion, instead of O₂% in the air entering the combustor, the O₂ content in O₂/CO₂ mixture is used in Eq. (12).

Fig. 4 compares NO_x and N₂O emissions and fuel-N to NO_x and N₂O conversions in air, O₂/CO₂, and O₂/RFG combustion modes. Emissions were compared at a constant T_{DB} in each combustion environment. These tests have been conducted for T_{DB} of 766 °C in air, 743 °C in OXY21, 793 °C in OXY30, 850 °C in OXY40, and 710 °C for OXY50 + RFG and OXY87 + RFG combustion modes. The results are similar for all tests under air and oxy-combustion; the NO_x emission increases by increasing λ_{pr} and fuel-N mass conversions to NO_x are more favoured at higher excess oxygen ratios. Many studies agree that elevating the excess oxygen ratio can lead to the enhancement of NO formation [9,41,66,67].

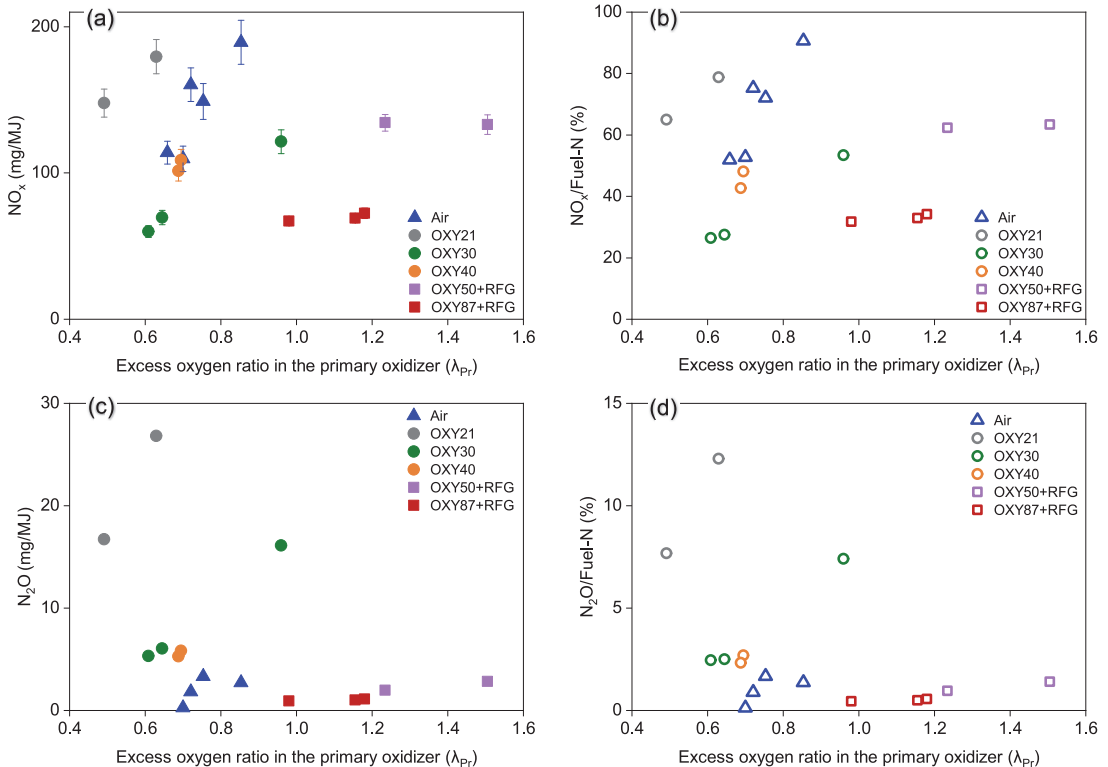


Fig. 4. Effect of excess oxygen ratio in the primary oxidizer (λ_{pr}) on; (a) Normalised NO_x emission (mg/MJ), (b) Fuel-N to NO_x conversion (%), (c) Normalised N₂O emission (mg/MJ) and (d) Fuel-N to N₂O conversion (%).

Under air conventional combustion, the NO_x emissions and fuel-N to NO_x mass conversion ratios increased by >36%, by increasing λ_{Pr} from 0.69 to 0.84. The effect of excess oxygen under air combustion has been reported in many studies [68], however, the effect can vary depending on the fuel used in the combustion process [26,69]. Under O_2/CO_2 combustion environment, results show a tendency to increase NO_x emission by 40% for OXY21, 44% for OXY30, and 22% for OXY40. The differences in increasing NO_x emissions percentages of different combustion modes can be explained by the effect of different temperatures between combustion environments.

Lupiáñez et al. [9,41] studied the effect of varied excess oxygen in a 90 kW fluidized bed test facility under 25/75 and 55/45 O_2/CO_2 modes, while the other parameters, such as temperature and limestone addition, were kept at a constant level. NO_x emissions noticeably increased from 590 to 685 mg/m^3 when the excess oxygen ratio increased from 1.1 to 1.7. A similar study was also reported by Tan et al. [67] in a 0.1 MWth CFB under a 50/50 O_2/CO_2 combustion environment. The excess oxygen ratio raised from 1.06 to 1.21 and the tests were performed at a constant temperature of 870 °C. The discussed literature results show that the influence of excess oxygen ratio was irrespective of the coal grade. The increase in NO_x emission can be explained by the fact that at oxygen-deficient conditions with lower excess oxygen ratios, higher N retention is obtained in the unburnt char, and by reducing λ_{Pr} , the NO_x emissions reduce too. CO can be produced in the combustion process and NO reacts with CO to form N_2 Eq. (13), which is helpful to the reduction of NO on the surface or in the pores of char [44]. By increasing oxygen concentration, the combustion of volatile matter and char is enhanced resulting in a higher NO_x formation [70].

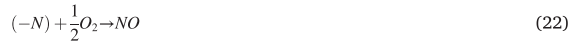
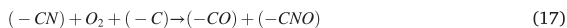


The obtained results also suggest that λ_{Pr} is the main variable controlling the NO_x formation in both combustion modes: air and O_2/CO_2 . Under O_2/RFG mode, NO_x emissions are slightly independent, as NO_x and N_2O concentrations are mainly affected by multiple factors as discussed earlier in the influence of flue gas recycled ratio.

N_2O emissions were increased with increasing λ_{Pr} for air and oxyfuel combustion atmospheres, as shown in Fig. 4(c) and (d). Miao et al. [69] studied the combustion of five types of high volatile fuels on N_2O and NO_x emissions and explained the increase in N_2O with increasing excess oxygen ratio, which can be accounted for the homogeneous gas-phase reactions of volatile-N. The higher conversion of volatile-N to N_2O via reactions (Eq.'s 14–16) and Eq. (9) occurred at a higher oxygen concentration.



In addition, the study also accounted for the increase of N_2O with increasing excess oxygen due to the char-N conversion to N_2O . As the intermediate product (-CNO) or (-N) can react with NO to form N_2O through reactions (Eq.'s 17–23) [69]:

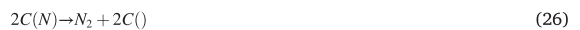


Another research reported by Li et al. [42] studied the influence of excess oxygen, temperature, and gas-staging on N_2O using 0.1 MWth oxyfuel CFB combustion with high oxygen concentration. The results show the increase in excess oxygen concentration in the primary stream increases N_2O emissions. Therefore, it can be concluded that both homogeneous gas-phase reactions and heterogeneous reactions affect the formation of N_2O . Overall, the lower the excess oxygen, the lower the NO_x , and N_2O emissions, but a practical limit must be prescribed to avoid disturbing either fluidization conditions or residence times.

Effect of bed temperature (T_{DB})

Fig. 5 displays the effect of dense bed temperature in air and O_2/CO_2 modes on the total NO_x and N_2O emissions as (mg/MJ), and fuel-N to NO_x and N_2O mass conversions (%). Emissions were compared at a constant λ_{Pr} for each combustion environment, λ_{Pr} is ~ 0.55 under air combustion and ~ 0.66 under OXY30. In air combustion mode, the average dense bed temperature (T_{DB}) ranges from 690 °C to 790 °C. NO_x emissions were affected by T_{DB} , first decreasing significantly by 36% as bed temperature increased from 690 °C to 740 °C. Then NO_x emissions were almost constant between 740 °C and 770 °C, and start increasing by 35% at higher $T_{\text{DB}} \sim 780$ °C. Under OXY30 tests, the combustion temperatures were higher, and NO_x emissions decreased by 34% with increasing T_{DB} from 750 °C to 835 °C, and at higher bed temperatures ($T_{\text{DB}} \sim 850$ °C) emissions were slightly increasing.

Generally, NO_x emission increases with the increase in bed temperature. Previous literature [54] shows a positive effect of temperature on NO emissions of oil shale combustion, and a decrease in N_2O emissions for coal combustion [38]. This can be explained by enhancing the char combustion and increasing char-N release. Duan et al. [26] explained the oxidation improvement of NO precursors by increasing the concentration of free radicals (-O and -OH) with the increase in bed temperature. However, the conversions of fuel char-N to NO_x and the following NO_x reduction reactions are quite complicated because of many homogeneous and heterogeneous reactions [71]. The reaction between NO and char is considered the primary reaction to reduce NO [72]. With increasing bed temperature, the char-N conversion rate to NO and the reduction rate of NO increase. In the meantime, the NO reduction rate is higher, which leads to a further decrease in NO emissions. The NO reduction reaction equations are proposed by Tomita et al. [73] as follows:



Where; $\text{C}()$, $\text{C}(\text{N})$, and $\text{C}(\text{O})$ represent the surface free site, surface nitrogen, and oxygen species, respectively.

Moreover, in CFB oil shale combustion, it was reported [52] that NO_x emissions increase with a low solid circulation ratio due to constant excess oxygen ratio, causing the catalytic effect of metal oxides on the reaction of CO and NO_x to increase gradually, until it finally reaches the dominant role in NO_x removal with increasing solid circulation ratio. In the current experiment, the temperature distribution and the rate of solid circulation ratio were investigated in detail in the previous work [57]. The lower the recirculation rate of the recycled ash, as the solid ash particles are used as a heat carrier agent, and the more entered the bottom end of the bed, the more heat was absorbed in the riser eventually decreasing the temperature of the dense bed region. To a certain extent, the emission of NO_x will decrease under a high solid circulating

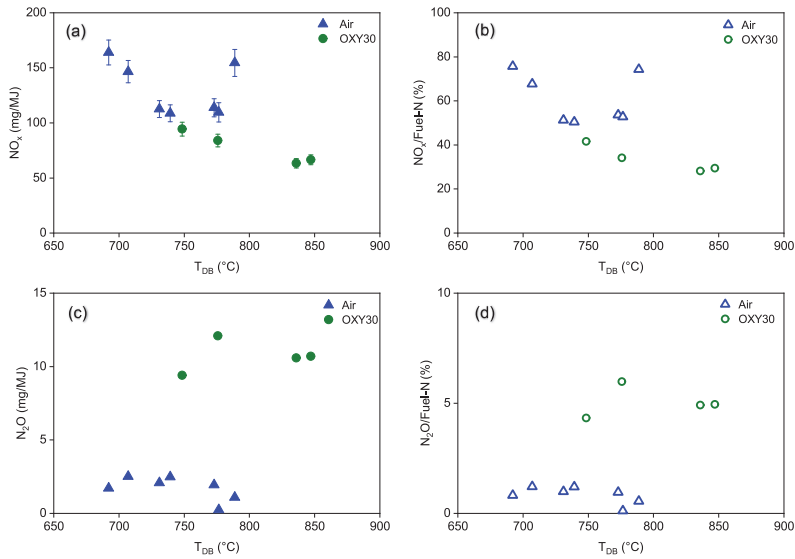


Fig. 5. Effect of bed temperature on; (a) Normalised NO_x emission (mg/MJ), (b) Fuel-N to NO_x conversion (%), (c) Normalised N₂O emission (mg/MJ), and (d) Fuel-N to N₂O conversion (%).

ratio.

In Fig. 5(c) and (d), N₂O emissions show an opposite behaviour for both combustion modes compared to NO_x emissions. As T_{DB} increases, at low operating temperatures, N₂O emissions increase by an average of 32% under air and OXY30 modes. At higher T_{DB} > 750 °C in air combustion and T_{DB} > 800 °C in OXY30, N₂O emissions decrease by >27%. This can be explained as at higher temperatures more free radicals (mainly H and OH) are promoting N₂O destruction via (Eq.'s 27 and 28) [36].



In addition, higher temperature causes the NCO reaction with O₂ more NO formation Eq. (9) and reduces the available NCO required for N₂O formation, similar to the influence of inlet O₂ concentration. The results are in line with [42,69]. Particularly [69] reported a decrease in N₂O emissions with increasing the temperature by using oil shale fuel in

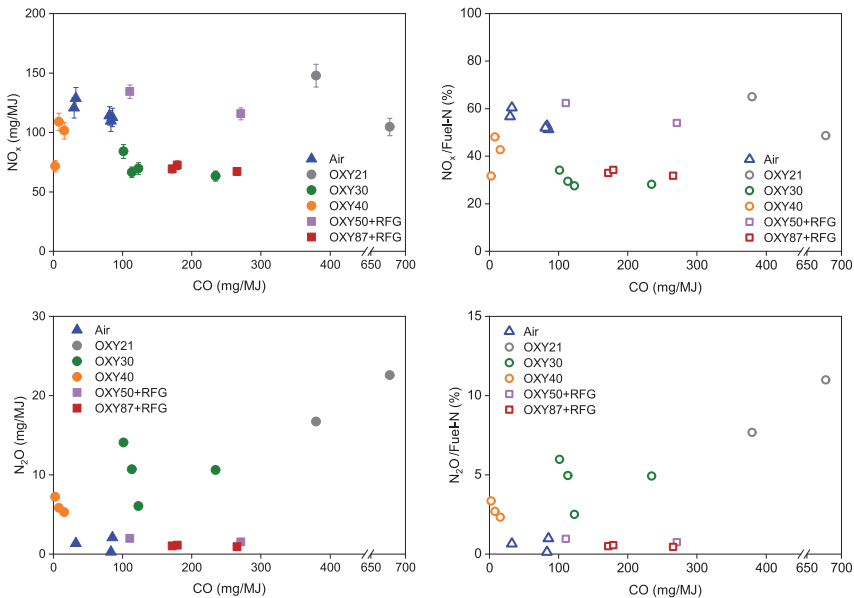
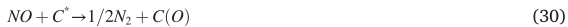


Fig. 6. Effect of CO concentrations on; (a) Normalised NO_x emission (mg/MJ), (b) Fuel-N to NO_x conversion (%), (c) Normalised N₂O emission (mg/MJ), and (d) Fuel-N to N₂O conversion (%).

air combustion, while the influence of temperature was not clear on NO_x emissions.

The concentration of CO could also affect the heterogeneous reduction by offering more active carbon sites on the char surface Eq. (29), which are effective to reduce NO through Eq. (30) [74,75]:



Where $\text{C}(\text{O})$ and C^* represent a carbon–oxygen complex and an active carbon site, respectively.

Fig. 6 shows the effect of CO concentrations in air, O_2/CO_2 , and O_2/RFG modes on the total NO_x and N_2O emission as (mg/MJ), and fuel-N to NO_x and N_2O mass conversions (%). NO_x emissions and fuel-N mass conversions decreased with increasing CO in the combustion atmosphere. During the combustion process, the CO emission originates in the combustor from partial oxidation of carbon and char, in addition to the CO_2 reduction [76]. The increased concentration of CO in the flue gas during oxyfuel combustion atmosphere is explained by the Boudouard reaction [77,78]:



As mentioned previously in the introduction part, nitrogen oxides from volatile-N and char-N can be reduced through homogeneous reactions with CO and H_2 , and a heterogeneous reaction with particles of soot and char [10]. Accordingly, a further reduction in NO emission occurs at higher CO concentrations in the combustor. Compared to NO, N_2O emissions have a little less significant impact at lower CO concentrations, and the latter tend to increase at higher CO releases under OXY21 and OXY30. The nitrogen-containing intermediates availability following Eq. (9), and the competition between the N release and NO, N_2O reduction over char determine generally the influence of combustion atmosphere on the total nitrogen emissions. By increasing inlet $\text{O}_2\%$, CO concentrations decrease under O_2/CO_2 mode as shown in Fig. 6, which indicates that higher inlet $\text{O}_2\%$ can improve combustion efficiency.

Li et al. [42] also reported the reason for N_2O emissions reduction with increasing the temperature, as both the formation of N_2O from NCO and the destruction by radicals are enhanced, similar to the influence of higher inlet O_2 as discussed in the previous section. In addition, the study reported that with increasing oxygen concentration from 35% to 50%, CO concentration and the amount of unburnt carbon in bottom ash decreased by 22%, which suggests the heterogeneous reduction reaction is suppressed, resulting in lower N_2O emissions.

Fig. 7 shows the TOC content in the bottom ash collected from the dense bed region of the riser and the combustion efficiencies as a function of λ_{pr} . Under OXY21 and OXY87 + RFG the lowest combustion efficiencies occurred, mainly because of the incomplete combustion of oil shale at an oxygen-deficient environment and low combustion temperature as shown in Table 4. At higher λ_{pr} , CO emissions decrease under OXY30 and OXY40, the TOC contents in the bottom ash are reduced and combustion efficiencies are enhanced. Overall, the increase in combustion efficiency, indicates that higher λ_{pr} promotes the combustion of oil shale under O_2/CO_2 mode, and with rising combustion temperature, the fuel burnout in the ash gradually decreases.

Overall, the presented results illustrate the operating variables including (excess oxygen ratios with CO concentrations, and bed temperatures) on the total nitrogen oxide emissions during the combustion of oil shale in air and different oxyfuel combustion environments with and without RFG. More differences can occur in the concentrations of NO_x and N_2O emissions when changing combustion environments. However, from the current results, the optimal operating parameters during CFB combustion can be confirmed after considering the discussed parameters. Yet, CO_2 formed in the oil shale oxyfuel flue gas stream may require further purification by post-combustion nitrogen reduction

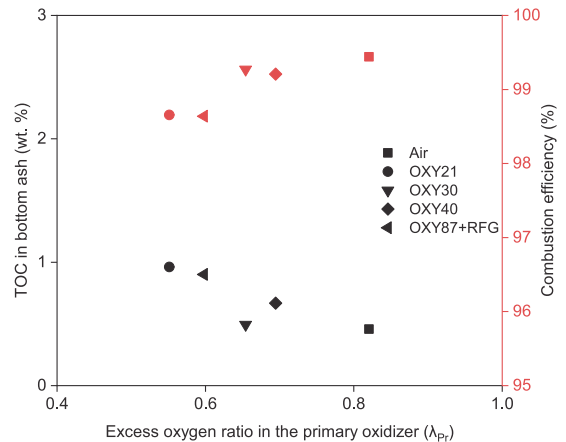


Fig. 7. Effect of excess oxygen in the primary oxidizer on total organic carbon content in bottom ash and combustion efficiency.

technologies, to achieve high CO_2 purity for further utilization or storage.

Conclusions

In this study, the first nitrogen oxide emissions results of multiple experiments in air and oxyfuel combustion with high inlet $\text{O}_2\%$ and with RFG application of kukersite type Estonian oil shale were presented. The 60 kWth CFB pilot facility operated with regular air as a base case, and pre-set gas mixtures under O_2/CO_2 and O_2/RFG environments of inlet $\text{O}_2\%$ (21–87) vol.%. The NO_x and N_2O emissions were normalised as mass per unit of energy released from the oil shale, and the fuel-N to NO_x and N_2O mass conversion ratios were calculated as well. The influence of some key operating factors, including combustion atmosphere, excess oxygen ratio in the primary oxidizer, bed temperature, and CO concentration were investigated in detail.

By switching from air to oxyfuel combustion, the specific NO_x reduction was from 120 mg/MJ in air to 105 mg/MJ in O_2/CO_2 mode, and 98 mg/MJ in O_2/RFG . N_2O emissions were highly increased in OXY21 compared to air combustion, and these emissions reduced significantly, from 20 mg/MJ to 4 mg/MJ, with increasing inlet $\text{O}_2\%$ to 52% in O_2/CO_2 mode. NO_x and N_2O emissions were the lowest of all combustion experiments at high inlet $\text{O}_2\%$ with RFG.

The volumetric excess oxygen ratio in the primary oxidizer is the main variable controlling NO_x and N_2O formations in both air and oxy-firing experiments, and emission values increased with increasing the ratios under all tested atmospheres.

NO_x emissions were decreasing with increasing bed temperature at low T_{DB} operating conditions, indicating a higher reduction rate of NO_x than formation rate in both air and O_2/CO_2 modes. While N_2O emissions were less affected by T_{DB} and decreased slightly at higher temperatures.

Oil shale combustion efficiency enhanced at higher inlet $\text{O}_2\%$ in O_2/CO_2 mode. A further reduction in NO_x emission occurred at higher CO concentrations for low inlet $\text{O}_2\%$. Although N_2O emissions increased relatively to CO concentrations.

To sum up the effect of primary measures on oil shale oxyfuel combustion, excess oxygen ratio can be the most influencing parameter affecting the formation of both NO_x and N_2O emissions. Higher inlet O_2 concentrations have a negative effect on the formation of both NO_x and N_2O nitrogen oxide emissions. RFG application is highly beneficial regarding emission reduction of oil shale oxy-fired conditions and these emissions are the lowest compared to air and O_2/CO_2 modes. The aforementioned optimal operating variables for oil shale oxyfuel

combustion atmospheres in O₂/CO₂ and O₂/RFG are presented. From the obtained results, the formation of NO_x and N₂O emissions is reduced under high inlet O₂% in O₂/CO₂ mode and with the application of RFG. Whereas these emissions are highly dependent on combustion parameters under both air and oxyfuel combustion environments. Therefore, further future research is needed to address the required purification by post-combustion nitrogen reduction technologies for CO₂ formed in the oil shale oxyfuel flue gas stream from technical perspective.

CRedit authorship contribution statement

Mais Baqain: Writing – original draft, Writing – review & editing. **Dmitri Neshumayev:** Conceptualization, Data curation, Writing – review & editing. **Alar Konist:** Funding acquisition, Project administration, Conceptualization, Supervision, Writing – review & editing.

Declaration of Competing Interest

The authors declare that they have no known competing financial interests or personal relationships that could have appeared to influence the work reported in this paper.

Data availability

Data will be made available on request.

Acknowledgements

This research was funded by the Estonian Research Council from the National Programme for Addressing Socio-Economic Challenges through R&D (RITA), which is supported by the Estonian Government and the European Regional Development Fund.

References

- [1] British Petroleum Company BP, Statistical Review of World Energy, London, 2020. <https://www.bp.com/en/global/corporate/energy-economics/statistical-review-of-world-energy>. (accessed April 1, 2022).
- [2] C. Le Quéré, R.M. Andrew, P. Friedlingstein, S. Sitch, J. Pongratz, A.C. Manning, et al., *Earth Syst. Sci. Data*. 10 (1) (2017) 405–448.
- [3] C.-Y. Cheng, C.-C. Kuo, M.-W. Yang, Z.-Y. Zhuang, P.-W. Lin, Y.-F. Chen, et al., CO₂ Capture from Flue Gas of a Coal-Fired Power Plant Using Three-Bed PSA Process, *Energies* 2021, Vol. 14, Page 3582. 14 (2021) 3582. <https://doi.org/10.3390/EN1423582>.
- [4] J. Poláčik, L. Šnajdárek, M. Špiláček, J. Pospíšil, T. Sitek, Particulate Matter Produced by Micro-Scale Biomass Combustion in an Oxygen-Lean Atmosphere, *Energies* 2018, Vol. 11, Page 3359. 11 (2018) 3359. <https://doi.org/10.3390/EN11123359>.
- [5] J.-P. Hettelingh, L. Hordijk, *Environmental conflicts: the case of acid rain in Europe*, Laxenburg, Austria, 1987.
- [6] L.L. Sloss, NO_x emissions from coal combustion, in: IEA Coal Research. (Ed.), IEA Coal Research, London, UK, 1991: p. 62.
- [7] L.L. Sloss, Trends in emission standards, in: IEA Coal Research, London, UK, 2003. <https://doi.org/10.13140/RG.2.2.30994.20162>.
- [8] J.A. Miller, C.T. Bowman, Mechanism and modeling of nitrogen chemistry in combustion, *Prog. Energy Combust. Sci.* 15 (1989) 287–338. [https://doi.org/10.1016/0360-1285\(89\)90017-8](https://doi.org/10.1016/0360-1285(89)90017-8).
- [9] C. Lupiáñez, L.I. Díez, L.M. Romeo, NO emissions from anthracite oxy-firing in a fluidized-bed combustor: Effect of the temperature, limestone, and O₂, *Energy Fuel* 27 (2013) 7619–7627. <https://doi.org/10.1021/ef4019228>.
- [10] J. Konttinen, S. Kallio, M. Hupa, F. Winter, NO formation tendency characterization for solid fuels in fluidized beds, *Fuel* 108 (2013) 238–246. <https://doi.org/10.1016/j.fuel.2013.02.011>.
- [11] P. Glarborg, A.D. Jensen, J.E. Johnsson, Fuel nitrogen conversion in solid fuel fired systems, *Prog. Energy Combust. Sci.* 29 (2003) 89–113. [https://doi.org/10.1016/S0360-1285\(02\)00031-X](https://doi.org/10.1016/S0360-1285(02)00031-X).
- [12] L.F. De Diego, C.A. Londono, X.S. Wang, B.M. Gibbs, Influence of operating parameters on NO_x and N₂O axial profiles in a circulating fluidized bed combustor, *Fuel* 75 (1996) 971–978. [https://doi.org/10.1016/0016-2361\(96\)00045-2](https://doi.org/10.1016/0016-2361(96)00045-2).
- [13] L.E. Amand, B. Leckner, Formation of N₂O in a Circulating Fluidized Bed Combustor, *Energy Fuel* 1097–1107 (1993).
- [14] S. Yadav, S.S. Mondal, A review on the progress and prospects of oxy-fuel carbon capture and sequestration (CCS) technology, *Fuel* 308 (2022), 122057. <https://doi.org/10.1016/j.fuel.2021.122057>.
- [15] M. Bui, C.S. Adjiman, A. Bardow, E.J. Anthony, A. Boston, S. Brown, et al., Carbon capture and storage (CCS): The way forward, *Energy Environ. Sci.* 11 (5) (2018) 1062–1176.
- [16] E. Morsch Filho, T.S. Possamai, V.d.P. Nicolau, R. Oba, Experimental investigation of the thermal behavior for oxy-fired and air-fired high temperature furnaces for the vitreous ceramic industry, *Therm. Sci. Eng. Prog.* 16 (2020), 100455. <https://doi.org/10.1016/j.tsep.2019.100455>.
- [17] S. Zinatloo-Ajabshir, R. Salehi, O. Amiri, M. Salavati-Niasari, Green synthesis, characterization and investigation of the electrochemical hydrogen storage properties of Dy₂Ce₂O₇ nanostructures with fig extract, *Int. J. Hydrogen Energy*. 44 (2019) 20110–20120. <https://doi.org/10.1016/j.ijhydene.2019.05.137>.
- [18] S. Zinatloo-Ajabshir, N. Ghasemian, M. Salavati-Niasari, Green synthesis of Ln₂Zr₂O₇ (Ln = Nd, Pr) ceramic nanostructures using extract of green tea via a facile route and their efficient application on propane-selective catalytic reduction of NO_x process, *Ceram. Int.* 46 (2020) 66–73. <https://doi.org/10.1016/j.ceramint.2019.08.231>.
- [19] S. Zinatloo-Ajabshir, N. Ghasemian, M. Mousavi-Kamazani, M. Salavati-Niasari, Effect of zirconia on improving NO_x reduction efficiency of Nd₂Zr₂O₇ nanostructure fabricated by a new, facile and green sonochemical approach, *Ultrason. Sonochem.* 71 (2021), 105376. <https://doi.org/10.1016/j.ultrsonch.2020.105376>.
- [20] S. Zinatloo-Ajabshir, S.A. Heidari-Asil, M. Salavati-Niasari, Rapid and green combustion synthesis of nanocomposites based on Zn–Co–O nanostructures as photocatalysts for enhanced degradation of acid brown 14 contaminant under sunlight, *Sep. Purif. Technol.* 280 (2022), 119841. <https://doi.org/10.1016/j.seppur.2021.119841>.
- [21] M. JabŁoniška, A.E. Palomares Gimeno, A. Węgrzyn, L. Chmielarz, A short review about NO_x storage/reduction catalysts based on metal oxides and hydroxalite-type anionic clays, *Acta Geodyn. Geomater.* 11 (2014) 175–186. <https://doi.org/10.13168/AGG.2013.0063>.
- [22] S. Zinatloo-Ajabshir, E. Shafaati, A. Bahrami, Facile fabrication of efficient Pr₂Ce₂O₇ ceramic nanostructure for enhanced photocatalytic performances under solar light, *Ceram. Int.* 48 (2022) 24695–24705. <https://doi.org/10.1016/j.ceramint.2022.05.116>.
- [23] C. Chao, Y. Deng, R. Dewil, J. Baeyens, X. Fan, Post-combustion carbon capture, *Renew. Sustain. Energy Rev.* 138 (2021), 110490. <https://doi.org/10.1016/j.rser.2020.110490>.
- [24] E.S. Rubin, J.E. Davison, H.J. Herzog, The cost of CO₂ capture and storage, *Int. J. Greenh. Gas Control.* 40 (2015) 378–400. <https://doi.org/10.1016/j.ijggc.2015.05.018>.
- [25] A.P. Melendo, R. Berbés, S.T. Blanco, J. Fernández, Effect of the impurities O₂ or NO present in non-purified flue gas from oxy-fuel combustion processes for carbon capture and storage technology, *Process Saf. Environ. Prot.* 172 (2023) 1120–1131. <https://doi.org/10.1016/j.psep.2023.02.086>.
- [26] L. Duan, C. Zhao, W. Zhou, C. Qu, X. Chen, Effects of operation parameters on NO emission in an oxy-fired CFB combustor, *Fuel Process. Technol.* 92 (2011) 379–384. <https://doi.org/10.1016/j.fuproc.2010.09.031>.
- [27] T. Czakiert, K. Sztokler, S. Karski, D. Markiewicz, W. Nowak, Oxy-fuel circulating fluidized bed combustion in a small pilot-scale test rig, *Fuel Process. Technol.* 91 (2010) 1617–1623. <https://doi.org/10.1016/j.fuproc.2010.06.010>.
- [28] K. El Sheikh, M.J.H. Khan, M. Diana Hamid, S. Shrestha, B.S. Ali, G.A. Ryabov, et al., Advances in reduction of NO_x and N₂O emission formation in an oxy-fired fluidized bed boiler, *Chinese, J. Chem. Eng.* 27 (2019) 426–443. <https://doi.org/10.1016/j.cjche.2018.06.033>.
- [29] T. Wall, Y. Liu, C. Spero, L. Elliott, S. Khare, R. Rathnam, F. Zeenathal, B. Moghtaderi, B. Buhre, C. Sheng, R. Gupta, T. Yamada, K. Makino, J. Yu, An overview on oxyfuel coal combustion-State of the art research and technology development, *Chem. Eng. Res. Des.* 87 (8) (2009) 1003–1016.
- [30] B. Engin, U. Kayahan, H. Atakül, A comparative study on the air, the oxygen-enriched air and the oxy-fuel combustion of lignites in CFB, *Energy* 196 (2020), 117021. <https://doi.org/10.1016/j.energy.2020.117021>.
- [31] J.A. Lasek, M. Janusz, J. Zuzwala, K. Glód, A. Iluk, Oxy-fuel combustion of selected solid fuels under atmospheric and elevated pressures, *Energy* 62 (2013) 105–112. <https://doi.org/10.1016/j.energy.2013.04.079>.
- [32] L. Duan, C. Zhao, Q. Ren, Z. Wu, X. Chen, NO_x precursors evolution during coal heating process in CO₂ atmosphere, *Fuel* 90 (2011) 1668–1673. <https://doi.org/10.1016/j.fuel.2010.12.014>.
- [33] M. Lupion, I. Alvarez, P. Otero, R. Kuivalainen, J. Lantto, A. Hotta, H. Hack, 30 MWh CIUDEN Oxy-CFB boiler - First experiences, *Energy Procedia* 37 (2013) 6179–6188. <https://doi.org/10.1016/j.egypro.2013.06.547>.
- [34] S. Li, H. Li, W. Li, M. Xu, E.G. Eddings, Q. Ren, Q. Lu, Coal combustion emission and ash formation characteristics at high oxygen concentration in a 1 MWh pilot-scale oxy-fuel circulating fluidized bed, *Appl. Energy*. 197 (2017) 203–211. <https://doi.org/10.1016/j.apenergy.2017.03.028>.
- [35] M. Xu, S. Li, Experimental study on N₂O emission in O₂/CO₂ combustion with high oxygen concentration in circulating fluidized bed, *J. Energy Inst.* 92 (2019) 128–135. <https://doi.org/10.1016/j.joei.2017.10.016>.
- [36] H. Zhou, Y. Li, N. Li, R. Qiu, K. Cen, Conversions of fuel-N to NO and N₂O during devolatilization and char combustion stages of a single coal particle under oxy-fuel fluidized bed conditions, *J. Energy Inst.* 92 (2019) 351–363. <https://doi.org/10.1016/j.joei.2018.01.001>.
- [37] D.G. Raheem, B. Yilmaz, U. Kayahan, S. Özdoğan, Effect of Recycled Flue Gas Ratio on Combustion Characteristics of Lignite Oxy-Combustion in a Circulating Fluidized Bed, *Energy Fuel* 34 (2020) 14786–14795. <https://doi.org/10.1021/acs.energyfuels.0c02464>.

- [38] H. Miettinen, M. Paulsson, D. Strömberg, Laboratory Study of N₂O Formation from Burning Char Particles at FBC Conditions, *Energy Fuel* 9 (1995) 10–19, <https://doi.org/10.1021/EF00049A002>, <https://doi.org/10.1021/EF00049A002.FP.PNG.V03>.
- [39] M. Vodička, J. Hrdlička, P. Skopec, Experimental study of the NO_x reduction through the staged oxygen supply in the oxy-fuel combustion in a 30 kWth bubbling fluidized bed, *Fuel* 286 (2021), 119343, <https://doi.org/10.1016/j.fuel.2020.119343>.
- [40] C. Lupiáñez, I. Guedea, I. Bolea, L.I. Díez, L.M. Romeo, Experimental study of SO₂ and NO_x emissions in fluidized bed oxy-fuel combustion, *Fuel Process. Technol.* 106 (2013) 587–594, <https://doi.org/10.1016/j.fuproc.2012.09.030>.
- [41] C. Lupiáñez, L.I. Díez, L.M. Romeo, Influence of gas-staging on pollutant emissions from fluidized bed oxy-firing, *Chem. Eng. J.* 256 (2014) 380–389, <https://doi.org/10.1016/j.cej.2014.07.011>.
- [42] S. Li, M. Xu, L. Jia, L. Tan, Q. Lu, Influence of operating parameters on N₂O emission in O₂/CO₂ combustion with high oxygen concentration in circulating fluidized bed, *Appl. Energy*. 173 (2016) 197–209, <https://doi.org/10.1016/j.apenergy.2016.02.054>.
- [43] T. Zhou, Z. Gong, Q. Lu, Y. Na, Y. Sun, Experimental Study on Enhanced Control of NO_x Emission from Circulating Fluidized Bed Combustion, *Energy Fuel* 29 (2015) 3634–3639, <https://doi.org/10.1021/ACS.ENERGYFUELS.5B00519>.
- [44] Z. Gong, Z. Liu, T. Zhou, Q. Lu, Y. Sun, Combustion and NO emission of shennu char in a 2 mw circulating fluidized bed, *Energy Fuel* 29 (2015) 1219–1226, <https://doi.org/10.1021/ef502768w>.
- [45] L.A.C. Tarelho, M.A.A. Matos, F.J.M.A. Pereira, Axial concentration profiles and NO flue gas in a pilot-scale bubbling fluidized bed coal combustor, *Energy Fuel* 18 (2004) 1615–1624, <https://doi.org/10.1021/ef049940l>.
- [46] M.E. Collings, M.D. Mann, B.C. Young, Effect of Coal Rank and Circulating Fluidized-Bed Operating Parameters on Nitrous Oxide Emissions, *Energy Fuel* 7 (1993) 554–558, <https://doi.org/10.1021/EF00040A016>, <https://doi.org/10.1021/EF00040A016.FP.PNG.V03>.
- [47] K. Okazaki, T. Ando, NO_x reduction mechanism in coal combustion with recycled CO₂, *Energy* 22 (1997) 207–215, [https://doi.org/10.1016/S0360-5442\(96\)00133-8](https://doi.org/10.1016/S0360-5442(96)00133-8).
- [48] F. Normann, K. Andersson, B. Leckner, F. Johnsson, Emission control of nitrogen oxides in the oxy-fuel process, *Prog. Energy Combust. Sci.* 35 (2009) 385–397, <https://doi.org/10.1016/j.pecs.2009.04.002>.
- [49] A. Ots, Oil shale fuel combustion, Tallinn University of Technology, Tallinn, Estonia, 2006.
- [50] A. Hotta, R. Parkkonen, M. Hiltunen, H. Arro, J. Loosaar, T. Parve, T. Pihu, A. Prikk, T. Tiikmaj, Experience of estonian oil shale combustion based on CFB technology at narva power plants, *Oil Shale*. 22 (4S) (2005) 381.
- [51] A. Ots, Formation of air-polluting compounds while burning oil shale, in: *Energy Environ., International Symposium on Energy and Environment*, Atlanta, Georgia, 1991: pp. 284–290. https://inis.iaea.org/search/search.aspx?orig_q=RN:28067889 (accessed March 31, 2022).
- [52] J. Xiumin, Y. Lijun, Y. Che, H. Xiangxin, Y. Hailong, Experimental investigation of SO₂ and NO_x emissions from Huadian oil shale during circulating fluidized-bed combustion, *Oil Shale*. 21 (2004) 249–257.
- [53] M. Aurela, F. Mylläri, A. Konist, S. Saarikoski, M. Olin, P. Simonen, et al., Chemical and physical characterization of oil shale combustion emissions in Estonia, *Atmos. Environ. X*. 12 (2021) 100139.
- [54] Y. Yang, Q. Wang, X. Lu, J. Li, Z. Liu, Combustion behaviors and pollutant emission characteristics of low calorific oil shale and its semi-coke in a lab-scale fluidized bed combustor, *Appl. Energy*. 211 (2018) 631–638, <https://doi.org/10.1016/j.apenergy.2017.10.071>.
- [55] L. Al-Makhdameh, J. Maier, G. Scheffknecht, Oxyfuel technology: NO reduction during oxy-oil shale combustion, *Fuel* 128 (2014) 155–161, <https://doi.org/10.1016/j.fuel.2014.03.003>.
- [56] L. Loo, A. Konist, D. Neshumayev, T. Pihu, B. Maaten, A. Siirde, Ash and flue gas from oil shale oxy-fuel circulating fluidized bed combustion, *Energies* 11 (5) (2018) 1218.
- [57] M. Baqain, C. Rüstü Yörük, D. Neşumajev, O. Järvik, A. Konist, Ash characterisation formed under different oxy-fuel circulating fluidized bed conditions, *Fuel* 338 (2023) 1–16, <https://doi.org/10.1016/j.fuel.2022.127244>.
- [58] A. Konist, L. Loo, A. Valtsev, B. Maaten, A. Siirde, D. Neshumayev, T. Pihu, Calculation of the amount of Estonian oil shale products from combustion in regular and oxy-fuel mode in a CFB boiler, *Oil Shale*. 31 (2014) 211–224, <https://doi.org/10.3176/oil.2014.3.02>.
- [59] B. Magnusson, et al., Calculation of Measurement Uncertainty in Environmental Laboratories, 4th ed., 2017. www.nordtest.info. (accessed January 26, 2023).
- [60] M. de las Obras-Loscertales, T. Mendiara, A. Rufas, L.F. de Diego, F. García-Labiano, P. Gayán, A. Abad, J. Adánez, NO and N₂O emissions in oxy-fuel combustion of coal in a bubbling fluidized bed combustor, *Fuel* 150 (2015) 146–153.
- [61] H. Watanabe, J.-I. Yamamoto, K. Okazaki, NO_x formation and reduction mechanisms in staged O₂/CO₂ combustion, *Combust. Flame*. 158 (7) (2011) 1255–1263.
- [62] L. Jia, Y. Tan, D. McCalden, Y. Wu, I. He, R. Symonds, E.J. Anthony, Commissioning of a 0.8 MWth CFB for oxy-fuel combustion, *Int. J. Greenh. Gas Control*. 7 (2012) 240–243, <https://doi.org/10.1016/j.ijggc.2011.10.009>.
- [63] J.-H. Moon, S.-H. Jo, S.J. Park, N.H. Khoi, M.W. Seo, H.W. Ra, S.-J. Yoon, S.-M. Yoon, J.-G. Lee, T.-Y. Mun, Carbon dioxide purity and combustion characteristics of oxy firing compared to air firing in a pilot-scale circulating fluidized bed, *Energy* 166 (2019) 183–192.
- [64] B. Roy, L. Chen, S. Bhattacharya, Nitrogen oxides, sulfur trioxide, and mercury emissions during oxy-fuel fluidized bed combustion of victorian brown coal, *Environ. Sci. Technol.* 48 (2014) 14844–14850, <https://doi.org/10.1021/es504667r>.
- [65] R. Yoshiie, T. Kawamoto, D. Hasegawa, Y. Ueki, I. Naruse, Gas-Phase Reaction of NO_x Formation in Oxyfuel Coal Combustion at Low Temperature, *Energy Fuel* 25 (2011) 2481–2486, <https://doi.org/10.1021/EF200277Q>.
- [66] L.W. Yang Xue-min, Emissions of SO₂, NO and N₂O in a circulating fluidized bed combustor during co-firing coal and biomass 19 (2010) 490–494.
- [67] L. Tan, S. Li, W. Li, E. Shou, Q. Lu, Effects of Oxygen Staging and Excess Oxygen on O₂/CO₂ Combustion with a High Oxygen Concentration in a Circulating Fluidized Bed, *Energy Fuel* 28 (2014) 2069–2075, <https://doi.org/10.1021/EF500051C>.
- [68] K. Svoboda, M. Pohorely, Influence of operating conditions and coal properties on NO_x and N₂O emissions in pressurized fluidized bed combustion of subbituminous coals, *Fuel* 83 (2004) 1095–1103, <https://doi.org/10.1016/j.fuel.2003.11.006>.
- [69] M. Miao, H. Kong, B. Deng, L. Chen, H. Yang, J. Lyu, M. Zhang, Experimental study on N₂O and NO_x emission characteristics of five high-volatile fuels in bubbling bed combustion, *Fuel Process. Technol.* 208 (2020), 106517, <https://doi.org/10.1016/j.fuproc.2020.106517>.
- [70] L.F. De Diego, C.A. Londono, X.S. Wang, B.M. Gibbs, Influence of operating parameters on NO_x and N₂O axial profiles in a circulating fluidized bed combustor, *Fuel* 75 (1996) 971–978, [https://doi.org/10.1016/0016-2361\(96\)00045-2](https://doi.org/10.1016/0016-2361(96)00045-2).
- [71] J. He, W. Song, S. Gao, L. Dong, M. Barz, J. Li, W. Lin, Experimental study of the reduction mechanisms of NO emission in decoupling combustion of coal, *Fuel Process. Technol.* 87 (2006) 803–810, <https://doi.org/10.1016/j.fuproc.2006.04.003>.
- [72] H. Teng, E.M. Suuberg, J.M. Calo, Studies on the Reduction of Nitric Oxide by Carbon: The NO-Carbon Gasification Reaction, *Energy Fuel* 6 (1992) 398–406, <https://doi.org/10.1021/EF00034A008>, <https://doi.org/10.1021/EF00034A008.FP.PNG.V03>.
- [73] A. Tomita, Suppression of nitrogen oxides emission by carbonaceous reductants, *Fuel Process. Technol.* 71 (2001) 53–70, [https://doi.org/10.1016/S0378-3820\(01\)00136-9](https://doi.org/10.1016/S0378-3820(01)00136-9).
- [74] I. Aarna, E.M. Suuberg, A review of the kinetics of the nitric oxide-carbon reaction, *Fuel* 76 (1997) 475–491, [https://doi.org/10.1016/S0016-2361\(96\)00212-8](https://doi.org/10.1016/S0016-2361(96)00212-8).
- [75] D. López, J. Calo, The N₂O-carbon reaction: The influence of CO and potassium on reactivity and populations of oxygen surface complexes, *Fuel* 86 (2007) 1900–1907, <https://doi.org/10.1016/j.fuel.2006.12.003>.
- [76] L. Duan, C. Zhao, W. Zhou, C. Qu, X. Chen, O₂/CO₂ coal combustion characteristics in a 50kWth circulating fluidized bed, *Int. J. Greenh. Gas Control*. 5 (2011) 770–776, <https://doi.org/10.1016/j.ijggc.2011.01.007>.
- [77] S.R. Dhaneswar, S.V. Pisupati, Oxy-fuel combustion: The effect of coal rank and the role of char-CO₂ reaction, *Fuel Process. Technol.* 102 (2012) 156–165, <https://doi.org/10.1016/j.fuproc.2012.04.029>.
- [78] C.R. Yörük, T. Meriste, A. Trikkel, R. Kuusik, Thermo-oxidation characteristics of oil shale and oil shale char under oxy-fuel combustion conditions, *J. Therm. Anal. Calorim.* 121 (2015) 509–516, <https://doi.org/10.1007/s10973-015-4484-5>.

Publication III

Baqain, M.; Neshumayev, D.; Konist, A. (2022). **Oxyfuel Conversion of Ca-rich fuel in a 60 kWth Circulating Fluidized Bed**. Proceedings of the 16th Greenhouse Gas Control Technologies Conference (GHGT-16) 23-24 Oct 2022. GHGT. DOI: 10.2139/ssrn.4276982.



16th International Conference on Greenhouse Gas Control Technologies, GHGT-16

23rd -27th October 2022, Lyon, France

Oxyfuel Conversion of Ca-rich fuel in a 60 kWth Circulating Fluidized Bed

Mais Baqain^{a*}, Dmitri Neshumayev^a, Alar Konist^a

^a*Department of Energy Technology, Tallinn University of Technology, 19086, Tallinn, Estonia*

Abstract

Carbon dioxide emissions produced from burning fossil fuels can be reduced by applying oxyfuel combustion, as one of the carbon capture methods, in circulating fluidized bed (CFB) boilers. Oxyfuel combustion for Estonia's energy sector represents promising carbon capture option. Estonia has one of the highest carbon intensities among the European countries as the power generation is dominated by domestically produced oil shale. To assess the suitability of applying oxyfuel technology in using Ca-rich Estonian oil shale, the presented paper is aimed to investigate the influence of different inlet O₂/CO₂ and O₂/RFG combustion modes on the used fuel. The combustion experiments were performed using a 60 kWth pilot facility under air and six different modes of inlet oxygen concentrations vol.% (21%-90%), with and without the application of recycled flue gas (RFG). Special attention was given on the produced pollutant emissions and the specific carbon emission as well. The obtained results show a total reduction in the SO₂ and NO_x emissions and a noticeable reduction exceeding 15% of the specific carbon factor in oxyfuel compared to air mode. In conclusion, the results outcomes indicate that oxyfuel technology is particularly suitable for oil shale combustion.

Keywords: Ca-rich fuel; oil shale; circulating fluidized bed; oxyfuel combustion; pollutant emissions.

1. Introduction

By limiting global warming to well below 2 °C, 196 countries set out a global framework to avoid dangerous climate change with the Paris agreement. To achieve this, the European Union has the goal to become the first climate-neutral continent and thus emit net zero greenhouse gases (GHGs) anymore [1]. The Estonian government announced plans to reach carbon neutrality by 2050 and an 80 % decrease in GHG emissions by that date (including 70 % by 2030) [2]. Estonia has a long history of using oil shale, the energy supply is dominated by domestically produced oil shale, an energy-rich sedimentary rock that can be either burned for heat and power generation or used for producing liquid fuels [3]. This gives the country a high degree of energy independence but also a high carbon intensity as well. Estonia's main challenge for the first time will be required to reduce emissions rather than solely control its growth.

The reduction of GHGs can be accomplished in several ways. These include: 1) Improving efficiency in combustion systems [4], 2) Utilizing alternative fuels, like biomass for achieving negative CO₂ emissions, [5], or co-firing blended fuels like biomass with oil shale for better GHGs emissions reduction [6], and 3) Implementing CO₂ capture technologies, such as pre-combustion, post-combustion and oxyfuel combustion captures [7]. The three major CO₂ capture technologies, in addition to chemical looping, have recently gained wide interest. The efficiency of the capture

* Corresponding author. *E-mail address:* mais.baqain@taltech.ee

technologies depends on the CO₂ concentrations in the flue gas stream. Increased concentrations of CO₂ in the exhaust gas stream result in a capture process that requires less chemically complicated treatments [8]. Therefore, CO₂ capture and sequestration will become more convenient and cost-effective.

In oxyfuel combustion, the main difference from regular firing is that the combustion occurs in a CO₂-based environment instead of air (O₂/N₂) [9]. A gaseous mixture of O₂ and recycled flue gas (RFG) is used as the combustion atmosphere. An air separation unit (ASU) is required to generate an O₂-rich stream (> 95 %). The produced flue gas stream is mainly consisting of CO₂ and water vapor, and before CO₂ transport/sequestration, water vapor is removed by condensation.

Oxy-firing currently has technology readiness level TRL > 7 [10]. One of the main drawbacks of oxyfuel combustion is the energy requirements for the ASU and the cost of O₂ production which reduces the total efficiency of the power plant [9]. The production of O₂ that is exceeding 95 % purity is considered the main challenge for this technology, followed by energy demand of the CO₂ compression and purification unit (CPU). However, it can be expected that amongst all the available options, oxyfuel CFB combustion for Estonia represents the most promising carbon capture technology in terms of the reduction potential of emissions, energy efficiency, and the ease to retrofit into currently operated power plants [11, 12]. 40 % of Estonia's electricity demand is fulfilled by oil shale, hence a special interest has already been given to studying different areas of oil shale oxyfuel combustion. These include thermogravimetric analysis (TGA) experiments to investigate the kinetics of oil shale combustion in a CO₂ environment [13, 14], small-scale batch laboratory reactor experiments [15], process simulator-based modeling of the oxyfuel combustion process with oil shale [16, 17], and pilot scale oxyfuel combustion experiments [18–20].

The extensive usage of Estonian oil shale, demands potential techniques to mitigate the CO₂ emissions, and the significant CO₂ reduction was achieved through decommissioning and retrofitting the pulverized combustion (PC) boilers with CFB technology [21], gives further hope to implementing oxyfuel combustion in the current oil shale power plants. In this context, Tallinn University of Technology within the ClimMit project's scope [22], has provided advanced experimental progress in investigating the combustion of kukersite oil shale for both oxyfuel and air combustion in a 60 kW_{th} CFB combustor. The main goal of this paper is to present the first experimental study of using oil shale oxyfuel combustion in a 60 kW_{th} pilot facility under multiple O₂/CO₂ combustion environments, and with the application of RFG. The results can be adopted to study the feasibility of retrofitting oxyfuel technology in Estonia's oil shale power plants to overcome the challenge associated with electricity production with near zero emissions.

Nomenclature

| | |
|---------------------------|--|
| k_{CO_2} | Extent of carbonate decomposition |
| q_c | Specific carbon emissions of oil shale firing, tC/TJ |
| M_C | Molar mass of C, 12.01 g/mol. |
| M_{CO_2} | Molar mass of CO ₂ , 44.01 g/mol. |
| M_{CaO} | Molar mass of CaO, 56.08 g/mol. |
| M_{MgO} | Molar mass of MgO, 40.30 g/mol. |
| $CO_{2(Mineral)}^{OS}$ | CO ₂ content in oil shale, wt% |
| $CO_{2(Mineral)}^{ash,i}$ | CO ₂ content in ash, wt% |
| CaO_i | CaO content in ash, wt% |
| MgO_i | MgO content in ash, wt% |
| TOC^r | Total organic carbon content, as received, wt% |
| Q_i^r | Net heating value of oil shale, MJ/kg |

2. Experimental work

2.1. Materials and Test facility

Estonian kukersite oil shale from Estonia's underground mines was used. The proximate and ultimate analysis in Table 1 shows that the Estonian oil shale has a high content of mineral matter, which consists of carbonates and sandy-clay parts [23]. The molar ratio of Ca/S is high exceeding 8 in the used fuel. Compared to coal oxyfuel combustion experiments, the Ca/S ratio is 2-3 times higher in oil shale than the ratio in coal [24, 25]. Therefore, no additional sorbent material is required for SO₂ capturing. The chemical compositions of the ashes and the oil shale fuel, as shown in Table 2 were measured using an X-ray fluorescence spectrometer (XRF).

Table 1. Oil shale proximate and ultimate analysis.

| Proximate analysis | | | | | |
|--|------------------|------|----------------|--------------------------|--------------------|
| Moisture, wt% | Ash, wt% | | | Net Heating Value, MJ/kg | |
| 0.18 | 52.6 | | | 10.10 | |
| Ultimate analysis, wt _{dry} % | | | | | |
| (CO ₂) _{Mineral} | ^a TOC | H | ^b O | N | S _{total} |
| 18.90 | 22.27 | 2.95 | 0.63 | 0.06 | 2.07 |

^aTOC% = (TC-TIC) %
^bO% = 100 - (W+A+CO₂+S+TOC+H+N) %

Table 2. Oil shale chemical composition.

| Components | Content, wt% |
|------------------------------------|--------------|
| SiO ₂ | 15.39 |
| Al ₂ O ₃ | 3.64 |
| Fe ₂ O ₃ | 2.03 |
| CaO | 22.52 |
| MgO | 3 |
| Na ₂ O | 0.09 |
| K ₂ O | 1.6 |
| SO ₃ | 3.91 |
| ^a LOI _{950 °C} | 47.12 |

^aLOI Loss of ignition

Experimental work is carried out with the 60 kWth CFB test bench which is specifically designed for operations of air, oxygen enriched environment O₂/CO₂, and oxyfuel combustion O₂/RFG, the operation parameters and the scheme of the test facility are shown in Table 3. and Fig. 1. The combustion experiments were performed under air and different inlet oxygen concentrations vol.% (21%-90%). The CFB test facility operated without RFG for combustion environment under O₂ concentrations ranging between -21% up to 40%, and with RFG for higher O₂ concentrations of 50% and 90%.

The CFB combustion chamber is designed and constructed for low-rank fuels with high ash content that can reach up to 70 wt. %. The main components shown in Fig.1 include a CFB boiler with a riser height of 4.9 m and an inner diameter of 0.12 m. The combustion chamber is isolated with ceramics and a high-temperature thermal isolation material with stainless-steel shell. The combustion air is supplied by a compressor and the oxyfuel combustion was performed using bottled CO₂ and O₂. The temperature measurements taps are distributed along the riser in six different locations. The concentrations of O₂, CO₂, CO, SO₂, NO_x, N₂O and H₂O in the flue gas were continuously monitored using a Fourier transform infrared (FTIR) spectrometer, which is located between cooler 1 and cooler 2. The collected bottom ash sample point is located below the CFB riser as shown in Fig. 1.

Table 3. Air and oxyfuel combustion experimental parameters.

| Combustion Mode | $T_{\text{Riser}}, ^\circ\text{C}$ | Oxygen ratio, λ | Fuel feed rate, kg/h |
|-----------------|------------------------------------|-------------------------|----------------------|
| Air | 814 | 1.38 | 9 |
| OXY21 | 808 | 1.45 | 6.5 |
| OXY25 | 896 | 1.31 | 10 |
| OXY30 | 868 | 1.40 | 10 |
| OXY40 | 886 | 1.61 | 16 |
| OXY50+RFG | 813 | 1.34 | 7 |
| OXY90+RFG | 807 | 1.16 | 6 |

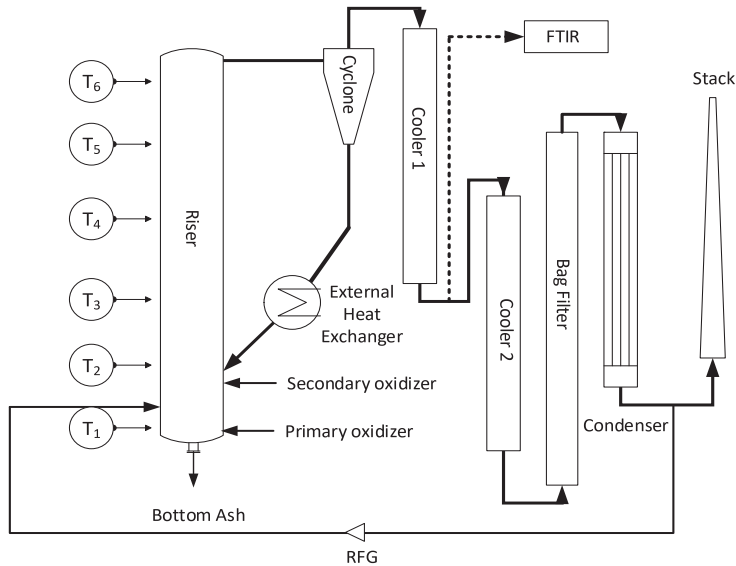


Fig. 1. 60 kWth CFB pilot facility.

2.2. Calculation of specific carbon emission

Oil shale is known to have high carbonate and dolomite content, specifically Estonian oil shale ash which is very rich in calcium [26]. The dissociation of both calcite (CaCO_3) and dolomite $\text{CaMg}(\text{CO}_3)_2$, during the combustion process, generates CO_2 emission. The shared CO_2 emission generated from the mineral part of the fuel depends on the content of mineral CO_2 , and the extent of carbonate decomposition ($k_{\text{CO}_2,i}$), where the $k_{\text{CO}_2,i}$ value is calculated based on the content of CaO , MgO and CO_2 in the ash part [27]. To calculate the specific emission of carbon (q_c), the heating value of oil shale can be assumed based on the net heating value of the fuel measured by the proximate analysis (the actual heat release at CFB conditions will be higher due to partial calcination and anhydrite formation). The average contents of carbonaceous CO_2 and total organic carbon (TOC) in the fuel need to be measured (as received). And the extent of carbonate decomposition ($k_{\text{CO}_2,i}$) value for each part of the ash (bottom, heat exchanger, filter ash, etc) should be calculated as well, in this paper the bottom ash only will be taken into consideration. Introducing the obtained initial data into Formulas (1) and (2) gives [27]:

$$k_{CO_2,i} = 1 - \frac{CO_{2(Mineral)}^{ash,i}}{\left(\frac{M_{CO_2}}{M_{CaO}} \times CaO_i\right) + \left(\frac{M_{CO_2}}{M_{MgO}} \times MgO_i\right)} \quad (1)$$

$$q_c \left(\frac{tC}{TJ}\right) = \frac{10 \times \left(TOC^r + k_{CO_2,i} \times CO_{2(Mineral)}^{OS} \times \frac{M_c}{M_{CO_2}}\right)}{Q_i^r} \quad (2)$$

3. Results and discussion

3.1. Air and oxyfuel overall combustion process

The inlet oxygen concentrations ratios with CO₂, and with RFG as vol.% are shown in Fig. 2(a). Under oxy-firing conditions, as the combustion process proceeds, the increasing temperature promotes oil shale combustion in the oxygen-rich environments (O₂/CO₂), as the CO₂ concentrations in the flue gas reach more than 90 % Fig. 2 (b). Additionally, a high CO₂ concentration would inhibit the calcination of limestone despite the increase in operating temperature because of the elevated O₂ concentrations [28]. As a result, a total increase in the solid waste material in oxyfuel could be expected compared to air firing.

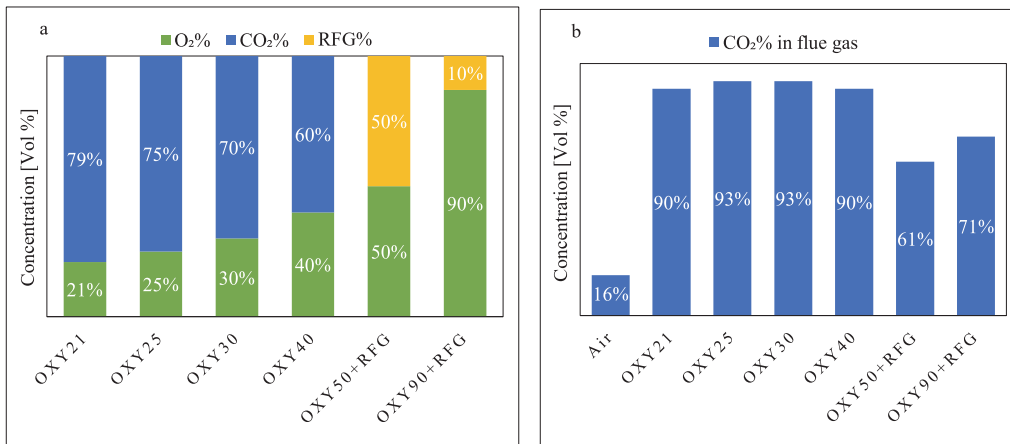


Fig. 2. (a) Oxyfuel gas mixtures used in the experiment; (b) CO₂ concentrations in the flue gas.

Fig. 3(a)-(c) show the full operating conditions of the 60 kWth CFB combustor from air to oxyfuel firing, all data are reported as time-averaged values. The CFB pilot facility was always started in the air-combustion mode. When the combustion process reached the desired experimental temperature, an air-combustion baseline test was carried out. Following the completion of the air test, at stable conditions, the switch from air to O₂/CO₂ or O₂/RFG combustion started. The transition was accomplished smoothly within a short period of time. After the transition from air to O₂/CO₂ or O₂/RFG combustion mode, tests under oxyfuel combustion commenced, including ash sampling and emissions monitoring. Fig. 3(b) shows that the bed temperatures at heights (0.9 m) and (0.11 m) are highly affected by the inlets of the secondary oxidizer and the solid's mass flow rate that is recycled back to the CFB riser. Respectively, from the results, can be seen a stable process inside the CFB combustor under both air and oxyfuel combustion environments.

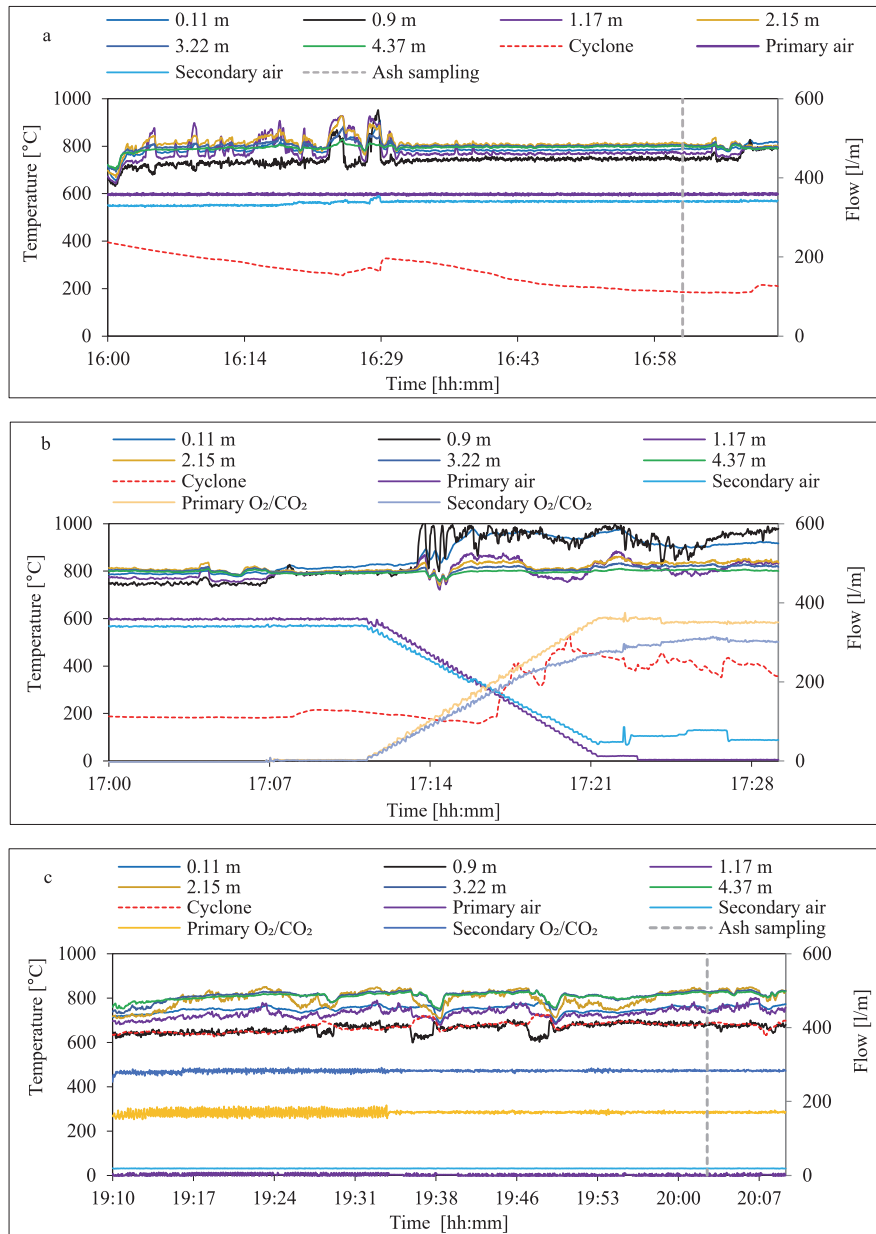


Fig. 3. Operating conditions of the CFB boiler at: (a) Stable air condition; (b) Trans; and (c) Stable oxy condition.

3.2. Emissions

The average emission values during stable operation under air and oxyfuel combustion experiments are shown in Fig. 4. The elevated partial pressure of CO₂ causing the oxy-firing atmosphere differs from air mode. The sulfur capture mechanisms may change from the normal sulfation path (CaCO₃ → CaO → CaSO₄) to the direct sulfation (CaCO₃ → CaSO₄). This change didn't affect the release of SO₂ emissions in oxyfuel combustion environment, and sulfur capture efficiency reached 99% in all combustion modes. As a reason for the high Ca/S molar ratio in the oil shale fuel, with a sufficient amount of excess calcium to bind with SO₂.

For nitrogen emissions, the variation of NO_x (NO and NO₂) formation and reduction is still a challenge in the application of oxy-fuel combustion as it depends on many factors [29]. NO emissions remained around 200 ppm under air conditions and 300 ppm under oxyfuel combustion mode as shown in Fig 4(a) and 4(b).

In Table 4 the emission rate of (SO₂, NO, NO₂ and CO) are defined as mass pollutants emitted per primary (oil shale) energy. Since oxyfuel combustion experiments were conducted under different inlet oxygen concentrations there are differences in the oil shale feeding rate. Thus, the emissions in the flue gas should be recalculated to take into consideration this difference. NO emissions under O₂/CO₂ and O₂/RFG were lower than in the air (except for OXY21). And fuel-N to NO_x conversions were reduced by 23% than in air under higher O₂ concentration, whereas the conversion reduction exceeded 50% under OXY90+RFG. A series of reported studies indicated that fuel nitrogen conversions were often about half that is seen in air-combustion experiments [30].

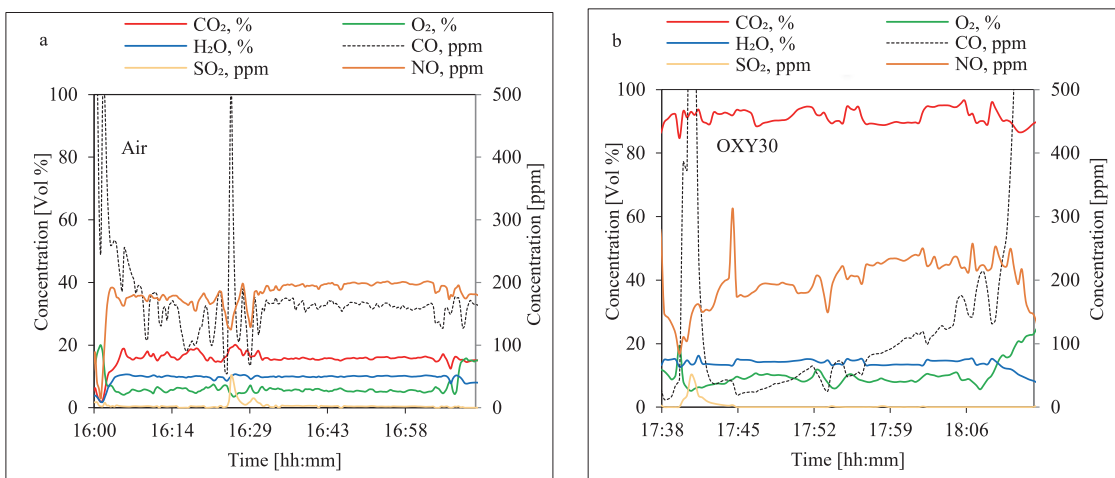


Fig. 4. Pollutant emissions during stable conditions under: (a) Air; (b) Oxyfuel combustion.

Table 4. Normalized emissions of oil shale under air and oxyfuel combustion.

| Combustion Mode | CO (mg/MJ) | SO ₂ (mg/MJ) | NO (mg/MJ) | NO ₂ (mg/MJ) | Fuel-N to NO _x Conversion (%) |
|-----------------|---------------|----------------------------|---------------|----------------------------|---|
| Air | 126 | 3 | 103 | 3 | 49 |
| OXY21 | 301 | 13 | 146 | 3 | 65 |
| OXY25 | 134 | 2 | 87 | 0 | 40 |
| OXY30 | 296 | 8 | 96 | 0 | 43 |
| OXY40 | 4 | 1 | 90 | 0 | 40 |
| OXY50+RFG | 202 | 3 | 80 | 48 | 38 |
| OXY90+RFG | 206 | 2 | 45 | 25 | 21 |

3.3. Specific carbon emission

All the bottom ash produced during stable conditions for each test run was collected in a container located underneath the CFB combustor chamber. Contents of CaO and MgO in bottom ash samples were identified through quantitative analysis X-ray diffraction (XRD), and the mineral CO₂ content through elemental analysis. Based on those results the extent of carbonate decomposition was calculated and so were the specific carbon emissions. The results in Table 5 show that the averaged specific carbon emission in the oxygen-enriched environment (O₂/CO₂) is less by 4.17 tC/TJ, and in oxyfuel combustion mode (O₂/RFG) is less by 4.14 tC/TJ. This reduction is corresponding to the total decrease in ($k_{CO_2,i}$) achieved by switching from air to oxy-fired mode. To point out the effect of oxyfuel combustion on the reduced carbon emissions factor, these results were compared to Estonian oil shale (EOS) in industrial boilers and other types of solid fuels as shown in Table 5. As can be seen in the table below, the adoption of oxyfuel in the combustion of Ca-rich oil shale fuel can reduce carbon emissions by more than 15% from oil shale air combustion and by 13 % from coal air combustion.

Table 5. Comparison of specific carbon emissions under air and oxyfuel combustion of Estonian oil shale with different solid fuels.

| Solid Fuel | qc (tC/TJ) | | | | | |
|---------------------------|------------|-------|-------|-------|-------|-----------|
| | Air | OXY21 | OXY25 | OXY30 | OXY40 | OXY90+RFG |
| 60 kWith EOS ^a | 26.69 | 22.48 | 22.52 | 22.53 | 22.58 | 22.56 |
| PC Boiler EOS | 27.85 | | | | | |
| CFB Boiler EOS, [27] | 26.94 | | | | | |
| Anthracite | 26.8 | | | | | |
| Lignite | 27.6 | | | | | |
| Coking coal, [31] | 25.8 | | | | | |

^aEOS = Estonian oil shale

3.4. Oxyfuel retrofit of Ca-rich oil shale power units

Based on the current results and the previous conclusion of [19, 32, 33] the essential aspects of Ca-rich oil shale power unit retrofitting into oxyfuel combustion are:

- Carbonate mineral decomposition is less than 40% under oxyfuel conditions. It means that in oxyfuel mode total CO₂ emissions can be reduced, and the total heat gain will be increased eventually leading to a lower reduction in power plant efficiency due to the CO₂ purification unit, and an increase in the overall efficiency.
- A larger amount of solid waste will be produced upon oxyfuel combustion compared to air-firing. In this case ash handling and disposal needs to be reconsidered, particularly for dense bed ashes.
- Stronger separation of fine particles into overhead zones is noticed in oxy-fired compared to air mode. This could require additional particulate filtering before preheater (if existed) and at electrostatic precipitator (ESP) as well.
- Air ingress during the application of RFG can reduce CO₂ concentration as shown in Fig. 2(b). The retrofitted structure should be tightly designed to prevent false air from entering the system.

The oxyfuel technology can be implemented in the CFB oil-shale firing units and consider technically feasible and does not require major changes in the boiler structures and heat surfaces if the adiabatic combustion temperature is close enough to that of air-combustion, whereas the maximum riser temperatures (T_6) under (OXY50+RFG and OXY90+RFG) are close to air-combustion. This can be achieved by controlling the mixing ratio of oxygen and recycled flue gas ratio.

Finally, it can be stated that an oxyfuel retrofit for producing a flue gas with a high CO₂ content using Estonian oil shale can be achieved, and changes in the overall process that include the three main components of oxyfuel CC are:

- ASU to supply pure oxygen into the CFB combustor
- CO₂ compression and purification unit (CPU)
- Flue gas recirculation system to maintain boiler performance

4. Conclusions

Experiments for oxyfuel combustion of Ca-rich oil shale in a 60kWth CFB pilot facility were carried out. A mixture of O₂, CO₂, and RFG was used, with an inlet O₂ concentration ranging from vol.% (21%-90%). The CFB pilot facility shows a stable process and a smooth transition from air to oxy-combustion. The average pollutant emission values during stable conditions under air and oxy-combustion experiments were monitored. Moreover, the specific carbon emission factor was calculated for each combustion experiment.

The results show that SO₂ emissions were almost near zero, and sulfur capture efficiency reached more than 99%. The reduction of fuel-N conversion to NO_x was the highest with the RFG application, followed by O₂/CO₂ environment and then air combustion. In comparison to oil shale air-firing, a total reduction in specific carbon emissions exceeding 15% was achieved under oxyfuel combustion in both O₂/CO₂ and O₂/RFG environments. The presented results served as a reference to help minimize GHG emissions from oil shale and to seek the feasibility of retrofitting oxyfuel technology in Estonia's oil shale power plants.

Acknowledgements

This research was funded by the Estonian Research Council (PSG266).

References

- [1] European Commission Communication. The European Green Deal. Brussels; 2019.
- [2] Ministry of the Environment of Estonia. National Development Plan for the Use of Oil Shale; 2016-2030. 2016; 75.
- [3] Konist A, Järvi O, Pikkor H, et al. Utilization of pyrolytic wastewater in oil shale fired CFBC boiler. *J Clean Prod* 2019; 234: 487–493.
- [4] Nowak W, Mirek P. Circulating fluidized bed combustion (CFBC). *Fluidized Bed Technologies for Near-Zero Emission Combustion and Gasification*; 2013. p. 701-764.
- [5] Kosowska-Golachowska M, Luckos A, Kijo-Kleczkowska A. Pollutant Emissions during Oxy-Fuel Combustion of Biomass in a Bench Scale CFB Combustor. *Energies* 2022; 15: 1–23.
- [6] Konist A, Pihu T, Neshumayev D, et al. Low grade fuel - oil shale and biomass co-combustion in CFB boiler. *Oil Shale* 2013; 30: 294–304.
- [7] Bui M, Adjiman CS, Bardow A, et al. Carbon capture and storage (CCS): The way forward. *Energy and Environmental Science* 2018; 11: 1062–1176.
- [8] Murugan A, Gardiner T, Brown RJC, et al. Purity requirements of carbon dioxide for carbon capture and storage. London, UK, 2019.
- [9] Yadav S, Mondal SS. A review on the progress and prospects of oxy-fuel carbon capture and sequestration (CCS) technology. *Fuel* 2022; 308: 122057.
- [10] Nemitallah MA, Habib MA, Badr HM, et al. Oxy-fuel combustion technology: current status, applications, and trends. *Int J Energy Res* 2017; 41: 1670–1708.
- [11] Cao H, Sun S, Liu Y, et al. Computational fluid dynamics modeling of NO_x reduction mechanism in oxy-fuel combustion. *Energy and Fuels* 2010; 24: 131–135.
- [12] Stanger R, Wall T, Spörl R, et al. Oxyfuel combustion for CO₂ capture in power plants. *Int J Greenh Gas Control* 2015; 40: 55–125.
- [13] Meriste T, Yörük CR, Trikkel A, et al. TG-FTIR analysis of oxidation kinetics of some solid fuels under oxy-fuel conditions. *J Therm Anal Calorim* 2013; 114: 483–489.
- [14] Loo L, Maaten B, Siirde A, et al. Experimental analysis of the combustion characteristics of Estonian oil shale in air and oxy-fuel atmospheres. *Fuel Process Technol* 2015; 134: 317–324.
- [15] Konist A, Valtsev A, Loo L, et al. Influence of oxy-fuel combustion of Ca-rich oil shale fuel on carbonate stability and ash composition. *Fuel* 2015; 139: 671–677.
- [16] Yörük CR, Meriste T, Trikkel A, et al. Oxy-fuel combustion of Estonian oil shale: Kinetics and modeling. *Energy Procedia* 2016; 86: 124–133.
- [17] Yörük CR, Trikkel A, Kuusik R. Prediction of Flue Gas Composition and Comparative Overall Process Evaluation for Air and Oxyfuel Combustion of Estonian Oil Shale, Using Aspen Plus Process Simulation. *Energy and Fuels* 2016; 30: 5893–5900.
- [18] Konist A, Loo L, Valtsev A, et al. Calculation of the amount of Estonian oil shale products from combustion in regular and oxy-fuel mode in a CFB boiler. *Oil Shale* 2014; 31: 211–224.
- [19] Loo L, Konist A, Neshumayev D, et al. Ash and flue gas from oil shale oxy-fuel circulating fluidized bed combustion. *Energies*; 11.
- [20] Konist A, Anthony EJ, Neshumayev D, et al. Mineral and heavy metal composition of oil shale ash from oxyfuel combustion. *ACS Omega* 2020; 5: 32498–32506.
- [21] Plamus K, Ots A, Pihu T, et al. Firing Estonian oil shale in CFB boilers -ASH balance and behaviour of carbonate minerals. *Oil Shale* 2011; 28: 58–67.
- [22] Uibu M, Siirde A, Järvi O, et al. ClimMIT - Climate change mitigation with CCS and CCU technologies. *SSRN Electron J*. 2021.
- [23] Ots A. Oil shale fuel combustion. Tallinn: Tallinn university of technology; 2006.
- [24] Wu Y, Wang C, Tan Y, et al. Characterization of ashes from a 100kWth pilot-scale circulating fluidized bed with oxy-fuel combustion. *Appl Energy* 2011; 88: 2940–2948.
- [25] Li W, Xu M, Li S. Calcium sulfation characteristics at high oxygen concentration in a 1MWth pilot scale oxy-fuel circulating fluidized

- bed. *Fuel Process Technol* 2018; 171: 192–197.
- [26] Maaten B, Konist A, Siirde A. High-speed thermogravimetric analysis of the combustion of wood and Ca-rich fuel. *J Therm Anal Calorim* 2019; 138: 2807–2811.
- [27] Arro H, Prikk A, Pihu T. Calculation of CO₂ emission from CFB boilers of oil shale power plants. *Oil Shale* 2006; 23: 356–365.
- [28] Khinast J, Krammer GF, Brunner C, et al. Decomposition of limestone: The influence of CO₂ and particle size on the reaction rate. *Chem Eng Sci* 1996; 51: 623–634.
- [29] Duan L, Zhao C, Zhou W, et al. Effects of operation parameters on NO emission in an oxy-fired CFB combustor. *Fuel Process Technol* 2011; 92: 379–384.
- [30] Jia L, Tan. Y, Anthony EJ. Emissions of SO₂ and NO_x during Oxy-Fuel CFB combustion tests in a mini-circulating fluidized bed combustion reactor. *Energy and Fuels* 2010; 24: 910–915.
- [31] IPCC. Revised 1996 IPCC Guidelines for National Greenhouse Gas Inventories. *Oceania* 3; 1996, 21–32.
- [32] Baqain M, Yörük C R, Nešumajev D, Järvik O, Konist A. Characterisation of Ashes Formed at CFB Oxy-fuel Combustion of Ca-rich Fuel. International Conference on Fluidized bed Conversion. Gothenburg, Sweden: Chalmers University of Technology; 2022.
- [33] Baqain M, Nešumajev D, Konist A. NO_x Emissions from Ca-rich Fuel Conversion in Oxy-fuel Circulating Fluidized Bed Combustion. 25th Conference on Process Integration, Modelling and Optimisation for Energy Saving and Pollution Reduction PRES22. Bol, Croatia; 2022.

Publication IV

Baqain, Mais; Neshumayev, Dmitri; Konist, Alar (2024). **TG-MS analysis and kinetic study of co-combustion of ca-rich oil shale with biomass in air and oxy-like conditions**. Carbon Capture Science & Technology, 10. DOI: 10.1016/j.ccst.2023.100162.



Contents lists available at ScienceDirect

Carbon Capture Science & Technology

journal homepage: www.elsevier.com/locate/ccst

Full Length Article

TG-MS analysis and kinetic study of co-combustion of ca-rich oil shale with biomass in air and oxy-like conditions



Mais Baqain, Dmitri Neshumayev, Alar Konist*

Department of Energy Technology, Tallinn University of Technology, Tallinn, 19086, Estonia

ARTICLE INFO

Keywords:

Oil shale
Biomass
Oxyfuel
Co-combustion
Thermogravimetric analysis
Synergy
MS
Kinetic analysis

ABSTRACT

In this study, the combustion behavior of ca-rich oil shale, spruce biomass, and their blends under air and oxyfuel environments of 21/79 % and 30/70 % O₂/CO₂ like conditions were investigated. Non-isothermal thermogravimetric (TG) experiments coupled with a quadrupole mass spectrometer (MS) were conducted to study individual fuels and their blends at 1:0, 4:1, 3:2, 2:3, 1:4, and 0:1 (0, 20, 40, 60, 80 and 100 wt.% Biomass) under three different heating rates 10, 30 and 50 °C/min. Co-combustion synergistic along with the kinetic analysis by the isoconversional Friedman method has been carried out to evaluate the combustion process.

The results show that the addition of biomass enhanced combustion performance and reduced burnout temperatures. Under oxy conditions, the ignition temperatures stabilized with a biomass ratio > 40 %. Ash content was reduced with biomass addition and when switching from air to oxyfuel combustion, the temperature of blends' carbonate decomposition was stable at ~ 720 °C. A positive synergistic effect in the devolatilization and the combustion of light hydrocarbons occurred at higher biomass ratios. Yet, the char oxidation peaks were below zero indicating a negative effect under 21 % of inlet O₂. With increasing the heating rate, the negative synergistic effect was weakened for the three combustion atmospheres. SO₂ emissions were reduced with increasing biomass ratio and increased under oxy mode along with H₂O release. The activation energy (*E*) was lower in oxy conditions than in air mode for individual fuel and their blends, compared to the OS sample, the reduction was higher with increasing BM ratios and for the BM fuel. Overall, this study determines the appropriate conditions for the co-combustion of oil shale and spruce biomass under air and oxy modes for future carbon-negative capture applications in industrial oil shale combustion boilers.

1. Introduction

The accelerating increase in energy utilization, the inadequacy of natural resources, environmental pollution, and the scarcity of conventional fossil fuels have stimulated the research on clean, renewable, and sustainable alternative sources for the synthesis of fuels and generation of energy (Sikarwar et al., 2016). The combustion of conventional fossil fuels and petrochemical products is the major contributor to CO₂ emissions, and this has led to the alteration of the carbon balance on earth (Powell and Lenton, 2012). Therefore, the EU Climate Action Plan set an interim target of reducing greenhouse gas (GHG) emissions to at least 55 % below 1990 levels by 2030 (EU Climate Policy, 2022). Undoubtedly, renewables, nuclear energy, and enhancement of energy efficiency are crucial for the establishment of a low-carbon economy, and these approaches will play an important role in the future. However, compared to the direct replacement of fossil fuels, strategies to reduce the emitted CO₂ are in high demand. This has urged the research and implementation of carbon capture and storage (CCS) (Carbon Clean, 2023), which is the only technology that allows the continued use of fossil fuels

while also substantially reducing GHG emissions. In addition, tremendous interest has been placed on the partial replacement of fossil fuels and reducing CO₂ emissions with the practice of co-combustion of carbon-neutral fuels, such as biomass.

Biomass is categorized as a CO₂-neutral fuel, that can be blended with different types of fossil fuels and burned in conventional power plants resulting in CO₂ reduction (Chirone et al., 2008). However, the direct combustion of biomass in boilers as an individual fuel is reported to have several operational problems which include agglomeration, deposit formation, and corrosion, due to the high alkali content, and these problems can be avoided by co-combustion (Deng et al., 2017; Konist et al., 2013). Konist et al. (2013) state that the challenges can be addressed with proper boiler design and operation, incorporation of alternative bed material or additives, and mainly with co-combustion with different fuels (coal, peat) that will aid the capturing of the problematic substances released from biomass. Recent studies show interest in analysing the combustion performance of fuel mixtures and obtaining the proper blend ratio (Aich and Bhattacharya, 2019). Other researchers have done studies with increasing biomass mix to coal, and no challenges concerning operations were found in the blend percentages of up to 50 % on an energy input basis (Tan et al., 2013; Varol et al., 2018). It has been approved that the co-utilization of biomass with other fu-

* Corresponding author.

E-mail address: Alar.konist@taltech.ee (A. Konist).<https://doi.org/10.1016/j.ccst.2023.100162>

Received 15 September 2023; Received in revised form 5 November 2023; Accepted 8 November 2023

2772-6568/© 2023 The Authors. Published by Elsevier Ltd on behalf of Institution of Chemical Engineers (IChemE). This is an open access article under the CC BY license (<http://creativecommons.org/licenses/by/4.0/>)

Nomenclature

| | |
|-----|----------------------------|
| BM | biomass |
| MS | mass spectrometer |
| OS | oil shale |
| RMS | root mean square |
| TG | thermogravimetric analysis |

els enhances the overall efficiency and cost effectiveness of large-scale biomass combusted plants (Nussbaumer, 2003; Vamvuka and Sfakiotakis, 2011), and a total reduction in SO_x emissions with an increasing biomass ratio (Kim et al., 2019; Nussbaumer, 2003). Yet, there are several limitations of the co-utilization of biomass which include (1) Cost associated with biomass handling and boiler modifications for co-firing, (2) Higher operational cost to manage the enhanced fouling and corrosion, and (3) Undesired alterations in ash composition due to the mix of the alkali metals from biomass ash (Nussbaumer, 2003).

The application of co-utilization is also extended to use an unconventional fuel such as oil shale (OS). There are OS reserves in many regions exceeding the amount of crude oil reserves (Altun et al., 2006), which is an important alternative to fossil fuels. The composition of OS is different, it is a Ca-rich fossil fuel and majorly comprised of organic matter- kerogen and mineral parts exceeding 60 % (Baqain et al., 2023). OS contains higher quantities of minerals, contrary to the biomass that contains a few percent of ash. As a result, the combustion performance of OS can yet be greatly improved to maximize process efficiency. Several studies investigate the interaction between the OS and biomass for the better design and operation of the combustion facilities (Konist et al., 2013; Maaten et al., 2019; Özgür et al., 2012; Torres et al., 2020; Wang et al., 2015). Maaten et al. (2019) utilized a biomass contribution of less than 50 % by weight, the results show that when analyzing the mixtures, the ignition temperatures were shifted towards lower temperatures in comparison with OS. Konist et al. (2013) showed that biomass and OS co-combustion, 15 % of biomass thermal contribution has reduced CO₂ emission by 14.6 % and ash formation by 16 % compared to conventional OS circulated fluidized bed (CFB) combustion. Moreover, Torres et al. (2020) reported that CO₂, CO, and SO₂ emissions were reduced with the addition of biomass to the OS. Further, (Özgür et al., 2012) have performed thermogravimetric analysis (TG) for co-firing of low volatile OS and biomass under combustion and reported that biomass 10 % and 20 % by weight blended with the low volatile OS are the best ratios for co-firing due to the formation of a sufficient amount of volatile matter to maintain a stable combustion process. The study by (Torres et al., 2019, 2020) shows that the co-combustion of samples between 0-50 % of OS-biomass produced the lowest total CO₂ emissions, and the reduction of the release of the emissions depends on the OS to biomass mass ratio, the characteristics of the fuels, the physicochemical properties, and the operating conditions of the combustion system (Torres et al., 2020). From the reported kinetic analysis studies (Özgür et al., 2012; Yörük et al., 2018; Mureddu et al., 2018), it was found that several differences in the activation energy values are based on the used biomass, OS volatile and ash content, and the co-combustion synergistic effect. Özgür et al. (2012) found a positive interaction in the reduction of activation energies during the combustion of the blend of OS and biomass, and (Yörük et al., 2018) reported that the value of activation energy decreased with the proportion of biomass ratio, while for the pine and eucalyptus wood chips, the activation energy of co-combustion with a different type of coal samples was higher (Mureddu et al., 2018).

Oxyfuel combustion is a process that uses O₂ and CO₂ or the blend of pure O₂ and a recycled exhaust gas stream for oxidation instead of using air (Baqain et al., 2022, 2023). Oxyfuel combustion combined with CCS-based CO₂ mitigation has been one of the main fields of interest in the energy sector of Estonia, as energy production is dominated by

OS with a share of 40 % of the electricity demand. Extensive research has been carried out at Tallinn University of Technology (Baqain et al., 2023; Baqain et al., 2022; Baqain et al., 2023; Konist et al., 2014, 2015; Loo et al., 2015, 2018; Meriste et al., 2013; Yörük et al., 2015, 2016, 2018). Studies reported several areas of oxyfuel combustion with OS including TG experiments to investigate the kinetics of OS combustion in the CO₂ rich oxyfuel atmosphere (Loo et al., 2015; Meriste et al., 2013; Yörük et al., 2015), small scale laboratory reactor experiments (Konist et al., 2015), process simulator-based modelling of the oxyfuel combustion process with OS (Yörük et al., 2015, 2016, 2018) and oxyfuel combustion tests with a 60 kWth CFB pilot facility (Baqain et al., 2022, 2023; Baqain et al., 2023; Loo et al., 2018).

In the case of biomass co-combustion with different fuels under oxy conditions, if the CO₂ produced is captured, the resulting emission from the combustion can be considered as a negative carbon emission. Recently there have been multiple studies on co-firing biomass and coal under oxy conditions (Kayahan and Özdoğan 2016; Liu et al., 2021; Tan et al., 2013; Xiao et al., 2022). Xiao et al. (2022) carried out a TG study of the co-combustion of lignite and lignocellulosic components and reported a strong positive synergistic effect in the devolatilization region during oxyfuel co-combustion experiments. Kayahan and Özdoğan (2016) reported that a 20 % biomass-to-coal blend ratio shows an improvement in combustion conditions in a 30 kWth circulating fluidized bed pilot facility under 30 % of O₂ enrichment condition. For OS biomass co-combustion, a recent techno-economic study (Saia et al., 2022) search into the viability of adopting CCS in the available OS power plants in Estonia, found that depending on the biomass share of the fuel blend supplied to the unit, the negative CO₂ emission can be as low as -40 % (an average of -0.7 Mt CO₂/y) of the initial level when the biomass is at 50 % of the fuel blend. Oxyfuel co-combustion of OS and biomass studies are very rare (Meriste et al., 2013; Yörük et al., 2018), further in depth theoretical and experimental studies are required. There is a knowledge gap around biomass fuels which vary widely in composition, sulfur, and nitrogen contents that can make oxyfuel utilization of these fuels with an unconventional fuel such as OS more challenging. Moreover, there is a critical need to study fundamental mechanisms associated with oxy-fuel co-combustion of OS and biomass. Further research is useful for improving the blending and cofiring of the fuel mixtures for additional reduction in emissions and solid waste in the OS industry. Therefore, the presented work provides a detailed observation of the co-combustion process under 21/79 % of O₂/N₂ environment as air combustion and 21 % and 30 % of inlet O₂ % under O₂/CO₂ environment as oxyfuel combustion. The results can provide reference information for the implementation and optimization of the OS biomass co-combustion field. The interaction of the fuel blends was studied at three combustion atmospheres under different heating rates 10, 30, and 50 °C/min. The main evolved emissions during co-combustion were also presented in this work. In addition, the activation energy (*E*) was obtained by the isoconversional Friedman method to evaluate the combustion process. The results stated in this paper could lead to a deeper understanding of the combustion characteristics of OS and biomass and such information would provide theoretical guidance and technical support for scaling up and deployment of oxyfuel co-combustion technology in the OS power industry.

2. Experimental work

2.1. Material

Typical kukersite OS and common spruce biomass (BM) samples were obtained from east Estonia. The samples were first dried at 105 °C for multiple hours and ground before the analysis, using a ball mill at 180 rpm for 20 min. The crushed samples were sieved using a sieve stack tensioning system with a 125-µm sieve. The OS sample with particles >125-µm was ground additionally at 220 and 280 rpm respectively for 20 min to make sure the whole sample passed the 125-µm sieve. The

Table 1
Proximate and ultimate analysis of the fuel.

| Fuel | Proximate analysis ^d (wt.%) | | | | | Ultimate analysis ^d (wt.%) | | | | | |
|------|--|-------|-------|-------|-------------|---------------------------------------|------|----------------|-------|------------------|-------|
| | Moisture | Ash | V | FC | LHV (MJ/kg) | C | H | ^a O | N | S | Cl |
| OS | 0.18 | 52.05 | 46.36 | 1.59 | 9.76 | 27.38 | 2.68 | 0.36 | 0.07 | 1.57 | 0.076 |
| BM | 6.00 | 0.27 | 84.67 | 15.06 | 20.21 | 50.04 | 6.35 | 37.24 | 0.103 | ^b n.d | 0.004 |

^a O% = 100-(W+A+CO₂+S+TOC+H+N) %

^b n.d = No detection

Table 2
Chemical composition of the mineral part of the oil shale.

| Components | SiO ₂ | Al ₂ O ₃ | Fe ₂ O ₃ | CaO | MgO | Na ₂ O | K ₂ O | SO ₃ | LOI _{950 °C} |
|---------------|------------------|--------------------------------|--------------------------------|-------|-----|-------------------|------------------|-----------------|-----------------------|
| Content, wt.% | 15.39 | 3.64 | 2.03 | 22.52 | 3 | 0.09 | 1.6 | 3.91 | 47.12 |

LOI_{950 °C} = Loss of ignition at 950 °C

Table 3
Mineralogical composition of the mineral part of the oil shale.

| Components | Quartz SiO ₂ | K-feldspar KAlSi ₃ O ₈ | Calcite CaCO ₃ | Dolomite CaMg(CO ₃) ₂ | Chlorite ClO ₂ | Pyrite FeS ₂ | Illite |
|---------------|-------------------------|--|---------------------------|--|---------------------------|-------------------------|--------|
| Content, wt.% | 11.6 | 6.5 | 43.1 | 20.3 | 3.5 | 1.9 | 13 |

OS and BM mixtures were prepared in the proportion of wt.% basis of OS:BM ratios at 1:0, 4:1, 3:2, 2:3, 1:4, and 0:1 (0, 20, 40, 60, 80, and 100 wt.% BM) using a ball mill grinding machine for a homogenous mixture. The fuel's proximate and ultimate analyses are given in Table 1. OS and BM samples characterization included proximate analysis (ash, moisture, and net heating value or lower heating value (LHV)), ultimate analyses include elemental analysis using Elementar Vario MACRO CHNS to measure carbon (C), hydrogen (H), nitrogen (N) and sulfur (S). The LHV was determined through calorimetric measurements with a bomb calorimeter IKA2000C. Chlorine content (Cl) was measured using ion chromatography. In comparison, Table 1 shows that the OS ash and S contents are significantly higher than in the BM, while moisture, volatiles (V), fixed carbon (FC), LHV, C, H, O, and N contents in BM are usually higher than in the OS. The chemical composition of the OS sample is given in Table 2, the results were obtained by using a Rigaku Primus II X-ray fluorescence (XRF) spectrometer, and the mineral composition, in Table 3, was obtained by using a Bruker D8 diffractometer fitted with a Lynx-Eye linear detector. X-ray diffraction (XRD) experiments were performed using Cu K α radiation in the 2θ range of 3–72 $^\circ$ with a step size of 0.02 $^\circ$ 2θ and a counting time of 0.1 s/step, and the X-ray tube operated at 40 kV and 40-mA. From Table 3 results it can be seen that the OS mineral part is mainly characterized by calcite and dolomite together exceeding 60 %.

2.2. Method

The influence of air and oxyfuel combustion environments on the combustion of OS and BM and their mixtures was investigated using NETZSCH STA 449 F3 Jupiter thermogravimetric analyser coupled with a Netzsch quadrupole mass spectrometer (MS) 403D Aeolos (mass 1–300 amu). The standard Al₂O₃ crucibles with 5 \pm 0.01 mg sample weight were used for the combustion analysis. The gas flow rate was 60 ml/min for a gas mixture of 21/79 % O₂/N₂ as air-base combustion and 21/79 % (OXY21) and 30/70 % (OXY30) of O₂/CO₂ as oxyfuel combustions. OXY30 mode was selected to study the influence of higher inlet O₂% on the combustion process. The non-isothermal TG was performed at a heating rate of 10, 30, and 50 $^\circ$ C/min from 40 $^\circ$ C up to the final combustion temperature of 1000 $^\circ$ C. The small temperature shift of \sim 6 $^\circ$ C was considered at higher heating rates (50 $^\circ$ C/min). The MS is used to investigate the dynamics of the following gaseous emissions (H₂O, CO₂, and SO₂). Each set of experiments was carried out by an empty crucible with a correction factor to eliminate the buoyancy effect that can

drift the TG curve. All the experiments were conducted at least twice, to reflect a good repeatability and reproducibility of the tests.

The combustion performance of the fuels was analyzed using combustion parameters that can be determined based on the TG curves and their derivatives (DTG) curves. The ignition temperature (T_i) was determined using the TG-DTG extrapolation method following other literature (Li et al., 2006; Liu et al., 2022; Niu et al., 2011). One or more weight loss peaks appear in the DTG curve of the sample, with the largest peak points indicating where the weight loss rate is the highest throughout the combustion process. The temperature corresponding to the peak (T_{max1} and T_{max2}) and the corresponding weight loss rate, namely $((dw/dt)_{max1})$ and $((dw/dt)_{max2})$ represents the maximum of the mass loss rate during the combustion process. Burnout temperature (T_b) is defined based on (Chen et al., 2020; Liu et al., 2022) and corresponds to the point when the sample mass at the end of combustion does not change substantially, at which the rate of weight loss decreases to 1 %/min. Combustion characteristic index (S) was also applied to this study, it is widely used in literature (Chansa et al., 2020; Fan et al., 2016), and it reflects the burning ability of samples. The higher S value the better the combustion capacity, and it is calculated as follows:

$$S = \frac{(dw/dt)_{max} \times (dw/dt)_{mean}}{T_i^2 T_b} \quad (1)$$

Where; $(dw/dt)_{max}$ – is the maximum average weight loss rate,

$(dw/dt)_{mean}$ – is the average weight loss rate,

T_i – is the ignition temperature, and

T_b – is the burnout temperature.

The following parameters for the carbonate decomposition were obtained: beginning temperature (T_{d1}) of the reaction; the temperature of the maximum mass loss rate (T_{max3}); the corresponding weight loss rate $((dw/dt)_{max3})$; and ending temperature (T_{e1}) of the carbonate decomposition, at which the rate of weight loss decreases to 1 %/min. In the OXY21 and OXY30 atmospheres, the decomposition of carbonate minerals occurs in two steps. The beginning temperature (T_{d2}) of the second decomposition step, the temperature of the maximum mass loss rate (T_{max4}); the corresponding weight loss rate $((dw/dt)_{max4})$ and ending temperature (T_{e2}) of the second step were measured.

2.3. Synergy evaluation

To further understand the occurrence of synergistic effects when co-processing two different fuels, and to evaluate the outcome variables

whether higher or lower than the individual feedstock processing, the synergy between OS and BM co-combustion is calculated. The parameters can be derived from the experimental value, while the theoretical weight loss value can be calculated as the following (Tian et al., 2023; Xiao et al., 2022):

$$TG_{cal} = x_i.TG_{BM} + (1 - x_i).TG_{OS} \quad (2)$$

Where; TG_{BM} , TG_{OS} and TG_{cal} – is the weight losses of BM, OS, and their blends respectively, and

x_i – is the mass fraction of the BM in the blend.

The difference between the calculated TG_{cal} and experimental TG_{exp} , that is obtained experimentally for the blend with the same x_i , weight loss can represent the extent of synergy and is calculated as the following:

$$\Delta TG\% = \frac{TG_{cal} - TG_{exp}}{TG_{exp}} \times 100\% \quad (3)$$

If the value of TG_{exp} is lower than the TG_{cal} and $\Delta TG > 0$, a positive synergy exists during the co-combustion of OS and BM, which contributes to more weight loss and larger volatiles evolved. On the contrary, if $\Delta TG < 0$, a suppressing effect occurs.

Moreover, the root mean square (RMS) value of ΔTG , is calculated to evaluate the synergistic effect generally for the fuel's combustion region. The RMS value is calculated as the following (Wu et al., 2016):

$$RMS = \sqrt{\frac{\sum_{i=1}^n (TG_{cal}^i - TG_{exp}^i)^2}{n}} \quad (4)$$

Where; i and n are the numbers of points selected in the TG profiles. The intensity of the interaction increases as the RMS value increases.

2.4. Kinetic model

An analysis of the kinetic methods and thermodynamic parameters was conducted for OS and BM and their blends under air, OXY21, and OXY30 combustion atmospheres. Isoconversional method is applied in this study, namely the non-linear form of the differential method introduced by Friedman (1964). Isoconversional methods give apparent kinetic parameters as a function of conversion (α), and this method is based on the isoconversional principle, stating that, at a fixed conversion, the conversion ratio is only a function of temperature. The application of isoconversional methods is quite common in the assessment of oil shale (Bai et al., 2019; Yörük et al., 2015), coal (Wang et al., 2023), and biomass (Barzegar et al., 2022; Samuelsson et al., 2015). The Arrhenius kinetic analysis approach is implemented, whereas the changes in activation energy (E) depending on the reaction progress were evaluated from the tests with 10, 30, and 50°C/min heating rates. According to this approach the reaction mechanism function $f(\alpha)$ becomes a constant at each fixed conversion degree α , and the relationship between the reaction rate $\ln[\beta \frac{d\alpha}{dT}]$ and $[\frac{1}{T}]$ is linear with the slope of $[-\frac{E}{RT}]$. The key advantage of this method is that it doesn't require assumptions about the specific reaction mechanism, making it suitable for reactions with unknown or complex mechanisms that occur in several steps. The general kinetic analysis for the thermal degradation of solid fuel during the combustion process is given by Mureddu et al. (2018):

$$\frac{d\alpha}{dt} = k(T)f(\alpha) = A \exp\left(-\frac{E}{RT}\right)f(\alpha) \quad (5)$$

Where, α – mass conversion ratio,

t – time (min),

k – reaction rate,

T – absolute temperature (K),

A – pre-exponential factor (min^{-1}),

E – activation energy (kJ/mol), and

R – ideal gas law constant (8.314 J/K mol),

α can be calculated by the following:

$$\alpha = \frac{m_0 - m_t}{m_0 - m_f} \quad (6)$$

Where, m_0 – the initial mass of the sample,

m_t – the mass of the sample at time t , and

m_f – the final mass of the sample.

Rearranging Eq. (5), with the introduction of the heating rate, $\beta = \frac{dT}{dt}$, Eq. (5) can be written as:

$$\beta \frac{d\alpha}{dT} = A \exp\left(-\frac{E}{RT}\right)f(\alpha) \quad (7)$$

Applying the natural logarithm on both sides of Eq. (7)

$$\ln\left[\beta \frac{d\alpha}{dT}\right] = \ln[Af(\alpha)] - \frac{E}{RT} \quad (8)$$

E was estimated from the inclination of the straight slope $-\frac{E}{RT}$ obtained by graph between $\ln[\beta \frac{d\alpha}{dT}]$ and $\frac{1}{T}$ for a constant conversion ratio (α).

3. Results and discussion

3.1. Thermal analysis of individual fuels and their blends at different atmospheres

Fig. 1 shows TG and DTG results of OS, BM, and their blends at 10 °C/min heating rate under air, OXY21, and OXY30 combustion atmospheres. In Fig. 1(a) and (b), the OS (OS:BM 1:0) in air combustion undergoes three stages of weight loss, in addition to the release of moisture prior to 150 °C. The first two regions denote the combustion of light hydrocarbon-bitumen and heavy hydrocarbon-kerogen (Han et al., 2006; Kaljuvee et al., 2007). Moreover, the region > 600 °C represents the mineral decomposition (Kaljuvee et al., 2007) indicating high mineral and ash content in the OS. As the height of the peaks of the DTG curves is proportional to the amount of mass loss in the reaction region at the maximum temperature where the mass loss occurred.

Fig. 1(c)-(f) shows the TG and DTG curves of OS combustion in OXY21 and OXY30 atmospheres, the differences between oxy and air combustions can be noted at higher temperature range > 600 °C, which represent the decomposition stage. The DTG curves in Fig. 1(d) and (f) have two peaks, compared to one peak in Fig. 1(b), whereas the peak corresponding to the temperature > 800 °C appeared. The main reason is that under an oxy-combustion atmosphere, the decomposition of carbonate is delayed and appears in two stages reference to the decomposition of dolomite and the second stage of calcite as discussed intensively in many literature (Baqain et al., 2023; Loo et al., 2015).

Table 4 shows in more detail the combustion and decomposition characteristics of the OS. Under air combustion, the bitumen and kerogen combustion of OS occurred at a temperature range of 300–500 °C. Generally, the region below 230 °C represents the vaporization of moisture and the devolatilization of the volatile matter (Loo et al., 2015). Under oxy conditions, T_i were slightly reduced compared to air combustion, and the reduction increased with increasing O₂ concentrations, this has also been noticed in previous literature (Bai et al., 2019; Loo et al., 2015). And can be explained as with the increment of O₂ concentration, the reaction rate increases, enhancing the release of heat. Moreover, temperatures at maximum mass loss T_{max1} and T_{max2} decreased by an average of 10 °C, and T_b were slightly reduced by ~4 °C, when increasing O₂% from 21 % to 30 % (Table 4). With higher O₂ concentration, the temperature of the particles becomes higher during the combustion process, and higher O₂ flux from the bulk towards inner particles, hence increasing the rate of combustion. However, when switching from O₂/N₂ to a 21/79 % O₂/CO₂ atmosphere, the molar heat capacity of CO₂ is higher and has lower O₂ diffusivity in CO₂, thus lowering the particles' temperature. Therefore, the T_{max1} , T_{max2} and T_b are higher in

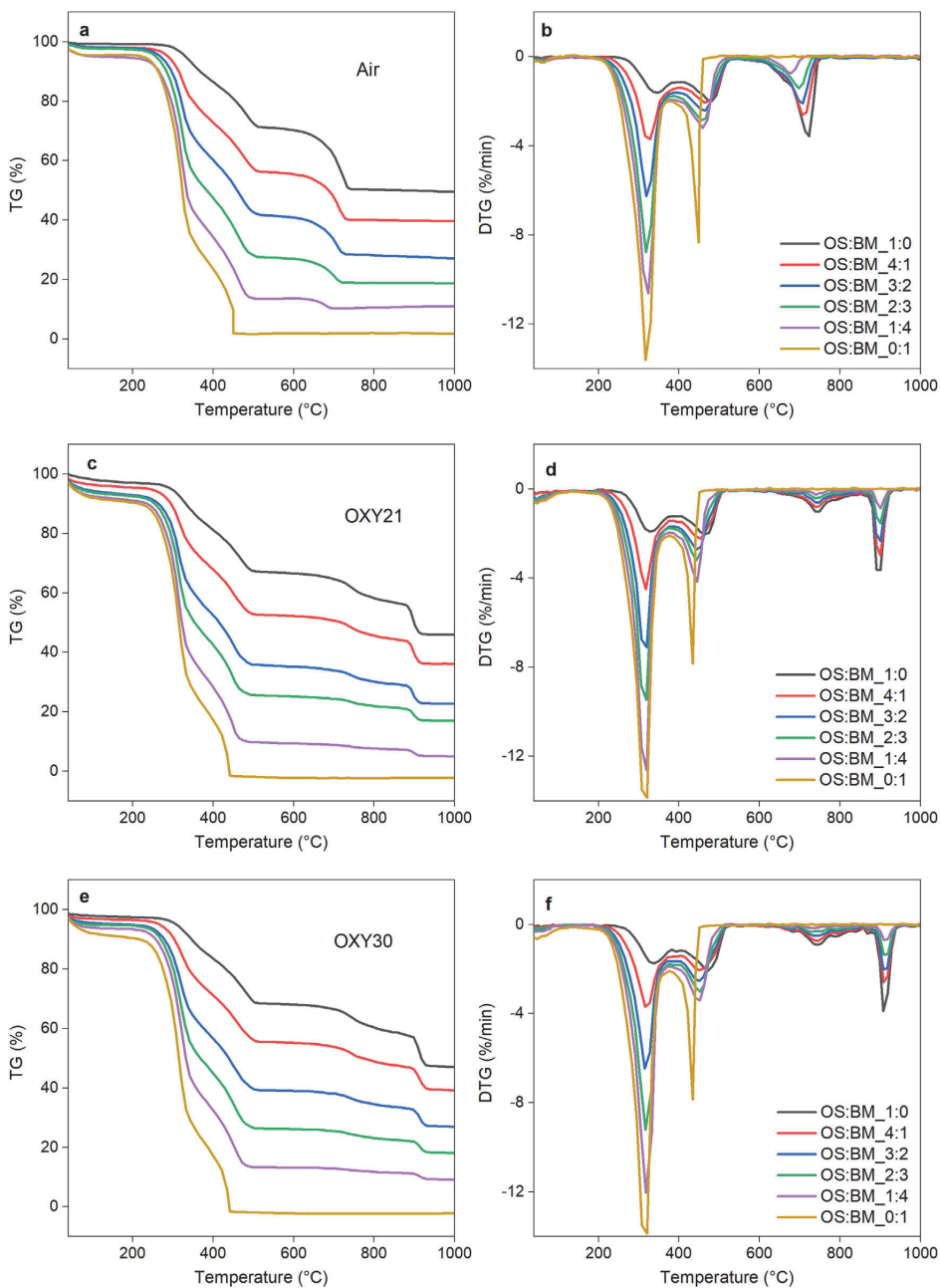


Fig. 1. TG-DTG Curves under; N_2/O_2 (air) (a) and (b), OXY21 (c) and (d), and OXY30 (e) and (f).

OXY21 compared to air combustion, and elevated O_2 concentration is required to maintain the same combustion characteristics as in air combustion. In Table 4, the first decomposition stage of OS under oxyfuel combustion, which refers to dolomite, occurred at a higher temperature of $\sim 39^\circ C$ compared to air combustion, due to the elevated CO_2 concentration that delays the decomposition of carbonates, as explained in the previous works (Baqain et al., 2023; Loo et al., 2015). While T_{d1} and

T_{d2} slightly reduced, and $(dw/dt)_{max3}$ and $(dw/dt)_{max4}$ values increased at higher O_2 concentrations when switching from OXY21 to OXY30.

Evaluating the combustion performance of the BM (OS:BM_0:1) sample, in Fig. 1(a) and (b), two significant regions can be observed in the TG and DTG curves, in addition to the release of moisture before $150^\circ C$. The first stage is a result of the combustion of the pyrolytic volatiles that occur in the temperature region of $200\text{--}400^\circ C$. The sec-

Table 4
Combustion characteristics of OS, BM, and their blends at N₂/O₂ (air), OXY21 and OXY30.

| Mode | Combustion | | | | | Carbonate decomposition | | | | | | | | | | |
|-------|----------------|--------------------------------------|-------------------|--------------------------------------|-------------------|-------------------------|----------------------|-----------------|--------------------------------------|-------------------|-----------------|-----------------|--------------------------------------|-------------------|-----------------|-----|
| | T _i | ($\frac{dw}{dt}$) _{max1}} | T _{max1} | ($\frac{dw}{dt}$) _{max2}} | T _{max2} | T _j | S (10 ⁶) | T _{d1} | ($\frac{dw}{dt}$) _{max3}} | T _{max3} | T _{e1} | T _{d2} | ($\frac{dw}{dt}$) _{max4}} | T _{max4} | T _{e2} | |
| Air | 1:0 | 307 | 1.63 | 346 | 2.03 | 478 | 0.13 | 692 | 3.6 | 721 | 735 | 909 | 4.66 | 916 | 927 | |
| | 4:1 | 300 | 4.15 | 325 | 2.08 | 466 | 0.43 | 690 | 2.8 | 712 | 727 | 909 | 3.74 | 918 | 927 | |
| | 3:2 | 295 | 6.84 | 323 | 2.45 | 465 | 1.00 | 673 | 2.19 | 702 | 720 | 911 | 2.82 | 919 | 929 | |
| | 2:3 | 293 | 9.72 | 322 | 2.98 | 462 | 1.94 | 668 | 1.56 | 701 | 715 | 912 | 2.03 | 919 | 927 | |
| | 1:4 | 292 | 12.37 | 323 | 3.47 | 461 | 3.05 | 661 | 0.84 | 687 | 698 | 911 | 0.96 | 919 | 926 | |
| | 0:1 | 288 | 14.03 | 321 | 8.48 | 441 | 6.76 | 722 | 1.02 | 745 | 773 | 909 | 4.66 | 916 | 927 | |
| | OXY21 | 1:0 | 305 | 1.68 | 349 | 2.07 | 482 | 0.15 | 720 | 1.06 | 746 | 775 | 902 | 4.76 | 910 | 921 |
| | | 4:1 | 300 | 4.01 | 326 | 2.16 | 460 | 0.44 | 720 | 0.78 | 746 | 766 | 902 | 3.6 | 911 | 918 |
| | | 3:2 | 293 | 7.08 | 325 | 2.51 | 461 | 1.08 | 722 | 0.58 | 750 | 762 | 911 | 2.82 | 919 | 929 |
| | | 2:3 | 293 | 9.82 | 325 | 2.88 | 461 | 1.93 | 722 | 0.38 | 750 | 762 | 912 | 2.03 | 919 | 927 |
| 1:4 | | 292 | 13.4 | 325 | 3.42 | 460 | 3.45 | 721 | 0.17 | 746 | 748 | 911 | 0.96 | 919 | 926 | |
| OXY30 | 0:1 | 292 | 15.22 | 315 | 8.61 | 429 | 7.33 | 717 | 1.06 | 746 | 775 | 902 | 4.76 | 910 | 921 | |
| | 1:0 | 300 | 1.72 | 338 | 2.04 | 473 | 0.16 | 719 | 0.85 | 746 | 768 | 903 | 3.6 | 911 | 922 | |
| | 4:1 | 290 | 4.38 | 322 | 2.22 | 446 | 0.53 | 719 | 0.58 | 743 | 766 | 904 | 2.6 | 912 | 923 | |
| | 3:2 | 288 | 7.03 | 320 | 2.56 | 447 | 1.14 | 719 | 0.58 | 743 | 774 | 905 | 1.76 | 913 | 923 | |
| | 2:3 | 286 | 10.42 | 320 | 3.05 | 452 | 2.32 | 719 | 0.36 | 744 | 754 | 904 | 0.97 | 914 | 921 | |
| 1:4 | 286 | 14.36 | 322 | 3.72 | 453 | 4.26 | 720 | 0.27 | 744 | 754 | 904 | 0.97 | 914 | 921 | | |
| 0:1 | 286 | 17.11 | 323 | 11 | 434 | 10.73 | | | | | | | | | | |

ond stage corresponds to the combustion of the fixed carbon between 400–500 °C. The DTG curve shows two significant peaks in the temperature range of 200–500°C. The first peak has a considerably high peak value of mass loss rate, and is wider compared to the second peak, as a reason of the high volatile matter in the BM. In addition, the combustion process of BM can be explained using the combustion of biomass model components- hemicellulose, cellulose, and lignin (Özgür et al., 2012). The key components of the BM or lignocellulose BM (cellulose, hemicellulose, and lignin) account for the shape of the profile and the temperature regions that contain the peaks. Generally, hemicellulose has a higher calorific value compared to other components in lignocellulose. Therefore, hemicellulose combustion will generate peaks with higher intensity. In contrast to this, the combustion of lignocellulose BM components with lower calorific values will lower the height of the generated peak (Giummarella et al., 2017). In addition, the reactivity and the lower oxidation stability of the lignocellulose are controlled mainly by hemicellulose and lignin. Table 4 shows the BM combustion profile, under air atmosphere, which comprises three significant stages: The region below 256 °C shows the devolatilization, next is the combustion of light volatile matters between 256 and 419 °C, followed by the combustion of heavy volatile and char oxidation 419–486 °C. However, in BM combustion above 480 °C, there is no further visible peak (Yörük et al., 2018), the presented literature data (Özgür et al., 2012) shows both the combustion of hemicellulose and lignin takes place in a broader temperature interval of 265–525 °C and 265–600 °C, respectively, while the combustion of cellulose is limited to a narrow temperature interval of 385–460 °C. This higher quantity of lighter compounds increases the reactivity of the sample, as shown for OS:BM_0:1, in Table 4. The effect of oxy conditions is clearly demonstrated in the thermal degradation of the OS sample but not in the BM sample. The number and the shape of the peaks under OXY21 and OXY30, Fig. 1(d) and (f), are similar to the BM sample in air combustion, Fig. 1(d). The differences between air and oxy conditions for the BM can be seen more clearly in Table 4, ($\frac{dw}{dt}$)_{max2} increases when switching from air to oxyfuel combustion and with the increment of O₂ concentration, while char oxidation ($\frac{dw}{dt}$)_{max3} enhances at higher O₂% only. Moreover, BM reactivity enhanced noticeably in oxy conditions, as the S index increased by 34 % when switching from air to OXY30, Table 4. This indicates that the degradation of BM is shown to accelerate significantly under a higher O₂ environment. A similar observation has been reported by Chansa et al. (2020), indicating that the combustion of BM with high O₂ concentrations was so quick that the curves became long sharp peaks. As the BM macromolecular components are bound together with weak ether bonds, oxygen-rich polymers such as cellulose and hemicelluloses have a strong tendency to decompose even at low temperatures, therefore the degradation of the biomasses is shown to accelerate significantly under greater enriched oxygen atmospheres.

TG and DTG curves for the OS and BM blends (4:1. 3:2, 2:3, and 1:4) under air and oxyfuel combustion conditions in Fig. 1 show that the weight loss trend is similar to the individual fuels. The thermal degradation curves of the blends were located between the OS and BM samples. The DTG curves in Fig. 1(b) show 3 main distinct peaks in air combustion, and those peaks correspond to the weight loss of both OS and BM. As the ratio of the BM in the blends increased, the DTG curve intensity increased, and the combustion intervals shifted toward a lower temperature region. Moreover, the co-combustion profiles show a reduction in mineral decomposition peak intensities at temperatures > 600 °C with the increase of the BM ratio, and T_d shifted to a lower temperature. This is due to the presence of lower ash/mineral contents for decomposition in BM compared to OS. As a result, the addition of BM has enhanced the combustion performance of the blends and increased the reaction rate intensity identified with the higher release of volatile and improved char combustion. The results are in line with the previous work presented by Konist et al. (2013), that CFB boiler efficiency increased slightly, and the amount of ash content decreased when co-combusting OS and BM up to 50 % of BM share thermal input in 215 MW CFB boiler of Balti

power plant. The effect of OS:BM blends under oxyfuel combustion are presented in the DTG curves in Fig. 1(d) and (f). The figures show 4 distinct peaks, and the intensity of combustion peaks increased with the increment of the BM blending ratio. However, the combustion intervals were similar to air combustion, and these intervals were shifted to a lower temperature region while the two decomposition stages' temperatures were the same as in the OS under oxy conditions.

Table 4 presents in more detail the co-combustion characteristics of the blends; under air combustion, it shows that the addition of BM slightly reduces T_i from 300 to 292 °C when increasing the BM blending ratio from 1-4. While under oxy conditions, when the BM ratio increased over 40% (OS:BM_2:3), the reduction rate of T_i stabilizes, the same behavior has been reported by Özgür et al. (2012). Moreover, the increase of the BM ratio in the blends led to accelerated combustion and reduce T_b significantly from 500 °C to 482 °C under air and OXY21, while further reduction occurred in OXY30 from 492 °C to 469 °C. The work studied by Kayahan and Özdoğan (2016) presents combustion in a 30 kWth CFB pilot facility under 30 % O₂ enrichment condition, with a 20 % BM to coal blend ratio, demonstrating an improvement of combustion conditions. As it can be indicated that the increment of O₂ concentration and the enriched oxy environment appear to be significantly more reactive atmosphere than in air and OXY21, which can also be seen in the increase of the S index of the fuel blends under OXY30, Table 4. Hence, the addition of BM improved the combustion of the OS by lowering both T_i and T_b and enhancing OS fuel reactivity. The calcite decomposition stage shows a decrease in T_{d1} by 30 °C, when reducing the OS:BM blending ratio from 4-1 in air combustion, while T_{d1} (dolomite decomposition) stabilizes at 720 °C in OXY21 and OXY30, and T_{d2} of fuel blends shifted from ~ 911 °C to 904 °C when switching from OXY21 to OXY30.

In conclusion, the blending method contributes a lot to improving the combustion of the OS. And switching from air to oxyfuel combustion, the behaviour of mineral decomposition is not affected by BM addition, on the contrary, it lowers the amount of ash and doesn't shift the carbonate decomposition to a lower temperature.

3.2. Synergistic effect

To verify the possible synergistic effect that occurred in the co-combustion of different mixing ratios of OS and BM, the experimental and calculated TG curves, following (Eq. (2)), and the differences between both experimental and calculated TG, as Δ TG curves (Eq. (3)) for 10 °C/min heating rate are shown in Fig. 2. In the case of 30 and 50 °C/min heating rates, the curves are shown in Figs. 1S and 2S (supplementary material). In air combustion mode, Fig. 2(a), the region between 290 and 460 °C shows that the TG calculated curve is higher than the experimental one, for an OS:BM_4:1, while with increasing BM ratios the TG experimental curve becomes higher, and the difference increases with increasing BM ratio. This can be explained as the co-combustion process under air conditions of OS and BM showed a negative synergistic effect in both volatile/light hydrocarbons and char oxidation regions, a sharp reduction in the Δ TG curve to below zero, and the increase in BM ratio corresponding to an inhibitory reaction effect of OS on BM combustion. However, in the decomposition region ($T > 650$ °C), a positive synergistic effect with increasing BM ratios is shown in Fig. 2(b), the peaks are significantly enhanced with increasing BM ratios.

Under OXY21 and OXY30 modes, Fig. 2(d) and 2(f), show that the peaks of Δ TG curves rose greater than zero at the combustion region of a temperature between (320 and 330 °C), indicating a positive synergistic effect that is associated with the devolatilization and the combustion of light hydrocarbons, and the intensity of the peaks increased with BM addition. In the meantime, the char oxidation (330–480 °C) exhibits the same behaviour as in air combustion, and the peaks were below zero under OXY21. The indicated peaks reduced noticeably under OXY30 showing a minimal inhibitory effect with the increase of O₂ concentration. As explained previously, this can be donated to the enhancement of combustion under higher O₂ concentrations. Xiao et al. (2022) studied syn-

Table 5

RMS values of Δ TG of various OS:BM blending ratios for the combustion region (250–500 °C) at 10 °C/min heating rate.

| OS:BM | Combustion atmosphere | | |
|-------|-----------------------|-------|-------|
| | Air | OXY21 | OXY30 |
| 4:1 | 0.53 | 0.14 | 1.15 |
| 3:2 | 0.85 | 1.17 | 1.44 |
| 2:3 | 2.58 | 0.49 | 4.04 |
| 1:4 | 3.31 | 0.09 | 5.06 |

ergistic effects during the co-combustion of lignite and lignocellulosic components under oxyfuel conditions and reported that a strong positive synergistic effect is noticed in the devolatilization region at 340 °C for a mixture with high cellulose. A possible explanation that can be deduced from Li et al. (2021), Xiao et al. (2022) is a considerable amount of hydrogen can be produced during the devolatilization of BM, which can prevent the recombination and cross-linking reactions of free radicals, thereby promoting the release of OS volatiles.

For the carbonate decomposition region under oxy conditions, Δ TG curves in Fig. 2(d) and (f) show a negative effect, which means that the actual mass loss of the experimental sample is lower than the calculated mass loss and indicates an inhibitory decomposition of ash mineral material. A possible explanation can be provided by comparing the temperature range of carbonate decomposition between air and oxy conditions, at the low-temperature range (air mode) the interactions between the OS and BM fuels were more significant, and the combustion of BM released more heat to accelerate the endothermic reaction which eventually promoted the combustion and decomposition of OS. This can also explain the shift in the TG experimental decomposition temperature compared to the TG calculated under air combustion, particularly at a higher BM ratio, Fig. 2(a). While under oxy conditions the decomposition temperature shifted to a much higher temperature lowering the effect of BM combustion heat release.

The synergistic effects at higher heating rates of 30 and 50 °C/min show that under the air mode combustion region, the negative effect was the strongest under 10 and 30 °C/min heating rates, and the weakest at the 50 °C/min heating rate. And under oxy conditions, the weakest negative effect was at 50 °C/min and the strongest positive effect in the devolatilization and the combustion of light hydrocarbons was also at 50 °C/min. Therefore, the synergistic effect of OS and BM blends enhanced under higher heating rates for the three combustion atmospheres. This is attributed to the strong combustion and faster heat transfer to the fuel particles, which can promote rapid volatilization and release of combustible gases. For the carbonate decomposition region, the positive Δ TG in air combustion and the negative Δ TG peaks in oxy conditions were weakened with a rising heating rate. However, the effect was much clearer in air mode than under oxy conditions.

Table 5 compares RMS values of the combustion region for a temperature range between 250 and 500 °C at different blending ratios in the three combustion atmospheres: air, OXY21, and OXY30 at 10 °C/min heating rate. The RMS values show that the synergistic effect was enhanced with the increase of BM blending ratio under air and OXY30, while OXY21 exhibits an opposite behaviour. This can be explained due to the high heat capacity of CO₂ and lower O₂ diffusivity under OXY21, however further explanation needs to be studied and addressed. While RMS values were the highest under OXY30.

Overall, based on the optimal stated conditions, increasing each of the BM ratios, heating rate, and O₂% in the combustion atmosphere can obtain a better positive synergistic effect during co-combustion of ca-rich OS and spruce BM.

3.3. Effect of the heating rate at different atmospheres

To study the effect of heating rates on individual and blended samples, Fig. 3 compares the 10, 30, and 50 °C/min heating rates of OS:BM

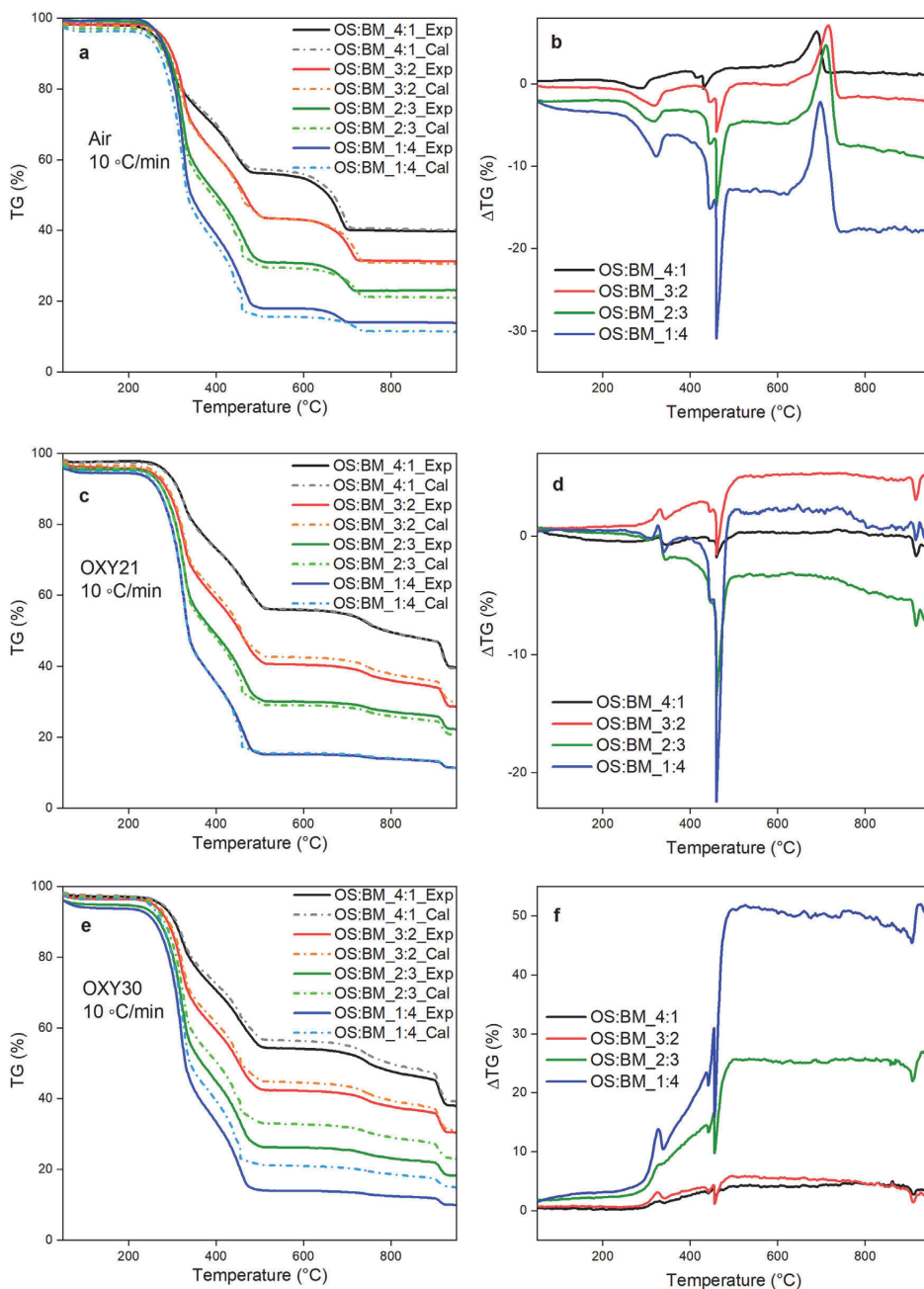


Fig. 2. TG curves comparison between the experimental and calculated value from the mixtures and the differences values ΔTG curves under; N_2/O_2 (air) (a) and (b), OXY21 (c) and (d), and OXY30 (e) and (f).

mixing ratios at 1:0, 3:2, and 0:1 under air, OXY21, and OXY30 combustion atmospheres. Similar thermal degradation trends can be seen as the heating rate increases, which indicates similar mechanisms of reaction. However, as the heating rate increased, the TG curves shifted to a higher temperature range, and the increase of the heating rate in-

creased the T_i , T_{max} and T_b temperatures of the reaction interval. This is due to the increase in the temperature gradients in the samples. In addition, the high heating rates increase the rate of mass loss in the specific interval, as shown in the DTG curves. Similar to the parent fuels, it is also observed that the increase in the heating rate increases the T_i and

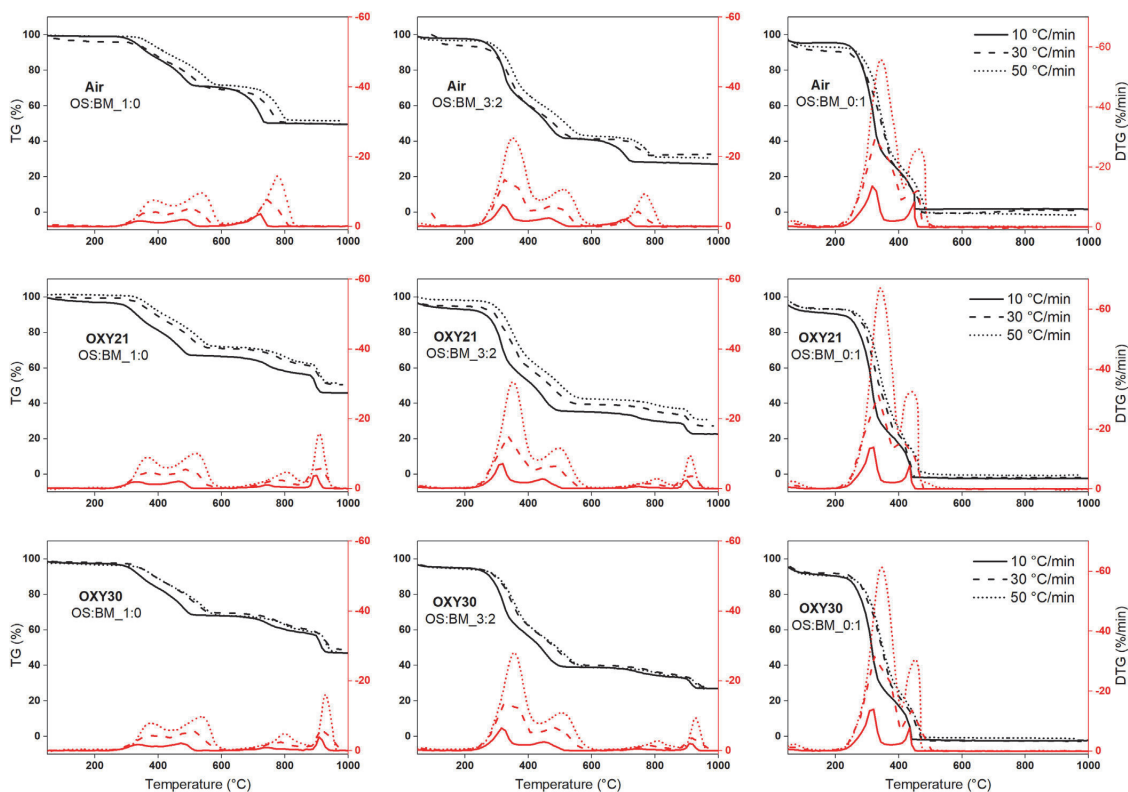


Fig. 3. Comparison of different heating rates on OS:BM mixing ratios of 1:0, 3:2, and 0:1 under air, OXY21, and OXY30 combustion atmospheres.

T_b temperatures and the rate of weight loss values in blends. For the OS sample the T_{i1} increased by 40 °C and T_b by 70 °C and the reactivity of the fuel (S) doubled when rising the heating rate from 10 to 50 °C/min under air combustion, while for the BM, T_{i1} increased by 20 °C, $T_b \sim 44$ °C, and $S \times 10^6$ increased significantly from 6.76 to 74.49 under the same air atmosphere. In an oxyfuel combustion environment, similar behaviour can be depicted from the TG and DTG curves compared to air mode with slightly lower temperature ranges of T_i and T_b , and the maximum mass reduction increased intensively with increasing heating rates of all samples. As an example, the BM reactivity increased by more than 10 times when increasing heating rates from 10 to 50 °C in OXY21 and OXY30 modes. For the OS, the reactivity increased more compared to the BM, from 0.13 in air mode to 2.95 and 2.05 under OXY21 and OXY30, respectively. Several literatures (Maaten et al., 2019; Vega et al., 2021; Yao et al., 2017) agreed that the heating rate significantly influences the combustion process. As with increasing heating rates, higher contact temperature at the particle surface at the specified temperature interval can explain this. This also clarifies the higher carbonate decomposition peaks at higher heating rates for all tested atmospheres. Whereas, the shorter residence time at a higher heating rate can affect the temperature evolution inside particles and the reaction time, which might be insufficient to fully burn the fuel if the heating rate is very quick. Yet, this can increase the fuel residue, however, this was not noticeable in the presented experiments.

3.4. MS of targeted gases at different atmospheres

Fig. 4 shows the monitored gases released during the combustion of individual fuels and their blends at the heating rate of 10 °C/min under

air, OXY21, and OXY30 combustion atmospheres. The MS ion current signal intensity at different temperatures reflects the major gas species that the MS was able to detect without noticeable overlap or noise. The two main gases that evolved in the combustion region of the fuels are CO_2 (ion numbers 44 and 46) and H_2O (ion number 18). In air combustion, Fig. 4(a) and (b), the MS shows a clear peak of CO_2 , while in the O_2/CO_2 atmosphere, the readings were covered by a CO_2 background. At a temperature of 350 °C the release of light hydrocarbons of OS:BM_1:0, is represented by the breakdown of organic matter with the release of CO_2 in the first peak, and the second peak at 490 °C represents char oxidation. With an increasing BM mixing ratio, the two peaks are shifted to a lower temperature and a higher intensity represents the more volatile emissions from the BM addition. For the OS:BM_0:1, the second peak of BM at 450 °C shows an intense and sharp increase of CO_2 within the char oxidation region. Yet, CO_2 peaks for the OS:BM_1:4 blend sample were observed to be much lower compared to OS:BM_0:1 for the combustion region. A possible explanation can be attributed to the inhibitory effect of OS addition in the light hydrocarbon combustion region; however, further study is needed to search for synergistic effects in MS results.

During the combustion process, the first gas emission peak generally represents water separation and hydrocarbon combustion, as in Fig. 4(c), 4(e), and 4(g) that is comparing H_2O release from the three combustion atmospheres. A significant increase in the H_2O peak is observed when increasing the BM ratio in air combustion due to the higher H and moisture contents in the BM sample, Fig. 4(c). While under oxy conditions the release of H_2O of OS:BM_1:0 is higher and the observed differences between OS and other mixing ratios or BM are less, as shown in Fig. 4(e) and (g). This can be explained as under oxyfuel combustion

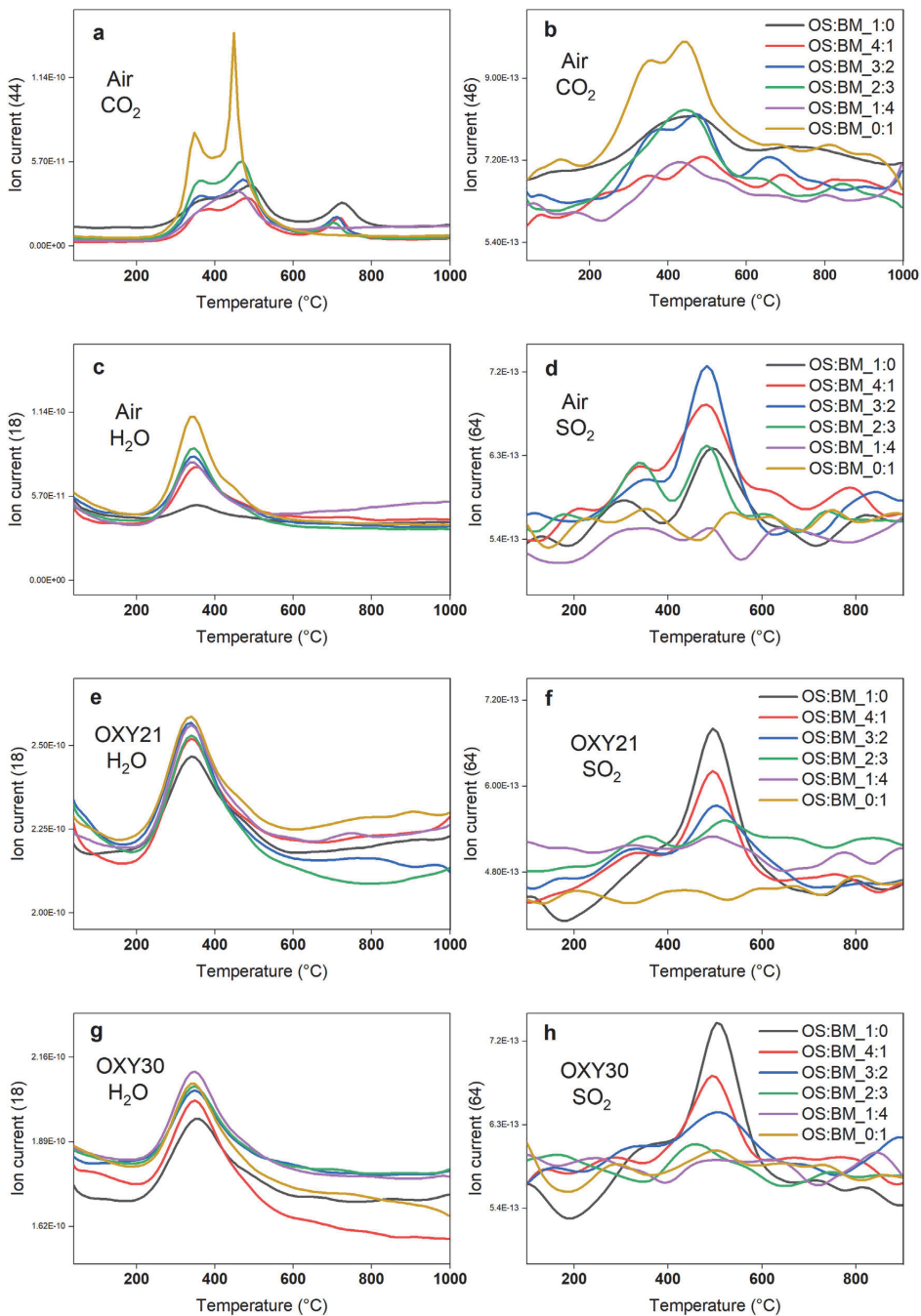


Fig. 4. Comparison between CO₂, H₂O, and SO₂ MS profiles of OS, BM, and their blends under; N₂/O₂ (air) (a)-(d), OXY21 (e), and (f), and OXY30 (g) and (h).

the H₂O and light hydrocarbon peaks correspond to the fast devolatilization, accelerating the release of gas emissions.

At a higher temperature range of 500 °C, the release of SO₂ during OS combustion occurred, Fig. 4(d), (f), and (h), which represent the pyritic sulfur decomposition, while the low peaks of organic sulfur burning occurred at lower combustion temperature at 300 °C. The SO₂ peak intensities were reduced with increasing BM ratio due to no sulfur content detected in the BM spruce sample, Table 1. Under oxy conditions, SO₂ emissions of OS increased noticeably, and higher peaks show for OXY21 and OXY30 compared to air combustion. Similar results were presented by Yörüük et al. (2015), which reported the release of SO₂ from the oxy-fuel combustion of OS sample and their blends with BM, as the first peak corresponds to the organic sulfur at 320 °C and the oxidation of iron sulfide at 480 °C.

Fig. 5 shows the effect of different heating rates on the release of gases under air and oxy conditions. As an example, CO₂ (ion numbers 44 and 46) and H₂O (ion numbers 17 and 18) under air, and SO₂ (ion numbers 48 and 64) under air and OXY21 were selected for OS:BM ratios at 1:0, 3:2, and 0:1. All MS compounds were identified according to the NIST-MS library to confirm the possible structure of the released compounds. It has been explained earlier that rising heating rate can influence combustion performance and increase thermal degradation, it can maximize the weight loss and provide higher thermal energy needed to enhance heat transfer from surrounding to inside the particles. The obtained MS results are in line with the TG and DTG results. Under air combustion, Fig. 5(a), (b), and (c) show that the fast temperature change and short residence time with increasing heating rate, delayed the release of CO₂ (44 and 46), and significantly increased the peak intensity. Moreover, with higher heating rates of 30 and 50 °C/min the two peaks of CO₂ in the temperature combustion region between 350 and 500 °C overlapped and merged to one wide peak. In Fig. 5(a), the first CO₂ peak under 10 °C/min heating rate occurred at a temperature of ~370 °C, if the temperature is compared with T_{max1} in Table 4, there's a delay of ~20 °C from the thermal degradation depicted from the DTG curves. This phenomenon has also been observed in other different literature using MS analysis (Liu et al., 2023; Pan et al., 2021). Liu et al., (2023) discussed the reason that as the thermal degradation occurred, the weight loss was detected first, while the volatile compounds generated can react in the gas phase undergoing secondary reactions, resulting in a time delay for the detection of the released product by MS. In the currently obtained results, the delay can also occur due to gas transfer in the TG-MS connection, however, further investigation needs to be studied further.

For the OS sample, raising the heating rate from 10–50 °C/min, a total shift of CO₂ released temperature by 50–60 °C occurred, while for the BM sample by 30–50 °C. Higher heating rates also enhanced the release of H₂O (ion numbers 17 and 18) due to the high moisture and H contents in BM, Fig. 5(d). The two peaks of SO₂ (ion numbers 48 and 64) are also overlapped with increasing heating rates under both air and oxy conditions for OS:BM 1:0 and their blends 3:2, Figures (e)–(h). The intensities of the peaks are largely increased, and the average SO₂ release temperatures from the OS combustion are shifted from 400–560 °C under air and OXY21 modes.

3.5. Kinetic study

Results of the isoconversional-Friedman method analysis for OS, BM, and their blends under air, OXY21, and OXY30 are presented in Tables 6–8, including E values at different α (0.2–0.8) with the correlation coefficient (R^2) (Muravyev et al. 2019) which reflects result satisfactory of the calculated E . The values of E can measure the difficulty of thermal degradation during the combustion process. As can be seen from Tables 6–8, the average values of E , which is calculated for $R^2 > 0.9$, increased with increasing BM ratio under the three combustion atmospheres: air, OXY21, and OXY30. Generally, the values of E depend on the BM type that is used in the combustion and the number of highly complex molecular weight compounds including cellulose, and lignin. The average E

values of parent fuel and their blends in the oxy conditions were lower than in air combustion, indicating that the O₂/CO₂ environment made it easier for the combustion process to proceed (Chansa et al., 2020).

For the OS sample, the E for α (0.2–0.8) were from 112–134 kJ/mol in air, while under oxy combustions were from 113–138 kJ/mol and 101–118 kJ/mol for OXY21 and OXY30, respectively, similar results were reported by Yörüük et al. (2015). The lower E values at the beginning of combustion represent the burning of volatile and light hydrocarbon materials (Wang et al., 2023), which is merely close between the three combustion atmospheres. While higher α values reflect the E values that are required for the combustion of fixed carbon and char oxidation (Yao et al., 2016). E values are reduced significantly under OXY30 compared to air and OXY21 modes at higher α (Yörüük et al., 2018). These results are in line with the TG and DTG curves, whereas O₂ increment under OXY30 has a significant effect on the char oxidation and the improvement of combustion as explained earlier.

The E values during the combustion process of the pure spruce BM sample were from 171–334 kJ/mol in air and from 180–445 kJ/mol and 194–354 kJ/mol under OXY21 and OXY30, respectively. The average E values were significantly reduced under oxyfuel combustion compared to air mode. The reduction of E values in oxy conditions than in air combustion is higher compared to the OS sample. Moreover, it was noticed that the E values under the three atmospheres were high at lower α , reducing slightly and increasing again at the end of the combustion process. As more E variation between different conversion ratios compared to OS, this can be attributed to the energy required for the beginning of hemicellulose and cellulose degradation (Idris et al., 2012). Interesting results were also reported by Mureddu et al. (2018), showing higher E values in two BM samples: stone pine and eucalyptus wood chips, compared to bituminous, sub-bituminous, and brown coal, and it was explained as no simple correlation exists between the activation energy and volatile matter of biomass, and a significant decrease in E could also be associated with an intensive burning of volatile matter. Adding to it that BM combustion proceeds with a complicated multistep reaction, the predominant combustion reactions take place through the gaseous volatile oxidation, as more volatile in BM, and the higher oxygen content in BM gives a greater thermal reactivity (Chansa et al., 2020).

The model fitting for the evaluation of kinetic parameters shows that D3-Jander's equation for diffusion-controlled solid-state reaction kinetics in a sphere and F3- the 3rd order reaction were the closest mechanisms for the reaction models.

Fig. 6 shows average E values at $R^2 > 0.9$ of OS, BM, and their blends under the three combustion atmospheres. The variation of E with α are indicated as line bars which represent the minimum and maximum values of E at different α (0.2–0.8). The increased variation of E with α indicates a kinetically complex process. This can be observed in the higher α values for OS:BM 1:4 and 0:1 samples. Moreover, in Table 7, OS:BM 1:4 sample under OXY21 mode shows a dependence of E value with α , due to the change in the oxidation mechanisms in dynamic experiments (Babiński et al., 2013; Mureddu et al., 2018), resulting in the loss of linearity of the straight line of calculated E that didn't give a clear indication of the behavior of the OS:BM 1:4 sample. Fig. 6 also indicates a gradual increase in E values as the BM blend ratio increases, this is attributed to the higher kinetic factors in BM than in OS as explained earlier, and reflects greater complex links that have relatively stronger chemical bonds in spruce BM than in the OS. Thus, the addition of spruce BM increases the energy required for the combustion process in the blends. While a clear positive effect can be noticed when switching from air to oxy conditions. The combustion process becomes more facile and E values were reduced under oxy conditions. Compared to the OS sample, the reduction was higher with increasing BM ratios and for the BM fuel. Yet, E values remained at the same level at OXY21 and OXY30 atmospheres. However, the line bars increased with BM addition, and for OS:BM 1:4 and 0:1 under OXY21 and air modes, the variations in E increase eventually raised the averaged values and affect the trend.

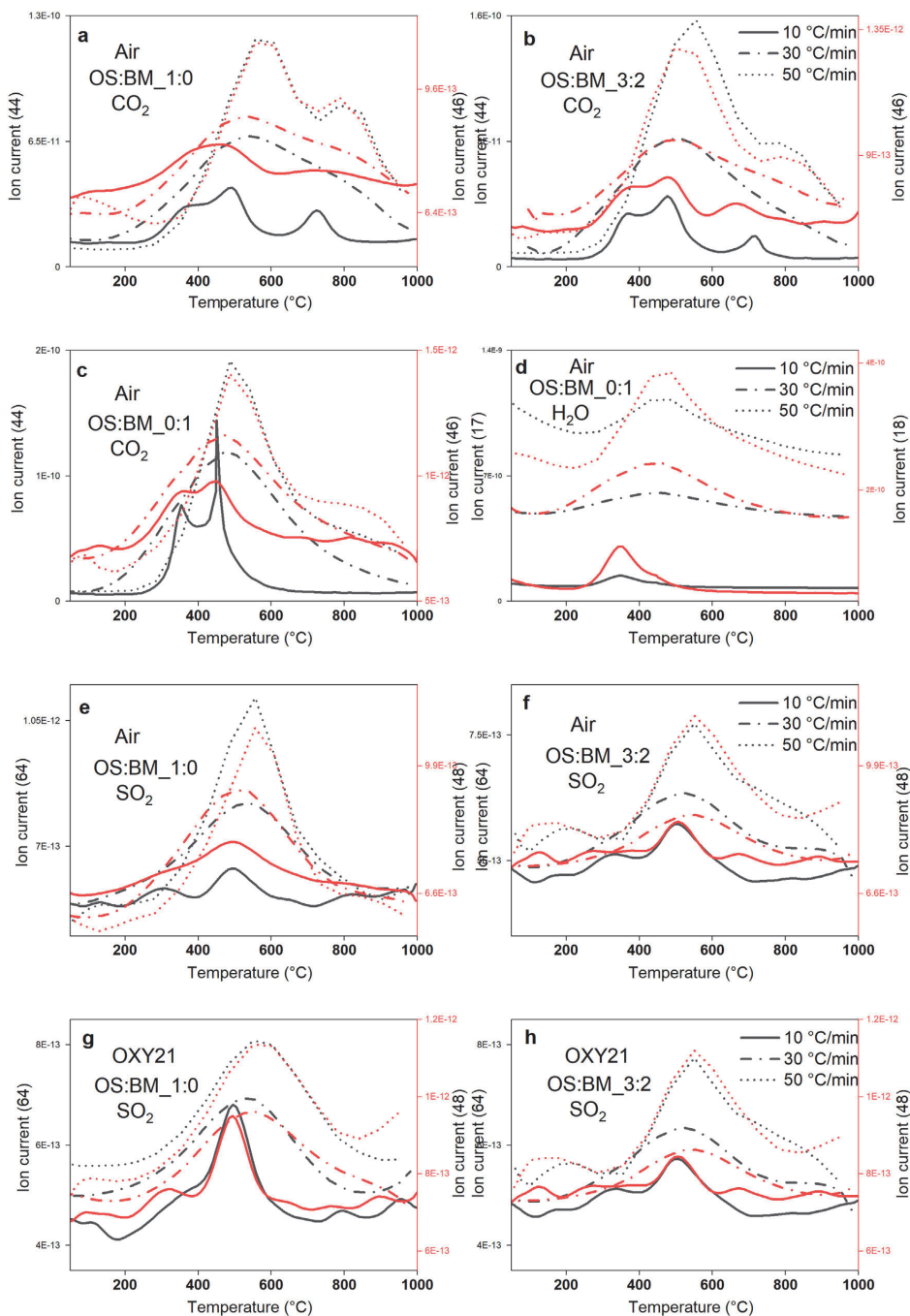


Fig. 5. Comparison of different heating rates on CO₂, H₂O, and SO₂ MS profiles of OS, BM, and their blends under; N₂/O₂ (air) (a-f), OXY21 (g), and (h).

Table 6Kinetic parameters for combustion stage of OS, BM, and their blends under N₂/O₂ (air) atmosphere.

| OS:BM α | 1:0 | | 4:1 | | 3:2 | | 2:3 | | 1:4 | | 0:1 | |
|-------------------|-------------------|----------------|-------------------|----------------|-------------------|----------------|-------------------|----------------|-------------------|----------------|-------------------|----------------|
| | <i>E</i> (kJ/mol) | R ² | <i>E</i> (kJ/mol) | R ² | <i>E</i> (kJ/mol) | R ² | <i>E</i> (kJ/mol) | R ² | <i>E</i> (kJ/mol) | R ² | <i>E</i> (kJ/mol) | R ² |
| 0.2 | 112.09 | 0.971 | 166.48 | 0.999 | 194.28 | 0.999 | 169.53 | 0.987 | 194.90 | 0.998 | 171.41 | 1.000 |
| 0.3 | 110.97 | 0.929 | 130.74 | 0.992 | 166.08 | 0.998 | 168.79 | 0.985 | 227.05 | 0.987 | 215.66 | 0.963 |
| 0.4 | 110.57 | 0.984 | 155.87 | 0.983 | 138.11 | 0.988 | 160.76 | 0.994 | 197.57 | 0.993 | 165.82 | 1.000 |
| 0.5 | 121.03 | 0.942 | 141.82 | 0.984 | 188.34 | 0.946 | 152.97 | 0.967 | 140.02 | 0.977 | 159.00 | 0.908 |
| 0.6 | 123.67 | 0.976 | 129.53 | 0.997 | 154.52 | 0.985 | 206.67 | 0.918 | 218.39 | 0.968 | 155.03 | 1.000 |
| 0.7 | 131.66 | 0.980 | 146.92 | 0.998 | 156.12 | 0.982 | 176.21 | 0.914 | 218.17 | 0.880 | 225.13 | 0.981 |
| 0.8 | 133.59 | 0.998 | 141.71 | 0.980 | 155.91 | 0.966 | 162.09 | 0.913 | 342.15 | 0.990 | 334.27 | 1.000 |
| Average* | 120.51 | – | 144.72 | – | 164.77 | – | 171.00 | – | 209.65 | – | 203.76 | – |

* Average *E* is calculated for R² > 0.90.**Table 7**

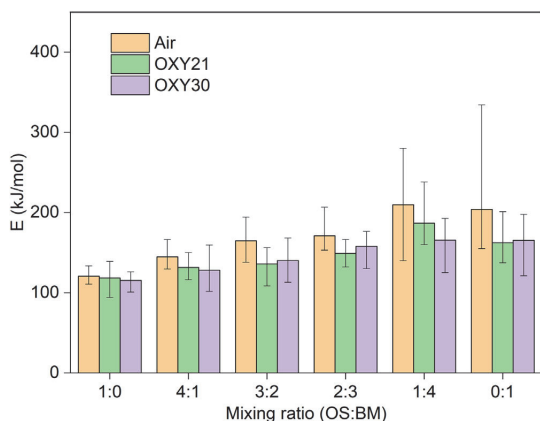
Kinetic parameters for combustion stage of OS, BM, and their blends under OXY21 atmosphere.

| OS:BM α | 1:0 | | 4:1 | | 3:2 | | 2:3 | | 1:4 | | 0:1 | |
|-------------------|-------------------|----------------|-------------------|----------------|-------------------|----------------|-------------------|----------------|-------------------|----------------|-------------------|----------------|
| | <i>E</i> (kJ/mol) | R ² | <i>E</i> (kJ/mol) | R ² | <i>E</i> (kJ/mol) | R ² | <i>E</i> (kJ/mol) | R ² | <i>E</i> (kJ/mol) | R ² | <i>E</i> (kJ/mol) | R ² |
| 0.2 | 113.06 | 0.984 | 150.04 | 0.994 | 156.35 | 0.999 | 166.31 | 0.992 | 180.391 | 0.975 | 180.50 | 0.984 |
| 0.3 | 94.00 | 0.990 | 116.33 | 1.000 | 128.19 | 0.997 | 160.21 | 0.991 | 188.583 | 0.957 | 187.15 | 0.998 |
| 0.4 | 107.86 | 0.997 | 135.36 | 0.994 | 108.49 | 0.993 | 132.74 | 0.994 | 166.346 | 0.947 | 162.47 | 0.963 |
| 0.5 | 104.93 | 0.985 | 120.26 | 0.988 | 141.76 | 0.994 | 132.11 | 1.000 | 159.989 | 0.922 | 123.48 | 0.931 |
| 0.6 | 131.30 | 0.992 | 129.08 | 0.992 | 132.72 | 0.998 | 150.35 | 0.996 | 238.017 | 0.920 | 135.03 | 0.955 |
| 0.7 | 139.10 | 1.000 | 143.22 | 0.991 | 141.58 | 0.999 | 148.84 | 0.999 | 252.165 | 0.333 | 185.17 | 1.000 |
| 0.8 | 138.45 | 0.999 | 126.65 | 1.000 | 141.90 | 1.000 | 152.76 | 1.000 | 68.221 | 0.020 | 445.43 | 0.833 |
| Average* | 118.39 | – | 131.56 | – | 135.86 | – | 149.05 | – | 186.67 | – | 162.30 | – |

* Average *E* is calculated for R² > 0.90.**Table 8**

Kinetic parameters for combustion stage of OS, BM, and their blends under OXY30 atmosphere.

| OS:BM α | 1:0 | | 4:1 | | 3:2 | | 2:3 | | 1:4 | | 0:1 | |
|-------------------|-------------------|----------------|-------------------|----------------|-------------------|----------------|-------------------|----------------|-------------------|----------------|-------------------|----------------|
| | <i>E</i> (kJ/mol) | R ² | <i>E</i> (kJ/mol) | R ² | <i>E</i> (kJ/mol) | R ² | <i>E</i> (kJ/mol) | R ² | <i>E</i> (kJ/mol) | R ² | <i>E</i> (kJ/mol) | R ² |
| 0.2 | 100.87 | 0.997 | 159.53 | 0.996 | 168.36 | 0.999 | 172.15 | 0.996 | 172.37 | 0.994 | 193.79 | 0.993 |
| 0.3 | 112.34 | 0.996 | 123.85 | 0.992 | 128.46 | 0.998 | 166.95 | 0.994 | 173.42 | 0.983 | 197.73 | 0.998 |
| 0.4 | 115.28 | 0.990 | 139.47 | 0.995 | 113.12 | 0.998 | 135.92 | 0.997 | 144.30 | 0.978 | 161.13 | 0.989 |
| 0.5 | 116.62 | 0.988 | 122.70 | 1.000 | 162.11 | 0.999 | 130.14 | 1.000 | 125.10 | 0.980 | 121.30 | 0.986 |
| 0.6 | 125.93 | 0.999 | 120.55 | 1.000 | 142.56 | 0.996 | 176.43 | 0.998 | 185.11 | 1.000 | 129.24 | 0.996 |
| 0.7 | 119.51 | 0.995 | 129.30 | 0.999 | 144.48 | 1.000 | 163.39 | 1.000 | 192.67 | 0.970 | 189.35 | 0.994 |
| 0.8 | 117.68 | 0.999 | 101.62 | 1.000 | 121.48 | 1.000 | 159.04 | 0.999 | 234.64 | 0.879 | 353.72 | 0.835 |
| Average* | 115.45 | – | 128.15 | – | 140.08 | – | 157.72 | – | 165.50 | – | 165.42 | – |

* Average *E* is calculated for R² > 0.90.**Fig. 6.** Comparison between the average *E* of OS, BM, and their blends under; N₂/O₂ (air), OXY21 and OXY30.

4. Conclusions

This study presents combustion characteristics of ca-rich OS, spruce BM, and their blends at 1:0, 4:1, 3:2, 2:3, 1:4, and 0:1 in air and O₂/CO₂ like conditions. Non-isothermal TG experiments coupled with an MS were carried out under three different heating rates: 10, 30, and 50 °C/min. The co-combustion synergistic effect along with the kinetic analysis by the isoconversional Friedman method were investigated. The obtained results show the addition of BM enhanced combustion performance and reduced *T_b* temperatures. The BM sample under oxy conditions shows higher maximum mass loss of the volatile, and the values increased with the increment of O₂% in the combustion atmosphere, while char oxidation enhances at higher O₂% only. A positive synergistic effect occurred in the devolatilization and the combustion of light hydrocarbons, and the intensity of the peaks increased towards higher BM ratios. At the higher heating rate of 50 °C/min, the OS and BM co-combustion synergistic effects were enhanced.

In air combustion, with the addition of BM, CO₂ release increased and shifted toward lower temperatures. Whereas an opposite behavior was obtained in the carbonate decomposition stage for the blend samples. SO₂ emissions were reduced while H₂O releases were higher with increasing BM ratio for all combustion atmospheres.

The samples' *E* results were reduced under oxy conditions and higher reduction occurred with increasing BM ratio and the BM fuel compared to the OS.

Overall, this study compares the co-combustion behaviors of OS and BM in air and oxyfuel combustion. The test results may differ from the actual situation, and OS is a complex fuel whereas several reactions can overlap during the combustion process. Yet, the presented work provides theoretical guidance for the partial replacement of OS fuel and combined application of BM in industrial oil shale combustion boilers to achieve negative CO₂ emissions.

Declaration of Competing Interest

The authors declare that they have no known competing financial interests or personal relationships that could have appeared to influence the work reported in this paper.

Acknowledgments

This research was funded by the Estonian Research Council from the National Programme for Addressing Socio-Economic Challenges through R&D (RITA), which is supported by the Estonian Government and the European Regional Development Fund

References

Aich, S., Kumar Nandi, B., Bhattacharya, S., 2019. Effects of eucalyptus leaves blending on combustion characteristics of an indian reject coal. *Energy Sources* 44 (1), 1437–1448. doi:10.1080/15567036.2019.1644397.

Altun, N.E., Hıçyılmaz, C., Hwang, J.Y., Saat Bağcı, A., Kök, M.V., 2006. Oil shale in the world and turkey; reserves, current situation, and future prospect: a review. *Oil Shale* 23 (3), 211–227.

Babiński, P., Labojko, G., Kotyczka-Morańska, M., Plis, A., 2013. Kinetics of coal and char oxycombustion studied by TG-FTIR. *J. Therm. Anal. Calorim.* 113 (1), 371–378. doi:10.1007/s10973-013-3002-x/FIGURES/7.

Bai, F., Zhao, J., Liu, Y., 2019. An investigation into the characteristics and kinetics of oil shale oxy-fuel combustion by thermogravimetric analysis. *Oil Shale* 36 (1), 1–18. doi:10.3176/oil.2019.1.01.

Baqain, M., Neshumayev, D., Konist, A., 2022. Oxyfuel conversion of ca-rich fuel in a 60 KWh circulating fluidized bed. *SSRN Electr. J.* doi:10.2139/SSRN.4276982.

Baqain, M., Neshumayev, D., Konist, A., 2023. NO_x and N₂O emissions from Ca-rich fuel conversion in oxyfuel circulating fluidized bed combustion. *Therm. Sci. Eng. Prog.* 42, 101938. doi:10.1016/j.tsep.2023.101938.

Baqain, M., Rüstü Yörük, C., Neşumajev, D., Järvi, O., Konist, A., 2023. Ash characterization formed under different oxy-fuel circulating fluidized bed conditions. *Fuel* 338 (November 2022), 1–16. doi:10.1016/j.fuel.2022.127244.

Barzegar, R., Yozgatligil, A., Atımtay, A.T., Co-combustion of high and low ash lignites with raw and torrefied biomass under air and oxy-fuel combustion atmospheres doi:10.1080/15567036.2022.2038313.

Clean, Carbon, 2023., COP27 carbon capture and storage. (<https://www.carbonclean.com/carbon-capture-cop27>). (accessed June 26, 2023)

Chansa, O., Luo, Z., Yu, C., 2020. Study of the kinetic behaviour of biomass and coal during oxyfuel co-combustion. *Chin. J. Chem. Eng.* 28 (7), 1796–1804. doi:10.1016/j.cjche.2020.02.023.

Chen, L., Wen, C., Wang, W., Liu, T., Liu, E., Liu, H., Li, Z., 2020. Combustion behaviour of biochars thermally pretreated via torrefaction, slow pyrolysis, or hydrothermal carbonisation and co-fired with pulverised coal. *Renew. Energy* 161, 867–877. doi:10.1016/j.renene.2020.06.148.

Chirone, R., Salatino, P., Scala, F., Solimene, R., Urciuolo, M., 2008. Fluidized bed combustion of pelletized biomass and waste-derived fuels. *Combust. Flame* 155 (1/2), 21–36. doi:10.1016/j.combustflame.2008.05.013, 1–2.

Deng, L., Ye, J., Jin, Xi, Zhu, T., Che, D., 2017. Release and transformation of potassium during combustion of biomass. *Energy Procedia* 142, 401–406. doi:10.1016/j.egypro.2017.12.063.

EU climate policy. 2022., 2030 climate & energy framework. Ministry of Environment. (https://climate.ec.europa.eu/eu-action/climate-strategies-targets/2030-climate-energy-framework_en). (accessed March 25, 2023).

Fan, Y., Yu, Z., Fang, S., Lin, Y., Lin, Y., Liao, Y., Ma, X., 2016. Investigation on the co-combustion of oil shale and municipal solid waste by using thermogravimetric analysis. *Energy Convers. Manage.* 117, 367–374.

Friedman, H.L., 1964. Kinetics of thermal degradation of char-forming plastics from thermogravimetry. application to a phenolic plastic. *J. Polym. Sci. Part C: Polym. Symp.* 6 (1), 183–195. doi:10.1002/POLC.5070060121.

Giummarella, N., Henriksson, G., Salmén, L., Lawoko, M., 2017. On the effect of hemi-cellulose removal on cellulose-lignin interactions. *Nordic Pulp Paper Res. J.* 32 (4), 542–549. doi:10.3183/NPPRJ-2017-32-04-p542-549.

Han, X., Jiang, X.M., Cui, Z.G., 2006. Thermal analysis studies on combustion mechanism of oil shale. *J. Therm. Anal. Calorim.* 84 (3), 631–636. doi:10.1007/s10973-005-7034-8/METRICS.

Idris, S.S., Rahman, N.A., Ismail, K., 2012. Combustion characteristics of Malaysian oil palm biomass, sub-bituminous coal and their respective blends via Thermogravimetric Analysis (TGA). *Bioresour. Technol.* 123, 581–591. doi:10.1016/j.biortech.2012.07.065.

Kaljuvee, T., Edro, E., Kuusik, R., 2007. Formation of volatile organic compounds at thermooxidation of solid fossil fuels. *Oil Shale* 24 (2), 117–133. doi:10.3176/OIL.2007.2.03.

Kayahan, U., Özdoğan, S., 2016. Oxygen enriched combustion and co-combustion of lignites and biomass in a 30 KWh circulating fluidized bed. *Energy* 116, 317–328. doi:10.1016/j.energy.2016.09.117.

Kim, J.H., Lee, Y.J., Yu, J., Jeon, C.H., 2019. Improvement in reactivity and pollutant emission by cofiring of coal and pretreated biomass. *Energy Fuels* 33 (5), 4331–4339. doi:10.1021/ACS.ENERGYFUELS.9B00396/SUPPL_FILE/EF9B00396_SI_001.PDF.

Konist, A., Valtsev, A., Loo, L., Pihu, T., Liira, M., Kirsimäe, K., 2015. Influence of oxy-fuel combustion of ca-rich oil shale fuel on carbonate stability and ash composition. *Fuel* 139, 671–677. doi:10.1016/j.fuel.2014.09.050.

Konist, A., Loo, L., Valtsev, A., Maaten, B., Siirde, A., Neshumayev, D., Pihu, T., 2014. Calculation of the amount of estonian oil shale products from combustion in regular and oxy-fuel mode in a CFB boiler. *Oil Shale* 31 (3), 211–224. doi:10.3176/oil.2014.3.02.

Konist, A., Tõnu, P., Neshumayev, D., Külaots, I., 2013. Low grade fuel - oil shale and biomass co-combustion in CFB boiler. *Oil Shale* 30 (2 SUPPL), 294–304. doi:10.3176/oil.2013.2S.09.

Li, H., Chi, H., Han, H., Hu, S., Song, G., Wang, Y., He, L., Wang, Yi, Su, S., Xiang, J., 2021. Comprehensive study on co-combustion behavior of pelletized coal-biomass mixtures in a concentrating photothermal reactor. *Fuel Process. Technol.* 211, 106596. doi:10.1016/j.fuproc.2020.106596.

Li, X.G., Ma, B.G., Xu, Li, Hu, ZWu, Wang, X.G., 2006. Thermogravimetric analysis of the co-combustion of the blends with high ash coal and waste tyres. *Thermochim. Acta* 441 (1), 79–83. doi:10.1016/j.tca.2005.11.044.

Liu, Q., Zhong, W., Tang, R., Yu, H., Gu, J., Zhou, G., Yu, A., 2021. Experimental tests on co-firing coal and biomass waste fuels in a fluidised bed under oxy-fuel combustion. *Fuel* 286, 119312. doi:10.1016/j.fuel.2020.119312.

Liu, T., Wen, C., Li, C., Yan, K., Li, R., Jing, Z., Zhang, B., Ma, J., 2022. Integrated water washing and carbonization pretreatment of typical herbaceous and woody biomass: fuel properties, combustion behaviors, and techno-economic assessments. *Renewable Energy* 200 (September), 218–233. doi:10.1016/j.renene.2022.09.073.

Liu, X., Tian, Ke, Chen, Z., Wei, W., Xu, B., Ni, B.J., 2023. Online TG-FTIR-MS analysis of the catalytic pyrolysis of polyethylene and polyvinyl chloride microplastics. *J. Hazard. Mater.* 441, 129881. doi:10.1016/j.jhazmat.2022.129881.

Loo, L., Konist, A., Neshumayev, D., Pihu, T., Maaten, B., Siirde, A., 2018. Ash and flue gas from oil shale oxy-fuel circulating fluidized bed combustion. *Energies* 11 (5). doi:10.3390/en11051218.

Loo, L., Maaten, B., Siirde, A., Pihu, T., Konist, A., 2015. Experimental analysis of the combustion characteristics of estonian oil shale in air and oxy-fuel atmospheres. *Fuel Process. Technol.* 134, 317–324. doi:10.1016/j.fuproc.2014.12.051.

Maaten, B., Konist, A., Siirde, A., 2019. High-speed thermogravimetric analysis of the combustion of wood and ca-rich fuel. *J. Therm. Anal. Calorim.* 138 (4), 2807–2811. doi:10.1007/s10973-019-08785-6.

Meriste, T., Yörük, C.R., Trikkel, A., Kaljuvee, T., Kuusik, R., 2013. TG-FTIR analysis of oxidation kinetics of some solid fuels under oxy-fuel conditions. *J. Therm. Anal. Calorim.* 114 (2), 483–489. doi:10.1007/s10973-013-3063-x/FIGURES/5.

Muravyev, N.V., Pivkina, A.N., Koga, N., 2019. Critical appraisal of kinetic calculation methods applied to overlapping multistep reactions. *Molecules* 24 (12), 2298. doi:10.3390/MOLECULES24122298, 2019Paper 2298 24.

Mureddu, M., Dessi, F., Orsini, A., Ferrara, A., Pettinau, A., 2018. Air- and oxygen-blown characterization of coal and biomass by thermogravimetric analysis. *Fuel* 212, 626–637. doi:10.1016/j.fuel.2017.10.005.

Niu, Sli, Han, K.H., Lu, C.M., 2011. Characteristic of coal combustion in oxygen/carbon dioxide atmosphere and nitric oxide release during this process. *Energy Convers. Manage.* 52 (1), 532–537. doi:10.1016/j.enconman.2010.07.028.

Nussbaumer, T., 2003. Combustion and co-combustion of biomass: fundamentals, technologies, and primary measures for emission reduction. *Energy Fuels* 17 (6), 1510–1521. doi:10.1021/EF030031Q.

Özgür, E., Miller, S.F., Miller, B.G., Kök, M.V., 2012. Thermal analysis of co-firing of oil shale and biomass fuels. *Oil Shale* 29 (2), 190–201. doi:10.3176/OIL.2012.2.07.

Pan, J., Jiang, H., Qing, T., Zhang, J., Tian, Ke, 2021. Transformation and kinetics of chlorine-containing products during pyrolysis of plastic wastes. *Chemosphere* 284, 131348. doi:10.1016/j.chemosphere.2021.131348.

Powell, T.W.R., Lenton, T.M., 2012. Future carbon dioxide removal via biomass energy constrained by agricultural efficiency and dietary trends. *Energy Environ. Sci.* 5 (8), 8116–8133. doi:10.1039/C2EE21592F.

Saia, A., Neshumayev, D., Hazak, A., Sander, P., Järvi, O., Konist, A., 2022. Techno-economic assessment of CO₂ capture possibilities for oil shale power plants. *Renew. Sustain. Energy Rev.* 169 (February). doi:10.1016/j.rser.2022.112938.

Samuelsson, L.N., Babler, M.U., Moriara, R., 2015. A single model-free rate expression describing both non-isothermal and isothermal pyrolysis of norway spruce. *Fuel* 161, 59–67. doi:10.1016/j.fuel.2015.08.019.

Sikarwar, V.S., Zhao, M., Clough, P., Yao, J., Zhong, X., Memon, M.Z., Shah, N., Anthony, E.J., Fennell, P.S., 2016. An overview of advances in biomass gasification. *Energy Environ. Sci.* 9 (10), 2939–2977. doi:10.1039/C6EE00935B.

Tan, Y., Jia, L., Wu, Y., 2013. Some Combustion characteristics of biomass and coal cofiring under oxy-fuel conditions in a pilot-scale circulating fluidized combustor. *Energy Fuels* 27 (11), 7000–7007. doi:10.1021/EF4011109.

Tian, B., Wang, J., Qiao, Y., Huang, H., Xu, L., Tian, Y., 2023. Understanding the pyrolysis synergy of biomass and coal blends based on volatile release, kinetics and char structure. *Biomass Bioenergy* 168, 106687. doi:10.1016/j.biombioe.2022.106687.

- Torres, M., Portugal, P., Castiglioni, J., Cuña, A., Yermán, L., 2020. Co-combustion behaviours of a low calorific uruguayan oil shale with biomass wastes. *Fuel* 266, 117118. doi:10.1016/J.FUEL.2020.117118.
- Torres, M., Portugal, P., Cuña, A., Castiglioni, J., Yermán, L., 2019. Pollutant gas emissions during the co-combustion of oil shales from uruguay with biomass wastes. In: *Proceedings of the 4th World Congress on Momentum, Heat and Mass Transfer*. Rome, Italy.
- Vamvuka, D., Sfakiotakis, S., 2011. Combustion behaviour of biomass fuels and their blends with lignite. *Thermochim. Acta* 526 (1–2), 192–199. doi:10.1016/J.TCA.2011.09.021.
- Varol, M., Symonds, R., Anthony, E.J., Lu, D., Jia, L., Tan, Y., 2018. Emissions from co-firing lignite and biomass in an oxy-fired CFBC. *Fuel Process. Technol.* 173, 126–133. doi:10.1016/J.FUPROC.2018.01.002.
- Vega, MF., Díaz-Faes, E., Barriocanal, C., 2021. Influence of the heating rate on the quality of metallurgical coke. *ACS Omega* 6 (50), 34615–34623. doi:10.1021/AC-SOMEGA.1C05007/ASSET/IMAGES/MEDIUM/AO1C05007_M003.GIF.
- Wang, Q., Xuan, Y., Liu, H., Li, X., Chi, M., 2015. Gaseous emission and thermal analysis during co-combustion of oil shale semicoke and sawdust using TG-FTIR. *Oil Shale* 32 (4), 356–372. doi:10.3176/oil.2015.4.05.
- Wang, R., Liu, Z., Song, X., Liu, S., 2023. Co-combustion of pulverized coal and walnut shells in air and oxy-fuel atmospheres: thermal behavior, synergistic effect and kinetics. *J. Energy Inst.* 108, 101243. doi:10.1016/J.JOIE.2023.101243.
- Wu, Z., Wang, S., Zhao, J., Chen, L., Meng, H., 2016. Thermochemical behavior and char morphology analysis of blended bituminous coal and lignocellulosic biomass model compound co-pyrolysis: effects of cellulose and carboxymethylcellulose sodium. *Fuel* 171, 65–73. doi:10.1016/J.FUEL.2015.12.057.
- Xiao, Z., Wang, S., Luo, M., Cai, J., 2022. Combustion characteristics and synergistic effects during co-combustion of lignite and lignocellulosic components under oxy-fuel condition. *Fuel* 310, 122399. doi:10.1016/J.FUEL.2021.122399.
- Yao, Z., Ma, X., Lin, Y., 2016. Effects of hydrothermal treatment temperature and residence time on characteristics and combustion behaviors of green waste. *Appl. Therm. Eng.* 104, 678–686. doi:10.1016/J.APPLTHERMALENG.2016.05.111.
- Yao, Z., Ma, X., Wang, Z., Chen, L., 2017. Characteristics of co-combustion and kinetic study on hydrochar with oil shale: a thermogravimetric analysis. *Appl. Therm. Eng.* 110, 1420–1427. doi:10.1016/J.APPLTHERMALENG.2016.09.063.
- Yörük, C.R., Meriste, T., Sener, S., Kuusik, R., Trikkel, A., 2018. Thermogravimetric analysis and process simulation of oxy-fuel combustion of blended fuels including oil shale, semicoke, and biomass. *Int. J. Energy Res.* 42 (6), 2213–2224. doi:10.1002/er.4011.
- Yörük, C.R., Meriste, T., Trikkel, A., Kuusik, R., 2015. Thermo-oxidation characteristics of oil shale and oil shale char under oxy-fuel combustion conditions. *J. Therm. Anal. Calorim.* 121 (1), 509–516. doi:10.1007/s10973-015-4484-5.
- Yörük, C.R., Meriste, T., Trikkel, A., Kuusik, R., 2016. Oxy-fuel combustion of estonian oil shale: kinetics and modeling. *Energy Procedia* 86, 124–133. doi:10.1016/j.egypro.2016.01.013.

Publication V

Neshumayev, Dmitri; Baqain, Mais; Konist, Alar (2024). **The emissions of NO_x, SO₂, CO and decomposition of carbonates during oxyfuel combustion of low heating value semicoke in CFB pilot facility.**

1 **The emissions of NO_x, SO₂, CO and decomposition of carbonates during oxyfuel**
2 **combustion of low heating value semicoke in CFB pilot facility**

3 Dmitri Neshumayev^{1*}, Mais Baqain¹, Alar Konist¹

4 ¹ Department of Energy Technology, Tallinn University of Technology, 19086, Tallinn, Estonia

6 **Abstract**

7 *Semicoke oxyfuel combustion is a technology that has the potential to play a role in transitioning to cleaner and*
8 *more sustainable energy generation in shale oil industry. Semicoke oxyfuel combustion offers several benefits and*
9 *serves specific purposes in the context of energy generation and environmental considerations by improving*
10 *semicoke combustion efficiency while reducing pollutant emissions and enabling the capture of CO₂ for storage or*
11 *utilization. However, oxyfuel combustion has not yet reached large-scale industrial application, but the technology*
12 *exists and has been validated in large pilot-scale incinerators. The current experimental study investigates*
13 *semicoke combustion behavior in air and O₂/CO₂ environments. Semicoke burning experiments both in air and in*
14 *oxygen-rich environments 21% and 30% of O₂/CO₂ were carried out in a 60 kW_{th} circulated fluidized bed (CFB) test*
15 *facility in the Department of Energy Technology of Tallinn University of Technology. The results show that the*
16 *temperature distributions are similar when burning in air and O₂/CO₂ (21/79%) environments. Under these*
17 *conditions, the temperature distribution is characterized by a temperature increase in the upper part of the riser.*
18 *When increasing the oxygen content in the supplied O₂/CO₂ mixture to 30%, the heat release is redistributed and*
19 *the temperature in the lower part of the riser increases. Under air combustion modes, at temperatures below 800 °C,*
20 *the thermal decomposition of carbonates does not occur and the content of free lime (CaO_{free}) in external heat*
21 *exchanger (EHE) is 3%. At higher temperatures >800 °C, most of the carbonates decompose thermally and the*
22 *content of CaO_{free} increased to 18%. When switching from air to oxyfuel combustion, the temperature of the thermal*
23 *decomposition of carbonates shifts to higher values lying in the range of 870 – 900 °C depending on the partial*
24 *pressure of CO₂. Oxyfuel combustion did not influence the release of SO₂, the concentration remained within a few*
25 *ppm since the high content of carbonates in the semi-coke still ensures almost complete binding of sulfur formed*
26 *during combustion. NO_x emissions are reduced by up to 40% with the same oxygen excess ratio in dense bed*
27 *under oxygen enriched environment compared to air combustion. The actual CO emissions (mg/MJ) are decreasing,*
28 *and a greater reduction is observed at higher O₂ content of supplied O₂/CO₂ mixture. These results are compatible*
29 *with other studies using oil shale fuel.*

* Corresponding author: e-mail Dmitri.Nesumajev@taltech.ee

30

31 **Keywords:** semicoke, oxyfuel combustion, shale-oil thermal processing, circulating fluidized bed, ash
32 behaviour, emissions

33 **1. Introduction**

34 Semi-coke (SC) is a solid organic-containing residue formed during the above-ground thermal process
35 of ex-situ shale oil production. SC is a potentially harmful solid material whose properties are greatly
36 dependent on the thermal processing technology used [1]. One of its peculiar characteristics is its low
37 energy content (low heating value 1-4 MJ/kg), the value of which depends on the type of technology
38 used and this generally determines the limited possibilities of its further efficient utilization. This is
39 particularly important in the case of oil shale processing technologies, where SC is the final residue
40 waste product, and no suitable efficient utilization at industrial level has been found for it due to various
41 technical and nontechnical obstacles. Herewith, its direct combustion for energy purposes to generate
42 steam and electricity was considered as the main direction of its further processing, but in addition,
43 efforts were made to use it as an additive (as a source of aluminosilicate) in cement production or as a
44 raw material in conjunction with ceramics in the production of mineral wool [2]. Recently, the potential
45 use of oil shale SC as an adsorbent for various pollutants has also been extensively investigated [3]. As
46 a technology of combustion of SC is mainly considered the fluidized bed or circulating fluidized bed [4]
47 [5], [6] and depending on the SC properties it is proposed to burn it alone or in a blend with other fuels
48 e.g. oil shale [7], [8], [5], [9], biomass [10], [11]. In the process of solid heat carrier (SHC) technology,
49 SC is burned to generate solid heat carrier, which is the hot ash formed during the combustion of semi-
50 coke, which in turn then serves as a source of energy for the pyrolysis of oil shale in retort [12] [13]. The
51 combustion of SC is realized in the separate so-called aero-fountain combustor integrated into the
52 technological scheme of SHC method and a distinctive feature and simultaneously its disadvantage is
53 that the combustion process proceeds under the reducing atmosphere [12] thereby causing
54 environmental concerns related to the incomplete oxidation of organic components. More recently, a
55 SHC method based shale oil unit (Enefit 280 technology) was commissioned in which circulating
56 fluidized bed combustion technology was successfully integrated to achieve a complete utilization of the
57 SC resulting from the pyrolysis process [14][13]. The principal scheme of Enefit-280 technology is
58 presented in Figure 1 [13]. In Estonia, shale oil production is mostly based on SHC processing

59 technology, exceeding the 980 t/h rated capacity of total operated oil plants [15]. Therefore, in the shale
60 oil production process through SHC method, greenhouse gases are mostly generated during the
61 production of a SHC by means of SC after burning, which is needed to heat the oil shale in the retort to
62 the pyrolysis temperature. As a product, the CO₂ footprint of shale oil naturally contains other sources
63 of greenhouse gases (e.g., from mining or the construction of an oil refinery), but their proportion is
64 smaller, and other measures should be used instead of CO₂ capture to further reduce them.

65 As a consequence, one possibility to decarbonize shale oil industry would be integrating one of the CO₂
66 capture technologies that has the potential to reduce CO₂ emissions by more than 90%. In recent years,
67 significant efforts have been made around the world to develop new techniques for capturing CO₂ in
68 various technological processes, including power generation, cement production, steel manufacturing
69 and many others [16]. This study focuses on the potential application of the so-called oxyfuel
70 combustion technology for SC combustion as one of the more technically mature ones, which has been
71 previously tested for oil shale combustion in a pilot unit [17] [18] [19].

72 Oxyfuel combustion is a technology that has the potential to play a role in transitioning to cleaner and
73 more sustainable energy generation from the shale oil industry. Oxyfuel combustion can offer several
74 benefits and serve specific purposes in the context of energy generation and environmental
75 considerations by improving combustion efficiency while reducing pollutant emissions and enabling the
76 capture of CO₂ for storage or utilization. However, oxyfuel combustion has not yet reached large-scale
77 industrial application, but the technology exists and has been validated in large pilot-scale incinerators
78 [20] [21].

79 The application of oxygen combustion technology affects combustion reactions and heat transfer in the
80 hearth. It should be considered that in the case of combustion in oxygen, the main component is CO₂
81 in the gas phase, not nitrogen. Since CO₂ has different properties (oxygen diffusivity in CO₂ environment,
82 radiation properties) compared to nitrogen, the transition to oxygen combustion technology can affect
83 both the combustion process and the composition of the resulting ash. SC combustion under oxygen
84 conditions has not been studied before, several literature and their results concerning the burning of oil
85 shale in an oxygen environment were presented in [22]–[25]. The results of these studies show that
86 compared to the air environment, the O₂ content in the CO₂ environment must be higher to achieve an
87 equal burning rate. To achieve the same temperature distribution, the O₂ content must be approximately
88 30%. Combustion in an oxygen and CO₂ environment does not significantly affect pollutant emissions.

89 Previous experimental studies carried out at the Institute of Energy Technology on different scales [17]–
90 [19], [26]–[28] have shown that burning in oxygen can be used for oil shale without significant effects
91 on burning efficiency or pollutant concentrations. These studies show that in a CO₂ environment, the
92 decomposition of carbonate minerals shifts to the region of much higher temperatures, which reduces
93 the release of CO₂ from the mineral part of the fuel, and the proportion of CaCO₃ in the ash composition
94 is higher. And NO_x formation emissions are lower under oxy conditions.

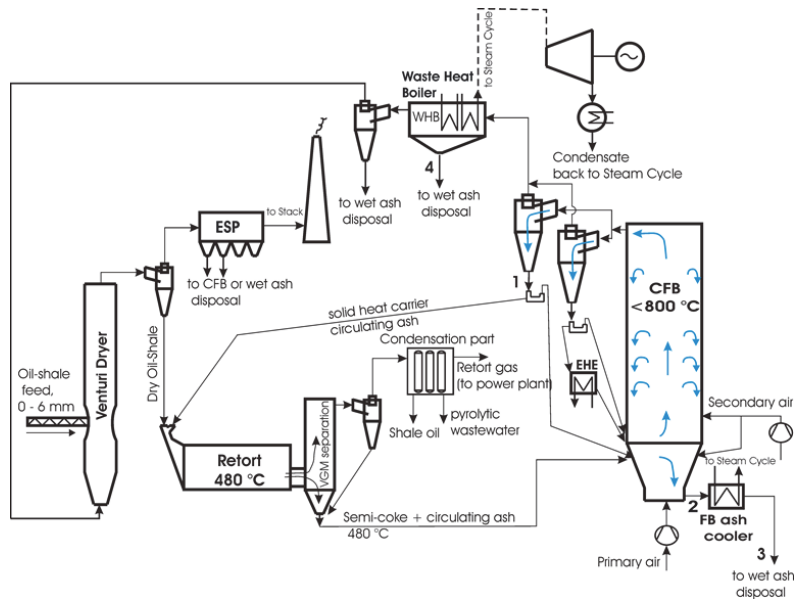
95

96 Herein, we present the first experimental result of pilot test campaigns to evaluate the extremely low
97 calorific SC oxyfuel combustion technology process. The pilot test results investigate the effect of
98 combustion atmosphere (air, O₂/CO₂) in semicoke burning behaviour in general and in terms of gaseous
99 emissions (CO, NO_x, SO_x) and compare it with air and the results from an industrial scale of Enefit 280
100 circulated fluidized bed (CFB) unit. Moreover, ash properties/composition including the thermal
101 decomposition of carbonate along with the primary pollutant emissions are studied as well, taking into
102 consideration the effect of different parameters. Semicoke combustion experiments both in air and in
103 oxygen-rich environments 21% and 30% of O₂/CO₂ were carried out in a 60 kW_{th} CFB test facility.

104

105

106



107

108

Figure 1. Scheme of Enefit 280 technology [13]

109

110 2. Experimental work

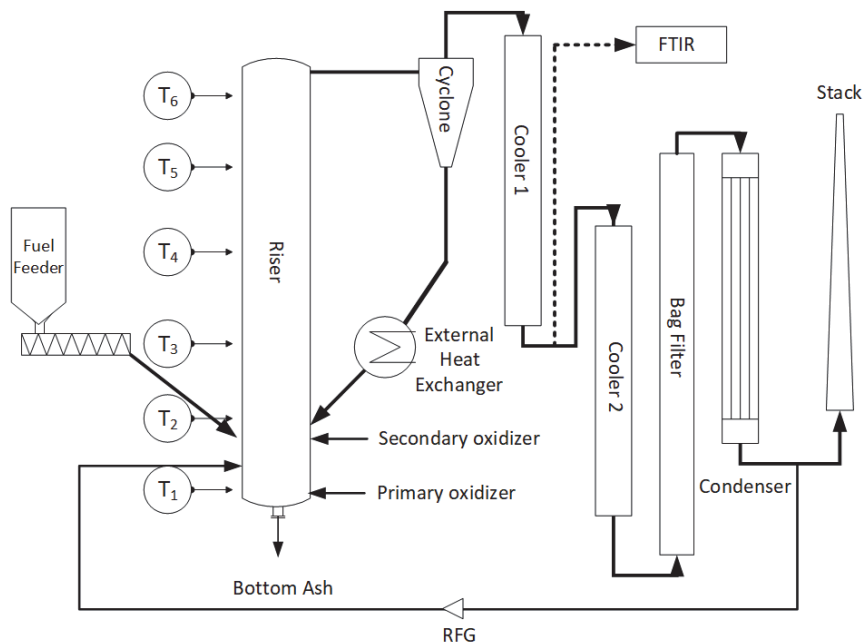
111 2.1. Pilot test facility

112 The experiments were conducted in a 60 kW_{th} CFB apparatus in the Department of Energy Technology
 113 of Tallinn University of Technology, the basic scheme is shown in Figure 2. The CFB test facility allows
 114 to study of the combustion of different fuels and their mixtures, it can be operated with regular air, pre-
 115 set gas mixtures, and flue gas recirculation as well. In recent years, this pilot has been successfully
 116 used to study the behavior of oil shale in an oxygen-rich environment, and the detailed description is
 117 presented elsewhere [18], [19], [26]. The total height of the riser is 4.40 m, and its inner diameter is 0.12
 118 m. The pilot is equipped with three fuel feeders, one of which is equipped with fuel preheating, a screw
 119 conveyor was used for feeding fuel at a height of 1.17 m. The unit is fully equipped with monitoring and
 120 thermal sensors and controlled with a LabVIEW system. The temperature measurements tap distributed
 121 along the riser are in six different locations and one in the heat exchanger as well. The flue gas
 122 composition is simultaneously analyzed using a Fourier transform infrared (FTIR) analyzer. To control
 123 the temperature of the fluidized bed, the recirculating ash is cooled in the loop seal. The remaining fly

124 ash is gradually removed from the cooled combustion gas both in coolers and in the bag filter. The
125 cleaned combustion gas that has passed through the bag filter moves to the condenser and eventually
126 to the stack.

127

128



129

130 *Figure 2. Circulating fluidized bed facility with 60 kWth capacity*

131

132 2.2. Material

133 The semicoke used in this experiment was collected from Enefit-280 retort. The proximate and ultimate
134 analyses of a representative semicoke sample are summarized in Table 1. Fuel sample characterization
135 included proximate analysis (ash and lower heating value (LHV)), ultimate analyses include elemental
136 analysis using Elementar Vario MACRO CHNS and TIC to measure (C, H, N, S), and total organic
137 carbon is measured by the difference between total carbon and inorganic carbon. Semicoke ash
138 chemical composition is presented in Table 2 and was prepared and tested using a Rigaku Primus II
139 XRF spectrometer. Table 3 shows semicoke quantitative X-ray diffraction (XRD) results. XRD

140 experiments were performed using Cu K α radiation in the 2 θ range of 3-72 $^\circ$ with a step size of 0.02 $^\circ$ 2 θ
 141 and a counting time of 0.1 s/step, and the X-ray tube operated at 40 kV and 40-mA.

142 *Table 1: Proximate and ultimate analysis of the semicoke.*

| | Proximate analysis | | Ultimate analysis ^d (wt.%) | | | | | |
|----------|-----------------------------|----------------|---------------------------------------|----------------|------|----------------|-------|------|
| | ^a Ash (wt. %) | LHV (MJ/kg) | C (total) | C (organic) | H | ^b O | N | S |
| Semicoke | 68.18 | < 1 | 10.81 | 2.90 | 0.24 | 18.49 | 0.035 | 2.24 |

143 ^aAsh at 815 $^\circ$ C

144 ^bO% = 100-(W+A+CO₂+S+TOC+H+N) %

145 *Table 2: Chemical composition of the semicoke.*

| Components | Content, wt.% |
|--------------------------------|---------------|
| SiO ₂ | 6.92 |
| Al ₂ O ₃ | 1.66 |
| Fe ₂ O ₃ | 2.48 |
| CaO | 45.1 |
| MgO | 3.58 |
| Na ₂ O | n.d. |
| K ₂ O | 0.51 |
| SO ₃ | 5.72 |
| P ₂ O ₅ | 0.13 |
| TiO ₂ | 0.101 |
| ZnO | 0.019 |
| SrO | 0.036 |

146 *Table 3: Mineralogical composition of the semicoke.*

| Components | Content, wt.% |
|--|---------------|
| Quartz (SiO ₂) | 4 |
| K-feldspar (KAlSi ₃ O ₈) | 2.4 |
| K-mica (Al ₂ K ₂ O ₆ Si) | 0.4 |
| Calcite (CaCO ₃) | 67.9 |
| Portlandite (Ca(OH) ₂) | 1.8 |
| Dolomite (CaMg(CO ₃) ₂) | 1.2 |
| Periclase (MgO) | 3.8 |
| Anhydrite (CaSO ₄) | 7.5 |
| Belite (C ₂ S) | 4.8 |
| Akermanite (Ca ₂ Mg(Si ₂ O ₇)) | 3.9 |
| Merwinite (Ca ₃ Mg(SiO ₄) ₂) | 0.5 |
| Hematite (Fe ₂ O ₃) | 1.4 |

147

148

149 2.3. Method

150 The working parameters were selected based on the main criteria that characterize the operation of the
151 Enefit-280 CFB combustion reactor. One of the specific features of the Enefit 280 CFB combustor
152 consists in maintaining such a temperature level (<800 °C) at which the decomposition of carbonates
153 would be minimized since the CaO formed as a result of this process when entering with solid heat
154 carrier into the retort negatively affects the oil yield. Another distinctive feature is that the semi-coke
155 feeding from the retort to the CFB reactor has a temperature of about 480 °C, which is higher than the
156 ignition temperature. Consequently, the selection of regimes for the experiments was primarily based
157 on the conditions of the existing CFB unit, where the temperature level in the combustor was the main
158 criterion. Since it is known that under oxy-fuel combustion, the carbonate decomposition shifts to a
159 higher temperature region due to the high partial pressure of CO₂, experiments covering higher
160 temperatures, which are typical for conventional CFB units, were also carried out.

161 During the tests, the semicoke was heated to a temperature of 100-200 °C before being fed into the
162 riser. In order to compensate for the physical heat content of the semicoke, the combustion air supplied
163 to the CFB riser was preheated to 500-550 °C. The mode was considered stable when the temperature
164 fluctuations were minimal. During the combustion tests, when the stability of the regime was achieved,
165 ash samples were taken from the following ash removal points: bottom ash from the bottom of the riser,
166 the first and second cooler, the external heat exchanger (EHE), and the bag filter. Corresponding
167 sampling locations can be followed in Figure 2. To collect the bottom ash and the ash of the external
168 heat exchanger, the corresponding valves were opened at the sampling point and the ash sample was
169 allowed to flow into metal containers, which were immediately sealed airtight to prevent the formation
170 of Ca(OH)₂ and carbonization. To carry out the oxygen combustion experiments, a stationary situation
171 was first achieved on the CFB pilot during the combustion of the semicoke in air mode. After working in
172 a stationary situation for a while, the combustion air was automatically changed to O₂/CO₂. The
173 transition to oxyfuel combustion mode (and vice versa if necessary) can be technically very successfully
174 carried out during work. As a result, the CO₂ content in the combustion gas increases significantly, up
175 to 90% by volume. During this process, continuous recording of basic parameters (temperatures,
176 pressure, etc., nearly 70 parameters in total) and continuous monitoring of the composition of the flue
177 gas in different places were carried out. Since the semicoke used in the experiments contains a relatively
178 small amount of organic matter, during some experiments other fuels (natural gas (NG) and oil shale

179 (OS)) were burned together with the semicoke (SC), and it is donated (SC+NG+OS), to keep the
 180 temperature in the CFB combustion riser at the required level.

181 *Table 4: Average working parameters of 60 kWth CFB unit during different combustion modes*

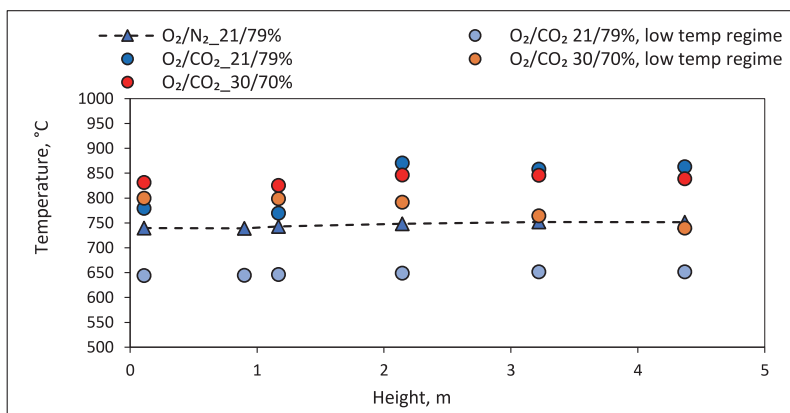
| Working parameter | Combustion Mode | |
|--------------------------------------|--------------------------------|---------------------------------|
| | Air | O ₂ /CO ₂ |
| Inlet O ₂ ratio (%) | 21 | 21-30 |
| CO ₂ in flue gas, dry (%) | 13-18 | 76-93 |
| T _{MAX} (°C) | 738-892 | 695-947 |
| Semicoke feed rate (kg/h) | 30-40 | 30-40 |
| Ash sampling point | Bottom ash and circulating ash | Bottom ash and circulating ash |

182

183 3. Results and discussion

184 3.1. Temperature profiles

185 The axial temperature change of the combustion chamber depending on the atmosphere at different
 186 riser mean temperatures is shown in Figure 3. The temperature distributions are qualitatively similar
 187 when burning in air and O₂/CO₂ (21/80%) environments. Under these conditions, the temperature
 188 distribution is characterized by a temperature increase in the upper part of the riser. When burning in
 189 an oxygen-rich environment, increasing the oxygen content in the supplied O₂/CO₂ mixture to 30%, the
 190 heat release is redistributed relative to the riser axis, as a result of which the temperature in the lower
 191 part of the CFB combustion chamber increases.



192

193 *Figure 3. Temperature profiles along the riser (from the grid) at different combustion modes.*

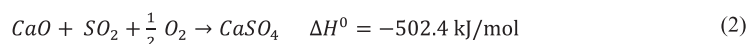
194 3.2. Emissions

195 3.2.1. Sulfur dioxide (SO₂)

196 The semicoke that is formed in the pyrolysis process at Enefit-280 technology contains both organic
197 and pyritic sulfur [29]. In CFB, the combustion process takes place largely in an excess of oxygen
198 (excess air factor >1), as a result of which combustible sulfur compounds are practically completely
199 oxidized to sulfur dioxide (SO₂). The transformation of sulfur compounds during combustion is a complex
200 series of reactions in which different gaseous components simultaneously participate: SO₂, H₂S, COS,
201 CS₂, O₂, CO, H₂, H₂O, and CO₂ [30]. In the presence of a sufficient concentration of oxygen (greater
202 than the stoichiometric amount), the formed sulfur compounds are basically completely oxidized to SO₂.
203 Figure 4 shows SO₂ concentrations (as ppm and as per MJ of semicoke energy input) are very low, as
204 a reason that semicoke contains carbonate minerals (mainly calcite CaCO₃ and to a lesser extent
205 dolomite CaMg(CO₃)₂) and the concentration of carbonates in semicoke ash is several times higher (>8,
206 molar based) than the stoichiometric ratio that is required for complete sulfur binding. Furthermore, the
207 long contact time between circulating ash particles and SO₂ is ensured in CFB, therefore SO₂ is totally
208 bound to the ash in the CFB riser [31] which is typical for oil shale combustion under CFB conditions.
209 It is generally believed that under oxyfuel combustion due to relatively high CO₂ partial pressure, the
210 binding of SO₂ to calcite obviously takes place mainly by a direct reaction [18] [32] [33] :



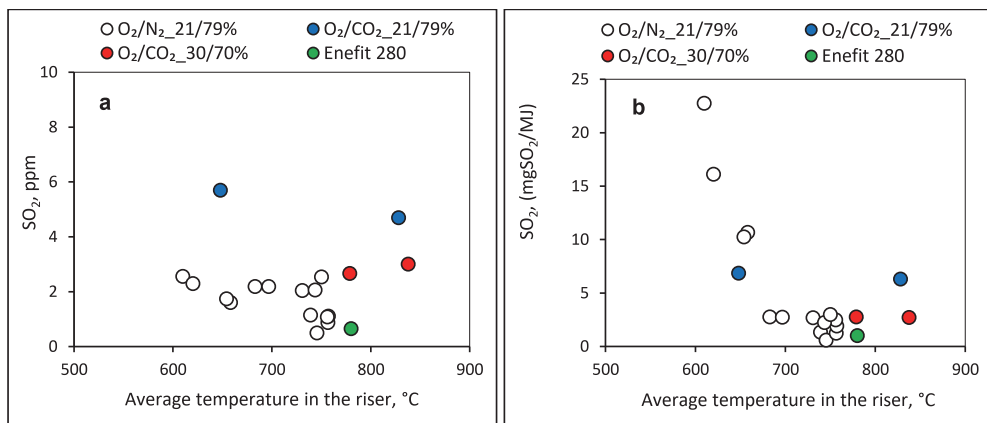
211 While under an air combustion atmosphere, the CFB combustor is operating in the region below the
212 equilibrium curve where the limestone calcination occurred, and indirect sulfation takes place as
213 limestone (CaO) reacts with SO₂:



214 In the existing CFB unit operating temperature is normally below 800 °C. Under these conditions, it is
215 believed that sulfur binding through direct sulfation mechanisms will be significant under air mode as
216 well.

217 The dependence of measured SO₂ concentrations (as ppm, in wet gases) on the average temperature
218 of the riser at different modes is presented in Figure 4(a). The combustion gas composition
219 measurements at the Enefit-280 plant are also compared in the same figure [13]. The figures show that
220 the SO₂ concentration is generally low due to favorable conditions for sulfur binding as mentioned earlier.

221 However, the concentration by itself does not reflect the actual emission, as it depends on the volume
 222 of combustion gas. Therefore Figure 4(b) is used here to show SO₂ emission per energy input of
 223 semicoke (mg/MJ), i.e., specific emission depending on the average temperature of the CFB riser. It
 224 turns out that when burning in air mode at lower temperatures, the SO₂ emission increases somewhat,
 225 and combustion in an oxygen-rich environment does not influence SO₂ emissions.
 226 Studies show that the behavior of sulfur when burned in an oxygen-rich environment is analogous to its
 227 behavior when burned in air [34]. At the same time, oxyfuel combustion affects the binding of the
 228 generated SO₂ due to the increased partial pressure of CO₂, as explained earlier, and calcite
 229 decomposition is shifted to a higher temperature, which in turn causes SO₂ to bind through direct
 230 sulfation. Therefore, the maximum SO₂ capture efficiency shifts to higher temperatures (around 900 °C).
 231 Experiments with different types of fuel have shown that SO₂ emissions (mg/MJ) in an oxygen-rich
 232 environment are lower or at the same level compared to burning in air [19], [26], [35].



234 *Figure 4: The dependence of SO₂ emissions on the riser average temperature under different*
 235 *combustion modes: (a) SO₂ emissions in ppm (b) Normalised SO₂ emissions (mgSO₂/MJ).*

236 3.2.2. Nitrogen oxides (NO_x)

237 Nitrogen oxides are mainly formed by the combination of nitrogen in the semicoke (fuel N) with oxygen
 238 in the CFB. Since the combustion temperature in CFB is low (<800 °C), direct thermal oxidation of
 239 nitrogen in the combustion air does not occur [36]. The main nitrogen compounds produced during
 240 combustion are nitrogen oxide (NO), nitrogen dioxide (NO₂), and nitrous oxide (N₂O). Oxidation of
 241 nitrogen (fuel N) in the organic part of the semicoke proceeds through complex reactions, discussed

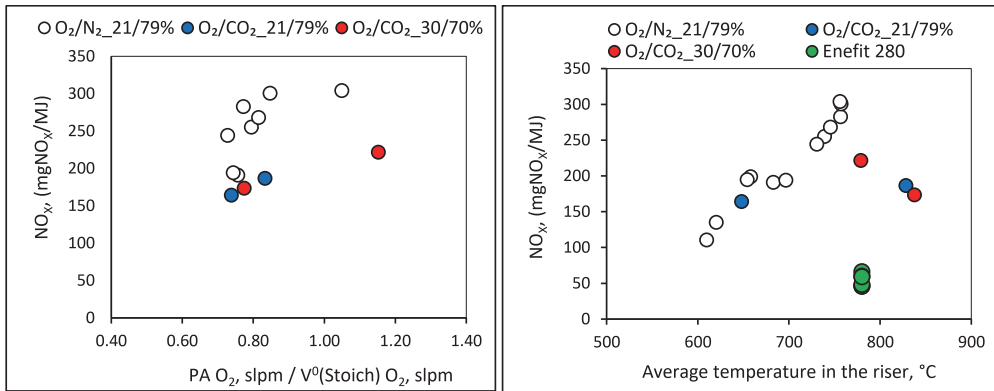
242 mainly elsewhere [17]. Nitrogen that has passed into the gas phase is converted into ammonia (NH_3)
243 and hydrogen cyanide (HCN) in the initial phase of the process. The mentioned compounds, in turn, are
244 further oxidized to NO and N_2O , which can later be reduced to molecular N_2 . The reduction of the
245 produced nitrogen oxides can proceed both through homogeneous reactions (for example, reaction with
246 CO and H_2) and through heterogeneous reactions, where the elements or minerals contained in the ash
247 particles (for example, CaO) can act as catalysts. In the combustion process, the nitrogen in the coke
248 is also partly oxidized to NO and N_2O and can be reduced to N_2 . A small amount of NH_3 and HCN is
249 also formed during this process.

250 The amount of nitrogen in the semicoke, as well as the O_2 concentration in the riser, the temperature,
251 and the degree of ash recirculation, greatly affect the NO_x concentration produced during the tests under
252 CFB conditions. In reality, today there is no complete understanding of fuel nitrogen conversion
253 processes. The formation of nitrogen oxides during the burning of semicoke in Enefit-280 technology
254 has not been studied in detail, but the general principles derived from other fuels and briefly described
255 above can be used. The NO_x emissions (mass of NO_x to semicoke mass consumption) obtained in the
256 experiments under different combustion modes depending on the average temperature in the CFB riser
257 and oxygen in the primary oxidizer (PA) are shown in Figure 5 respectively. For comparison purposes,
258 the NO_x emissions measured in the combustion gases generated in the Enefit-280 CFB riser are also
259 included in the same figure. It can be seen from the figures that NO_x emissions are lower when burning
260 in oxygen compared to burning in air. This result is compatible with the results of previous studies using
261 oil shale [17] or other solid fuels [21], [33], [38], [36], [39]. Experiments also showed that NO_x formation
262 during semicoke combustion is generally consistent with the mechanism described above: NO_x
263 emission is reduced by creating a reduction zone Figure 5(a). The latter, however, causes an increase
264 in CO emissions Figure 5(c). The difference in NO_x concentrations generated in the test facility and in
265 the Enefit-280 CFB can be explained mainly by the scale effect, in addition, to some extent by the
266 influence of other parameters, such as the difference in the initial temperature of the semicoke particle
267 when entering the riser and the difference in the temperature of the combustion air supplied to the
268 combustion chamber, Figure 5(b) and (c).

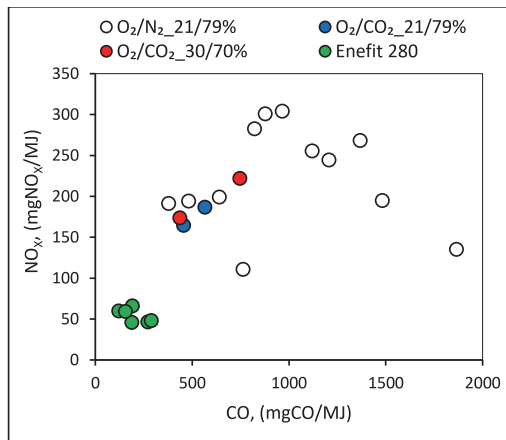
269 Previous studies have shown that when burning in oxygen at different gas velocities (under CFB
270 conditions), NO_x concentrations in the combustion gases (expressed in ppm or mg/Nm^3) are generally
271 about the same or higher compared to burning in air [35]. However, the actual NO_x emission (i.e.

272 converted to the energy unit mg/MJ or mass consumption of the input fuel) is lower. This is caused by
 273 the lower conversion of nitrogen in the fuel to NO during combustion in a CO₂-rich environment
 274 compared to conventional combustion [40]–[42]. During combustion in oxygen, the conversion of N to
 275 NO increases with increasing temperature, but it has also been shown experimentally that the total
 276 concentration of nitrogen oxides decreases [17], [41], [42].

277



278



279 *Figure 5: The dependence of normalised NO_x emissions under different combustion modes on (a)*
 280 *Excess O₂ supplied in the primary oxidizer (PA O₂, slpm / V⁰(Stoich) O₂, slpm); (b) Average*
 281 *temperature in the riser and (c) Normalised CO emissions (mgCO/MJ).*

282 3.2.3. Carbon monoxide (CO)

283 Besides being a poisonous compound, CO is one of the essential indicators of combustion efficiency
 284 as it characterizes the completeness of combustion of carbon-containing fuel compounds. Under
 285 conventional combustion of solid fuels in air environment, the major contributor to the production of CO

286 is heterogeneous reactions during char conversion and as a result of homogeneous reactions in the
287 gas phase [43]. The subsequent mechanism and rate of oxidation of the produced CO are influenced
288 by such factors as temperature level, concentrations of O₂, CO and H₂O, and gas mixing [43]. However,
289 the mechanism of CO formation changes significantly when the atmosphere in which combustion takes
290 place is changed from N₂ to CO₂. It was found that there are several factors responsible for these
291 changes. Thus, the high chemical activity of CO₂ itself leads to the fact that CO₂-char gasification
292 becomes more prominent, causing a higher ratio of CO formation relative to CO₂ [44] [45] [46] [47] [48]
293 which can be significant even at relatively low temperatures (700 °C) [49].

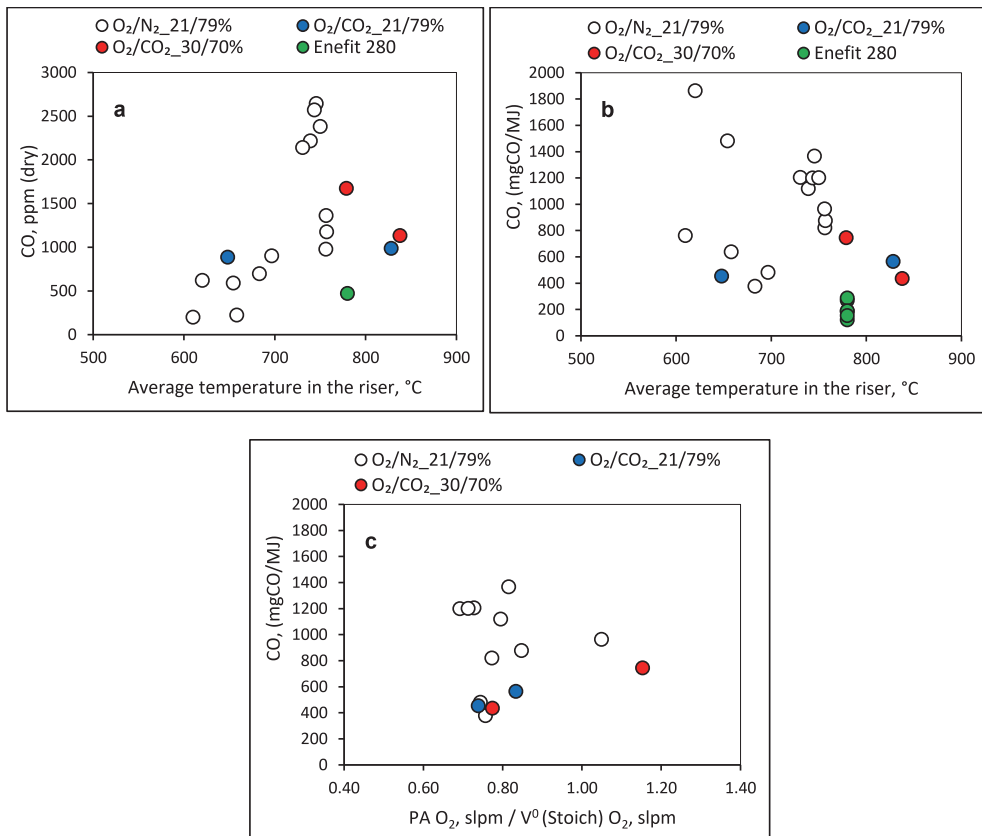
294 Diffusion of O₂ in CO₂ medium is less intensive, leading to a decrease in particle burnout rate for
295 conditions where the combustion process is controlled by O₂ external diffusion [45] [50]. The differences
296 in particle burnup rate are thereby negligible at higher O₂ contents (> 30%) [45] [48]. In the gas phase,
297 the main difference between combustion in O₂/N₂ and O₂/CO₂ atmospheres consists in the formation of
298 CO by homogeneous reactions of CO₂ with hydrogen radicals [47] and inhibiting effect of CO₂ on the
299 oxidation of the CO [51] [43]. In general, during the pilot scale experiments, one can observe higher CO
300 concentrations in the O₂/CO₂ environment, which is most likely due to the smaller flue gas volume in
301 oxyfuel regime. However, when concentrations are normalized to the fuel energy unit (MJ), CO
302 concentrations tend to be lower in O₂/CO₂ [32] [51] [52] [53] [38] [54].

303 CO concentrations obtained during the semicoke combustion in different combustion modes depending
304 on the riser average temperature and excess O₂ level are shown in Figure 6. Given the same figure,
305 the CO concentrations generated in the Enefit-280 CFB. It can be seen that the CO concentrations
306 obtained during the experimental tests are generally higher compared to Enefit-280 CFB. This can be
307 explained mainly by the scale effect - namely, the shorter residence time of the gas. The CO oxidation
308 to CO₂ is greatly influenced by the residence time of CO at the corresponding temperature, and the
309 efficiency of oxygen (combustion air) mixing with CO and semicoke. Further adjusting the combustion
310 parameters (increasing the primary air share to stoichiometric), would allow for a reduction of the
311 concentration of CO in the exhaust gas, Figure 6(c). However, certain limits are applied to avoid the
312 increase in the formation of nitrogen oxides. When burning in oxygen, the concentration of CO is
313 generally at the same level compared to the burning mode in air. However, the specific emission of CO
314 (per MJ of semicoke) is generally lower in oxyfuel combustion modes, Figure 6(a) and (b). For oil shale

315 combustion in CFB, the concentration of CO is relatively low, as the combustion temperature exceeds
316 800 °C.

317 Under oxyfuel CFB combustion, the obtained results show that the concentration of CO in the
318 combustion gas remains at the same level or increases slightly compared to burning in air. At the same
319 time, the actual CO emissions reduced to the energy unit of the supplying fuel (mg/MJ) in the O₂/CO₂
320 environment are lower than when burning in air [40][52]. In addition, it should be mentioned that the CO
321 concentration is strongly influenced by the residence time of the combustion gas at a high temperature,
322 which, however, generally turns out to be insufficient in laboratory test stands [55]. Therefore, a direct
323 comparison of the CO concentration values obtained on the test bench and in the Enefit 280 CFB
324 combustor is not correct, and this fact must be kept in mind when making such a comparison.

325



326

327

328 *Figure 6: (a) The dependence of CO emissions in ppm (dry) on the average temperature in the riser;*

329 *(b) The dependence of normalised CO emissions in (mgCO/MJ) on the average temperature in the*

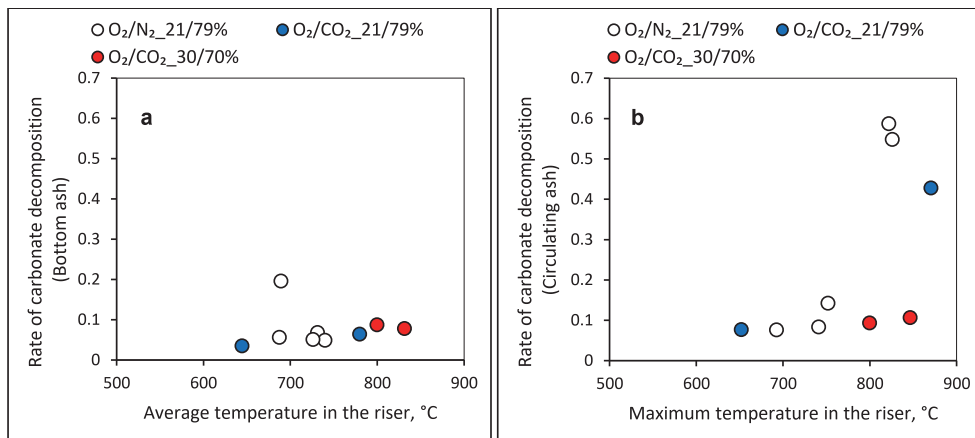
330 riser, and (c) the dependence of normalised CO emissions in (mgCO/MJ) on the excess O₂ supplied
331 in the primary oxidizer (PA O₂, slpm / V⁰ (Stoich) O₂, slpm).

332 **3.3 Thermal decomposition of carbonate minerals**

333 The thermal decomposition of calcium carbonate (one of the main components in the semicoke mineral)
334 in a CO₂-containing environment, depends on the temperature of the environment and the partial
335 pressure of CO₂ [18], [35]. When semicoke is burned in air, the degree of decomposition of carbonates
336 in the bottom ash is very low, Figure 7, being less than 10% on average.

337 The degree of decomposition of carbonates (essentially mainly calcite, as the content of dolomite in the
338 investigated semicoke) was calculated separately for all ash streams based on their mineralogical
339 compositions, the calculation methodology for the rate of carbonate decomposition has been described
340 more thoroughly by Arro et al. [56]. The original amount of calcite in the ash was calculated from the
341 measured undecomposed calcite and minerals such as free lime (CaO) and anhydrite (CaSO₄). These
342 compounds are formed as a result of the decomposition of calcite. Thus, the original content of these
343 minerals in the semicoke was considered. The main factors affecting the content of carbonates in the
344 ash are the relatively low temperature in the dense bed region of the riser, where the bottom ash
345 circulates due to its particle sizes and hydrodynamic conditions, and from where the particle size and
346 residence time are later collected. In addition, calculations show that in this zone the partial pressure of
347 CO₂ exceeds the equilibrium of the thermal decomposition of CaCO₃. Carbonates (mainly calcite) also
348 do not thermally decompose when switched to burning in oxygen, and this situation continues even at
349 higher operating temperatures, Figure 7(a).

350 A similar behaviour of carbonates is found in circulating ash (ash particles, which circulate through the
351 external circuit of the CFB; riser - cyclone - external heat exchanger - riser) in air combustion modes at
352 riser temperature below 800 °C, as shown in Figure 7(b), an intensive thermal decomposition of
353 carbonates does not occur. At temperatures above 800 °C, most of the carbonates decompose
354 thermally. When switching to oxyfuel combustion, the temperature of thermal decomposition of
355 carbonates shifts to higher values, which in turn is compatible with the other previous studies [18], [26],
356 [27].



357

358 *Figure 7: (a) The dependence of bottom ash carbonate decomposition on the average temperature in*
 359 *the riser and (b) the dependence of circulating ash carbonate decomposition on the maximum*
 360 *temperature in the riser.*

361

362 4. Conclusions

363 The first experimental results studied the potential of transitioning to cleaner and sustainable energy
 364 generation in the shale oil industry. Semicoke air and oxyfuel combustion tests were carried out in a
 365 60 kW_{th} CFB pilot facility. Air, 21/79%, and 30/70% O₂/CO₂ combustion modes were presented. The
 366 results show that the temperature distributions are similar when burning in air and O₂/CO₂ (21/79%)
 367 environments. When increasing the oxygen content in the supplied O₂/CO₂ mixture to 30%, the heat
 368 release is redistributed and the temperature in the lower part of the riser increases. SO₂ emissions are
 369 slightly increased in air combustion mode under lower operation temperatures, and oxyfuel combustion
 370 did not influence SO₂ release. Actual NO_x emissions (per MJ) are reduced under oxygen oxygen-
 371 enriched environment compared to air combustion. Experiments also showed that NO_x generation
 372 during semicoke combustion is generally reduced by creating a reduction zone, which causes an
 373 increase in CO concentration. Under air combustion modes, at temperatures below 800 °C, the thermal
 374 decomposition of carbonates does not occur. At higher temperatures >800 °C, most of the carbonates
 375 decompose thermally and when switching from air to oxyfuel combustion, the temperature of the thermal
 376 decomposition of carbonates shifts to a higher value.

377 **Acknowledgements**

378 The Eesti Energia AS and Estonian Research Council funded this research from the National
379 Programme for Addressing Socio-Economic Challenges through R&D (RITA), which is supported by
380 the Estonian Government and European Regional Development Fund

381 **References**

- 382
383 [1] X. Han, I. Kulaots, X. Jiang, and E. M. Suuberg, "Review of oil shale semicoke and its
384 combustion utilization," *Fuel*, vol. 126, pp. 143–161, Jun. 2014, doi:
385 10.1016/J.FUEL.2014.02.045.
- 386 [2] A. Trikkel, R. Kuusik, A. Martins, T. Pihu, and J. M. Stencel, "Utilization of Estonian oil shale
387 semicoke," *Fuel Process. Technol.*, vol. 89, no. 8, pp. 756–763, 2008, doi:
388 <https://doi.org/10.1016/j.fuproc.2008.01.010>.
- 389 [3] H. Lees, I. Kulaots, and E. M. Suuberg, "Oil shale kerogen-derived adsorbents and their
390 application to trichloroethylene adsorption from aqueous solutions," *Microporous Mesoporous*
391 *Mater.*, vol. 354, p. 112523, 2023, doi: <https://doi.org/10.1016/j.micromeso.2023.112523>.
- 392 [4] R. Kuusik *et al.*, "Fluidized bed combustion of oil shale retorting solid waste," *Oil Shale*, vol. 21,
393 no. 3, pp. 237–248, 2004.
- 394 [5] H. Arro, A. Prikk, T. Pihu, and I. Öpik, "Utilization of semi-coke of Estonian shale oil industry,"
395 *Oil Shale*, vol. 19, no. 2, pp. 117–125, 2002.
- 396 [6] Y. Yang, X. Lu, Q. Wang, L. Mei, D. Song, and Y. Hong, "Experimental Study on Combustion
397 of Low Calorific Oil Shale Semicoke in Fluidized Bed System," *Energy & Fuels*, vol. 30, no. 11,
398 pp. 9882–9890, Nov. 2016, doi: 10.1021/acs.energyfuels.6b01870.
- 399 [7] Y. Yang, Q. Wang, X. Lu, J. Li, and Z. Liu, "Combustion behaviors and pollutant emission
400 characteristics of low calorific oil shale and its semi-coke in a lab-scale fluidized bed
401 combustor," *Appl. Energy*, vol. 211, pp. 631–638, Feb. 2018, doi:
402 10.1016/J.APENERGY.2017.10.071.
- 403 [8] T. KALJUVEE, R. KUUSIK, A. TRIKKEL, and N. MALJUKOVA, "BEHAVIOR OF SULPHUR
404 COMPOUNDS AT COMBUSTION OF OIL SHALE SEMICOKE," *Oil Shale*, vol. 20, no. 2, pp.
405 113–125, 2003, doi: <https://doi.org/10.3176/oil.2003.2.03>.
- 406 [9] Q. Wang, H. Wang, B. Sun, J. Bai, and X. Guan, "Interactions between oil shale and its semi-
407 coke during co-combustion," *Fuel*, vol. 88, no. 8, pp. 1520–1529, 2009, doi:
408 <https://doi.org/10.1016/j.fuel.2009.03.010>.
- 409 [10] H. Liu, W.-X. Liang, H. Qin, and Q. Wang, "Thermal behavior of co-combustion of oil shale
410 semi-coke with torrefied cornstalk," *Appl. Therm. Eng.*, vol. 109, pp. 413–422, 2016, doi:
411 <https://doi.org/10.1016/j.applthermaleng.2016.08.084>.
- 412 [11] H. Liu, W. Liang, H. Qin, and Q. Wang, "Synergy in co-combustion of oil shale semi-coke with
413 torrefied cornstalk," *Appl. Therm. Eng.*, vol. 109, pp. 653–662, Oct. 2016, doi:
414 10.1016/J.APPLTHERMALENG.2016.08.125.
- 415 [12] N. Golubev, "Solid heat carrier technology for oil shale retorting," *Oil Shale*, vol. 20, no. 3, pp.
416 324–332, 2003.
- 417 [13] D. Neshumayev, T. Pihu, A. Siirde, O. Järvik, and A. Konist, "Solid heat carrier oil shale
418 retorting technology with integrated CFB technology," *Oil Shale*, vol. 36, no. 2S, pp. 99–113,
419 2019, doi: 10.3176/oil.2019.2S.02.
- 420 [14] T. Hensler, C. Binder, H. Sieger, I. Aarna, and A. Orth, "The multi-functional role of high-
421 throughput CFB's in the oil shale industry," in *12th International Conference on Fluidized Bed*,

- 422 2017, pp. 773–780.
- 423 [15] A. Konist, O. Järvik, Z. Steven Baird, and D. Neshumayev, “A technical analysis of oil shale
424 firing power units retrofitting for Carbon Capture and Storage (CCS),” 2021.
- 425 [16] C. Wu *et al.*, “A comprehensive review of carbon capture science and technologies,” *Carbon*
426 *Capture Sci. Technol.*, p. 100178, 2023, doi: <https://doi.org/10.1016/j.ccst.2023.100178>.
- 427 [17] M. Baqain, D. Neshumayev, and A. Konist, “NO_x and N₂O emissions from Ca-rich fuel
428 conversion in oxyfuel circulating fluidized bed combustion,” *Therm. Sci. Eng. Prog.*, vol. 42, p.
429 101938, Jul. 2023, doi: 10.1016/J.TSEP.2023.101938.
- 430 [18] M. Baqain, C. Rüstü Yörük, D. Nešumajev, O. Järvik, and A. Konist, “Ash characterisation
431 formed under different oxy-fuel circulating fluidized bed conditions,” *Fuel*, vol. 338, no.
432 November 2022, pp. 1–16, 2023, doi: 10.1016/j.fuel.2022.127244.
- 433 [19] M. Baqain, D. Neshumayev, and A. Konist, “Oxyfuel Conversion of Ca-rich fuel in a 60 kWth
434 Circulating Fluidized Bed,” *SSRN Electron. J.*, Nov. 2022, doi: 10.2139/SSRN.4276982.
- 435 [20] G. Chen, L. Shiyuan, and W. Linwei, “Current investigation status of oxy-fuel circulating
436 fluidized bed combustion,” *Fuel*, vol. 342, p. 127699, 2023, doi:
437 <https://doi.org/10.1016/j.fuel.2023.127699>.
- 438 [21] M. Lupion *et al.*, “30 MWth CIUDEN Oxy-CFB boiler - First experiences,” *Energy Procedia*, vol.
439 37, pp. 6179–6188, 2013, doi: 10.1016/j.egypro.2013.06.547.
- 440 [22] L. Al-Makhadmeh, J. Maier, M. Al-Harashsheh, and G. Scheffknecht, “Oxy-fuel technology: An
441 experimental investigations into oil shale combustion under oxy-fuel conditions,” *Fuel*, vol. 103,
442 pp. 421–429, 2013.
- 443 [23] L. Al-Makhadmeh, J. Maier, M. Al-Harashsheh, and G. Scheffknecht, “Oxyfuel technology: Oil
444 shale desulphurisation behaviour during unstaged combustion,” *Fuel*, vol. 158, pp. 460–470,
445 2015.
- 446 [24] L. Al-Makhadmeh, J. Maier, and G. Scheffknecht, “Oxyfuel technology: NO reduction during
447 oxy-oil shale combustion,” *Fuel*, vol. 128, pp. 155–161, 2014.
- 448 [25] C. Rüstü Yörük, “Experimental and Modeling Studies of Oil Shale Oxy-fuel Combustion
449 THESIS ON CHEMISTRY AND CHEMICAL ENGINEERING G46,” Tallinn University of
450 Technology, Tallinn, Estonia, 2016.
- 451 [26] L. Loo, A. Konist, D. Neshumayev, T. Pihu, B. Maaten, and A. Siirde, “Ash and Flue Gas from
452 Oil Shale Oxy-Fuel Circulating Fluidized Bed Combustion,” *Energies*, vol. 11, no. 5, p. 1218,
453 2018.
- 454 [27] L. Loo, B. Maaten, A. Siirde, T. Pihu, and A. Konist, “Experimental analysis of the combustion
455 characteristics of Estonian oil shale in air and oxy-fuel atmospheres,” *Fuel Process. Technol.*,
456 vol. 134, pp. 317–324, Jun. 2015, doi: 10.1016/j.fuproc.2014.12.051.
- 457 [28] M. Baqain, D. Neshumayev, and A. Konist, “TG-MS analysis and kinetic study of co-
458 combustion of ca-rich oil shale with biomass in air and oxy-like conditions,” *Carbon Capture*
459 *Sci. Technol.*, vol. 10, no. November 2023, p. 100162, 2024, doi: 10.1016/j.ccst.2023.100162.
- 460 [29] B. Maaten, O. Järvik, O. Pihl, A. Konist, and A. Siirde, “Oil shale pyrolysis products and the
461 fate of sulfur,” *Oil Shale*, vol. 37, no. 1, pp. 51–69, 2020, doi:
462 <https://doi.org/10.3176/oil.2020.1.03>.
- 463 [30] H. Ma, L. Zhou, S. Lv, J. W. Chew, and Z. Wang, “Review on Reaction Mechanisms of Sulfur
464 Species During Coal Combustion,” *J. Energy Resour. Technol.*, vol. 141, no. 10, May 2019,
465 doi: 10.1115/1.4043554.
- 466 [31] D. Neshumayev, T. Pihu, A. Siirde, O. Järvik, and A. Konist, “Solid heat carrier oil shale
467 retorting technology with integrated CFB technology,” *Oil Shale*, vol. 36, no. 2S, 2019, doi:
468 10.3176/oil.2019.2S.02.
- 469 [32] R. Stanger *et al.*, “Oxyfuel combustion for CO₂ capture in power plants,” *Int. J. Greenh. Gas*

- 470 *Control*, vol. 40, pp. 55–125, Sep. 2015, doi: 10.1016/J.IJGGC.2015.06.010.
- 471 [33] L. Duan, H. Sun, C. Zhao, W. Zhou, and X. Chen, “Coal combustion characteristics on an oxy-
472 fuel circulating fluidized bed combustor with warm flue gas recycle,” *Fuel*, vol. 127, pp. 47–51,
473 Jul. 2014, doi: 10.1016/J.FUEL.2013.06.016.
- 474 [34] J. Reinik *et al.*, “Changes in trace element contents in ashes of oil shale fueled PF and CFB
475 boilers during operation,” *Fuel Process. Technol.*, vol. 115, pp. 174–181, Nov. 2013, doi:
476 10.1016/J.FUPROC.2013.06.001.
- 477 [35] R. Stanger *et al.*, “Oxyfuel combustion for CO₂ capture in power plants,” *Int. J. Greenh. Gas*
478 *Control*, vol. 40, pp. 55–125, Sep. 2015, doi: 10.1016/J.IJGGC.2015.06.010.
- 479 [36] J. E. Johnsson, “Formation and reduction of nitrogen oxides in fluidized-bed combustion,” *Fuel*,
480 vol. 73, no. 9, pp. 1398–1415, 1994, doi: [https://doi.org/10.1016/0016-2361\(94\)90055-8](https://doi.org/10.1016/0016-2361(94)90055-8).
- 481 [37] T. Fujimori and T. Yamada, “Realization of oxyfuel combustion for near zero emission power
482 generation,” *Proc. Combust. Inst.*, vol. 34, no. 2, pp. 2111–2130, Jan. 2013, doi:
483 10.1016/J.PROCI.2012.10.004.
- 484 [38] S. Li *et al.*, “Coal combustion emission and ash formation characteristics at high oxygen
485 concentration in a 1MWth pilot-scale oxy-fuel circulating fluidized bed,” *Appl. Energy*, vol. 197,
486 pp. 203–211, 2017, doi: <https://doi.org/10.1016/j.apenergy.2017.03.028>.
- 487 [39] L. Duan, C. Zhao, W. Zhou, C. Qu, and X. Chen, “Effects of operation parameters on NO
488 emission in an oxy-fired CFB combustor,” *Fuel Process. Technol.*, vol. 92, no. 3, pp. 379–384,
489 2011, doi: <https://doi.org/10.1016/j.fuproc.2010.09.031>.
- 490 [40] G. Hofbauer, T. Beisheim, H. Dieter, and G. Scheffknecht, “Experiences from Oxy-fuel
491 Combustion of Bituminous Coal in a 150 kWth Circulating Fluidized Bed Pilot Facility,” *Energy*
492 *Procedia*, vol. 51, pp. 24–30, Jan. 2014, doi: 10.1016/J.EGYPRO.2014.07.003.
- 493 [41] T. Pikkarainen, J. Saastamoinen, H. Saastamoinen, T. Leino, and A. Tourunen, “Development
494 of 2nd Generation Oxyfuel CFB Technology – Small Scale Combustion Experiments and
495 Model Development Under High Oxygen Concentrations,” *Energy Procedia*, vol. 63, pp. 372–
496 385, 2014, doi: 10.1016/j.egypro.2014.11.040.
- 497 [42] A. Tourunen, T. Leino, T. Pikkarainen, H. Nevalainen, and R. Kuivalainen, “Small pilot scale
498 CFB experiments under air- and oxygen-firing conditions,” 2011.
- 499 [43] S. Seddighi K., D. Pallarès, F. Normann, and F. Johnsson, “Carbon Monoxide Formation
500 during Oxy-fuel-Fired Fluidized-Bed Combustion,” *Energy & Fuels*, vol. 27, no. 4, pp. 2275–
501 2282, Apr. 2013, doi: 10.1021/ef3021393.
- 502 [44] H. Saastamoinen, T. Leino, and A. Tourunen, “Comparison of emission formation during
503 pyrolysis and char combustion in air and oxyfuel conditions in fluidized bed,” in *Proceedings of*
504 *the 21st International Conference on Fluidized Bed Combustion*, 2012.
- 505 [45] C. Bu *et al.*, “Effect of CO₂ on oxy-fuel combustion of coal-char particles in a fluidized bed:
506 Modeling and comparison with the conventional mode of combustion,” *Appl. Energy*, vol. 177,
507 pp. 247–259, 2016, doi: <https://doi.org/10.1016/j.apenergy.2016.05.108>.
- 508 [46] C. Gonzalo-Tirado, S. Jiménez, and J. Ballester, “Kinetics of CO₂ gasification for coals of
509 different ranks under oxy-combustion conditions,” *Combust. Flame*, vol. 160, no. 2, pp. 411–
510 416, 2013, doi: <https://doi.org/10.1016/j.combustflame.2012.10.020>.
- 511 [47] D. Kühnemuth, F. Normann, K. Andersson, and F. Johnsson, “On the carbon monoxide
512 formation in oxy-fuel combustion—Contribution by homogenous and heterogeneous reactions,”
513 *Int. J. Greenh. Gas Control*, vol. 25, pp. 33–41, 2014, doi:
514 <https://doi.org/10.1016/j.ijggc.2014.02.014>.
- 515 [48] C. Geng, Y. Shao, Z. Bian, and W. Zhong, “Experimental study on oxy-fuel combustion
516 behavior of lignite char and carbon transfer mechanism with isotopic tracing method,” *Chem.*
517 *Eng. J.*, vol. 386, p. 123977, 2020, doi: <https://doi.org/10.1016/j.cej.2019.123977>.

- 518 [49] K. Jamil, J. Hayashi, and C.-Z. Li, "Pyrolysis of a Victorian brown coal and gasification of
519 nascent char in CO₂ atmosphere in a wire-mesh reactor," *Fuel*, vol. 83, no. 7, pp. 833–843,
520 2004, doi: <https://doi.org/10.1016/j.fuel.2003.09.017>.
- 521 [50] W. Wang *et al.*, "O₂/CO₂ and O₂/N₂ combustion of bituminous char particles in a bubbling
522 fluidized bed under simulated combustor conditions," *Chem. Eng. J.*, vol. 336, pp. 74–81,
523 2018, doi: <https://doi.org/10.1016/j.cej.2017.11.027>.
- 524 [51] L. Duan, C. Zhao, W. Zhou, C. Qu, and X. Chen, "O₂/CO₂ coal combustion characteristics in a
525 50kWth circulating fluidized bed," *Int. J. Greenh. Gas Control*, vol. 5, no. 4, pp. 770–776, 2011,
526 doi: <https://doi.org/10.1016/j.ijggc.2011.01.007>.
- 527 [52] L. Duan, H. Sun, C. Zhao, W. Zhou, and X. Chen, "Coal combustion characteristics on an oxy-
528 fuel circulating fluidized bed combustor with warm flue gas recycle," *Fuel*, vol. 127, pp. 47–51,
529 2014, doi: [10.1016/j.fuel.2013.06.016](https://doi.org/10.1016/j.fuel.2013.06.016).
- 530 [53] S. Seddighi K., D. Pallarès, F. Normann, and F. Johnsson, "Progress of Combustion in an Oxy-
531 fuel Circulating Fluidized-Bed Furnace: Measurements and Modeling in a 4 MWth Boiler,"
532 *Energy & Fuels*, vol. 27, no. 10, pp. 6222–6230, Oct. 2013, doi: [10.1021/ef4011884](https://doi.org/10.1021/ef4011884).
- 533 [54] B. Engin, U. Kayahan, and H. Atakül, "A comparative study on the air, the oxygen-enriched air
534 and the oxy-fuel combustion of lignites in CFB," *Energy*, vol. 196, p. 117021, Apr. 2020, doi:
535 [10.1016/J.ENERGY.2020.117021](https://doi.org/10.1016/J.ENERGY.2020.117021).
- 536 [55] F. Scala, *Fluidized bed technologies for near-zero emission combustion and gasification*.
537 Woodhead Publishing Limited, 2013.
- 538 [56] H. Arro, A. Prikk, and T. Pihu, "Calculation of CO₂ emission from CFB boilers of oil shale
539 power plants," *Oil Shale*, vol. 23, no. 4, pp. 356–365, 2006.
- 540

Publication VI

Wu, Chunfei; Huang, Qi; Xu, Zhicheng; Sipra, Ayesha Tariq; Gao, Ningbo; Vandenberghe, Luciana Porto de Souza; et al. (2023). **A comprehensive review of carbon capture science and technologies.** **Carbon Capture Science & Technology.** DOI: 10.1016/j.ccst.2023.100178.



Contents lists available at ScienceDirect

Carbon Capture Science & Technology

journal homepage: www.elsevier.com/locate/ccst

Review

A comprehensive review of carbon capture science and technologies



Chunfei Wu^{a,*}, Qi Huang^a, Zhicheng Xu^b, Ayesha Tariq Sipra^b, Ningbo Gao^{b,†},
 Luciana Porto de Souza Vandenberghe^{c,†}, Sabrina Vieira^c, Carlos Ricardo Soccol^c, Ruikai Zhao^d,
 Shuai Deng^{d,†}, Sandra K.S. Boetcher^{e,†}, Shijian Lu^{f,*}, Huancong Shi^g, Dongya Zhao^{h,†},
 Yupeng Xing^h, Yongdong Chen^{i,†}, Jiamei Zhu^j, Dongdong Feng^{k,†}, Yu Zhang^k, Lihua Deng^k,
 Guoping Hu^{l,†}, Paul A. Webley^m, Daxin Liang^{n,†}, Zhichen Baⁿ, Agata Mlonka-Mędrala^o,
 Aneta Magdziarz^{o,†}, Norbert Miskolczi^{p,†}, Szabina Tomasek^p, Su Shiung Lam^{q,†},
 Shin Ying Foong^q, Hui Suan Ng^r, Long Jiang^{s,†}, Xinlong Yan^t, Yongzhuo Liu^u, Ying Ji^s,
 Hongman Sun^{v,†}, Yu Zhang^v, Haiping Yang^{w,†}, Xiong Zhang^w, Mingzhe Sun^x,
 Daniel C.W. Tsang^{x,†}, Jin Shang^y, Christoph Muller^{z,*}, Margarita Rekhchina^z, Maximilian Krödel^z,
 Alexander H. Bork^z, Felix Donat^z, Lina Liu^{aa,†}, Xin Jin^{h,†}, Wen Liu^{bb,†}, Syed Saqline^{bb},
 Xianyu Wu^{bb}, Yongqing Xu^{cc}, Asim Laeeq Khan^{dd,†}, Zakawat Ali^{dd}, Haiqing Lin^{ee,†},
 Leiqing Hu^{ee}, Jun Huang^{ff,†}, Rasmeet Singh^{ff}, Kaifang Wang^{gg,hh,†}, Xuezhong He^{gg,hh,†},
 Zhongde Dai^{ii,†}, Shouliang Yi^{ij,*}, Alar Konist^{kk,†}, Mais Hanna Suleiman Baqain^{kk}, Yijun Zhao^k,
 Shaozeng Sun^k, Guoxing Chen^{ll,†}, Xin Tu^{mm}, Anke Weidenkaff^{ll,nm}, Sibudjing Kawi^{oo,†},
 Kang Hui Lim^{oo}, Chunfeng Song^{pp,†}, Qing Yang^{qq,†}, Zhenyu Zhao^{rr}, Xin Gao^{rr,†}, Xia Jiang^{ss,†},
 Haiyan Ji^{ss}, Toluleke E. Akinola^{tt}, Adekola Lawal^{uu}, Olajide S. Otitoju^{tt}, Meihong Wang^{tt,*},
 Guojun Zhang^{vv}, Lin Ma^{vv,†}, Baraka C. Sempuga^{ww}, Xinying Liu^{ww,†}, Eni Oko^{xx,†},
 Michael Daramola^{yy}, Zewei Yu^{zz}, Siming Chen^f, Guojun Kang^f, Qingfang Li^{aaa}, Li Gao^{aab},
 Ling Liu^f, Hui Zhou^{cc,*}

^a School of Chemistry and Chemical Engineering, Queen's University Belfast, Belfast, BT7 1NN, UK^b School of Energy and Power Engineering, Xi'an Jiaotong University, Xi'an, Shaanxi, 710049, China^c Department of Bioprocess Engineering and Biotechnology, Federal University of Paraná, Brazil^d State Key Laboratory of Engines, Tianjin University, Tianjin 300350, China^e Embry-Riddle Aeronautical University, Daytona Beach, Florida 32114 USA^f China University of Mining and Technology, China^g Huzhou Research Institute of Zhejiang University, China^h College of Chemistry & Chemical Engineering, China University of Petroleum (East China), Qingdao 266580, Chinaⁱ College of Chemistry and Chemical Engineering, Southwest Petroleum University, Chengdu 610500, China^j School of Chemical Engineering and Technology, China University of Mining & Technology, Xuzhou, Jiangsu 221116, China^k School of Energy Science and Engineering, Harbin Institute of Technology, 150001, China^l Key Laboratory of Rare Earths, Ganjiang Innovation Academy, Chinese Academy of Sciences, Ganzhou, Jiangxi, 341000, China^m Department of Chemical Engineering, Monash University, Victoria 3800, Australiaⁿ Key Laboratory of Bio-based Material Science and Technology (Ministry of Education), Northeast Forestry University, Harbin 150040, China^o AGH University of Krakow, Al. A. Mickiewicza 30, 30-059 Krakow, Poland

* Corresponding authors.

E-mail addresses: c.wu@qub.ac.uk (C. Wu), lushijian@cumt.edu.cn (S. Lu), muelchri@ethz.ch (C. Muller), slyi@chbe.gatech.edu (S. Yi), meihong.wang@sheffield.ac.uk (M. Wang), zhouhui.10@tsinghua.org.cn (H. Zhou).

[†] Section leaders: 2.1&2.2 - Professor Ningbo Gao; 2.3 - Professor Luciana Porto de Souza Vandenberghe; 2.4 - Professor Shuai Deng; 2.4 & 5.3 - Professor Sandra Boetcher; 3.1.1.5 - Professor Dongya Zhao; 3.1.2 - Professor Yongdong Chen; 3.1.3 - Dr Dongdong Feng; 3.2.1 - Dr Guoping Hu; 3.2.2-Dr Daxin Liang; 3.2.3.1 - Dr Aneta Magdziarz; 3.2.3.2 - Dr Norbert Miskolczi; 3.2.3.3 - Professor Su Shiung Lam; 3.2.4 - Dr Long Jiang; 3.2.5.1 - Dr Hongman Sun; 3.2.5.2 - Professor Haiping Yang; 3.2.5.3 - Professor Dan Tsang; 3.4.1, 3.4.2 & 3.5.1 - Professor Christoph Muller; 3.4.3 - Dr Lina Liu; 3.5.2 - Dr Xin Jin; 3.5.3, 5.1.2 & 5.3 - Dr Wen Liu; 4.1 & 4.2.1 - Dr Asim Khan 4.2 - Professor Haiqing Lin; 4.3, 3.2.2, 3.2.5.1 - Professor Jun Huang; 4.4 - Dr Xuezhong He; 4.5 - Dr Zhongde Dai; 5.1.1 Professor Alar Konist; 5.1.4 - Dr Guoxing Chen; 5.2 - Dr Sibudjing Kawi; 5.3 Professor Chunfeng Song; 5.3.8 - Professor Qing Yang; 5.4 - Professor Xin Gao; 5.5 - Professor Xia Jiang; 6.1&6.2 - Professor Meihong Wang; 6.3 & 6.4 - Professor Lin Ma 6.5 -Professor Xinying Liu; 6.6 - Dr Eni Oko; 7.1 - Professor Shijian Lu; 7.2 - Dr Siming Chen; 7.3 - Dr Ling Liu

<https://doi.org/10.1016/j.ccst.2023.100178>

Received 6 September 2023; Received in revised form 3 December 2023; Accepted 8 December 2023

2772-6568/© 2023 The Authors. Published by Elsevier Ltd on behalf of Institution of Chemical Engineers (IChemE). This is an open access article under the CC BY license (<http://creativecommons.org/licenses/by/4.0/>)

- ^p MOL Department of Hydrocarbon and Coal Processing, University of Pannonia, H-8200, Veszprém, Egyetem u. 10, Hungary
- ^q Institute of Tropical Aquaculture and Fisheries (AKUATROP), Universiti Malaysia Terengganu, 21030 Kuala Nerus, Terengganu, Malaysia
- ^r Centre for Research and Graduate Studies, University of Cyberjaya, Persiaran Bestari, 63000 Cyberjaya, Selangor, Malaysia
- ^s Institute of Refrigeration and Cryogenics, Zhejiang University, Hangzhou, 310027, China
- ^t School of Chem. Eng. Technol., China University of Mining and Technology, Xuzhou 221116, China
- ^u College of Chemical Engineering, Qingdao University of Science & Technology, Qingdao, 266042, China
- ^v State Key Laboratory of Heavy Oil Processing, College of Chemistry and Chemical Engineering, China University of Petroleum, Qingdao 266580, China
- ^w State Key Laboratory of Coal Combustion, School of Energy and Power Engineering, Huazhong University of Science and Technology, Wuhan, 430074, China
- ^x Department of Civil and Environmental Engineering, The Hong Kong University of Science and Technology, Clear Water Bay, Hong Kong
- ^y School of Energy and Environment, City University of Hong Kong, Tat Chee Avenue, Kowloon, Hong Kong, China
- ^z Institute of Energy and Process Engineering, ETH Zürich, Leonhardstrasse 21, Zürich 8092, Switzerland
- ^{aa} College of Environmental Science and Engineering, Ministry of Education Key Laboratory of Pollution Processes and Environmental Criteria, Nankai University, Tianjin 300350, China
- ^{ab} School of Chemistry, Chemical Engineering and Biotechnology, Nanyang Technological University, 62 Nanyang Drive, Singapore 637459, Singapore
- ^{ac} Department of Energy and Power Engineering, Tsinghua University, Beijing, 100084, China
- ^{ad} Chemical Engineering Department, COMSATS University Islamabad, Lahore, Pakistan
- ^{ae} Department of Chemical and Biological Engineering, University at Buffalo, The State University of New York, Buffalo, NY 14260, USA
- ^{af} School of Chemical and Biomolecular Engineering, University of Sydney, Sydney, Australia
- ^{ag} Department of Chemical Engineering, Guangdong Technion - Israel Institute of Technology, 241 Daxue Road, Shantou, Guangdong, 515063, China
- ^{ah} The Wolfson Department of Chemical Engineering, Technion - Israel Institute of Technology, Haifa 3200003, Israel
- ^{ai} College of Carbon Neutrality Future Technology, Sichuan University, Chengdu 610065, China
- ^{aj} Department of Energy, National Energy Technology Laboratory, Pittsburgh, PA 15236, USA
- ^{ak} Department of Energy Technology, Tallinn University of Technology, 19086, Tallinn, Estonia
- ^{al} Fraunhofer Research Institution for Materials Recycling and Resource Strategies IWKS, Brentanostraße 2a, 63755 Alzenau, Germany
- ^{am} Department of Electrical Engineering and Electronics, University of Liverpool, Liverpool L69 3GJ, UK
- ^{an} Department of Materials and Earth Sciences, Technical University Darmstadt, Alarich-Weiss-Str. 2, 64287 Darmstadt, Germany
- ^{ao} Department of Chemical and Biomolecular Engineering, National University of Singapore, P.O. Box 117585, Singapore
- ^{ap} School of Environmental Science and Engineering, Tianjin University, Tianjin, China
- ^{aq} School of Energy and Power Engineering, Huazhong University of Science and Technology, Wuhan, China
- ^{ar} School of Chemical Engineering and Technology, Tianjin University, Tianjin 300072, China
- ^{as} College of Carbon Neutrality Future Technology, Sichuan University, Chengdu, 610065, China
- ^{at} Department of Chemical and Biological Engineering, University of Sheffield, Sheffield S1 3JD, UK
- ^{au} Petrofac, Woking GU21 5BH, UK
- ^{av} Department of Mechanical Engineering, University of Sheffield, Sheffield S1 3JD, UK
- ^{aw} Institute for Catalysis and Energy Solutions, University of South Africa, c/o Christiaan de Wet & Pioneer Avenue, Florida, 1709, Johannesburg, South Africa
- ^{ax} School of Engineering, Newcastle University, Newcastle upon Tyne NE1 7RU, UK
- ^{ay} Department of Chemical Engineering, Faculty of Engineering, Built Environment and Information Technology, University of Pretoria, Pretoria, South Africa
- ^{za} International CCS Knowledge Centre, 198-10 Research Drive Regina, SK S4S 7J7, Canada
- ^{aab} Sinopec Engineering Incorporation, Dongying, Shandong, 257088, China
- ^{aab} China Energy Jin Jie Power Station, Yulin, Shanxi, 719319, China

1. Introduction

CO₂ is one of the major anthropogenic greenhouse gases in the atmosphere contributing to global warming (Blamey et al., 2010; Mikkelsen et al., 2010). In the last half-century, the concentration of CO₂ has exhibited a dramatic growth from about 310 to over 415 ppm owing to the large-scale utilization of fossil fuels and various chemical refinery processes (Hu et al., 2016; Lackner, 2003; Yu et al., 2008). Thus, worldwide efforts have been devoted to developing new technologies for reducing CO₂ emissions and most of the United Nations members have approved Paris Climate Agreements for greenhouse gas reduction (He et al., 2016; Jacobson, 2009; Obergassel et al., 2016; Wang et al., 2011). The 21st conference on global warming (COP21) reached a landmark agreement (the Paris Agreement) to limit the increase of the global average temperature to 2.0 °C in 2100 (Rhodes, 2016). CO₂ emissions from energy- and industry-related sources must decrease dramatically after 2030 and reach net-zero levels between 2050 and 2060 (Rogelj et al., 2016) to enable this target to be reached.

Carbon capture removing CO₂ before releasing it into the atmosphere plays an important role in a zero and/or negative CO₂ emission. It has three categories: pre-combustion, post-combustion, and oxyfuel combustion. For oxyfuel combustion, pure oxygen is used in combustion to produce flue gas with high purity of CO₂. In the pre-combustion CO₂ capture process, fuels are partially oxidized by steam or oxygen to produce synthetic gas, followed by water gas shift reaction to form hydrogen-enriched gas. The third category of CO₂ capture is post-combustion, which refers to capturing CO₂ after the combustion of hydrocarbon fuels. Among these CO₂ capture technologies, post-combustion with amine solvents is the state-of-the-art mature technol-

ogy (Rochelle, 2009). In addition, directly capturing CO₂ from the air could meet global climate goals. However, a new study reported that the process needs as much as a quarter of global energy supplies in 2100 (Realmondo et al., 2019).

The direct use of carbonaceous fuels such as fossil fuels and biomass is unavoidable in the future. Therefore, a large amount of CO₂ is still expected to be emitted into the atmosphere. Therefore, post-combustion CO₂ capture, oxyfuel combustion and direct air capture (DAC) represent key technologies to reduce CO₂ emissions and mitigate climate change. Review papers are available regarding the development of carbon capture technologies (Al-Hamed and Dincer, 2021; Buckingham et al., 2022; Mikulčić et al., 2019). However, a more comprehensive review of carbon capture will be beneficial to the research community. Therefore, this paper provides a thorough description and analysis of carbon capture technologies, including solid and liquid-based sorbents for capturing CO₂ from different sources (e.g. flue gas, biogas, syngas and air). Various liquid solvents, including amines, ion liquid and ammonia, were studied. In addition, solid adsorbents were analysed based on their working temperatures, such as low-temperature adsorbents (carbon, biochar, zeolite, amine-loaded solid, covalent organic frameworks (COFs) and aerogels), medium-temperature adsorbents (MgO and K₂CO₃) and high-temperature adsorbents (CaO). In Section 4 of this review paper, membrane-based CO₂ separation is critically analysed, followed by the investigation of oxyfuel combustion, chemical looping, cryogenic CO₂ capture, and bioenergy-related CO₂ capture. Process modelling using Aspen, CFD and machine learning for CO₂ capture is also included and critically analysed in this review paper. Furthermore, techno-economic analysis and evaluation of typical large-scale CO₂ capture plants were carried out.

2. CO₂ capture from various CO₂ sources

2.1. Flue gas as the CO₂ source

2.1.1. Current status of flue gas

Currently, as the world's second-largest energy source, coal contributes to more than 40% of the total global emissions (Rahman et al., 2017; Younas et al., 2020). Around 60% and 39% of the total carbon emissions from the electricity industry were derived from coal-fired and natural gas-fired power plants, respectively (Administration, 2020). Therefore, carbon capture from flue gas as the CO₂ source is the key to achieving net-zero global CO₂ emissions. In addition, capturing and utilising CO₂ in flue gas will reduce the pressure of greenhouse gas emissions and generate substantial economic benefits (Khalifa et al., 2022; Maina et al., 2021).

Carbon capture from flue gas refers to the process of separating and collecting CO₂ from industrial production and energy use, such as power plants, cement manufacturing and stainless-steel factory, etc. (Cheng et al., 2022; Wang and Song, 2020a). CO₂ emissions from fossil fuel-fired flue gas in the power industry are characterised by large flue gas volume, low CO₂ partial pressure (0.03–0.2 bar), high total emissions and relatively low CO₂ concentration (3–20%) (Buvik et al., 2021; Figueroa et al., 2008). Usually, the flue gas from other manufacturing industries contains a higher CO₂ concentration than that from the power plant. As for the components of flue gas from power plants, except for N₂ in air, CO₂, O₂ and H₂S are approximately 20%, 5% and < 1%, respectively, produced by complete fuel combustion, together with large amounts of water vapour generation (Cheah et al., 2015; Maina et al., 2021; Wang and Song, 2020a). The properties of a few typical flue gases from different sources are summarised in Table 2.1.

2.1.2. Challenges to CO₂ capture from flue gas

Until now, the use of fossil fuels is still increasing for electricity generation in future (Zou et al., 2017). Thereby, as an “end-of-pipe” process, post-combustion carbon capture is the most widely used and mature carbon capture technology due to its good viability and feasibility for existing power plants, without the requirement for large-scale renovation and upgrading (Cheng et al., 2022; Han et al., 2020; Zhao et al., 2018). The main post-combustion CO₂ capture technologies include absorption separation (physical and chemical absorption) (Fang et al., 2020; Wang et al., 2015), adsorption separation (physical and chemical adsorption) (Wilcox et al., 2014; Zhao et al., 2018) and membrane separation (Feron et al., 2020; Han et al., 2020). According to the statistics, there are more than 60% of post-combustion technologies employing absorption-based methods. Among those, the chemical absorption method, represented

by the MEA absorption, is considered the most promising for industrial applications because of its applicability to large air volumes and simplicity of operation, which mainly consists of two important processes, including chemical absorption of CO₂ in the absorption tower and thermal regeneration of the absorber in the desorption tower (Akeeb et al., 2022).

However, carbon capture from flue gas sources is still confronted with major challenges, restraining its further development and commercialisation (D'Alessandro et al., 2010; Notz et al., 2011). First, after fossil fuel combustion, there is a high volumetric flow rate together with a large amount of CO₂ in flue gas derived from most conventional thermal power plants, which is in the temperature range of 50–150 °C because of a series of gas cleaning procedures after fuel combustion. Then, the discharge flue gas is mainly in atmospheric pressure, but the partial pressure of CO₂ is at a relatively low level due to insufficient volumetric concentration of CO₂ in flue gas, as discussed above. Last, the surplus O₂ used during the combustion process results in the presence of SO_x and NO_x, and the humidity due to the existing steam poses additional difficulties for the currently preferred CO₂ capture process, such as amine-based absorption technology.

Solid amine-based adsorbents are promising candidates for carbon capture from flue gas, especially at low CO₂ partial pressure (10–15%) (Wang and Song, 2020a). However, the low oxidative stability of amines could significantly influence the performance of flue gas carbon capture using amine-based adsorbents, because the presence of O₂ (3–4%) can result in the rapid oxidative degradation of amines (Sreedhar et al., 2017). Min et al. investigated amine-based solids for CO₂ capture by enhancing the oxidation resistance of polyethyleneimine (PEI)/silica adsorbent, as shown in Fig. 2.1, with two strategies adopted. First, 1, 2-epoxybutane was used to functionalise PEI to produce tethered 2-hydroxybutyl groups. Besides, metals that could assist amine oxidation were poisoned through using chelator. After improvement, only a surprisingly low decay of CO₂ capture capacity (8.5%) was observed under aging by flue gas with oxygen at 110 °C after 30 d, 50 times higher stability compared with conventional PEI/silica (Min et al., 2018). This work may provide the further commercialisation prospect of these adsorbents when used for carbon capture from flue gas containing oxygen, which may cause the oxidation of adsorbents (Bali et al., 2013; Heydari-Gorji and Sayari, 2012).

It is known that traditional amine-containing adsorbents are vulnerable to acidic conditions in flue gas caused by SO_x and NO_x, which could lead to irreversible poisoning effects and, eventually, fast deactivation of sorbents. Thus, the basic sites in amine-based adsorbents can be significantly influenced by acidic compounds (Maina et al., 2021; Zhao et al., 2018). Hence, designing and developing SO_x- and NO_x-resistant amine-

Table 2.1
Typical CO₂ concentration and impurities of flue gas from various sources.

| Flue gas source | CO ₂ conc. (vol%) | Pressure (atm) | CO ₂ partial pressure (atm) | Impurities | Ref. |
|--|------------------------------|----------------|--|--|--|
| Aluminum production | 1–2 | 1 | 0.01–0.02 | SO _x and NO _x present, fluoride | Husebye et al., 2012 |
| Gas turbine exhaust | 3–4 | 1 | 0.03–0.04 | low SO _x and NO _x levels, O ₂ : 12%–15% | Samanta et al., 2011 |
| Fired boiler of oil refinery and petrochemical plant | ~8 | 1 | 0.08 | SO _x and NO _x present | Wang and Song, 2020a |
| Natural gas fired boilers | 7–10 | 1 | 0.07–0.10 | SO _x and NO _x present | Wang and Song, 2020a |
| Oil-fired boilers | 11–13 | 1 | 0.11–0.13 | high SO _x and NO _x levels, O ₂ : 2%–5% | Wang and Song, 2020a |
| Coal-fired boilers | 12–14 | 1 | 0.12–0.14 | high SO _x and NO _x levels, O ₂ : 2%–5% | Samanta et al., 2011 |
| IGCC syngas turbine | 12–14 | 1 | 0.12–0.14 | low SO _x and NO _x levels | Wang and Song, 2020a; Song et al., 2019b |
| Hydrogen production | 15–20 | 22–27 | 3–5 | high NO _x levels | Husebye et al., 2012 |
| Steel production (Blast furnace) | 20–27 | 1–3 | 0.2–0.6 | SO _x and NO _x present | Husebye et al., 2012 |
| Cement process | 14–33 | 1 | 0.14–0.33 | SO ₂ and NO _x , trace elements, particulates | Husebye et al., 2012 |

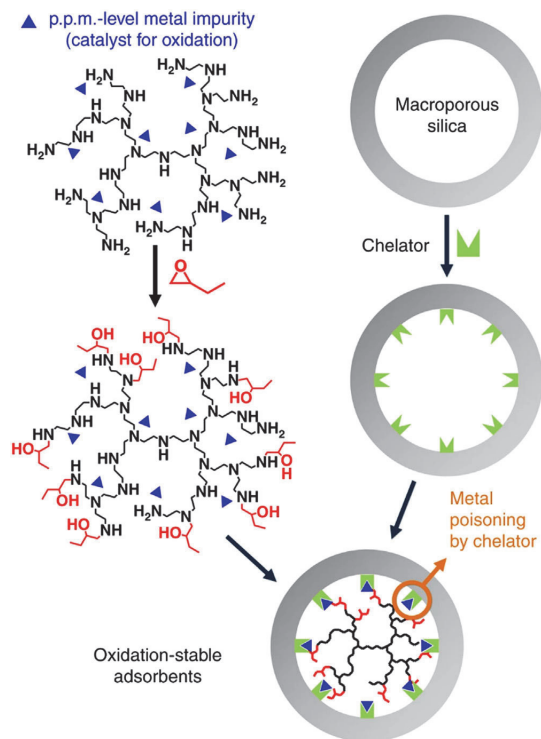


Fig. 2.1. Synthesis of oxidation-stable PEI functionalised CO_2 adsorbent (Min et al., 2018). (For interpretation of the references to color in this figure legend, the reader is referred to the web version of this article.)

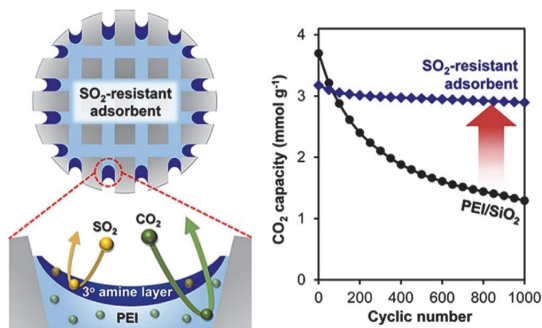


Fig. 2.2. Synthesis of SO_2 -resistant CO_2 adsorbent. Tertiary-amine-rich layer plays a role of protection for CO_2 capture by beneath PEI layer (Kim et al., 2019). (For interpretation of the references to color in this figure legend, the reader is referred to the web version of this article.)

based adsorbents are of great importance for carbon capture from flue gas in terms of solid adsorption technologies. Kim and co-workers (Kim et al., 2019) employed a facile fabrication route to impregnate porous silica with PEI to form a surface layer composed of tertiary amines, which exhibited improved SO_2 resistance during flue gas CO_2 capture. As shown in Fig. 2.2, the tertiary amine layer can capture SO_2 to enhance CO_2 adsorption by the beneath layer. The results showed that, compared with conventional PEI/silica for 65.1% carbon uptake abil-

ity, this novel sorbent achieved a significant reduction of capacity loss (only 8.52%) after 1000 cycles for simulated flue gas carbon capture with 50 ppm SO_2 (Kim et al., 2019). In addition to the improvement of adsorbents for carbon capture from flue gas with existing impurities of SO_x and NO_x as CO_2 resources, another method is to establish desulfurisation and denitrification units for enhancing sorbents regenerability during real-world power plant applications.

In most cases of practical power plants, the flue gas after post-combustion could be in humid conditions between 40°C to 80°C . The presence of moisture in wet flue gas may be detrimental to carbon capture, because the resulting steam not only results in competitive adsorption to CO_2 , but could decompose the adsorbents due to their low hydrothermal stability (Ray et al., 2021). However, modifying the existing power plant for pretreatment of water removal in flue gas may significantly aggregate the economic burden of the overall process. Therefore, novel sorbent materials should be designed and fabricated with high hydrothermal stability and high CO_2 uptake selectivity.

Soubeyrand-Lenoir et al. (2012) studied three different MOFs (HKUST-1, UiO-66 (Zr) and MIL-100 (Fe)) for CO_2 uptake with varying relative humidity (RH). As shown in Fig. 2.3a, 5 times higher carbon capture ability (105 mg/g) was achieved by MIL-100 (Fe) with escalating RH from 3% to 40%, compared with the other two MOFs. As depicted in Fig. 2.3b, the filled water on MIL-100 (Fe) formed microporous pockets to enhance CO_2 capture (A, B and C). However, the water in microporous MOFs could antagonise the carbon uptake by blocking CO_2 molecules (D and E) (Soubeyrand-Lenoir et al., 2012). In addition to the route of water-enhanced CO_2 uptake from flue gas reported in the above research, there are other key strategies for improving the carbon capture from wet flue gas, including hydrophobic modifications, the introduction of functional groups and amine modifications.

Therefore, it is essential to optimise the post-combustion CO_2 capture processes to deal with flue gas impurities, for example, O_2 , moisture, SO_x and NO_x , in terms of cost reduction, sorbents performance and regeneration, together with power plant units of drying, desulfurisation and denitrification. First, it is recommended to develop advanced materials with favourable stability, high capture capacity and low cost for promotion of the CO_2 capture from flue gas. Second, system and process optimisation is also crucial to make the new approach from bench-scale experiments to practical application. Besides, most of the research work in current literature used simulated gas or pure CO_2 as the carbon sources. In the future, the real-world flue gas with impurities should be applied for carbon capture investigations, in order to obtain more viable and feasible processes for carbon capture from flue gas to facilitate CO_2 reduction, collection and utilisation.

2.2. Syngas as the CO_2 source

2.2.1. Characteristics of syngas

Syngas is comprised of methane (CH_4), hydrogen (H_2), carbon monoxide (CO), water vapours (H_2O), carbon dioxide (CO_2), condensable compounds, and hydrocarbons (HCs). It is the major product of the gasification of carbonaceous materials, like natural gas, heavy oil and coal. Syngas is a favourable alternative fuel because it burns cleanly and has low greenhouse gas emissions. Its composition largely depends on the choice of feedstock and the production process. The main source of carbon dioxide emissions is coal. Syngas obtained from coal is non-renewable; however, producing syngas from coal gasification by Integrated Gasification Combined Cycle (IGCC) power plants will help reduce CO_2 emissions compared to burning coal directly (Casleton et al., 2008).

As described in the previous section, there are three key approaches for capturing CO_2 from fossil fuel-based power plants: post-combustion, oxy-fuel combustion and pre-combustion. In an IGCC power plant with pre-combustion carbon capture, syngas generated from the gasification of coal are processed in a water-gas shift (WGS) unit where after desulfurisation most of CO is converted to CO_2 and steam. This allows for

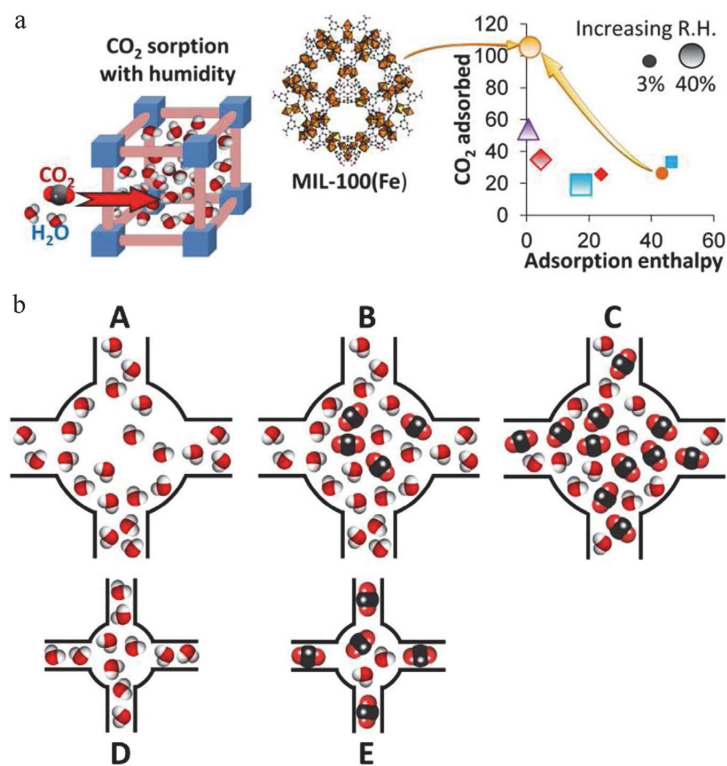


Fig. 2.3. Three MOF samples studied under various R.H. levels (a); Schematic representation of possible mechanisms of CO₂ adsorption in the presence of humidity (b) (Soubeyrand-Lenoir et al., 2012). (For interpretation of the references to color in this figure legend, the reader is referred to the web version of this article.)

Table 2.2

Advantages of syngas over flue gas in terms of CO₂ capture (Wang and Song, 2020b).

| Factors | Pre-combustion (Syngas) | Post-combustion (Flue gas) |
|----------------------------------|---|---|
| CO ₂ Partial pressure | High | Low |
| CO ₂ concentration | High (~40%) | Low (~3-15%) |
| Plant modifications | Minimal; requires the addition of only absorber and regenerator | Needs larger and more expensive equipment due to less CO ₂ concentration in the exhaust stream |

the separation of CO₂ before the combustion of the fuel (H₂) (Subraveti et al., 2019b). The CO₂ in the syngas can be separated by various methods like adsorption, absorption, membranes etc. According to Table 2.2, CO₂ concentration in the syngas is much higher compared to flue gas, pre-combustion CO₂ capture is a potentially cheaper method than post-combustion CO₂ capture. This is because, for an equal quantity of CO₂ captured, a relatively smaller volume of gas needs to be processed, resulting in lower capital costs due to smaller equipment size. Therefore, syngas is a better and more economical source for CO₂ capture as compared to flue gas in IGCC power plants (Trapp et al., 2015). However, further research needs to be carried out in order to integrate pre-combustion CO₂ capture technologies into IGCC power plants successfully.

2.2.2. Challenges of CO₂ capture from syngas

Since gasification is required to produce syngas in the pre-combustion process, various factors in the gasification process can pose challenges to CO₂ capture from syngas. The gasification can be classified into oxygen-blown and air-blown processes. The oxygen-blown gasifier

contains no nitrogen, having an evidently different composition from the air-blown gasifier syngas, which have a large nitrogen content (Cao et al., 2021). Therefore, both processes can have different configurations for the CO₂ capture process. The type of fuel (coal, oil, natural gas or biomass) can also affect the composition of syngas, which in turn affects the CO₂ capture system. Coal is an abundant fossil fuel used for electricity production. Besides, it's up-gradation and developments in better efficiency at present power plants, researchers are concentrating on the growth of innovative technologies, for example, supercritical and ultra-supercritical coal fired power plants and IGCCs. Amongst these technologies, IGCCs exhibit the most promising efficiency and environmental performance, along with the facility to incorporate various kinds of feedstock (James et al., 2019). These power plants are also good for low carbon applications, as syngas has a higher concentration of CO₂ which favours the separation process. At present, absorption is considered to be the most reliable method for CO₂ separation from syngas. The absorption process can utilise chemical solvents like aqueous solutions of amines or hot potassium carbonate and physical solvents (Rectisol, Selexol, Purisol) (Notz et al., 2011). As IGCC power plants yield high partial pressure of CO₂ in the syngas with higher plant operating pressure, physical solvents are deemed more appropriate than chemical ones for CO₂ absorption (Jansen et al., 2015). Therefore, vast research has been performed on pre-combustion CO₂ capture processes using various physical solvents (Park et al., 2015; Siefert et al., 2016; Smith et al., 2022). The cost of carbon capture IGCC facility depends on thermal recovery and pumping, heating and cooling of the liquid and gas stream. Compared to other commercial physical solvent processes, the Selexol process has lower strength, which would result in reduced lower heating value, thereby increasing the overall plant efficiency (Cormos, 2011; Dave et al., 2016). Alternative methods for CO₂ capture are gaining research attention, such as the utilisation of H₂ or CO₂-selective

membranes. The type of membrane selection also depends on the gasification process, which subsequently affects the cost of the pre-combustion capture process (Scholes et al., 2012). Furthermore, the syngas flow rate, hydrogen production, output power, hydrocarbon flow rate, and apparent thermal efficiency also affect the CO₂ capture system. Therefore, all these factors must be considered while selecting appropriate CO₂ capture systems.

From the above discussion, it can be concluded that pre-combustion carbon capture is considered to be the most effective method as compared to other carbon capture methods. This is because of high CO₂ partial pressure. Separating carbon dioxide from syngas is considerably easier than in the post-combustion carbon capture system. Moreover, pre-combustion holds better environmental, economic and social impact as compared to other carbon capture technologies (Olabi et al., 2022). Recently, two commercial pre-combustion carbon capture facilities have been working in the United States, where around 90 % of CO₂ is captured by using physical solvent absorption processes (Olabi et al., 2022). Two more power plants are operating in Spain and Netherlands, but only a part of syngas is being treated for carbon capture (Rubin et al., 2012). Therefore, there is a need to study the commercialisation prospects of the pre-combustion carbon capture process extensively.

2.3. Biogas as the CO₂ source

2.3.1. Biogas production and the upgrade necessity

Anaerobic digestion is a process that involves organic matter digestion to form biogas through hydrolysis, acidogenesis, acetogenesis, and methanogenesis (Fu et al., 2021). The produced biogas is considered to be one of the most important renewable energy sources, whose technology has been used worldwide for organic waste treatment and bioenergy production. In fact, the world is impacted by limited energy alternatives and significant environmental problems, which have stimulated the search for new bioenergy and environmental solutions. That is why the biogas industry has faced accelerated development and increase in the last decades. The annual biogas production in Europe and China is expected to reach 300 billion m³ by 2020 (Fu et al., 2021), representing around 1.43 exajoules (Sönnichsen, 2022).

Traditionally, most of the raw biogas is used to produce electricity and heat directly (Khan et al., 2021). In general, biogas is a mixture of gases consisting of 50–75 % methane (CH₄), 25–50 % carbon dioxide (CO₂), 0–10 % nitrogen (N₂), 0–3 % hydrogen sulfide (H₂S), 0–1 % hydrogen (H₂) and a minimal concentration of other gases (Aghel et al., 2022). With this composition, it does not meet natural gas specifications, so the content of CH₄ in biogas should be upgraded, and, in this case, it can be called biomethane or natural gas, enlarging its commercial value and range of applications, such as vehicle fuel (Yanuka-Golub et al., 2019). Natural gas contains 98–75 % of CH₄, promoting higher burning energy, with higher burning velocity and flammability. Also, when used as vehicle fuel, CO₂ gas occupies more space in the cylinder tanks, which leads to the necessity of additional energy during biogas compression, thus, increasing costs. So, CO₂ content must be reduced through biogas upgrade solutions for the elimination of impurities using different techniques (Aghel et al., 2022a).

2.3.2. Developed technologies for CO₂ capture from biogas

The main applied technologies worldwide for biogas upgrade are: absorption (water scrubbing, chemical absorption, physical absorption), swing adsorption (temperature, electrical, pressure), and membrane-based gas permeation are employed worldwide for biogas up-gradation (Shah et al., 2021) (Fig. 2.4). High-pressure water scrubbing is the most simple and reliable biogas absorption technology. This technology promotes large-volume biogas processing. However, it presents higher electricity consumption (0.30–33.0 kWh/Nm³) (Aghel et al., 2022a). So, the development and optimisation of biogas upgrade must pass through less energy consumption and the generation of methane-rich gas high-energy biogas. In situ technologies for methane enrichment have been explored,

which include cryogenic separation, and hybrid membrane-cryogenic technologies to limit energy costs and improve CO₂ capture efficiency (Shah et al., 2021). Apparently, hybrid technologies seem to be more economic, but they must still be tested on a large scale (Scholz et al., 2013). Table 2.3 presents the characteristics, parameters, and advantages of the most employed biogas purification techniques, which will be described as follows (Fu et al., 2021; Shah et al., 2021).

Water purification is the most common and well-developed method for removing CO₂ from biogas, and is based on the principle of physical absorption of gas in water, because of the property of gas solubility. Temperature is a factor that directly influences the process, because the solubility of gases increases with the decrease in temperature. Pressurised biogas is injected through the bottom of the absorption column, and water is channelled inward through the top of a column. The absorption of CO₂ in the water washing process is usually performed at 8–10 bar, although pressures are also used in the range of 10–20 bar. Biogas flows up in the column, and water flows from the top to the bottom of the column. Biomethane with more than 90 % CH₄ is obtained from the top of the purifier, while water containing CO₂ and absorbed H₂S is channelled from the bottom of the column to a flash vessel. Pressure reduction (2.5–3.5 bar) is applied, which results in the release of a gaseous mixture rich in CO₂ (80–90 %) (Kapoor et al., 2019). The main advantages of this technology are simplicity of design, low overall cost, and low loss of methane during the process (less than 2 %). The accumulation of elemental sulphur, corrosion, and unpleasant odour, results of simultaneous absorption of H₂S in water, are problems that occur in this process.

Aqueous organic or inorganic compounds are used to bind the CO₂ or H₂S molecules contained in biogas. The commonly used chemical solvents are amines and aqueous solutions of alkaline salts (sodium hydroxide, potassium, ammonium, and calcium) (Abdeen et al., 2016). The solubility of CO₂ in sodium hydroxide is higher than amines. For example, to absorb 1 ton of CO₂, 1.39 tons of monoethanolamine will be required, and 0.9 tons of sodium hydroxide are needed (Angelidaki et al., 2018). Aqueous alkaline salts are more economical and readily available compared to amines; however, the regeneration of alkaline solutions is expensive due to the high energy requirement. However, if carbonation products from the inorganic absorption process are used in other applications, such as chemical manufacturing, the process may be advantageous. The chemical purification system consists of a packaged bed column integrated into a desorption unit equipped with a reboiler. In chemical purification, biogas is injected into the packaged bed absorber operating at 1–2 bar from the bottom, and the chemical solvent is supplied from the top counter. The CO₂-rich solution obtained from the bottom of the absorber is pumped into a stripping column through a heat exchanger. Solvent regeneration is performed in the stripping column at a pressure of 1.5 bar and heating it to 120–160 °C (Ullah Khan et al., 2017). Foaming, the cost of chemicals, solvent loss due to evaporation and contaminant accumulation, amine degradation, solvent losses, composition problems, corrosion, and operational problems make this system complex compared to other techniques (Kapoor et al., 2019).

Organic solvents, such as methanol mixtures and polyethylene glycol dimethyl ethers, can be used for the physical absorption of CO₂ from biogas. The use of organic solvents has advantages: reduction of recycling rates of absorbents, investment, and operating costs. In addition, another advantage of organic solvent is the low vapour pressure of polyethylene glycol dimethyl ethers, which leads to a low solvent loss during the washing process. During the process, the raw biogas is compressed to 7–8 bar, and the column is cooled to 20 °C before injection into the absorption. The organic solvent is also cooled before being injected from the top. After washing, the organic solvent is regenerated by heating and depressurisation at 80 °C and 1 bar, respectively, in a desorption column. The first step of the process is the compression and cooling of the crude biogas (7–8 bar, 20 °C), followed by its injection into the bottom of the absorption column. The regeneration of the organic solvent is done in the desorption column by heating it to 80 °C while

Table 2.3
Biogas purification technologies and their characteristics (Modified from (Fu et al., 2021; Shah et al., 2021)).

| Technology | Operation | Pressure (bar) | Electrical Consumption (kWh/Nm ³) | Methane losses (%) | Methane purity (%) | Investment (€/Nm ³ biogas) | Maintenance per year (€/year) | Advantages | Disadvantages |
|----------------------------------|------------------------------|----------------|---|--------------------|--------------------|---------------------------------------|-------------------------------|--|---|
| <i>Water scrubbing</i> | Absorption | 6 – 10 | 0.30 – 33.0 | < 1 % | >97 % | 0.13 – 15 | 15,000 | Easy to handle and simple in operation; The large volume of processed gas; Useful in cold regions where CO ₂ solubility increases; High methane purity with less methane loss. | High investment High pressure and energy needed A huge amount of water needed High risk of biological contamination |
| <i>Chemical scrubbing</i> | Absorption | 1 – 1.5 | < 0.15 | < 0.1 % | >99 % | 0.28 | 59,000 | High efficiency; High CH ₄ purity up to 99%; Easy operation; Low CH ₄ loss (<0.1 %); Simultaneous removal of CO ₂ and H ₂ S. | High investment in amine solvents; Toxic solvents are needed; Solutions are needed for reasonable disposal. |
| <i>Solvents scrubbing</i> | Absorption | 4-7 | < 0.25 – 0.33 | 2 – 4 % | >96 % | 0.25 | 39,000 | Fewer liquid inputs, smaller dimensions of the upgrading unit; High CH ₄ purity up to 98%; Simultaneous removal of CO ₂ and H ₂ S; Simple process and easy operation; Low CH ₄ loss. | Use of toxic organic solvents; Difficult regeneration of organic solvents (presence of CO ₂); High temperatures are required for H ₂ S separation. |
| <i>Membrane separation</i> | Permeation | 20-36 | < 0.18 – 0.35 | < 5 % | 90 – 99 % | 0.22 | 25,000 | Dry process; High selectivity to impurities; Removes water vapour; Less mechanical deterioration; No usage of chemicals. | High cost of membranes; Multiple steps are required for high purity; Low membrane selectivity; Pretreatment is needed |
| <i>Cryogenic separation</i> | Compression and condensation | 40 | < 0.18 – 0.66 | < 0.1 % | >99 % | 0.40-0.44 | - | Methane purity is high No use of chemicals and water Possible reuse of CO ₂ | High investment and operation costs; High energy is needed; Under development. |
| <i>Pressure swing adsorption</i> | Adsorption/desorption | 4 -8 | 0.25 | < 3 % | >96 % | 0.26 | 56,000 | Dry process No solvent to dispose No water requirement No microbial impurity Adsorbent usable for up to 3 years | Higher CH ₄ loss; Prepurification equipment is needed to remove H ₂ S from biogas; Pre-drying is needed for water remove from biogas; Contamination by impurities in the biogas. |
| <i>Biological methods</i> | Photosynthetic reaction | Atmospheric | - | - | >99 % | - | - | High methane recovery up to ~97 % Transformation of CO ₂ into other products Production of active biomass Low requirements in terms of land and water | High investment cost and energy; Low photosynthetic CO ₂ uptake; Natural sources are required; High risk of biological contamination. |
| | Chemoautotrophic reaction | Atmospheric | - | - | >99 % | - | - | High selectivity, process efficiency, and CH ₄ purity Conversion of CO ₂ into CH ₄ ; Reduction of CO ₂ emission; Moderate temperatures and atmospheric pressure; Can be integrated with the AD process; Environmentally friendly. | A high amount of reductant is needed; This technology is still under development. |

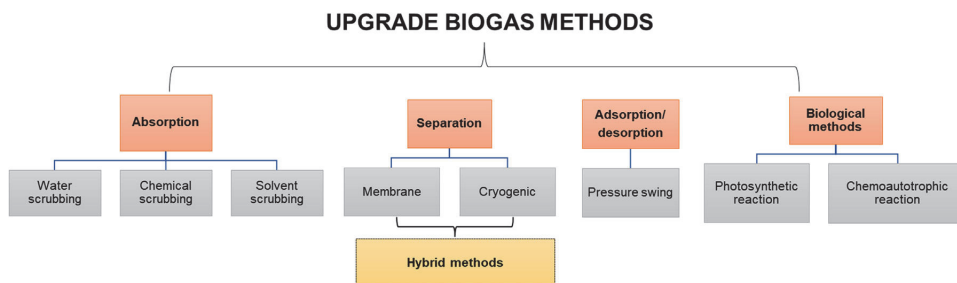


Fig. 2.4. Methods for CO₂ capture from biogas. (For interpretation of the references to color in this figure legend, the reader is referred to the web version of this article.)

the pressure is decreased to 1 bar. The final methane content in the biogas updated using this technology can reach 96–98.5% and less than 2% of CH₄ losses, which can be achieved in an optimised plant on a full scale.

Adsorption involves the selective adhesion or bonding of one or more components to the surface of a microporous solid. The adsorption is classified according to the adsorbent regeneration method. The procedure can occur: a) in a cyclic operation by closing the inlet valve or by using a vacuum (vacuum swing adsorption -VSA), by reducing the pressure to atmospheric level (pressure swing adsorption - PSA), or by varying temperature (30–120 °C) that is carried out at the same pressure level (temperature swing adsorption - TSA) (Nie et al., 2013). Pressure swing adsorption - PSA presents interesting advantages to remove CO₂ from biogas because it employs compact equipment, has low energy requirements, and requires low investment. It is safe, simple, and stable compared to other methods. Another point is that it is suitable for small-scale plants (Aghel et al., 2020). It uses structural adsorbents in the form of granules, pellets, and laminates to separate CO₂ from biogas, which is based on size-selective adsorption strategies (Kadam and Panwar, 2017). Porous carbon is widely used in gas phase separation, and it can be produced by the thermal decomposition of natural and synthetic polymers. However, natural polymers are advantageous due to their high availability and lower costs. Activated carbon is commonly used as an adsorbent due to its high surface area, developed microporosity, thermal stability, ease of reduction, and low production costs (Aghel et al., 2022a).

Vacuum pressure oscillation adsorption (VPSA) technology for CO₂ removal from biogas has low capital investment and low energy consumption and greater applicability in areas with water deficiency (Shen et al., 2018). In adsorption, atoms, molecules or ions adhere to the surface of materials creating an adsorbent layer on the adsorbent surface. Gas adsorption can be based on temperature and pressure, as high pressures and low temperatures promote adsorption efficiency (Zhou et al., 2017). VPSA methods drew more attention to the removal of CO₂ from biogas due to its low capital investment and low energy consumption, which can be applied in areas with water deficiency (Shen et al., 2018).

Cryogenic processes are based on temperature differences for the liquefaction of biogas compounds (Ma et al., 2018). The separation depends on different sublimation points where CH₄ (−161.5 °C) has a lower sublimation point than CO₂ (−78.5 °C). Another strategy is the gradual temperature reduction, which allows the selective separation of CH₄ from other components (Aghel et al., 2022a). In this case, biogas is cooled and compressed until CO₂ is liquefied. With the lower sublimation point of CH₄, the two gases can be separated through distillation (Budzianowski et al., 2017). In cryogenic separation, the difference in the boiling point of the various gas components is explored to separate the components, and obtain high content of CH₄ and CO₂ recovery, generating biomethane of high purity and with minimal methane losses (<1 %). In addition, liquid CO₂ can be generated (usually up to 98 % pu-

riety), and this high-purity liquid CO₂ can be produced at a high-pressure level, which makes it interesting, especially about storage, saving dense compression of energy to store CO₂ as gas (Hashemi et al., 2019). However, some obstacles are encountered by separating CO₂ under the required very low-temperature conditions, hindering its development and applicability: the dense consumption of energy via refrigeration cycles used for separation and the formation of dry ice due to cryogenic separation of CO₂, which generates serious operating problems such as clogging of pipes or other equipment (Yousef et al., 2018b). Although the separation by this method is interesting because it results in very high-purity gas, this method has high electricity consumption and requires a cryogenic production technology of up to −125 °C temperature at pressures of 20–50 bar (Mehrpooya et al., 2020). In a study on cryogenic technologies for biogas update and CO₂ separation, three main systems were identified. In the first system, the biogas is first cooled, and the water is removed, then it is cooled, compressed, and gets CO₂ liquid. In the distillation system, a distillation column is used to remove and liquefy CO₂. In the desublimation process, CO₂ is removed during its phase change from steam to solid inside a heat exchanger (Tan et al., 2017).

Biological biogas update involves the application of microorganisms for the conversion of CO₂ and H₂ into methane. The two metabolic pathways involved in the updating of biological biogas are that with hydrogenotrophic methanogens involved in the direct conversion of CO₂ into CH₄, and another with homoacetogenic bacteria that first convert CO₂ into acetate, and then for conversion into methane by acetoclastic methane (Kapoor et al., 2019).

In biological upgrading methods, microorganisms are employed as catalysts to convert CO₂ and H₂ into CH₄. Different advantages of biological processes can be pointed out over chemical processes, such as the use of moderate temperatures and atmospheric pressure, compared to chemical processes. In addition, higher resistance to gas contaminations, including H₂S, organic acids, and NH₄ is observed (Aghel et al., 2022a). The most important advantage of biological processes is that CO₂ is captured and recycled to be used in the production of new bioproducts. Biological upgrading methods can involve methanogens binding CO₂ into CH₄, dicarboxylic-acid-producing bacteria binding CO₂ into dicarboxylic acids such as biosuccinic acid, or algae binding CO₂ into algal biomass (Fu et al., 2021).

In the last years, microalgae, bacteria, or archaea have been used in upgrading biogas processes (Zhu et al., 2020). According to processes' configurations, these technologies are classified into *in situ* biogas upgrading, *ex situ* biogas upgrading, and hybrid biogas upgrading. In *in situ* configuration, H₂ is injected directly into the biogas reactor to capture the endogenously produced CO₂. In the *ex-situ* strategy, H₂ and biogas are injected into a separate reactor. Hybrid upgrading is a combination of *in situ* and *ex situ* strategies, where the initial *in situ* process occurs in a favourable pH for biological processes, while the last upgrading step is

carried out in an ex-situ process. An advantage of *in situ* biogas upgrading is the integration of biomethanation and biogas upgrading in the same bioreactor in an economically and feasible way (Fu et al., 2021).

2.4. Direct air capture (DAC)

2.4.1. Technological family of DAC

Large-scale direct air capture (DAC) has been considered since the late 1990s as an additional way to mitigate the growing atmospheric CO₂ concentrations. Lackner et al. (1999), Zeman and Lackner (2004) presented an optimistic look regarding DAC. Although ambient CO₂ concentrations are very low, DAC may not totally be unfeasible and detailed a carbon-capture approach utilising Ca(OH)₂. A number of DAC approaches have been proposed using adsorption and absorption technologies, although the topic is still developing (Goepfert et al., 2012; Jones, 2011). DAC is a technique for permanently capturing and storing CO₂ in geological storage sites by separating it from ambient air using chemical, physical, or mechanical methods. Since the CO₂ in the atmosphere is quite diluted (~415 ppm), substantial energy is required while utilising specialised materials. Therefore, the process design and ensuing techno-economic and environmental performances will have a significant impact on their future deployment and participation in climate change mitigation (Qiu et al., 2022).

Pressure swing adsorption (PSA) is utilised in many industrial processes to separate specified gas species from a mixture of gases (usually air). An adsorbent bed (e.g., activated carbon, zeolites, etc.) is used to trap target gas species while the mixture is pressurised. When the pressure is released, the trapped gas species are released. Membranes, such as zeolites, have the potential to become useful for DAC (Gao et al., 2022a; Hong, 2022). Another promising technology is utilising nitrogen-enriched biochar as a CO₂ adsorbent (Sanz-Pérez et al., 2016).

Another technology for carbon capture is temperature swing adsorption (TSA), which alternates the temperature of the sorbent to adsorb and desorb CO₂. TSA is attractive because it is generally less costly than PSA (Zhao et al., 2017c). Veselovskaya et al. (2013) presented an extensive study of utilising K₂CO₃ in g-AL₂O₃ as a composite inorganic sorbent for a TSA cycle for direct air capture.

Removing CO₂ from the atmosphere using alkaline solutions has been investigated since the 1940s (A and Dodge, 1946; Tepe and Dodge, 1943). In various wet-scrubbing techniques, CO₂ is absorbed into a NaOH solution, which leaves behind an aqueous solution of NaOH and Na₂CO₃. Packed scrubbing towers (Baciacchi et al., 2006; Zeman, 2007) and large convective towers (Lackner et al., 1999) are the most frequently used designs for putting NaOH in contact with CO₂. Other investigators (Stolaroff et al., 2008) have generated a fine spray of the absorbing solution to the air through an open tower. It has since been proposed that DAC using CO₂ absorption exclusively by an aqueous solution of NaOH is unfeasible economically (Socolow et al., 2011).

Another alternative to chemisorption- and physisorption-based approaches is to take advantage of the temperature advantage that naturally cold climates, such as the arctic and Antarctica, can provide to desublimite CO₂ directly from the air. Since the outside air temperature is very cold, the idea is not as much energy is needed to cool the air to desublimite CO₂. DAC via cryogenic heat exchangers is still very nascent. Serious consideration to such devices started in the early 2010s with lab-scale benchtop demonstrations (Agee et al., 2013; Agee and Orton, 2016). Follow-up work by several other studies quantified the theoretical energy associated with DAC cryogenic carbon capture plants placed in arctic climates (Boetcher et al., 2020; Perskin et al., 2022; von Hippel, 2018).

2.4.2. DAC performance from real world

2.4.2.1. Performance map of DAC: adsorption as a case study. The chronological results of the amount and proportion of publications on direct air capture (DAC) since 2004 are presented in Fig. 2.5. The keywords of (TS= (direct air capture or DAC) AND TS= (CO₂ or carbon

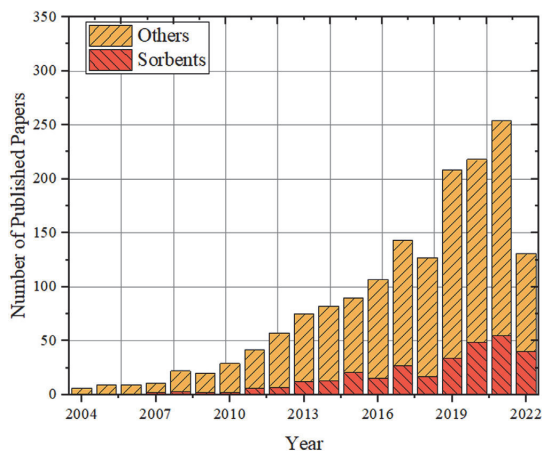


Fig. 2.5. The database pool of DAC performance from 2004 to 2022 (Data collected in July 2022 based on search results of papers from Web of Science). (For interpretation of the references to color in this figure legend, the reader is referred to the web version of this article.)

dioxide) NOT (DT== ("PATENT")) is applied for the literature research. Until July 2022, a total of 1673 articles were collected, with a significant increase in the past four years. Furthermore, the keywords of (TS= (direct air capture or DAC) AND TS= (CO₂ or carbon dioxide) AND TS= (sorbent or *sorbent)) NOT (DT== ("PATENT")) were applied to final obtain 306 articles among these published articles on DAC sorbents, accounting for 18.2% of the total number of articles. Such results are applied to establish a data pool of DAC performance to explore specific development trends.

However, after a detailed screening of summarised data, it could be found that the real-world performance of DAC has not yet demonstrable a clear development trend among various technologies. Due to the relatively active status of research and demonstration, adsorption DAC is taken as the example of the technological family to demonstrate the real-world performance analysis of DAC (Baus and Nehr, 2022; Belmabkhout et al., 2010; Chaikittisilp et al., 2011; Chan et al., 2013; Custelcean et al., 2021; Elfving and Sainio, 2021; Fujikawa et al., 2021; Hemmatifar et al., 2022; Keith et al., 2018; Keller et al., 2018; Mazzotti et al., 2013; Mukherjee et al., 2019; Ruuskanen et al., 2021; Sadiq et al., 2020; Sinha et al., 2017; Sinha and Realf, 2019; Wang et al., 2014; Wang et al., 2020; Wurzbacher et al., 2016; Xu et al., 2020; Zhu et al., 2021). Two main performance indicators of adsorption capacity and energy consumption are employed in Fig. 2.6 with three physical scales: adsorbent-scale, contactor-scale, and system-scale. Due to a lack of standard methods of test and data-report on DAC with different TRLs (Technology Readiness Levels), it is challenging to conduct a fair performance comparison without a classification on various physical scales.

In addition to direct screening of Fig. 2.6, several points are summarised as follows based on the current data pool:

- (1) The adsorbents with large sorption capacities, fast reaction kinetics, strong selectivity, as well as low energy consumption, are so-called 'intrinsic' pursuit of researches not only on adsorbent scale, but also on contactor and system scale.
- (2) The adsorption heat of adsorbent is expected to on a reasonable level of 45-92 kJ/mol CO₂ for potential scale-application of DAC. Thus, amine-modified porous materials have become a primary option due to their excellent comprehensive properties.
- (3) Moisture cannot be ignored in the DAC performance analysis, especially some active candidates of adsorbent, such as amine-modified porous materials. Though the presence of water could

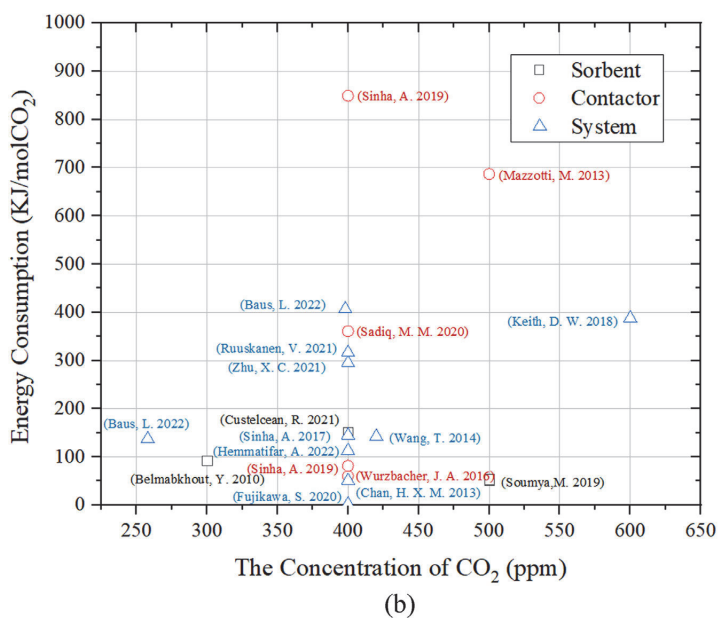
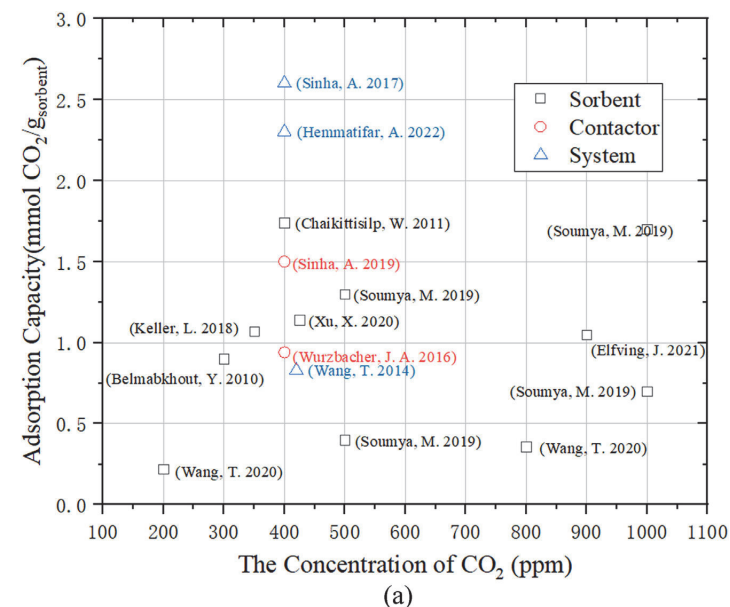


Fig. 2.6. Performance map of adsorption DAC (a) Adsorption Capacity (b) Energy Consumption. (For interpretation of the references to color in this figure legend, the reader is referred to the web version of this article.)

increase the capture performance on some specific moisture level, the adsorption of water would increase the heat of adsorption during the desorption process (Jung and Lee, 2020). Drechsler proposed that a well-designed desorption step of DAC could significantly reduce the co-desorption effect of moisture, and the heat of water vapour can be recovered to further compensate for the desorption heat loss (Drechsler and Agar, 2020).

- (4) Currently, the condition window for DAC research is commonly in a range of 400–420 ppm and 20–25 °C. Considering scenarios of carbon sources are still emerging for potential exploration

in industrial, building, etc. sectors, some relatively concentrated range, e.g. 5% vol, of distributed carbon source, could lead DAC application to a wonderland, with improved capture performance and lower energy-consumption (Zhao et al., 2019b), though it may increase the complexity of the capture system to a certain extent.

- (5) Integrating DAC technology with other technologies could result in an intensive process with a reasonable energy-consumption and improved energy-efficiency of the entire system (Wang et al., 2014).

2.4.2.2. Re-thinking the methodology of performance evaluation of DAC. The efficient operation with reasonable energy consumption is a key prerequisite to the practical application of DAC. Hence, a clear and complete performance evaluation method, especially on energy-consumption or energy-efficient aspects, is critical to scale-up. [Chen et al. \(2021\)](#) employed the benchmarking analysis method to compare the energy-consumption results of temperature swing adsorption (TSA) carbon capture systems with various physical boundaries. It was found that the selection of benchmarking boundary has an important influence on the performance evaluation results, as shown in [Table 2.4](#).

In [Table 2.4](#), e_1 – e_7 are elements of energy consumption during the heating process, depending on which scale is applied in performance evaluation, which commonly includes the sensible heat of adsorbent, the sensible heat of adsorbed gas, the heat of desorption, the sensible heat of adsorption chamber, the heat dissipation of adsorption chamber, the sensible heat of pipelines and auxiliary equipment, and the heat dissipation of pipelines and auxiliary equipment. The e_8 and e_9 are the energy consumption of the blower and the vacuum pump, respectively. By analysing the elements of the energy consumption of DAC technology in [Table 2.4](#), it can be found that there are a few consensuses on which evaluation framework should be applied for the performance analysis of DAC, as a standard framework. Such a knowledge gap would lead to a direct performance comparison among various studies difficult. A simplified guideline would be helpful: according to the specific research aim, the energy consumption of DAC, taking adsorption-kind technology as an example, could be divided into three physical scales: the adsorbent, the adsorption chamber, and the adsorption system. Such rough classification, at least, could be considered as a small step in the scholar community to re-think whether the current confused methodology of performance evaluation is beneficial to the development of DAC.

2.4.2.3. Discussion on DAC performance in real world. In addition to capturing rate and purity, energy consumption is taken into consideration in the performance evaluation framework with the emerging attention on initial investment and operation management of DAC. Although it is a widely-applied indicator for the performance evaluation of DAC, the specific amount of energy consumption during operation is deeply affected by operating conditions such as the composition of the air source and the temperature of the heat source (e.g. heat regeneration). Hence, it is challenging to compare the performance of various DAC systems directly without specific descriptions of design or operation conditions. In addition, this indicator should clearly reflect the energy-saving potential of various DAC technology, as well as the maturity degree of technology, in a direct way.

The efficiency of the second law of thermodynamics (ESLT), which has been successfully applied in the performance evaluation of heat pump, organic rankie cycle, etc., can also be applied in the performance evaluation of DAC to solve the above-mentioned problems ([Landelle et al., 2017](#)). Generally, the ESLT is applied to evaluate the irreversibility of the energy system with a viewpoint of thermodynamics, which could be considered as an indicator to demonstrate the ratio of performance of actual DAC to that of real DAC. In reference [Zhao et al. \(2017a\)](#), it is expressed as follows:

$$\eta_{2nd} = \frac{W_{min}}{W_{ac}} = \frac{W_{min}}{W_{min} + LW}, \quad (2.1)$$

where W_{ac} is the equivalent work input of the actual system; W_{min} is the minimum separation work, that is, the work required for the reversible separation of the ideal mixture under constant temperature and pressure; $LW = T_0\Delta S$ and indicates the irreversibility of the actual system.

Based on the common calculation method, the ESLT of DAC cases from the pool of existing publications is obtained. Due to the lack of real performance data of DAC, more cases of carbon capture are included. The final-chosen cases include absorption, sorption, membrane separation, cryogenics, and integrated technologies ([Berstad et al., 2022](#); [Bounaceur et al., 2006](#); [Cau et al., 2014](#); [Clausse et al., 2011](#);

Table 2.4
The boundary with various elements of energy-consumption: TSA DAC system as a case study.

| Reference | Organisation | Heat consumption (MJ/kg) | Electricity consumption (MJ/kg) | e_1 | e_2 | e_3 | e_4 | e_5 | e_6 | e_7 | e_8 | e_9 |
|---|------------------------------------|--------------------------|---------------------------------|-------|-------|-------|-------|-------|-------|-------|-------|-------|
| Deutz et al. (Deutz and Bardow, 2021) | RWTH Aachen University; ETH Zurich | 11.9 | 2.52 | ✓ | ✓ | ✓ | ✓ | ✓ | ✓ | ✓ | ✓ | ✓ |
| Young et al. (Young et al., 2021) | Heriot-Watt University | 9.93 | 0.8 | ✓ | ✓ | ✓ | ✓ | ✓ | ✓ | ✓ | ✓ | ✓ |
| Zhu et al. (Zhu et al., 2021) | Shanghai Jiao Tong University | 16.23 | 1.3 | ✓ | ✓ | ✓ | ✓ | ✓ | ✓ | ✓ | ✓ | ✓ |
| Sinha et al. (Sinha et al., 2017, 2020) | Georgia Institute of Technology | 0.77 | 2.5 | ✓ | ✓ | ✓ | ✓ | ✓ | ✓ | ✓ | ✓ | ✓ |
| Wurzbacher et al. (Wurzbacher et al., 2012) | ETH Zurich; Chineseworks Ltd. | 11.2 | 0.28 | ✓ | ✓ | ✓ | ✓ | ✓ | ✓ | ✓ | ✓ | ✓ |

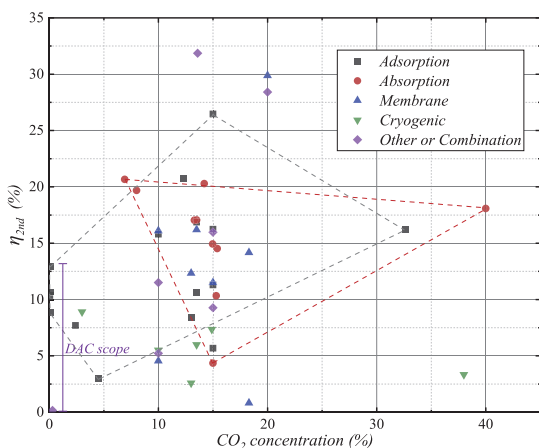


Fig. 2.7. The efficiency of the second law of thermodynamic of different technologies (Zhao et al., 2017a). (For interpretation of the references to color in this figure legend, the reader is referred to the web version of this article.)

Cormos, 2015; Giordano et al., 2017; Grande and Rodrigues, 2008; Hussain and Hägg, 2010; Jiang et al., 2020; Kim and Lee, 2016; Knapik et al., 2018; Krekel et al., 2018; Landelle et al., 2017; Li et al., 2020, 2022; Li et al., 2016; Lin et al., 2021; Lindqvist et al., 2014; Liu et al., 2020; Matthews and Lipiński, 2012; Mletzko et al., 2016; Oexmann et al., 2008; Oreggioni et al., 2015; Pirngruber et al., 2013; Rezaei et al., 2022; Ruan et al., 2014; Sanpasertparnich et al., 2010; Seo et al., 2022; Shen et al., 2012, 2017; Song et al., 2017; Tajima et al., 2004; Tian et al., 2021; Tuinier et al., 2011a, 2011b; Veneman et al., 2015; Versteeg and Rubin, 2011; Wang and Gan, 2014; Wurzbacher et al., 2012; Xie et al., 2014; Zhang et al., 2016; Zhao et al., 2017a), as well as some DAC cases.

As can be seen in Fig. 2.7, the ESLT of adsorption-based carbon capture and DAC ranges from 3–26%, while the absorption-based technologies range from 4–21%. The area enclosed by the grey and red dotted lines represents the ELST ranges of the state-of-art of adsorption and absorption technologies, respectively. It is worth noting that the purple area shows ELST of DAC-related technologies is in a range of 0.15–13%. The fact of ESLT of DAC is relatively lower compared to that of high-concentration CO₂ capture. It is implied that the current knowledge system has weaker support for DAC than that of carbon capture; more efforts should be input into the DAC field to explore its potential for system optimisation.

2.4.3. DAC cost from the real world

2.4.3.1. Cost controversy of DAC. The cost of DAC is uncertain and hotly disputed. Due to the limited research that has been done, the available data are not unified and sometimes even inconsistent. The reason is that the research methods are different, and the method of data report is not systematic and comprehensive. The results of different research projects are inconsistent, and the results of the same project are constantly updated to overturn the existing knowledge. Currently, the cost of DAC typically includes the investment cost, operating cost, material loss, and system maintenance cost of the DAC equipment. Other studies also consider the cost of CO₂ transportation, storage, and utilisation. Early studies on CO₂ capture from the atmosphere primarily focused on producing synthetic fuels (Steinberg and Dang, 1977). Subsequently, the concept of DAC was proposed in the field of carbon capture and storage (CCS) (Lackner et al., 1999). Fig. 2.8 shows the context of the DAC cost battle in recent years.

Some researchers believe that the cost of DAC will be so high that investment in DAC is a mistake because it undermines the incentives for a major clean-modification of the original energy structure. In 2003,

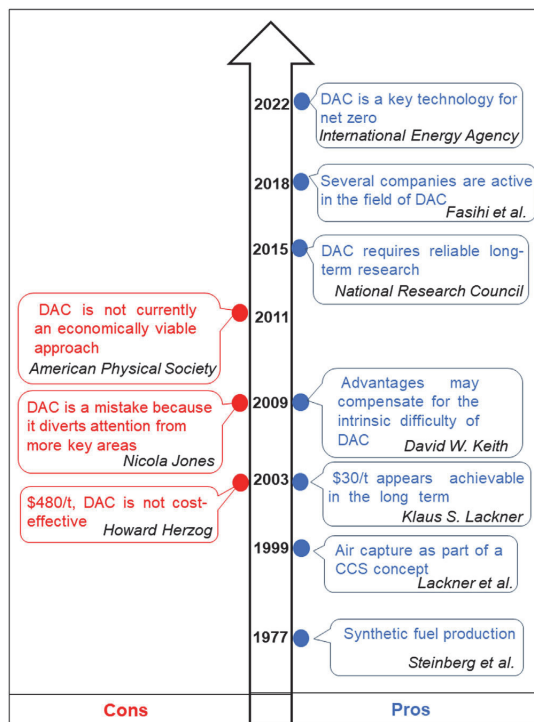


Fig. 2.8. Controversy of DAC development. (For interpretation of the references to color in this figure legend, the reader is referred to the web version of this article.)

Howard Herzog of the Massachusetts Institute of Technology calculated that the cost of DAC technology was as high as \$480–540/t (H, 2003). In 2009, Jones N. of Columbia University argued that the study on DAC may be a complete mistake because it diverted attention and resources from other important fields (Jones, 2009). In 2011, the American Physical Society released a report on *Direct Air Capture of CO₂ with Chemicals*, and stated that DAC was not an economically feasible solution to mitigate climate change (Socolow et al., 2011). The report used a simplified method to calculate the CO₂ avoidance cost of DAC using a sodium hydroxide solution that was \$600/t. In comparison, the CO₂ avoidance cost of post combustion carbon capture from flue gas using the same solution was only \$80/t. Hence, the cost of DAC is approximately eight times that of the post combustion carbon capture. In addition, the report also states that DAC cost is likely to decline as technology advances and new concepts are introduced. However, industry experience suggests that considering the necessary compromises in material selection, process conditions, component efficiency, and component lifetime, the cost of all systems will increase after the pilot operation. Therefore, the report concluded that the adoption of DAC technology should be postponed.

In stark contrast, supporters argue that DAC is relatively inexpensive and plays a key role in managing carbon dioxide emissions. In 2003, Klaus S. Lackner of Columbia University showed that the cost of CO₂ emission reduction would be reduced in the long run (Lackner, 2003). In 2009, David W. Keith reported that although the DAC cost would be higher than the cost of power plants with post combustion carbon capture under the same economic conditions. However, DAC enables the partial decoupling of carbon capture from the energy infrastructure, easing the constraints that arise when new energy technologies must be integrated into the existing infrastructures and making it easier to build

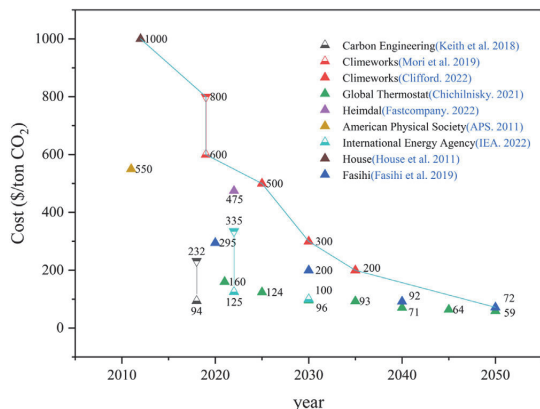


Fig. 2.9. The cost summary of DAC. (For interpretation of the references to color in this figure legend, the reader is referred to the web version of this article.)

a capture plant near the best sequestration sites (Keith, 2009). These advantages can compensate for the inherent difficulties of DAC.

After the report of 2014 International Panel on Climate Change (IPCC) (Pachauri and Meyer, 2014), the international academic community generally changed their views on DAC. In 2015, the National Research Council of the United States released a report stating that long-term research support for DAC is required (Board and Council, 2015). Subsequently, Keith et al. designed a plant for DAC using a potassium hydroxide (KOH) sorbent and calcium-alkali coupling cycle. A detailed calculation showed that the cost of CO₂ was \$94–232/t (Keith et al., 2018). DAC has gradually become a major research focus in the United States, Europe, China, and Japan. For example, the Negative Carbon Plan launched by the U.S. Department of Energy in November 2021 enlisted DAC technology as a key development goal. This strategy aims to reduce the DAC cost to less than \$100/t.

2.4.3.2. How high is the DAC cost in the real-world right now? As shown in Fig. 2.9, many scholars have conducted an economic evaluation of DAC (Baylin-Stern et al., 2022; Chichilnisky, 2021; Clifford, 2022; Fasihi et al., 2019; House et al., 2011; Keith et al., 2018; Mori et al., 2019; Peters, 2022; Socolow et al., 2011). In Mori et al. (2019) conducted a cost assessment of the pilot DAC plant of Climeworks in Iceland. Since the technology and commercial scale was still in the development stage, the cost was approximately \$600–800/t. In 2022, according to Fast company, a start-up company called Heimdall launched the first ocean-assisted carbon removal plant in Hawaii that is currently capable of capturing CO₂ at the cost of \$475/t (Peters, 2022). Some researchers believe that the DAC cost will show a clear downward trend in the long term. In a techno-economic assessment of DAC plants by Fasihi et al. (2019) in 2019, it was reported that the cost of DAC systems would be significantly reduced with large-scale applications in the 2040s and 2050s. By using a low-temperature sorption DAC system that utilises a hybrid photovoltaic power cell system in Morocco as an example, the CO₂ capture costs in 2020, 2030, 2040, and 2050 were estimated to be \$295, \$200, \$92, and \$72/t, respectively. Jan Wurzbacher, co-founder and co-CEO of Climeworks, told CNBC in an interview that the company is focusing on cost reduction in addition to increasing capacity (Clifford, 2022). It is expected that the cost in 2025, 2030, and 2035, can be reduced to \$500, \$300, and \$200/t, respectively. In December 2021, NOAA Zurich report, Graciela Chichilnisky described the DAC technology of Global Thermostat that captures carbon dioxide from the air using waste heat at 85 °C and a proprietary solvent. According to the use of the captured carbon (e.g., beverage filling, carbon dioxide concrete, synthetic fuels, and se-

questration), Global Thermostat has divided the 2020 to 2050 period into nine phases and assessed the cost of each phase. It is estimated that the cost will be as low as \$54/t by 2050 (Chichilnisky, 2021). According to the IEA's report on DAC in Baylin-Stern et al. (2022), assuming different capture technologies, energy prices, and financial assumptions, the cost of DAC capture under a large-scale application of 1 Mt CO₂/year is estimated to be in the range of \$125–335/t. In addition, the IEA also predicts that by 2030, the cost of DAC is likely to be less than \$100/t with the large-scale application of the technology.

2.4.3.3. High or relatively high cost? Currently, the high cost has become the primary factor that limits the commercialisation of DAC technology. However, a good question that needs to be addressed is whether the DAC cost is high or relatively high compared to the environmental cost. The hidden cost can be quantified to a certain extent using external tools such as a carbon tax. As shown in Fig. 2.10, as the amount of captured carbon increases, the cost of DAC increases as well. According to IEA, the cost of DAC under large-scale application conditions (1 Mt CO₂/year) is between \$125–335/t. Low heat and electricity prices could reduce the projected cost to just above the industry target of \$100/t (Baylin-Stern et al., 2022). If the captured carbon could be monetised using some form of carbon pricing scheme, the levelized cost of DAC would be well below \$100/t. Furthermore, a carbon price above \$160/t could make DAC-based capture profitable.

Due to the high flexibility of DAC technology in terms of plant site selection, the best power generation and heating technology could be used in areas with high renewable energy potentials. By 2030, the cost of DAC could be reduced to less than \$100/t. In addition to strong policy and financial support, technological research and development may also cause industrial upgrades. Therefore, cost reduction could be achieved through technological research and development, learning-by-doing, and large-scale implementation (Fasihi et al., 2019).

Other factors, such as social acceptability, policies, and regulations, can also play a critical role in the cost of DAC (Chauby and Dubois, 2022). For instance, DAC systems would be difficult to be adopted without a policy-driven carbon tax price. It is worth mentioning that most of the key levers in existing studies are also necessary to facilitate the implementation of other low-carbon technologies, such as photovoltaics and wind power (Chauby and Dubois, 2022). Therefore, a cost assessment of DAC should not merely focus on a step-by-step reduction of the cost of the DAC technology itself, but a moderately accurate quantitative method should be developed for the environmental cost related to global warming.

2.4.4. Perspectives on DAC

In order to meet specific climate targets, such as those outlined in the Paris agreement, it is imperative that all CO₂ removal technologies be explored (Allen, 2019; Shayegh et al., 2021). Capturing CO₂ at the source, such as at power plants, may not be enough. Other avenues, such as DAC, although more costly than capturing at the source, will be required. Although several groups are conducting research on various DAC approaches such as adsorption, absorption, and cryogenic capture, considerable research will need to go into scaling up these technologies so that they can be feasibly implemented in real-world systems. The risks of implementing such systems are enormous, including environmental, ethical, and technical risks (Lenzi, 2018). Furthermore, massive spending, estimated to reach a third of government general expenditures in developed countries, will be required (Bednar et al., 2019).

The five pillars of DAC, as shown in Fig. 2.11, are (1) capture technology, (b) energy demand, (c) cost, (d) environmental impact, and (e) political support (Ozkan et al., 2022). Currently, DAC technologies need to be improved to reduce costs. Costs of less than \$100/tonne of CO₂ are needed to make DAC viable economically. The costs include capital equipment, maintenance, and operation due to the very low concentrations of CO₂ found in the atmosphere.

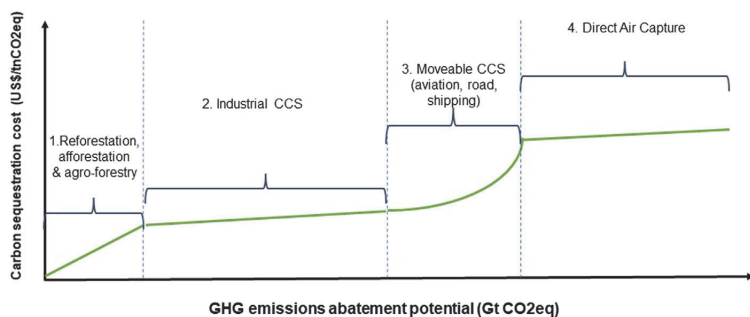


Fig. 2.10. Carbon abatement cost curve (Research, 2019). (For interpretation of the references to color in this figure legend, the reader is referred to the web version of this article.)

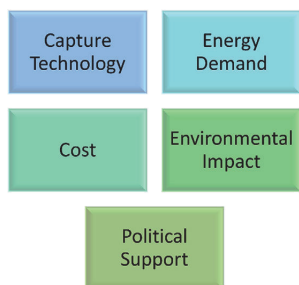


Fig. 2.11. The five of DAC as outlined by Ozkan et al. (2022). (For interpretation of the references to color in this figure legend, the reader is referred to the web version of this article.)

According to a recent report (Budinis, 2022), there are currently 18 DAC plants in Europe, Canada, and the United States that are in operation that captures nearly 0.01 MtCO₂/year. As stated by the “net-zero emissions by 2050 scenario,” (IEA, 2021) DAC should be scaled-up to capture at least 60 Mt/CO₂ by 2030. The first 1 Mt/CO₂ DAC plant is expected to be fully operating in the United States by 2025, with even more DAC facilities planned.

3. CO₂ capture with sorbents

3.1. Liquid-based sorbents amine solutions

3.1.1. Amine solution

Chemical absorption using amine solvent is a relatively mature post-combustion CO₂ capture method at present, which has realized industrial application from large fixed emission sources such as coal/gas power plant flue gas (Wang et al., 2021; Zhang and Liu, 2013) It is an important technical route to achieve large-scale CO₂ reduction at this stage, and it is also the only low-concentration CO₂ capture technology in the world that can achieve large-scale commercial applications (Weidong et al., 2009). Taking monoethanolamine (MEA) as an example, CO₂ can react with it to form corresponding water-soluble salt and release CO₂ when heating it at 100~140 °C, thus realizing the capture and enrichment of CO₂. The CO₂-rich MEA solvent enters the digestion unit after being heated by the heat exchanger and releases CO₂. However, the shortcomings of the chemical absorption method using amine solvents are also very obvious (Xuepeng, 2014) Due to the large flue gas flow and low CO₂ partial pressure, the investment cost and operation energy consumption of the chemical absorption method are high. Secondly, amine solvents such as MEA have poor stability and are easy to degrade in contact with oxygen in the air. (Lin Haizhou et al. (2019)) In addition, it is necessary to control the concentration of sulphur oxide

and nitrogen oxide in the combustion tail gas of the separation unit below 10 ppm to prevent the amine liquid from reacting with the above impurities and deteriorating rapidly. In addition, this kind of solution is highly corrosive and requires relatively expensive pipeline and equipment investment in the early stage.

The average energy consumption of amine chemical absorption carbon capture technology in China is about 2.4~3.2 GJ/t CO₂, reaching the same level in the world, but it is still in the industrial demonstration stage due to lack of large-scale industrial or commercial application. China has designed large-scale and major CCUS demonstration projects, such as the Huaneng Shanghai Shidongkou Carbon Capture Demonstration Project (100000 tons/year) put into operation in 2009, the Shengli Oil Field Flue Gas Carbon Capture Project (40000 tons/year) put into operation in 2010, the CCUS Test Platform Project of China Resources Power Haifeng Company (20000 tons/year) put into operation in 2019, and the National Energy Group Jinjie Carbon Capture Demonstration Project (150000 tons/year) put into operation in 2021, The relatively mature chemical absorption technology of mixed amine solution is adopted.

Internationally, the amine liquid chemical absorption method has a high maturity and is widely used in the existing coal-fired power plants and other flue gas CO₂ capture, and has completed the industrial demonstration and large-scale commercial operation stage internationally. In 2014, Canada put into operation the SaskPower boundary dam project with a capacity of 1 million tons/year, the United States put into operation the world's largest PetraNova project with a capacity of 1.4 million tons/year in 2017, and Japan put into operation the Mikawa biomass combustion power plant with a capacity of 150000 tons/year carbon capture project in 2020, all of which use amine chemical absorption capture technology. The average energy consumption of amine regeneration is 2.6~3.0 GJ/tCO₂.

3.1.1.1. Mixed amine solution. The mixed amine technology combines the advantages of different organic amines. (Han Shuyi et al. (2014)) It reduces the energy consumption of regeneration by optimizing the proportion of amine liquid in different proportions and is widely used in the post-combustion chemical absorption method at this stage. A mini review studied several commercial amine blend solvents licensed by companies such as BASF, DOW, Fluor Daniel Co. MHI Shell Co, etc., with high “energy efficiency”. Aghel et al. (2022b) Most primary amines exhibit enthalpy of CO₂ solubility that represents CO₂ absorption heat about 80–90 kJ/mol CO₂, and secondary amines contain lower enthalpy of 70–75 kJ/mol, and tertiary amines contain the reduced enthalpy within the range of 40–55 kJ/mol. (Flores-Segura and Torres, 1997) The lower enthalpy of amine reflects lower heat duties but with higher absorption rates. The amine blends can reach very low heat duty and moderate absorption rates with optimized combination ratios.

Based on literature review, Table 3.1 plotted 5 famous branches of solvent improvement / blended amine solution, along with the most re-

Table 3.1
Major solvent improvement methods in amine blend in CO₂ absorption.

| System | Use of reagent | Time |
|--|---|------------|
| MEA based blended amine | MEA + R ₃ N | Since 2005 |
| PZ based blended amine | PZ + K ₂ CO ₃ , PZ + R ₃ N | Since 2005 |
| AMP based blended amine | AMP + DETA, AMP + EAE, AMP + DETA + PZ | Since 2016 |
| The selection rules developed based on structure -performance correlation | MDEA, DEEA, 1DMA-2P, 3DMA-1P | Since 2016 |
| The "absorption-desorption parameter" studies of single and blended amines | BEA, AMP, BEA + AMP | Since 2017 |
| The "coordinative effect" of MEA + RR'NH of single amine | MEA (activator) + DEA (dominant) | Since 2018 |

cent 6th one: tri-blends containing coordinative effects. The 1st branch was famous and common, which is blending MEA with various tertiary amines MEA + R₃N (5 + 0~2 mol/L) since 2005. (Decardi-Nelson et al., 2017; Gao et al., 2017; Liao et al., 2017; Liu H et al., 2017; Raphael Idem et al., 2006; Roongrat et al., 2005; Sema et al., 2012; Shi et al., 2014b; Srisang et al., 2018; Zhang et al., 2019) Several typical examples were MEA + MDEA, MEA + DEAB, MEA + DEEA and etc. (Decardi-Nelson et al., 2017; Gao et al., 2017; Liao et al., 2017; Liu H et al., 2017; Raphael et al., 2006; Roongrat et al., 2005; Sema et al., 2012; Srisang et al., 2018; Vega et al., 2020; Zhang et al., 2019) It integrated the advantages of MEA (quick CO₂ absorption reaction rates) with tertiary amines (lower energy cost and larger cyclic capacity) and offset the disadvantage of MEA (higher energy cost of desorption and smaller cyclic capacity) with tertiary amine (slower absorption rates). For example, Zhang et al. used MEA (5M), MEA MDEA (5:1 molar ratio, total content 6M) and MEA-1DMA2P (5:1 molar ratio, total content 6M) as blended amine solution. The results show that as an additive in MEA, 1DMA2P has better potential than MDEA to generate bicarbonate ions under the condition of poor CO₂ load and reduce the regeneration energy. (Zhang et al., 2016) The 2nd branch was mixing piperazine (PZ) with various types of tertiary amines PZ + R₃N or K₂CO₃, etc. (Brüder et al., 2011; Cullinane and Rochelle, 2004; Gao et al., 2018; Li et al., 2014; Zhao et al., 2017) The concept integrates the advantage of PZ (faster absorption rate) with tertiary amine (lower energy cost and larger cyclic capacity) and offsets the disadvantage of PZ (easy to precipitate and poison to human life) and tertiary amine (lower absorption rates).

The 3rd branch was blending AMP based amine with either bi-amine blends or tri- amine blends, which fully exerted the advantage of AMP (higher desorption performance with moderate absorption performance). The carbamate of AMP was unstable, which was easy to hydrolyze under heat. Ciftja et al. (2014) After 2016, a large number of studies involved tri-solvents of MEA + AMP + PZ, (Nwaoha et al., 2017, 2016b) MDEA + DETA + AMP (Nwaoha et al., 2016a) and bi-solvents: AMP + PZ, (Brüder et al., 2011) and AMP + DETA, (Wai et al., 2018). Zhang et al. studied the regeneration behaviour of 6M MEA-AMP-PZ (monoethanolamine, 2-amino-2-methyl-1-propanol and piperazine) tri-solvent mixtures loaded with CO₂ with different AMP/PZ molar ratios and blank mixtures at 96 °C. For non-catalytic operation, the results show that compared with 5M MEA, all three solvent mixed amines greatly increase the CO₂ desorption rate, and cycle capacity and reduce the relative heat load. ¹³C NMR analysis showed that 3M MEA-2.5M AMP-0.5M PZ blend with the highest AMP/PZ ratio produced the largest amount of bicarbonate and less carbamate, which led to the best desorption performance (Zhang et al., 2018c).

The 4th branch started to investigate the chemical property of amines by their molecular structure (hindrance), kinetics (k₂) and basicity (pKa), and correlate the performance with its CO₂ absorption and desorption performance such as absorption rates, equilibrium CO₂ solubility (α_{eq}), heat duty (H), etc. (Singto et al., 2016). Several studies developed various selection rules of tertiary amines (R₃N), (Xiao et al., 2016) which is named as "fast screen method" in 2016. (Xiao et al., 2016) Other studies (Singto et al., 2016), (Luo et al., 2016; Muchan et al., 2017) also reported the selection rules of different amines based on "structure-activity correlations" based on equilibrium solubility, pKa analysis, and absorption rates after 2016–2017.

The 5th branch developed a set of comprehensive "absorption-desorption" parameters of various single amines, such as primary, secondary and tertiary amines in order to compare various single amines at a consistent level. Later on, these sets of parameters were extended to a blended amine solution (Shi et al., 2018). The absorption and desorption parameters integrated the initial absorption rates, equilibrium CO₂ solubility, initial desorption rates, heat duty and cyclic capacity, etc. into two equations. That study discovered that BEA and AMP possessed optimised absorption parameters and desorption parameters (Narku-Tetteh et al., 2017). AMP had a very high desorption parameter with a relatively adequate absorption parameter, while BEA had a very high absorption parameter with relatively good desorption parameter (Narku-Tetteh et al., 2017). Based on intensive analysis, the 2 + 2 mol/L BEA + AMP blended amine solvents were prepared, and tested with heterogeneous catalysts in both absorber and desorber in a batch process and bench scale pilot plant study (Afari et al., 2018; Narku-Tetteh et al., 2018; Natewong et al., 2019; Prasongthum et al., 2019). After studies of these 5 branches, the methodologies of liquid amine solutions were upgraded to highly accurate quantitative analysis. The preparation method was developed from "combination of the advantage of two amine blends" since 2005, (Roongrat et al., 2005) to "structure-activity correlation" since 2016 (Singto et al., 2016) and "absorption-desorption parameter analyses" since 2017 (Narku-Tetteh et al., 2017). The research focus was always at "heat duty oriented analysis" (energy efficient and low cost) by analysing the individual energy contribution: such as absorption enthalpy, sensible heat, and heat of vapourization (Narku-Tetteh et al., 2018; Nwaoha et al., 2017).

The 6th branch was developed in 2018. It is the application of "coordinative effect" onto "bi-solvents" or "tri-solvents", together with absorption-desorption parameters analysis (Narku-Tetteh et al., 2017) of the 5th branch to analyse the performance of amine solution comprehensively. Firstly, Liu et al.³¹ and Shi et al. (2020), (2018) discovered "coordinative effect" of MEA + RR'NH, which could facilitate CO₂ absorption (Shi et al., 2022) and desorption (Shi et al., 2020, 2018) simultaneously. This performance was contradictory to the general rule that MEA enhance CO₂ absorption performance and weakens desorption performance. (Nwaoha et al., 2017). The coordinative effect was already verified to exist within MEA + DEA (RR'NH) bi-solvent at the ratio of 0~0.5/2 (Shi et al., 2020) and MEA + BEA (RR'NH) + AMP tri-solvent at 0.1~0.5 + 2 + 2 mol/L³⁴. Experimental results confirmed that their absorption and desorption performance was better than that of BEA + AMP 2 + 2 mol/L simultaneously (Hsa et al. 2021). Recently, other similar tri-solvents with the coordinative effect of MEA + EAE + AMP (Shi et al., 2022; Zhang et al., 2022) MEA + BEA + DEEA (Shi et al., 2022) were also studied by Shi et al. and exhibited higher absorption desorption performance.

3.1.1.2. Non-aqueous amine solution. It has been well understood that energy consumption was the main factor affecting the efficiency of power plants when employing the CO₂ capture process (Chakma, 1995; Oexmann and Kather, 2010; Tan et al., 2011). Water evaporation in conventional aqueous amine solutions is the major reason for the high energy consumption (Guo et al., 2014; Leites, 1998; Li et al., 2012). Using organic solvents instead of water provides significant advantages. For example, it can reduce decomposition at high temperature and

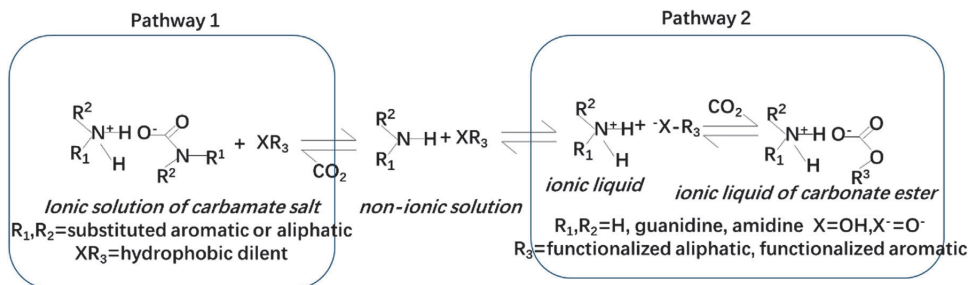


Fig. 3.1. Reaction pathways for RTI's NASs. (For interpretation of the references to color in this figure legend, the reader is referred to the web version of this article.)

energy cost in the regeneration step due to their low heat of vapourization and high boiling temperature (Barzagli et al., 2013; Yu et al., 2013). Recently, non-aqueous amine solutions have been extensively investigated. Lail et al. (2014) developed improved RILs called "non aqueous solvents" (NASs). These solvents are composed of hydrophobic, steric, carbamate forming amine (with low water solubility) and an unspecified amount of low vapour pressure organic diluents to produce NASs with minimum foaming, viscosity reduction and water accumulation. Two families of promising NASs have been discovered and the general reaction pathways with CO_2 are depicted in Fig. 3.1.

Barpaga et al. (2022) found that dilute water solvents have unique thermodynamic and physical properties that can be used to improve efficiency. Water-poor solvents have shown water resistance. The reboiler load is lower and the mass transfer rate is higher than expected, but the increase of intrinsic viscosity must be balanced. David et al. Heldebrant et al. (2017) also studied the comprehensive examination of GAP/TEG solvent system at a molecular level to slow down hydrolysis and reduce viscosity. This discovery makes it possible to design one-component silicone-free diamine derivatives, which can reduce viscosity by adding selective chemical groups at specific positions, direct placement and directional hydrogen bonding. Compared with the original GAP/TEG formulation, the viscosity is reduced by 98%. Chen et al. (2015) studied that compared with the use of triethylene glycol (TEG) or diethylene glycol (DEG) cosolvent, the CO_2 capture formula produced by ethyl monoethanolamine (EMEA) solution in tertiary ethanolamine cosolvent (such as diethylethanolamine (DEEA) or MDEA) has higher equilibrium solubility and high cycle capture capacity. DEEA participates in chemical absorption by extracting protons from EMEA carbamate intermediates. Moreover, using tertiary amine DEEA in non-aqueous solvent has better performance than using alcohol and glyco (Chen, S. et al., 2016).

Sada et al. studied the kinetics of CO_2 absorption with mono- and diethanolamine in non-aqueous solvents, such as methanol, ethanol and 2-propanol (Sada et al., 1985). Versteeg et al. developed a CO_2 absorption system of MDEA in ethanol and concluded that in non-aqueous solutions, no reaction, even no alkylcarbonate formation, occurred between CO_2 and tertiary alkanolamines (Versteeg and van Swaaij, 1988). Sami et al. observed the pseudo-first-order rate constant value for the reaction of aniline/cyclohexamine/hexamine with carbon dioxide in ethanol and the results favoured the zwitterion intermediate mechanism (Ali et al., 2000). Park et al. measured the chemical absorption rate of CO_2 with DEA, DIPA, TEA and MDEA in non-aqueous solvents, such as methanol, ethanol, n-propanol, n-butanol (NBA), ethylene glycol, propylene glycol, and propylene carbonate (Hwang et al., 2010; Park et al., 2006, 2005, 2006). Tan et al. explored the CO_2 capture process with a mixture composed of MEA and triethylene glycol (TEG) (Tan et al., 2011). Li et al. studied the mixed non-aqueous solutions of MEA, DEA, and diglycolamine (DGA) with polyethylene glycol (PEG) as non-aqueous solvent for CO_2 capture (Li et al., 2012). Zheng et al. examined the CO_2 solubility in the non-aqueous solutions of AMP–diethylene glycol

(DEG) and AMP–triethylene glycol (TEG) (Zheng et al., 2012). Guo et al. investigated a mixture of 2- (2-aminoethylamine)ethanol with benzylalcohol (BP) as absorbent for CO_2 capture. Guo et al. (2014) Barpaga team (Cantu et al., 2020) developed and studied the aqueous diamine solvent N1- (2-ethoxyethyl)- N_2 , N_2 -diisopropylethane-1,2-diamine (2-EEDIPEDA).

The CO_2 capture performance of the solvent was evaluated from the aspects of adsorption characterization such as vapour-liquid equilibrium adsorption kinetics and viscosity, and it was found that its performance was ahead of that of aqueous dilute amine solvent and its economic cost was as low as 46.8 USD/ton. The results of Fu et al. (2020) showed that the viscosity of the three EHA non-aqueous solutions was smaller (<3 mPa·s) at the temperature range of 303.2 K ~ 323.2 K, which was conducive to the mass transfer and initial absorption rate of CO_2 absorption. These three non-aqueous adsorbents had good application potential in the process of CO_2 capture.

Zheng et al. (2016) studied the process mechanism of lean water CO_2 combined with organic liquid (CO_2 BOL) solvent platform and polar swing assisted regeneration (PSAR). From thermodynamics, dynamics and bench scale data, combined with Aspen Plus, the full-size process performance under three CO_2 BOL/PSAR conditions were predicted, the material performance was discussed, and the viscosity was determined as the key characteristic that most seriously limited the viability of the water-poor solvent platform.

The Water-poor solvents retain the chemical selectivity of water amine and utilise the lower specific heat of organic matter relative to water to reduce the load of the reboiler, that is, the energy required for the regeneration of solvent. In terms of time and cost, the dilute water solvent can be used as a drop-in solvent substitute that can use the first and second generation of water amine infrastructure. In addition to the characteristics of high boiling point, low specific heat and low evaporation enthalpy of organic solvent, the use of organic solvent instead of water to build an anhydrous absorbent system is expected to reduce the energy consumption of regeneration, and also reduce solvent loss and equipment corrosion. The future experimental work will focus on testing the new iteration of a similar amino-based dilute water solvent with different hydrophilicity to understand the impact on carbon dioxide capture while developing new configuration and process design to further improve the efficiency and cost of the solvent, and testing the use of lean water solvent for carbon dioxide capture after combustion with large-scale platform, testing its efficiency and calculating its cost.

3.1.1.3. Phase-change amine solution. Recently, biphasic solvents, forming two immiscible phases (CO_2 -rich and CO_2 -lean phases) during the CO_2 capture process, have attracted increasing interest because the process only transports the CO_2 -rich phase into the desorption tower, which greatly reduces the volume of solution to be desorbed and regenerated and reduces the energy consumption for water evaporation and

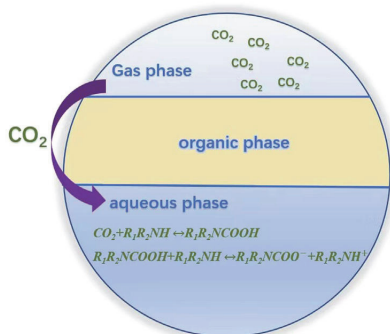
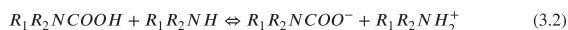


Fig. 3.2. Phase separation schematic diagram of biphasic solvents. (For interpretation of the references to color in this figure legend, the reader is referred to the web version of this article.)

sensible heat, thus reducing the energy consumption for regeneration reduced (Raynal et al., 2011; Zhou et al., 2019). A biphasic solvent typically consists of active amines and a phase-separation agent. As shown in Fig. 3.2, the active amine is a primary or secondary amine with a fast reaction rate, and the phase separation agent is a tertiary amine that cannot react directly with CO_2 , so it plays a role as a catalyst in the absorption process (Ye et al., 2015).

The primary or secondary amine ($\text{R}_1\text{R}_2\text{NH}$) can absorb CO_2 and form a carbamate acid (Reaction 3.1), which can then be deprotonated by a base (Reaction 3.2) such as tertiary amine. The formation of the carbamate greatly increases the solvent polarity and changes the density. Phase separation occurs if the carbamate is immiscible with a phase-separation agent. Phase separation can occur, a phenomenon known as the salting-out effect.



Tertiary amines such as *N,N*-diethylethanolamine (DEEA), *N,N*-dimethylcyclohexylamine (DMCA), and pentamethyldiethylenetriamine (PMDTA) are used as phase-separation agent because of their low polarity, which allows the salting out of the carbamate to form aqueous and organic phase (Liu et al., 2019a; Liu et al., 2019b; Pinto et al., 2014a, 2014b; Ye et al., 2015; Zhang et al., 2018). Pinto et al. proposed an aqueous biphasic solvent comprising 5 M DEEA mixed with 2 M *N,N*-methyl-1,3-diaminopropane (MAPA), compared with 5 M MEA, the DEEA-MAPA biphasic solvent requires lower heat to absorb, and can regenerate at high pressure or low temperature, which has a high cyclic absorption capacity (2 mol kg^{-1}) and a low regeneration energy consumption ($2.2\text{--}2.4 \text{ GJ t}^{-1} \text{ CO}_2$) (Pinto et al., 2014b). Zhang et al. studied the phase change behaviour of five different tertiary amines (DEEA, DMCA, PMDETA, 3-(diethylamino)-1,2-propanediol (DEAPD), and bis(2-dimethylaminoethyl)ether (BDMAEE)) on triethylenetetramine (TETA), total amine concentration is 4M, the molar ratio of DMCA and TETA is 3:1, and found that TETA-BDMAEE and TETA-PMDETA were inferior to MEA in absorption capacity, TETA-DEAPD had the strongest absorption capacity, but due to the low hydrophobicity of DEAPD no phase separation occurred during absorption, TETA-DEEA formed a homogeneous phase at high CO_2 loading, and only TETA-DMCA showed high stability in absorption capacity and phase change behaviour, the rate of CO_2 absorption into this biphasic solvent was comparable to that of the 5 M MEA solution, while the regeneration energy reduced by approximately 40% compared with that achieved with MEA (Zhang et al., 2018). Zhou et al. explored a novel biphasic solvent comprising PMDTA and diethylenetriamine (DETA) with a CO_2 -absorption

loading of $0.613 \text{ mol CO}_2 \cdot \text{mol}^{-1}$ amine, in which 99.7% of the absorbed CO_2 was distributed in the lower phase, accounting for 57% of the total volume. The regeneration energy was reduced to $2.40 \text{ GJ t}^{-1} \text{ CO}_2$. (Lv et al., 2019; Zhou et al., 2017).

Organic physical solvents such as diethylene glycol dimethyl ether (DGM), diethylene glycol diethyl ether, 1-propanol, *N*-heptanol, and sulfone are often used as physical solvents and phase splitters (Luo et al., 2016; Wang et al., 2019; Xu et al., 2019). For example, Wang et al. (2021) used 1-propanol as a phase splitter mixed with an aqueous MEA solvent and triggered the liquid-liquid phase-change. Compared with pure MEA solution, the cycle capacity was increased from 1.01 mol/kg to 2.51 mol/kg after the addition of 1-propanol, and the biphasic solvent was able to reduce the energy consumption to $2.87 \text{ GJ t}^{-1} \text{ CO}_2$ (Wang et al., 2019). Liu et al. developed 2-amino-2-methyl-1-propanol (AMP)/MEA blend-based biphasic solvents using diethylene glycol dimethyl ether and sulfolane as phase splitters, and shows that AMP/MEA blends with physical solvents have higher CO_2 absorption rate, with the most excellent being 69% higher CO_2 -absorption capacity and 36% lower regeneration energy than those achieved using 30 wt% MEA (Liu et al., 2019a). Hu et al. developed a biphasic solvent consisting of 2-(methylamino) ethanol (MAE), 3-(dimethylamino)propan-1-ol (3DMA1P), DGM and water with a CO_2 loading of 1.59 mol/kg , which is 74.2% higher compared to 30 wt% MEA, and demonstrated by simulation that the concentration of DGM has an effect on the absorption rate of CO_2 (Hu et al., 2022).

Non-aqueous solutions generally use organic reagents as solvents such as alcohols, polyethers, and alcohol (Tao et al., 2018; Zhuang and Clements, 2018). However, precipitation often occurs when alcohols or polyethers are used as phase splitters, forming a solid-liquid biphasic solvent (Chen et al., 2020). The liquid-solid biphasic solvents have significant advantages such as good absorption performance and low regeneration energy consumption, but the formation of solid products makes it difficult to transport to the resolution tower for desorption and regeneration. In addition, it can cause operational problems such as equipment fouling and plugging. Therefore, liquid-liquid biphasic solvents are more attractive. Zhou et al. proposed a novel non-aqueous liquid-liquid biphasic solvent composed of 2-(2-aminoethyl-amino)ethanol (AEEA) as an active amine, dimethyl sulfoxide (DMSO) as a diluent, and *N,N,N,N'*,*N'*-pentamethyldiethylenetriamine (PMDETA) as a phase splitter with a high CO_2 -absorption loading ($1.75 \text{ mol mol}^{-1}$); 96.8% of the absorbed CO_2 was in the lower phase. The regeneration energy consumption could be reduced to $1.66 \text{ GJ t}^{-1} \text{ CO}_2$. Moreover, the biphasic solvent in the CO_2 saturated state did not exhibit corrosion behaviour on carbon steel CO_2 absorption products with high polarity are more willing to dissolve in the polar DMSO solvent rather than in the less polar PMDETA, resulting in phase-change behaviour (Li et al., 2021; Zhou et al., 2020). Hence, phase-change behaviour can be obtained by modifying the solvent polarity. Note that the polarity of the phase-splitting agent should be lower than those of the active amine and diluent.

3.1.1.4. Amine solution regeneration using catalysts. The addition of solid acid catalysts to CO_2 -rich amine solution is considered as one of the potential methods to reduce the energy consumption for CO_2 regeneration, as it can help decompose the carbamate by providing protons to increase the desorption rate and reduce the desorption temperature (Sun et al., 2021; Zhang et al., 2019b). The principle of catalytic desorption with solid acid catalyst is shown in Fig. 3.3.

Domestic and international research based on solid acid catalysts has focused on metal oxides, zeolites, mesoporous silica, sulfated metal oxides, and composite catalysts (Alivand et al., 2020; Zhang et al., 2019b). Metal oxides have a wide range of industrial applications as solid acid catalysts because of the acidic sites provided by surface defects (Lewis acidity, Brønsted acidity). The addition of $\gamma\text{-Al}_2\text{O}_3$ as a catalyst to the rich solution was first proposed by Idem et al., and experimental data showed a 27% decrease in energy consumption for the regeneration

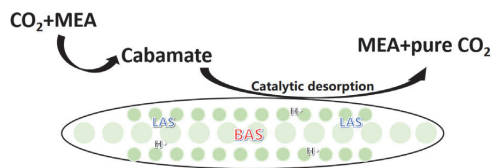


Fig. 3.3. Principle of catalytic desorption with a solid acid catalyst (Xing et al., 2021). (For interpretation of the references to color in this figure legend, the reader is referred to the web version of this article.)

of 5 M MEA aqueous solution (Shi et al., 2014a; 2014b). The catalytic properties of metal oxides (TiO₂, SiO₂) were investigated by Wang et al. and compared with γ -Al₂O₃. The result showed that TiO₂ was the most effective and that the addition of TiO₂ to MEA increased the desorption rate by more than 10% and reduced the desorption time by more than 40% compared to MEA with no catalysts (Wang, T. et al., 2016). Bhatti et al. systematically investigated the desorption kinetics of MEA aqueous solutions with metal oxide catalyse and found that V₂O₅, MoO₃, Ag₂O, and Nb₂O₅ exhibited better catalytic performance due to the presence of both Lewis and Brønsted acids on the surface (Bhatti et al., 2018a, 2017, 2018b). Ji et al. (2022) found that adding ZrO (OH)₂ and FeOOH to CO₂-rich amine solution can reduce the desorption heat load by 45% and 47%, respectively. Jiang et al. prepared metal hydroxyl oxide AlOOH and applied it to CO₂ desorption, and found that the addition of AlOOH increased the desorption rate by 560% and the amount of desorption by 251% (Jiang et al., 2022).

Previous studies have shown that the addition of synthetic zeolites (HZSM-5, HY, HB, SAPO-34) to the CO₂-rich amine solutions can also improve CO₂ desorption performance. Xu et al. found that HZSM-5 could effectively promote CO₂ regeneration and reduce regeneration energy consumption by 23.9% (Xu et al., 2020). Bhatti et al. prepared a range of HZSM-5 with different properties and investigated its catalytic performance in CO₂-rich amine solutions and found that optimally adjusted HZSM-5 could reduce the relative heat load by 62.7% (Bhatti et al., 2020). Zhang et al. found that HB with a larger mesoporous specific surface area and more Brønsted acid centers could improve CO₂ desorption performance by 1360.8% and reduce regeneration energy consumption by 66.1% (Zhang et al., 2019a). Through their study, Srisang et al. found that the catalytic performance of HY in CO₂-rich amine solutions was significantly inferior to HZSM-5 (Srisang et al., 2017). A commercial SAPO-34 had a similar surface area, average pore width and Brønsted to Lewis acid ratio to HZSM-5, but SAPO-34 showed a lower catalytic efficiency in CO₂-rich amine solutions than HZSM-5 due to the lower number of total acid sites on SAPO-34 compared to HZSM-5 (Zhang et al., 2018c). Natural zeolites are considered an ideal alternative to CO₂ desorption catalysts due to their unique advantages such as low price and high availability. However, only H-mordenite zeolite was reported to be applied as a catalyst for CO₂ desorption, showing similar catalytic performance to HZSM-5 (Zhang et al., 2019a). Mesoporous silica such as MCM-41 and SBA-15 has also been used to catalyse CO₂ desorption due to their regular mesoporous structure and small amounts of Brønsted acid. However, their catalytic performance was inferior under the same conditions compared to that of HZSM-5 (Gao et al., 2020; Liu H et al., 2017; Zhang et al., 2017).

Sulphated metal oxides exhibit more acidic sites due to the presence of sulphur atoms in their structure (Almeida et al., 2008; HINO and ARATA, 1979; López et al., 2000). As reported in previous years, the catalytic effects of sulfated zirconia (SO₄²⁻/ZrO₂), sulfated TiO₂ (SO₄²⁻/TiO₂), and sulfated Fe₂O₃ (SO₄²⁻/Fe₂O₃) was inferior to HZSM-5 and MCM-41 because of the lower number of Lewis and Brønsted acid sites and mesoporosity (Ali Saleh Bairq et al., 2019; Xing, Lei et al., 2021). Idem et al. investigated the preparation of solid super acid catalyst Ce (SO₄)₂/ZrO₂ and its catalytic effect on CO₂ desorption and found that Ce (SO₄)₂/ZrO₂ has a large number of Brønsted acid sites even well

beyond HZSM-5 (Natewong et al., 2019; Prasongthum et al., 2019). Hybrid composite catalysts are usually composed of two materials with different properties, which combine the unique advantages of different materials to further reduce energy consumption for CO₂ regeneration.

For instance, composite amine catalyst γ -Al₂O₃/HZSM-5 is more effective in catalysing desorption than γ -Al₂O₃ or HZSM-5 alone (Liang et al., 2016b; Zhang et al., 2018b). The catalysts were prepared by loading SO₄²⁻/ZrO₂ onto mesoporous structures (e.g., γ -Al₂O₃, SiO₂, SBA-15, and MCM-41) and used to catalyse CO₂ desorption with a higher catalytic effect than HZSM-5 (Ali Saleh Bairq et al., 2019; Gao et al., 2020; Zhang et al., 2018a, 2019b). Gao et al. synthesized composite catalyst SO₄²⁻/ZrO₂/SBA-15 and used it to reduce heat duty for the regeneration of CO₂-loaded MEA solution. The results of the study showed that SO₄²⁻/ZrO₂/SBA-15 increased the desorption factor by 100–200% and reduced energy consumption for regeneration by 20–26.50% (Gao et al., 2020). A series of composite catalysts (CMK-3-SiO₂, CMK-3-MCM-41 and CMK-3-SBA-15) were prepared, and their catalytic performance was compared and analysed by Bairq et al. It was found that CMK-3-SiO₂ gave the best catalytic performance, being able to reduce the energy requirement by 37.41% and increase the desorption rate by 195% (Bairq et al., 2020).

3.1.1.5. Life cycle assessment of amine solutions based carbon capture.

3.1.1.5.1. Introduction. LCA is an important environmental management tool. The term "life cycle" refers to the whole process of an object from raw materials, through production and use, to abandonment (that is, from cradle to grave). The International Organization for Standardization (ISO) defines LCA as the assessment of environmental factors and potential impacts in the life cycle and mentions that LCA is generally carried out through four stages (target and scope definition, inventory analysis, impact assessment, and interpretation) to quantify the main potential environmental impacts associated with related products or services. Literature (Wang et al., 2022) introduces the four stages of LCA in detail:

1. Definition of objectives and scope: "clear objectives," "determine the boundary," "time span of evaluation," and "specify the functional units of quantitative description."
2. Inventory analysis: collect relevant data and prepare a list of inputs and outputs related to the environment and resources of the evaluated objects. When the data is missing or unclear, it needs to be analysed at the interpretation stage.
3. Impact assessment: The results of the inventory analysis are classified according to the type of impact, and the assessment method is selected and quantified for the resulting environmental impact.
4. Interpretation: analyse the results of the impact assessment phase, improve the data through sensitivity and uncertainty analysis, and draw conclusions.

In this paper, the life cycle impact of a part of the CCS system (the amine solution carbon capture system) is studied. The important problems involved in the LCA of an amine solution carbon capture system are analysed, and the limitations and shortcomings of the system are pointed out.

3.1.1.5.2. Life cycle assessment of amine solution carbon capture systems.

Goals and Scope

At present, the life cycle evaluation of carbon capture systems in amine solutions is very limited. Tim Grant et al. studied the life cycle evaluation of coal-fired power plants using MEA and potassium carbonate solution as absorbents (Grant et al., 2014). Ben Young et al. evaluated the life cycle of CCS in oil refineries, amine production plants, and coal-fired power plants in the United States (Young et al., 2019). There is extensive research on the life cycle evaluation of carbon capture systems, but there is a lack of research on amine-based carbon capture systems. The carbon capture system is a part of the CCS system, and the research on it can learn to a certain extent from the research experience

of the CCS system life cycle. When the object of LCA is transferred from the CCS system to the ammonium solution carbon capture system, the focus of LCA should turn to the impact of the ammonium solution carbon capture system on the environment without considering the impact of the sequestration part on the environment.

In LCA, the definition of the functional unit should be based on its ability to serve as a reference for the impact of the evaluated system on the environment to facilitate the comparison between different studied systems. In general, functional units need to be defined in terms of research objectives, and the defined functional units need to be consistent with the goals of the overall system. Most research has focused on the environmental burden of CCS systems using different absorbents. Since most studies are based on coal-fired power plants, the LCA of CCS systems usually uses a functional unit based on power generation without capturing a certain amount of CO₂ as a functional unit. For example, Letitia Petrescu et al. (2017) selected 1 MWh of net generation as a functional unit in the LCA of a supercritical pulverised coal power plant with post-combustion carbon capture and storage (Petrescu et al., 2017). Francois Saunier et al. (2019) selected "separation of 1 tonne of CO₂ from smoke streams from a 550 MW coal-fired power plant in the Midwest of the United States in 2017" as a functional unit in a study on bio-catalysing and facilitating a comparison of the LCA of a K2 carbonate process with amine-based carbon capture technologies (Saunier et al., 2019). The purpose of defining functional units in this way is to compare the environmental impacts of different CO₂ separation methods. In future studies, more consideration should be given to defining CO₂-based functional units to make better comparisons between different studies.

The whole amine solution carbon capture system is a relatively complete process in the CCS system, which connects all devices in series by absorbing and desorbing carbon dioxide. By determining system boundaries, relevant processes can be included in the LCA of the target system, performing a full life cycle evaluation or a partial life cycle evaluation on the target system. In general, the boundaries of the target system should encompass the entire process from cradle to grave. For example, the boundaries of the life cycle evaluation of CCS systems for sub-critical coal-fired power plants include the entire chain of CCS systems, i.e., the entire process from generation to CO₂ storage (Giordano et al., 2018). Generally, the boundary of the target system should be selected according to different research purposes. When defining the system boundary, we can purposefully simplify the system boundary according to the research focus, which helps us better study the relatively complex system. However, the boundary of the target system should be simplified in line with the actual situation rather than arbitrarily. In particular, processes with less than 1% environmental impact are considered negligible. Kristina Zakuciova et al. defined the system boundary as the operation part of the power plant and the activated carbon production, emission treatment, carbon dioxide capture process, and waste generation in the life cycle evaluation of coal-fired power plants and carbon capture systems based on activated carbon (Zakuciová et al., 2020). However, the definition of the system boundary does not need to consider the operation part of the power plant or the production of activated carbon. Instead, it needs to focus on the production and deterioration processes of the amine solution. Since this paper only takes the carbon capture system as the object, carbon dioxide compression, transport, and oil displacement are excluded from the system boundary. When comparing amine solution carbon capture systems applied to different combustion power generation plants, it should be fully considered that the different coal-fired power plants may have an impact on the life cycle evaluation of amine solution carbon capture systems.

Inventory analysis

The rationality, timeliness, and accuracy of the required data can affect the final evaluation results to a large extent. When the available data cannot support the research, a variety of assumptions need to be added to the target system, which may affect the accuracy of the evaluation to some extent, and the relevant database cannot provide comprehensive

life cycle inventory (LCI) data. Real data, rather than average or average data, should be used as far as possible for LCA, as many aspects, such as average data in geographical space, time span, and technical level, may lead to large errors in LCA. The improvement of the accuracy and timeliness of the data involved in the studied system can provide more experience for the construction of various carbon capture systems. Usually, researchers are faced with the problem of limited available data, so they will use relevant average data for research, which will reduce the accuracy of the results. It is particularly important to reduce the difficulty and improve the accuracy of data collection. In addition, with the continuous innovation of target system technology, researchers need more and more types of data, so they should pay more attention to data collection.

Most of the information used in this study is taken from published works, studies by international and national agencies (such as the IEA, IPCC, and Global CCS Institute), and a number of commercial databases (like Ecoinvent, Environmental Footprint, and Impact World+). In the areas of agriculture, building, chemical manufacture, power generation, fishing, metals, refineries, textiles, tourism, transportation, waste treatment and recycling, water supply, etc., the Ecoinvent database includes 140 nations. Due to the openness, depth, and dependability of its data, it is frequently utilised by businesses and has more than 18,000 data for roughly 3,200 items. The geographic variability of the data can be reduced in the IMPACT World Plus database, which provides country- or region-specific characterisation parameters.

Impact assessment

Two accepted approaches to life cycle impact assessment are problem-oriented midpoint impacts and damage-oriented end effects. The former was chosen in most LCA studies of amine-based carbon capture systems. Selecting appropriate impact categories is the first and most significant step for the first method. The selection of impact categories usually depends on the purpose of the study, the time span considered in the study, and the geographical location of the object of study (Wang et al., 2022). The role of carbon capture systems is to reduce greenhouse gas emissions by separating CO₂ from fixed emission sources, which include cement, steel production, hydrogen production from fossil fuels, waste incineration, power generation, and other industries. However, the construction and operation of the infrastructure for carbon capture systems, as well as the production, regeneration, and degradation of amine solutions, will cause certain negative environmental impacts. Therefore, we should not only select the "global warming potential" (GWP) as the impact category but also select other impact categories for comprehensive analysis and assessment in the LCA studies of amine-based carbon capture systems. Table 3.2 lists the impact categories selected in the LCA study of the amine-based carbon capture system.

Interpretation

There is a certain gap between the results of the LCA and the actual situation, so we need to analyse the cause of this gap. In the process of LCA, the evaluation is not accurate due to the data (such as the gap in the application of existing databases and some data caused by the integration of heterogeneous data sets). Furthermore, the emission trends of small-scale-related emissions have expanded to large-scale applications with factors that cause large errors and other factors that make the results of the life cycle subject to a certain degree of uncertainty. Therefore, we need to analyse the life cycle results and uncertainty to optimise the results of the parameters. Therefore, we should solve these uncertain issues in future research (Gibon et al., 2015).

Sensitivity and uncertainty analysis

The application of the CCS system can reduce the GWP indicator of the coal power generation system, but it will also affect some other environmental indicators to a certain extent. In the literature (Petrescu and Cormos, 2017), the condition of the IGCC power plant without CCS is compared with the IGCC power plant with calcium circulation for the carbon dioxide capture before burning. The results showed that the GWP of the CCS coal-fired power plant was 917.25 kg CO₂-EQ/MWh,

Table 3.2
Selected impact categories for LCA studies on carbon capture in amine solutions.

| Study | GWP | AP | EP | PCOP | ADP | HTP | ETP | ODP | PMFP |
|---------------------------|-----|----|----|------|-----|-----|-----|-----|------|
| Kathrin Volkart (2013) | | | | ✓ | | ✓ | | | ✓ |
| Longlong Tang (2014) | ✓ | ✓ | ✓ | ✓ | ✓ | ✓ | ✓ | | |
| Tim Grant (2014) | ✓ | ✓ | ✓ | ✓ | ✓ | ✓ | ✓ | | |
| Utrecht University (2014) | ✓ | ✓ | ✓ | ✓ | ✓ | ✓ | ✓ | ✓ | ✓ |
| Xiangping Zhang (2014) | ✓ | ✓ | ✓ | ✓ | ✓ | ✓ | ✓ | ✓ | ✓ |
| M.A. Morales Mora (2016) | ✓ | ✓ | ✓ | ✓ | ✓ | ✓ | ✓ | ✓ | ✓ |
| Stefanie Troy (2016) | ✓ | ✓ | ✓ | ✓ | ✓ | ✓ | ✓ | ✓ | ✓ |
| Tang Daqing (2016) | ✓ | ✓ | ✓ | ✓ | ✓ | ✓ | ✓ | ✓ | ✓ |
| Letitia Petrescu (2017) | ✓ | ✓ | ✓ | ✓ | ✓ | ✓ | ✓ | ✓ | ✓ |
| Lorena Giordano (2018) | ✓ | ✓ | ✓ | ✓ | ✓ | ✓ | ✓ | ✓ | ✓ |
| Ben Young (2019) | ✓ | ✓ | ✓ | ✓ | ✓ | ✓ | ✓ | ✓ | ✓ |
| Yi-Ming Wei (2019) | ✓ | ✓ | ✓ | ✓ | ✓ | ✓ | ✓ | ✓ | ✓ |
| Albert Ratner (2020) | ✓ | ✓ | ✓ | ✓ | ✓ | ✓ | ✓ | ✓ | ✓ |
| Alireza Aslani (2022) | ✓ | ✓ | ✓ | ✓ | ✓ | ✓ | ✓ | ✓ | ✓ |
| Andrea Mio (2022) | ✓ | ✓ | ✓ | ✓ | ✓ | ✓ | ✓ | ✓ | ✓ |

GWP = Global Warming Potential; AP = Acidification Potential; EP = Eutrophication Potential; PCOP = Photochemical Oxidation Potential; ADP = Abiotic Depletion Potential; HTP = Human Toxicity Potential; ETP = Ecotoxicity Potential; ODP = Ozone Depletion Potential; PMFO = Particulate Matter Formation

and the GWP was 373.09 kg CO₂-EQ/MWH under CCS. The use of CCS reduced GWP by more than 50%. However, other environmental indicators have increased. The AP index of the power plant system that has not been used in CCS technology was 0.49 kg SO₂-EQ/MWH. After using the CCS technology, the AP index increased to 1.47 kg SO₂-EQ/MWH. The literature (Petrescu et al., 2017) compared the SC pulverised coal power plant without CCS with the SC pulverised coal power plant using amine-based (MDEA) combustion CCS. The GWP value of an SC pulverised coal power plant without CCS is 970.37 kg CO₂ equiv./MWh, and the total GWP value of an SC pulverised coal power plant using amine (MDEA) combustion was 495.93 kg CO₂ equiv./MWh. However, after the application of amine-based combustion, the AP environmental index has reached 4.57 kg SO₂ eq/MWh, while the AP index of pulverised coal power plants without CCS is 0.49 kg SO₂ eq/MWh, with an increase of about 9 times. Not only that, EP, ADP, and other relevant environmental indicators have also increased to varying degrees. According to the analysis, the MDEA production process and the upstream and downstream processes of CCS have made great contributions to these growth indicators. Therefore, the reduction of CO₂ emission in the power generation system can not only focus on the emissions of the power plant itself but also combine the whole process to analyse the environmental benefits of the system comprehensively. In addition, the cost of establishing the emission reduction system should also be considered.

The fate of some other harmful substances other than carbon dioxide is also an important uncertainty. The amine solution absorbent may absorb other harmful substances besides carbon dioxide during the actual absorption process, which may make the whole system have better environmental performance. If the power plant system can effectively treat these substances, some environmental assessment indicators will be greatly reduced, and the environmental impact of the entire system will be smaller (Pehnt and Henkel, 2009). In addition, the energy efficiency of the system itself has an important impact on LCA. The literature (Young et al., 2019) indicated that in ammonia production systems and petroleum production systems, when the energy efficiency of the system was improved, almost the entire life cycle impact was reduced by 20–30%, and the photochemical smoke formation potential (PSFP) in ammonia production systems reduced by 60%. The PSFP effect of CO₂ reduction per unit equivalent ammonia production system was greatest, while the increase in PSFP was minimal when energy efficiency was sensitive. Therefore, when a more energy-efficient carbon capture system is used, the environmental impact of the entire system can be significantly improved.

3.1.1.5.3. Environmental impact of amine solution carbon capture systems. After the application of a carbon capture system to a coal-fired

power plant, its direct CO₂ emissions decrease, but other negative environmental impacts increase. It was pointed out (Young et al., 2019) that the operation of carbon capture systems and the degradation of amine solutions caused negative impacts on the environment, such as abiotic depletion, acidification, and eutrophication. In another literature (Volkart et al., 2013), LCA was performed on a coal-fired power plant with a carbon capture system. The results showed that the plant was superior to the plant without a carbon capture system in terms of the impact categories of GWP and AP but had greater negative impacts on other impact categories (such as HTP, PMFP, ETP, ADP, etc.).

To justify whether the carbon capture system reduces the environmental burden, it is necessary to understand whether the environmental benefits generated by the system are higher than the environmental damage it brings. As a result, the method of a damage-oriented end impact assessment must be introduced for further analysis. For example, the end-point impact assessment method was applied for human health, and ecological environment damage was used to conduct an LCA for biomass co-fired power plants combined with CO₂ capture systems (Schakel et al., 2014). The results showed that the overall environmental performance of the power plant was improved, even though the CO₂ capture system itself produced various negative environmental impacts.

In the carbon capture system, the production and degradation of chemical absorbents are one of the main factors that cause negative environmental impacts, and different absorbents have different impacts on the environment. In the literature Barbera et al. (2022) and Grant et al. (2014), carbon capture systems with different absorbents (monoethanolamine (MEA) and potassium carbonate) were compared. The results showed that in the natural gas power plant with a carbon capture system, the GWP of MEA was lower than that of potassium carbonate, but its ETP and HTP were higher than those of potassium carbonate. In the lignite power plant with a carbon capture system, the potassium carbonate process showed less environmental impact than MEA on the basic environmental indicators such as GWP, ETP, HTP, and ADP. It can be seen that the selection of absorbents depends on CO₂ emission sources, and selecting different absorbents for different CO₂ emission sources can improve the overall environmental performance. In addition, LCA was carried out on two carbon capture systems with MEA and strong hydroxide as absorbents (Zahedi et al., 2022). The results showed that except for eutrophication and nonbiological resource consumption, MEA had less impact on the environment than strong hydroxide in other impact categories. In addition to chemical absorbent separation, CO₂ capture systems can also use membrane separation methods to separate CO₂. Compared with MEA, membrane separation not only consumes less energy but also has a lower negative environmental impact (Giordano et al., 2018; Zhang et al., 2014).

The energy consumption of the CO₂ capture system can be reduced by using clean energy to supply energy to the MEA regeneration system. It was found that the temperature range of the solar collector had a good match with the regeneration temperature of MEA; thus solar energy can be used to supply heat for the MEA regeneration system. Junyao Wang et al. (2017) analysed the solar-assisted coal-fired power plant with a CO₂ capture system by using the LCA method. The results showed that when the CO₂ capture rate was 90%, in terms of GHG reduction performance, the implementation of CCS reduced the life cycle GHG emissions by 67.1% and 73.7% for coal-fired power plants with an amine-based CO₂ capture system and solar-assisted repowering of coal-fired power plants, respectively. This was because solar energy reduced greenhouse gases for carbon capture power plants more than the greenhouse gases emitted by the construction and operation of solar heat collection systems. Therefore, the application of solar heat collection systems is conducive to reducing the negative environmental impact of coal-fired power plants with CO₂ capture systems.

According to the LCA findings, carbon capture systems based on amine solutions can increase environmental performance while lowering greenhouse gas emissions and CO₂ levels. Additionally, it can be shown from a comparison of amine solution and other chemical absorbents that there is a small difference between the pros and cons of each absorbent. However, amine-based carbon capture technology is currently more advanced. Therefore, the primary technique for reducing CO₂ can be an amine solution carbon capture device. According to a life cycle study, reducing the running energy usage of a carbon capture system can greatly increase the total environmental benefits of the whole system.

3.1.1.5.4. Disadvantages and limitations.

Accuracy of results

Although the CCS system has attracted much attention in recent years, its application has been greatly hindered due to the constraints of cost and economy, the legal and regulatory framework, social acceptability, uncertainty, and scalability. The application popularity of CCS overall technology is extremely low, among which the application of amine solution carbon capture systems is less popular, which leads to the very limited data required. The enterprise application of amine solution carbon capture systems is only to reduce CO₂ emissions and pay little attention to other data collection related to the environment, resulting in extremely low accuracy of the required data. Because the required data is very limited and the accuracy is low, the LCA analysis of the amine solution carbon capture system often uses the average value and makes a series of assumptions, resulting in inaccurate LCA results.

Interdisciplinary and large-scale implementation assessment

At present, most of the research on CCS systems focuses on the analysis of applications. Few researchers have studied the potential impact of CCS systems on the environment, and there are few studies on the CCS system (the amine solution carbon capture system). The amine solution carbon capture system employs both the LCA and the technical-economic assessment (TEA) methods for CCS evaluation (Wang et al., 2022). In this section, the LCA of an amine solution carbon capture system is carried out, but it is not combined with TEA or other methods for a comprehensive evaluation. It is limited to the study of a single discipline, which makes the evaluation results unreasonable. At present, there is no mature integrated method for the comprehensive evaluation of an amine solution carbon capture system, and even the comprehensive evaluation method for a CCS system is not mature. Therefore, the large-scale deployment of amine solution carbon capture systems is normally carried out without comprehensive evaluation of their economic and environmental benefits. Future research on amine solution carbon capture systems should focus on the interdisciplinary evaluation of environmental impact, economic cost, and geographical factors. A high level of evaluation combined with a variety of effective disciplines is conducive to better decision-making by decision-makers and helps make decisions more convincing and credible.

3.1.2. Ionic liquids in CO₂ capture

Ionic liquids (ILs), a class of room temperature molten salt composed of cations and anions, have been intensively investigated as novel solvents and soft functional materials for CO₂ capture, owing to their low vapour pressure, high thermal stability, superior solvation ability and designable structures (Gao et al., 2020). Brennecke et al. (Blanchard et al., 1999) first reported that CO₂ has a high solubility in ILs. Subsequently, research demonstrated the application possibility of ILs in CO₂ absorption at room temperature. Classification of ILs apart from the hybrid ILs can be broadly done, as indicated in the diagram (Fig. 3.4). In this part, we mainly review novel IL-based materials and hybrid ILs-based materials for CO₂ capture.

Although the CO₂ solubility in traditional ILs is relatively low compared to amine-based absorbents, the ILs properties can be improved by functionalization of cations or anions to increase the physical and chemical interactions between ILs and CO₂. Effects of CO₂ solubility in ILs have been widely investigated to increase CO₂ capture performance, and the factors affecting CO₂ capture through ILs are listed in Fig. 3.5. The longer alkyl chains on cation and fluorinated anions are profitable to facilitate the CO₂ capture process (Almantariotis et al., 2010; Zheng et al., 2020). The hydrophobic nature of the cation or anion can enhance the interaction between ILs and CO₂. Water content in ILs also has a positive effect on fluidity and CO₂ absorption (Hu et al., 2014). From the viewpoint of industrial practice, the high viscosity of ILs is one of the main reasons that cause slow gas diffusion (Hussain et al., 2021). In addition, ILs can be combined with numerous types of materials to form hybrid materials. However, doping an excessive amount of ILs may cause pore-blocking, there could be detrimental for immobilized ILs to capture CO₂ (Lian et al., 2021).

3.1.2.1. Amino ILs. On the basis of the chemical reaction of CO₂ with the amino group, a large number of amino functionalized ionic liquids were developed as absorbents. Studies have found that more amino groups in ILs lead to higher CO₂ absorption capacity, and water content has a great influence on CO₂ absorption capacity. When the moisture content increased from 0% to 40%, the absorption capacity of poly-amino-based ionic liquids [TETAH][BF₄] increased from 0.96 mol CO₂/mol IL to 2.04 mol CO₂/mol IL (Hu et al., 2014). A bifunctional ionic liquid [APmim][Gly] consisting of amine and amino acid has the advantages of high efficiency and high CO₂ capacity, which was as high as 1.23 mol CO₂/mol IL (Lv et al., 2016a). A polyamine functionalized ionic liquid [APmim][Lys] by introducing amine and lysine functionalization groups into imidazole ILs was reported and its absorption load was 1.80 mol CO₂/mol IL (Zhou et al., 2016). A novel hydrophilic amino acid ILs [C₂OHmim][Gly] was designed and the level of capture capacity reached 0.575 mol CO₂/mol IL (Lv et al., 2016b), which makes it has great potential to make up for the deficiency of water-based MEA and is beneficial to industrial application.

However, the formation of intermolecular hydrogen bonds in ILs-CO₂ complex may lead to a sharp increase in viscosity after absorbing CO₂, thus affecting mass transfer performance and limiting the application of amine ILs (Cui et al., 2016). Bhattacharyya and Shah (2016) synthesized the ether functionalized choline amino acid ILs [N_{1,1,6,204}][Lys] with low viscosity and high CO₂ sorption capacity. Luo et al. (Luo et al., 2016) introduced hydrogen receptors such as N or O atoms into amino-functionalized ILs, and showed that ILs such as [P₆₆₆₁₄][4NH₂-NC], [P₆₆₆₁₄][Ac-Gly], [P₆₆₆₁₄][Me-Gly], [P₆₆₆₁₄][Ac-PhO] and [P₆₆₆₁₄][MA-Tetz] have two active sites for CO₂ on an amine group through the formation of intramolecular hydrogen bonds and proton transfer processes, and the viscosity of these amino-functionalized ILs slightly increased or even decreased during CO₂ capture.

In order to achieve low regenerative energy consumption and low viscosity, a novel CO₂ capture method for [TEPAH][2-MI] combined with organic solvents was proposed (Liu et al., 2020). The absorption load of [TEPAH][2-MI]/N-propanol/ethylene glycol was 1.72 mol CO₂/mol IL, which was much higher than MEA/water. The regeneration

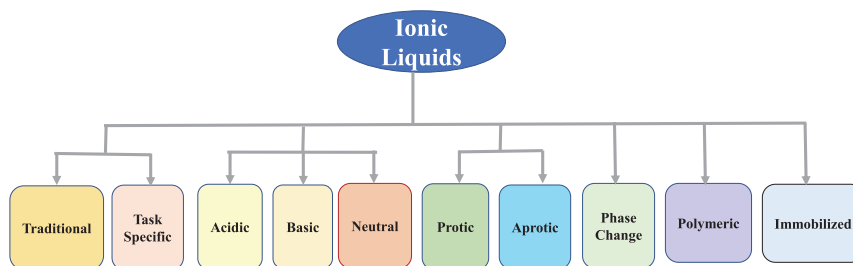


Fig. 3.4. Classification of ILs. (For interpretation of the references to color in this figure legend, the reader is referred to the web version of this article.)

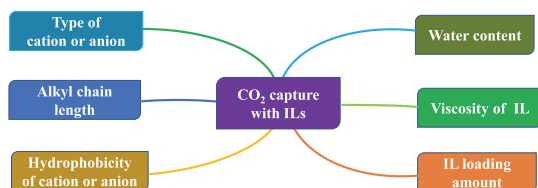


Fig. 3.5. Factors affecting the CO₂ absorption with ILs. (For interpretation of the references to color in this figure legend, the reader is referred to the web version of this article.)

efficiency remained at 90.7% after the fifth regeneration cycle, and the viscosity of the solution before and after absorption was only 3.66 and 7.65 mPa s.

3.1.2.2. Protic ILs. Protic Ionic Liquids (PILs) generally include proton donor and proton acceptor, and a hydrogen bond network can be formed in the structure with strong polarity (Cohen et al., 2019; Er et al., 2019; Sun et al., 2014), which not only has typical ILs properties, but also builds the hydrogen bond network due to the proton that can migrate in its structure. In general, PILs have high viscosity, which is a result of strong interactions between the ions through, mainly, the hydrogen bonds of hydroxyl groups and protic ion-ion interactions. Therefore, when PILs are used to absorb CO₂, it is generally mixed with water, methanol, ethanol and other solvents and then used in its two-phase system.

The viscosity of PILs is an important property in studying its application range. The structure of anions in PILs has a great influence on the viscosity, and the anions such as F (HF)_n⁻, N (CN)₂⁻, N (CN)₃⁻ have relatively low viscosity (Ignat'ev et al., 2015; Seki et al., 2010). Weak intermolecular interactions (such as van der Waals forces and hydrogen bonds) have a certain effect on the viscosity of PILs. The stronger the intermolecular interaction, the greater the viscosity of PILs. Delocalization of charges on anions in PILs (e.g. fluorination) can weaken hydrogen bond interactions and reduce viscosity.

Zheng et al. (2017) determined the solubility of CO₂ in the cation PILs 3-(dimethyl amino)-1-propylamine (DMAPA) and different anions, and the results showed that the solubility of CO₂ in [DMA-PAH][F] aqueous solution reached 3.62 mol/kg at 0.1 MPa and 35.2 °C. A series of etoxyacetic anionic PILs containing three different amine cations were designed (Wei et al., 2020), and the CO₂ solubility in [3-(dimethylamino)-1-propylamine][ethanol amine] ([DMAPAH][EOAc]) was as high as 2.44 mol/kg. An anionic functionalized PIL synthesized by superbase 1,8-diazabicyclo [5.4.0]-undec-7-ene (DBU) and imidazole was synthesized (Zhu et al., 2017), which can reversibly capture CO₂ with a capacity of 1 mol CO₂/mol IL. In addition, there are many studies on fluorine substituents. Dimethyl-1,3-malon-2,3,5-difluorophenol salt ([DMAPAH][3,5F-PhO]) was synthesized, and its optimal absorption

capacity was 3.99 mol CO₂/kg IL (0.86 mol CO₂/mol IL) (Zhao et al., 2018).

As for the influence of cations and anions of PILs on CO₂ absorption, other researchers have given their own ideas. Ma et al. (2021) found that the absorption path by the anion of dimethylethylenediamine 4-fluorophenolate ([DMEDA][4-F-Pho]) was favourable in kinetics, while the absorption path by the cation was thermodynamically beneficial. Moreover, dimethylethylenediamine acetate ([DMEDA][OAc]) only showed the possibility of cation absorption.

For the application of PILs in CO₂ capture, in addition to their CO₂ absorption performance, selectivity should also be considered as an important performance. Alcantara et al. (2018) measured the phase equilibria data of low viscous diethylammonium butanoate [Bu] with CO₂, CH₄ and N₂ from 30 °C to 60 °C and up to 20 MPa. The results were shown that this PIL presented moderate to low CO₂ solubility, but it would display higher CO₂/CH₄ selectivity than most ILs studied at high pressures. Swati et al. (2021) synthesized several ionic liquids, namely, 1-butylsulfonate-3-methylimidazolium P-toluene sulfonate ([BSmim][tos]), 1-butylsulfonate pyridine P-toluene sulfonate ([BSmpyl][tos]), 1-butyl-3-methylimidazolium chloride ([Bmim]Cl) and 1-butylpyridine chloride ([Bpy]Cl) for the separation of CO₂/N₂ and CO₂/CH₄ by supported ionic liquid membranes (SILMs). It was found that the presence of sulfonic group in proton ionic liquid would increase Lewis acid-base force and enhance the affinity of CO₂ to ILs, resulting in PILs having certain advantages in selectivity. The selectivity of [BSmim][tos] and [BSmpyl][tos] to pure CO₂/CH₄ was 47.4 and 40.7, respectively.

3.1.2.3. Phase change ILs. CO₂ capture using phase change ILs has attracted increased interest for the potential to reduce the cost of energy consumption. Upon CO₂ absorption, phase change ILs form a two-phase system, namely a CO₂-enriched phase and a CO₂-lean phase. The CO₂-lean phase is a liquid phase and the CO₂-enriched phase is either a liquid or solid phase. Only the CO₂-enriched liquid phase is used for solvent regeneration; thus, the heat required to regenerate the solvent is reduced. Recently, the research on PILs has been mainly focused on ionic liquid-amine composite and pure ionic liquids systems (Lv et al., 2020; Tiwari et al., 2021; Wu et al., 2019; Zalewski et al., 2021).

The blends of diethanolamine (DEA) with one of three IL, [EMIM][Tf₂N], [BMIM][Tf₂N] and [HMIM][Tf₂N], were able to form a solid phase during CO₂ absorption (Hasib-ur-Rahman and Larachi, 2013; Hasib-ur-Rahman et al., 2012; Iliuta et al., 2014). The solid products of this IL-amine composite system are mainly carbamates and alkyl carbonates, and more than 99% are concentrated in the CO₂ rich phase. The precipitation of the carbamate product allowed CO₂ absorption to proceed beyond the equilibrium limitation exerted on a liquid phase system.

To enhance CO₂ capture capacities, some researchers investigated functionalized ILs in such phase change systems. Triethylenetetramine L-lysine ([TETAH][Lys]) was dissolved in ethanol-water solvent to form a phase change solvent, and the CO₂ capacity reached 2.35 mol CO₂/mol

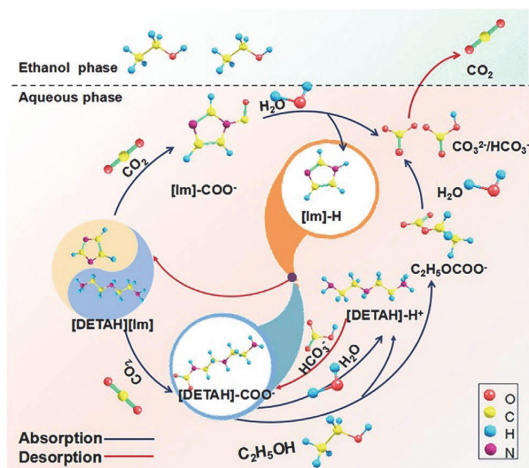


Fig. 3.6. The mechanism of CO₂ capture into [DETAH][Im]-EtOH-H₂O (Lü B, 2021). (For interpretation of the references to color in this figure legend, the reader is referred to the web version of this article.)

IL as well as the volume ratio of the CO₂-rich phase was 66% (Huang et al., 2018). At the same time, the regeneration energy consumption (1.29 GJ/t CO₂) and solvent loss during the regeneration process are also reduced. The CO₂ capacity of triethylenetetramine hydrobromide [TETA]Br-PMDETA-H₂O phase change system was high to 2.631 mol CO₂/L at 30 °C and 0.1 MPa, and the regeneration efficiency remained above 95% after four cycles at 150 °C (Zhou et al., 2020).

Recently, an amino-azolyl dual-functional IL/ethanol/water system ([DETAH][Im]-CH₃CH₂OH-H₂O) for CO₂ capture was constructed via dissolution of a diethylenetriamine-imidazole functionalized ionic liquid ([DETAH][Im]) in the mixed ethanol-water solvent and the CO₂ loading was reported to be 1.548 mol CO₂/mol absorbent whereas the volume only accounted for 32% (Lü B, 2021). As shown in Fig. 3.6, in the process of absorption, [DETAH][Im] as the main absorbent, cations can react with CO₂ to form carbamates (RN⁺COO⁻), whileazolyl anions can react with CO₂ to form HCO₃⁻/CO₃²⁻, which ensures the efficient CO₂ trapping ability of the system. At the same time, [Im]-H and ethanol can promote the decomposition of carbamate (RN⁺COO⁻) and produce easily decomposed HCO₃⁻/CO₃²⁻ and ethyl carbonate products, while leads to the high regeneration efficiency of the rich liquid.

3.1.2.4. Immobilized ILs. Supported ILs (SILs) or encapsulated or nanoconfined ILs (ENILs) are loading or incorporating ILs into the pore structure of solid matrices (Zheng et al., 2021). ENILs are new types of ILs hybrid materials with high gas-liquid contact area and a large amount of ILs is wrapped in the shell structure of the support (Silva et al., 2020). The ILs in ENILs are physically restricted by the cavity of the support, which can keep the complete molecular structure, fluidity and CO₂ affinity of the ILs (Luo and Pentzer, 2020; Santiago et al., 2018). Both SILs and ENILs improve CO₂ adsorption capacity and selectivity by introducing CO₂-philic reactive sites compared with blank porous matrices, so these improvements render SILs and ENILs with great potential for large scale application. In this section, we will provide a comprehensive review of the above two types of immobilized ILs in application in CO₂ capture, emphasizing the alternative porous matrices for supporting or encapsulating ILs (Fig. 3.7).

Porous silica and zeolite are the preferred matrices for ILs considering their porosity, nontoxicity and facile synthesis. The interaction between the pore wall and ILs plays a key role in affecting the properties of the corresponding SILs or ENILs, which depends on both silica

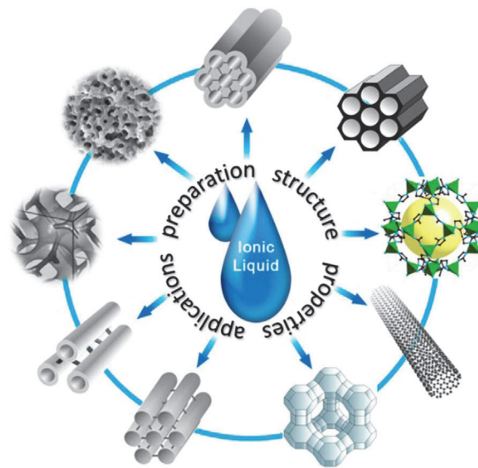


Fig. 3.7. Concept of ILs immobilized by various porous solid matrices (Zhang et al., 2017). (For interpretation of the references to color in this figure legend, the reader is referred to the web version of this article.)

surface properties and the functional groups of ILs. The surface of silica and zeolite mainly contains Si, Al, Si-O groups and Si-OH groups, which serve as interaction sites for the supported ILs (Wang et al., 2011; Zhang et al., 2017). For example, Zhu et al. (2018) immobilized imidazolium and phosphonium ILs into porous silica supports and suggested that the CO₂ adsorption through the porous nature of the silica dominated the adsorption behavior of the hybrid adsorbent. Pohako-Esko et al. (2016) prepared the ENILs by encapsulating chitosan containing ILs with nanoporous fumed silica. The results showed that dissolution chitosan in ILs increased the CO₂ adsorption capacity of chitosan about 10 times. In addition, functional groups usually increase the interaction between ILs and CO₂, resulting in increased CO₂ capacity. Zhang et al. (2019) prepared multi-amino functionalized IL adsorbent supported on SBA-15, which exhibited a high CO₂ capacity of 2.15 mmolCO₂/g-adsorbent under 60 °C and 0.015 MPa. Arellano et al. (2015) reported the SBA-15 supported metal-based zinc-functionalized ILs. It was shown that an excellent CO₂ capacity of 4.70 mmolCO₂/g-adsorbent was achieved under 40 °C and 0.015 MPa after incorporating EZT3 into SBA-15. As displayed in Fig. 3.8, the CO₂ capacity of EZT3@SBA-15 is 600% and 250% of the pristine ILs and SBA-15, owing to the creation of abundantly accessible CO₂ adsorption sites and the elimination of the viscosity-imposed limitation on mass transfer. Yu et al. (2014) applied NaY zeolite as support to encapsulate [C_nmim][Br] (n=4, 6, 8, 10). It was shown that the encapsulated [C_nmim][Br]@NaY was more thermal stable than the neat one. Moreover, the results showed that the CO₂ capacity under 35 °C and 0.015 MPa increased with decreasing length of the side chain on the cation. Besides, immobilization methods affect the performance of the SILs a lot. Zhu et al. (2018) studied the effect of immobilization methods (impregnation and grafting) on the CO₂ selectivity of silica-supported ILs. They found that compared with the impregnated adsorbent, grafting ILs on the support surface caused a weak loss of microporosity, leading to a slight decrease in CO₂ adsorption capacity, and had better recycling. The grafted silica exhibited diffusivities faster than those of the impregnated one, indicating that excessive filling of with ILs was unfavourable for CO₂ diffusion. According to Yin's report Yin et al. (2018), the CO₂ capacity of [C₄mim][BF₄]₂@SBA-15 synthesized by supercritical fluid method (0.79 mmol CO₂/g-adsorbent) is higher than that of the impregnation method (0.63 mmolCO₂/g-adsorbent) under 25 °C and 0.003 MPa. The authors proposed that the supercritical fluid method

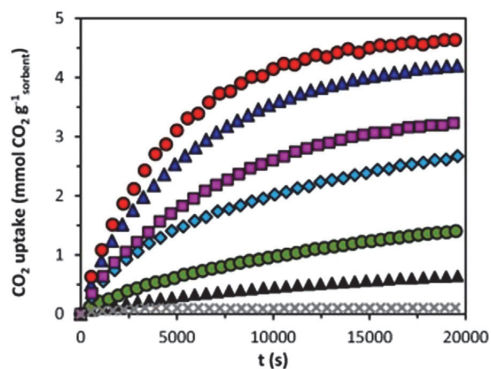


Fig. 3.8. Dynamic CO₂ uptake capacity for SBA-15 (green), nonfunctionalized IL ET (grey), EZT3 (black), and EZT3@SBA-15 with different IL loadings: 10 wt% (cyan), 25 wt% (dark blue), 50 wt% (red), and 80 wt% (pink) (Arellano et al., 2015). (For interpretation of the references to color in this figure legend, the reader is referred to the web version of this article.)

could make ILs more homogeneously distributed on the support and increase the loading amount of ILs, resulting in the increased CO₂ adsorption capacity.

CO₂ adsorption on pristine carbon materials is physical and weak, thus, the adsorption is sensitive to the reaction temperature and CO₂ selectivity is very low (Wang et al., 2011). Immobilizing ILs on carbon materials, such as activated carbons (AC) and carbon nanotubes (CNT), is particularly interesting to overcome the drawbacks of both pristine carbon materials and ILs, and combine their respective advantages. CNTs are investigated the most since their initially empty channel could spontaneously be filled with surrounding ILs in the container to achieve a saturated state. Fig. 3.9 displays one of the typical ENILs, where the [Me₃NC₂H₄OH][ZnCl₂] is encapsulated inside CNTs with different diameters (Chen, S. et al., 2009). Maurya and Singh (2019) compared the CO₂ adsorption capacity of MOFs (InOF-1, UiO-66 and ZIF-8), COFs (COF-108 and COF-300) and carbon based materials (single-wall carbon nanotube SWCNT), and the results showed that SWCNT had the highest CO₂ adsorption capacity. Moreover, the CO₂ adsorption capacity and selectivity further improved by impregnating with ILs. Zeng et al. (2018) synthesized a series of ENILs using carbon nanotube (CNT) as shell material, including [C₄mim][PF₆]@CNT, [C₄mim][SCN]@CNT and [C₄mim][Tf₂N]@CNT, to study the effect of anions on the ENILs for CO₂ capture. The results showed that [C₄mim][PF₆]@CNT exhibited the highest CO₂ capacity of 1.30 mmolCO₂/g-adsorbent under 30 °C and 0.1 MPa, because [PF₆]⁻ had a stronger interaction with CO₂ than [SCN]⁻ and [Tf₂N]⁻. As a consequence of the reduced pore volume by the larger anion inside CNT, [C₄mim][Tf₂N]@CNT showed the low CO₂ capacity. In general, the CO₂ selectivity of SILs and ENILs synthesized by impregnation method is higher than that of the grafting method.

He et al. Wang et al. (2019a) incorporated the phosphonium ILs [(EtO)₃SiP⁸⁸⁸³][Tf₂N] into activated carbon (AC) by the grafting method and the impregnation method, respectively. The results showed that the CO₂/N₂ selectivity of the adsorbent synthesized by the impregnation method is higher than that of the grafted one. This is because the thin film of ILs formed on the support after impregnation is beneficial for permitting the entry of CO₂ but blocking N₂ (Wang et al., 2019a; Zhu et al., 2018). Besides, Karousos et al. (2016) found that the CO₂/SO₂ selectivity of the AC-impregnated [C₂mim][OAc] is much higher than that of the AC-grafted one under 50 °C and 0.1 MPa. The similar conclusions for other supports (SBA-15 and MOF-177) were also obtained. Graphene oxide was also reported to construct ILs-based solid CO₂ adsorbent. For example, Huang et al. (2019) synthesized the encapsulated

imidazolium-based ILs with alkylated graphene oxide as the shell with ILs loading of 80 wt%. The shell material was permeable to CO₂ and allowed CO₂ to reach the inner IL core effectively, resulting in the increased CO₂ adsorption rate. As shown in Fig. 3.10, the time to reach CO₂ adsorption equilibrium for encapsulated ILs was shortened from 271 to 97 min compared with the agitated ILs. This result proves that the encapsulating ILs in special structure can increase the gas-liquid contact area and improves the mass transfer.

Metal-Organic Frameworks (MOFs) are constructed from transition metal ions and bridging organic ligands, which are a new family of porous materials. Impregnation of ILs on MOFs has been proposed as a promising alternative to traditional ILs, because they are non-volatile, non-flammable and thermal stable and therefore are categorized as green adsorbents. Fig. 3.11 shows the schematics of [C₂mim][SCN] incorporated into Cu-BTC. Silva et al. (2015) proposed MOF-supported ILs for CO₂ capture and proved that the incorporation of [C₄mim][PF₆] to Cu-BTC enhanced the CO₂ adsorption capacity compared with pristine MOFs. However, the CO₂ adsorption capacity of [C₄mim][PF₆]@Cu-BTC with 5 wt% ILs loading (1.2 mmol CO₂/g-adsorbent) under 25 °C and 0.025 MPa was lower than pure Cu-BTC (1.3 mmolCO₂/g-adsorbent). Besides, a further decrease in CO₂ adsorption capacity was observed as the ILs loading increased. This might be caused by channel jam after the incorporation of excessive ILs. Although loading conventional ILs suppressed the CO₂ adsorption capacity of MOFs, it is worth noting that the conventional ILs have a positive effect on CO₂ selectivity (Vicent-Luna et al., 2018). Kinik et al. (2016) incorporated [C₄mim][PF₆] into zeolitic imidazolate frameworks-8 (ZIF-8) and found that the CO₂ adsorption capacity of [C₄mim][PF₆]@ZIF-8 (0.10 mmolCO₂/g-adsorbent) was twice as high as that of the pristine ZIF-8 under 25 °C and 0.00065 MPa. Furthermore, CO₂ selectivity in CO₂/CH₄ and CO₂/N₂ was improved. Ferreira et al. (2019) found that incorporating [C₁₀mim][Tf₂N]@ZIF-8 onto ZIF-8 enhanced the CO₂/CH₄ selectivity of 3.1 under 0.05 MPa, which increased by 35 % compared with the blank ZIF-8. Besides, the nonpolar and long side chain of [C₁₀mim][Tf₂N] strengthened its interaction with CO₂, making [C₁₀mim][Tf₂N]@ZIF-8 show better CO₂ separation performance than other ILs@ZIF-8. The functional groups, like amino group and carboxyl group, also play a key role in CO₂ adsorption, considering their interaction with CO₂. For instance, Mohamedali et al. (2018) incorporated the acetate-based ILs into ZIF-8, which enhanced the CO₂ capacity and CO₂/N₂ selectivity. In comparison with the pristine ZIF-8, the CO₂ uptake of [C₄mim][OAc]@ZIF-8 was increased by more than seven times, and the CO₂/N₂ selectivity reached 18 times. By increasing the ILs loading to 83.04 wt%, Wang et al. (2019) prepared a [C₄Py][Tf₂N]@ZIF-8 adsorbent with 1.36 mmolCO₂/g-adsorbent under 30 °C and 1.8 MPa, which increased by 24 % compared with pristine ILs. Mohamed et al. (2019) investigated six ENILs with different ILs and the same ZIF-8 support via Monte Carlo simulations. The results showed that the encapsulation of [C₄mim][B(CN)₄] and [C₄mim][TCM] into ZIF-8 can achieve higher CO₂/N₂ and CO₂/CH₄ selectivity than that of [C₄mim][Tf₂N]@ZIF-8. For explanation, the authors proposed that more ILs pairs in ZIF-8 cages provided more CO₂ adsorption sites, consequently the higher CO₂ selectivity.

In addition to the intensively studied rigid inorganic matrices, ILs could also be confined into organic polymer matrices. The application of polymers as porous hosts for ILs gives rise to the easy and convenient formation of flexible membranes, although this system often experiences a loss of mechanical when the loading of immobilized ILs is too high. Polymer-immobilized ILs are usually prepared by either in situ polymerization of monomers in ILs (Guyomard-Lack et al., 2015) or a solvent casting method (Tang et al., 2015; Yang et al., 2015). Several polymers have been explored for supporting ILs, such as polymethyl methacrylate (PMMA) (Uehara et al., 2018; Wang et al., 2013), fluorinated copolymer poly(vinylidene fluoride-co-chlorotrifluoroethylene) (P(VDF-CTFE)) (Yang et al., 2015), biopolymers (Guyomard-Lack et al., 2015; Trivedi et al., 2015), and

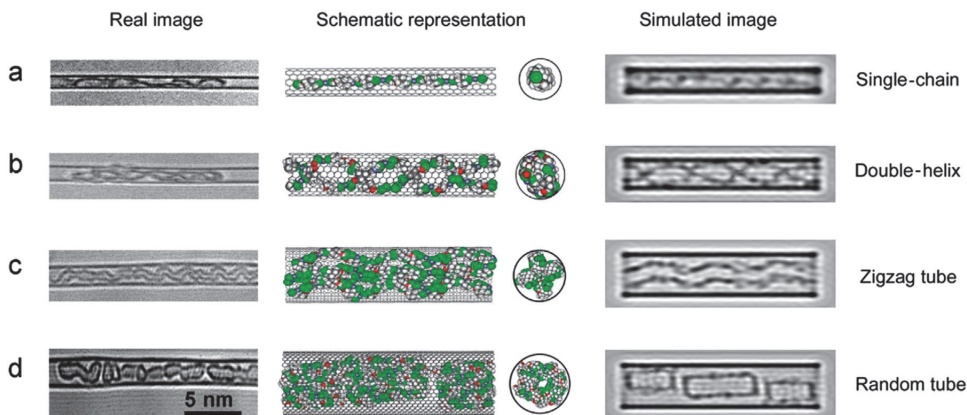


Fig. 3.9. Images of $[\text{Me}_3\text{NC}_2\text{H}_4\text{OH}][\text{ZnCl}_3]$ encapsulated inside SWCNTs with different diameters (Chen et al., 2009). (For interpretation of the references to color in this figure legend, the reader is referred to the web version of this article.)

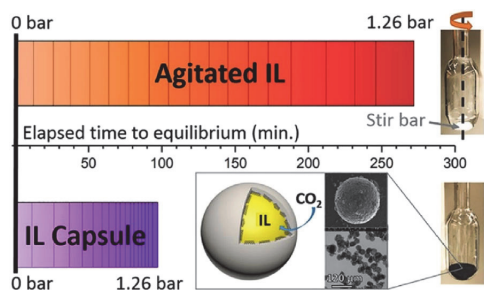


Fig. 3.10. The elapsed time to reach CO_2 adsorption equilibrium and schematic of encapsulated $[\text{C}_2\text{mim}][\text{TF}_2\text{N}]$ (Huang et al., 2019). (For interpretation of the references to color in this figure legend, the reader is referred to the web version of this article.)

epoxy resins (Matsumoto and Endo, 2008). Ren et al. (2018) synthesized a series of SILs by impregnating tetramethylammonium glycinate ($[\text{N}_{1111}][\text{Gly}]$) into four supports, including polymethyl methacrylate (PMMA), titanium oxide (P25), MCM-41 and silica gel (SG). Among them, PMMA- $[\text{N}_{1111}][\text{Gly}]$ displayed the best CO_2 adsorption behavior in terms of adsorption capacity and rate. The CO_2 adsorption capacity reached up to $2.14 \text{ mmolCO}_2/\text{g-adsorbent}$ at 35°C . Pristine ILs and supported ILs might exhibit opposite behavior. For instance, Uehara et al. (2018) synthesized a series of polymethyl methacrylate (PMMA) supported ILs, including $[\text{C}_2\text{mim}][\text{Lys}]@PMMA$, $[\text{C}_2\text{mim}]@PMMA$, $[\text{C}_2\text{mim}][\text{Gly}]@PMMA$, $[\text{P}_{4444}][\text{Lys}]@PMMA$, $[\text{P}_{4444}]@PMMA$ and $[\text{P}_{4444}][\text{Gly}]@PMMA$. It was found that $[\text{Lys}]^-$ exhibited higher CO_2 capacity than $[\text{Gly}]^-$. However, the CO_2 capacity was the opposite when these ILs were supported on PMMA. The $[\text{C}_2\text{mim}][\text{Gly}]@PMMA$ had a higher CO_2 capacity ($0.88 \text{ mmolCO}_2/\text{g-adsorbent}$) than $[\text{C}_2\text{mim}]@PMMA$ ($0.63 \text{ mmolCO}_2/\text{g-adsorbent}$) under 30°C and 0.0023 MPa . This was because the side chains with amino groups blocked the pore structure of PMMA, which inhibited the entry of CO_2 and thus reduced CO_2 capacity. Lee et al. (2020) combined $[\text{C}_2\text{mim}][2\text{-CNpyr}]$ with polyurethane and graphene oxide nanosheet shells to prepare the reactive ENILs. As shown in Fig. 3.12, the CO_2 capacity of this adsorbent was $1.30 \text{ mmolCO}_2/\text{g-adsorbent}$ under 25°C and 0.0005 MPa . In comparison with the most advanced zeolite 13X, these ENILs had better stability, recyclability and higher CO_2 capacity. Kaviani et al. (2018) investigated the feasibility of ILs encapsulation within a polymeric shell and

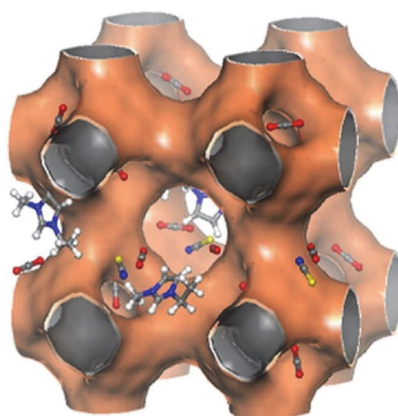


Fig. 3.11. Schematics of $[\text{C}_2\text{mim}][\text{SCN}]@Cu\text{-BTC}$ (Manuel Vicent-Luna et al., 2013). (For interpretation of the references to color in this figure legend, the reader is referred to the web version of this article.)

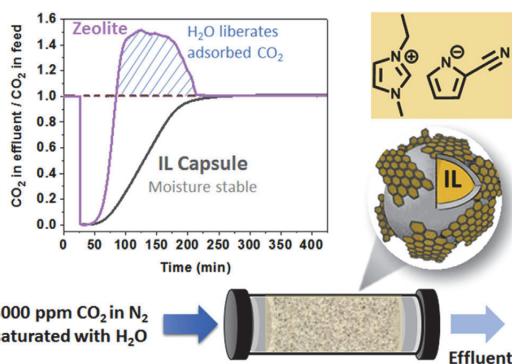


Fig. 3.12. Schematics of encapsulated $[\text{C}_2\text{mim}][2\text{-CNpyr}]$ with polyurethane and graphene oxide nanosheet shells (Lee et al., 2020). (For interpretation of the references to color in this figure legend, the reader is referred to the web version of this article.)

Table 3.3
Qualitative comparison between amines and ammonia as CO₂ absorbers.

| Characteristics | Amines | Ammonia |
|--|---|---|
| CO ₂ capture capacity | 0.5 mol- CO ₂ /mol-MEA | 1.0 mol- CO ₂ /mol-NH ₃ |
| Regeneration energy (GJ/t _{CO2}) | 4.2 (MEA) | < 2.5 |
| Absorption rate | Fast | Slow |
| Corrosiveness | Severe | Mild |
| Volatility | Low | High |
| Absorbent cost | Expensive | Cheap |
| Advantages | Fast reaction kinetics and high absorption capacity | Absorption at high loading, low corrosion, and degradation, easy regeneration |
| Disadvantages | High regeneration energy, high corrosion rate, easily oxidized and degraded | Ammonia escape, secondary pollution |

evaluated the hybrid adsorbent in CO₂ absorption. The proper choice of chemistry for the polymeric matrix allows the ENILs to outperform the pristine ILs. The improvement was ascribed to the synergistic effect between the fluorine-containing polymer and ILs on the CO₂ adsorption of the ENILs.

3.1.3. New ammonia-based CO₂ capture

As the most feasible post-combustion CO₂ capture technology, the chemical absorption method shows great prospects for industrial applications. Currently, the main industrial method is alcohol-amine solution-ethanolamine (MEA) absorption. However, there are many problems in the practical application, such as high regeneration energy consumption, serious equipment corrosion, and easy solvent volatilization and decomposition (Liang et al., 2016a). Therefore, ammonia-based carbon capture technology may become the main theme of CO₂ capture technology, but its ammonia escape problem is serious. The advent of additives brings a turnaround, and ammonia and additives can promote each other to some extent to improve the CO₂ absorption rate of ammonia. Ethanol as an additive excels in all aspects, and a new ammonia-based carbon capture technology (ammonia-ethanol hybrid absorber) (Zhang et al., 2019) was born. Due to the high corrosiveness of MEA and regeneration problems, ammonia-based CO₂ capture is a viable carbon capture technology over conventional amine-based CO₂ capture technology, technically and economically.

3.1.3.1. Ammonia-based CO₂ capture technology. Reliable absorbents for low concentration CO₂ capture are amine- and amino-based CO₂ capture technologies. The thermochemistry of CO₂-NH₃-H₂O systems with ammonia as an alternative to amine-based absorbents is reasonably well understood, including vapour-liquid-solid equilibria, species formation, absorption heat, reaction kinetics, and thermodynamic model development. Many thermodynamic models based on CO₂-NH₃-H₂O systems were developed by Thomsen and Rasmussen (1999), and Que and Chen (2011), which accurately predicted the gas-liquid-solid phase equilibrium. Fig. 3.13 shows the typical post-combustion ammonia carbon capture system and the proportion of electricity consumption of each part of the process. The existing typical processes of this technology are as follows: Alstom refrigerated ammonia process, Powerspan ECO₂ process, CSIRO ammonia process of Australian Federal Science and Industry Commission, RIST ammonia process of Korea Industrial Science and Technology Research Center, etc.

During CO₂ capture, ammonia reacts with carbon dioxide (aq) to form carbamate, which is immediately deprotonated to give carbamate. Due to the reversal of the equilibrium as the pH changes with continued CO₂ uptake, the carbamate eventually decomposes to produce protonated ammonia and bicarbonate. The carbamate equilibrium constant of MEA is much higher than that of ammonia, indicating that the yield of ammonia-derived carbamate is lower than that of the equivalent monoethanolic ammonium carbamate ammonia possesses a higher CO₂ capture capacity compared to MEA. Based on equilibrium calculations (Darde et al., 2009), the cold ammonia method resulted in significantly lower energy consumption in the regeneration step than the

amine-based method. Table 3.3 shows a qualitative comparison between amine and ammonia as CO₂ capture absorbents. Ammonia-based CO₂ capture technology outperforms conventional amine-based CO₂ capture technology in terms of technical and economic advantages, with high CO₂ absorption capacity, low heat of absorption reaction, and less susceptibility to downgrading by O₂ in the flue gas, low corrosiveness, and low feedstock prices (Darde et al., 2009; Pellegrini et al., 2010).

3.1.3.2. Ammonia escape. While ammonia solution as a CO₂ absorber has the above-mentioned significant advantages, there are also common shortcomings and deficiencies in the current application.

- 1) Low CO₂ absorption rate, the reaction rate of CO₂ absorption by ammonia at the same temperature is about an order of magnitude lower than that of MEA.
- 2) Serious ammonia escape, the concentration of escaped ammonia during CO₂ absorption can be as high as 2 vol.%, and the concentration of escaped ammonia during rich liquid regeneration reach 10–20 vol.%; with 14% ammonia, for example, the total ammonia loss is as high as 43.1% (Jilvero et al., 2015).
- 3) High energy consumption for desorption and regeneration and up to 4–4.2 MJ/kgCO₂ for regeneration in the pilot experiment of ammonia decarbonization (Yu, 2018).

The main drawbacks of ammonia-based CO₂ capture technology are slower absorption kinetics and higher volatility than amine solutions. The ammonia escape mechanism is shown in Fig. 3.14, and the ammonia escape problem is becoming one of the most critical technical and economic challenges in the commercial application of ammonia-based CO₂ capture technology. A high NH₃ escape rate also reduces the concentration of NH₃ in the solution, thus reducing the CO₂ uptake capacity (Wang et al., 2018). In addition, ammonia can leak into the air, thus causing serious secondary pollution. Therefore, it is imperative to develop effective methods to suppress ammonia leakage or recover the leaked ammonia. Optimizing process parameters through acid and aqueous washing, membrane technology, additives and accelerators, and applying cold ammonia processes and mixed salts are common strategies to control ammonia escapes.

3.1.3.3. Ammonia-ethanol mixture absorber. To solve the ammonia escape problem, many scholars have proposed the modification of CO₂ absorption by ammonia solutions using additives, which inhibit not only NH₃ escape but also improve CO₂ absorption performance. Table 3.4 provides the results of studies on CO₂ capture by ammonia additive in the last five years. Gao et al. (2015), Zhang et al. (2019) have shown significant advantages of using ethanol as an additive in various aspects. Ammonia and ethanol can promote each other to improve the CO₂ absorption rate of ammonia (Yang et al., 2014). However, there is a slight contradiction between the hybrid absorber increasing the absorption rate and inhibiting ammonia escape (Ma et al., 2016). The additive mainly binds the free ammonia in the ammonia solution through hydrogen bonding. It thus inhibits ammonia escape, but when the hybrid absorber absorbs CO₂, the additive does not achieve effective ammonia

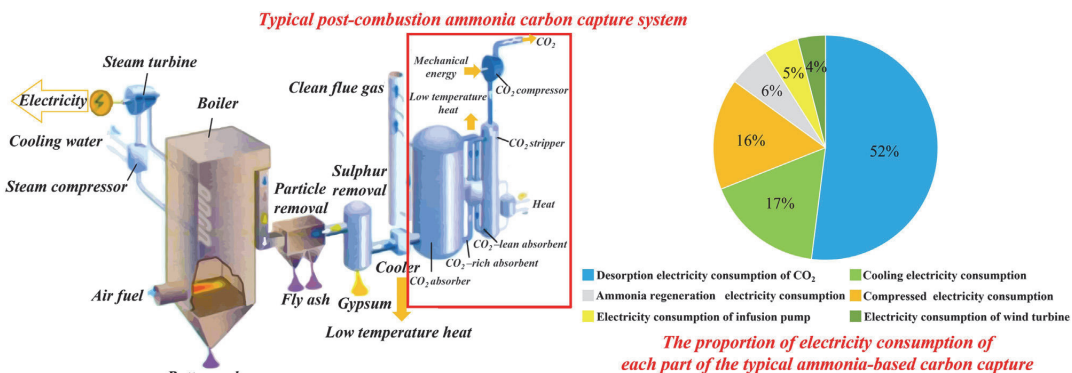


Fig. 3.13. Typical post-combustion ammonia-based carbon capture system and the proportion of electricity consumption of each part of the process diagram (Yu and Wang, 2015). (For interpretation of the references to color in this figure legend, the reader is referred to the web version of this article.)

Table 3.4
Comparison of ammonia CO₂ capture performance with different additives.

| Parameters | Additives | CO ₂ loading (mol/mol) | CO ₂ removal efficiency | Reference |
|---|---|-----------------------------------|------------------------------------|--------------------------------|
| 8.22 mol NH ₃ /kg H ₂ O, T = 27 °C | 1.5 mol K ₂ CO ₃ /kg H ₂ O | 0.4 | 90 % | (Pachitsas and Bonalumi, 2022) |
| 6.31 mol NH ₃ /kg H ₂ O, T = 27 °C | 1.0 mol K ₂ CO ₃ /kg H ₂ O | 0.3 | 90 % | |
| 4 M NH ₃ , T = 25 °C, CO ₂ = 12 vol% | 0.25 mol Piperazine /kg H ₂ O | 0.43 | 85.0 % | (Jiang et al., 2018) |
| 2.5 M NH ₃ , T = 25 °C | 1.50 M K ₂ CO ₃ | 0.35 | >90 % | (Lillia et al., 2019) |
| 0.85 mol/L NH ₃ , T = 20 °C | Ethanol | - | 1.64 kg/kg | (Gao et al., 2015) |
| 3 mol/L NH ₃ , T = 26 °C | Capacitive deionization | 0.24 | 87.0 % | (Ullah et al., 2017) |
| 3.6 wt.% NH ₃ , T = 25 °C | 20 mL microalgae | - | 76.8 % | (Song et al., 2019a) |
| 5 wt.% NH ₃ , T = 20 °C, CO ₂ = 15 vol % | 0.1 mol/L Piperazine /kg H ₂ O | - | 60.0 % | (Xu et al., 2019) |
| 247 mg/L NH ₃ , T = 25 °C, CO ₂ = 5 vol % | 423 mg/L microalgae | 17 mg/L | 87.0 % | (Song et al., 2019c) |

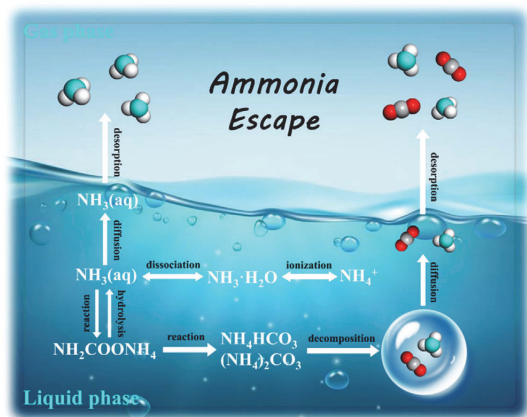


Fig. 3.14. Schematic diagram of ammonia escape. (For interpretation of the references to color in this figure legend, the reader is referred to the web version of this article.)

release, thus decreasing the liquid-phase partial pressure of free ammonia, which adversely affects the absorption process. Ethanol does not show significant differences in this regard. In addition, Pellegrini et al. (2010) pointed out that partial replacement of water in chemical absorbents by ethanol solvents with a smaller specific heat can significantly reduce the regeneration energy consumption (the specific heat of anhydrous ethanol is 2.4×10^3 J/(kg·°C), which is only 57 % of that of water, i.e., the same mass of solvent can save nearly 40 % of the heat by increasing the same temperature), which shows that "ammonia-ethanol mixture (i.e., the same mass of solvent can save nearly 40 %

of the heat by increasing the same temperature), which shows that the "ammonia-ethanol mixture" has significant advantages for CO₂ absorption and capture (Zhang et al., 2019).

The solubility of the products in the reaction process of CO₂ absorption by ammonia is known. Ammonium carbamate is soluble in water and soluble in ethanol, and ammonium bicarbonate is soluble in water-insoluble in ethanol. As reported (Gao et al., 2015; Zhang et al., 2019), the ammonia carbon capture process could be controlled to a low carbonation degree (<0.5) (Fig. 3.15) to ensure the efficient carbon capture rate of the system and adopted a new decarbonization and regeneration process of "ammonia-ethanol mixed absorption leading to solvation crystallization and crystal regeneration instead of rich liquid regeneration." It has been proved that the ammonia-ethanol liquid-phase mixed absorption of the CO₂ dissolution crystallization process is mainly precipitated by NH₄HCO₃ crystals.

The regeneration tower only needs to heat the NH₄HCO₃ crystal products, indicated in Fig. 3.16. NH₄HCO₃ crystals could be decomposed into CO₂, NH₃, and H₂O above 36 °C and completely decompose at 60 °C. This can greatly reduce the system's energy consumption by eliminating the energy consumed by heating and vaporizing the solvent during conventional liquid-rich desorption.

3.1.3.4. Applications and outlook. The mainstream CO₂ liquid-phase chemical absorption method is difficult to avoid high regeneration energy consumption, degradation problems, and high corrosiveness. The discovery of ethanol additives has further improved the techno-economic of the amino CO₂ absorption system. The new ammonia carbon capture technology ("ammonia-ethanol hybrid absorber") shows great potential in carbon capture. With the rapid development of CO₂ solid-phase adsorption technology, biochar is considered the most promising solid CO₂ adsorbent for application (Creamer et al., 2014). Suppose biochar particles are used as modified materials to enhance the liquid-phase mass transfer characteristics. In that case, their stronger

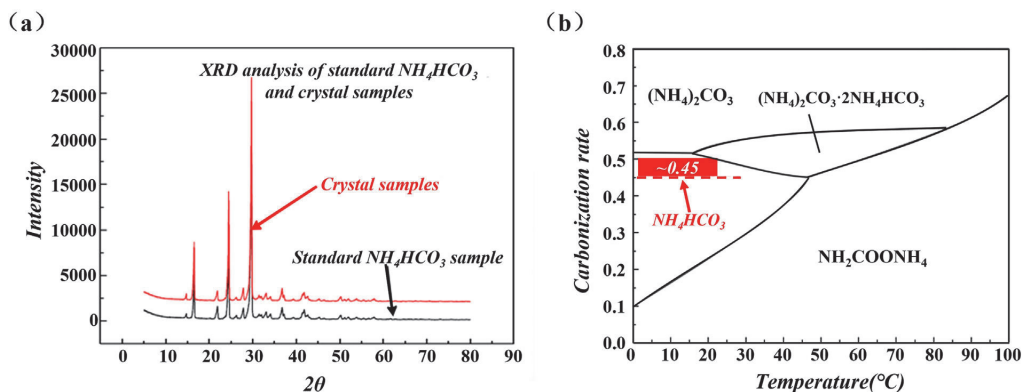


Fig. 3.15. (a) Crystal and standard NH_4HCO_3 sample analysed by X-ray diffractometer (b) The effect of carbonization rate on the "carbon balance" of ammonia-based carbon capture system (Gao et al., 2015). (For interpretation of the references to color in this figure legend, the reader is referred to the web version of this article.)

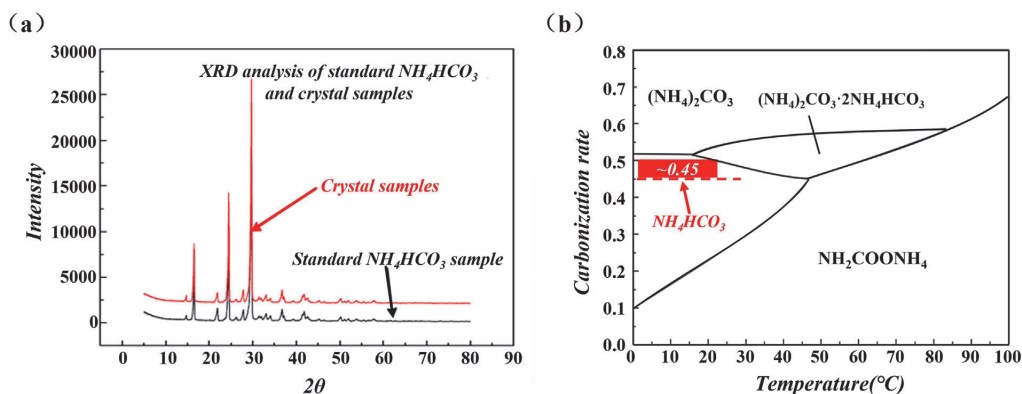


Fig. 3.16. The crystal sample after reaction (Gao et al., 2015). (For interpretation of the references to color in this figure legend, the reader is referred to the web version of this article.)

CO_2 diffusion characteristics can be fully utilized to improve the overall carbon-negative degree and CO_2 capture rate of the CO_2 capture system, enhance the solid-liquid two-phase mass transfer enhancement and suppress ammonia escape (Zhang, et al., 2022). The high-quality rice husk nano-pore carbon was prepared using agricultural waste rice husk, combined with the new ammonia CO_2 capture technology to improve the overall performance of carbon dioxide capture. In addition, the intermediate product NH_4HCO_3 from the new ammonia CO_2 capture and the intermediate product K_2SiO_3 from the preparation of rice husk nano-pore carbon were used to prepare nanoscale silica through process regulation, which significantly solved the problems of CO_2 capture product dissipation, agricultural waste pollution, and high-value product preparation. The production of high-value products - rice husk nano-pore carbon and nano-grade silica - also helps form an integrated system of energy and product laddering and integrated removal of various pollutants, which provides a new idea for a CO_2 capture system.

3.2. Low-temperature solid sorbents

3.2.1. Cyclic adsorption processes for carbon capture

Advanced sorbents, process design and swing technologies are the fundamentals for adsorptive carbon capture technologies. The adsorbents and their shaping and pellet sizes have been demonstrated to have

a significant impact on the separation performances (Hedin et al., 2013; Zapata Ballesteros et al., 2022). Bed design such as multilayer packing has been employed to selectively pre-remove minor impurities including SO_x , NO_x and H_2O , with part of the adsorbents being replaced by activated alumina, silica gel or zeolites (Hefti and Mazzotti, 2018).

One of the most challenging tasks in adsorption is the ranking of the performances of different adsorbents, in which isotherm based selectivity and working capacity are often unsatisfying (Khurana and Farooq, 2016a). Simplified cycles have been used for adsorbent screening, which provides rapid (seconds to minutes) solutions to pre-select suitable adsorbents for various functions (Ajjenifuja et al., 2020; Gutierrez-Ortega et al., 2022; Maring and Webley, 2013b; Rajagopalan et al., 2016; Subramanian Balashankar et al., 2019; Wang, Jiajun et al., 2021). Moreover, efficient engineering processes are the key to the development of operable and economical adsorption technologies. The fine-tuning of both adsorbents and processes is crucial to commercializing adsorption technologies (Zanco et al., 2017).

Almost all adsorbents appear to have a strong affinity to CO_2 over other major components, i.e., N_2 and O_2 , due to the large quadrupole moment and high polarizability of CO_2 , which means CO_2 is always the heavy component that is adsorbed and regenerated from adsorbents. CO_2 selective adsorbents are also favoured due to the low concentration of CO_2 in carbon capture applications, e.g. confined space (0.7%) (Zhan et al., 2020), air (0.04%), flue gas in natural gas fired (3–5%) and coal

fired (10–15%) power plants. The target of these cycles is to recover the heavy product at high purities.

CO₂ capture using adsorption can be classified as temperature swing adsorption (TSA) and pressure swing adsorption (PSA) based on their dominant regeneration mechanism, i.e. increase in temperature or decrease in pressure (Webley, 2014). Other effects must also be taken into account, such as heat and mass transfer, pressurization, and energy consumption, and there is still no straightforward way to design regenerative cycles for adsorption processes (Subramanian Balashankar et al., 2019).

3.2.1.1. Pressure/vacuum swing adsorption (P/VSA). P/VSA cycles have been developed over the last several decades through various applications, reported by Skarstrom (1960) for gas mixture separation, Sircar and Kratz (1988) for hydrogen purification, Grande et al. (2010) for propane/propylene separation. P/VSA is the most frequently studied for the adsorptive carbon capture process, with multiple pilot scale demonstrations reported (Cho et al., 2004; Krishnamurthy et al., 2014b; Wang et al., 2013a,b). PSA cycles are the most suitable for pre-combustion conditions as the feed gas is often at high pressures, while VSA is more often used for post-combustion, where vacuum evacuation is employed for the regeneration of adsorbents. Adsorption at high pressure and regeneration under vacuum may also be considered to enhance the working capacity of adsorbents. A typical P/VSA cycle includes two necessary steps: adsorption at high pressure and desorption at low pressure, with a few modifications available to improve separation performances and process efficiencies, such as depressurization, purge, pressure equalization, repressurization.

The high flexibility of PSA makes it possible to meet the specifications of feed conditions and desired separation targets, through one or multiple stages. However, it seems a single stage PSA struggles to reach the > 95% CO₂ purity target with > 90% recovery from a 15% feed gas, which often requires extremely low vacuum conditions (Khurana and Farooq, 2016b; Ntiamoah et al., 2015; Yan et al., 2016). Another concern regarding P/VSA is that the energy consumption is often underestimated as high grade energy (electricity) must be used for pressure variation (Zhao et al., 2017b), where a thermal energy conversion is necessary to compare its performance with the benchmark amine processes fairly.

Dual reflux pressure swing adsorption (DR-PSA), also known as duplex PSA, is a special format of PSA in which the feed position is not constrained to the end of an adsorption column. An adsorption column can then be divided into a rectifying section and an enriching section, and two high purity product streams can be achieved simultaneously (Diagne et al., 1994; Leavitt, 1992). DR-PSA cycles consist of four fundamental steps, i.e., adsorption/feed, pressurization, purge and blowdown. It can be applied via four basic configurations, i.e., DR-PL-A, DR-PH-A, DR-PL-B and DR-PH-B, depending on the feed position and purged streams (Guo et al., 2021; Kearns and Webley, 2006a,b). Here, PL and PH refer to the feed injected into the high- and low-pressure column, respectively; A and B denote the types of the purged gas, adsorbate (heavy component) and less adsorbed component, respectively.

DR-PSA has been a rapidly developing process in the past two decades, with many researchers dedicated to providing process optimization methods, such as the Triangular Operating Zone (TOZ) (Rossi et al., 2020), Capacity Ratio (C) (May et al., 2017) and feed position (z_{feed}) analysis (Guo et al., 2021). Zhang et al. achieved 99% CO₂ purity with 99% recovery from a 15% feed gas in a simulated work (Li et al., 2016). In a pilot investigation, Wawrzyńczak et al. compared a 9-step DR-PSA with an 8-step PVSA cycle with a 4-bed system using 540 kg activated carbon as adsorbents (Wawrzyńczak et al., 2019). The DR-PSA cycle showed a 14% higher CO₂ purity and 28% higher energy costs, 29% lower CO₂ recovery and 30% lower productivity. This may be due to the cycles are not fully optimized, such as feed position, pressure ratio and purged quantity (Bhatt et al., 2017, 2018).

3.2.1.2. Temperature swing adsorption (TSA). TSA cycles regenerate the adsorbents via lifting the column temperature. The packed adsorption column also serves as a heat exchanger packed with adsorbents (Masuda et al., 2021). Researchers have explored multiple ways to heat the entire column to the desired temperature, via direct or indirect heating. TSA has drawn great interest in carbon capture from power plants, given that available waste heat reuse is an advantage. For example, the temperature of low grade heat in power plants, such as waste steam and flue gases, can be over 300 °C, which perfectly suits the regeneration of adsorbents (Leppänen et al., 2014; Zanco et al., 2017).

Direct heating often refers to the adsorbents in direct contact with heating media such as hot steam, air or CO₂. As direct heating using nonadsorbing gases leads to the dilution of CO₂ products, hot steam or CO₂ product are preferred to serve as the heating sources (Ntiamoah et al., 2016). Indirect heating does not incur the dilution problem and refers to heating sources such as heating/cooling jacket and inner heating/cooling pipes, which often requires a less adsorbing sweep gas (N₂, air or flue gases) to recover the desorbed CO₂.

The basic step sequence of a TSA cycle is adsorption, heating and regeneration, and cooling, where CO₂ product purity can rarely reach the 95% target in carbon capture applications. Several novel design concepts have been employed to achieve better separation performances. For example, a purge using feed prior to adsorption can push the regenerated CO₂ out of bed to enhance recovery; a purge step using the CO₂ product prior to the heating and regeneration step can push the free gas out of bed to increase the product purity; other internal purge steps can also be used to integrate the heat and reduce energy consumptions, e.g., a novel 5-step cycle consists of adsorption, heavy reflux using the light purged gas stream, desorption/heating, light purge, cooling (Joss et al., 2017). Mazzotti et al. compared four TSA cycles and concluded that the cycle with purge and recycle steps outperformed others, reaching the DOE target of 95% CO₂ purity with 90% recovery from flue gases containing 12% CO₂ (Joss et al., 2017; Peh et al., 2022). The major issue with TSA is the long time required for heating and cooling, resulting in the long cycle time ranging from minutes to days. Hence, the number of columns and the time schedule of TSA cycles are crucial in assessing their separation performances.

3.2.1.3. Pressure temperature swing adsorption (PTSA). Separation performance is extremely sensitive to the regeneration temperature and evacuation pressure, which is dependent on the properties of adsorbents (Plaza and Rubiera, 2019; Zhan et al., 2021). The productivity of conventional PSA cycles is often reduced due to the exothermic nature of adsorption, i.e., high bed temperature during adsorption and low bed temperature during desorption (Plaza and Rubiera, 2019). Hybrid cycles by combining the effects of temperature and pressure, i.e., pressure temperature swing adsorption (PTSA), may be capable of solving this problem and allowing for milder regeneration conditions which are easier to achieve for large scale CO₂ capture plants, i.e., lower regeneration temperature compared with TSA and higher desorption pressure than PSA (Wang et al., 2012; Wurzbacher et al., 2011). Such lower temperature is easier to be integrated with waste heat in power plants than conventional TSA. Hence, PTSA possibly requires lower energy consumption and achieves higher process efficiency/productivity, although with higher cycle complexity (Su and Lu, 2012).

A simple PTSA process consists of the following steps: adsorption, heating and depressurization or evacuation, cooling and/or pressurization (Wang et al., 2021). More complex cycles are also reported, such as a 7-step cycle, including adsorption, pressure equalization, depressurization, vacuum heating, vacuum cooling, pressure equalization, and pressurization (Zhan et al., 2021). Cooling water may also be introduced to maintain the column temperature during the adsorption step to avoid the capacity drop due to the released heat of adsorption. Tsutsumi et al. reported a 40% energy penalty reduction via energy recovery measures such as pressure recovery through an expander and adsorption heat recovery through a chemical heat transformer (Song et al., 2016). Plaza

and Rubiera simulated a PTSA carbon capture process in an 820 MWe power plant using a desorption temperature of 80 °C and pressure of 5 kPa. Results showed the energy penalty is 2.41 MJ (heating)/kg CO₂ and 1.15 MJ (evacuation)/kg CO₂, which is mainly due to the extremely low desorption pressure (Plaza and Rubiera, 2019).

3.2.1.4. Electric swing adsorption (ESA). ESA has been reported as commercially viable for volatile organic compounds (VOC) removal (Subrenat and Le Cloirec, 2006). Adsorptive carbon capture using ESA aims to solve the lengthy heating time issue related to conventional TSA and improve the overall productivity of adsorbents (Zhao et al., 2019), in which rapid and homogeneous heating can be achieved via electrification by Joule effect (or Ohmic heating). The temperatures of adsorbents can be raised to 70 °C in 22 s at a potential of 24 V (Mendes et al., 2021) or 10 V (Pereira et al., 2022), 101 °C in 90 s at a potential of 60.5 V (Zhao et al., 2019), and 150 °C in less than 30 s at a potential of 8 V (Verougstraete et al., 2022). Even though the electric power for ESA is of a higher exergetic energy format than thermal energy required by TSA, such low voltage requirements in ESA cycles offer an opportunity to integrate with renewable electricity.

A simple operational ESA cycle consists of the following steps: adsorption, electrification, rinse/purge or evacuation, and cooling. More complex cycles have also been demonstrated for high CO₂ purity and recovery, with extra internal rinse, purge and depressurization steps (Grande et al., 2009); 89.7% purity and 72.0% recovery were achieved from 3.5% CO₂ flue gases.

ESA cycles require that adsorbents must be conductive, such as activated carbons, hybrid adsorbents combining zeolite and activated carbon, and uniform adsorbents to allow heat to be transferred homogeneously (Zhao et al., 2018). Uneven heating may lead to hot spots and damage the adsorbents due to partial overheat. Three-dimensional (3D) printing is an ideal methodology to replace conventional pelleting, which shows lower pressure drop, no fluidization and better heat transfer. This also provides a pathway to create hybrid adsorbents, which may combine the best properties of multiple adsorbents, CO₂ uptake capacity, CO₂/N₂ selectivity and mass transfer coefficient. It should be noted that the cooling step still requires quite a significant time, which may be a major hurdle for its application. According to Grande et al., electric heating only accounts for 1.5% of the cycle time (2225 s) (Lillia et al., 2018), with enormous time put into the cooling of adsorbents.

3.2.1.5. Rapid pressure or temperature swing adsorption (RPSA/RTSA). A 600 MWe coal power plant emits 500 m³/s of flue gas with 13% CO₂ (Merkel, et al., 2010). Hence, it is critical to develop economical CO₂ separation technologies to handle flue gases with massive flow rates. Rapid swing adsorption shows its superiority as CO₂ capture from flue gases is often at a very large scale, and the structuring of adsorbents becomes crucial to allow a high flow rate and avoid sorbent pulverization. The cycle sequence in rapid swing adsorption is similar to conventional ones, with modifications in different aspects. In a reported rapid pressure swing adsorption process, the total cycle time is 18 s, which employs the same cycle as conventional PSA, i.e., adsorption (8 s), desorption (8 s), purge (1 s) and repressurization (1 s) (Luberti et al., 2017). The superficial velocity is as high as 1.6 m/s, which is much higher than conventional PSA cycles (0.1–0.5 m/s), resulting in a significant pressure drop of 16 kPa at the column length to diameter ratio of 1:1.

Rapid temperature swing adsorption (RTSA) can be achieved via direct heating using hot steam, which involves quick heating through the latent heat and adsorption competition between water vapour and CO₂. A hot air stream is essential to remove the condensed steam right after CO₂ regeneration (prior cooling) to avoid a significant capacity drop. The cycle time can also be reduced to 20–330 s, which is much lower than conventional TSA cycles (≥ 15 min) (Verougstraete et al., 2020). RTSA may also be achieved using hybrid materials, which employ a hollow fiber embedded with porous adsorbents, as demonstrated by Lively et al. (2009). Such hollow fiber adsorbent performs as both a heat

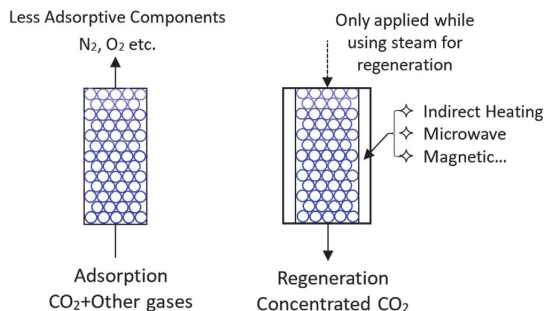


Fig. 3.17. A simplified schematic adsorptive cycle. Adsorption occurs at high pressure and/or low temperatures. Regeneration occurs at low pressure and/or high temperatures, where the heating can be achieved by heat conduction, Joule effect, magnetic effect, microwave etc. (For interpretation of the references to color in this figure legend, the reader is referred to the web version of this article.)

exchanger and gas contactor (or “adsorbing heat exchangers” (Lively et al., 2010)), for which 90% adsorption occurs within the first 2 s (Lively et al., 2012), and thermal equilibrium can also be achieved within seconds. A high linear velocity of 1.6 m/s was also tested (Lively et al., 2012). This setup also enables internal cooling during adsorption so the adsorption enthalpy can be quickly removed to maintain a high CO₂ uptake capacity. The hollow fiber RTSA cycles have also been extended to air separation by integrating LiX zeolites on thermally stable polymers (Sujan et al., 2018).

Other novel design concepts are also seen in literature such as the rotary adsorption system for MOF based carbon capture systems (Lin et al., 2021), fin coil heat exchangers filled with an adsorbent that allows internal heating and cooling (Masuda et al., 2021, 2022) and structured honeycomb carbon monolith adsorbents which can tolerate high linear velocities of flue gases as high as 3.4 m/s (Verougstraete et al., 2020).

3.2.1.6. Other swing concepts. Hybrid cycles combining two or more of the above mentioned swing technologies have been widely investigated, such as those combining ESA and VSA, namely VESA (Zhao et al., 2019); ESA and TSA, namely TESA (Lillia et al., 2018); ESA ad VSA, namely VESA (Zhao et al., 2019). Different adsorption column configurations are also considered including fixed beds, fluidized beds, moving beds and simulated moving beds to improve the separation performances (Yi et al., 2007). Fixed beds are still the most commonly used configuration due to their simplicity and low requirement in the mechanical strength of adsorbents.

Novel swing concepts are continuously proposed to improve the energy efficiency and separation performances of adsorptive carbon capture technologies. Microwave, commonly interpreted by three mechanisms, i.e. ionic conduction, dipolar rotation of polar molecules and dielectric polarization (Lee et al., 2019), has been applied to the regeneration of adsorbents using a hybrid adsorbent of graphene oxide and MIL-91 (Muschi et al., 2021), in which desorption occurred faster and under lower temperature, i.e. 50 °C for 150 s using microwave versus 80 °C for 215 s using conventional electrical heating. High microwave absorption allows temperature increases through energy dissipation. Sound assisted adsorption/desorption is reported to enhance kinetics and cut overall energy consumption (Ammendola et al., 2015; Raganati et al., 2020). Magnetic induction swing adsorption (MISA) has also attracted interest due to its high energy efficiency (Bellucci et al., 2021; Li et al., 2016a). However, these concepts are rather immature and needs more exploration.

In summary, adsorptive swing technologies can be as simple as shown in Fig. 3.17, which consists of an adsorption and a desorption step. The adsorption step occurs at high pressure and/or low temper-

atures. Regeneration occurs at low pressure and/or high temperatures. Any form of radiation may be used for adsorbents regeneration as long as the adsorbents can absorb the form of radiation, such as evacuation (PVSA), heating (TSA), Joule effect (ESA), magnetic effect (MSA), microwave (MCSA) etc. However, efficient processes, which can heavily impact the performance of cyclic adsorption processes, are much more complicated than the two-step cycles. There is yet no best way to design and optimize such processes.

3.2.2. MOF-based materials for CO₂ capture

Metal organic frameworks (MOFs) are deemed to be the most promising materials for CO₂ adsorption due to their high porosity, large specific surface area, designability, tunability, rich spatial topology, and unsaturated metal sites. Zn (BDC) became the first reported MOFs material for CO₂ adsorption (Li et al., 1998), and then Yaghi synthesized a series of MOFs to systematically investigate the effects of structural and porous attributes on CO₂ adsorption performance (Millward and Yaghi, 2005). The results showed that the higher pressure and larger specific surface area were favourable for CO₂ adsorption, which opened the door to explore MOFs in the field of CO₂ adsorption capture and separation. Several MOFs have been prepared and commercialized on a large scale, such as MOF-177, HKUST-1, ZIF-8, UIO-66, and MIL-127 (Gargiulo et al., 2020).

3.2.2.1. Influence of pressure on CO₂ capture. The adsorption of gases can be divided into high and low pressure. For high pressure condition, CO₂ adsorption is generally related to the specific surface area and pore volume of MOFs. Hu et al. (Hu et al., 2013) studied the behavior of ZIF-8 for high pressure CO₂ adsorption using situ FTIR spectroscopy, the results showed that the chemical and mechanical robustness of the framework formed by the relatively stiffer metal centered tetrahedrons as joints but with flexible linkers makes ZIF-8 a promising agent for the storage of CO₂ at high pressure conditions. Arstad et al. (2008) synthesized USO-2 using Ni (NO₃)₂ as a metal ion source and 1,4-phenylene terephthalic acid (1,4-H₂BDC) as a ligand, which increased CO₂ adsorption at 25 atm compared to atmospheric pressure adsorption by 46%. Qasem et al. (2018) prepared MOF-177, which has excellent storage capacity at high pressure (≥10 bar) and gradually increases its adsorption capacity with increasing external pressure, from 0.07 kg kg⁻¹ at 5 bar to 1.58 kg kg⁻¹ at 30 bar, with a 22-fold increase in its adsorption capacity. Llewellyn et al. (2008) prepared mesoporous MIL-101 and found a high adsorption capacity of 40 mmol g⁻¹ by activating it with ethanol and KF at 5 MPa and 303 K. To further increase the surface area of the adsorbent material, Farha et al. (2010) designed a new MOF material (NU-100) with Cu²⁺ as the metal center and hexatopic carboxylate as the organic ligand through calculation and simulation, and successfully prepared it through experiments. The MOF has a super high surface area of 6143 m² g⁻¹ and the total pore volume is 2.82 cm³ g⁻¹, and its CO₂ adsorption capacity reaches 2315 mg g⁻¹ at 40 bar and 298 K. Furukawa et al. (2010) synthesized MOFs using Zn²⁺ as the metal center and various carboxylate organic ligands, among which MOF-210 has a larger surface area (6240 m² g⁻¹) and a large pore volume (3.6 cm³ g⁻¹), so that its adsorption capacity also reaches an impressive values of 2870 mg g⁻¹ at 50 bar and 298 K. In addition to the selection of ligands with longer molecular chains, the surface area of MOFs can also be increased by introducing defects. Wu et al. (2013) adjusted the degree of defects by adding different concentrations of acetic acid to the UIO-66 system and setting different reaction times, and the porosity of UIO-66 increased dramatically with increasing dosage and longer reaction times, which results in an increase in pore volume from 0.44 cm³ g⁻¹ to 1 cm³ g⁻¹ and an increase in surface area from 1000 m² g⁻¹ to 1600 m² g⁻¹. Moreover, the hydroxyl group on the surface of UIO-66 was found to contribute to the adsorption of CO₂ due to the presence of the Coulombic interactions between the negatively charged O (of CO₂) and the positively charged H (of the -OH group), making the CO₂ uptake in the hydroxylated MOF

(2.50 mmol g⁻¹) at 300 K and 1 bar is more than 50 % higher than that in the dehydroxylated MOF (1.60 mmol g⁻¹).

Compared with high-pressure adsorption, low-pressure adsorption is more common in industrial production and is mainly used to capture CO₂ from combustion exhaust gases. Low-pressure adsorption is mainly related to the heat of CO₂ adsorption, which can be improved by introducing unsaturated metal sites, ligand group modification, and introducing defects.

- (i) Introduction of coordinated unsaturated metal sites and ion doping. During the preparation of MOFs, solvent molecules will be coordinated with metal sites, and the unsaturated metal sites are obtained by removing solvent molecules through the solvent exchange, vacuum heating, and freeze-drying to enhance the adsorption capacity of MOFs. MOF-74 is a common low-pressure CO₂ adsorption material, which is prepared from divalent metal ions (Fe²⁺, Co²⁺, Ni²⁺, Mg²⁺, Zn²⁺, etc.) and 2,5-dihydroxyterephthalic acid, where Mg-MOF-74 has excellent low-pressure CO₂ adsorption (8.6 mmol g⁻¹) at 100 kPa and 298 K. This is due to the high density of open metal sites in MOF-74 and the presence of Mg–O bonds that improve the CO₂ adsorption capacity relative to the chemical bonds formed by other metal ions (Bahamon and Vega, 2016; Caskey et al., 2008). In addition to this, HKUST-1 is also a common material for low-pressure CO₂ adsorption, due to the high charge density of Cu²⁺, which allows a strong interaction with CO₂ (Hamon et al., 2010; Yazaydin et al., 2009). After treatment with ethanol and NH₄Cl at 338 K, it also has a high adsorption capacity (11.6 mmol g⁻¹) at 1 atm and 273 K (Yan et al., 2014). To further improve the adsorption performance, bimetallics can be introduced to the MOF framework as metal sites and optimal results have been obtained by adjusting the ratios, Gao et al. (2021) prepared Zn_{0.75}Mg_{0.25}-MOF-74 by one-step hydrothermal synthesis (Fig. 3.18a), due to the large surface area (667.6 m² g⁻¹) and affinity for CO₂, its CO₂ adsorption capacity of 128.3 cm³ g⁻¹ at 1 bar and 273 K. Also, due to the multiple active sites of the unsaturated metal centers as active Lewis acid sites and O atoms from Zn–O and Mg–O as Lewis basic sites, conferring excellent catalytic properties. Kadi et al. (2020) prepared Cu_{1.5}Mg_{1.5} (BTC)₂ with a molar ratio of Cu to Mg of 1:1, and this MOF maintained the original crystalline shape of HKUST-1. The substitution of Cu of atomic radius 128 pm by larger ions of Mg of atomic radius 173 pm may lead to electrostatic unbalance in the surface of the MOF, which enhance the adsorption efficiency due to the created synergetic phenomenon, resulting in a significant increase in adsorption to 23.85 mmol g⁻¹, which is much higher than Cu-BTC (5.95 mmol g⁻¹) and Mg-BTC (4.57 mmol g⁻¹). In addition to this, unsaturated alkali metal ions can be introduced into the framework of MOF to enhance the adsorption performance, for example, K⁺ can be immobilized in NKU-521 through a tetrazole based motif and are effectively embedded in a trinuclear Co²⁺-tetrazole coordination motif (Fig. 3.18b), resulting in a 24 % increase in isosteric heat for CO₂, with a CO₂ adsorption capacity of 139 cm³ g⁻¹ at 273 K and 1 atm (Li et al., 2019). Bae et al. (2011) introduced Li⁺ into Zn-MOF using different methods to enhance the adsorption performance, and after experimental analysis, it is known that the chain structure can be replaced and the pore capacity can be reduced by the chemical reduction method leading to improved adsorption, while the ion exchange method is due to the stronger interaction of the desolvated Li⁺ with CO₂ (Fig. 3.18c).
- (ii) Organic ligand selection and group modification. Since the acid-base and dipole-quadrupole interactions between N atoms and CO₂ molecules induce dispersion and electrostatic forces between CO₂ and MOFs, thus enhancing the adsorption capacity of MOFs, the current chemical modifications are mainly based on the selection of organic ligands containing N elements or the

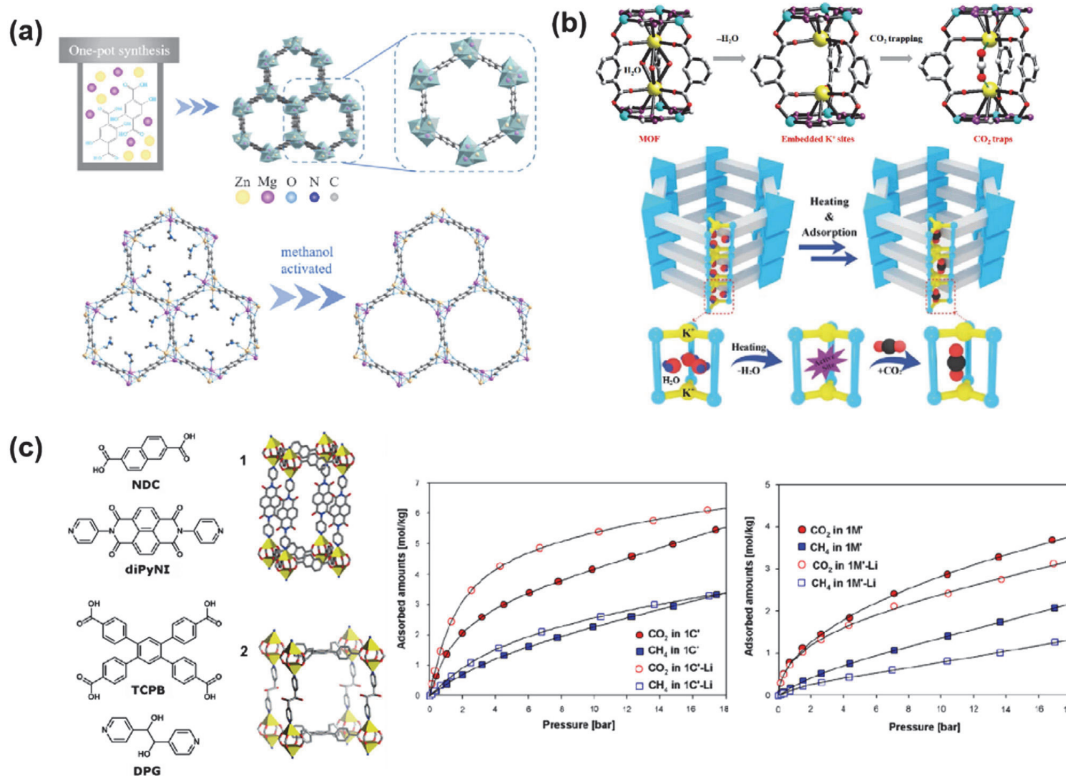


Fig. 3.18. (a) facile one-pot method to synthesize bimetallic Zn/Mg-MOF-74, and 2D structure of original and methanol-activated Zn/Mg-MOF-74 (Gao et al., 2021); (b) the structures of the framework of NKU-521 and Co-K MBB, and schematic illustration of the MOF featuring novel K^+ binding sites for CO_2 (Li et al., 2019); (c) chemical structures of ligands, the crystal structure of MOFs and effect of chemical reduction on the CO_2 and CH_4 isotherms in 1C and 1M at 298 K (Bae et al., 2011). (For interpretation of the references to color in this figure legend, the reader is referred to the web version of this article.)

introduction of Lewis bases. The direct selection of ligands containing N element can eliminate the complex preparation process, such as nitrogen heterocycles, aromatic amines, adenine, triazole and so on. Hong et al. (2017) used 4-(2-hydroxy-3-methoxy-benzyl)-dene-hydrazinocarbonyl)-N-pyridin-4-yl-(benzamide) compounds as organic ligands for the synthesis of Cd-MOF, which has a heat of adsorption of 26 kJ mol^{-1} and an adsorption capacity of 1.5 mmol g^{-1} at 273 K and 1 bar. Maity et al. (2019) chose Cu^{2+} and Zn^{2+} with adenine and terephthalic acid as organic ligands for the preparation of IISEPR-MOF26 and IISEPR-MOF27, which exhibited excellent cyclic stability with CO_2 adsorption amounts of 4.3 mmol g^{-1} and 3.8 mmol g^{-1} at 273 K and 1 atm, respectively, due to the lower heat of adsorption and thus ease of desorption. In addition, the synthesized MOFs also have excellent water stability with no decay of adsorption properties in water as well as exposure to water vapour for more than 24 h. The above synthesized MOFs can be seen to only rely on nitrogen-containing ligands for CO_2 adsorption, which has a low adsorption capacity. Therefore, post-modification of the MOFs by introducing Lewis bases (amino acids, alkyl amines, etc.) is needed to further enhance the adsorption performance. Khan et al. (2018) synthesized ZIF-8 nanoparticles with $n_{Zn^{2+}}:n_{Hmim} = 1:8$. At the same time, a small amount of triethylamine was added to the synthesis process. Due to the introduction of N-H group, it helped to improve the adsorption capacity of CO_2 , reaching $22.43 \text{ mmol g}^{-1}$. Li et al. (2016b),

Li et al. (2019) used Brønsted Acid-Base Reaction and solvent effect to access alkylamines to Cr-MIL-101 (Fig. 3.19a), and the use of low-polar cyclohexane as dispersant could make higher chemical potential of alkylamine and enhanced driving force from cyclohexane to MOF, allowing for introduce more amino groups into the MOF and enhancing the adsorption capacity of CO_2 , which was 4.21 mmol g^{-1} at 150 mbar and 298 K. Yoo and Jung (2022) used aminosilanes for UIO-67 modification and by choosing different types and amounts of aminosilanes (Fig. 3.19b), the heat of adsorption after treatment was found to be between $35\text{--}50 \text{ kJ mol}^{-1}$, due to the formation of a carbamate via the interaction between primary/secondary amino groups and CO_2 , resulting in good adsorption of amino acids on CO_2 at 298 K and 15 kPa, the highest adsorption capacity can reach 0.58 mmol g^{-1} . In addition, the experimental analysis revealed no major difference in the adsorption of CO_2 between primary and secondary amino groups. Yang et al. (2011) investigated the effect of different group modifications on the adsorption properties by means of simulated calculations (Fig. 3.19c), and the heat of adsorption increased with increasing group polarity: $-SO_3H > -CO_2H > -NH_2 > -OH > -NO_2 > -Br > -CF_3$. Although the polarity of the $-CF_3$ group is the lowest, the strongest CO_2 adsorption mainly results from the highest confinement caused by the significant decrease of the accessible pore volume.

(iii) Pore size tuning. The molecular size of CO_2 is between 0.3–0.4 nm, so tuning the pore size of MOFs and using the size effect

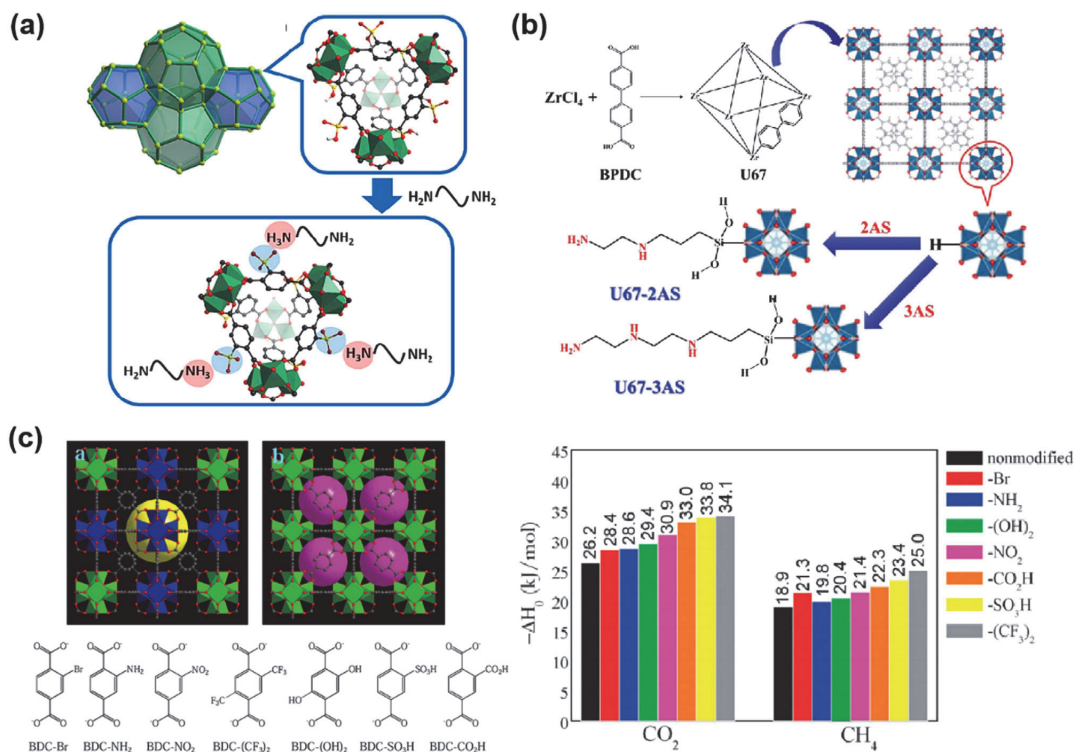


Fig. 3.19. (a) Cr-MIL-101-SO₃H topology and illustration of electrostatic interaction between sulfonate groups and ammonium groups (Li et al., 2016b); (b) a scheme to introduce amino groups on the U67 MOF (Yoo and Jung, 2022); (c) illustration of the UiO-66 (Zr) crystalline structure, including: octahedral cages, tetrahedral cages and functionalized ligands, calculated low-coverage adsorption enthalpies of pure CO₂ and CH₄ gases in the non-modified UiO-66 (Zr) and its functionalized derivatives at 303 K (Yang et al., 2011). (For interpretation of the references to color in this figure legend, the reader is referred to the web version of this article.)

for adsorption is also an effective way. Jiang et al. (2018) synthesized highly symmetric NJU-Bai35 with Cu²⁺ as metal sites and isonicotinic acid and [Cu (N₂)_∞] as dual ligands (Fig. 3.20a). Its internal space has homogeneous dimensions in the a, b, and c axis with dimensions of 3.6°3.6, 3.4°3.4, and 3.6°3.6 Å², respectively, which are close to those of CO₂, resulting in CO₂ adsorption up to 7.2 wt.% at 298 K and 0.15 bar. Bao et al. (2015) used biphenyl-carboxylic acid derivatives as ligands to synthesize [Zn₂L₂]-2DMF (Fig. 3.20b), which has a high heat of adsorption (33 kJ mol⁻¹) and a high adsorption capacity of 79.9 cm³ cm⁻³ at 298 K and 100 kPa due to the presence of N elements in the structure and a one-dimensional nanochannel with a diameter of 3.6 Å. By fine design of the pore size structure of MOFs, a size matching CO₂ can be obtained. However, the more complicated preparation process and the screening of organic ligands are not suitable for large-scale applications. Compared with directly designing MOFs with the size matching CO₂, the intercalated structure is a more convenient method. Yao et al. (2012) synthesized three SUMOFs with intercalated structures using Zn₄O clusters and rigid dicarboxylate anions (Fig. 3.20c), all of which have two different types of small pores and high pore volumes. Among them, MOF synthesized with terephthalic acid as a ligand has a structure closer to the molecular size of CO₂ (5.9 Å and 7.7 Å). In addition, with the aid of interpenetration in these MOFs, the electric field gradients in the small pores are increased, and therefore enhancing the interaction between CO₂ and the host framework. At 273 K and 100 kPa, The three MOFs synthesized have high low-pressure adsorption properties of 4.26, 3.44 and 3.6 mmol g⁻¹, respectively.

Pal et al. (2017) added a flexible N-containing donor to the Zn²⁺ and sulfonyldibenzoic acid system and synthesized {[CO₂ (SDB)₂ (L)]·(H₂O)₄·(DMF)_n} with a double interpenetrating structure by hydrothermal method. The MOF material has a rhombic channel with a size of 3.4°5.0 Å inside, and its adsorption heat is 23 kJ mol⁻¹, the CO₂ adsorption capacity is 50.6 cm³ g⁻¹ at 273 K and 1 bar.

Due to the structural limitations, MOFs suitable for high-pressure adsorption have low CO₂ adsorption performance under low pressure environment due to the larger pore size, which reduces the potential energy superposition between the pore walls and the interaction between CO₂ molecules and the material (Mason et al., 2011). MOFs suitable for low-pressure adsorption have lower surface area, which limits the performance of CO₂ adsorption. In contrast, MIL-53 has a unique double-cage structure that allows it to have a "breathing effect", which can achieve low-pressure adsorption in the internal small frame and high-pressure adsorption in the external large frame, giving the desired adsorption performance of CO₂ at different air pressures. Finsy et al. (2009) synthesized MIL-53 using Al³⁺ as the metal site and found that at pressures below 5 bar, CO₂ adsorption led to the contraction of the framework and the formation of a narrow pore, while at high pressures, further adsorption of CO₂ reopened the framework, leading to a sudden increase in adsorption above 6 bar. Mahdipour et al. (2021) synthesized three MOFs (Fe-MIL-53, Fe-MIL-101, Fe-MIL-101-NH₂) and investigated the adsorption capacity of CO₂ at different pressures (0-40 bar), compared to the other two, Fe-MIL-101-NH₂ has a larger specific surface area (915 m² g⁻¹) and pore volume (0.4 cm³ g⁻¹) with heat of adsorption of 46.7 kJ

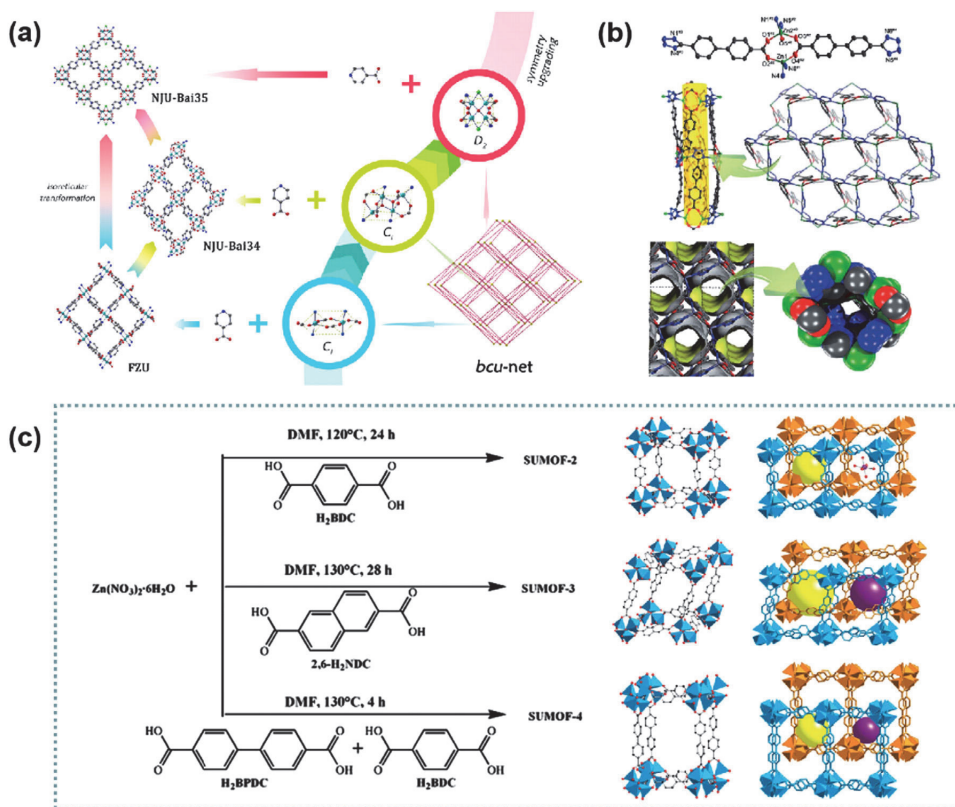


Fig. 3.20. (a) isoreticular transformation of bcu-type MOF by symmetry-upgrading inorganic clusters (Jiang et al., 2018); (b) the structure of NENU-520 obtained by Pore size design (Bao et al., 2015); (c) synthesis of the SUMOFs, non-interpenetrated models and crystal structures of the doubly interpenetrated frameworks (Yao et al., 2012). (For interpretation of the references to color in this figure legend, the reader is referred to the web version of this article.)

mol^{-1} . Moreover, the adsorption capacity increased sharply between 15–20 bar, and finally reached 13 mmol g^{-1} at 298 K and 40 bar.

In addition, MOF materials are often combined with other materials to enhance the adsorption effect. Policicchio et al. (2014) investigated the adsorption performance of urea-modified graphene oxide with Cu-BTC for CO_2 at different temperatures and pressures, and the surface area and total pore volume of the composites were $1367 \text{ m}^2 \text{ g}^{-1}$ and $0.663 \text{ cm}^3 \text{ g}^{-1}$, respectively. Compared to MOF, the surface area and total pore volume of the composites were $1367 \text{ m}^2 \text{ g}^{-1}$ and $0.663 \text{ cm}^3 \text{ g}^{-1}$, which were improved by 53.25% and 54.91%, respectively, and the heat of adsorption reached 30 kJ mol^{-1} with 7.27 mmol g^{-1} at low pressure (0.1 MPa) and 15 mmol g^{-1} at high pressure (1.5 MPa) at 277 K. In addition, it also has a fully reversible adsorption process to recover its CO_2 adsorption capacity without heat treatment. Chakraborty and Maji (2014) prepared composites for CO_2 adsorption at room temperature by immobilizing nanocrystals of Mg-MOF-74 in the mesopores of SBA-15 rods by in situ growth, and the CO_2 adsorption capacity was 88 ml g^{-1} at 293 K and P/P_0 , the heat of adsorption was 30.3 kJ mol^{-1} . Ghahramaninezhad et al. (2018) synthesized Li^+ -doped polyoxometalate ($\{\text{Mo}132\}$)-coated ZIF-8 with a surface area of $237 \text{ m}^2 \text{ g}^{-1}$ and a CO_2 adsorption of 16 mmol g^{-1} at 298 K and 10 bar, and the composite also has excellent water stability. After being exposed to humid air for 7 months, the adsorption capacity of CO_2 has not changed significantly. Qasem et al. (2017) modified multi-walled carbon nanotubes with HNO_3 and grew Cr-MIL-101 in situ on their surface. Compared with Cr-MIL-101, the surface area and pore volume of the prepared compos-

ites were $4004 \text{ m}^2 \text{ g}^{-1}$ and 2.07 cc g^{-1} , which were increased by 6.92% and 4.62%, respectively. At 298 K and 20 kPa, the maximum adsorption capacity was 1.2 mmol g^{-1} .

3.2.2.2. Surface chemistry of MOFs based CO_2 capture. The intrinsic capacity for CO_2 uptake by MOFs is influenced through either structural or functional routes.

- (i) Structural route: it involves reducing the size of micropores in the 0.5–1.2 nm range by penetration or intercalation to encourage intermolecular interactions and achieve molecular sieving (Han et al., 2013). IRMOF-9, 13, and 15 have an interpenetrated MOF-5 scaffolding, however, it has less pore size than its parent framework (Eddaoudi et al., 2002). Transition metal interpenetrated $\text{Co}_2(\text{ndc})_2$ (bipym) having pore cross-section of $4.4 \times 3.4 \text{ \AA}$ is another example of such strategy (Choi et al., 2004; Lee et al., 2003).
- (ii) Functional route: it involves the creation of frameworks with coordinatively unsaturated metal sites acting like charge-binding sites for adsorption. These could be obtained by dissolving the material in a vacuum or at high temperatures (Bae et al., 2008; Moon et al., 2006). One of the examples of such material is $[\text{M}_2(\text{DOBDC})(\text{EG})_2]$ ($\text{M} = \text{Mg}, \text{Co}, \text{Ni}$) frameworks, with open Mg (II), Co (II), and Ni (II) sites offering zero-loading enthalpies as 44.0, 35.0 and 62 kJ/mol , respectively (Kim et al., 2019).

Apart from the above two approaches, MOFs can also be modified post-synthesis through heterogeneous chemical transformations of metal groups and ligands without disturbing the overall geometry of the structure (Demessence et al., 2009; Hoskins and Robson, 1990; Jones and Bauer, 2009; Wang and Cohen, 2007). Some MOFs have been post-synthetically functionalized with alkylamines like $\text{HCu}[(\text{Cu}_4\text{Cl})_3(\text{BTri})_3]$ ($\text{H}_3\text{BTri} = 1,3,5\text{-tris}(1\text{H-}1,2,3\text{-triazol-}4\text{-yl})\text{benzene}$) and diamines like N,N' -dimethylenediamine (McDonald, 2011). Few MOFs undergoing this approach are ethylenediamine modified $\text{Mg}_2(\text{dobdc})$ having unsaturated sites of Mg (II) (Choi et al., 2012), $\text{Mg}_2(\text{dobpc})$, and $\text{Zn}_2(\text{dobpc})$ (McDonald et al., 2012). The functionalization with ethylenediamine not only enhances the CO_2 uptake capacity, but also improves the material regenerability. ZIF-68, -69, and -70 show excellent adsorption and CO_2/CO separation capacities after modification with alkaline/polar charges and N-functionalization with 4&5-azabenzimidazole and purinate ligands (Bastin et al., 2008; Chen et al., 2008; Liu and Smit, 2010; McCarthy et al., 2010). Apart from this, ZIF-related compounds like $\text{Zn}(\text{bdc})(4,4'\text{-bipy})_{0.5}$ showed improved CO_2 separation from CO_2/N_2 and $\text{CO}_2/\text{CH}_4/\text{N}_2$ gas mixtures (Bastin et al., 2008).

Unsaturated metal sites can also be created in MOFs via post-synthesis treatment. One of the examples is impregnated $[\text{Zn}_3(\text{tcpt})_2(\text{HCOO})][\text{NH}_2(\text{CH}_3)_2]$ with Li^+ , Mg^{2+} , Ca^{2+} , Co^{2+} , and Ni^{2+} cations. This in return results in increased zero-loading CO_2 uptake isosteric heat from 29.3 to 34.5–37.4 kJ mol^{-1} in $[\text{Zn}_3(\text{tcpt})_2(\text{HCOO})][\text{NH}_2(\text{CH}_3)_2]$ and cation-doped compounds, respectively (Park and Suh, 2013).

3.2.2.3. Effect of water on CO_2 adsorption. Contrary to zeolites, the adsorption capacity of MOFs can be highly affected by water due to weak metal-ligand bonds, which sometimes may result in structure collapse. Steam stability routes have been reported for MOFs over wide range of temperatures (Park and Suh, 2013). The most common example to hydrothermally unstable MOF is MOF-5. IRMOF series with Zn carboxylate clusters are also less hydrothermally stable due to quick hydrolysis of Zn-carboxylate bonds (Kaye et al., 2007; Li and Yang, 2007; Schröck et al., 2008). MIL family compounds show the highest hydrothermal stability, especially robust MIL-100 and M101 having clusters of Cr (III) (Férey et al., 2005, 2004; Küsgens et al., 2009), Zr (IV)-MOFs (i.e., $\text{Zr}_6\text{O}_4(\text{OH})_4(\text{CO}_2)_{12}$ (UiO-66) (Cavka et al., 2008), and $\text{Ni}_3(\text{bt})_2$ -based on azolate linkers (Colombo et al., 2011).

Apart from hydrothermal stability, water also plays an important role in identifying CO_2 over other gases and improve adsorption capacity. Half pore blockage by H_2O upon CO_2 adsorption is also reported in rigid MOFs. $\text{Mg}_2(\text{dobdc})$ shows a sturdy deactivation when H_2O is adsorbed via reduction of CO_2 binding energy (Yu and Balbuena, 2013). However, Co_2dobdc and $\text{Ni}_2(\text{dobdc})$ performed better after H_2O exposure and kept a stable CO_2 adsorption (Kizzie et al., 2011; Liu et al., 2011). KHUST-1 impregnated with unsaturated Cu (II) showed reduction in CO_2 capacity after two H_2O molecule coordinated at Cu sites (Liu et al., 2010). However, when one H_2O molecules coordinated, the framework showed a major improvement in CO_2 adsorption. This is due to the presence of selective electrostatic interactions among coordinated H_2O molecule and CO_2 molecule (Yazaydin et al., 2009). On the other hand, in hydrated MIL-101, the terminal H_2O molecules act as an extra binding set for CO_2 adsorption.

A very special type of property has been observed in flexible MOFs (such as the MIL-53 family) where H_2O can promote reversible structural changes. Flexible MOFs can perform adsorption/desorption cycles but become less stable over time (Cheng et al., 2009). In pure MIL-53 (Al)- NH_2 , water improves the stability of narrow pores and provides an excellent material for membrane design (Bureekaew et al., 2008). Since the flue gas contains 5–15% of water, the evaluation of MOF-based membranes in humid environment, and ternary breakthroughs tests for the mixture of CO_2 , N_2 , and H_2O are needed. MOF adsorbents, particularly those with unoccupied Lewis acid sites, generally have reduced CO_2 adsorption capabilities when exposed to moisture due to the higher affini-

ty of H_2O compared to CO_2 . For instance, Mason et al. (Mason et al., 2015) proposed 83% decrease in total CO_2 adsorption (from 5.87 mmol g^{-1} (Hu et al., 2017b) to 1 mmol g^{-1}) for Mg-MOF-74 under wet condition. In the case of MOFs with small apertures, the same trend is followed as in the case of opt-UiO-66 (Zr)- $(\text{OH})_2$, which shows 90% (from 2.47 mmol g^{-1} to 0.7 mmol g^{-1}) reduction in CO_2 adsorption capacity (Nguyen et al., 2014). The water-repellent characteristics of MOFs can be improved by either doping chemical functions like alkyl amines, or by boosting the hydrophobicity. For example, doping with hydrazine (N_2H_4), N,N' -dimethylethylenediamine (mmen), and 2,2-dimethyl-1,3-diaminopropane (dmpn) can result in 100% retention of CO_2 uptake. Nguyen et al. (2014) developed a hydrophobic chabazite-type ZIF-300, capable of upholding constant CO_2 uptake capacity within 80% relative humidity. Furthermore, Hu et al. (2017a) synthesized a triphasic hydrothermal approach for introducing ligands into parental UiO-66 structures and demonstrated that UiO-66 (Zr)- $\text{NH}_2\text{-F}_4\text{-0.53}$ show a loss of only 30% in CO_2 capture capacity under 70% relative humidity and $\text{CO}_2(15)/\text{N}_2(85)$ mixture.

In summary, it can be seen that MOFs have made a big breakthrough in CO_2 adsorption due to their advantages such as designable chemical structure, adjustable pore size, and high chemisorption capacity. However, there are still problems that need to be solved. Firstly, we should continue to improve the adsorption capacity of MOFs, especially under atmospheric pressure, and conduct in-depth research on the adsorption mechanism; secondly, we should improve the environmental stability of MOFs, so that they have high thermal stability, water stability, and high selective adsorption; thirdly, the current research mainly focuses on the adsorption of CO_2 , and in the future, we can focus on the desorption, enrichment, and conversion of CO_2 ; fourthly, the ligands used in MOFs are mainly derived from chemical materials, which is not conducive to sustainable development, the use of biomass materials (e.g., lignin derivatives, furandicarboxylic acid, etc.) as ligands and their structure and adsorption properties can be explored.

3.2.3. Carbon materials (biochar and activated carbon) for CO_2 capture

3.2.3.1. Biochar for CO_2 adsorption.

3.2.3.1.1. Introduction of biochar and its properties. Biochar is an eco-friendly adsorbent that is produced from different kinds of biomass and organic wastes. Although many carbon-based porous materials are available on the market, biomass-derived adsorbents seem attractive for biomass and waste management. Biochars and activated biochars might be used as adsorbents for carbon dioxide capturing thanks to their developed porous structure, noticeable carbon dioxide adsorption capacities (Singh et al., 2019) and also high thermal, chemical and mechanical resistance (Amer et al., 2022). Biochars are also about ten times cheaper than other CO_2 adsorbents due to the wide availability of biomass on the market and relatively simple and cheap synthesis methods. Additionally, to minimize the cost of the adsorbent, waste materials are used as a raw feedstock in a pure state or as a mixture with biomass, usually woody or lignocellulosic (Ibrahim et al., 2022; Igalavithana et al., 2020; Liu, 2019; Xu et al., 2016).

The physicochemical properties of biochar are greatly affected by the pyrolysis operating parameters (e.g., temperature, retention time, carrier gas flow rate, and heating rate) (Foong et al., 2020). For instance, slow pyrolysis was reported to produce biochar with a larger pore volume and surface area. This is because a longer reaction time/slow heating rate enhanced the release of volatile organic matter from the feedstock, thus creating a more porous structure on the surface of biochar (Foong et al., 2020).

Pristine biochar obtained through pyrolysis was reported to have a low total pore volume (0.016–0.083 cm^3/g) and surface area (8–132 m^2/g). The pore size of the pristine biochar is contributed mainly by micropores (12.1–58.0%) and mesopores (18.9–31.7%), which is within pore size of < 50 nm (Leng et al., 2021). Sajjadi et al. (2019a) also reported that cellulose-rich biomass produces highly microporous biochar while lignin-rich biomass produces highly macroporous

biochar. Besides that, high pyrolysis temperature and activation temperature enhanced the formation of larger surface area and pore size on the biochar (Feng et al., 2017; Lam et al., 2018). However, micropores are highly desired in CO₂ capture for sorption and storage of the gas molecules via the micropores' diffusional activation energy (Ghanbari and Kamath, 2019; Lahijani et al., 2018). Thus, pyrolysis or activation at lower temperatures is preferable to avoid excess widening of the pores that lead to a decrease in CO₂ adsorption capacities.

The physicochemical properties of biochar have been shown to affect CO₂ adsorption capacities. These properties include microporosity, total pore volume, specific surface area, surface chemistry, and pore size. Microporosity and specific surface area are interrelated. A high volume of micropores contributes to a larger surface area, which in turn promotes CO₂ adsorption capacities (Durá et al., 2016; Serafin et al., 2017). Besides that, the CO₂ adsorption capacity in micropores is dependent on the adsorption pressure and temperature. The CO₂ adsorption at temperature and pressure of 0 °C and < 0.1 bar as well as 25 °C and < 1 bar is governed by the pore size of < 0.7 nm (ultra-micropore) and < 1 nm (micropore), respectively (Adeniran and Mokaya, 2016; Presser et al., 2011).

Surface chemistry plays an important role in CO₂ capture. For instance, an increase in the N-containing functional group (e.g., amino group) on the biochar surface facilitates the adsorption of CO₂ via interactions such as H-bonding, dipole-dipole interaction, and covalent bonding (Shafeeyan et al., 2010). The presence of O-containing functional groups (e.g., phenols, carboxylic acids, carbonyl) on the biochar surface was shown to affect CO₂ adsorption as most of them are acidic. The O-containing functional group and N-containing functional group are removed via pyrolysis at a temperature higher than 100 °C and 400 °C, respectively (Sajjadi et al., 2019a). S-doped on biochar surfaces also plays an important role in CO₂ adsorption. The S-containing functional group present on the biochar surface is basic in nature, thus facilitating the adsorption of weak acidic CO₂ via acid-base interaction (Seema et al., 2014). A strong pole-pole interaction is also present between the polar sites of S functional groups and the large quadrupole moment of CO₂, thus enhancing the adsorption of CO₂ onto the biochar surface (Xia et al., 2012).

Hydrophobicity and polarity of biochar were reported to influence the CO₂ capture performance. It can be determined through the content of oxygen (O), hydrogen (H), nitrogen (N), and sulphur (S) as well as the aromaticity of the biochar. Low content of O, H, the ratio of (O+N)/C and (O+N+S)/C contributed to high hydrophobicity and low polarity, thus limiting the adsorption of polar molecules (e.g., H₂O) and enhancing the adsorption of non-polar molecules (e.g., CO₂) (Shafawi et al., 2021; Shen et al., 2016). The presence of alkali (e.g., K, Na) and alkaline earth metals (e.g., Ca, Mg) in the biochar was also reported to affect the CO₂ adsorption through chemisorption, as the presence of metal can improve the basicity of biochar (Xu, X. et al., 2016). For instance, Lahijani et al. (2018) reported that the introduction of Mg to biochar (82.0 mg/g) improved the CO₂ adsorption capacities as compared to pristine biochar (72.6 mg/g) due to the enhancement of basicity of the modified biochar. In another research, Xu, X. et al. (2016) reported that biochar prepared from pig manure is highly basic (pH = 10.4), which showed high CO₂ adsorption capacities (23.5 mg/g) as compared to biochar prepared from sewage sludge (18.2 mg/g) with lower pH (pH = 8.44).

Over the few decades, various types of activation methods and advanced pyrolysis techniques have been introduced to improve the porous characteristics of biochar used in CO₂ capture. The activation methods include chemical activation (e.g., KOH, NaOH, HCl) (Liew et al., 2018; Sakhiya et al., 2021) and physical activation (e.g. CO₂, steam) (Sangon et al., 2018), while advanced pyrolysis techniques include microwave pyrolysis (Huang et al., 2015), catalytic pyrolysis (Jalalabadi et al., 2019), CO₂ pyrolysis (Kwon et al., 2019), and co-pyrolysis (Igalavithana et al., 2020a). These methods were introduced to resolve the limitation of pristine biochar in CO₂ adsorption as pristine biochar possesses low surface area, porosity, limited surface functional

group, and low basicity (Shafawi et al., 2021). Pristine biochar is tuned via these methods to produce “engineered biochar” with optimum characteristics for CO₂ capture (high basicity, surface area, pore volume, pore size, and high hydrophobicity).

Among them, co-pyrolysis shows the potential to produce biochar with higher CO₂ adsorption capacities, as shown in Table 3.5. Besides that, the ratio of feedstock selected during co-pyrolysis plays an important role as it may change the surface chemistry and porous structure of the biochar produced, which in turn affects the CO₂ adsorption capacities. As reported by Igalavithana et al. (2020a), an increased ratio of food waste during co-pyrolysis produced biochar with reduced amounts of N%, S%, and C%, as well as micropores on the surface, thus lowering the CO₂ adsorption capacities. Interestingly, there is positive synergy by adding wood waste to the co-pyrolysis, as it can help to reduce the moisture content contributed by the food waste in the gasifier and increase the C% in the biochar produced. Igalavithana et al. (2020a) also modified the co-pyrolyzed biochar from food and wood waste with KOH and reported an increase in microporous structure, thus increasing the CO₂ adsorption (148 mg/g) compared to that without activation (115 mg/g). Another research by Liu and Huang (2018) converted coffee ground into biochar via pyrolysis, then performed ammoxidation, followed by KOH activation to produce engineered biochar with higher surface area ranging from 990 m²/g to 1684 m²/g compared to those without KOH activation (0.8 – 402 m²/g) and pristine biochar (34 m²/g). The CO₂ adsorption capacities of the engineered biochar is higher (89.8 – 117.5 mg/g) compared to biochar without KOH activation (18.0 – 37.4 mg/g) and pristine biochar (6.2 mg/g). The research reported that N-doped ammoxidation and KOH activation had significant effects on CO₂ adsorption by improving the biochar basicity and amount of microporosity. Although previous research reported promising result on using biochar in CCT, however, limited research is performed for optimization of different methods as well as combination of these methods, where the synergy presence in the processes still remain unknown. CO₂ adsorption test should also be performed with larger scale or in real industry to identify the feasibility of using biochar for CO₂ capture. Table 3.5 summarizes the production of biochar from various techniques.

3.2.3.1.2. Biochar activation. Activated carbons are obtained through several processes, starting from carbonization under inert atmosphere. Initially, the raw biochar product does not have a developed porous structure; therefore, its activation is carried out through physical processes such as high-temperature carbon dioxide or steam gasification or by chemical treatment. A general concept of biochar and activated carbon synthesis is presented in Fig. 3.21.

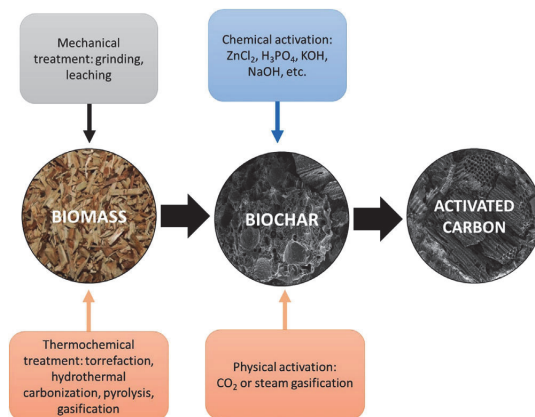


Fig. 3.21. Biochar and activated carbon synthesis methods, based on (Karimi et al., 2022). (For interpretation of the references to color in this figure legend, the reader is referred to the web version of this article.)

Table 3.5
Summary of biochar as CO₂ adsorbent.

| Feedstock | Preparation and modification of biochar | Biochar porous characteristic | | | CO ₂ adsorption capacity (mg/g) (adsorption temperature) | Ref. |
|---------------------------------------|---|--------------------------------------|--|-------------------------|---|------------------------------|
| | | BET surface area (m ² /g) | Total pore volume (cm ³ /g) | Average pore width (nm) | | |
| Taihu blue algae | Conventional pyrolysis Temp: 500 °C | 29.18 | 0.02 | 18.8 | 89.8 (0 °C) 62.9 (25 °C) | (Wang et al., 2021) |
| Rice straw | Microwave pyrolysis Power: 200 W Temp: 300 °C Time: 20 min | 122.2 | 0.08 | 5.0 | 86.2 (20 °C) | (Huang et al., 2015) |
| Chicken manure | CO ₂ pyrolysis Temp: 700 °C | 13.59 | - | 9.3 | - | (Kwon et al., 2019) |
| Sewage sludge | Slow pyrolysis Temp: 500 °C Time: 4 h | 10.12 | 0.02 | - | 18.2 (25 °C) | (Xu et al., 2016) |
| Pig manure | Slow pyrolysis Temp: 500 °C Time: 4 h | 31.57 | 0.04 | - | 23.5 (25 °C) | (Xu et al., 2016) |
| Walnut shell | Slow pyrolysis Temp: 900 °C Time: 90 min Modification: Mg | 292.0 | 0.16 | 2.15 | 82.0 (25 °C) | (Lahijani et al., 2018) |
| Coffee ground | Fast pyrolysis Temp: 400 °C Time: 60 min | 34.0 | 0.18 | - | 6.2 (35 °C) | (Liu and Huang, 2018) |
| Coffee ground | Fast pyrolysis Temp: 400 °C Time: 60 min Modification: Ammoxidation | 0.8 – 402 | 0.01 – 0.22 | - | 18.0 – 37.4 (35 °C) | (Liu and Huang, 2018) |
| Coffee ground | Fast pyrolysis Temp: 400 °C Time: 60 min Modification: Ammoxidation followed by KOH activation | 990 - 1684 | 0.55 – 0.94 | - | 89.8 – 117.5 (35 °C) | (Liu and Huang, 2018) |
| Food waste (20 %) + wood waste (80 %) | Gasification Temp: 800-1000 °C | 294.7 | 0.05 | 2.3 | 115.1 (25 °C) | (Igalavithana et al., 2020a) |
| Food waste (40 %) + wood waste (60 %) | Gasification Temp: 800-1000 °C Activation: KOH | 841.3 | 0.36 | 2.9 | 148.0 (25 °C) | (Igalavithana et al., 2020a) |

“Temp” denoted temperature.

Several modification methods were also implemented to enhance the adsorption properties of the biochar-derived activated carbons (Dissanayake et al., 2020). In terms of gaseous species, adsorption capacity and selectivity of the carbonaceous material are important factors (Ben Petrovic, 2022) for CO₂ adsorption selectivity toward nitrogen, and the presence of steam is another key factor (Manya et al., 2018). Specific properties of the materials are adjusted to the end-user requirements by proper modifications of production method and process conditions, raw material kind, its properties and additional post modifications (impregnation, doping etc.) (Xie et al., 2022). In addition, CO₂ adsorption using biochar-based materials is favourable at low-temperature adsorption; normally, its adsorption capacity increases with a temperature decrease (Cao et al., 2022).

The physical and chemical properties of biochars depend on the origin of biomass. Lignocellulosic biomass cell walls (e.g. woody, agriculture, food waste) are composed of three main components: two polysaccharides (hemicellulose - (C₅H₈O₄)_m, cellulose - (C₆H₁₀O₅)_n) and an aromatic polymer (lignin -[C₉H₁₀O₃ (OCH₃)_{0.9–1.7}]_x) and also other organic components (with acetyl groups, phenolic compounds) and mineral matter (Ashokkumar et al., 2022; Nahak et al., 2022). The content of each fiber component in biomass feedstocks is different: 6 – 38 % of hemicellulose, 10–50 % of cellulose, and 6–46 % of lignin (Saravanan et al., 2022). Cellulose is a polymer built with glucose monomers connected by glycosidic bonds, whereas hemicellulose is not a homogeneous polymer. It consists of glucose, mannose, arabinose, rhamnose, and other sugars. Because of their similar structure and nature, cellulose and hemicellulose make the stability of the matrix of biomass cell walls (Nagarajan et al., 2017). Lignin is a hydrophobic polymer

built by aliphatic and aromatic hydrocarbons with a developed structure. Lignin plays the binding role between cellulose and hemicellulose, providing strong mechanical support to increase the recalcitrance of lignocellulosic biomass (Afzal et al., 2022). On the other side, lignin has a negative impact on cellulose conversion during conversion of thermochemical conversion of biomass (Zoghلامي and Paes, 2019). It should be emphasised that lignocellulosic biomass was found as a good feedstock for biochar and activated carbon (AC) production (Duan et al., 2021; Kielbasa et al., 2022). For biochar and AC production, the content of particular fiber components and mineral content are crucial because they determine the properties of obtained products. H. Tian et al. found that biochar derived from the highest content of lignin in biomass characterized the highest reactivity, whereas cellulose biochar had a rich porous structure (Tian et al., 2022). The literature revealed that cellulose could be obtained the activated carbon with a surface area of more than 1000 m²/g (Suhās et al., 2016). Cellulose can also be used to produce nanofibrils and cellulose nanocrystals, which after modification, have a large surface area and high selectivity towards CO₂ and high CO₂ capacity (Ho and Leo, 2021).

The most suitable activated carbon synthesis method in the case of biomass is thermochemical treatment and chemical activation. Biochars obtained from pyrolysis or hydrothermal carbonisation of lignocellulosic biomass can be successfully activated to produce active carbon with a very high specific area (Shen et al., 2021). Cao et al. (2022) proved that high adsorbent properties for CO₂ capture and good reusability characterised biochar produced from woody and straw biomass. As well as biochar from palm biochar is a porous carbon-based material with high CO₂ adsorption capacity through physisorption and chemisorption

processes (Ben Salem et al., 2021a), whereas biochar from rice straw produced by using microwave pyrolysis was characterised by CO₂ adsorption ability (Huang et al., 2015). Pyrolysis and further chemical activation using KOH of carbonaceous material of sugar cane bagasse resulted in the formation of phenolic and carboxylic functional groups with high affinity to CO₂ (Peres et al., 2022). During biochar synthesis, a pyrolysis process temperature favours the development of porous structure, which directly affects the CO₂ adsorption capacity of the material (Mukherjee et al., 2021). The development of the microporous structure of biochar is directly associated with the adsorption capacity of the carbonaceous material at low pressures in the range of 5–15 kPa (Manya et al., 2020). The main mechanism of CO₂ adsorption with biochar is a physical method (physisorption) through van der Waals forces which adsorb CO₂ molecules (Zhang et al., 2022). According to the literature, specific surface area and pore size are the main factors affecting the process of CO₂ physical adsorption (Majchrzak-Kuceba and Soltysik, 2020; Xu, X.Y. et al., 2016).

Synthesis of adsorbents from biowaste is an important challenge nowadays. Constant economic progress, urbanization and industrialization are leading to a significant increase of the amount of municipal waste, food waste, bio-waste and sewage sludge. Therefore, the most important challenges for people are related to the reduction of waste generation and waste utilization in the circular economy concept bringing effective solutions (where re-materials generation, which can be returned into production processes) and environmental benefits for humans. One of the possibilities to reduce the use of natural resources is, in line with the waste management hierarchy, the use of waste to produce new products through material or energy recovery. The use of waste fuels, such as industrial non-hazardous waste, municipal waste, sewage sludge or the solid fraction after anaerobic digestion of the organic fraction of municipal waste in thermal conversion processes enables the production of valuable products, including gaseous energy carriers and solid products used in adsorption processes. The results presented by M. Karimi et al. in Karimi et al. (2020) show that compost from municipal solid wastes might be a valuable resource for adsorbent synthesis through chemical activation using sulfuric acid and activation at 800 °C. The results of carbon dioxide capture were comparable to those obtained for commercial samples (Karimi et al., 2020). Biowaste, as a mixture of food waste and wood waste, was also a potential material for microporous activated carbon synthesis through gasification; combining with chemical activation using KOH gives better results of porosity of the material (Igalavithana et al., 2020).

A mixture of sewage sludge and leucaena wood was tested as a precursor of biochar synthesis through microwave co-torrefaction. The results show that the adsorption capacity of pure leucaena wood biochar was almost four times higher than that of pure sewage sludge biochar (Huang, Y.F. et al., 2019). Biochar-derived carbons prepared from coffee grounds were studied by Liu and Huang (2018). The activated carbons were obtained through carbonisation, ammoxidation and KOH activation. A highly developed microporous structure resulted in high CO₂ adsorption capacity. Peanut shells were tested as a potential raw material for the synthesis of biochar through catalytic pyrolysis in the molten salt of ZnCl₂, giving a high capacity of CO₂ and selectivity over other gases. It was reported by Manya et al. (2018) that chemical activation of vine shoots results in 20–30% higher CO₂ adsorption capacity of produced biochars compared with physical activation with CO₂.

Due to the chemical reactions of mineral matter components to form carbonates, an enhanced process of CO₂ adsorption was observed. Mineral matter components, especially Mg, Al, Fe, Ni and Ca promote the chemical sorption of carbon dioxide. Additionally, high temperature and water vapour content in the gas stream enhance chemisorption (Xu et al., 2016). Mineral matter also influences the activation process and gases released during the process. For example, during the activation process of chicken manure, which is a fuel rich in CaCO₃, an enhanced generation of CO and suppressed dehydrogenation was observed (Kwon et al., 2019).

3.2.3.1.3. Modifications enhancing carbon dioxide capture. To enhance the CO₂ adsorption capacity of carbonaceous materials, it is possible to introduce different modifications, increasing the role of the chemisorption mechanism in the process of adsorption. An overview of modification methods to enhance the porous structure and enhance the adsorption capacity of biochar towards carbon dioxide adsorption, using both chemical and physical methods, is presented in Fig. 3.22.

It was proved that the adsorption capacity of biochar towards CO₂ might be enhanced by increasing the alkalinity of the material surface (Dissanayake et al., 2020). It is possible to enhance CO₂ adsorption on carbon-based material by incorporating chemisorption and modifying biochar with metal oxides and amine-containing materials (Ben Salem et al., 2021a). Especially in the case of waste materials, such modifications are implemented, as organic waste usually contains smaller amounts of carbon, which directly affects the material's adsorption capacity. More advanced procedures are implemented and described in the literature to enhance biochars' adsorption capacity, for both physically and chemically activated samples. For example, A. Igalavithana et al. defined modification of biochars through hetero atoms doping as a promising strategy to further increase CO₂ adsorption (Igalavithana et al., 2020). A nitrogen doped biochar derived from chicken manure possessed a well-developed porous structure of above 300 m²/g, resulting in very high adsorption capacity and selectivity (Nguyen and Lee, 2016). Anaerobic digestion solid residue might also be a raw material for biochar-based synthesis. It was observed that nitrogen-functionalised porous carbon synthesised in a one-step process using urea seems to be effective in improving the uptake of CO₂ (Qiao et al., 2020). However, modifications before the chemical treatment of sawdust biochar by a simple impregnation method resulted in pores clogging and reduction of sample adsorption capacity (Madzaki et al., 2016). Pore blockage was also observed after K₂CO₃ impregnation of conocar-pus biochar (Al-Wabel et al., 2019).

A biochar dedicated to biogas treatment and capturing CO₂ and H₂S was produced from sawdust biochar treated with urea phosphate to improve the porosity and surface N-containing functional groups of biochars (Ma et al., 2021). An enhanced adsorption process of CO₂ was observed on metalized-biochar in the sequence of metals: Mg > Al > Fe > Ni > Ca (Lahijani et al., 2018), due to a change of physical mechanism to the chemical reaction between e.g., iron oxyhydroxides and carbon dioxide (Xu et al., 2020). Sorption properties might also be enhanced using mechanical treatment e.g. using ball mining (Xu et al., 2020).

Biochars, on the example of coconut shell biochar, might be used for a simultaneous NO/CO₂ removal system which uses biochar and calcined limestone in the calcium looping process (Zhang et al., 2020b). To further enhance adsorption properties, Cu-modification of biochar was proposed together with CaO in the carbonation stage of calcium looping (Zhang et al., 2020a).

In Table 3.6, the review of adsorption capacities toward carbon dioxide of biomass-derived adsorbents was shown. Biochars are produced from a wide range of feedstocks characterizing different CO₂ adsorption capacities.

3.2.3.2. Sewage sludge char for CO₂ adsorption.

3.2.3.2.1. Composition and main characteristics of sewage sludge derived biochar. The biochar product of sewage sludge pyrolysis is a carbon-like material that contains sulphur, nitrogen and oxygen-containing compounds, polycyclic aromatic hydrocarbons, valuable nutrients for the soil (e.g. N, P, K, Ca, Fe, Mg, Cu, Zn) and heavy metals (e.g. As, Cd, Cr, Ni, Pb, Se). Depending on the raw material and the reaction parameters, the yield of biochar is usually between 20 and 70% (Table 3.7). The amount of ash, fixed carbon and volatile compounds is 29–86%, 7–64%, 1–39%, respectively (Chen et al., 2021; Hossain et al., 2011; Moško et al., 2021; Stylianou et al., 2020; Tong et al., 2021). It is also known, that the ash content of sewage sludge derived biochar is generally higher, than that of based on biomass, which can be attributed

BIOCHAR MODIFICATIONS

Towards formation and development of:

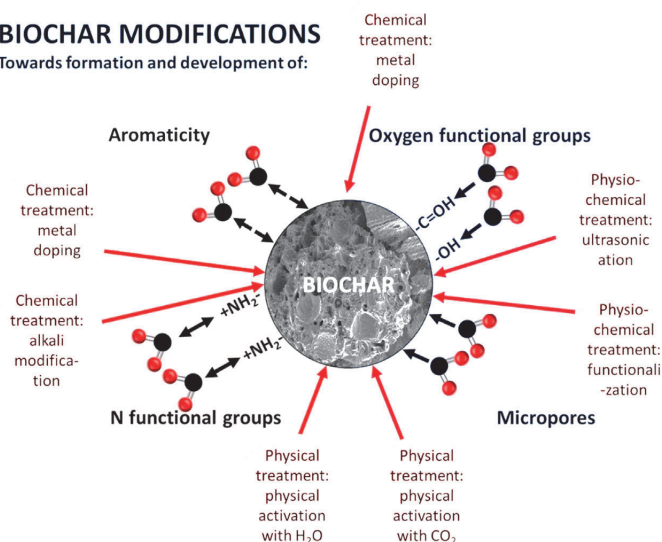


Fig. 3.22. Biochar modification methods towards enhanced CO₂ adsorption capacity, based on (Kumar et al., 2022; Shafawi et al., 2021). (For interpretation of the references to color in this figure legend, the reader is referred to the web version of this article.)

Table 3.6

CO₂ adsorption capacities of biomass-derived adsorbents.

| No. | Sample | CO ₂ adsorption capacity, mmol/g | Adsorption process parameters | Reference |
|-----|--|---|---------------------------------|---------------------------------------|
| 1 | Biochar-derived carbons from coffee grounds | 2.04 - 2.67 | Ambient pressure, 35 °C | (Liu and Huang, 2018) |
| 2 | Biochar from compost from municipal solid wastes | 2.5 | 2.5 bar and 40 °C | (Karimi et al., 2020) |
| 3 | Biochar prepared by catalytic pyrolysis of waste roasted peanut shell in the molten salt of ZnCl ₂ | 3.8 | 100 kPa and 0 °C | (Guo et al., 2018) |
| 4 | Carbonaceous material of sugar cane bagasse | 1.22 | Ambient pressure, 25 °C | (Peres et al., 2022) |
| 5 | Biochar derived from chicken manure chemically treated with HNO ₃ and NH ₃ at 450 °C | 10.15 | Ambient pressure (1 bar), 20 °C | (Nguyen and Lee, 2016) |
| 6 | Leucaena wood biochar | 1.20 | Ambient pressure (1 bar) | (Huang et al., 2019) |
| 7 | Vine shoots-derived biochar using both chemical and physical methods | 0.92-2.42 | 15 kPa, 0 °C | (Manya et al., 2018) |
| 8 | pine cone biochars activated with KOH | 3.64 | 1 bar, 25 °C | (Kaya and Uzun, 2021) |
| 9 | Pecan nut shell biochar obtained through microwave pyrolysis | 2.5 (2.0) | 1 bar, 0 °C (25 °C) | (Duran-Jimenez et al., 2021) |
| 10 | Vine shoots biochar obtained at 600 °C and activated with CO ₂ (at 0.1 MPa and 800 °C) | 2.35-2.67 | 1 bar, 25 °C | (Manya et al., 2020) |
| 11 | Wheat straw biochar obtained at 500 and activated with CO ₂ (at 0.1 MPa and 800 °C) | 2.44-2.63 | 1 bar, 25 °C | (Manya et al., 2020) |
| 12 | Sawdust biochar activated using urea phosphate at 700 °C | 2.42 | 1 bar, 25 °C | (Ma et al., 2021) |
| 13 | Bamboo chips biochar modified by ZIF-8 grafting | 1.8 | 1 bar, 30 °C | (Zhang et al., 2022) |
| 14 | Anaerobic digestion solid residue biochar modified by urea | 1.22 | 1 bar, 25 °C | (Qiao et al., 2020) |
| 15 | Lignin impregnated with sodium lignosulfonate | 2.34 | 1 bar, 25 °C | (Zhang et al., 2022) |
| 16 | Rape straw, soybean straw, corn stalk, wheat straw, walnut shell, hickory wood, and pine wood biochar obtained at 600 °C | 0.69-1.02 | 1 bar, 25 °C | (Cao et al., 2022) |
| 17 | Conocarpus biochar obtained at 400 °C | 4.47 | 1 bar, 25 °C | (Al-Wabel et al., 2019) |
| 18 | Date palm waste biochar obtained at 500 °C | 0.38 | 1 bar, 25 °C | (Ben Salem et al., 2021b) |
| 19 | Biocarbon | 0.6 | 30 mbar, 30 °C | (Majchrzak-Kuceba and Soltysik, 2020) |
| 20 | Walnut shell biochar (Mg metalized) | 1.65 (1.86) | Ambient pressure, 25 °C | (Lahijani et al., 2018) |
| 21 | biochar/Fe oxyhydroxide composite | 3.63 | Ambient pressure, 25 °C | (Xu et al., 2020) |
| 22 | Spent coffee grounds obtained at 600 °C | 2.8 | 1 bar, 25 °C | (Mukherjee et al., 2021) |
| 23 | Pig manure biochar obtained at 500 °C | 0.53 | 1 bar, 25 °C | (Xu et al., 2016) |
| 24 | Wheat straw biochar obtained at 500 °C | 0.78 | 1 bar, 25 °C | (Xu et al., 2016) |
| 25 | Peanut shell derived activated carbon with KOH | 7.06 (4.61) | 1 bar, 0 °C (25 °C) | (Deng et al., 2015) |
| 26 | Rambutan peel-derived KOH-activated hydrochar using KOH:HC ratio of 2:1 at 850 °C for 120 min with the involvement of water-soaking pretreatment | 2.78 | 1 bar, 30 °C | (Zubbri et al., 2021) |
| 27 | Sugarcane bagasse biochar produced at 600 °C | 1.67 | 1 bar, 25 °C | (Creamer et al., 2014) |
| 28 | Argan fruits shells obtained through dry physical mixing with KOH | 5.63 | 1 bar, 25 °C | (Boujibar et al., 2018) |
| 29 | Rice straw biochar produced by microwave pyrolysis (200 W and 300 °C) | 1.75 | 1 bar, 20 °C | (Huang et al., 2015) |
| 30 | Rambutan peel biochar impregnated with magnesium nitrate (raw biochar) | 1.71 (1.56) | 1 bar, 30 °C | (Zubbri et al., 2020) |

Table 3.7
Yields, composition and main characteristics of biochar products of sewage sludge pyrolysis.

| Raw material | Pyrolysis conditions | Biochar yield, % | Properties, elemental composition, % | | | | Other properties | | | | | Ref. | | | |
|--|--|------------------|--------------------------------------|--------------------|--------------|-----------|------------------|---------|---------|-----------|------------|------------|-------------------------------------|---------------------------------|---------------------------|
| | | | Ash | Volatile compounds | Fixed carbon | C | H | N | S | O | HHV, MJ/kg | | BET surface area, m ² /g | Pore volume, cm ³ /g | Average pore diameter, nm |
| Sewage sludge (100 g) | T = 400-800 °C, τ = 2 h, He atmosphere (150 ml/min) quartz reactor | 46.3-61.7 | 67.9-80.8 | 0.9-21.5 | 10.6-18.3 | 17.2-23.1 | 0.3-1.6 | 0.9-3.0 | 0.8-0.8 | <3.6 | 8.0-9.5 | 14.9-85.7 | <0.1 | - | (Wośko et al., 2021) |
| Sewage sludge (10 g) | T = 300-500 °C, 10 °C/min heating rate, N ₂ atmosphere (100 ml/perc), quartz reactor | 55-68 | 50.7-62.5 | 24.4-39.0 | 9.9-13.1 | 21.5-29.6 | 1.4-5.3 | 2.8-5.1 | 0.6-1.3 | 12.3-24.4 | 8.2-12.5 | - | - | - | (Chen et al., 2021) |
| Sewage sludge + rice husk (5 g) | Hydrothermal treatment, T = 600 °C, τ = 0.5 h, N ₂ atmosphere (200 ml/min) high pressure autoclave | 24.4-62.4 | 28.8-86.1 | 5.6-9.5 | 8.2-63.6 | 2.5-62.1 | 0.9-2.2 | 0.7-0.8 | 0.1-0.2 | 6.2-8.4 | 3.9-23.0 | 13.7-211.9 | 0.1-0.3 | 2.5-17.5 | (Tong et al., 2021) |
| Sewage sludge (Kb, 250 g) | T = 300-700 °C, N ₂ atmosphere (50 ml/min) Horizontal fixed-bed reactor | 52.4-72.3 | 52.8-72.5 | 15.8-33.8 | 6.8-9.1 | 20.2-25.6 | 0.5-2.6 | 1.2-3.3 | - | <8.3 | - | - | - | - | (Hossain et al., 2011) |
| Sewage sludge, cattle manure, used coffee grounds (20-24 kg) | T = 550 °C, N ₂ atmosphere, τ = 1.5 h | 21.2-41.6 | - | - | - | 28.5-87.4 | 0.9-2.4 | 1.6-5.7 | 0.3-0.5 | - | - | 1.5-14.0 | <0.1 | 3.9-60.4 | (Styllianou et al., 2020) |

to the higher mineral content of sewage sludge (Li et al., 2018). The properties of biomass and sewage sludge derived bio-carbons should be different depending on the composition of raw materials and process parameters (Li et al., 2018; Zhang et al., 2019).

The sewage sludge derived biochar can be used for many purposes, e.g. as a sorbent, catalyst and soil amendment. The application is determined by the physico-chemical properties (e.g. specific surface area, pore volume, average pore diameter), the relative proportions of volatile compounds, fixed carbon and ash in the biochar (Yuan et al., 2015). Biochar obtained at higher pyrolysis temperature ($T > 450^\circ\text{C}$) has higher specific surface area and increased adsorption capacity (Peng et al., 2011; Yuan et al., 2015). As it was mentioned earlier, sewage sludge derived biochar also contains heavy metals, that accumulate in the carbonaceous residue; e.g. Pb, Zn, Ni, Cd, As, Cu or Cr. Their concentrations should be significant (>5000 ppm) and it can be increased as function of temperature (Cao and Harris, 2010; Xiong et al., 2021; Yin et al., 2021; Zheng et al., 2013).

For sequestering CO_2 , many technologies (e.g. absorption, adsorption, membrane separation, chemical or Ca looping, pre- and post-combustion and oxy-fuel) have been developed (Osman et al., 2021). Among the variety of routes, adsorption technologies seem to be the most promising. Based on this fact, different types of porous solid sorbents such as synthetic or natural zeolites, mesoporous silica, metal organic frameworks, active carbon, etc. have already been studied for CO_2 removal (Creamer et al., 2014; Lahijani et al., 2018; McEwen et al., 2013). Although the listed sorbents have high adsorption capacity, the application of metal organic frameworks and zeolites is limited (Ahmed et al., 2016). In case of metal organic frameworks, the instability should be mentioned (Guo et al., 2022), and in the case of zeolites, the fast deactivation, the irreversible adsorption, the steric hindrance of the heavy compounds and the high regeneration temperature are the main disadvantages (Perot and Guisnet, 1990). Biochar can also be an excellent CO_2 sequestering sorbent (Singh et al., 2022). However, before its usage, it is inevitable to create the appropriate pore structure, alkalinity and surface functional groups with different modification methods (Guo et al., 2022; Miricioiu et al., 2021).

3.2.3.2.2. Modification of sewage sludge derived biochar for CO_2 reduction. In order to create the appropriate pore structure, alkalinity and surface functional groups, physical, chemical, physical-chemical modification of the biochar and co-pyrolysis of sewage sludge and biomass have been proposed in the literature (Shafawi et al., 2021; Xiao et al., 2022). The reason for the latter is that biomass also contains alkali elements and alkali earth metals and thus enabling the alkalinity and CO_2 adsorption capacity of the produced biochar to be increased (Huang et al., 2017).

The modification processes have three types. One of them is physical modification, which involves two steps: (i) carbonization carried out at low temperature ($T = 400\text{--}750^\circ\text{C}$) in the presence of physical agents, heat, gases (e.g. $\text{CO}_2/\text{He}/\text{N}_2$) or steam and (ii) activation in gas atmosphere at a relatively high temperature ($T = 800\text{--}1200^\circ\text{C}$) in order to further increase the porosity (Singh et al., 2020). The process that takes place is slow oxidation, which leads not only to the formation of new pores, but also to an increase in the diameter of the existing pores (Wang et al., 2017).

Physical treatment has already been studied by several research groups, especially in the case of biomass derived bio-carbons (González et al., 2013; Plaza et al., 2011, 2010; Shahkarami et al., 2015; Xiong et al., 2013). In these cases, a CO_2 adsorption capacity of even more than 100 mg/g can be achieved. In an interesting way, considerably less information is available about physical modification of sewage sludge derived bio-carbons. Despite the fact, that Tinnirello and co-workers (Tinnirello et al., 2020) observed a CO_2 adsorption capacity of 103 mg/g (temperature = 600°C , dwell time = 2 h, nitrogen flow rate = 300 Nml/min) when they studied the physical activation of the anaerobically digested sewage sludge derived biochar. It is important to note that the reported value (2.3 mmol/g) is consistent with the ad-

sorption capacity of activated carbon (2.6 mmol/g) (Siriwardane et al., 2001).

In addition to nitrogen, steam and CO_2 can also be used for biochar activation. According to Pallarés et al. (2018) CO_2 activation is more beneficial than steam modification, because CO_2 activation allows the formation of the desired micropores. The beneficial temperature of CO_2 activation is about $600\text{--}650^\circ\text{C}$ and the resulting biochar has basic/alkaline character. In those cases, when nitrogen is used as activating agent the temperature should be around 700°C or even higher (Gao et al., 2014).

To increase the CO_2 sequestration capacity, chemical modification can also be used. This type of modification can be done in two ways: (i) impregnation of sewage sludge or biomass sample with the chemical agent and thermal treatment, (ii) impregnation of sewage sludge or biomass based biochar with the chemical reagent and thermal treatment (Ahmed et al., 2016; Sajjadi et al., 2019b). Increasing the CO_2 adsorption capacity, it may be beneficial to create nitrogen-containing functional groups (e.g. amide, imide, nitriles, etc.) on the surface of the biochar. For this purpose, ammonia, amines and nitric acid are the most widely used compounds (Shen and Fan, 2013). In case of ammonia treatment/ammonification the most commonly used temperature is between 600 and 900°C , where ammonia first decomposes to free NH_2 , NH radicals, atomic hydrogen and nitrogen and then the nitrogen containing functional groups are formed from the reaction of the resulting radicals and the carbon (Stöhr et al., 1991). Between the functional groups and the ammonification temperature correlations have been observed (Mangun et al., 2001). It was found that amides, imides, imines, amines and nitriles are the most dominating functional groups below 600°C , while the thermally stable aromatic rings-like functionalities are dominated at higher temperatures (Plaza et al., 2009; Shafeeyan et al., 2010). It was also reported, that C-N and C=N chemical groups had been introduced into the char surface, by the using of $200\text{--}1000^\circ\text{C}$ ammonification temperature till 2 h (Przepiórski et al., 2004). In another study (Zhang et al., 2016) soybean straw derived biochar and $500\text{--}900^\circ\text{C}$ ammonification temperature was applied before the CO_2 adsorption capacity was determined. The resulting biochar had a micropore surface area of $311\text{--}461\text{ m}^2/\text{g}$ and the adsorption capacities changed between 48 and 74 mg/g (CO_2 adsorption temperature = 30°C). It was found that increasing the temperature is beneficial from the point of view of micropore production, but the ammonification temperature has a maximum ($T = 800^\circ\text{C}$) and above this value both the surface area and the adsorption capacity decreased.

The chemical treatment can also be conducted using alkaline solutions such as KOH and NaOH (Jin et al., 2014), but impregnation of biochar with metal salt solution can also be a promising option. In case of KOH and NaOH activation O-containing functional groups (e.g. carboxyl, hydroxyl etc.) are formed on the surface of the biochar and enhance the adsorption capacity for CO_2 . The reason for this is that carboxyl and hydroxyl groups led to intermolecular forces and dipole-dipole interaction with the molecule of CO_2 (Shafawi et al., 2021; Shafeeyan et al., 2012). As a result of this, the CO_2 adsorption capacity can be higher than 70 mg/g at ambient conditions, but in some cases it can be over 100 mg/g (Du et al., 2020; Manyà et al., 2018; Quan et al., 2020).

The literature results are also promising in the case of metal or metal oxide modification. In this case, aluminium chloride, magnesium chloride and iron chloride are the most widely used metal salts to impregnate the biochar. The first step is impregnation, which is followed by a thermal treatment, where the metal salts are converted into metal oxides (Ahmed et al., 2016; Jung and Ahn, 2016). Lahijani et al. (2018) studied more individual metals (Mg, Al, Fe, Ni, Ca, Na) for the activation of biochar. It was found that Mg derived compounds have the highest CO_2 adsorption capacity (82 mg/g) and Na derived compounds are the least suitable for sequestering CO_2 . The latter had an even lower adsorption capacity than raw biochar. In Table 3.8 some of the results of chemical

Table 3.8
Results of chemical modification of sewage sludge derived bio-carbons.

| Raw material | Conditions for biochar production | Chemical activation | BET surface area, m ² /g | Micropore volume, cm ³ /g | Adsorption temperature (°C) and pressure | CO ₂ adsorption capacity, mg/g (mmol/g) | Ref. |
|----------------|-----------------------------------|--|-------------------------------------|--------------------------------------|--|--|-------------------------------|
| Chicken manure | 400 °C | KOH, activation under N ₂ at 700 °C for 1 h | 22 | N/A | 25.1 bar | 76.8 | (Huang et al., 2017) |
| Chicken manure | 400 °C | HCl, activation under N ₂ at 700 °C for 1 h | 137 | N/A | 25.1 bar | 85.7 | (Huang et al., 2017) |
| Sewage sludge | 400 °C | KOH, activation under N ₂ in the temperature range of 500–900 °C for 30 min | 984 | 0.6 | - | - | (Hunsom and Auththanit, 2013) |

modification are summarized, particularly focusing on sewage sludge based bio-carbons.

3.2.3.2.3. Mechanism of adsorption. The CO₂ reduction should be taken by physical and chemical adsorption at low temperature or even by chemical looping at high temperatures (Igalavithana et al., 2020b; Jung et al., 2019; Shafawi et al., 2021). The adsorption properties of biochar obtained from sewage sludge pyrolysis are based on the surface characteristics of the solid particle. The adsorption ability is greatly influenced not only by the pore size or surface area of the macropores and microporous, but also by their chemical properties. Micropores have a significant role in the physical aspects of adsorption, while the surface groups can affect rather the formation of chemical relationships (Igalavithana et al., 2020b; Jung et al., 2019). When carbon dioxide is adsorbed, the groups containing nitrogen or oxygen usually form chemical linkage through acid-base (Lewis-acid and Lewis-base) reactions, while the groups containing aromatics form chemical linkage through van der Waals bonds (Igalavithana et al., 2020b; Jung et al., 2019). As a result of activation and surface modifications carried out in different ways, the relative ratio of before discussed chemical groups can be changed. This can also change the adsorption ability significantly. However during desorption, the strong chemical linkage is disadvantageous in many cases, because it does not exclude the fully removal of the adsorbed components (Igalavithana et al., 2020b; Jung et al., 2019; Shafawi et al., 2021).

3.2.3.3. Chitosan for CO₂ capture. Chitosan is a deacetylated-derivative of chitin (abundantly available biopolymer after cellulose) that has been used in various fields, including cosmetics, food industry, pharmaceuticals, biomedicine, agricultural and wastewater treatment (Pakizeh et al., 2021). Chitin can be extracted from various sources, including crustaceans, mollusks, insect shells, and cell walls of fungi (Said Al Hoqani et al., 2020; Sayari et al., 2016; Soetemans et al., 2020). Similar to biochar, chitosan possesses excellent properties that are suitable for CCT, which are biodegradability, non-toxicity, functionality, biocompatibility, and high adsorption capacity (El Knidri et al., 2016). The quality of chitosan is characterized by molecular weight (Mw) and degree of deacetylation (DD%), where commercial chitosan has a DD% ranging from 70 to 95% and Mw ranging from 50 kDa to 200 kDa (Sun et al., 2009). In general, chitosan with high Mw (>1000 kDa) exhibits better mechanical properties (suitable to use as an adsorbent), while medium (100–1000 kDa) to low (<100 kDa) Mw exhibit better biological properties (suitable for pharmaceutical applications) (Gonçalves et al., 2021; Kou et al., 2021).

Chitosan as an adsorbent/precursor for CO₂ capture has recently caught the attention of researchers owing to the natural basicity of chitosan, where the free amino group in the chitosan structure can provide basic sites for CO₂ adsorption. Other advantages of chitosan as an adsorbent/precursor include high thermal stability, chemically inert, tunable surface functional group, minimal energy for recovery, and it is inexpensive due to the ability of mass production from chitin sources (Kamran and Park, 2020). Previous studies applied chitosan-based adsorbents in CO₂ capture and revealed that CO₂ could be adsorbed on the adsorbent surface and converted into ammonium carbamates at room tempera-

ture, then released as CO₂ from the adsorbent upon heating (Ababneh and Hameed, 2021). However, pure chitosan possesses low CO₂ adsorption and therefore, modification of the surface properties of chitosan is required to improve or maximize its adsorption efficiency toward CO₂ (Kumar et al., 2018; Peng et al., 2019). The chitosan adsorbent can be prepared via thermochemical technology such as hydrothermal carbonization, or surface functionalization with chemicals or structural modification.

Hydrothermal carbonization (HTC) operated at a temperature ranging from 180 to 260 °C with the presence of water and autogenous pressure, is a promising method for preparing chitosan-based adsorbent. It is a simple, low-cost process without the use of a catalyst or organic solvents. Thus, it has been introduced as a greener approach for the synthesis of functionalized chitosan and improving its CO₂ adsorption efficiency (Titirici and Antonietti, 2010). Research by Chagas et al. (2020) reported an outstanding performance of HTC chitosan adsorbent where the CO₂ uptake is 4-fold higher than the pure chitosan. The HTC of chitosan has been shown to increase the carbon content, and reduce the oxygen content but does not significantly change the amount of nitrogen in chitosan. Interestingly, the structural characterization of chitosan revealed the production of more aromatic amines at a longer HTC reaction time, hence causing lower basicity of chitosan, but showed a higher CO₂ adsorption capacity, suggesting that aromatic structure in HTC chitosan exposed the N atom for CO₂ adsorption (Chagas et al., 2020). Modification of the chitosan into a spherical structure via HTC was an alternative to improve the CO₂ adsorption efficiency of chitosan due to the carbon sphere providing properties such as a large contact area, adjustable surface chemistry, and open-pore structure for adsorption reactions. For instance, Wu et al. (2019) have reported that the chitosan sphere (3.28 mmol/g) has a higher BET surface area (462 m²/g), with up to 85.5% of micropore structure and ultra-micropore (<0.9 nm) able to enhance CO₂ capture compared to rod-structure (1.36 mmol/g) and 2D sheet structure (2.61 mmol/g) of chitosan. However, chitosan hydrochar still possesses low CO₂ adsorption efficiency and thus HTC combined with a different technique such as chemical impregnation is required to modify the surface chemistry to enhance the CO₂ capture performance.

Physical activation such as steam activation usually requires a long reaction time to achieve a high temperature, which may lead to high energy consumption (Yek et al., 2020). In contrast, chemical activation requires chemical reagents to carbonize and develop the porosity of the chitosan under low-temperature conditions and short reaction time, thus reducing energy consumption (Wang et al., 2021). In particular, NaOH, KOH, and K₂CO₃ have been discovered as effective chemical activation agents that can enhance the development of porosity in carbonaceous materials (Liew et al., 2018, 2019). For instance, Wang et al. (2021) reported on the use of mild KOH as an activation agent to enhance the porosity of chitosan hydrochar, resulting in the production of a high surface area of chitosan hydrochar (up to 2547 m²/g). Chitosan hydrochar produced at a temperature of 600 °C exhibited the highest CO₂ capture capacity (4.41 mmol/g) compared to the other carbon produced under different precursors (e.g., walnut shell) and activating agents (e.g., NaNH₂), which only possessed CO₂ uptake of

Table 3.9
Summary of chitosan as CO₂ adsorbent.

| Sample | Biochar porous characteristic | | | N content (wt%) | CO ₂ adsorption capacity (mg/g) (adsorption temperature) | Ref. |
|---|--------------------------------------|--|-------------------------|-----------------|---|-----------------------|
| | BET surface area (m ² /g) | Total pore volume (cm ³ /g) | Average pore width (nm) | | | |
| Chitosan hydrochar | 2.6 | N/A | N/A | 7.5 | 19.8 (25 °C) | (Chagas et al., 2020) |
| Carbon sphere | 462 | 0.27 | 2.04 | 4.6 | 142 (25 °C) | (Wu et al., 2019) |
| Carbon sphere | 384 | 0.27 | N/A | 11.6 | 154 (0 °C) | (Primo et al., 2012) |
| Chitosan hydrochar | 1249 | 0.67 | N/A | 7.6 | 304 (0 °C) | (Wang et al., 2021) |
| | | | | | 194 (25 °C) | |
| N,P-co-doped chitosan | 895 | 0.73 | 6.56 | N/A | 234 (25 °C) | (Xiao et al., 2022) |
| KOH activated N-doped chitosan | 1928 | 0.72 | N/A | 4.1 | 172 (25 °C) | (Li et al., 2022) |
| KAc activated N-doped chitosan | 1273 | 0.46 | N/A | 5.4 | 156 (25 °C) | (Li et al., 2022) |
| K ₂ CO ₃ activated N-doped chitosan | 1147 | 0.42 | N/A | 5.3 | 155 (25 °C) | (Li et al., 2022) |
| KHCO ₃ activated N-doped chitosan | 1054 | 0.38 | N/A | 8.4 | 146 (25 °C) | (Li et al., 2022) |
| K ₂ CO ₃ activated chitosan | 1673 | 0.73 | 0.60 | 5.3 | 169 (25 °C) | (Fan et al., 2013) |
| NaNH ₂ modified chitosan | 1740 | 0.98 | N/A | 5.1 | 278 (0 °C) | (Yang et al., 2022) |

3.06 mmol/g (Yang et al., 2019). This suggests the potential of chitosan hydrochar as a desirable precursor and KOH as an effective activation agent in producing carbon with high porosity as an adsorbent for CO₂ uptake.

Other than alkalis, acids can also be used as an alternative activation agent. Xiao et al. (2022) introduced phytic acid into the carbon network of chitosan gel to fabricate N, P-co-doped porous carbon materials (NPPCs). The surface area of NPPCs (690–1010 m²/g) was lower than carbon produced using alkali but exhibited a higher CO₂ uptake (5.31 mmol/g) as compared to chitosan hydrochar in the previous study (2547 m²/g and 4.41 mmol/g, respectively) (Wang et al., 2021), thus showing the better potential of NPPC to be used as a CO₂ capture. The effects of different chemical activators for chitosan activation were performed by Li et al. (2022) using KOH, potassium acetate (KAc), potassium carbonate (KHCO₃), and potassium bicarbonate (K₂CO₃). The research revealed that activation via KOH produces a chitosan-based adsorbent with a high surface area (1928 m²/g) and high CO₂ adsorption capacity (3.91 mmol/g). However, KOH is highly corrosive, and an alternative has been provided by the author by using KAc activation that produced a chitosan-based adsorbent with comparable surface area (1273 m²/g) and CO₂ adsorption capacity (3.52 mmol/g).

Physical impregnation has emerged as a new research area for the synthesis of chitosan-based adsorbents for CO₂ adsorption. For instance, Peng et al. (2019) synthesized an amine-impregnated adsorbent by impregnating chitosan-derived adsorbent with a pentaethylenehexamine (PEHA), which was inspired by conventional CO₂ adsorption using liquid amine. Chitosan loaded with PEHA showed higher CO₂ (3.72 mmol/g) uptake compared to pure chitosan-derived adsorbent (0.21 mmol/g) at 100 °C, thus implying the effectiveness of amines-impregnated carbon to capture CO₂. Besides that, Yang et al. (2022) developed N-doped porous carbon via mixing and ball-milled chitosan and NaNH₂. The use of NaNH₂ as the source of nitrogen and porogen during carbonization has increased the surface area and pore structures of the N-doped porous carbon. N-doped carbon material showed a high surface area (2398 m²/g) and high CO₂ adsorption capacity (6.33 mmol/g), showing better CO₂ adsorption performance compared to carbon-based adsorbent produced using ZnCl₂ (2.62 mmol/g) (Xu et al., 2020). Although much research has been carried out to modify the physicochemical properties of chitosan to be used in CO₂ adsorption, there are many research gaps to be filled as compared to biochar as CO₂ adsorbents, such as the optimization of carbonization parameters, utilization of suitable activator and the CO₂ adsorption temperature and pressure. It is worth noting that chitosan has a more desirable properties such as high surface N-functional group in nature, low cost, biodegradable and non-

toxic as compared to biochar, thus, novel and optimize research for chitosan-based adsorbent for CCT should be performed. Table 3.9 summarizes the synthesis techniques of chitosan-based adsorbent for CO₂ capture.

The CO₂ adsorption mechanism of biochar and chitosan are similar as both carbon materials have N-containing functional group on the surface, and pore structure that facilitates the adsorption processes. Studies have indicated that CO₂ adsorption to the adsorbent occurs via physisorption and chemisorption. Physisorption of CO₂ is dominated by the pore structure and surface area, where micropore sizes of 0.3–0.8 nm are preferable, and < 0.5 nm are optimum for CO₂ adsorption (Igalavithana et al., 2020c). Physisorption is mainly induced by van der Waals and micropore-filling effects (Shafawi et al., 2021). The chemisorption of CO₂ is dominated by Lewis acid-base interaction and hydrogen bond interaction. The hydrogen bond is formed between CO₂ and O-containing functional groups. In general, O-containing functional groups are acidic, which may hinder the adsorption of acidic CO₂. Interestingly, some studies revealed that hydroxyl (-OH) and carboxyl group (-COOH) enhance the hydrogen bond interaction. This is attributed to the electronegativity different of H atom (2.1) and O atom (3.5), causing the H atom from -COOH and -OH having high electropositivity to interact with the O atom from CO₂ via hydrogen bond (Liu and Wilcox, 2012). However, this hydrogen bond is weak and the presence of H₂O molecules would hinder the formation of the hydrogen bond. This is because the presence of H₂O molecules created a strong dipole moment on the adsorbent surface compared to the weak quadrupole moment of CO₂ (Liu and Wilcox, 2012). Thus, H₂O molecules are selected for hydrogen bonding instead of CO₂ with the adsorbent.

Lewis acid-based interaction occurs between N-containing functional group on the adsorbent surface and the CO₂ molecule. Generally, the N atom is electron-rich, attributed to the presence of a lone pair of electrons, thus it facilitates the adsorption of CO₂. Other than Lewis acid-based interaction, some N-containing functional groups can form hydrogen bonds with CO₂ molecules owing to their naturally high electropositivity (Lim et al., 2016; Liu et al., 2013). Thus, CO₂ can form hydrogen bonds with the N-containing functional group on the adsorbent. For instance, Fan et al. (2013) reported that a major of pyridone was present in the chitosan-derived CO₂ adsorbent, and contributed mainly to CO₂ adsorption. The presence of -OH adjacent to the N atom resulted in a p- π conjugation effect (from -OH) with the π bond, thus increasing the adsorbent's electron density and improving its Lewis basicity. Fig. 3.23 shows the possible reaction that occurs during CO₂ adsorption to biochar/chitosan adsorbent. Although many studies have been carried out to identify the possible reaction mechanism for CO₂ adsorption

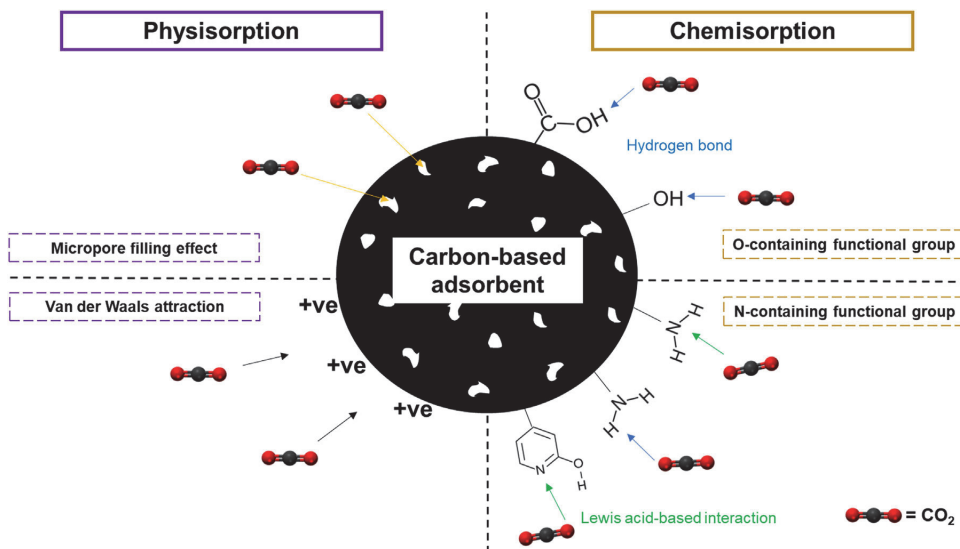


Fig. 3.23. Possible reaction mechanism of CO₂ adsorption on carbon-based adsorbent. (For interpretation of the references to color in this figure legend, the reader is referred to the web version of this article.)

on the carbon-based adsorbent, the variation of feedstock types can significantly affect the functional groups of the adsorbent, thus affecting the adsorption efficiency of CO₂.

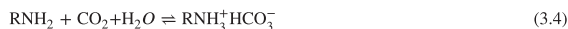
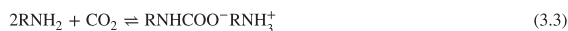
3.2.4. Solid amine-based sorbent

Amine-based adsorbents have the advantages of high adsorption capacity, thermal stability, and good regeneration performance in comparison with granular solid adsorbents (Raganati et al., 2021). By means of the addition of amine functional groups, it could evenly disperse in solid adsorbents, providing alkaline sites for the adsorption of acid gas (CO₂). Porous solid supports, such as porous silica, alumina, porous carbons, zeolites, polymers, and metal organic frameworks (MOFs), always have large pore volumes and specific area. CO₂ adsorption performances of diverse amino-solids are discussed in the following sections.

3.2.4.1. Reaction mechanism. Solid amine-based sorbents are the functional combination of aqueous amine and porous solid adsorbents. As for existing amines, tethered amines onto solid adsorbents could substantially reduce energy requirements to liberate captured CO₂ from the relatively dilute amine solutions, and avoid equipment corrosion occurring during the amine scrubbing process. Conceivably, the interaction between amino groups is strengthened within the constrained space of porous solid material. From the perspective of porous solid adsorbents, the incorporated amine will dramatically improve CO₂ capacity and selectivity via chemical adsorption even at low pressure, but might increase mass transfer resistance of adsorbate to contact amine groups within microporous materials. Therefore, the performance of solid amine-based sorbents reflects a compromise on the advantages and disadvantages between aqueous amine and porous solid adsorbents. To deeply uncover adsorption-desorption mechanism, the structure of amines and their reaction routes with adsorbate, the texture of different solid supports and their physisorption properties, as well as the interaction between amines and solid supports, should be taken complete account. Three aspects i.e. reaction mechanism of CO₂ with amines, adsorption thermodynamics and kinetics, and the deactivation mechanism, are discussed.

3.2.4.1.1. Adsorption mechanism. CO₂ adsorption mechanism of solid amine-based sorbents is analogous to one that occurs by absorp-

tion of amine solutions via acid-base interaction, which is confirmed by numerous in situ spectroscopic studies using solution- and solid-state nuclear magnetic resonance (SSNMR) and infrared (IR) spectroscopy combined with theoretical calculations (Chen et al., 2018; Forse and Milner, 2020). Under dry conditions, the formation of carbamate is achieved by substituting hydrogen of amine with CO₂, which means only H-containing amines, i.e. primary and secondary amines are available. According to Reaction 3.3, two amidogens are necessitated to capture one molecule of CO₂. Whereas the introduction of moisture, which exists widely in various sources for CO₂ capture, could improve amine efficiency by one fold via the formation of bicarbonate or carbonate compared with that without moisture. In Reaction 3.4, water attributes a hydroxide to CO₂ molecule. Therefore, it is suitable for all primary, secondary and tertiary amines. Obviously, amine-based adsorbents could achieve higher CO₂ adsorption under humid conditions, while moisture is deleterious on the CO₂ adsorption capacity of porous zeolites and MOFs owing to their hydrophilic nature over exposed metal ions. It should be noted that the amine efficiency is limited to 0.5-1 under humid conditions because of kinetically controlled bicarbonate formation (Serna-Guerrero, 2008).



Said et al. (2020) proposed a unified approach to CO₂-amine reaction mechanism in Fig. 3.24. At high amine loading under dry conditions, nucleophilic attack of CO₂ by amines is primarily assisted by a neighbouring amine (X = N, Y = N), which leads to a 1,_n-zwitterion (n > 3) or to alkylammonium carbamate, and it depends on whether two amines involved are linked or separated. At low amine loading, nucleophilic attack of CO₂ by isolated amines may be assisted by hydroxyl groups (X = N, Y = O), leading to carbamic acid or hydronium carbamate. Under humid conditions, water may assist nucleophilic attack of CO₂ by amines (X = N, Y = O) to form hydronium carbamate or play a role of a nucleophile assisted by amines to form ammonium bicarbonate (X = O, Y = N) at the expense of carbamate. The latter mechanism applies for tertiary and hindered amines, regardless of surface density.

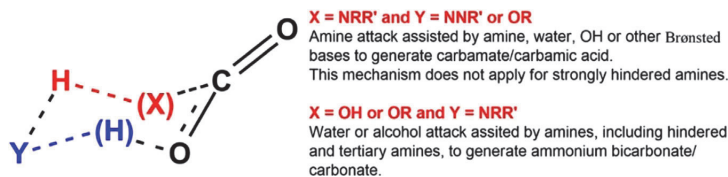


Fig. 3.24. The unified schematic mechanism for CO₂-amine-water interactions (Said et al., 2020). (For interpretation of the references to color in this figure legend, the reader is referred to the web version of this article.)

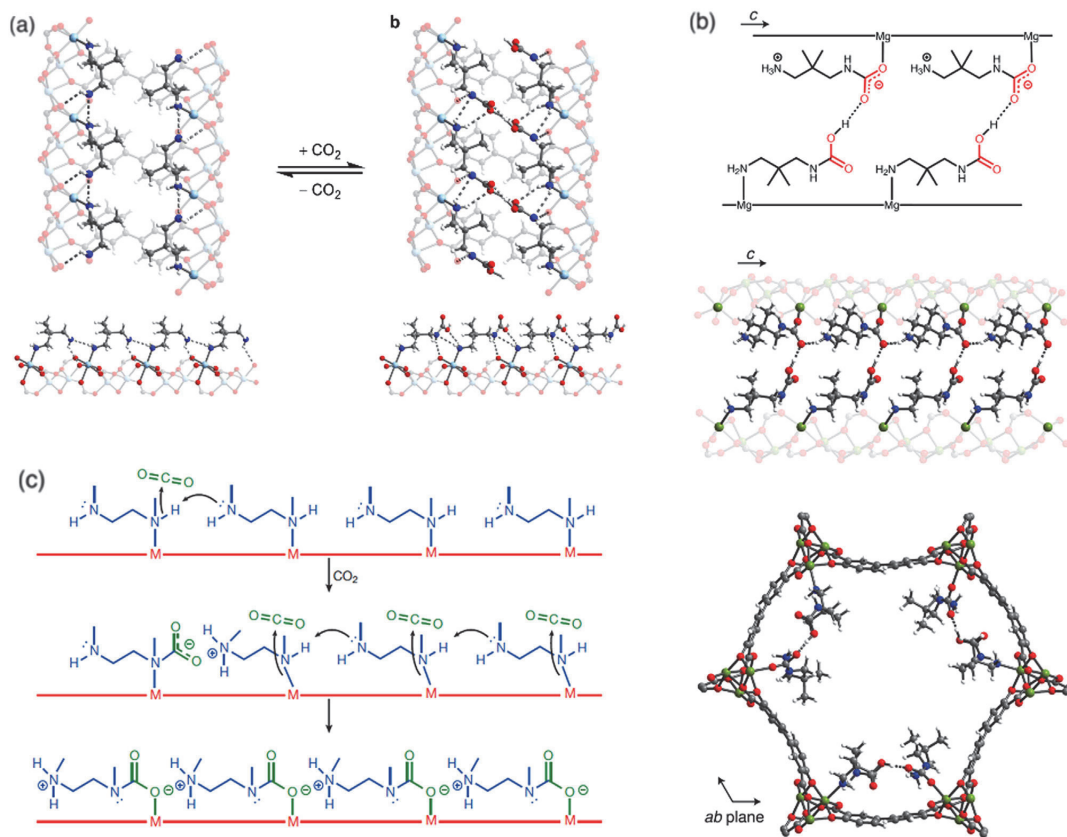


Fig. 3.25. The cooperative mechanism over amine-functionalized MOFs sorbents (a) The formation of carbamic acid pairs over dmpn-Zn₂ (dobpdc) (Milner et al., 2017); (b) Mixed chemisorption structure with ammonium carbamate and carbamic acid in a 1:1 ratio for dmpn-Mg₂ (dobpdc) (Forse et al., 2018); (c) The formation of carbamic acids and mixed ammonium carbamates/carbamic acids over mmen-M₂ (dobpdc) (mmen = N,N'-dimethylethylenediamine, M = Mg, Mn, Fe, Co, Zn) (McDonald et al., 2015). (For interpretation of the references to color in this figure legend, the reader is referred to the web version of this article.)

Initially, amine-based silica sorbents are widely investigated. Therefore, classical preparation methods, referring to impregnation and grafting by silane linkage, are derived from amine-silica adsorbents. Meanwhile, the proposed reaction mechanism above is based on amino-silicas. In the last decade, thriving porous materials such as MOFs, covalent organic polymers (COPs), and their amine functionalized adsorbents have drawn more attention. New reaction pathways beyond the traditional formation of ammonium carbamates are then proposed (Forse and Milner, 2020). Long et al. proposed a unique cooperative mechanism of CO₂ adsorption involving the formation of ammonium carbamate chains (Milner et al., 2017; Siegelman et al., 2017), and firstly demonstrated the feasible formation of carbamic acid pair to compete with ammonium carbamate chain during CO₂ adsorption over dmpn-Zn₂ (dobpdc) (dmpn = 2,2-dimethyl-1,3-diaminopropane) (Fig. 3.25a)

(Milner et al., 2017). Later, they elucidated a new chemisorption mechanism using dmpn-Mg₂ (dobpdc), which involved the formation of a 1:1 mixture of ammonium carbamate and carbamic acid (Fig. 3.25b) (Forse et al., 2018). Also, a cooperative mechanism, the formation oxygen-bound carbamate chains by CO₂ inserting into the metal-N bonds, given rise to unusual step-shaped CO₂ adsorption (Fig. 3.25c) (Kim, 2020; McDonald et al., 2015). It was anticipated that coordination forms of amine and porous material with different structure could give rise to a spectacular mechanism in the future.

3.2.4.1.2. Adsorption thermodynamics & kinetics. Equilibrium adsorption capacity, reaction heat, and kinetics are key parameters for overall evaluation. These parameters could be obtained by adsorption isotherms. The distinction caused by amine functionalization is principally summarised. As for amine-functionalized solid sorbents,

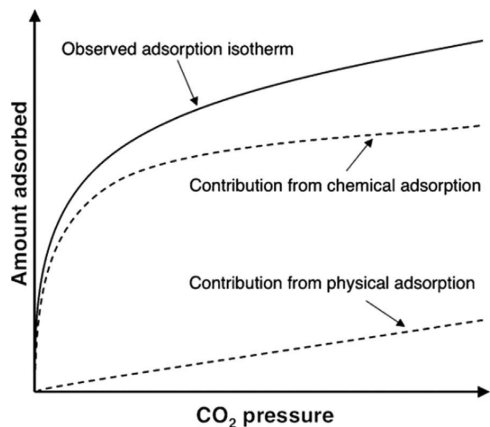


Fig. 3.26. Schematic representation of CO₂ adsorption on amine-functionalized mesoporous adsorbents (Serna-Guerrero et al., 2010). (For interpretation of the references to color in this figure legend, the reader is referred to the web version of this article.)

CO₂ adsorption is implemented via two independent mechanisms, i.e. chemisorption with amine-functionalized groups and physisorption on surface of solid adsorbent. In Fig. 3.26, chemical adsorption contributes to a high initial CO₂ uptake at the lower partial pressure while physisorption is enhanced with the increasing partial pressure. Langmuir isotherm model and Freundlich isotherm model, suitable for both chemisorption and physisorption processes, are widely adopted for describing the adsorption behaviour of amine functionalized adsorbent. However, Serna-Guerrero et al. (2010) pointed out that these two isotherm models were acceptable for describing adsorption profiles at low concentrations of CO₂ but less reliable at higher pressures. Therefore, they adapted a semi-empirical two-site Toth isotherm model, including two parts to represent chemisorption and physisorption, respectively. The model was successfully employed on different amine-functionalized materials with various adsorbates (Bollini et al., 2012a; Gebald et al., 2014).

Adsorption heat can be calculated from the adsorption isothermic curve by applying Clausius–Clapeyron. Generally, adsorption heat lower than 50 kJ/mol indicates weak physical adsorption, while that higher than 50 kJ/mol indicates the effects of chemical adsorption or reaction (Gelles et al., 2019; Siriwardane et al., 2005). High adsorption heat demonstrates strong interaction between CO₂ and amine, and further improves CO₂ selectivity, however, will increase the temperature of the process. Higher temperatures can decrease the adsorption capacity of the adsorbents, meanwhile resulting in higher desorption energy demands. To reduce energy consumption, two approaches are listed as follows:

- 1) Tuning the structure of solid support material and its interaction with suitable amine types through a new reaction mechanism. For instance, the distinct adsorption route of dmpn-Mg₂ (dobpdc) to CO₂, i.e. the formation of both ammonium carbamates and carbamic acids, results in high entropy penalty (-74 kJ/mol) coupled with a large entropic penalty (-204 J/mol/K). It can reduce the temperature required to desorb CO₂ in a temperature-swing adsorption process to lower than 100 °C (Milner et al., 2017). Long et al. prepared serials of diamine-appended MOFs, which could behave as ‘phase-change’ adsorbents with unusual step-shaped CO₂ adsorption isotherms (McDonald et al., 2015). As shown in Fig. 3.27, adsorption isotherm shifts markedly with temperature, resulting that a large working capacity can be achieved with only a small increase in temperature. Besides, they demonstrated tetraamine-appended

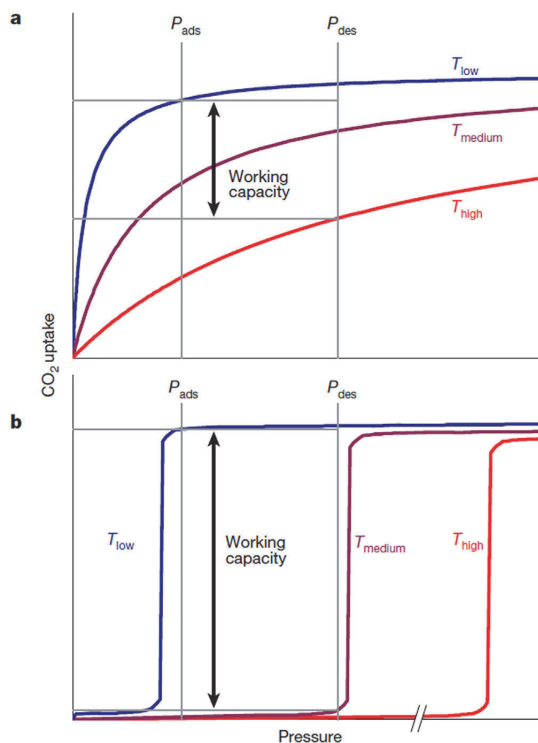


Fig. 3.27. Variation in the idealized adsorption isotherm behaviour with temperature for a classical microporous adsorbent (a) The usual Langmuir-type isotherm shape, compared with that of a phase-change adsorbent (b) Step-shaped (sometimes referred to as ‘S-shaped’) isotherms (Kim, 2020). (For interpretation of the references to color in this figure legend, the reader is referred to the web version of this article.)

- 2) System analysis and optimization of the whole reaction process. Zhang et al. (Zhang et al., 2016) systematically evaluated the effect of significant parameters, i.e. adsorbent property, adsorption heat, specific capacity, working capacity, moisture adsorption, swing temperature difference and heat recovery degree. The calculated regeneration heat for PEI/silica adsorbent was 2.47 GJ/tCO₂, while this value was 3.9 and 3.3 GJ/tCO₂ for a typical aqueous and an advanced MEA system, respectively.

Similar to porous adsorbents, kinetics for amine-functionalized adsorbents can be modelled by pseudo-first order law, pseudo-second order law, Elovich equation, Avrami model, and film diffusion model, among which pseudo-first order and pseudo-second order models are the simplest to understand the interaction mechanism of gas-solid adsorption (Syeda Saba Fatima, 2021). In Fig. 3.28, compared with benchmark adsorbent, the dynamic adsorption breakthrough curve of CO₂ over amine-functionalized adsorbents displayed a relatively sharp trend followed by a long tail. The sharp trend inferred favourable interactions between CO₂ and amine groups, while long tails signified large mass transfer resistance because of diffusion hindrance of amine groups (Bollini et al., 2012a, b). It has been well established that the adsorption behaviour of CO₂ onto benchmark adsorbent was driven by thermodynamic effects, while an opposing trend for amine functionalized adsorbent was controlled by kinetic effects. It is of significance to balance the thermodynamic and kinetic effects of CO₂ adsorption. Besides, adsorp-

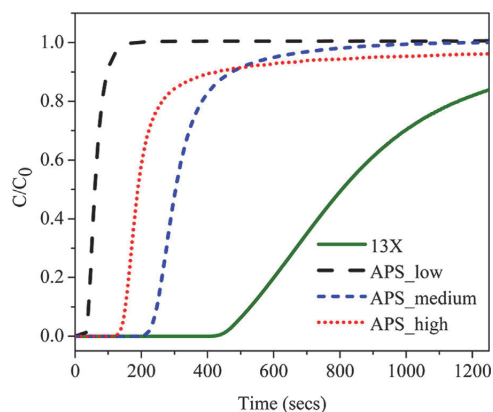


Fig. 3.28. APS-functionalized silica adsorbents at three different amine loadings compared to the benchmark zeolite 13X at 25 °C (Bollini et al., 2012a, b). (For interpretation of the references to color in this figure legend, the reader is referred to the web version of this article.)

tion kinetics are largely influenced by the process temperature, amine type, amine loading, and support material, which have been widely discussed in previous literature.

3.2.4.1.3. Deactivation mechanism. Stabilities of amine-functionalized CO₂ adsorbents during multiple adsorption-desorption cycles are the prerequisite for its industrial applications. A robust adsorbent should withstand many adverse effects including physical and chemical properties, feed gas composition and characteristics, and operational parameters. More detailed reviews have been summarized by Jahandar Lashaki et al. (2019) and Fan and Jia (2022). Herein, chemical deactivation associated with the interaction between amines and different gas compositions is focused, such as O₂, SO_x, NO_x and CO₂.

Due to the existence of oxygen in the feeding gas, such as 3–15% from power plant flue gas (Siegelman et al., 2021), 21% in the air, oxidative degradation of adsorbents has to be concerned. Akin to gas-liquid absorption systems, amine in adsorbents is prone to be oxidized to imine, imide, amide or nitron groups when exposed to high O₂ concentration, elevated temperature and metal ions (Heydari-Gorji et al., 2011a). Amine structure obviously affects its oxidative degradation, which indicates that single secondary amines and mixed amines readily degrade to oxygen-containing gas mixtures at high temperatures (Bali et al., 2013). Though strategies such as converting primary amines into secondary/tertiary amines (Choi et al., 2016; Zhang et al., 2012), chelating ppm-level metal impurities of PEI (Min et al., 2018), and using longer linkers between amine groups in amino-polymers (Pang et al., 2018) could mitigate the adverse effect of oxygen, the mechanism of oxidative degradation is still unclear.

CO₂-induced deactivation refers to the formation of stable urea between amine and CO₂. In Fig. 3.29, urea groups may form readily by direct interaction between amine species and CO₂ at high temperature under dry conditions. When moisture-containing gases are employed, urea formation can be strongly inhibited, even at a relatively low humidity (Belmabkhout, 2010; Li et al., 2016). Sayari et al. (2012) investigated the interaction between CO₂ and amines-containing mesoporous silica under dry condition, and proposed different reaction pathways depending on the structure and nature of amine-containing species (Fig. 3.30). As for primary amines, CO₂-induced deactivation undergoes through intermediacy of isocyanate followed by reaction with primary or secondary amine into di- and trisubstituted open-chain urea or N-substituted imidazolidinones. As for materials containing ethylene-diamine units with secondary amines, formation of the corresponding

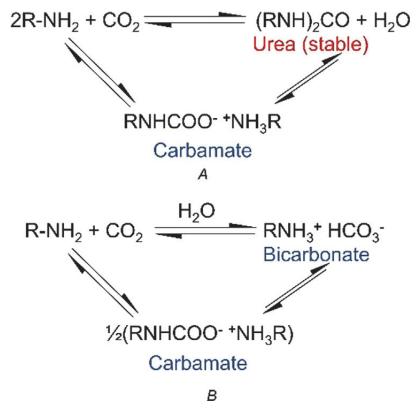
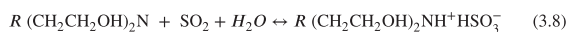
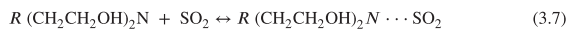


Fig. 3.29. (A) Schematic representation of urea formation under dry adsorption conditions, and (B) Inhibition thereof in the presence of added water vapour (Belmabkhout, 2010). (For interpretation of the references to color in this figure legend, the reader is referred to the web version of this article.)

N,N'-disubstituted imidazolidinones takes place through the dehydration of ammonium carbamate or carbamic acid. Also, they pointed out that all or some CO₂-deactivated materials may be regenerated via urea hydrolysis using a humidified inert gas under relatively high temperature (100–200 °C). Furthermore, Jung et al. (2017) found that the conversion of primary into secondary amines in different oligomers and polymers via functionalization with 1,2-alkylepoxyde, 1,3-butadiene diepoxide and epichlorohydrin could effectively inhibit the formation of urea linkages.

Generally, SO_x and NO_x in the flue gases potentially cause adsorbent deactivation by competing adsorption with CO₂, resulting from adsorption reversibility on amines in the order of CO₂ > SO₂ > NO₂ (A. Diaf, 1994). Since SO₂ is a stronger Lewis acid, SO₂ can interact strongly with all amines, including tertiary amines, through Reaction 3.5 under dry conditions and Reaction 3.6 under humid conditions, respectively. Nevertheless, Tailor and Sayari (Heldebrant et al., 2010; Tailor and Sayari, 2016; Yang et al., 2013) found that SO₂ could react with tertiary amines by Reaction 3.7 and Reaction 3.8 to form non-covalent charge transfer complexes, leading to adsorbent deactivation.



3.2.4.2. Modification of different adsorbents.

3.2.4.2.1. Description of three subclasses (I, II, III class). Considering bond structures and preparation methods, amine-based adsorbents could be divided into three subclasses in Fig. 3.31. Class I materials are prepared by physical impregnation with monomeric or polymeric within the pore of the supports, bonding through hydrogen bonds and/or dipole interactions. Class II materials are obtained by covalently grafting the targeted amines with relatively low molecule weight onto the surface of the support. As for Class III materials, they are prepared via in-situ polymerization of amine-containing monomers. Also, Class I materials are considered as promising candidates for industrial CO₂ capture because of high CO₂ adsorption capacity under the condition of low CO₂ concentration. However, shorter chained amines are preferable for the formulation of class II or class III adsorbents due to lower activation energies which aid in the facilitation of tethering (Bollini et al., 2011).

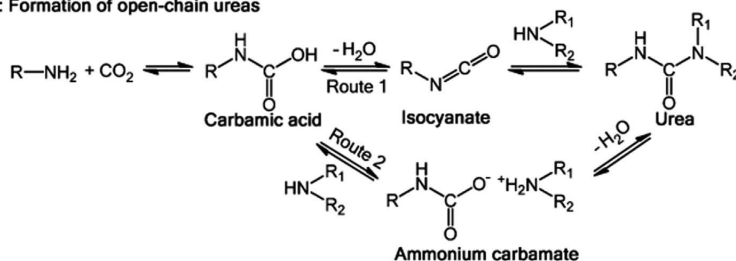
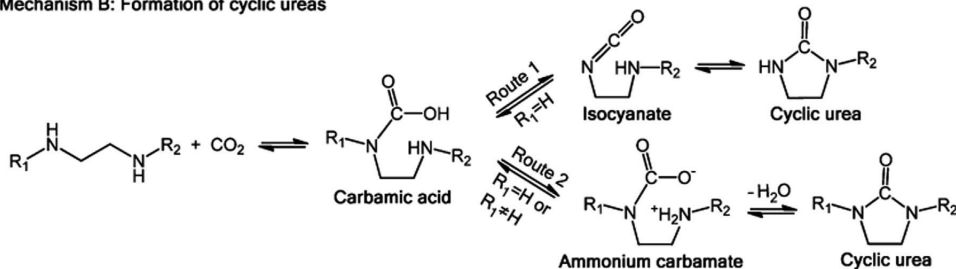
Mechanism A: Formation of open-chain ureas**Mechanism B: Formation of cyclic ureas**

Fig. 3.30. Mechanisms of CO₂-induced degradation of supported amines (Sayari et al., 2012). (For interpretation of the references to color in this figure legend, the reader is referred to the web version of this article.)

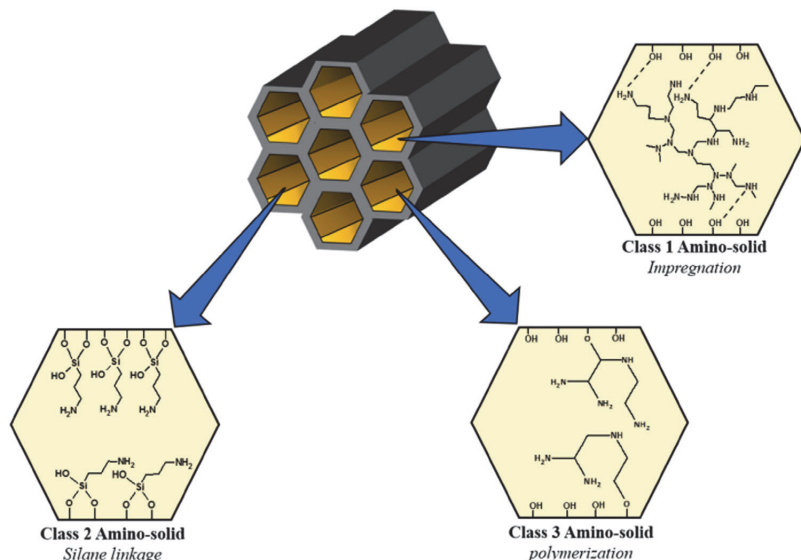


Fig. 3.31. Amino-solids based on preparation methods (Didas et al., 2015). (For interpretation of the references to color in this figure legend, the reader is referred to the web version of this article.)

3.2.4.2.2. Porous silica supports (I, II, III). As one of the important porous materials, porous silica is a chemically and thermally stable material with tunable textural and surface properties, e.g. pore size, pore distribution, surface area, and surface hydroxyl groups (Gawande et al., 2015; K, 1979; Verma et al., 2020). These features make it versatile and used in various technological or industrial applications, e.g. adsorption, medical, energy, catalyst and support materials (Liang et al., 2017). Thus, a variety of porous silica materials functionalized with amine have been synthesized and characterized to chemisorb CO₂ from different gas streams. For three classes of supported amine adsorbents, recent advances in porous silica support are summarized and discussed in this section.

Class 1: Amine-impregnated silica

The first ever literature reported in the field of amines impregnated silica was reported in 2002 (Xu, 2002), and the authors used a high surface area mesoporous silica MCM-41 as the support material for PEI loading, and the resulting adsorbent was termed as “molecular basket”. With PEI loading amount of 75 wt%, the highest CO₂ adsorption capacity of 3.02 mmol/g was achieved at a pure CO₂ atmosphere and 75 °C. The pore structure of porous silica was an important factor that affected the distribution of PEI. Son et al. (2008) further synthesized mesoporous silica with different pore structures and impregnated it with the same amount of PEI (50 wt%). CO₂ uptake capacity was in the order of KIT-6 (3D) > SBA-15 (1D) ~ SBA-16 (3D) > MCM-48 (3D) > MCM-41 (1D). The highest CO₂ adsorption capacity achieved by KIT-6 was mainly attributed to the large pore size and 3D structure. To further investigate

Table 3.10
Amine-porous silica CO₂ adsorbent prepared by physical impregnation method.

| Support material | Amine type | Temperature (°C) | CO ₂ partial pressure (atm) | Adsorption capacity (mg/g, dry CO ₂) | Ref. |
|-----------------------------|---------------------------------------|------------------|--|--|-------------------------------|
| MCM-41 | PEI | 75 | 0.15 | 89 | (Xu, 2005) |
| Pore expanded MCM-41 | PEI | 75 | 1 | 210 | (Heydari-Gorji et al., 2011b) |
| SBA-15 | PEI | 75 | 0.15 | 105 | (Yan et al., 2011b) |
| As-syn SBA-15 | PEI | 75 | 1 | 173 | (Yue et al., 2006) |
| | Tetraethylenepentamine | | | | |
| HMS | PEI | 75 | 1 | 184 | (Chen et al., 2010) |
| KIT-6 | PEI | 75 | 1 | 135 | (Son et al., 2008) |
| As-syn KIT-6 | PEI | 75 | 1 | 139 | (Kishor and Ghoshal, 2016) |
| Silica monolith | PEI | 75 | 1 | 210 | (Chen et al., 2009) |
| Mesocellular silica foam | PEI | 75 | 0.15 | 152 | (Yan et al., 2011a) |
| MSU-F silica | PEI | 50 | 1 | 260 | (Goepfert et al., 2011) |
| | Tetraethylenepentamine/diethanolamine | | | | |
| Fumed silica | PEI | 25 | 0.0004 | 52 | (Goepfert et al., 2011) |
| CARiACT G10 silica | PEI | 80 | 1 | 123 | (Ebner et al., 2011) |
| Mesoporous silica nanotubes | PEI | 85 | 0.6 | 121 | (Niu et al., 2016) |
| Rice husk derived silica | PEI | 75 | 0.15 | 159 | (Zeng and Bai, 2015) |
| TUD-1 mesoporous sponge | PEI | 75 | 0.15 | 116 | (Wang et al., 2014) |
| Hollow silica microspheres | PEI | 25 | 1 | 149 | (Cecilia et al., 2016) |

the influence of the pore structure of silica on CO₂ adsorption, Yan et al. (2011b) investigated PEI impregnated SBA-15 with different pore structures, and found that CO₂ adsorption amount increased proportionally with the total pore volume of SBA-15 support. However, pore size was not the main factor influencing CO₂ adsorption capacity. Besides, roles of micropores in SBA-15 were found not obvious as they have been blocked by amine (Yan et al., 2013). Overall, the ideal silica support would have high pore volume, which can load a high amount of amines and it should leave the voids in the pores for CO₂ diffusion. Thus, extensive research on the amine-impregnated porous silica for CO₂ capture have been reported. Some typically porous silica supports used for amine impregnation are summarized and given in Table 3.10.

Class 2: Amine-containing silane modified silica

The grafted amines on silica often have better thermal stability up to 200–250 °C when compared with physically impregnated silica (Sayari, 2006). Hydroxyl groups of silica supports played an important role because covalent bonds will be formed between hydroxyl groups and amino-silanes. Thus, available hydroxyl groups determine the content of amines grafted. Similar to the amine physically impregnated silica, the CO₂ adsorption capacity of amine containing silane modified silica was also affected by the pore structure of the silica support. Fayaz et al. (Fayaz and Sayari, 2017) found that P10 silica with a pore size of 21 nm exhibited a high CO₂ adsorption capacity of 86 mg/g after 3-[2-(2-aminoethylamino)ethylamino] propyltrimethoxysilane grafted. Jahandar Lashaki et al. (2017) synthesized SBA-15 with different pore structures, and functionalized them with 3-[2-(2-aminoethylamino)ethylamino] propyltrimethoxysilane for CO₂ adsorption. Results indicated that amine-silane grafted SBA-15 with larger pore size exhibited a higher CO₂ adsorption capacity. The CO₂ capture performance of amine-silane-modified silica is included in Table 3.11.

Class 3: In situ polymerized amine on silica

Class 3 adsorbents bind amines covalently to hydroxyl groups of the support, which is similar to class 2 sorbents. However, the densities of amine groups are similar to class 1. Thus, Jones et al. defined class 3 as a combination of class 1 and 2 (Sanz-Perez et al., 2016a). Usually, the adsorption capacities of Class 3 sorbents are higher than that of Class 2 adsorbents due to their high amine loading amounts, and they also have good reusability in successive runs. Porous silica support has a large surface area, pore volume and plenty of surface -OH groups, which facilitate the grafting of the amines. Thus, different kinds of silica materials have attracted considerable research interest since 2000s (Acosta et al., 2004; Chaikittisilp et al., 2011; Lunn and Shantz, 2009). A summary of the CO₂ adsorption capacity of graft-

ing amines by in-situ polymerization onto porous silica is given in Table 3.12.

3.2.4.2.3. *Polymer supports (I, II, III)*. Polymers can refer to inorganic polymers (e.g. geopolymer, clay etc.), organic polymers (i.e. porous organic polymers, POPs) and inorganic-organic coordination polymers (e.g. MOFs). Since geopolymer, MOFs and their amine-tethered adsorbents have been introduced in other sections, amine-tethered POPs adsorbents are especially focused. Amine adsorbent known as HSC+, which was applied by NASA to regeneratively remove CO₂ from space shuttle in 20 years ago, belongs to the amine-tethered polymer adsorbents (Satyapal et al., 2001). This proprietary material bonds polyethyleneimine (PEI) to solid polymethyl methacrylate polymeric support, with poly (ethylene glycol) (PEG), to enhance CO₂ adsorption and desorption rates. POPs with ultrahigh surface areas, tunable pore structure and adjustable chemical properties can be synthesized diversely from organic molecular building blocks (Cooper, 2009; Dawson et al., 2012), and are ideal supports for amine functionalization because of their chemically inert, high stability, and low production cost (Slater and Cooper, 2015). Amine modification can improve POPs not only for CO₂ adsorption capacity, but also for CO₂ selectivity (Lu et al., 2012). For example, amine e.g. EDA DETA, TETA, TAEA, AA, PEI and 2,5-dibromoaniline anchored onto PPN-6, CMP-1, polymethylmethacrylate (PMMA) could increase CO₂ uptake when compared with corresponding pristine supports (Gelles et al., 2019; Han et al., 2015; Hu, Xiayi et al., 2020; Jahandar Lashaki et al., 2019; Jiang et al., 2013; Mukhtar et al., 2020). A detailed list of amine-modified POPs and their CO₂ adsorptive properties can be found in a recent review (Zou et al., 2017).

For amine-loaded polymers, researchers have focused on amine selection and polymer preparation. Jafari et al. (2017) synthesized mesoporous polydivinylbenzene (PDVB) materials using 2, 2'-Azobis (2-methylpropionitrile) (AIBN) as the initiator through microwave-assisted polymerization and then impregnated the material with the amine-rich co-monomers of vinylimidazole (VI) and vinyl triazole (VT). With more active sites, VT-modified PDVB had a maximum CO₂ adsorption of 2.65 mmol/g at 0 °C under 100 kPa, while the adsorption capacity of VI-modified PDVB was 2.35 mmol/g under the same conditions. Liu F. et al. (2017) prepared PDVB through one-pot, timsolvothermal polymerization and impregnated them with PEI. The optimum formulation was 58 wt% PEI (to the adsorbent) impregnated PDVB (0.58PEI@PDVB) with maximum adsorption capacities of 3.76 and 3.00 mmol/g under pure CO₂ and 10 % CO₂, respectively, at 75 °C. The stability under both conditions was maintained after ten adsorption cycles under both dry

Table 3.11
Amine-porous silica CO₂ adsorbent prepared by the amine-silane grafting method.

| Support material | Amine type | Temperature (°C) | CO ₂ partial pressure (atm) | adsorption capacity (mg/g, dry CO ₂) | Ref. |
|-------------------------------|--|------------------|--|--|---------------------------------|
| Pore-expanded MCM-41 | N- (3-trimethoxysilylpropyl) diethylenetriamine | 75 | 0.2 | 92 | (Loganathan and Ghoshal, 2017) |
| MCM-48 | 2-[2- (3-trimethoxysilylpropylamino) ethylamino]ethylamine | 25 | 0.15 | 70 | (Nigar et al., 2016) |
| SBA-15 | 3-[2- (2-Aminoethylamino) ethylamino] propyltrimethoxysilane | 25 | 0.05 | 83 | (Jahandar Lashaki et al., 2017) |
| HMS | Aminopropyltrimethoxysilane | 20 | 0.9 | 53 | (Knowles and Chaffee, 2016) |
| P10 silica | 3-[2- (2-Aminoethylamino)ethylamino] propyltrimethoxysilane | 50 | 0.05 | 86 | (Fayaz and Sayari, 2017) |
| Amorphous silica | [3- (methylamino)propyl]trimethoxysilane | 30 | 0.17 | 60 | (Park et al., 2016) |
| SBA-16 | N- (2-Aminoethyl)-3-aminopropyltrimethoxysilane | 60 | 0.15 | 32 | (Wei et al., 2008) |
| SBA-12 | 3-Aminopropyltrimethoxysilane | 25 | 0.1 | 46 | (Zelenak et al., 2008) |
| MSU-F silica | 3-[2- (2-Aminoethylamino)ethylamino] propyltrimethoxysilane | 45 | 0.3 | 72 | (Lee et al., 2011) |
| Silica gel | 3-Aminopropyltrimethoxysilane | 27 | 1 | 18 | (Leal, 1995) |
| Fumed silica | 3-[2- (2-Aminoethylamino) ethylamino]propyltrimethoxysilane | 25 | 1 | 41 | (Czaun et al., 2013) |
| SiO ₂ aerogel | 3-Aminopropyltrimethoxysilane | 25 | 0.1 | 86 | (Cui et al., 2011) |
| Double-walled silica nanotube | 3-[2- (2-Aminoethylamino)ethylamino] propyl trimethoxysilane | 25 | 1 | 98 | (Ko et al., 2013) |

Table 3.12
Amine-porous silica CO₂ adsorbent prepared by the in-situ polymerization method.

| Support material | Amine type | Temperature (°C) | CO ₂ partial pressure (atm) | adsorption capacity (mg/g, dry CO ₂) | Ref. |
|--------------------------|---|------------------|--|--|------------------------------|
| Pore-expanded -MCM-41 | 3-[2- (2-aminoethylamino)ethylamino]propyl trimethoxysilane | 25 | 0.05 | 62 | (Sayari, 2006) |
| SBA-15 | 3-aminopropyltrimethoxysilane | 25 | 0.1 | 50 | (Chaikittisilp et al., 2011) |
| Mesoporous Silica | Polyethenimine | 75 | 0.15 | 124 | (Klinthong et al., 2016) |
| Silica spheres | Trimethoxy [3- (methylamino)propyl]silane | 50 | 0.1 | 44 | (Hahn et al., 2016) |
| Silsesquioxane aerogel | (3-Aminopropyl) triethoxysilane | 50 | 0.01 | 134 | (Kong et al., 2016) |
| Precipitated silica | (3-Aminopropyl) triethoxysilane | 50 | 0.14 | 45 | (Quang et al., 2017) |
| Silica monolith | tetraethylenepentamine | 75 | 1 | 171 | (Wen et al., 2010) |
| SiO ₂ aerogel | 3-Aminopropyltriethoxysilane | 25 | 0.1 | 86 | (Cui, Sheng et al., 2011) |

and wet conditions. Zheng et al. (2019) synthesized an N-abundant and mesopores-rich POPs by solvothermal copolymerization of divinylbenzene (DVB) and 1-vinylimidazole (VI) without the use of any templates. It was found that PEHA-impregnated P (DVB-VI) adsorbents displayed CO₂ capacities as high as 4.56 mmol/g at 75 °C and atmospheric pressure, together with excellent CO₂/N₂ selectivity and good recycling stability.

To reduce the cost of material development, a simplified preparation route and utilization of existing polymers have drawn more attention. Wang et al. (2022) reported a novel synthesis method by in situ ring-opening grafting copolymerization of aziridine with the poly-HIPE (HIPE = high internal phase emulsion). The adsorption capacity of 2.40 and 3.25 mmol/g could be achieved under dry and humid conditions at 0.1 atm partial pressure of CO₂, respectively. Further, they fabricated 4.0PEI70k@polyHIPE adsorbent by one-step method (Fig. 3.32), which indicated a maximum adsorption capacity of 4.18 mmol/g at 20 °C under humid conditions (Wang et al., 2021). Stiernet et al. (2022) combined Radziszewski's multicomponent reaction and high internal phase emulsion (HIPE) polymerization in a one-pot manner (Fig. 3.32). The bifunctional amine/imidazolium foams revealed superior CO₂ capture performances when compared to their monofunctional counterparts, indicating the synergy between functional groups. Yang et al. (2019) developed a facile strategy that converted a cost-effective porous organic polymer, which was synthesized by Friedel-Crafts alkylation reaction of dichloro-*p*-xylene, into outstanding CO₂ adsorbents through one-step post-synthesis functionalization with polyamines. Adsorbents showed good CO₂ uptake capacity, fast adsorption-desorption kinetics and excellent stability toward both water vapour and regeneration cycles under dynamic flow conditions. As for existing polymers,

Meng et al. (2021) found that tethering PEI onto conventional porous supports HP20 could achieve superior adsorption properties with above 4 mmol/g and cyclic stability with around 1 % loss after 30 cycles, which were rather than ones synthesized through complex approaches.

3.2.4.2.4. Zeolite supports (I, II, III). Zeolites, possessing the merit of tunable textural properties, variable pore sizes, and interconnecting channels and cavities, have been widely used in CO₂ via their steric effect, kinetic effect, equilibrium effect and trapdoor effect (Bai et al., 2022; Yue et al., 2022). However, hydrophilic nature and physical adsorption behavior incapacitate zeolites for CO₂ separation under the conditions of humidity, high temperature (>30 °C), and low pressure (<2 bar). Amine-functionalized zeolites have been demonstrated to empower CO₂ capture from humid streams and improve selectivity (Chen et al., 2015; Kim et al., 2016; Kolle et al., 2021; Jadhav, 2007; Su et al., 2010). Two kinds of amine-functionalized zeolites, prepared by impregnation and grafting, are discussed as follows respectively. (Fig. 3.33)

Class I: Physical impregnation of monomeric and polymeric amines.

Impregnation is a cost-effective method for the preparation of amine-functionalized zeolites. However, two issues should be addressed. Firstly, microporous zeolite is prone to be blocked by impregnated amines, resulting in the decrease of adsorption capacity. Murge et al. (2019) found that the adsorption capacity of in-house-synthesized zeolites decreased with increasing TEPA loading. Meanwhile, the decrease in physisorption capacity was several times higher than the expected increase in chemisorption capacity. However, commercial zeolites had an optimal amine loading 2.5 %. On the contrary to high amine loading up to 70 %, Panda et al. (2019) synthesized a binder-containing zeolite 4A bodies (IBA-Z4A) modified with 0.3 % iso-butylamine, which

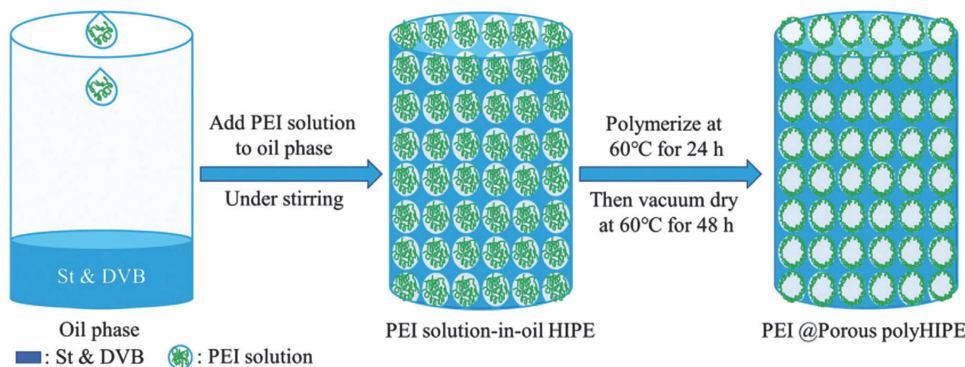


Fig. 3.32. Synthetic procedure for PEI functionalized polyHIPE (Wang et al., 2021). (For interpretation of the references to color in this figure legend, the reader is referred to the web version of this article.)

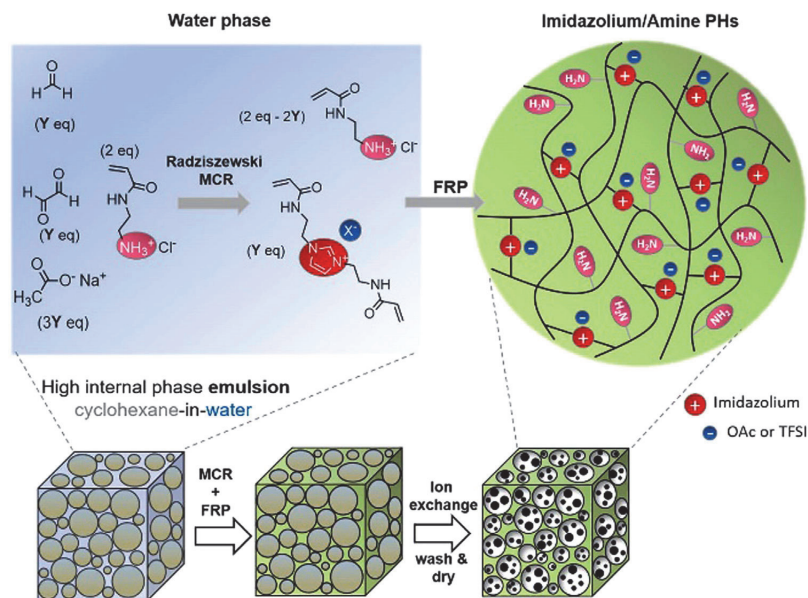


Fig. 3.33. Imidazolium/amine polyHIPEs synthesis combining Radziszewski MCR and emulsion templating polymerization (Stiernet et al., 2022). (For interpretation of the references to color in this figure legend, the reader is referred to the web version of this article.)

exhibited excellent CO₂ adsorption performance with adsorption capacity of 2.56 mmol/g and remarkably high CO₂/N₂ selectivity of 335 at 25 °C and 1 bar. Whereas CO₂/N₂ selectivity of pristine binder-containing zeolite 4A bodies was only 24. The other issue is that the impregnated amines is liable to evaporate at elevated temperature, especially for small-molecular amines. It remarkably affects adsorption thermal stability. To hinder the amine loss, Yu et al. (2014) proposed a ship-in-a-bottle method to prepare NaY zeolites loaded with amine functionalized ionic liquids (Fig. 3.34) by employing unique cage structures of microporous zeolites. The trick of this method lay in the in-situ synthesis of large molecular ionic liquid, 1-aminopropyl-3-methylimidazolium bromide ([APMIM]Br) within super cage using the smaller precursors (e. g. N-methylimidazole and 3-bromopropylamine) that can diffuse through zeolite windows. Whereas the host-guest systems exhibited superb adsorption capacity up to 4.94 mmol/g and good cyclic ability with 5% decreasing adsorption capacity after 20 working cycles.

Heat consumption and cost should be taken into account for industrial applications. Kalantarifard et al. Cheng et al. (2021b) synthesized EDA impregnated ZSM-5 for CO₂ adsorption, with the highest CO₂ adsorption capacity of 6.13 mmol/g in the presence of water at 75 °C. Microwave heating was employed for the desorption process, and the fastest desorption time was 9 min for 70% EDA loaded ZSM-5. Recently, Cheng et al. (2021a) tethered monoethanolamine (MEA) and hydroxyethyl ethylenediamine (AEEA) onto HZSM-5 zeolites via wet impregnation method, respectively. The result indicated that MEA and AEEA fixed HZSM-5 zeolites had good CO₂ adsorption capacities, with maximum values of 4.27 and 4.44 mmol/g, respectively. Notably, the CO₂ desorption process of AEEA loaded HZSM-5 exhibited a low activation energy of 54.27 kJ/mol. HZSM-5 zeolite provided a large number of free H⁺ ions to directly participate in carbamate breakdown, and metal atoms (Al) that attached to N atom of carbamate, thereby stretching the C–N bond and promoting decomposition. To further reduce the cost of adsorbents, Thakkar et al. (2017) prepared ZSM-5, zeolite-Y and SAPO-34 from kaolin clay and modified them with TEPA for capturing CO₂ from

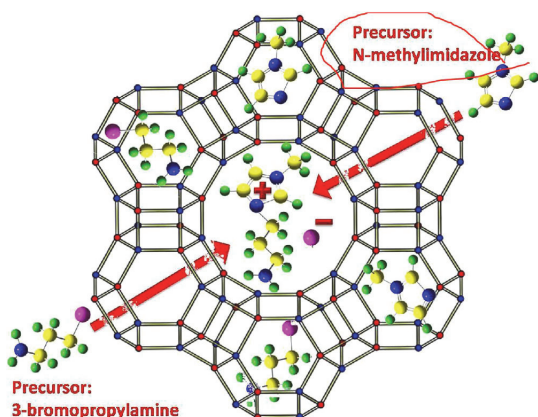


Fig. 3.34. Schematic illustration of ship in a bottle synthesis of [AP-MIM]Br@NaY (Liu F. et al., 2017). (For interpretation of the references to color in this figure legend, the reader is referred to the web version of this article.)

the air. The best adsorption capacity was 1.12 mmol/g for the TEPA-loaded ZY at 25 °C using 5000 ppm CO₂ in nitrogen.

Class II: Grafting.

Similar to the impregnated amine onto zeolites, the grafted amine can reduce adsorption capacity, but improve the selectivity over other gas and amine stability. Kim et al. (2013) functionalized SAPO-34 with 3-aminopropyltrimethoxysilane (APMS). It demonstrated that the functionalized mesoporous SAPO-34 (NH₂-SAPO (M)-34) had a lower CO₂ adsorption capacity than its pristine counterparts. However, it exhibited improved CO₂/N₂ selectivity. Bezerra et al. (2014) found that increasing amine grafted to zeolite 13X adsorbent tended to reduce micropore volume of the resulting adsorbents by pore blocking with MEA. Liu F. et al. (2017) synthesized an ethylenediamine-grafted Y zeolite with working capacities higher than 1.1 mmol/g over 20 temperature swing adsorption (TSA) cycles, and reported that the strongly co-adsorbed H₂O within the hydrophilic zeolite micropores suppressed urea formation under desorption conditions according to Le Chatelier's principle. Yang et al. (2012) concluded that CO₂ adsorption capacity varied in the sequence of MCM-22 (2.09) > NH₂-ITQ-2 (1.73) > ITQ-2 (1.64) > NH₂-MCM-22 (1.52) > MCM-36 (1.32) > NH₂-MCM-36 (1.20) > Fe-MCM-22 (1.20 mmol/g) at 298 K, but NH₂-ITQ-2 showed exceptionally high CO₂/N₂ selectivity of 10.8.

To further boost the stability of APTES grafted zeolite β , Liu et al. (2020) proposed an alkyl-functionalization method for the stoichiometric conversion of primary amines to secondary amines. Alkyl-functionalized-APTES zeolite exhibited the adsorption capacity of 1.44 mmol/g of 15% CO₂ at 90 °C and a very high sorption rate ($t_{1/2}$ = 0.69 min of over 90% of total sorption capacity within 5 min). Also, long-term stability after 20 cycles in a TSA operation with above 0.9 mmol/g at pure CO₂ regeneration was observed.

Recently, another zeolite-like adsorbent, geopolymer, was adopted as efficient amine support. Chen et al. (2022) grafted APTES onto the geopolymer treated with nitric acid and achieved a high grafting amount of 3.5 mmol N/g due to the large specific surface area of 412 m²/g and superior silanol density of 4.25 mmol/g. The as-prepared amine functionalized solid sorbent showed a remarkable adsorption capacity of 1.82 mmol/g with fast adsorption kinetics and low energy requirement for regeneration.

Class III

Liang et al. (2022) immobilized monoethanolamine (MEA) and ethylenediamine (ED) via ionic bond to the zeolite Y framework to overcome amine degradation. The elemental analysis demonstrated that ED

had successfully grafted almost twice as many amino groups as MEA within the same solvent concentration. It indicated that 20% ED@HY had the highest CO₂ adsorption capacity of 1.76 mmol/g at 90 °C with superior performance in cyclic thermal stability in the condition of the adsorption temperature of 90 °C and the desorption temperature of 150 °C. Wahono et al. (2021) deposited a solid-state amine adsorbent on natural mordenite-clinoptilolite zeolite through a simple plasma polymerization. The plasma deposition of amine polymer under certain conditions resulted in a significant increase in surface area-weighted CO₂ adsorption capacity and weakened the strength of the interaction between CO₂ and the adsorbent.

Post-synthetic functionalization by organic molecules has been proposed as an effective strategy to tailor the adsorption properties of zeolites (Nik et al., 2011). Small amine molecules can be chemisorbed onto micropore walls via conjugate acid-base formation between the Brønsted acid sites of the zeolite and the basic N atoms. Kwon et al. (2022) adopted this method to covalently attached various functional groups (-PhNH₂, -PhCH₂NH₂, -PhCOOH, -PhOH, -Ph) onto the micropore walls of beta zeolites to modify their adsorption properties. The results conducted that the benzylamine functionalized β zeolite exhibited higher CO₂ adsorption than its pristine counterpart under flue gas conditions with 10.5% CO₂, 5% H₂O and 84.5% N₂, which might be attributed to the synergistic effect of the hydrophobic benzene and basic amine moieties in the benzylamine group.

Hierarchical microporous and amorphous is another strategy for improving the properties of amine functionalized zeolite (Ge et al., 2021; Jia et al., 2022). Liu et al. (2016) fabricated a series of 5A zeolite-based hybrids with a shell of mesoporous silica-supported-amine (5A@MSAs) to dynamically hinder the diffusion of water molecules into the zeolite core. 5A@MSA-30 was demonstrated to be the best candidate for CO₂ capture with the CO₂ uptake as high as 5.05 mmol/g at 298 K and 10 cyclic stable adsorption/desorption operation.

3.2.4.2.5. MOF supports (I, II, III). MOFs as porous crystalline materials are composed of metal nodes that are combined with organic linkers. In view of their well-ordered porous structures, such as high specific surface area, pore volume and easily adjustable composition and pore structure, MOFs have been viewed as promising candidates for CO₂ capture technology. Over the last two decades, research on MOFs and MOFs-amine composites has been the study button and widely studied. However, the crystalline or microcrystalline form factor has limited the development of MOFs for commercialization application (Sanz-Perez et al., 2016a). Therefore, the modification of MOFs by amines has been sought in an effort to advance the utility of MOFs.

Class I

Class I amine-modified MOFs are common in adsorption applications because large pore volume allows the loading of high amine contents, which results in physisorption and chemisorption conducted at the same time. Therefore, Class I amino-MOFs always show high CO₂ adsorption capacity. However, unlike traditional mesoporous amine-based adsorbents, MOFs are microporous materials. The bulky amino polymers have the possibility to block the pores during the impregnation process and even decompose the structure (Gelles et al., 2019). A majority of Class I amino-MOFs select MIL-101 as support in view of its chemical stability, which could prevent pore degradation as a result of unintended side reactions (Gelles et al., 2019). For example, the impregnation of PEI onto MIL-101 was first reported in 2013. The results demonstrated an increase in CO₂ adsorption capacity, reaching 5.1 mmol/g at 25 °C, 1.75 bar when the amine loading is 100% (Lin et al., 2013). Also, Uio-66 was impregnated with PEI and achieved a CO₂ adsorption capacity of 1.65 mmol/g and 2.41 mmol/g under the condition of a dry and humid environment. After several adsorption and regeneration experiments, the composite could recover the capture performance completely (Xian et al., 2015a). Typical class I amino-MOFs are summarized in Table 3.13.

Class II

Class II amine-MOFs CO₂ adsorbents are rarely reported due to the lack of functionalized sites, which are suitable for silane attachment.

Table 3.13
CO₂ adsorption capacity of class I amine-MOFs CO₂ adsorbent.

| Support material | Amine type | Temperature (°C) | CO ₂ partial pressure (kPa) | Adsorption capacity (mmol/g, dry CO ₂) | Reference |
|------------------------------------|------------|------------------|--|--|-------------------------|
| MIL-101 | PEI | 25 | 175 | 5.10 | (Lin et al., 2013) |
| MIL-101 | PEI | 25 | 100 | 3.30 | (Xian et al., 2015a) |
| MIL-101 (Cr) | PEI | 25 | 10 | 1.30 | (Yan et al., 2013) |
| MIL-101 (Cr) | DETA | 23 | 100 | 3.56 | (Hu et al., 2014) |
| MIL-101 (Fe) | DETA | 25 | 100 | 1.82 | (Mutyalu et al., 2019b) |
| MIL-101 (Cr,Mg) | PEI | 25 | 100 | 3.04 | (Gaikwad et al., 2019) |
| MIL-101 (Cr) | PEI | 75 | 100 | 3.81 | (Mutyalu et al., 2019a) |
| MIL-101 | TREN | 25 | 0.04 | 2.60 | (Darunte et al., 2016) |
| MIL-53 | TEPA | 45 | 500 | 1.40 | (Martínez et al., 2016) |
| UiO-66 | PEI | 65 | 100 | 1.65 | (Xian et al., 2015a) |
| UiO-66 | PEI | 35 | 10 | 0.75 | (Xian et al., 2015a) |
| Cu ₃ (BTC) ₂ | PEI | 25 | 100 | 10.0 | (Aarti et al., 2016) |
| HKUST-1 | TEPA | 45 | 500 | 2.3 | (Martínez et al., 2016) |
| ZIF-8 | TEPA | 45 | 500 | 2.0 | (Martínez et al., 2016) |
| ZIF-8 | PEI | 35 | 10 | 1.4 | (Yang et al., 2022) |
| ZIF-8 | PEI | 65 | 100 | 1.61 | (Xian et al., 2015b) |
| Zn/Co ZIF | PEI | 25 | 100 | 1.82 | (Cheng et al., 2019) |
| MOF-177 | DETA | 25 | 100 | 2.83 | (Gaikwad et al., 2021) |
| MOF-177 | TEPA | 25 | 100 | 3.82 | (Gaikwad et al., 2021) |
| MOF-177 | TEPA | 55 | 100 | 4.6 | (Gaikwad et al., 2021) |
| Mg-MOF-74 | TEPA | 25 | 100 | 5.68 | (Su et al., 2017) |

Pokhrel et al. (2018) grafted APTES onto ZIF-8, and the results suggested CO₂ adsorption capacity of 0.8 mmol·g⁻¹ was achieved under the condition of 1 bar dry CO₂ atmosphere at 25 °C. Also, the capture performance of class II amino-ZIF didn't change (0.8 mmol/g) under 10% RH humid condition and humidified stability was improved. Also, deprotonated MEA was grafted onto UiO-66, which reveals a CO₂ capacity of 0.8 mmol·g⁻¹ at 0.15 bar CO₂ and 298 K, and it could maintain the adsorption performance even at high relative humidity (82%) (Li et al., 2015). When it comes to adsorption performance, markedly improvement was not observed between class II and class III amino-MOFs. Therefore, considering the inefficient synthesis procedure of preparation of amino-MOFs, class II amino-MOFs prepared by the grafting method are not suitable for scaled applications (Gelles et al., 2019).

Class III

As for class III amine-MOFs CO₂ adsorbents, less energy is required for amine-tethering in comparison with the energy used for silane attachment of class II amino-MOFs making them attractive candidates for capture application. As for class III materials, ED was first incorporated into ZIF-8, and the experimental results demonstrated the potential for stable CO₂ adsorption. At 1 bar, the composite showed a CO₂ adsorption capacity of 0.68 mmol/g (Pokhrel et al., 2018). Since then, various supports have been selected for amine modification with different amines. For example, MIL-101 was grafted with PEHA and TEPA, and increased CO₂ adsorption capacities were observed, with the highest adsorption capacity up to 3.1 mmol/g at 25 °C, 1 bar (Huang et al., 2016). Similarly, a number of attempts have been conducted for Mg₂/DOPDC and Mg₂ (dobpdc). And class III amino-MOF adsorbents are listed in Table 3.14 (Gelles et al., 2019).

3.2.4.2.6. Carbon supports (I, II, III). Carbonaceous adsorbents are utilized widely in the field of gas adsorption and separation processes due to high surface area, large pore volume, high stability and relatively low adsorption/desorption temperatures (Lee et al., 2015). Amine-modified carbonaceous materials, such as activated carbon (AC), carbon nanotubes (CNTs) and porous carbon supports, could perform similar CO₂ adsorption performance as amine-modified porous silica because of their stable structural pores. Among various carbonaceous materials, cost-effective ACs are the most common in practical applications. ACs supports always use lignocellulose and coal, e.g. coconut shell, bamboo and coke, as raw materials. After the physical or chemical activation process, pore structures of ACs are improved. The high surface area of ACs allows for subsequent amine modification. After surface amine modification, ACs display higher affinities towards CO₂, which could then improve CO₂ adsorption capacity. As advanced materials, CNTs have

been investigated widely in recent years in light of their high thermal and chemical stability as well as their unique physicochemical properties. Additionally, CNTs exhibit similar CO₂ adsorption performance as functionalized high surface area ACs (Lawson et al., 2018).

Class I

Class I materials have been widely investigated due to the simplicity of the physical impregnation method. Gholidoust et al. impregnated DEA onto oil sands coke-based ACs and reported the highest CO₂ adsorption capacity of 5.63 mmol/g at 50 °C. The results suggested a 75% improvement in comparison with commercial zeolite 13X (Gholidoust et al., 2017). Moreover, the effects of different amines, including DEA, MDEA and TEPA were investigated. The results indicated that ACs impregnated with secondary amines (DEA) have a more profound reaction with CO₂ than tertiary amines (MDEA), which agreed with CO₂ and amine reactivity: order primary > secondary > tertiary (Gholidoust et al., 2017). Also, the stimulatory effect of water was proven by MDEA@AC, increasing from 0.58 mmol/g to 1.70 mmol/g at 20% RH. Gibson physically impregnated EDA and TETA onto microporous and mesoporous ACs. The results demonstrated that microporous ACs were not suitable for amine-impregnation because the filling of the external channel led to the blockage of pores and then restrained further diffusion into the inner pores (Gibson et al., 2015). For CNTs, Zhou compared the CO₂ capture capacity of two types PEI-modified CNTs (L-PEI and B-PEI). The results suggested that although lower CO₂ adsorption capacity was achieved by L-PEI-impregnated CNT when compared with CNT modified by B-PEI, it exhibited lower desorption and better stability, which allowed for practical application for a long time (Zhou et al., 2017). CO₂ adsorption capacity of class I amine-carbon materials are shown in Table 3.15.

Class II

Class II amino-carbon materials are always focused on CNTs supports rather than ACs supports because covalent functionalization on the CNTs interface does not compromise the structural integrity of the supports (Gelles et al., 2019). By means of covalently bonding PEI onto functionalized-single wall CNTs (SWCNTs), enhanced CO₂ adsorption capacity could reach 1.77 mmol/g at 75 °C, 1 bar (Eoghan, 2008). Similarly, increased CO₂ uptake was also observed by APTES-modified multi-wall CNTs (MWCNTs), reaching 1.25 mmol/g 60 °C and 0.15 bar with 5 wt% APTES loading. Also, in the presence of water, CO₂ capture capacity increased with the increase of water content. Under the same condition of temperature, pressure and amine loading, CO₂ uptake increased from 1.25 mmol/g to 1.53 mmol/g at 35% RH (Su et al., 2009). What's more, due to the combined adsorption capacities of chemisorp-

Table 3.14
CO₂ adsorption capacity of class III amine-MOFs CO₂ adsorbent.

| Support material | Amine Type | Temperature (°C) | CO ₂ partial pressure (kPa) | Adsorption capacity (mmol/g, dry CO ₂) | Reference |
|--------------------------|------------|------------------|--|--|---------------------------|
| ZIF-8 | ED | 25 | 100 | 0.68 | (Pokhrel et al., 2018) |
| ZIF-8 | ED | 25 | 2500 | 10.0 | (Zhang et al., 2013) |
| ZIF-8 | ED | 35 | 1000 | 4.8 | (Thompson et al., 2013) |
| MIL-101 | PEHA | 25 | 100 | 1.3 | (Anbia and Hoseini, 2012) |
| NH ₂ -MIL-101 | TEPA | 25 | 100 | 3.1 | (Huang et al., 2016) |
| MIL-101 (Cr) | TEPA | 25 | 100 | 2.75 | (Wang et al., 2012) |
| Mg ₂ /DOPDC | m-2 | 25-120 | 100 | 5.0 | (Siegelman et al., 2017) |
| Mg ₂ /DOPDC | mm-2 | 25-120 | 100 | 5.1 | (Siegelman et al., 2017) |
| Mg ₂ /DOPDC | mnen | 25-120 | 100 | 5.0 | (Siegelman et al., 2017) |
| Mg ₂ /DOPDC | i-2 | 25-120 | 100 | 4.9 | (Siegelman et al., 2017) |
| Mg ₂ /DOPDC | ii-2 | 25-120 | 100 | 5.1 | (Siegelman et al., 2017) |
| Mg ₂ /DOPDC | e-2 | 25-120 | 100 | 4.5 | (Siegelman et al., 2017) |
| Mg ₂ /DOPDC | ee-2 | 25-120 | 100 | 4.4 | (Siegelman et al., 2017) |
| Mg ₂ /DOPDC | e-2-e | 25-120 | 100 | 4.6 | (Siegelman et al., 2017) |
| Mg ₂ (dobpdc) | dmen | 40 | 100 | 4.34 | (Lee et al., 2015) |
| Mg/DOBDC | ED | 25 | 100 | 4.5 | (Lee et al., 2015) |
| Mg/DOBDC | ED | 25 | 0.04 | 1.6 | (Choi et al., 2012) |
| Mg/DOBDC | mnen | 25-75 | 100 | 4.0 | (McDonald et al., 2015) |
| Mg ₂ (dobpdc) | pn | 40 | 100 | 4.6 | (Milner et al., 2017) |
| Mg ₂ (dobpdc) | mpn | 40 | 100 | 3.8 | (Milner et al., 2017) |
| Mg ₂ (dobpdc) | dmpn | 40 | 100 | 4.2 | (Milner et al., 2017) |
| Co/DOBDC | mnen | 25-75 | 100 | 3.9 | (McDonald et al., 2015) |
| Fe/DOBDC | mnen | 25-75 | 100 | 3.5 | (McDonald et al., 2015) |
| Mn/DOBDC | mnen | 25-75 | 100 | 3.5 | (McDonald et al., 2015) |
| Ni/DOBDC | mnen | 25-75 | 100 | 3.9 | (McDonald et al., 2015) |
| Zn/DOBDC | mnen | 25-75 | 100 | 3.0 | (McDonald et al., 2015) |

Table 3.15
CO₂ adsorption capacity of class I amine-carbon materials CO₂ adsorbent.

| Support material | Amine type | Temperature (°C) | CO ₂ partial pressure (kPa) | Adsorption capacity (mmol/g, dry CO ₂) | Ref. |
|-------------------------|------------|------------------|--|--|---------------------------|
| Oil sands coke-based AC | DEA | 50 | 66 | 5.63 | (Gholidoust et al., 2017) |
| Oil sands coke-based AC | MDEA | 50 | 66 | 0.58 | (Gholidoust et al., 2017) |
| Oil sands coke-based AC | TEPA | 50 | 66 | 0.90 | (Gholidoust et al., 2017) |
| AC | MEA | 75 | 10 | 1.70 | (Bezerra et al., 2011) |
| AC | TEA | 75 | 10 | 0.27 | (Bezerra et al., 2011) |
| Palm shell-based AC | AMP | 25 | 30 | 1.50 | (Lee et al., 2013) |
| Palm shell-based AC | AMPD | 25 | 30 | 1.20 | (Lee et al., 2013) |
| AC | AMP | 26 | 15 | 0.77 | (Khalil et al., 2012) |
| AC | MEA | 25 | 15 | 1.11 | (Khalil et al., 2012) |
| Mesoporous AC | BPEI | 25 | 0.04 | 2.25 | (Wang et al., 2015) |
| Mesoporous AC | BPEI | 25 | 0.5 | 3.34 | (Wang et al., 2015) |
| Nanoporous carbon | PEI | 75 | 100 | 0.26 | (Tang et al., 2013) |
| Nanoporous carbon | PEI | 75 | 100 | 1.01 | (Tang et al., 2013) |
| Nanoporous carbon | PEI | 75 | 10 | 0.23 | (Tang et al., 2013) |

Table 3.16
CO₂ adsorption capacity of class II amine-carbon materials CO₂ adsorbent.

| Support material | Amine type | Temperature (°C) | CO ₂ partial pressure (kPa) | Adsorption capacity (mmol/g, dry CO ₂) | Reference |
|------------------|------------|------------------|--|--|-----------------------|
| SWCNT | PEI | 75 | 100 | 1.77 | (Eoghan et al., 2008) |
| MWCNT | APTES | 60 | 15 | 1.25 | (Su et al., 2009) |
| MWCNT | APTES | 50 | 15 | 1.95 | (Su et al., 2011) |
| MWCNT | PEI | 70 | 20 | 0.98 | (Zhou et al., 2018) |
| CNTs | APTS | 25 | 10 | 0.93 | (Chungsyng Lu, 2008) |
| CNTs | APTS | 25 | 50 | 2.19 | (Chungsyng Lu, 2008) |
| Granular AC | APTS | 25 | 50 | 1.81 | (Chungsyng Lu, 2008) |
| CNTs | APTS | 20 | 15 | 0.98 | (Su et al., 2009) |

tion and physisorption for amine-based CNTs, CO₂ adsorption capacity enhanced with the increase of amine loading amounts. The investigation of PEI-modified MWCNTs demonstrated the steam and resultant suitability for CO₂ capture in post-combustion process after eleven working cycles (Zhou et al., 2018). Class II amine-carbon adsorbents are listed in Table 3.16.

Class III

CO₂ adsorption capacities of Class III amine-carbon materials have also been investigated widely, especially for ACs. Firstly, after anchoring TETA onto the surface of carbonaceous material, the highest CO₂

adsorption performance was 1.90 mmol/g with 10 wt% TAEA loadings at 70 °C and 1 bar, and CO₂/N₂ selectivity also increased. Zhao et al. (2010) modified graphene oxide with ED, DETA and TETA. In particular, ED modified graphene oxide showed the highest CO₂ adsorption capacity in the presence of a longer amine chain and enhanced N content, reaching 1.06 mmol/g with 50 wt% ED loadings (Zhao et al., 2012). Houshand et al. grafted ED and DETA onto AC. The results suggested that the inclusion of toluene in the solvent resulted in increased active sites (Lee, C.S. et al., 2013). The CO₂ adsorption capacity of class III amine-carbon materials is summarized in Table 3.17.

Table 3.17
CO₂ adsorption capacity of class III amine-carbon materials CO₂ adsorbent.

| Support material | Amine type | temperature (°C) | CO ₂ partial pressure (kPa) | Adsorption capacity (mmol/g, dry CO ₂) | Ref. |
|-----------------------|------------|------------------|--|--|---------------------|
| Carbonaceous material | TAEA | 70 | 100 | 1.90 | (Zhao et al., 2010) |
| Graphene oxide | ED | 30 | 100 | 1.06 | (Zhao et al., 2012) |
| Palm shell-based AC | MMEA | 25 | 30 | 1.00 | (Lee et al., 2013) |
| Mesoporous carbon | PEI | 30 | 100 | 3.80 | (Wang et al., 2013) |

3.2.5. Other low-temperature solid adsorbents

3.2.5.1. COF-based materials for CO₂ capture. Covalent organic frameworks (COFs), a newly emerging class of porous crystalline materials, have been regarded as a promising alternative for CO₂ capture due to their easy pore surface engineering, ordered pore distribution, structural tenability endow them with excellent CO₂ selectivity, good stability, and low energy requirement for regeneration even under moist conditions (Cote et al., 2005; El-Kaderi et al., 2007; Tilford et al., 2006). COFs are constructed by strong organic covalent bonds in a periodic arrangement entirely from light elements such as C–C, C–N, C–O, B–O, C=N, and C–Si (Biswal et al., 2013; Wan et al., 2008). Since the first pioneering work of CO₂ adsorption of COFs in 2009, great efforts have been devoted to improving the CO₂ capture performance of COFs, including Boron-based COFs, Triazine-Based COFs, and Imine-Based COFs (Aksu et al., 2022; Van Der Jagt et al., 2021; Zeng et al., 2016).

Boron-based COFs. According to the structural dimensionality and corresponding pore size, the boron-based COFs can be classified into three groups: Group 1 consists of 2D structures with 1D small pores (9 Å for each of COF-1 and COF-6), group 2 includes 2D structures with large 1D pores (27, 16, and 32 Å for COF-5, COF-8, and COF-10, respectively), and group 3 is comprised of 3D structures with 3D medium-sized pores (12 Å for each of COF-102 and COF-103) (Fig. 3.35) (Furukawa and Yaghi, 2009; Modak and Jana, 2019). As previously reported, Ar adsorption isotherm of COFs follows the sequence of BET surface area, COF-102 (3620–3530 m² g⁻¹) > COF-10 (1760 m² g⁻¹) > COF-5 (1670 m² g⁻¹) > COF-8 (1350 m² g⁻¹) > COF-1 and COF-6 (750 m² g⁻¹). However, CO₂ uptake capacity at 273 K and 1 bar decreased in the order of COF-6 > COF-1 > COF-103 > COF-102 > COF-8 > COF-5 > COF-10, that is, group 1 > group 3 > group 2 COFs. COF-6 with a 9 Å pore diameter can adsorb CO₂ as high as 85 cm³ g⁻¹ at 273 K and 1 bar, outperforming the other six COFs despite its lowest BET surface area of (750 m² g⁻¹), indicating that the low-pressure CO₂ uptake mainly depends on the pore width of COFs rather than the BET surface area and pore volume. The adsorbed amount of CO₂ at 298 K and 55 bar follows the order of COF-102 (611 cm³ g⁻¹) > COF-103 (606 cm³ g⁻¹) > COF-10 (514 cm³ g⁻¹) > COF-5 (443 cm³ g⁻¹) > COF-8 (321 cm³ g⁻¹) > COF-6 (158 cm³ g⁻¹) > COF-1 (117 cm³ g⁻¹), that is group 3 > group 2 > group 1 COFs, revealing that the high-pressure CO₂ uptake capacities are dominantly determined by pore volumes and BET surface area of COFs (Olajire, 2017).

Triazine-based COFs. Compared to boron-based COFs, triazine-based COFs exhibit excellent thermal and chemical stability, high CO₂ capacity, and selectivity even in water vapour, making them ideal candidates for CO₂ capture (Bhunja et al., 2013; Katekomol et al., 2013). The first triazine-based COF (CTF-1), possessing a hexagonal structure with 1D pore channels and a BET surface area of 1000 m² g⁻¹, was synthesized by Thomas and co-workers via the ionothermal synthesis method (Kuhn et al., 2008). They constructed CTF-1 by cyclotrimerization of 1,4-dicyanobenzene in the presence of ZnCl₂ at 400 °C. As previously reported, perfluorinated alkanes not only exhibit more hydrophobic and lipophobic characteristics than their corresponding hydrocarbons but also show an extraordinary affinity to CO₂ molecules. Han et al. designed and synthesized a perfluorinated triazine-based COF (FCFT-1) for selective CO₂ capture (Zhao et al., 2013). It was found that the CO₂ capture capacity of FCTF-1 was as high as 1.76 mmol g⁻¹ at 273 K and 0.1 bar due to the enhanced CO₂ electrostatic interaction caused by the

high electronegativity of F. In addition, FCTF-1 exhibited an exceptional CO₂–N₂ selectivity of 77 under kinetic flow conditions in mixed-gas breakthrough experiments because the incorporation of F groups produced a significant amount of ultra-micropores (<0.5 nm). Moreover, FCTF-1 proved to be tolerant to water and its CO₂ capture performance remained excellent when there was moisture in the gas mixture, due to the hydrophobic nature of the C–F bonds. Because only a few triazine-based COFs exhibit crystallinity to some extent and their performance greatly depends on the synthetic conditions, the abovementioned drawbacks are inevitable issues during their further development (Ren et al., 2012).

Imine-based COFs. Another class of COFs is the imine-based COFs, first developed by Yaghi and co-workers using the strategy of dynamic covalent chemistry (Uribe-Romo et al., 2009). Compared with the CTFs, the imine-based COFs have much better crystallinity and structural regularity, which are beneficial to tuning the order of pore size (Kandambeth et al., 2013; Kandambeth et al., 2015). Imine-based COFs are divided into two types based on the covalent formation of distinct –C=N– bonds. One is the “Schiff base” type formed by the co-condensation of aldehydes and amines, and the other is the “hydrazine” type built by the co-condensation of aldehydes and hydrazides (Uribe-Romo et al., 2011). The first application of imine-based COFs in CO₂ adsorption was reported by Banerjee et al. in 2012 (Kandambeth et al., 2012). They reported two chemically stable (acid and base) 2D COFs (TpPa-1 and TpPa-2) through reversible and irreversible routes, which were constructed from 1,3,5-triformylphloroglucinol (Tp) with p-phenylenediamine (Pa-1) and 2,5-dimethylp-phenylenediamine (Pa-2), respectively. The CO₂ uptake of TpPa-1 and TpPa-2 was measured to be 78 and 64 cm³ g⁻¹ at 273 K and 1 bar, respectively. More COFs were prepared using similar building blocks with different functional groups (Chandra et al., 2013). The order of CO₂ capacity at 273 K and 1 bar is TpPa-1 > TpPa-NO₂ (73 cm³ g⁻¹) > TpPa-2 (64 cm³ g⁻¹) > TpBD-(NO₂)₂ (52 cm³ g⁻¹) > TpBD (40 cm³ g⁻¹) > TpBDMe₂ (37 cm³ g⁻¹) > TpPa-F₄ (35 cm³ g⁻¹) > TpBD-(OMe)₂ (27 cm³ g⁻¹). Interestingly, these water and chemically stable COFs can be delaminated using the mechanical grinding route to transform into covalent organic nanosheets that were characterized via transmission electron microscopy and atomic force microscopy. The stability of COFs is a central issue before any applications, and the stability of imine-based COFs in most organic solvents and water, when compared with boron-based COFs, has motivated researchers to incorporate several polar groups in the pore walls of imine-based COFs for enhanced CO₂ capture. More importantly, the good water and chemical stabilities of some imine-based COFs also favour their regeneration without loss of their CO₂ uptake performance. All these merits of imine-based COFs coupled with high CO₂ selectivity, large CO₂ capacity, and moderate heat of adsorption will provide a powerful platform for designing functional materials for CO₂ capture.

Surface chemistry of COF based CO₂ capture

El-Mahdy et al. (2018) in 2018 conducted an experiment to synthesize and adsorb CO₂ on triphenylamine COFs (TPA-3NH₂) and (triphényltriazine COFs) (TPT-3NH₂). Various triacrylaldehydes were used in the synthesis of COFs. These varied in planarity, nitrogen concentrations, and symmetry. Through monitoring the monomer symmetry and planarity, specific crystalline COFs can be prepared targeting particular applications.

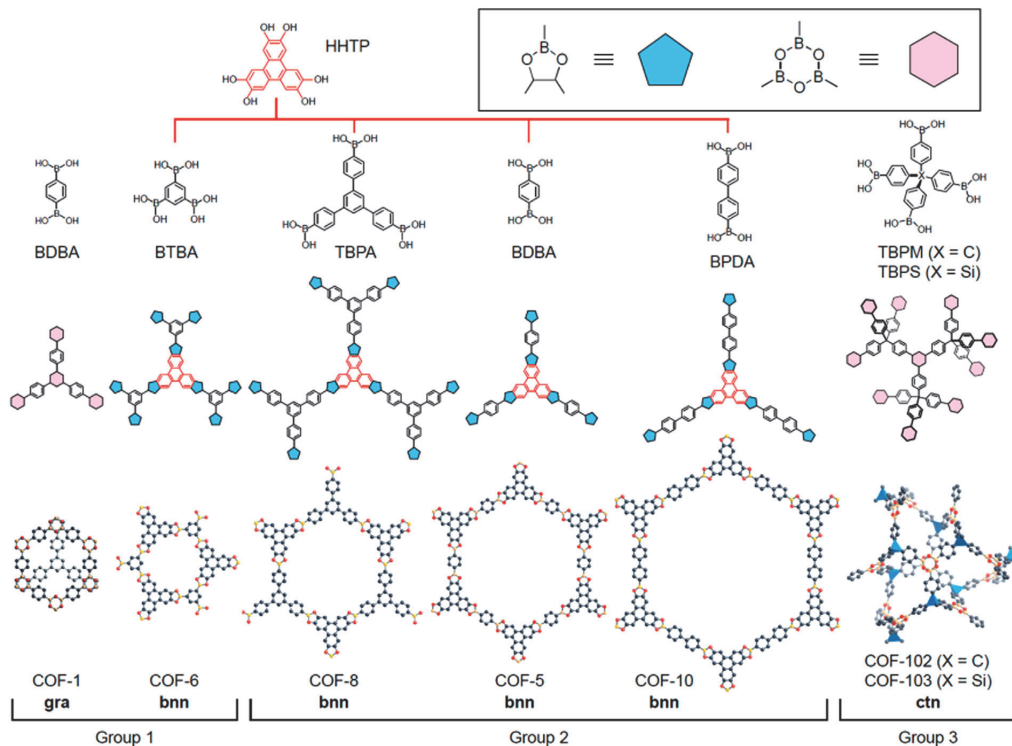


Fig. 3.35. Condensation reactions of boronic acids and HHTP are used to produce COFs (top) and resulting fragments of COFs (middle). Atomic connectivity and structures of crystalline 2D and 3D COFs (bottom). The topology and the group classification number are indicated for each COF. Inset: the C_2O_2B (blue) and the B_3O_3 (pink) rings are formed by condensation reactions (Furukawa and Yaghi, 2009). (For interpretation of the references to color in this figure legend, the reader is referred to the web version of this article.)

Symmetrical monomers were also used in many studies (Gao et al., 2018; Haase et al., 2017; Zhai et al., 2017), but none showed good gas storage properties. El-Mahdy et al. (2018) thought to control the fluctuation in the crystallinity of COFs and study its effect on CO_2 adsorption. The XRD confirmed the crystallinity of the material, which increased with increasing monomers. The surface area of TPT-COF-6 synthesized from most planar and symmetrical linkers came out to be $1535\text{ m}^2\text{ g}^{-1}$ (calculated with BET). Although, another material (TPT-COF-5) reported a surface area of $1747\text{ m}^2\text{ g}^{-1}$, the highest CO_2 uptake capacity was still shown by TPT-COF-6. The study concluded that planarity and symmetry were the two most important factors to vary the total surface area of COFs.

Very few numbers of research have been seen about synthetic routes which can affect the structural variations of COFs. Gao et al. (2018) discovered that the combination of tetraphenylethane (Ascherl et al., 2016; Pang et al., 2016) will give [4 + 4] TPE-COF-I and [2 + 4] TPE-COF-I upon heating in *o*-dichlorobenzene and *n*-butanol solvents, respectively. Keeping it as a basis, the new TPE-COF-II was prepared. It showed surprisingly high CO_2 uptake of 23.2 wt% at 1 bar and 273 K, whereas TPE-COF-I showed only 13.4 wt% CO_2 adsorption. TPE-COF-I and TPE-COF-II displayed a BET surface area of $1535\text{ m}^2\text{ g}^{-1}$ and $2168\text{ m}^2\text{ g}^{-1}$, respectively.

Effect of water on CO_2 adsorption using COF

While many COFs have shown good future for CO_2 capture, the industrial implementation of COFs is affected by their intolerance towards harsh conditions like water (Li et al., 2018; Uribe-Romo et al., 2011; Zhang et al., 2018). The crystal structure of COFs depends on

the reversible reactions in synthesis process. In the reactions, the amorphous products first dominate the structure, but slowly the formation of low energy products take place, making COF crystals as major products (Zhu and Zhang, 2017). The reactions with which may COFs are synthesized are generally reversible and thus the crystals suffer degradation in mild aqueous surroundings (Spitler et al., 2011). Due to all these complications of reversible reactions, it is emphasized to prepare MOFs from non-reversible reactions. It is a very challenging task, but effective if possible. For the first time, Kandambeth et al. (2012) prepared COF (TpPa-1 and TpPa-2) from an irreversible reaction. The developed technique was a two-step method; first is reversible Schiff base reactions, and the second is an irreversible keto-enol tautomerization. The CO_2 adsorption capacity of TpPa-1 at 273K was 153 mg g^{-1} . This capacity is in relation to COF-6 (Furukawa and Yaghi, 2009), but with high stability. To further test the material, COFs were immersed in water for 7 days and various analysis were carried. There was no change in the pXRD peaks, and no new peaks were noticed in FTIR testing. Furthermore, the TpPa-2 did not show any change in surface area, FTIR, and XRD analysis even after soaking in NaOH for 7 days. This exceptional stability is due to the irreversible keto-enol tautomerization reaction.

Abdelnaby et al. (2018) prepared amine-functionalized crosslinked porous polymer (KFUPM-1) using 1,4-benzenediamine, formaldehyde, and pyrrole with HCl as the catalyst. High concentration of primary and secondary amines in the framework offered very high selectivity for CO_2 over N_2 (i.e. 14 at 298K) with CO_2 uptake of $15.1\text{ cm}^3\text{ g}^{-1}$ in wet conditions. The material also exhibited stable activity for 45 cycles with similar selectivity. Later, Abdelnaby et al. (2019) prepared another

novel crosslinked microporous organic polymer (KFUPM-2) via Friedel-Crafts alkylation between pyrrole and phenothiazine, crosslinked by paraformaldehyde. The material processed $39.1 \text{ cm}^3 \text{ g}^{-1}$ CO_2 uptake at 273 K with CO_2/N_2 selectivity value of 51. Another polymer KFUPM-4 developed from different monomer exhibited superior CO_2 uptake in wet conditions. The presence of aniline and pyrrole monomers dispenses CO_2 -philic properties to the material. It also offers high CO_2/N_2 selectivity of 79 and CO_2/CH_4 selectivity of 16. It was also reported that the existence of water vapours in feed improves the CO_2 uptake capacity, which is due to the strong solubility of CO_2 in the presence of water (Alloush et al., 2020).

3.2.5.2. Conjugated microporous polymers (CMPs) for CO_2 capture. CMPs (Conjugated Microporous Polymers), represent another class of amorphous covalent organic polymers with a considerable conjugated skeletal structure. These polymers are constructed using π - π conjugated rigid structural units, resulting in a rigid framework that can achieve complete conjugation system through tautomerism involving single, double, and triple bonds. The covalent bonds connecting the structural elements ensure the stability of CMPs even at elevated temperatures, making them highly suitable for CO_2 adsorption applications. CMPs have attracted great attention as a versatile platform for CO_2 adsorption, primarily owing to their remarkably high specific surface area (BET), total volume (V_{total}), and exceptional thermal stability. Through manipulating the structural design and synthetic approach, CMPs are then allowed for tuning their CO_2 adsorption capacity and selectivity.

For example, Su et al. (Xu et al., 2019) synthesized two distinct porphyrin-contained CMPs, namely Porp-TPE-CMP and Porp-Py-CMP, using a FeCl_3 -catalyzed coupling reaction. The specific surface area of Porp-TPE-CMP measured at $547 \text{ m}^2 \text{ g}^{-1}$ exceeded that of Porp-Py-CMP registered at $31 \text{ m}^2 \text{ g}^{-1}$. This considerable higher BET values of Porp-TPE-CMP is indicative of the substantially higher CO_2 adsorption capacity (88.75 mg g^{-1}) when compared to Porp-Py-CMP (54.41 mg g^{-1}) under conditions of 273 K and 0.1 MPa. Furthermore, the selectivity ratios for CO_2/N_2 and CO_2/CH_4 between Porp-TPE-CMP and Porp-Py-CMP were evaluated and found to be 55.3 and 40.8, as well as 4.1 and 5.1, respectively.

CMPs are typically prepared through various reactions and by employing different monomers, leading to the fabrication of polymers with diverse CO_2 adsorption properties attributed to variations in porosity and functional groups. Hu and his group (Zhou et al., 2019) synthesized three distinct CMPs using cationic cyclization polymerization, employing monomers with multiple enediyne moieties. The specific surface area measurements for CMP1, CMP2, and CMP3 were found to be 767, 624, and $780 \text{ m}^2 \text{ g}^{-1}$, respectively. Moreover, the values for specific microporous surface area (S_{micro}) and micropore volume (V_{micro}) for CMP1 were notably higher, at $481 \text{ m}^2 \text{ g}^{-1}$ and $0.19 \text{ cm}^3 \text{ g}^{-1}$, than those of CMP2 ($302 \text{ m}^2 \text{ g}^{-1}$ and $0.12 \text{ cm}^3 \text{ g}^{-1}$) and CMP3 ($134 \text{ m}^2 \text{ g}^{-1}$ and $0.02 \text{ cm}^3 \text{ g}^{-1}$). This enhanced S_{micro} and V_{micro} of CMP1 contribute to its excellent CO_2 adsorption performance, registering at 129.60 mg g^{-1} under conditions of 273 K and 0.1 MPa. Porphyrin-based polymers are widely recognized for their structural stability and inherent porosity. When doped with metal ions, these polymers exhibit increased activity at active sites, thereby improving their performance in gas adsorption applications.

3.2.5.3. Aerogels for CO_2 capture. Aerogel have received extensive attention due to well-developed pore structure. There is a wide variety of aerogel materials and numerous synthetic procedures for obtaining aerogel materials. The most common method of synthesizing aerogel is the sol-gel followed by drying. The drying procedures determine the final state of the aerogel. An ambient drying will destroy the structure due to capillary forces. Freeze drying eliminates the capillary forces during the solvent evaporation process. However, during the freezing process, the structure may be slightly damaged. Through supercritical drying,

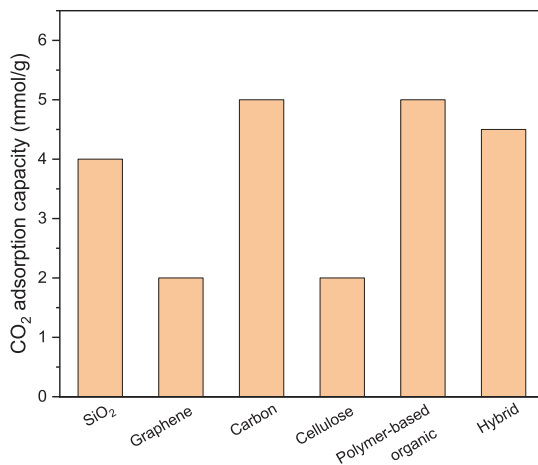


Fig. 3.36. The approximate adsorption capacity of CO_2 (Keshavarz et al., 2021; Kong et al., 2017; Lee and Park, 2020; Shao et al., 2018; Vinayakumar et al., 2022b; Wang et al., 2020; Wu et al., 2022; Yay and Gizli, 2019; Zhang et al., 2020; Zhu et al., 2020). (For interpretation of the references to color in this figure legend, the reader is referred to the web version of this article.)

the structure can be preserved completely. After drying, a great number of mesopores and macropores can be obtained, which can provide abundant active sites for gas adsorption (Vinayakumar et al., 2022a; Wu et al., 2022). Competitive adsorption of coexisting gas components often has an adverse effect on the adsorption of target gases. Therefore, most of the research work in recent years has focused on modifying aerogels to improve their adsorption capacity or selectivity for target gases (Ho and Leo, 2021; Keshavarz et al., 2021; Maleki, 2016; Vinayakumar et al., 2022a). In terms of CO_2 adsorption and capture, for SiO_2 aerogels (Cui et al., 2011; Cui et al., 2017; Lin et al., 2013; Zhou et al., 2021), SiC aerogels (Cui et al., 2017; Guo et al., 2018; Han et al., 2014), graphene aerogels (Pruna et al., 2021) and other new aerogels (Wang et al., 2019b). At present, basic active centers are mainly introduced by amino functionalization, nitrogen doping, etc. (Jeon et al., 2015; Li et al., 2020; Tian et al., 2021; Wormeyer et al., 2012; Wormeyer and Smirnova, 2013; Xu et al., 2021). Chemisorption can also improve the adsorption capacity and selectivity of CO_2 by aerogels. For aerogels, the specific surface area and micropores can be further increased by activation, which also plays a key role in CO_2 adsorption at the same time. The CO_2 adsorption capacity of a few common aerogels is shown in Fig. 3.36.

SiO_2 aerogel. As an adsorption material, SiO_2 aerogel has the advantages of high adsorption efficiency, convenient desorption, and stable performance. It is the most studied and mature aerogel material, and was first applied to the field of gas adsorption and purification. The current research work focuses on amino functionalization or hydrophobic modification of SiO_2 aerogel to further improve its adsorption performance for CO_2 . There are two main modification methods: one is grafting, and impregnation after the formation of wet gel or after supercritical drying (Fang et al., 2020; Linneen et al., 2014). The other method is to functionalize the surface of SiO_2 aerogel, which is to introduce functionalized precursors in the sol-gel reaction process, and use a mixed silicon source to endow SiO_2 aerogel with specific properties through in-situ polymerization (Liu et al., 2021; Xu et al., 2018). Amino functionalization of SiO_2 aerogels is currently the main method to improve its selectivity to CO_2 , increase the saturated adsorption capacity and accelerate the CO_2 adsorption rate. The presence of an appropriate amount of water vapour in the mixed gas can significantly improve the adsorption capacity of CO_2 by aerogels.

Carbon aerogel. Activation is a common method to control the pore structure of porous carbon materials. During the activation, the microporous structure can be introduced into the mesoporous pores of carbon aerogels, increasing the specific surface area further. Therefore, it is beneficial to the application of carbon aerogels as CO₂ adsorption materials. Similar to SiO₂ aerogels, the adsorption performance of carbon aerogels for CO₂ can also be improved by means of amino functionalization, nitrogen doping, and the introduction of active metals (Geng et al., 2020; Li et al., 2019; Marques et al., 2013; Robertson and Mokaya, 2013; Xie et al., 2017; Zhuo et al., 2016).

Graphene aerogel. Graphene sheet layers stacked on top of each other can form graphene aerogels with three-dimensional porous network structures, which have not only the characteristics of fast graphene electron transport rate, but also rich surface oxygen groups, large aerogel specific surface area, high porosity, and easy for further modification (Pruna et al., 2021; Ren et al., 2020).

Metal oxides aerogel. Metal oxide aerogel is a type of inorganic aerogel. Whether it is the preparation of one-component or multi-component metal oxide aerogels, the metal salts are first dissolved in organic solvents or water, and the reaction reagents can be added after adjusting the concentration and pH value of the solution to form a gel. Metal oxide aerogels are rich in surface active sites such as metal centers, active hydroxyl groups, etc., which have high chemical adsorption capacity and selectivity. (Li et al., 2019)

Polymer-based organic aerogels. Polymer-based organic aerogels are polymer molecules passed with glue, and the body particles are formed by combining hydrogen bonds or van der Waals forces organic compounds with porous network structures. Compared to conventional inorganic aerogels, the performance of organic aerogels depends mainly on the type of polymer. Therefore, the polymer based organic aerogels offer flexible design and performance adjustability. Assemble synth-based organic aerogels mainly include polyurethane (PU), polyurea (PUA), polyimide (PI), etc (Kong et al., 2015; Li et al., 2019).

3.2.5.4. Zeolites materials for CO₂ capture. Zeolites have been widely used as CO₂ adsorbents due to the large surface area, high stability, and tunable physicochemical properties. Zeolites are porous aluminosilicates with three-dimensional rigid frameworks consisting of corner-sharing SiO₄ and AlO₄ tetrahedra through shared oxygen atoms. The framework of zeolites contains the periodic arrangement of cages and channels with molecular dimensions (3–15 Å in diameter). According to the number of oxygen atoms forming the largest pore aperture, zeolites can be divided into small-pore zeolites (8-membered ring), medium-pore zeolites (10-membered ring), large-pore zeolites (12-membered ring) and extra-large-pore zeolites (≥14-membered ring). The frameworks of pure silica zeolite are electrically neutral. The isomorphous replacement of Si⁴⁺ by Al³⁺ in the lattice will induce negative charges on the framework, which require extra-framework cations for charge balance. The physicochemical properties of zeolites can be tuned by incorporating extra-framework cations via ion exchange or impregnation methods. Zeolites with desired properties can be achieved for target applications by tuning the topology of zeolites (Fig. 3.37), and the type and density of extra-framework cations.

Zeolites show outstanding CO₂ adsorption performance in terms of high CO₂ capacity and selectivity, and excellent regenerability, which highly rely on the properties of zeolites. Generally, materials with large surface areas show high adsorption capacities. However, the high surface area with non-specific nature benefits the adsorption of both target and unwanted adsorbates, which is not enough when the selectivity is considered. The selectivity on the other hand is governed by the distinct adsorbent/adsorbate interaction, which relates to the type of the adsorption sites (e.g., extra-framework cations, functional groups etc.). In the case of CO₂ separation, a higher affinity of zeolite towards CO₂ over other accompanying species is desired, such as N₂ and CH₄ in flue gas and biogas/natural gas, respectively. However, an overly strong gas-host interaction requires a high energy consumption during the regen-

eration process. CO₂ adsorption on various zeolites is reviewed aiming to provide references for its utilization in industrial processes.

Separating molecules with similar sizes (e.g., CO₂, 3.3 Å; N₂, 3.6 Å; CH₄, 3.8 Å) is challenging through the sieving effect due to the difficulty in precisely adjusting the pore size locating just in between the sizes of molecules. (Shang et al., 2012, 2013) Small-pore zeolites are effective and highly selective adsorbents for CO₂ capture due to the similar sizes of the window aperture (3–5 Å) and the kinetic diameters of adsorbates (CO₂, 3.3 Å; N₂, 3.6 Å; CH₄, 3.8 Å), which enables the separation through size sieving and “molecular trapdoor” mechanism. (Shang et al., 2012) In addition, the high thermal and mechanical stability make small-pore zeolites attractive in industrial processes. Shang et al. have studied the CO₂ and N₂ adsorption on alkali metal ion-exchanged chabazite (CHA) zeolites (Si/Al of 1~50). (Shang et al., 2012, 2013) They achieved ultra-high selectivity for CO₂/N₂ (325, 20 kPa, 273 K) and CO₂/CH₄ (98, 100 kPa, 233 K) by Cs⁺CHA (Si/Al = 2.2) and K⁺CHA (Si/Al = 2.2), respectively. The high selectivity was attributed to the temperature-dependent “molecular trapdoor” mechanism (Fig. 3.38), which describes the different capability of gas molecules to deviate the cation from the center of the 8-ring windows to enter the pores of zeolites. Molecules such as CO₂ with high polarizability can interact with the “door-keeping” cation (e.g., Cs⁺ and K⁺) strongly and need to pay lower energy toll than the “weak molecules” (e.g., CH₄ and N₂). In terms of the zeolites, the key factors for realizing this mechanism are the cations with proper size, and the proper Al distribution on the pore aperture providing enough electronegativity for cations to coordinate to large extent for the effective blockage. The kinetics on the other hand is an important parameter to evaluate the CO₂ capture performance, especially during the industrial processes, which is determined by the energy barrier for cation deviation. The cation with smaller size or a weaker cation-window interaction strength requires lower energy for deviation, which can help in improving the kinetics. Further tunings among the zeolites topology, the Si/Al ratio and the type of cations are required for developing CO₂ adsorbents with both high selectivity and promising kinetics.

Typically, high selectivity and high regenerability cannot be attained simultaneously. Highly selective materials tend to consume lots of energy for the completed regeneration, and conventional physisorption-driven adsorbents with easy regeneration always feature low selectivity. To address this contradiction, Sun et al. prepared transition metal (Co, Ni, Zn, Fe, Cu, Ag, La, and Ce) ion-exchanged SSZ-13 zeolites (CHA type, Si/Al = 12) for flue gas (CO₂/N₂:15/85) separation. (Sun et al., 2019) The selectivity of Co²⁺SSZ-13 and Ni²⁺SSZ-13 reached above 50 at 273 K, which was higher than the alkali metal ion-exchanged SSZ-13 zeolites (23–36). (Bower et al., 2018) The improvement was attributed to the Pi-complexation interaction (Fig. 3.39) formed between CO₂ and the transition metal ions, which is with moderate interaction strength between those of physisorption and chemisorption. The isosteric heat of adsorption of CO₂ is 30~60 kJ/mol, much lower than that of chemisorption (>80 kJ/mol), which enables regeneration under mild conditions.

Considering the higher polarizability and quadrupole moment of CO₂ than the unwanted gases (N₂ or CH₄) in the mixture, cations with strong polarizing power are highly desired, which can improve the affinity of adsorbents towards CO₂. Researchers have studied the CO₂ adsorption behavior on alkali metal (Li, Na, K, Rb, Cs) ion-exchanged FAU (X and Y) and MFI (ZSM-5) zeolites. (Dunne et al., 1996; Kato et al., 2000; Walton et al., 2006; Wirawan and Creaser, 2006a, b; Yamazaki et al., 1993) Generally, the CO₂ capacity is reduced in the order of LiZ > NaZ > KZ > RbZ > CsZ (Z representing zeolite), which is coincident with the order of increasing ionic radius. For the ions with the same valance state, those with smaller ionic radius feature higher polarizing power: Cs⁺ (3.3 Å) < Rb⁺ (2.9 Å) < K⁺ (2.7 Å) < Na⁺ (1.9 Å) < Li⁺ (1.4 Å). The result indicates the interaction of CO₂ with alkali metal is electrostatic interaction dominated. The consistent results were also demonstrated on alkali metal ion-exchanged X zeolite through density functional theory calculations. (Plant et al., 2006) The CO₂ adsorption

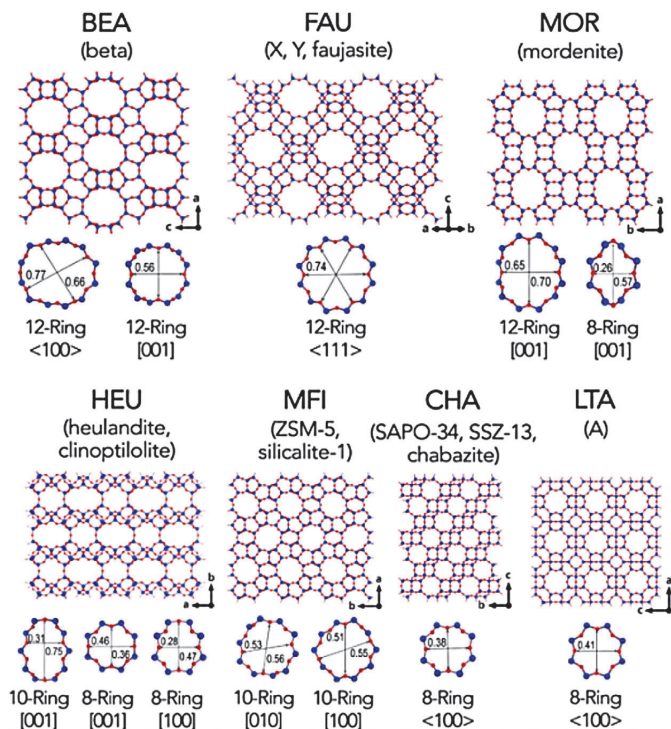


Fig. 3.37. Selected widely applied zeolite frameworks. The three-letter code relates to the type of framework, assigned by the International Zeolite Association (IZA) (in bold). The size of the pore window and the ball-stick atomic model are given. Blue and red spheres represent T atoms and oxygen atoms, respectively (Li et al., 2017). (For interpretation of the references to color in this figure legend, the reader is referred to the web version of this article.)

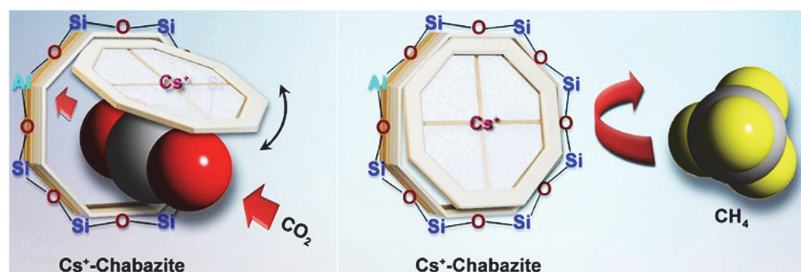


Fig. 3.38. Illustration of the “molecular trap-door” mechanism in discriminative gas separation: Cs^+ locating in the middle of SMR acts as a door keeping cation, which can only be deviated by strong gas molecules (e.g., CO_2), but not by weak molecules (e.g., CH_4) at certain temperature (Shang et al., 2012). (For interpretation of the references to color in this figure legend, the reader is referred to the web version of this article.)

enthalpies at low coverages vary from 33.20 to 17.17 kJ/mol, decreasing with the increase of the ionic radius. The smaller cations are with higher affinity towards CO_2 , which was also evidenced by the shorter distance between the oxygen of carbon dioxide and the cations with smaller sizes.

The presence of moisture is unavoidable in the gas separation process, which is another challenge when adopting zeolites as adsorbents due to the extremely hydrophilic nature. Featuring high polarizability, H_2O is indeed a main inhibitor for CO_2 adsorption even when the water is at a low concentration, by forming a favourable interaction with the adsorption sites, especially the extra-framework cations in the cationic forms of zeolites, which can dramatically reduce the CO_2 capacity. (Brandani and Ruthven, 2004) Grafting amine functional groups in zeolites was found as a powerful approach for CO_2 capture under wet conditions. (Kim et al., 2016) Kim et al. prepared ethylenediamine (ED)-modified Y zeolite prepared via the gas-phase titration method and tested the CO_2 capture performance in wet flue gas (Kim et al., 2016). CO_2 was effectively captured through interacting with the amine groups,

and H_2O was co-adsorbed in the micropores of zeolites without forming urea. The CO_2 working capacity was maintained at a stable level (> 1.1 mmol/g) during 20 temperature swing adsorption (TSA) cycles. The ED-modified Y zeolite features a high H_2O tolerance and remarkable resistance against the urea formation simultaneously.

In the industrial separation process, the energy lost due to the undesirable pressure drop in the fixed bed needs additional blower power to maintain the constant flow. Fabricating zeolite powder into monoliths with desired channel sizes, wall thicknesses, and high mechanical properties by 3D printing is a promising strategy to tackle this issue. Wang et al. prepared mechanically robust binder-free 3D printing zeolite monoliths (ZM-BF) as a superior configuration for CO_2 capture (Wang et al., 2019). Halloysite nanotubes (HNTs) with high strength were used as printing ink additives, which benefited the formation of robust interfacial “HNTs-bridges” for individual zeolite crystals. ZM-BF showed a promising equilibrium CO_2 capacity of 5.58 mmol/g (298 K, 1 bar), which is higher than other reported 3D-printed CO_2 adsorbents. Compared with the commercial benchmark NaX zeolites, ZM-BF showed

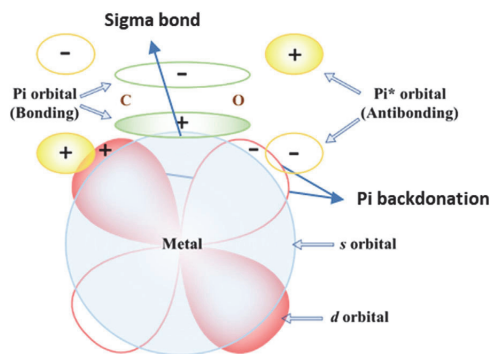


Fig. 3.39. Pi-complexation interaction formed between Pi-structured molecules and transition metal ion (Sun et al., 2019). (For interpretation of the references to color in this figure legend, the reader is referred to the web version of this article.)

superiority in dynamic adsorption breakthrough tests in terms of dynamic, CO₂ capture capacity and selectivity. In addition, the binder-free ZM-BF shows outstanding mechanical properties (with a robust compressive strength of up to 5.24 MPa), higher than most of the reported monoliths with binders. The “3D printing and zeolite soldering” strategy developed in this study afforded a promising approach for precisely fabricating monoliths with desirable configurations, which may provide references for other related applications, such as catalysis and sensing.

The zeolite topology and the type/density of adsorption sites in zeolites are the essential factors for CO₂ adsorption on zeolite materials. The CO₂ capacity can be affected by the type/density of adsorption sites and the surface area of zeolites, as well as the presence of high-affinity components (e.g., H₂O) in the gas mixture. The high selectivity can be attained by introducing the adsorption sites with high CO₂ affinity, as well as through the “molecular trapdoor” mechanism. However, it still requires efforts to achieve easy regeneration and fast kinetics simultaneously. Thus, tuning the physicochemical properties of zeolites together with optimizing the experimental conditions are required for approaching effective CO₂ capture in industries.

3.3. Photo-responsive adsorbents for low-energy CO₂ capture and release

For post combustion CO₂ capture techniques to achieve widespread feasibility, energy cost must be substantially reduced. Traditional CO₂ liberation technologies highly relied on pressure (pressure swing adsorption, PSA), temperature (temperature swing adsorption, TSA), vacuum (vacuum swing adsorption, VSA), or any combination of them (Li and Hill, 2017). Both VSA and PSA are in demand of large amounts of electrical energy to alter the pressure for driving the CO₂ to be liberated from adsorbents (Mason et al., 2011). Although waste heat can be exploited in the TSA method, some adsorbents are so thermally insulating that these methods cannot be applied on a large scale unless the heating transformation distance can be designed into the gas adsorbent contactor (Labreche et al., 2015). Apart from that, the long cycle time and the demand for high vapour to heat the column also resist the development of the TSA method (Qiao et al., 2022). Considering that the traditional triggers for the liberation of adsorbed CO₂, such as high temperature and vacuum, are so energy consuming (Lyndon et al., 2013), it's necessary to establish new stimuli that are more naturally abundant and renewable resources such as solar light. In this case, the adsorbents with maximum CO₂ uptake capacity and further reduced energy will obtain a more prospective and wide application (Huang et al., 2022).

Light, particularly concentrated solar light, as a naturally abundant, renewable resource, is an extremely appealing trigger for regenerating the adsorbents. Compared to traditional technologies, light can be re-

garded as the most energy-efficient method (Li and Hill, 2017). When the adsorbents show strong light absorption, combined with the large amounts of CO₂ desorption, much energy cost could be saved (Jiang et al., 2019). Therefore, through the different directions of adsorbents functionalization, light triggered different applications can be developed.

3.3.1. Photo responsive porous polymer adsorbents for CO₂ switching capture

Recently, porous materials have been reported as attractive light responsive candidates for low energy CO₂ capture (Heinke and Wöll, 2019). Because of their large surface area, structural variety and easy functionalization ability, high CO₂ adsorption performance and the potential for integration with light responsive photochromic units in the pore channels can be realized. Such light triggered CO₂ release performance of porous materials can be achieved by the functionalization of photochromic units into the structural molecules of porous materials (Huang and Wu, 2022). Such photochromic organic molecules can undergo a reversible photoisomerization process, and then change the electronic state and molecular structures under light irradiation. Up until now, azobenzene (AB), diarylethene (DET) and spiropyran (SP) are the most reported photochromic units that were successfully reported to be incorporated into porous materials (Fig. 3.40) (Jones et al., 2016). Among them, azobenzene can transition between the trans/cis state through different wavelength number of light irradiation, and DET can undergo a structural transition through ring-open/close reaction while SP molecules can switch between the zwitterionic merocyanine counterpart upon light exposure (Bigdeli et al., 2020). These photo switchable compounds can be either integrated into the backbones or side chain of porous materials or directly loaded as the guest to pore channels (Haldar et al., 2019). Therefore, the light triggered photoisomerization transition of these materials can finally contribute to a remote light controlled CO₂ capture and release recycle.

3.3.1.1. Photo responsive MOFs for CO₂ switching. Photo switching MOFs are the most widely reported porous materials for low energy CO₂ capture owing to their high uptake capacity, crystallinity and adjustable structures (Mukhopadhyay et al., 2014). For photoswitching MOFs, azobenzene functionalized photo switching MOFs were widely reported because of the easy functionalization method. For example, azobenzene based PCN-123 can switch the conformation upon UV light irradiation and lateral thermal heating (Park et al., 2012). Such material was fabricated by the introduction of azobenzene pendants to the organic linkage. After UV light irradiation, a release of 54%, from 22.9 cm³/g to 10.5 cm³/g, in CO₂ uptake capacity could be realized. In addition, the CO₂ uptake ability could also be recovered by thermal heating. Apart from functionalization as linkage pendants, azobenzene groups could also be incorporated as backbones of MOF materials. Matthew et al. Lyndon et al. (2013) reported an azobenzene based Zn (AzDC) (4,4'-BPE)_{0.5} by directly incorporating the azobenzene units into the backbone of the framework. The switching of CO₂ uptake capacity was found to be tremendously strong, with up to 64% changes under dynamic light switch on/off conditions. In addition, azobenzene molecules were also reported to be directly loaded as a guest in MOF materials. Matthew et al. Lyndon et al. (2015b) also reported Mg-MOF-74 materials. Through methyl red loading, such MOF exhibited 84% tailored CO₂ uptake changes after visible light irradiation.

DET and SP based MOFs are also other promising alternatives for low energy CO₂ capture. For example, a photochromic diarylethene linkage was utilized to fabricate a photo responsive DMOF material (Luo et al., 2014). The local photoisomerization reactions induced by UV and lateral visible light irradiation in DMOF frameworks contributed to a 76% desorption of CO₂ capacity. Apart from that, Deanna et al. (Healey et al., 2016) also reported a photoactive spiropyran based MOF-808-SP adsorbent through a post-synthetic modification strategy. Such MOF material suggested both photo responsive BET surface area and light trig-

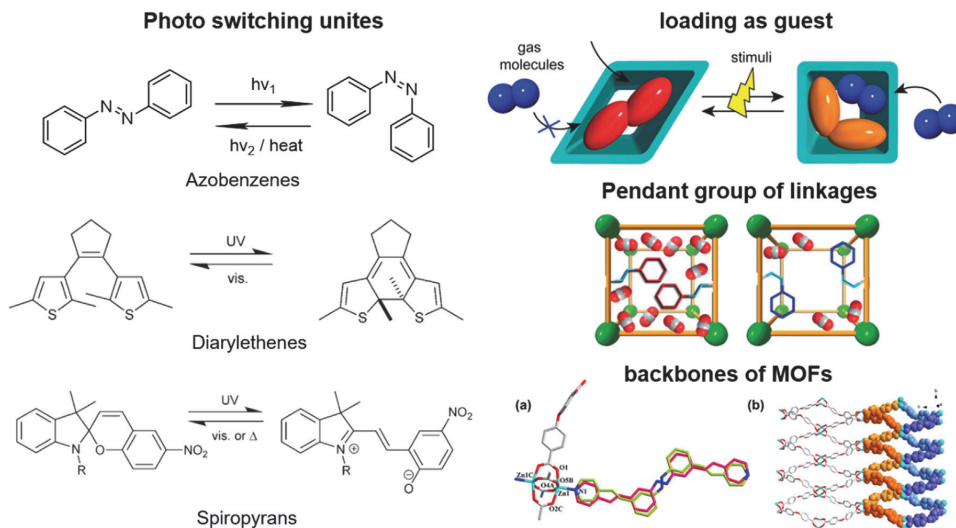


Fig. 3.40. A schematic representation of different strategy to integrate photo switchable components into a metal-organic framework (MOF) (Jones et al., 2016). (For interpretation of the references to color in this figure legend, the reader is referred to the web version of this article.)

gered tailorable CO_2 capture performance, which provides a promising, remote light controlled, low energy cost gas separation and storage method.

3.3.1.2. Other photo responsive porous polymer adsorbents for CO_2 switching. Considering the structural tunability, some other porous materials are also promising candidates for fabricating the light responsive adsorbents for tailorable carbon capture. For instance, porous organic polymers are one of the most developed adsorbents for carbon capture, which possess many similar inherent properties as MOFs, such as high porosity and gas uptake capacity. Bradley et al. (Lyndon et al., 2015a) fabricated a diarylethene based porous aromatic framework-1 materials. Such DArE@PAF-1 material exhibited an up to 26 wt.% desorption capacity of CO_2 at the 50 wt.% DArE guest molecules loading. The photo responsive ability could also be modulated by different guest loading content, which provided greatly controlling for carbon capture and release for industrial applications.

Zhang et al. Zhu and Zhang (2014) also reported the first example of azobenzene based porous organic polymer. Under UV light irradiation and, consequently thermal heating, both the pore size distribution and the CO_2 uptake ability could be reversibly changed. In contrast to most reported azobenzene based MOFs, the trans to cis isomerization in this material suggested increasing adsorption of CO_2 because of the enhanced dipole-quadrupole interactions between CO_2 molecules and cis isomer pendants. In detail, the UCBA-1 showed a dramatic increase in CO_2 adsorption capacity, up to 29%, which could complement the most reported photo responsive MOF materials so far.

3.3.1.3. Photo responsive chemicals for CO_2 switching. Fabian et al. Wilm et al. (2022) first fabricated photo responsive superbases containing the photochromic DET units. The reported N-heterocyclic imines can undergo a reversible electronic isomerization under UV light exposure and lateral visible light irradiation, with multiple cycles. The transition between ring opening and ring closing states was accompanied by a remarkable pK_a shift (up to 8.7 units). The ring closing isomers of these imines are effectively basic to act as CO_2 capture sites via the production of zwitterionic bases, which enable the light triggered CO_2 capture and release cycles. Such light stimulated basicity alterations provided guid-

ance for developing new photo switching transformations in a variety of fields of research.

3.2.2. Photothermal conversion applied in low light-triggered temperature of CO_2 adsorbents regeneration

Endowing the adsorbents with photothermal conversion capability is also another alternative way to utilize the sunlight for CO_2 adsorbent regeneration. Through combining photothermal conversion ability, thermos sensitivity with the high density of amino sites with CO_2 affinity, an energy saved light triggered high capacity of CO_2 capture and release process can be achieved. He et al. Lu et al. (2022) synthesized solar energy triggered cellulose nanofiber based thermos responsive fiber adsorbents. The contained poly (N-isopropylacrylamide), graphene oxide and polyethyleneimine served as thermos responsive switchers, photothermal conversion switchers and CO_2 uptake sites. Therefore, the prepared CNF-TBFA fiber adsorbents exhibited a high CO_2 uptake capacity of up to 6.52 mmol/g, and low regeneration temperature (60 °C) at the same time. These provide a great promising strategy for energy saved CO_2 adsorbents regeneration method.

Since noble metal crystals such as Ag and Au can effectively absorb sunlight photons and convert them to thermal energy, Paolo et al. (Li, Haiqing et al., 2016) utilized Ag nanocrystals as “nanoheaters” to form silver incorporated Ag/Uio-66 composites. Considering the low-cost and high CO_2 adsorption performance of Uio-66 MOF, such composites are an ideal adsorbent for remote light triggered CO_2 low energy CO_2 capture and release. Under visible light irradiation, 90.5% captured CO_2 in Ag/Uio-66 composites can be released out, which demonstrates a promising energy saved method for remotely regenerating the MOF adsorbents under the natural abundant light resources.

3.3. Medium temperature solid sorbents

3.3.1. MgO-based materials for CO_2 capture

Depending on the origin of the CO_2 -containing gas stream, e.g. a combustion process, it may be more efficient thermodynamically to operate the CO_2 process at elevated temperature, instead of cooling the gas stream to near-ambient temperatures prior to CO_2 removal. Sections 3.3 – 3.4 review recent developments of CO_2 capture processes with

Table 3.18
Overview of properties of binary alkali metal oxide/carbonate pairs for CO₂ capture applications.

| Alkali metal oxide /carbonate pair (MeO/MeCO ₃) | Reaction enthalpy in kJ/mol _{MeO} (at 298 K) | Melting temperature in °C of MeO/MeCO ₃ | CO ₂ uptake capacity in g _{CO2} /g _{MeO} (mmol _{CO2} /g _{MeO}) | Equilibrium temperature in °C for P _{CO2} = 1 bar * | Potential applications |
|---|---|--|--|--|--|
| MgO/MgCO ₃ | ±101 | 2825/990 | 1.094 (24.86) | 395 | Pre-combustion CO ₂ capture, Sorption enhanced conversion reactions |
| CaO/CaCO ₃ | ±178 | 2900/1330 | 0.786 (17.86) | 885 | Pre-combustion CO ₂ capture, Post-combustion CO ₂ capture, Sorption enhanced conversion reactions, Thermochemical energy storage |
| SrO/SrCO ₃ | ±241 | 2530/1495 | 0.426 (9.68) | 1225 | Thermochemical energy storage |
| BaO/BaCO ₃ | ±272 | 1973/1555 | 0.288 (6.54) | 1560 | Thermochemical energy storage |

* Below the equilibrium temperature CO₂ sorption and the formation of MeCO₃ are favored thermodynamically, whereas above the equilibrium temperature CO₂ release and the formation of MeO are favored for a given partial pressure of CO₂, P_{CO2}, in the gas environment.

solid sorbents at medium (>250 °C) and high (>500 °C) temperatures, respectively. To this end, mostly alkali or alkaline earth metal oxides have been used as sorbents, often mixed with other metal oxides that themselves are not active for CO₂ sorption. Such “inactive” metal oxides function as support materials, or structural stabilizers, for binary oxides to mitigate the cyclic decay in CO₂ sorption activity that all alkali or alkaline earth metal oxides have in common due to the rather low melting temperatures of the carbonates formed (Dunstan et al., 2021); they also can play an important role in the carbonation mechanism of ternary oxide sorbents. The formation of carbonate phases, rather than adsorbed carbonate species upon exposure to CO₂, is one of the most significant differences of medium- to high temperature solids sorbents when compared to low temperature solid sorbents, and influences the overall process design appreciably. Table 3.18 provides an overview of binary alkali metal oxide/carbonate pairs that have been investigated frequently for CO₂ capture.

3.3.1.1. Introduction of MgO-based sorbents. Thermodynamically, MgO-based sorbents are suitable materials for CO₂ capture (MgO + CO₂ → MgCO₃, ΔH_{298K} = -100.9 kJ·mol⁻¹) at intermediate temperatures, with CO₂ sorption being feasible up to ~400 °C when the partial pressure of CO₂ is 1 bar. MgO-based materials have a lower energy penalty associated with the decomposition of the carbonate phase (i.e. the regeneration of the metal oxide phase) than other alkali metal oxide/carbonate pairs (e.g. CaO/CaCO₃, Table 3.18) due to their lower reaction enthalpy and the lower regeneration temperatures (<500 °C). Further, they possess a high theoretical CO₂ sorption capacity (1.09 g_{CO2}/g_{MgO} – the highest among the alkali earth metals) (Chi et al., 2014). Mg-containing minerals are abundant (the earth crust contains ca. 2 mol. % of Mg) (Goff and Lackner, 1998), environmentally benign and are less extensively used in other industries, e.g. building and construction, than limestone, such that there is less competition for raw materials with these industries compared to CaO/CaCO₃.

3.3.1.2. CO₂ capture capacity and kinetics of MgO-based sorbents. Despite the promising theoretical characteristics, there has been only little interest in using MgO-based sorbents for CO₂ capture applications due to their slow CO₂ sorption (i.e. carbonation) kinetics, resulting in low actual CO₂ uptakes (typically less than 0.02 g_{CO2}/g_{MgO} when using commercial MgO). Two reasons for the poor carbonation performance are (i) the formation of a CO₂-impermeable mono-dentate surface carbonate layer (Harada and Hatton, 2015; Harada et al., 2015), and (ii) the high lattice enthalpy of crystalline MgO (Glasser and Jenkins, 2000; Zhang et al., 2014). Several ways have been suggested to improve the carbonation performance of MgO, including (i) the synthesis of high surface area MgO (in particular for low temperature CO₂ adsorption) (Bhagiyalakshmi et al., 2010; Ruminski et al., 2011), (ii) the synthesis of MgO supported by e.g. ZrO₂, TiO₂, Al₂O₃ or C to improve also its

structural stability (Han et al., 2014; Hiremath et al., 2019; Jeon et al., 2012; Li et al., 2017; Liu et al., 2008; Liu et al., 2013), or (iii) the promotion of MgO with molten alkali metal salts (AMS, predominantly nitrates) (Dunstan et al., 2021; Hu et al., 2019). The first two approaches have led only to limited improvement of the CO₂ uptake, typically up to 0.1–0.3 g_{CO2}/g_{MgO} both at low and medium temperatures (Hu et al., 2019). The maximum CO₂ uptake of these sorbents scales with their surface area and is reached within several minutes of exposure to CO₂ when the surface is saturated with carbonates. No crystalline MgCO₃ is formed upon exposure of unpromoted MgO to CO₂ (Wang et al., 2014). Modification of MgO with molten AMS, however, enables the rapid formation of crystalline MgCO₃ and leads to a significant improvement in the carbonation performance. With AMS promotion, the conversion of MgO into MgCO₃ proceeds through a nucleation and growth mechanism (Bork et al., 2021), with the type of the AMS influencing the number of nucleation sites (Jo et al., 2017) and the solubility of CO₂ and MgO in the salt (Dal Pozzo et al., 2019).

3.3.1.3. Chemical composition of MgO-based sorbents. The discovery that the addition of AMS to MgO enhances its CO₂ sorption rate (Zhang et al., 2013) appreciably has led to the research community focusing on two broad aspects: The optimization of the sorbent's CO₂ capture performance (largely by trial and error) (Harada and Hatton, 2015; Harada et al., 2015; Hu et al., 2019), and the understanding of the promotion mechanism by the AMS (Bork et al., 2021; Gao et al., 2021; Lin et al., 2021; Harada et al., 2015; Jo et al., 2017; Landuyt et al., 2022; Zhang et al., 2014).

The former includes the optimization of the carbonation conditions (Harada and Hatton, 2015), the amount of the AMS promoter (Dal Pozzo et al., 2019; Harada and Hatton, 2015; Harada et al., 2015), the selection of various synthesis routes for MgO production (Zhao et al., 2018) and, most predominantly, the variation and optimization of the promoter's composition (Dal Pozzo et al., 2019; Huang et al., 2017; Qiao et al., 2017). The promoters investigated range from the single nitrates (LiNO₃, NaNO₃ or KNO₃) to their binary and ternary mixtures with lower melting points. Furthermore, the addition of alkali nitrites, such as NaNO₂, was shown to improve the carbonation performance of sorbents. Some reports, however, have shown that NaNO₂ itself is not stable and transforms into NaNO₃ and Na₂CO₃ upon cyclic operation (Gao et al., 2021; Gao, Wanlin et al., 2021; Gao et al., 2018).

The beneficial effect of the addition of carbonates (e.g. Na₂CO₃ or CaCO₃) on the carbonation performance of alkali nitrate-promoted MgO has been demonstrated relatively early on (Zhang et al., 2015). Furthermore, it was shown that the presence of residual amounts of MgCO₃ (obtained by partial regeneration of the sorbent) also has led to an improved carbonation performance in the following reaction cycle (Prashar et al., 2016). Some carbonate additives readily form double carbonates with magnesium, e.g. Na₂Mg(CO₃)₂, K₂Mg(CO₃)₂

(Wang et al., 2017) and CaMg (CO₃)₂ (Cui et al., 2020, 2018; Dong et al., 2022; Hu et al., 2019; Papalas et al., 2021), whereas others do not, e.g. SrCO₃ (Jo et al., 2017). It was suggested that the addition of carbonates enhances the CO₂ sorption performance of alkali nitrate-promoted MgO further by (i) acting as stabilizers (or spacers), preventing the sintering of MgO (Cui et al., 2020), (ii) being dissolved in the molten alkali nitrate promoter increasing the concentration of carbonate ions (Wang et al., 2017) that act as “CO₂ carrier” (Vu et al., 2016), or (iii) acting as nucleation seeds for the MgCO₃ nucleation (Jo et al., 2017).

3.3.1.4. Regeneration and cyclic stability of MgO-based sorbents. The major factors governing the long-term stability of other solid sorbents (e.g. CaO) and their CO₂ uptake rate are the available surface area, the sorbent's porosity and the average crystallite size (Alvarez and Abanades, 2005; Sun et al., 2007). The formation of MgCO₃ in AMS-promoted MgO proceeds via a nucleation and growth mechanism (Bork et al., 2021; Harada and Hatton, 2015; Jo et al., 2017); therefore, the stability of the sorbent is influenced by a larger number of parameters, including the properties of MgO, of the promoters and the interaction between them. Importantly, after promotion with AMS, the available surface area of MgO has a much lesser influence on the overall CO₂ uptake capacity than without AMS (Dal Pozzo et al., 2019; Rekhina et al., 2020; Zhao et al., 2018). Still, other surface properties of MgO (e.g. surface defects and secondary phases acting as nucleation points) area play an important role in the cyclic stability of the sorbent since MgCO₃ is formed via a nucleation mechanism. An in-depth understanding of how these surface parameters evolve upon cycling between carbonation and calcination, and how they correlate with the carbonation performance is yet to be obtained. The cyclic evolution of AMS is another important and, thus far, largely under-investigated factor influencing the cyclic performance of sorbent. It has been proposed that the segregation of the molten salt from the MgO surface can lead to a decrease in the cyclic CO₂ uptake performance of sorbent (Dal Pozzo et al., 2019; Jo et al., 2017). Yet, these conclusions were drawn based on ex-situ contact angle measurements between the salt and the MgO surface, and do not represent the distribution of the molten promoter in the sorbent under operation conditions. Furthermore, the thermal stability of the molten promoter and its effect on the overall performance must be considered in greater detail (Chen et al., 2021; Gao et al., 2021), since the thermal decomposition temperatures of many nitrates, e.g. LiNO₃ or NaNO₃, are below or equal to the typical sorbent regeneration temperature of 450 °C (Hoshino et al., 1981; Qiao et al., 2017).

3.3.1.5. Effect of the gas composition. Flue gas contains, besides CO₂, a variety of compounds in different concentrations depending on the preceding process, and they all can potentially affect the CO₂ sorption performance of alkali metal oxide-based sorbents (Aaron and Tsouris, 2005). The presence of water vapour in the CO₂-containing gas stream was observed to improve the carbonation performance of both pristine (Fagerlund et al., 2012) and promoted MgO-based sorbents (Jin et al., 2017; Vu et al., 2016; Yang, Xinfang et al., 2016; Zarghami et al., 2015). It was suggested that the MgO is hydrated partially, forming reaction intermediates (e.g. Mg (OH)₂) that have an intrinsically higher reactivity with CO₂, and also that the presence of steam alters the morphology of the sorbent such that the surface area is increased (Béarat et al., 2002; Zarghami et al., 2015). Furthermore, it has been shown that the addition of liquid water to a used MgO-NaNO₃ sorbent, followed by calcination, is effective in regenerating its activity, because the water helps to distribute the NaNO₃ promoter on the surface of MgO and to decrease the average crystallite size of MgO (Dal Pozzo et al., 2019).

MgO can theoretically react with SO₂ and O₂ to form MgSO₄, which is thermodynamically stable at typical regeneration temperatures of sorbents (< 600 °C) (Scheidema and Taskinen, 2011). The accumulation of MgSO₄ in the sorbent with time would lead to a loss of MgO for CO₂ capture, and hence to a gradual reduction of the CO₂ uptake capacity. However, the formation of MgSO₄ does not occur on pristine

MgO at a fast rate at typical carbonation temperatures such that the presence of SO₂ may practically not impair the CO₂ sorption performance of MgO (Bakshi Ani et al., 2021). Thus far, it remains unclear whether molten salts promote the formation of MgSO₄ at lower temperatures, similar to their promoting effect on the formation of MgCO₃.

3.3.1.6. CO₂ capture applications. MgO-based sorbents, even when promoted with AMS, require high CO₂ partial pressures (> 1 bar) for fast CO₂ sorption rates and high theoretical CO₂ capture efficiencies (i.e. the thermodynamic limit of the fraction of CO₂ that can be removed from a gas stream) (Donat and Müller, 2022). Therefore, they are much more suitable for pre-combustion CO₂ capture than post-combustion CO₂ capture in which CO₂ partial pressures are rather low (usually between 3 and 10 vol.% in a flue gas stream). Experimental studies using MgO-based sorbents in packed bed reactors have demonstrated the efficient removal of CO₂ from high-pressure coal gas (Abbasi et al., 2014; Zarghami et al., 2015) or water-gas shift processes (Hu et al., 2019; Sikarwar et al., 2022) (sorption enhanced water-gas shift reaction, SEWGS).

3.3.2. Hydrotalcites for CO₂ adsorption

Hydrotalcite (HTL) compounds have attracted much attention in the context of CO₂ capture due to their potential application for the CO₂ capture from flue gas (Ding and Alpay, 2001; Ram Reddy et al., 2006) and in particular sorption enhanced reactions (SER) for H₂ production (Bassani et al., 2019; Fang et al., 2019; Gil et al., 2018; Halabi et al., 2012; Qi et al., 2018; Reijers et al., 2006; Yong and Rodrigues, 2002). They exhibit beneficial features including low cost, a wide range of preparation variables, high specific surface area, good regenerability, and high selectivity towards adsorption of CO₂ over gases like CH₄, CO, N₂ and steam at medium temperature, i.e. 200–500 °C (Baskaran et al., 2015; Cavani et al., 1991; Hufton et al., 1999; Lee et al., 2007; Vaccari, 1998).

Hydrotalcites, which belong to the class of layered double hydroxides (LDH, also known as anionic clays), are naturally occurring minerals (Vaccari, 1998). Since their natural occurrence is limited, the HTLs in use today are prepared by chemical companies (e.g. BASF, Sigma-Aldrich, SASOL, Clariant, Kisuma, Chemicals, or Sakei Chemicals) that sell tons of synthetic hydrotalcite-like compounds yearly (Forano et al., 2013). Synthetic hydrotalcites can be prepared via co-precipitation, urea hydrolysis, hydrothermal, sol-gel, microwave irradiation, steam activation, or solvothermal routes, as detailed in recent reviews (Forano et al., 2013; Othman et al., 2009). Furthermore, Mg-Al hydrotalcites can be prepared even from waste products, for example, using coal fly ash from coal-fired power plants (Muriithi et al., 2017; Yong and Rodrigues, 2002), and hazardous aluminum waste from the aluminum industry (Bui et al., 2018; Galindo et al., 2015; Gil et al., 2018).

HTLs are described by the general formula [M²⁺_{1-x}M³⁺_x(OH)₂][Aⁿ⁻_{x/n}mH₂O] or [M²⁺_{1-x}M³⁺_x(OH)₂][Aⁿ⁻_{(2x-1)/n}mH₂O], where the metal cations M⁺ = Li, M²⁺ = Mg, Ni, CO, Zn, and M³⁺ = Al, Cr, Fe, and usually, x has a value between 0.25 and 0.33 for the most widely used HTLs with M²⁺ and M³⁺ (Vaccari, 1998). The metal cations together with the hydroxide form a di-metal hydroxide layer, and Aⁿ⁻ denotes anions which, together with the molecules of water, constitute the anionic layer. The hydrotalcite structure can accommodate a plethora of anions including inorganic (e.g. CO₃²⁻, NO₃²⁻), organic (e.g. oxalate, citrate, tartrate), and complex anions (e.g. Fe-, Cr-, porphyrin complexes). A comprehensive list of anions used in the hydrotalcite-like compounds can be found in the review by Baskaran et al. (2015). The structural flexibility of hydrotalcite-like compounds to accommodate a high variety of metals and anions is reflected by their use in a wide range of applications (Corma et al., 1992; Kagunya et al., 1996; Kung and Ko, 1996; Laycock et al., 1991; Orthman et al., 2003; Reichle, 1985; Salam et al., 2020; Takuo et al., 1979).

3.3.2.1. CO₂ adsorption capacity and kinetics of Mg-Al hydrotalcite compounds. Among the considered HTLs, the Mg-Al hydrotalcite, where M²⁺ is magnesium and M³⁺ is aluminum, has received the most attention for CO₂ sorption at medium temperature due to the highest CO₂ capture performance (Ding and Alpay, 2000; Lee et al., 2010; Oliveira et al., 2008; Yong et al., 2001; Yong and Rodrigues, 2002). HTLs can adsorb CO₂ at higher temperature (200–500 °C), compared to other adsorbents that capture CO₂ below 200 °C such as zeolites, supported amines, or metal organic frameworks (Dunstan et al., 2021). The adsorption capacity is typically <1 mmol per g sorbent, which is low in comparison with alkali metal oxide solid sorbents (Table 3.18) and is a major challenge for their practical applications (Choi et al., 2009; Ding and Alpay, 2000). For example, Ding and Alpay (2000) observed equilibrium adsorption capacities of 0.65 and 0.58 mmol g⁻¹ during isothermal measurements at 400 and 480 °C, respectively. Generally, the saturation capacity increases with an increase in pressure. Interestingly, Reddy et al. (Ram Reddy et al., 2008) found that diluting the concentration of CO₂ (from 14 % at atmospheric pressure) in the gas feed by almost seven times did not affect the CO₂ sorption capacity. Most of the tested HTLs are powder samples with particle sizes ranging from nanometer to micrometer. Recently, Veerabhadrapa et al. (2021) produced pelletized (2 mm) exfoliated LDH-based nanosheets to investigate whether they can be used in industrial-scale applications. The best sample displayed a high surface area (264 m²/g) and a CO₂ sorption capacity of 1.4 mmol/g at 200 °C and 86 % CO₂ at 1 bar.

The use of alkali metal impregnation has been used widely to increase the HTL's basicity and thereby improve its CO₂ sorption capacity. When Mg-Al hydrotalcites are impregnated with K₂CO₃ (commonly referred to as K-promoted HTL), an optimum of 20 wt.% offers the maximum adsorption capacity (Choi et al., 2009; Hutson and Attwood, 2008; Yang and Kim, 2006; Yong and Rodrigues, 2002). Also, it has been found that the CO₂ sorption capacity depends more strongly on the basicity of the surface of the modified HTL than the associated changes in the surface area (Hutson and Attwood, 2008).

There is some debate in the literature about how to best describe and accurately model the kinetics of CO₂ uptake by HTLs (Ebner et al., 2006, 2007; Lee et al., 2007; Singh et al., 2009). Considering K-promoted HTL, the reaction has been described as a diffusion limited reaction similar to a physical adsorption process (Ding and Alpay, 2000, 2001). Comparing the values of the fitted mass-transfer coefficients, as determined by a diffusion limited reaction model, show large differences suggesting that the adsorption mechanism is more complex, as pointed out by Ebner et al. (2007). For example, mass transfer coefficients for adsorption have been determined as low as 0.0058 s⁻¹ for K₂CO₃ promoted Mg-Al hydrotalcites (Ding and Alpay, 2000). In contrast, other works have shown steep break-through curves for the same type of HTL, suggesting fast kinetics and a high mass transfer coefficient with a fitted value of 0.0151 s⁻¹ (Soares et al., 2005). Ebner et al. (2006, 2007) observed that the CO₂ uptake reached equilibrium saturation only after a very long adsorption time (700 min). To describe this behavior, the authors developed a non-equilibrium model consisting of three reversible reactions and four phases which had a better fit throughout the slow adsorption process. However, the discrepancies in interpretation and modelling can to a large extent, be related to preparation of the HTL, variations in composition, impregnation degree and coverage, pressure range, and temperature range (Halabi et al., 2012). Recent kinetic studies were able to accurately model the CO₂ adsorption kinetics between 300 and 500 °C in dry and wet conditions, where there is competitive adsorption of H₂O and CO₂ (Coenen et al., 2019).

3.3.2.2. Chemical composition of hydrotalcites. There have been several efforts towards modifying the chemistry of HTLs to improve their CO₂ adsorption capacity and kinetics (Aschenbrenner et al., 2011; Oliveira et al., 2008; Yang and Kim, 2006; Yong et al., 2001). Yong et al. considered different combinations of di- and trivalent cations, including Ni-Al, Co-Al, Cu-Al, Zn-Al, and Mg-Al, and found that the latter showed the

best performance (Yong and Rodrigues, 2002). Further optimizing the ratio of Mg and Al affects the number of basic sites and capacity. A high content of Al increases the charge density, providing a higher number of basic sites, but at the same time decreases the interlayer spacing and void space, thereby accommodating less CO₂ molecules (Baskaran et al., 2015; Choi et al., 2009). Increasing the Mg content provides more basic sites, which suggests that there exists an optimal ratio of Mg and Al for highest CO₂ adsorption capacity (Yang and Kim, 2006; Yong et al., 2001). For K-promoted Mg-Al HTL, with 20 wt.% of K₂CO₃ impregnation, an optimum ratio of Mg/Al = 2 provided the highest CO₂ adsorption capacity (0.77 mmol/g) at 450 °C and 1 bar (Yang and Kim, 2006). While an optimum ratio of Mg/Al = 2 was found specifically for K-promoted HTL under those conditions, a large variation in the optimum ratios of Mg/Al between 1 and 3 has been reported depending on the type of interlayer anion, whether other metal cations were used, the synthesis procedure, and which conditions they have been tested under (Baskaran et al., 2015; Choi et al., 2009).

The HTL composition changes with temperature and gas atmosphere, exhibiting hydroxylation, decomposition of carbonate and formation of oxides (mixed metal oxide, MMO). The decomposition occurs in four steps: (i) The desorption of interlayer water molecules at 100–200 °C, (ii) the loss of OH⁻ groups bonded to Al³⁺ at 200–300 °C, (iii) the loss of OH⁻ groups bonded to Mg²⁺ at 250–450 °C, and (iv) the loss of carbonates at 400–600 °C (León et al., 2010; Othman et al., 2009). The calcination temperature to achieve the highest CO₂ adsorption capacity has generally been reported as 400 °C, providing an optimum balance between surface area and basic sites (Ram Reddy et al., 2006). Under reaction conditions for sorption enhanced water gas shift (SEWGS), 400 °C and 5 bar, the layered clay structure decomposes and the material can be described as a mixed magnesium aluminum oxide with basic adsorption properties, and the basicity is further enhanced by the addition of potassium carbonate (van Dijk et al., 2011).

3.3.2.3. Regeneration of hydrotalcites. Hydrotalcites possess good capabilities for regeneration as measured by a small loss in the successive adsorption/desorption CO₂ capacity. For example, Halabi et al. (2012) assessed the regenerability of K-promoted HTL over 30 cycles at 400 °C and 1.5 bar. The sorbent displayed an uptake of 0.96 mmol g⁻¹ in the first cycle, which decreased to 0.89 mmol g⁻¹ in the second cycle and remained stable afterwards. The synthesis route also affects the ability to regenerate the HTLs. León et al. (2010) studied the adsorption/desorption mechanism and regenerability of hydrotalcites prepared by different methods. They observed that co-precipitation led to 86 % regenerability (with a low CO₂ adsorption capacity of 0.72 mmol g⁻¹ at 100 °C and 1 bar) opposed to only 67 % for sonication (with a higher initial CO₂ adsorption capacity of 0.84 mmol g⁻¹ at 100 °C and 1 bar). The reason for the differences was attributed to the bonding strength of the basic sites. The HTL prepared by sonication conditions had the strongest basic sites due to the formation of unidentate CO₂-adsorbent species causing irreversibility. On the other hand, co-precipitation produced materials with weaker basic sites with the formation of bidentate and surface bicarbonates causing highly reversible adsorption (León et al., 2010).

3.3.2.4. Effect of the gas composition. The impact of gas composition including H₂O and impurities such as H₂S, SO₂ have been investigated with respect to the CO₂ adsorption capacity. Generally, steam enhances both the CO₂ adsorption capacity and the cyclic stability of hydrotalcites (Ding and Alpay, 2000, 2001; Hufton et al., 1999; León et al., 2010; Ram Reddy et al., 2008). Ding et al. measured a 10 % increase in the CO₂ adsorption capacity under humid conditions compared to dry conditions at 480 °C (Ding and Alpay, 2000). They also found no further increase in the CO₂ adsorption capacity when the partial pressure of steam was increased from 0.03 to 2.45 bar, similar to what has been observed for CaO/CaCO₃ where only low partial pressures of steam have a positive impact on the CO₂ sorption capacity (Donat et al., 2012). The reason for the CO₂ sorption enhancement of Mg-Al HTLs, measured in the range

of 300–480 °C, has been attributed to the formation of magnesium and aluminum hydroxides, a higher hydroxyl concentration of the surface, and/or avoiding coke deposition (Choi et al., 2009; Ding and Alpay, 2000). Due to the independence of the water concentration in the CO₂ sorption step, it has also been suggested that new adsorption sites are created through the surface coverage of water (Ram Reddy et al., 2008). Furthermore, performing the regeneration of the HTL with steam has proven to be more effective in maintaining a high regenerability than with N₂, demonstrated by 30–40% higher CO₂ recovery in the presence of steam at 300 °C and 1 bar (Ding and Alpay, 2001).

Hydroxalicates promoted with K₂CO₃ are able to reversibly capture both H₂S and CO₂ with high selectivity. With up to 2000 ppm of H₂S, the CO₂ sorption capacity is not affected compared to the sulphur-free conditions (van Dijk et al., 2011). The high selectivity and reversibility suggest that SEWGS can eliminate CO₂ and H₂S simultaneously from the syngas, and an almost CO₂ and H₂S-free H₂ stream and a separate CO₂ and H₂S stream can be produced (Bassani et al., 2019; van Dijk et al., 2011). On the other hand, SO_x has a severe negative impact on the CO₂ adsorption capacity of HTLs, as the adsorbents deactivate rapidly due to irreversible SO_x adsorption. Also, the adsorption of SO_x is favoured over CO₂ due to strong acid-base interactions, such that a desulfurization unit upstream of CO₂ capture unit is necessary on a process scale (Ram Reddy et al., 2008).

3.3.2.5. CO₂ capture applications. Similar to MgO-based sorbents, at medium temperatures HTLs are most suitable for pre-combustion CO₂ capture when CO₂ partial pressures are high. Recent European Horizon 2020 projects (e.g. STEPWISE or FREsMe) have demonstrated the large potential of SEWGS using HTLs to reduce CO₂ emissions from the iron and steel industry (Cobden et al., 2018; Gazzani et al., 2015; Manzolini et al., 2020; Sebastiani et al., 2021). Here, the sorbent is operated through a pressure swing adsorption approach (CO₂ sorption at >20 bar, and CO₂ removal from the sorbent at ~1 bar) (Gentile et al., 2022).

3.3.3. Alkali-metal-based carbonates

Among the various solid sorbents, dry alkali-metal-based solid sorbents are considered promising candidates for post-combustion CO₂ capture, which are expected to be cost-effective and energy-efficient (Dong et al., 2015; Rodriguez-Mosqueda et al., 2018). Alkali-metal carbonates, such as K₂CO₃ and Na₂CO₃, can react with CO₂ to form alkali hydrogen carbonates in the presence of H₂O at low temperatures (60–80 °C) as displayed in Reaction 3.9, which can be easily regenerated at 120–200 °C via the reverse reaction of Reaction 3.9 (Qin et al., 2014). By comparison, K₂CO₃ has been revealed to give better performance than Na₂CO₃ in terms of both CO₂ adsorption capacity and kinetics, and thus most attention has been diverted to the former (Jaiboon et al., 2013). Nevertheless, the employment of pure K₂CO₃ is mainly restricted by their low conversion and poor reaction kinetics, which has been proven to be limited by the adsorption, instead of chemical reaction. Furthermore, pure K₂CO₃ is a deliquescent substance with a compact structure and a relatively low surface area, leading to its inferior CO₂ adsorption capacity (Bararpour et al., 2019; Zeng et al., 2022). It has been reported that the hydration of K₂CO₃ (Reaction 3.10) generally occurs as a competing reversible reaction in parallel with Reaction 3.9 during the carbonation process in the presence of a high amount of moisture in the inlet gas, which converts the active adsorption sites to hydrated by products with poor CO₂ capture capacity (Fig. 3.41) (Bararpour et al., 2020; Gomez et al., 2016). Therefore, the modification of K₂CO₃ sorbents is required to enhance their CO₂ capture capacity and durability before use for cyclic carbonization and regeneration operations.

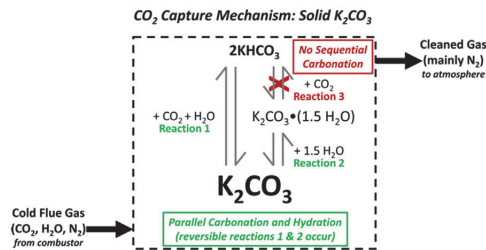
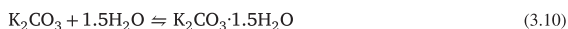
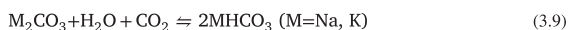


Fig. 3.41. Reaction mechanism of solid K₂CO₃ for CO₂ capture (Gomez et al., 2016). (For interpretation of the references to color in this figure legend, the reader is referred to the web version of this article.)

The most extensively studied method is to support K₂CO₃ by a stable and porous material, which contributes to better contact between the sorbent and CO₂ and hence increases the overall carbonation rate. The commonly used supports include activated carbon (AC), TiO₂, CaO, MgO, ZrO₂, silica gel, zeolites and Al₂O₃ (Li et al., 2011). Al₂O₃ and MgO are the most widely employed supports because of their excellent CO₂ capture capacity. However, the main drawback of Al₂O₃ and MgO supported K₂CO₃ sorbents is their easy deactivation because of the generation of undesirable by products, such as KAl (CO₃)₂ (OH)₂, K₂Mg (CO₃)₂, and K₂Mg (CO₃)₂·4 (H₂O), which could not be completely regenerated to the original K₂CO₃ phase (Lee et al., 2008; Qin et al., 2018). For example, Lee et al. (2014), Lee et al. (2013) investigated the phase of Al₂O₃ on the CO₂ capture performance of supported K₂CO₃ sorbents by calcining Al₂O₃ at various temperatures of 300, 600 (γ-Al₂O₃), 950 (δ-Al₂O₃) and 1200 °C (α-Al₂O₃). They demonstrated that the regeneration capacity of the sorbents increased with elevating the calcination temperature due to the production of less inactive KAl (CO₃)₂ (OH)₂ byproducts, in spite of the decreased surface area of the sorbents at higher calcination temperature. In this case, the regeneration capacity of the sorbents was more dependent on the structure properties of alumina, rather than the texture properties. In comparison, AC and TiO₂ supported K₂CO₃ sorbents are more promising in retaining the CO₂ capture capacity with the formation of mainly KHCO₃ in the carbonation process (Lee et al., 2008; Qin et al., 2018).

It has been proven that the nature and physiochemical properties of the support, such as the surface area, pore structure, and surface property, play a significant role in determining the CO₂ capture capacity of supported K₂CO₃ sorbents. For instance, Qin et al. (2014) discovered that for K₂CO₃ sorbents supported by various materials (fly ash, Portland cement, clay, Al₂O₃, and calcium aluminate cement), K₂CO₃/Al₂O₃ displayed the highest CO₂ capture capacity of 71 mg CO₂/g sorbent, which was stable in 10 cycles. The reason could be explained by the developed mesoporous structure and high surface area of K₂CO₃/Al₂O₃ sorbents. Similar results have been reported by Wang et al. that among various Al₂O₃-based supports (i.e., activated alumina (Al₂O₃), Bayer aluminum hydroxide (Bah), kaolinite clay (KC) and calcium aluminate cement (CA)), Bah supported K₂CO₃ displayed the highest CO₂ sorption capacity of 1.85 mmol CO₂/g, which might be ascribed to its loose surface and well-developed pore structure, as well as its highest surface area and pore volume (Fig. 3.42) (Wang et al., 2019). In addition, Masoud et al. (2021) studied the role of surface oxygen groups on the carbon supports (i.e. polarities of the support) in CO₂ capture by K₂CO₃ sorbents. The result showed that the apolar carbon support was more favourable to CO₂ capture, since an apolar support accelerated the adsorption of apolar CO₂ molecules while decreasing the local concentration of polar H₂O on the sorbent, contributing to a higher carbonation degree. On the contrary, a polar support was expected to promote the hydrate formation by attracting more polar H₂O molecules on the K₂CO₃ sorbent, which thereby limited the carbonation reaction.

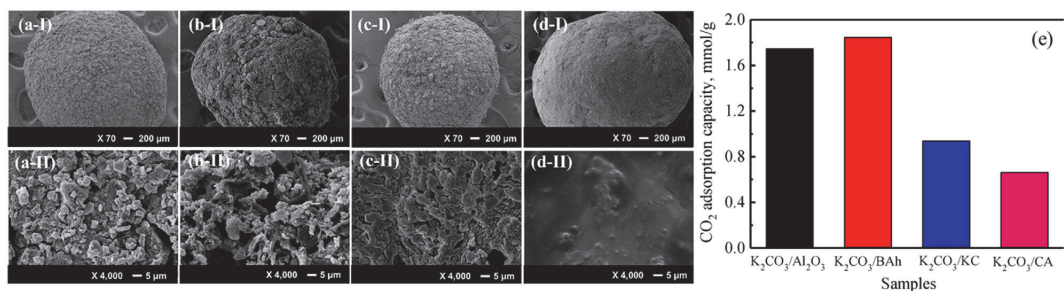


Fig. 3.42. SEM images of K_2CO_3 -based sorbents supported by (a) Al_2O_3 ; (b) BAH; (c) KC and (d) CA, and (e) CO_2 adsorption capacities of K_2CO_3 -based sorbents with different supports (Wang et al., 2019). (For interpretation of the references to color in this figure legend, the reader is referred to the web version of this article.)

In addition to the support properties, the loading amount of K_2CO_3 on the support is another important parameter affecting the CO_2 capture performance of the composite sorbents. It has been proven that a proper K_2CO_3 loading favours the achievement of well-developed pore structures and surface morphology with active components uniformly distributed on the support, contributing to the enhancement of CO_2 capture performance. On the contrary, excessive K_2CO_3 loading will result in the agglomeration of K_2CO_3 crystallites and hence the coverage and blocking of the surface and pores of the sorbents, which could be responsible for the deteriorated CO_2 capture capacity (Wang et al., 2019). Guo et al. (2018) evaluated the CO_2 sorption capacity of silica aerogel supported K_2CO_3 sorbents with various K_2CO_3 loadings of 0–30 wt%. The maximum CO_2 capture capacity of 1.32 mmol CO_2 /g was achieved at a K_2CO_3 loading of 20 wt%, which should be attributed to its best particle morphology with a uniform dispersion of K_2CO_3 and small pores. Zeng et al. (2022) also varied the content of K_2CO_3 on Al_2O_3 support from 20 to 60 wt% and discovered a decrease of the surface area and pore volume with increasing the K_2CO_3 content. In spite of the relatively inferior texture properties of K30Al to that of K20Al, K30Al achieved the highest CO_2 capture capacity because of its higher amount of active K_2CO_3 . With the further increase of K_2CO_3 content to 40–60 wt%, the CO_2 capture capacity decreased sharply due to the blockage of the pores, leading to the increase of the internal diffusion resistance of CO_2 .

The synthesis method is another crucial factor influencing the physicochemical properties of the sorbents. In recent years, various methods have been developed for the preparation of K_2CO_3 -based sorbent, in order to enhance its CO_2 capture performance. For example, Sengupta et al. (2015) compared the performance of K_2CO_3/Al_2O_3 sorbents synthesized by single- and multi-step impregnation (SI and MI) methods. They found that the sorbent synthesized by the MI method was more promising than that synthesized by the SI method in terms of CO_2 adsorption capacity and regeneration efficiency. The reason could be the more uniform dispersion of K_2CO_3 in the broad macropores without the blockage of narrower mesopores of Al_2O_3 in the sorbent synthesized by the MI method, which enabled a higher loading of accessible K_2CO_3 for CO_2 adsorption. On the contrary, the blockage of narrower mesopores by large K_2CO_3 aggregates could be obviously observed in the sorbent synthesized by the SI method, which limited the accessibility of CO_2 towards active K_2CO_3 species. In order to eliminate the adverse effect of H_2O on the CO_2 capture performance of supported K_2CO_3 sorbent, Bararpour et al. (2020) synthesized a core-shell structured support with γ -alumina as the core and TiO_2 as the shell. The result showed that the CO_2 capture performance of K_2CO_3/γ -alumina was significantly enhanced after shelling the support with TiO_2 , due to the low hydrophilicity of the sorbent, which restricted the occurrence of reaction (2). The effect of calcination temperature on the CO_2 adsorption performance of Al_2O_3 -supported K_2CO_3 pellets synthesized by graphite-casting method (Fig. 3.43 (a)) has also been investigated in a previous

study (Zeng et al., 2022). Although it is widely accepted that a high calcination temperature will lead to a less developed microstructure and hence an inferior CO_2 adsorption capacity because of the aggregation of active components at higher temperatures, the K_2CO_3 -based pellets calcinated at 900 °C displayed a 2.5 times higher CO_2 adsorption capacity than that of the sorbent calcinated at 300 °C (Fig. 3.43 (b) and (c)). The reason could be explained by that the residual graphite coating on the sorbent surface calcinated at 300 °C suppressed the diffusion of H_2O to K_2CO_3 because of the hydrophobicity of graphite.

On account of the relatively poorer CO_2 adsorption rate of Na_2CO_3 than that of K_2CO_3 , the studies on CO_2 capture using Na_2CO_3 -based sorbents are limited. However, the primary advantages of using Na_2CO_3 over K_2CO_3 are its easier accessibility, lower regeneration temperature, and lower CO_2 capture costs (Wu et al., 2020). If the reaction kinetics of CO_2 capture could be dramatically improved via proper modifications of Na_2CO_3 -based sorbents, their applications in large-scale CO_2 capture could be significantly broadened. Therefore, the understanding of the rate-limiting steps of CO_2 capture by Na_2CO_3 is critical to systematically improving the kinetics. Cai et al. (2019) employed first-principles density functional theory (DFT) to study the structural, mechanistic, and energetic properties of CO_2 adsorption on the low-index (001) and high-index ($\bar{1}0\bar{1}2$) surfaces of unmodified Na_2CO_3 sorbent, in order to clarify the actual reason of the slow kinetics. They discovered that the reaction barriers for bicarbonate formation on the above two facets were comparable with that on K_2CO_3 surfaces. However, on account of the much lower overall kinetics of CO_2 capture by Na_2CO_3 observed by experiments, they assumed that the kinetics of CO_2 captured on Na_2CO_3 was controlled by surface diffusion, rather than by surface carbonation reaction as that observed for K_2CO_3 .

In order to enhance the reaction kinetics of CO_2 capture on Na_2CO_3 , the dispersion of Na_2CO_3 on various supports is considered as the most dominant strategy, where the support effect and Na_2CO_3 loading are important factors in developing efficient Na_2CO_3 -based sorbents (Cai et al., 2020; Luo and Kanoh, 2017). It is well accepted that the textural properties of the support play a crucial role in determining the CO_2 capture performance of the sorbent. Kazemi et al. (2020) tried to improve the specific surface area and pore volume of γ - Al_2O_3 -supported Na_2CO_3 sorbent using a modified sol-gel process with the addition of polyethylene glycol (PEG). They demonstrated that the surface area and pore volume of the modified sorbent were around 38% and 340% higher than that of the sorbent synthesized without the addition PEG. As a result, the CO_2 capture capacity of the sorbent increased by 34%. In addition to the texture properties such as surface area and pore structure, the morphology and distribution of Na_2CO_3 have also been confirmed to affect the CO_2 capture performance. As observed by Cai et al. (2020), the morphology of Na_2CO_3/γ - $AlOOH$ sorbent could be changed by varying the loading amount of Na_2CO_3 , which thereby influences the CO_2 capture capacity significantly. At lower Na_2CO_3 loadings of <17 wt%, Na_2CO_3

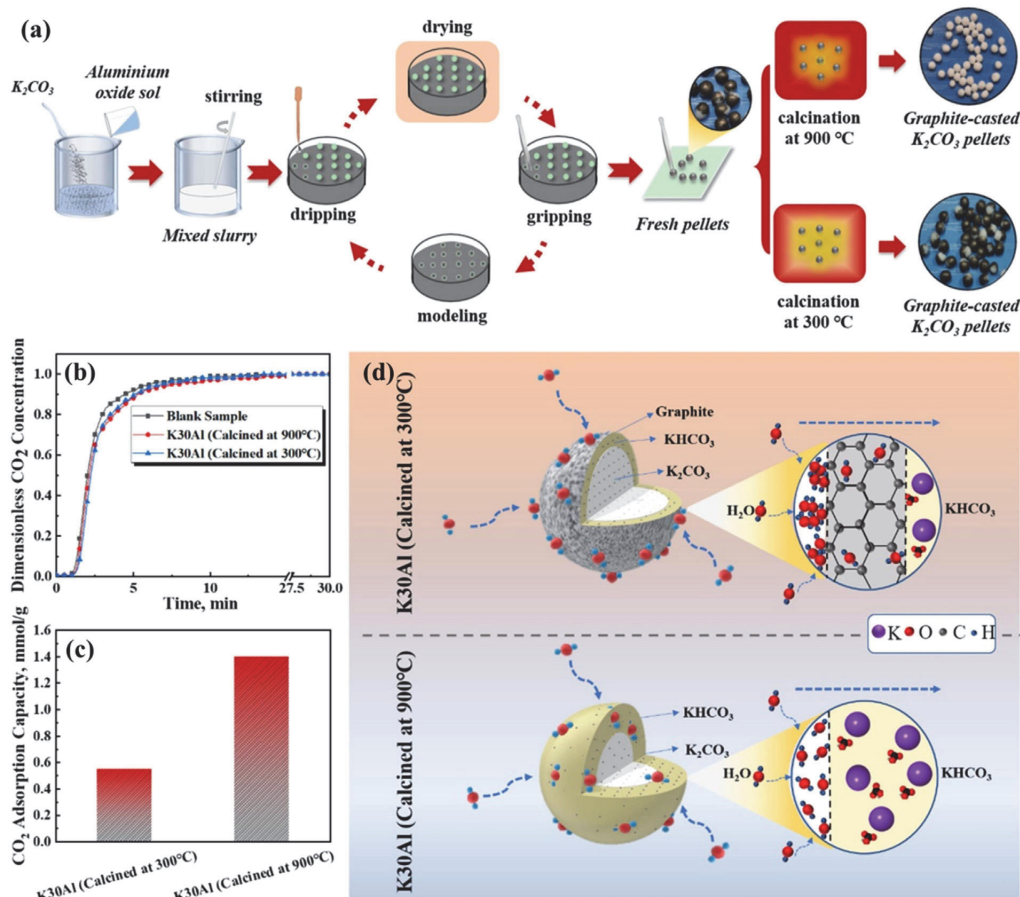


Fig. 3.43. (a) Scheme for the preparation of graphite-casted K_2CO_3 pellets, (b) breakthrough curves of CO_2 adsorption, (c) CO_2 adsorption capacity of K30Al calcined at 300 and 900 °C, and (d) mechanism of the adverse effect of residual graphite coating on CO_2 adsorption (Zeng et al., 2022). (For interpretation of the references to color in this figure legend, the reader is referred to the web version of this article.)

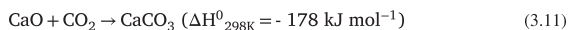
was uniformly dispersed on γ -AlOOH surface sites as a monolayer amorphous form. With the increase of Na_2CO_3 loading up to 23–29 wt%, the Na_2CO_3 crystallites grew uniformly to form nanoparticles on the inner surface of γ -AlOOH, contributing to the exposure of more high-index facets of Na_2CO_3 (such as (1 1 2) and (−4 0 2) facets) and hence the enhancement of the CO_2 capture capacity.

In summary, alkali-metal-based carbonates of K_2CO_3 and Na_2CO_3 are proven as promising candidates for CO_2 capture, while the practical applications of pure carbonates were restricted by their poor capacities and kinetics. As a result, the proper design of efficient K_2CO_3 - and Na_2CO_3 -based sorbents is of significant importance in broadening their application prospects. The most potential method for modification of K_2CO_3 and Na_2CO_3 is to load them on a porous support, where the optimization of the support materials, K_2CO_3/Na_2CO_3 loading amounts, and preparation methods are expected to improve the texture properties and surface morphology, enhance the dispersion of active K_2CO_3/Na_2CO_3 , and hence accelerate the CO_2 adsorption. In spite of the extensive studies on this topic, the influence of the abundant impurities in flue gases, such as sulphur- and chlorine-containing species, on the CO_2 capture performance of alkali-metal-based sorbents was rarely studied systematically, which is critical in evaluating their durability and regeneration efficiency in practical applications.

3.4. High-temperature solid sorbents

3.4.1. CaO for CO_2 capture

Among the alkali earth metal oxides CaO, SrO, and BaO, CaO has been studied most thoroughly for CO_2 sorption applications at high temperatures (Kierzkowska et al., 2013; Krödel et al., 2020; Omodolor et al., 2020; Yu et al., 2012). Many of the early studies in the 1990s and 2000s benefitted from experience with CaO-based sorbents in the context of flue gas desulfurization, when SO_2 was considered more problematic than CO_2 (Dunstan et al., 2021). The CO_2 capture process using CaO-based sorbents, also referred to as calcium looping (CaL), utilizes the reversible reaction between CaO and CO_2 at elevated temperatures, viz Reaction 3.11:



The operational windows for the carbonation and the calcination reactions are defined by the reaction equilibrium, i.e. the equilibrium partial pressure of CO_2 at a given temperature (Samanta et al., 2012). In sorbent research, calcination is commonly conducted at 800–950 °C in air, N_2 or pure CO_2 ; at the process level, the calcination reaction would have to be carried out in (almost) pure CO_2 to process the CO_2 released

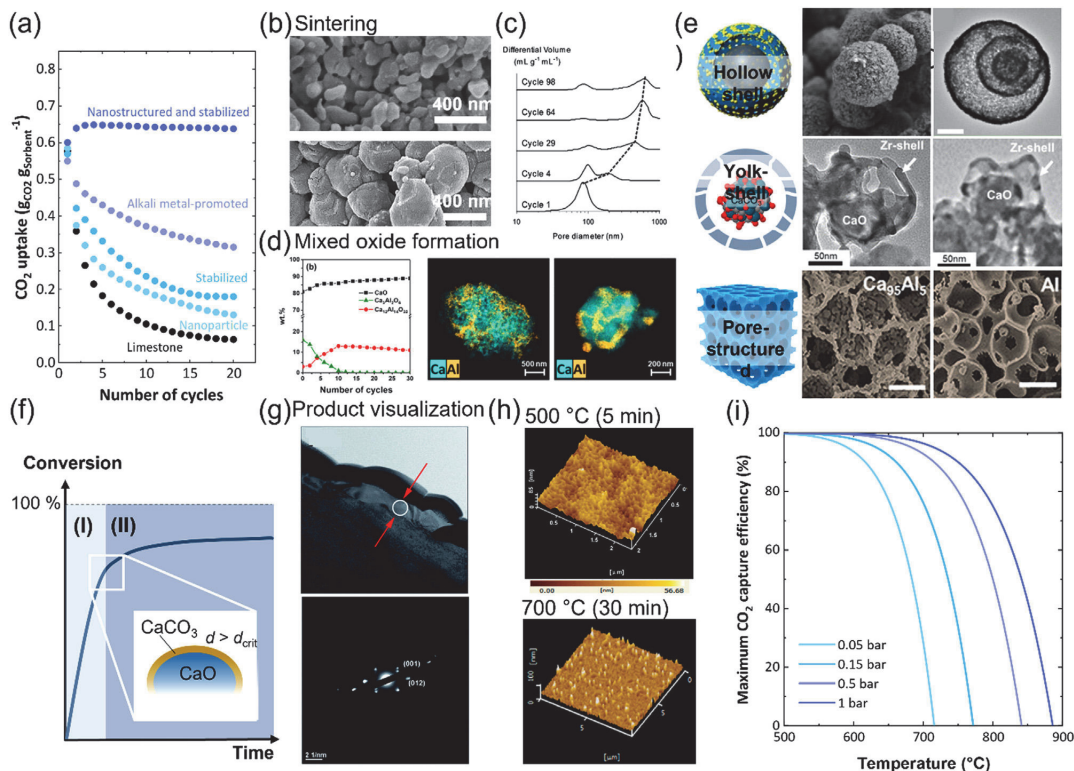


Fig. 3.44. (a) Typical cyclic CO₂ uptake of selected CaO-based sorbents over 20 carbonation-regeneration cycles, illustrating the performance improvement compared to bare limestone via stabilization, promotion or nanostructuring of the sorbent. (b) SEM micrographs of limestone after the 1st calcination (top) and after 10 cycles (bottom) (Naeem et al., 2018). (c) Evolution of the pore volume of La Blanca limestone measured via Hg intrusion porosimetry over 98 carbonation-calcination cycles (Alvarez and Abanades, 2005). (d) Changes in the phase composition of a Ca₃Al₂O₆-stabilized CaO-based sorbent over carbonation-regeneration cycling derived from in situ XRD using Rietveld analysis (Kim et al., 2018). (e) Electron micrographs of a nanostructured hollow multishell CaO-based sorbent reported by Naeem et al. (Naeem et al., 2018), a yolk-shell-type CaO-based sorbent reported by Krödel et al. (Krödel et al., 2022), and pore-structured (via a sacrificial template) CaO-based sorbent reported by Kim et al. (Kim et al., 2019) (f) Conversion over time curve for CaO-based sorbents exhibiting the two typically observed regimes: (I) a kinetically-controlled regime and (II) a diffusion-controlled regime. (g) Visualization of the CaCO₃ product formation on CaO single crystal at two different carbonation times and after varying carbonation times (Li et al., 2012). (i) Maximum CO₂ capture efficiency for CaO-based sorbents as a function of temperature and the partial pressure of CO₂ in the gas stream. (For interpretation of the references to color in this figure legend, the reader is referred to the web version of this article.)

from the sorbent further (e.g. compression and storage) and avoiding additional downstream gas purification. Typically investigated carbonation conditions range between 550 °C and 700 °C as well as 10–15 vol.% CO₂ in air or N₂ to reflect CO₂ concentrations in off-gases from (coal) combustion processes. During the carbonation reaction, two reaction regimes are observed: (Bhatia and Perlmutter, 1983; Cai et al., 2017). A fast, kinetically-controlled regime and a slow, diffusion-controlled regime, see Fig. 3.44f. The CO₂ uptake in the kinetically-controlled regime correlates directly with the initially available surface area of the CaO-based sorbent, which is usually supplied by pores with diameters smaller than 100 nm (Alvarez and Abanades, 2005; Alvarez and Abanades, 2005; Bhatia and Perlmutter, 1983). The shift between the two reaction regimes is often explained with the CaCO₃ product layer reaching a critical thickness, estimated at 30–50 nm at which the reaction becomes limited by CO₂ diffusion through CaCO₃ (Fig. 3.44g and h).

For practical CO₂ capture applications at high temperature, CaO-based sorbents need to be repeatedly cycled between their oxide and carbonate states, making the cyclic CO₂ uptake an important metric for the CO₂ capture costs (Hanak et al., 2015a). Generally, the cyclic CO₂

uptake should be as close as possible to the theoretical maximum CO₂ uptake capacity of 0.78 g_{CO₂}/g_{CaO} and stable over ideally thousands of cycles. In reality, the cyclic CO₂ uptake of sorbents derived from natural limestones decreases rapidly with cycling, as shown exemplarily in Fig. 3.44a. The deactivation of the sorbent is a result of material sintering (Fig. 3.44b and c), which (i) reduces the surface area of the regenerated CaO available for the reaction with CO₂, and (ii) increases the diffusional resistance of CO₂ into the bulk sorbent, such that both the rate and the extent of CO₂ uptake during the carbonation step are reduced (Barker, 2007; Li et al., 2006; Wang et al., 2014). To mitigate the sintering-induced deactivation, research efforts have focused on either reactivating the sorbents, e.g. using a steam treatment at high temperatures, or stabilizing and promoting the sorbent using non-alkali metal oxides and alkali metal salts, respectively (Salaudeen et al., 2018).

3.4.1.1. Synthetic stabilized and promoted sorbents. The cyclic CO₂ uptake performance of CaO-based sorbents can be stabilized using metal oxides with high Tammann temperatures such as Al₂O₃, ZrO₂ or MgO (Kierzkowska et al., 2013; Krödel et al., 2020; Naeem et al., 2017; Radfarnia and Iliuta, 2013; Salaudeen et al., 2018). These stabilizers

are mixed into the CaO matrix in contents of typically 5–20 wt.%, e.g. through ball-milling, co-precipitation, sol-gel or more advanced techniques like atomic layer deposition, and they are assumed to act as physical barriers against the sintering of CaO particles (Kim et al., 2018; Kurlov et al., 2020a; Kurlov et al., 2016; Liu et al., 2010). Stabilizers effectively reduce the cyclic decrease of the surface area and pore volume of the sorbents, thereby improving their cyclic CO₂ uptake. For example, Kim et al. reported a Ca₃Al₂O₆-stabilized CaO-based sorbent showing a CO₂ uptake of 0.38 g_{CO₂}/g_{Sorbent} after 30 cycles, an increase of 300% compared to the benchmark limestone (Kim et al., 2018). Other materials utilizing ZrO₂, MgO or SiO₂ showed similar CO₂ uptakes of up to 0.37, 0.31 or 0.39 g_{CO₂}/g_{Sorbent} after 10 cycles, respectively (Kurlov et al., 2016; Sanchez-Jimenez et al., 2014; Zhao et al., 2014). Despite these improvements, even stabilized materials deactivate with cycling via mixed phase formation with CaO, viz. a loss of the reactive phase for CO₂ sorption, or the agglomeration of the stabilizing phase as surface-segregated particles, reducing the effectiveness of the stabilizer as a physical barrier against sintering of CaO grains/particles (Fig. 3.44d) (Kim et al., 2018; Kurlov et al., 2016). Hence, optimizing both the distribution and the mobility of the stabilizer phase in the material are crucial aspects for the design of stabilized, long-lasting CaO-based sorbents. Works by Naeem et al. (2018) and Armutulu et al. (2017) have employed means of stabilization as well as morphological design techniques to derive sorbents with even more stable cyclic CO₂ uptakes (Fig. 3.44e). For example, one of the best performing sorbents to date consists of a double shell structure of a CaO-MgO nanocrystalline matrix. This material exhibited a CO₂ uptake of 0.65 g_{CO₂}/g_{Sorbent} after 10 cycles, which equals 93% of the theoretical maximum CO₂ uptake of a sorbent containing 10 wt.% MgO.

The promotion of CaO-based sorbents using alkali metal salts (AMS), e.g. Na₂CO₃, NaCl, K₂CO₃ or KCl, is another approach to improve their cyclic CO₂ uptake (González et al., 2011; Kurlov et al., 2020b; Lee et al., 2018; Xu, Yongqing et al., 2018). Added in relatively large amounts (>5 wt.%), these low Tammann-temperature promoters increase the sintering of the sorbents, thereby reducing the cyclic CO₂ uptake performance significantly compared to benchmark materials without AMS (Krödel et al., 2020). In addition, some alkali metals form low-melting mixed phases with CaO that tend to form either large surface-segregated particles or a layer around the bulk CaO particles (Kurlov et al., 2020b). For example, Kurlov et al. reported the formation of Na₂Ca (CO₃)₂ coatings around Na₂CO₃-modified CaO particles due to the melting of the mixed phase under calcination conditions (900 °C, 100 vol.% CO₂), negatively affecting the accessibility of CaO for reaction with CO₂. On the other hand, low AMS contents of < 1 wt.% have been reported to have a positive effect on both the carbonation and calcination reaction, therefore increasing the cyclic CO₂ uptake (Xu et al., 2023; Xu et al., 2017; Yang et al., 2018). The best reported sorbents to achieve CO₂ uptakes of up to 0.5 g_{CO₂}/g_{Sorbent} after 10 cycles with < 1 wt.% of promoter added. In nature, various alkali metals are found in the structure of CaCO₃, which may explain the large differences in the cyclic CO₂ uptake of limestone-derived sorbents of different origin/geographical location (Fennell et al., 2007; Grasa and Abanades, 2006; Valverde et al., 2015; Yoshimura et al., 2017). Similarly, researchers have proposed that alkali metal promoters may be incorporated into the structure of the CaCO₃ product forming during carbonation (Leukel et al., 2018). This could positively affect the rate of carbonation, e.g. by enhancing CO₂ diffusion through CaCO₃, but evidence for this mechanism is still lacking. It has been reported that AMS affects the transition temperature between CaO and CaCO₃, leading to the onset of the decomposition of CaCO₃ at lower temperatures which may be interesting from a process perspective. For the CaL process to be implemented at industrially relevant scales, also the mechanical stability of sorbent particles is important, and maintaining a high stability with cycling is currently an active area of sorbent research (Pi et al., 2019; Sun et al., 2019; Sun et al., 2015).

3.4.1.2. Effect of the gas composition. Unburnt fuel gases (e.g. CO, H₂, CH₄) hardly affect the rate of the carbonation or calcination reaction of CaO-based sorbents (Dunstan et al., 2021); under conditions that favour the reverse water-gas shift reaction, H₂ was observed to react with CO₂ released from the CaCO₃, thereby accelerating its decomposition. The presence of SO₂ and steam is more influential, and affects the sorbent behavior during both the carbonation and calcination reaction.

SO₂ forms CaSO₄ with CaO in the presence of oxygen, a reaction that has been utilized for high-temperature flue gas desulfurization (He et al., 2021). As the decomposition of CaSO₄ does not proceed rapidly below ~ 1200 °C (viz. at temperatures much higher than typical decomposition temperatures of CaCO₃) (Tian et al., 2008), the presence of SO₂ in a flue gas stream is problematic and with time reduces the amount of CaO that is available for CO₂ to form CaCO₃ (Grasa et al., 2008). The carbonation reaction is faster at typical carbonation conditions (15 vol.% CO₂, 550–700 °C) than the sulfation reaction, but sulfation rates increase with rising temperatures. The CaSO₄ product also has an approximately 25% higher molar volume than CaCO₃, increasing the diffusional resistance for CO₂ further, which shifts the transition between the kinetically-controlled regime and the diffusion-controlled regime to lower CO₂ uptakes, and also negatively affects the CO₂ uptake in the diffusion-controlled regime (Borgwardt et al., 1987).

Contrarily, the presence of steam usually enhances both the rate and extent of CO₂ uptake, mainly in the diffusion-controlled regime (Arias et al., 2012; Dong et al., 2020; Li et al., 2016). It has been shown both experimentally and computationally that steam concentrations <1 vol.% are sufficient to achieve this effect. From a morphological point of view, the presence of steam has a positive effect on the surface area and pore volume for pores with diameters < 100 nm, enhancing the rate of carbonation (Dong et al., 2020; Wang et al., 2014). It has also been reported that the presence of steam lowers the driving forces ($p_{\text{CO}_2} - p_{\text{CO}_2, \text{eq}}$) for the carbonation reaction to commence at a fast rate (Blamey et al., 2015). Structurally, it has been proposed that the presence of steam may lead to the formation of Ca(OH)₂ as an intermediate product. However, bulk Ca(OH)₂ is not thermodynamically stable under typical carbonation conditions (600–700 °C).

3.4.1.3. CO₂ capture applications using CaO-based sorbents. CaO-based sorbents can be used for a range of applications involving CO₂ capture, and thus far, post-combustion CO₂ capture has most frequently been investigated. Different from MgO-based sorbents, relatively high CO₂ capture efficiencies can be realized with CaO-based sorbents even at low CO₂ partial pressures as in flue gases from combustion processes. Several pilot-scale reactor units, typically operated as interconnected fluidized bed reactors involving the transfer of CaO-based sorbents between them, have shown CO₂ capture efficiencies of 90% or higher with steam present, close to the thermodynamic limit (Fig. 3.44i) (Dieter et al., 2013; Duelli et al., 2015; Hanak et al., 2015a). Large demonstration plants at the MW scale have demonstrated the feasibility of the CaL process for post-combustion CO₂ capture (Chang et al., 2014; Diego and Arias, 2020; Hilz et al., 2017; Ströhle et al., 2020), yet there are currently no industrial units in operation.

Closer to the industrial application may be CaO-based CO₂ capture processes that offer, besides the removal or the elimination of CO₂ emissions, additional economic value, e.g. hydrogen through sorption-enhanced reforming or water-gas shift reactions (Chirone et al., 2022; Di Giuliano and Gallucci, 2018; Harrison, 2008; Ma et al., 2021; Masoudi Soltani et al., 2021; Zhang et al., 2022; Zhu et al., 2020) or thermal energy (Arcenegui-Troya et al., 2020; Medina-Carrasco and Valverde, 2022; Perejón et al., 2016).

3.4.2. Challenges and emerging technologies: a life cycle thinking

Compared with other alternative technologies, calcium looping is expected to substitute amine looping in dealing with fuel gas with low CO₂ concentration ranging from 5–15%. But successful installation and

operation of calcium looping should be relied on techno-economically competitiveness. High CO₂ concentration is obviously the main advantage for calcium looping. In addition, this CO₂ from post-combustion unit then only needs to be conditioned and dehydrated prior to compression, transport and commercial purposes. However, despite of the simple chemistry and efficient recycling involved in calcium looping, the following challenges are believed to hinder wider applications of such technology for CO₂ capture.

- 1) The net efficiency of tail-end configuration is reduced by integrating cryogenic air separation unit (Plaza et al., 2020; Yang et al., 2021).
- 2) The combustion temperature must be controlled to avoid hot spots in the combustion zone that would enhance NO_x production in the boiler (Chen et al., 2020; Hu et al., 2020).
- 3) Fast catalyst deactivation and poor reaction engineering technologies for optimum operations.

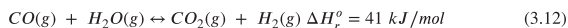
Those challenges could be addressed by applying advanced reaction technologies. However, those solutions should be proposed based on techno-economic thinking. (Colelli et al., 2022; Galusnyak et al., 2022; Kong et al., 2022; Moore et al., 2022) From a perspective of process development, the overall techno-economic advantages or disadvantages should be quantitatively assessed to evaluate the feasibility prior to practical implementation. The following aspects have been the main R&D focus in the past five years.

Emerging technologies from a life cycle assessment

(1) Combinatory processes with H₂ generation technologies

The combinatory technologies involving CO₂ capture and in-situ transformation could be a most promising solution to enhance environmental sustainability and technological viable. (Han et al., 2022; Hashemi et al., 2022; Li et al., 2022) Researchers have been proposing a variety of combinatory processes to integrate calcium looping with advanced H₂ generation techniques.

The commercial technologies based on the fuels reforming and gasification processes involve the production of syngas (H₂, CO, CO₂, and some CH₄ and hydrocarbons). (Han et al., 2022; Madejski et al., 2022; Yang et al., 2021) Downstream applications of molecular H₂ usually demand high purity with 99.99% and CO-free composition. This purpose has been achieved through water gas shift reaction (WGS), where CO reacts with water vapour to produce additional H₂ and CO₂. However, this reaction (Reaction 3.12) is equilibrium-limited, but if CO₂ is continuously removed, the reaction will be shifted in favour of increased H₂ production.



Consequently, the syngas produced during the reforming or gasification (>600 °C) is upgraded in an independent WGS reactor (250–500 °C). The capture of CO₂ generated in-situ during the reforming and gasification processes, or syngas upgrade in a separate reactor, can favourably shift the thermodynamic equilibrium of the above-mentioned reactions toward a higher efficiency of H₂ production.

Another advanced energy efficient technique is called sorption-enhanced steam reforming. CaO is incorporated in this process in sorbents and immobilized with active metallic catalytic materials to enhance the overall the economics of CO₂ capture. Ni-based reforming catalysts, synergistically working with trace amounts of noble Rh, Pt, Pd and Ru have better performances in coke resistance for converting natural gas into highly purified molecular H₂. The flow scheme is present in Fig. 3.45, where reformer/shift reactors are working with calciner in a synchronizing fashion, coupled with pressure swing adsorption (PSA) for producing high quality H₂. Life cycle assessment has confirmed that, such novel combination could lower the H₂ production cost by 3–5% comparatively with no capture conventional reforming (approximately \$40/MWh capacity).

(2) Solar thermal calcium looping

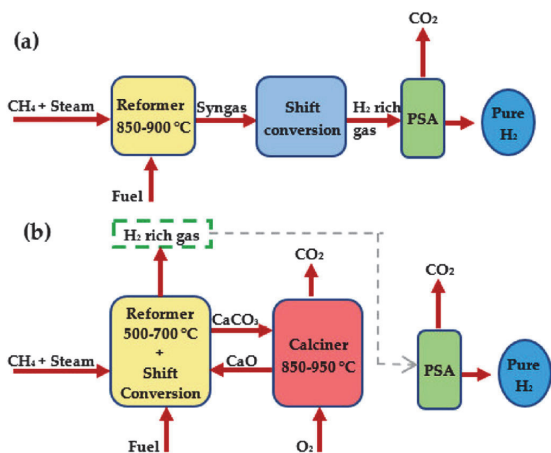


Fig. 3.45. Flow diagram of (a) steam methane reforming and (b) sorption-enhanced steam methane reforming (CaCO₃ as sorbent). (For interpretation of the references to color in this figure legend, the reader is referred to the web version of this article.)

Grey H₂ production from natural gas conversion, or dry reforming of CH₄ and CO₂ could enhance the overall sustainability of CO₂ capture processes. However, carbon footprint analysis shows that, using solar energy as primary source could potentially reduce process cost by almost 12–25%, simply using solar heat as energy carrier. (Khosa et al., 2019; Salaudeen et al., 2018; Valverde, 2018)

An earlier version of solar thermal-assisted calcium looping has been involving compressed CO₂ and high-pressure air in carbonation stage. It assumed that CO₂ was completely converted in the carbonator, and then only high-temperature and high-pressure air was sent to the turbine to generate work. The power generation efficiency of the system was maximum, as high as 40–43%. It is worth mentioning that the complete consumption of CO₂ in the carbonator is an ideal situation.

Heat storage would favour the efficiency enhancement for calcium looping. An indirect integration of the steam Rankine cycle in calcium looping can be optimized from both energy and economic aspects, which determined the size and operating conditions of the main components. A complete exergy analysis show that, exergy loss occurs in the solar receiver (about 37%), the calcination section (26%), and the steam Rankine cycle (about 21%). (Erans et al., 2016; Perejon et al., 2016) In sharp contrast, the exergy loss that occurred in the carbonation section was relatively small, lower than 5%. The improved solar thermal-assisted calcium looping (shown in Fig. 3.46) leads to a much higher process efficiency of 51%. (Ortiz et al., 2019; Tregambi et al., 2021)

(3) Nanomaterials

The use of functionalized materials not only could reduce the carbon footprint by combining H₂ generation technologies with calcium looping, in addition, nanomaterials with high surface areas would significantly enhance heat transfer in carbonation and calcination, leading to lowered loss of exergy. Experimental studies have suggested that the coupling of a solid looping cycle, for example, Fe/FeO and Cu/CuO, can deliver the heat required in the calcination step in a faster way. The improvement is achieved by the exothermic oxidation of the Fe (Cu) to FeO (CuO) with air, which took place in the same fixed bed reactor as the calcination. (Santos and Hanak, 2022)

Nanostructured CaO and CaCO₃ materials could also slow sorbent and catalyst deactivation during high temperature looping. In earlier stages of looping operation, reactions occur in a kinetic controlled regime. In this stage, catalyst size is small thus reactions are consid-

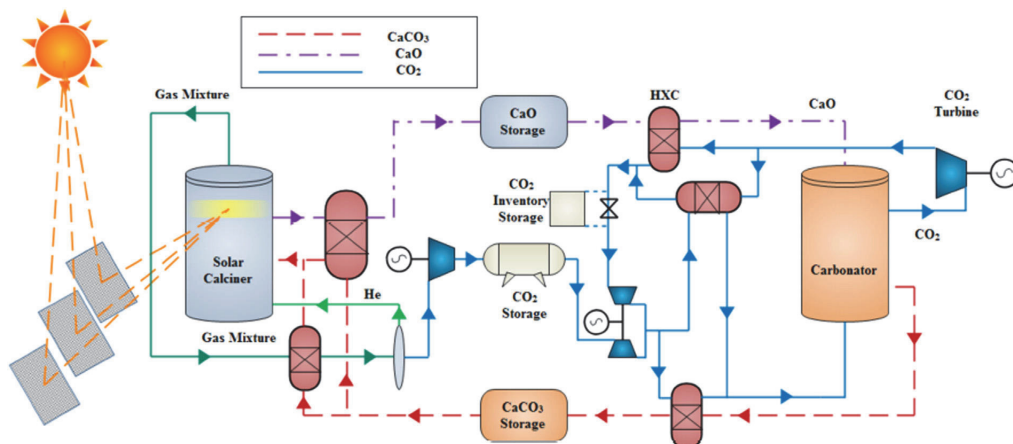


Fig. 3.46. Solar thermal calcium looping (Chacartegui et al., 2016). (For interpretation of the references to color in this figure legend, the reader is referred to the web version of this article.)

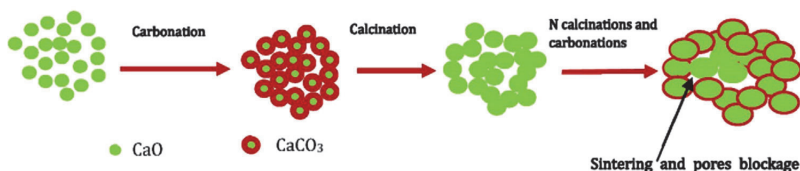


Fig. 3.47. Particle sintering during carbonation-calcination cycles (Teixeira et al., 2022). (For interpretation of the references to color in this figure legend, the reader is referred to the web version of this article.)

ered as rate limiting step. However, catalyst size has been enhanced significantly after several cycles, leading to poor surface area and loss of sorbent reactivity by particle sintering and pore blockage (Fig. 3.47).

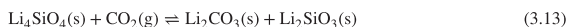
Recent experimental studies have demonstrated the advantages of using nano-sized CaO and CaCO₃ materials in calcium looping. Unfortunately, no life cycle assessment has been conducted to quantitatively evaluate the environmental impact of preparation steps on the overall sustainability in calcium looping. (Li et al., 2022; Xu et al., 2021)

3.4.3. Li-, Na-, Sr-, and Ba-based sorbents

Unlike MgCO₃ and CaCO₃, other carbonates of alkali metal or alkaline earth metals, e.g., Li₂CO₃, Na₂CO₃, SrCO₃ and BaCO₃, are hard to decompose in practically achievable conditions, making them unsuitable for reversible CO₂ capture in their monometallic forms. To address this issue, transition metals and/or semi-metals are often incorporated into oxides of Li, Na, Sr and Ba to form ternary oxide sorbents. The incorporation of the transition metals modifies the basicity of the oxides, thus rendering their regenerability over CO₂ capture cycles. This section discusses some developments in Li, Na, Sr and Ba based CO₂ sorbents. Table 3.19 summarises the stoichiometric CO₂ capacities and experimental CO₂ uptakes of these sorbents.

3.4.3.1. Li-based sorbents.

3.4.3.1.1. Lithium silicates. Lithium silicates, including Li₄SiO₄ and Li₈SiO₆, are the most often studied lithium based sorbents. Li₄SiO₄ reacts with CO₂ between 450 and 700 °C with a stoichiometric CO₂ capacity of 36.7 wt.%:

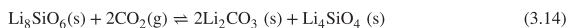


The carbonation mechanism of these ternary oxides is different from simple oxides like CaO or MgO, because more than one solid phase will be produced. The two solid products, Li₂CO₃ and Li₂SiO₃, form an outer

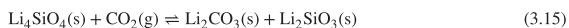
shell and an inner shell surrounding the unreacted Li₄SiO₄ core, respectively, generating a double-shell structure, as shown in 8 (Yang et al., 2016b).

The subsequent carbonation requires the transport of CO₂ through the Li₂CO₃ layer, and the migration of Li⁺ and O₂⁻ ions out of the Li₂SiO₃ layer. As the shells grow thicker during carbonation, the diffusion resistances of both CO₂ and ions will increase, slowing down the carbonation. It is believed that the rate limiting step is the CO₂ gas diffusion through the Li₂CO₃ layer. Owing to these product layer diffusion resistances, the experimental CO₂ uptake capacity of Li₄SiO₄ is always lower than the stoichiometric value. Increasing the surface area of the chemically unmodified lithium silicates is one of the most effective means to enhance the CO₂ uptake performance of Li₄SiO₄.

Li₈SiO₆, as a CO₂ sorbent with higher Li contents than Li₄SiO₄, also has a higher theoretical CO₂ uptake of 98 wt.%. The process of Li₈SiO₆ carbonation consists of 3 steps (Cova et al., 2019). Steps 1 and 2 involve the CO₂ adsorption on the surface and in bulk:



Step 3 involves the reaction between CO₂ and the formed Li₄SiO₄:



Lithium silicates can be synthesised by mechanically mixing solid particles of lithium and silicon precursors at stoichiometric ratios, followed by drying and calcination. Commonly used lithium precursors include Li₂CO₃ (Chen, X. et al., 2016; Wang, Haiyang et al., 2018), Li₂O (Lara-García et al., 2019), and LiNO₃ (Wang, K. et al., 2019), while the silicon precursor is almost always SiO₂. However, the lithium silicates obtained by solid-state reactions typically have low surface areas (<1 m²/g) and low experimental CO₂ uptakes (28–35 wt.% for Li₄SiO₄ (Chen, X. et al., 2016; Wang, Haiyang et al., 2018) and 42 wt.% for Li₈SiO₆) (Cova et al., 2019). Additionally, the poor sintering resistance of the Li₂SiO₃ results in a rapid decrease in CO₂ capture capacity over carbonation cycles (Chen, X. et al., 2016; Yang et al., 2016b).

Table 3.19
Stoichiometric CO₂ capacities and experimental CO₂ uptakes of Li, Na, Sr and Ba based sorbents.

| Sorbent | Stoichiometric CO ₂ capacity [wt.%] | Experimental CO ₂ uptake [wt.%] | Carbonation Temperature [°C] | Calcination Temperature [°C] | Carbonation CO ₂ partial pressure [bar] | Calcination CO ₂ partial pressure [bar] | Max No. of Cycles | Ref |
|--|--|--|------------------------------|------------------------------|--|--|-------------------|---|
| Li ₄ SiO ₄ | 36.7 | 1.8-36.0 | RT-700* | 550-900 | 0.04-1.0 | 0 | 250 | (Chen et al., 2016; Lara-García et al., 2019; Seggiani et al., 2018; yang et al., 2018; Wang et al., 2019; Yang et al., 2016a, b) (Cova et al., 2019) |
| Li ₆ SiO ₆ | 98.0 | 0-42.0 | 25-776* | - | 1.5 | - | - | (Gómez-Garduño and Pfeiffer, 2019; Peltzer et al., 2019; Peltzer et al., 2018) |
| Li ₂ ZrO ₃ | 28.7 | 0.01-23.0 | 500-575 | 600-700 | 0.10-2.0 | 0-0.585 | 30 | (Gaultois et al., 2018) (Bernabé-Pablo et al., 2020) |
| Li ₆ WO ₆ | 41.1 | 3.6-25.9 | 30-710* | 730-760 | 0.60 | 0 | 4 | (Harada and Hatton, 2017) |
| Li ₆ CoO ₄ | 80.0 | 5.0-76.4 | 300-700 | 700-750 | 0.20-1.0 | 0 | 10 | (Martínez-Cruz et al., 2020; Martínez-Cruz et al., 2020; Yañez-Aulestia et al., 2020) |
| Li ₂ BO ₃ | 69.1 | 0-47.2 | 500-650 | 650 | 0.20-1.0 | 0 | 10 | (Blanco et al., 2018) |
| Li ₂ CuO ₂ | 40.2 | 3.6-37.4 | 30-750* | 750-850 | 1.0-5.0 | 0 | - | (Togashi et al., 2007) |
| Li ₃ FeO ₄ | 71.2 | 0-62.0 | 30-700* | - | 1.0 | - | - | (Liu et al., 2019) |
| Li ₄ TiO ₄ | 47.3 | 0-42.0 | 300-856 | - | 1.0 | - | - | (Ji et al., 2017; Martínez-díCruz and Pfeiffer, 2012; Munro et al., 2020; Zhao et al., 2007) |
| Na ₄ SiO ₄ | 23.9 | 7.7-19.2 | 50-840* | - | 0.80 | - | - | (Vera et al., 2019) |
| Na ₂ ZrO ₃ | 23.8 | 4.5-23.8 | 150-800 | 680-900 | 0.025-1.0 | 0 | 70 | (Miccio et al., 2016) |
| NaCoO ₂ | 15.0 | 3.3-11.1 | 100-800 | - | 0.050-1.0 | - | - | (Yang and Lin, 2006) |
| SrO | 42.5 | 3.0-37.1 | 1100-1200 | 1100-1200 | 0.30-0.50 | 0 | 10 | (Homonnay et al., 2002; Juhasz et al., 2001; Nomura et al., 1996) |
| La _{0.1} Sr _{0.9} Co _{0.5} Fe _{0.5} O _{3-δ} | 20.7 | 0-17.3 | 600-800 | - | 0.10-1.0 | - | - | (Lu et al., 2011) |
| Sr _x Ca _{1-x} Fe _{0.5} Co _{0.5} O _{3-δ} | 15.1 | 0.4-17.0 | RT-950* | - | 1.0 | - | - | (Galven et al., 2010) |
| SrCo _{1-2x} (Fe,Nb) _x O _{3-δ} | 11.6 | 0-13.1 | 925 | - | 0.75 | - | - | (Nomura et al., 1996) |
| Li ₂ SrTa ₂ O ₇ | 5.1 | 0-4.9 | 140 | 700 | - | - | 6 | (Lu et al., 2011) |
| Ba _{0.95} Ca _{0.05} Co _{1-x} Fe _x O _{3-δ} | 9.3 | 2.8-12.0 | 850 | - | 0.10 | - | - | (Fujishiro et al., 2011; Yi et al., 2013) |
| Ba _{0.5} Sr _{0.5} Co _{0.8} Fe _{0.2} O _{3-δ} | 10.1 | 0-14.9 | RT-950* | - | 1.0 | - | - | (Sneha and Thangadurai, 2007) |
| Ba ₂ Fe ₂ O ₅ | 9.4 | 0-9.4 | 1000 | 1000 | 1.0 | 0 | - | (Dunstan et al., 2013) |
| BaCe _{0.9} Y _{0.1} O _{2.95} | 13.8 | 0-13.1 | 600-1000 | - | 1.0 | - | - | |
| Ba ₄ Sb ₂ O ₉ | 14.1 | 9.5-14.0 | 650-750 | 950 | 0.42 | 1 | 100 | |

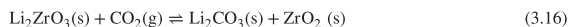
* indicates temperature programmed CO₂ capture experiments in a TGA.

To overcome the product layer diffusion resistances during carbonation, wet chemistry methods (e.g., impregnation suspension) are applied to synthesise Li₄SiO₄ with high surface areas (Yang et al., 2016a, b). With improved specific surface areas (1.65-2.09 m²/g), Li₄SiO₄ prepared by impregnation suspension afforded higher CO₂ uptake (up to 37 wt.%) and better cyclability (over 40 cycles) than those prepared by solid-state reactions (Yang et al., 2016b).

The CO₂ capture performance of Li₄SiO₄ can also be improved by metal doping. Low melting-point dopants, e.g. Na₂CO₃, K₂CO₃, NaNO₃ and KNO₃, can accelerate the migration of CO₂ through the Li₂CO₃ product layer (Seggiani et al., 2018; Wang, K. et al., 2019; Yang et al., 2016a). Alternatively, redox-active dopants, such as salts containing Fe³⁺, are able to promote the transport of O²⁻ through the Li₂SiO₃ shell (Lara-García et al., 2019). Some practical methods to introduce the dopants into Li₄SiO₄ sorbents include adding dopant precursors during the solid-state reactions (Chen, X. et al., 2016; Wang, Haiyang et al., 2018), impregnating the solid-state synthesised Li₄SiO₄ with soluble dopants, and conducting further solid-state synthesis between Li₄SiO₄ particles and the dopant precursors (Lara-García et al., 2019). Wang et al. (2018) chose acid-leached blast furnace slag, which contains TiO₂, Fe₂O₃, Al₂O₃, CaO and K₂O, as an economic and sustainable alternative for silicon precursor of Li₄SiO₄ (Wang, Haiyang et al., 2018). In many cases, doped Li₄SiO₄ showed many improvements, including higher specific surface area, enhanced CO₂ uptake (up to 35 wt.%) (Chen et al., 2016), improved cyclic stability (for up to 250 cycles) (Seggiani et al., 2018) and faster carbonation rate at lower temperatures and/or in lower CO₂ concentrations (Lara-García et al., 2019).

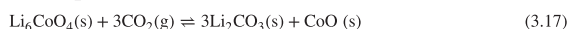
3.4.3.1.2. Other Li-based sorbents. Lithium zirconate (Li₂ZrO₃) is the second most studied Li based sorbent. It has a stoichiometric CO₂ capacity of 28.7 wt.% when used within a temperature range

of 450–650 °C:



Like lithium silicates, the carbonated Li₂ZrO₃ also exhibit a double-shell structure, with ZrO₂ and Li₂CO₃ forming the inner layer and the outer layer, respectively. Similarly, the CO₂ diffusion through the Li₂CO₃ layer is believed to be rate limiting. Li₂ZrO₃ can be prepared by a solid-state reaction between Li₂CO₃ and ZrO₂. However, solid-state synthesised Li₂ZrO₃ shows relatively slow carbonation and low capacities (5.9 - 10 wt.%) (Gómez-Garduño and Pfeiffer, 2019; Peltzer et al., 2018). Likewise, metal doping methods e.g. (i) doping low-melting point salts (Peltzer et al., 2018) (ii) doping redox-active Fe³⁺ chemicals (Gómez-Garduño and Pfeiffer, 2019), and (iii) impregnation suspension method (Peltzer et al., 2019) have been adopted to improve the performance of Li₂ZrO₃ sorbents. Both (i) and (iii) could effectively improve CO₂ uptake (20 - 22 wt.%), whereas the Fe-doping method gives marginal enhancements (7.0 - 9.2 wt.%).

Other Li-based ternary oxide phases have also been studied for CO₂ capture (Bernabé-Pablo et al., 2020; Blanco et al., 2018; Gaultois et al., 2018; Martínez-Cruz et al., 2020; Togashi et al., 2007; Yañez-Aulestia et al., 2020). Among these ternary oxides, Li₆CoO₄ shows the highest stoichiometric CO₂ capacity and experimental uptake of 80.0 and 74.5 wt.%, respectively (Bernabé-Pablo et al., 2020). Li₆CoO₄ reacts with CO₂ according to:



However, the CO₂ capture uptake of Li₆CoO₄ decreases quickly over cycles in the presence of O₂, reaching 30.5 wt.% after 10 cycles. This deterioration is attributed to the irreversible oxidation of Co²⁺ to Co³⁺ (Bernabé-Pablo et al., 2020). In contrast, for Li₅FeO₄, O₂ appears to accelerate the ion diffusion through the LiFeO₂ layer, improving its CO₂

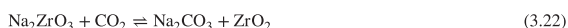
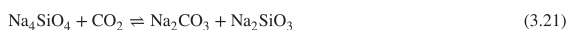
capture performance (Lara-García et al., 2019). Similar to lithium silicates and lithium zirconates, doping is an effective strategy to enhance the CO₂ capture performance of lithium-transition metal oxides. Several dopants, including second transition metal salts (e.g. Mn, Fe or Ni) (Martínez-Cruz et al., 2020) or alkali metal nitrates (MNO₃, M = Li, Na, K) (Yañez-Aulestia et al., 2020), were found to increase the CO₂ uptake and cyclic stability of Li₂CuO₂. Recently, Li₆WO₆ nanowires were developed and showed the capability to capture CO₂ at ambient temperatures in the presence of moisture, owing to the hydration and activation of Li₆WO₆, which promoted the carbonation kinetics. At 30 °C and with a relative humidity = 58 ± 3 %, Li₆WO₆ was able to achieve a CO₂ uptake of 7.6 wt.% within 1 min (Bernabé-Pablo et al., 2020).



Lastly, Li₃BO₃, with a stoichiometric CO₂ uptake capacity of Li₃BO₃ of 41.4 wt.% has shown an experimental CO₂ uptake of 35.4 wt.% (Harada and Hatton, 2017), through Reaction 3.17. However, the cyclic stability of Li₃BO₃ is inferior. Doping with NaNO₂ or KNO₂, which facilitates the formation of a molten layer, could accelerate product layer diffusion and the carbonation of Li₃BO₃. Interestingly, adding 10 mol % (Na-K)NO₂ achieved an experimental uptake of 47.2 wt.%, exceeding the stoichiometric capacity. The enhanced CO₂ uptake may have originated from the deeper carbonation, which was induced by the incorporation of alkali metal nitrites. Accordingly, Reactions 3.18 and 3.19 corresponds to improved stoichiometric uptake capacities of 69.1 and 55.4 wt.%, respectively.



3.4.3.2. Na-based sorbents. Na-based sorbents share similar chemical formulae with Li based ones. On one hand, Na-based sorbents are cheaper as Na is more earth abundant. On the other hand, Na based sorbents generally have lower stoichiometric CO₂ capacities than the Li equivalents in terms of weight percentage because Na is a heavier element. Experimentally, Na₄SiO₄, Na₂ZrO₃ and other Na based ternary oxides have shown promising CO₂ capture performance up to 850 °C:



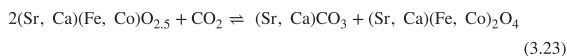
Similarly, Na based sorbents can be obtained by either solid-state reactions or wet-chemistry methods, e.g., sol-gel synthesis (Ji et al., 2017; Zhao et al., 2007), using several combinations of precursors, e.g. Na₂SiO₃ + NaOH (Liu et al., 2019), Na₂CO₃ + ZrO₂ (Martínez-dlCruz and Pfeiffer, 2012), and Na₂CO₃ + CoCO₃ (Vera et al., 2019). Na₄SiO₄ has a stoichiometric capacity of 23.9 wt.%, an experimental uptake of 19.2 wt.% at 840 °C, and a generally good performance above 750 °C (Liu et al., 2019). To improve the capture performance of Na₄SiO₄ at lower temperatures (< 700 °C), modification with alkali carbonates (M₂CO₃, M = Li, Na, K) could be a good choice, because the molten can accelerate the diffusion of O₂⁻ through the product layer (Liu et al., 2019). In particular, K₂CO₃-doped Na₄SiO₄ has shown a CO₂ uptake of 4.7 wt.% at 300 °C, doubling that of undoped Na₄SiO₄.

Unlike the silicates, the gas permeability through the product layer during the carbonation of Na₂ZrO₃ is higher. Therefore, the Na₂ZrO₃ sorbents do not appear to encounter serious product layer diffusion resistance, as shown in Fig. 3.48 (a) and (b). Ji et al. prepared Na₂ZrO₃ by a sol-gel method, and achieved an experimental uptake of 22.6 wt.%, (stoichiometric uptake = 23.8 wt.%), which lasted over 5 cycles (Ji et al., 2017). The authors attributed the high performance of Na₂ZrO₃ to the partly sintered product layer, which could form channels to facilitate fast sodium diffusion, as illustrated in Fig. 3.49c. For NaCoO₂, partially doping the Co sites with Fe could increase the CO₂ capture performance

by enhancing the redox activity and ionic conductivity of the sorbent. For instance, NaCo_{0.7}Fe_{0.3}O₂ showed increased uptake of 10.6 wt.% in 20 % CO₂ at 700 °C, while undoped NaCoO₂ could only achieve 3.3 wt.% (Vera et al., 2019). (Fig. 3.49)

3.4.3.3. Sr-based sorbents. SrO itself can be directly used as a CO₂ sorbent, functioning at temperatures > 1000 °C. Miccio et al. (2016) synthesised coarse SrO particles by calcining SrCO₃ and fine SrO particles by wet-granulation method (Fig. 3.50). Both SrO sorbents showed relatively high initial CO₂ uptakes of 37.1 and 30.5 wt.%, respectively. On the other hand, the capture capacities dramatically dropped after 5 cycles due to severe sintering. To increase the cyclic durability, it could be helpful to load SrO onto Al₂O₃ to form the thermally stable Sr₃Al₂O₆ and/or SrAl₂O₄ sorbents.

In fact, Sr-containing CO₂ sorbents are more often perovskite structured, where Sr occupies the A sites in the ABO₃ lattice. The CO₂ capture performance of the perovskites are greatly affected by both A and B site metals, which can be adjusted by changing the compositions of precursors during the sol-gel synthesis (Yang and Lin, 2006). For example, La_{0.1}Sr_{0.9}Co_{0.5}Fe_{0.5}O_{3-δ} is able to adsorb more CO₂ (17.3 wt.%) than Sr_{0.95}Ca_{0.05}Fe_{0.5}Co_{0.5}O_{3-δ} (4.37 - 8 wt.%) (Homonnay et al., 2002; Juhasz et al., 2001). Further changing Sr:Ca ratio to Sr_{0.5}Ca_{0.5}Fe_{0.5}Co_{0.5}O_{3-δ} could improve the uptake to 17 wt.% (Juhasz et al., 2001), owing to the formation of more ordered oxygen vacancies, which is considered to be helpful for CO₂ uptake (Homonnay et al., 2002; Nomura et al., 1996):



Lu et al. (2011) studied the effects of B-site occupancies for Sr based, perovskite structures. They prepared SrCo_{1-2x}(Fe,Nb)_xO_{3-δ} with equimolar Fe and Nb. The fresh SrCo_{1-2x}(Fe,Nb)_xO_{3-δ} sorbents had CO₂ uptake of 13.1 wt.% and 11.1 wt.%, when x = 0.05 and 0.10 respectively. The increased Nb occupancy of the B sites would reduce the carbonation activity due to the weakened basicity of the perovskite (Yi et al., 2010). Besides the perovskite-structured Sr-based sorbents, a Li₂SrTa₂O₇ sorbent having a Ruddlesden-Popper (RP) phase (A₂[A_{n-1}B_nO_{3n+1}]) was reported by Galven et al. (2010) to achieve 4.90 wt.% experimental uptake (with a stoichiometric capacity of 5.11 wt.%) at 140 °C, 30 bar. Additionally, the Li₂SrTa₂O₇ sorbent exhibited good cyclability after 5 carbonation-regeneration cycles.



3.4.3.4. Ba-based sorbents. Similar to Sr based sorbents, most Ba based sorbents are perovskite-structured oxides with Ba occupying the A sites. These sorbents can be prepared by either state reactions (Sneha and Thangadurai, 2007) or sol-gel synthesis (Nomura et al., 1996). The capture performance of the Ba based perovskites also depends on the metal site occupancies. For example, Nomura et al. (1996) discovered that if the Fe contents in (Ba_{0.95}Ca_{0.05})(Co_{1-x}Fe_x)O_{3-δ} is increased from 0.2 to 0.9, the CO₂ uptake will drop from 10.0 wt.% to 8.7 wt.%. The BaFeO_{3-δ} (0 < δ < 0.5) structures could switch phases between perovskite (ABO₃) and brownmillerite (A₂B₂O₅), representing oxygen uptake and release. It is believed that these phase changes are beneficial to the CO₂ capture performance. For instance, the thermal decomposition of perovskite structured Ba_{0.95}Ca_{0.05}Co_{0.8}Fe_{0.2}O_{3-δ} to brownmillerite in the absence of O₂ would improve CO₂ uptake of 12 wt.%; this phenomenon is in line with the findings of Lu et al. (2011) and Fujishiro et al. (2011) Like Sr based perovskites, doping B-sites with Nb will hinder the carbonation of Ba based perovskites as well. Yi et al. (2013) reported low CO₂ uptake (0 - 1.3 wt.%) of the Nb-doped BaFeO_{3-δ}. It is possible that the reduced performance may be related to the electron-donating behaviour of Nb dopant, which makes the perovskite sorbents more thermodynamically inert towards CO₂.

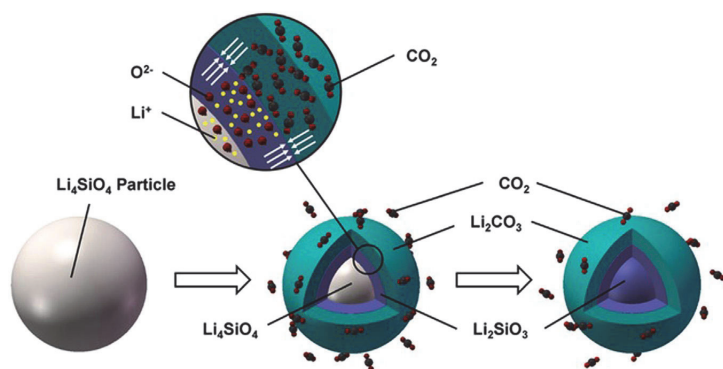


Fig. 3.48. Schematic illustration of the "double shell" model describing Li_4SiO_4 carbonation. Reprinted with permission (Yang et al., 2016b). (For interpretation of the references to color in this figure legend, the reader is referred to the web version of this article.)

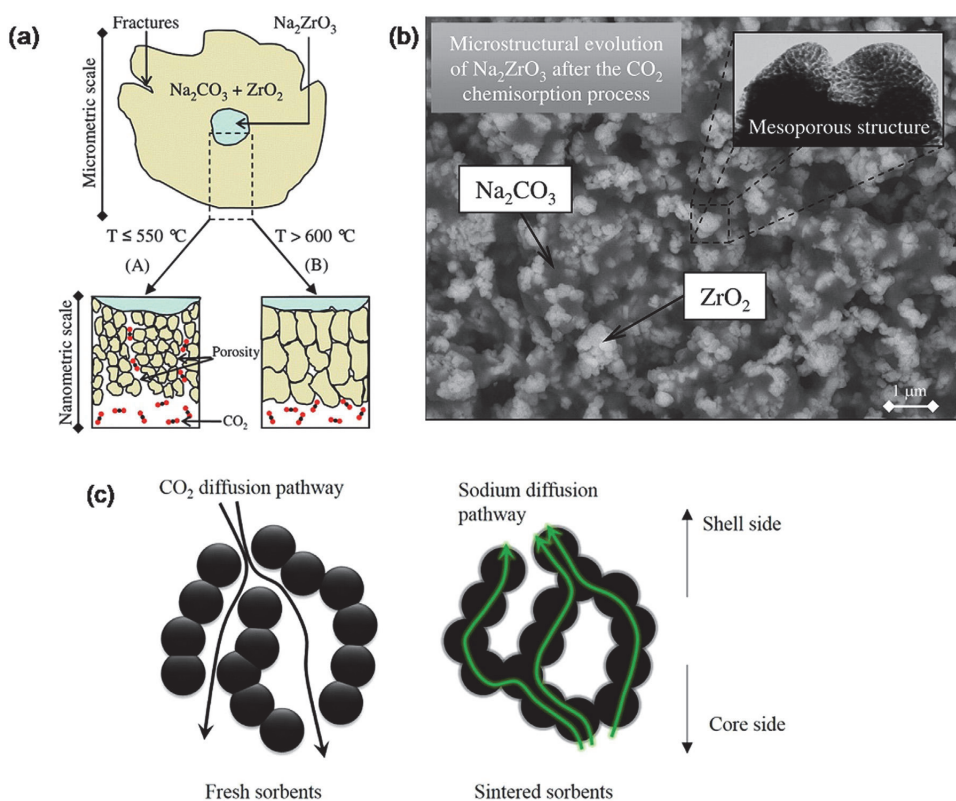


Fig. 3.49. (a) Scheme of the carbonation of Na_2ZrO_3 at different temperatures. Reprinted with permission (Martínez-dlCruz and Pfeiffer, 2012) (b) SEM image of growth of ZrO_2 and Na_2CO_3 after the carbonation of Na_2ZrO_3 . Reprinted with permission (Martínez-dlCruz and Pfeiffer, 2012) (c) Scheme of the CO_2 and Na^+ diffusion in fresh and sintered Na_2ZrO_3 sorbents. Reprinted with permission (Ji et al., 2017). (For interpretation of the references to color in this figure legend, the reader is referred to the web version of this article.)

The most outstanding Ba based sorbent so far is probably be the 6H-perovskite $\text{Ba}_4\text{Sb}_2\text{O}_9$ reported by Dunstan et al. (2013) $\text{Ba}_4\text{Sb}_2\text{O}_9$ has a stoichiometric capacity of 14.1 wt.%:



Experimentally, a near-stoichiometric CO_2 uptake of 13.8 wt.% was achieved at 750°C . During cyclic carbonation-regeneration, $\text{Ba}_4\text{Sb}_2\text{O}_9$ exhibited >10 wt.% CO_2 uptake over 100 cycles (Fig. 3.51a). The excellent cyclic stability of $\text{Ba}_4\text{Sb}_2\text{O}_9$ was attributed to its outstanding regenerability: its pore structure could be fully recovered after calcination in each cycle (Fig. 3.51b). The authors also discovered that $\text{Ba}_4\text{Nb}_{2-x}\text{Ta}_x\text{O}_9$

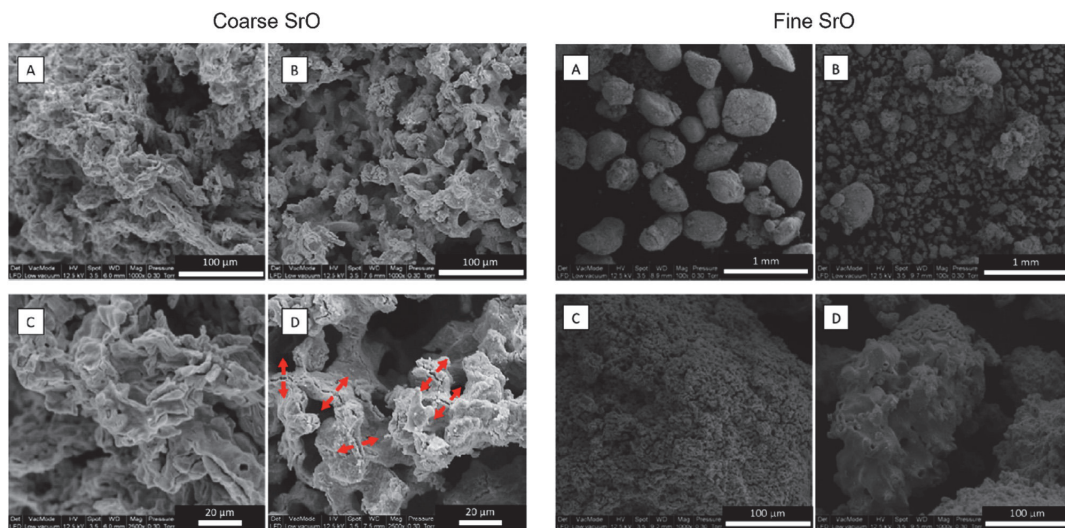


Fig. 3.50. SEM images of coarse and fine SrO particles before (A & C) and after (B & D) five cycles of carbonation–calcination at 1100 °C. Reprinted with permission (Miccio et al., 2016). (For interpretation of the references to color in this figure legend, the reader is referred to the web version of this article.)

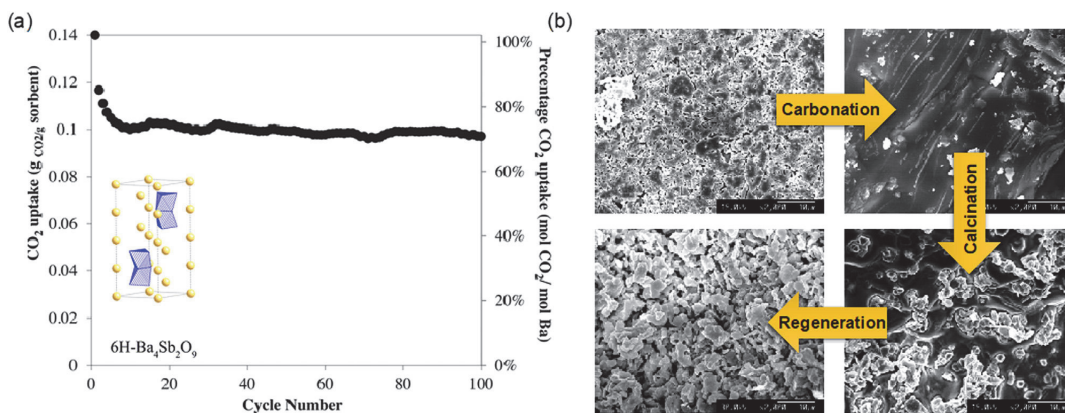


Fig. 3.51. (a) CO₂ uptake by 6H perovskite Ba₄Sb₂O₉ over 100 carbonation–calcination cycles in at TGA. (b) surface morphology Ba₄Sb₂O₉ as it evolves over carbonation–calcination cycles. Reprinted with permission (Dunstan et al., 2013). (For interpretation of the references to color in this figure legend, the reader is referred to the web version of this article.)

is a poor CO₂ sorbent, with only <0.07 wt.% in 100% CO₂ at 1000 °C (Dunstan et al., 2011).

4. Membrane based CO₂ capture

4.1. Polymeric membranes

4.1.1. Introduction for polymeric membranes CO₂ capture

Membrane technology (a thin interface that acts as a permselective for two-phase separation, typically in a range of 100 nm to a few micrometers) has emerged as one of the promising alternative technologies in CO₂ capture compared to the conventional gas–liquid contactors, due to their inherent attribution such as smaller footprint, simpler setup, and operation, energy-saving and do not involve in phase transformation (Fujikawa et al., 2020; Ramasubramanian et al., 2013). But still, the highly permeable membrane is a big challenge for efficient CO₂ capture. Thanks to the unique architectural properties of polymeric

chemistry, it has great potential to design a versatile membrane with outstanding properties for gas separation, especially for CO₂ capture (Robeson et al., 2009; Wang et al., 2016). Polymeric membrane technology has been used widely for CO₂ capture and is considered a next-generation technology for CO₂ capture due to its inherent properties such as cost-effectiveness, efficiency, separation performance, mechanical stability, and applicability for large scale-manufacturing (Feron and Jansen, 2002). Over the past decade, an extensive research quest has been devoted to the polymeric membrane with unprecedented transport properties for CO₂ capture from post-combustion (CO₂/N₂), syngas processing (CO₂/H₂), and natural gas sweetening (CO₂/CH₄).

One of the major challenges associated with the commercialization of membrane technology is the permeability and selectivity trade-off, i.e., high permeability is achieved always at the cost of lower selectivity and vice versa, for a specific component of the mixture. Robeson's proposed the empirical upper bounds limit in 1991 and updated the upper bounds in 2008 to explain such a limiting behavior (Robeson, 1991;

Table 4.1
Physical properties of CO₂, N₂, and CH₄

| Gas | Kinetic diameter/nm | Critical temperature/K |
|-----------------|---------------------|------------------------|
| CO ₂ | 0.330 | 304.1 |
| N ₂ | 0.364 | 126.2 |
| CH ₄ | 0.380 | 190.6 |

Robeson, 2008). The paradigm shift is desirable in developing a new polymer-based membrane to outreach the Robeson's upper bounds limit along with long-term stability to be able to mitigate a massive volume of CO₂ emission.

In this section, we will review the recent efforts of the membrane's main research theme to surpass Robeson's upper bond limit focusing on polymeric materials. The unique structural properties of polymeric materials exhibit high permeability of CO₂ with sufficient selectivity. We categorized polymeric-based membranes into two categories based on the transport mechanism, 1) solution-diffusion membranes, including polyethylene oxide (PEO) (copolymer membranes, blend membranes, crosslinking membranes), perfluoro polymers, polymers of intrinsic microporosity, thermally rearrange polymers; and 2) facilitated transport membranes, including Amin based membranes, RTIL and other carriers for facilitated transport membranes.

4.1.2. Solution - diffusion transport mechanism

The driving force in membrane separation is pressure or concentration gradient. Firstly, the gas molecules dissolve in the dense polymeric membrane at the higher-pressure side for non-reactive polymer, then diffuse across the membrane and desorb at the lower-pressure side. This simple approach to gas transportation is known as the solution diffusion transport mechanism. This mechanism can be expressed as a product of the solubility coefficient (S_x) and diffusion coefficient (D_x) term as permeability coefficient (P_x) (Doong et al., 1995).

$$P_x = S_x \times D_x \quad (4.1)$$

The permeability is commonly expressed in terms of Barrer, whereas 1 Barrer = 1 Barrer = $1 \times 10^{-10} \text{ cm}^3 (\text{STP}) \cdot \text{cm} \cdot \text{cm}^{-2} \cdot \text{s}^{-1} \cdot (\text{cm Hg})^{-1}$. The permeability is an inherent property of polymeric materials, as solubility is the thermodynamic affinity of materials toward gas and diffusivity is dependent upon the morphology of the material and the size of gas molecules. The separation performance of the membrane can be expressed in terms of the permeability of the membrane divided by the thickness of the membrane.

The separation efficiency of the membrane is described by selectivity. The selectivity of the membrane is termed as the ability of a membrane to separate one component from another component of the mixture. The ideal selectivity is the ratio of two gas (x, y) permeability as shown in the equation below, which can further be extended in terms of solubility selectivity and diffusivity selectivity as:

$$\alpha_{x/y} = \frac{S_x}{S_y} \times \frac{D_x}{D_y} \quad (4.2)$$

The perm selectivity is deeply rooted in the solubility or diffusivity of gas molecules into the polymeric membrane. The solubility selectivity is enthalpy driven, dependent upon the condensability (increase with the increasing critical temperature) of penetrant gas molecules in the polymer and the affinity of penetrant gas toward the polymeric membrane (Frisch, 1970; Zydney, 1995). The solubility of CO₂ is higher as compared to other gases due to its significantly high critical temperature, $T_{c, \text{CO}_2} = 304.1 \text{ K}$ shown in Table 4.1 (Bondar et al., 2000). The diffusivity selectivity kinetic diameter of penetrant gas molecules is dependent, and the gas molecules migrate through the free voids of polymer, which is the inherent characteristic of the polymer. The diffusivity selectivity of CO₂ is also higher as compared to other gases due to its smallest kinetic diameter, $d_k = 0.330 \text{ nm}$. The less packing density and chain to chain spacing allows penetrant molecules to diffuse. Typically, the diffusivity

increases with the decreasing in the kinetic diameter of gas molecules as well as increasing in free voids.

The fractional free volume (FFV) plays a vital role in the gas transport phenomenon in glassy polymeric membranes. Free volume is obtained during the condensation, as the less packing density leads to a more void not occupied by the polymer chain. Contrary to glassy polymer in rubbery polymer, solubility selectivity is more favourable (Lee, 1980). But the aging and plasticization of the membrane limit the fractional free volume and decrease the performance of the membrane (Du et al., 2011). It is required to mitigate such a challenge to fabricate an efficient and long-term durable membrane to move forward toward commercial applications.

4.1.2.1. PEO based polymeric membrane. Poly (ethylene oxide) (PEO) containing polymers have been extensively studied and shown a great potential to capture CO₂ due to their outstanding affinity toward CO₂ attributed to its dipole- quadrupole interaction between ethylene oxide (EO) group and CO₂ (Rindfleisch et al., 1996). Due to the inherent property of polar ether linkage (-c-c-o-) in PEO (rubbery polymer), it has a reasonable separation performance of CO₂ from other light gases. However, the limitation of PEO is its tendency toward crystallinity and film-forming ability due to its polar oxygen atoms, which are prone to reduce the free volume leading to the poor separation performance of CO₂, poor mechanical strength, and ultimately hampering their commercial applications (Sangroniz et al., 2021). Therefore the current effort of the researchers is to overcome the crystallinity constrain by cross-linking to form a highly branched polymeric network, copolymerization with the hard segment, and blending with the low MW polymer PEG, to enhance the separation performance as well as the thermal stability of the PEO based membrane. The PEO based membranes have been widely investigated via different synthesis approaches and some examples are summarized in Table 4.2.

PEO based copolymeric membrane. To overcome the limitation of crystallinity in the PEO based membrane is the copolymerization approach with the different rigid segments (Han and Ho, 2018). The transport properties of these membranes are controlled by altering the PEO phase and the unit length of soft and rigid segments (Yave et al., 2010). Luo et al. investigated the copolymer membranes of commercial polyether amines, pentiptycene-based diamine, and 6FDA, which exhibited high CO₂ gas permeability of 39 Barrer with CO₂/H₂ selectivity of 4.1 and CO₂/N₂ of 46 (Luo et al., 2016). The supramolecular chain threading and interlocking induced by the pentiptycene structures, effectively minimize the inherent crystallization ability of PEO, leading to an amorphous structure. Jankowski et al. synthesized a series of PEO based copolyimides with varying hard segment structures and found OPDA-ODA-PEO is the best copolyimide, with CO₂ permeability of 52 Barrer with CO₂/N₂ selectivity of 63 (Jankowski et al., 2021). A CO₂ selective copolymer based on aromatic poly ethers tethered with flexible PEO side chains was synthesized via polycondensation by Ioannidi et al. showing maximum CO₂ permeability of 11.2 Barrer along with CO₂/H₂ and CO₂/CH₄ ideal selectivity of 9.6 and 68 respectively surpassing the upper bond limit for H₂ (Ioannidi et al., 2021). An asymmetric TF-MMM with ZIF-8 in the copolymer of PVI-POEM was synthesized by Lee et al. observed high CO₂ performance of 4474 GPU with high CO₂/N₂ and CO₂/CH₄ ideal selectivity of 32 and 12.4, respectively (Lee et al., 2022).

PEO based crosslinked membrane. The crosslinking approach is also the best alternative to overcome the crystallinity limitation of PEO based membranes. The crosslinking strategy is the transformation to a highly branched polymer by the free radical polymerization of ethylene oxide monomers and oligomers. At the incipient, the crosslinked PEO based polymers were designed by the free radical polymerization of different methyl acrylate monomers. Another noticeable building block for designing of PEO crosslink network is the addition reaction of amino and epoxy groups shows a high separation performance as well as thermal stability (Lin et al., 2006). Zhang et al. explored the crosslinking of PEO with nitrogen-rich polyamines network (PAN-NH₂) to synthesized CO₂-

Table 4.2
Examples of polymeric-based membranes with their performances (solution diffusion mechanism).

| Material | p (CO ₂)/atm | T/°C | P (CO ₂)/Barrer | α (CO ₂ /N ₂) | α (CO ₂ /CH ₄) | References |
|---|----------------------------|------|-------------------------------|---|--|--------------------------------|
| PEO based polymeric membrane | | | | | | |
| HPEO ₂ -800 | 30 psig | 35 | 540 | 43 | 14 | (Zhang and Tran et al., 2022) |
| PAN-NH ₂ /PEO | 5bar | 35 | 1160 | 73 | 19.7 | (Zhang et al., 2022) |
| DME240-45 | 3bar | 35 | 1400 | 45 | - | (Guo et al., 2022) |
| STA-PEO | 0.5MPa | 35 | 1294 | 50 | - | (Li et al., 2022) |
| PEO/PDMS-PEGBEM | 1 bar | 35 | 240 | 34.6 | 12.2 | (Kang et al., 2021b) |
| PEO/PEGDEI 37 | 1 bar | 35 | 201.1 | 49.3 | 15.7 | (Min et al., 2021) |
| OPDA-ODA-PEO | 6 bar | 30 | 52 | 63 | - | (Jankowski et al., 2021) |
| PEGDME-500 | | | 2281.1 | 48.1 | - | (Li et al., 2019) |
| XLPP3-30 | 5 bar | 25 | 92 | 92 | - | (Motahari and Raisi, 2020) |
| PEO/PGP-POEM | 1 bar | 35 | 120.9 | 44.9 | 14.5 | (Kim et al., 2020) |
| XLPEO/C6-60 | 30 psig | 35 | 1340 | 48 | - | (Huang et al., 2020) |
| 1-GEF-M | 4 bar | 35 | 460 | 57 | 18 | (Liu, et al., 2022) |
| PVI-POEM -PZ-50 | 1bar | 30 | 4474 | 32 | 12.4 | (Lee et al., 2022) |
| PEO/PTMSP EFCM | 0.3MPa | 25 | 281 | 32.94 | - | (Zheng et al., 2022) |
| XLPEO | | 35 | 761.9 | 40.3 | 11.5 | (Cheng et al., 2020a) |
| Perfluoro based polymeric membrane | | | | | | |
| Teflon AF1600 | 1000kPa | 35 | 489 | | 12 | (Scholes et al., 2016) |
| Poly (PFMMD-co-CTFE) | 50psig | 22 | 44.3 | | 49 | (Fang et al., 2018) |
| PEBAXs 2533 | 350kpa | 35 | 1860 | 22 | - | (Schofield et al., 2016b) |
| F-SPEEK/Matrimid | 10 bar | 25 | 33.2 | 51.11 | 47.45 | (Asghar et al., 2018) |
| PEBAX 1657/P1 (60 wt%) | 350kpa | 35 | 226 | 39 | - | (Schofield et al., 2016a) |
| PIM-COOH-360h | | 30 | 96.43 | 53.6 | 25.2 | (Jeon et al., 2017) |
| PIM-1/SNW-1 | 2 bar | 30 | 7553 | 22.7 | 13.5 | (Wu et al., 2017) |
| PIM-1/PEG-POSS-10 | 1 bar | 30 | 1300 | 31 | 30 | (Yang et al., 2017) |
| PIM-TMN-Trip | | 31 | 16,500 | 11 | - | (Stanovsky et al., 2020) |
| PIM-SBI-Trip | 1bar | 25 | 35 600 | 15.4 | 7.74 | (Bezzu et al., 2021) |
| PIM-1/SBI-Trip | 1bar | 25 | 24 410 | 18.8 | 9.69 | (Wang et al., 2017) |
| PAO-PIM-1/NH ₂ -UiO-66 (30%) | 1bar | 35 | 8425 | 27.5 | 23.0 | (Wang et al., 2017) |
| 3-SCPIM-6/24 | 1 atm | 25 | 4008 | 58.1 | 40.9 | (Zhou et al., 2020b) |
| PIM-BM-70 | 50psi | 25 | 48.3 | 30.1 | 43.9 | (Chen et al., 2020) |
| PIM-MP-TB | 1 bar | 25 | 633 | 29.6 | 24.4 | (Williams et al., 2018) |
| PIM-1-450 | 3.5 atm | 35 | 40 | 40 | 110 | (He et al., 2020) |
| AOPIM-1-9 | 1 atm | 35 | 2483.6 | 31.2 | 30.1 | (Wang et al., 2020) |
| PIM-1/sPPSU-3.5 (98:2) | 3.5 atm | 35 | 3003 | 22.9 | 18.0 | (Kammakam et al., 2021) |
| TR polymeric based membrane | | | | | | |
| Im-PBO[onene] + [2-IL] | 2 atm | 20 | 44.7 | 34.1 | 51.9 | (Kammakam et al., 2021) |
| TR400-0 | 76 cmhg | 25 | 184 | 26 | 63 | (Suzuki, 2021) |
| 6F-AP-450 | 100 psi | 35 | 200.3 | | 28 | (Suzuki, 2021) |
| TR-coated PBOA | 0.5 Mpa | 25 | 24.0 gpu | 18.9 | 18.2 | (Ye et al., 2021) |
| ODA/APAF (3:7) | | | 127.4 | 20.6 | 34.2 | (Jia et al., 2022) |
| PIOAc30 | 3 bars | 30 | 1036 | 23 | 28 | (Aguilar-Lugo et al., 2021) |
| XTR-PBOI | 3 bars | 75 | 400 GPU | 20 | - | (Lee et al., 2017) |
| TR-PBOI-AD5 | | 25 | 481 GPU | 17.7 | - | (Woo et al., 2016a) |
| XTR425 | 1 atm | 35 | 271 | 20 | - | (Lee et al., 2019) |
| TR-PBOI-375 | | | 560 GPU | 16.8 | - | (Woo et al., 2016b) |
| 2D-diXTR | 3 bar | 35 | 4,590 GPU | 18.0 | - | (Lee, Jongmyeong et al., 2020) |
| 6F-TM-Ac-425 | 1 bar | 35 | 205 | 25 | 33 | (Hu, Xiaofan et al., 2020) |
| rGO-PBOI | 1 atm | 25 | 1784 GPU | 17.7 | 32.4 | (Kim et al., 2018) |

philic mixed matrix membrane, showing the excellent separation performance of CO₂ 1160 Barrer along with CO₂/N₂, CO₂/CH₄ selectivity of 73, 19.7 respectively, surpassing the Robeson's upper bond (2019) limit (Zhang et al., 2022). Recently, a highway built up in PEO based membrane via a solvothermal annealing approach, offered a superior CO₂ permeability of 1299 Barrer with CO₂/N₂ selectivity of 50 along with long-term stability of 110 h, beyond the Robeson's upper bond line (Li et al., 2022). The solvothermal annealing approach enhances the flexibility of PEO chain and rearranges the side chain, which is an essential tuning permanent to boost the membrane performance, opening a new dimension for PEO based membrane for CO₂ capture towards industrialization.

PEO based blended membrane. The blending approach with a low molecular weight (100–200) polymer like PEG is also a suitable strategy not only to circumvent the limitations of crystallinity but also to obtain superior separation performance and thermal stability (Chen et al., 2016b). The introduction of low MW polymer in the backbone of PEO leads the crystalline PEO to the amorphous materials with outstanding separation performance. In addition it provides another tun-

ing parameter to reduce the strong hydrogen bonding among the ether groups. Kang et al. synthesized an amphiphilic combo copolymer PDMS-PEGBEM via free radical polymerization and incorporated it into commercially available polymer PEO, resulting in extremely enhanced selectivity of CO₂/N₂ and CO₂/CH₄ from 0.78 and 0.71 to 41.7 and 13.3 respectively (Kang et al., 2021a)

4.1.2.2. Perfluoro based polymeric membrane. Perfluoro polymers are a fluorinated polymeric family, which attracted the most attention because of its mostly or all hydrogen atoms are replaced by fluorine atoms. The enrichment in strong C–F and C–C covalent bonds, transformed the per fluoropolymers to extremely thermally and chemically stable, which is the beneficial trait of this class of polymer to be a prospective candidate for commercial application (Merkel et al. 2006) Although it has a low tendency toward swelling because of its insolubility in many organic compounds and its semi-crystalline nature, it limits the applicability of perfluoro polymer in membrane advancement for gas separation (Prabhakar and Freeman, 2002). Since 1980, a new family of perfluoro polymers like Teflon AF, Hyflon AD, and Cytop polymers have been de-

signed for gas separation. The bulky dioxole monomer as a copolymer or cyclic homopolymer in these polymers reduces the chain mobility and crystallinity, leading to an amorphous polymer with exponential FFV, which renders the superior gas separation performance (Hellums et al., 1989; Tanaka et al., 1992). Fang et al. reported a new class of amorphous perfluorinated polymeric membranes to exhibit tuneable transport properties, which showed excellent separation performance for important gas pairs including CO₂/CH₄ (Wang et al., 2019). The summarized membrane performance mentioned is in Table 4.2.

4.1.2.3. Polymer of intrinsic microporosity-based membrane. In 2004 Budd and McKeown et al. introduced a new family of glassy polymers with a unique backbone feature having rigid ladder-like and contorted macromolecular structures, which are called polymers of intrinsic microporosity (PIMs) (Budd et al., 2004). The restricted chain rotation due to the absence of a single bonded chain in the backbone, kink chain, and their three-dimensional contorted conformation due to the tetrahedral carbon atom interaction with five-membered carbon rings, inhibit the macromolecules to effectively compact packing leads to the higher fractional free volume of typically 20% FFV (McKeown, 2012; Rose et al., 2017). Therefore, PIM exhibits unprecedented permeability with moderate selectivity of CO₂ in a CO₂/N₂ and CO₂/CH₄ mixture. These versatile features of PIM attract the attention of researchers to focus on the designing of highly permeable and selective membranes. In recent years many efforts have been employed to enhance the CO₂ selectivity of PIM-based membranes. Some are summarized in Table 4.2. Bezzu et al. synthesized polymer of intrinsic microporosity (PIMs) by blending with rigid and bulky triptycene to the spirobisindane (SBI) and showed excellent permselective for the CO₂/CH₄ and CO₂/N₂ gas pairs (Bezzu et al., 2021). A hybrid mixed matrix membrane of PIM with the metal-organic framework synthesized by Wang et al., 2021 exhibited excellent performance with CO₂ permeability of 8425 Barrer and CO₂/N₂ and CO₂/CH₄ selectivity of 27.5 and 23, respectively, surpassing the 2008 Robeson's upper bound (Bandeali et al., 2021). Recently, thermally self-crosslinked Bromo alkylated PIM-based membranes were constructed by Xiuling Chen and co-workers and treated for gas separation, indicating superior CO₂ permeability of 48.3 Barrer along with CO₂/CH₄ selectivity of 43.9 (Halder et al., 2018). Jeon et al. reported, highly carboxylate functionalized PIMs (HCPIMs), due to their smaller interchain distance and CO₂ affinity exhibited high separation performance for CO₂ separation with a selectivity of 53.6 for CO₂/N₂ separation (Zhou et al., 2019).

4.1.2.4. Thermally rearranged (TR) polymeric-based membrane. Park et al. first introduced a new concept of more rigid and planer macromolecules from ortho-functionalized polyimides or polyamides by thermal rearrangement, named thermally rearranged (TR) polymer (Park et al., 2007). The TR polymer engineered with an unprecedented inherent feature of bimodal narrow cavity distribution (3–10 Å) and structural rigidity led to a high free volume, which was attributed to the excellent gas separation performance of TR-based polymeric membranes (Chern et al., 1983; Zhuang et al., 2015). Several examples TR based polymeric membranes are listed in Table 4.2 with their transport properties for lighter gas pairs. The ortho-position hydroxy group of polyimides or polyamides thermally rearranged via polycondensation reaction and formed twisted rigid-rod structure with a uniform microporosity, i.e., Poly benzoxazole (PBO) or polybenzimidazole (PBI) (Calle et al., 2015; Kim and Lee, 2015). The intrinsic uniform and small size micropores, result in the TR polymer to outstanding rapid gas transportation along with high selectivity for lighter gas pairs (Budd and McKeown, 2010). These inherent properties of TR polymer can further modify by tuning the thermal treatment protocol to surpass Robeson's upper bound along with the major bottleneck of TR polymer such as fragility and brittleness for gas separation.

Many research endeavours have been done due to the unprecedented intrinsic property of TR polymer. Recently, a new TR polymer incorpo-

ration of ionic components to obtain a novel imidazolium mediated poly benzoxazole by Kammakakam et al. in order to enhance the gas separation performance (Kammakakam et al., 2021). Suzuki et al. synthesized a novel TR-PBI-silica hybrid membrane and found an outstanding gas separation performance for CO₂/CH₄ due to the enlargement in the FFV and d-spacing with size-selective CO₂/CH₄ free volume holes at polymer-silica interfacial region (Suzuki, 2021). Lugo et al. synthesized mixed matrix membrane (TROH and TROAc-MMMs), notably increasing the permeation of CO₂ with 1036 Barrer CO₂/N₂ and CO₂/CH₄ surpassing the 2008 Robeson's upper bound limit, with a selectivity of 28 for CO₂/CH₄ bit lower than the pristine TR-PBO membrane (Aguilar-Lugo et al., 2021). The thermal densification of the skin layer in the hollow fiber membrane of TR polymer hindered the permeance, and Lee et al. exploited this limitation by ultrathin skin layer. The crosslinking thermally rearranged diXTR hollow fiber, exhibits remarkable permeance of 4600 GPU with CO₂/N₂ selectivity of 18 (Lee et al., 2020).

4.1.3. Facilitated transport mechanism

Contrary to the solution-diffusion transport mechanism, membranes with a reactive carrier (amino group, -NH₂) which enhanced the reversible reaction between CO₂ and reactive carriers, refer to facilitated transport membranes (Schultz et al., 1974; Tong et al., 2017). The reactive carriers either be chemically embedded onto a backbone (fixed site carrier) or in the form of mobile carriers (mobile carriers) in a polymer matrix (Noble, 1990). Initially, CO₂ diffused into the polymer metrics, herein CO₂ reacts with the carrier and forms a CO₂-carrier complex at the high-pressure side, as due to the concentration gradient, it transports towards the low-pressure side by intramolecular diffusion (fixed-site carrier) or intermolecular diffusion (mobile carrier) where it released CO₂ and the reactive-carrier been regenerated back (Meldon et al., 1982).

While on the other hand, the small magnitude of inert gas molecules to the carrier transports through the membrane by the phenomenon of solution-diffusion mechanism. Worth noticeable that in the facilitated transport mechanism, the solution-diffusion mechanism is important. In general, the total CO₂ flux through the membrane is the combination of facilitated transport and solution diffusion transport mechanism, which can be represented by the following equation:

$$J_{CO_2} = \frac{D_{CO_2}}{l} (\Delta C_{CO_2}) + \frac{D_{Carrier+CO_2}}{l} (\Delta C_{Carrier+CO_2}) \quad (4.3)$$

Where, D_{CO_2} and $D_{Carrier+CO_2}$ are the diffusion coefficient of Fick's diffusion (solution-diffusion) and carrier-CO₂ complex diffusion (facilitated diffusion), respectively. The thickness of the membrane is represented as l . The above equation clearly shows that the reactive carrier can drastically increase the total flux in addition to the solution diffusion, which can be attributed to the outstanding performance of facilitated transport-based membranes. However, the strong interaction between carrier and CO₂ hindered the desorption of CO₂ at permeate side. Contrary to this weak interaction between carrier and CO₂, it induced additional CO₂ partial pressure due to the CO₂ saturation in the membrane, consequently having an adverse effect on the performance of the membrane. Therefore, it is required to optimize reaction kinetics and CO₂ loading capacity for the outstanding separation performance of facilitated transport-based membranes.

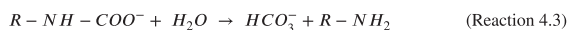
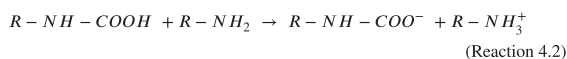
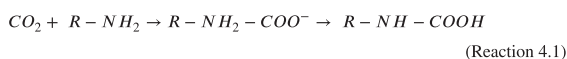
4.1.3.1. Amine-based polymeric membranes. The most investigated reactive carrier in the facilitated transport of CO₂ captures is amines. The inherent features of amines provide structural versatility with tuneable of fast reaction kinetics and the extraordinary capacity of CO₂ loading (Perinu et al., 2017). The chemistry of CO₂ and amines is shortly explained in this section. Primary and secondary amine (electron-rich) acts as a nucleophile and attacks the electron-deficient carbonyl group CO₂ from zwitterion as shown in the below Equation (Caplow, 1968). The immediate proton transformation of another amine zwitterions transforms to a stable carbamate and ammonium ion as shown in Reactions 4.1, 4.2 and 4.3, in the nutshell 2 mol of amines are required for 1 mol

Table 4.3

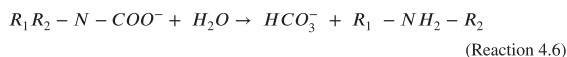
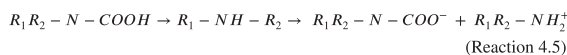
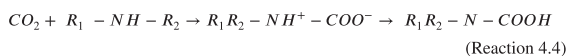
Examples of polymeric based membranes with their performances (facilitated transport mechanism).

| Material | $p(\text{CO}_2)/\text{atm}$ | $T/^\circ\text{C}$ | $P(\text{CO}_2)/\text{Barrer}$ | $\alpha(\text{CO}_2/\text{N}_2)$ | $\alpha(\text{CO}_2/\text{CH}_4)$ | Reference |
|--|-----------------------------|--------------------|--------------------------------|----------------------------------|-----------------------------------|--------------------------------|
| Amine-based polymeric membranes | | | | | | |
| 65/35 PG/PVAm | 1.5 psig | 57 | 1100 GPU | 200 | | (Chen et al., 2016a) |
| TFC-a-Tertiary amine | 0.11 Mpa feed pressure | 70 | 173 GPU | 70 | 37 | (Yu et al., 2010) |
| PEBAX/AFS-15 | 2 bar | 25 | 145 | | 28 | (Isanejad and Mohammadi, 2018) |
| PAA-C3H7/PVA | 2 atm F | 110 | 308.6 | 346.9 | | (Zhao and Ho, 2012) |
| zeolite Y/Biomax PES | 1 atm | 57 | 745 GPU | 25.4 | | (Zhaot et al., 2016) |
| PVAm/PG | | 57 | 1100 GPU | 140 | | (Chen, Y. and Ho, W.W. 2016) |
| poly (N-methyl-N-vinylamine) | 1 atm | 102 | 6804 | 350 | | (Tong and Ho, 2017) |
| PES | 4 atm | 67 | 1451 GPU | 165 | | (Han et al., 2019c) |
| HMMP-1 | 0.2 MPa | 298 K | 1544 GPU | 252 | | (Yuan et al., 2021) |

of CO_2 (Danckwerts, 1979). Hydrolysis of carbamate ions can occur at low PH to produce bicarbonate regenerating free amine. However, it is not favourable due to the stability of carbamate, as shown in the below Equation.



The sterically hindered amino group effectively contributes to fast reaction kinetics with CO_2 , leading to an equimolar stoichiometry between CO_2 and amine. Consequently, it increases the CO_2 loading capacity of amine (Sartori et al., 1983). The sterically hindered destabilized the carbamate intermediate by restricting the C-N bond in carbamate. As the carbamate is destabilized by the bulky substituted amino group, it forms bicarbonate, releasing the free amine as shown in the Reactions 4.4, 4.5 and 4.6.



A common polymer matrix that attracted much attention from a researcher is poly (vinyl alcohol) (PVA), polyvinyl amine (PVAm), and polyallylamine (PAA) for facilitated-based membranes. Some examples are summarized in Table 4.3. Chen et al. synthesized a polyvinyl amine (PVAm) based membrane featuring the fixed-site carrier also with different amino acid salts mobile carries for CO_2 facilitated transport, demonstrated a CO_2 permeance of 1100 GPU and selectivity of 200 for CO_2/N_2 (Chen et al., 2016b). Zhao et al. studied the steric hindrance effect on amine and observed that it has a great advantage to enhance CO_2 transport (Zhao and Winston Ho, 2012). A hindered polyamines cross-linked with polyvinyl alcohol and obtained polymeric membrane of the fixed-site carrier, which exhibits an outstanding transport property of 440 % enhancement in CO_2 permeability along with 311 % increment in CO_2/N_2 selectivity. The same group studied again a sterically hindered polyvinyl amine effect more comprehensively by Tong et al. (2017b) the modified poly (N-methyl-N-vinylamine) demonstrated superior performance of CO_2 permeability of 6804 Barrer with a selectivity

of 350 for CO_2/N_2 and 162 for CO_2/H_2 (Tong and Ho 2017b). Polyvinyl amine/piperazine glycinate membrane is fabricated by Chen and co-workers, consequently achieving the excellent performance of about 1100 GPU of CO_2 permeability and selectivity of 140 for CO_2/N_2 mixture, such high performance is attributed to the PVAm fixed-site-carrier whereas piperazine glycinate mobile carrier (Chen and Ho, 2016).

4.1.3.2. RTIL and other carrier based facilitated polymeric membranes. The designer solvent, room temperature ionic liquids (RTIL), nowadays are highly investigated as a potential candidate to replace other conventional materials, especially in CO_2 capture, due to its extraordinary features, such as low vapour pressure, high CO_2 uptake capacity, task-specific tuneable features, high thermally and chemical stability (Gan et al., 2011). These unique features supported ionic liquid-based membranes (SILMs) attracted much attention from a researcher for light gas separation. For instance, supported ionic liquid-based membranes have been investigated by Scovazzo et al. and exhibited an excellent separation with CO_2 permeability of 1000 Barrer along with the selectivity of 22 for CO_2/N_2 . The major challenges for SILMs are the leaching of ionic liquids at the low-pressure difference from the polymer matrix due to its weak interactions limiting their mechanical stability (Tomé and Marucho, 2016). To minimize these limitations, different approaches have been applied such as poly (ionic liquids) PIL by direct polymerization of IL monomers, embedding of IL into a compatible polymer matrix, and ion-gel membranes showing robust mechanical stability along with outstanding separation performance. For instance, Mannan et al. reported polyether sulfone/emim (Tf2N) ionic liquid polymeric membrane, observed 124-fold enhancement than the neat PES membrane, CO_2 permeability of 298.84 Barrer with 57.53 (3.6-fold enhancement) selectivity of CO_2/CH_4 (Mannan et al., 2016).

A small molecule of diamine and polyamine-based ionic liquid is used by Dai et al. to cross-link PEG diglycidyl ether (PEGDE) to obtain poly (ethylene glycol)-based epoxy-amine networks, exhibiting good separation performance due to CO_2 -phillic ionic liquids along with robust mechanical strength due to the cross-linking. Moghadam et al. fabricated an interesting double-network ion-gel membrane of triethyl (2-methoxymethyl) phosphonium indazole ([P222 (101)] [Inda]), displaying an excellent CO_2 separation performance and excellent mechanical strength. By tuning the cross-linking loading, the impact of CO_2 separation performance significantly increases such as 4 mol% loading showing CO_2 permeability of 2254 Barrer with 210 selectivity of CO_2/N_2 (Moghadam et al., 2017). Ionic liquid based epoxy-amine ion gel membrane designed by M.McDaniel et al. for fixed-site-carrier facilitated transport of CO_2 (Kasahara et al., 2014). The CO_2 -phillic free RTIL carrier in membranes enhances the CO_2/N_2 separation performance of epoxy-amine ion-gel membrane drastically and surpasses the 2008 Robeson's upper bound limit. Ionic liquids featured with highly CO_2 -phillic functional groups make them more interesting alternatives for CO_2 separation. Its CO_2 -phillic functional groups lead it to a highly facilitated transport for CO_2 as well as also provide a solution-diffusion transport effect. Zhang et al. first introduced diamine-monocarboxylate-based protic ionic liquids (PILs) as a supported ionic liquid membrane

(SILMs), exhibit an excellent separation performance of CO₂ permeability of 3028 Barrer with ideal selectivity of CO₂/N₂ and CO₂/CH₄ is 151 and 72 respectively (Zhang et al., 2017a). A series of imidazolium based phenolate ionic liquid feature with dual sites of interaction with CO₂ reported by Zhang et al. The outstanding separation performance of CO₂ permeability of 2540 Barrer with ideal selectivity of CO₂/N₂ of 127, such an excellent performance is attributed to facilitated transport of CO₂ from carbene to phenolated anion based on theoretical calculations (Zhang et al., 2019).

Beyond the amine and RTIL, many other carriers also have been widely investigated for CO₂ separation and show a vibrant separation performance with mechanically stable such as nanotube, GO, nanoparticles, etc. A novel nanotube-reinforced facilitated transport membrane is fabricated by Han et al., a selective layer of 170 nm coated on the polyether sulfone substrate demonstrates a CO₂ permeance of 975 GPU along with a CO₂/N₂ ideal selectivity of 140 (Han et al., 2018). This excellent separation performance is attributed to the amino group bound to the polymer backbone acting as a fixed-site carrier and 2-(1-piperazinyl) ethylamine as a mobile carrier. Zhang et al. reported a mixed matrix membrane (MMMs) by introducing amino silane functionalized graphene oxides (f-GO) nanosheet into the Pebax polymer matrix, demonstrating a high CO₂ permeability of 934.3 Barrer along with CO₂/CH₄ and CO₂/N₂ ideal selectivity of 40.9 and 71.1 respectively (Zhang et al., 2019b). The amino groups on graphene oxides introduce facilitated transport effects in the MMMs, leading to surpassing Robeson's upper bound limit. An interesting hollow fiber thin film composite membrane with a three-phase hybrid facilitated transport effect (host polymeric matrix feature with fixed-site carriers, 2D-GO filler, CO₂-reactive mobile carrier) is investigated by Janakiram, showed a CO₂ permeance of 825 GPU with CO₂/N₂ and CO₂/CH₄ separation factor of 31 and 20 respectively (Janakiram et al., 2020).

Although much research focus has been made to explore the efficient membrane for CO₂ separation still far to make it applicable for industrial applications. In view of the exponential increment of carbon dioxide levels in the atmosphere, a high efficiency, low cost, energy effective, and stable membrane is required urgency.

4.2. Mixed matrix membranes

Although polymeric membranes have been extensively investigated for gas separation due to their inherent features such as low costs, mechanical stability and easy processability, they are hindered due to their trade-off relationship between selectivity and permeability for industrial application (Sanders et al., 2013). Many researchers have devoted an effort to the advancement of polymeric materials like thermally rearranged polymer (TR) (Meis et al., 2022) and polymer of intrinsic microporosity (PIMs) (Zhou et al., 2020a) as discussed in the above section, proved its potential to surpass Robeson's upper bound.

However, in the past few decades, mixed matrix membranes (MMMs) gained much attention from researchers due to their outstanding property to surpass Robeson's upper bound limit (Katare et al., 2023). In 1970, Paul and Kemp reported MMMs of zeolite 5 Å into polydimethylsiloxane (PDMS) for the first time (Paul and Kemp, 1973). MMMs generally comprise inorganic fillers dispersed into a polymeric matrix that exhibit excellent permeability and selectivity for gas separation (Zornoza et al., 2015). MMMs featured with the dispersed phase (inorganic-fillers) provide the selectivity and continuous phase (polymer matrix) enhanced permeability and mechanical strength. MMMs are potential alternatives to a conventional polymeric membrane to overcome the trade-off between permeability and selectivity for gas separation.

Generally, the transport behaviour of small gas molecules through membranes depends upon the pore size of the porous membrane and solubility or reactivity in the case of the dense membrane, as explained in the above section (Kanehashi and Nagai, 2005). However, the transport property of MMMs is dependent upon many factors such as the compatibility of filler and polymer matrix, loading of filler, size, and

shape of filler, etc. Maxwell model is a well-known model for the prediction of the transport mechanism of gas through MMMs for low loading and good compatibility between polymer and filler (Kanehashi et al., 2015). For higher loading and ideal morphology, Lewis-Nielsen models are more appropriate (Lewis and Nielsen, 1970). Many inorganic fillers such as carbon molecular sieves (CMS) (Rafizah and Ismail, 2008), graphene oxides (GOs) (Li et al., 2015), zeolite imidazolate framework (ZIFs) (Yuan et al., 2017), metal-organic framework (MOFs) (Fu et al., 2016), covalent organic framework (COFs) (Fan et al., 2021) are investigated as filler into a polymeric matrix for gas separation. Recently, Fan et al. reported an interesting approach to enhance MOF/polymer interaction. However, it affects the permeability and selectivity of MMMs (Fan et al., 2022b). Deng et al. reported the effect of the morphology of filler (ZIFs 0D, ZIFs 1D, and ZIFs 2D) on the performance of MMMs (Deng et al., 2020a). Zhang et al. investigated 2D MFI nanosheet as a filler in Pebax polymeric matrix showing an excellent CO₂ permeability of 159.1 Barrer with a selectivity of 27.4 for CO₂/CH₄ (Zhang et al., 2021b). Yoo et al. studied defects in metal-organic frameworks, a highly porous defect-engineered UiO-66 incorporated into PEGDA exhibit superior CO₂ permeability of 470 Barrer with CO₂/N₂ selectivity of 41 (Lee et al., 2021b). Although by incorporating different and effective fillers into an appropriate polymer matrix we can achieve high separation performance, the defects exist at the polymer and filler interface. Therefore, evenly dispersion of fillers and appropriate fillers are still existing challenges for the researchers.

The separation of H₂/CO₂ is extremely difficult due to its kinetic diameters (Zhu, L et al., 2019). However, the exponential separation performance, sieving effects, high thermal, chemical, and mechanical stability of MMMs is extensively investigated for H₂/CO₂ or CO₂/H₂ separation. In this section, we discussed the pre-combustion and post-combustion CO₂ capture through MMMs.

4.2.1. Mixed matrix membranes for pre-combustion CO₂ capture

The separation of CO₂ or H₂ before the combustion is an effective strategy to limit the CO₂ concentration level in the atmosphere, generally termed pre-combustion CO₂ capture (Babu et al., 2016). After the water gas shift reaction, a mixture of CO₂/H₂ is obtained with high temperature and high pressure from the IGCC system (Kanniche et al., 2010). Membrane technology is a promising alternative to the conventional separation technologies such as cryogenic distillation, chemical absorption, and physical sorption. Membrane materials must be considered especially for pre-combustion separation. MMMs have the potential to sustain such extreme conditions due to their thermal and mechanical stability. For precombustion CO₂ capture, the membrane must either be H₂ selective or CO₂ selective (Al-Rowaili et al., 2023). We categorized MMMs as H₂ selective and CO₂ selective. H₂ selective membranes have been investigated mostly, which might be due to the increasing demand for pure hydrogen fuel. Among the polymer classes polybenzimidazole (PBI) exhibit excellent H₂/CO₂ selectivity. However, permeation is not significant (Zhu et al., 2017). MMMs provide an interesting window for such a polymer to enhance the permeability along with reasonable selectivity by incorporation of suitable fillers. For example, recently, Etxebarria-Benavides et al. studied the effect of zeolitic-imidazolate framework (ZIF-8) filler into the polybenzimidazole (PBI) matrix, found superior H₂ permeance of 65 GPU to 170 GPU with ideal selectivity of 18 for H₂/CO₂ at 150 °C and 7 bar (Etxebarria-Benavides et al., 2020). Asymmetric PBI/ZIF-8 MMMs with 1 μm skin layer designed by Sanchez-Lainez et al. exhibit unprecedented H₂ permeability of 20.3 GPU and H₂/CO₂ ideal selectivity of 35.6 at 250 °C and 6 bar (Sánchez-Lainez et al., 2018). Cheng et al. work on Zn/CO zeolitic imidazolate framework filler into a PEBAX polymer matrix to fabricate CO₂ selective MMMs showing CO₂ permeability of 102.5 Barrer along with 9.4 CO₂/H₂ selectivity (Cheng et al., 2020b).

Metal-organic frameworks (MOFs) are also emerging material that has been reported as filler due to their pore size and functional groups giving superior gas transportation property (Lin et al., 2018). Friebe

et al. fabricated NH_2 -MIL-125 MOF layer MMMs for shown enhanced selectivity and H_2 permeability (Friebe et al., 2016). The morphology of fillers is also a good tuning property to enhance the separation performance of MMMs. Kang et al. reported an effect of filler morphology on membrane performance. $\text{PBI}/[\text{Cu}_2(\text{ndc})_2(\text{dabci})\text{In}]$ MMMs with different morphology (bulk crystal (BC), nanocube (NC), and nanosheet (NS)), stacking orientation of NS MOF in MMMs provide a CO_2 barrier and enhance the H_2/CO_2 selectivity of 26.7 along with the H_2 permeability of 6.13 Barrer (Kang et al., 2015). Ashtiani et al. demonstrated defect-free CO_2 selective MMMs by dispersing UiO-66- NH_2 (MOF) into a polyethyleneimine (PEI) (Ashtiani et al., 2021). Interestingly polymer-filler interfacial interaction enhanced by covalently bounding polyvinylpyrrolidone (PVP) with polymer and filler, exhibit CO_2 permeability of 394 Barrer along with a 12.7 separation factor. Ma et al. demonstrated ZIF-7@PI MMMs as a superior H_2 performance of $3.0 \times 10^{-7} \text{ molm}^{-2}\text{s}^{-1}\text{Pa}^{-1}$ with 128.4 of separation factor for H_2/CO_2 and 91.5 for H_2/CH_4 due to the high channelling effects of ZIF-7 (Ma et al., 2019). Mei et al. modified the ZIF-8/Polysulfone MMMs with polydopamine, which enhanced the performance of MMMs showing H_2 permeability of 23.3 along with the selectivity of 9.3 for H_2/CO_2 (Mei et al., 2020). MMMs can thus be considered as a next-generation membrane for pre-combustion and post-combustion CO_2 capture due to their potential for industrial application. The novel design of inorganic fillers, such as MOFs, COFs, GOs, ZIFs, etc., makes this area more attractive.

4.2.2. Mixed matrix membranes (MMMs) for post-combustion carbon capture

MMMs containing dispersed inorganic fillers in continuous polymer matrices have emerged as an effective and versatile platform to obtain superior CO_2/N_2 separation properties for post-combustion carbon capture (Buddin and Ahmad, 2021; Hu et al., 2022b). The addition of nanofillers may also improve physical and chemical stabilities against plasticization and aging (Ahmad et al., 2020; Chi et al., 2019; Smith et al., 2020; Zhao et al., 2019). More importantly, the diversity of polymers and fillers offers enormous possibilities for designing membranes with desirable properties (Budhathoki et al., 2019).

A variety of functional polymers have been used as polymer matrices to construct MMMs to achieve superior CO_2/N_2 separation properties (Han and Ho, 2020; Hu et al., 2022b; Hu et al., 2018; Lee and Gurkan, 2021), including glassy polymers such as PIMs (Chen et al., 2021; Fan et al., 2022a; Shen et al., 2019) and polyimides (Hu et al., 2020; Jiang et al., 2021; Wang, Hongliang et al., 2018), and rubbery polymers such as Pebax (Nadeali et al., 2019; Sanaeepur et al., 2019; Thankamony et al., 2019), Polyactive (Rahman et al., 2018; Sabetghadam et al., 2019), and polyethers (Alebrahim et al., 2022; Hu et al., 2018; Liu et al., 2020). Polymers containing fixed CO_2 carrier sites, including poly(vinyl alcohol) (PVA) (Cao et al., 2019; Gao et al., 2018; Jia et al., 2020) and poly(ionic liquids) (PILs) (Dunn et al., 2019; Lee and Gurkan, 2021; Yang et al., 2022) were also used to realize facilitated transport for CO_2 , but not for N_2 .

Porous or non-porous fillers can be used to create MMMs, while most studies focus on porous nanofillers with well-designed pores, such as metal-organic frameworks (MOFs) (Hu et al., 2018; Knebel et al., 2020), metal-organic polyhedra (MOPs) (Guo et al., 2021; Liu et al., 2020), porous organic frameworks (POFs) (Duan et al., 2019; Zhang et al., 2022), and two-dimensional (2D) nanosheets (Shi et al., 2021; X X Li et al., 2019). These porous fillers have high porosities that can tremendously improve gas diffusivity and solubility or well-controlled pore sizes that exhibit precise cut-off between CO_2 and N_2 . Non-porous fillers with affinities towards CO_2 have also been used to improve CO_2 solubility and CO_2/N_2 solubility selectivity (Matteucci et al., 2008; Zhu, L et al., 2019). Additionally, non-porous fillers might disrupt polymer chain packing, increasing free volume and thus gas diffusivity (Hu et al., 2020; Merkel et al., 2002). Typical non-porous fillers include silica (SiO_2) (Aghaei et al., 2018; Hu et al., 2020), metal oxide (MO_x)

(Qiu et al., 2022; Sanaeepur et al., 2019), and polyhedral oligomeric silsesquioxane (POSS) (Kanezashi et al., 2019; Ren et al., 2019).

In addition to the rapid growth of advanced materials, various empirical models are employed to describe gas transport properties in MMMs, such as the Maxwell model, modified Maxwell model, Lewis-Nielsen model, and Kang-Jones-Nair model (Hoang and Kaliaguine, 2013; Monsalve-Bravo and Bhatia, 2018). Computational simulations have also been applied to predict the structure/property relationship in MMMs, such as molecular dynamics simulation (Erucar and Keskin, 2016), Monte Carlo simulation (Harami et al., 2019), computational fluid dynamics calculation (Kattula et al., 2015; Safaei et al., 2021), and artificial neural network model (Rezazakemi and Mohammadi, 2013; Rostamizadeh et al., 2013).

Despite tremendous progresses made in the last decades, the MMMs are faced with key challenges for practical applications, including particle agglomeration, interfacial incompatibility, brittleness, and poor thin-film formability. This section will highlight various strategies to address these challenges for the MMMs containing porous nanofillers, as well as the improvement of CO_2/N_2 separation properties. Tables 4.4 and 4.5 record separation properties for the key materials and thin-film composite (TFC) membranes developed, respectively.

4.2.2.1. MOF-based MMMs. MOFs have well-controlled apertures with sizes similar to gas molecules, such as ZIF-8 (3.4 Å) (Hu et al., 2018) and ZIF-90 (3.5 Å) (Huang et al., 2010). However, MOFs have flexible structures and show “gate-opening” behavior, leading to lower intrinsic CO_2/N_2 selectivity than most polymers (Bondorf et al., 2022; Ryder et al., 2014). Consequently, the MOF-based MMMs confine to the trade-off between CO_2 permeability and CO_2/N_2 selectivity, though their separation properties can still be described by empirical models such as the Maxwell model. Additionally, polymers (particularly glass polymers) do not have affinities towards MOFs, generating interfacial defects that can degrade separation performance and mechanical properties.

Compared to the blending of polymers and MOFs to form MMMs, *in-situ* growth of MOF nanoparticles (NPs) in polymers or *in-situ* polymerization of polymers provides an effective approach to improve interfacial compatibility by wetting the NPs with the polymers or precursors (Hu et al., 2022a; Park et al., 2020). Moreover, *in-situ* growth of the NPs can effectively control the NP sizes and avoid their aggregation (Ma et al., 2019). The NP sizes and shapes (or dimensions) can also be optimized to improve gas separation performance. Interestingly, low loadings of the NPs with optimized morphologies were reported to unexpectedly increase gas permeability because of the percolation networks formed by the highly porous NPs (Ashtiani et al., 2021; Chi et al., 2019).

Creating strong interactions between MOFs and polymers can efficiently enhance interfacial compatibility (Hu et al., 2022b). Specifically, the surface of the MOF NPs can be modified to exert affinities towards the polymer phase (Guo et al., 2019; Jiang et al., 2021; Lee, Jooyeon et al., 2020). For example, Fig. 4.1a shows that the ZIF-8 was modified using dopamine (a bio-inspired adhesive) before mixing. The addition of ZIF-8-DA substantially increased gas permeability without reducing selectivity (Fig. 4.1b,c), breaking the permeability/selectivity trade-off.

The surface of the ZIF-67 NPs was functionalized with N-heterocyclic carbene ligands to achieve excellent mechanical and separation properties (Knebel et al., 2020). Polymer chains can also be grafted onto the MOF surface, acting as brushes and generating favourable interactions with the polymer (Wang et al., 2018). Compatibilizers like ionic liquids (ILs) were also used to modify the MOF surface (Lu et al., 2021). Additionally, the MOF was even used to cross-link polymers to improve both interfacial compatibility and size-sieving ability. For example, UiO-66 NPs were functionalized with nitrile groups and then covalently bonded to PIM-1 by thermal treatment (Yu et al., 2019). The cross-linking with 20 wt% UiO-66 increased CO_2 permeability by 4 times to 12,000 Barrer and CO_2/N_2 selectivity by 2 times to 54 at 25 °C.

Table 4.4
CO₂/N₂ separation performance of representative MMMs.

| MMMs | | | T (°C) | CO ₂ permeability (Barrer) | CO ₂ /N ₂ selectivity | Ref. |
|-----------------------|-----------------------------------|----------------|--------|---------------------------------------|---|---------------------------|
| Polymers | Fillers | Loading (wt.%) | | | | |
| PEGDA-co-PEGMEA | - | 0 | 35 | 424 | 33 | (Ma et al., 2019) |
| | ZIF-8 | 49.7 | | 910 | 33 | |
| | ZIF-7 | 34.3 | | 1084 | 38 | |
| XLPEGDA | - | 0 | 35 | 130 | 50 | (Hu et al., 2018) |
| | ZIF-8 | 50 | | 1300 | 33 | |
| 6FDA-DAM | - | 0 | 35 | 970 | 18 | (Chi et al., 2019) |
| | HKUST-1 | 30 | | 2360 | 16 | |
| sPIM-1 | - | 0 | 25 | 5929 | 24 | (Yu et al., 2019) |
| | UiO-66-CN | 20 | | 12063 | 54 | |
| XLPEO | UiO-66-H | 30 | 35 | 70 | 49 | (Lee et al., 2020) |
| | UiO-66-Vinyl | 30 | | 110 | 47 | |
| | UiO-66-NO ₂ | 30 | | 115 | 44 | |
| | UiO-66-Naph | 30 | | 82 | 47 | |
| ODPA-DAM | - | 0 | 35 | 65 | 17 | (Wang et al., 2018) |
| | UiO-66-NH ₂ @PI | 27 | | 142 | 27 | |
| PIM-1 | - | 0 | 20 | 7062 | 10 | (Lu et al., 2021) |
| | UiO-66-NH ₂ @IL | 10 | | 8283 | 23 | |
| XLPEGDA | - | 0 | 35 | 110 | 55 | (Liu et al., 2020) |
| | MOP-3 | 50 | | 480 | 42 | |
| XLPDXLA | - | 0 | 35 | 190 | 70 | (Zhang et al., 2022) |
| | MOP-3 | 30 | | 580 | 62 | |
| XLPEO | - | 0 | 35 | 440 | 35 | (Zhang et al., 2022) |
| | COF | 6-9.6 | | 804 | 61 | |
| 6FDA-DAM | - | 0 | 25 | 812 | 25 | (Cheng et al., 2019) |
| | COF300 | 7 | | 1205 | 33 | |
| | COF@PEI | 10 | | 1154 | 49 | |
| PIM-1 | - | 0 | 35 | 4500 | 14 | (Li et al., 2019) |
| | Azo-COP-2 | 15 | | 10,500 | 12 | |
| Pebax®1657 | - | 0 | 20 | 53 | 51 | (Thankamony et al., 2019) |
| | CTPP | 0.025 | | 73 | 79 | |
| PTMSP | - | 0 | - | 43,000 | 7 | (Smith et al., 2020) |
| | p-DCX | - | | 42,000 | 12 | |
| Pebax®1657 | - | 0 | 25 | 94 | 32 | (He et al., 2019) |
| | POP-PGO | 2 | | 233 | 81 | |
| Pebax®1657/ PEGMEA | - | 0 | 35 | 590 | 43 | (Shin et al., 2019) |
| | GO | 0.3 | | 610 | 56 | |
| Pebax®1657 | - | 0 | 25 | 125 | 65 | (Shamsabadi et al., 2017) |
| | AS-TiO ₂ | 3 | | 189 | 85 | |
| | CMC-TiO ₂ | 3 | | 195 | 82 | |
| | - | 0 | | 67 | 28 | |
| ODPA-TFMB | - | 0 | 35 | 210 | 31 | (Hu et al., 2020) |
| | SiO ₂ -NH ₂ | 20 | | 210 | 31 | |
| XLPEO | - | 0 | 35 | 520 | 52 | (Alebrahim et al., 2022) |
| | LiClO ₄ | 2 | | 710 | 53 | |
| Pebax®1657 | - | 0 | RT | 71 | 30 | (Deng et al., 2020b) |
| | ZIF-C | 20 | | 387 | 47 | |
| Pebax®1657 | - | 0 | 35 | 96 | 39 | (Zhang et al., 2019a) |
| | f-GO | 0.9 | | 934 | 71 | |

Table 4.5
CO₂/N₂ separation performance of representative TFC membranes based on MMMs.

| MMMs | | | | Gutter layer | T (°C) | CO ₂ permeance (GPU) | CO ₂ /N ₂ selectivity | Ref. |
|--------------|-------------------------|-----------------|----------------|--------------|--------|---------------------------------|---|--|
| Polymers | Fillers | Loading (wt.%) | Thickness (μm) | | | | | |
| Pebax 1657 | ZIF-8 | 30 | ~1.5 | PTMSP | 25 | 350 | 31 | (Sutrisna et al., 2017; Sutrisna et al., 2018) |
| | ZIF-7 | 30 | 1–1.5 | | | 300 | 48 | |
| | UiO66-NH ₂ | 50 | 1–1.5 | | | 340 | 57 | |
| PEGDME | NH ₂ -MIL-53 | 47.4 | 4.9 | None | 35 | 560 | 35 | (Xie et al., 2018) |
| PIM-1 | MOF-74-Ni | 10 | 0.65 | PDMS@aMOF | 35 | 1200 | 30 | (Liu et al., 2020) |
| PGMA-co-POEM | UiO-66-NH ₂ | 28.6 | <0.1 | PTMSP | 25 | 1300 | 31 | (Kim et al., 2019) |
| PEGDMA | EG3-MOP | 5 | ~0.29 | PTMSP | 35 | 300 | 16 | (Sohail et al., 2021) |
| Pebax 1657 | GO/IL | 0.05 | ~0.1 | PTMSP | 25 | 900 | 45 | (Huang et al., 2018) |
| Pebax 1657 | MXene | 0.05 | 0.07 | PTMSP | 25 | 1360 | 31 | (Shamsabadi et al., 2019) |
| PSF | Montmorillonite | NA ^c | 0.1 | None | 50 | 800 | 125 | (Qiao et al., 2016) |
| PA | MIL-101 (Cr) | NA | 0.2 | PDMS | NA | 930 | 220 | (Wang et al., 2020) |
| PIL-IL | GO | ~1 | 0.9 | None | 22 | 3090 | 1180 | (Lee and Gurkan, 2021) |
| PVAm | PEI-g-ZIF-8 | 16.7 | 0.33 | None | 30 | 2000 | 80 | (Gao et al., 2018) |
| PVAm | HMP (F) | NA | ~0.3 | PDMS/PVA | 25 | 1800 | 65 | (Wang et al., 2020) |

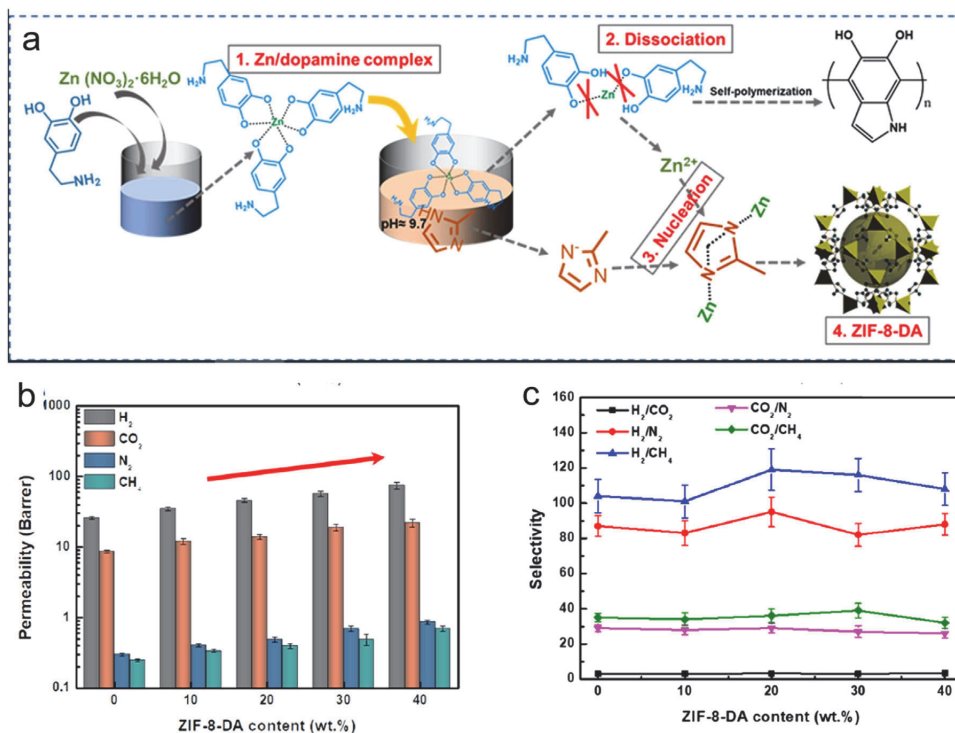


Fig. 4.1. (a) Illustration of the dopamine-modulated synthesis process of ZIF-8-DA. Effect of the ZIF-8-DA loading in Matrimid on (b) gas permeability and (c) selectivity (Jiang et al., 2021). (For interpretation of the references to color in this figure legend, the reader is referred to the web version of this article.)

2D MOF nanosheets (NSs), especially ZIF, have been widely used to form MMMs (Bi et al., 2020; Feng et al., 2020). For instance, metal-tetrakis (4-carboxyphenyl) porphyrin (M-TCPP) NSs have open metal sites and affinities towards polymer chains and CO₂, increasing CO₂ solubility and interfacial compatibility (Wang et al., 2019; X Li, 2019; Zhao et al., 2017; Zhao et al., 2018). In addition, the M-TCPP NSs have intrinsic micropores and interlayer spacing near 1 nm, which can be utilized to enhance gas separation properties (Lee et al., 2021a; X Li, 2019).

4.2.2.2. MOP- and POF-based MMMs. MOPs are highly porous molecular cages formed via the self-assembly of metal ions and organic ligands, similar to MOFs. However, MOPs are discrete cages of 1–5 nm, which can be dissolved in solvents and easily processed into TFC membranes, as shown in Fig. 4.2a (Fulong et al., 2018). MOPs were incorporated in glassy or rubbery polymers to improve CO₂/N₂ separation properties (Fulong et al., 2018; Liu et al., 2020; Liu et al., 2018). In particular, the metal ions on the MOPs can have favourable interactions with polymers such as polyethers, enhancing interfacial compatibility. For instance, MOP-3 NPs have a uniform size of ≈5 nm (Fig. 4.2b) with aperture sizes of 1.1 and 0.89 nm. Fig. 4.2c shows a photo of a freestanding film containing 50% MOP-3, and the SEM photo confirmed the well-dispersed NPs in the polymer (Fig. 4.2d). The introduction of 50% MOPs in the polyether increased CO₂ permeability from 190 to 580 Barrer while retaining high CO₂/N₂ selectivity of 62 (Fig. 4.2e). Interestingly, low loadings of MOPs can also significantly increase CO₂ permeability and retain CO₂/N₂ selectivity because of the percolation networks derived from the MOP NPs (Hosono et al., 2019).

Unlike MOFs and MOPs containing metal atoms, POFs are assembled by pure organic compounds and can be categorized as covalent

organic frameworks (COFs), covalent organic polymers (COPs), and porous aromatic frameworks (PAFs). Due to their high crystallinity and well-defined porous structures, COFs have been intensively investigated for gas separations. However, most COFs have pore sizes far larger than gas molecules, increasing gas permeability but decreasing selectivity (Zhang, Yahui et al., 2022). Several approaches have been adopted to reduce COF pore sizes to increase the size-sieving ability (Fan et al., 2018; Yang et al., 2019). For instance, 3D COF-300 NPs were constructed from 2D COF layers to attain pore sizes of 4 Å, and the incorporation of the NPs in Pebax increased both CO₂ permeability and CO₂/N₂ selectivity (Cheng et al., 2019). One of the challenges in using COFs for MMMs is their hydrophobicity, leading to poor interactions with polymers. To mitigate this problem, the COFs are often functionalized with ions or hydrophilic groups to enhance interfacial compatibility (Cheng et al., 2018; Liu et al., 2021). Additionally, the hydrophilic groups, such as PEO and polyethylenimine (PEI), can have affinities towards CO₂, further improving CO₂/N₂ separation properties (Liu et al., 2021).

POFs can also be further functionalized with N₂-phobic groups, such as azo groups (–N=N–), decreasing N₂ solubility and increasing CO₂/N₂ solubility selectivity (Patel et al., 2013). For example, the addition of 15% azo-COP-2 in polysulfone increased CO₂/N₂ solubility selectivity by ~90% (Li, Siyao et al., 2019). Other POFs have also been developed and used in MMMs to improve CO₂/N₂ separation properties, such as PAFs (Smith et al., 2020, 2019) and covalent triazine piperazine polymer (CTPP) (Thankamony et al., 2019; Zhang, Yahui et al., 2022).

4.2.2.3. MMMs containing 2D nanomaterials. 2D nanomaterials with tunable channels are another popular type of porous fillers used to con-

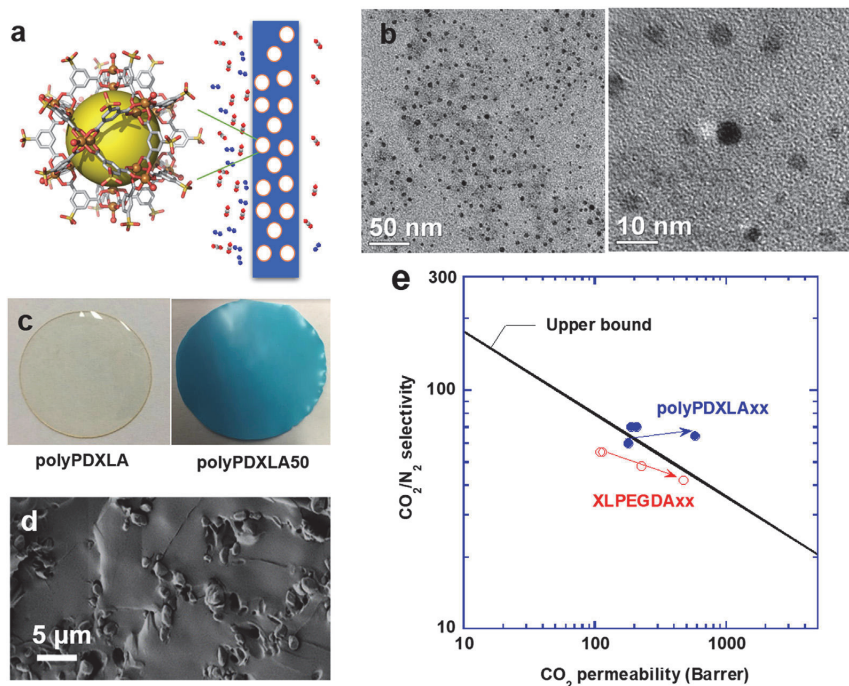


Fig. 4.2. (a) Schematic of the MOP-based MMMs for CO₂/N₂ separation. (b) TEM images of MOP-3 NPs. (c) Photos of polyPDXLA and polyPDXLA50 (containing 50 mass% MOP-3). (d) Cross-sectional SEM image of the XLPEGDA30. (e) CO₂/N₂ separation performance of XLPEGDAxx and polyPDXLaxx in 2008 upper bound (Liu et al., 2020). (For interpretation of the references to color in this figure legend, the reader is referred to the web version of this article.)

struct MMMs, such as 2D COF and MOFs, graphene-based NSs, and MXene NSs (Shi et al., 2021). For instance, porous graphene was demonstrated with the potential to achieve CO₂ permeance of 100,000 GPU and CO₂/N₂ selectivity of ~ 300 (Liu et al., 2013). Graphene oxide (GO) NSs have high aspect ratios and can be stacked to form sub-nm channels for gas molecular sieving. Furthermore, GO NSs can be chemically modified by grafting or blending to enhance interfacial compatibility with polymers and affinity toward CO₂ (He et al., 2019; Li et al., 2015). For example, the addition of 0.3 wt% GO NSs in Pebax/PEGMEA increased CO₂/N₂ selectivity from 42 to 56 with enhanced stability against physical aging (Shin et al., 2019).

MXenes contain metal carbides and carbonitrides and have a large surface area and hydrophilicity (Huang et al., 2021). MXene nanosheets can be stacked to attain interlayer spacings near gas molecule sizes, thus achieving a strong size-sieving ability for CO₂/N₂ separation. For example, Ti₃C₂T_x NSs showed an interlayer spacing of 3.5 Å, larger than CO₂ but smaller than N₂ (Shamsabadi et al., 2019), and the addition of 0.1 wt% Ti₃C₂T_x in Pebax increased CO₂/N₂ selectivity by 41 % to 43 and CO₂ permeability by 83 % to 1810 Barrer because of the disrupted polymer chain packing and increased free volume.

4.2.2.4. Facilitated transport MMMs. MMMs with facilitated CO₂ transport have also been investigated to obtain superior CO₂/N₂ separation properties, and typical polymers can be poly (vinyl amine) (PVAm) and PolyILs (Cao et al., 2019; Lee and Gurkan, 2021). For example, MMMs were prepared by self-assembly of PVAm and modified MIL-101 (Cr) (MKP) (Wang et al., 2020), and a TFC membrane with 200-nm MKP/PVAm exhibited CO₂ permeance of 823 GPU and CO₂/N₂ selectivity of 242 in the presence of water vapour.

Nanofillers can also be functionalized with CO₂ carrier groups to achieve facilitated CO₂ transport (Deng et al., 2020b; Zhang et al., 2019a). Fig. 4.3 presents the structure and properties of the MMMs containing ZIF NSs in Pebax (Deng et al., 2020b). The ZIF NSs showed good dispersion in MMMs (Fig. 4.3b). Increasing the relative humidity (RH) generally improves the CO₂/N₂ separation properties due to the facilitated CO₂ transport. An MMM film containing 20 wt% NSs exhibited high CO₂ permeability of 390 Barrer and CO₂/N₂ selectivity of 47 in the presence of saturated water vapour (Fig. 4.3c,d).

4.3. Inorganic membranes for CO₂ capture

Polymeric inorganic membranes (PIMs) are still at the initial stage of research; they display prospective characteristics for pre- and post-combustion CO₂ capture. These membranes offer high permeabilities, thus reducing the total investment as compared to polymeric membranes. Moreover, PIMs can be operated in a continuous operation and can withstand high flow rates.

The market of inorganic membranes is very small and is expected to rise in the near future. Inorganic membranes like zeolites, porous glass, microporous beryllium oxide, silicon nitride, carbon, and silica are quite popular because of their characteristic of high permeability and selectivity (Ogieglo et al., 2019; Sazali et al., 2021; Shi et al., 2020). The phenomenon of high permeability and selectivity is known as the upper bound trade-off curve, first introduced by Robeson (1991) in 1991 and later updated in 2008 (Robeson, 2008). The phenomenon describes an inverse dependency of selectivity and permeability for gas separation of membranes. For example, as the gas selectivity decreases, the permeability decreases, and vice versa. For this reason, inorganic membranes have superior performance as compared to glassy mem-

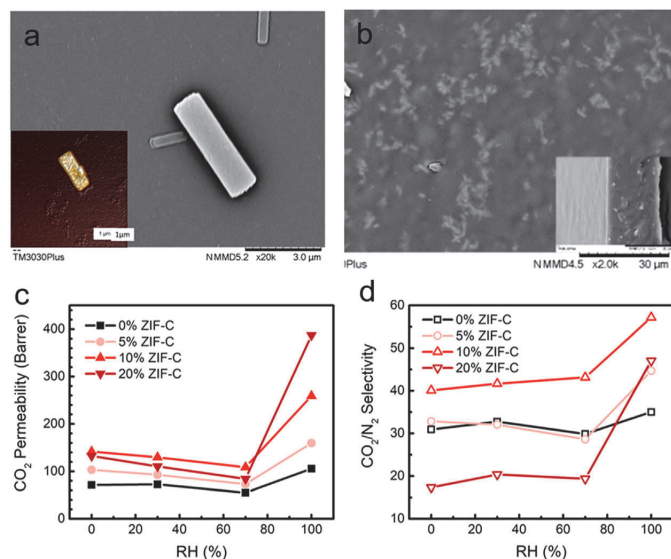


Fig. 4.3. Morphology of (a) ZIF-C 85–124 NS and (b) MMM with 10 wt% ZIF-C 85–124 NS. (c) CO₂ permeability and (d) CO₂/N₂ selectivity of MMMs as a function of relative humidity (Deng et al., 2020b). (For interpretation of the references to color in this figure legend, the reader is referred to the web version of this article.)

branes. J.W. McBain introduced the first ever inorganic polymeric membrane in 1930s. This membrane was initially utilized as a molecular sieve material and surprisingly displayed excellent selectivity (McBain, 2002). Apart from the processes of permeability and selectivity, membrane properties play another important role in carbon capture and separation. Primarily, the support material for any membrane is selected based on the requirements of mechanical strength, chemical resistance, and durability (Lee et al., 2016). In most cases, the support material is porous in nature to experience minimal gas/water transport resistance. Porous inorganic membranes contain either contain porous metal or ceramic support structures, with additional porous layers on top with different structures and morphologies. Inorganic membranes have different pore shapes like (i) straight pores of equal diameter extending from end to end of the membrane, and (ii) conical pores smaller at the bottom and a larger diameter at the surface of the membrane.

In addition to the general advantages of the PIM, new generation hybrid materials of zeolites, silica, and organometallic frameworks (MOFs) offer an abundance of opportunities to produce new membranes with selective functional groups for carbon recovery (Ding et al., 2019; Shi et al., 2020). Recent reviews of CO₂ capture on hybrid membranes have provided only brief insights into membrane design for CO₂ and H₂ separation.

4.3.1. Zeolite based inorganic membrane

Zeolites, also known as semi-stable silicates or alumina silicates, with a uniform topology, giving an intracrystalline network of voids and channels. They also have an abundant surface chemistry that varies with the Si/Al ratio, amount, and type of exchangeable cations. Cations in zeolites sometimes act as Lewis acids, while the framework oxide ions nearby cations may act as Bronsted/Lewis bases. Furthermore, the silanol groups might act as Bronsted acids. The CO₂ adsorption capacity of zeolites are highly affected by their topology, modelling the energy interactions, segregating, and clustering effects. The dependence of zeolites on topology is not always precise as most of the zeolites are very complex to prepare in pure silica form or in proper Si/Al ratios. Noteworthy exceptions to this statement are silicate-1 (Tawalbeh et al., 2021; Zhu et al., 2006), clathrasil DD3R (Himeno et al., 2007; Van Den Bergh et al., 2010), CHA (Debost et al., 2020; Miyamoto et al., 2012), and ITQ-

29 (Palomino et al., 2010). Silicalite-1 composite membranes with thin zeolite layers, prepared by Wirawan et al. (2011) provided a simulated results of 9.8 and 4.0 mol/ (m²s) for CO₂/H₂ separation factor and CO₂ flux, respectively. Faujasite (FAU)-type zeolites with low Si/Al ratio often provide the highest adsorption selectivity for CO₂. Study by Krishna and van Baten (2010), proposed that FAU-type membrane can achieve a selectivity of 500 and permeability of 10000 Barrer for CO₂/N₂ separation. The presence of aluminum in the silicon-aluminum framework creates a negative charge that must be neutralized by the metal cations in the pores. The most observed configurations involve the presence of Na⁺ ions as counterions, termed NaX and NaY. Compared to N₂, CO₂ exhibits a stronger interaction with the electric field of the micropores, influenced by the number and type of cations present. NaX, which has a lower Si/Al ratio than NaY and contains more cations, exhibits higher selectivity for CO₂ over N₂, despite having a smaller pore volume than NaY (Maurin et al., 2005). White et al. (2010) developed a zeolite Y membrane on alumina, which gave CO₂ permeance of 300 GPU and more than 500 selectivity factors for CO₂/N₂.

4.3.1.1. Surface chemistry. The Si/Al ratio in zeolite surface is highly responsible for influencing its ability to adsorb CO₂ by pitching the number and setting of exchangeable cations, including the acid-base character of zeolite topology. Among the most famous zeolite structures, faujasites provide the highest CO₂ uptake capacity of 5-10 mmol CO₂/g at 101 kPa and 303 K. The CO₂ affinity follows the order of NaA > NaX > NaY. This trend can be explained by decreasing pore size and the presence of a high number of type III cations at the starting of super-cage structure, leading to preferential interaction with CO₂ (Li and Pidko, 2019). The CO₂ uptake in ITQ-29 dramatically increase with Si/Al ratio (Fig. 4.4). This property is exceptional for membrane design as it enables preferential separation of CO₂ by precisely modulating the polarity and surface science of LTA scaffold in specific separations. In the case of Aluminosilicate-based zeolites, CO₂ adsorption Henry's coefficients are 1-2 orders greater than corresponding N₂ and CH₄. This difference is attributed to the high heat of adsorption of CO₂ as compared to N₂ and CH₄.

The zeolite basicity increases with Al content and cation electropositivity (Barthomeuf, 2003; Verdoliva et al., 2019). Ward and Habgood (1966) supported the hypothesis of chemical interactions among

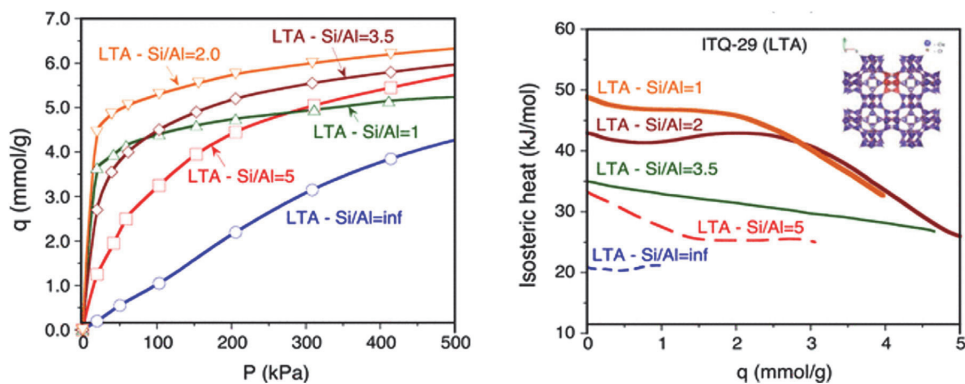


Fig. 4.4. Effect of the Si/Al ratio on the isosteric heat of CO₂ adsorption for a series of ITQ-29 zeolites displaying the LTA (Pera-Titus, 2014). (For interpretation of the references to color in this figure legend, the reader is referred to the web version of this article.)

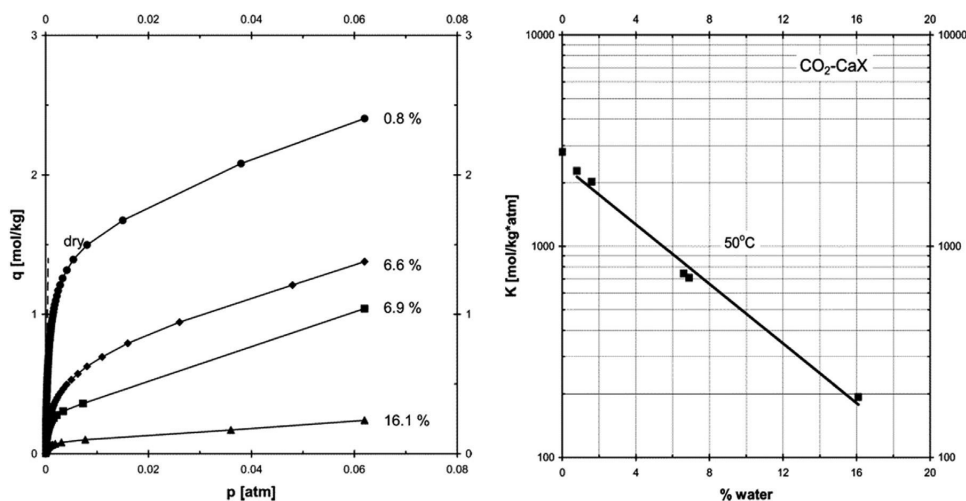


Fig. 4.5. CO₂ adsorption isotherms (left) and Henry's constants (right) on CaX at 323 K for different pre-adsorbed water loadings (Brandani and Ruthven, 2004). (For interpretation of the references to color in this figure legend, the reader is referred to the web version of this article.)

adsorbed CO₂ and alkaline cations. They reported the characteristic IR bands of carbonates for CO₂ adsorption in KX, NaX, and LiX zeolites. Heavy cations (Rb and Cs) compensate for the strong basicity with electrostatic interactions of cation and quadrupole (Walton et al., 2006). The basicity of zeolite structure can further be devised by incorporating amine groups, resulting in phase alteration of zeolite, and the formation of Si-N-Si moieties (Han et al., 2005).

4.3.1.2. Effect of water on CO₂ adsorption. Water is studied as a simple molecule to increase the CO₂ adsorption of zeolites. The CO₂ uptake can be highly influenced by high water partial pressure as CO₂ and H₂O molecules compete for the sorbent sites (Kolle et al., 2021). H₂O favourably adsorb on exchangeable cations, lessening the electrical field on zeolite cavities. For instance, as reported by Brandani and Ruthven (2004), the CO₂ uptake in CaX-zeolite at 0.06 bar and 323 K decreases between 2.5 and 0.1 mmol/g on increasing H₂O concentration from 0.8 wt% to 0.1 wt% (Fig. 4.5). Meanwhile, in case of CO₂ concentration less than 300 ppm, H₂O pre-adsorption may promote CO₂ adsorption capacity by forming surface bicarbonate species. This improvement automatically normalises CO₂ uptake as the CO₂ concentration

reaches 1000 ppm, stating that CO₂ loadings are higher for dry adsorption.

In zeolites with high Si/Al ratios, the H₂O isotherm deviates from the characteristic type-I trend (i.e., Langmuir type), as noticed in LTA and FAU zeolites. The H₂O adsorption proceeds through the formation of clusters in MFI channels, resulting in the reduction of CO₂ uptake capacity (Ahunbay, 2011; Cailliez et al., 2008; Trzpit et al., 2007). The deviation from Langmuir-type is generally known as type-II behaviour. Introducing germanium in the MFI structure also improves hydrophobic properties. Fig. 4.6 represents water adsorption on MFI zeolite improved with Al, B, and Ge species.

MFI membranes have yielded comparatively low amounts of CO₂/N₂ separation factors. However, their use for the separation of CO₂/N₂ mixtures is still being investigated because of their low Al content. This gives the membranes better reproducibility and chemical stability. Ando et al. (Ando et al., 1998) reported a separation factor of 25.5 at a CO₂ permeance of 6.6×10^{-7} mol/(m² s Pa). The MFI membranes synthesized by Guo et al. (2006) show CO₂/N₂ separation of about 65 μmol·m⁻²·s⁻¹·Pa⁻¹ at room temperature with equimolar CO₂/N₂ mixtures under Wicke-Lallenbach conditions. In addition, the

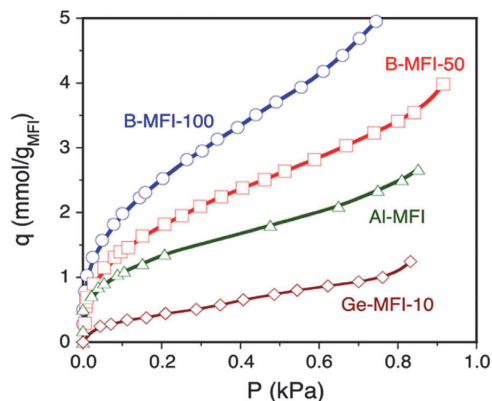


Fig. 4.6. Water adsorption at 303 K on crushed Al-MFI (Si/Al = 30), B-MFI-100 (Si/B = 100), B-MFI-50 (Si/B = 50), and Ge-MFI-10 (Si/Ge = 10) (Nicolas and Pera-Titus, 2012). (For interpretation of the references to color in this figure legend, the reader is referred to the web version of this article.)

CO₂ molecules were seen to pass at the rate of 0.7 $\mu\text{mol}\cdot\text{m}^{-2}\cdot\text{s}^{-1}\cdot\text{Pa}^{-1}$ through the membrane. These factors were better than the pre-recorded values for silicate-1, BaZSM-5, B-NaZSM-5, and BHZSM-5. The isomorphous substitution of Si (IV) in place of B (III) results in materials with comparable CO₂ permeation, but with better stability. Sublet et al. (2012) reported the post-combustion separation of CO₂/N₂ using α -supported MFI zeolite membrane. At higher water concentrations, MFI membranes show static reduction of gas permeance of 40% for water concentration. The insertion of water improves CO₂/N₂ separation due to the development of (bi)carbonate stable intermediates. In addition, the MFI membranes like HZSM-5 (Guo et al., 2006) and NaZSM-5 (Shin et al., 2005) show a good perspective for CO₂/N₂ separation in the presence of water. These two membranes compete with the best reported NaY membranes in terms of CO₂/N₂ separation, CO₂ permeances, and permeabilities. Shin et al. (2005) proposed an increased membrane selectivity of ZSM-5 for the separation of an equimolar CO₂/N₂ mixture saturated with moisture. At room temperature, the separation factor for the dry mixture was 50, while it was 60 for the wet mixture. Due to the higher ratio of Si/Al in ZSM-5, these membranes can be a potential candidate for future membranes in CO₂ separation technologies.

4.4. Carbon molecular sieve membranes for post-combustion carbon capture

4.4.1. Introduction for carbon molecular sieve membranes

The rapid increase of greenhouse gas emissions causes global climate change (Hoegh-Guldberg et al., 2019; Malhi et al., 2021), and CO₂ capture, utilization and storage (CCUS) is becoming one of the most attractive solutions for the reduction of CO₂ emissions (Figueroa et al., 2008; Hassanlouei et al., 2013). Different technologies such as chemical absorption, adsorption, membranes, and cryogenic distillation, have been developed for CO₂ capture (Araújo et al., 2022; Shah et al., 2020). Among them, membrane-based gas separation technology is one of the most promising strategies due to its high adaptability and reliability, energy-saving, and being environmentally friendly (Agaton and Karl, 2018; Araújo et al., 2022; He et al., 2022; Kunalan and Palanivelu, 2022; Rodrigues et al., 2019). Various membrane materials have been investigated for CO₂ capture (Kunalan and Palanivelu, 2022; Lei et al., 2020; Liu et al., 2022; Shah et al., 2020), such as polymer membranes (Meixia Shan et al., 2018; Zhu et al., 2018), mixed matrix membranes (MMMs) (Guo et al., 2022; Voon et al., 2022; Zhang et al., 2021a), fixed-site-carrier (FSC) membranes (Hägg et al., 2017;

He et al., 2017b), two-dimensional (2D) nanosheets (Achari et al., 2016; Cacho-Bailo et al., 2017; Ding et al., 2018; Ying et al., 2018; Yu et al., 2011) and carbon molecular sieve membranes (CMSMs) (Araujo et al., 2020; Cao et al., 2019; Karousos et al., 2020; Lei et al., 2021; Szali et al., 2021; Tseng et al., 2016). Among them, CMSMs are considered the next-generation gas separation membranes due to their high separation performance, and thermal and chemical stability, which shows great potential for pre- and post-combustion carbon capture (Koros and Zhang, 2017; Lei et al., 2020). Importantly, the development of flexible carbon hollow fiber membranes (CHFMs) is expected to produce practical membrane modules with a low cost and a high packing density (Liu et al., 2016). In this section, a systematic review of CMSMs for CO₂ capture or removal related to both material and process performances will be conducted.

4.4.2. Carbon membrane structure and gas transport mechanisms

Under inert purge gas or vacuum conditions, CMSMs are prepared by pyrolysis of precursors at high temperatures. During the pyrolysis process, the polymeric precursors are transformed to ordered carbon plates, which usually results in a bimodal structure with ultramicropores (3–7 Å) and micropores (7–20 Å) (Ma et al., 2019; Qiu et al., 2019; Rungta et al., 2017; Zhang and Koros, 2017). Fig. 1 illustrates the proposed pyrolysis mechanism from a cellulosic precursor to CMSMs (Lei et al., 2020). The polymeric precursors start aromatization and fragmentation with temperature ramping and afterwards transform into rigidly aromatic carbon strands (Fig. 4.7 (i) & (ii)). Next, the rigid carbon strands align and form carbon “plates” due to higher entropy to the system (Fig. 1 (iii)). The final CMSMs usually result in a microstructure with imperfectly packed plates due to the kinetic restrictions (limited time at high temperature) (Fig. 4.7 (iv)). In the end cooling stage, the micropore “cells” are stacked to form a cellular structure (Fig. 4.7 (v)) in which the ultra-micropores share the “walls” between micropores.

There are four different mechanisms related to mass transfer of gas through a porous carbon membrane: Poiseuille flow; Knudsen diffusion; partial condensation/capillary diffusion/selective adsorption and molecular sieving, as it is shown in Fig. 4.8 (Hamm et al., 2017). The dominating mechanism will be dependent on the membrane properties, the permeated gases and the operating conditions such as feed temperature and pressure (Anne Julbe, 2001), and quite often more than one mechanism will contribute to the gas separation performance together. Carbon membranes with a selective surface flow mechanism (with micropores of < 20 Å) may be applied to the separation of heavy hydrocarbons (HHCs) in the petroleum industry, while carbon molecular sieve membranes with ultramicropores (3–7 Å) can potentially be used for the separation of small gas molecules that are alike in size such as CO₂-N₂, and CO₂-O₂ (i.e., post-combustion carbon capture) (Kumakiri, 2020).

4.4.3. Carbon membranes for CO₂/N₂ separation

Carbon membranes for pre-combustion carbon capture and CO₂ removal from biogas and natural gas have been critically reviewed in the previous work (Lei et al., 2020). Therefore, the main focus in this section is to discuss the status and challenges of applying carbon membranes for post-combustion carbon capture. The low feed pressure (~1 bar), the low CO₂ concentration and similar sizes like CO₂, O₂ and N₂ in the flue gas are the main challenges for post-combustion CO₂ capture. Development of high performance CMSMs with high CO₂/N₂ selectivity is of emerging interest in this application. Fig. 4.9 summarizes the gas separation performances of CMSMs for CO₂/N₂, which clearly surpass the Robeson upper bound. To improve the separation performance of CMSMs, the pore size and distribution of CMSMs can be finely tuned by the chemical deposition method. Tseng and Itta (2012) selected poly (propylene oxide) (PPO) polymers as the segment-forming agent, and applied the self-deposition method to adjust the pore structure of CMSMs. The modified PPO/polyimide (PI)-derived CMSMs presented CO₂ permeability of 1318.2 ± 37.6 Barrer and a CO₂/N₂ selectivity of 156.4, respectively.

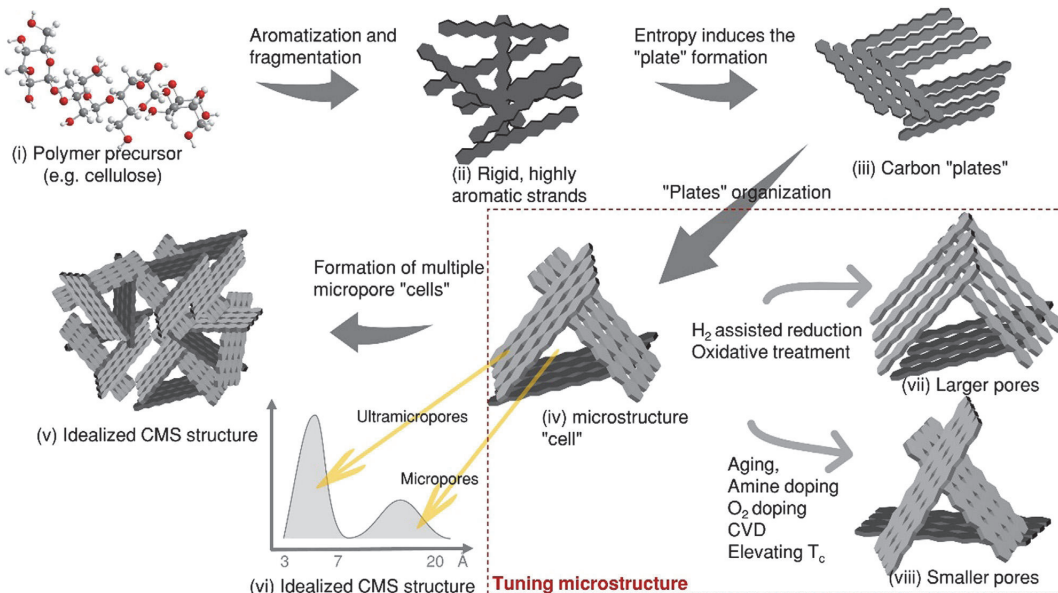


Fig. 4.7. Illustration of pyrolysis mechanism from a cellulosic precursor to CMSMs (Lei et al., 2020). (For interpretation of the references to color in this figure legend, the reader is referred to the web version of this article.)

The porous N-doped carbon as an advanced adsorbent has been investigated for CO₂ separation as the polar N-doped sites within the carbonaceous framework provide a strong and selective dipole-quadrupole interaction with CO₂ molecules. Zhu et al. (2013) prepared polymeric membranes through superacid-based method using the trimerization of aromatic nitriles with a superacid catalyst (trifluoromethanesulfonic acid, CF₃SO₃H), and the obtained precursors were further used to synthesize the N-doped CMSMs. The final carbon membranes showed a CO₂ permeability of 1149.3 Barrer and a CO₂/N₂ selectivity of 43.2, respectively. Moreover, the resorcinol–formaldehyde (RF) with high char yield and thermal stability, can be applied as nanoporous carbon membranes (NCMs). Zhang et al. prepared NCMs through pyrolysis of thermosetting RF resin blending with thermally labile F-127 in the presence of a basic catalyst. The RF resin/F-127-based NCMs have CO₂ permeabilities of 4862 ± 350.8 Barrer and CO₂/N₂ selectivity of 85.9, respectively (Zhang et al., 2014). To enhance gas separation performance of CO₂/N₂, the introduction of functional materials to the pore of CMSMs has been proven to be a versatile strategy (Hou, 2016). Ionic liquids (ILs) are promising candidates for CO₂ capture and separation due to their low vapour pressure, high thermal stability, good mechanical stability, non-toxic nature, non-flammable, designability and high CO₂ affinity (Patil et al., 2022; Tome and Marrucho, 2016). Guo et al. prepared the IL/CMS hybrid membrane spin-coating IL dissolved in ethanol at different concentrations on Matrimid®-derived CMSMs with CO₂ permeability of 675 Barrer and CO₂/N₂ selectivity of 53, respectively (Guo et al., 2020). Interestingly, the covalent triazine frameworks (CTFs)-derived materials with fluorine functional groups have been proved to significantly enhance the CO₂ sorption properties. Yang et al. reported fluorinated CMS hybrid membrane has CO₂ permeability of 2140 Barrer and CO₂/N₂ selectivity of 36, respectively (Yang et al., 2020).

Although some previous work reported the evolution mechanism of polyimide-based precursors to carbon membranes, the design and synthesis of novel polyimide precursors are still required to fabricate high-performance carbon membranes for gas separation due to the complicated rearrangement of the pyrolytic aromatic fragments of the decomposed precursors (Hazazi et al., 2019; Ngamou et al., 2019;

Ogieglo et al., 2019; Pérez-Francisco et al., 2020). Deng et al. synthesized new binaphthol-6FDA polyimide precursors and pyrolyzed into the CMS membranes. The binaphthol-6FDA polyimide-derived CMSMs have CO₂ permeability of 2674 Barrer and CO₂/N₂ selectivity of 37.1, respectively (Deng et al., 2021). It is well-known that the gas separation performance of CMSMs is highly dependent on the intrinsic property of polymer precursors, so the pyrolysis of polymeric precursors comprising thermally-stable microporous fillers has been promising as a simple approach to improve gas separation performance of CMSMs (Li et al., 2019). Chuah et al. (2021) fabricated mixed matrix carbon membranes (MMCMs) including SAPO-34 zeolites have CO₂ permeabilities of 2248 ± 4 Barrer and CO₂/N₂ selectivity of 33.2 ± 0.7 , respectively. Moreover, the MMCMs with activated carbon (YP-50F) presented a high CO₂ permeability of 1833 Barrer and a CO₂/N₂ selectivity of 30.4, respectively (Chuah and Lee et al., 2021). Yang et al. prepared polyimide/sepiolite derived MMCMs have CO₂ permeability of 6711.5 Barrer and a CO₂/N₂ selectivity of 30.4, respectively (Yang et al., 2021). Overall, it can be found that CMS membranes have been proven attractive for post-combustion carbon capture due to their rigid, typical tunable and bimodal pore structure, which could effectively transport CO₂ molecules.

4.4.4. Techno-economic feasibility of CMSMs for post-combustion carbon capture

The current and fairly established technology (such as chemical absorption) allows for effective CO₂ capture from flue gas with a low concentration at low temperatures, but it is expensive owing to the large size of columns and equipment installation. Additionally, thermal efficiency is also reduced. Utilizing membrane separation units could be a different approach. A carbon membrane separation unit was designed to be integrated into typical post-combustion power plants, as it was previously described (He et al., 2009). To ensure a significant reduction in emissions and to reduce the future costs for compression and transport, the criteria of purity and recovery of CO₂ from flue gas are highly required, generally higher than 90% (Yang et al., 2009). The CO₂ content in flue gas is low (10–20%), rendering it difficult to

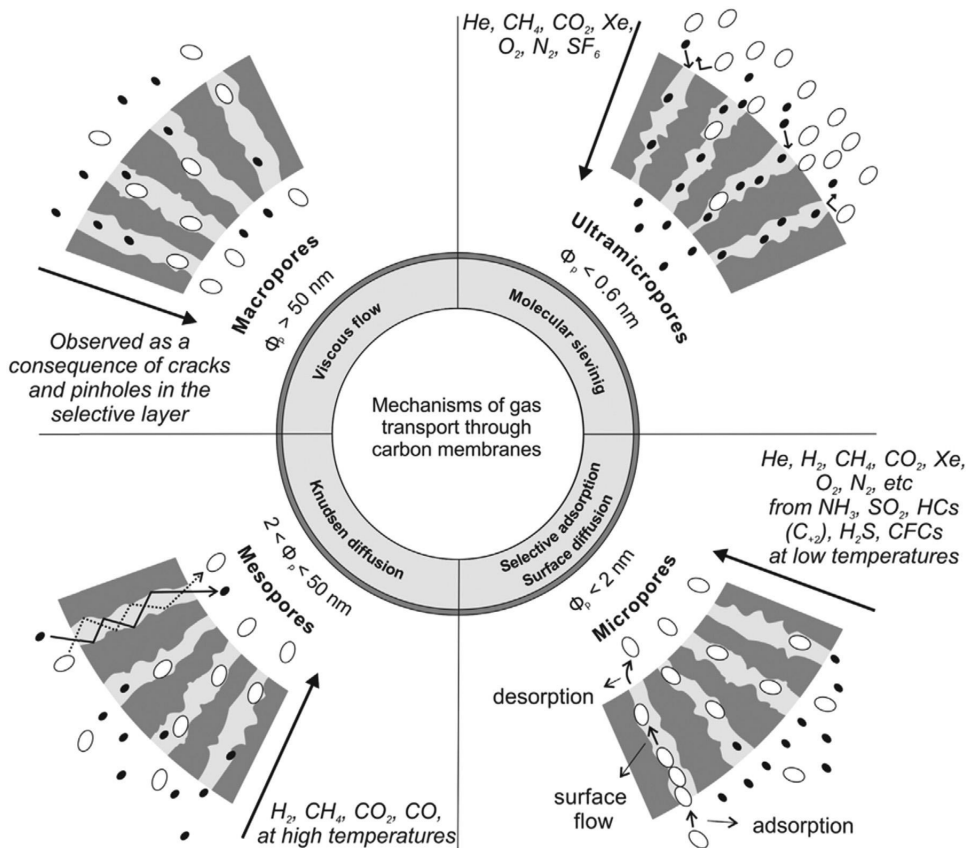


Fig. 4.8. Different mechanisms of gas transport through carbon membranes (Hamm et al., 2017). (For interpretation of the references to color in this figure legend, the reader is referred to the web version of this article.)

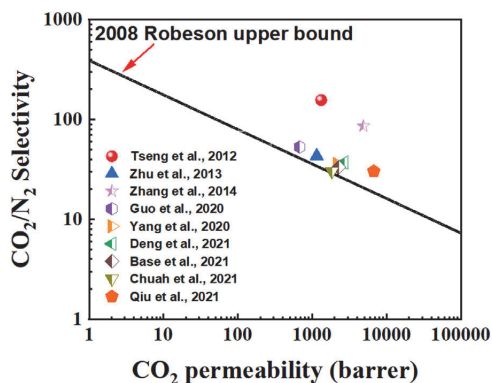


Fig. 4.9. The CO₂/N₂ separation performances of different CMSMs. (For interpretation of the references to color in this figure legend, the reader is referred to the web version of this article.)

accomplish through a single-stage membrane technique. Consequently, implementing a multi-stage membrane arrangement becomes necessary, and two-stage membrane systems have been reported to be the effective

configuration to achieve the separation target (Xu et al., 2019; Yang et al., 2009). For the purpose of creating a driving force for CO₂ diffusion, several studies on the techno-economic feasibility analysis of a process by combining the feed compression with the vacuum suction on the permeate side (Merkel et al., 2010; Yang et al., 2009). The operating conditions (e.g., feed temperature, feed and permeate pressures), membrane properties (CO₂ permeance, selectivity, membrane lifetime), and corresponding costs were typically reported along with representative parameters such as specific area [m²/(kgCO₂/s)], specific energy [MJ/kgCO₂], and CO₂ capture cost [\$/tonCO₂] (energy cost and capital cost for membranes, pumps, compressors, etc.).

Favre et al. outlined the major difficulties in applying membranes for post-combustion capture and indicated the ranges of operating conditions within which the membrane process can compete with cutting-edge absorption technology (Favre, 2007). Due to the significant energy consumption of the compression step, it has been claimed that the membrane process with feed compression can only be competitive when the inlet CO₂ content is more than 20%. Benchmarking was performed by Roussanaly et al. to determine the required CO₂ permeance and membrane selectivity to ensure the membrane process is competitive with absorption technology (Roussanaly et al., 2016). It was revealed that simple membrane process configurations and more sophisticated configurations, including recycling or sweep could be economically competitive with the absorption technology. He et al. explored the techno-economic feasibility of hollow fiber carbon membranes which is based

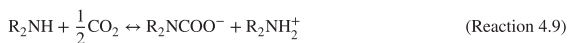
on the carbonization of deacetylated cellulose acetate (He and Hägg, 2011). It was reported that the CO₂ recovery of 67% and the CO₂ purity of 88% could be achieved with a total required membrane area of $1.62 \times 10^7 \text{ m}^2$ and a total compressor duty of $1.37 \times 10^5 \text{ kW}$ [1]. In addition, He et al. also contrasted the feasibility of single-stage membrane process and two-stage cascade membrane process. It was indicated that the single stage membrane process cannot achieve high CO₂ purity and CO₂ recovery simultaneously employing such hollow fiber carbon membrane whereas the two-stage cascade membrane technology can be economically competitive with the chemical absorption method (He and Hägg, 2011).

4.4.5. Future perspectives

Although carbon membrane technology is considered one of the energy-efficient processes for CO₂ separation, the application of CMSMs for post-combustion CO₂ capture is still challenging: (1) the relatively low CO₂ permeance compared to polymeric membranes, which requires a large carbon membrane area and thus increases the membrane unit cost significantly; (2) many CMSMs are sensitive to water vapour existing in flue gas, which may reduce the membrane durability and lifetime; (3) difficult in the flat-sheet carbon membrane upscaling and production cost as well as the brittleness of carbon structure. To address these challenges, the development of hydrophilic, ultra-thin supported carbon membranes or flexible asymmetric CHFMs should be pursued in future work. It should be noted the advantage of its strong mechanical strength may direct the operation of carbon membranes for CO₂ capture at a relatively higher feed pressure, but the optimal operating conditions should be identified based on cost minimization by balancing capital expenditure and operation cost.

4.5. Facilitated transport membranes

In facilitated transport (FT) membranes, the transport of CO₂ molecules can be enhanced through specific reversible reactions (Li et al., 2015). Many studies have shown that the transport of CO₂ occurs in the form of carbamate and bicarbonate in FT membranes (Caplow, 1968). In most cases, water is required in FT processes (Chiwaye et al., 2021). The reaction equations for primary amine, secondary amine, and tertiary amine with CO₂ are given in Reaction 4.7-4.11 below.



The scheme of FT processes is illustrated in Fig. 4.10. In comparison to conventional polymeric membranes, where gas is transported through the membrane via a solution-diffusion model, gas transport in FT membranes involves a reversible reaction, which is depicted in Eq. (4.4) (Kim et al., 2013).

$$J_A = \frac{D_A}{l}(c_{A,0} - c_{A,l}) + \frac{D_{A,B}}{l}(c_{AB,0} - c_{AB,l}) \quad (4.4)$$

Compared to solution-diffusion based membranes, FT membranes can achieve much higher CO₂ fluxes at relatively low CO₂ concentration conditions by utilizing reversible reactions between CO₂ and carriers, as shown in Fig. 4.11. This property makes FT membranes ideal for flue gas CO₂ capture, as flue gas is usually present in large amounts and at low pressures (Chao et al., 2021; Kárszová et al., 2020). However, the phenomenon of ‘carrier saturation’ (Han and Ho, 2022; Li et al., 2015)

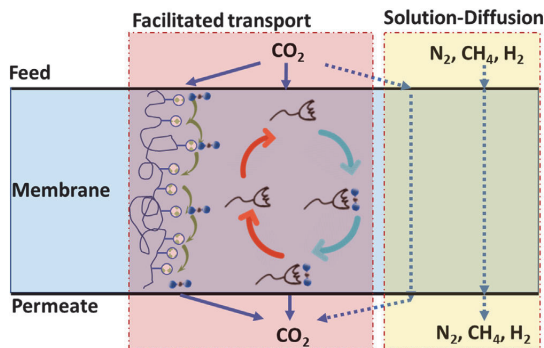


Fig. 4.10. Gas transport through the facilitated transport membrane.

causes a gradual reduction in CO₂ permeance as the CO₂ partial pressure increases in the feed. As a result, the CO₂ separation performance of FT membranes is sensitive to the CO₂ partial pressure.

4.5.1. Mobile carrier

Mobile carriers have been intensively studied for CO₂ separation purposes, with representative examples including alkaline solutions (e.g., KOH) (Ansaroni et al., 2015), amino acid salts (e.g., GlyK, ProK) (Dai et al., 2019a; Dai et al., 2019b), small amine molecules (e.g., MEA, DEA) (Teramoto et al., 1996), and ionic liquids (ILs) (Klemm et al., 2020) (Fig. 4.12). In the early stage of FT membrane research, these mobile carriers were incorporated into supported liquid membranes (SLMs) (Bao and Trachtenberg, 2006; Peng et al., 2022; Teramoto et al., 1997), which exhibited rather high intrinsic CO₂ separation performance for CO₂/N₂, CO₂/CH₄, and CO₂/H₂ separations. However, the stability of SLMs is always a serious issue, especially under high operational pressure conditions. Additionally, reducing the thickness of an SLM to ensure a feasible CO₂ flux across the membrane is difficult. As a result, mobile carrier-based SLMs are less competitive in practical CO₂ separation applications.

On the other hand, mobile carriers are also widely used in TFC membranes for CO₂ separation applications (Tong and Ho, 2017a). Exceptional separation performances have been obtained for many of these materials. However, similar to SLMs, long-term stability is always an issue, as the small molecules may easily leach out of the membrane, especially if there is water vapour condensation on the surface of the membranes.

4.5.2. Fixed site carrier

Fixed site carrier (FSC) membranes are a group of polymers with functional groups that can undergo reversible reactions with CO₂ to facilitate its transport (Deng et al., 2009; He et al., 2017a). Normally these materials contain different kinds of amine groups, including primary amine, secondary amine, and tertiary amine (Fig. 4.13). In some cases, -COOH group can also function as an effective carrier for CO₂ transport (Zhao et al., 2006). Compared to mobile carrier FT membranes, FSC membranes typically exhibit better stability. On the other hand, since many FSC membranes contain a large amount of amine groups, they can be rather brittle in the dry state due to strong hydrogen bonding, and their mechanical strength is not good. Therefore, in many cases, a second polymer is blended with the FSC polymer to improve its mechanical strength and sometimes to promote water uptake as well (Han et al., 2020; Han and Ho, 2021a; Han et al., 2018).

Fig. 4.13 presents a few representative FSC polymers. In principle, for primary and secondary amines, with the help of water vapour, one mole of amine could react with more than one mole of CO₂, thus making it a very promising option for CO₂ separation. However, it has been found that tertiary amines only react with one mole of CO₂, even with

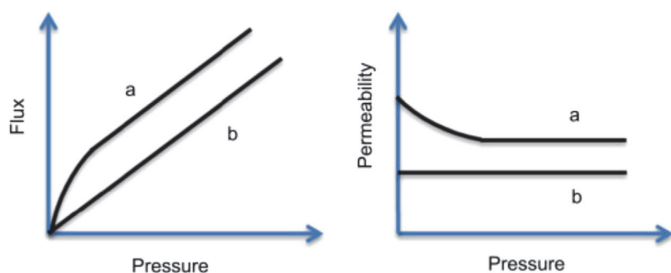


Fig. 4.11. FT membrane presents higher CO₂ flux at lower CO₂ partial pressure conditions but the CO₂ permeance gradually reduces due to carrier saturation. (For interpretation of the references to color in this figure legend, the reader is referred to the web version of this article.)



Fig. 4.12. Typical mobile carrier used in FT membranes, reproduced from (Zhang et al., 2021). (For interpretation of the references to color in this figure legend, the reader is referred to the web version of this article.)

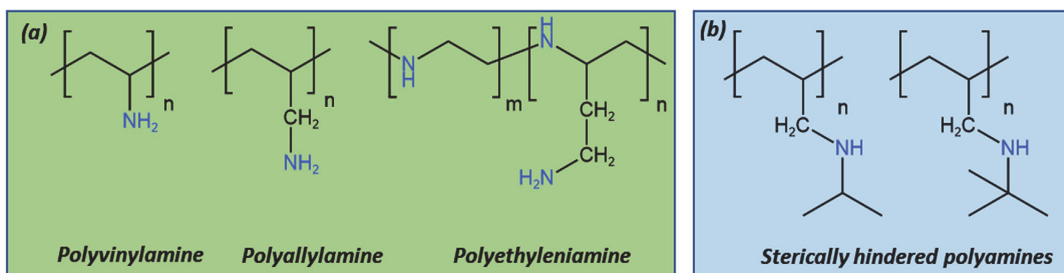
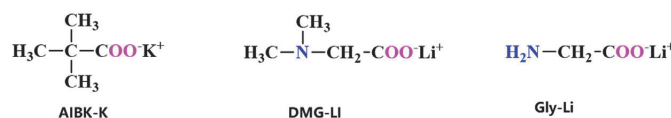


Fig. 4.13. (a) Typical fixed site carrier materials used in FT membranes, (b) sterically hindered membranes exhibited higher CO₂ separation performances, reproduced from (Han et al., 2020). (For interpretation of the references to color in this figure legend, the reader is referred to the web version of this article.)

one mole of tertiary amine. In some cases, if the amine is sterically hindered, it can be more effective than primary and secondary amines (Tong and Ho, 2017b). There have been several reviews discussing this topic (He, 2021; Rafiq et al., 2016; Tong and Ho, 2017a).

4.5.3. Hybrid membranes

Compared to the pure mobile carrier or fixed site FT membranes, in many cases, both mobile carrier and fixed site carrier can be employed in FT membranes. The polymeric phase works as a hosting matrix for mobile carriers (Han and Ho, 2021b). In addition, to improve the mechanical strength of the membrane, the hosting matrix is sometimes crosslinked (Deng and Hägg, 2015; Han et al., 2019b). Another category of facilitated transport hybrid membranes includes those membranes containing functionalized nanoadditives (Nithin Mithra and Ahankari, 2022). Compared to conventional mixed matrix membranes (MMMs), which are fabricated by blending nanoadditives and polymer phases together, facilitated transport membranes contain nanoparticles with amine-functionalized groups. Representative nanofillers include MOFs (Kim, Jiyoung et al., 2016; Wu et al., 2014), GO (Dong et al., 2016), and CNT (Ansaloni et al., 2015; Saeed et al., 2017). Additionally, hybrid membranes containing three different components are also being studied (Guo et al., 2019), which typically consist of a liquid phase, a polymer phase, and a solid phase. The liquid phase works as both facil-

itated transport carriers and fillers for the non-selective voids between the polymer phase and solid additives (Kalantari et al., 2020).

Many facilitated transport membranes are made using thick films with a thickness in the range of dozens of micrometers, while others have been fabricated as thin-film-composite (TFC) membranes with feasible CO₂ permeances. Dip-coating is the most commonly used method to fabricate FT TFC membranes, with both flat-sheet and hollow fiber geometries (Dai et al., 2016). Other methods, such as interfacial polymerization (Zhao et al., 2006), knife casting (Pate et al., 2022), and spin-coating (Zhang et al., 2018) have also been reported. The thickness of TFC membranes varies a lot. In principle, the thickness of the selective layer should be as thin as possible to ensure a high CO₂ flux across the membrane. Interestingly, for facilitated transport membranes, as there is a need for a proper carrier in the selective layer, it is sometimes found that membranes with thinner selective layers present lower CO₂ permeances (Kim et al., 2004), which is different from conventional membranes based on solution-diffusion model.

The CO₂/CH₄ separation performances of FT membranes developed in the past few years are listed in Fig. 4.14. As can be seen from the figure, many FT membranes showed very promising CO₂ separation performances, which are far above the Upper Bound. Meanwhile, for FT TFC membranes, both high CO₂ permeance and high CO₂/CH₄ selectivity have also been documented, indicating that FT membranes are very competitive materials in CO₂ capture.

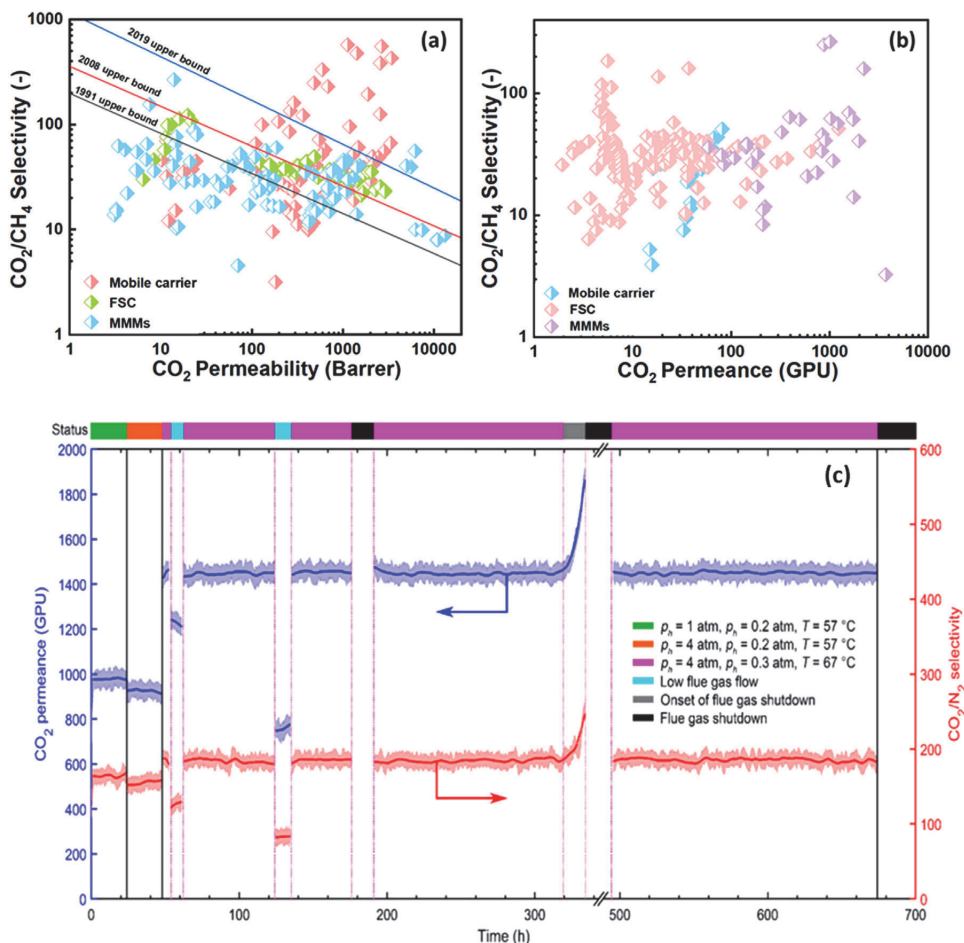


Fig. 4.14. Comparison of CO₂ separation performances of the thick film (a) and TFC FT membranes (b). Data obtained from ref (Aframehr et al., 2022; Alkhouzaam et al., 2016; Chen et al., 2012; Guo et al., 2015; Hanioka et al., 2008; Iarikov et al., 2011; Isanejad and Mohammadi, 2018; Li et al., 2010; Li et al., 2020; Liu et al., 2021; Liu et al., 2014; Mashhadikhan et al., 2020; Mubashir et al., 2018; Murugiah et al., 2018; Park et al., 2009; Peng et al., 2017; Pu et al., 2022; Qu et al., 2020; Regmi et al., 2022; Sasikumar et al., 2021; Shahkaramipour et al., 2014; Shamair et al., 2020; Swati et al., 2021; Tu et al., 2021a; Tu et al., 2021b; Wang et al., 2020; Wang et al., 2021; Wu et al., 2014; Yu et al., 2020; Zhang et al., 2021; Zhang et al., 2018; Zhang et al., 2017b; Zhang et al., 2022). (c) long-term stability performances of FT membranes tested under industrial conditions. Reproduced from ref (Han et al., 2019a). (For interpretation of the references to color in this figure legend, the reader is referred to the web version of this article.)

The long-term stability of the FT membrane has also been investigated. Unlike conventional glassy polymeric membranes, which suffer from physical aging problems (Brunetti et al., 2017; Merrick et al., 2020; Xu et al., 2014), there are few reports about physical aging of FT membranes. In addition, though the presence of impurities in the feed (e.g., SO_x and NO_x) may negatively affect the CO₂ separation performances of FT membranes, as long as the impurities are removed from the feed, the CO₂ separation performances will gradually recover to the original value (Liao et al., 2014). Ho et al. also investigated the separation performances of FT membranes under industrial conditions and concluded that the FT membrane demonstrated excellent stability over the testing period (Han et al., 2019a).

Overall, FT membranes are promising CO₂ capture membrane materials showing exceptionally high CO₂ separation performances. Future research can be carried out to develop more efficient carriers for CO₂

transport, which could work under high CO₂ partial conditions. On the other hand, developing novel FT membranes with good RH variation tolerance can also be useful for practical CO₂ capture applications.

5. Other CO₂ capture technologies

5.1. Oxy-fuel combustion

5.1.1. Oxygen production technologies (OPTs)

This section aims to analyse oxygen production Technologies (OPTs) that are most widely utilized for oxygen production. Fig. 5.1 shows the technologies that are discussed in this work and divided into conventional OPTs: Cryogenic Distillation and Pressure Swing Adsorption, and novel OPTs: Membranes, Chemical Looping Air Separation and electrochemical water splitting technologies.

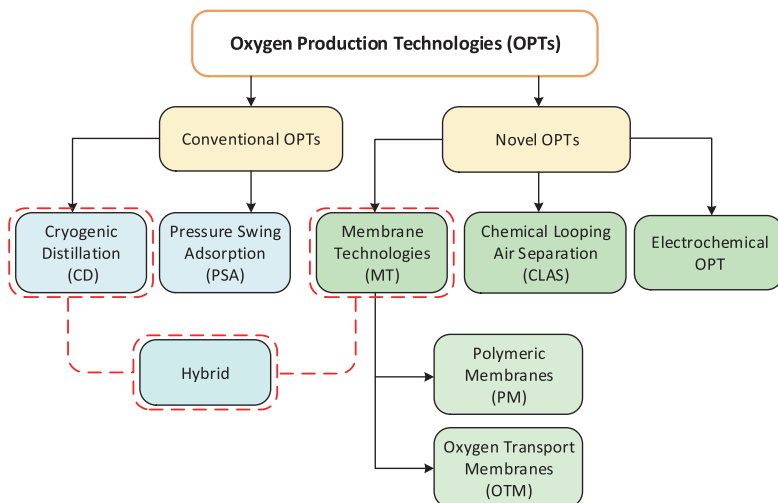


Fig. 5.1. Main oxygen production technologies for oxyfuel combustion process. (For interpretation of the references to color in this figure legend, the reader is referred to the web version of this article.)

Table 5.1

Main advantages and disadvantages of CD (Agrawal and Herron, 2000; Cao et al., 2016; Chen and Yu, 2021; Smith and Klosek, 2001; Zhu et al., 2006).

| Advantages | Disadvantages |
|---|--|
| Mature and reliable technology suitable for large-scale air separation with high O ₂ volume production | The air compression and fractional distillation of its constituents are very energy-intensive, accounting for around 85% of the total energy consumption in the ASU (Zhu et al., 2006) |
| Cryogenic air separation units produce oxygen with a purity of 99.5% by volume at an oxygen recovery rate of 97.85% (Agrawal and Herron, 2000) | The technique results in a 3–4% energy penalty and the capital investment for the CAS technique contributes to around 14% of the overall oxy-fuel plant cost (Cao et al., 2016) |
| Cryogenic technology can also produce high-purity nitrogen as a useful byproduct stream at a relatively low incremental cost (Smith and Klosek, 2001) | Inappropriate for processes requiring fast startup and shutdowns |
| Established technology | large units with a large physical footprint |
| | Not profitable for processes that consume small amounts of oxygen (Chen and Yu, 2021) |
| | Requires moisture pre-removal |

5.1.1.1. Cryogenic distillation. The cryogenic air separation (ASU) is a traditional process for producing large quantities of oxygen, nitrogen, and argon as gaseous or liquid. The technology is considered one of the most developed (Wu et al., 2018) and feasible methods for high-volume oxygen production that is required for the oxyfuel combustion process (Yadav and Mondal, 2022). The idea behind the technology is to use fractional distillation at low pressure and temperature to separate oxygen (with a purity of 99.5%) from air elements based on their different boiling temperatures. The most important design parameters of the distillation column are the number of stages, feed stage, and reflux ratio. These parameters are selected based on distillation requirements. Table 5.1 shows the main advantages and disadvantages of the cryogenic air separation method. One added benefit is that cryogenic air separation is specifically suitable for oxyfuel technology due to the high O₂ volume production. Oxy-combustion requires high O₂ production capacity; for example, a 500 MWE coal-fired oxy-combustion power plant requires 9000–10,000 tO₂/d (Chorowski and Gizicki, 2015; Higginbotham et al., 2011). On the other hand, one of the main drawbacks of the cryogenic air separation unit is high energy intensity, as mentioned earlier. The energy demand for the system oxygen production is about 240 kWh/tO₂ resulting in an overall efficiency drop of a power plant of around 8–10% (Davison, 2007). CD ASU at lower oxygen product purities, the separation of oxygen and nitrogen is only required, which is relatively easier than the separation of oxygen and argon. Fig. 5.2 illustrates that the rapid decrease in separation energy required takes place as the product oxygen purity is decreased from 99.5% to 97.5%, corresponding to the

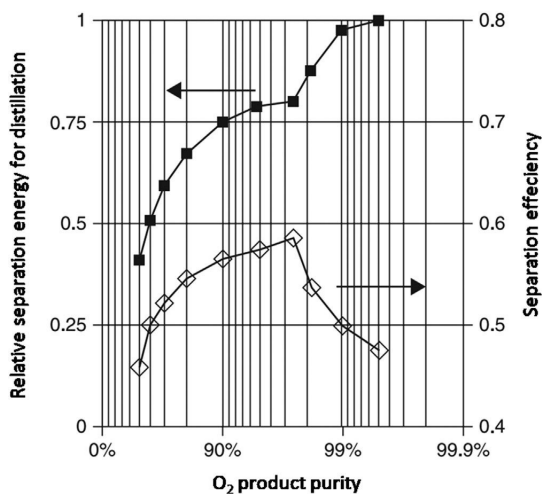


Fig. 5.2. Effect of oxygen purity on ASU separation energy (Prosser and Shah, 2011). (For interpretation of the references to color in this figure legend, the reader is referred to the web version of this article.)

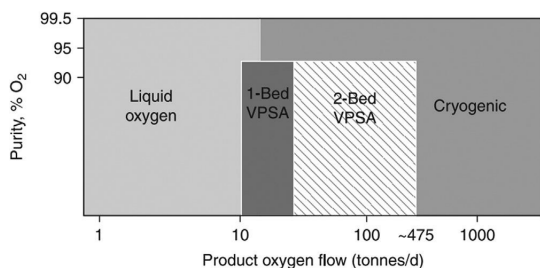


Fig. 5.3. PSA Oxygen supply system typical economic ranges (Prosser and Shah, 2011). (For interpretation of the references to color in this figure legend, the reader is referred to the web version of this article.)

change from oxygen–argon separation to an oxygen–nitrogen separation and the switch to an improved low purity oxygen process (Shash, 2011).

Cryogenic technology has greatly contributed to scientific research, specifically for oxyfuel combustion (Scaccabarozzi et al., 2016; Xiong et al., 2011, 2012; Ziółkowski et al., 2013). Beysel G. found that the energy consumption to produce O_2 with a purity of 95% instead of 99%, can reduce the energy consumption from 245 to 175 kWh/ton (Beysel). Tranier J. et al. reported that if the oxygen purity up to 95% is acceptable, then the auxiliary power consumption of oxygen production can be reduced from 350 to 200 kWh/ton of oxygen (Tranier et al., 2011). Šulc and Ditl (2021) obtained a relation between energy consumption per ton of oxygen and cryogenic plant capacity and reported that the specific energy consumption per ton of oxygen remains constant up to a value of 200 kWh/t of oxygen. Overall, the power consumption of the cryogenic air separation unit to produce O_2 of 95% purity varies between 184 and 260 kWh/ tO_2 (Chorowski and Gizicki, 2015; Skorek-Osikowska et al., 2015; Ströhle et al., 2009).

Despite the widespread of cryogenic air separation units in industrial use and their major benefits, the high energy demands of cryogenic distillation commonly contribute to over 50% of plant operating costs reported by Li and Bai (2012a). And S. García-Luna reported that cryogenic distillation is responsible for 54.42% of the total power consumption of plant net electric power of 242.24 MWe to provide the required amount of oxygen with 95% purity (García-Luna et al., 2022). However, R. López, based on techno-economic analysis, found that the use of cryogenic ASU makes oxy-coal fired plants unattractive for inversion due to its high total equipment plant cost (López et al., 2016).

5.1.1.2. Pressure swing adsorption (PSA). Pressure swing adsorption (PSA) is a separation method that is much newer as compared to cryogenic ASU. The first PSA technology for oxygen enrichment using nitrogen-selective zeolite was designed by Skarstrom and Attorney (1958). PSA devices take atmospheric air into a pressurized tank, a sorbent that is filled inside the tank. Zeolites are typically used and can selectively adsorb nitrogen while allowing oxygen gas to pass depending on the chosen sorbent dipole that has been created under high pressure (Ruthven and Farooq, 1990). After a certain volume of air has been separated, the adsorption sorbent will become saturated and eventually require regeneration. The adsorbent is regenerated by blowdown and a low-pressure purge using a part of the oxygen that was produced. The PSA has found use in medium and small-scale productions including industrial and health care. The performance of the adsorption system depends highly on the properties of adsorbents including: sorbent selectivity, adsorption capacities, sorption and desorption kinetics, and regeneration method (Yang et al., 2002).

One of the main drawbacks of PSA is the low oxygen purity, as shown in Fig. 5.3. Whereas PSA devices are best suited for processes that do not require extremely high purities of oxygen. Since the output of oxygen is largely controlled by the bed size, costs will rise drastically when higher

Table 5.2

Main advantages and disadvantages of PSA (Banaszkiwicz et al., 2014; Cao et al., 2016; Smith and Klosek, 2001; Zhao et al., 2015)

| Advantages | Disadvantages |
|--|---|
| Oxygen production, typically approximately 300 ton/day (Banaszkiwicz et al., 2014) | Limited scalability |
| Quick installation and start-up (minutes) | Not profitable for processes that consume small amounts of oxygen (Chen and Yu, 2021) |
| Low capital investment | Low Oxygen purity is typically 93–95 vol. % (Smith and Klosek, 2001) |
| Established technology | Energy penalty for large-scale applications is considerably high (Zhao et al., 2015) |
| Low waste generation, due to adsorbent recycling | Pretreatment is required to maintain the performance of the major adsorbents in the system, which makes process design more complicated |
| | It is not possible to obtain other separation products (nitrogen, argon) |

volumes of oxygen are required. In addition, the installation of multiple volume PSA plants is generally required for higher capacities, as shown in Fig. 5.3. However, due to economies of scale, there is a practical limit above which cryogenic supply becomes more economically attractive.

Another disadvantage of this method is that it has limited adsorbent capacity for large-scale applications (Prosser and Shah, 2011). The rest main advantages and disadvantages of PSA are summarized in Table 5.2. The reported literature shows that from an energy consumption perspective, the oxygen production for a small unit using the vacuum-pressure-temperature swing adsorption technology is between 500–888 kWh/ton of oxygen (Banaszkiwicz and Chorowski, 2018).

5.1.1.3. Membrane technology for oxygen production. Membrane separation is simpler than the cryogenic separation method. One such alternative approach is to use polymeric membranes or ion transport membranes (ITM). The difference between these two techniques is that polymer membranes are used for applications at ambient temperature, while for high-temperature applications, inorganic solid-oxide ceramic materials are mainly used [23]. The differences between the two approaches are shown in Table 5.3. Membrane technology has quick start-up times and operates at near ambient conditions. In contrast, capital costs with membrane systems increase linearly with the output volume desired. However, compared to cryogenic distillation and PSA, they are less complicated since they do not require regenerative steps (Murali et al., 2013).

A general polymeric membrane-based air separation is the feed gas that is passed across the membrane surface under a pressure driving force. The permeate is the gas that penetrates through the membrane and comes out as the low-pressure stream. The retentate is the remaining gas that exits as the high-pressure stream (Wijmans and Baker, 1995). Both permeate and retentate can be used if they meet the desired product purities (Murali et al., 2013). Polymeric membranes have received the most attention due to their advantages: high selectivity between gases, good mechanical properties, and economical processing capability. Polymeric membranes are often preferred to inorganic or ceramic membranes as they have a low environmental impact, are easy to incorporate into large-scale modules, and have the lowest capital costs among the different membranes [35]

Polymeric membranes are characterised by two factors: permeability and selectivity. The higher the permeability, the lower the selectivity, and vice versa (tradeoff) (Freeman, 1999). Consequently, the tradeoff between permeability and selectivity limits the use of polymeric membranes in large-scale applications (Robeson et al., 2015). A purity of 90% with one stage polymer membrane system is not practically achievable currently. A purity of 90% O_2 can be achieved by using two and three stages, depending on the type of membrane that is used

Table 5.3

Main advantages and disadvantages of MT (Bai et al., 2021b; Hofs et al., 2011; Hosseini et al., 2015; Sidhikku Kandath Valappil et al., 2021).

| Membrane separation technology | Advantages | Disadvantages |
|--------------------------------|---|--|
| Polymeric | <p>Lowest capital costs among the different membranes (Hosseini et al., 2015)</p> <p>Low environmental impact</p> <p>They can easily be modified and fabricated according to the specified requirements (Hofs et al., 2011)</p> <p>have competitive selectivity and permeability with ceramic and metallic counterparts</p> | <p>less competitive in improving oxygen purity in large-scale production compared with other conventional technologies</p> <p>Low oxygen purity ~ 40% (Sidhikku Kandath Valappil et al., 2021)</p> |
| OTM | <p>High chemical, mechanical and thermal stabilities</p> <p>can obtain 99.99% high purity oxygen (Bai et al., 2021b)</p> | <p>Very Brittle</p> <p>More expensive than organic polymer materials (Sidhikku Kandath Valappil et al., 2021)</p> |

(Adhikari et al., 2021). Up-to-date large-scale oxy-fuel combustion process, the feed stream is composed of an oxygen concentration higher than 21 % but lesser than 40 % in the best cases (Kianfar and Cao, 2021; Sidhikku Kandath Valappil et al., 2021).

Oxygen Transport membrane OTM or ion transport membrane (ITM) is an inorganic oxide ceramic material that is solid at the molecular level and acts as a membrane by allowing oxygen ions to pass through the ceramic crystalline structure. To conduct oxygen, the temperature of the OTM must be maintained above 800 °C and an oxygen partial pressure gradient must be applied across the membrane (Boot-Handford et al., 2014). The significant advantage of this approach is the potential reduction of capital cost and energy demand (Rastogi and Nayak, 2011).

Several studies (Engels et al., 2010; Stadler et al., 2011) have been conducted to reduce the energy consumption of the ASU by investigating the use of high-temperature OTM technology for oxygen production as an alternative to conventional cryogenic distillation methods. Reported literature shows that the OTM approach can be integrated into the front-end of combustion equipment, which results in the effective energy demand reduction to 147 kWh/ton of oxygen (Bai et al., 2021b). Normally, the conventional process has an associated consumption of 201.38 kWh/ton O (Dillon et al., 2005), whereas literature estimated a decrease in power consumption ranging between 85–362 kWh/ton of oxygen (Dillon et al., 2005; Shin and Kang, 2018). While some researchers maintain that OTM technology may replace cryogenic ASU in the long term because this alternative achieves energy and economic savings of 0.5–9 and 10.5–17.5 % (Portillo et al., 2019). Compared to cryogenic ASUs, a small-scale OTM unit consumes 60 % less energy and costs 35 % less to produce 500 kg O₂/day (Bernardo et al., 2009).

Integration of membrane and cryogenic technologies has recently attracted attention (Chen and Yu, 2021; Janusz-Szymańska and Dryjańska, 2015), as many researchers tried to evaluate the feasibility of oxy-combustion-based plants utilizing air separation units (ASUs) via cryogenic or membrane technology (Castillo, 2011; Pfaff and Kather, 2009; Skorek-Osikowska et al., 2015). Considering the implementation of a hybrid membrane-cryogenic ASU for further power reduction, Szymańska et al. (Janusz-Szymańska and Dryjańska, 2015) Demonstrated that the cryogenic ASU's reduced power usage for 99.8 % oxygen purity was 179 kWh/tO₂. In addition, Skorek-Osikowska et al. (2015) reported that the hybrid membrane cryogenic oxygen separation method has a 1.1 % higher net efficiency than the conventional cryogenic ASU.

5.1.1.4. Chemical looping. Chemical Looping Air Separation (CLAS) is based on the oxidative and reductive reactions of two interconnected reactors: air reactor and fuel reactor, which are oxidized to CO₂ and water vapour. The reduced oxygen carrier (typically metal oxide) is then transported to the air reactor where it reacts with the oxygen to reform the original metal oxide for recirculation back to the fluidized reactor (Mattisson, 2013). CLAS has been developed from chemical looping combustion (CLC), which has several challenges including the used material, mechanical stability and oxygen transfer rates, the temperature

at which the oxygen carrier is active, reactor capacity, and solid handling (Shah et al., 2015; Wu et al., 2018). Yet, on the other hand, CLAS is considered a promising approach capable of reducing the cost of oxygen production required for oxyfuel combustion technology (Cormos, 2020; Zhou et al., 2015b).

Shah et al. (2013) studied the integrated chemical looping air separation (ICLAS) modes with oxy-fuel coal-fired power plants. The results show that the specific energy required to produce oxygen in an ICLAS using flue gas (ICLAS[FG]) is 71 kWh/ton (CH integration) and 69 kWh/ton (solar integration) and in an ICLAS using steam (ICLAS[S]) and solar integration of 64 kWh/ton (without NSC) and 43 kWh/ton (with NSC). While in a conventional cryogenic ASU of 415 kWh/ton (99 % purity) and 330 kWh/ton (95 % purity), in an advanced cryogenic-based ASU (CASU) of 250 kWh/ton (99 % purity) and 200 (95 % purity). Zhou et al. (2015a) reported that by replacing a CASU with an ICLAS unit, the average reduction in the ASU power demand was up to 47 % and 76 %, respectively, for ICLAS[S] and ICLAS[FG]. Similarly, the average thermal efficiency penalty associated with the CASU, the ICLAS[S] and ICLAS[FG] units was found to be about 9.5 %, 7.5 %, and 5 %, respectively, indicating that the ICLAS[FG] unit is the most energy-efficient option for oxy-fuel plants. The levelized cost of electricity associated with the cryogenic and the ICLAS[S] and ICLAS[FG] units for the NSW fleet of coal-fired power plants were found to be about 118, 105, and 95 \$/MWh, respectively.

Cai et al. (2022) developed a one-dimensional packed bed model using perovskite sorbent to investigate the CLAS operation. The power consumption was 115 kWh/ton and 161 kWh/ton at 90 % and 95 % oxygen purities, respectively, while for a 5-step cycle configuration, the power consumption was 118 kWh/ton at 95 %. Cormos (2020) demonstrated that by using manganese-based CLAS, the energy efficiency was higher than the cryogenic process by 2–3.5 net percentage points. However, it was approved that the utilization of the CLAS system in coal and lignite-based oxy-combustion and gasification power plants significantly reduce the capital investment by about 12–18 % (Cormos, 2018), and the ICLAS offers between 40–70 % lower operational expenses as compared to conventional O₂ production technologies (Zhou et al., 2016).

5.1.1.5. Electrochemical water splitting. Electrochemical separation of hydrogen and oxygen using the electrolysis process dissociate water molecule by means of oxidation-reduction reactions taking place in two electrodes: cathode and anode, and separated by a medium (electrolyte) through which the ionic species transfers from one electrode to another (Bailera et al., 2020). Lately, the interest in the promotion of hydrogen energy to decarbonize the current energy system has strongly increased and is based on the Renewable Energy Roadmap (REmap) analysis. Hydrogen share will be increased by 6 % of total final energy consumption by 2050 (Gielen et al., 2019). Fig. 5.4 shows a schematic structure of the four types of electrolysis available in the market based on the difference in the operating temperature range and the ions exchange. These types include high temperature operation as; (a) solid-oxide steam

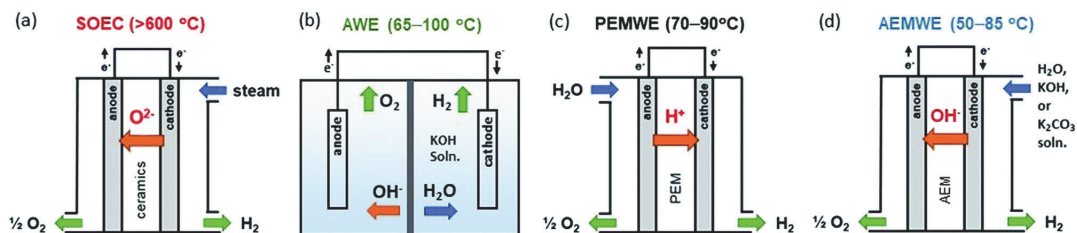


Fig. 5.4. Types of electrolysis technologies (Li et al., 2021). (For interpretation of the references to color in this figure legend, the reader is referred to the web version of this article.)

electrolyzer (SOEC) and low temperature operation as; (b) Alkaline water electrolyzer (AWE), (c) Proton exchange membrane water electrolyzer (PEMWE) and (d) Anion exchange membrane water electrolyzer (AEMWE).

Very limited publications regarding considering the potential of co-production of the energy free oxygen supplied from renewable base electrolysis for oxy-fuel combustion plants. As a reason, the high-power demand of such a process makes this option less competitive with other oxygen production methods. Yet, the efficiency of this process can be improved by using the co-product hydrogen to generate the power required for electrolysis (Iora and Chiesa, 2009).

Bailera et al. reported in different studies on hybrid power-to-gas oxy-combustion power plants where the co-product of oxygen in the water electrolysis for hydrogen production was used for the combustion (Bailera et al., 2015, 2016, 2021). The simulation of an electrolyser using Aspen Plus software that consumed 4.3–4.9 kWh/Nm³ to produce hydrogen with integration with methanation results in an increase in the overall efficiency from 55.9% to 67.5% since the OPT is avoided in the oxy-coal combustion. Kezibri and Bouallou (2017) demonstrated a conceptual model of a 200 MW power supply to the electrolysis process that leads to a corresponding 155 MW of Synthetic Natural Gas (SNG) produced in a thermally integrated methanation process with an efficiency of 83.1%. And found that by producing and storing enough amount of SNG and oxygen, an oxy-combustion power plant can be subsequently used to recover up to 480 MW of electric power as well as to produce CO₂ rich gas with an overall efficiency of 51.8%.

5.1.2. Allam cycle

Oxy fuel combustion utilizes a pure stream of oxygen (generally > 95%) as the oxidant for fuel combustion to achieve a product stream consisting solely of CO₂ and water vapour. The N₂ from air functions as a temperature regulator in conventional combustion; an oxidant stream devoid of N₂ can result in high flame temperatures, and this is controlled by recycling a part of the CO₂ flue gas back to the combustor. The difference in the two diluting gases (CO₂ and N₂) causes significant differences such as the density of the flue gas, heat capacity, diffusivity of oxygen and radiative properties of the furnace gases (Wall et al., 2009b). A process flow diagram of a general oxy-fuel combustion plant is shown in Fig. 5.5.

The Allam cycle, also known as the NET Power cycle or Allam-Fetvedt cycle, is an oxy-fuel based cycle which uses trans-critical CO₂ used as the thermal fluid (Allam et al., 2013a). The schematic of the cycle, as proposed by the original inventors, is shown in Fig. 5.6. The combustion chamber (6) operating at 300 bar is fed with pressurized gaseous fuel (3) and an oxidant mixture (4) of recycled supercritical CO₂ and pure O₂ from an Air Separation Unit (ASU) (27). The products (7) consisting of CO₂ and water vapour are expanded at an approximate pressure ratio of 10 in a gas turbine (9), co-fed with a bypassed coolant flow (8) of recycled supercritical CO₂ to avoid critical damage to the turbomachinery blades due to the high turbine inlet temperature. The gases (10) exiting the turbine are recuperated in a multi-stream heat exchanger (11) where the extracted heat is transferred to the incom-

ing supercritical streams (32, 23 & 24). The cooled flue gas (12) is sent through a condenser where water (13) is eliminated, and a portion of the remaining pure CO₂ (15) stream is exported to a CO₂ processing unit (CPU) for capture, sequestration, or utilization. The rest (~95%) is recycled (16) by compressing, cooling, and pumping to supercritical conditions. A split stream (25) is drawn to be mixed with the pure oxygen (29) from the ASU (27), forming the oxidant feed (30) to the combustion zone. The second split stream (21) is further divided (23 & 24) to form the cooling media (5 & 8) to the combustion chamber and the gas turbine, respectively.

The cycle developers evaluated the process efficiency (LHV basis) to be 58.9% for natural gas (simulated using pure methane) and 51.4% for coal (Allam et al., 2017). The extremely high efficiency was attributed to the difference in the thermodynamic properties of the working fluid, i.e., supercritical CO₂, which enables more energy recovery by eliminating losses typically encountered in Rankine cycles due to the phase changes (Allam et al., 2013b). While the cycle was initially developed for natural gas, it was adopted for solid fuel such as coal with some minor changes to the layout, such as the addition of a gasifier and ash filtration system upstream of the combustion chamber and flue gas desulphurization, deNO_x, and particulate removal units downstream. In addition to the high target efficiencies, the cycle claims a small plant footprint owing to the use of only a single turbine. For a power supply of 25 MW, the sCO₂ turbine is 90% smaller than an equivalent steam turbine (Service, 2017). The Allam cycle offers 100% carbon capture with the resulting CO₂ gas pressurized at pipeline conditions for sequestration, EOR and storage. The capital costs are expected to be lower than conventional plants without carbon capture due to the simplicity of operation (Allam et al., 2017).

The inventors have partnered with Toshiba Corporation to design the sCO₂ turbine and the oxyfuel combustor for use in the 50 MW demo plant at La Porte facility in Texas, USA, where the first run was conducted in May 2018. Planned commercialization in collaboration with multiple industrial partners has resulted in NET Power, the business venture of 8 Rivers, the inventors of the Allam cycle, announcing multiple 280+ MW scale plants at various locations across the United States and United Kingdom. With a goal of net zero emissions by 2050, each plant is capable of avoiding 1 million tons of CO₂ emissions annually.

There are, however, many challenges associated with the design components of this cycle. One such part is the heat recuperator section which handles multiple hot and cold streams. There is a large pressure gradient between the various streams, the required heat transfer area is large and the hot side may corrode the equipment as it contains CO₂ and condensing water (Scaccabarozzi et al., 2016). It is also noted that there is a significant imbalance between the heat requirement by the high pressure recycle streams and the heat supplied by the low pressure turbine exhaust, which can be corrected by adding external heat either from the ASU air compressors or the CO₂ recycle compressors into the recuperator (Allam et al., 2017). This adds to the complexity of the whole process and reduces the novelty of flexible operation. While there are several ways to provide pure oxygen to the process, the most mature technology is the cryogenic distillation of air. This is integrated

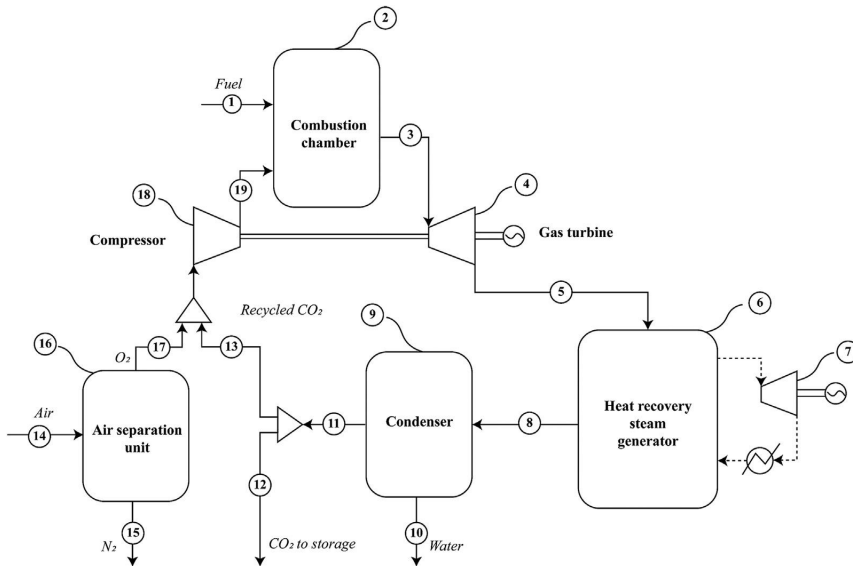


Fig. 5.5. Schematic of the general combined cycle oxy-fuel combustion process. (For interpretation of the references to color in this figure legend, the reader is referred to the web version of this article.)

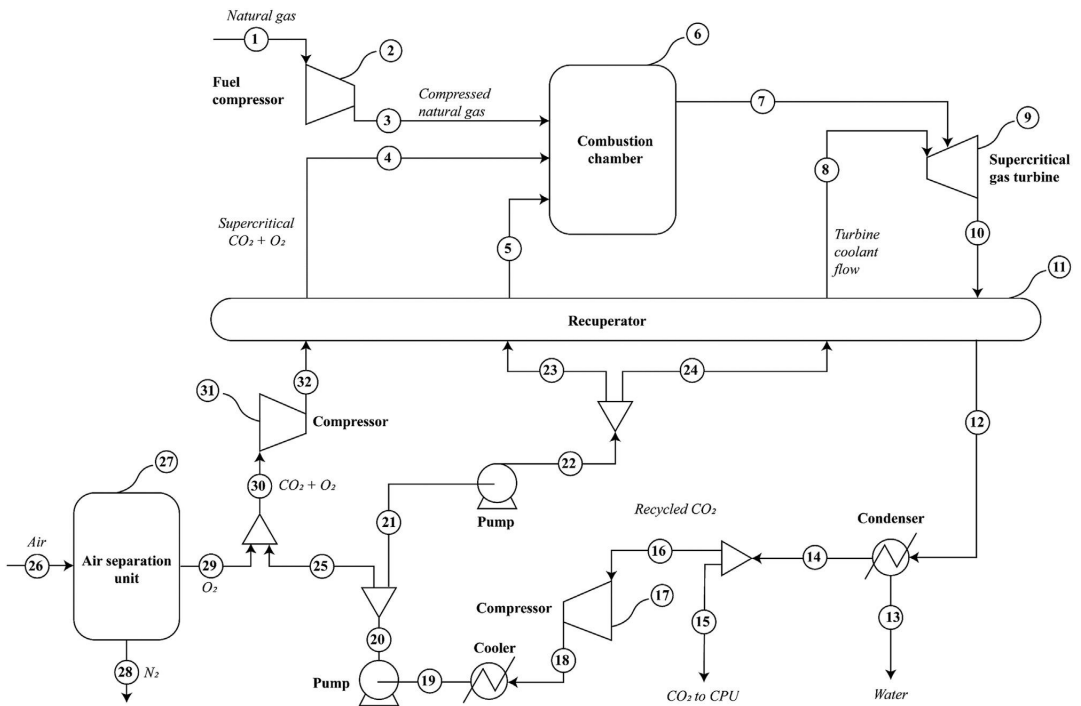


Fig. 5.6. Schematic of the natural gas fueled Allam power cycle (Allam et al., 2013b).

into the Allam cycle as a standalone unit operation. However, the compression and air separation units impose an energy penalty on the Allam cycle; when combined, they account for one-third of the gross turbine power production. Several potential modifications have been proposed in the literature to reduce this power consumption and further increase the performance of the Allam cycle.

Saccabarozzi et al. (2016) performed a thorough thermodynamic analysis and optimization of the Allam cycle. Their study indicates the existence of an optimal range where the cycle efficiency is maximum for the turbine inlet pressure between 260 and 300 bar and turbine inlet temperature between 1100 and 1200 °C. The turbine backpressure of the cycle was increased by Zhu et al. (2019a) to keep the turbine outlet gases at near supercritical value so that all gas compressors can be eliminated and replaced by pumps, thus increasing the performance by 2.15% at a turbine inlet temperature (TIT) of 700 °C and 2.96% at a TIT of 900 °C. This modified process, also known as the Allam-Z cycle, also introduced the utilization of cold energy of liquified natural gas (LNG) and liquid O₂ into the cycle, but the performance enhancement was subject to the TIT not being higher than 900 °C. While the substitution of multi-stage adiabatic compression with centrifugal pumps does decrease power consumption, it also requires extreme cooling and liquefaction of the flue gas. Chan et al. (2021) proposed to do this by utilising the cold energy of LNG through a series of condensers and chillers. This, however, leads to the demand for an excessive amount of LNG (87.5 kg/s), far beyond the actual amount required for combustion (2 kg/s). Accordingly, the authors propose to send the regasified natural gas (85.5 kg/s) to other potential end users. A secondary source of power output was included as a natural gas expander, which could raise the overall efficiency to 65.7%, much higher than the efficiency of the basic Allam cycle design, with the assumption that the cold energy associated with LNG regasification is freely available and does not constitute energy usage. A similar LNG heat sink concept, with a dual pressure Allam cycle for the cascade utilization of LNG cold energy, was proposed by Li et al. (2021); they suggested that their process could achieve 70.56% electricity efficiency at its optimal operation point. On the other hand, an optimization study to determine the best configuration to utilize the LNG cold energy suggests that it may be difficult to justify the additional capital cost associated with employing a standalone organic Rankine cycle to recover additional energy, because the performance of the modified Allam cycle only marginally increases (Yu et al., 2021).

Some design changes have been proposed by Allam and co-workers, e.g. the introduction of a low-pressure reheat loop with a two-turbine system, which was found to afford a 57.5% net efficiency (Allam et al., 2014). The authors also suggested that, in comparison to a single loop system, the net power output could increase by 2.5 times. Recently, Chan et al. (2020) described a reheating configuration for the Allam cycle. They added a low-pressure turbine and decoupled the ASU from the heat exchange network of the power island, at the expense of an increase the capital cost owing to the extra turbomachinery, a potentially more hazardous operation associated with the reheating of fuel and oxygen mixture and a decline in net efficiency.

The concept of Allam cycle is not limited to the combustion of natural gas, as its original designers also considered the efficient utilization of gasified coal. In fact, studies of coal-fired Allam cycle have also been conducted as part of the effort to develop clean-coal technologies. An analysis of the type of gasifiers and coal feedstock was conducted to determine the optimal performance by the Allam cycle using solid fuels (Lu et al., 2016). The key finding of the study validated the original hypothesis that a coal-fired Allam cycle could perform at higher efficiencies than the state-of-the-art integrated gasification combined cycle (IGCC) processes without carbon capture. While it was found that the different feedstock quality does not have a significant impact on cycle performance, emphasis is given to the future development of DeSNOx (de-sulphurisation and nitrogen oxide removal) processes, heavy metal removal, fouling prevention and corrosion pre-

vention, all of which are important considerations for developing truly clean coal technologies, which are less commonly studied in the context of Allam cycle. A detailed exergy analysis of a coal-fueled Allam cycle, by Luo et al. (2021) revealed that 50% of the exergy destruction comes from just three components, the gasifier, the turbine and the combustion chamber. These insights are important for determining the focus of further R&D efforts to improve the performance of the Allam cycle systems.

Zhu et al., who proposed the Allam-Z cycle (Zhu et al., 2019a), also proposed a similar scheme for coal-fired Allam cycle, denoted as the Allam-ZC cycle (Zhu et al., 2019b). In the Allam-ZC cycle, supercritical water coal gasification technology was employed to produce a syngas which can be directly sent to the Allam cycle with a higher turbine backpressure. As such, there is no need to add costly syngas cleaning procedures as supercritical water gasification ensures the complete conversion of contaminating elements such as N, S, P and Hg to inorganic salts and deposits. Even though a lower net efficiency of 47.3% was reported (c.f. the original Allam coal cycle efficiency of 51.4%), the authors argued that the Allam-ZC is still superior over the state-of-the-art to IGCC and other coal-fired plants without carbon capture.

An economic evaluation of the Allam cycle found it has a levelized cost of electricity of 91.7 €/MWh, which is higher than that of a typical natural gas CCGT (62.5 €/MWh) (Rodríguez Hervás and Petrakopoulou, 2019). Indeed, Allam cycle remains a relative new power generation technology with relatively few dedicated studies and analyses. The economic viability of the Allam cycle would also depend heavily on the CAPEX of highly specialized equipment, such as a supercritical CO₂ turbine, the cost of which may be far from being commercially competitive at its current state of development. The shortage of comprehensive experimental data in the open domain also imposes great uncertainties in validating the performance and cost-effectiveness of the Allam cycle and its various process variations (Haseli, 2021). In addition, the energy efficiency of the ASU units and their integration with the thermal power cycle would further impact the net efficiency of the Allam cycle. Optimistically, future near-commercial scale demonstration projects will provide the research community with more data validating the practical performance of the Allam cycle, highlighting the needs for further R&D and encouraging more research efforts to improve its competitiveness, e.g. by exploring integrating and hybridizing Allam cycles with other cryogenic, thermal and/or chemical processes, under a variety of operating scenarios, including the use of gasified solid fuels.

5.1.3. O₂/CO₂ and O₂/H₂O oxy-fuel combustion

Oxy-fuel combustion is considered one of the technologies applied to capture and sequester CO₂ in coal-fired power plants, and three generations of combustion technology have been developed so far. The circulating flue gas in the first-generation oxy-fuel combustion technology is about 70%, and flue gas recirculation (FGR) results in exergy losses and additional auxiliary loads (Gopan et al., 2020). The air separation unit (ASU) and the CO₂ purification unit (CPU) will cause about 8% carbon capture efficiency loss. The second-generation and third-generation combustion technologies are the main development targets. According to the combustion atmosphere, they are divided into O₂/CO₂ and O₂/H₂O combustion. Combustion pressure develops towards higher, making the entire technology economically competitive.

5.1.3.1. Characteristics of O₂/CO₂ combustion. The reactive gases in O₂/CO₂ combustion are O₂ and recycled flue gas. Pure oxygen and partially recovered flue gas produced in the ASU control the flame temperature and supplement the missing N₂ volume to transfer heat to the boiler (Stanger et al., 2015). Compared with air combustion, replacing N₂ with CO₂ will significantly reduce the combustion gas temperature (Khatami et al., 2012), but the combustion temperature of O₂/CO₂ can match the air combustion temperature curve when the O₂ concentration exceeds 30% (Scheffknecht et al., 2011).

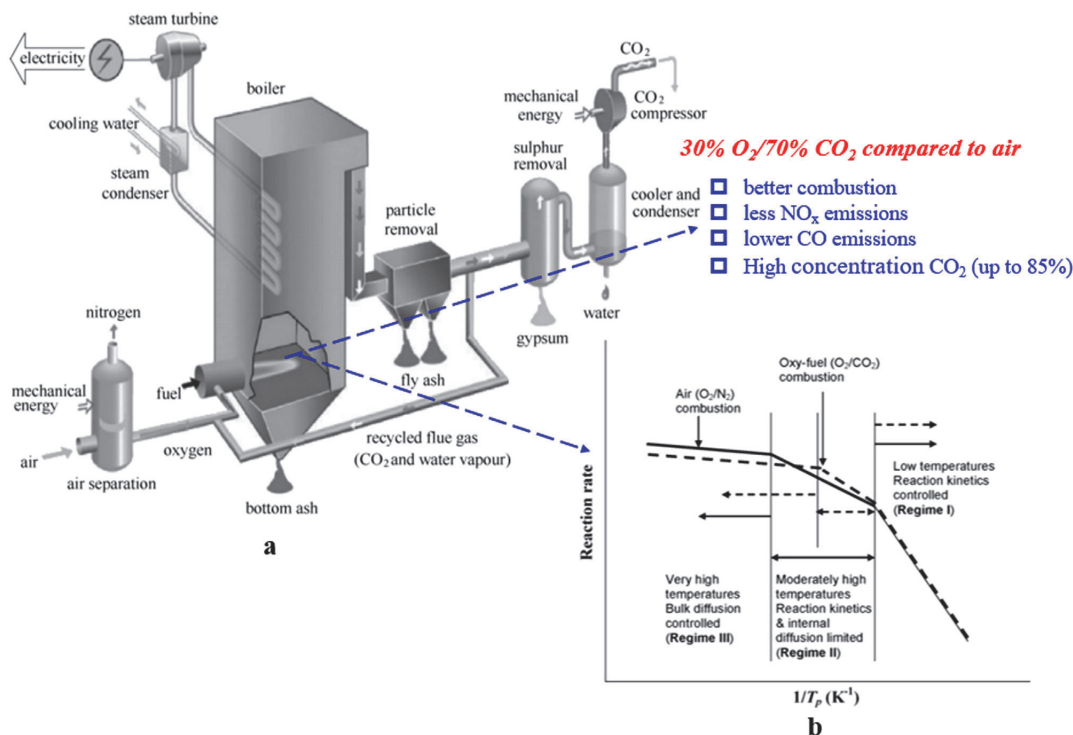


Fig. 5.7. a: technical route of oxy-fuel combustion (Horn and Steinberg, 1982), b: schematic diagram of control stage in air and O₂/CO₂ atmosphere (Wall et al., 2009a), comparison of char combustion characteristics in 30% O₂/70% CO₂ and air combustion (Stanger et al., 2015; Toftegaard et al., 2010).

The comparison of the characteristics between the second-generation oxy-fuel combustion technology and air combustion and its technical schematic diagram is shown in Fig. 5.7. O₂/CO₂ combustion has advantages in combustion characteristics and is conducive to CO₂ capture compared with air combustion. However, the flue gas circulation will enhance the coupling of the boiler, making it difficult to start and stop (Toftegaard et al., 2010), and cause pollutant accumulation and air leakage, which will increase the cost of CO₂ capture (Croiset and Thambimuthu, 2001). Chen et al. (2012) systematically reviewed the research on combustion thermodynamics, ignition, kinetics, pollutant emissions, combustion stability, and CFD simulation design of O₂/CO₂ before 2011. However, the research on pressurized oxy-fuel combustion has not been thoroughly analysed.

5.1.3.2. Pressurized O₂/CO₂ combustion. The ASU and CPU in the traditional oxy-fuel combustion system are carried out under high pressure, but the working pressure of the fuel combustion unit (pulverized coal boiler or fluidized bed) is normal. The pressure conversion process in the system results in a reduction in power generation efficiency of around 10% (Tranier et al., 2011). Therefore, the concept of pressurized oxy-fuel combustion (POFC) was proposed to overcome the energy loss by increasing the pressure of the combustion unit. In addition, pressurized oxy-fuel combustion has the following advantages:

- 1) The size of boiler equipment is reduced, and the cost of infrastructure is reduced;
- 2) More latent heat of steam in flue gas can be recovered;
- 3) Avoid system air leakage and reduce CPU energy consumption;
- 4) Convective heat transfer is improved at the same speed.

Current research shows that the optimal working pressure of pressurized fluidized bed combustion is around 1 MPa (Shi et al., 2019; Ying et al., 2016). Studies on pressurized oxy-fuel combustion systems have shown that the elevated pressure of the combustion unit can improve the power plant system's net power efficiency (LHV), reduce pollutant emissions, and obtain high concentrations of CO₂ (Soundararajan and Gundersen, 2013). Chen et al. (2019) analysed the 600 MW pressurized fluidized bed oxy-fuel combustion power plant and found that more phase change heat in the flue gas can be recovered under pressurized conditions, which can increase the net power efficiency by 36.83%. Hong et al. (2009,2010) and Gopan et al. (2014) reported that the net power plant cycle efficiency increased by 3%–6% when the pressure was increased beyond 1 MPa. Shi et al. (2019) showed that circulating compression work on pressurized circulating fluidized bed (PCFB) systems are negligible at a lower pressure than PC boilers. The higher combustion pressure is beneficial to the oxy-fuel circulating fluidized bed combustion, the net efficiency is increased from 27.2% to 30.5%, and the mole fraction of CO₂ can reach 92%.

The research on a laboratory-scale oxy-fuel-PFBC platform found that elevated pressure can improve pulverized coal combustion performance, thereby reducing CO, NO_x, and SO₂ emissions (Duan et al., 2019; Lasek et al., 2013; Wu et al., 2011). Zhang, W.D. et al. (2020) studied the O₂/CO₂ thermal conversion characteristics of bituminous coal at 1273 K using a pressurized drop tube furnace (PDTF) and found that the char yield decreased from 59.18% to 44.47% when the CO₂ partial pressure was increased from 0 to 0.45 MPa. Axelbaum et al. (2017) proposed a staged pressurized oxy-combustion (SPOC) process and successfully operated it at 1.5 MPa and ~100 kW of pilot scale. The results show that the system can capture more than 90% of CO₂ with high efficiency and

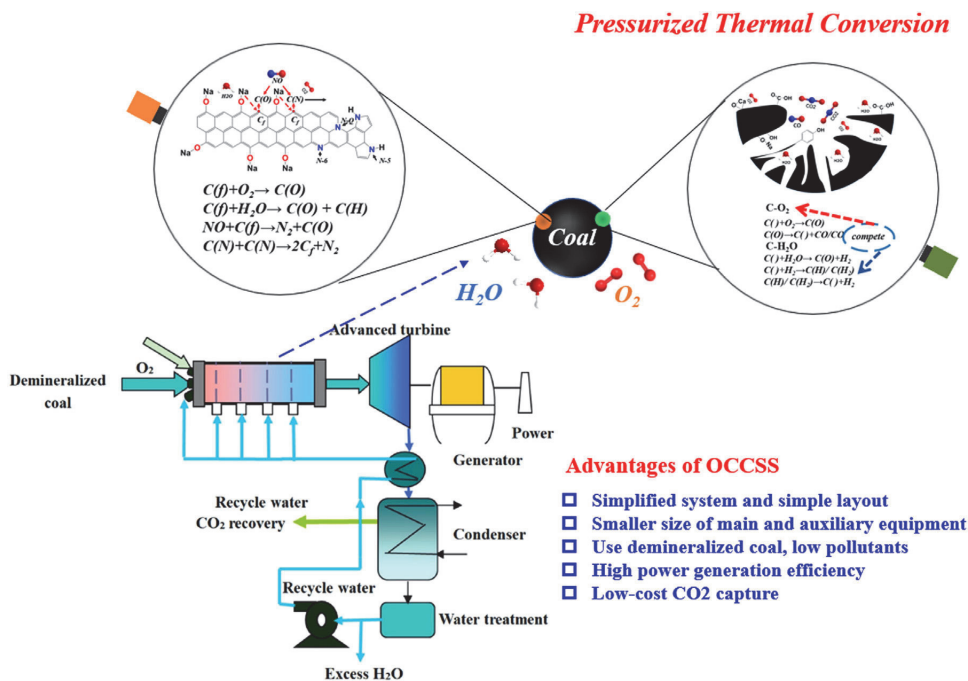


Fig. 5.8. OCCSS system diagram and technical advantages (Deng et al., 2021a, b; Zhao et al., 2019).

Table 5.4

Comparison of air combustion, O₂/CO₂ and O₂/H₂O combustion technologies (Deng et al., 2022).

| | Air combustion | O ₂ /CO ₂ combustion | O ₂ /H ₂ O combustion |
|-------------------------|----------------|--|---|
| Flame temperature | low | high | low |
| Combustion rate | low | high | high |
| Smoke volume | high | low | |
| System layout | | complex | simplify |
| Pollutant emissions | | low | low |
| CO ₂ capture | low | high (<90%) | high (>95%) |
| Cost | | higher | high |

affordable cost, and the efficiency is at least 3.5% higher than that of traditional oxy-fuel combustion devices (Yang et al., 2021).

The oxy-fuel combustion of pulverized coal mixed with biomass for power generation to reduce carbon emissions has also attracted widespread interest. Long et al. (Spiegel et al., 2021) performed a series of works on the oxy-fuel combustion of pulverized coal mixed with biomass using a laboratory-scale fluidized bed reactor, demonstrating the feasibility of mixed fuel blending. Zhong et al. (Liu et al., 2022) used a pressurized fluidized bed to achieve stable combustion of the mixed fuel, but the working pressure was only 0.1–0.3 MPa and found that the increased pressure can increase the combustion efficiency and facilitate CO₂ enrichment.

5.1.3.3. Characteristics of O₂/H₂O combustion. The O₂/H₂O combustion technique was originally proposed by Carlos et al. Salvador (2007), Seepana and Jayanti (2010), which was called steam-moderated oxy-fuel combustion (SMOC). The CANMET Energy Technology Center in Canada proposed a zero-emission power generation system based on O₂/H₂O combustion. The system uses steam to adjust the flame temperature, reducing the size of the power generation system by 2/5, and the energy consumption is greatly reduced compared with the second-generation oxy-fuel combustion technology (Zou et al., 2014b).

The O₂/H₂O combustion system eliminates the flue gas circulation system. And the flue gas condensed water is heated by the residual heat of the flue gas into steam, which is injected into the furnace to adjust the temperature. This series of processes improves the heat utilization rate of the system and removes the impurity gas in the water through the condensation and vapourization of steam, which is beneficial to the later CO₂ purification [30] (Cai et al., 2015). Deng et al. (2022) compared the characteristics of air combustion, O₂/CO₂, and O₂/H₂O combustion in the review of O₂/H₂O combustion of pulverized coal, as shown in Table 5.4.

5.1.3.4. Atmospheric pressure O₂/H₂O combustion. The H₂O concentration in O₂/H₂O atmosphere under oxygen-enriched conditions is between 25% and 35% (Hecht et al., 2012), which affects the ignition mode of char. Zou et al. (2015b) studied the ignition behavior of pulverized coal particles in an O₂/H₂O atmosphere (reaction temperature of 1373K, H₂O concentration of 50–79%) and found that the addition of steam promoted the formation of a large amount of CO and H₂ on the char surface. Under the same oxygen concentration, pulverized coal ignites earlier in O₂/H₂O atmosphere than in O₂/N₂ atmosphere (Zou et al., 2014a). The high concentration of steam strengthens the reactions of C + H₂O → CO + H₂ and CO + H₂O → CO₂ + H₂. A large amount of H₂ and CO in the char particle boundary layer will affect the heterogeneous

Table 5.5
Economic comparison of different CO₂ emission reduction system technologies.

| Power generation method | CES (Marin, 2003) | Hydroxy-fuel | OCCSS | IGCC wCO ₂ (EPRI, 2000) | USC Oxy-fuel (Dillon, 2005) |
|------------------------------------|-------------------|--------------|-------|------------------------------------|-----------------------------|
| Thermal Efficiency | 50.7 | 35 | 53.4 | 39 | 35.4 |
| CO ₂ emissions (Kg/MWh) | 0 | 0 | 0 | 83 | 83.7 |
| Equipment cost (US\$/kW) | 1210 | – | – | 1642 | 1857 |
| Electricity price (\$/kWh) | 0.054 | – | – | 0.069 | 0.062 |

reaction of char, making the char combustion mode change to joint ignition (Moors, 1999; Zou et al., 2015a). Blackwood et al. (1958) found that the CO₂ generated around the particles in O₂/H₂O atmosphere was mainly attributed to the homogeneous reaction (CO + H₂O → CO₂ + H₂).

A high concentration of H₂O affects the combustion mode of char. The enhanced gasification reaction and the thermal effect significantly affect the combustion process of char. Therefore, many scholars quantitatively analyse the consumption of char in the H₂O gasification reaction to study the effect of H₂O concentration on the combustion characteristics of char. Hecht et al. (2012) found that the H₂O gasification reaction of char in the wet flue gas cycle of oxy-fuel combustion contributed 8.7% to the overall char consumption. The gasification reaction accounted for about 20% of the carbon consumption under low oxygen conditions. Zhang and Pratioto et al. (2015) studied the char gasification-combustion model and found that under 31% O₂/CO₂-18% H₂O atmosphere (reaction temperature is 1373K), the char-H₂O gasification reaction contributed 26.2% to the char consumption. Chen et al. (2022) found that the contribution of gasification reaction to carbon consumption in the O₂/H₂O atmosphere increased with the increase in temperature and H₂O concentration. Increasing the H₂O concentration from 5% to 15% increased the gasification reaction's contribution to carbon consumption by 1.96 at 1373K.

5.1.3.5. Pressurized O₂/H₂O combustion. The research on O₂/H₂O combustion technology is still at the laboratory scale. Due to the complexity and high requirements of the experimental equipment, the understanding of the combustion characteristics of pulverized coal pressurized O₂/H₂O is still in its infancy. As shown in Fig. 5.8, Sun et al. (Zhao et al., 2019) proposed the concept of an oxy-coal combustion steam system of near-zero emissions (OCCSS).

The fuel of the system in the O₂/H₂O atmosphere is demineralized coal, and the high temperature and pressure mixed gas (the final steam concentration is about 90%, and the rest is mainly CO₂) drives the advanced turbine to work. Then the exhaust gas is condensed to obtain high concentrations of CO₂. The economic comparison between this system and other different CO₂ emission reduction systems is shown in Table 5.5. The CES (based on coal gasification technology) and OCCSS show absolute advantages over IGCC and USC (ultra-supercritical) oxy-fuel combustion power generation systems.

Macneil and Basu (1998) found that when the oxygen concentration was constant, the combustion rate of char first increased and then decreased with the elevated pressure. The experimental work on pressurized O₂/H₂O combustion of pulverized coal is currently being carried out by Harbin Institute of Technology (Bai et al., 2022; Deng et al., 2021a, b) and Southeast University (Zan et al., 2020). Fig. 5.9 (Deng et al., 2021a, b) summarizes the char thermal conversion process of demineralized coal in the context of OCCSS under different pressure conditions, H₂O concentration, and temperature. The increase of pyrolysis pressure helps increase the yield of pyrolysis char, and the increase of pressure and H₂O concentration can both promote the combustion of char. Under pressurized conditions, the temperature exceeds 1173K, and the thermal transformation of char is significantly promoted. At equal intervals of the reaction time, the char is transformed linearly.

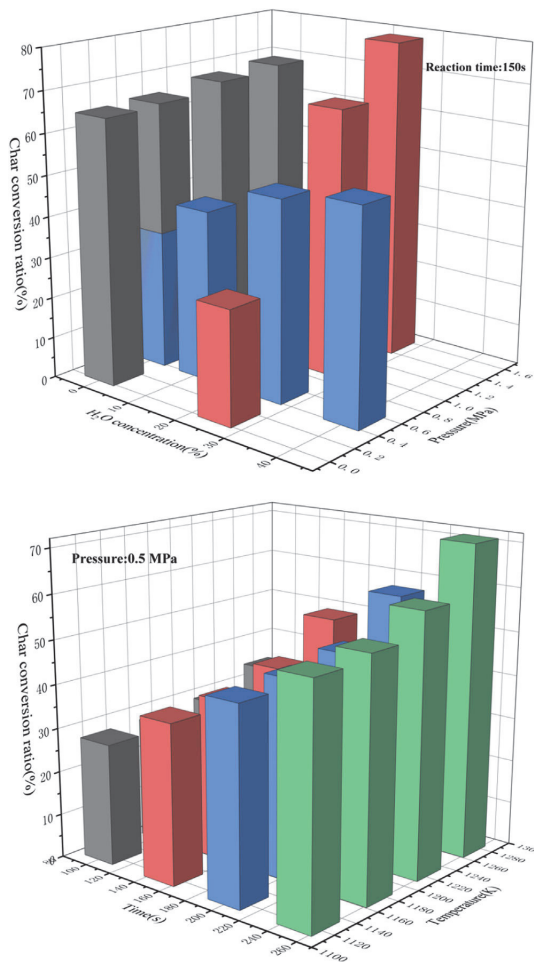


Fig. 5.9. Char conversion rate of demineralized char under different pressure, H₂O concentration and temperature, data adapted from (Deng et al., 2021a, b). (For interpretation of the references to color in this figure legend, the reader is referred to the web version of this article.)

The chemical kinetics in the pressurization stage is the rate-limiting reaction, and the pore diffusion becomes the rate-limiting reaction at high pressure (Turnbull et al., 1984). The char-H₂O reaction fully develops the micropore surface area, and pore development is achieved by consuming 5–10% of the char (Jasieñko-Hałat and Kędzior, 2005).

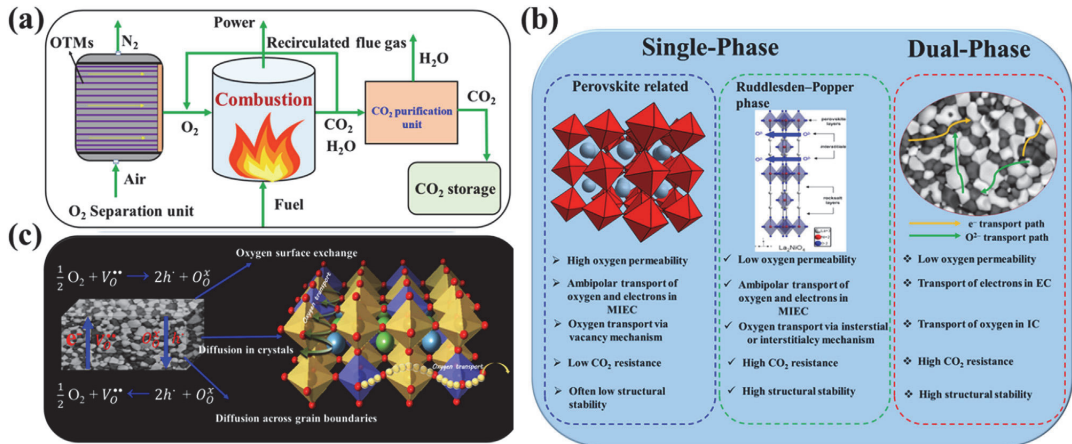


Fig. 5.10. (a) Schematic representation of using OTMs reactors for oxy-fuel combustion (b) the most common types of OTMs used for oxygen permeation and (c) a diagram of the oxygen transport mechanism (Chen et al., 2022). (For interpretation of the references to color in this figure legend, the reader is referred to the web version of this article.)

Therefore, under pressurized O_2/H_2O conditions, the change of char pore structure strongly affects its combustion process. Deng et al. (Deng et al., 2021a, b) studied the effect of H_2O concentration and pressure on char pores and found that the development of char pore structure increases first and then decreases with the increase of H_2O and pressure. When the H_2O concentration is 25%, and the pressure is 1MPa, the specific surface area of the char is the largest.

Therefore, pressure can inhibit NO production is consistent, but the optimal pressure is not unified. Zan et al. (2020) found that increased system pressure significantly suppressed NO emissions, and H_2O suppressed the formation of NO and N_2O . Bai et al. (2022) found that pressure affects NO emission, and the lowest relative migration of char-N to NO is 0.4 MPa. In summary, the application of pressurized oxy-fuel combustion technology to coal-fired power plants has great potential to achieve CO_2 emission reduction, especially to improve the combustion efficiency of pulverized coal and reduce pollutant emissions.

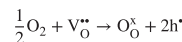
5.1.4. Oxygen transport membranes for oxy-fuel combustion

5.1.4.1. Status. To meet expanding global energy demand, the power generation sectors have integrated carbon capture and sequestration technology (CCS) into their current infrastructures in order to reduce combustion emissions while maximizing process efficiency (Li et al., 2022; Shaw and Mukherjee, 2022). Directly capturing CO_2 emissions from power plants is a potential route and oxyfuel combustion technology using pure oxygen for fuel combustion has gained increasing interest from many researchers and governments since it is easy to be integrated into current power generation facilities. The massive amounts of oxygen can be obtained by incorporating oxygen transport membrane (OTMs) reactors that filter pure oxygen directly from air (Fig. 5.10 (a)), with the required heat for the oxygen permeation reaction provided by the combustion process itself. The oxygen transport membrane reactors can also be used in many other industrial sectors, such as iron and glass factories, to capture enormous quantities of CO_2 emissions. Academic and industrial communities are becoming increasingly interested in OTMs. In theory, these oxygen permeable membranes can separate oxygen with 100% permeation selectivity and provide a cost-effective and simplified method for producing O_2 . In comparison to current cryogenic technology, the revolutionary method based on OTMs can save 60% of energy consumption and reduce production costs by 35% (Chen et al., 2022, 2015; Kiebach et al., 2022). Another appealing advantage of OTMs is

the ability to directly implement oxygen separation units into high-temperature processes such as oxy-fuel combustion. Recently, OTMs are also becoming increasingly appealing for use in membrane reactors for chemical and fuel production, in addition to O_2 separation (Chen et al., 2022; Plazaola et al., 2019).

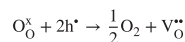
5.1.4.2. Transport mechanism of OTMs. OTMs for oxygen separation have been extensively researched in recent decades and are broadly classified into two types, as shown in Fig. 5.10 (b): single-phase and dual-phase. The selective permeability of oxygen from the high oxygen partial pressure side to the low oxygen partial pressure side can be realized based on a driving force created by oxygen partial pressure difference on the two sides of the dense OTMs. The oxygen ionic transfer in one direction and the simultaneous electronic transfer in the opposite direction allow oxygen to permeate through dense OTMs membranes at high temperatures. The oxygen transport process is generally comprised of the following steps (Bai et al., 2021a; Garcia-Fayos et al., 2020; Kiebach et al., 2022):

- 1) Diffusion of oxygen from the feed stream to the OTMs surface
- 2) Adsorption of O_2 on the surface of the OTMs
- 3) The adsorbed oxygen on the OTMs surface undergoes dissociation surface exchange reaction:



where V_O^{**} represents oxygen vacancies, O_O^x represents lattice oxygen and h^* represents electron holes.

- 1) Oxygen ion incorporation into membrane crystal lattice to form lattice oxygen.
- 2) Lattice oxygen diffusion and electrons diffusion via electron bands inside OTMs.
- 3) Lattice oxygen undergoes charge transfer on the OTMs surface to create chemisorbed oxygen.
- 4) Recombination surface exchange reaction:



- 5) O_2 molecule desorption from the OTMs surface

The oxygen permeation process involves a number of physical and chemical processes that are primarily controlled jointly by surface exchange and bulk diffusion in most cases. It is important to note that

the rate-limiting steps are determined by several parameters, including membrane material, operating conditions, and membrane geometry. To obtain accurate prediction of the oxygen permeation fluxes for various limiting cases, intensive efforts have been devoted to developing empirical equations or models that integrate surface exchange and bulk diffusion reactions. More detailed descriptions of the existing oxygen permeation flux models on the basic assumptions and transport mechanism of OTMs can be found in the previous excellent reviews (Li et al., 2018; Sunarso et al., 2008).

5.1.4.3. Performance overview of different types of OTMs. Single-phase perovskite-type OTMs materials with a general formula of $A_xA'_{1-x}B'_yB''_{1-y}O_{3-\delta}$ are among the most studied and promising candidates for oxygen separation since they exhibit high mixed ionic and electronic conductivity, which allow transporting the oxygen ions sustainably. An ion is typically an alkaline-earth metal like Ba^{2+} or/and Sr^{2+} , whereas B ion is generally a transition metal like Fe^{3+} or/and Co^{3+} . Based on the literature (Chen et al., 2022; Han et al., 2022; Widenmeyer et al., 2020), the chemical compound combinations $Ba_xSr_{1-x}Co_yFe_{1-y}O_{3-\delta}$ (BSCF) appear to be the best candidates with the highest oxygen permeation flux, which is generally more than $1 \text{ mL min}^{-1} \text{ cm}^{-2}$ for a 1 mm-thick membrane at 950°C and can even reach to more than $10 \text{ mL min}^{-1} \text{ cm}^{-2}$ for an ultra-thin BSCF membrane at 1000°C (Zhang et al., 2017). Despite exhibiting good performances for oxygen separation, the low chemical stability of BSCF membranes in CO_2 -containing atmospheres resulted in oxygen permeation flux deterioration because of the formation of strontium or barium carbonates, which limits their applicability for oxy-fuel combustion. In addition, the high thermal expansion arising from the phase transition in the OTMs operating temperature range will lead to mechanical instability. Based on the reported studies, several major approaches have been taken to improve the chemical stability of perovskite-based OTMs towards CO_2 (Chen et al., 2022; Chen et al., 2019; Zhang et al., 2017):

- Partially substituting the transition metal components in the B-site with more stable or acidic metal components.
- Reducing the Co content in the B-site;
- Using a rare earth metal cation as the A-site cation (e.g. La or Pr);

Although the proposed approaches (partial substitution of A- and B-site cations) can enhance the CO_2 resistance of perovskite-type OTMs, performance degradation is unavoidable due to the formation of an alkaline-earth carbonate layer over time when exposed to CO_2 -containing atmospheres.

An attractive alternative to perovskite is the Ruddlesden-Popper single-phase membrane material with a general formula $A_{n+1}B_nO_{3n+1}$ (A is an alkaline earth or lanthanide and B is a transition metal; $n = 1, 2, 3, 4, \dots$). One of the most studied examples is $\text{Ln}_2\text{NiO}_{4+d}$ (Ln is referred to rare earth metals such as Nd, Pr or La), which has been proved to be totally CO_2 tolerant during long-term oxygen permeation test in a CO_2 atmosphere (Chen et al., 2019; Xue et al., 2015). However, when compared to perovskite-type OTMs, the oxygen permeability of Ruddlesden-Popper single-phase membrane is significantly lower. Furthermore, it is reported that the presence of a small amount of SO_2 was sufficient to damage the Ruddlesden-Popper phase membranes because of the formation of sulphur containing products (Kiebach et al., 2022), which instantaneously blocks the active sites of the membranes for oxygen transport.

Dual-phase membranes, which are composed of an electronic phase and an ionic phase, have a high potential for oxygen separation and can address the issues of low chemical stability of single-phase OTMs (Bai et al., 2021a; Chen et al., 2021; Fang et al., 2015; Garcia-Fayos et al., 2020). Ideally, they combine the best properties of the electronic and ionic conductors to achieve both good oxygen permeation fluxes and satisfied chemical and mechanical stability in harsh operating conditions (for example, CO_2 and SO_2) at high temperatures. The successful materials for dual-phase membranes should meet the basic requirements: (a)

no reactions between these two phases at working temperature; (b) the creation of good percolation paths for the diffusion of electrons and ions; (c) a proper ratio between these two phases; (d) high electrical conductivities of both electronic and ionic conductors. Noble metals such as Ag or Pd were used as electronic conductors in early approaches. More recently, conductive oxide phases were selected as the electronic conductor. It is well accepted that the incorporation and release of oxygen are restricted to triple-phase boundaries (gas phase / electronic conductor / ionic conductor). The concept of combining two mixed ionic-electronic conductors in the dual phase OTMs is a promising route to overcome this limitation, where one shows superior electronic conductivity while the other has excellent ionic conductivity. Although dual-phase membranes also exhibit high CO_2 resistance after long-term CO_2 exposure, their oxygen permeability is lower than that of perovskite-type single-phase OTMs, similar to ruddlesden–popper single-phase membranes. To sum up, there is a trade-off between oxygen permeability and CO_2 tolerance. It is difficult to achieve high oxygen permeation flux while maintaining excellent chemical stability for the designed OTMs. Often, improving one property comes at the expense of sacrificing another. Reduced membrane thickness or optimization of OTMs geometry are two alternatives that do not induce such a trade-off. Since oxygen flux and membrane thickness are inversely related, reducing membrane thickness generally increases the oxygen permeation flux of the membrane. This is true up to a certain thickness known as characteristic thickness, after which the predominant bulk diffusion is limited by the oxygen surface exchange at gas/solid interfaces.

5.1.4.4. Membrane geometry and strategies for improving CO_2 resistance and oxygen permeability. At present, three shaped membrane configurations of OTMs have been widely studied: disk, tubular, and hollow fiber membranes. Despite being relatively simple to fabricate, the oxygen permeation performance of disk and tubular membranes is constrained by their small surface area, thick wall, sealing, and connection issues. The hollow fiber membranes have been considered as the most promising and practical one to improve O_2 permeation flux, which solves the problems faced by disk and tubular membranes. It is important to note that when the thickness of the membrane is reduced in order to achieve high oxygen permeability, the mechanical strength of the membrane decreases. A promising method for simultaneously obtaining high oxygen permeability and satisfied mechanical strength was an asymmetric structure membrane supported by a porous substrate. Aside from structural and chemical modifications to improve the oxygen permeability and CO_2 resistance of the OTMs, engineering approaches are effective methods to be applied. Coating the membrane surface with a porous CO_2 resistant layer is currently used as an effective approach to protect the single-phase perovskite-type membranes from CO_2 poisoning. For an ideal CO_2 protective layer material, high ionic conductivity, good chemical and mechanical stability towards CO_2 at working temperatures, and compatibility with the protected membrane are required. It is possible for the protected dense membrane and the porous protective layer to be made of the same material. If oxygen surface exchange predominates the transport process, it may be possible to increase the oxygen permeation fluxes by speeding up the surface exchange reaction rate by depositing a surface decoration (catalyst) layer on the membrane surface. Some intriguing ideas for improving oxygen permeability include using external electronic short-circuit methods to enhance the electronic conductivity of the membrane and utilizing plasma-based approaches that decouple oxygen molecule splitting and oxygen incorporation from the OTMs surface (Buck et al., 2021; Zhang et al., 2017; Zheng et al., 2022).

5.1.4.5. Existing developments for potential industrial applications of OTMs. The design of modules is a critical step in enabling OTM technology for large-scale purity oxygen production. Significant efforts are being made to improve the performance and stability of OTMs materials, and significant steps are also being taken in the design and integration of OTMs with oxy-fuel combustion systems. There are several developed

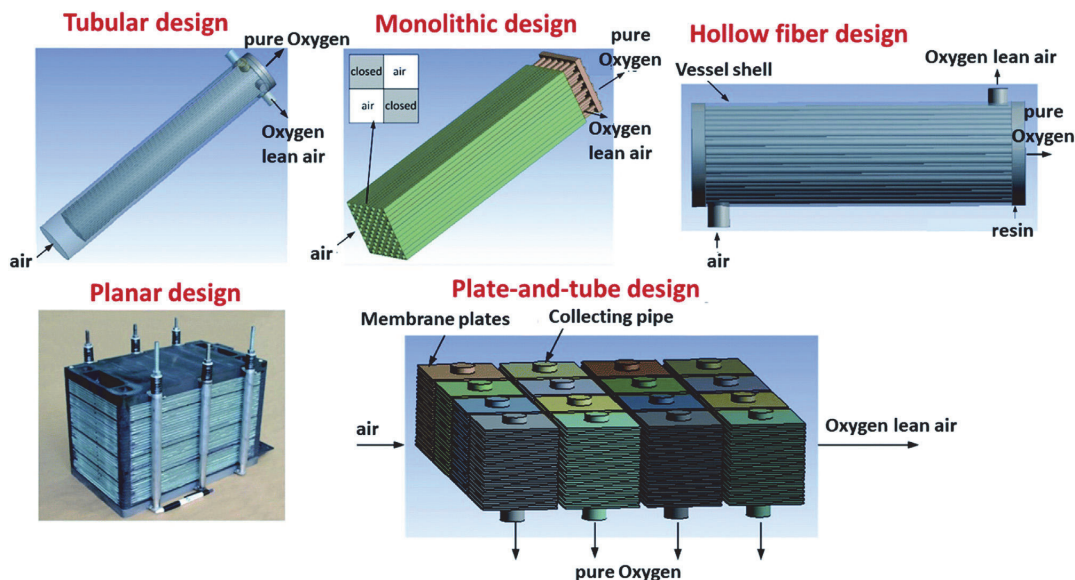


Fig. 5.11. Different design configurations for OTM modules for large-scale oxygen production. Reprinted with permission from (Kiebach et al., 2022). (For interpretation of the references to color in this figure legend, the reader is referred to the web version of this article.)

OTMs membrane modules (Fig. 5.11.) with different design configurations targeted at small and medium scale oxygen production, as recently summarized by Kiebach et al. (2022). A number of companies and academic research institutions have been working to scale up OTM concepts, developing membrane modules and successfully integrating them into industrial environments. Praxair, Inc. (now Linde plc) has made significant progress towards applications of dual-phase OTMs containing multipanel tubular reactor systems to improve the syngas produced by coal-gasification (Gupta et al., 2016). Currently, the pilot scale infrastructure is being reconfigured to connect OTM technology with steam methane reforming for blue hydrogen production by Linde. In terms of technology readiness levels and O₂ production rates, Air Products and Chemicals Inc. has made the most advanced developments. A membrane vessel with a total capacity of 2000 ton-per-day (TPD) O₂ production was developed, consisting of several 1 TPD OTM modules. However, no new information about OTM development activities was revealed, which was most likely due to a significant company restructuring in 2015 (Garcia-Fayos et al., 2020). It's also important to mention the OTM pilot module research conducted by the two Germany academic research organizations - RWTH Aachen University and Fraunhofer Institute for Ceramics Technologies and Systems (IKTS), both of which used Ba_{0.5}Sr_{0.5}Co_{0.8}Fe_{0.2}O_{3-δ} (BSCF) as the membrane material. With regard to the pilot module developed by RWTH Aachen University, a membrane module with a total of 596 tubular BSCF membranes was created and tested in a variety of environments (Nauels et al., 2019). It was possible to operate continuously for a maximum of 1800 h with an operating pressure of 10 bars and a temperature of 880 °C. The testing results demonstrated their concept is generally feasible. However, significant improvement is still needed to address the problems of breakages of membrane tubes. Since 2009, Fraunhofer IKTS has developed various OTM pilot plants with a growing oxygen production rate and a decreasing energy demand. A 18,000 h long-term oxygen permeation measurement was carried out using 93 capillaries, and the results showed the O₂ permeation flux dropped only by approximately 6% during the last 14,000 h continuous operation (Chen et al., 2022). The pilot plant design is still being refined, and more information can be found in

(Chen et al., 2022). Similarly, a perovskite membrane module made up of 889 La_{0.6}Sr_{0.4}Co_{0.2}Fe_{0.8}O_{3-δ} hollow fiber membranes has also been developed and could be operated continuously for 1067 h at about 960 °C (Tan et al., 2010).

It is worth noting that the majority of the above results were obtained in the absence of CO₂. Considered the harsh operation environments of the oxy-fuel combustion process, the membranes should deliver high stability while maintaining satisfied performance. In this context, special attention should be given to the development of dual-phase OTMs by optimizing the preparation approaches and microstructures, which have shown high resistance towards CO₂ and acceptable oxygen permeation flux. Engineering approaches such as depositing a surface decoration (catalyst) layer and designing an appropriate module should also be considered. Despite many advancements, there are still many research and technological challenges to overcome before OTMs for oxy-fuel combustion in power plants can be commercialized.

5.2. Chemical looping related carbon capture

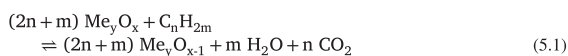
In a fuel-based power generation unit, the combustion of fuels is the route for energy generation, and carbon capture and storage (CCS) technology is necessarily employed to minimize CO₂ emissions combustion reactions (Gao et al., 2022b; Song et al., 2018b). CO₂ capture can be implemented in post-, oxy- or pre-combustion, wherein post-combustion is the conventional fuel oxidation method of combining fuel and air in a single heated reactor to give power (Alalwan and Alminshid, 2021). The flue gas containing CO₂ emitted has a low CO₂ partial pressure (i.e., < 0.15 atm), which makes current CO₂ technology challenging due to difficulties in separation and absorption. Progressing toward more efficient carbon capture, oxy-combustion, as described in Section 5.1, is the alternative to improve energy efficiency for the separation of CO₂ due to using pure oxygen from separation for fuel combustion to give only CO₂ and water vapour (Figuerola et al., 2008). More importantly, the CO₂-rich stream could be obtained by condensing water vapour, which is favourable for more-energy efficient carbon capture. Similar to oxy-combustion, pre-combustion primarily aims to form synthesis gas or syn-

gas, a mixture of H₂ and CO, from gasification or reforming. Thereafter, CO₂ is produced from CO via a water-gas shift reaction to produce more H₂ for combustion to give energy (Alalwan and Alminshid, 2021). Hence CO₂ before the combustion stage is captured (i.e., pre-combustion).

In any case, combustion technologies that require either CO₂ separation or O₂ separation from the air will incur high economic and energy costs. With the desire to avail of more energy-efficient process technologies for energy and material conversions, chemical looping processes, whereby a reaction or separation is divided into at least two sub-reactions that take place in a decoupled manner, have emerged as a competitive alternative in terms of the facile intrinsic CO₂ capture ability (Zeng et al., 2018). Typically, the chemical looping process involves circulating a chemical intermediate or looping material, such as metal oxides (MeO), that oxidizes feedstocks and reduces MeO. The reduced MeO (i.e., metals; M) would be re-oxidized, typically with air, in another unit. Such process is known as Chemical Looping Full Oxidation (CLFO), or conventionally also known as Chemical Looping Combustion (CLC). Some researchers labelled CLC as a pre-combustion CO₂ capture technology or a standalone fourth technique after post-, oxy- and pre-combustion CO₂ capture (Mukherjee et al., 2015). Importantly, CLC differentiates itself from pre-combustion CO₂ capture due to much higher concentrations of CO₂ in an effluent stream (i.e., up to 100%) compared to only 50% in that of pre-combustion. While many carbon capture technologies are being developed (e.g., solvent scrubbing, integrated gasification combined cycle), chemical looping is the most competitive technology by means of carbon capture cost (Bhave et al., 2017; Fan et al., 2012). Presently, most of the chemical-looping technologies for carbon capture in the power generating sector are still under laboratory research development stage, with several pilot-scale setups in operation for at least 11 000 h in 46 chemical looping combustors (Lyngfelt et al., 2019).

5.2.1. Chemical looping techniques

Chemical looping concept dates back to the 19th century by Quentin and Arthur Brin for air separation, with BaO as the looping material (i.e., BaO + 1/2O₂ = BaO₂) (Hepworth, 1892). CLC, the most widely adopted concept for chemical looping, was first introduced and patented by Lewis and Gilliland for the production of pure CO₂ using a solid oxygen carrier or any oxidizable carbon-based materials in two interconnected fluidized bed reactors. (Lewis and Gilliland, 1954) More scholars began to explore a deeper understanding of the process design (Mattisson et al., 2018, 2009), looping material selection (Tian et al., 2021; Zeng et al., 2018; Zhang, Z. et al., 2022), and the energetics of CLC, (Mukherjee et al., 2015) and expanded to a broad range of applications, depending on the nature of the recyclable reaction or looping reaction (Hu et al., 2018; Zeng et al., 2018). CLC consists of two mutually exclusive reaction steps that are performed sequentially and in a cycle with two interconnected fluidized bed reactors (i.e., fuel combustion reactor; reducer and air reactor; oxidizer) and solid oxygen carriers like metal oxides (Fig. 5.12 A1). In the first reaction step within the fuel combustion reactor, fossil fuel feedstock such as natural gas is oxidized by lattice oxygen found in MeO. Complete combustion with oxygen resulted in the formation of CO₂ and H₂O (Reaction 5.1), for which pure CO₂ can be obtained by condensation, thus doing away with costly CO₂ separation. Sequentially, in the second reactor (i.e., air reactor; oxidizer), the reduced oxygen carrier is subjected to airflow for re-oxidation (Reaction 5.2). The oxidized MeO is then circulated back to the first reactor for complete feedstock combustion.



The reduction reaction (equation 1) is, in general, an endothermic reaction for most oxygen-carrier metal oxides, while the re-oxidation of

MeO is exothermic. (Peltola et al., 2013) The heat released from equation (2) is of the same magnitude as if for complete conventional combustion of fossil fuel in the air, thus making CLC intrinsically advantageous. (Lyngfelt et al., 2001)

Chemical looping processes can be broadly classified into two groups depending on the type of looping material carriers, oxygen-carrier or non-oxygen carriers (e.g., CO₂-carrier). (Fan et al., 2012) Others may classify the different chemical looping processes as either CO₂-producing or separation is involved or not. CLC or CLFO process is one of the processes that only use oxygen carriers for energy generation (Fig. 5.12 A1), and others include partial oxidation or selective oxidation for syngas or hydrocarbons production, respectively, thus going beyond energy generation efficiency (Fig. 5.12 A2,3). Chemical looping can be extended to hydrogen production (i.e., chemical looping hydrogen production; CLH), and other forms of chemical looping, such as sorption enhanced reforming (SER) and sorption enhanced chemical looping reforming (SECLR). (Chisalita and Cormos, 2019) Regardless of the choice of looping materials (i.e., oxygen-carriers, non-oxygen-carriers, or both in tandem), chemical looping has been shown to effectively give better yields and product selectivity while having better CO₂ management, either by concentrating the CO₂ stream for capture or efficient CO₂ utilization. For example, Chisalita and co-workers conducted a techno-economic analysis of CLH with iron-based oxygen carriers for natural gas reforming to hydrogen and found that the chemical looping process is expected to have a production cost of 41.84 €/MWh, lower than 42.43 €/MWh from that of a conventional natural gas reforming without carbon capture. (Chisalita and Cormos, 2019) Furthermore, CLH allows for a very high carbon capture rate of > 99%, the unexpected inherent advantage of using chemical looping. The techno-economic assessment was applied to the natural gas combined cycle using oxy-fuel and carbon capture technologies with and without chemical looping design. With CO₂ and H₂O splitting chemical looping that permitted CO₂ recycling, the parasitic power load was reduced and thus resulted in an increase in net energy efficiency by 7.5% from 43.25%. (Farooqui et al., 2018) Hence, the chemical looping process can improve economic viability for chemical processes with 100% intended carbon capture. Fig. 5.12 briefly describes possible chemical looping processes, including more advanced hybrid chemical looping processes with three reactors for desulfurization and ammonia synthesis (Laassiri et al., 2018; Xuan et al., 2018).

5.2.2. Chemical looping materials

Ideal carriers, be it to carry oxygen or other atoms, require good reactivity with respective carrying atoms (e.g., oxidation in the air in oxidizers) or reduction with carbonaceous feed in the reducer reactor. Secondly, the carriers should have sufficient mechanical strength to minimize attrition and excellent resistance to carbon deposition, sintering, and agglomeration at high temperatures. Carriers also need to be fluidizable, and their physical and chemical properties remain robust against repeated reduction and oxidation kinetics at high temperatures. Transition metals such as Co, Ni, Cu, Fe and Mn have been investigated as oxygen carriers with their corresponding oxides CoO, NiO, CuO, Fe₂O₃ and Mn₃O₄ (Zhang, et al., 2022).

Among the transition metals, Ni and Co are among the costlier metals, but both have good reactivity with hydrocarbons (Dewangan et al., 2019; Hu et al., 2021a; Zhou et al., 2022), making them good candidates for the chemical looping process with carbonaceous feedstock. Close to 100% CH₄ conversions can be obtained over Ni-based oxygen carriers during a CLR process (Han et al., 2021; Huang et al., 2018). However, Ni sintering and the loss of metallic Ni, owing to partial re-oxidation into NiO, resulted in a reduction of the overall active surface area and hence catalytic performance after repetitive chemical looping cycles. Ni-based catalyst also suffers from sulfur-poisoning with the formation of nickel sulfide, Ni₃S₂. (García-Labiano et al., 2009) Co possesses high oxygen transport capacity, and readily undergoes a redox process between Co and CoO at above 900 °C (Fig. 5.13A). However,

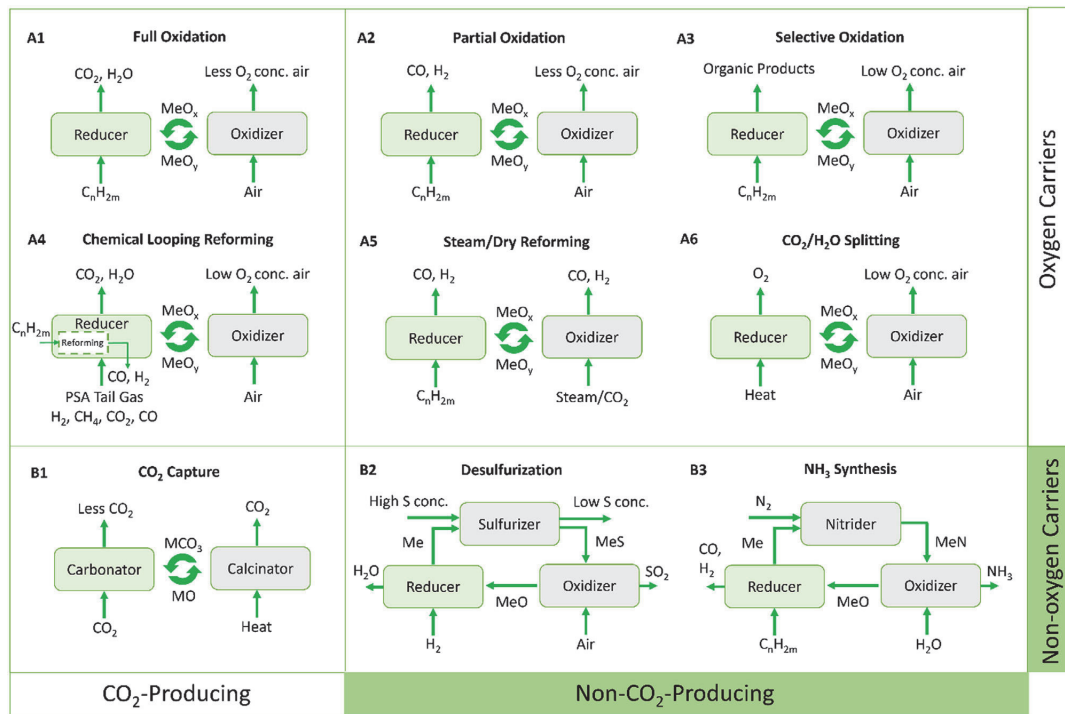


Fig. 5.12. Chemical looping techniques with different looping materials, broadly classified as either oxygen carriers (A) or non-oxygen carriers (B), and with different process designs, broadly classified as either CO₂-producing (A1, A4, B1) or non-CO₂-producing (A2, A3, A5, A6, B1-3). A1) Conventional chemical looping full oxidation (CLFO) or chemical looping combustion (CLC) (Alalwan and Alminshid, 2021). A2) Partial oxidation of carbonaceous feed to give syngas (Zhang et al., 2022). A3) Selective oxidation of carbonaceous feed affords high-value higher order hydrocarbons such as alkanes and alkenes. A4) Chemical looping reforming (CLR) with separate standalone conventional stream reforming in a reducing reactor (Luo et al., 2018). A5) Alternate chemical looping reforming (CLR) via steam or dry reforming process to convert carbonaceous feed into syngas (Hu et al., 2018; Hu et al., 2021c). A6) Thermochemical splitting chemical looping reactors for CO₂ to give CO and H₂O to give H₂ (Kim et al., 2022). B1) Carbon capture with carbonates to trap CO₂ (Zhang et al., 2022). B2) Hybrid chemical looping to carry O and S atoms for desulfurization (Xuan et al., 2018). B3) Hybrid chemical looping to carry O and N atoms for NH₃ synthesis (Laassiri et al., 2018). (For interpretation of the references to color in this figure legend, the reader is referred to the web version of this article.)

CoO has a strong affinity with common catalyst support materials like Al₂O₃, MgO, and TiO₂ to give thermally-stable and unreactive CoAl₂O₄, Mg_{0.4}Co_{0.6}O, and CoTiO₃ phases (Hu et al., 2018).

Cu-based catalyst has increasingly gained attention for their flexible redox ability from Cu with +2 oxidation state in CuO to +1 or 0 oxidation state in Cu₂O or Cu. Moreover, Cu is less toxic and low cost, and has a sulfur-resistant ability that Ni-based oxygen carrier lacks (Forero et al., 2010). Drawbacks of Cu include severe agglomeration at high temperatures due to its low melting point (i.e., 1085 °C) (Fig. 5.13 B), but strategies with tuning metal-support interaction to disperse Cu can overcome the limitation to give high chemical and mechanical stability (Izquierdo et al., 2021).

Fe-based oxygen carriers also face similar agglomeration problems with the formation of magnetite (Ryden et al., 2010). But, among the metals, Fe is environmentally-friendly, low cost, and possesses high mechanical strength – suitable for fluidization. While Fe falls short in the spectrum of oxygen transport capacity and reactivity towards hydrocarbons, its flexible oxidation states (i.e., Fe, FeO, Fe₂O₃, and Fe₃O₄) allow for use in different reaction systems (e.g., counter-flow moving bed reactor (Hu et al., 2020; Luo et al., 2014; Yu et al., 2019) Akin to Cu, Fe has modest resistance against H₂S poisoning, with H₂S being instead oxidized to SO₂ in the flue gas (Cabello et al., 2014), making Fe the most common versatile choice, together with Ni, for oxygen-carriers in many chemical looping processes and applications (Zhang et al., 2022).

Lastly, Mn-based catalysts as oxygen carriers are beneficial in terms of toxicity and cost, comparable with Fe, except that they boast higher oxygen transport capacity. However, Mn has flaws consisting of sulfur intolerance and the ability to form unreactive phases with Al₂O₃, SiO₂ and TiO₂ (Tian et al., 2009; Zafar et al., 2006). Fig. 5.13 C shows a broad overview of the possible metal-based oxygen carriers, contingent on a certain desirable chemical looping process (i.e., activity, sulfur-tolerance, cost etc.) To better meet the practicality and commercial viability of chemical looping processes, strategies to improve the shortcomings in the monometallic oxygen-carriers have been reported with 1) introducing promoters (Hu et al., 2021b, 2021c; Machida et al., 2015), 2) mixed oxide or bimetallic catalysts (Hossain and de Lasa, 2007; Mungse et al., 2015), and 3) unique structures (e.g., perovskites (He et al., 2013), core-shell (Neal et al., 2015; Tian et al., 2017) etc.).

Conventional oxygen carriers generally function by 1) generating oxygen vacancies or ions and electron-hole pairs, 2) permitting bulk diffusion of the oxygen species and electron-hole pairs, and 3) providing surface sites for reactions (Fig. 5.13D). In the reduction step of the chemical looping process, where the oxygenated oxygen carriers are subjected to a reducing gas (e.g., carbonaceous feedstock, hydrogen, etc.), oxygen anions are first generated due to the exposure and absorption of thermal energy, which would diffuse from within the bulk (i.e., higher oxygen potential) to the surface (i.e., lower oxygen potential) with a concomitant counter-current flow of electrons to ensure charge neutrality. The

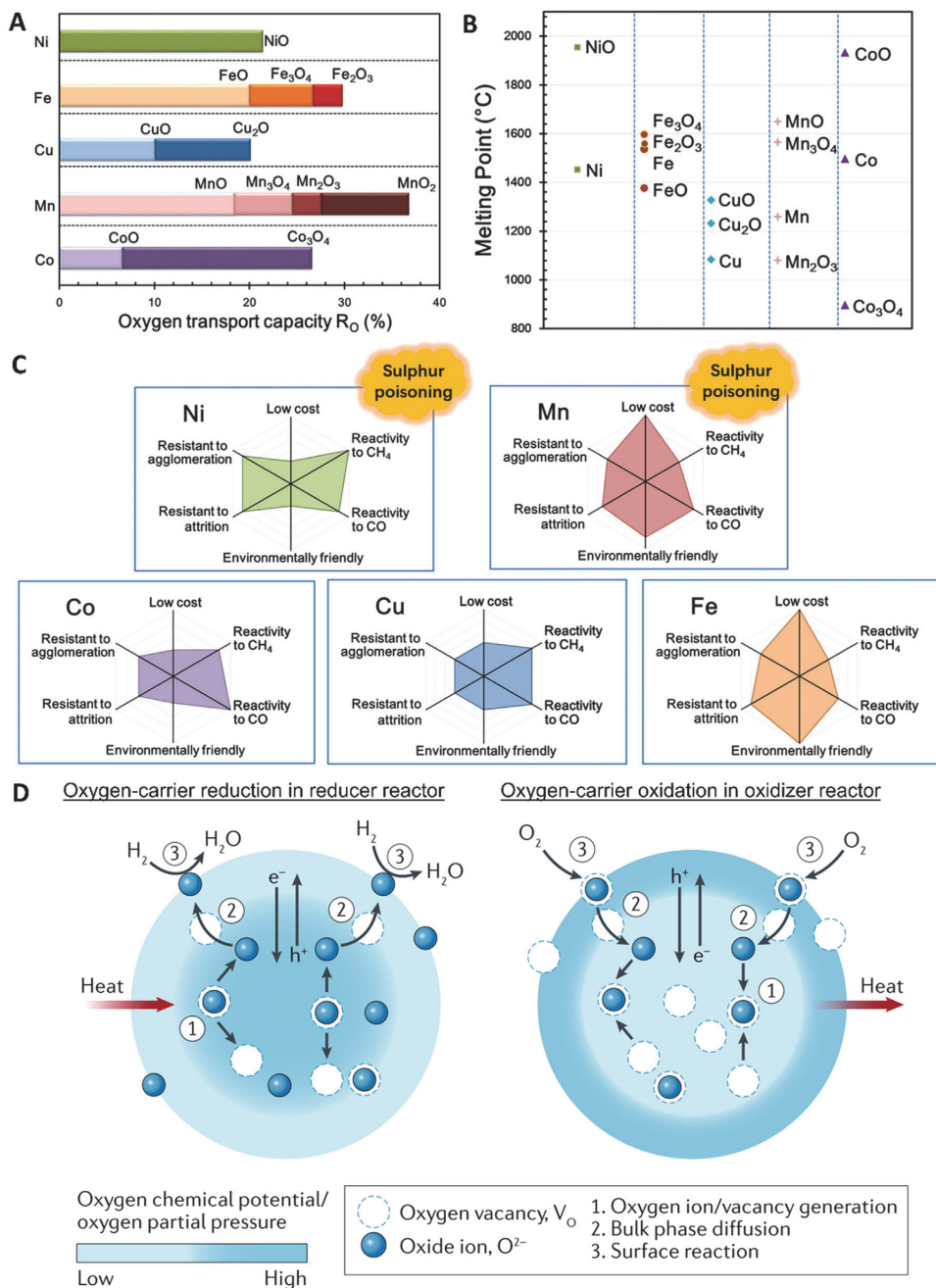


Fig. 5.13. Chemical and mechanical properties of oxygen carriers. A) Oxygen transport capacities comparison among Ni, Fe Cu, Mn and Co. B) Melting points of common metal oxides as oxygen carriers. C) Catalytic performance, cost, environmental-friendliness, agglomeration, and attrition resistance comparison (Zhao et al., 2017). D) Lattice oxygen generation and consumption of oxygen carriers in reducer and oxidizer segments of the chemical looping process (Zeng et al., 2018). (For interpretation of the references to color in this figure legend, the reader is referred to the web version of this article.)

active oxygen anions that have diffused to the surface can react and oxidize the reacting gas. On the other side, in the oxidation reactor, the oxidation of the oxygen-deficient oxygen carriers proceeds with oxygen occupying the oxygen vacancies on the surface before moving towards the bulk down an oxygen concentration gradient.

Another variant of the chemical looping process is chemical looping with oxygen uncoupling (CLOU), wherein the oxygen carriers do not just generate oxygen anions or vacancies, but rather release oxygen gas (O_2) to the gaseous phase in the reducer. The separated oxygen available for direct combustion overcomes the rate-limiting surface reaction with lattice oxygen on the typical oxygen carriers (Skulimowska et al., 2017). The common types of oxides capable of uncoupling oxygen are Cu and Mn-based, which allow the uncoupling of oxygen with sufficient oxygen partial pressures for combustion at elevated temperatures (Abián et al., 2017; Rydén et al., 2014). Interestingly, the majority of these carriers are Mn-based, either pure Mn_2O_3 or combined with other oxides (i.e., Ni, Fe, Mg, and Si) to give mixed oxides (Abián et al., 2017; Azimi et al., 2013; Shulman et al., 2009, 2011). The mixed oxides allowed higher oxygen partial pressures than pure Mn_2O_3 from between 850 to 1000 °C for combustion – a temperature range that is unsuitable for low-melting point Cu-based oxides.

Non-oxygen-carriers such as carbonates, sulfides, and nitrides for carbon capture, desulfurization, and ammonia production deviated from conventional oxygen carriers to allow novel applications (Zeng et al., 2018). Super-dry reforming is one example of hybrid chemical looping with both oxygen-carrier (e.g., Fe_3O_4) and carbon dioxide-carrier (e.g., $CaCO_3$), to convert CO_2 and CH_4 in a 3 by 1 molar ratio to H_2O in the reducer unit (Buelens et al., 2016). The work demonstrated that carriers can be used in tandem with other carriers (for a different purpose) to achieve broader applications. Also, the chemical looping concept can also be ingeniously exploited in a way without the use of an existing carrier. Hu and co-workers demonstrated that carbon deposits formed from dry reforming reaction (i.e., $CO_2 + CH_4 \rightleftharpoons 2H_2 + 2CO$) on the catalyst could serve as a transient looping material for NO reduction in a sequential step (i.e., $C + xNO \rightarrow CO_x + \frac{x}{2} N_2$) (Hu et al., 2021a). Henceforth, chemical looping technologies have high commercial-deployability value in the near future for efficient carbon capture, CO_2 utilization, or higher exergy efficiency with immediate CO_2 mitigation.

5.3. Cryogenic CO_2 capture

5.3.1. Introduction for cryogenic CO_2 capture

Cryogenic CO_2 capture refers to a physical separation process operating at sub-zero temperatures, which induces the anti-sublimation and, or liquefaction of CO_2 from process streams that require CO_2 removal, often combustion flue gases. Prior to cryogenic CO_2 capture, the flue gas should be completely de-humidified to prevent extensive frost formation in the pipeline and the process vessels. The advantages of this separation process include little or no usage of chemicals, a high rate of recovery, and high purity of the CO_2 product. In general, cryogenic CO_2 capture is considered economically viable when the feed stream is appropriately conditioned (Berstad et al., 2013), or when sufficient cold energy is available with fairly low cost.

The phase diagram for pure CO_2 is shown in Fig. 5.14. With a triple point at $-56.6^\circ C$ and 5.1 bar, cooling the process stream at CO_2 partial pressures below 5.1 bar would produce dry ice, while cryogenic capture with CO_2 partial pressure above 5.1 bar would produce liquid CO_2 upon direct cooling. To decarbonise flue gases from thermal powerplants with a typical CO_2 concentration of ca. 3–14%, depending on fuel sources, cryogenic carbon capture can be retrofitted as a post-combustion capture technology. For instance, to achieve 90% capture rate from a coal-fired powerplant (with a typical CO_2 concentration of 13 vol%), a maximum operating temperature of $-120^\circ C$ is required at 1 atmospheric pressure. To capture CO_2 from the flue gases of natural gas-fired powerplants (e.g. NGCC powerplant) that contains ~ 5 vol% CO_2 , a maximum

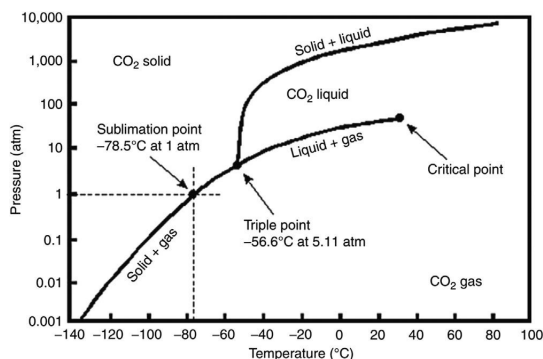


Fig. 5.14. Phase diagram for pure CO_2 . Image reproduced from (McCullom, 2011). (For interpretation of the references to color in this figure legend, the reader is referred to the web version of this article.)

operation temperature of $-140^\circ C$ is required to achieve 90% capture rate.

5.3.2. Vapour-to-liquid cryogenic separation

Distillation is the most common type of separation technique. As shown in Fig. 5.15, the traditional Ryan-Holmes process has been proposed for the purification of natural gas (Holmes and Ryan, 1982). Cryogenic distillation is a technique for separating biogas, natural gas and flue gas with careful consideration of CO_2 freezing temperature and pressure. The specific process of cryogenic distillation is as follows: The feed gas is pre-cooled and then chilled to a cryogenic temperature by a heat exchanger and enters the distillation column, which usually has a certain number of gas-liquid contact devices (e.g. trays or packing materials). After the distillation column, the raw gas is divided into two parts: the gas product at the top and the liquid product at the bottom of the column, respectively. Normally, in the biogas upgrading process, the methane after upgrading is discharged at the top of the column through a partial condenser, and the condensed CO_2 is passed through a reboiler at the bottom of the column to provide the heat required for evaporation. Eventually, the purified liquefied CO_2 is obtained through the separator.

Avoiding CO_2 freezing out during the cryogenic distillation process is an important point worth noting. Yousef et al. investigate the effect of tray temperature on CO_2 freezing by pressurizing biogas to 4.9 MPa and cooling it to $-61^\circ C$ to obtain liquefied CO_2 at the bottom of the column and biomethane with 94.4% purity at the top of the column (Yousef et al., 2018a). Although widely used in industry, cryogenic distillation is still characterized by high energy consumption, often reaching more than half of the overall operating costs (Ebrahimzadeh et al., 2016; Li and Bai, 2012b). A dual column cryogenic distillation process was proposed to use the cold energy of biomethane to pre-cool the biogas, thus reducing energy consumption to 0.236 kWh/Nm³ CH_4 , while the purity of biomethane was improved to 97.16% (Yousef et al., 2018b). Process intensification and mixed hybrid cryogenic distillation networks were explored in Maqsood's work, and the result shows a significant reduction in energy reduction and an enhancement in purification performance (Maqsood et al., 2014a; Maqsood et al., 2014b). In addition, a number of energy-efficient methods have been applied to the distillation process, such as recompression distillation (Kazemi et al., 2016), and heat integrated distillation column (Jana, 2016). In general, studies on cryogenic distillation focus on the reduction of energy consumption and the improvement of methane purity.

The controlled freeze zone (CFZ) is a solution based on single-tower cryogenic distillation for the removal of acidic impurities from natural gas because the presence of acidic gases (CO_2 and H_2S) in natural gas has

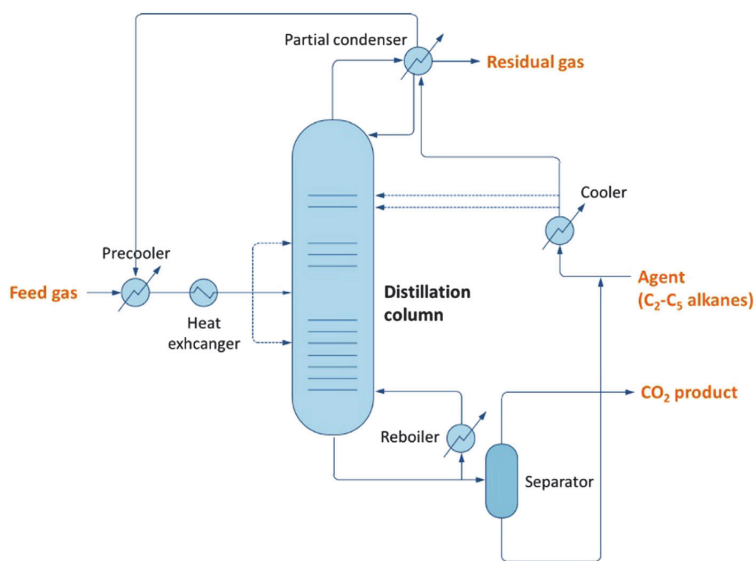


Fig. 5.15. The schematic flow diagram of Ryan Holmes process (Holmes and Ryan, 1982). (For interpretation of the references to color in this figure legend, the reader is referred to the web version of this article.)

a negative impact on both its combustion and transportation (Rufford et al., 2012). In this technology, the cryogenic distillation column consists of three parts: a controlled freezing zone, an upper distillation section and a lower distillation section. After dehydration and cooling, the feed enters the CFZ through a nozzle where the CH_4 evaporates above due to the higher temperature above than below. The solidified CO_2 is collected in the melt tray, and the temperature is kept moderately above the CO_2 solidification temperature so that CO_2 leaves at the bottom as a high concentration of liquefied CO_2 (Michael et al., 2011). The Exxon-Mobil Upstream Research Company developed this technology in 1983 and successfully demonstrated it in a commercial demonstration plant (Michael et al., 2011). The project results show that the technology has a natural gas processing capacity of 0.02 MNm^3 and a maximum operating capacity of $28.3 \text{ MNm}^3/\text{day}$, and that most of the captured CO_2 can be used for enhanced oil recovery (EOR). However, it should be mentioned that CFZ is not economical when there is a high content of ethane or higher hydrocarbon in the feed gas (Kelley et al., 2011).

5.3.3. Vapour-to-solid cryogenic separation

Antisublimation carbon capture technology is a vapour-to-solid cryogenic process in which CO_2 is converted directly from the gas phase to the solid phase at atmospheric pressure (or below the three-phase point pressure). The process of antisublimation CO_2 capture can be roughly divided into five steps (Pan et al., 2013): 1) chilling of flue gas to -40°C and removal of moisture and other impurities, 2) heat exchange between rich and poor flue gases, 3) refrigeration integrated cascade (RIC) process, 4) freezing heat exchange of CO_2 , 5) recovery of CO_2 .

Clodic et al. used lab-scale tests for an antisublimation carbon capture process in a 660 MW boiler under flue gas conditions of 15.47% CO_2 concentration at 60°C and 120 KPa, respectively (Clodic et al., 2005a, 2005b). The result shows that the energy loss in total power efficiency is controlled between 3.8% and 7.2%, which is a relatively low level compared to other technologies (Clodic et al., 2005a). Schach et al. performed simulations by reproducing the gas-liquid and solid-liquid phase equilibrium models, where the flue gas was chilled to 155 K at 100 KPa, and the specific electric demand was $0.286 \text{ kWh}/\text{kgCO}_2$ (Schach et al., 2011). In this process, the carbon capture performance is further improved by improving the compression cooling cycle, and the power consumption is further reduced to $0.193 \text{ kWh}/\text{kgCO}_2$, but the

high equipment investment cost is a major bottleneck problem. A similar process mechanism was reported by Spitoni, where the optimized process was able to recover both liquid CO_2 and liquid biogas with an electrical power consumption of $1.093 \text{ kWh}/\text{kgCO}_2$, which is 23% and 22% lower than the energy consumption levels of the alternative processes (Spitoni et al., 2019).

The CO_2 concentration in raw biogas has a significant effect on electricity consumption, which varies from 1.093 to $1.574 \text{ kWh}/\text{kgCO}_2$ when the CO_2 concentration is raised from 5% to 50%. CO_2 concentration also affects its freezing point during flue gas carbon capture. The freezing point of pure CO_2 gas is -78.5°C . However, it reduces to -99.3°C when the CO_2 concentration is low to 15% that in the flue gas condition, undoubtedly increasing the overall energy consumption (Song et al., 2014). Therefore, low CO_2 concentration and high expected capture target increase the overall energy consumption of the antisublimation process in flue gas (Clodic et al., 2005a). For the carbon capture process in biogas, even though the overall energy consumption increased and the liquid biogas revenue decreased when the feed CO_2 concentration was in the worst condition (50% CO_2 content), the total energy cost increased up to 5% due to 50% increment of by-product (liquefied CO_2) (Spitoni et al., 2019).

Generally speaking, the advantage of antisublimation carbon capture is that it has lower energy requirements in certain carbon capture scenarios (Clodic et al., 2005a; Spitoni et al., 2019). Another advantage of antisublimation technology is that the CO_2 thawed on the heat exchanger surface can be used for heat recovery, providing pre-cooling (Clodic et al., 2005b; Spitoni et al., 2019). At the same time, the latent heat during melting can be used to cool the refrigerant before evaporation (Clodic et al., 2005a). However, there are some limitations with the antisublimation process. For example, the moisture in the flue gas and raw biogas must be removed to less than 5 ppm to avoid clogging and other adverse effects. In addition, the choice of heat exchanger material is crucial to the effect of heat transfer efficiency after frosting. Finally, the concentration of CO_2 in the flue gas and raw biogas plays an equally important role in the evaluation of economic technology.

Stirling coolers are specific for their small size and low refrigeration temperature and can be used in the antisublimation capture process of flue gas and biogas. Song et al. designed a Stirling-based cryogenic capture process for post-combustion flue gas (Song et al., 2012c). This

carbon capture system consists of three parts. The pre-cooling tower removes the water from the flue gas to avoid blockage. The dehydrated flue gas is continuously cooled down to -99.3°C by cooling towers. The CO_2 in the flue gas is frosted on the storage tower, the solid CO_2 is collected by scrapers, and the remaining flue gas (the main component is N_2) is discharged to the atmosphere. The parameter analysis, energy consumption, study and energy integration of the system are also reported in the relevant articles, where the energy consumption of the simulated flue gas carbon capture at the experimental scale is controlled below 0.55 MJ/kgCO_2 (Song et al., 2012a; Song et al., 2012b; Song et al., 2017). However, the antisublimation carbon capture technology based on the Stirling cooler may be limited by the real flue gas conditions (impurities, high temperature, atmospheric volume, etc.), which is the focus of further research.

5.3.4. Heat exchangers

Heat exchangers can be utilized to cryogenically antisublimation CO_2 concentrations at atmospheric pressure for both high concentrations of CO_2 found in the flue gas of post-combustion processes ($\sim 13\text{--}15\%$) and for very low concentrations of CO_2 found directly in the atmosphere ($\sim 0.04\%$). While the idea of antisublimating CO_2 directly from exhaust gas streams at atmospheric pressure using a cryogenic heat exchanger has been around for around 20 years, newer studies are beginning to explore thermally capturing CO_2 directly from the atmosphere utilizing massive heat exchangers placed in arctic climates. Even though the two situations have drastically different CO_2 concentrations, the technology needed to design cryogenic heat exchangers to antisublimation CO_2 is analogous.

5.3.4.1. Heat exchangers: CO_2 cryogenic flue gas capture at atmospheric pressure. While considerable research to directly capture CO_2 from the atmosphere via chemical- and adsorption-based methods (Deng et al., 2021; Lai et al., 2021; Sanz-Perez et al., 2016b) is ongoing, due to the immaturity of the technology, questions remain on how and at what cost these techniques will scale to the gigaton level (Baxter et al., 2009; Keith et al., 2006; Lackner et al., 2012). On the other hand, cryogenic CO_2 removal is better understood, making potential faster scale-up possible. Cryogenic heat exchangers may be used for post-combustion carbon remover as well as for direct-air capture. Cryogenic CO_2 removal directly from the atmosphere or from power plant effluent is based on the thermal sublimation of CO_2 at very low temperatures, thus creating solid CO_2 for disposal. Post-combustion carbon removal from power plant exhaust streams using cryogenic heat exchangers is a mature technology that has been utilized for some time. Recently, several researchers have been exploring potential direct air capture cryogenic CO_2 heat exchanger designs for placement in Arctic and/or Antarctic climates (Boetcher et al., 2020; Perskin et al., 2022; von Hippel, 2018).

Clodic and Younes (2003) investigated the energy consumption associated with antisublimating CO_2 from flue gas using cryogenic refrigeration at atmospheric pressure. Theoretically, they determined that more than 93% of a 15% flue-gas CO_2 concentration could be captured at plate-heat-exchanger surface temperatures between -99 and 122°C . Since flue gases exit at high temperatures, above 85°C , water must first be condensed out of the mixture, then, after the CO_2 “frosts” onto the surface, it must be removed by a “defrosting process,” so a multi-step process is needed cryogenically removing CO_2 from effluent at atmospheric pressure. Follow-on test-bench work by Clodic et al. (2005b) presented an experimental examination of the defrosting process. Water from flue gas, at 15% CO_2 concentration, is first removed to equal 0.01 g of water per kg of dry flue gas, by multi-stage condensation. The flue gas is then routed to a low-temperature evaporator, where the flue gas is cooled to -120°C , energy recovery is utilized, and an energy cost is determined by process steps. Excluding other steps, such as pre-cooling to remove condensate, the energy cost of the cryogenic process was determined to be approximately 1.12 MJ/kg CO_2 , including a defrosting waste-energy recovery of around 0.26 MJ/kg CO_2 .

In the process proposed by Baxter et al. (2009), the flue gas is cooled, dried, and moderately compressed before it is cryogenically formed into a solid. In their process, with a concentration of CO_2 less than 15%, 99% of the CO_2 is antisublimated at -135°C . The advantage of the system proposed by Baxter et al. (2009) is that it can be easily retrofitted to existing carbon removal systems. Energy cost per mass CO_2 was not reported.

Haddad et al. (2019) modelled the frost growth and formation of CO_2 cryogenically antisublimating on a flat plate from biogas and flue gas stream utilizing simplified heat and mass transfer equations. The heat and mass transfer equations include heat and mass transfer coefficients which are determined using existing correlations in the literature. The exact starting CO_2 concentrations in the biogas and flue gas streams are unclear. Utilizing parabolic trough solar collectors to power a vapour absorption refrigeration cycle, Sateesh et al. (2021) tried to capture post-combustion CO_2 . The authors assumed a flue-gas composition of 15% CO_2 , 75% N_2 , and 10% H_2O and claimed a 100% CO_2 capture rate at an energy penalty of 1.25 MJ/kg of CO_2 .

5.3.4.2. Heat exchangers: cryogenic direct air capture of CO_2 . Pure CO_2 at 1 atm pressure antisublimates (changes phase from vapour to solid) at -78.5°C . However, for CO_2 in the atmosphere, which has partial pressures much below 1 atm, a much lower temperature is required to extract solid CO_2 from power plant streams or the air. Power plant exhaust CO_2 concentrations can reach up to 14%. Recent measurements of the concentration of CO_2 in the atmosphere at the Muana Loa Atmospheric Baseline Observatory have reached 419 ppm (NOAA, 2022), which equals a partial pressure of 0.000419 atm , which corresponds to an antisublimation temperature of -141.5°C . However, it should be noted that the CO_2 continues to antisublimates, and the partial pressure also decreases, which corresponds to a decrease in antisublimation temperature. Temperatures as low as -162°C may be required to antisublimation 99% of the CO_2 from the atmosphere. Air is primarily made up of N_2 and O_2 . At 1 atm, O_2 and N_2 begin to liquefy at -181°C and -195.8°C , respectively. Since the partial pressures of those components in the air are less than 1 atm, the liquefaction temperature will be even lower, allowing CO_2 to be cryogenically removed before liquefying O_2 or N_2 .

In the last decade, due to the urgency of the global CO_2 problem, research has emerged on thermally capturing CO_2 directly from the environment via antisublimation using a cryogenically cooled plate heat exchanger. The heat exchanger would be a part of a CO_2 deposition plant placed in Antarctica. The cold-air temperatures in Antarctica allow the inlet temperature to be as low as possible and closer to the CO_2 antisublimation temperature, thus reducing the cooling the sensible load needed to reach that temperature. Another advantage of Antarctica is that at those low temperatures, the air is virtually completely dry. Agee et al. (2013) were one of the first to conceptually propose such a system, referring to it as a CO_2 “snow” maker. An initial laboratory prototype was analysed by Agee and Orton (2016). The prototype was a benchtop-scale sequestration chamber situated with an aluminum plate interfaced with LN_2 . This experiment showed proof-of-concept, but the authors did not perform an in-depth energy analysis.

A systems-level energy analysis for a CO_2 deposition plant hypothetically placed in three candidate arctic climate scenarios (Snag, Yukon, Oymyakon, Russia, and Vostok Station, Antarctica) was performed by von Hippel (von Hippel, 2018). Using a simplified energy balance, von Hippel determined that CO_2 heat exchanger antisublimation in an arctic environment may be competitive with other technologies. Follow-on work, using a more sophisticated thermodynamic model and investigating more cases, including exploring pre-compression, was conducted by Boetcher et al. (2020) and Perskin et al. (2022). There, the energy performance of a waste-heat (or better, a “waste-cool”) precooler heat exchanger attached to the antisublimation heat exchanger was evaluated. It was found that this type of system could theoretically antisublimation

90% of 405 ppmv concentration ($\sim 0.04\%$) atmospheric CO_2 for as low as 133 MJ/kg in an arctic environment.

5.3.5. Cryogenic liquids

In addition to heat exchangers, cryogenic liquid as a cold source can directly take away the heat of flue gas containing CO_2 , resulting in the solidification of CO_2 . Then, the mixture liquid slurry of CO_2 and the cryogenic liquid goes through a filter to produce a CO_2 -rich product (Jensen et al., 2015). Generally, the vapour pressures of cryogenic liquids should be low in order to reduce losses during evaporation. Fazlollahi et al. have chosen isopentane to prevent CO_2 solidification on the surfaces, which would end the process (Fazlollahi et al., 2015). In Jensen's work, the heat duty is provided by an internal CF_4 refrigeration and an external cooling loop of CH_4 , and the result shows that the parasite power loading is about 15% (82.6 MW_e) and the energy consumption is 0.74 MJ_e/kgCO₂ (Jensen et al., 2015).

In most carbon capture processes, the biggest challenge is the high energy consumption. For the cryogenic carbon capture process, the waste cold energy like LNG (liquefied natural gas) is a promising approach to reduce the energy consumption by a thermal process, an inertial carbon extraction system or an external cooling loop. A hybrid cryogenic carbon capture process with an external cooling loop (CCCECL) was proposed (Baxter et al., 2009; Jensen et al., 2015). Briefly, the CCCECL system concludes: 1) dehydrated and cooled flue gas was sent from the system to the CCCECL process, 2) the flue gas was compressed and chilled to a temperature above the solidification of CO_2 , 3) the gas was expanded to be further chilled, 4) an amount of CO_2 was precipitated, 5) the CO_2 was pressured and reheated via the inlet gases, 6) the liquid CO_2 product was achieved for further utilization and the N_2 -rich exhausted gas was discharged. Some configurations of the CCCECL process can store energy as LNG (Jensen et al., 2015). In such system, the refrigerant was regenerated during low-demand periods, and then it was used to drive the cryogenic carbon capture process during peak demand periods. As a result, the parasitic load to the grid reduces. Besides, renewable intermittent power sources could be integrated with conventional power generation systems via CCCECL, resulting in a low energy intensive compared to the conventional capture process (0.98 MJ_e/kgCO₂) (Safdarnejad et al., 2015).

5.3.6. Packed beds

Packed beds have been worked as a heat transfer surface for the cryogenic carbon capture process that is usually filled with cold bed materials like steel monolith structure (Tuinier et al., 2011b). The capture process follows the steps: 1) chilled N_2 stream is sent to precooled bed material, 2) the N_2 steam is stopped, and the flue gas is sent to cryogenic packed bed, 3) CO_2 frost on the surface of bed materials till saturation, 4) a CO_2 frost front happen through the column, 5) a regeneration step is required when the packed column is saturated. The advantages of a cryogenic packed bed are that both CO_2 and H_2O can be separated from flue gas simultaneously via the difference of their dew and solidification points and the cold energy can be provided by LNG (Tuinier et al., 2010). Tuinier proposed a dynamically cryogenic packed bed, and the results show that the low volume fraction of frosted CO_2 leads to a low requirement of the elevated pressure value (Tuinier et al., 2011b). This indicated that the pressure drop and clogging phenomenon are mitigated in the cryogenic packed bed process. Apart from the carbon capture process in flue gas, cryogenic packing is also applied to the biogas upgrading process (Tuinier and van Sint Annaland, 2012). A novel cryogenic packed bed has been proposed for biogas treatment, and the result shows that the purity and recovery of biomethane products are higher. Meanwhile, the bed capacity is much higher (350.2 kg CH_4 h⁻¹ m⁻³ packing), and the energy consumption is lower (2.9 MJ/kgCH₄), compared to the conventional vacuum pressure swing adsorption process (Tuinier and van Sint Annaland, 2012). Moreover, the removal of H_2S content in raw biogas can be simultaneously achieved when the initial cryogenic packed bed temperature as low as -150°C

(Abatzoglou and Boivin, 2009). However, this may lead to an augment in operating cost on required cold energy. Fortunately, the cold energy required in the cryogenic packed beds process may be provided by LNG, making it competitive (Abatzoglou and Boivin, 2009). Moreover, the thermal insulation of cryogenic packed bed is another challenge that should be taken into consideration to reduce latent heat loss.

5.3.7. Compression

Compression is an important part in the cryogenic carbon capture process. The vapour-to-liquid and vapour-to-solid routes are determined by the pressure and cryogenic temperature of the carbon capture process. In Baxter's work, flue gas was compressed to 5–7 bar before cooling and chilled and then was expanded to form CO_2 solidification, which was called cryogenic carbon capture with compressed flue gas (CCC-FG) (Baxter et al., 2009). Similarly, in the cryogenic distillation process, the feed gas is compressed to 4.9 bar via four stage compressor and then cooled to 35°C by water (Yousef et al., 2018a, b, 2019). Maqsood et al. compared the effect of pressure on liquid and solid formation during cryogenic separation. The result showed that the vapour-solid region decreased with the pressure (-60 to -98°C for 20 bar and -62 to -75°C for 40 bar) and the CH_4 purity was higher at 40 bar under the same cryogenic temperature (Maqsood et al., 2017).

The energy consumption in the cryogenic process is one of the main challenges for the scale-up application of cryogenic carbon capture processes. In the cryogenic distillation process, the power penalty for the compression process accounts for 43.1–50.9% of the total biogas upgrading energy consumption, and the energy consumption for CO_2 capture is 1.66–1.79 MJ/kgCO₂ (Yousef et al., 2018a, b). Energy saving technologies have been applied to cryogenic carbon capture processes. Compared with the conventional distillation carbon capture process, more than 34% energy reduction was observed when the multibed hybrid network was introduced into cryogenic distillation for the natural gas sweetening process (Maqsood et al., 2014c). Moreover, the energy consumption can be further reduced when the capture process is applied with intensified side mounted and integrated switch cryogenic antishublimation bed, resulting in a 69.24% profit increment (Maqsood et al., 2017). Moreover, Pellegrini et al. compared three cryogenic purification technologies for natural gas upgrading, including the dual pressure cryogenic distillation process, Ryan-Holmes and antishublimation process (Pellegrini et al., 2018). Compared with Ryan-Holmes process, the mechanical power consumption of dual pressure cryogenic distillation is higher because the raw biogas required to be compressed to 50 and 40 bar, and for antishublimation process, 99.84% of the energy requirement is the cooling duties consumption (Pellegrini et al., 2018). Up to now, the reduction of energy consumption in the cryogenic carbon capture processes requires further development and research to be applied in practical sceneries.

5.3.8. Life cycle assessment of cryogenic CO_2 capture

An overview of cryogenic-based carbon capture pathways and technology challenges, which mean the extreme utilization of cold energy and energy consumption barriers, is provided by Shen et al. (2022). A recent review paper by (Song et al. (2019b) focused on cryogenic carbon capture technology progress, including cryogenic system structure and optimal system parameters, which revealed that cryogenic carbon capture technology provided remarkable cost and efficiency benefits. However, most of the studies involved cryogenic carbon capture considering its energy consumption (Esfilar et al., 2018), technical feasibility (Naquash et al., 2022) and economic performance, without taking its carbon abatement and other environmental impacts into consideration (Markewitz et al., 2013). Only a few studies provided a far-reaching insight into the life-cycle environmental impacts or life-cycle cost analysis of systems combined with cryogenic technologies and other carbon capture pathways, which shows a possibility to be deployed in biogas upgrading (Hiloidhari and Kumari, 2021), air separation unit (Schreiber et al., 2013; Troy et al., 2016; Zhang et al., 2014), natural

gas purification (Rocco et al., 2019) and biomass-coal co-gasification (Esfilar et al., 2018). Herein, all selected LCAs report significant carbon capture processes with regard to cryogenic technologies. However, global warming potential (GWP) can hardly be compared, since each cryogenic LCA exhibits specific system boundary and functional unit, use different life cycle inventory source and database, such as Ecoinvent, Simapro and Gabi. The uniform and comprehensive framework principles should be further investigated and paid more attention to, including system boundaries, functional units and inventory analysis.

System boundaries: System boundaries vary to different extents for all kinds of cryogenic capture systems, but it is necessary to take some vital processes into consideration, such as raw material production and transportation, energy conversion, carbon capture and storage. Biogas-related cryogenic systems usually contain the whole supply chain of biogas from cradle to gate, which includes biomass feedstocks cultivation, harvesting and transportation processes, and bioenergy conversion processes (Florio et al., 2019). However, there are still few studies that considered the product end-use process (Adelt et al., 2011). Cryogenic air separation units are the most common forms while talking about cryogenic carbon capture, which can be deployed in steel production, liquefied natural gas (LNG) production and combined with membrane capture. Some studies have taken the whole life cycle of air separation and carbon capture processes into consideration, which included up-stream processes (O₂ production process, MDEA and membrane production), main processes (steel production and CO₂ capture), and down-stream processes (CO₂ transport and storage), but not considering the end-of-life processes of different equipment (Luca and Petrescu, 2021). More comprehensive frameworks have considered waste treatment processes in the life cycle of IGCC and oxy-fuel plants (Schreiber et al., 2013; Zhang et al., 2014).

Functional unit: Per unit of product (biogas, biomethane, electricity, heat etc.) produced (Adelt et al., 2011; Florio et al., 2019) or per unit CO₂ removal from biogas (Starr et al., 2012) are usually selected as functional units of biogas upgrading systems. Electricity or heat supply is selected to be functional units since air separation is usually connected with generation processes.

Environmental categories: Most of the LCAs of cryogenic-related systems considered ReCiPe 2016 midpoint (H), CML 2001 and Eco-indicator 99 Hierarchist as the impact assessment methods with various impact categories, among which GWP is the most cared one. Hence, it seems that there is an agreement to consider multiple environmental impact categories for the assessment of cryogenic systems.

Cryogenic carbon capture technologies have been studied for thermodynamic performance and technical feasibility with a limited understanding of overall environmental implications. Because of the lack of large-scale deployment or pilot demonstration, there is a huge knowledge gap in the availability of operation parameters and related energy/resource consumption data on cryogenic carbon capture, which is the direct reason for the shortage of LCAs about cryogenic carbon capture. This part aims to conclude the LCA of the cryogenic carbon capture situation to fully understand the environmental benefits and potential trade-offs associated with cryogenic carbon capture technologies. Based on the available body of cryogenic carbon capture LCA literature, we conclude that existing LCA results for most cryogenic technologies are not representative of cryogenic carbon capture schemes since these studies are all related to cryogenic air separation or biogas upgrading processes. However, a high-purity CO₂ product in either a compressed liquid or solid phase and utilization of organic solvents and sorbents is the main advantage of cryogenic carbon capture technologies, indicating the environmental benefit potential for ecosystems. Furthermore, due to dramatic temperature variations and high-pressure conditions, large energy losses exist during the whole capture process. Therefore, more efficient cryogenic carbon capture option designing will be an inevitable challenge for commercial applications. In order to explore more possibilities for the application of cryogenic carbon capture technologies, life-cycle environmental or cost assessments should be deployed under

comprehensive and suitable evaluation frameworks. Moreover, life cycle environmental assessment should also quantify the environmental burden shift to reveal more realistic environmental benefits connecting with various ecologic co-benefits and compare with different conventional CCS options.

5.4. Process intensification

Currently, the improvement of carbon capture efficiency generally needs high investment, including more expensive materials and increasing operating cost. This scenario has sent researchers fleeing to the application of process intensification (PI) techniques in the field of carbon capture for saving energy and decreasing consumption. For example, in the commonly alkanolamine method, the chemical reaction is fast while the efficiency of carbon capture is limited by the gas-liquid/gas-solid mass transfer in most cases. Therefore, it is promising to break through the limitation of low-speed heat and mass transfer via drastic improvement of equipment and process efficiency. According to the principle of PI (Van Gerven and Stankiewicz, 2009), the intensified strategies for carbon capture can be classified into four domains: spatial, functional, energy, and temporal. Specifically, the PI of carbon capture can be achieved by (1) developing novel structures to enhance mass transfer; (2) combining a variety of technologies to maximize the synergistic effect; (3) designing rational process to minimize the energy cost; and (4) shortening the process time to improve the whole efficiency.

5.4.1. Spatial domain: novel structure for ample transfer

With the aim to enhance mass transfer, many researchers tried to optimize the internal structure of the absorption columns, such as the geometry of aperture and baffles (Garcia-Abuin et al., 2010), the structure of packing (Smith et al., 2015), etc. and adjust the operating conditions, including gas velocity, gas-liquid ratio, and liquid height in the column (Yan et al., 2019). The experimental results of these studies showed that installing baffles and using smaller apertures, lower sorption temperature, higher regeneration temperature, and lower regeneration pressure exerted positive effects on CO₂ capture. The principle of above studies is to increase gas-liquid mass transfer coefficient by enhancing fluid turbulence or enlarge the gas-liquid contact area by changing the fluid flow patterns, including the deformation, splitting, stretching and breakup of bubbles (Yin et al., 2022).

With the idea of intensifying gas-liquid mass transfer, microchemical technology has recently attracted great attention in the field of CO₂ capture due to the various advantages including efficient mass and heat transfer, safer operation, higher integration and superior controllability. By performing the processes in the scale of sub-millimeter, microreactors can dramatically intensify the gas-liquid mass transfer. As reported, the volumetric mass transfer coefficient in the micro-reactor can be several orders of magnitude higher than that in traditional gas-liquid vessels, such as plate column, packed column and stirred tank (Ganapathy et al., 2016). For example, Yue et al. (2007) investigated the absorption of pure CO₂ in a 667 μm channel. The experimental demonstrated an enhancement in mass transfer characteristics, as compared to conventional absorption systems. A comparison of mass transfer performance among different gas-liquid contactors reveals that the gas-liquid microchannel contactor of this study can provide at least one or two orders of magnitude higher liquid side volumetric mass transfer coefficients and interfacial areas than the others. Besides, Ganapathy et al. (2015) compared a microreactor to most conventional absorption systems including packed columns, plate columns, bubble columns, tube reactors, bubble reactors and venturi reactors. The experimental results showed that the interfacial areas and liquid-side volumetric mass transfer coefficients achieved using the present reactors are between 1 and 4 orders of magnitude higher than the mentioned conventional macroscale gas-liquid absorption systems, which is considered an indication of the high level of process intensification and enhancement that can be achieved by using microreactors. The high mass transfer

efficiency of micro-reactors is bound to reduce the operating consumption of carbon capture. Shao et al. (2010) investigated the influence of channel length of micro-reactors on their absorption efficiencies of CO₂ and found that when the channel length increased by 100%, the mass transfer coefficient was higher by 290%, improving utilization of the absorption capacity of the amine solution for a given reactor volume.

Although microchemical technology has exhibited promising performance in carbon capture, the industrial application of this method still faces many obstacles. First, smaller diameters yield substantial enhancement in mass transfer characteristics, while the pressure drop is also considerably higher (Niu et al., 2009). For the various microchannel contactors tested, an enhanced mass transfer rate was observed for smaller microchannel contactors. The shortening of the diffusion length from channel size reduction is beneficial to achieve fast mass transfer rates, and this is the size effect of mass transfer (Ganapathy et al., 2014). However, the rapidly increasing pressure drop limits the application of micro-reactors for large handling capacity. Besides, the strong interfacial force makes it very difficult to operate counter-current at microscale, not only for absorption but also for stripping, distillation and extraction (Wang et al., 2021), which limits the design of more rational structures. Therefore, in order to better utilize the advantages of microscale to carbon capture, the micro-channel should be optimally designed to ensure the inherently higher surface area to volume ratio of these systems substantially while keeping the pressure drop at moderate levels.

5.4.2. Functional domain: hybrid techniques for maximal synergism

Apart from the optimization of reactor structures, the combination of two or more standalone CO₂ capture technologies, named as hybrid processes, has also provided novel ideas to overcome the challenges of standalone CO₂ capture technologies due to the potentially high capture efficiency and low energy requirement. The hybrid processes usually consist of two or more conventional technologies (i.e. absorption, adsorption, membrane, cryogenic and hydrate, etc.). The integration of different technologies may be superior to the standalone process and avoid their disadvantages. Currently, there are four types of hybrid carbon capture technologies, including (1) absorption-based processes, including membrane contactor (Zhao et al., 2016) and absorption-adsorption (Breault et al., 2016); (2) adsorption-based processes, including adsorption-catalysis (Marono et al., 2015) and adsorption-hydrate (Yang et al., 2014); (3) membrane-based processes, including membrane-cryogenic (Burdyny and Struchtrup, 2010), and membrane-absorption (Kundu et al., 2014); (4) low-temperature-based processes, including cryogenic-hydrate (Suroutseua et al., 2011) and low temperature-absorption (Hanak et al., 2015b).

Appropriate hybrid CO₂ capture strategy can be a potential alternative of exiting standalone processes in terms of efficiency, as screening of suitable hybrid carbon capture processes highly depends on the properties of feed gas (e.g. CO₂ concentration, gas temperature and pressure, etc.), the requirement of product (e.g. purity, etc.) and the availability of the capture equipment. In addition, CO₂ recovery and energy consumption are also significantly affected by the source of CO₂ emission when using different capture technologies (Song et al., 2018b). For example, Song et al. (Song et al., 2018a; Song et al., 2017) employed a membrane-cryogenic hybrid system to CO₂ capture and exhibited that compared to the standalone methods, hybrid processes showed the superiority not only in CO₂ recovery and energy penalty, but also in the installation investment.

The synergistic effect existed in the hybrid processes can no doubt lead to energy saving and consumption reduction. Liao et al. (2019) designed and optimized a hybrid membrane-cryogenic system for both pre-combustion and post-combustion carbon capture, which reduced 33% of operating cost and 28% of total annualized cost. Besides, Scholes et al. (2013) postulated a post combustion capture process equipped with three membrane stages and a cryogenic separation to ensure the feed burner air supply is not oxygen-deficient. By employing this strat-

egy, \$43/ton CO₂ can be avoided, and the carbon capture cost of membrane contactor technology can be decreased to \$48/ton CO₂ with over 90% CO₂ recovery and 97% CO₂ purity.

Although increasing interest in the CO₂ capture by hybrid processes has been attracted in recent years and exciting results have been reported, amount of existing research is undertaken by simulation or lab-scale, because the overall cost of the hybrid process has to be taken into consideration in terms of capital costs, operating costs and maintenance costs. Most costs are very site-specific, and for a full-scale system these costs strongly depend on properties (e.g. CO₂ concentration, flow rate, temperature and pressure) of feed gas, the configuration of separation units, as well. Meanwhile, the concentration of CO₂ is limited to higher than 15%, and the capture condition is also moderate than that in industrial emissions. In addition, the hybrid processes may result in the more stringent requirements on materials and equipment, such as cold resistance of membrane in the membrane-cryogenic system, and poison resistance of membrane in the adsorption-catalysis-membrane hybrid system etc. To overcome these problems, it is essential to understand the interactions between membranes and absorbents/solvents and develop novel membranes and green solvents for hybrid processes, which requires further investigation.

5.4.3. Energy domain: process optimization for low cost

From the perspective of energy domain, it is necessary for industrializing carbon capture technologies to design rational processes via the combination of flowsheet design and rigorous optimization, with the aim to lower the energy cost and higher the environmental performance. In order to deliver better performance in recovery rates, energy consumption and solvent slip, the design and improvement of a standalone CO₂ capture flowsheet generally follows these steps: (1) Design equilibrium-based process flowsheet to obtain process specifications; (2) Conduct sensitivity analysis on the process variables to obtain process model and variables; (3) Perform multi-objective optimization to obtain the results of energy and mass balances; (4) Calculate equipment dimension and process productivity (Sharma et al., 2016). These processes are always achieved by using commercial software packages, including Aspen Plus, HYSIS, or gPROMS, because these tools contain the required physicochemical models and can provide property databanks for numerical calculation.

Different with traditional flowsheets design, the decision makers in the current society focus more on emission reduction efficiency, energy penalty, and carbon cyclic capacity among different solvents, rather than just energy consumption (Ji et al., 2021). However, the multi-objective problem leads to a time-consuming design process because of the highly non-linear nature of the model equations and the high complexity of the processes. In this case, many researches abstracted this problem as a Mixed Integer Non-Linear Problem (MINLP) to assist them in the selection of optimal retrofitting options of CO₂ capture technologies. Take a design process for a coal-fired plant as example, post-combustion capture by monoethanolamide (MEA) scrubbing is currently the commercial technology used worldwide, while oxy-fuel combustion is still on an earlier stage of development (Zhu and Fan, 2011). Many preliminary studies have shown that the latter technology is technically and economically feasible for retrofitting existing coal-fired power plants (Hu and Yan, 2012). In order to evaluate these two techniques, Bravo et al. (2021) considered economic and environmental criteria at the early stages of the process development and conducted multi-objective optimization to address the trade-off problems between different economic and environmental indicators. The numerical results indicated that carbon capture with MEA scrubbing performs better for soft environmental limits while oxy-fuel combustion is the preferred choice when more stringent environmental limitations are considered.

However, the optimal design of carbon capture processes is always time-consuming due to the highly non-linear nature of the model equations and the high complexity of the processes. Besides, the convergence management of the process simulations limits the combined flowsheet

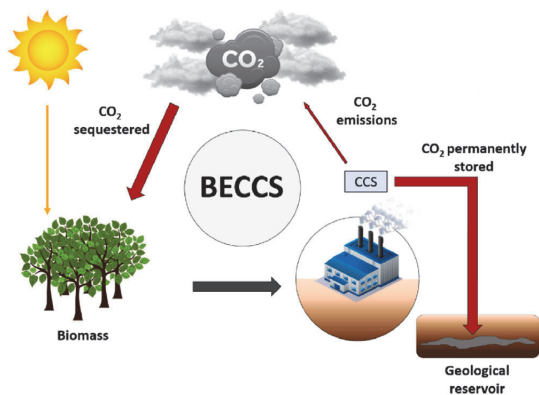


Fig. 5.17. The carbon flow of BECCS. When BECCS systems are employed, a negative carbon flow from the atmosphere into storage is created. (Almena et al., 2022). (For interpretation of the references to color in this figure legend, the reader is referred to the web version of this article.)

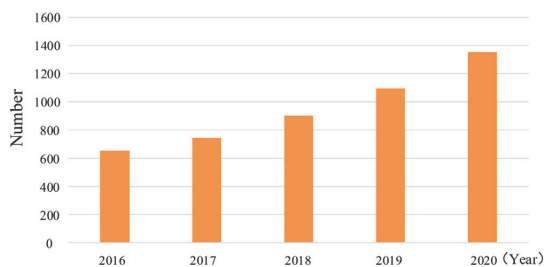


Fig. 5.18. Number of biomass power generation projects in operation (Guo et al., 2022). (For interpretation of the references to color in this figure legend, the reader is referred to the web version of this article.)

5.5.1. Biomass power generation

Biomass power generation is the largest and most mature modern biomass energy utilization technology. The number of biomass power generation projects that have been put into operation from 2016 to 2020 are shown in Fig. 5.18. China is rich in biomass resources, mainly including agricultural waste, forestry waste, livestock and poultry waste, municipal solid waste, organic wastewater and waste, etc. The total amount of biomass resources for energy is equivalent to about 460 million standard coal. Biomass power generation technology can be divided into three categories according to the working principle: direct combustion power generation technology, gasification power generation technology and coupled combustion power generation technology.

Direct combustion of biomass for power generation is very similar to coal-fired boilers in principle. It is to add biomass fuel into appropriate steam boilers for biomass combustion, convert chemical energy in biomass fuel into internal energy of high temperature and pressure steam through high temperature combustion process, convert into mechanical energy through steam power cycle. Finally, the mechanical energy is eventually converted into electricity by a generator.

Biomass gasification power generation should go through the following steps: (1) biomass gasification, after crushing and drying and other pretreated biomass pyrolysis gasification under high temperature environment, to produce gas containing combustible components such as CO, CH₄ and H₂; (2) Gas purification, the combustible gas generated in the gasification process is passed into the purification system to remove impurities such as ash, coke and tar, so as to meet the inlet requirements of downstream power generation equipment; (3) Gas combustion

power generation, purified gas into the gas turbine or internal combustion engine combustion power generation, can also be passed into the boiler combustion, the use of high temperature and high pressure steam to drive steam turbine power generation.

Due to the dispersion of biomass resources, low energy density, and difficulty in collection and transportation, direct combustion of biomass for power generation is highly dependent on the sustainability and economy of fuel supply, resulting in high cost of biomass power generation. Biomass coupled power generation is a power generation method that uses biomass fuel to replace some other fuels (usually coal) for mixed firing. It can improve the flexibility of biomass fuel and reduce the consumption of coal at the same time, so as to achieve CO₂ emission reduction of coal-fired thermal power units. At present, biomass coupled power generation technology mainly includes: direct mixed combustion coupled power generation technology, indirect combustion coupled power generation technology and steam coupled power generation technology.

As we all know, biomass itself is generally considered to have zero carbon emissions. In other words, the CO₂ produced by biomass combustion or conversion is equal to the CO₂ absorbed during the growth process, so the CO₂ stored by biomass becomes negative carbon emissions after deducting the additional emissions in related processes. The life cycle assessment (LCA) method was used to evaluate CO₂ emissions from different power generation technologies. The system boundary consists of three parts: forest management (FM), collection, processing and transportation (CPT), and electricity generation with Carbon Capture and Storage (EG-CCS) through a Biomass Heat & Power Plant (BHP-CCS) (Fig. 5.19) (Briones-Hidrovo et al., 2022). The life analysis of the entire system is 25 years. As opposed to integrated coal gasification combined cycle (ICGCC), biomass integrated combined cycle (BIGCC) combined with CO₂ capture can greatly reduce CO₂ emissions.

5.5.2. Biomass liquid fuel

Biomass is the only renewable carbon resource that can be converted into liquid fuel. It has the potential to replace petroleum, provide diversified clean energy supply for transportation, and greatly reduce carbon emissions. At present, the raw materials of aviation biofuel mainly include animal and vegetable oil, lignocellulose, sugar and starch, etc. Animal and vegetable oil based jet fuel has great development potential, with its high energy density, molecular structure close to aviation biofuel, and high blending degree with fossil jet fuel (up to 50%). It is an important source of sustainable jet fuel at present (Gnanasekaran et al., 2022).

Microalgae biosequestration technology is a process that uses microorganisms to convert a large amount of carbon dioxide into biomass. Algae cells synthesize organic matter through photosynthesis using CO₂ and light energy and release oxygen to realize photosynthetic carbon sequestration (Figuerola et al., 2008). Micrococcoid genetically engineered using tools including CRISPR-Cas9 can produce twice as much oil as its wild parent and grow at a similar rate (Ajajawi, 2017). Zhang et al. found a novel "blue light" enhancement pathway and established an induction pathway for related oil synthesis, achieving a peak productivity of triacylglycerol twice that of unmodified microalgae (Zhang et al., 2022). The advantages of microalgae carbon sequestration technology are high carbon sequestration efficiency, strong environmental adaptability, reduction of industrial carbon emissions, production of high value-added products, and creation of economic value.

5.5.3. Biomass based materials and chemical

At present, there are also many studies that use waste biomass as raw materials to generate zero-carbon plastics. By providing long-chain bio-based epoxides and innovating and efficient synthesis of CO₂ to produce polymers such as biomass polycarbonate materials, the secondary utilization of waste biomass and CO₂ brings greater emission reduction potential. Sichuan University has made a breakthrough in the efficient depolymerization of biodegradable cyclic ester copolymer to obtain its

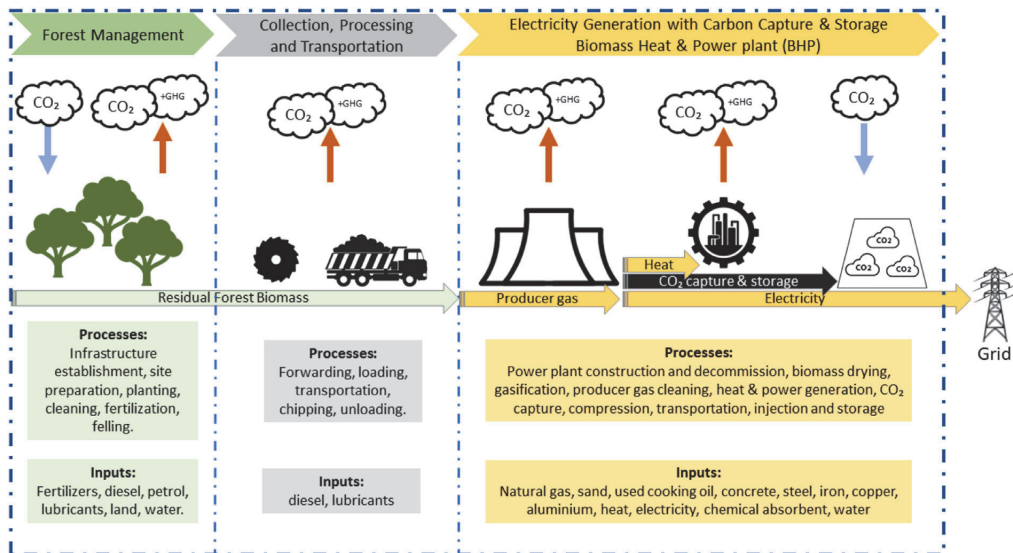


Fig. 5.19. System boundaries of the Biomass Heat and Power Plant with Carbon Capture and Storage. (Briones-Hidrovo et al., 2022). (For interpretation of the references to color in this figure legend, the reader is referred to the web version of this article.)

Table 5.6
Global BECCS project distribution.

| Project title | Capture source | Capture scale / (Mt a ⁻¹) | CO ₂ storage method |
|--|------------------------------|---------------------------------------|--------------------------------|
| Illinois Industrial Carbon Capture | Bioethanol plant | 1.0000 | Saline sequestration |
| Arkalon CO ₂ Compression Facilities | Bioethanol biplant | 0.2900 | EOR |
| Bonanza Carbon Capture | Bioethanol plant | 0.1000 | EOR |
| Husky CO ₂ Inject | Bioethanol plant | 0.0900 | EOR |
| Farnsworth Inject | Bioethanol/fertilizer plants | 0.0070 | EOR |
| Mikaua Power plant capture after combustion | Biomass power plants | 0.1800 | Offshore storage |
| Drax Power CCS | Biomass power plants | 0.0003 | Geological storage |
| Norwegian Full Process CCS | Waste-to-energy/cement | 0.8000 | Geological storage |

Note: EOR (Enhanced Oil Recovery) refers to enhanced oil recovery or enhanced extraction.

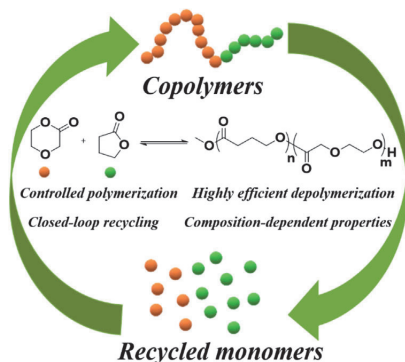


Fig. 5.20. Schematic diagram of controlled synthesis and closed loop chemical cycle of biodegradable copolymers (Yan et al., 2022). (For interpretation of the references to color in this figure legend, the reader is referred to the web version of this article.)

copolymerized cyclic ester monomer under mild conditions (no catalyst, no solvent, 120°C). Through the repolymerization of recovered monomer, a regenerated copolymer with the same structure and properties as the original depolymerization copolymer was synthesized un-

der controlled control (Fig. 5.20). The closed-loop chemical cycle of the polymer was realized for the first time (Yan et al., 2022). Based on the characteristics of biomass unit structure, it is advisable to vigorously develop bioenergy, biochemical and biological materials, and cultivate and strengthen the biomass industry.

5.5.4. BECCS project distribution

The application of BECCS technology in the power industry is still in a stage of rapid development. In 2019, the UK Drax 6*660MW biomass fuel power plant started to capture CO₂, capturing 1000 kg of carbon from flue gas emissions every day. This is the first time in the world that CO₂ is captured from 100% biomass combustion.

As of 2019, the distribution of 8 BECCS projects in the global geological sequestration is shown in Table 5.6. Five of these are already in operation, including one large-scale demonstration project and four demonstration and pilot-scale projects, with an annual CO₂ capture of about 1.5Mt. Among them, the Illinois Industrial Carbon Capture Project in the United States is currently the largest BECCS project and the only BECCS project in operation in the world. The project captures high-purity CO₂ from maize ethanol production for geological storage in the saline aquifer on a capture scale of 1 Mt/a. The capture sources for the remaining four operating BECCS projects are small-scale ethanol production plants, all of which capture enhanced oil recovery (EOR). In addition, three BECCS geological storage projects are still being planned, with CO₂ capture sources from power plants and cement plants.

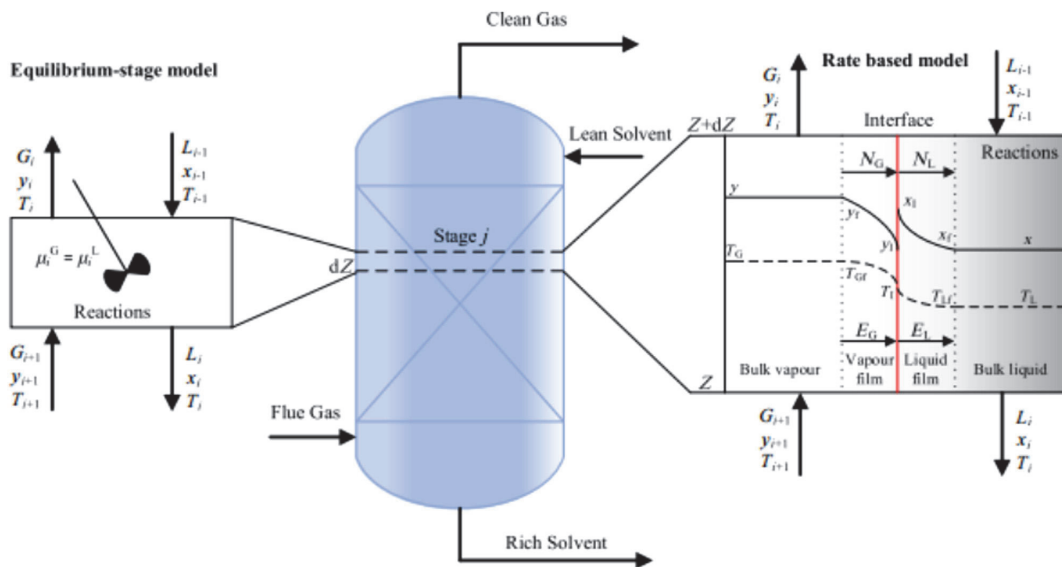


Fig. 6.1. the equilibrium-stage model and rate-based model approaches for the PCC based on chemical absorption using PB. Adapted from (Otitoju, 2022). (For interpretation of the references to color in this figure legend, the reader is referred to the web version of this article.)

5.5.5. BECCS development trend and potential

Biomass energy is highly integrated with fossil energy to provide electricity, gas, heat and oil in a stable and secure manner without changing the existing energy infrastructure and architecture to achieve seamless energy replacement. Moreover, in the period of adjusting the energy structure in our country, only biomass energy can cover all the energy goods of industrial civilization and assume the task of new energy transformation, which is not possessed by other renewable energy.

The influence factors of BECCS technology application potential include biomass resource quantity and biomass utilization technology maturity. Biomass resources are mainly divided into agricultural and forestry residues, solid wastes and energy crops, and the availability of resources is uncertain. It is predicted that the total biomass resources will be 17.24 EJ/a in 2050. In terms of biomass utilization technology, biomass processing, combustion, anaerobic digestion, densification technology and final products have reached the commercial level. Some advanced biomass energy utilization technologies, for example, cellulosic ethanol, F-T synthetic biofuel and biomass integrated gasification combined cycle (BIGCC) are still in the demonstration stage of development, and the future development is more uncertain.

BECCS is likely to play an important role in climate change mitigation and energy transition along with renewables, other negative emission technologies, and deep emission reduction technologies. The efficient conversion of biomass into energy, chemicals and materials to replace petrochemical based products is an important zero-carbon/negative-carbon technology to achieve the dual carbon target. Earlier deployment of BECCS greatly increases its climate change mitigation potential, suggesting that policymakers should use BECCS alongside measures for GHG abatement and carbon removal.

6. Process modelling and techno-economic analysis

6.1. Modelling, simulation and TEA for PCC based on chemical absorption using packed bed

Different mathematical models have been developed and reported in literature to describe the operation of the PCC process based on chemi-

cal absorption using packed bed (PB) column. Most of these studies have focused on steady state operation. It is imperative that the models are realistic and accurate to perform model-based application such as process design, operation and control. Investigations on the PCC process using dynamic models are required to investigate the dynamic operations such as start-up, shutdown and load following, capturing the interactions within the PCC process and the influence of the disturbances on the PCC process. Commonly used commercially available software to carry out modelling and simulation studies of the PCC-chemical absorption process using PB include Aspen Plus®, Aspen HYSYS®, gPROMS®, Aspen Custom Modeller®, Aspen Dynamics®, Aspen Dynamics®, Aspen Custom Modeller®, gPROMS® are tools capable of developing efficient dynamic models that could adequately explain the process (Bui et al., 2014).

6.1.1. Modelling principles

Modelling and simulating the solvent-based PCC process is vital for the quick prediction of CO₂ capture efficiency by avoiding many expensive experimental tests (Chatziasteriou et al., 2022). PCC based on chemical absorption using a PB column involving simultaneous gas-liquid mass transfer and chemical reactions, is best described using either the equilibrium-stage or the rate-based model approach. The equilibrium-based approach assumes theoretical stages, where liquid and vapour attain equilibrium. This assumption is unrealistic and does not reflect the real stage performance of the column (Bui et al., 2014; Chatziasteriou et al., 2022). The rate-based approach, however, accounts for multi-component mass transfer, heat transfer and chemical reactions within the column, making it more appropriate for describing the PCC process based on chemical absorption as it gives an accurate representation of the process (Lawal et al., 2009; Otitoju, 2022). In the rate-based modelling approach, the gas-liquid mass transfer can be described using different established theories such as the penetration theory (Rahimpour and Kashkooli, 2004), the surface renewal theory (Danckwerts, 1970), and the two-film theory (Biliyok et al., 2012; Lawal et al., 2009; Nittaya et al., 2014; Otitoju, 2022). The two-film theory whereby the mass transfer within the film arises from steady-state molecular diffusion, mass transfer resistance is assumed only in the vapour film and liquid film is

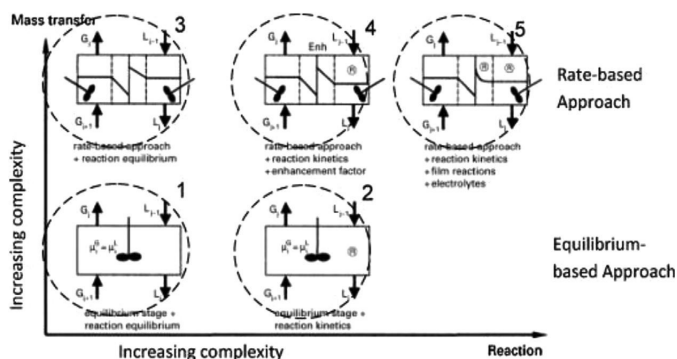


Fig. 6.2. Complexity in models for PCC based on chemical absorption using PB column. Adapted from (Kenig et al. 2001; Wang et al. 2011). (For interpretation of the references to color in this figure legend, the reader is referred to the web version of this article.)

the most widely used (Kenig et al., 2001). The Maxwell-Stefans equations are used to describe the diffusion in the film, the compositions for both bulk liquid and gas phases are assumed to be uniform.

The reaction of CO_2 with an amine in PCC based on chemical absorption using PB column is described using three reaction mechanisms: the Zwitterion mechanism, the termolecular mechanism and the base-catalysed hydration mechanism. The details of these reaction mechanisms have been extensively discussed in literature (Aboudheir et al., 2003; Littell et al., 1992). The reaction kinetics of fast-reacting solvents such as MEA and PZ can be approximated, assuming these reactions reach equilibrium. For slow-reacting solvents such as DEA and MDEA, accurate reaction kinetics is therefore needed to describe the reactions (Zhang et al., 2009). In first-principle modelling, the reaction kinetics is accounted for using the enhancement factor based on pseudo-first-order reaction kinetics. Thus, based on the level of detail required in the mass transfer and reaction kinetics, the model of the PCC process based on chemical absorption can be developed according to the level of complexities shown in Fig. 6.2. The level of accuracy increases with complexity thus, Model 5 is the most accurate as it accounts for mass transfer and reaction kinetics via the rate-based approach. Model 1 is regarded as the least accurate of all. The main assumptions in most of the models for chemical absorption process using PB column include (Koronaki et al., 2015):

- Adiabatic absorber is considered with constant pressure inside it.
- All reactions take place in the liquid film, while the liquid bulk is at chemical equilibrium.
- A plug flow model describes the movement of both gas and liquid streams into the column.
- The flowrates of gas and liquid phases are constant in the absorber.
- Axial diffusion and solvent evaporation may be ignored.
- The interface and bulk phase temperatures are equal.
- The two phases are considered as ideal.

6.1.2. Modelling, simulation and process analysis of PCC based on chemical absorption using RPB

Some studies on the modelling and simulation of the PCC process using MEA in PB have focused on the development of single components such as absorber and stripper (Kvamsdal et al., 2009; Lawal et al., 2009; Zhang et al., 2009; Ziari et al., 2009), the whole solvent-based PCC plant (Gaspar and Cormos, 2012; Harun et al., 2011; Lawal et al., 2010), and integration of the PCC plant to CO_2 emitters such as power plants (Biliyok et al., 2012; Lawal et al., 2012). These studies have been analysed and summarized in various review papers (Bui et al., 2014; Oko et al., 2017; Wang et al., 2011). Zhang et al. (2009) presented a rate-based model for PCC using MEA solvent in Aspen Plus®. The developed model was validated against pilot plant experimental data and accurately predicted using the measurements for lean and rich CO_2 loadings,

capture level and temperature profile. Khan et al. (2011) investigated the impact of various mass transfer correlations on the predictability of the rate-based model. The selection/suitability of mass transfer and hydraulic correlations depends on the type of alkanolamines, packing and flow conditions. Thus, it is important to benchmark the correlations against experiments based on various operating conditions and packing types (Gaspar and Cormos, 2012). Razi et al. (2013) investigated the impact of mass transfer coefficient correlation, kinetic models and effective interfacial area correlation on the model prediction of the pressure drop, CO_2 capture level and temperature profile in the column. The study revealed that the model prediction accuracy is dependent on the kinetic model and mass transfer correlations. MEA solvent is volatile, corrosive and requires high regeneration energy. Thus, it is imperative to focus on PCC process using alternative solvents with lower regeneration energy, high reactivity with CO_2 , high resistance to degradation and environmentally friendly (Zhou et al., 2010). Modelling and simulation studies of PCC process using alternative solvent such as PZ (Otitaju et al., 2021) and AMP and PZ blend (Zhang et al., 2017) solvent. For example, Otitaju et al. (2021) developed a rate-based model for the PCC process using PZ. The model was validated at pilot scale and scaled-up to treat flue gas from a 250 MWe NGCC power plant (Dillon et al., 2005). Therefore, further modelling and simulation studies of PCC process using suitable novel solvents should be explored.

The model development of the solvent-based PCC process with process configuration modifications has received much attention because the modified process has shown better economic performance and flexibility in operation (Wu et al., 2020). Mostafavi et al. (2021) proposed combinations of process modifications such as absorber intercooling, lean vapour recompression and parallel exchanger arrangement to reduce the reboiler duty and cost of the PCC process. They found that the combination of the absorber intercooling and the lean vapour recompression resulted in an 8% reduction in steam consumption for regeneration and consequently a significant reduction in the total costs (i.e. fixed and variable costs).

Karimi et al. (2011, 2012) developed rate-based models for five different stripper configurations of the PCC process including: standard configuration, split-stream, multi-pressure stripper, vapour recompression and compressor integration. The capital cost and CO_2 avoidance cost are calculated to evaluate the steady-state performance of different processes (Karimi et al. 2011). The dynamic performance of PCC processes with standard configuration, split-stream and vapour recompression configurations were then investigated. The simulation results showed that the standard configuration has the best dynamic behavior and is the most stable one. For the other two configurations, the vapour recompression configuration can handle disturbances better than the split-stream configuration (Karimi et al., 2012).

In the same vein, Biliyok et al. (2012) developed a dynamic model for the PCC process with inter-cooled absorber in gPROMS®. The model

was validated with dynamic experimental data and accurately predicted the behavior of the plant, especially for the trend of dynamic change. Analysis of the impact of inter-cooled solvent and flue gas moisture content on the CO₂ capture process performance was investigated using the validated model. Results revealed that the inter-cooling can slightly enhance the absorber performance when the temperature bulge is located around it. However, the moisture content in flue gas could strongly influence the temperature profile of the absorber but only had a trivial influence on the capture level. Similar study by Walters et al. (2016) using PZ solvent revealed that PZ solvent capacity could be improved by absorber intercooling.

Investigating the PCC process integrated with either a power plant or industrial process is critical to improving its operation performance. Lawal et al. (2012) integrated dynamic models for a 500MWe sub-critical coal-fired power plant with PCC in gPROMS. The simulation results illustrated that the PCC process response was much slower than the coal-fired power plant. Olaleye et al. (2016) investigated the dynamic behaviour of a large-scale PCC model integrated with a 600MWe super-critical coal-fired power plant on load following mode of operation of the coal-fired power plant. The simulation results showed that about 4.67% of the maximum power of the coal-fired power plant could be quickly produced by the stripper stop mechanism, which has potential benefit for the wide-range load-varying operation of the power plant.

6.1.3. Techno-economic analysis (TEA) of PCC based on chemical absorption using PB

Several studies have focused on the model-based optimization of PCC process based on chemical absorption to establish the operating conditions that achieve the CO₂ capture targets at minimum cost. Abu-Zahra et al. (2007) investigated the minimal thermal energy duty required for MEA solvent regeneration. Studies revealed significant energy savings could be achieved by optimizing lean solvent loading, amine solvent concentration, and stripper operating pressure. A minimum thermal energy requirement of 3.0 GJ/ton CO₂ was attained at a lean MEA loading of 0.3, using 40wt% MEA and stripper operating pressure of 210 kPa compared with the base case of 3.9 GJ/ton CO₂. Comprehensive sensitivity analysis and optimization of solvent-based PCC process using MEA based on total annual cost was carried out by Arias et al. (2016). The study revealed that rich solvent, lean solvent, and flue gas temperatures are very sensitive to the total annual cost.

Further studies on TEA of the chemical absorption process focused on the process configuration modification. Dubois and Thomas (2018) presented a technical analysis of different CO₂ capture process configurations (rich solvent recycle (RSR), solvent split flow (SSF), lean/rich vapour compression (L/RVC)) using different solvents (MEA, PZ, PZ-MDEA blend). The study revealed that the configurations studied attained regeneration energy savings within 4–18% range. The minimal regeneration energy of 2.38 GJ/ton CO₂ was obtained with PZ-MDEA blend (30 wt% PZ and 10 wt% MDEA) solvent and RVC process configuration.

Oh et al. (2020) conducted a TEA on various modified PCC processes using 30 wt% MEA. Five stripper configurations modified with two or more components of lean vapour compression (LVC), cold solvent split (CSS), and stripper overhead compression (SOC) were investigated to reduce the total equivalent work. The study revealed that the thermal energy required from the reboiler could be reduced by 8.1–32.8% through the modified configurations. The study suggested that for a combined configuration implementation, the total equivalent work could be up to 9.0%, and the operating cost could be saved by up to 10.2%. However, an increase in capital cost is attained due to the process modifications.

An investigation by Zhang et al. (2017) on the energy performance of CO₂ capture process with AMP and PZ aqueous solvent with process modifications, including intercooled absorber (ICA), lean vapour compressor (LVC) and rich solvent split (RSS) revealed that the energy demand were reduced by 6.7%, 2.7%, and 8.5%, respectively. The combination of LVC + RSS, ICA + LVC and ICA + RSS modifications obtained

energy savings of 9.3%, 8.5% and 14% respectively. The energy demand for the combination of ICA + RSS + LVC was reduced by 15.2%.

Otitoju et al. (2021) investigated the technical and economic performance of three different PCC process configurations using PZ solvent for 250 MWe NGCC compared with the standard process using 30 wt% MEA solvent. Results revealed that the total energy demand of the standard CO₂ capture process using 30 wt% PZ is 3.56 GJ/ton CO₂, which is 33% less than the energy demand of the standard PCC process using 30 wt% MEA. Amongst the configurations considered, the lowest energy demand of 2.76 GJ/ton CO₂ was attained using an advanced flash stripper (AFS) using 40 wt% PZ. Results also showed that the lowest CO₂ capture cost of \$34.65 per ton CO₂ was achieved using the AFS process configuration with 40 wt% PZ.

6.1.4. Summary: advantages, limitations and future prospect

Modelling and simulation of the PCC process based on chemical absorption using PB column has matured through many years of development and improvement. Many models have been developed to gain in-depth knowledge or insights into the PCC process using different solvents and configurations under steady-state and dynamic conditions. However, dynamic operating/experimental data is still insufficient to verify PCC dynamic models at different process configurations. From the validation point of view, more experimental tests should be carried out on the PCC process with different process configurations at pilot scale.

6.2. Modelling, simulation and techno-economic assessment of intensified PCC based on chemical absorption using RPB

The rotating packed bed (RPB) is the most commonly used Higee (high gravity) technology for the solvent-based PCC process. It comprises an annular packed bed connected to two disks erected on a rotating shaft. A cross-sectional view of the RPB is shown in Fig. 6.3. The RPB assembly is housed in a casing and operates in a high centrifugal field attained by rotating a cylindrical rigid bed (Cortes Garcia et al., 2017). The liquid and the vapour flow either co-currently or counter-currently in the horizontal direction. This is in opposition to the packed bed (PB) where liquid and vapour flow is vertical. Thus in RPB, the separation efficiency and capacity are determined by the rotor diameter and the axial height respectively. This is in contrast with PB where capacity is determined by the column diameter and the separation efficiency is determined by column height (see Fig. 6.4) (Cortes Garcia et al., 2017; Kiss, 2014).

Because of these fundamental structural differences, the modelling and simulation of the PB are significantly different from that of the RPB. For instance, mass transfer is considered to occur only along the packing in PB modelling whereas, mass transfer is considered to occur both along the packing and in the space between the rotor and the casing in modelling of RPB. Additionally, unlike the PB which is modelled as a straight bed with a constant cross-sectional area and constant gas and liquid velocities, the RPB is modelled as a tapered bed with a varied cross-sectional area and varied gas and liquid velocities (Cortes Garcia et al., 2017). This leads to varying gas and liquid mass transfer coefficients along the radius in RPB. The schematic of the PB and RPB, which highlights their structural and modelling differences, is shown in Fig. 6.4.

There are many research activities on the modelling and simulation of the PCC process using the RPB technology (Joel et al., 2014, 2017; Im et al., 2020; Luo et al., 2021). The majority of these studies have focused on the modelling and simulation of CO₂ capture either in the RPB absorber (Joel et al., 2014; Luo et al., 2021) or in the RPB stripper (Joel et al., 2017). The modelling and simulation of the whole intensified carbon capture process consisting of the RPB absorber, RPB stripper, heat exchanger, pumps etc. have also been reported (Im et al., 2020). Discussions on these are provided in the following subsections.

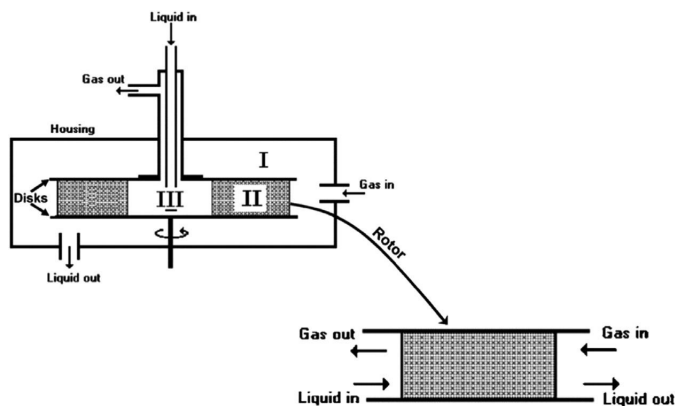


Fig. 6.3. The cross-sectional view of the RPB (Chavez and Larachi, 2009). (For interpretation of the references to color in this figure legend, the reader is referred to the web version of this article.)

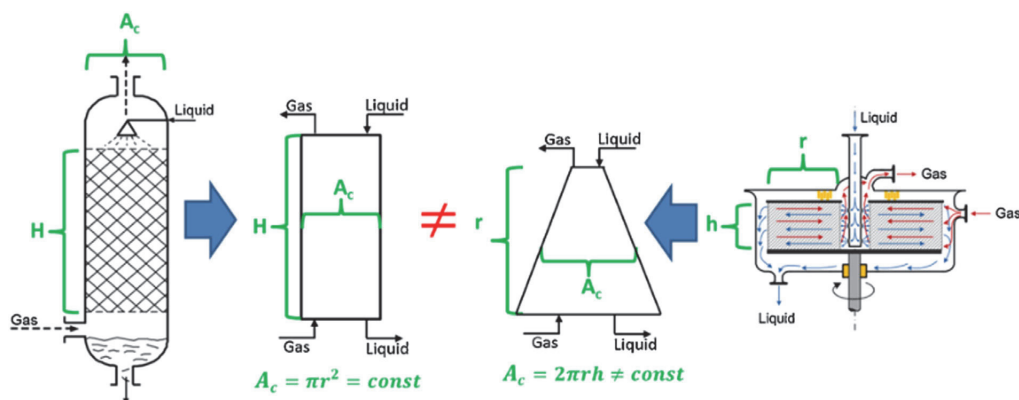


Fig. 6.4. Schematic of the PB modelling (left) vs. RPB modelling (right) (Neumann et al., 2018).

6.2.1. Modelling and simulation of CO₂ absorption in RPB absorber

Modelling and simulation of CO₂ absorption with different solvents in RPB absorbers have been reported. The absorption of CO₂ using Benfield solution (amine-promoted hot potassium carbonate) was investigated in an experimental and modelling study conducted by Yi et al. (2009). The steady-state model was developed in Matlab® based on the two-film theory and accounted for kinetics and CO₂ balance in the liquid droplets. The model was validated with experimental data collected in RPB with an inner radius of 0.040 m, outer radius of 0.10 m and axial height of 0.031 m. The model generally predicted the CO₂ mole fraction in the outlet gas and revealed the presence of an end effect zone at the inlet region of the packing where mass transfer efficiency in the RPB was the highest (Yi et al., 2009). Zhang Z., et al. (2014) developed a steady-state model of CO₂ absorption with an MDEA concentration of 10–30 wt% in a pilot-scale RPB absorber packed with multi-layer stainless steel. The model was implemented in Fortran® and uses Higbie's penetration theory. The model was validated and accurately predicted the CO₂ capture level at rotating speeds less than 1100 rpm. Beyond this rotating speed, there were sharp deviations between the experimental values and model predictions. The CO₂ capture levels were generally lower than 50 % due to slow reaction and low concentration of MDEA.

More studies have focused on the modelling and simulation of CO₂ absorption with MEA in RPB absorbers. Joel et al. (2014) modified the rate-based model in Aspen Plus® to simulate a steady-state pro-

cess of CO₂ absorption with MEA in an RPB absorber. The default mass transfer and hydrodynamic correlations in the rate-based model were modified by replacing the gravitational acceleration term (g) in the correlations with centrifugal acceleration ($r\omega$). The modified correlations were written in visual Fortran® and linked dynamically with the rate-based model in Aspen Plus®. The model was validated at the pilot scale and was used to investigate the effects of various operating variables on the CO₂ capture level. Process analysis showed that no temperature bulge was observed in the temperature profile of the pilot-scale RPB absorber because of the high liquid-to-gas (L/G) ratio (30 kg/kg). Furthermore, it was reported that the RPB absorber achieved a 12 times volume reduction factor compared to a PB absorber when 30 wt% MEA was used. A steady-state rate-based model of an MEA-based RPB absorber was developed by Kang et al. (2014). The model equations and the different correlations were implemented and solved in gPROMS ModelBuilder®. Their model used a modified enhancement factor which is based on the apparent reaction rate constant of Aboudheir et al. (2003) to improve the agreements between the model predictions and experimental data. Additionally, they investigated the effects of various mass transfer and liquid holdups correlations on model predictions of CO₂ mole fraction, $K_G a$ and CO₂ capture level. It was concluded that a combination of Onda et al. (1968) for liquid phase mass transfer coefficient and interfacial area, Burns et al. (2000) for liquid holdup and Tung and Mah (1985) for gas phase mass transfer coefficient improved model predictions and were adequate to

Table 6.1
Specifications of RPB stripper.

| Institutions | Dimensions r_i, r_o, h (m) | Packing type | a_p (m^2/m^3) | ϵ | References |
|---------------------------------------|------------------------------|--------------|---------------------|------------|-----------------------|
| Newcastle University | 0.078, 0.199, 0.02 | Expamet | 2132 | 0.76 | (Jassim et al., 2007) |
| National Tsing Hua University, Taiwan | 0.038, 0.08, 0.02 | Wire mesh | 803 | 0.96 | (Cheng et al., 2013) |

predict the effect of changes in liquid and gas flow rates in the RPB absorber.

Thiels et al. (2016) examined the process design for the RPB absorber to achieve varying CO₂ capture levels in Aspen Custom Modeler. They proposed a series arrangement of the RPB and PB absorbers to minimize the absorber packing volume. Borhani et al. (2018) studied the effect of different reaction models and enhancement factors on CO₂ absorption in a pilot-scale RPB absorber operated with MEA concentrations of 55 wt% to 75 wt%. In addition to this, the influence of rotor speed, lean MEA concentrations, flow rates and temperatures on CO₂ capture level was also evaluated. Oko et al. (2018) used their steady-state RPB absorber model developed in gPROMS ModelBuilder® to show that the liquid phase temperature in RPB could rise significantly and hence demonstrated the need for intercoolers in RPB absorbers. Following this, the authors proposed and investigated various intercooler design options suitable for application in RPB absorbers. In a recent study, Oitotoju et al. (2023) developed, validated and scaled up a steady-state rate-based model of an RPB absorber in Aspen Custom Modeller®. The authors reported that the large-scale RPB absorber achieved a 4–13 times reduction in volume and a 3–35 % reduction in capital expenditures compared to a PB absorber. Recently Luo et al. (2021) reported the dynamic modelling and simulation of CO₂ absorption in a pilot-scale RPB absorber based on the surface renewal mass transfer theory. The RPB absorber model was developed in gPROMS ModelBuilder® and the embedded SAFT-VR EOS was used for the modelling of the thermodynamic properties. They performed steady-state process analysis to investigate the effects of key process variables such as rotating speed (300–1450 rpm), L/G ratio (2–6 kg/kg) and MEA concentrations (30–80 wt%) on the absorption performance. They also carried out dynamic simulations of the RPB absorber to study its response to changes in the flow rates of both the flue gas and the solvent. It was concluded that the RPB absorber responds quickly to process changes (Luo et al., 2021).

6.2.2. Modelling and simulation of CO₂ desorption in RPB stripper

Although there are many experimental studies of CO₂ desorption in RPB strippers, experimental data collected from two of those studies are commonly used to validate the model of the RPB stripper. Table 6.1 shows the specifications of the RPB used in those studies (Jassim et al., 2007; Cheng et al., 2013). There are fewer model-based studies on CO₂ desorption using an RPB stripper compared to their RPB absorber counterpart. There are only two studies in the open literature on the modelling and simulation of CO₂ desorption in RPB stripper (Joel et al., 2017). This may be due to the complexity and difficulty involved in modelling the RPB Stripper compared to the RPB absorber. The first modelling and simulation study for CO₂ desorption in a RPB stripper was reported by Joel et al. (2017). The rate-based RPB stripper model was developed using Aspen Plus® and Fortran®. Their model was validated with experimental data from Jassim et al. (2007) and Cheng et al. (2013). Model validation results were in agreement with experimental data for specific reboiler duty and lean CO₂ loading. Process analysis indicated that the regeneration efficiency increases with rotor speed, but with an increase in heat and mass transfers that subsequently resulted in a decrease in regeneration energy. The authors also reported that the RPB stripper volume was reduced by 9.692 times compared to that of a PB stripper. Borhani et al. (2019) used an equation-oriented approach to develop the model of the RPB stripper. The partial pressure, the heat of desorption and K-values were calculated from correlation developed by regression of experimental data collected for different concentrations of

MEA. The model was implemented in gPROMS ModelBuilder® and was used to analyse the effect of changes in liquid flow rate, pressure, rotor speed and reboiler temperature on the regeneration energy of the RPB stripper. They concluded that the desorption energy reduces with an increase in reboiler temperature until 120 °C. Beyond this temperature, desorption energy increases.

6.2.3. Modelling, simulation and optimization of the whole solvent-based intensified PCC process

Modelling and simulation of the CO₂ absorption/desorption using RPB have been carried out mostly for individual RPB absorbers and RPB strippers. Only one study reported the modelling and simulation of the RPB absorber and RPB stripper as a connected system for the solvent-based PCC process at the lab scale (Im et al., 2020). In that study, the authors first developed and validated the model of the MEA-based RPB absorber and RPB stripper separately and then they developed the whole intensified PCC system by integrating the RPB absorber and RPB stripper with other process units in gPROMS ModelBuilder®. The integrated process was operated with varied MEA concentrations (30–80 wt%). Optimal design and workable operating conditions for the integrated intensified PCC process were investigated using a flue gas flow rate of 71 kg/h and design specifications including 90 % CO₂ capture level, lean solvent temperature of 40 °C, absorber and stripper pressures of 1 atm and 1.6 atm, CO₂ lean lading of 0.364 molCO₂/molMEA, flash drum temperature of 40 °C, temperature approach of 10 °C, condenser temperature of 40 °C and rotor speeds of 800 and 600 rpm for the RPB absorber and RPB stripper respectively. Steady-state optimization of the whole intensified process was performed by setting the minimization of the total energy consumption (reboiler, rotation and pumps) as the optimisation objective and parameters such as rotor speed, MEA concentration, reboiler temperature, lean solvent flow rate, condenser temperature and stripper pressure as decision variables. In addition to this, the CO₂ capture level, CO₂ purity and percentage flooding in the absorber and the stripper were chosen as constraints. The optimization results showed that the lowest total energy consumption of 4.62 GJ/ton CO₂ (3.04 GJ/ton CO₂ for reboiler duty and 1.57 GJ/ton CO₂ for rotational energy) was achieved at 90 % CO₂ capture level and 73 wt% MEA concentration. The authors concluded that although the specific reboiler duty was lower for the MEA-based PCC process using RPB its overall energy consumption could be higher than that of the MEA-based PCC process using PB due to the additional energy consumed for rotating the RPB.

6.2.4. Scale-up of RPB for solvent-based PCC

Unlike the solvent-based PCC process using PB as absorbers and strippers, there are not many scale-up studies on solvent-based PCC with RPB as absorbers and strippers. Hence existing studies on CO₂ capture in RPB are based on small RPB rigs with a maximum outer diameter of 0.396 m and flue gas capacity of 0.66 kg/s or less (Jassim et al., 2007). Oitotoju et al. (2023) performed the first scale-up study by scaling up a validated pilot-scale model of an MEA-based RPB absorber to a large-scale MEA-based RPB absorber with capacity for flue gas flow rate (356 kg/s) from a 250 MW_e CCGT power plant. The large-scale RPB absorber was designed by estimating its basic dimensions (i.e. inner radius, outer radius, axial height and casing) using a rigorous iterative scale-up procedure developed by the authors based on the design approach of Agarwal et al. (2010). The scale-up uses the area of a transfer unit (ATU) to address the polar coordinate issue in RPBs. The results of the scale-up studies

showed that a large-scale RPB absorber operated with 55 wt% would require an inner radius of 1.48 m while the one with a 75 wt% MEA would require an inner radius of 1.47 m. According to the authors, this inner radius would be sufficient to house the liquid distributor, not lead to excessive gas velocity and allow for gas withdrawal from the RPB without causing a very high pressure drop. Furthermore, the outer radius of the large-scale RPB absorber with 55 wt% MEA and 75 wt% MEA were estimated to be 4.86 m and 4.61 m, respectively, while their axial heights were estimated to be 1.26 and 1.19 respectively. The author used the scale-up results to carry out a techno-economic assessment and quantified the size and cost of a large-scale RPB absorber operated with MEA concentration of (55–75 wt%).

6.2.5. Techno-economic assessment of the solvent-based intensified PCC process

Although there are existing techno-economic studies for systems where RPBs are used for distillation (Sudhoff et al., 2015), recovery and purification of bioethanol (Gudena et al., 2013) and absorption of aroma from a bioreactor off-gas (Lukin et al., 2020). So far only Otitoju et al. (2023) has reported on the techno-economic assessment of the solvent-based PCC process using RPB, though the study was limited to the RPB absorber only. Technical assessments of the MEA-based RPB absorber performed by Otitoju et al. (2023) included the effects of certain process variables (i.e. lean solvent CO₂ loading, lean MEA flow rate and rotor speed) on the CO₂ absorption performance. The authors reported that the RPB absorber operated with 55 wt% MEA has a 4–11 times volume reduction factor while that operated with 75 wt% MEA has a 5–13 times volume reduction factor when compared to those of the PB absorbers. Furthermore, economic assessments showed that the capital expenditure (CAPEX), operating expenditure (OPEX) and CO₂ capture cost of the RPB absorber were lower compared to that of the PB absorbers. For instance, the CAPEX was lowered by 3–53% with the RPB absorber while the CO₂ capture cost was lowered by \$8.5/tCO₂ – \$15/tCO₂ with the RPB absorber compared to that of the PB absorbers.

6.2.6. Summary: advantages, limitations and future prospect

The RPB is the most commonly used technology in the intensified solvent-based PCC process because of its lower flooding tendency and ability to operate at higher gas and/or liquid flow rates compared to PBs. RPB is self-cleaning and can intensify the mass transfer process in the CO₂ capture process. It can reduce the process equipment footprint by reducing the size of the absorber by 5–13 times (Joel et al., 2014) and that of the stripper by 9.69 times compared to PB (Joel et al., 2017). Hence, RPB could be used in space-limited applications like ships and mobile skid plants. Furthermore, it can fulfil larger flue gas treatment than PB because mass transfer intensification in RPB could lead to a gas retention time below 1.5 s. This is significantly lower than a gas retention time of 20.4 s obtained in PBs. RPB can deal with viscous solvents and has been mostly operated with higher solvent concentrations (e.g. 55 wt% or 80 wt% MEA). The cost of the solvent-based PCC process could also be reduced by RPB technology.

Despite the many advantages of RPB, its modelling and application in the solvent-based PCC process are limited to being used separately as an absorber or as a stripper. This is due majorly to the lack of experimental data to validate the model of the whole solvent-based PCC process using RPB. Additionally, existing studies on solvent-based PCC using RPB are conducted at lab and pilot scales. To accelerate the commercial deployment of the process, there is a need for more studies involving the detailed and accurate modelling and scale-up of the whole intensified PCC process using RPB. Such studies are critical to gaining insights into the design and operation of the whole intensified process. Additionally, a detailed economic assessment of the whole process is necessary to quantify the CO₂ capture cost for the entire process. Detailed optimization studies incorporating environmental and life cycle analysis (LCA) of the intensified PCC process should be carried out and

the results thereof compared with the that of solvent-based PCC process using PB.

6.3. CFD study of post-combustion carbon capture based on chemical absorption using packed bed

Packed bed (PB) has been used as multiphase contactors and reactors for post-combustion carbon capture (PCC). Like many other industry sectors, computational fluid dynamics (CFD) has been employed to design and optimize the packed bed technology for PCC. By solving a series of governing equations for fluid flows, chemical reactions, and heat and mass transfers, CFD simulation can reveal details of hydrodynamics, heat and mass transfer performance inside the packed beds.

Due to the packed bed's multi-scale nature, CFD simulation of the CO₂ capture processes in large scale PBs is still prohibitively computationally expensive when the processes at the pore scale are to be resolved. In order to reduce the computational costs, two general approaches to the CFD PB simulations are employed, i.e. the micro- and macro-scale approaches. For example, the details of the flow behaviour in the PB can be investigated using the micro-scale modelling approach, whereas the overall column performance, such as the CO₂ capture rate and pressure drop, can be analysed using the macro-scale approach (Li et al., 2016). Different models, such as the element scale, corrugation scale, and column scale models, have been proposed, as illustrated in Fig. 6.5.

6.3.1. Element scale model

For mesoscale simulations, 3D representative element units (REUs) can be employed (Petre et al., 2003). The REU can be viewed as the smallest element in the PB, representing the bed dissipation mechanisms. Petre et al. (2003) utilized numerous REUs to resemble the flow at different positions in the column and they were used to simulate the gas flows over a wide range of Reynolds numbers: from pure creeping flows to fully developed turbulent flows. The overall pressure drop across the column was reconstructed based on each REU's obtained pressure loss. Furthermore, Said et al. (2011) investigated the dry pressure drop for the fully developed turbulent gas flow using two periodic REUs with different slice directions. In addition, the counter-current gas-liquid flow in the PB was studied using the VOF method based on a 3D REU, and the total liquid holdup and wetted area were estimated by Chen et al. (2009). It should be noted that although the use of the REUs can save the computing resources and time, the accuracy of the simulation results is directly related to the setting of the boundary conditions for the REUs, especially the wall effects, which may lead to an inaccurate result. It has been reported that the predicted pressure drop using REUs is usually more significant than the pressure drop measured from the experiment due to the intersection of the two adjacent flow channels (Raynal et al., 2004).

6.3.2. Corrugation scale model

The 2D corrugation scale model is usually employed to study the two-phase flow behaviours in the PB, such as the dry pressure drop, liquid holdup, and liquid film thickness using the VOF method. For example Gu et al. (2004), studied the counter-current gas-liquid flows on inclined plates using the VOF method for various packing surface microstructures, fluid properties and gas flow rates. It was concluded that the gas flow rate noticeably influenced the liquid flow pattern and film thickness. Further, the complex geometry of the structured packing in the PB was simplified as a 2D vertical cross-section channel between two neighbouring packing sheets (Raynal et al., 2004; Hosseini et al., 2012). The process of the liquid film formation on the packing surface was simulated, and the liquid film thickness and pressure drop were compared with the experimental data. In addition, Haroun et al. (2012) investigated the liquid holdup and the no-reacting mass transfer rate based on co-current gas-liquid flows in a 2D corrugation scale model. The results showed that the liquid flow rate and packing geometry mainly affected

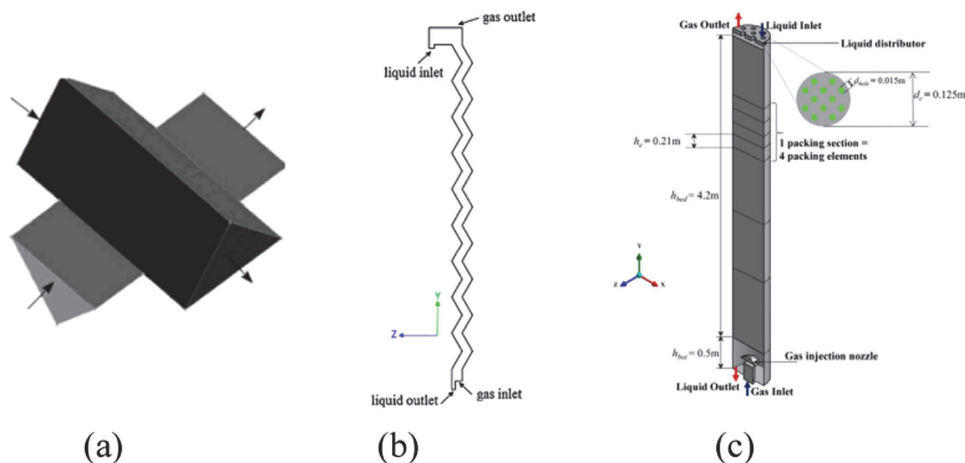


Fig. 6.5. Typical computational models employed. (a) element scale model (Chen et al., 2009); (b) corrugation scale model (Hosseini et al., 2012); (c) column scale model (Kim et al., 2016).

the mass transfer. Nevertheless, the use of the 2D geometry for the simulation of two-phase flow in the PB, although generally successful, has limitations due to the presence of highly anisotropic structured packings.

6.3.3. Column scale model

In general, the hydrodynamics and mass transfer processes have been explored in a packing column considering gas flow only or gas-liquid flows using the VOF and Eulerian methods. For the simulations of the gas flow, Wen et al. (2007) investigated the single-component (air) and two-component (air and CO₂) gas flows in a column with complex packing geometries. Then, the influence of the geometry features of the packing on the dry pressure drop was explored (Sun et al., 2021). Haghshenas Fard et al. (2007) modelled the dry and wet pressure drops in a packing column model similar to the actual geometry of the structured ceramic packing. The simulation showed that the wet pressure drop was larger than the dry pressure drop under the same gas load. This indicates that the modelling of the dry pressure drop cannot accurately describe the actual pressure drop in the packing column, where both the upward gas and downward liquid stream flows exist. Therefore, the simulations of both gas and liquid flows are essential for better understanding the flow dynamics in the packed bed.

It should be noted that the size of the column models employed in most studies such as those in the above-mentioned works, are relatively small but the required numbers of the computational mesh are still quite large. A promising approach for modelling a large-scale or industrial column is to take the packing as a porous medium without resolving the details of the packing geometry, i.e. using the Eulerian porous medium model. To utilize this approach, it is very important to accurately determine a proper resistance force model to describe the gas-liquid interfacial force and drag force from the packing (Kołodziej and Łojewska, 2009). Mirzaie et al., 2020 estimated the porous resistance using the general Ergun's equation. However, the force models employed did not consider the effect of the various geometry of the packing, which may cause an inaccurate flow behaviour prediction. As a result, various porous medium resistance force models, such as those for spherical packing (Attou et al., 1999), structured slit packing (Iliuta et al., 2004), wire gauze packing (Kołodziej and Łojewska, 2009), and tube bundle packing (Zhang and Bokil, 1997) have been proposed. These models are developed based on the packings of different types and they consider the influence of the packing geometry on the fluids across the packing region. It has been shown that the flow characteristics could

be accurately predicted in the packed beds by employing these models (Fourati et al., 2013; Iliuta et al., 2014; Pham et al., 2015; Pham et al., 2015; Uwitonze et al., 2021; Zhang et al., 2017).

In addition, liquid dispersion occurs in the packed bed. Fig. 6.6 (a) shows the experimentally observed spreading of the liquid in a 3D column model with a point liquid jet source located at the top of the packing. Without considering the dispersion forces in the CFD model, the predicted liquid mal-distribution can be quite different (Tan et al., 2021).

Liquid dispersion in the packed bed may be divided into the capillary pressure induced dispersion and mechanical dispersion (Wang et al., 2013). The capillary pressure force is produced by the difference in the pressures across the fluid interface. Two main models, i.e. the Grosser model (Grosser et al., 1988) and the Attou and Ferschneider model (Attou and Ferschneider, 1999), have been widely used to model the liquid dispersion resulting from the capillary dispersion (Boyer et al., 2005; Gunjal et al., 2005; Iliuta et al., 2014; Jiang et al., 2002; Wang et al., 2013). In Grosser's models, it was assumed that the capillary pressure force was inversely proportional only to the packing's porosity and particle diameter. It is reported that the Grosser model may fail to reproduce the steep rise in the capillary pressure as the liquid saturation approaches zero, and thus fail to catch the effect of the capillary pressure force in some packed bed models (Zhang et al., 2022).

The mechanical dispersion is caused by the complex advection of the momentum by the fluid at the pore scale (Fourati et al., 2013) or, in other words, the variation in the velocity with respect to the main flow at the macroscopic scale (Carney and Finn, 2016). The gas dispersion force is relatively small compared with the liquid dispersion force because the momentum exchange between the gas and liquid is usually small. As a result, the gas dispersion force is usually ignored (Fourati et al., 2013) in the CFD simulations. The drift velocity, which is a function of the gradient of the phase volume fraction, will lead to a driving force to cause the liquid to flow from the high liquid concentration region to the low liquid concentration region and subsequently increase the liquid holdup. Although many mechanical dispersion force models have been developed, the model proposed by Lappalainen et al. (2009) based on spherical particle packings is the most popular, and it has been employed in many works for the PB simulations (Kim et al., 2017; Lappalainen et al., 2011, 2009; Solomenko et al., 2015).

Lappalainen et al. (2009) employed their porous resistance model and dispersion force models to investigate the liquid dispersion phenomenon in a trickle bed. The results showed that the mechanical dispersion force was always larger than the capillary dispersion force under

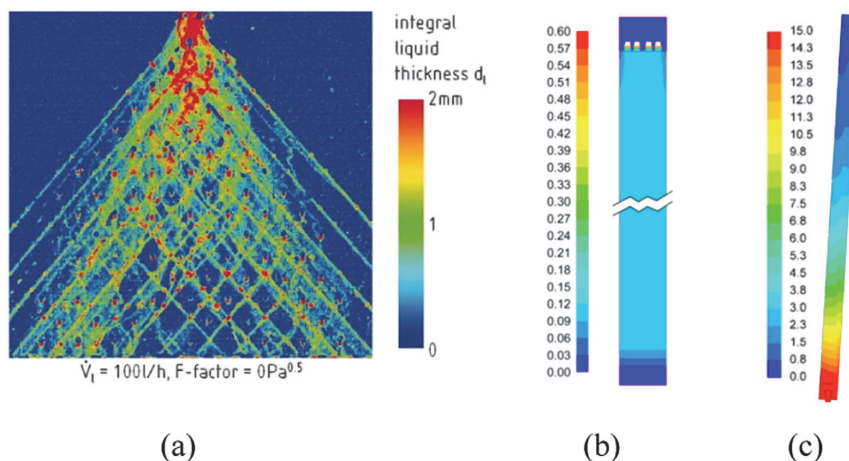


Fig. 6.6. Contours of (a) the spreading of the liquid fed from a point source (Mahr and Mewes, 2008); (b) the liquid holdup (Kim et al., 2016); and (c) CO₂ concentration (Pham et al., 2015). (For interpretation of the references to color in this figure legend, the reader is referred to the web version of this article.)

different particle sizes. Also, it was reported that the capillary dispersion force could be ignored for large particles and high packing porosity (Fourati et al., 2013). Thus, the mechanical dispersion force is the only force employed in most simulation works (Pham et al., 2015, 2015). Furthermore, Hossain et al. (2020) used the mechanical dispersion model to simulate the liquid dispersion in a structured packed bed, and the simulation results agreed with the experimental data. It was proven that the mechanical dispersion model that initially derived from the random packing was also suitable for structured packings (Fourati et al., 2013), thus indicating that this model had a wide range of adaptability to model the flow in different types of packings.

Based on the column scale models combining the porous resistance and dispersion forces, the fluid flows were investigated in randomly and structured packed beds (Pham et al., 2015a; Kim et al., 2016; Uwitonze et al., 2021). An example of the simulated liquid holdup contour is shown in Fig. 6.6 (b). By further coupling with the mass transfer model and some empirical correlations of the effective interfacial area and mass transfer coefficient, the CO₂ capture process could be successfully analysed (Gbadago et al., 2020; Pan et al., 2018). Then, the effect of the sloshing on the liquid flow mal-distribution and CO₂ capture performance (Fig. 6.6 (c)) may be investigated by using the sliding mesh method (Kim et al., 2017; Zhang et al., 2017).

6.3.4. Summary on CFD simulations of the PB

The PB's flow characteristics and mass transfer have been studied using the CFD method, mostly for small lab and pilot scale models. It has been demonstrated that employing the CFD is an efficient and effective way to simulate the carbon capture processes inside the PB, either for simulating the single or multiphase flows and for evaluating the hydrodynamics and/or mass transfer performances. Also, it can achieve much more detailed information about the processes occurring in the bed, which may not be obtained from the experimental measurements.

In order to model the gas-liquid flow and mass transfer in the PBs, different approaches have been employed. The details of the flow behaviour in the PB are usually investigated in the micro-scale model. When using this model, small and complex packing geometry can be considered and it requires a large mesh number. Some methods, such as using the REUs could be used to save computing resources and time. However, the accuracy of the simulation results is directly related to the setting of the boundary conditions and the established packing geometry. Some overall column performance parameters can be obtained using the macro scale model, such as the CO₂ capture rate and pressure drop. To make the simulation of large scale PB feasible and accurate, the Eu-

lerian porous medium model can be used without resolving the complex geometry of the packing structure, but the sub-models for expressing the forces, including the porous resistance and dispersion forces, should be carefully considered.

6.4. CFD study of post-combustion carbon capture based on chemical absorption using rotating packed bed

The rotating packed bed (RPB) has shown great potential to capture CO₂ due to its increased effective interfacial area between the gas and liquid phases under the centrifugal force and excellent mass transfer performance. Among the studies on the RPB, CFD has been widely used to investigate the gas and liquid flows inside the 2D and 3D RPB models. For the single-phase, the gas flow behaviours, including the pressure drop and its distribution, have been studied in various RPB models. While for the gas-liquid flows, two methods, i.e. the VOF and Eulerian methods, have been employed to investigate the wet pressure drop, liquid holdup, liquid dispersion, etc., within the RPB. In addition, the mass transfer performance has been explored by using the CFD method coupled with user-defined functions (UDF).

6.4.1. Fluid flow study in the RPB

The flow characteristics, such as the gas pressure drop and liquid holdup, affect the CO₂ capture performance within the RPB and these have been investigated by using the CFD.

6.4.1.1. Single phase gas flow and pressure drop.

The distribution of the dry gas pressure and pressure drop were simulated for the gas flow passing through a 3D packing region with a complex wire mesh matrix by Liu F. et al. (2017). The influence of the liquid flow was not considered in these simulations. Liu F. et al. (2017) concluded that a considerable part of the gas pressure drop usually occurred from the gas pressure drop in the inner cavity zone of the rotating bed. Also, strong turbulence and mixing, named as the gas-side end effect, were observed in the outer packing zone of the RPB. In this study, a grid of over 90 million computational cells was used to accurately describe the gas flow by resolving at the pore scale in the wire mesh packing of a volume of just 0.009 m³.

In addition, the packing region may be regarded as a porous medium without computationally resolving the geometry of the packing in order to reduce the required computing resources. In this way Yang et al. (2015) and Wu et al. (2018) investigated the mal-distribution of the gas pressure in the 3D RPB models. Then the optimum design of the RPB

was obtained by modifying the gas feed configurations and inserting internals or baffles in the packing region to reduce the mal-distribution and increase the gas-side mass transfer. Again, the simulations did not consider the influence of the liquid phase on the gas flow. The difference between the dry and wet pressure drops in the RPB can be pretty significant.

6.4.1.2. Characteristics of the liquid flow.

The characteristics of the liquid flow, such as the liquid holdup, liquid velocity, and liquid residence time, significantly influence the CO₂ capture in the RPB and therefore attract more attention than the gas flow. A two-phase flow model, either the VOF or the Eulerian model, must be adopted to investigate the liquid flow behaviours accurately. In particular, the VOF method has been widely used since it is well-suited for capturing the gas-liquid interface and the evolution of droplets when impacting on the packing surface, if sufficiently fine computational meshes are employed.

Using 2D VOF method, the liquid flow patterns in wire mesh and foam packings have been obtained under various operating conditions. The flow patterns can be primarily divided into three types: pore flow, droplet flow and film flow (Shi et al., 2013; Xie et al., 2017; Ouyang et al., 2018a, 2018b, 2019; Liu et al., 2019, 2020). In addition, the simulation investigations showed that the flow patterns varied mainly depending on the rotational speed of the RPB. The liquid distribution in the packing region became more uniform with the increased rotational speed, thus producing improved micro-mixing. Furthermore, Yang et al. (2016) and Liu et al. (2020) visually explored the liquid holdup and the liquid distribution within the packing under different operating conditions using the VOF method. The predicted liquid holdup agreed well with the correlations of Burns et al. (2000) and Yang et al. (2016).

However, the actual liquid flow in the RPB is 3D. The flow characteristics obtained under the 2D assumption are limited (Shi et al., 2013). Xie et al. (2019) analysed the gas-liquid flow by using 3D REUs of the RPB where different gravitational forces were employed in the REU to model the flow at different locations across a typical RPB, so that the overall characteristics of the liquid flow in the RPB was successfully assembled. In addition, the correlation of the effective interfacial area was proposed which has been further utilized in the work of Lu et al. (2019) and Zhang et al. (2022a, 2022b). In addition, using the VOF method, Guo et al. (2017) and Zhang et al. (2020) investigated the liquid holdup, liquid droplet size and residence time in a complete RPB model in 3D. However, the multilayer wire mesh packing was simplified as straight wires parallel to the rotor axis without considering the effect of the horizontal wire meshes. Thus, the difference of the liquid holdup obtained from the experiment, simulation and Bruns correlation was large. Therefore, it is important to model the packing geometry exactly in 3D when using VOF method. However, this would lead to a huge computational mesh.

Recently, Zhang et al. (2021) and modelled a sector of the 3D RPB model using the VOF model incorporating a periodic boundary condition. The model considered both the latitude and longitude structured wires to predict the liquid flow behaviours in the packing region accurately. Using this model, the formations of the liquid droplets when impacting on the single-layer or multi-layer wire meshes were simulated (Guo et al., 2017; Xu et al., 2019; Wei et al., 2020; Zhang et al., 2021). The results obtained were compared with the photographs recorded using high-speed cameras, as shown in Fig. 6.7. The observed liquid dispersion indicated that the gas-liquid contact area and the mixing were enhanced at the inner edge of the packing (Zhang et al., 2017). Although various liquid flow characteristics could be clearly captured by employing the VOF method in this study, it will become computationally prohibitively expensive to be used for the simulations of large/full scale RPBs (Liu Y. et al., 2017).

The Eulerian approach has shown great potential for reducing the computational cost in modelling the RPBs (Vlahostergios et al., 2020). Eulerian porous medium method has been utilized in the single-phase

model to investigate the dry gas pressure drop in RPBs. When it is employed to study the liquid flow, the appropriate mathematical models need to be added to the governing momentum equations, such as the porous resistance and liquid dispersion forces. (Lu et al., 2019) proposed some beneficial mathematical models for estimating the gas-liquid interfacial force and the drag forces from the packing to be used with the two-phase Eulerian porous media model for simulating liquid flow in the RPB. These equations were derived based on the correlations originally proposed by Kołodziej and Lojewska (2009) for single-phase flow through a wire mesh. The equations have been successfully employed to investigate the gas-liquid flows in the RPBs to predict the liquid holdup and gas pressure drop. Recently, Zhang and Xie et al. (2022) further developed this model by considering the dispersion forces mentioned in Section 6.3.3, including the capillary and mechanical dispersion forces. The results showed that the predicted liquid holdup matched the experimental data after considering the liquid dispersion force, as shown in Fig. 6.8. Employing the Eulerian porous medium models and the proposed models by Lu et al. (2019) and Zhang and Ingham et al. (2022), the simulation time for a full pilot scale RPB in 3D was significantly reduced. Although the trade-off of the Eulerian porous medium model is that it does not allow a clear capture of the gas-liquid interface, it does provide a feasible and effective way to simulate the CO₂ capture process in a full-scale RPB in 3D.

6.4.2. Predicting the mass transfer performance in the RPB

As is well known, the mass transfer can be greatly enhanced in the RPB due to the centrifugal force resulting from the rotation of the packed bed. Both the VOF and the porous medium approaches have been employed in studying the mass transfer process within the RPB, especially for CO₂ capture. Guo et al. (2016) employed the VOF, together with Yang et al. (2016) investigated the oxygen absorption in the water in the packing region by employing the VOF model and Chen's liquid side mass transfer coefficient correlation via a UDF. They found that the micro-mixing behaviour was extreme in the 'end effect' zone due to the liquid dispersion produced by the collision between the liquid and the packing. Since the semi-empirical mass transfer correlation was used, it may not be able to accurately predict the mass transfer process in a practical RPB as the correlation was too general. As mentioned before, using VOF method requires a prohibitively large number of computational cells to model a full-scale RPB where multiple-length scales which exist in the RPB have to be resolved in order to obtain an acceptable accuracy of the CFD simulation. Therefore, the Eulerian porous medium approach is preferred.

Lu et al. (2019) developed a 2D axisymmetric Eulerian porous medium model incorporating the two-film chemical-enhanced mass transfer model to investigate the CO₂ capture in an RPB, as is illustrated in Fig. 6.9 (a). The model uses a much coarser computer mesh than that typically employed in a VOF model without resulting in significant errors in the model results. The two-film reaction-enhanced mass transfer model has shown sufficient accuracy for expressing the CO₂ mass transfer among the phases in many PB investigations (Kim et al., 2017; Pham et al., 2015). Figs. 6.9 (b) and 6.9 (c) show the predicted CO₂ capture and temperature distributions in the RPB. The results are in good agreement with the experimental observations. Using a similar approach, a complete 3D RPB model, including the packing, inner and outer cavity zones, has been simulated (Zhang et al., 2023). Fig. 6.10 shows the CO₂ and liquid temperature distributions in the RPB with a 50% MEA concentration solvent. The simulation results showed that the CO₂ capture performance agreed well with the experimental data, indicating that the porous medium approach can accurately predict the carbon capture process within the entire RPB.

6.4.3. Summary on CFD for the RPB

The flow characteristics and mass transfer in the RPB have been successfully investigated using CFD. Unlike modelling the static packing in the PB, the RPB models usually employ multiple reference frames or

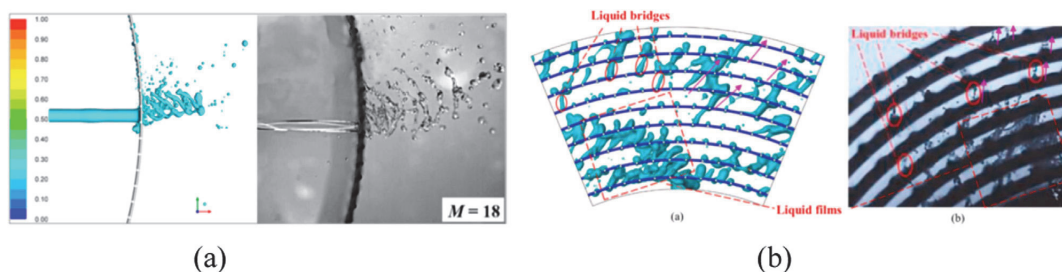


Fig. 6.7. Comparison of the simulated and visualized liquid flow across the rotating (a) single-layer wire mesh packing (Xu et al., 2019); and (b) multi-layer wire mesh packing (Zhang et al., 2021). (For interpretation of the references to color in this figure legend, the reader is referred to the web version of this article.)

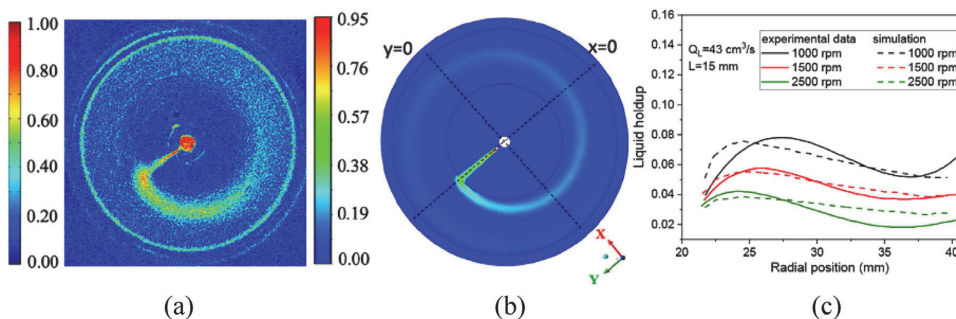


Fig. 6.8. (a) Map of the liquid holdup from the experiment (Yang et al., 2015); (b) contour of the liquid holdup from the simulation; (c) comparison of the liquid holdup along the radial position (Zhang and Ingham et al., 2022). (For interpretation of the references to color in this figure legend, the reader is referred to the web version of this article.)

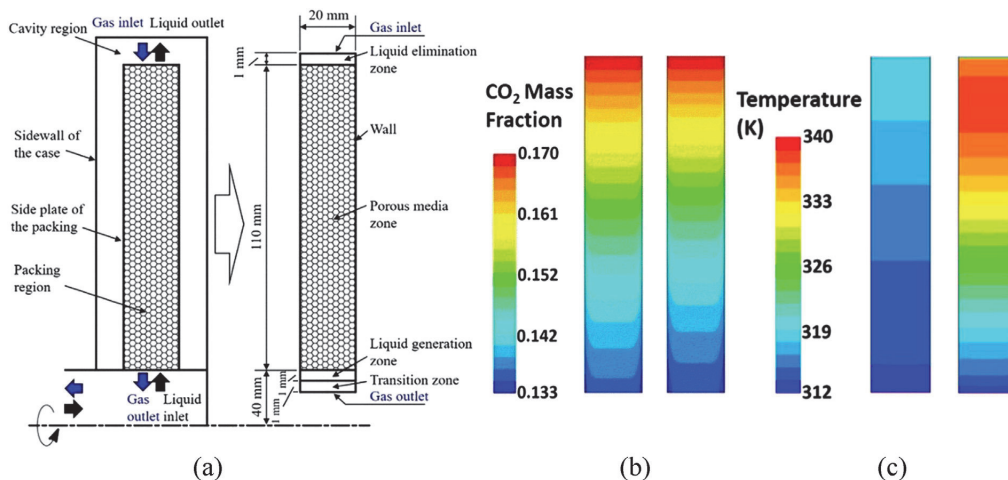


Fig. 6.9. (a) Schematic diagram of the physical 2D RPB model; contours of the (b) CO_2 mass fraction in the gas phase and (c) liquid temperature for 30% MEA and 90% MEA (Lu et al., 2019). (For interpretation of the references to color in this figure legend, the reader is referred to the web version of this article.)

a dynamic mesh to simulate the rotation of the packed bed. To model the gas-liquid flow and CO_2 capture in the RPBs, both the VOF and Eulerian methods have been employed. The VOF can clearly capture the gas-liquid interface and the process of droplet formation when a sufficiently fine computational mesh is employed. However, it is computationally time-consuming and can become prohibitively expensive to simulate large-scale RPBs using the VOF method. Using the Eulerian

method coupled with the porous medium sub-models could save computational resources and simulation time significantly. Therefore, it has shown an excellent potential to be used to simulate large-scale RPBs for process design optimization and scaling up. Nevertheless, the model's accuracy depends on the sub-models employed, such as the porous resistance force model, effective interfacial area model, etc. Finally, as for any CFD model development, including those for both PB and RPB sim-

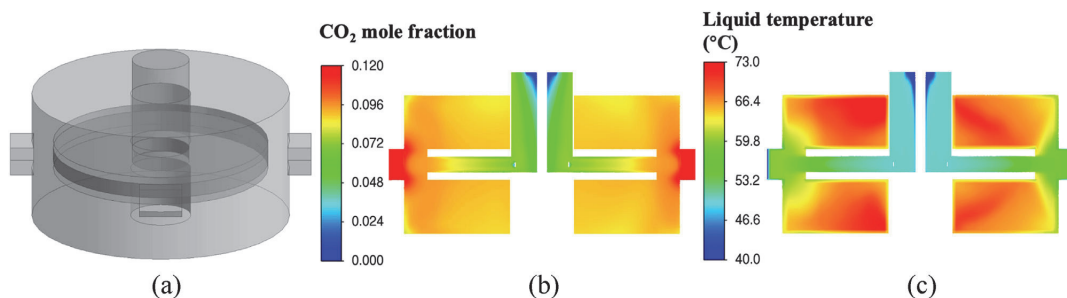


Fig. 6.10. (a) Schematic diagram of the physical 3D RPB model; contours of the (b) CO₂ mole fraction in the gas phase and (c) liquid temperature for 50% MEA (Zhang et al., 2023). (For interpretation of the references to color in this figure legend, the reader is referred to the web version of this article.)

ulations, model validation needs to be performed before it is employed for the modelling of a specific type of packing for CO₂ capture.

6.5. Modelling, simulation and techno-economic analysis of solid adsorbent-based post combustion carbon capture (PCC)

6.5.1. Introduction for modelling, simulation and techno-economic analysis of solid adsorbent-based post combustion carbon capture (PCC)

Post combustion CO₂ adsorption is usually done in fixed bed columns (Siahpoosh et al., 2009), but it is also done in fluidized beds (Akinola et al., 2022). The design of an adsorption column based on empirical data can be expensive and time-consuming, due to the extensive experimentation required. However, predictive models that consider all important transport phenomena can be used to understand the behavior of adsorption column systems and to screen adsorbents without the need for experimentation (Maring and Webley, 2013a).

Pai et al. (2021) described three main concepts involved in modelling adsorption columns, i.e., mass transfer, heat transfer and fluid dynamics. Mathematical models that include solving coupled partial differential equations with appropriate boundary conditions are used to describe the mass and energy balance and fluid flow, to predict the behavior of the adsorption process. The models are then validated with experimental data before they are used for design, optimization, and economic analysis (Yan et al., 2016). Solving partial differential equations simultaneously can be tedious and time-consuming. Therefore, simplified models can usually be used satisfactorily by developing assumptions that simplify the representation of mainly the mass transfer phenomena within the adsorbent particles, to decrease the complexity of the model and the computational time (Shafeeyan et al., 2014). In general, mathematical models of fixed bed adsorption reflect a dynamic state, since a steady-state condition is never attained during adsorption (Valenciano et al., 2015).

6.5.2. Current status on model development of solid adsorption-based carbon capture

6.5.2.1. Fixed bed adsorption column modelling. A set of partial differential and algebraic equations derived from the conservation of mass, energy, and momentum balance are typically used in the modelling of bed columns described in the literature. These equations are used to predict the transient concentration and temperature profile in a fixed bed column. For the equations to be solved, initial conditions for a few key factors, such as concentration, temperature, and flow rate, are necessary. By using the appropriate transport rate equations and equilibrium isotherms, these conservation equations consider the restrictions imposed by the mass transfer rate and the equilibrium between the gas phase and the solid particles. Fixed-bed adsorption models differ in terms of mass transfer rate, equilibrium isotherms, thermal effect and the pressure drop equations used.

6.5.2.2. Mass balance model. Eq. (6.1) is the mathematical equation used to determine the concentration distribution of components in the gas phase along the bed. It includes the terms for: axial dispersion, convection flow, accumulation of the components in the gas phase and the mass transfer term that accounts for the adsorption process on the adsorbent particles.

$$-D_{zi} \frac{\partial^2 c_i}{\partial z^2} + \frac{\partial}{\partial z} (uc_i) + \frac{\partial c_i}{\partial t} + \left(\frac{1 - \epsilon_b}{\epsilon_b} \right) \rho_p \frac{\partial q_i}{\partial t} = 0 \quad (6.1)$$

- D_{zi} is the axial dispersion coefficient, which lumps together the effects that contribute to axial mixing. It can be estimated using the following correlation:

$$\frac{\epsilon_b D_{zi}}{D_{mi}} = 20 + 0.5 Sc Re \quad (6.2)$$

Where D_{mi} , Sc and Re are the molecular diffusivity of component i , the Schmidt number and the Reynolds number respectively.

- c_i is the adsorbate concentration in the gas phase; z is the distance along the bed length; u is the fluid velocity; t is the time; ϵ_b is the bed voidage; ρ_p is the particle density.
- q_i represents the average concentration of component i in the adsorbent particle. It is the link between the gas and solid phase mass balance equations.
- It is often assumed that there is no radial variation in concentration in both the gas and the solid phase, therefore c_i and q_i represent radial average concentrations.
- The axial mixing term, $-D_{zi} (\partial^2 c_i / \partial z^2)$ is often assumed to be insignificant and therefore excluded from Eq. (6.1). This assumption is reasonable for large industrial adsorption units (Simo et al., 2008).

In Eq. (6.1), $\frac{\partial q_i}{\partial t}$ is the rate of mass transfer to the solid adsorbent. It can be expressed as function of the concentration in the gas and solid phase as shown in Eq. (6.3). It is a kinetic model that describes the mass transfer mechanism within an adsorbent. There are different models for different adsorbents, which provide an accurate representation of the mass transfer mechanism (Zhao et al., 2019a).

$$\frac{\partial q_i}{\partial t} = f(q_i, c_i) \quad (6.3)$$

The main types of mass transfer kinetic models include the local equilibrium model and the mass transfer resistance model.

The local equilibrium model assumes a fast mass transfer rate between the gas and solid phase and local equilibrium is reached at every point and time in the column. The equilibrium relationship between the gas and the solid phase can be represented using equilibrium isotherms. The most common isotherms used by researchers include the Langmuir, Freundlich and Toth isotherms (Zhao et al., 2019a). An example of these models can be found in Zhao et al. (2019a), who have used various equilibrium isotherms to evaluate the performance of a PCC adsorption

system when using different adsorbents. The local equilibrium models exclude the effect of mass transfer resistance in the particle and thus do not accurately represent what is observed in adsorption columns. However, due to their simplicity, they can be used to provide an approximate representation of column behavior and they can provide valuable information about the process dynamics and the behavior of the system during the preliminary design stage of the process. Equilibrium models are also useful for designing systems in which the adsorptive selectivity depends on the difference in the equilibrium of the species in the gas mixture, but they will not be useful when the selectivity is based on kinetics when separation is achieved by the difference in the gas-adsorbent mass transfer rates between the components (Hassan et al., 1986). Therefore, a non-equilibrium model will be required to describe the behavior of such processes.

Mass transfer resistance models are based on the three potential types of resistance to diffusion into the adsorbent particles, namely: external fluid resistance and intraparticle diffusion resistance, macropore diffusion resistance, and micropore diffusion resistance. These models have been shown to predict the behavior of adsorbents in a column adequately (Mulgundmath et al., 2012). A detailed description of these models can be found in Shafeeyan et al. (2014). Although these models provide a close approximation of reality in adsorption columns, their main drawback is the complex mathematical formulation, which is difficult and time-consuming to solve, which makes them impractical for column design and optimization. In general, simplified models are adopted by applying assumptions that increase the practicability of the model without reducing its accuracy. The most used of such models is the Linear Driving Force (LDF) approximation, which suggests that the mass transfer rate of a component into the adsorbent is proportional to the linear difference between the concentration on the outer surface of the adsorbent particle and the average concentration inside the particle. The outer surface concentration is assumed to be at equilibrium with the bulk gas phase concentration. The mass transfer is therefore expressed as follows (Shafeeyan et al., 2014):

$$\frac{\partial q_i}{\partial t} = k_i (q_i^* - q_i) \quad (6.4)$$

Where q_i^* is the adsorbed-phase concentration in equilibrium with the gas phase concentration of component i , which can be obtained from various equilibrium isotherms models (Zhao et al., 2019a), an example of which is the Langmuir isotherm. This can be expressed as shown in Eq. (6.5), where: q_i^s is the saturation loading of the adsorbent; K is the Langmuir isothermal equilibrium constant.

$$q_i^* = q_i^s \frac{K(T)P_i}{1 + K(T)P_i} \quad (6.5)$$

In Eq. (6.4), k_i is the effective linear driving force rate coefficient that lumps together all the resistance to mass transfer. To predict k_i accurately, many forms that have been developed can be found in the literature, with these depending on what type of mass transfer resistance is dominant. For instance, Farooq and Ruthven (1990) suggested the following model for k_i , if both macropore and micropore diffusion resistance are dominant:

$$\frac{1}{k_i} = \frac{R_p q_0}{3k_{fi} c_0} + \frac{R_p^2 q_0}{15\epsilon_p D_{pi} c_0} + \frac{R_c^2}{15D_{\mu i}} \quad (6.6)$$

Where:

- q_0 is the value of q (concentration in the solid state) at equilibrium, while c_0 is the concentration in the gas phase at feed temperature.
- D_{pi} and $D_{\mu i}$ are the effective macropore diffusivity and the micropore diffusivity respectively.
- R_p and R_c are the macropore and micropore radius.
- k_{fi} is the external film mass transfer coefficient.

6.5.2.3. Energy balance. Although there are several isothermal adsorption models that do not take the energy balance into account (Moreira

et al., 2006; Shen et al., 2010), temperature variations in the adsorption column can affect adsorption equilibrium and the adsorption rate. Therefore, in order to accurately predict packed bed adsorption, the effect of heat generation due to the adsorption process must be considered. Three control volumes are usually considered - the gas, the solid and the wall of the column - and the heat transfer rate in these volumes can be modelled as follows (Shafeeyan et al., 2014):

The gas phase energy balance that is used to determine the gas temperature profile in the bed:

$$-\lambda_L \frac{\partial^2 T_g}{\partial Z^2} + \rho_g C_g \frac{\partial(uT_g)}{\partial Z} + \rho_g C_g \frac{\partial T_g}{\partial t} + \left(\frac{1 - \epsilon_b}{\epsilon_b} \right) h_f a_s (T_g - T_s) + \frac{4h_w}{\epsilon_b d_{int}} (T_g - T_w) = 0 \quad (6.7)$$

Where:

- T_g , T_s and T_w are the gas, solid particles, and wall temperature, respectively.
- C_g and ρ_g are the bulk heat capacity and density of the gas.
- h_f is the coefficient of the film heat transfer between the gas and the solid particles; h_w is the coefficient of the internal convective heat transfer between the gas and column wall; a_s is the ratio of the particle's external surface area to its volume; d_{int} is the internal diameter of the column; λ_L is the effective axial heat dispersion given by Grande and Rodrigues, (2005).

The solid phase energy balance:

$$\rho_p C_s \frac{\partial T_s}{\partial t} = h_f a_s (T_g - T_s) + \sum_{i=1}^n (-\Delta H_i) \frac{\partial q_i}{\partial t} \quad (6.8)$$

Where: ρ_p and C_s are the particle density and heat capacity, respectively; ΔH_i is the isosteric enthalpy of adsorption for component, which can be calculated as given in Yang et al. (1997).

The column wall energy balance:

$$\rho_w C_w \frac{\partial T_w}{\partial t} = h_w a_w (T_g - T_w) + U a_a (T_\infty - T_w) \quad (6.9)$$

Where: ρ_w and C_w are the density and the heat capacity of the wall, respectively; a_w is the ratio of the internal surface area to the volume of the column wall; a_a is the ratio of the external surface area to the volume of the wall; U is the external overall heat transfer coefficient between the wall and the air outside the wall; T_∞ is the temperature of the outside air.

6.5.2.4. Momentum balance. The moment balance accounts for the pressure drop and the change in gas velocity in the column. Any model that estimates the pressure drop across a fixed bed can be used. The most common in the Ergun equation:

$$\frac{\partial P}{\partial Z} = - \frac{150\mu(1 - \epsilon_b)^2}{\epsilon_b^3 d_p^2} + \frac{1.75(1 - \epsilon_b)\rho_g u^2}{\epsilon_b^3 d_p} \quad (6.10)$$

Where: P is the total pressure; μ is the gas viscosity; d_p is the particle diameter.

6.5.2.5. Fluidized bed adsorption modelling. When compared to fixed-bed systems, where hotspot generation is frequently unavoidable due to insufficient heat and mass transfer across the bed, fluidized-bed adsorption has the main advantage of improved adsorption due to enhanced heat and mass transfer caused by uniformity of temperature in the bed. However, modelling the behaviour of a fluidized bed is more difficult and requires the use of a complex computational method to describe the different fluidization regimes (Lee and Miller, 2013).

In addition to the gas-solid interactions phenomena that we have addressed for fixed bed column modelling (Li et al., 2022), fluidized bed adsorption modelling also requires characterization of the hydrodynamics (Jung and Lee, 2022b). Simple models that consider the important

hydrodynamic characteristics of a fluidized bed and require less computational power have been used (Akinola et al., 2022). In recent years, the use of computation fluid dynamic (CFD) has become more prevalent among researchers due to the advances in computational power (Balice et al., 2022; Cai et al., 2022; Lian and Zhong, 2022; Luo et al., 2022). According to Nikam et al. (2022), two approaches are used in these models: the Eulerian-Eulerian approach, which considers two fluid phases, i.e., the gas phase and the fluidized solid phase; the Eulerian-Lagrangian approach, which treats the solid fluidized phase as a discrete phase and keeps track of the position of individual particles in the bed. The latter approach provides a more precise description of the fluidized phase, although it requires more processing power.

6.5.3. Study of the adsorption-based carbon capture process based on process simulation

The simulation and modelling of PCC processes are usually done to screen and evaluate the performance of different adsorbent materials, and to evaluate different process configurations. According to Nikolaidis et al. (2018), the relationship between ideal process performance, operating conditions, and adsorbent properties is complicated and cannot be quantified by only considering isotherms, selectivity and data of equilibrium working capacity: detailed simulation and optimization are required. The common performance indicators used in most PCC simulations and modelling include CO₂ purity and recovery, energy efficiency, productivity, and economics (Akinola et al., 2022). Simulation and modelling packages such as gPROMS, Matlab and Aspen Adsorption are often used when evaluating these processes (Hasan et al., 2013; Leperi et al., 2019; Subraveti et al., 2019a). Several authors, including (Farmahini et al., 2018), Hasan et al. (2013), Leperi et al. (2019) and Subramanian Balashankar and Rajendran (2019) have used simulation and modelling to screen adsorbent materials. Recently, Burns et al. (2020) screened 1632 metal-organic framework (MOF) materials for PCC by integrating molecular simulation with a macroscopic process simulation of vacuum swing adsorption (VSA). They concluded that: 482 materials met the regulatory target of 95% purity and 90% recovery of CO₂ (95/90 CO₂ PRT); 365 of these materials had a parasitic energy requirement below that of solvent-based capture of 290 kWh per metric ton of CO₂. They also used a machine learning model to predict a given material's ability to achieve the required 95/90 CO₂ PRT.

Energy consumption is one of the important parameters, which has been extensively investigated using modelling and simulation in adsorption-based PCC and which ties up closely with process operating conditions such as feed pressurization and blowdown pressure, plant productivity and capital cost. For instance, Haghpanah et al. (2013) did a simulation exercise in which they optimized pressure-vacuum swing adsorption (PVSA) using Zeochem zeolite 13X. They concluded that a minimum energy requirement of 149 kWh/ton of CO₂ is achievable when the process operates at low pressure, with an inlet pressure of 1 bar and a vacuum blowdown pressure of 0.02 bar to achieve a productivity of 0.49 mol of CO₂/m³ of adsorbent corresponding to an 11% energy penalty. They also noted that energy consumption increases with higher productivity and that a combination of feed pressurization and low blowdown pressure can reduce the plant size and the capital cost significantly. Nikolaidis et al. (2018) corroborated that energy consumption increases with increased productivity when they compared the optimized performance of zeolite 13X and modified zeolite 13X in a simulation of a single stage PVSA. In a simulation run by Subramanian Balashankar and Rajendran, (2019), more than 120 000 zeolite materials were compared, including hypothetical and existing zeolite materials. It was shown that low N₂ affinity, not high CO₂ affinity, is characteristic of a low energy consuming adsorbent. It was also shown that the best performing adsorbent materials consumed 16% less energy than Zeolite 13X, which is considered the current benchmark for adsorbent materials.

6.5.4. Techno-economic analysis

In industrial settings, solid adsorbents have been used to remove CO₂ from hydrogen and natural gas. Unlike the flue gas from power plants, these gases are typically present at high pressure and low temperature. When the International Energy Agency (IEA) conducted a study on applying PSA to adsorption-based PCC in the early 1990s (IEA, 1992); thus, the authors concluded that this technology was not suitable for the bulk capture of CO₂ from fossil fuel power plants.

Interest in using adsorbents for CO₂ PCC only surfaced in late 2000s. Ho et al. (2008) reported the first Techno-Economic Analysis (TEA) study after the publication of the IEA 1992 report. In this study, the VSA process was compared to the PSA process, as shown in Fig. 6.11. Zeolite 13 X was selected as the adsorbent, with a capacity of 2.2 mol/kg of adsorbent, and CO₂/N₂ selectivity of 54. When the four-step Skarstrom cycle was used, the VSA showed promising results compared to PSA, with a capture cost of \$51/ton of CO₂ avoided (2006 USD), close to MEA adsorption process, which is \$49/ton CO₂. The CO₂ capture rate was set at 85% in the study, but the purity of the CO₂ in the recovery stream was less than 50%. Most of the cost comes from compression (both unit cost and energy cost), seconded by the adsorbent unit and adsorbent replacement. When a seven-step PSA cycle was applied, the capture cost was lowered to \$41/ton with an improved purity of 70%. The drawback of using the seven-step PSA cycle is that more adsorbent is needed to compensate for the reduced CO₂ recovery rate. The authors proposed that the most cost can be reduced further if a better adsorbent is used (Ho et al., 2008). This result was very promising, as the estimated capture cost was close to that of the MEA adsorption processes.

The impact of process factors on the VSA for PCC was investigated by Zhang et al., 2008. The cost results were not comparable to those reported in previous studies since a straightforward economic assessment method was used to compare the merits of various VSA situations. However, the study did show that input CO₂ with a high concentration increases the recovery rate and purity of CO₂, which can significantly reduce the capture cost. Using a six-step VSA cycle, the study found that ordinary flue gas with a CO₂ concentration of about 12% by volume is good for VSA, with good recovery (>70%) and purity (>90%). Increased purity can be attained using a nine-step VSA cycle, but the cost penalty is higher.

In their review paper, Samanta et al. (2012) evaluated the studies on PCC and noted that relatively few economic analyses were done because there was insufficient data on the performance of solid sorbents in various contactor configurations. The assessment also made it clear that the reactor and process design are crucial for the development of the PCC technology and that the sorbent is not the only important factor in the process. This assessment still holds true.

The impact of water on adsorption-based PCC was taken into consideration by Leperi et al. (2016). The study found that removing water before the PSA cycle is crucial. When moisture was eliminated during the pre-treatment phase, with zeolite 13X being used as the adsorbent, it resulted in a 90% recovery rate with 90% purity at a cost of \$32.1/ton CO₂. Pre-treatment can cut the overall cost of capture by about 6%.

More and more parameters can be added into the TEA as computer power and simulation models improve. Khurana and Farooq (2019) reported on an integrated optimization platform that can use a simulator based on a non-isothermal and non-isobaric linear driving force model. This platform was demonstrated using two VSA cycles: a four-step VSA cycle with light pressurization and a six-step cycle with dual reflux Fig. 6.12. The method was optimized in relation to the leveled cost of electricity (LCOE). MOF UTSA-16 was used to obtain a minimum LCOE of \$114/MWh for the four-step cycle, which is less expensive than NETL's Shell Cansolv-based PCC solution. The cost of CO₂ capture is claimed to be \$21.1/ton CO₂ captured and \$26.3/ton CO₂ avoided, with CO₂ purity exceeding 90% (Khurana and Farooq, 2019). This is much lower than that reported in prior research, and it meets the \$40/ton CO₂ objective for second-generation PCC technologies.

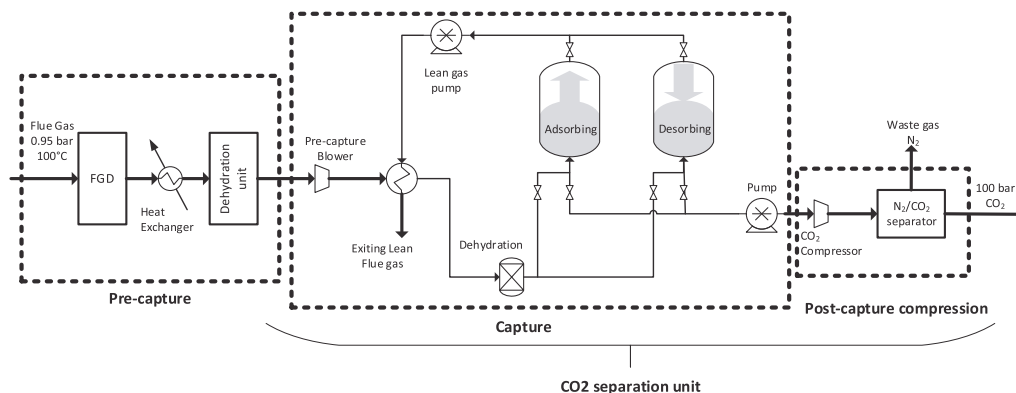


Fig. 6.11. Simplified process flow diagram for the PSA/VSA CO₂ capture process applied by Ho et al. (2008). (For interpretation of the references to color in this figure legend, the reader is referred to the web version of this article.)

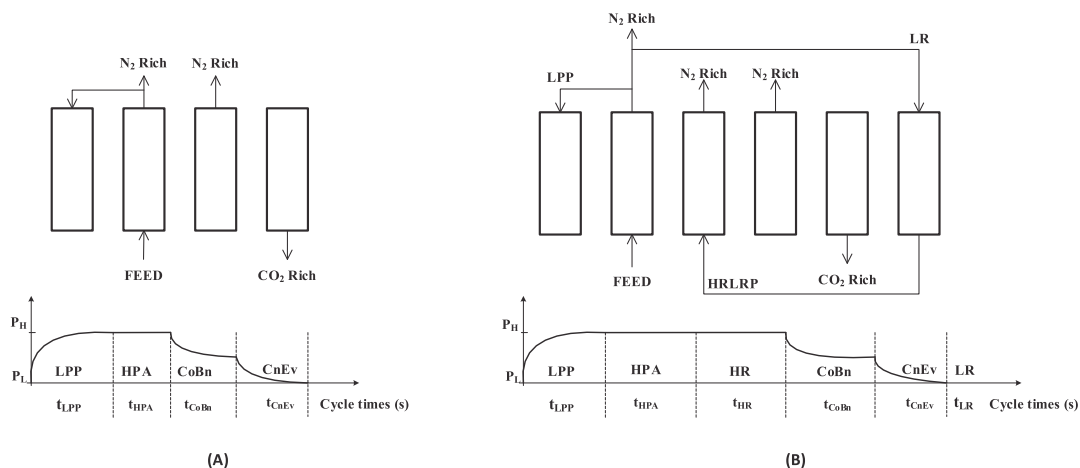


Fig. 6.12. (A) The four-step VSA cycle with LPP and (B) the six-step dual-reflux VSA cycle studied by Khurana and Farooq (2019). (For interpretation of the references to color in this figure legend, the reader is referred to the web version of this article.)

Danaci et al. (2020) created another screening tool. Twenty-two MOFs, two zeolites and activated carbon were tested against CO₂ purity, recovery rate and cost. CO₂ emissions from four sources were considered: natural gas power plants, coal-fired power plants, cement manufacture and the steel industry. UTSA-16, which is similar to zeolite 13X, was found to be the best MOF among the adsorbents examined; however, the cost of the adsorbent was higher than that of an amine-based adsorption technique. The study found that the most relevant qualities of the adsorbent are its low N₂ adsorption and moderate enthalpies of adsorption, rather than its CO₂ capacity or surface area. This work showed a new direction for adsorbent design, as well as the complexity of the PSA system.

Subraveti et al. (2021) confirmed that the cost of the VSA process when using the new proposed adsorbents Zeolite 13X and two MOFs, is still higher than that of the MEA process. The study reported that IISERP MOF 2 outperformed Zeolite 13X, which is the benchmark material for the four-step cycle process. When the CO₂ concentration in the flue gas was 20%, the capture cost was €33.6/ton of CO₂, with a corresponding CO₂ averted cost of €73/ton, which is more than that of MEA. The study reported that optimizing the VSA process for proxy objectives, such as reducing energy used and maximizing productivity, does not

automatically translate into the lowest cost. The adsorbents identified as being superior due to their high energy/productivity performance did not always result in reduced cost. The rationale offered was that the minimum cost configuration does not lay in the minimal energy vs. maximum productivity Pareto curves, due to the complexity of the VSA process scaling up. This explanation adds to the already-complex VSA process and poses a new hurdle in adsorbent screening. The study also indicated that: due to the constraint of a single VSA unit, it is difficult to profit from economies of scale; the VSA process is probably better suited to small and medium-sized operations rather than large-scale operations (Subraveti et al., 2021). It was also stated that a different strategy is required to further reduce capture costs, and the proposed solutions were to use monoliths, contact passes paired with quick cycling and using other cycles.

Jung and Lee, (2022b) claimed that the solid sorbent process outperforms the MEA process. Four processes were evaluated in their study: fluidized bed, fixed bed, moving bed and rapid thermal swing. The amine functionalized SiO₂/0.37EB-PEI powder, pellet and hollow fibre were employed as the solid sorbent. The study revealed that, except for the fluidized bed process, the proposed processes had a lower capture cost than the 30% MEA process. The best performing process had a

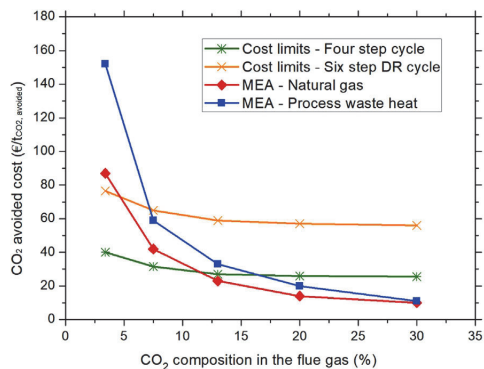


Fig. 6.13. Comparison of the cost limit of the four-step and six-step DR PVSA cycles with CO₂ avoided cost obtained using the MEA-based CO₂ capture with two streams supply scenario (Subraveti et al., 2022). (For interpretation of the references to color in this figure legend, the reader is referred to the web version of this article.)

capture cost of \$48 per ton of CO₂, which was 24% less expensive than the 30% MEA process and only 3% more expensive than the Water Lean Solvents method.

Subraveti et al. (2022) investigated the cost limits of the PVSA process. In this investigation, the cost of the adsorbent was adjusted to zero to determine the effect of sorbent characteristics. It was determined that the optimal adsorbent should have close to 0% N₂ adsorption, which agrees with Danaci et al. (2020)'s conclusions, as well as linear isotherms. Based on the four-step cycle, morphological change can result in a 9–22% lower CO₂ avoidance cost. The optimal pellet porosity and diameter was 0.42–0.76% and 3–5 mm, respectively. When compared to the four-step cycle, the six-step DR cycle cost 15–42% less. As shown in Fig. 6.13, compared to the MEA process, the four stage PVSA cycle is at least 8% less expensive, and the six-step DR PVSA is at least 35% less expensive for input gasses with more than 7.5% CO₂ concentration. CO₂ averted costs ranged from €10.4 to 87.1/ton for feed gas with CO₂ concentrations ranging from 3.50% to 30%, while MEA costs ranged from €54.8 to €76.8, which indicates that PSA is well suited to high CO₂ concentration gas treatment.

The two most recent studies (Jung and Lee, 2022a; Subraveti et al., 2022) indicated that under certain conditions, the solid adsorbent could deliver a reduced CO₂ capture cost. It is worth noting that in the study by Subraveti et al. (2022), the optimal CO₂ adsorption isotherm varied according to the different process options and different CO₂ compositions. Examples of the CO₂ isotherms are shown in Fig. 6.14.

According to Akinola et al. (2022), although TEA research on the solid adsorbent system for PCC is still limited, the trend over the last two decades has shown that advancements in the computational capacity of available modelling and simulation tools has enabled detailed model development and simulation studies, particularly in the case of a fixed bed, which has thus far been seen as the most promising option. The detailed simulation demonstrated the difficulty of adsorbent and process screening, particularly when the best performing adsorbent does not always result in the lowest cost, and the best performing process for single unit operation does not always result in a superior large-scale setup. More creative cycle and column configurations are required to enable cost-effective PCC adsorption.

6.5.5. Summary: advantages, limitations, and prospects

Table 6.2 summarizes some of the important developments in PCC modelling, simulation, and economic analysis. Even though there are still few process simulations and economic evaluations, it is evident that more information on identifying the lowest-cost option has been

reported thanks to increased computing capacity and model development. It is promising to see that the cost of solid-based PCC processes has decreased over the years, according to the simulation results. The second-generation PCC technologies' target cost of \$40/ton of CO₂ has been met, and additional cost reductions are possible.

Furthermore, the work done so far has indicated that the traditional way of doing materials screening, with only the CO₂ capacity and surface area being considered, was not sufficient to determine the best adsorbent. Adsorption enthalpies and N₂ adsorption both contribute significantly to reducing capture costs. The "best adsorbent" also depends on the process configuration. Various processes have different needs in terms of the optimal adsorbent. This makes material screening more changing because the best adsorbent selected for a single unit might not be the best candidate for a large-scale operation. To reduce capture cost, it would therefore be more crucial to consider different process configuration options. As recommended by Akinola et al. (2022), the key to develop more cost-effective PCC processes would lie on the development of more creative cycle and column configurations. Setting the process performance target first, understanding the process requirements for the adsorbent to reach the target, and using this as a criterion for material screening should be the philosophy for more cost-effective PCC.

6.6. Machine learning application for modelling, simulation, optimization and control of carbon capture systems

Carbon capture systems involve a highly nonlinear and complicated interplay of heat and mass transfer, thermodynamics and chemical reactions (Lawal et al., 2009). Accurately modelling their behaviour from the first principle is time-consuming, computationally difficult and requires advanced capabilities in process systems engineering. Data-based modelling using machine learning, which is simpler and easier to implement, has been proven to accurately model and predict the highly complex underlying relationships in carbon capture systems with reduced computational load (Li et al., 2018). Machine learning, a branch of artificial intelligence, uses empirical data to obtain models that can predict relationships and patterns. Machine learning models use algorithms, common among which are decision trees, naïve Bayes, support vector machines, random forest, AdaBoost, k-means clustering, particle swarm, genetic algorithm and artificial neural networks (Yan et al., 2021), to achieve specific tasks such as regression, classification, clustering, outlier detection and dimension reduction. The tasks are achieved by 'training' the algorithms using the selected data to 'learn' the relationships and patterns in a dataset. The methods for machine learning model training includes supervised, unsupervised and reinforcement learning (Bonetto and Latzko, 2020). Unsupervised learning algorithms use only input datasets to 'train' machine learning models to 'learn' the commonalities within a dataset, enabling clustering or association of unlabelled datasets. On the other hand, supervised and reinforcement learning uses an input-output dataset and 'trains' the machine learning model to 'learn' the input-output relationship (Bonetto and Latzko, 2020).

Supervised machine learning has been widely used in carbon capture modelling, simulation, control and optimisation due to its relative simplicity and suitability for a wide range of machine learning algorithms. Machine learning-based modelling application in carbon capture has become expedient with the growing availability of experimental and/or operating datasets of carbon capture systems as the number of test and demonstration plants commissioned worldwide continues to increase (Oko et al., 2017). State-of-the-art machine learning applications in the wider area of carbon capture storage and utilisation (CCUS) have been reported (Gupta and Li, 2022; Rahimi et al., 2021; Yan et al., 2021). Given the wide-ranging nature of the existing reviews, their discussions on machine learning applications in carbon capture are limited with no critical analysis of existing models. Therefore, this section of this review provides an in-depth critical analysis, identifies the grey areas and limitations in existing machine learning applications in carbon

Table 6.2

Summary of some of the work done on modelling, simulation, and techno-economic analysis of PCC processes and their results on capture cost and energy consumption.

| Application | Authors | Method | Adsorption Type | Operation mode | Cost/ energy consumption | Software used |
|--------------------------------|---|---|--------------------------------------|----------------|---|-------------------------|
| Adsorbent material screening | (Farmahini et al., 2018) | Molecular simulation, Equilibrium adsorption, Process simulation | Fixed bed | VSA, PSA | | CySim, Platypus, Python |
| Adsorbent material screening | (Hasan et al., 2013) | ZEOMICS, Isotherms, Process simulation, NAPDE, NLP | Fixed bed | VSA, PSA | \$23.63-\$41.45 per ton CO ₂ | ZEOMICS |
| Adsorbent material screening | (Leperi et al., 2019) | Molecular Simulation, Equilibrium Isotherms, Process simulation | Fixed bed | PSA | \$30-\$40 per ton CO ₂ | Matlab-S-ODE |
| Adsorbent material screening | (Subramanian Balashankar and Rajendran, 2019) | BAAM, Process simulation, Equilibrium Isotherms | Fixed bed | VSA | 123.21 kWh/ton CO ₂ | Matlab-S-PDE |
| Adsorbent material screening | (Burns et al., 2020) | Molecular Simulation (GCMC), Process Simulation, Machine Learning | Fixed bed | VSA | < 290 kWh/ ton CO ₂ | |
| Adsorbent material screening | (Jung and Lee, 2022a) | Process simulation | Fixed bed, Fluidized bed, Moving bed | TSA | \$48.1-\$75.2/ton CO ₂ | |
| Energy evaluation | (Haghpahanah et al., 2013) | Process simulation -Finite Volume Method | Fixed bed | PSA, VSA, PVSA | 148.96-499.65 kWh/ ton CO ₂ | Matlab-ode23s |
| Energy evaluation wet flue gas | (Krishnamurthy et al., 2014a) | Process Simulation, Equilibrium model | Fixed bed | VSA | 177 kWh/ton CO ₂ | Matlab-ODE |
| Energy Evaluation | (Nikolaïdis et al., 2018) | Equilibrium Isotherms, LDF | Fixed bed | P/VSA | 0.89-1.08 MJ/kg CO ₂ | gPROMS/ gOPT |
| Energy Evaluation | (Jung and Lee, 2022b) | Process simulation | Fluidized bed | TSA | 258.6 kWh/ton CO ₂ | |

capture and gives recommendations to guide future research and development.

6.6.1. Machine learning algorithm: artificial neural network

Although a handful of machine learning algorithms have been developed for handling different tasks (Yan et al., 2021), artificial neural network (ANN) is the most widely used algorithm due to their versatility and accuracy for all task categories (Shalaby et al., 2021). ANN mimics the structure of biological neural networks and their way of encoding and decoding problems and is therefore able to identify complex underlying relationships based on input-output datasets. They include the interconnection of neurones and the basic building blocks, organised in input, hidden and output layers (Fig. 6.15). Feedforward ANN with signals flowing from the input to the output through a single hidden layer

is very commonly used, although they are very likely to overfit the data and therefore have poor generalisation capability (Caruana et al., 2000). To address this limitation, NN algorithms with multiple hidden layers and recurrent networks with feedback loops are emerging. The following sections describe machine learning application in different areas of carbon capture.

6.6.2. Machine learning for thermodynamic and physical property prediction

The CO₂ solubility and other thermodynamic and physical property data, used for representing the vapour-liquid equilibria (VLE) in solutions of chemical solvent-CO₂, are essential for the design and modelling of the absorber and stripper in carbon capture systems. The VLE in these systems is commonly predicted using the electrolyte Non-Randon

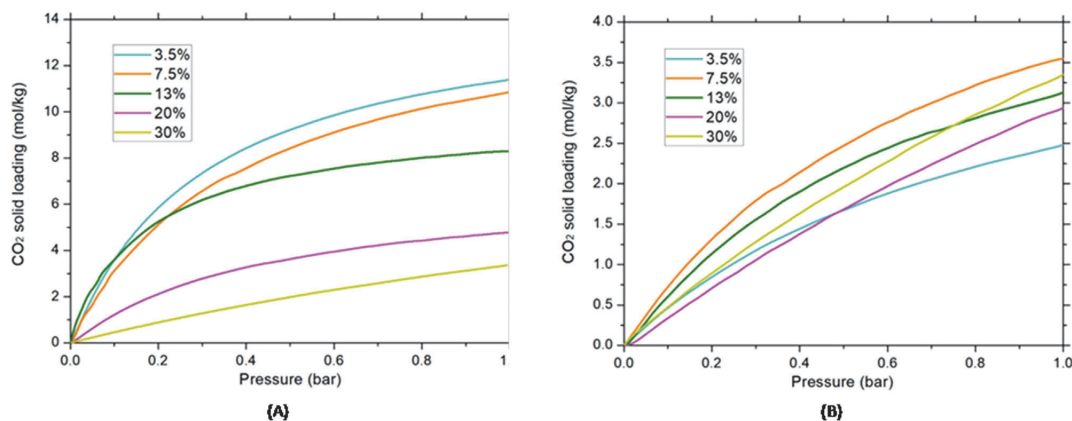


Fig. 6.14. Optimal adsorbent properties that correspond to the cost limit of (A) four-step PVSA process, and (B) six-step DR cycle with different CO₂ feed concentrations Subraveti et al. (2022). (For interpretation of the references to color in this figure legend, the reader is referred to the web version of this article.)

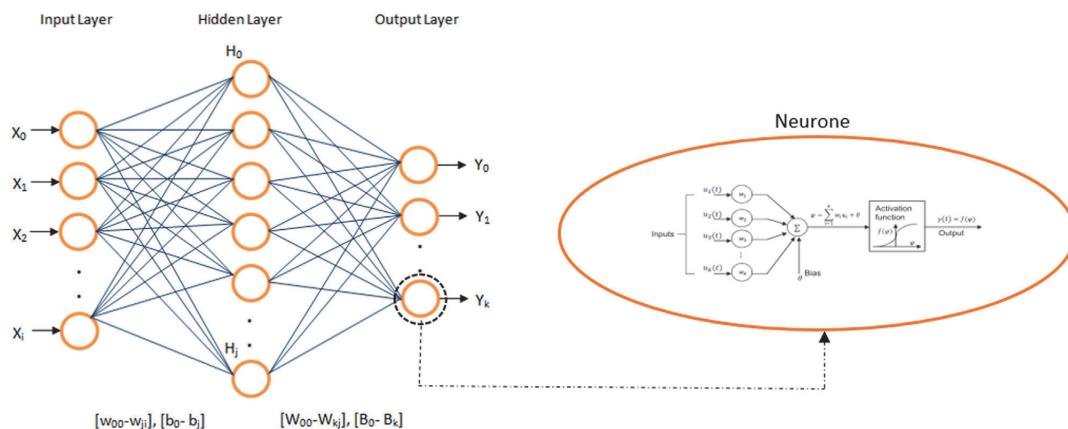


Fig. 6.15. Neural network showing the structure of the neurone (Shalaby et al., 2021). (For interpretation of the references to color in this figure legend, the reader is referred to the web version of this article.)

Two-Liquid (NRTL) or models such as the extended UNIQUAC, SAFT-VR and SAFT- γ (Aronu et al., 2011; Mac Dowell et al., 2010). The electrolyte NRTL, an activity coefficient model, is the most accurate thermodynamic equilibrium model (Austgen et al., 1989). The model predictions are based on the excess Gibbs free energy model with the Pitzer-Debye-Huckel equation used to describe the long-range interaction effects. The electrolyte NRTL model has been widely used to correlate CO₂ solubility data in 30 wt% MEA solution. Unless where these thermodynamic models are available such as in commercial simulators, developing them is non-trivial making a strong case for machine learning-based models.

ANN has proven to successfully accurately model the VLE and physical properties of solutions of the different solvents-CO₂ systems as obtained in carbon capture systems (Chen et al., 2015; Norouzbahari et al., 2015; Zhang et al., 2018). Single hidden layer back-propagation neural networks (BPNN), radial basis function neural networks (RBFNN) and general regression neural networks among others have all been shown to accurately predict the CO₂ solubility and other properties of different amine solutions (Chen et al., 2015; Zhang et al., 2018). Although BPNN show slightly better performance, these models have limited generalisation due to the one hidden-layer structure. A more robust structure, namely multiple hidden layer BPNN, showed improved accuracy (Norouzbahari et al., 2015) although this model appeared to have overfitted the data. Extreme machine learning algorithms where the input-hidden layer and hidden layer-output neurone weightings of the ANN are assigned random and via one-step regression respectively have also been shown to improve the predictive performance for CO₂ solubility and other properties (Nabipour et al., 2020). Other machine learning algorithms, namely Least Square Support Vector Machine, have comparable performance for CO₂ solubility predictions as an ANN-based model (Nabipour et al., 2020). On the other hand, ANN has also been used to predict isotherms for CO₂ capture by adsorption (Khurana and Farooq, 2019). The isotherms relate the adsorbates in the surrounding phase to the adsorbates on the adsorbent at equilibrium and constant temperature conditions and is a critical thermodynamic requirement for modelling the process. The ANN-based isotherm model can be effectively and rapidly used to screen and select adsorbents.

6.6.3. Machine learning for modelling and simulation of the CO₂ capture system

ANN model with a single hidden layer has been developed and used to evaluate carbon capture performance through chemical absorption

(Wu et al., 2010). As this type of ANN model generally has poor generalisation capability beyond the training data, new solutions involving bootstrapping multiple single-layered neural networks into one network have been developed for CO₂ capture application (Li et al., 2015). Bootstrapped ANN models have a slow training process due to the increased number of calculations. The extreme learning machine algorithm, where the input-hidden layer and hidden layer-output neurone weightings are assigned randomly and via one-step regression respectively, can be employed to greatly enhanced the training speed of the bootstrapped ANN models (Li et al., 2017). Notwithstanding, the hidden single-layer nature of the bootstrapped primary networks, makes them vulnerable to accurately capturing the complicated phenomena in carbon capture systems as they may become trapped in the local optima (Dong and Li, 2012). More sophisticated deep belief networks (DBN) has been proposed to address this problem in carbon capture application (Li et al., 2018). DBN comprises multiple hidden layers of restricted Boltzmann machines that learn the input dataset's probability distribution, rather than the deterministic values. DBN is trained in batches including the unsupervised training phase to obtain initial weights of the neurones and a subsequent supervised phase via back-propagation. The DBN model of carbon capture systems has been shown to have better prediction accuracy than others (Li et al., 2018). Other machine learning algorithms, namely tree regression and Gaussian process regression, have also been used for modelling and simulating solvent-based carbon capture systems, but ANN generally performs better (Shalaby et al., 2021). ANN and other machine algorithms namely support vector machine, gradient boosting and tree regression have also been applied to estimate the CO₂ adsorption capacity for different adsorbents (Yuan et al. 2021; lian et al. 2022) with ANN similarly showing superior predictive capability compared to other algorithms (Fathalian et al. 2022). Many existing machine learning models for CO₂ capture by adsorption are mainly for predicting the CO₂ adsorption capacities for different adsorbents. These models are therefore not suitable for process optimisation and control.

6.6.4. Machine learning for control of the CO₂ capture process

CO₂ capture via chemical absorption exhibits large time inertia due to the high solvent circulation rate and huge volume of the absorber and stripper (Liao et al., 2020). This impacts the capability of the plant to be operated flexibly to follow the rapid dynamics of their host power plant as required, making the process control very challenging and conventional PID controllers insufficient for achieving desired control (Liao et al., 2020). Machine learning-based predictive controllers effectively reach setpoints with zero bias at all conditions (Li et al., 2018;

Akinola et al., 2020; Liao et al., 2020). Conventional model predictive controllers (MPC) are based on first principle models often linearised around the operating point to reduce the associated complexity and computational loads. Although these MPCs show better performance than PID-based controllers, their performance deteriorates quickly due to the linear models. In contrast, the machine learning-based MPC is non-linear; in some cases, the parameters can be conveniently tuned online (Li et al., 2018). The machine learning-based MPC for CO₂ capture has also been assessed for large-scale applications involving a carbon capture plant integrated into a 500 MW coal-fired power plant modelled via the first principle (Liao et al., 2020).

6.6.5. Machine learning for optimisation of the carbon capture process

Process optimisation, which involves an iterative solution of non-linear equations, can be computationally challenging when based on mechanistic models of the process. As a result, reduced-order models are widely used for optimisation (Eason and Biegler, 2020). However, reduced order models sacrifice accuracy and in dynamic scenarios may not capture some critical dynamics of a process, making a case for more accurate machine learning models. Machine learning models of carbon capture systems by chemical absorption using the ANN algorithm have been used for optimising the operating condition of the process using a genetic algorithm and sequential quadratic programming algorithm (Shalaby et al., 2021). More sophisticated systems, involving reinforcement learning using actor-critic neural networks that address the limitation of standard single hidden layer ANN, have also been used to optimize carbon capture systems (Chen and Wang, 2014).

6.6.6. Summary: advantages, limitations and future prospects

Although machine learning has been largely proven for obtaining models of carbon capture and other process systems the models are rarely used. Sipócz et al. (2011) recommended incorporating machine learning models in component libraries of commercial simulators. This will greatly promote their use and enable hybrid models to leverage the strengths of machine learning and first principle modelling, diminishing their limitations. Machine learning models of carbon capture systems are also mostly obtained from first principle models. While this is sufficient for demonstrating the efficacy of the methodology, the models must be developed using actual operating plant data in practice as assumptions in modelling may oversimplify the practical realities. In addition, overfitting appears to go unnoticed in many reported models showing near-perfect predictions. These studies do not show any rigorous attempt to check for overfitting and the generalisation capability of the models cannot, therefore, be trusted. Finally, machine learning application in CO₂ capture adsorption is limited with many reported models focusing mainly on predicting the capture capacity of different adsorbents without consideration for other operating conditions.

7. Large scale applications of carbon capture technologies

7.1. SaskPower boundary dam CCS facility

7.1.1. Introduction for large scale carbon capture technologies

Given the dominant role that fossil fuels continue to play in primary energy consumption for a prolonged future to come, carbon capture, use and storage (CCUS) will remain a critical greenhouse gas reduction solution. The enormous challenge for implementing CCUS lies in the integration of component technologies through large-scale commercial demonstration projects. CCS is applicable beyond the energy sectors and can be applied to industrial sources of emissions from sectors such as iron, steel, and concrete, which are hard to decarbonize. In recent years, it has been recognized widely recognized by governments and experts that some of the world's most carbon-intensive industries may have no alternatives to CCS for deep emissions reduction.

On 2 October 2014, the first-ever, commercial-scale, coal-fired power plant incorporating amine solvent absorption carbon capture be-

gan operation near Estevan, Saskatchewan, Canada. This was a global landmark event, demonstrating a number of high-risk technology and business issues have been overcome. The project has proven to the world that commercial scale carbon dioxide capture at a coal-fired power generating station is possible rather than an elusive future option (Preston, 2015). SaskPower's Boundary Dam 3 Carbon Capture & Storage Facility (BD3 CCS Facility) is fully integrated with a coal-fired power plant. Renowned for being a key part of a full chain operation, the facility includes a power plant burning coal, a CO₂ capture facility, transportation infrastructure (pipelines), use and storage in enhanced oil recovery (EOR), and deep underground storage. The Province of Saskatchewan, Canada, becomes the hub for full-cycle CCUS knowledge, with the large-scale full chain of CCUS operations and demonstration, which is an ideal model for carbon capture, use and storage (CCUS) because the EOR creates revenue from the sale of carbon dioxide (CO₂). Any additional capacity the off-taker of CO₂ does not require can be permanently stored underground.

7.1.2. BD3 CCS project background

BD3 CCS Facility of the SaskPower Boundary Dam Power Station is located in the southeast corner of Saskatchewan near the border with the USA, named after the Boundary Dam Reservoir, which is the surface water source for power plants cooling. The region is endowed with 300-year supply of lignite coal that is affordable, abundant, and accessible and has been fuelling power plants in Saskatchewan for nearly a century. New Canadian greenhouse gas regulations on CO₂ emissions from fossil fuel power generation came into effect on 1 July 2015. Essentially, the regulations require existing and new coal-fired power generation facilities to operate with the same emissions as natural gas-fired plants: 420 tonnes CO₂/GWh. In addition to the performance standard under the Regulation, the current Pan-Canadian Regulation for reducing carbon emission charges a carbon tax at a price of \$40 on fossil fuel consumption. Prior to modification, Boundary Dam's Unit #3 emitted 1110 tonnes CO₂/GWh, but at a 90% capture rate, the plant will, at full capacity, operate with emission at 140 tonnes CO₂/GWh—essentially four times less carbon emissions than a natural gas facility. However, According to SaskPower, the federal government's carbon pricing is having an impact on SaskPower, with emissions payments going up to an estimated \$180 million in 2022 from \$56 million in 2020. The investment in the BD3 power unit's retrofit and carbon capture plant was C\$1.467 billion, of which the carbon capture plant accounted for about 50%. That gave 30 years of prolonged life to a power unit which could produce 115–120 MW clean base load power 24 h a day (Jonathan and Crawford, 2013).

7.1.3. Technology selection of BD3 CCS project

SaskPower pursued various technology options for carbon capture from oxyfuel combustion to amine solvent absorption that ultimately led to the decision to select the commercially unproven CANSOLV amine solvent carbon dioxide capture process. SaskPower then coupled that technology with Shell Cansolv's proven sulphur dioxide capture process to simplify the capture plant operation and to further reduce emissions. By the end of 2009, Shell Cansolv's CO₂ amine absorption capture process was the leading technology option due, in part, to its proven record of deployment of very similar SO₂ capture technology in coal-fired power plants and other industrial facilities at various global locations. This assured SaskPower of a lower risk of scale-up by selecting the CANSOLV technology for CO₂. SaskPower had forged ahead with the design and construction of the BD3 ICCS retrofit well in advance of GHG Regulations being enacted in Canada, which came into effect on 1 July 2015. This was a strategic and environmentally-responsible decision to ensure the continued use of lignite coal reserves in Saskatchewan that could last 250–500 years.

After it is piped to the adjacent capture plant, the emissions are put through a flue gas cooler to bring the temperature down from 199 °C to around 89 °C, which helps enhance the adsorption of the CO₂ and SO₂.

SaskPower enhances this process by adding a polymer heat exchanger which pre-heats the condenser water used for steam generation in the power plant. The cooler also condenses out the moisture that comes from the lignite–poor-quality coal–burned at the plant. This moisture is not wasted; it is diverted to the cooling tower.

In the tower, the gas first passes through a pre-scrubber that further cools the gas and removes contaminants; then bubbles up through the scrubber, where liquid amines absorb the SO₂. Moreover, the gas is introduced to the caustic polisher section reusing residual caustic generated in the CO₂ capture system to remove the remaining SO₂. The captured CO₂ comes out of the stripper at 16 psi and is passed through an eight-stage compressor to ramp it up to around 2,500 psi, producing supercritical CO₂. A carbon dioxide stripper, made of stainless steel, which weighs roughly 250 tonnes, 44 metres Tall and 26 feet in diameter. The rectangular absorber tower with ceramic tiles inside is even taller, at 54M X11, according to online information.

7.1.4. Design and construction process and considerations

The BD3 capture facility is fully integrated with its host power plant from which it draws its steam and power needs. The BD3 facility includes CO₂ capture, compression, and transport infrastructure. CO₂ produced at the BD3 operation is mainly utilized and stored at nearby enhanced oil recovery (EOR) operations near Weyburn, Saskatchewan, while also providing CO₂ for injection and permanent geological storage at a depth of 3,400 m in a deep saline aquifer at Aquistore Project at the SaskPower Carbon Storage and Research Centre, located near the Boundary Dam Power Station, an onsite CO₂ measurement, monitoring and verification (MMV) project, managed by the Petroleum Technology Research Centre in Regina, Saskatchewan. Key factors contributed to the decision to retrofit BD3 to convert it to clean coal power include the value that would be realized over the next 30 years of operating the retrofitted power plant from the sale of three valuable by-products: carbon dioxide, sulphuric acid and fly ash. This would help to offset the cost of capture. The latter two by-products provide the off-taker market with essential materials for the production of fertilizer and cement, respectively. A 2010 study comparing the cost of building a new NGCC with the retrofit with CCS showed the levelized electricity cost was equal while the clean coal would have one 3rd emission of natural gas. This would satisfy SaskPower's core mission to deliver steady power to its customers, while capturing CO₂, which would mitigate the environmental impact of coal use, with the associated generation of a revenue stream to offset the cost of capture.

7.1.5. Operational status and performances updates

The carbon capture facility at Boundary Dam was designed to be capable of capturing 3,200 metric tons of CO₂ daily, or 1 million metric tons annually. The current performance status of the project, which through a full-scale flue gas post-combustion capture process, produces 115 megawatts (MW) of clean power, captures 90% of CO₂, 100% of SO₂, and lowers NO_x and PM emissions, and recovers vaporised water from the flue gas to meet half (34 M/H) of the cooling water demand. SaskPower reports that the parasitic energy requirements are 21%, lower than the typical 24% to 40% reported for other CCS schemes (Giannaris et al., 2021).

BD3 CCS Facility has achieved a significant milestone recently with a total of cumulative five million tonnes captured since start-up (Stephene, 2015). As of the end of 2022, 5,001,707 tonnes of CO₂ have been captured and prevented from entering the atmosphere, and the majority has been stored on oilfield through EOR, with about 10% permanently sequestered deep underground. The BD3 CCS facility is on track to achieve an 800,000-tonne target for the fiscal year of 2022–23 (Total capture for the 2022 calendar year was 749,035 tonnes).

During the fourth quarter of 2022 (1 October – 31 December), the CCS facility was available 79% of the time, capturing 192,703 tonnes of CO₂. While online, the facility had a daily average capture rate of 2,631 tonnes in Q4, with a peak one-day capture of 2,874 tonnes. A

Table 7.1
Gas composition list (design value).

| Number | Component | Content (mol%) | |
|--------|------------------|--------------------|---------------------------|
| | | Raw gas components | liquefaction purification |
| 1 | H ₂ | 0.5% | 0.012% |
| 2 | N ₂ | 7.3796% | 0.6289% |
| 3 | CO | 0.403% | 0.0363% |
| 4 | CO ₂ | 91.62% | 99.2931% |
| 5 | CH ₄ | 0.002% | 0.0003% |
| 6 | Ar | 0.07% | 0.0095% |
| 7 | H ₂ S | 0.0004% | 0.0004% |
| 8 | COS | 0 | 0 |
| 9 | methanol | 0.015% | 0.0191% |
| 10 | water | 0.01% | 0.0001% |

Table 7.2
Physical parameters (0.1013 MPa (g), 25°C).

| Physical parameters | Index |
|------------------------------|---------|
| Average molecular weight | 42.55 |
| Cp/Cv | 1.291 |
| Viscosity (cP) | 0.01501 |
| Thermal conductivity (W/m·K) | 0.01786 |
| Compressibility factor | 0.9950 |
| Density (kg/m ³) | 1.747 |

two-week planned maintenance outage in Q4 allowed SaskPower to undertake scheduled work to enable the facility to run smoothly until the next planned outage in May 2023 (Preston et al., 2018).

7.2. Research and design experience of Qilu Petrochemical-Shengli OilField 1 million tons/year CCUS project capture and transport unit

7.2.1. Project purpose and project scope

Qilu Petrochemical-Shengli Oil Field project is China's first million-tonne CCUS (Carbon Capture, Utilization, and Storage) project and is the largest CCUS full industry chain demonstration base and benchmark project in China. It sets a precedent for the construction of million-tonne CCUS projects in China, and it lays a solid foundation for the large-scale industrial application of CCUS projects. The project is of great significance to constructing the "artificial carbon cycle" model, which will significantly improve China's carbon emission capacity and effectively push forward the achievement of China's "double carbon" target. When completed, the project can reduce CO₂ emissions by 1 million tons each year. This is equivalent to planting nearly 9 million trees each year, stopping nearly 600,000 economy cars from being driven each year, and an additional 2.965 million tons of fuel is expected to be added over the next 15 years. The project is composed of CO₂ capture and CO₂ transportation in Qilu Petrochemical. After being captured in Qilu Petrochemical Company, CO₂ is transported to Shengli Oilfield for oil drive, and sequestered in a green way, realising the integrated application of CO₂ capture, oil drive and storage.

7.2.2. Introduction of construction scale and capture process

7.2.2.1. Gas source and component. The raw gas is supplied by the exhaust gas of the gas installation of the Qilu Petrochemical Company Second Fertilizer Plant, which has a large handling capacity, low inlet pressure and high CO₂ purity. The component of the raw gas, the liquefied and refined gas, are shown in Table 7.1, and the physical properties are shown in Table 7.2.

7.2.2.2. Construction scale and design principles. The project is based on the exhaust gas of the gas installation of the Qilu Petrochemical Company Second Fertilizer Plant to demonstrate CO₂ capture technology, with the designed CO₂ production capacity of 1 million tons/year. Taking the variation in waste gas composition into account, the installation

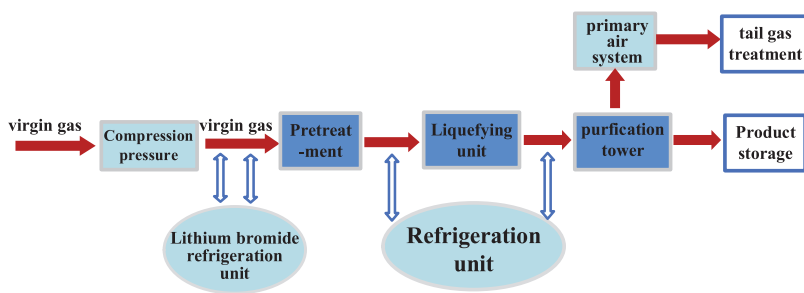


Fig. 7.1. Carbon dioxide recycling process flow chart. (For interpretation of the references to color in this figure legend, the reader is referred to the web version of this article.)

Table 7.3
Gas composition after liquefaction.

| Composition | CO ₂ | H ₂ S | H ₂ O |
|----------------------------------|-----------------|------------------|------------------|
| Molar molecular percentage, mol% | ≥0.99 | ≤0.001 | ≤10 ppm |

is intended to run smoothly within 60~105 % of the rated production capacity, with the maximum load of the installation intended to be 105 % of the normal load. The installation has an annual continuous operating time of 8,000 h. Currently, the project team has fully integrated with the owner unit, taking the steam, electricity, recycled water, and other supporting facilities necessary for the 1 million tons/year CO₂ capture into account adequately. The project makes full use of the reserved supporting facilities and land for the CO₂ capture project to reduce the impact on production and engineering investment of Qilu Petrochemical and lay the foundation for the good operation of the CO₂ capture project. The project requires water, electricity and steam to be connected to the main project.

7.2.3. Product programs

7.2.3.1. Product categories. The raw gas is supplied by the exhaust gas of the gas installation of the Qilu Petrochemical Company Second Fertilizer Plant, whose main components are CO₂ and N₂. The Qilu Petrochemical Company Second Fertilizer Plant captures, compresses, dries and liquefies CO₂, eventually obtaining liquid CO₂ with a purity greater than 99 % (mol%). Liquid CO₂ products are transported to Shengli Oil-field via pipelines for oil drive and sequestration.

7.2.3.2. Actual indicators of product quality. The raw gas is dried and liquefied under pressure to obtain liquid CO₂ products with a pressure of 1.9 MPa and a temperature of -27 °C. The main component of the product gas is shown in Table 7.3. The product gas meets the purity requirements for on-site geological sequestration.

7.2.4. Process description

7.2.4.1. CO₂ capture process. The process of "compression-condensation-purification" is adopted to recover CO₂. The raw gas is first pressurised by a compressor unit, then passes through a lithium bromide refrigeration unit to recover waste heat for cooling, and then sequentially enters the drying dehydration and liquefaction purification system. The raw gas is condensed and liquefied at low temperatures to obtain a liquid CO₂ product. The liquid CO₂ product is ready to be stored in tanks once it has been qualified.

In accordance with its function, the production process can be divided into compression units, liquid purification units, refrigeration units, tank storage units, loading unit and conveying units. The process flow of CO₂ recycling is shown in Fig. 7.1.

7.2.4.1.1. Compression unit. Compressor is an essential piece of equipment to keep the system running, and its stability is the key factor affecting the normal operation of the system. Currently, centrifugal compressor, reciprocating compressor and screw compressor are the more commonly used types of compressors. The capacity of the unit is key to compressor selection, while the gas composition and final pressure also have a certain influence on compressor selection. Centrifugal compressors are mostly driven by steam, and they are adapted for use in high-flow conditions. Currently, screw compressors and reciprocating compressors are often used to handle the small and medium flow. The project has low gas pressure and high gas volume, so the MCL706 centrifugal compressor is chosen. Horizontal split welded casing is selected, and the speed regulation mode is variable speed when used. The flow ranges from 60 % ~ 105 %. The shaft power of the centrifugal compressor is large. Taking the utility conditions at the project site into consideration, steam turbine is used as the drive mechanism of the centrifugal compressor for this project.

7.2.4.1.2. Liquid purification units. The project has a high concentration of CO₂, so low temperature distillation technology, indicated in Fig. 7.2, is chosen to liquefy and purify CO₂. The selective removal of impurities without the use of chemicals results in dry liquid CO₂.

(1) Dry Dehydration System

The CO₂ raw gas passes through the compression unit and then enters the drying tower for dehydration treatment. The dehydration process is based on a double tower + pre-sorption tower technology.

Commonly used solid desiccants consist of molecular sieve, lithium oxide, activated carbon, alumina, silica gel and compound desiccant. Molecular sieve has poor absorption ability. Lithium oxide has good water absorption properties, but it is corrosive and has a high heat release when absorbing water which affects its cooling capacity. Silica gel has the advantages of good adsorption performance, economic and practical, but it is easy to break after the adsorption of a significant amount of water. Alumina has poor adsorption capacity, only 50 % of silica gel, its regeneration temperature is high, and its regeneration time is long. Composite desiccant is unstable and deliquescent, but its adsorption performance is good.

The CO₂ raw gas is dehydrated using molecular sieves as adsorption carriers, and the water content after dehydration is decreased to less than 10 ppm. When used as a solid desiccant, a molecular sieve carries out gas adsorption by adsorption; that is, water molecules are adsorbed on the surface of the solid. A molecular sieve has a capillary or cylindrical surface, and therefore its adsorption force is more concentrated. When the diameter of the capillary pores approaches that of the adsorbed molecules, Capillary coagulation means that the cohesion starts to concentrate when the diameter of the capillary pores approaches that of the adsorbed molecules. Because of the high cohesion, water can be drawn out from the airflow and condensed into a liquid phase in the capillary pores when the temperature is higher than the boiling point.

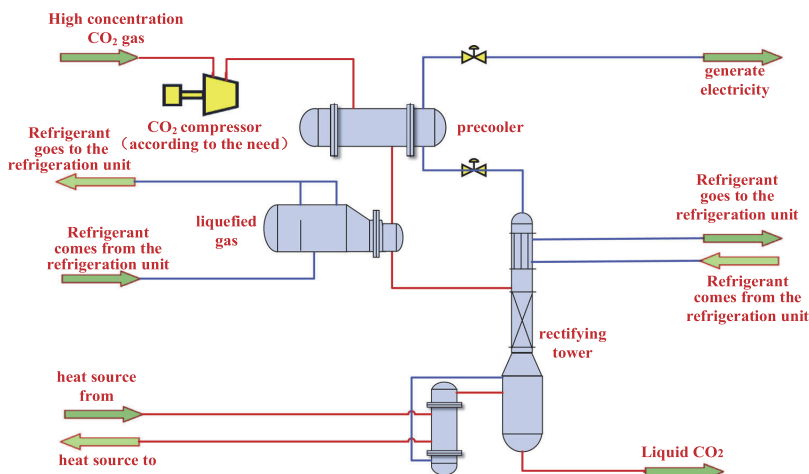


Fig. 7.2. Low-temperature distillation process flow chart. (For interpretation of the references to color in this figure legend, the reader is referred to the web version of this article.)

Table 7.4
Comparison of advantages and disadvantages of common solid desiccants.

| Refrigeration circle | Merit | Defect |
|-------------------------|---|---|
| Lithium oxide desiccant | big amount of water absorption | Corrosive, large heat release when absorbing water, affecting cooling capacity |
| silica-gel drier | Good adsorption value performance, economical and practical | Easy to crack, high regeneration temperature, long time, limited use times (usually 10-30 times, the first regeneration after the drying effect is almost the same as the original finished product, and the second regeneration effect is reduced to 90%, after 10-30 times of regeneration, the drying effect is reduced to the original 80%, generally no desiccant regeneration |
| Molecular sieve | Strong adsorption, high temperature can still accommodate water molecules, pore size can be controlled by different processes | Relatively low dehydration capacity |
| Alumina drier | Large water absorption, fast drying speed | Aluminum oxide adsorption capacity is weak, and high regeneration temperature (usually 250-350 °C), long time (3-5 h) |
| Composite desiccant | Good moisture absorption | Unstable, easy to deliquesce |

The advantages and disadvantages of commonly used solid desiccants are shown in Table 7.4 below.

(2) Liquefaction system

After pressurised dehydration, the product gas is cooled to less than -20°C by a horizontal shell and tube liquefier. Three horizontal shell and tube liquefiers are put into use. The shell medium is propylene, while the tube medium is CO_2 . The raw CO_2 gas is condensed into liquid CO_2 due to the evaporation of liquid propylene. CO_2 is completely liquefied and then sent to the purification system for deeper purification.

(3) Purification system

Purify the product gas from the liquefaction system. MellapakPlus TM structured filler is Sulzer's latest generation of structured filler, which effectively increases the handling capacity of the filler. The ripple direction of the upper and lower parts of each filler unit gradually approaches the vertical direction. This can not only reduce the pressure drop and shear force caused by the interaction between vapour and liquid phase, but also reduce the possibility of liquid flooding so as to eliminate local bottlenecks. MellapakPlus TM structured filler also offers significant advantages, such as high mechanical strength and strong corrosion resistance. The new MellapakPlus TM filler design allows for a significant reduction in tower diameter to reduce the customer's upfront investment costs.

(4) Expander

The expansion generator unit recovers the pressure energy of the exhaust gas, and the electricity generated is integrated into the plant grid. The low-temperature exhaust gas, after the expansion is heat exchanged with the raw gas.

Principle of the expansion generator unit: exhaust gas enters the expansion generator unit to be expanded and cooled, and the power output of the expansion generator unit is passed through the gearbox and transmitted to the generator to generate electricity. An emergency shut-off valve is provided at the inlet of the expansion generator unit. When the unit interlocks and shuts down, the emergency shut-off valve immediately cuts off the gas supply to the expansion generator unit. At the same time, the bypass control valve is opened to bring the gas supply directly into the subsequent process to ensure system balance and stability.

(5) Fresh air system

Three fans are put into use, and the flow of each fan is $20000\text{ Nm}^3/\text{h}$. The non-condensable exhaust gas discharged from the expansion generator exchanges heat with air and then enters the exhaust buffer tank. Then it is transported to the RCO unit for exhaust gas treatment.

7.2.4.1.3. *Refrigeration units.* The main advantages of propylene refrigeration units and lithium bromide refrigeration units are low noise, energy saving and environmental friendliness. In this project, a combination of a centrifugal propylene refrigeration unit and a lithium bromide refrigeration unit is put into use.

Table 7.5
Main equipment of spherical tank area and loading unit.

| Equipment name | Quantity | Major parameter |
|-----------------------------------|----------|---|
| Carbon dioxide spherical tank | 2 | Volume 4000 m ³ , material 07MnNiMoDR, design temperature-45 ~ 50 °C, design pressure 2.2MPa |
| Carbon dioxide loading pump | 2 | Flow 30 ~ 120 m ³ /h, head 50 m |
| Carbon dioxide loading crane tube | 14 | DN50/DN50-304 |

Table 7.6
Utility consumption.

| No. | Name | Unit | Specification | Unit consumption/t products | Time consume | Energy conversion value (kg standard oil) | Energy consumption (kg standard oil/t) |
|-----|------------------------------------|-----------------|---------------|-----------------------------|--------------|---|--|
| 1 | Electricity | kWh | 6000/380 V | 13.428 | 1180 | 0.22 | 2.954 |
| 2 | Circulating water | t | 0.45 MPa | 86.373 | 7590 | 0.06 | 5.182 |
| 3 | Medium- pressure superheated steam | t | 4.0 MPaG | 0.624 | 54.6 | 88 | 54.912 |
| 4 | Instrument air | Nm ³ | 0.7 MPaG | 3.414 | 300 | 0.038 | 0.130 |
| 5 | Medium nitrogen gas | / | 1.3 MPa | 0.569 | 50 | 0.15 | 0.085 |
| 6 | Footing | / | / | / | / | / | 63.263 |

The propylene refrigeration unit provides the necessary cryogenic conditions for the condensation and liquefaction of CO₂. The project is processed on a large scale with a turbine-driven centrifugal refrigeration unit.

The lithium bromide aqueous solution absorbs heat by the low boiling point vapourisation of water in a high vacuum state for the purpose of refrigeration. The refrigerant cycle is the cycle of lithium bromide aqueous solution in the machine from dilute to concentrated and concentrated to dilute, refrigerant water from liquid to vapour and from vapour to liquid. The two cycles are carried out simultaneously. The lithium bromide refrigeration unit produces cryogenic cooling water by the waste heat of the final stage outlet of the CO₂ raw gas compressor. The compressed CO₂ raw gas is further cooled to 8 °C using cryogenic cooling water and then transported to subsequent liquefaction and purification installation.

7.2.4.1.4. Spherical tank area and loading units. The CO₂ raw gas is processed by the liquefaction and purification installation to obtain liquid CO₂ product, which is respectively stored in the corresponding spherical tanks and then conveyed by a loading crane. The main equipment of the spherical tanks area and loading units is shown in Table 7.5 below.

7.2.4.1.5. Integrated optimisation of the capture process. The CO₂ capture process of this project adopts two energy-saving processes: the recovery of waste heat by the additional refrigeration unit and the recovery of exhaust pressure energy by the expansion generator. The recovery of waste heat by the additional refrigeration unit can reduce the operating load and electricity consumption of the ice machine and reduce carbon emission. The expansion generator unit recovers the pressure energy of the exhaust gas, and the electricity generated is integrated into the plant grid. The low-temperature exhaust gas, after expansion, can exchange heat with the raw gas to maintain system balance and stability. After the energy-saving process is put into use, the combined energy consumption of capture is 63.263 kg standard oil/tCO₂. In light of the "Standard for Calculation of Energy Consumption for Petrochemical Design" (GB/T50441-2016), the energy consumption is converted to 2.649 GJ/tCO₂. Table 7.6 shows the consumption of utilities for capture and compression drying in each scheme:

7.3. Research and design experience of a 150 kt/a CO₂ capture and purification project

7.3.1. Project purpose and scope

The Guohua Jinjie Power Plant CO₂ capture project relies on the Shenhua Jin Guohua 600 MW sub-critical coal-fired unit to investigate advanced chemical absorption and CO₂ capture processes to capture

Table 7.7
Flue gas composition (design value).

| Component | Molecular weight | Mole fraction / (mol %) |
|--------------------|------------------|-------------------------|
| CO ₂ | 44.011 | 11.1 |
| O ₂ | 31.999 | 6.1 |
| N ₂ | 28.014 | 70.7 |
| SO ₂ | 64.065 | 35 mg/Nm ³ |
| SO ₃ | 80.064 | / |
| Dust concentration | — | <10 mg/Nm ³ |
| HCl | 36.461 | 0.0001 |
| HF | 20.006 | 0.0001 |
| H ₂ O | 18.015 | 12.1 |
| NO _x | — | 50 mg/Nm ³ |

and store post-combustion CO₂ in a brine layer. The project includes a 150,000 ton/year CO₂ capture system that utilizes a CO₂ capture system built by Shenhua Coal to Oil Company. A storage unit (located in Erdos, Inner Mongolia) was used for geological storage. The successful implementation of this project will help optimize the entire process of post-combustion CO₂ capture and brine storage, mastering various key technologies to achieve near-zero emissions from coal-fired power plants.

7.3.2. Introduction of construction scale and capture technology

7.3.2.1. Source and composition of the flue gas. The flue gas is introduced from the flue at the outlet of the desulfurization absorption tower of the King Street Power Plant. The composition of the flue gas is shown in Table 7.7.

7.3.2.2. CO₂ stream. The flue gas of the project was introduced from the outlet of the desulfurization absorption tower, and the main components of the flue gas are CO₂ and N₂. After trapping, compression, drying and liquefaction, liquid CO₂ with 99.5% (V%) purity was obtained at Shenhua Jinjie Power Plant and then transported to the storage site of Shenhua CCS project in Ulanmulun Town, Ijinhuluo Banner, Ordos City, Inner Mongolia for geological storage. After pressurizing, drying, and liquefying, the pressure of the product was 2.2 MPaG and the temperature was -20 °C. The main components in the product are shown in Table 7.8, and the purity of CO₂ in the product gas meet the requirements for geological storage on site.

7.3.2.3. Process description. For the characteristics of low partial pressure and complex composition of CO₂ in the flue gas of coal-fired power plants, the project integrated and applied design technologies such as a new high-efficiency CO₂ absorber, plastic packed absorption tower, flue

Table 7.9
Raw materials, utilities, and major consumption quotas.

| Serial number | Description & specification | Unit | Quantity | Remark |
|---------------|--|----------------------|----------|--|
| 1 | Design scale: product gas (dry gas) | Nm ³ /h | 87217 | / |
| 2 | Flue gas (dry gas) | Nm ³ /h | 100000 | / |
| | Chemicals | | | 400 m ³ for original start-up solution |
| | Amine solvent | t | ~80 | |
| | Corrosion inhibitor | t | ~1 | |
| | Antioxidant | t | ~0.6 | |
| 3 | Chemicals | | | Annual operation demand |
| | Amine solvent | t/a | ~150 | |
| | Corrosion inhibitor | t/a | ~3.75 | |
| | Antioxidant | t/a | ~3.75 | |
| | Sodium hydroxide | t/a | ~100 | |
| 4 | Public works | | | 1.0 MPag steam for drying skid, and 0.63 MPag steam for amine recovery |
| | Circulating water | t/h | ~2594 | |
| | Electric | kwh | ~4942.75 | |
| | 0.3 MPag steam | t/h | ~23.76 | |
| | 1.0 MPa steam | t/h | ~1.5 | |
| | 0.63 MPag steam | t/h | ~5 | |
| | Desalted water | t/h | ~4.5 | |
| 5 | Rate of expenditure | | | |
| | Circulating water | t/tCO ₂ | ~115 | / |
| | Electric | kW /tCO ₂ | ~263 | / |
| | Steam | t/tCO ₂ | ~1.27 | / |
| | Amine solvent | kg/tCO ₂ | ≤1.0 | / |
| | Corrosion inhibitor | kg/tCO ₂ | ≤0.025 | / |
| | Antioxidants | kg/tCO ₂ | ≤0.025 | / |
| | Sodium hydroxide | kg/tCO ₂ | ≤0.67 | / |
| | Desalted water | kg/tCO ₂ | ~240 | / |

Table 7.10
Consumption of public works.

| Project | Unit | Quantity | | | | | Total | |
|--------------|---------------------------------|--------------------------|------------------------|----------------|-----------------|---------------------|-------|---------|
| | | Capture and purification | Compressing components | Drying section | Liquefying part | Storage and loading | | |
| Public works | Circulation water | t/h | ~1800 | ~190 | ~30 | ~574 | – | 2594 |
| | Electrical | kW | ~2007.75 | ~1700 | 175 | ~1042 | ~18 | 4942.75 |
| | Steam | t/h | ~21 | – | – | – | – | 21 |
| | Desalinated water | t/h | ~4.5 | – | – | – | – | 4.5 |
| | Makeup of the circulating water | t/h | ~33 | ~4 | ~1 | ~12 | – | 50 |
| | | | | | | | | |

7.3.5. Estimation of total investment

The construction investment consisted of engineering costs, other engineering construction costs and basic reserve costs. Among them, the engineering cost was 992,322,000 yuan, the engineering secondary cost, including management, design, supervision, protection, seismic assessment and environmental assessment cost was 234,235,000 yuan, and the basic reserve cost was 613,280,000 yuan, totalling 128,788,500 yuan. The project cost was 9,923,220,000 RMB, including 6,995,540,000 RMB for equipment purchase, 1,122,290,000 RMB for main materials, 6,656,680,000 RMB for installation and 113,911,000 RMB for construction. Other expenses: Other costs totalled RMB 2,432,350,000, including construction site acquisition and clearing fees, project construction management fees, project construction technical service fees, complete set of start-up and test freight fees, production preparation fees, and large transportation measures. The basic reserve cost was calculated as 5% of the sum of construction cost and other costs, totalling 6,132,800 yuan. The project consisted of all own funds and was interest-free during the construction period. The total investment reported and approved was the sum of construction investment and interest and working capital during the construction period. The total investment reported and approved was 13,839,800 yuan.

8. Conclusions and outlook

Carbon capture from flue gas, the primary CO₂ source, is pivotal for achieving net-zero global CO₂ emissions. Post-combustion carbon capture, the most mature and widely utilized technology, presents significant viability and feasibility for existing power plants, requiring no

substantial renovation or infrastructure upgrades. The primary post-combustion CO₂ capture technologies encompass absorption separation (physical and chemical), adsorption separation (physical and chemical), and membrane separation. Over 60% of post-combustion technologies employ absorption-based methods. Particularly, the chemical absorption method, typified by MEA absorption, is highly promising for industrial applications due to its suitability for handling large air volumes and its operational simplicity. It primarily consists of two critical processes: the chemical absorption of CO₂ in the absorption tower and the thermal regeneration of the absorbent in the desorption tower. Nonetheless, CO₂ capture from flue gas sources still faces considerable challenges impeding further development and commercialization. Accordingly, more extensive studies are required to explore the commercial prospects of the pre-combustion CO₂ capture process. Since the late 1990s, large-scale direct air capture (DAC) has been proposed as an additional method for mitigating rising atmospheric CO₂ concentrations. Despite the ambient CO₂ concentrations being extremely low, several DAC approaches have been put forward, utilizing adsorption and absorption technologies. Nevertheless, the topic remains under development. Ensuring efficient operation with reasonable energy consumption is a prerequisite for the practical application of DAC. This review discusses in detail a clear and complete performance evaluation method, focusing on energy consumption and energy efficiency.

Chemical absorption with amine solvents currently serves as a relatively mature post-combustion CO₂ capture method, with practical applications in large fixed emission sources, such as coal/gas-fired power plant flue gas. However, it is still in the industrial demonstration stage due to the absence of large-scale industrial or commercial applications.

Replacing conventional aqueous amine solutions with organic solvents or ionic liquids could provide significant benefits. Additionally, life cycle assessment can be employed to evaluate the environmental and economic impacts of carbon capture and storage. Alkali-metal-based carbonates of K_2CO_3 and Na_2CO_3 are proven as promising candidates for CO_2 capture, while the practical applications of pure carbonates were restricted by their poor capacities and kinetics. As a result, the proper design of efficient K_2CO_3 - and Na_2CO_3 -based sorbents is of significant importance in broadening their application prospects. The most promising method for modification of K_2CO_3 and Na_2CO_3 is to load them on a porous support, where the optimization of the support materials, K_2CO_3/Na_2CO_3 loading amounts, and preparation methods are expected to improve the texture properties and surface morphology, enhance the dispersion of active K_2CO_3/Na_2CO_3 , and hence accelerate the CO_2 adsorption. In spite of the extensive studies on this topic, the influence of the abundant impurities in flue gases, such as sulphur- and chlorine-containing species, on the CO_2 capture performance of alkali-metal-based sorbents was rarely studied systematically, which is critical in evaluating their durability and regeneration efficiency in practical applications.

Apart from liquid-based sorbents, solid sorbents are emerging as potential candidates for large-scale CO_2 capture. These can be categorized as low, medium, and high-temperature solid sorbents. CaO has a high capacity for CO_2 capture. Although it can be deactivated during the CO_2 capture process, the spent CaO could be used for cement industries. One of the key challenges of CaO-based carbon capture is the use of high temperatures (up to 900 °C). MgO is an excellent medium-temperature adsorbent for carbon capture. However, it has very slow reaction kinetics. Key breakthroughs are needed for MgO-based materials development towards its commercial applications.

Furthermore, membrane technology has emerged as a promising alternative for CO_2 capture due to its inherent attributes, such as a smaller footprint, simpler setup and operation, energy savings, and the absence of phase transformation. However, designing a highly permeable membrane remains a significant challenge for efficient CO_2 capture. Other CO_2 capture technologies, including oxy-fuel combustion technology and chemical looping process, have also been reviewed. Techno-economic analysis and process modelling of CO_2 capture technologies are being developed to gain in-depth insights into the CO_2 capture process under various conditions.

The primary factor limiting the commercialization of CO_2 capture technology is its high cost. However, the International Energy Agency (IEA) forecasts that by 2030, the cost of CO_2 capture, such as DAC, is likely to decrease to less than \$100/t with the large-scale application of technology. To meet specific climate targets, it is imperative to explore all CO_2 removal technologies thoroughly, as capturing CO_2 at the source, such as power plants, is insufficient. Novel reaction systems such as RPB and process intensification (integrated with CO_2 conversion) and broad system optimization are required. However, for novel high-efficient systems (e.g., RPB), large-scale demonstration is needed to validate process modelling. Process modelling and simulation (e.g., CFD) of carbon capture systems should be further carried out. However, more research is required to enhance the accuracy of modelling and simulation results. Furthermore, extensive process conditions such as adsorption enthalpies should be considered for post-combustion CO_2 capture modelling.

Declaration of Competing Interest

The first author Dr Chunfei Wu is also the Editor-in-Chief of the journal Carbon Capture Science and Technology, however he was not involved in the peer review or handling this paper for the journal. The paper was handled by the Editor Dr. Yeshui Zhang. Furthermore, co-authors Sandra Boetcher, Shijian Lu, Dongdong Feng, Guoping Hu, Paul Webley, Daxin Liang, Aneta Magdziarz, Norbert Miskolczi, Su Shiung Lam, Hongman Sun, Haiping Yang, Mingzhe Sun, Dan Tsang, Jin Shang,

Christoph Müller, Lina Liu, Xin Jin, Yongqing Xu, Asim Khan, Haiqing Lin, Xuezhong He, Zhongde Dai, Shouliang Yi, Alar Konist, Xin Tu, Sibudjing Kawi, Chunfeng Song, Meihong Wang, Eni Oko, Li Gao, Hui Zhou are either Editors or board members for this journal, but none of them were involved in the peer review or handling of this paper.

References

- Šulc, R., Dittl, P., 2021. A technical and economic evaluation of two different oxygen sources for a small oxy-combustion unit. *J. Clean. Prod.* 309 (May). doi:10.1016/j.jclepro.2021.127427.
- A, S.N., Dodge, B.F., 1946. Removal of carbon dioxide from atmospheric air. *Trans. Am. Inst. Chem. Eng.* 42 (5-6), 827-848.
- Aaron, D., Tsouris, C., 2005. Separation of CO_2 from flue gas: a review. *Sep. Sci. Technol.* 40 (1-3), 321-348. doi:10.1081/SS-200042244.
- Aarti, A., Bhaduria, S., Nanoti, A., Dasgupta, S., Divekar, S., Gupta, P., Chauhan, R., 2016. [Cu3 (BTC)2]-polyethyleneimine: an efficient MOF composite for effective CO_2 separation. *RSC Adv.* 6 (95), 93003-93009. doi:10.1039/c6ra10465g.
- Ababneh, H., Hameed, B.H., 2021. Chitosan-derived hydrothermally carbonized materials and its applications: A review of recent literature. *Int. J. Biol. Macromol.* 186, 314-327. doi:10.1016/j.ijbiomac.2021.06.161.
- Abatzoglou, N., Boivin, S., 2009. A review of biogas purification processes. *Biofuels Bioprod. Bioref.* 3 (1), 42-71. doi:10.1002/bbb.117.
- Abbasi, E., Hassanzadeh, A., Zarghami, S., Arastoopour, H., Abbasian, J., 2014. Regenerable MgO-based sorbent for high temperature CO_2 removal from syngas: 3. CO_2 capture and sorbent enhanced water gas shift reaction. *Fuel* 137, 260-268. doi:10.1016/j.fuel.2014.07.088.
- Abdeen, F.R.H., Mel, M., Jami, M.S., Ihsan, S.I., Ismail, A.F., 2016. A review of chemical absorption of carbon dioxide by syngas upgrading. *Chin. J. Chem. Eng.* 24 (6), 693-702. doi:10.1016/j.cjche.2016.05.006.
- Abdelnaby, M.M., Alloush, A.M., Qasem, N.A., Al-Maythaly, B.A., Mansour, R.B., Cordova, K.E., Al Hamouz, O.C.S., 2018. Carbon dioxide capture in the presence of water by a amine-based crosslinked porous polymer. *J. Mater. Chem. A* 6 (15), 6455-6462.
- Abdelnaby, M.M., Qasem, N.A., Al-Maythaly, B.A., Cordova, K.E., Al Hamouz, O.C.S., 2019. A microporous organic copolymer for selective CO_2 capture under humid conditions. *ACS Sustain. Chem. Eng.* 7 (16), 13941-13948.
- Abián, M., Abad, A., Izquierdo, M.T., Gayán, P., de Diego, L.F., García-Labiano, F., Adánez, J., 2017. Titanium substituted manganese-ferrite as an oxygen carrier with permanent magnetic properties for chemical looping combustion of solid fuels. *Fuel* 195, 38-48. doi:10.1016/j.fuel.2017.01.030.
- Aboudheir, A., Tontiwachuthikul, P., Chakma, A., Idem, R., 2003. Kinetics of the reactive absorption of carbon dioxide in high CO_2 -loaded, concentrated aqueous monoethanolamine solutions. *Chem. Eng. Sci.* 58 (23-24), 5195-5210. doi:10.1016/j.ces.2003.08.014.
- Abu-Zahra, M.R.M., Niederer, J.P.M., Feron, P.H.M., Versteeg, G.F., 2007. CO_2 capture from power plants. Part II. A parametric study of the economical performance based on mono-ethanolamine. *Int. J. Greenh. Gas Control* 1 (2), 135-142. doi:10.1016/S1750-5836(07)00032-1.
- Achari, A., S, S., Eswaramoorthy, M., 2016. High performance MoS2 membranes: effects of thermally driven phase transition on CO_2 separation efficiency. *Energy Environ. Sci.* 9 (4), 1224-1228. doi:10.1039/c5ee03856a.
- Acosta, E.J., Carr, C.S., Simanek, E.E., Shantz, D.F., 2004. Engineering nanospaces: iterative synthesis of melamine-based dendrimers on amine-functionalized SBA-15 leading to complex hybrids with controllable chemistry and porosity. *Adv. Mater.* 16 (12), 985-989. doi:10.1002/adma.200306323.
- Adelt, M., Wolf, D., Vogel, A., 2011. LCA of biomethane. *J. Nat. Gas Sci. Eng.* 3 (5), 646-650. doi:10.1016/j.jngse.2011.07.003.
- Adeniran, B., Mokaya, R., 2016. Is N-doping in porous carbons beneficial for CO_2 storage? experimental demonstration of the relative effects of pore size and N-doping. *Chem. Mater.* 28 (3), 994-1001. doi:10.1021/acs.chemmater.5b05020.
- Adhikari, B., Orme, C.J., Klachn, J.R., Stewart, F.F., 2021. Technoeconomic analysis of oxygen-nitrogen separation for oxygen enrichment using membranes. *Sep. Purif. Technol.* 268. doi:10.1016/j.seppur.2021.118703, 118703-118703.
- Administration, U.S.E.I., 2020. Annual Energy Outlook 2020. U.S. Energy Information Administration, Washington, DC, USA.
- Afari, D.B., Coker, J., Narku-Tetteh, J., Idem, R., 2018. Comparative kinetic studies of solid absorber catalyst (K/MgO) and solid desorber catalyst (HZSM-5)-aided CO_2 absorption and desorption from aqueous solutions of MEA and blended solutions of BEA-AMP and MEA-MDEA. *Ind. Eng. Chem. Res.* 57 (46), 15824-15839. doi:10.1021/acs.iecr.8b02931.
- Aframehr, W., Molki, B., Bagheri, R., Sarami, N., 2022. Capturing CO_2 by a fixed-site-carrier polyvinylamine-/matrimid-facilitated transport membrane. *ACS Appl. Polym. Mater.* 4 (5), 3380-3393. doi:10.1021/acsapm.1c01603.
- Afzal, R.A., Pennells, J., Yamauchi, Y., Annamalai, P.K., Nanjundan, A.K., Martin, D.J., 2022. Lignocellulosic plant cell wall variation influences the structure and properties of hard carbon derived from sorghum biomass. *Carbon Trends* 7, 100168. doi:10.1016/j.cartre.2022.100168.
- Agarwal, L., et al., 2010. Process intensification in HiGee absorption and distillation: Design procedure and applications. *Ind. Eng. Chem. Res.* 49 (20), 10046-10058.
- Agaton, C.B., Karl, H., 2018. A real options approach to renewable electricity generation in the Philippines. *Energy, Syst. Soc.* 8 (1). doi:10.1186/s13705-017-0143-y.
- Agee, E.M., Orton, A., 2016. An initial laboratory prototype experiment for sequestration of atmospheric CO_2 . *J. Appl. Meteorol. Climatol.* 55 (8), 1763-1770.

- Agee, E., Orton, A., Rogers, J., 2013. CO₂ snow deposition in antarctica to curtail anthropogenic global warming. *J. Appl. Meteorol. Clim.* 52 (2), 281–288. doi:10.1175/Jamc-d-12-0110.1.
- Aghaei, Z., Najji, L., Asl, V.H., Khanbabaee, G., Dezhagah, F., 2018. The influence of fumed silica content and particle size in poly (amide 6-b-ethylene oxide) mixed matrix membranes for gas separation. *Sep. Purif. Technol.* 199, 47–56. doi:10.1016/j.seppur.2018.01.035.
- Aghel, B., Sahraie, S., Heidaryan, E., 2020. Comparison of aqueous and non-aqueous alkaline amines sorbents for carbon dioxide desorption in a microreactor. *Energy* 201, 117618. doi:10.1016/j.energy.2020.117618.
- Aghel, B., Behaein, S., Alobaid, F., 2022a. CO₂ capture from biogas by biomass-based adsorbents: A review. *Fuel* 328, 125276. doi:10.1016/j.fuel.2022.125276.
- Aghel, B., Janati, S., Wongwises, S., Shadloo, M.S., 2022b. Review on CO₂ capture by blended amine solutions. *Int. J. Greenh. Gas Control* 119. doi:10.1016/j.jggc.2022.103715.
- Agrawal, R., Herron, D.M., 2000. Air liquefaction: distillation. *Encycl. Sep. Sci.* 1895–1910. doi:10.1016/B0-12-226770-2/04821-3.
- Aguilar-Lugo, C., Lee, W.H., Míguez, J.S.A., de la Campa, J.G., Prádanos, P., Bae, J.Y., Lee, Y.M., Álvarez, C., Lozano, A.N.E.J.A.A.P.M., 2021. Highly permeable mixed matrix membranes of thermally rearranged polymers and porous polymer networks for gas separations. *ACS Appl. Polym. Mater.* 3 (10), 5224–5235.
- Ahmad, M.Z., Castro-Muñoz, R., Budd, P.M., 2020. Boosting gas separation performance and suppressing the physical aging of polymers of intrinsic microporosity (PIM-1) by nanomaterial blending. *Nanoscale* 12 (46), 23333–23370. doi:10.1039/D0NR07042D.
- Ahmed, E., Deep, A., Kwon, E.E., Brown, R.J.C., Kim, K.-H., 2016. Performance comparison of MOF and other sorbent materials in removing key odors emitted from pigpen slurry. *Sci. Rep.* 6 (1), 31283. doi:10.1038/srep31283.
- Ahmed, M.B., Zhou, J.L., Ngo, H.H., Guo, W., Chen, M., 2016. Progress in the preparation and application of modified biochar for improved contaminant removal from water and wastewater. *Bioresour. Technol.* 214, 836–851. doi:10.1016/j.biortech.2016.05.057.
- Ahunbay, M.G.K., 2011. Monte Carlo simulation of water adsorption in hydrophobic MFI zeolites with hydrophilic sites. *Langmuir* 27 (8), 4986–4993.
- Ajenifuja, A., Joss, L., Jobson, M., 2020. A new equilibrium shortcut temperature swing adsorption model for fast adsorbent screening. *Ind. Eng. Chem. Res.* 59 (8), 3485–3497. doi:10.1021/acs.iecr.9b05579.
- Ajjawi, I., Verruto, J., Aquil, M., et al., 2017. Lipid production in *Nannochloropsis gadiata* is doubled by decreasing expression of a single transcriptional regulator. *Nat. Biotechnol.* 35, 647–652. doi:10.1038/nbt.3865.
- Akeeb, O., Wang, L., Xie, W., Davis, R., Alkassawi, M., Toan, S., 2022. Post-combustion CO₂ capture via a variety of temperature ranges and material adsorption process: A review. *J. Environ. Manage.* 313, 115026. doi:10.1016/j.jenvman.2022.115026.
- Akinola, T.E., Bonilla Prado, P.L., Wang, M., 2022. Experimental studies, molecular simulation and process modelling/simulation of adsorption-based post-combustion carbon capture for power plants: A state-of-the-art review. *Appl. Energy* 317. doi:10.1016/j.apenergy.2022.119156, 119156–119156.
- Aksu, G.O., Erucar, I., Haslak, Z.P., Keskin, S., 2022. Accelerating discovery of COFs for CO₂ capture and H₂ purification using structurally guided computational screening. *Chem. Eng. J.* 427, 131574.
- Al-Hamed, K.H.M., Dincer, I., 2021. A comparative review of potential ammonia-based carbon capture systems. *J. Environ. Manage.* 287, 112357. doi:10.1016/j.jenvman.2021.112357.
- Al-Rowaili, F.N., Khaled, M., Jamal, A., Zahid, U., 2023. Mixed matrix membranes for H₂/CO₂ gas separation— a critical review. *Fuel* 333, 126285. doi:10.1016/j.fuel.2022.126285.
- Al-Wabel, M., Elfaki, J., Usman, A., Hussain, Q., Ok, Y.S., 2019. Performance of dry water- and porous carbon-based sorbents for carbon dioxide capture. *Environ. Res.* 174, 69–79. doi:10.1016/j.envres.2019.04.020.
- Alalwan, H.A., Alminshid, A.H., 2021. CO₂ capturing methods: Chemical looping combustion (CLC) as a promising technique. *Sci. Total Environ.* 788, 147850. doi:10.1016/j.scitotenv.2021.147850.
- Alcantara, M.L., Santos, J.P., Loreno, M., Ferreira, P.I.S., Paredes, M.L.L., Cardozo, L., Silva, A.K., Liao, L.M., Pires, C.A.M., Mattedi, S., 2018. Low viscosity protic ionic liquid for CO₂/CH₄ separation: Thermophysical and high-pressure phase equilibria for diethylammonium butanoate. *Fluid Phase Equilibria* 459, 30–43. doi:10.1016/j.fluid.2017.12.001.
- Alebrahim, T., Chakraborty, A., Hu, L., Patil, S., Cheng, S., Acharya, D., Doherty, C.M., Hill, A.J., Cook, T.R., Lin, H., 2022. Gas transport characteristics of supramolecular networks of metal-coordinated highly branched poly (ethylene oxide). *J. Membr. Sci.* 644, 120063. doi:10.1016/j.memsci.2021.120063.
- Ali, S.H., Merchant, S.Q., Fahim, M.A., 2000. Kinetic study of reactive absorption of some primary amines with carbon dioxide in ethanol solution. *Sep. Purif. Technol.* 18 (3), 163–175.
- Ali Saleh Bairq, Z., Gao, H., Huang, Y., Zhang, H., Liang, Z., 2019. Enhancing CO₂ desorption performance in rich MEA solution by addition of SO₄²⁻/ZrO₂/SiO₂ bifunctional catalyst. *Appl. Energy* 252. doi:10.1016/j.apenergy.2019.113440.
- Alivand, M.S., Mazaheri, O., Wu, Y., Stevens, G.W., Scholes, C.A., Mumford, K.A., 2020. Catalytic solvent regeneration for energy-efficient CO₂ capture. *ACS Sustain. Chem. Eng.* 8 (51), 18755–18788. doi:10.1021/acscchemeng.0c07066.
- Alkhouzaam, A., Khraishbeh, M., Atilhan, M., Al-Mutaseb, S.A., Qi, L., Rooney, D., 2016. High-pressure CO₂/N₂ and CO₂/CH₄ separation using dense polysulfone-supported ionic liquid membranes. *J. Nat. Gas Sci. Eng.* 36, 472–485.
- Allam, R.J., Palmer, M., Brown, G.W., 2013a. System and method for high efficiency power generation using a carbon dioxide circulating working fluid. Google Patents.
- Allam, R.J., Palmer, M.R., Brown Jr., G.W., Fetvedt, J., Freed, D., Nomoto, H., Itoh, M., Okita, N., Jones Jr., C., 2013b. High efficiency and low cost of electricity generation from fossil fuels while minimizing atmospheric emissions, including carbon dioxide. *Energy Procedia* 37, 1135–1149.
- Allam, R., Fetvedt, J., Forrest, B., Freed, D., 2014. The oxy-fuel, supercritical CO₂ Allam Cycle: New cycle developments to produce even lower-cost electricity from fossil fuels without atmospheric emissions. In: *Turbo Expo: Power for Land, Sea, and Air*. American Society of Mechanical Engineers V03BT36A016.
- Allam, R., Martin, S., Forrest, B., Fetvedt, J., Lu, X., Freed, D., Brown Jr., G.W., Sasaki, T., Itoh, M., Manning, J., 2017. Demonstration of the Allam Cycle: an update on the development status of a high efficiency supercritical carbon dioxide power process employing full carbon capture. *Energy Procedia* 114, 5948–5966.
- Allen, M., 2019. Technical Summary: Global warming of 1.5 C. An IPCC Special Report on the impacts of global warming of 1.5 C above pre-industrial levels and related global greenhouse gas emission pathways, in the context of strengthening the global response to the threat of climate change, sustainable development, and efforts to eradicate poverty.
- Aloulsh, A.M., Abdelnaby, M.M., Cordova, K.E., Qasem, N.A., Al-Maythaly, B.A., Jililov, A., Mankour, Y., Al Hamouz, O.C.S., 2020. Selectively capturing carbon dioxide from mixed gas streams using a new microporous organic copolymer. *Microporous Mesoporous Mater.* 305, 110391.
- Almantariotis, D., Gefflaut, T., Padua, A.A.H., Coxam, J.Y., Gomes, M.F.C., 2010. Effect of fluorination and size of the alkyl side-chain on the solubility of carbon dioxide in 1-Alkyl-3-methylimidazolium Bis (trifluoromethylsulfonyl)amide Ionic Liquids. *J. Phys. Chem. B* 114 (10), 3608–3617. doi:10.1021/jp912176n.
- Almeida, R.M.d., Noda, L.C.K., Goncalves, N.S., Meneghetti, S.M.P., Meneghetti, M.R., 2008. Transesterification reaction of vegetable oils, using superacid sulfated TiO₂-base catalysts. *Appl. Catal. A* 347 (1), 100–105. doi:10.1016/j.apcata.2008.06.006.
- Almena, A., Thornley, P., Chong, K., Röder, M., 2022. Carbon dioxide removal potential from decentralised bioenergy with carbon capture and storage (BECCS) and the relevance of operational choices. *Biomass Bioenergy* 159. doi:10.1016/j.biombioe.2022.106406.
- Alvarez, D., Abanades, J.C., 2005. Determination of the critical product layer thickness in the reaction of CaO with CO₂. *Ind. Eng. Chem. Res.* 44 (15), 5608–5615.
- Alvarez, D., Abanades, J.C., 2005. Pore-size and shape effects on the recarbonation performance of calcium oxide submitted to repeated calcination/recarbonation cycles. *Energy Fuels* 19 (1), 270–278. doi:10.1021/ef049864m.
- Amer, N.M., Lahijani, P., Mohammadi, M., Mohamad, A.R., 2022. Modification of biomass-derived biochar: A practical approach towards development of sustainable CO₂ adsorbent. *Biomass Conv. Bioref.* doi:10.1007/s13399-022-02905-3.
- Ammendola, P., Raganati, F., Chirone, R., 2015. Effect of operating conditions on the CO₂ recovery from a fine activated carbon by means of TSA in a fluidized bed assisted by acoustic fields. *Fuel Process. Technol.* 134, 494–501. doi:10.1016/j.fuproc.2015.03.010.
- Anbia, M., Hoseini, V., 2012. Enhancement of CO₂ adsorption on nanoporous chromium terephthalate (MIL-101) by amine modification. *J. Nat. Gas Chem.* 21 (3), 339–343. doi:10.1016/s1003-9953 (11)60374-5.
- Ando, Y., Hirano, Y., Mase, S., Taguchi, H., 1998. Preparation and characterization of monolithic and planar element of zeolite membranes. In: *Proc. ICIM*, p. 124.
- Angelidaki, I., Treu, L., Tsaepkos, P., Luo, G., Campanaro, S., Wenzel, H., Kougias, P.G., 2018. Biogas upgrading and utilization: Current status and perspectives. *Biotechnol. Adv.* 36 (2), 452–466. doi:10.1016/j.biotechadv.2018.01.011.
- Anne Julbe, D.F., Guizard, Christian, 2001. Porous ceramic membranes for catalytic reactors — overview and new ideas. *J. Membr. Sci.* 181, 3–20.
- Ansalmi, L., Zhao, Y., Jung, B.T., Ramasubramanian, K., Bascchetti, M.G., Ho, W.S.W., 2015. Facilitated transport membranes containing amino-functionalized multi-walled carbon nanotubes for high-pressure CO₂ separations. *J. Membr. Sci.* 490, 18–28. doi:10.1016/j.memsci.2015.03.097.
- Araújo, T., Andrade, M., Bernardo, G., Mendes, A., 2022. Stable cellulose-based carbon molecular sieve membranes with very high selectivities. *J. Membr. Sci.* 641. doi:10.1016/j.memsci.2021.119852.
- Araujo, T., Bernardo, G., Mendes, A., 2020. Cellulose-based carbon molecular sieve membranes for gas separation: a review. *Molecules* 25 (15). doi:10.3390/molecules25153532.
- Arcenegui-Troya, J., Sánchez-Jiménez, P.E., Perejón, A., Valverde, J.M., Chacartegui, R., Pérez-Maqueda, L.A., 2020. Calcium-looping performance of biomimetic CaCO₃ for CO₂ capture and thermochemical energy storage. *Ind. Eng. Chem. Res.* 59 (29), 12924–12933. doi:10.1021/acs.iecr.9b05997.
- Arellano, I.H., Huang, J., Pendleton, P., 2015. Synergistic enhancement of CO₂ uptake in highly ordered mesoporous silica-supported zinc-functionalized ionic liquid sorbents. *Chem. Eng. J.* 281, 119–125. doi:10.1016/j.cej.2015.06.083.
- Arias, B., Grasa, G., Abanades, J.C., Manovic, V., Anthony, E.J., 2012. The effect of steam on the fast carbonation reaction rates of CaO. *Ind. Eng. Chem. Res.* 51 (5), 2478–2482. doi:10.1021/ie202648p.
- Arias, A.M., Mores, P.L., Scenna, N.J., Mussati, S.F., 2016. Optimal design and sensitivity analysis of post-combustion CO₂ capture process by chemical absorption with amines. *J. Clean. Prod.* 115, 315–331. doi:10.1016/j.jclepro.2015.12.056.
- Armuthulu, A., Naem, M.A., Liu, H.J., Kim, S.M., Kierzkowska, A., Fedorov, A., Müller, C.R.J.A.M., 2017. Multishelled CaO microspheres stabilized by atomic layer deposition of Al₂O₃ for enhanced CO₂ capture performance. *Adv. Mater.* 29 (41), 1702896.
- Aronu, U.E., Gondal, S., Helsen, E.T., Haug-Warberg, T., Hartono, A., Hoff, K.A., Svendsen, H.F., 2011. Solubility of CO₂ in 15, 30, 45 and 60 mass% MEA from 40 to 120°C and model representation using the extended UNIQUAC framework. *Chem. Eng. Sci.* 66 (24), 6393–6406. doi:10.1016/j.ces.2011.08.042.

- Arstad, B., Fjellvåg, H., Kongshaug, K.O., Swang, O., Blom, R., 2008. Amine functionalised metal organic frameworks (MOFs) as adsorbents for carbon dioxide. *Adsorption* 14 (6), 755–762. doi:10.1007/s10450-008-9137-6.
- Aschenbrenner, O., McGuire, P., Alsaamaq, S., Wang, J., Supasitmongkol, S., Al-Duri, B., Styring, P., Wood, J., 2011. Adsorption of carbon dioxide on hydroxalite-like compounds of different compositions. *Chem. Eng. Res. Des.* 89 (9), 1711–1721. doi:10.1016/j.cherd.2010.09.019.
- Ascherl, L., Sick, T., Margraf, J.T., Lapidus, S.H., Calik, M., Hettstedt, C., Karaghiosoff, K., Döblinger, M., Clark, T., Chapman, K.W., 2016. Molecular docking sites designed for the generation of highly crystalline covalent organic frameworks. *Nat. Chem.* 8 (4), 310–316.
- Asghar, H., Ilyas, A., Tahir, Z., Li, X., Khan, A.L., 2018. Fluorinated and sulfonated poly (ether ether ketone) and Matrimid blend membranes for CO₂ separation. *Sep. Purif. Technol.* 203, 233–241. doi:10.1016/j.seppur.2018.04.047.
- Ashokkumar, V., Venkatkarthick, R., Jayashree, S., Chuetor, S., Dharmaraj, S., Kumar, G., Chen, W.H., Ngamcharussivichai, C., 2022. Recent advances in lignocellulosic biomass for biofuels and value-added bioproducts-A critical review. *Bioresour. Technol.* 344. doi:10.1016/j.biortech.2021.126195.
- Ashtiani, S., Khoshnamvand, M., Bouša, D., Šturala, J., Sofer, Z., Shaliutina-Kolešová, A., Gardenő, D., Friess, K., 2021. Surface and interface engineering in CO₂-philic based UiO-66-NH₂-PEI mixed matrix membranes via covalently bridging PVP for effective hydrogen purification. *Int. J. Hydrogen Energy* 46 (7), 5449–5458. doi:10.1016/j.ijhydene.2020.11.081.
- Attou, A., Ferschneider, G., 1999. A two-fluid model for flow regime transition in gas-liquid trickle-bed reactors. *Chem. Eng. Sci.* 54 (21), 5031–5037. doi:10.1016/S0009-2509(99)00226-2.
- Austgen, D.M., R. G.T.P.X., Chen, C.C., 1989. Model of vapor-liquid equilibria for aqueous acid gas-alkanolamine systems using the electrolyte-NRTL equation. *Ind. Eng. Chem. Res.* 28, 1060–1073–1060–1073.
- Axelbaum, R., Kümfer, B., Gopan, A., Yang, Z., Phillips, J., Pint, B., 2017. Staged, High-Pressure Oxy-Combustion Technology. Development and Scale-Up Washington Univ, St. Louis, MO (United States).
- Azimi, G., Leon, H., Rydén, M., Mattisson, T., Lyngfelt, A., 2013. Investigation of different Mn-Fe oxides as oxygen carrier for chemical-looping with oxygen uncoupling (CLOU). *Energy Fuels* 27 (1), 367–377. doi:10.1021/ef301120r.
- Béarat, H., McKelvey, M.J., Chizmeshya, A.V.G., Sharma, R., Carpenter, R.W., 2002. Magnesium hydroxide dehydroxylation/carbonation reaction processes: implications for carbon dioxide mineral sequestration. 85 (4), 742–748. <https://doi.org/10.1111/j.1151-2916.2002.tb00166.x>.
- Babu, P., Ong, H.W.N., Linga, P., 2016. A systematic kinetic study to evaluate the effect of tetrahydrofuran on the clathrate process for pre-combustion capture of carbon dioxide. *Energy* 94, 431–442.
- Bacocchi, R., Storti, G., Mazzotti, M., 2006. Process design and energy requirements for the capture of carbon dioxide from air. *Chem. Eng. Process.: Process Intensif.* 45 (12), 1047–1058. doi:10.1016/j.ccep.2006.03.015.
- Bae, Y.-S., Farha, O.K., Spokoyny, A.M., Mirkin, C.A., Hupp, J.T., Snurr, R.Q., 2008. Carborane-based metal-organic frameworks as highly selective sorbents for CO₂ over methane. *Chem. Commun.* (35) 4135–4137.
- Bae, Y.-S., Hauser, B.G., Farha, O.K., Hupp, J.T., Snurr, R.Q., 2011. Enhancement of CO₂/CH₄ selectivity in metal-organic frameworks containing lithium cations. *Microporous Mesoporous Mater.* 141 (1–3), 231–235. doi:10.1016/j.micromeso.2010.10.048.
- Bahamon, D., Vega, L.F., 2016. Systematic evaluation of materials for post-combustion CO₂ capture in a temperature swing adsorption process. *Chem. Eng. J.* 284, 438–447. doi:10.1016/j.ccej.2015.08.098.
- Bai, W., Feng, J., Luo, C., Zhang, P., Wang, H., Yang, Y., Zhao, Y., Fan, H., 2021a. A comprehensive review on oxygen transport membranes: development history, current status, and future directions. *Int. J. Hydrogen Energy* 46, 36257–36290. doi:10.1016/J.IJHYDENE.2021.08.177.
- Bai, W., Feng, J., Luo, C., Zhang, P., Wang, H., Yang, Y., Zhao, Y., Fan, H., 2021b. A comprehensive review on oxygen transport membranes: development history, current status, and future directions. *Int. J. Hydrogen Energy* 46 (73), 36257–36290. doi:10.1016/j.ijhydene.2021.08.177.
- Bai, C., Zhang, W., Deng, L., Zhao, Y., Sun, S., Feng, D., Wu, J., 2022. Experimental study of nitrogen conversion during char combustion under a pressurized O₂/H₂O atmosphere. *Fuel* 311, 122529. doi:10.1016/j.fuel.2021.122529.
- Bai, R., Song, X., Yan, W., Yu, J., 2022. Low-energy adsorptive separation by zeolites. *Natl. Sci. Rev.* doi:10.1093/nsr/nwac064.
- Bailera, M., Lisbona, P., Romeo, L.M., 2015. Power to gas-oxyfuel boiler hybrid systems. *Int. J. Hydrogen Energy* 40 (32), 10168–10175. doi:10.1016/J.IJHYDENE.2015.06.074.
- Bailera, M., Lisbona, P., Romeo, L.M., Espatolero, S., 2016. Power to Gas-biomass oxycombustion hybrid system: Energy integration and potential applications. *Appl. Energy* 167, 221–229. doi:10.1016/J.APENERGY.2015.10.014.
- Bailera, M., Lisbona, P., Peña, B., Romeo, L.M., 2020. *Energy Storage*. Springer International Publishing.
- Bailera, M., Peña, B., Lisbona, P., Marín, J., Romeo, L.M., 2021. Lab-scale experimental tests of power to gas-oxycombustion hybridization: System design and preliminary results. *Energy* 226. doi:10.1016/j.energy.2021.120375, 120375–120375.
- Bairq, Z.A.S., Gao, H., Murshed, F.A.M., Tontiwachwuthikul, P., Liang, Z., 2020. Modified heterogeneous catalyst-aided regeneration of CO₂ capture amines: a promising perspective for a drastic reduction in energy consumption. *ACS Sustain. Chem. Eng.* 8 (25), 9526–9536. doi:10.1021/acscchemeng.0c02582.
- Bakhshi Ani, A., Ale Ebrahim, H., 2021. Comprehensive kinetic study of sulfur dioxide removal by magnesium oxide using TG. *J. Therm. Anal. Calorimetry* 146 (6), 2587–2599.
- Bali, S., Chen, T.T., Chaikittisilp, W., Jones, C.W., 2013. Oxidative stability of amino polymer-alumina hybrid adsorbents for carbon dioxide capture. *Energy Fuels* 27 (3), 1547–1554. doi:10.1021/ef4001067.
- Balice, D.M., Molenaar, C.W.C., Fochesato, M., Venier, C.M., Roghair, I., Deen, N.G., van Sint Annaland, M., 2022. CFD modeling of droplet permeability in fluidized beds. *Int. J. Multiph. Flow* 152. doi:10.1016/j.ijmultiphaseflow.2022.104069, 104069–104069.
- Banaszkiewicz, T., Chorowski, M., 2018. Energy consumption of air-separation adsorption methods. *Entropy (Basel, Switzerland)* 20 (4). doi:10.3390/e20040232, 232–232.
- Banaszkiewicz, T., Chorowski, M., Gizicki, W., 2014. Comparative analysis of oxygen production for oxy-combustion application. *Energy Procedia* 51, 127–134. doi:10.1016/j.egypro.2014.07.014.
- Bandehali, S., Ebadi Amoghini, A., Sanaeepour, H., Ahmadi, R., Fuoco, A., Jansen, J.C., Shirazian, S., 2021. Polymers of intrinsic microporosity and thermally rearranged polymer membranes for highly efficient gas separation. *Sep. Purif. Technol.* 278, 119513. doi:10.1016/j.seppur.2021.119513.
- Bao, L., Trachtenberg, M.C., 2006. Facilitated transport of CO₂ across a liquid membrane: Comparing enzyme, amine, and alkaline. *J. Membr. Sci.* 280 (1), 330–334. doi:10.1016/j.memsci.2006.01.036.
- Bao, S.-J., Krishna, R., He, Y.-B., Qin, J.-S., Su, Z.-M., Li, S.-L., Xie, W., Du, D.-Y., He, W.-W., Zhang, S.-R., Lan, Y.-Q., 2015. A stable metal-organic framework with suitable pore sizes and rich uncoordinated nitrogen atoms on the internal surface of micropores for highly efficient CO₂ capture. *J. Mater. Chem. A* 3 (14), 7361–7367. doi:10.1039/c5ta00256g.
- Bararpour, S.T., Karami, D., Mahinpey, N., 2019. Investigation of the effect of alumina-aerogel support on the CO₂ capture performance of K₂CO₃. *Fuel* 242, 124–132. doi:10.1016/j.fuel.2018.12.123.
- Bararpour, S.T., Adanez, J., Mahinpey, N., 2020. Application of core-shell-structured K₂CO₃-based sorbents in postcombustion CO₂ capture: Statistical analysis and optimization using response surface methodology. *Energy Fuels* 34 (3), 3429–3439. doi:10.1021/acs.energyfuels.9b03442.
- Barbera, E., Mio, A., Massi Pavan, A., Bertuccio, A., Fermeglia, M., 2022. Fueling power plants by natural gas: An analysis of energy efficiency, economical aspects and environmental footprint based on detailed process simulation of the whole carbon capture and storage system. *Energy Convers. Manage.* 252. doi:10.1016/j.enconman.2021.115072.
- Barker, R., 2007. The reversibility of the reaction CaCO₃ ⇌ CaO+CO₂. *J. Appl. Chem. Biotechnol.* 23, 733–742. doi:10.1002/jctb.5020231005.
- Barpaga, D., Jiang, Y., Zheng, R.F., Malhotra, D., Koeck, P.K., Zwoster, A., Mathias, P.M., Heldebrandt, D.J., 2022. Evaluation of a third generation single-component water-lean diamine solvent for post-combustion CO₂ capture. *ACS Sustain. Chem. Eng.* 10 (14), 4522–4528. doi:10.1021/acscchemeng.1c08401.
- Barthomeuf, D., 2003. Framework induced basicity in zeolites. *Microporous Mesoporous Mater.* 66 (1), 1–14.
- Barzagli, F., Mani, F., Peruzzini, M., 2013. Efficient CO₂ absorption and low temperature desorption with non-aqueous solvents based on 2-amino-2-methyl-1-propanol (AMP). *Int. J. Greenh. Gas Control* 16 (10), 217–223. doi:10.1016/j.jggcc.2013.03.026.
- Baskaran, T., Christopher, J., Sakthivel, A., 2015. Progress on layered hydroxalite (HT) materials as potential support and catalytic materials. *RSC Adv.* 5 (120), 98853–98875. doi:10.1039/C5RA19909D.
- Bassani, A., van Dijk, H.A.J., Cobden, P.D., Spigno, G., Manzolini, G., Manenti, F., 2019. Sorption Enhanced Water Gas Shift for H₂ production using sour gases as feedstock. *Int. J. Hydrogen Energy* 44 (31), 16132–16143. doi:10.1016/j.ijhydene.2019.04.199.
- Bastin, L., Bércia, P.S., Hurtado, E.J., Silva, J.A., Rodrigues, A.E., Chen, B., 2008. A microporous metal-organic framework for separation of CO₂/N₂ and CO₂/CH₄ by fixed-bed adsorption. *J. Phys. Chem. C* 112 (5), 1575–1581.
- Baus, L., Nehr, S., 2022. Potentials and limitations of direct air capturing in the built environment. *Build. Environ.* 208. doi:10.1016/j.buildenv.2021.108629.
- Baxter, L., Baxter, A., Burt, S., 2009. Cryogenic CO₂ capture as a cost-effective CO₂ capture process. In: 26th Annual International Pittsburgh Coal Conference 2009, PCC 2009, p. 1.
- Baylin-Stern, A., Beck, L., Beutler, C., Bolesta, C., Dailey, M., Dixon, T., Edwards, R., 2022. Direct Air Capture A Key Technology for Net Zero. International Energy Center.
- Bednar, J., Obersteiner, M., Wagner, F., 2019. On the financial viability of negative emissions. *Nat. Commun.* 10 (1), 1783. doi:10.1038/s41467-019-09782-x.
- Bellucci, M., Masi, A., Albino, M., Peddis, D., Petrecca, M., Sangregorio, C., La Barbera, A., Varsano, F., 2021. Fe₂O₃@HKUST-1 magnetic composites by mechanochemical route for induction triggered release of carbon dioxide. *Microporous Mesoporous Mater.* 328. doi:10.1016/j.micromeso.2021.111458.
- Belmabkhout, Y., Serna-Guerrero, R., Sayari, A., 2010. Adsorption of CO₂-containing gas mixtures over amine-bearing pore-expanded MCM-41 silica: application for gas purification. *Ind. Eng. Chem. Res.* 49 (1), 359–365. doi:10.1021/ie900837t.
- Belmabkhout, A.S.Y., 2010. Stabilization of amine-containing CO₂ adsorbents: dramatic effect of water vapour. *J. Am. Chem. Soc.* 132, 6312–6314.
- Ben Petrovic, M.G., Soltani, S.M., 2022. Impact of surface functional groups and their introduction methods on the mechanisms of CO₂ adsorption on porous carbonaceous adsorbents. *Carbon Cap. Sci. Technol.* 3. doi:10.1016/j.cest.2022.100045.
- Ben Salem, I., El Gamal, M., Sharma, M., Hameedi, S., Howari, F.M., 2021a. Utilization of the UAE date palm leaf biochar in carbon dioxide capture and sequestration processes. *J. Environ. Manage.* 299. doi:10.1016/j.jenvman.2021.113644.
- Ben Salem, I., Saleh, M.B., Iqbal, J., El Gamal, M., Hameed, S., 2021b. Date palm waste pyrolysis into biochar for carbon dioxide adsorption. *Energy Rep.* 7, 152–159. doi:10.1016/j.egyrs.2021.06.027.
- Bernabé-Pablo, E., Plascencia-Hernández, F., Yañez-Aulestia, A., Pfeiffer, H., 2020. High and efficient carbon dioxide chemisorption on a new high lithium-content ceramic; hexalithium cobaltate (Li₆CoO₄). *Chem. Eng. J.* 384, 123291. doi:10.1016/j.ccej.2019.123291.

- Bernardo, P., Drioli, E., Golemme, G., 2009. Membrane gas separation: a review/state of the art. *Ind. Eng. Chem. Res.* 48 (10), 4638–4663. doi:10.1021/ie801903z.
- Berstad, D., Anantharaman, R., Nekså, P., 2013. Low-temperature CO₂ capture technologies – Applications and potential. *Int. J. Refrig.* 36 (5), 1403–1416. doi:10.1016/j.ijrefrig.2013.03.017.
- Berstad, D., Skaugen, G., Roussanaly, S., Anantharaman, R., Nekså, P., Jordal, K., Trædal, S., Gundersen, T., 2022. CO₂ Capture from IGCC by low-temperature synthesis gas separation. *Energies* 15 (2), 515. doi:10.3390/en15020515.
- Beysel, G., Enhanced Cryogenic Air Separation. Cottbus, Germany, pp. 38–38.
- Bezerra, D.P., Oliveira, R.S., Vieira, R.S., Cavalcante, C.L., Azevedo, D.C.S., 2011. Adsorption of CO₂ on nitrogen-enriched activated carbon and zeolite 13X. *Adsorption* 17 (1), 235–246. doi:10.1007/s10450-011-9320-z.
- Bezerra, D.P., Silva, F.W.M.d., Moura, P.A.S.d., Sousa, A.G.S., Vieira, R.S., Rodriguez-Castellon, E., Azevedo, D.C.S., 2014. CO₂ adsorption in amine-grafted zeolite 13X. *Appl. Surf. Sci.* 314, 314–321. doi:10.1016/j.apsusc.2014.06.164.
- Bezzu, C.G., Fuoco, A., Esposito, E., Monteleone, M., Longo, M., Jansen, J.C., Nichol, G.S., McKeown, N.B., 2021. Ultrapermeable polymers of intrinsic microporosity containing spirocyclic units with fused triptycenes. *Adv. Fun. Mater.* 31 (37), 2104474. doi:10.1002/adfm.202104474.
- Bhagiyalakshmi, M., Lee, J.Y., Jang, H.T., 2010. Synthesis of mesoporous magnesium oxide: Its application to CO₂ chemisorption. *Int. J. Greenh. Gas Control* 4 (1), 51–56. doi:10.1016/j.jggc.2009.08.001.
- Bhattia, S.K., Perlmutter, D.D., 1983. Effect of the product layer on the kinetics of the CO₂-lime reaction. *Aiche J.* 29 (1), 79–86. doi:10.1002/aic.690290111.
- Bhatt, T.S., Storti, G., Denayer, J.F.M., Rota, R., 2017. Optimal design of dual-reflux pressure swing adsorption units via equilibrium theory: Process configurations employing heavy gas for pressure swing. *Chem. Eng. J.* 311, 385–406. doi:10.1016/j.cej.2016.11.111.
- Bhatt, T.S., Storti, G., Denayer, J.F.M., Rota, R., 2018. Equilibrium theory-based assessment of dual-reflux pressure swing adsorption cycles that utilize light gas for pressure swing. *Ind. Eng. Chem. Res.* 58 (1), 350–365. doi:10.1021/acs.iecr.8b04415.
- Bhattacharyya, S., Shah, F.U., 2016. Ether functionalized choline tethered amino acid ionic liquids for enhanced CO₂ capture. *ACS Sustain. Chem. Eng.* 4 (10), 5441–5449. doi:10.1021/acsuschemeng.6b00824.
- Bhatti, U.H., Shah, A.K., Kim, J.N., You, J.K., Choi, S.H., Lim, D.H., Nam, S., Park, Y.H., Baek, I.H., 2017. Effects of transition metal oxide catalysts on MEA solution regeneration for the post-combustion carbon capture process. *ACS Sustain. Chem. Eng.* 5 (7), 5862–5868. doi:10.1021/acsuschemeng.7b00604.
- Bhatti, U.H., Nam, S., Park, S., Baek, I.H., 2018a. Performance and mechanism of metal-oxide catalyst-aided amine solvent regeneration. *ACS Sustain. Chem. Eng.* 6 (9), 12079–12087. doi:10.1021/acsuschemeng.8b02422.
- Bhatti, U.H., Sivanesan, D., Lim, D.H., Nam, S.C., Park, S., Baek, I.H., 2018b. Metal oxide catalyst-aided solvent regeneration: A promising method to economize post-combustion CO₂ capture process. *J. Taiwan Inst. Chem. Eng.* 93, 150–157. doi:10.1016/j.jtice.2018.05.029.
- Bhatti, U.H., Shah, A.K., Hussain, A., Khan, H.A., Park, C.Y., Nam, S.C., Baek, I.H., 2020. Catalytic activity of freshly synthesized mesoporous HZSM-5 catalysts for optimizing the CO₂ desorption rate from CO₂-rich amine solutions. *Chem. Eng. J.* 389. doi:10.1016/j.cej.2019.123439.
- Bhave, A., Taylor, R.H., Fennell, P., Livingston, W.R., Shah, N., MacDowell, N., Dennis, J., Kraft, M., Pourkashanian, M., Insa, M., 2017. Screening and techno-economic assessment of biomass-based power generation with CCS technologies to meet 2050 CO₂ targets. *Appl. Energy* 190, 481–489.
- Bhown, A.S., Freeman, B.C., 2011. Analysis and status of post-combustion carbon dioxide capture technologies. *Environ. Sci. Technol.* 45 (20), 8624–8632. doi:10.1021/es104291d.
- Bhunia, A., Boldog, L., Möller, A., Janiak, C., 2013. Highly stable nanoporous covalent triazine-based frameworks with an adamantane core for carbon dioxide sorption and separation. *J. Mater. Chem. A* 1 (47), 14990–14999.
- Bi, X., Zhang, Y.a., Zhang, F., Zhang, S., Wang, Z., Jin, J., 2020. MOF nanosheet-based mixed matrix membranes with metal-organic coordination interfacial interaction for gas separation. *ACS Appl. Mater. Interfaces* 12 (43), 49101–49110. doi:10.1021/acami.0c14639.
- Bigdeli, F., Lollar, C.T., Morsali, A., Zhou, H.C., 2020. Switching in metal-organic frameworks. *Angew. Chem. Int. Ed. Engl.* 59 (12), 4652–4669. doi:10.1002/anie.201900666.
- Bililyok, C., Lawal, A., Wang, M., Seibert, F., 2012. Dynamic modelling, validation and analysis of post-combustion chemical absorption CO₂ capture plant. *Int. J. Greenh. Gas Control* 9, 428–445. doi:10.1016/j.jggc.2012.05.001.
- Biswal, B.P., Chandra, S., Kandambeth, S., Lukose, B., Heine, T., Banerjee, R., 2013. Mechanochemical synthesis of chemically stable isoreticular covalent organic frameworks. *J. Am. Chem. Soc.* 135 (14), 5328–5331.
- Blackwood, J.D., McGrory, F., Blackwood, J.D., McGrory, F., 1958. The carbon-steam reaction at high pressure. *Aust. J. Chem.* 11 (1), 16–33.
- Blamey, J., Anthony, E., Wang, J., Fennell, P., 2010. The calcium looping cycle for large-scale CO₂ capture. *Prog. Energy Combust.* 36 (2), 260–279.
- Blamey, J., Manovic, V., Anthony, E.J., Dugwell, D.R., Fennell, P.S., 2015. On steam hydration of CaO-based sorbent cycled for CO₂ capture. *Fuel* 150, 269–277. doi:10.1016/j.fuel.2015.02.026.
- D.H. Blanchard, L.A., Beckman, E.J., Brennecke, J.F., 1999. Green processing using ionic liquids and CO₂. *Nature* 399 (6731), 28–29. doi:10.1038/19887.
- Blanco, M.V., Kohopää, K., Snigireva, I., Cova, F., 2018. Low temperature solid state synthesis of Li₂FeO₄ and CO₂ capture mechanism via real time in situ synchrotron X-ray diffraction. *Chem. Eng. J.* 354, 370–377. doi:10.1016/j.cej.2018.08.017.
- Board, O.S., Council, N.R., 2015. Climate Intervention: carbon Dioxide Removal and Reliable Sequestration. National Academies Press.
- Boetcher, S.K.S., Traum, M.J., von Hippel, T., 2020. Thermodynamic model of CO₂ deposition in cold climates. *Clim. Change* 158 (3), 517–530. doi:10.1007/s10584-019-02587-3.
- Bollini, P., Didas, S.A., Jones, C.W., 2011. Amine-oxide hybrid materials for acid gas separations. *J. Mater. Chem.* 21 (39). doi:10.1039/c1jm12522b.
- Bollini, P., Brunelli, N.A., Didas, S.A., Jones, C.W., 2012a. Dynamics of CO₂ adsorption on amine adsorbents. 1. Impact of heat effects. *Ind. Eng. Chem. Res.* 51 (46), 15145–15152. doi:10.1021/ie301790a.
- Bollini, P., Brunelli, N.A., Didas, S.A., Jones, C.W., 2012b. Dynamics of CO₂ adsorption on amine adsorbents. 2. Insights into adsorbent design. *Ind. Eng. Chem. Res.* 51 (46), 15153–15162. doi:10.1021/ie3017913.
- Bondar, V.I., Freeman, B.D., Pinnau, I., 2000. Gas transport properties of poly (ether-b- amide) segmented block copolymers. *J. Polym. Sci. Part B Polym. Phys.* 38 (15), 2051–2062. doi:10.1002/1099-0488(20000801)38:15<2051::AID-POLB100>3.0.CO;2-D.
- Bondorf, L., Fiorio, J.L., Bon, V., Zhang, L., Malluta, M., Ehrling, S., Senkowska, I., Evans, J.D., Joswig, J.-O., Kaskel, S., 2022. Isotope-selective pore opening in a flexible metal-organic framework. *Sci. Adv.* 8 (15), eabn7035. doi:10.1126/sciadv.abn7035.
- Bonetto, R., Latzko, V., 2020. Chapter 8 - Machine learning, in: Fitzek, F.H.P., Granelli, F., Seeling, P.B.T.C.I.C.N. (Eds.), Academic Press, pp. 135–167. https://doi.org/10.1016/B978-0-12-820488-7.00021-9.
- Boot-Handford, M.E., Abanades, J.C., Anthony, E.J., Blunt, M.J., Brandani, S., MacDowell, N., Fernández, J.R., Ferrari, M.-C., Gross, R., Hallett, J.P., Haszeldine, R.S., Heptonstall, P., Lyngfelt, A., Makuch, Z., Mangano, E., Porter, R.T.J., Pourkashanian, M., Rochelle, G.T., Shah, N., Yao, J.G., Fennell, P.S., 2014. Carbon capture and storage update. *Energy Environ. Sci.* 7 (1), 130–189. doi:10.1039/c3ee42350f.
- Borgwardt, R.H., Bruce, K.R., Blake, J., 1987. An investigation of product-layer diffusivity for calcium oxide sulfation. *Ind. Eng. Chem. Res.* 26 (10), 1993–1998. doi:10.1021/ie00070a010.
- Borhani, T.N., Oko, E., Wang, M., 2018. Process modelling and analysis of intensified CO₂ capture using monoethanolamine (MEA) in rotating packed bed absorber. *J. Clean. Prod.* 204, 1124–1142.
- Borhani, T.N., Oko, E., Wang, M., 2019. Process modelling, validation and analysis of rotating packed bed stripper in the context of intensified CO₂ capture with MEA. *J. Ind. Eng. Chem.* 75, 285–295.
- Bork, A.H., Rehkina, M., Willinger, E., Castro-Fernandez, P., Drnec, J., Abdala, P.M., Müller, C.R., 2021. Peering into buried interfaces with X-rays and electrons to unveil MgCO₃ formation during CO₂ capture in molten salt-promoted MgO. *Proc. Natl. Acad. Sci. U S A* 118 (26), e2103971118. doi:10.1073/pnas.2103971118.
- Boujibar, O., Souikny, A., Ghamouss, F., Achak, O., Dahbi, M., Chafik, T., 2018. CO₂ capture using N-containing nanoporous activated carbon obtained from argan fruit shells. *J. Environ. Chem. Eng.* 6 (2), 1995–2002. doi:10.1016/j.jece.2018.03.005.
- Bouaceur, R., Lape, N., Roizard, D., Vallieres, C., Favre, E., 2006. Membrane processes for post-combustion carbon dioxide capture: A parametric study. *Energy* 31 (14), 2556–2570. doi:10.1016/j.energy.2005.10.038.
- Bower, J.K., Barpaga, D., Prodingler, S., Krishna, R., Schaeff, H.T., McGrail, B.P., Derewinski, M.A., Motkuri, R.K., 2018. Dynamic adsorption of CO₂/N₂ on cation-exchanged chabazite SSZ-13: a breakthrough analysis. *ACS Appl. Mater. Interfaces* 10 (17), 14287–14291.
- Boyer, C., Koudil, A., Chen, P., Dudukovic, M.P., 2005. Study of liquid spreading from a point source in a trickle bed via gamma-ray tomography and CFD simulation. *Chem. Eng. Sci.* 60 (22), 6279–6288. doi:10.1016/j.ces.2005.03.049.
- Brüder, P., Grimstedt, A., Mejdell, T., Svendsen, H.F., 2011. CO₂ capture into aqueous solutions of piperazine activated 2-amino-2-methyl-1-propanol. *Chem. Eng. Sci.* 66 (23), 6193–6198. doi:10.1016/j.ces.2011.08.051.
- Brandani, F., Ruthven, D.M., 2004. The effect of water on the adsorption of CO₂ and C₃H₈ on type X zeolites. *Ind. Eng. Chem. Research* 43 (26), 8339–8344.
- Bravo, J., Drapanauskaite, D., Sarunac, N., Romero, C., Jesikiewicz, T., Baltusaitis, J., 2021. Optimization of energy requirements for CO₂ post-combustion capture process through advanced thermal integration. *Fuel* 283. doi:10.1016/j.fuel.2020.118940.
- Breault, R.W., Spenik, J.L., Shadle, L.J., Hoffman, J.S., Gray, M.L., Panday, R., Stehle, R.C., 2016. Carbon capture test unit design and development using amine-based solid sorbent. *Chem. Eng. Res. Des.* 112, 251–262. doi:10.1016/j.cherd.2016.06.020.
- Brienes-Hidrovo, A., Copa Rey, J.R., Cláudia Dias, A., Tarelho, L.A.C., Beauchet, S., 2022. Assessing a bio-energy system with carbon capture and storage (BECCS) through dynamic life cycle assessment and land-water-energy nexus. *Energy Convers. Manage.* 268. doi:10.1016/j.enconman.2022.116014.
- Brunetti, A., Cersosimo, M., Kim, J.S., Dong, G., Fontananova, E., Lee, Y.M., Drioli, E., Barbieri, G., 2017. Thermally rearranged mixed matrix membranes for CO₂ separation: An aging study. *Int. J. Greenh. Gas Control* 61, 16–26. doi:10.1016/j.jggc.2017.03.024.
- Buck, F., Wieggers, K., Schulz, A., Schiestel, T., 2021. MIEC hollow-fibre membranes in a plasma membrane reactor. *Intercom - Int. Ceramic Rev.* 70 (2), 40–45. doi:10.1007/s42411-021-0445-0, 202170.
- Buckingham, J., Reina, T.R., Duyar, M.S., 2022. Recent advances in carbon dioxide capture for process intensification. *Carbon Cap. Sci. Technol.* 2, 100031. doi:10.1016/j.ccsr.2022.100031.
- Budd, P.M., McKeown, N.B., 2010. Highly permeable polymers for gas separation membranes. *J. Polym. Chem.* 1 (1), 63–68.
- Budd, P.M., Ghanem, B.S., Makhseed, S., McKeown, N.B., Msayib, K.J., Tattershall, C.E., 2004. Polymers of intrinsic microporosity (PIMs): robust, solution-processable, organic nanoporous materials. *Chem. Commun.* (2) 230–231. doi:10.1039/B311764B.

- Buddin, M., Ahmad, A.L., 2021. A review on metal-organic frameworks as filler in mixed matrix membrane: Recent strategies to surpass upper bound for. *J. CO₂ Util.* 51, 101616. doi:10.1016/j.jcou.2021.101616.
- Budhathoki, S., Ajayi, O., Steckel, J.A., Wilmer, C.E., 2019. High-throughput computational prediction of the cost of carbon capture using mixed matrix membranes. *Energy Environ. Sci.* 12 (4), 1255–1264. doi:10.1039/c8ee02582g.
- Budinis, S., 2022. Direct air capture technology deep dive. <https://www.iea.org/reports/direct-air-capture>. (Accessed Sep. 2022).
- Budzianowski, W.M., Wyllock, C.E., Marciniak, P.A., 2017. Power requirements of biogas upgrading by water scrubbing and biomethane compression: Comparative analysis of various plant configurations. *Energy Convers. Manage.* 141, 2–19. doi:10.1016/j.enconman.2016.03.018.
- Buelens, L.C., Galvita, V.V., Poelman, H., Detavernier, C., Marin, G.B., 2016. Super-dry reforming of methane intensifies CO₂ utilization via Le Chatelier's principle. *Science* 354 (6311), 449–452. doi:10.1126/science.aah7161.
- Bui, M., Gunawan, I., Verheyen, V., Feron, P., Meuleman, E., Adeloju, S., 2014. Dynamic modelling and optimisation of flexible operation in post-combustion CO₂ capture plants-A review. *Comput. Chem. Eng.* 61, 245–265. doi:10.1016/j.compchemeng.2013.11.015.
- Bui, M., Adjiman, C.S., Bardow, A., Anthony, E.J., Boston, A., Brown, S., Fennell, P.S., Fuss, S., Galindo, A., Hackett, L.A., 2018. Carbon capture and storage (CCS): the way forward. *Energy Environ. Sci.*
- Burdyny, T., Struchtrup, H., 2010. Hybrid membrane/cryogenic separation of oxygen from air for use in the oxy-fuel process. *Energy* 35 (5), 1884–1897. doi:10.1016/j.energy.2009.12.033.
- Burekacw, S., Shimomura, S., Kitagawa, S., 2008. Chemistry and application of flexible porous coordination polymers. *Sci. Technol. Adv. Mater.*
- Burns, J.R., Jamil, J.N., Ramshaw, C., 2000. Process intensification: Operating characteristics of rotating packed beds - determination of liquid hold-up for a high-voidage structured packing. *Chem. Eng. Sci.* 55 (13), 2401–2415. doi:10.1016/S0009-2509(99)00520-5.
- Burns, T.D., Pai, K.N., Subraveti, S.G., Collins, S.P., Krykunov, M., Rajendran, A., Woo, T.K., 2020. Prediction of MOF performance in vacuum swing adsorption systems for postcombustion CO₂ capture based on integrated molecular simulations, process optimizations, and machine learning models. *Environ. Sci. Technol.* 54 (7), 4536–4544. doi:10.1021/acs.est.9b07407.
- Buvik, V., Høisæter, K.K., Vevelstad, S.J., Knuutila, H.K., 2021. A review of degradation and emissions in post-combustion CO₂ capture pilot plants. *Int. J. Greenh. Gas Control* 106. doi:10.1016/j.jggc.2020.103246.
- Cabello, A., Dueso, C., García-Labiano, F., Gayán, P., Abad, A., de Diego, L.F., Adnéz, J., 2014. Performance of a highly reactive impregnated Fe₂O₃/Al₂O₃ oxygen carrier with CH₄ and H₂S in a 500Wth CLC unit. *Fuel* 121, 117–125. doi:10.1016/j.fuel.2013.12.027.
- Cacho-Bailo, F., Matito-Martos, I., Perez-Carballo, J., Etxebarria-Benavides, M., Karvan, O., Sebastian, V., Calero, S., Tellez, C., Coronas, J., 2017. On the molecular mechanisms for the H₂/CO₂ separation performance of zeolite imidazolate framework two-layered membranes. *Chem. Sci.* 8 (1), 325–333. doi:10.1039/c6sc02411d.
- Cai, L., Zou, C., Liu, Y., Zhou, K., Han, Q., Zheng, C., 2015. Numerical and experimental studies on the ignition of pulverized coal in O₂/H₂O atmospheres. *Fuel* 139, 198–205. doi:10.1016/j.fuel.2014.08.038.
- Cai, J., Wang, S., Kuang, C., 2017. A modified random pore model for carbonation reaction of CaO-based limestone with CO₂ in different calcination-carbonation cycles. *Energy Procedia* 105, 1924–1931. doi:10.1016/j.egypro.2017.03.561.
- Cai, T., Johnson, J.K., Wu, Y., Chen, X., 2019. Toward understanding the kinetics of CO₂ capture on sodium carbonate. *ACS Appl. Mater. Interfaces* 11 (9), 9033–9041. doi:10.1021/acsami.8b20000.
- Cai, T., Chen, X., Zhong, J., Wu, Y., Ma, J., Liu, D., Liang, C., 2020. Understanding the morphology of supported Na₂CO₃/γ-ALOOH solid sorbent and its CO₂ sorption performance. *Chem. Eng. J.* 395, 124139. doi:10.1016/j.cej.2020.124139.
- Cai, R., Dou, J., Krzystowczyk, E., Richard, A., Li, F., 2022. Chemical looping air separation with Sr_{0.8}Ca_{0.2}Fe_{0.9}Co_{0.1} perovskite sorbent: Packed bed modeling, verification, and optimization. *Chem. Eng. J.* 429. doi:10.1016/J.CEJ.2021.132370, 132370-132370.
- Cai, W., Kong, X., Ye, Q., Wang, L., Ren, D., Lu, H., 2022. Numerical modelling of hydrodynamics of molten salt fluid-particles fluidized beds using CFD-DEM and TFM approaches. *Powder Technol.* 410. doi:10.1016/j.powtec.2022.117882, 117882-117882.
- Cailliez, F., Stirnemann, G., Boutin, A., Demachy, I., Fuchs, A.H., 2008. Does water condense in hydrophobic cavities? A molecular simulation study of hydration in heterogeneous nanopores. *J. Phys. Chem. C* 112 (28), 10435–10445.
- Calle, M., Jo, H.J., Doherty, C.M., Hill, A.J., Lee, Y.M., 2015. Cross-linked thermally rearranged poly (benzoxazole-co-imide) membranes prepared from ortho-hydroxycopolyimides containing pendant carboxyl groups and gas separation properties. *Macromolecules* 48 (8), 2603–2613.
- Cantu, D.C., Malhotra, D., Nguyen, M.T., Koech, P.K., Zhang, D., Glezakou, V.A., Rousseau, R., Page, J., Zheng, R., Perry, R.J., Heldebrandt, D.J., 2020. Molecular-level overhaul of gamma-aminopropyl aminosilicone/triethylene glycol post-combustion CO (2) -capture solvents. *ChemSusChem* 13 (13), 3429–3438. doi:10.1002/cssc.202000724.
- Cao, X., Harris, W., 2010. Properties of dairy-manure-derived biochar pertinent to its potential use in remediation. *Bioresour. Technol.* 101 (14), 5222–5228. doi:10.1016/j.biortech.2010.02.052.
- Cao, Y., He, B., Ding, G., Su, L., Duan, Z., 2016. Performance modeling of integrated chemical looping air separation and IGCC with CO₂ capture. *Energy Fuels* 30 (11), 9953–9961. doi:10.1021/ACS.ENERGYFUELS.6B01894.
- Cao, X., Wang, Z., Qiao, Z., Zhao, S., Wang, J., 2019. Penetrated COF channels: Amino environment and suitable size for CO₂ preferential adsorption and transport in mixed matrix membranes. *ACS Appl. Mater. Interfaces* 11 (5), 5306–5315. doi:10.1021/ac-sami.8b16877.
- Cao, Y., Zhang, K., Sanyal, O., Koros, W.J., 2019. Carbon molecular sieve membrane preparation by economical coating and pyrolysis of porous polymer hollow fibers. *Angew. Chem. Int. Ed. Engl.* 58 (35), 12149–12153. doi:10.1002/anie.201906653.
- Cao, M., Zhao, L., Xu, D., Parsley, D., Ciora, R., Liu, P.K.T., Manoussiotakis, V.I., Tsoisis, T.T., 2021. A reactive separation process for pre-combustion CO₂ capture employing oxygen-blown coal gasifier off-gas. *Chem. Eng. J.* 420, 127694. doi:10.1016/j.cej.2020.127694.
- Cao, L.Y., Zhang, X.Y., Xu, Y., Xiang, W., Wang, R., Ding, F.J., Hong, P.Z., Gao, B., 2022. Straw and wood based biochar for CO₂ capture: Adsorption performance and governing mechanisms. *Sep. Purif. Technol.* 287. doi:10.1016/j.seppur.2022.120592.
- Caplow, M., 1968. Kinetics of carbamate formation and breakdown. *J. Am. Chem. Soc.* 90, 6795–6803.
- Caplow, M., 1968. Kinetics of carbamate formation and breakdown. *J. Am. Chem. Soc.* 89, 6795–6803.
- Carney, J.E., Finn, J.R., 2016. NETL Technical Report Series. National Energy Technology Lab. (NETL), Albany, OR (United States) 48-48.
- Caruana, R., Lawrence, S., C. L.G., 2000. Overfitting in Neural Nets: Backpropagation, Conjugate Gradient, and Early Stopping. *Advances in Neural Information Processing Systems* 13, 402–408.
- Caskey, S.R., Wong-Foy, A.K., Matzger, A.J., 2008. Dramatic tuning of carbon dioxide uptake via metal substitution in a coordination polymer with cylindrical pores. *J. Am. Chem. Soc.* 130 (33), 10870–10871.
- Casleton, K.H., Breault, R.W., Richards, G.A., 2008. System issues and tradeoffs associated with syngas production and combustion. *Combust. Sci. Technol.* 180 (6), 1013–1052.
- Castillo, R., 2011. Thermodynamic analysis of a hard coal oxyfuel power plant with high temperature three-end membrane for air separation. *Appl. Energy* 88 (5), 1480–1493. doi:10.1016/J.APENERGY.2010.10.044.
- Cau, G., Cocco, D., Tola, V., 2014. Performance assessment of USC power plants integrated with CCS and concentrating solar collectors. *Energy Convers. Manage.* 88, 973–984. doi:10.1016/j.enconman.2014.09.040.
- Cavani, F., Trifiro, F., Vaccari, A., 1991. Hydrotalcite-type anionic clays: preparation, properties and applications. *Catal. Today* 11 (2), 173–301. doi:10.1016/0920-5861(91)80068-K.
- Cavka, J.H., Jakobsen, S., Olsbye, U., Guillou, N., Lamberti, C., Bordiga, S., Lillerud, K.P., 2008. A new zirconium inorganic building brick forming metal organic frameworks with exceptional stability. *J. Am. Chem. Soc.* 130 (42), 13850–13851.
- Cecilia, J.A., Vilarrasa-García, E., García-Sancho, C., Saboya, R.M.A., Azevedo, D.C.S., Cavalcante, C.L., Rodríguez-Castellón, E., 2016. Functionalization of hollow silica microspheres by impregnation or grafted of amine groups for the CO₂ capture. *Int. J. Greenh. Gas Control* 52, 344–356. doi:10.1016/j.jggc.2016.07.018.
- Chacartegui, R., Alovizio, A., Ortiz, C., Valverde, J.M., Verda, V., Becerra, J.A., 2016. Thermochemical energy storage of concentrated solar power by integration of the calcium looping process and a CO₂ power cycle. *Appl. Energy* 173, 589–605. doi:10.1016/j.apenergy.2016.04.053.
- Chagas, J.A.O., Crispim, G.O., Pinto, B.P., San Gil, R.A.S., Mota, C.J.A., 2020. Synthesis, characterization, and CO₂ uptake of adsorbents prepared by hydrothermal carbonization of chitosan. *ACS Omega* 5 (45), 29520–29529. doi:10.1021/ac-somega.0c04470.
- Chaikittisilp, W., Kim, H.-J., Jones, C.W., 2011. Mesoporous alumina-supported amines as potential steam-stable adsorbents for capturing CO₂ from simulated flue gas and ambient air. *Energy Fuels* 25 (11), 5528–5537. doi:10.1021/ef201224v.
- Chaikittisilp, W., Lunn, J.D., Shantz, D.F., Jones, C.W., 2011. Poly (L-lysine) brush-mesoporous silica hybrid material as a biomolecule-based adsorbent for CO₂ capture from simulated flue gas and air. *Chemistry* 17 (38), 10556–10561. doi:10.1002/chem.201101480.
- Chakma, A., 1995. An energy efficient mixed solvent for the separation of CO₂. *Energy Convers. Manage.* 36 (6–9), 427–430. doi:10.1016/0196-8904(95)00036-D.
- Chakraborty, A., Maji, T.K., 2014. Mg-MOF-74@SBA-15 hybrids: Synthesis, characterization, and adsorption properties. *APL Mater.* 2 (12). doi:10.1063/1.4902816.
- Chan, H.X.M., Yap, E.H., Ho, J.H., 2013. Overview of axial compression technology for direct capture of CO₂. *Adv. Mater. Res.* 744, 392–395. doi:10.4028/www.scientific.net/AMR.744.392.
- Chan, W., Lei, X., Chang, F., Li, H., 2020. Thermodynamic analysis and optimization of Allam cycle with a reheating configuration. *Energy Convers. Manage.* 224, 113382.
- Chan, W., Li, H., Li, X., Chang, F., Wang, L., Feng, Z., 2021. Exergoeconomic analysis and optimization of the Allam cycle with liquefied natural gas cold exergy utilization. *Energy Convers. Manage.* 235, 113972.
- Chandra, S., Kandambeth, S., Biswal, B.P., Lukose, B., Kunjir, S.M., Chaudhary, M., Babarao, R., Heine, T., Banerjee, R., 2013. Chemically stable multilayered covalent organic nanosheets from covalent organic frameworks via mechanical delamination. *J. Am. Chem. Soc.* 135 (47), 17853–17861.
- Chang, M.-H., Chen, W.-C., Huang, C.-M., Liu, W.-H., Chou, Y.-C., Chang, W.-C., Chen, W., Cheng, J.-Y., Huang, K.-E., Hsu, H.-W., 2014. Design and experimental testing of a 1.9 MWth calcium looping pilot plant. *Energy Procedia* 63, 2100–2108.
- Chao, C., Deng, Y., Dewil, R., Baeyens, J., Fan, X., 2021. Post-combustion carbon capture. *Renew. Sustain. Energy Rev.* 138, 110490. doi:10.1016/j.rser.2020.110490.
- Chatzisteriou, C.C., Kikkinides, E.S., Georgiadis, M.C., 2022. Recent advances on the modeling and optimization of CO₂ capture processes. *Comput. Chem. Eng.* 165. doi:10.1016/j.compchemeng.2022.107938, 107938-107938.

- Chauvy, R., Dubois, L., 2022. Life cycle and techno-economic assessments of direct air capture processes: An integrated review. *Int. J. Energy Res.* 46 (8), 10320–10344. doi:10.1002/er.7884.
- Chavez, H., Larachi, F., 2009. Analysis of flow in rotating packed beds via CFD simulations—Dry pressure drop and gas flow maldistribution. *Chemical Engineering Science* 64(9), 2113–2126. <https://doi.org/10.1016/j.ces.2009.01.019>.
- Cheah, W.Y., Show, P.L., Chang, J.S., Ling, T.C., Juan, J.C., 2015. Biosequestration of atmospheric CO₂ and flue gas-containing CO₂ by microalgae. *Bioresour. Technol.* 184, 190–201. doi:10.1016/j.biortech.2014.11.026.
- Chen, Y., Ho, W.S.W., 2016. High-molecular-weight polyvinylamine/piperazine glycinate membranes for CO₂ capture from flue gas. *J. Membr. Sci.* 514, 376–384. doi:10.1016/j.memsci.2016.05.005.
- Chen, J., Wang, F., 2014. Cost reduction of CO₂ capture processes using reinforcement learning based iterative design: A pilot-scale absorption-stripping system. *Separation and Purification Technology* 122, 149–158.
- Chen, S.J., Yu, B.Y., 2021. Rigorous simulation and techno-economic evaluation on the hybrid membrane/cryogenic distillation processes for air separation. *J. Taiwan Instit. Chem. Eng.* 127, 56–68. doi:10.1016/j.jtice.2021.08.001.
- Chen, B., Ji, Y., Xue, M., Fronczek, F.R., Hurtado, E.J., Mondal, J.U., Liang, C., Dai, S., 2008. Metal-organic framework with rationally tuned micropores for selective adsorption of water over methanol. *Inorg. Chem.* 47 (13), 5543–5545.
- Chen, C., Yang, S.T., Ahn, W.S., Ryoo, R., 2009. Amine-impregnated silica monolith with a hierarchical pore structure: enhancement of CO₂ capture capacity. *Chem. Commun. (Camb.)* (24) 3627–3629. doi:10.1039/b905589d.
- Chen, S., Kobayashi, K., Miyata, Y., Imazu, N., Saito, T., Kitaura, R., Shinohara, H., 2009. Morphology and melting behavior of ionic liquids inside single-walled carbon nanotubes. *J. Am. Chem. Soc.* 131 (41), 14850–14856. doi:10.1021/ja904283d.
- Chen, C., Son, W.-J., You, K.-S., Ahn, J.-W., Ahn, W.-S., 2010. Carbon dioxide capture using amine-impregnated HMS having textural mesoporosity. *Chem. Eng. J.* 161 (1–2), 46–52. doi:10.1016/j.cej.2010.04.019.
- Chen, L., Yong, S.Z., Ghoniem, A.F., 2012. Oxy-fuel combustion of pulverized coal: Characterization, fundamentals, stabilization and CFD modeling. *Prog. Energy Combust. Sci.* 38 (2), 156–214. doi:10.1016/j.peccs.2011.09.003.
- Chen, X.Y., Vinh-Thang, H., Rodrigue, D., Kallaguine, S., 2012. Amine-functionalized MIL-53 metal-organic framework in polyimide mixed matrix membranes for CO₂/CH₄ separation. *Ind. Eng. Chem. Res.* 51 (19), 6895–6906. doi:10.1021/ie3004336.
- Chen, C., Kim, S.-S., Cho, W.-S., Ahn, W.-S., 2015. Polyethyleneimine-incorporated zeolite 13X with mesoporosity for post-combustion CO₂ capture. *Appl. Surf. Sci.* 332, 167–171. doi:10.1016/j.apsusc.2015.01.106.
- Chen, S., Chen, S., Fei, X., Zhang, Y., Qin, L., 2015. Solubility and Characterization of CO₂ in 40 mass% N-ethylmonoethanolamine solutions: explorations for an efficient nonaqueous solution. *Ind. Eng. Chem. Res.* 54 (29), 7212–7218. doi:10.1021/acs.iecr.5b01654.
- Chen, W., van der Ham, L., Nijmeijer, A., Winnubst, L., 2015. Membrane-integrated oxy-fuel combustion of coal: Process design and simulation. *J. Membr. Sci.* 492, 461–470. doi:10.1016/j.memsci.2015.05.062.
- Chen, S., Chen, S., Zhang, Y., Qin, L., Guo, C., Chen, J., 2016. Species distribution of CO₂ absorption/desorption in aqueous and non-aqueous N-ethylmonoethanolamine solutions. *Int. J. Greenh. Gas Control* 47, 151–158. doi:10.1016/j.jggcc.2016.01.046.
- Chen, X., Xiong, Z., Qin, Y., Gong, B., Tian, C., Zhao, Y., Zhang, J., Zheng, C., 2016. High-temperature CO₂ sorption by Ca-doped Li₄SiO₄ sorbents. *Int. J. Hydrogen Energy* 41 (30), 13077–13085. doi:10.1016/j.ijhydene.2016.05.267.
- Chen, Y., Zhao, L., Wang, B., Dutta, P., Ho, W.S.W., 2016a. Amine-containing polymer/zeolite Y composite membranes for CO₂/N₂ separation. *J. Membr. Sci.* 497, 21–28. doi:10.1016/j.memsci.2015.09.036.
- Chen, Y., Zhao, L., Wang, B., Dutta, P., Winston Ho, W.S., 2016b. Amine-containing polymer/zeolite Y composite membranes for CO₂/N₂ separation. *J. Membr. Sci.* 497, 21–28. doi:10.1016/j.memsci.2015.09.036.
- Chen, C.H., Shimon, D., Lee, J.J., Mentink-Vigier, F., Hung, I., Sievers, C., Jones, C.W., Hayes, S.E., 2018. The “Missing” bicarbonate in CO₂ chemisorption reactions on solid amine sorbents. *J. Am. Chem. Soc.* 140 (28), 8648–8651. doi:10.1021/jacs.8b04520.
- Chen, G., Liu, W., Widenmeyer, M., Ying, P., Dou, M., Xie, W., Bubeck, C., Wang, L., Fyta, M., Feldhoff, A., Weidenkaff, A., 2019. High flux and CO₂-resistance of La_{0.6}Ca_{0.4}Co_{1-x}FexO_{3-δ} oxygen-transporting membranes. *J. Membr. Sci.* 590, 117082. doi:10.1016/j.memsci.2019.05.007.
- Chen, S., Yu, R., Soomro, A., Xiang, W., 2019. Thermodynamic assessment and optimization of a pressurized fluidized bed oxy-fuel combustion power plant with CO₂ capture. *Energy* 175, 445–455. doi:10.1016/j.energy.2019.03.090.
- Chen, J., Duan, L.B., Sun, Z.K., 2020. Review on the development of sorbents for calcium looping. *Energy Fuels* 34 (7), 7806–7836. doi:10.1021/acs.energyfuels.0c00682.
- Chen, X., Zhang, Z., Wu, L., Liu, X., Xu, S., Efome, J.E., Zhang, X., Li, N., 2020. Polymers of intrinsic microporosity having bulky substituents and cross-linking for gas separation membranes. *ACS Appl. Polym. Mater.* 2 (2), 987–995.
- Chen, Z., Jing, G., Lv, B., Zhou, Z., 2020. An efficient solid-liquid biphasic solvent for CO₂ capture: crystalline powder product and low heat duty. *ACS Sustain. Chem. Eng.* 8 (38), 14493–14503. doi:10.1021/acscchemeng.0c04616.
- Chen, G., Snyders, R., Britun, N., 2021. CO₂ conversion using catalyst-free and catalyst-assisted plasma-processes: Recent progress and understanding. *J. CO₂ Util.* 49, 101557. doi:10.1016/j.jcou.2021.101557.
- Chen, J., Duan, L.B., Donat, F., Muller, C.R., 2021. Assessment of the effect of process conditions and material characteristics of alkali metal salt promoted MgO-based sorbents on their CO₂ capture performance. *ACS Sustain. Chem. Eng.* 9 (19), 6659–6672. doi:10.1021/acscchemeng.1c00262.
- Chen, L.J., Deng, S., Zhao, R.K., Zhao, L., Li, S.J., Guo, Z.H., Lu, Y.N., Zhao, J., Wu, K.L., 2021. The thermodynamics-based benchmarking analysis on energy-efficiency performance of CO₂ capture technology: temperature swing adsorption as case study. *Energy Technol.* 9 (1). doi:10.1002/ente.202000756.
- Chen, R., Sheng, Q., Dai, X., Dong, B., 2021. Upgrading of sewage sludge by low temperature pyrolysis: Biochar fuel properties and combustion behavior. *Fuel* 300, 121007. doi:10.1016/j.fuel.2021.121007.
- Chen, W., Zhang, Z., Yang, C., Liu, J., Shen, H., Yang, K., Wang, Z., 2020. PIM-based mixed-matrix membranes containing MOF-801/ionic liquid nanocomposites for enhanced CO₂ separation performance. *J. Membr. Sci.* 636, 119581. doi:10.1016/j.memsci.2021.119581.
- Chen, G., Feldhoff, A., Weidenkaff, A., Li, C., Liu, S., Zhu, X., Sunarso, J., Jiang, K., Wu, X.Y., Ghoniem, A.F., Yang, W., Xue, J., Wang, H., Shao, Z., Duffy, J.H., Brinkman, K.S., Tan, X., Zhang, Y., Jiang, H., Costa, R., Friedrich, K.A., Kriegel, R., 2022. Roadmap for sustainable mixed ionic-electronic conducting membranes. *Adv. Funct. Mater.* 32, 2105702. doi:10.1002/adfm.202105702.
- Chen, H., Dong, S., Zhang, Y., He, P., 2022. Robust structure regulation of geopolymer as novel efficient amine support to prepare high-efficiency CO₂ capture solid sorbent. *Chem. Eng. J.* 427. doi:10.1016/j.cej.2021.131577.
- Chen, K., Zhang, W., Bai, C., Deng, L., Zhao, Y., Zhang, L., Feng, D., Sun, S., Qin, Y., 2022. Modeling of single-particle char combustion under O₂/H₂O conditions: Effects of temperature and steam concentration. *Fuel Process. Technol.* 227, 107131. doi:10.1016/j.fuproc.2021.107131.
- Cheng, Y., Kondo, A., Noguchi, H., Kajiro, H., Urita, K., Ohba, T., Kaneko, K., Kanoh, H., 2009. Reversible structural change of Cu-MOF on exposure to water and its CO₂ adsorptivity. *Langmuir* 25 (8), 4510–4513.
- Cheng, H.H., Lai, C.C., Tan, C.S., 2013. Thermal regeneration of alkanolamine solutions in a rotating packed bed. *Int. J. Greenh. Gas Control* 16, 206–216. doi:10.1016/j.jggcc.2013.03.022.
- Cheng, Y., Zhai, L., Tong, M., Kundu, T., Liu, G., Ying, Y., Dong, J., Wang, Y., Zhao, D., 2018. Selective gas permeation in mixed matrix membranes accelerated by hollow ionic covalent organic polymers. *ACS Sustain. Chem. Eng.* 7 (1), 1564–1573. doi:10.1021/acscchemeng.8b05333.
- Cheng, J., Liu, N., Hu, L., Li, Y., Wang, Y., Zhou, J., 2019. Polyethyleneimine entwined thermally-treated Zn/Co zeolitic imidazolate frameworks to enhance CO₂ adsorption. *Chem. Eng. J.* 364, 530–540. doi:10.1016/j.cej.2019.02.026.
- Cheng, Y., Zhai, L., Ying, Y., Wang, Y., Liu, G., Dong, J., Ng, D.Z., Khan, S.A., Zhao, D., 2019. Highly efficient CO₂ capture by mixed matrix membranes containing three-dimensional covalent organic framework fillers. *J. Mater. Chem. A* 7 (9), 4549–4560. doi:10.1039/C8TA10333J.
- Cheng, J., Wang, Y., Hu, L., Liu, N., Xu, J., Zhou, J., 2020a. Using lantern Zn/Co-ZIF nanoparticles to provide channels for CO₂ permeation through PEO-based MMMs. *J. Membr. Sci.* 597, 117644. doi:10.1016/j.memsci.2019.117644.
- Cheng, J., Wang, Y., Liu, N., Hou, W., Zhou, J., 2020b. Enhanced CO₂ selectivity of mixed matrix membranes with carbonized Zn/Co zeolitic imidazolate frameworks. *Appl. Energy* 272, 115179.
- Cheng, H., Song, H., Toan, S., Wang, B., Gasem, K.A.M., Fan, M., Cheng, F., 2021a. Experimental investigation of CO₂ adsorption and desorption on multi-type amines loaded HZSM-5 zeolites. *Chem. Eng. J.* 406, 126882. doi:10.1016/j.cej.2020.126882.
- Cheng, H., Song, H., Toan, S., Wang, B., Gasem, K.A.M., Fan, M., Cheng, F., 2021b. Experimental investigation of CO₂ adsorption and desorption on multi-type amines loaded HZSM-5 zeolites. *Chem. Eng. J.* 406. doi:10.1016/j.cej.2020.126882.
- Cheng, Z., Li, S., Liu, Y., Zhang, Y., Ling, Z., Yang, M., Jiang, L., Song, Y., 2022. Post-combustion CO₂ capture and separation in flue gas based on hydrate technology: a review. *Renew. Sustain. Energy Rev.* 154. doi:10.1016/j.rser.2021.111806.
- Cherbanski, R., Molga, E., 2009. Intensification of desorption processes by use of microwaves—An overview of possible applications and industrial perspectives. *Chem. Eng. Process-Process Intensif.* 48 (1), 48–58. doi:10.1016/j.cep.2008.01.004.
- Chern, R.T., Koros, W.J., Sanders, E.S., Yui, R., 1983. Second component[†] effects in sorption and permeation of gases in glassy polymers. *J. Membr. Sci.* 15 (2), 157–169. doi:10.1016/S0376-7388(00)80395-6.
- Chi, J., Zhao, L., Wang, B., Li, Z., Xiao, Y., Duan, Y., 2014. Thermodynamic performance assessment and comparison of IGCC with solid cycling process for CO₂ capture at high and medium temperatures. *Int. J. Hydrog. Energy* 39 (12), 6479–6491.
- Chi, W.S., Sundell, B.J., Zhang, K., Harrigan, D.J., Hayden, S.C., Smith, Z.P., 2019. Mixed-matrix membranes formed from multi-dimensional metal-organic frameworks for enhanced gas transport and plasticization resistance. *ChemSusChem* 12 (11), 2355–2360. doi:10.1002/cssc.201900623.
- Chichilnisky, G., 2021. 21 Dec NOAA Zurich 2021. Global Thermostat.
- Chirone, R., Paulillo, A., Coppola, A., Scala, F., 2022. Carbon capture and utilization via calcium looping, sorption enhanced methanation and green hydrogen: A techno-economic analysis and life cycle assessment study. *Fuel* 328, 125255. doi:10.1016/j.fuel.2022.125255.
- Chisalita, D.-A., Cormos, C.-C., 2019. Techno-economic assessment of hydrogen production processes based on various natural gas chemical looping systems with carbon capture. *Energy* 181, 331–344.
- Chiwaye, N., Majazi, T., Daramola, M.O., 2021. Optimisation of post-combustion carbon dioxide capture by use of a fixed site carrier membrane. *Int. J. Greenh. Gas Control* 104, 103182. doi:10.1016/j.jggcc.2020.103182.
- Cho, S.-H., Park, J.-H., Beum, H.-T., Han, S.-S., Kim, J.-N., 2004. A 2-stage PSA process for the recovery of CO₂ from flue gas and its power consumption. *Stud. Surf. Sci. Catal.* 153, 405–410.
- Choi, E.Y., Park, K., Yang, C.M., Kim, H., Son, J.H., Lee, S.W., Lee, Y.H., Min, D., Kwon, Y.U., 2004. Benzene-templated hydrothermal synthesis of metal-organic frameworks with selective sorption properties. *Chem.-A Eur. J.* 10 (21), 5535–5540.
- Choi, S., Drese, J.H., Jones, C.W., 2009. Adsorbent materials for carbon dioxide capture from large anthropogenic point sources. *ChemSusChem* 2 (9), 796–854. doi:10.1002/cssc.200900036.

- Choi, S., Watanabe, T., Bae, T.H., Sholl, D.S., Jones, C.W., 2012. Modification of the Mg/DOBDC MOF with amines to enhance CO₂ adsorption from ultradilute gases. *J. Phys. Chem. Lett.* 3 (9), 1136–1141. doi:10.1021/jz300328j.
- Choi, W., Min, K., Kim, C., Ko, Y.S., Jeon, J.W., Seo, H., Park, Y.K., Choi, M., 2016. Epoxide-functionalization of polyethyleneimine for synthesis of stable carbon dioxide adsorbent in temperature swing adsorption. *Nat. Commun.* 7, 12640. doi:10.1038/ncomms12640.
- Chorowski, M., Gizicki, W., 2015. Technical and economic aspects of oxygen separation for oxy-fuel purposes. *Arch. Thermodyn.* 36 (1), 157–170. doi:10.1515/aoter-2015-0011.
- Chuah, C.Y., Lee, J., Bao, Y., Song, J., Bae, T.-H., 2021. High-performance porous carbon-zeolite mixed-matrix membranes for CO₂/N₂ separation. *J. Membr. Sci.* 622. doi:10.1016/j.memsci.2020.119031.
- Chuah, C.Y., Lee, J., Song, J., Bae, T.H., 2021. Carbon molecular sieve membranes comprising graphene oxides and porous carbon for CO₂/N₂ separation. *Membranes (Basel)* 11 (4). doi:10.3390/membranes11040284.
- Chungsyng Lu, H.B., Wu, B., Su, F., Hwang, J.F., 2008. Comparative study of CO₂ capture by carbon nanotubes, activated carbons, and zeolites. *Energy Fuels* 22, 3050–3056.
- Ciftja, A.F., Hartono, A., Svendsen, H.F., 2014. Experimental study on carbamate formation in the AMP-CO₂-H₂O system at different temperatures. *Chem. Eng. Sci.* 107, 317–327. doi:10.1016/j.ces.2013.12.028.
- Clauss, M., Merel, J., Meunier, F., 2011. Numerical parametric study on CO₂ capture by indirect thermal swing adsorption. *Int. J. Greenh. Gas Control* 5 (5), 1206–1213. doi:10.1016/j.ijggc.2011.05.036.
- Clifford, C., 2022. From milligrams to gigatons: Startup that sucks carbon dioxide from the air is building a big plant in Iceland. CNBC.
- Clocic, D., Younes, M., 2003. A new method for CO₂ capture: frosting CO₂ at atmospheric pressure. In: Gale, J., Kaya, Y. (Eds.), *Greenhouse Gas Control Technologies - 6th International Conference*. Pergamon, Oxford, pp. 155–160. doi:10.1016/B978-008044276-1/50025-8.
- Clocic, D., Hitti, R.E., Younes, M., Bill, A., Casier, F., 2005a. CO₂ capture by anti-sublimation Thermo-economic process evaluation.
- Clocic, D., Younes, M., Bill, A., 2005b. Test results of CO₂ capture by anti-sublimation capture efficiency and energy consumption for boiler plants. In: Rubin, E.S., Keith, D.W., Gilboy, C.F., Wilson, M., Morris, T., Gale, J., Thambimuthu, K. (Eds.), *Greenhouse Gas Control Technologies 7*. Elsevier Science Ltd, Oxford, pp. 1775–1780. doi:10.1016/B978-008044704-9/50210-X.
- Cobden, P.D., Lukashuk, L., de Water, L.v., Lundqvist, M., Manzolini, G., Cormos, C.-C., van Dijk, C., Mancuso, L., Johns, J., Bellqvist, D., 2018. Stepwise project: Sorption-enhanced water-gas shift technology to reduce carbon footprint in the iron and steel industry.
- Coenen, K., Gallucci, F., Hensen, E., van Sint Annaland, M., 2019. Kinetic model for adsorption and desorption of H₂O and CO₂ on hydrotalcite-based adsorbents. *Chem. Eng. J.* 355, 520–531. doi:10.1016/j.cej.2018.08.175.
- Cohen, D.T., Zhang, C., Fadzén, C.M., Mijalis, A.J., Hie, L.N., Johnson, K.D., Shriver, Z., Plante, O., Miller, S.J., Buchwald, S.L., Pentelute, B.L., 2019. A chemoselective strategy for late-stage functionalization of complex small molecules with polypeptides and proteins. *Nat. Chem.* 11 (1), 78–85. doi:10.1038/s41557-018-0154-0.
- Colelli, G., Chacartegui, R., Ortiz, C., Carro, A., Arena, A.P., Verda, V., 2022. Life cycle and environmental assessment of calcium looping (CaL) in solar thermochemical energy storage. *Energy Convers. Manage.* 257, 14. doi:10.1016/j.enconman.2022.115428.
- Colombo, V., Galli, S., Choi, H.J., Han, G.D., Maspero, A., Palmisano, G., Masciocchi, N., Long, J.R., 2011. High thermal and chemical stability in pyrazolate-bridged metal-organic frameworks with exposed metal sites. *Chem. Sci.* 2 (7), 1311–1319.
- Cooper, A.I., 2009. Conjugated microporous polymers. *Adv. Mater.* 21 (12), 1291–1295. doi:10.1002/adma.200801971.
- Corra, A., Fornés, V., Martín-Aranda, R.M., Rey, F., 1992. Determination of base properties of hydrotalcites: condensation of benzaldehyde with ethyl acetoacetate. *J. Catal.* 134 (1), 58–65. doi:10.1016/0021-9517(92)90209-Z.
- Cormos, C.-C., 2011. Evaluation of power generation schemes based on hydrogen-fuelled combined cycle with carbon capture and storage (CCS). *Int. J. Hydrogen Energy* 36 (5), 3726–3738. doi:10.1016/j.ijhydene.2010.12.042.
- Cormos, C.-C., 2015. Assessment of chemical absorption/adsorption for post-combustion CO₂ capture from Natural Gas Combined Cycle (NGCC) power plants. *Appl. Therm. Eng.* 82, 120–128. doi:10.1016/j.applthermaleng.2015.02.054.
- Cormos, C.-C., 2018. Techno-economic evaluations of copper-based chemical looping air separation system for oxy-combustion and gasification power plants with carbon capture. *Energies* 11 (11). doi:10.3390/en11113095, 3095–3095.
- Cormos, C.C., 2020. Energy and cost efficient manganese chemical looping air separation cycle for decarbonized power generation based on oxy-fuel combustion and gasification. *Energy* 191. doi:10.1016/j.energy.2019.116579, 116579–116579.
- Cortes Garcia, G.E., van der Schaaf, J., Kiss, A.A., 2017. A review on process intensification in HiGeC distillation. *J. Chem. Technol. Biotechnol.* 92 (6), 1136–1156. doi:10.1002/jctb.5206.
- Cote, A.P., Benin, A.I., Ockwig, N.W., O'Keeffe, M., Matzger, A.J., Yaghi, O.M., 2005. Porous, crystalline, covalent organic frameworks. *Science* 310 (5751), 1166–1170.
- Cova, F., Amica, G., Kohopää, K., Blanco, M.V., 2019. Time-resolved synchrotron powder X-ray diffraction studies on the synthesis of Li₆SiO₆ and its reaction with CO₂. *Inorg. Chem.* 58 (2), 1040–1047. doi:10.1021/acs.inorgchem.8b01297.
- Creamer, A.E., Gao, B., Zhang, M., 2014. Carbon dioxide capture using biochar produced from sugarcane bagasse and hickory wood. *Chem. Eng. J.* 249, 174–179.
- Croiset, E., Thambimuthu, K.V., 2001. NO_x and SO₂ emissions from O₂-CO₂ recycle coal combustion. *Fuel* 80 (14), 2117–2121. doi:10.1016/S0016-2361(00)00197-6.
- Cui, S., Cheng, W., Shen, X., Fan, M., Russell, A., Wu, Z., Yi, X., 2011. Mesoporous amine-modified SiO₂ aerogel: a potential CO₂ sorbent. *Energy Environ. Sci.* 4 (6). doi:10.1039/c0ee00442a.
- Cui, S., Cheng, W.W., Shen, X.D., Fan, M.H., Russell, A., Wu, Z.W., Yi, X.B., 2011. Mesoporous amine-modified SiO₂ aerogel: a potential CO₂ sorbent. *Energy Environ. Sci.* 4 (6), 2070–2074. doi:10.1039/c0ee00442a.
- Cui, G., Wang, J., Zhang, S., 2016. Active chemisorption sites in functionalized ionic liquids for carbon capture. *Chem. Soc. Rev.* 45 (15), 4307–4339. doi:10.1039/c5cs00462d.
- Cui, S., Yu, S.W., Lin, B.L., Shen, X.D., Zhang, X., Gu, D.M., 2017. Preparation of amine-modified SiO₂ aerogel from rice husk ash for CO₂ adsorption. *J. Porous Mater.* 24 (2), 455–461. doi:10.1007/s10934-016-0280-2.
- Cui, H.J., Zhang, Q.M., Hu, Y.W., Peng, C., Fang, X.C., Cheng, Z.M., Galvita, V.V., Zhou, Z.M., 2018. Ultrafast and stable CO₂ capture using alkali metal salt-promoted MgO-CaCO₃ sorbents. *ACS Appl. Mater. Interfaces* 10 (24), 20611–20620. doi:10.1021/acsami.8b05829.
- Cui, H., Cheng, Z., Zhou, Z., 2020. Unravelling the role of alkaline earth metal carbonates in intermediate temperature CO₂ capture using alkali metal salt-promoted MgO-based sorbents. *J. Mater. Chem. A* 8 (35), 18280–18291. doi:10.1039/D0TA06170K.
- Cullinane, J.T., Rochelle, G.T., 2004. Carbon dioxide absorption with aqueous potassium carbonate promoted by piperazine. *Chem. Eng. Sci.* 59 (17), 3619–3630. doi:10.1016/j.ces.2004.03.029.
- Custelcean, R., Garrabrant, K.A., Agullo, P., Williams, N.J., 2021. Direct air capture of CO₂ with aqueous peptides and crystalline guanidines. *Cell Rep. Phys. Sci.* 2 (4), 100385. doi:10.1016/j.xcrp.2021.100385.
- Czaun, M., Goepfert, A., May, R.B., Peltier, D., Zhang, H., Prakash, G.K.S., Olah, G.A., 2013. Organoamines-grafted on nano-sized silica for carbon dioxide capture. *J. CO₂ Util.* 1, 1–7. doi:10.1016/j.jcou.2013.03.007.
- D'Alessandro, D.M., Smit, B., Long, J.R., 2010. Carbon dioxide capture: prospects for new materials. *Angew. Chem. Int. Ed.* 49 (35), 6058–6082. doi:10.1002/anie.201000431.
- Dai, Z., Ansaloni, L., Deng, L., 2016. Recent advances in multi-layer composite polymeric membranes for CO₂ separation: a review. *Green Energy Environ.* 1 (2), 102–128. doi:10.1016/j.gee.2016.08.001.
- Dai, Z., Deng, J., Ansaloni, L., Janakiram, S., Deng, L., 2019a. Thin-film-composite hollow fiber membranes containing amino acid salts as mobile carriers for CO₂ separation. *J. Membr. Sci.* 578, 61–68. doi:10.1016/j.memsci.2019.02.023.
- Dai, Z., Fabio, S., Giuseppe Marino, N., Riccardo, C., Deng, L., 2019b. Field test of a pre-pilot scale hollow fiber facilitated transport membrane for CO₂ capture. *Int. J. Greenh. Gas Control* 86, 191–200. doi:10.1016/j.ijggc.2019.04.027.
- Dal Pozzo, A., Armutulu, A., Rekhina, M., Abdala, P.M., Müller, C.R., 2019. CO₂ uptake and cyclic stability of MgO-based CO₂ sorbents promoted with alkali metal nitrates and their eutectic mixtures. *ACS Appl. Energy Mater.* 2 (2), 1295–1307. doi:10.1021/acsaeam.8b01852.
- Danaci, D., et al., 2020. Exploring the limits of adsorption-based CO₂ capture using MOFs with PVSA – from molecular design to process economics. *Molecular Systems Design & Engineering* 5 (1), 212–231.
- Danckwerts, P.V., 1970. Gas-liquid reactions.
- Danckwerts, P.V., 1979. The reaction of CO₂ with ethanolamines. *Chem. Eng. Sci.* 34 (4), 443–446. doi:10.1016/0009-2509(79)85087-3.
- Darde, V., Thomsen, K., van Well, W.J., Stenby, E.H., 2009. Chilled ammonia process for CO₂ capture. *Energy Procedia* 1 (1), 1035–1042.
- Darunte, L.A., Oetomo, A.D., Walton, K.S., Sholl, D.S., Jones, C.W., 2016. Direct air capture of CO₂ using amine functionalized MIL-101 (Cr). *ACS Sustain. Chem. Eng.* 4 (10), 5761–5768. doi:10.1021/acsuschemeng.6b01692.
- Dave, A., Dave, M., Huang, Y., Rezvani, S., Hewitt, N., 2016. Process design for CO₂ absorption from syngas using physical solvent DMEPEG. *Int. J. Greenh. Gas Control* 49, 436–448. doi:10.1016/j.ijggc.2016.03.015.
- Davidson, J., 2007. Performance and costs of power plants with capture and storage of CO₂. *Energy* 32 (7), 1163–1176. doi:10.1016/j.energy.2006.07.039.
- Dawson, R., Cooper, A.I., Adams, D.J., 2012. Nanoporous organic polymer networks. *Prog. Polym. Sci.* 37 (4), 530–563. doi:10.1016/j.progpolymsci.2011.09.002.
- Debst, M., Klar, P.B., Barrier, N., Clatworthy, E.B., Grand, J., Laine, F., Brázda, P., Palatinus, L., Nesterenko, N., Boullay, P., 2020. Synthesis of discrete CHA zeolite nanocrystals without organic templates for selective CO₂ capture. *Angew. Chem. Int. Ed.* 59 (52), 23491–23495.
- Decardi-Nelson, B., Akachuku, A., Osei, P., Srisang, W., Pouryousefi, F., Idem, R., 2017. A flexible and robust model for low temperature catalytic desorption of CO₂ from CO₂-loaded amines over solid acid catalysts. *Chem. Eng. Sci.* 170, 518–529. doi:10.1016/j.ces.2016.12.068.
- Demessence, A., D'Alessandro, D.M., Foo, M.L., Long, J.R., 2009. Strong CO₂ binding in a water-stable, triazolate-bridged metal-organic framework functionalized with ethylenediamine. *J. Am. Chem. Soc.* 131 (25), 8784–8786.
- Deng, L., Hägg, M.-B., 2015. Fabrication and evaluation of a blend facilitated transport membrane for CO₂/CH₄ separation. *Ind. Eng. Chem. Res.* 54 (44), 11139–11150. doi:10.1021/acs.iecr.5b02971.
- Deng, L., Kim, T.-J., Hägg, M.-B., 2009. Facilitated transport of CO₂ in novel PVAm/PVA blend membrane. *J. Membr. Sci.* 340 (1), 154–163. doi:10.1016/j.memsci.2009.05.019.
- Deng, S.B., Hu, B.Y., Chen, T., Wang, B., Huang, J., Wang, Y.J., Yu, G., 2015. Activated carbons prepared from peanut shell and sunflower seed shell for high CO₂ adsorption. *Adsorpt.-J. Int. Adsorpt. Soc.* 21 (1–2), 125–133. doi:10.1007/s10450-015-9655-y.
- Deng, J., Dai, Z., Deng, L., 2020a. Effects of the morphology of the ZIF on the CO₂ separation performance of MMMs. *Ind. Eng. Chem. Res.* 59 (32), 14458–14466.

- Deng, J., Dai, Z., Hou, J., Deng, L., 2020b. Morphologically tunable MOF nanosheets in mixed matrix membranes for CO₂ separation. *Chem. Mater.* 32 (10), 4174–4184. doi:10.1021/acs.chemmater.0c00020.
- Deng, G., Wang, Y., Zong, X., Luo, J., Wang, X., Zhang, C., Xue, S., 2021. Structure evolution in carbon molecular sieve membranes derived from binaphthol-6FDA polyimide and their gas separation performance. *J. Ind. Eng. Chem.* 94, 489–497. doi:10.1016/j.jiec.2020.11.024.
- Deng, Y., Li, J., Miao, Y., Izikowitz, D., 2021. A comparative review of performance of nanomaterials for direct air capture. *Energy Rep.* 7, 3506–3516. doi:10.1016/j.egy.2021.06.002.
- Deng, L., Zhang, W., Sun, S., Bai, C., Zhao, Y., Feng, D., Zhang, L., Wu, J., 2021a. Effect of pressure on the structure and reactivity of demineralized coal during O₂/H₂O thermal conversion process. *Energy*, 122632 doi:10.1016/j.energy.2021.122632.
- Deng, L., Zhang, W., Sun, S., Bai, C., Zhao, Y., Feng, D., Zhang, L., Wu, J., 2021b. Study on the thermal conversion characteristics of demineralized coal char under pressurized O₂/H₂O atmosphere. *Fuel*, 122429 doi:10.1016/j.fuel.2021.122429.
- Deng, L., Zhao, Y., Sun, S., Feng, D., Zhang, W., 2022. Review on thermal conversion characteristics of coal in O₂/H₂O atmosphere. *Fuel Process. Technol.* 232, 107266. doi:10.1016/j.fuproc.2022.107266.
- Deutz, S., Bardow, A., 2021. Life-cycle assessment of an industrial direct air capture process based on temperature-vacuum swing adsorption. *Nat. Energy* 6 (2), 203–213. doi:10.1038/s41560-020-00771-9.
- Dewangan, N., Ashok, J., Sethia, M., Das, S., Pati, S., Kus, H., Kawi, S., 2019. Cobalt-based catalyst supported on different morphologies of alumina for non-oxidative propane dehydrogenation: effect of metal support interaction and Lewis acid sites. *ChemCatChem* 11 (19), 4923–4934. doi:10.1002/cctc.201900924.
- Di Giuliano, A., Gallucci, K., 2018. Sorption enhanced steam methane reforming based on nickel and calcium looping: a review. *Chem. Eng. Process. - Process Intensif.* 130, 240–252. doi:10.1016/j.ccep.2018.06.021.
- Diáf, A., Garcia, J.L., Beckman, E.J., 1994. Thermally reversible polymeric sorbents for acid gases: CO₂, SO₂, and NO_x. *J. Appl. Polym. Sci.* 53, 857–875.
- Diagne, D., Goto, M., Hirose, T., 1994. New PSA process with intermediate feed inlet position operated with dual refluxes: application to carbon dioxide removal and enrichment. *J. Chem. Eng. Jpn.* 27 (1), 85–89.
- Didas, S.A., Choi, S., Chaikittisilp, W., Jones, C.W., 2015. Amine-oxide hybrid materials for CO₂ capture from ambient air. *Acc. Chem. Res.* 48 (10), 2680–2687. doi:10.1021/acs.accounts.5b00284.
- Diego, M.E., Arias, B., 2020. Impact of load changes on the carbonator reactor of a 1.7 MWh calcium looping pilot plant. *Fuel Process. Technol.* 200, 106307. doi:10.1016/j.fuproc.2019.106307.
- Dieter, H., Hawthorne, C., Zieba, M., Scheffknecht, G., 2013. Progress in calcium looping post combustion CO₂ capture: successful pilot scale demonstration. *Energy Procedia* 37, 48–56. doi:10.1016/j.egypro.2013.05.084.
- Dillon, D.J., Panesar, R.S., Wall, R.A., Allam, R.J., White, V., Gibbins, J., Haines, M.R., 2005. Ox-combustion processes for CO₂ capture from advanced supercritical PF and NGCC power plant. *Greenh. Gas Control Technol.* 211–220. doi:10.1016/B978-008044704-9/50022-7.
- Dillon, D., 2005. Proc 7th Intern. Conf. Greenhouse Gas Control Technol.
- Ding, Y., Alpay, E., 2000. Equilibria and kinetics of CO₂ adsorption on hydrotalcite adsorbent. *Chem. Eng. Sci.* 55 (17), 3461–3474. doi:10.1016/S0009-2509(99)00596-5.
- Ding, Y., Alpay, E., 2001. High temperature recovery of CO₂ from flue gases using hydrotalcite adsorbent. *Process. Saf. Environ. Prot.* 79 (1), 45–51. doi:10.1205/095758201531130.
- Ding, L., Wei, Y., Li, L., Zhang, T., Wang, H., Xue, J., Ding, L.-X., Wang, S., Caro, J., Gogotsi, Y., 2018. MXene molecular sieving membranes for highly efficient gas separation. *Nat. Commun.* 9 (1), doi:10.1038/s41467-017-02529-6.
- Ding, M., Fläig, R.W., Jiang, H.-L., Yaghi, O.M., 2019. Carbon capture and conversion using metal-organic frameworks and MOF-based materials. *Chem. Soc. Rev.* 48 (10), 2783–2828.
- Dissanayake, P.D., You, S.M., Igalavithana, A.D., Xia, Y.F., Bhatnagar, A., Gupta, S., Kua, H.W., Kim, S., Kwon, J.H., Tsang, D.C.W., Ok, Y.S., 2020. Biochar-based adsorbents for carbon dioxide capture: A critical review. *Renew. Sustain. Energy Rev.* 119. doi:10.1016/j.rser.2019.109582.
- Donat, F., Müller, C.R., 2022. Prospects of MgO-based sorbents for CO₂ capture applications at high temperatures. *Curr. Opin. Green Sustain. Chem.*, 100645 doi:10.1016/j.cogsc.2022.100645.
- Donat, F., Florin, N.H., Anthony, E.J., Fennell, P.S., 2012. Influence of high-temperature steam on the reactivity of CaO sorbent for CO₂ capture. *Environ. Sci. Technol.* 46 (2), 1262–1269. doi:10.1021/es202679w.
- Dong, Y., Li, D., 2012. Efficient and effective algorithms for training single-hidden-layer neural networks. *Pattern Recognit. Lett.* 33 (5), 554–558. doi:10.1016/j.patrec.2011.12.002.
- Dong, W., Chen, X., Yu, F., Wu, Y., 2015. Na₂CO₃/MgO/Al₂O₃ solid sorbents for low-temperature CO₂ capture. *Energy Fuels* 29 (2), 968–973. doi:10.1021/ef502400s.
- Dong, G., Zhang, Y., Hou, J., Shen, J., Chen, V., 2016. Graphene oxide nanosheets based novel facilitated transport membranes for efficient CO₂ capture. *Ind. Eng. Chem. Res.* 55 (18), 5403–5414. doi:10.1021/acs.iecr.6b01005.
- Dong, J., Tang, Y., Nzihou, A., Weiss-Hortala, E., 2020. Effect of steam addition during carbonation, calcination or hydration on re-activation of CaO sorbent for CO₂ capture. *J. CO₂ Util.* 39, 101167. doi:10.1016/j.jcou.2020.101167.
- Dong, H., Cui, H., Zhou, Z., 2022. Promoting effects of Li₃PO₄ and CaCO₃ on the intermediate-temperature CO₂ adsorption over molten NaNO₃-promoted MgO-based sorbents. *Chem. Eng. J.* 442, 136133. doi:10.1016/j.cej.2022.136133.
- Doong, S.J., Ho, W.S., Mastondrea, R.P., 1995. Prediction of flux and selectivity in pervaporation through a membrane. *J. Membr. Sci.* 107 (1), 129–146. doi:10.1016/0376-7388(95)00109-P.
- Drechsler, C., Agar, D.W., 2020. Investigation of water co-adsorption on the energy balance of solid sorbent based direct air capture processes. *Energy* 192, 116587. doi:10.1016/j.energy.2019.116587.
- Du, N., Park, H.B., Robertson, G.P., Dal-Cin, M.M., Visser, T., Scoles, L., Guiver, M.D., 2011. Polymer nanosieve membranes for CO₂-capture applications. *Nat. Mater.* 10 (5), 372–375. doi:10.1038/nmat2989.
- Du, Y., Fan, Z., Guo, T., Xu, J., Han, Z., Pan, Y., Xiao, H., Sun, Y., Yan, Q., 2020. Characteristics of as-prepared biochar derived from catalytic pyrolysis within moderate-temperature ionic liquid for CO₂ uptake. *Can. J. Chem. Eng.* 98 (3), 690–704. doi:10.1002/cjce.23671.
- Duan, K., Wang, J., Zhang, Y., Liu, J., 2019. Covalent organic frameworks (COFs) functionalized mixed matrix membrane for effective CO₂/N₂ separation. *J. Membr. Sci.* 572, 588–595. doi:10.1016/j.memsci.2018.11.054.
- Duan, Y., Duan, L., Wang, J., Anthony, E.J., 2019. Observation of simultaneously low CO, NO_x and SO₂ emission during oxy-coal combustion in a pressurized fluidized bed. *Fuel* 242, 374–381. doi:10.1016/j.fuel.2019.01.048.
- Duan, D.L., Chen, D.H., Huang, L.Y., Zhang, Y.C., Zhang, Y.Y., Wang, Q., Xiao, G.S., Zhang, W.L., Lei, H.W., Ruan, R., 2021. Activated carbon from lignocellulosic biomass as catalyst: A review of the applications in fast pyrolysis process. *J. Anal. Appl. Pyrol.* 158. doi:10.1016/j.jaap.2021.105246.
- Dubois, L., Thomas, D., 2018. Comparison of various configurations of the absorption-regeneration process using different solvents for the post-combustion CO₂ capture applied to cement plant flue gases. *Int. J. Greenh. Gas Control* 69, 20–35. doi:10.1016/j.jggc.2017.12.004.
- Duelli, G., Charitos, A., Diego, M.E., Stavroulakis, E., Dieter, H., Scheffknecht, G., 2015. Investigations at a 10kWh calcium looping dual fluidized bed facility: Limestone calcination and CO₂ capture under high CO₂ and water vapour atmosphere. *Int. J. Greenh. Gas Control* 33, 103–112. doi:10.1016/j.jggc.2014.12.006.
- Dunn, C.A., Shi, Z., Zhou, R., Gin, D.L., Noble, R.D., 2019. Cross-linked poly (ionic liquid)-ionic liquid-zeolite) mixed-matrix membranes for CO₂/CH₄ gas separations based on curable ionic liquid prepolymer. *Ind. Eng. Chem. Res.* 58 (11), 4704–4708. doi:10.1021/acs.iecr.8b06464.
- Dunne, J., Rao, M., Sircar, S., Gorte, R., Myers, A., 1996. Calorimetric heats of adsorption and adsorption isotherms. 2. O₂, N₂, Ar, CO₂, CH₄, C₂H₆, and SF₆ on NaX, H-ZSM-5, and Na-ZSM-5 zeolites. *Langmuir* 12 (24), 5896–5904.
- Dunstan, M.T., Southon, P.D., Kepert, C.J., Hester, J., Kimpton, J.A., Ling, C.D., 2011. Phase diagram, chemical stability and physical properties of the solid-solution Ba₄Nb₂-xTaxO₉. *J. Solid State Chem.* 184 (10), 2648–2654. doi:10.1016/j.jssc.2011.07.036.
- Dunstan, M.T., Liu, W., Pavan, A.F., Kimpton, J.A., Ling, C.D., Scott, S.A., Dennis, J.S., Grey, C.P., 2013. Reversible CO₂ adsorption by the 6H perovskite Ba₄Sb₂O₉. *Chem. Mater.* 25 (24), 4881–4891. doi:10.1021/cm402875v.
- Dunstan, M.T., Donat, F., Bork, A.H., Grey, C.P., Müller, C.R., 2021. CO₂ capture at medium to high temperature using solid oxide-based sorbents: fundamental aspects, mechanistic insights, and recent advances. *Chem. Rev.* 121 (20), 12681–12745. doi:10.1021/acs.chemrev.1c00100.
- Durá, G., Budarin, V.L., Castro-Osma, J.A., Shuttleworth, P.S., Quek, S.C.Z., Clark, J.H., North, M., 2016. Importance of micropore-mesopore interfaces in carbon dioxide capture by carbon-based materials. *Angew. Chem. Int. Ed.* 55 (32), 9173–9177. doi:10.1002/anie.201602226.
- Duran-Jimenez, G., Kostas, E.T., Stevens, L.A., Meredith, W., Erans, M., Hernandez-Montoya, V., Buttress, A., Uguna, C.N., Binner, E., 2021. Green and simple approach for low-cost bioproducts preparation and CO₂ capture. *Chemosphere* 279. doi:10.1016/j.chemosphere.2021.130512.
- Eason, J.P., Biegler, L.T., 2020. Model reduction in chemical process optimization. *De Gruyter, Boston* doi:10.1515/9783110499001-001.
- Ebner, A.D., Reynolds, S.P., Ritter, J.A., 2006. Understanding the adsorption and desorption behavior of CO₂ on a K-promoted hydrotalcite-like compound (HTlc) through nonequilibrium dynamic isotherms. *Ind. Eng. Chem. Res.* 45 (18), 6387–6392. doi:10.1021/ie060389k.
- Ebner, A.D., Reynolds, S.P., Ritter, J.A., 2007. Nonequilibrium kinetic model that describes the reversible adsorption and desorption behavior of CO₂ in a K-promoted hydrotalcite-like compound. *Ind. Eng. Chem. Res.* 46 (6), 1737–1744. doi:10.1021/ie061042k.
- Ebner, A.D., Gray, M.L., Chisholm, N.G., Black, Q.T., Mumford, D.D., Nicholson, M.A., Ritter, J.A., 2011. Suitability of a solid amine sorbent for CO₂ capture by pressure swing adsorption. *Ind. Eng. Chem. Res.* 50 (9), 5634–5641. doi:10.1021/ie2000709.
- Ebrahimzadeh, E., Matagi, J., Fazlollahi, F., Baxter, L.L., 2016. Alternative extractive distillation system for CO₂-ethane azeotrope separation in enhanced oil recovery processes. *Appl. Therm. Eng.* 96, 39–47. doi:10.1016/j.applthermaleng.2015.11.082.
- Eddoudi, M., Kim, J., Rosi, N., Vodak, D., Wächter, J., O'Keeffe, M., Yaghi, O.M., 2002. Systematic design of pore size and functionality in isoreticular MOFs and their application in methane storage. *Science* 295 (5554), 469–472.
- El Knidri, H., El Khalifaouy, R., Laajeb, A., Addaou, A., Lahsini, A., 2016. Eco-friendly extraction and characterization of chitin and chitosan from the shrimp shell waste via microwave irradiation. *Process. Saf. Environ. Prot.* 104, 395–405. doi:10.1016/j.psep.2016.09.020.
- El-Kaderi, H.M., Hunt, J.R., Mendoza-Cortés, J.L., Côté, A.P., Taylor, R.E., O'Keeffe, M., Yaghi, O.M., 2007. Designed synthesis of 3D covalent organic frameworks. *Science* 316 (5822), 268–272.
- El-Mahdy, A.F., Kuo, C.-H., Alshehri, A., Young, C., Yamauchi, Y., Kim, J., Kuo, S.-W., 2018. Strategic design of triphenylamine- and triphenyltriazine-based two-dimensional covalent organic frameworks for CO₂ uptake and energy storage. *J. Mater. Chem. A* 6 (40), 19532–19541.
- Elfvig, J., Sainio, T., 2021. Kinetic approach to modelling CO₂ adsorption from humid air using amine-functionalized resin: Equilibrium isotherms and

- column dynamics. *Chem. Eng. Sci.* 246, 116885. doi:10.1016/j.ces.2021.116885.
- Engels, S., Beggel, F., Modigell, M., Stadler, H., 2010. Simulation of a membrane unit for oxyfuel power plants under consideration of realistic BSCF membrane properties. *J. Membr. Sci.* 359 (1–2), 93–101. doi:10.1016/j.memsci.2010.01.048.
- Eoghain, P., Dillon, C.A.C., Barron, A.R., 2008. Synthesis, characterization, and carbon dioxide adsorption of covalently attached polythyleneimine functionalized single-wall carbon nanotubes. *ACS Nano* 2 (2), 156–164.
- EPRI Report, 2000. Interim Report #1000316 Dec.
- Er, H., Xu, Y., Zhao, H., 2019. Properties of mono-protic ionic liquids composed of hexylammonium and hexylethylenediaminium cations with trifluoroacetate and bis (trifluoromethylsulfonyl) imide anions. *J. Mol. Liq.* 276, 379–384. doi:10.1016/j.molliq.2018.11.132.
- Erans, M., Manovic, V., Anthony, E.J., 2016. Calcium looping sorbents for CO₂ capture. *Appl. Energy* 180, 722–742. doi:10.1016/j.apenergy.2016.07.074.
- Erucar, I., Keskin, S., 2016. Computational methods for MOF/polymer membranes. *Chem. Rec.* 16, 703–718. doi:10.1002/cr.201500275.
- Esfilari, R., Mehropooya, M., Moosavian, S.M.A., 2018. Thermodynamic assessment of an integrated biomass and coal co-gasification, cryogenic air separation unit with power generation cycles based on LNG vaporization. *Energy Convers. Manage.* 157, 438–451. doi:10.1016/j.enconman.2017.12.026.
- Exeberria-Benavides, M., Johnson, T., Cao, S., Zornoza, B., Coronas, J., Sanchez-Lainez, J., Sabteghadam, A., Liu, X., Andres-Garcia, E., Kaptejin, F., 2020. PBI mixed matrix hollow fiber membrane: Influence of ZIF-8 filler over H₂/CO₂ separation performance at high temperature and pressure. *Sep. Purif. Technol.* 237, 116347.
- Férey, G., Serre, C., Mellot-Draznieks, C., Millange, F., Surlblé, S., Dutour, J., Margiolaki, I., 2004. A hybrid solid with giant pores prepared by a combination of targeted chemistry, simulation, and powder diffraction. *Angew. Chem.* 116 (46), 6456–6461.
- Férey, G., Mellot-Draznieks, C., Serre, C., Millange, F., Dutour, J., Surlblé, S., Margiolaki, I., 2005. A chromium terephthalate-based solid with unusually large pore volumes and surface area. *Science* 309 (5743), 2040–2042.
- Fagerlund, J., Highfield, J., Zevenhoven, R., 2012. Kinetics studies on wet and dry gas-liquid carbonation of MgO and Mg (OH)₂ for CO₂ sequestration. *RSC Adv.* 2 (27), 10380–10393. doi:10.1039/C2RA21428H.
- Fajardý, M., Morris, J., Gurgel, A., Herzog, H., Mac Dowell, N., Paltsev, S., 2021. The economics of bioenergy with carbon capture and storage (BECCS) deployment in a 1.5°C or 2°C world. *Glob. Environ. Change* 68, doi:10.1016/j.gloenvcha.2021.102262.
- Fan, Y., Jia, X., 2022. Progress in amine-functionalized silica for CO₂ capture: important roles of support and amine structure. *Energy Fuels* 36 (3), 1252–1270. doi:10.1021/acs.energyfuels.1c03788.
- Fan, L.-S., Zeng, L., Wang, W., Luo, S., 2012. Chemical looping processes for CO₂ capture and carbonaceous fuel conversion—prospect and opportunity. *Energy Environ. Sci.* 5 (6), 7254–7280.
- Fan, X., Zhang, L., Zhang, G., Shu, Z., Shi, J., 2013. Chitosan derived nitrogen-doped microporous carbons for high performance CO₂ capture. *Carbon* 61, 423–430. doi:10.1016/j.carbon.2013.05.026.
- Fan, H., Mundstock, A., Feldhoff, A., Knebel, A., Gu, J., Meng, H., Caro, J.R., 2018. Covalent organic framework-covalent organic framework bilayer membranes for highly selective gas separation. *J. Am. Chem. Soc.* 140 (32), 10094–10098. doi:10.1021/jacs.8b05136.
- Fan, H., Peng, M., Strauss, I., Mundstock, A., Meng, H., Caro, J., 2021. MOF-in-COF molecular sieving membrane for selective hydrogen separation. *Nat. Commun.* 12 (1), 38.
- Fan, D., Özcan, A., Ramsahye, N.A., Maurin, G., Semino, R., 2022a. Putting Forward NUS-8-CO₂H/PIM-1 as a Mixed Matrix Membrane for CO₂ Capture. *ACS Appl. Mater. Interfaces* 14 (14), 16820–16829. doi:10.1021/acsmi.2c00909.
- Fan, D., Özcan, A., Shekhal, O., Semino, R., Eddaoudi, M., Maurin, G., 2022b. Engineering MOF surface defects in mixed matrix membranes: an effective strategy to enhance MOF/polymer adhesion and control interfacial gas transport. *J. Membr. Sci. Lett.* 2 (2), 100029.
- Fang, W., Liang, F., Cao, Z., Steinbach, F., Feldhoff, A., 2015. A mixed ionic and electronic conducting dual-phase membrane with high oxygen permeability. *Angew. Chem. Int. Ed.* 54, 4847–4850. doi:10.1002/anie.201411963.
- Fang, M., He, Z., Merkel, T.C., Okamoto, Y., 2018. High-performance perfluorodioxolane copolymer membranes for gas separation with tailored selectivity enhancement. *J. Mater. Chem. A* 6 (2), 652–658. doi:10.1039/C7TA09047A.
- Fang, X., Men, Y., Wu, F., Zhao, Q., Singh, R., Xiao, P., Du, T., Webley, P.A., 2019. Promoting CO₂ hydrogenation to methanol by incorporating adsorbents into catalysts: Effects of hydrothermalite. *Chem. Eng. J.* 378, 122052. doi:10.1016/j.cej.2019.122052.
- Fang, M., Yi, N., Di, W., Wang, T., Wang, Q., 2020. Emission and control of flue gas pollutants in CO₂ chemical absorption system – A review. *Int. J. Greenh. Gas Control* 93. doi:10.1016/j.jggc.2019.102904.
- Fang, Q.-X., Huang, W.-Q., Wang, H.N., 2020. Role of additives in silica-supported polyethyleneimine adsorbents for CO₂ adsorption. *Mater. Res. Exp.* 7 (3) 1010882053-1591/ab80eb.
- Farha, O.K., Yazaydin, A.O., Eryazici, I., Malliakas, C.D., Hauser, B.G., Kanatzidis, M.G., Nguyen, S.T., Snurr, R.Q., Hupp, J.T., 2010. De novo synthesis of a metal-organic framework material featuring ultrahigh surface area and gas storage capacities. *Nat. Chem.* 2 (11), 944–948. doi:10.1038/nchem.834.
- Farmahini, A.H., Krishnamurthy, S., Friedrich, D., Brandani, S., Sarkisov, L., 2018. From crystal to adsorption column: challenges in multiscale computational screening of materials for adsorption separation processes. *Ind. Eng. Chem. Res.* 57 (45), 15491–15511. doi:10.1021/acs.iecr.8b03065.
- Farooqui, A., Bose, A., Ferrero, D., Llorca, J., Santarelli, M., 2018. Techno-economic and exergetic assessment of an oxy-fuel power plant fueled by syngas produced by chemical looping CO₂ and H₂O dissociation. *J. CO₂ Util.* 27, 500–517.
- Fasili, M., Efimova, O., Breyer, C., 2019. Techno-economic assessment of CO₂ direct air capture plants. *J. Clean. Prod.* 224, 957–980. doi:10.1016/j.jclepro.2019.03.086.
- Favre, E., 2007. Carbon dioxide recovery from post-combustion processes: Can gas permeation membranes compete with absorption? *J. Membr. Sci.* 294 (1–2), 50–59. doi:10.1016/j.memsci.2007.02.007.
- Fayaz, M., Sayari, A., 2017. Long-term effect of steam exposure on CO₂ capture performance of amine-grafted silica. *ACS Appl. Mater. Interfaces* 9 (50), 43747–43754. doi:10.1021/acsmi.7b15463.
- Fazlollahi, F., Bown, A., Ebrahimzadeh, E., Baxter, L.L., 2015. Design and analysis of the natural gas liquefaction optimization process- CCC-ES (energy storage of cryogenic carbon capture). *Energy* 90, 244–257. doi:10.1016/j.energy.2015.05.139.
- Feng, D., Zhao, Y., Zhang, Y., Zhang, Z., Zhang, L., Gao, J., Sun, S., 2017. Synergistic effects of biochar structure and AAEM species on reactivity of H₂O-activated biochar from cyclone air gasification. *Int. J. Hydrogen Energy* 42 (25), 16045–16053. doi:10.1016/j.ijhydene.2017.05.153.
- Feng, S., Bu, M., Pang, J., Fan, W., Fan, L., Zhao, H., Yang, G., Guo, H., Kong, G., Sun, H., 2020. Hydrothermal stable ZIF-67 nanosheets via morphology regulation strategy to construct mixed-matrix membrane for gas separation. *J. Membr. Sci.* 593, 117404. doi:10.1016/j.memsci.2019.117404.
- Fennell, P.S., Pacciani, R., Dennis, J.S., Davidson, J.F., Hayhurst, A.N., 2007. The effects of repeated cycles of calcination and carbonation on a variety of different lime-stones, as measured in a hot fluidized bed of sand. *Energy Fuels* 21 (4), 2072–2081. doi:10.1021/ef060506o.
- Feron, P.H.M., Jansen, A.E., 2002. CO₂ separation with polyolefin membrane contactors and dedicated absorption liquids: performances and prospects. *Sep. Purif. Technol.* 27 (3), 231–242. doi:10.1016/S1383-5866(01)00207-6.
- Feron, P.H.M., Cousins, A., Jiang, K., Zhai, R., Garcia, M., 2020. An update of the benchmark post-combustion CO₂-capture technology. *Fuel* 273. doi:10.1016/j.fuel.2020.117776.
- Ferreira, T.J., Ribeiro, R.P.P.L., Mota, J.P.B., Rebelo, L.S.P.N., Esperança, J.M.S.S., Esteves, I.A.A.C., 2019. Ionic liquid-impregnated metal-organic frameworks for CO₂/CH₄ separation. *ACS Appl. Nano Mater.* doi:10.1021/acsnan.9b01936.s001.
- Figueroa, J.D., Fout, T., Plasynski, S., McIlvried, H., Srivastava, R.D., 2008. Advances in CO₂ capture technology—The U.S. department of energy’s carbon sequestration program. *Int. J. Greenh. Gas Control* 2 (1), 9–20. doi:10.1016/s1750-5836(07)00094-1.
- Finsy, V., Ma, L., Alaerts, L., De Vos, D.E., Baron, G.V., Denayer, J.F.M., 2009. Separation of CO₂/CH₄ mixtures with the MIL-53 (Al) metal-organic framework. *Microporous Mesoporous Mater.* 120 (3), 221–227. doi:10.1016/j.micromeso.2008.11.007.
- Flores-Segura, H., Torres, L.A., 1997. Enthalpies of formation of primary, secondary, and tertiary amineborane adducts in tetrahydrofuran solution. *Struct. Chem.* 8.
- Florio, C., Fiorentino, G., Corcelli, F., Ulgiati, S., Dumontet, S., Güsewiler, J., Eltrop, L., 2019. A life cycle assessment of biomethane production from waste feedstock through different upgrading technologies. *Energy*.
- Foong, S.Y., Liew, R.K., Yang, Y., Cheng, Y.W., Yek, P.N.Y., Wan Mahari, W.A., Lee, X.Y., Han, C.S., Vo, D.-V.N., Van Le, Q., Aghabashlo, M., Tabatabaie, M., Sonne, C., Peng, W., Lam, S.S., 2020. Valorization of biomass waste to engineered activated biochar by microwave pyrolysis: Progress, challenges, and future directions. *Chem. Eng. J.* 389, 124401. doi:10.1016/j.cej.2020.124401.
- Forano, C., Costantino, U., Prévot, V., Gueho, C.T., 2013. Chapter 14.1 - layered double hydroxides (LDH). In: Bergaya, F., Lagaly, G. (Eds.), *Developments in Clay Science*. Elsevier, pp. 745–782. doi:10.1016/B978-0-08-098258-8.00025-0.
- Forero, C., Gayán, P., García-Labiano, F., De Diego, L., Abad, A., Adánez, J., 2010. Effect of gas composition in chemical-looping combustion with copper-based oxygen carriers: fate of sulphur. *Int. J. Greenh. Gas Control* 4 (5), 762–770.
- Forse, A.C., Milner, P.J., 2020. New chemistry for enhanced carbon capture: beyond ammonium carbamates. *Chem. Sci.* 11 (2), 508–516. doi:10.1039/d0sc06059c.
- Forse, A.C., Milner, P.J., Lee, J.H., Redfern, H.N., Oktawiec, J., Siegelman, R.L., Martell, J.D., Dinakar, B., Zasada, L.B., Gonzalez, M.I., Neaton, J.B., Long, J.R., Reimer, J.A., 2018. Elucidating CO₂ chemisorption in diamine-appended metal-organic frameworks. *J. Am. Chem. Soc.* 140 (51), 18016–18031. doi:10.1021/jacs.8b10203.
- Fourati, M., Roig, V., Raynal, L., 2013. Liquid dispersion in packed columns: Experiments and numerical modeling. *Chem. Eng. Sci.* 100, 266–278. doi:10.1016/j.ces.2013.02.041.
- Freeman, B.D., 1999. Basis of permeability/selectivity tradeoff relations in polymeric gas separation membranes. *Macromolecules* 32 (2), 375–380. doi:10.1021/MA9814548.
- Friebe, S., Mundstock, A., Unruh, D., Renz, F., Caro, J., 2016. NH₂-MIL-125 as membrane for carbon dioxide sequestration: Thin supported MOF layers contra Mixed-Matrix-Membranes. *J. Membr. Sci.* 516, 185–193. doi:10.1016/j.memsci.2016.06.015.
- Frisch, H.L., 1970. “Diffusion in polymers” edited by J. Crank and G. S. Park, Academic Press, London and New York, 1968; 452 pp. 14 (6), 1657–1657. <https://doi.org/10.1002/appr.1970.070140623>.
- Fu, J., Das, S., Xing, G., Ben, T., Valtchev, V., Qiu, S., 2016. Fabrication of COF-MOF composite membranes and their highly selective separation of H₂/CO₂. *J. Am. Chem. Soc.* 138 (24), 7673–7680.
- Fu, K., Zhang, P., Wang, L., Huang, X., Fu, D., 2020. Viscosity of 2-ethylhexan-1-amine (EHA)-diglyme, EHA-triglyme and EHA-tetraglyme non-aqueous solutions and its effect on initial absorption rate. *J. Mol. Liq.* 302. doi:10.1016/j.molliq.2020.112518.
- Fu, S., Angelidaki, I., Zhang, Y., 2021. In situ biogas upgrading by CO₂-to-CH₄ bioconversion. *Trends Biotechnol.* 39 (4), 336–347. doi:10.1016/j.tibtech.2020.08.006.
- Fujikawa, S., Selyanchyn, R., Kunitake, T., 2020. A new strategy for membrane-based direct air capture. *Polym. J.* 53, 111–119.

- Fujikawa, S., Selyanchyn, R., Kunitake, T., 2021. A new strategy for membrane-based direct air capture. *Polym. J.* 53 (1), 111–119. doi:10.1038/s41428-020-00429-z.
- Fujishiro, F., Fukasawa, K., Hashimoto, T., 2011. CO₂ absorption and desorption properties of single phase Ba₂Fe₂O₇ and analysis of their mechanism using thermodynamic calculation. *J. Am. Ceramic Soc.* 94 (11), 3675–3678. doi:10.1111/j.1551-2916.2011.04842.x.
- Fulong, C.R.P., Liu, J., Pastore, V.J., Lin, H., Cook, T.R., 2018. Mixed-matrix materials using metal-organic polyhedra with enhanced compatibility for membrane gas separation. *Dalton Trans.* 47 (24), 7905–7915. doi:10.1039/C8DT00082D.
- Furukawa, H., Yaghi, O.M., 2009. Storage of hydrogen, methane, and carbon dioxide in highly porous covalent organic frameworks for clean energy applications. *J. Am. Chem. Soc.* 131 (25), 8875–8883.
- Furukawa, H., Ko, N., Go, Y.B., Aratani, N., Choi, S.B., Choi, E., Yazaydin, A.Ö., Snurr, R.Q., M.O.K., Kim, J., Yaghi, O.M., 2010. Ultrahigh porosity in metal-organic frameworks. *Science* 329 (5990), 424–428.
- Gómez-Garduño, N., Pfeiffer, H., 2019. Thermokinetic evaluation of iron addition on lithium metazirconate (Fe-Li₂ZrO₃) for enhancing carbon dioxide capture at high temperatures. *Thermochim. Acta* 673, 129–137. doi:10.1016/j.tca.2019.01.017.
- Gaikwad, S., Kim, S.-J., Han, S., 2019. CO₂ capture using amine-functionalized bimetallic MIL-101 MOFs and their stability on exposure to humid air and acid gases. *Microporous Mesoporous Mater.* 277, 253–260. doi:10.1016/j.micromeso.2018.11.001.
- Gaikwad, S., Kim, Y., Gaikwad, R., Han, S., 2021. Enhanced CO₂ capture capacity of amine-functionalized MOF-177 metal organic framework. *J. Environ. Chem. Eng.* 9 (4). doi:10.1016/j.jece.2021.105523.
- Galindo, R., López-Delgado, A., Padilla, I., Yates, M., 2015. Synthesis and characterisation of hydrotalcites produced by an aluminium hazardous waste: a comparison between the use of ammonia and the use of triethanolamine. *Appl. Clay Sci.* 115, 115–123. doi:10.1016/j.clay.2015.07.032.
- Galsunyak, S.C., Petrescu, L., Cormos, C.C., 2022. Environmental impact assessment of post-combustion CO₂ capture technologies applied to cement production plants. *J. Environ. Manage.* 320, 10. doi:10.1016/j.jenvman.2022.115908.
- Galven, C., Fourquet, J.-L., Suard, E., Crosnier-Lopez, M.-P., Le Berre, F., 2010. Mechanism of a reversible CO₂ capture monitored by the layered perovskite Li₂SrTa₂O₇. *Dalton Trans.* 39 (17), 4191–4197. doi:10.1039/C002233N.
- Gan, Q., Zou, Y., Rooney, D., Nancarrow, P., Thompson, J., Liang, L., Lewis, M., 2011. Theoretical and experimental correlations of gas dissolution, diffusion, and thermodynamic properties in determination of gas permeability and selectivity in supported ionic liquid membranes. *Adv. Colloid Interface Sci.* 164 (1), 45–55. doi:10.1016/j.cis.2011.01.005.
- Ganapathy, H., Shooshtari, A., Dessiatoun, S., Alshehhi, M., Ohadi, M., 2014. Fluid flow and mass transfer characteristics of enhanced CO₂ capture in a minichannel reactor. *Appl. Energy* 119, 43–56. doi:10.1016/j.apenergy.2013.12.047.
- Ganapathy, H., Shooshtari, A., Dessiatoun, S., Ohadi, M.M., Alshehhi, M., 2015. Hydrodynamics and mass transfer performance of a microreactor for enhanced gas separation processes. *Chem. Eng. J.* 266, 258–270. doi:10.1016/j.cej.2014.12.028.
- Ganapathy, H., Steinmayer, S., Shooshtari, A., Dessiatoun, S., Ohadi, M.M., Alshehhi, M., 2016. Process intensification characteristics of a microreactor absorber for enhanced CO₂ capture. *Appl. Energy* 162, 416–427. doi:10.1016/j.apenergy.2015.10.010.
- Gao, N., Li, J., Qi, B., Li, A., Duan, Y., Wang, Z., 2014. Thermal analysis and products distribution of dried sewage sludge pyrolysis. *J. Analyt. Appl. Pyrol.* 105, 43–48. doi:10.1016/j.jaap.2013.10.002.
- Gao, J., Zhang, Y., Feng, D., Du, Q., Yu, M., Xie, M., Sun, L., Wu, S., 2015. A new technique of carbon capture by ammonia with the reinforced crystallization at low carbonized ratio and initial experimental research. *Fuel Process. Technol.* 135, 207–211. doi:10.1016/j.fuproc.2015.02.008.
- Gao, H., Xu, B., Han, L., Luo, X., Liang, Z., 2017. Mass transfer performance and correlations for CO₂ absorption into aqueous blended of DEEA/MEA in a random packed column. *AIChE J.* 63 (7), 3048–3057. doi:10.1002/aic.15673.
- Gao, H., Liu, S., Gao, G., Luo, X., Liang, Z., 2018. Hybrid behavior and mass transfer performance for absorption of CO₂ into aqueous DEEA/PZ solutions in a hollow fiber membrane contactor. *Sep. Purif. Technol.* 201, 291–300. doi:10.1016/j.seppur.2018.03.027.
- Gao, Q., Li, X., Ning, G.-H., Xu, H.-S., Liu, C., Tian, B., Tang, W., Loh, K.P., 2018. Covalent organic framework with frustrated bonding network for enhanced carbon dioxide storage. *Chem. Mater.* 30 (5), 1762–1768.
- Gao, W., Zhou, T., Gao, Y., Wang, Q., Lin, W., 2018. Study on MnO₃/NO₂ (M = Li, Na, and K)/MgO composites for intermediate-temperature CO₂ capture. *Energy Fuels* 33 (3), 1704–1712. doi:10.1021/acs.energyfuels.8b02749.
- Gao, Y., Qiao, Z., Zhao, S., Wang, Z., Wang, J., 2018. In situ synthesis of polymer grafted ZIFs and application in mixed matrix membrane for CO₂ separation. *J. Mater. Chem. A* 6 (7), 3151–3161. doi:10.1039/C7TA10322K.
- Gao, H., Huang, Y., Zhang, X., Bairq, Z., Huang, Y., Tontiwachwuthikul, P., Liang, Z., 2020. Catalytic performance and mechanism of SO₄2-/ZrO₂/SBA-15 catalyst for CO₂ desorption in CO₂-loaded monoethanolamine solution. *Appl. Energy* 259.
- Gao, H., Huang, Y., Zhang, X., Bairq, Z.A.S., Huang, Y., Tontiwachwuthikul, P., Liang, Z., 2020. Catalytic performance and mechanism of SO₄2-/ZrO₂/SBA-15 catalyst for CO₂ desorption in CO₂-loaded monoethanolamine solution. *Appl. Energy* 259. doi:10.1016/j.apenergy.2019.114179.
- Gao, W., Liang, S., Wang, R., Jiang, Q., Zhang, Y., Zheng, Q., Xie, B., Toe, C.Y., Zhu, X., Wang, J., Huang, L., Gao, Y., Wang, Z., Jo, C., Wang, Q., Wang, L., Liu, Y., Louis, B., Scott, J., Roger, A.-C., Amal, R., Heh, H., Park, S.-E., 2020. Industrial carbon dioxide capture and utilization: state of the art and future challenges. *Chem. Soc. Rev.* 49 (23), 8584–8686. doi:10.1039/d0cs00025f.
- Gao, W., Vasilades, M.A., Damaskinos, C.M., Zhao, M., Fan, W., Wang, Q., Reina, T.R., Efstathiou, A.M., 2021. Molten salt-promoted MgO adsorbents for CO₂ capture: transient kinetic studies. *Environ. Sci. Technol.* 55 (8), 4513–4521. doi:10.1021/acs.est.0c08731.
- Gao, Z., Liang, L., Zhang, X., Xu, P., Sun, J., 2021. Facile one-pot synthesis of Zn/Mg-MOF-74 with unsaturated coordination metal centers for efficient CO₂ adsorption and conversion to cyclic carbonates. *ACS Appl. Mater. Interfaces* 13 (51), 61334–61345. doi:10.1021/acscami.1c20878.
- Gao, W., Xiao, J., Wang, Q., Li, S., Vasilades, M.A., Huang, L., Gao, Y., Jiang, Q., Niu, Y., Zhang, B.J.A.M., 2021. Unravelling the mechanism of intermediate-temperature CO₂ interaction with molten NaNO₃ salt promoted MgO. 2106677.
- Gao, X., Wang, Z., Chen, T., Hu, L., Yang, S., Kawi, S., 2022a. State-of-art designs and synthesis of zeolite membranes for CO₂ capture. *Carbon Cap. Sci. Technol.* 5, 100073. doi:10.1016/j.cst.2022.100073.
- Gao, X., Yang, S., Hu, L., Cai, S., Wu, L., Kawi, S., 2022b. Carbonaceous materials as adsorbents for CO₂ capture: synthesis and modification. *Carbon Cap. Sci. Technol.* 3, 100039. doi:10.1016/j.cst.2022.100039.
- García-Labiano, F., de Diego, L.F., Gayán, P., Adanez, J., Abad, A., Dueso, C., 2009. Effect of fuel gas composition in chemical-looping combustion with Ni-based oxygen carriers. 1. Fate of sulfur. *Ind. Eng. Chem. Res.* 48 (5), 2499–2508.
- García-Luna, S., Ortiz, C., Carro, A., Chacartegui, R., Pérez-Maqueda, L.A., 2022. Oxygen production routes assessment for oxy-fuel combustion. *Energy* 254 (September), 1–58. doi:10.1016/j.energy.2022.124303.
- García-Abuín, A., Gomez-Diaz, D., Navaza, J.M., Vidal-Tato, I., 2010. CO₂ capture by aqueous solutions of glucosamine in a bubble column reactor. *Chem. Eng. J.* 162 (1), 37–42. doi:10.1016/j.cej.2010.04.050.
- García-Fayos, J., Serra, J.M., Luitien-Olieman, M.W.J., Meulenber, W.A., 2020. Gas separation ceramic membranes. *Adv. Ceram. Energy Convers. Storage* 321–385. doi:10.1016/B978-0-08-102726-4.00008-9.
- Gargiulo, N., Peluso, A., Caputo, D., 2020. MOF-based adsorbents for atmospheric emission control: a review. *Processes* 8 (5). doi:10.3390/pr8050613.
- Gaspar, J., Cormos, A.M., 2012. Dynamic modeling and absorption capacity assessment of CO₂ capture process. *Int. J. Greenh. Gas Control* 8, 45–55. doi:10.1016/j.jggcc.2012.01.016.
- Gaultois, M.W., Dunstan, M.T., Bateson, A.W., Chan, H.S.C., Grey, C.P., 2018. Screening and characterization of ternary oxides for high-temperature carbon capture. *Chem. Mater.* 30 (8), 2535–2543. doi:10.1021/acs.chemmater.7b04679.
- Gawande, M.B., Monga, Y., Zboril, R., Sharma, R.K., 2015. Silica-decorated magnetic nanocomposites for catalytic applications. *Coord. Chem. Rev.* 288, 118–143. doi:10.1016/j.ccr.2015.01.001.
- Gazzani, M., Romano, M.C., Manzolini, G., 2015. CO₂ capture in integrated steelworks by commercial-ready technologies and SEWGS process. *Int. J. Greenh. Gas Control* 41, 249–267. doi:10.1016/j.jggcc.2015.07.012.
- Gbadago, D.Q., Oh, H.T., Oh, D.H., Lee, C.H., Oh, M., 2020. CFD simulation of a packed bed industrial absorber with interbed liquid distributors. *Int. J. Greenh. Gas Control* 95. doi:10.1016/j.jggcc.2020.102983, 102983–102983.
- Ge, L., Wei, J., Geng, L., Chen, S., Liao, L., 2021. Amine-bifunctionalized ZSM-5/SBA-16 composite for CO₂ adsorption. *J. Porous Mater.* 29 (1), 19–31. doi:10.1007/s10934-021-01146-5.
- Gebald, C., Wurzbacher, J.A., Borgschulte, A., Zimmermann, T., Steinfeld, A., 2014. Single-component and binary CO₂ and H₂O adsorption of amine-functionalized cellulose. *Environ. Sci. Technol.* 48 (4), 2497–2504. doi:10.1021/es404430g.
- Gelles, T., Lawson, S., Rowngah, A.A., Rezaei, F., 2019. Recent advances in development of amine functionalized adsorbents for CO₂ capture. *Adsorption* 26 (1), 5–50. doi:10.1007/s10450-019-00151-0.
- Geng, S.Y., Wei, J.Y., Jonasson, S., Hedlund, J., Oksman, K., 2020. Multifunctional carbon aerogels with hierarchical anisotropic structure derived from lignin and cellulose nanofibers for CO₂ capture and energy storage. *ACS Appl. Mater. Interfaces* 12 (6), 7432–7441. doi:10.1021/acscami.9b19955.
- Gentile, G., Bonalumi, D., Pieterse, J.A.Z., Sebastiani, F., Lucking, L., Manzolini, G., 2022. Techno-economic assessment of the FReSMe technology for CO₂ emissions mitigation and methanol production from steel plants. *J. CO₂ Util.* 56, 101852. doi:10.1016/j.jcou.2021.101852.
- Gahramanizhad, M., Soleimani, B., Niknam Shahrak, M., 2018. A simple and novel protocol for Li-trapping with a POM/MOF nano-composite as a new adsorbent for CO₂ uptake. *New J. Chem.* 42 (6), 4639–4645. doi:10.1039/c8nj00274f.
- Ghanbari, S., Kamath, G., 2019. Dynamic simulation and mass transfer study of carbon dioxide capture using biochar and MgO-impregnated activated carbon in a swing adsorption process. *Energy Fuels* 33 (6), 5452–5463. doi:10.1021/acs.energyfuels.9b00923.
- Gholidoust, A., Atkinson, J.D., Hashisho, Z., 2017. Enhancing CO₂ adsorption via amine-impregnated activated carbon from oil sands coke. *Energy Fuels* 31 (2), 1756–1763. doi:10.1021/acs.energyfuels.6b02800.
- Giannaris, S., Janowczyk, D., Ruffini, J., Hill, K., Jacobs, B., Bruce, C., Feng, Y., Srisang, W., 2021. SaskPower's Boundary Dam Unit 3 Carbon Capture Facility - The Journey to Achieving Reliability. *Social Science Electronic Publishing*.
- Gibon, T., Wood, R., Arvesen, A., Bergesen, J.D., Suh, S., Hertwich, E.G., 2015. A methodology for integrated, multiregional life cycle assessment scenarios under large-scale technological change. *Environ. Sci. Technol.* 49 (18), 11218–11226. doi:10.1021/acs.est.5b01558.
- Gibson, J.A.A., Gromov, A.V., Brandani, S., Campbell, E.E.B., 2015. The effect of pore structure on the CO₂ adsorption efficiency of polyamine impregnated porous carbons. *Microporous Mesoporous Mater.* 208, 129–139. doi:10.1016/j.micromeso.2015.01.044.
- Gielen, D., Taibi, E., Miranda, R., 2019. Hydrogen: a renewable energy perspective.
- Gil, A., Arrieta, E., Vicente, M.A., Korili, S.A., 2018. Synthesis and CO₂ adsorption properties of hydrotalcite-like compounds prepared from aluminum saline slag wastes. *Chem. Eng. J.* 334, 1341–1350. doi:10.1016/j.cej.2017.11.100.

- Giordano, L., Roizard, D., Bounaceur, R., Favre, E., 2017. Energy penalty of a single stage gas permeation process for CO₂ capture in post-combustion: a rigorous parametric analysis of temperature, humidity and membrane performances. *Energy Procedia* 114, 636–641. doi:10.1016/j.egypro.2017.03.1206.
- Giordano, L., Roizard, D., Favre, E., 2018. Life cycle assessment of post-combustion CO₂ capture: A comparison between membrane separation and chemical absorption processes. *Int. J. Greenh. Gas Control* 68, 146–163. doi:10.1016/j.jggc.2017.11.008.
- Glasser, L., Jenkins, H.D.B., 2000. Lattice energies and unit cell volumes of complex ionic solids. *J. Am. Chem. Soc.* 122 (4), 632–638.
- Gnanasekaran, L., Priya, A.K., Thanigaivel, S., Hoang, T.K.A., Soto-Moscoco, M., 2022. The conversion of biomass to fuels via cutting-edge technologies: Explorations from natural utilization systems. *Fuel* 331. doi:10.1016/j.fuel.2022.125668.
- Goepfert, A., Czaun, M., May, R.B., Prakash, G.K., Olah, G.A., Narayanan, S.R., 2011. Carbon dioxide capture from the air using a polyamine based regenerable solid adsorbent. *J. Am. Chem. Soc.* 133 (50), 20164–20167. doi:10.1021/ja2100005.
- Goepfert, A., Czaun, M., Surya Prakash, G.K., Olah, G.A., 2012. Air as the renewable carbon source of the future: an overview of CO₂ capture from the atmosphere. *Energy Environ. Sci.* 5 (7), 7833–7853. doi:10.1039/C2EE21586A.
- Goff, F., Lackner, K., 1998. Carbon dioxide sequestering using ultramafic rocks. *Environ. Geosci.* 5 (3), 89–101.
- Gomez, A., Jayakumar, A., Mahinpey, N., 2016. Experimental verification of the reaction mechanism of solid K₂CO₃ during postcombustion CO₂ capture. *Ind. Eng. Chem. Res.* 55 (41), 11022–11028. doi:10.1021/acs.iecr.6b02916.
- Gonçalves, C., Ferreira, N., Lourenço, L., 2021. Production of low molecular weight chitosan and chito oligosaccharides (COS): A review. *Polymers* 13 (15). doi:10.3390/polym13152466.
- González, B., Blamey, J., McBride-Wright, M., Carter, N., Dugwell, D., Fennell, P., Abanades, J.C., 2011. Calcium looping for CO₂ capture: sorbent enhancement through doping. *Energy Procedia* 4, 402–409. doi:10.1016/j.egypro.2011.01.068.
- González, A.S., Plaza, M.G., Rubiera, F., Pevida, C., 2013. Sustainable biomass-based carbon adsorbents for post-combustion CO₂ capture. *Chem. Eng. J.* 230, 456–465. doi:10.1016/j.cej.2013.06.118.
- Gopan, A., Kumfer, B.M., Phillips, J., Thimsen, D., Smith, R., Axelbaum, R.L., 2014. Process design and performance analysis of a staged, pressurized oxy-combustion (SPOC) power plant for carbon capture. *Appl. Energy* 125, 179–188. doi:10.1016/j.apenergy.2014.03.032.
- Gopan, A., Verma, P., Yang, Z., Axelbaum, R.L., 2020. Quantitative analysis of the impact of flue gas recirculation on the efficiency of oxy-coal power plants. *Int. J. Greenh. Gas Control* 95, 102936. doi:10.1016/j.jggc.2019.102936.
- Grande, C.A., Rodrigues, A.E., 2008. Electric Swing Adsorption for CO₂ removal from flue gases. *Int. J. Greenh. Gas Control* 2 (2), 194–202. doi:10.1016/S1750-5836(07)00116-8.
- Grande, C.A., Ribeiro, R.P.L., Oliveira, E.L.G., Rodrigues, A.E., 2009. Electric swing adsorption as emerging CO₂ capture technique. *Energy Procedia* 1 (1), 1219–1225. doi:10.1016/j.egypro.2009.01.160.
- Grande, C.A., Poplow, F., Rodrigues, A.E., 2010. Vacuum pressure swing adsorption to produce polymer-grade propylene. *Sep. Sci. Technol.* 45 (9), 1252–1259.
- Grant, T., Anderson, C., Hooper, B., 2014. Comparative life cycle assessment of potassium carbonate and monoethanolamine solvents for CO₂ capture from post combustion flue gases. *Int. J. Greenh. Gas Control* 28, 35–44. doi:10.1016/j.jggc.2014.06.020.
- Grasa, G.S., Abanades, J.C., 2006. CO₂ capture capacity of CaO in long series of carbonation/calcination cycles. *Ind. Eng. Chem. Res.* 45 (26), 8846–8851. doi:10.1021/ie0606946.
- Grasa, G.S., Alonso, M., Abanades, J.C., 2008. Sulfation of CaO particles in a carbonation/calcination loop to capture CO₂. *Ind. Eng. Chem. Res.* 47 (5), 1630–1635. doi:10.1021/ie070937+.
- Grosser, K., Carbonell, R.G., Sundaresan, S., 1988. Onset of pulsing in two-phase concurrent downflow through a packed bed. *AIChE J.* 34 (11), 1850–1860. doi:10.1002/aic.690341111.
- Gu, F., et al., 2004. CFD simulation of liquid film flow on inclined plates. *Chemical Engineering and Technology* 27 (10), 1099–1104.
- Gudena, K., Rangaiah, G.P., Lakshminarayana, S., 2013. HiGee stripper-membrane system for decentralised bioethanol recovery and purification. *Ind. Eng. Chem. Res.* 52 (12), 4572–4585. doi:10.1021/ie302557f.
- Gunjal, P.R., Kashid, M.N., Ranade, V.V., Chaudhari, R.V., 2005. Hydrodynamics of trickle-bed reactors: experiments and CFD modeling. *Ind. Eng. Chem. Res.* 44 (16), 6278–6294. doi:10.1021/ie0491037.
- Guo, H., Zhu, G., Li, H., Zou, X., Yin, X., Yang, W., Qiu, S., Xu, R., 2006. Hierarchical growth of large-scale ordered zeolite silicalite-1 membranes with high permeability and selectivity for recycling CO₂. *Angew. Chem. Int. Ed.* 45 (42), 7053–7056.
- Guo, C., Chen, S., Zhang, Y., Wang, G., 2014. Solubility of CO₂ in Nonaqueous Absorption System of 2-(2-Aminoethylamine)ethanol + Benzyl Alcohol. *J. Chem. Eng. Data* 59 (6), 1796–1801. doi:10.1021/je401028g.
- Guo, X., Huang, H., Ban, Y., Yang, Q., Xiao, Y., Li, Y., Yang, W., Zhong, C., 2015. Mixed matrix membranes incorporated with amine-functionalized titanium-based metal-organic framework for CO₂/CH₄ separation. *J. Membr. Sci.* 478, 130–139. doi:10.1016/j.memsci.2015.01.007.
- Guo, T.-Y., et al., 2016. Computational Fluid Dynamics Analysis of the Micromixing Efficiency in a Rotating-Packed-Bed Reactor. *Ind. Eng. Chem. Res.* 55 (17), 4856–4866.
- Guo, T.-Y., Cheng, K.-P., Wen, L.-X., Andersson, R., Chen, J.-F., 2017. Three-dimensional simulation on liquid flow in a rotating packed bed reactor. *Ind. Eng. Chem. Res.* 56 (28), 8169–8179. doi:10.1021/acs.iecr.7b01759.
- Guo, T.X., Ma, N., Pan, Y.F., Bedane, A.H., Xiao, H.N., Eic, M., Du, Y.R., 2018. Characteristics of CO₂ adsorption on biochar derived from biomass pyrolysis in molten salt. *Can. J. Chem. Eng.* 96 (11), 2352–2360. doi:10.1002/cjce.23153.
- Guo, Y.F., Zhao, C.W., Sun, J., Li, W.L., Lu, P., 2018. Facile synthesis of silica aerogel supported K₂CO₃ sorbents with enhanced CO₂ capture capacity for ultra-dilute flue gas treatment. *Fuel* 215, 735–743. doi:10.1016/j.fuel.2017.11.113.
- Guo, Y., Zhao, C., Sun, J., Li, W., Lu, P., 2018. Facile synthesis of silica aerogel supported K₂CO₃ sorbents with enhanced CO₂ capture capacity for ultra-dilute flue gas treatment. *Fuel* 215, 735–743. doi:10.1016/j.fuel.2017.11.113.
- Guo, X., Qiao, Z., Liu, D., Zhong, C., 2019. Mixed-matrix membranes for CO₂ separation: role of the third component. *J. Mater. Chem. A* 7 (43), 24738–24759. doi:10.1039/C9TA09012F.
- Guo, X.Y., Qiao, Z.H., Liu, D.H., Zhong, C.L., 2019. Mixed-matrix membranes for CO₂ separation: role of the third component. *J. Mater. Chem. A* 7 (43), 24738–24759. doi:10.1039/c9ta09012f.
- Guo, W., Mahurin, S.M., Wang, S., Meyer, H.M., Luo, H., Hu, X., Jiang, D.-e., Dai, S., 2020. Ion-gated carbon molecular sieve gas separation membranes. *J. Membr. Sci.* 604. doi:10.1016/j.memsci.2020.118013.
- Guo, X., Xu, S., Sun, Y., Qiao, Z., Huang, H., Zhong, C., 2021. Metal-organic polyhedron membranes for molecular separation. *J. Membr. Sci.* 632, 119354. doi:10.1016/j.memsci.2021.119354.
- Guo, Y., Hu, G., Chen, K., Guo, J., Webley, P.A., Li, G.K., 2021. Capture of dilute methane with a novel dynamic-feed dual-reflux pressure swing adsorption process. *AIChE J.* 68, e17390. doi:10.1002/aic.17390.
- Guo, F., Li, D., Ding, R., Gao, J., Ruan, X., Jiang, X., He, G., Xiao, W., 2022. Constructing MOF-doped two-dimensional composite material ZIF-90@C3N₄ mixed matrix membranes for CO₂/N₂ separation. *Sep. Purif. Technol.* 280. doi:10.1016/j.seppur.2021.119803.
- Guo, H., Cui, J., Li, J., 2022. Biomass power generation in China: status, policies and recommendations. *Energy Rep.* 8, 687–696. doi:10.1016/j.egypr.2022.08.072.
- Guo, S., Li, Y., Wang, Y., Wang, L., Sun, Y., Liu, L., 2022. Recent advances in biochar-based adsorbents for CO₂ capture. *Carbon Cap. Sci. Technol.*, 100059.
- Guo, W., Tran, T.N., Mondal, H., Schaefer, S., Huang, L., Lin, H., 2022. Superior CO₂/N₂ separation performance of highly branched Poly (1,3 dioxolane) plasticized by polyethylene glycol. *J. Membr. Sci.* 648, 120352. doi:10.1016/j.memsci.2022.120352.
- Gupta, S., Li, L., 2022. The potential of machine learning for enhancing CO₂ sequestration, storage, transportation, and utilization-based processes: a brief perspective. *JOM* 74 (2), 414–428. doi:10.1007/s11837-021-05079-x.
- Gupta, S., Adams, J.J., Wilson, J.R., Eddings, E.G., Mahapatra, M.K., Singh, P., 2016. Performance and post-test characterization of an OTM system in an experimental coal gasifier. *Appl. Energy* 165, 72–80. doi:10.1016/j.apenergy.2015.12.077.
- Gutierrez-Ortega, A., Nomen, R., Sempere, J., Parra, J.B., Montes-Morán, M.A., Gonzalez-Olmos, R., 2022. A fast methodology to rank adsorbents for CO₂ capture with temperature swing adsorption. *Chem. Eng. J.* 435. doi:10.1016/j.cej.2022.134703.
- Guymard-Lack, A., Buchtová, N., Humbert, B., Le Bideau, J., 2015. Ion segregation in an ionic liquid confined within chitosan based chemical ionogels. *Phys. Chem. Chem. Phys.* 17 (37), 23947–23951. doi:10.1039/C5CP04198H.
- Hägg, M.B., Lindbräthen, A., He, X., Nodeland, S.G., Cantero, T., 2017. Pilot demonstration-reporting on CO₂ capture from a cement plant using hollow fiber process. *Energy Procedia* 114, 6150–6165. doi:10.1016/j.egypro.2017.03.1752.
- H, H., 2003. Assessing the Feasibility of Capturing CO₂ from the Air. Massachusetts Institute of Technology, Laboratory for Energy and the Environment Publication No. LFEE 2.
- Haase, F., Gottschling, K., Stegbauer, L., Germann, L., Gutzler, R., Duppl, V., Vyas, V., Kern, K., Dinneber, R., Lotsch, B., 2017. Tuning the stacking behaviour of a 2D covalent organic framework through non-covalent interactions. *Mater. Chem. Front.* 1 (7), 1354–1361.
- Haddad, S., Rivera-Tinoco, R., Bouallou, C., 2019. Modelling of CO₂ frost formation and growth on a flat plate. *Chem. Eng. Trans.* doi:10.3303/cet1976112.
- Haghighanar, M., Majumder, A., Nilam, R., Rajendran, A., Farooq, S., Karim, I.A., Amanullah, M., 2013. Multiobjective optimization of a four-step adsorption process for post-combustion CO₂ capture via finite volume simulation. *Ind. Eng. Chem. Res.* 52 (11), 4249–4265. doi:10.1021/ie302658y.
- Haghsheenas Fard, M., et al., 2007. CFD Simulation of Mass Transfer Efficiency and Pressure Drop in a Structured Packed Distillation Column. *Chemical Engineering & Technology* 30 (7), 854–861.
- Hahn, M.W., Jelic, J., Berger, E., Reuter, K., Jentys, A., Lercher, J.A., 2016. Role of amine functionality for CO₂ chemisorption on silica. *J. Phys. Chem. B* 120 (8), 1988–1995. doi:10.1021/acs.jpcc.5b10012.
- Haizhou, Lin, Hui, Yang, Haizhong, Luo, Aiguo, Pei, Mengxiang, F., 2019. Research progress on amine adsorbent for CO₂ capture from flue gas. *South. Energy Construct.* 6 (01), 16–21.
- Halabi, M.H., de Croon, M.H.J.M., van der Schaaf, J., Cobden, P.D., Schouten, J.C., 2012. High capacity potassium-promoted hydrocalcite for CO₂ capture in H₂ production. *Int. J. Hydrogen Energy* 37 (5), 4516–4525. doi:10.1016/j.ijhydene.2011.12.003.
- Haldar, R., Heinke, L., Woll, C., 2019. Advanced photoreponsive materials using the metal-organic framework approach. *Adv. Mater.*, e1905227. doi:10.1002/adma.201905227.
- Halder, K., Neumann, S., Bengtson, G., Khan, M.M., Filiz, V., Abetz, V., 2018. Polymers of intrinsic microporosity postmodified by vinyl groups for membrane applications. *Macromolecules* 51 (18), 7309–7319. doi:10.1021/acs.macromol.8b01252.
- Hamm, J.B.S., Ambrosi, A., Griebeler, J.G., Marcellio, N.R., Tessoro, I.C., Pollo, L.D., 2017. Recent advances in the development of supported carbon membranes for gas separation. *Int. J. Hydrogen Energy* 42 (39), 24830–24845. doi:10.1016/j.ijhydene.2017.08.071.
- Hamon, L., Jolimaire, E., Pirngruber, G.D., 2010. CO₂ and CH₄ separation by adsorption using Cu-BTC metal-organic-framework. *Ind. Eng. Chem. Res.* 49, 7497–7503.
- Han, Y., Ho, W.S.W., 2018. Recent advances in polymeric membranes for CO₂ capture. *Chin. J. Chem. Eng.* 26 (11), 2238–2254. doi:10.1016/j.cjche.2018.07.010.

- Han, Y., Ho, W.S.W., 2020. Recent advances in polymeric facilitated transport membranes for carbon dioxide separation and hydrogen purification. *J. Polym. Sci.* 58 (18), 2435–2449. doi:10.1002/pol.20200187.
- Han, Y., Ho, W.S.W., 2021a. Facilitated transport membranes for H₂ purification from coal-derived syngas: A techno-economic analysis. *J. Membr. Sci.* 636, 119549. doi:10.1016/j.memsci.2021.119549.
- Han, Y., Ho, W.S.W., 2021b. Polymeric membranes for CO₂ separation and capture. *J. Membr. Sci.* 628, 119244. doi:10.1016/j.memsci.2021.119244.
- Han, Y., Ho, W.S.W., 2022. Mitigated carrier saturation of facilitated transport membranes for decarbonizing dilute CO₂ sources: An experimental and techno-economic study. *J. Membr. Sci. Lett.* 2 (1), 100014. doi:10.1016/j.memlet.2022.100014.
- Han, A.-J., He, H.-Y., Guo, J., Yu, H., Huang, Y.-F., Long, Y.-C., 2005. Studies on structure and acid-base properties of high silica MFI-type zeolite modified with methylamine. *Microporous Mesoporous Mater.* 79 (1–3), 177–184.
- Han, S.S., Jung, D.-H., Heo, J., 2013. Interpenetration of metal organic frameworks for carbon dioxide capture and hydrogen purification: Good or bad? *J. Phys. Chem. C* 117 (1), 71–77.
- Han, S.J., Bang, Y., Kwon, H.J., Lee, H.C., Hiremath, V., Song, I.K., Seo, J.G., 2014. Elevated temperature CO₂ capture on nano-structured MgO-Al₂O₃ aerogel: Effect of Mg/Al molar ratio. *Chem. Eng. J.* 242, 357–363. doi:10.1016/j.cej.2013.12.092.
- Han, J., Du, Z., Zou, W., Li, H., Zhang, C., 2015. Moisture-responsive hydrogel impregnated in porous polymer foam as CO₂ adsorbent in high-humidity flue gas. *Ind. Eng. Chem. Res.* 54 (31), 7623–7631. doi:10.1021/acs.iecr.5b01305.
- Han, Y., Wu, D., Ho, W.S.W., 2018. Nanotube-reinforced facilitated transport membrane for CO₂/N₂ separation with vacuum operation. *J. Membr. Sci.* 567, 261–271. doi:10.1016/j.memsci.2018.08.061.
- Han, Y., Salim, W., Chen, K.K., Wu, D., Ho, W.S.W., 2019a. Field trial of spiral-wound facilitated transport membrane module for CO₂ capture from flue gas. *J. Membr. Sci.* 575, 242–251. doi:10.1016/j.memsci.2019.01.024.
- Han, Y., Wu, D., Ho, W.S.W., 2019b. Simultaneous effects of temperature and vacuum and feed pressures on facilitated transport membrane for CO₂/N₂ separation. *J. Membr. Sci.* 573, 476–484. doi:10.1016/j.memsci.2018.12.028.
- Han, Y., Wu, D., Ho, W.S.W., 2019c. Simultaneous effects of temperature and vacuum and feed pressures on facilitated transport membrane for CO₂/N₂ separation. *J. Membr. Sci.* 573, 476–484.
- Han, Y., Yang, Y., Ho, W.S.W., 2020. Recent progress in the engineering of polymeric membranes for CO₂ capture from flue gas. *Membranes (Basel)* 10 (11). doi:10.3390/membranes10110365.
- Han, Y., Tian, M., Wang, C., Kang, Y., Kang, L., Su, Y., Huang, C., Zong, T., Lin, J., Hou, B., Pan, X., Wang, X., 2021. Highly active and anticoke Ni/CeO₂ with ultralow Ni loading in chemical looping dry reforming via the strong metal–support interaction. *ACS Sustain. Chem. Eng.* 9 (51), 17276–17288. doi:10.1021/acscuschemeng.1c06079.
- Han, N., Shen, Z., Zhao, X., Chen, R., Thakur, V.K., 2022. Perovskite oxides for oxygen transport: Chemistry and material horizons. *Sci. Total Environ.* 806, 151213. doi:10.1016/j.scitotenv.2021.151213.
- Han, R., Wang, Y., Xing, S., Pang, C.H., Hao, Y., Song, C.F., Liu, Q.L., 2022. Progress in reducing calcination reaction temperature of Calcium-Looping CO₂ capture technology: a critical review. *Chem. Eng. J.* 450, 15. doi:10.1016/j.cej.2022.137952.
- Hanak, D.P., Anthony, E.L., Manovic, V., 2015a. A review of developments in pilot-plant testing and modelling of calcium looping process for CO₂ capture from power generation systems. *Energy Environ. Sci.* 8 (8), 2199–2249. doi:10.1039/C5EE01228G.
- Hanak, D.P., Bilyok, C., Manovic, V., 2015b. Rate-based model development, validation and analysis of chilled ammonia process as an alternative CO₂ capture technology for coal-fired power plants. *Int. J. Greenh. Gas Control* 34, 52–62. doi:10.1016/j.jggcc.2014.12.013.
- Hanioka, S., Maruyama, T., Sotani, T., Teramoto, M., Matsuyama, H., Nakashima, K., Hanaki, M., Kubota, F., Goto, M.J., 2008. CO₂ separation facilitated by task-specific ionic liquids using a supported liquid membrane. *J. Membr. Sci.* 314 (1–2), 1–4.
- Harada, T., Hatton, T.A., 2015. Colloidal nanoclusters of MgO coated with alkali metal nitrates/nitrites for rapid, high capacity CO₂ capture at moderate temperature. *Chem. Mater.* 27 (23), 8153–8161. doi:10.1021/acs.chemmater.5b03904.
- Harada, T., Hatton, T.A., 2017. Tri-lithium borate (Li₃BO₃): a new highly regenerable high capacity CO₂ adsorbent at intermediate temperature. *J. Mater. Chem. A* 5 (42), 22224–22233. doi:10.1039/C7TA06167F.
- Harada, T., Simeon, F., Hamad, E.Z., Hatton, T.A., 2015. Alkali metal nitrate-promoted high-capacity MgO adsorbents for regenerable CO₂ capture at moderate temperatures. *Chem. Mater.* 27 (6), 1943–1949. doi:10.1021/cm503295g.
- Harami, H.R., Fini, F.R., Rezakazemi, M., Shirazian, S., 2019. Sorption in mixed matrix membranes: experimental and molecular dynamic simulation and grand canonical Monte Carlo method. *J. Mol. Liq.* 282, 566–576. doi:10.1016/j.molliq.2019.03.047.
- Haroun, Y., Raynal, L., Legendre, D., 2012. Mass transfer and liquid hold-up determination in structured packing by CFD. *Chem. Eng. Sci.* 75, 342–348.
- Harrison, D.P., 2008. Sorption-enhanced hydrogen production: a review. *Ind. Eng. Chem. Res.* 47 (17), 6486–6501. doi:10.1021/ie800298z.
- Harun, N., Douglas, P.L., Ricardez-Sandoval, L., Croiset, E., 2011. Dynamic simulation of MEA absorption processes for CO₂ capture from fossil fuel power plant. *Energy Procedia* 1478–1485.
- Hasan, M.M.F., First, E.L., Floudas, C.A., 2013. Cost-effective CO₂ capture based on an silico screening of zeolites and process optimization. *Phys. Chem. Chem. Phys.* 15 (40), 17601–17618. doi:10.1039/c3cp53627k.
- Haseli, Y., 2021. Approximate relations for optimum turbine operating parameters in al-alam cycle. *J. Eng. Gas Turbines Power* 143 (6), 064501.
- Hashemi, S.E., Sarker, S., Lien, K.M., Schnell, S.K., Austbo, B., 2019. Cryogenic vs. absorption biogas upgrading in liquefied biomethane production – An energy efficiency analysis. *Fuel* 245, 294–304. doi:10.1016/j.fuel.2019.01.172.
- Hashemi, S.M., Sedghkarder, M.H., Mahinpey, N., 2022. Calcium looping carbon capture: progress and prospects. *Can. J. Chem. Eng.* 100 (9), 2140–2171. doi:10.1002/cjce.24480.
- Hasib-ur-Rahman, M., Larachi, F., 2013. Kinetic behavior of carbon dioxide absorption in diethanolamine/ionic-liquid emulsions. *Sep. Purif. Technol.* 118, 757–761. doi:10.1016/j.seppur.2013.08.027.
- Hasib-ur-Rahman, M., Sijaj, M., Larachi, F., 2012. CO₂ capture in alkanolamine/room-temperature ionic liquid emulsions: A viable approach with carbamate crystallization and curbed corrosion behavior. *Int. J. Greenh. Gas Control* 6, 246–252. doi:10.1016/j.jggcc.2011.10.014.
- Hassan, M.M., Ruthven, D.M., Raghavan, N.S., 1986. Air separation by pressure swing adsorption on a carbon molecular sieve. *Chem. Eng. Sci.* 41 (5), 1333–1343. doi:10.1016/0009-2509(86)87106-8.
- Hassanlouei, R.N., Pelalak, R., Daraei, A., 2013. Wettability study in CO₂ capture from flue gas using nano porous membrane contactors. *Int. J. Greenh. Gas Control* 16, 233–240. doi:10.1016/j.jggcc.2013.03.018.
- Hazazi, K., Ma, X., Wang, Y., Ogieglo, W., Alhazmi, A., Han, Y., Pinnau, I., 2019. Ultra-selective carbon molecular sieve membranes for natural gas separations based on a carbon-rich intrinsically microporous polyimide precursor. *J. Membr. Sci.* 585, 1–9. doi:10.1016/j.memsci.2019.05.020.
- He, X., Hägg, M.-B., 2011. Hollow fiber carbon membranes: investigations for CO₂ capture. *J. Membr. Sci.* 378 (1–2), 1–9. doi:10.1016/j.memsci.2010.10.070.
- He, X., Arvid Lie, J., Sheridan, E., Hägg, M.-B., 2009. CO₂ capture by hollow fibre carbon membranes: Experiments and process simulations. *Energy Procedia* 1 (1), 261–268. doi:10.1016/j.egypro.2009.01.037.
- He, F., Li, X., Zhao, K., Huang, Z., Wei, G., Li, H., 2013. The use of La_{1-x}Sr_xFeO₃ perovskite-type oxides as oxygen carriers in chemical-looping reforming of methane. *Fuel* 108, 465–473. doi:10.1016/j.fuel.2012.11.035.
- He, D., Shao, Y., Qin, C., Pu, G., Ran, J., Zhang, L., 2016. Understanding the sulfation pattern of CaO-based sorbents in a novel process for sequential CO₂ and SO₂ capture. *Ind. Eng. Chem. Res.* 55 (39), 10251–10262.
- He, X., Lindbräthen, A., Kim, T.-J., Hägg, M.-B., 2017a. Pilot testing on fixed-site-carrier membranes for CO₂ capture from flue gas. *Int. J. Greenh. Gas Control* 64, 323–332. doi:10.1016/j.jggcc.2017.08.007.
- He, X., Lindbräthen, A., Kim, T.-J., Hägg, M.-B., 2017b. Pilot testing on fixed-site-carrier membranes for CO₂ capture from flue gas. *Int. J. Greenh. Gas Control* 64, 323–332. doi:10.1016/j.jggcc.2017.08.007.
- He, R., Cong, S., Wang, J., Liu, J., Zhang, Y., 2019. Porous graphene oxide/porous organic polymer hybrid nanosheets functionalized mixed matrix membrane for efficient CO₂ capture. *ACS Appl. Mater. Interfaces* 11 (4), 4338–4344. doi:10.1021/acsmi.8b17599.
- He, S., Jiang, X., Li, S., Ran, F., Long, J., Shao, L., 2020. Intermediate thermal manipulation of polymers of intrinsic microporous (PIMs) membranes for gas separations. *AIChE J.* 66 (10), e16543.
- He, D., Gong, H., Chen, Y., Jiao, Z., Liu, Y., Zhang, X., Qin, C., Yin, H., 2021. Experimental and density functional theory study of the synergistic effect between steam and SO₂ on CO₂ capture of calcium-based sorbents. *Fuel* 295, 120634.
- He, X., Chen, D., Liang, Z., Yang, F., 2022. Insight and comparison of energy-efficient membrane processes for CO₂ capture from flue gases in power plant and energy-intensive industry. *Carbon Cap. Sci. Technol.* 2. doi:10.1016/j.cscst.2021.100020.
- He, X., 2021. Polyvinylamine-based facilitated transport membranes for post-combustion CO₂ capture: challenges and perspectives from materials to processes. *Engineering* 7 (1), 124–131. doi:10.1016/j.eng.2020.11.001.
- Healey, K., Liang, W., Southon, P.D., Church, T.L., D'Alessandro, D.M., 2016. Photoreversible spiropran-functionalised MOF-808: postsynthetic incorporation and light dependent gas adsorption properties. *J. Mater. Chem. A* 4 (28), 10816–10819. doi:10.1039/c6ta04160d.
- Hecht, E.S., Shaddix, C.R., Geier, M., Molina, A., Haynes, B.S., 2012. Effect of CO₂ and steam gasification reactions on the oxy-combustion of pulverized coal char. *Combust. Flame* 159 (11), 3437–3447.
- Hedin, N., Andersson, L., Bergström, L., Yan, J., 2013. Adsorbents for the post-combustion capture of CO₂ using rapid temperature swing or vacuum swing adsorption. *Appl. Energy* 104, 418–433. doi:10.1016/j.apenergy.2012.11.034.
- Hefti, M., Mazzotti, M., 2018. Postcombustion CO₂ capture from wet flue gas by temperature swing adsorption. *Ind. Eng. Chem. Res.* 57, 15542–15555. doi:10.1021/acs.iecr.8b03580.
- Heinke, L., Wöll, C., 2019. Surface-mounted metal-organic frameworks: crystalline and porous molecular assemblies for fundamental insights and advanced applications. *Adv. Mater.* 31 (26). doi:10.1002/adma.201806324.
- Heldebrand, D.J., Koehn, P.K., Yonker, C.R., 2010. A reversible zwitterionic SO₂-binding organic liquid. *Energy Environ. Sci.* 3 (1), 111–113. doi:10.1039/b916550a.
- Heldebrand, D.J., Koehn, P.K., Rousseau, R., Glezakou, V.-A., Cantu, D., Malhotra, D., Zheng, F., Whyatt, G., Freeman, C.J., Bearden, M.D., 2017. Are water-lean solvent systems viable for post-combustion CO₂ capture? *Energy Procedia* 114, 756–763. doi:10.1016/j.egypro.2017.03.1218.
- Hellums, M.W., Koros, W.J., Husk, G.R., Paul, D.R., 1989. Fluorinated polycarbonates for gas separation applications. *J. Membr. Sci.* 46 (1), 93–112. doi:10.1016/03076-7388(00)81173-4.
- Hemmatifar, A., Kang, J.S., Ozbek, N., Tan, K.-J., Hatton, T.A., 2022. Electrochemically mediated direct CO₂ capture by a stackable bipolar cell. *ChemSusChem* 15 (6), e202102533. doi:10.1002/cssc.202102533.
- Hepworth, T., 1892. Oxygen for limelight. *Nature* 47 (1208), 176–177.
- Heydari-Gorji, A., Sayari, A., 2012. Thermal, oxidative, and CO₂-induced degradation of supported polyethyleneimine adsorbents. *Ind. Eng. Chem. Res.* 51 (19), 6887–6894. doi:10.1021/ie3003446.

- Heydari-Gorji, A., Belmabkhout, Y., Sayari, A., 2011a. Degradation of amine-supported CO₂ adsorbents in the presence of oxygen-containing gases. *Microporous Mesoporous Mater.* 145 (1–3), 146–149. doi:10.1016/j.micromeso.2011.05.010.
- Heydari-Gorji, A., Belmabkhout, Y., Sayari, A., 2011b. Polyethylenimine-impregnated mesoporous silica: effect of amine loading and surface alkyl chains on CO₂ adsorption. *Langmuir* 27 (20), 12411–12416. doi:10.1021/ja202972t.
- Higginbotham, P., White, V., Fogash, K., Govegluoglu, G., 2011. Oxygen supply for oxyfuel CO₂ capture. *Int. J. Greenh. Gas Control* 5 (SUPPL. 1), S194–S203. doi:10.1016/j.jggc.2011.03.007.
- Hiloidhari, M., Kumari, S., 2021. Chapter 15 - Biogas upgrading and life cycle assessment of different biogas upgrading technologies. In: Aryal, N., Mørck Ottosen, L.D., Wegener Kofeod, M.V., Pant, D. (Eds.), *Emerging Technologies and Biological Systems for Biogas Upgrading*. Academic Press, pp. 413–445. doi:10.1016/B978-0-12-822808-1.00015-5.
- Hilz, J., Helbig, M., Haaf, M., Daikeler, A., Ströhle, J., Epple, B., 2017. Long-term pilot testing of the carbonate looping process in 1MWh scale. *Fuel* 210, 892–899. doi:10.1016/j.fuel.2017.08.105.
- Himeno, S., Tomita, T., Suzuki, K., Yoshida, S., 2007. Characterization and selectivity for methane and carbon dioxide adsorption on the all-silica DD3R zeolite. *Microporous Mesoporous Mater.* 98 (1–3), 62–69.
- HINO, M., ARATA, K., 1979. Solid catalyst treated with anion. 2. Reactions of butane and isobutane catalyzed by zirconium oxide treated with sulfate ion. *Solid superacid catalyst. Chem. Soc. Jpn.* 101 (21), 6439–6441.
- Hiremath, V., Trivino, M.L.T., Seo, J.G.J.J.o.E.S., 2019. Eutectic mixture promoted CO₂ sorption on MgO-TiO₂ composite at elevated temperature. *76*, 80–88.
- Ho, N.A.D., Leo, C.P., 2021. A review on the emerging applications of cellulose, cellulose derivatives and nanocellulose in carbon capture. *Environ. Res.* 197. doi:10.1016/j.envres.2021.111100.
- Ho, M.T., Allinson, G.W., Wiley, D.E., 2008. Reducing the cost of CO₂ capture from flue gases using pressure swing adsorption. *Ind. Eng. Chem. Res.* 47 (14), 4883–4890. doi:10.1021/ie070831e.
- Hoang, V.T., Kaliaguine, S., 2013. Predictive models for mixed-matrix membrane performance: a review. *Chem. Rev.* 113 (7), 6439–6441. doi:10.1021/cr3003888.
- Hoegh-Guldberg, O., Jacob, D., Taylor, M., Guillen Bolanos, T., Bindi, M., Brown, S., Camilloni, I.A., Diedhiou, A., Djalante, R., Ebi, K., Engelbrecht, F., Guiot, J., Hi-joka, Y., Mehrotra, S., Hope, C.W., Payne, A.J., Portner, H.O., Seneviratne, S.I., Thomas, A., Warren, R., Zhou, G., 2019. The human imperative of stabilizing global climate change at 1.5 degrees C. *Science* 365 (6459). doi:10.1126/science.aaw6974.
- Hofs, B., Ogier, J., Vries, D., Beerendonk, E.F., Cornelissen, E.R., 2011. Comparison of ceramic and polymeric membrane permeability and fouling using surface water. *Sep. Purif. Technol.* 79 (3), 365–374. doi:10.1016/j.seppur.2011.03.025.
- Holmes, A.S., Ryan, J.M., 1982. *Cryogenic Distillate Separation of Acid Gases from Methane*. Koch Press Systems, Inc., United States.
- Homonny, Z., Nomura, K., Juhász, G., Gál, M., Sölymos, K., Hamakawa, S., Hayakawa, T., Vértes, A., 2002. Simultaneous probing of the Fe and Co sites in the CO₂-absorber perovskite Sr_{0.95}Ca_{0.05}Co_{0.5}Fe_{0.5}O_{3-δ}: a Mössbauer study. *Chem. Mater.* 14 (3), 1127–1135. doi:10.1021/cm011190v.
- Hong, J., Chaudhry, G., Brisson, J.G., Field, R., Gazzino, M., Ghoniem, A.F., 2009. Analysis of oxy-fuel combustion power cycle utilizing a pressurized coal combustor. *Energy* 34 (9), 1332–1340. doi:10.1016/j.energy.2009.05.015.
- Hong, J., Field, R., Gazzino, M., Ghoniem, A.F., 2010. Operating pressure dependence of the pressurized oxy-fuel combustion power cycle. *Energy* 35 (12), 5391–5399. doi:10.1016/j.energy.2010.07.016.
- Hong, X.J., Wei, Q., Cai, Y.P., Zheng, S.R., Yu, Y., Fan, Y.Z., Xu, X.Y., Si, L.P., 2017. 2-fold interpenetrating bifunctional Cu-metal-organic frameworks: highly selective adsorption for CO₂ and sensitive luminescent sensing of nitro aromatic 2,4,6-trinitrophenol. *ACS Appl. Mater. Interfaces* 9 (5), 4701–4708. doi:10.1021/acsmi.6b14051.
- Hong, W.Y., 2022. A techno-economic review on carbon capture, utilisation and storage systems for achieving a net-zero CO₂ emissions future. *Carbon Cap. Sci. Technol.* 3, 100044. doi:10.1016/j.cst.2022.100044.
- Horn, F.L., Steinberg, M., 1982. Control of carbon dioxide emissions from a power plant (and use in enhanced oil recovery). *Fuel* 61 (5), 415–422. doi:10.1016/0016-2361(82)90064-3.
- Hoshino, Y., Utsunomiya, T., Abe, O., 1981. The thermal-decomposition of sodium-nitrate and the effects of several oxides on the decomposition. *B Chem. Soc. Jpn.* 54 (5), 1385–1391. doi:10.1246/bcsj.54.1385.
- Hoskins, B.F., Robson, R., 1990. Design and construction of a new class of scaffolding-like materials comprising infinite polymeric frameworks of 3D-linked molecular rods. A reappraisal of the zinc cyanide and cadmium cyanide structures and the synthesis and structure of the diamond-related frameworks [N(CH₃)₄][CuZnII(CN)₄] and [CuI₄ 4⁻], 4⁻-tetracyano(tetraphenylmethane) BF₄. *xC6HSNO₂*. *J. Am. Chem. Soc.* 112 (4), 1546–1554.
- Hosono, N., Guo, W., Omoto, K., Yamada, H., Kitagawa, S., 2019. Bottom-up synthesis of defect-free mixed-matrix membranes by using polymer-grafted metal-organic polyhedra. *Chem. Lett.* 48 (6), 597–600. doi:10.1246/cl.190131.
- Hossain, M.M., de Lasa, H.L., 2007. Reactivity and stability of Co-Ni/Al₂O₃ oxygen carrier in multicycle CLC. *AIChE J.* 53 (7), 1817–1829. doi:10.1002/aic.11188.
- Hossain, M.K., Strezov, V., Chan, K.Y., Ziolkowski, A., Nelson, P.F., 2011. Influence of pyrolysis temperature on production and nutrient properties of wastewater sludge biochar. *J. Environ. Manage.* 92 (1), 223–228. doi:10.1016/j.jenvman.2010.09.008.
- Hossain, M.A., Nabavi, S.A., Ranganathan, P., Könözy, L., Manovic, V., 2020. 3D CFD modelling of liquid dispersion in structured packed bed column for CO₂ capture. *Chem. Eng. Sci.* 225. doi:10.1016/j.ces.2020.115800, 115800-115800.
- Hosseini, S.H., Shojaei, S., Ahmadi, G., Zivdar, M., 2012. Computational fluid dynamics studies of dry and wet pressure drops in structured packings. *J. Ind. Eng. Chem.* 18 (4), 1465–1473. doi:10.1016/j.jiec.2012.02.012.
- Hosseini, S.S., Najari, S., Kundu, P.K., Tan, N.R., Roodsathi, S.M., 2015. Simulation and sensitivity analysis of transport in asymmetric hollow fiber membrane permeators for air separation. *RSC Adv.* 5 (105), 86359–86370. doi:10.1039/C5RA13943K.
- Hou, X., 2016. Smart gating multi-scale pore/channel-based membranes. *Adv. Mater.* 28 (33), 7049–7064. doi:10.1002/adma.201600797.
- House, K.Z., Baclig, A.C., Ranjan, M., van Nierop, E.A., Wilcox, J., Herzog, H.J., 2011. Economic and energetic analysis of capturing CO₂ from ambient air. *Proc. Natl. Acad. Sci.* 108 (51), 20428–20433. doi:10.1073/pnas.1012253108.
- Hsa, B., Mc, C., Ji, A., Wd, A., Min, H.A., Jh, A., Lq, A., Pt, B., Zlb, D., 2021. Application of “coordinative effect” into tri-solvent MEA+BEA+AMP blends at concentrations of 0.1 + 2 + 20.5 + 2 + 2 mol/L with absorption, desorption and mass transfer analyses - ScienceDirect. *Int. J. Greenh. Gas Control* 107.
- Hu, Y., Yan, J., 2012. Characterization of flue gas in oxy-coal combustion processes for CO₂ capture. *Appl. Energy* 90 (1), 113–121. doi:10.1016/j.apenergy.2011.03.005.
- Hu, Y., Liu, Z., Xu, J., Huang, Y., Song, Y., 2013. Evidence of pressure enhanced CO₂ storage in ZIF-8 probed by FTIR spectroscopy. *J. Am. Chem. Soc.* 135 (25), 9287–9290. doi:10.1021/ja403635b.
- Hu, H., Li, F., Xia, Q., Li, X., Liao, L., Fan, M., 2014. Research on influencing factors and mechanism of CO₂ absorption by poly-amino-based ionic liquids. *Int. J. Greenh. Gas Control* 31, 33–40. doi:10.1016/j.jggc.2014.09.021.
- Hu, Y., Verdegaeal, W.M., Yu, S.H., Jiang, H.L., 2014. Alkylamine-tethered stable metal-organic framework for CO₂ (capture from flue gas. *ChemSusChem* 7 (3), 734–737. doi:10.1002/cssc.201301163.
- Hu, Y., Liu, W., Chen, H., Zhou, Z., Wang, W., Sun, J., Yang, X., Li, X., Xu, M., 2016. Screening of inert solid supports for CaO-based sorbents for high temperature CO₂ capture. *Fuel* 181, 199–206.
- Hu, Z., Gami, A., Wang, Y., Zhao, D., 2017a. A triphasic modulated hydrothermal approach for the synthesis of multivariate metal-organic frameworks with hydrophobic moieties for highly efficient moisture-resistant CO₂ capture. *Adv. Sustain. Syst.* 1 (11), 1700092.
- Hu, Z., Wang, Y., Farooq, S., Zhao, D., 2017b. A highly stable metal-organic framework with optimum aperture size for CO₂ capture. *AIChE J.* 63 (9), 4103–4114.
- Hu, J., Galvita, V.V., Poelman, H., Marin, G.B., 2018. Advanced chemical looping materials for CO₂ utilization: a review. *Materials* 11 (7), 1187.
- Hu, L., Liu, J., Zhu, L., Hou, X., Huang, L., Lin, H., Cheng, J., 2018. Highly permeable mixed matrix materials comprising ZIF-8 nanoparticles in rubbery amorphous poly (ethylene oxide) for CO₂ capture. *Sep. Purif. Technol.* 205, 58–65. doi:10.1016/j.seppur.2018.05.012.
- Hu, Y.C., Guo, Y.F., Sun, J., Li, H.L., Liu, W.Q., 2019. Progress in MgO sorbents for cyclic CO₂ capture: a comprehensive review. *J. Mater. Chem. A* 7 (35), 20103–20120. doi:10.1039/c9ta06930e.
- Hu, Y.W., Cui, H.J., Cheng, Z.M., Zhou, Z.M., 2019. Sorption-enhanced water gas shift reaction by *in situ* CO₂ capture on an alkali metal salt-promoted MgO-CaCO₃ sorbent. *Chem. Eng. J.* 377, 119823. doi:10.1016/j.cej.2018.08.209.
- Hu, J., Poelman, H., Marin, G.B., Detavernier, C., Kawi, S., Galvita, V.V., 2020. FeO controls the sintering of iron-based oxygen carriers in chemical looping CO₂ conversion. *J. CO₂ Util.* 40, 101216. doi:10.1016/j.jcou.2020.101216.
- Hu, X., Liu, L., Luo, X., Xiao, G., Shiko, E., Zhang, R., Fan, X., Zhou, Y., Liu, Y., Zeng, Z., Li, C.e., 2020. A review of N-functionalized solid adsorbents for post-combustion CO₂ capture. *Appl. Energy* 260. doi:10.1016/j.apenergy.2019.114244.
- Hu, X., Lee, W.H., Zhao, J., Kim, J.S., Wang, Z., Yan, J., Zhuang, Y., Lee, Y.M.J., 2020. Thermally rearranged polymeric membranes containing highly rigid biphenyl ortho-hydroxyl diamine for hydrogen separation. *J. Membr. Sci.* 604, 118053.
- Hu, C., Cheng, P., Chou, S., Lai, C., Huang, S., Tsai, H., Hung, W., Lee, K., 2020. Separation behavior of amorphous amino-modified silica nanoparticle/polyimide mixed matrix membranes for gas separation. *J. Membr. Sci.* 595, 117542. doi:10.1016/j.memsci.2019.117542.
- Hu, Y.C., Lu, H.Y., Liu, W.Q., Yang, Y.D., Li, H.L., 2020. Incorporation of CaO into inert supports for enhanced CO₂ capture: a review. *Chem. Eng. J.* 396, 16. doi:10.1016/j.cej.2020.125253.
- Hu, J., Galvita, V.V., Poelman, H., Wang, Z., Marin, G.B., Kawi, S., 2021a. Coupling CO₂ utilization and NO reduction in chemical looping manner by surface carbon. *Appl. Catal. B: Environ.* 297, 120472. doi:10.1016/j.apcatb.2021.120472.
- Hu, J., Hongmanorom, P., Chirawatkul, P., Kawi, S., 2021b. Efficient integration of CO₂ capture and conversion over a Ni supported CeO₂-modified CaO microsphere at moderate temperature. *Chem. Eng. J.* 426, 130864. doi:10.1016/j.cej.2021.130864.
- Hu, J., Hongmanorom, P., Galvita, V.V., Li, Z., Kawi, S., 2021c. Bifunctional Ni-Ca based material for integrated CO₂ capture and conversion via calcium-looping dry reforming. *Appl. Catal. B: Environ.* 284, 119734. doi:10.1016/j.apcatb.2020.119734.
- Hu, H.T., Fang, M.X., Liu, F., Wang, T., Xia, Z.X., Zhang, W., Ge, C.L., Yuan, J.J., 2022. Novel alkanolamine-based biphasic solvent for CO₂ capture with low energy consumption and phase change mechanism analysis. *Appl. Energy* 324. doi:10.1016/j.apenergy.2022.119570.
- Hu, L., Bui, V.T., Pal, S., Guo, W., Subramanian, A., Kissinger, K., Fan, S., Nam, C.Y., Ding, Y., Lin, H., 2022a. In situ growth of crystalline and polymer-incorporated amorphous ZIFs in polybenzimidazole achieving hierarchical nanostructures for carbon capture. *Small*, 2201982. doi:10.1002/smll.202201982.
- Hu, L., Clark, K., Alebrahim, T., Lin, H., 2022b. Mixed matrix membranes for post-combustion carbon capture: From materials design to membrane engineering. *J. Membr. Sci.* 644, 120140. doi:10.1016/j.memsci.2021.120140.
- Huang, Q., Wu, C., 2022. Photoswitching metal organic frameworks development and applications on environmental related topics. *Mater. Today Sustain.* 18. doi:10.1016/j.mtsust.2022.100149.

- Huang, A., Dou, W., Caro, J.R., 2010. Steam-stable zeolitic imidazolate framework ZIF-90 membrane with hydrogen selectivity through covalent functionalization. *J. Am. Chem. Soc.* 132 (44), 15562–15564. doi:10.1021/ja108774v.
- Huang, Y.-F., Chiueh, P.-T., Shih, C.-H., Lo, S.-L., Sun, L., Zhong, Y., Qiu, C., 2015. Microwave pyrolysis of rice straw to produce biochar as an adsorbent for CO₂ capture. *Energy* 84, 75–82. doi:10.1016/j.energy.2015.02.026.
- Huang, X., Lu, J., Wang, W., Wei, X., Ding, J., 2016. Experimental and computational investigation of CO₂ capture on amine grafted metal-organic framework NH₂-MIL-101. *Appl. Surf. Sci.* 371, 307–313. doi:10.1016/j.apsusc.2016.02.154.
- Huang, H.-j., Yang, T., Lai, F.-y., Wu, G.-q., 2017. Co-pyrolysis of sewage sludge and sawdust/rice straw for the production of biochar. *J. Anal. Appl. Pyrol.* 125, 61–68. doi:10.1016/j.jaap.2017.04.018.
- Huang, L., Zhang, Y., Gao, W., Harada, T., Qin, Q., Zheng, Q., Hatton, T.A., Wang, Q., 2017. Alkali carbonate molten salt coated calcium oxide with highly improved carbon dioxide capture capacity. *Energy Technol.*
- Huang, Q., Jing, G., Zhou, X., Lv, B., Zhou, Z., 2018. A novel biphasic solvent of amino-functionalized ionic liquid for CO₂ capture: High efficiency and regenerability. *J. CO₂ Util.* 25, 22–30. doi:10.1016/j.jcou.2018.03.001.
- Huang, G., Isfahani, A.P., Muchtar, A., Sakurai, K., Shrestha, B.B., Qin, D., Yamaguchi, D., Sivaniah, E., Ghalei, B., 2018. Pebax/ionic liquid modified graphene oxide mixed matrix membranes for enhanced CO₂ capture. *J. Membr. Sci.* 565, 370–379. doi:10.1016/j.memsci.2018.08.026.
- Huang, J., Liu, W., Yang, Y., Liu, B., 2018. High-performance Ni-Fe redox catalysts for selective CH₄ to syngas conversion via chemical looping. *ACS Catal.* 8 (3), 1748–1756. doi:10.1021/acscatal.7b03964.
- Huang, Q., Luo, Q., Wang, Y., Pentzer, E., Gurkan, B., 2019. Hybrid ionic liquid capsules for rapid CO₂ capture. *Ind. Eng. Chem. Res.* 58 (24), 10503–10509. doi:10.1021/acs.iecr.9b00314.
- Huang, Y.F., Chiueh, P.T., Lo, S.L., 2019. CO₂ adsorption on biochar from co-torrefaction of sewage sludge and leucaena wood using microwave heating. *Innov. Solut. Energy Trans.* 158, 4435–4440. doi:10.1016/j.egypro.2019.01.772.
- Huang, L., Liu, J., Lin, H., 2020. Thermally stable, homogeneous blends of cross-linked poly(ethylene oxide) and crown ethers with enhanced CO₂ permeability. *J. Membr. Sci.* 610, 118253. doi:10.1016/j.memsci.2020.118253.
- Huang, L., Ding, L., Wang, H., 2021. MXene-based membranes for separation applications. *Small Sci.* 1 (7), 2100013. doi:10.1002/smssc.202100013.
- Huang, Q., Mu, J., Zhan, Z., Wang, F., Jin, S., Tan, B., Wu, C., 2022. Steric hindrance alleviation strategy to enhance the photo switching efficiency of azobenzene functionalized metal-organic framework toward tailorabe carbon dioxide capture. *J. Mater. Chem. A* doi:10.1039/d1ta09270g.
- Huften, J.R., Mayorga, S., Sircar, S., 1999. Sorption-enhanced reaction process for hydrogen production. *Process. Saf. Environ. Protect.* 45 (2), 248–256. doi:10.1002/aic.690450205.
- S.J.W. Huften, J., Nataraj, S., Rao, M., Sircar, S., 1999. Proceedings of the 1999 US DOE Hydrogen Program Review National Renewable Energy Lab. (NREL), Golden, CO (United States).
- Hunsom, M., Authanit, C., 2013. Adsorptive purification of crude glycerol by sewage sludge-derived activated carbon prepared by chemical activation with H₃PO₄, K₂CO₃ and KOH. *Chem. Eng. J.* 229, 334–343. doi:10.1016/j.cej.2013.05.120.
- Husebye, J., et al., 2012. Techno Economic Evaluation of Amine based CO₂ Capture: Impact of CO₂ Concentration and Steam Supply. *Energy Procedia* 23, 381–390.
- Hussain, A., Hägg, M.-B., 2010. A feasibility study of CO₂ capture from flue gas by a facilitated transport membrane. *J. Membr. Sci.* 359 (1), 140–148. doi:10.1016/j.memsci.2009.11.035.
- Hussain, S., Dong, H., Zeng, S., Ahmad, M.U., Shehzad, F.K., Wu, H., Zhang, Y., 2021. Investigation uncovered the impact of anions on CO₂ absorption by low viscous ether functionalized pyridinium ionic liquids. *J. Mol. Liq.* 336. doi:10.1016/j.molliq.2021.116362.
- Hutson, N.D., Attwood, B.C., 2008. High temperature adsorption of CO₂ on various hydroxalite-like compounds. *Adsorption* 14 (6), 781–789. doi:10.1007/s10450-007-9085-6.
- Hwang, K.-S., Park, S.-W., Park, D.-W., Oh, K.-J., Kim, S.-S., 2010. Absorption of carbon dioxide into diisopropanolamine solutions of polar organic solvents. *J. Taiwan Instit. Chem. Eng.* 41 (1), 16–21.
- Iarikov, D., Hacırlıoğlu, P., Oyama, S.T., 2011. Supported room temperature ionic liquid membranes for CO₂/CH₄ separation. *Chem. Eng. J.* 166 (1), 401–406.
- Ibrahim, M., Hameed, B.H., Ouakouk, A., Din, A.T.M., 2022. Effect of hydrothermal carbonization parameters and performance of carbon dioxide adsorption on pineapple peel waste biochar. *Chem. Eng. Technol.* doi:10.1002/ceat.202200089.
- Agency, I.E., 2021. CO₂ capture: an examination of potential gas-solid adsorption technologies for the capture of CO₂ and other greenhouse gases arising from power generation using fossil fuel. 1992.
- IEA, 2021. Net zero by 2050: A roadmap for the global energy sector. <https://www.iea.org/reports/net-zero-by-2050> (Accessed Oct. 2021).
- Igalavithana, A.D., Choi, S.W., Dissanayake, P.D., Shang, J., Wang, C.-H., Yang, X., Kim, S., Tsang, D.C.W., Lee, K.B., Ok, Y.S., 2020a. Gasification biochar from biowaste (food waste and wood waste) for effective CO₂ adsorption. *J. Hazard. Mater.* 391, 121147. doi:10.1016/j.jhazmat.2019.121147.
- Igalavithana, A.D., Choi, S.W., Shang, J., Hanif, A., Dissanayake, P.D., Tsang, D.C.W., Kwon, J.-H., Lee, K.B., Ok, Y.S., 2020b. Carbon dioxide capture in biochar produced from pine sawdust and paper mill sludge: Effect of porous structure and surface chemistry. *Sci. Total Environ.* 739, 139845.
- Igalavithana, A.D., Choi, S.W., Shang, J., Hanif, A., Dissanayake, P.D., Tsang, D.C.W., Kwon, J.-H., Lee, K.B., Ok, Y.S., 2020c. Carbon dioxide capture in biochar produced from pine sawdust and paper mill sludge: Effect of porous structure and surface chemistry. *Sci. Total Environ.* 739, 139845. doi:10.1016/j.scitotenv.2020.139845.
- Ignat'ev, N.V., Finze, M., Sprenger, J.A.P., Kerpen, C., Bernhardt, E., Willner, H., 2015. New hydrophobic ionic liquids with perfluoroalkyl phosphate and cyanofluoroborate anions. *J. Fluorine Chem.* 177, 46–54. doi:10.1016/j.jfluchem.2015.03.007.
- Iliuta, I., Petre, C.F., Larachi, F., 2004. Hydrodynamic continuum model for two-phase flow structured-packing- containing columns. *Chem. Eng. Sci.* 59 (4), 879–888. doi:10.1016/j.ces.2003.11.020.
- Iliuta, I., Hasib-ur-Rahman, M., Larachi, F., 2014. CO₂ absorption in diethanolamine/ionic liquid emulsions - Chemical kinetics and mass transfer study. *Chem. Eng. J.* 240, 16–23. doi:10.1016/j.cej.2013.11.063.
- Iliuta, I., Larachi, F., Fourati, M., Raynal, L., Roig, V., 2014. Flooding limit in countercurrent gas-liquid structured packed beds-Prediction from a linear stability analysis of an Eulerian two-fluid model. *Chem. Eng. Sci.* 120, 49–58. doi:10.1016/j.ces.2014.08.053.
- Im, D., Jung, H., Lee, J.H., 2020. Modeling, simulation and optimization of the rotating packed bed (RPB) absorber and stripper for MEA-based carbon capture. *Comput. Chem. Eng.* 143. doi:10.1016/j.compchemeng.2020.107102, 107102–107102.
- Ioannidis, A., Vroliadis, D., Kallitidis, J., Ioannidis, T., Deimede, V., 2021. Synthesis and characterization of poly(ethylene oxide) based copolymer membranes for efficient gas/vapour separation: effect of PEO content and chain length. *J. Membr. Sci.* 632, 119353. doi:10.1016/j.memsci.2021.119353.
- Iora, P., Chiesa, P., 2009. High efficiency process for the production of pure oxygen based on solid oxide fuel cell-solid oxide electrolyzer technology. *J. Power Sources* 190 (2), 408–416. doi:10.1016/j.jpowsour.2009.01.045.
- Isanejad, M., Mohammadi, T., 2018. Effect of amine modification on morphology and performance of poly(ether-block-amide)/fumed silica nanocomposite membranes for CO₂/CH₄ separation. *Mater. Chem. Phys.* 205, 303–314.
- Izquierdo, M.T., García-Labiano, F., Abad, A., Cabello, A., Gayán, P., de Diego, L.F., Adánez, J., 2021. On the optimization of physical and chemical stability of a Cu/Al₂O₃ impregnated oxygen carrier for chemical looping combustion. *Fuel Process. Technol.* 215, 106740. doi:10.1016/j.fuproc.2021.106740.
- Jacobson, M.Z., 2009. Review of solutions to global warming, air pollution, and energy security. *Energy Environ. Sci.* 2 (2), 148–173.
- R.V.C. Jadhav, P.D., Biniwale, R.B., Labhsetwar, N.K., Devotta, S., Rayalu, S.S., 2007. Monoethanol Amine Modified Zeolite 13X for CO₂ Adsorption at Different Temperatures. *Energy Fuels* 21, 3555–3559.
- Jafari, T., Moharreri, E., Tloueinia, P., Amin, A.S., Sahoo, S., Khakpash, N., Noshadi, I., Alpay, S.P., Suib, S.L., 2017. Microwave-assisted synthesis of amine functionalized mesoporous polydivinylbenzene for CO₂ adsorption. *J. CO₂ Util.* 19, 79–90. doi:10.1016/j.jcou.2017.03.004.
- Jahandar Lashaki, M., Ziaei-Azad, H., Sayari, A., 2017. Insights into the hydrothermal stability of triamine-functionalized SBA-15 silica for CO₂ adsorption. *ChemSusChem* 10 (20), 4037–4045. doi:10.1002/cssc.201701439.
- Jahandar Lashaki, M., Khiavi, S., Sayari, A., 2019. Stability of amine-functionalized CO₂ adsorbents: a multifaceted puzzle. *Chem. Soc. Rev.* 48 (12), 3320–3405. doi:10.1039/c8cs00877a.
- Jaiboon, O.-a., Chalermsinuwan, B., Mekasut, L., Piumsomboon, P., 2013. Effect of flow patterns/regimes on CO₂ capture using K₂CO₃ solid sorbent in fluidized bed/circulating fluidized bed. *Chem. Eng. J.* 219, 262–272. doi:10.1016/j.cej.2012.12.081.
- Jalalabadi, T., Glenn, M., Tremain, P., Moghtaderi, B., Donne, S., Allen, J., 2019. Modification of biochar formation during slow pyrolysis in the presence of alkali metal carbonate additives. *Energy Fuels* 33 (11), 11235–11245. doi:10.1021/acs.energyfuels.9b02865.
- James, I.I.R.E., Keairns, D., Turner, M., Woods, M., Kuehn, N., Zoelle, A., 2019. Cost and Performance Baseline for Fossil Energy Plants Volume 1: Bituminous Coal and Natural Gas to Electricity. National Energy Technology Laboratory, United States.
- Jana, A.K., 2016. A new divided-wall heat integrated distillation column (HIDIc) for batch processing: feasibility and analysis. *Appl. Energy* 172, 199–206. doi:10.1016/j.apenergy.2016.03.117.
- Janakiram, S., Espejo, Martín, Juan, L., Høisæter, K.K., Lindbråthen, A., Ansaloni, L., Deng, L., 2020. Three-phase hybrid facilitated transport hollow fiber membranes for enhanced CO₂ separation. *Appl. Mater. Today* 21, 100801. doi:10.1016/j.apmt.2020.100801.
- Jankowski, A., Grabiec, E., Nocoń-Szmajda, K., Marcinkowski, A., Janeczek, H., Wolińska-Grabczyk, A., 2021. Polyimide-based membrane materials for CO₂ separation: a comparison of segmented and aromatic (Co)polyimides. 11 (4), 274.
- Jansen, D., Gazzani, M., Manzolini, G., Dijk, E.v., Carbo, M., 2015. Pre-combustion CO₂ capture. *Int. J. Greenh. Gas Control* 40, 167–187. doi:10.1016/j.jggc.2015.05.028.
- Janusz-Szymańska, K., Dryjańska, A., 2015. Possibilities for improving the thermodynamic and economic characteristics of an oxy-type power plant with a cryogenic air separation unit. *Energy* 85, 45–61. doi:10.1016/j.energy.2015.03.049.
- Jasiński-Hałat, M., Kędzior, K., 2005. Comparison of molecular sieve properties in micro-porous chars from low-rank bituminous coal activated by steam and carbon dioxide. *Carbon* 43 (5), 944–953.
- Jassim, M.S., Rochelle, G., Eimer, D., Ramshaw, C., 2007. Carbon dioxide absorption and desorption in aqueous monoethanolamine solutions in a rotating packed bed. *Ind. Eng. Chem. Res.* 46 (9), 2823–2833. doi:10.1021/ie051104r.
- Jensen, M.J., Russell, C.S., Bergeson, D., Hoeger, C.D., Frankman, D.J., Bence, C.S., Baxter, L.L., 2015. Prediction and validation of external cooling loop cryogenic carbon capture (CCC-ECL) for full-scale coal-fired power plant retrofit. *Int. J. Greenh. Gas Control* 42, 200–212. doi:10.1016/j.jggc.2015.04.009.
- Jeon, H., Min, Y.J., Ahn, S.H., Hong, S.-M., Shin, J.-S., Kim, J.H., Lee, K.B., 2012. Graft copolymer templated synthesis of mesoporous MgO/TiO₂ mixed oxide nanoparticles and their CO₂ adsorption capacities. *Colloids Surf. A: Physicochem. Eng. Aspects* 414, 75–81.
- Jeon, D.H., Min, B.G., Oh, J.G., Nah, C., Park, S.J., 2015. Influence of Nitro-

- gen moieties on CO₂ capture of Carbon Aerogel. *Carbon Lett.* 16 (1), 57–61. doi:10.5714/Cl.2015.16.1.057.
- Jeon, J.W., Kim, D.-G., Sohn, E.-h., Yoo, Y., Kim, Y.S., Kim, B.G., Lee, J.-C., 2017. Highly carboxylate-functionalized polymers of intrinsic microporosity for CO₂-selective polymer membranes. *Macromolecules* 50 (20), 8019–8027. doi:10.1021/acs.macromol.7b01332.
- Ji, L., et al., 2022. Metal oxyhydroxide catalysts promoted CO₂ absorption and desorption in amine-based carbon capture: a feasibility study. *ACS Omega* 7 (49), 44620–44630. doi:10.1021/acsomega.2c02851.
- Ji, G., Memon, M.Z., Zhuo, H., Zhao, M., 2017. Experimental study on CO₂ capture mechanisms using Na₂ZrO₃ sorbents synthesized by soft chemistry method. *Chem. Eng. J.* 313, 646–654.
- Ji, C., Yuan, S., Huffman, M., El-Halwagi, M.M., Wang, Q., 2021. Post-combustion carbon capture for tank to expeller via process modeling and simulation. *J. CO₂ Util.* 51. doi:10.1016/j.jcou.2021.101655.
- Jia, X., Qiao, Z., He, B., Zhong, C., 2020. Highly selective filler–polymer gaps in situ fabricated in mixed matrix membranes for gas separation. *J. Mater. Chem. A* 8 (24), 11928–11932. doi:10.1039/D0TA03378B.
- Jia, P., Liu, J., Kong, J., Hu, M., Qi, N., Chen, Z., Xu, S., Li, N., 2022. Tailoring the micropore structure of 6FDA-based polyimide membrane for gas permselectivity studied by positron annihilation. *Sep. Purif. Technol.* 282, 120044.
- Jia, Y., Wei, J., Yuan, Y., Geng, L., Chen, S., Liao, L., 2022. Tetraethylenepentamine impregnated composite material ZSM-5/SBA-16 for CO₂ adsorption. *J. Mater. Res.* 37 (2), 543–553. doi:10.1557/s43578-021-00469-y.
- Jiang, Y., Khadilkar, M.R., Al-Dahhan, M.H., Dudukovic, M.P., 2002. CFD of multiphase flow in packed-bed reactors: II. Results and applications. *AIChE J.* 48 (4), 716–730. doi:10.1002/aic.690480407.
- Jiang, B., Wang, X., Gray, M.L., Duan, Y., Luebke, D., Li, B., 2013. Development of amino acid and amino acid-complex based solid sorbents for CO₂ capture. *Appl. Energy* 109, 112–118. doi:10.1016/j.apenergy.2013.03.070.
- Jiang, J., Lu, Z., Zhang, M., Duan, J., Zhang, W., Pan, Y., Bai, J., 2018. Higher symmetry multinuclear clusters of metal-organic frameworks for highly selective CO₂ capture. *J. Am. Chem. Soc.* 140 (51), 17825–17829. doi:10.1021/jacs.8b07589.
- Jiang, K., Li, K., Yu, H., Feron, P.H.M., 2018. Piperazine-promoted aqueous-ammonia-based CO₂ capture: process optimisation and modification. *Chem. Eng. J.* 347, 334–342. doi:10.1016/j.cej.2018.04.103.
- Jiang, Y., Tan, P., Qi, S.C., Liu, X.Q., Yan, J.H., Fan, F., Sun, L.B., 2019. Metal-organic frameworks with target-specific active sites switched by photoresponsive motifs: efficient adsorbents for tailorable CO₂ capture. *Angew. Chem. Int. Ed. Engl.* 58 (20), 6600–6604. doi:10.1002/anie.201900141.
- Jiang, Y., Zhang, Z., Fan, J., Yang, L., Liu, J., 2020. Experimental study on postcombustion systems including a hollow fiber membrane and a packed column. *ACS Omega* 5 (28), 17692–17702. doi:10.1021/acsomega.0c02251.
- Jiang, X., He, S., Han, G., Long, J., Li, S., Lau, C.H., Zhang, S., Shao, L., 2021. Aqueous one-step modulation for synthesizing monodispersed ZIF-8 nanocrystals for mixed-matrix membrane. *ACS Appl. Mater. Interfaces* 13 (9), 11296–11305. doi:10.1021/acami.0c22910.
- Jiang, C., Fan, M., Gao, G., Jiang, W., Li, X., Luo, C., Zhang, L., Wu, F., 2022. Nanostructured AlOOH - A promising catalyst to reduce energy consumption for amine-based CO₂ capture. *Sep. Purif. Technol.* 303. doi:10.1016/j.seppur.2022.122232.
- Jilvero, H., Normann, F., Andersson, K., Johnsson, F., 2015. Ammonia-based post combustion-The techno-economics of controlling ammonia emissions. *Int. J. Greenh. Gas Control* 37, 441–450.
- Jin, H., Capareda, S., Chang, Z., Gao, J., Xu, Y., Zhang, J., 2014. Biochar pyrolytically produced from municipal solid wastes for aqueous As (V) removal: Adsorption property and its improvement with KOH activation. *Bioresour. Technol.* 169, 622–629. doi:10.1016/j.biortech.2014.06.103.
- Jin, S., Ho, K., Vu, A.-T., Lee, C.-H., 2017. Salt-composition-controlled precipitation of triple-salt-promoted MgO with enhanced CO₂ sorption rate and working capacity. *Energy Fuels* 31 (9), 9725–9735.
- Jo, S.I., An, Y.I., Kim, K.Y., Choi, S.Y., Kwak, J.S., Oh, K.R., Kwon, Y.U., 2017. Mechanisms of absorption and desorption of CO₂ by molten NaNO₃-promoted MgO. *Phys. Chem. Phys.* 19 (8), 6224–6232. doi:10.1039/c6cp07787k.
- Joel, A.S., Wang, M., Ramshaw, C., Oko, E., 2014. Process analysis of intensified absorber for post-combustion CO₂ capture through modelling and simulation. *Int. J. Greenh. Gas Control* 21, 91–100. doi:10.1016/j.jggc.2013.12.005.
- Joel, A.S., Wang, M., Ramshaw, C., Oko, E., 2017. Modelling, simulation and analysis of intensified regenerator for solvent based carbon capture using rotating packed bed technology. *Appl. Energy* 203, 11–25. doi:10.1016/j.apenergy.2017.05.157.
- Jonathan, C., 2013. SaskPower expects 30% savings in carbon capture following Boundary Dam project. *SNL Energy Coal Rep.*
- Jones, S.C., Bauer, C.A., 2009. Diastereoselective heterogeneous bromination of stilbene in a porous metal–organic framework. *J. Am. Chem. Soc.* 131 (35), 12516–12517.
- Jones, C.L., Tansell, A.J., Easun, T.L., 2016. The lighter side of MOFs: structurally photoresponsive metal–organic frameworks. *J. Mater. Chem. A* 4 (18), 6714–6723. doi:10.1039/c5ta09424k.
- Jones, N., 2009. Climate crunch: sucking it up. *Nature* 458 1094+.
- Jones, C.W., 2011. CO₂ Capture from dilute gases as a component of modern global carbon management. *Ann. Rev. Chem. Biomol. Eng.* 2 (1), 31–52. doi:10.1146/annurev-chembioeng-061010-114252.
- Joss, L., Gazzani, M., Mazzotti, M., 2017. Rational design of temperature swing adsorption cycles for post-combustion CO₂ capture. *Chem. Eng. Sci.* 158, 381–394. doi:10.1016/j.ces.2016.10.013.
- Juhasz, G., Homonnay, Z.o., Nomura, K., Hayakawa, T., Hamakawa, S., Vértés, A., 2001. Microstructural study of the CO₂ absorption in SrCa_{1-x}Fe_{0.5}Co_{0.5}O_{3-δ}. *Solid State Ionics* 139, 219–231. doi:10.1016/S0167-2738 (01)00690-7.
- Jung, K.-W., Ahn, K.-H., 2016. Fabrication of porosity-enhanced MgO/biochar for removal of phosphate from aqueous solution: Application of a novel combined electrochemical modification method. *Bioresour. Technol.* 200, 1029–1032. doi:10.1016/j.biortech.2015.10.008.
- Jung, W., Lee, K.S., 2020. Isotherm and kinetics modeling of simultaneous CO₂ and H₂O adsorption on an amine-functionalized solid sorbent. *J. Nat. Gas Sci. Eng.* 84, 103489. doi:10.1016/j.jngse.2020.103489.
- Jung, W., Lee, J., 2022a. Economic evaluation for four different solid sorbent processes with heat integration for energy-efficient CO₂ capture based on PEI-silica sorbent. *Energy* 238. doi:10.1016/j.energy.2021.121864, 121864–121864.
- Jung, W., Lee, J., 2022b. Pseudo counter-current turbulent fluidized bed process with sensible heat recovery for energy-efficient CO₂ capture using an amine-functionalized solid sorbent. *Energy* 240. doi:10.1016/j.energy.2021.122803, 122803–122803.
- Jung, H., Jeon, S., Jo, D.H., Huh, J., Kim, S.H., 2017. Effect of crosslinking on the CO₂ adsorption of polyethyleneimine-impregnated sorbents. *Chem. Eng. J.* 307, 836–844. doi:10.1016/j.cej.2016.09.005.
- Jung, S., Park, Y.-K., Kwon, E.E., 2019. Strategic use of biochar for CO₂ capture and sequestration. *J. CO₂ Util.* 32, 128–139. doi:10.1016/j.jcou.2019.04.012.
- Kárszová, M., Zach, B., Petrusová, Z., Červenka, V., Bobák, M., Šyc, M., Izák, P., 2020. Post-combustion carbon capture by membrane separation. *Review. Sep. Purif. Technol.* 238, 116448. doi:10.1016/j.seppur.2019.116448.
- Kisgens, P., Rose, M., Senkowska, I., Fröde, H., Henschel, A., Siegle, S., Kaskel, S., 2009. Characterization of metal-organic frameworks by water adsorption. *Microporous Mesoporous Mater.* 120 (3), 325–330.
- K, U.K., 1979. Porous Silica. Elsevier.
- Kadam, R., Panwar, N.L., 2017. Recent advancement in biogas enrichment and its applications. *Renew. Sustain. Energy Rev.* 73, 892–903. doi:10.1016/j.rser.2017.01.167.
- Kadi, M.W., El Salam, H.M.A., Zaki, T., Mohamed, R.M., 2020. Adsorption of carbon dioxide on CuxMg (BTC) MOFs: influence of Cu/Mg ratio. *J. Nanoparticle Res.* 22 (6). doi:10.1007/s11051-020-04855-1.
- Kagunya, W., Hassan, Z., Jones, W., 1996. Catalytic properties of layered double hydroxides and their calcined derivatives. *Inorg. Chem.* 35 (21), 5970–5974. doi:10.1021/ic960047e.
- Kalantari, S., Omidkhan, M., Ebadi Amooghini, A., Matsuura, T., 2020. Superior interfacial design in ternary mixed matrix membranes to enhance the CO₂ separation performance. *Appl. Mater. Today* 18, 100491. doi:10.1016/j.apmt.2019.100491.
- Kammakam, I., O’Harra, K.E., Jackson, E.M., Bara, J.E.J.P., 2021. Synthesis of imidazolium-mediated Poly (benzoxazole) Ionenone and composites with ionic liquids as advanced gas separation membranes. 214, 123239.
- Kamran, U., Park, S.J., 2020. Tuning ratios of KOH and NaOH on acetic acid-mediated chitosan-based porous carbons for improving their textural features and CO₂ uptakes. *J. CO₂ Util.* 40. doi:10.1016/j.jcou.2020.101212.
- Kandambeth, S., Mallick, A., Lukose, B., Mane, M.V., Heine, T., Banerjee, R., 2012. Construction of crystalline 2D covalent organic frameworks with remarkable chemical (acid/base) stability via a combined reversible and irreversible route. *J. Am. Chem. Soc.* 134 (48), 19524–19527.
- Kandambeth, S., Shinde, D.B., Panda, M.K., Lukose, B., Heine, T., Banerjee, R., 2013. Enhancement of chemical stability and crystallinity in porphyrin-containing covalent organic frameworks by intramolecular hydrogen bonds. *Angew. Chem. Int. Ed.* 52 (49), 13052–13056.
- Kandambeth, S., Venkatesh, V., Shinde, D.B., Kumari, S., Halder, A., Verma, S., Banerjee, R., 2015. Self-templated chemically stable hollow spherical covalent organic framework. *Nat. Commun.* 6 (1), 1–10.
- Kanehashi, S., Nagai, K., 2005. Analysis of dual-mode model parameters for gas sorption in glassy polymers. *J. Membr. Sci.* 253 (1–2), 117–138.
- Kanehashi, S., Chen, G.Q., Scholtes, C.A., Ozcelik, B., Hua, C., Ciddor, L., Southon, P.D., D’Alessandro, D.M., Kentish, S.E., 2015. Enhancing gas permeability in mixed matrix membranes through tuning the nanoparticle properties. *J. Membr. Sci.* 482, 49–55.
- Kanezashi, M., Tomarino, Y., Nagasawa, H., Tsuru, T., 2019. Tailoring the molecular sieving properties and thermal stability of carbonized membranes containing polyhedral oligomeric silsesquioxane (POSS)-polyimide via the introduction of norbornene. *J. Membr. Sci.* 582, 59–69. doi:10.1016/j.memsci.2019.04.003.
- Kang, J.-L., Sun, K., Wong, D.S.-H., Jang, S.-S., Tan, C.-S., 2014. Modeling studies on absorption of CO₂ by monoethanolamine in rotating packed bed. *Int. J. Greenh. Gas Control* 25, 141–150. doi:10.1016/j.jggc.2014.04.011.
- Kang, Z., Peng, Y., Hu, Z., Qian, Y., Chi, C., Yeo, L.Y., Tee, L., Zhao, D., 2015. Mixed matrix membranes composed of two-dimensional metal–organic framework nanosheets for pre-combustion CO₂ capture: a relationship study of filler morphology versus membrane performance. *J. Mater. Chem. A* 3 (41), 20801–20810. doi:10.1039/C5TA03739E.
- Kang, M., Min, H.J., Kim, N.U., Kim, J.H., 2021a. Amphiphilic micelle-forming PDMS-PEGBEM comb copolymer self-assembly to tailor the interlamellar nanospaces of defective poly (ethylene oxide) membranes. *Sep. Purif. Technol.* 257, 117892. doi:10.1016/j.seppur.2020.117892.
- Kang, M., Min, H.J., Kim, N.U., Kim, J.H., 2021b. Amphiphilic micelle-forming PDM-S-PEGBEM comb copolymer self-assembly to tailor the interlamellar nanospaces of defective poly (ethylene oxide) membranes. *Sep. Purif. Technol.* 257, 117892.
- Kanniche, M., Gros-Bonnivard, R., Jaud, P., Valle-Marcos, J., Amann, J.-M., Bouallou, C., 2010. Pre-combustion, post-combustion and oxy-combustion in thermal power plant for CO₂ capture. *Appl. Therm. Eng.* 30 (1), 53–62.
- Kapoor, R., Ghosh, P., Kumar, M., Vijay, V.K., 2019. Evaluation of biogas upgrading technologies and future perspectives: a review. *Environ. Sci. Pollut. Res.* 26 (12), 11631–11661. doi:10.1007/s11356-019-04767-1.
- Karimi, M., Hillestad, M., Svendsen, H.F., 2011. Capital costs and energy considerations of different alternative stripper configurations for post combustion CO₂

- capture. *Chem. Eng. Res. Des.* 89 (8), 1229–1236. doi:10.1016/j.cherd.2011.03.005.
- Karimi, M., Hillestad, M., Svendsen, H.F., 2012. Investigation of the dynamic behavior of different stripper configurations for post-combustion CO₂ capture. *Int. J. Greenh. Gas Control* 7, 230–239. doi:10.1016/j.jggc.2011.10.008.
- Karimi, M., de Tuesta, J.L.D., Gonçalves, C., Gomes, H.T., Rodrigues, A.E., Silva, J.A.C., 2020. Compost from municipal solid wastes as a source of biochar for CO₂ capture. *Chem. Eng. Technol.* 43 (7), 1336–1349. doi:10.1002/ceat.201900108.
- Karimi, M., Shirzad, M., Silva, J.A.C., Rodrigues, A.E., 2022. Biomass/Biochar carbon materials for CO₂ capture and sequestration by cyclic adsorption processes: A review and prospects for future directions. *J. Co2 Util.* 57. doi:10.1016/j.jcou.2022.101890.
- Karousos, D.S., Vangeli, O.C., Athanasekou, C.P., Sapalidis, A.A., Kouvelos, E.P., Romanos, G.E., Kanellopoulos, N.K., 2016. Physically bound and chemically grafted activated carbon supported 1-hexyl-3-methylimidazolium bis (trifluoromethylsulfonyl)imide and 1-ethyl-3-methylimidazolium acetate ionic liquid adsorbents for SO₂/CO₂ gas separation. *Chem. Eng. J.* 306, 146–154. doi:10.1016/j.cej.2016.07.040.
- Karousos, D.S., Lei, L., Lindbråthen, A., Sapalidis, A.A., Kouvelos, E.P., He, X., Favvas, E.P., 2020. Cellulose-based carbon hollow fiber membranes for high-pressure mixed gas separations of CO₂/CH₄ and CO₂/N₂. *Sep. Purif. Technol.* 253. doi:10.1016/j.seppur.2020.117473.
- Kasahara, S., Kamio, E., Otani, A., Matsuyama, H., 2014. Fundamental investigation of the factors controlling the CO₂ permeability of facilitated transport membranes containing amine-functionalized task-specific ionic liquids. *Ind. Eng. Chem. Res.* 53, 2422–2431. doi:10.1021/ie403116t.
- Katara, A., Kumar, S., Kundu, S., Sharma, S., Kundu, L.M., Mandal, B., 2023. Mixed matrix membranes for carbon capture and sequestration: challenges and scope. *ACS Omega* 8 (20), 17511–17522. doi:10.1021/acsomega.3c01666.
- Katekomol, P., Roeser, J.r.m., Bojids, M., Weber, J., Thomas, A., 2013. Covalent triazine frameworks prepared from 1, 3, 5-tricyanobenzene. *Chem. Mater.* 25 (9), 1542–1548.
- Katoh, M., Yoshikawa, T., Tomonari, T., Katayama, K., Tomida, T., 2000. Adsorption characteristics of ion-exchanged ZSM-5 zeolites for CO₂/N₂ mixtures. *J. Colloid Interface Sci.* 226 (1), 145–150.
- Kattula, M., Ponnuru, K., Zhu, L., Jia, W., Lin, H., Furlani, E.P., 2015. Designing ultrathin film composite membranes: the impact of a gutter layer. *Sci. Rep.* 5, 15016. doi:10.1038/srep15016.
- Kaviani, S., Kolahchyan, S., Hickenbottom, K.L., Lopez, A.M., Nejadi, S., 2018. Enhanced solubility of carbon dioxide for encapsulated ionic liquids in polymeric materials. *Chem. Eng. J.* 354, 753–757. doi:10.1016/j.cej.2018.08.086.
- Kaya, N., Uzun, Z.Y., 2021. Investigation of effectiveness of pine cone biochar activated with KOH for methyl orange adsorption and CO₂ capture. *Biomass Conv. Bioref.* 11 (3), 1067–1083. doi:10.1007/s13399-020-01063-8.
- Kaye, S.S., Dailly, A., Yaghi, O.M., Long, J.R., 2007. Impact of preparation and handling on the hydrogen storage properties of Zn4O (1, 4-benzenedicarboxylate) 3 (MOF-5). *J. Am. Chem. Soc.* 129 (46), 14176–14177.
- Kazemi, A., Hosseini, M., Mehrabani-Zeinabad, A., Faizi, V., 2016. Evaluation of different vapour recombination distillation configurations based on energy requirements and associated costs. *Appl. Therm. Eng.* 94, 305–313. doi:10.1016/j.applthermeng.2015.10.042.
- Kazemi, H., Shahhosseini, S., Bazayari, A., Amiri, M., 2020. A study on the effects of textural properties of γ-Al₂O₃ support on CO₂ capture capacity of Na₂CO₃. *Process. Saf. Environ. Prot.* 138, 176–185. doi:10.1016/j.psep.2020.03.001.
- Kearns, D.T., Webley, P.A., 2006a. Modelling and evaluation of dual-reflux pressure swing adsorption cycles: Part I. Mathematical models. *Chem. Eng. Sci.* 61 (22), 7223–7233. doi:10.1016/j.ces.2006.07.040.
- Kearns, D.T., Webley, P.A., 2006b. Modelling and evaluation of dual reflux pressure swing adsorption cycles: part II. productivity and energy consumption. *Chem. Eng. Sci.* 61 (22), 7234–7239. doi:10.1016/j.ces.2006.07.043.
- Keith, D.W., Ha-Duong, M., Stolaroff, J.K., 2006. Climate strategy with CO₂ capture from the air. *Clim. Change* 74 (1), 17–45. doi:10.1007/s10584-005-9026-x.
- Keith, D.W., Holmes, G., St Angelo, D., Heidel, K., 2018. A process for capturing CO₂ from the atmosphere. *Joule* 2 (8), 1573–1594. doi:10.1016/j.joule.2018.05.006.
- Keith, D.W., 2009. Why Capture CO₂ from the atmosphere? *Science* 325 (5948), 1654–1655. doi:10.1126/science.1175680.
- Keller, L., Ohs, B., Lemhart, J., Abdul, L., Blanke, P., Wessling, M., 2018. High capacity polyethyleneimine impregnated microtubes made of carbon nanotubes for CO₂ capture. *Carbon* 126, 338–345. doi:10.1016/j.carbon.2017.10.023.
- Kelley, B.T., Valencia, J.A., Northrop, P.S., Mart, C.J., 2011. Controlled Freeze Zone™ for developing sour gas reserves. *Energy Procedia* 4, 824–829. doi:10.1016/j.egypro.2011.01.125.
- Kenig, E.Y., Schneider, R., Górak, A., 2001. Reactive absorption: optimal process design via optimal modelling. *Chem. Eng. Sci.* 56 (2), 343–350. doi:10.1016/S0099-2509(00)00234-7.
- Keshavarz, L., Ghaani, M.R., MacElroy, J.M.D., English, N.J., 2021. A comprehensive review on the application of aerogels in CO₂ adsorption: Materials and characterisation. *Chem. Eng. J.* 412, 128604. doi:10.1016/j.cej.2021.128604.
- Keshavarz, L., Ghaani, M.R., MacElroy, J.M.D., English, N.J., 2021. A comprehensive review on the application of aerogels in CO₂ adsorption: Materials and characterisation. *Chem. Eng. J.* 412. doi:10.1016/j.cej.2021.128604.
- Kezibri, N., Bouallou, C., 2017. Conceptual design and modelling of an industrial scale power to gas-oxy-combustion power plant. *Int. J. Hydrogen Energy* 42 (30), 19411–19419. doi:10.1016/j.ijhydene.2017.05.133.
- Khalifa, O., Alkhatib, I.L.I., Bahamon, D., Alhajaj, A., Abu-Zahra, M.R.M., Vega, L.F., 2022. Modifying absorption process configurations to improve their performance for Post-Combustion CO₂ capture – What have we learned and what is still Missing? *Chem. Eng. J.* 430. doi:10.1016/j.cej.2021.133096.
- Khalil, S.H., Aroua, M.K., Daud, W.M.A.W., 2012. Study on the improvement of the capacity of amine-impregnated commercial activated carbon beds for CO₂ adsorbing. *Chem. Eng. J.* 183, 15–20. doi:10.1016/j.cej.2011.12.011.
- Khan, F.M., Krishnamoorthi, V., Mahmud, T., 2011. Modelling reactive absorption of CO₂ in packed columns for post-combustion carbon capture applications. *Chem. Eng. Res. Des.* 89 (9), 1600–1608. doi:10.1016/j.cherd.2010.09.020.
- Khan, I.U., Othman, M.H.D., Jilani, A., Ismail, A.F., Hashim, H., Jaafar, J., Rahman, M.A., Rehman, G.U., 2018. Economical, environmental friendly synthesis, characterization for the production of zeolitic imidazolate framework-8 (ZIF-8) nanoparticles with enhanced CO₂ adsorption. *Arab. J. Chem.* 11 (7), 1072–1083. doi:10.1016/j.arabj.2018.07.012.
- Khan, M.U., Lee, J.T.E., Ashir, M.A., Dissanayake, P.D., Ok, Y.S., Tong, Y.W., Shariati, M.A., Wu, S., Ahning, B.K., 2021. Current status of biogas upgrading for direct biomethane use: A review. *Renew. Sustain. Energy Rev.* 149, 111343. doi:10.1016/j.rser.2021.111343.
- Khatami, R., Stivers, C., Joshi, K., Leventis, Y.A., Sarofim, A.F., 2012. Combustion behavior of single particles from three different coal ranks and from sugar cane bagasse in O₂/N₂ and O₂/CO₂ atmospheres. *Combust. Flame* 159 (3), 1253–1271. doi:10.1016/j.combustflame.2011.09.009.
- Khosa, A.A., Xu, T.X., Xia, B.Q., Yan, J., Zhao, C.Y., 2019. Technological challenges and industrial applications of CaCO₃/CaO based thermal energy storage system - A review. *Sol. Energy* 193, 618–636. doi:10.1016/j.solener.2019.10.003.
- Khurana, M., Farooq, S., 2016a. Adsorbent screening for postcombustion CO₂ capture: A method relating equilibrium isotherm characteristics to an optimum vacuum swing adsorption process performance. *Ind. Eng. Chem. Res.* 55 (8), 2447–2460. doi:10.1021/acs.iecr.5b04531.
- Khurana, M., Farooq, S., 2016b. Simulation and optimization of a 6-step dual-reflux VSA cycle for post-combustion CO₂ capture. *Chem. Eng. Sci.* 152, 507–515. doi:10.1016/j.ces.2016.06.033.
- Khurana, M., Farooq, S., 2019. Integrated adsorbent process optimization for minimum cost of electricity including carbon capture by a VSA process. *AIChE J.* 65 (1), 184–195. doi:10.1002/aic.16362.
- Kianfar, E., Cao, V., 2021. Polymeric membranes on base of PolyMethyl methacrylate for air separation: a review. *J. Mater. Res. Technol.* 10, 1437–1461. doi:10.1016/j.jmrt.2020.12.061.
- Kiebas, K., Bayar, Ş., Varol, E.A., Sreńieck-Nazzal, J., Bosacka, M., Michalkiewicz, B., 2022. Thermochemical conversion of lignocellulosic biomass - olive pomace - into activated biochar for CO₂ adsorption. *Ind. Crops Prod.* 187, 115416. doi:10.1016/j.indcrop.2022.115416.
- Kiebach, R., Pirou, S., Martinez Aguilera, L., Haugen, A.B., Kaiser, A., Hendriksen, P.V., Balaguer, M., Garcia-Fayos, J., Serra, J.M., Schulze-Küppers, F., Christie, M., Fischer, L., Meulenber, W.A., Baumann, S., 2022. A review on dual-phase oxygen transport membranes: from fundamentals to commercial deployment. *J. Mater. Chem. A* 10, 2152–2195. doi:10.1039/D1TA07898D.
- Kierzkowska, A.M., Pacciani, R., Müller, C.R., 2013. CaO-Based CO₂ sorbents: from fundamentals to the development of new, highly effective materials. *ChemSusChem* 6 (7), 1130–1148.
- Kim, S., Lee, Y.M.J.P.i.P.S., 2015. Rigid and microporous polymers for gas separation membranes. 43, 1–32.
- Kim, H., Lee, K.S., 2016. Design guidance for an energy-thrift absorption process for carbon capture: Analysis of thermal energy consumption for a conventional process configuration. *Int. J. Greenh. Gas Control* 47, 291–302. doi:10.1016/j.jggc.2016.02.003.
- Kim, T.-J., Li, B., Hägg, M.-B., 2004. Novel fixed-site-carrier polyvinylamine membrane for carbon dioxide capture. 42 (23), 4326–4336. https://doi.org/10.1002/polb.20282.
- Kim, J.-Y., Kim, J., Yang, S.-T., Ahn, W.-S., 2013. Mesoporous SAPO-34 with amine-grafting for CO₂ capture. *Fuel* 108, 515–520. doi:10.1016/j.fuel.2012.12.020.
- Kim, T.-J., Vrålstad, H., Sandru, M., Hägg, M.-B., 2013. Separation performance of PVAm composite membrane for CO₂ capture at various pH levels. *J. Membr. Sci.* 428, 218–224. doi:10.1016/j.memsci.2012.10.009.
- Kim, C., Cho, H.S., Chang, S., Cho, S.J., Choi, M., 2016. An ethylenediamine-grafted Y zeolite: a highly regenerable carbon dioxide adsorbent via temperature swing adsorption without urea formation. *Energy Environ. Sci.* 9 (5), 1803–1811. doi:10.1039/c6ee00601a.
- Kim, J., Pham, D.A., Lim, Y.I., 2016. Gas-liquid multiphase computational fluid dynamics (CFD) of amine absorption column with structured-packing for CO₂ capture. *Comput. Chem. Eng.* 88, 39–49. doi:10.1016/j.compchemeng.2016.02.006.
- Kim, J., Choi, J., Soo Kang, Y., Won, J., 2016. Matrix effect of mixed-matrix membrane containing CO₂-selective MOFs. 133 (1). https://doi.org/10.1002/app.42853.
- Kim, J., Pham, D.A., Lim, Y.I., 2017. Effect of gravity center position on amine adsorbent with structured packing under offshore operation: Computational fluid dynamics approach. *Chem. Eng. Res. Des.* 121, 99–112. doi:10.1016/j.cherd.2017.03.008.
- Kim, S.M., Liao, W.-C., Kierzkowska, A.M., Margossian, T., Hosseini, D., Yoon, S., Broda, M., Copéret, C., Müller, C.R., 2018. In Situ XRD and dynamic nuclear polarization surface enhanced NMR spectroscopy unravel the deactivation mechanism of CaO-based, Ca3Al2O6-stabilized CO₂ sorbents. *Chem. Mater.* 30 (4), 1344–1352. doi:10.1021/acs.chemmater.7b05034.
- Kim, S., Hou, J., Wang, Y., Ou, R., Simon, G.P., Seong, J.G., Lee, Y.M., Wang, H.J.J.o.M.C.A., 2018. Highly permeable thermally rearranged polymer composite membranes with a graphene oxide scaffold for gas separation. 6 (17), 7668–7674.
- Kim, C., Choi, W., Choi, M., 2019. SO₂-resistant amine-containing CO₂ adsorbent with a surface protection layer. *ACS Appl. Mater. Interfaces* 11 (18), 16586–16593. doi:10.1021/acsaami.9b02831.

- Kim, H., Sohail, M., Yim, K., Park, Y.C., Chun, D.H., Kim, H.J., Han, S.O., Moon, J.-H., 2019. Effective CO₂ and CO separation using [M2 (DOBDC)] (M = Mg, Co, Ni) with unsaturated metal sites and excavation of their adsorption sites. *ACS Appl. Mater. Interfaces* 11 (7), 7014–7021.
- Kim, N., Park, B., Lee, J., Kim, J., 2019. High-performance ultrathin mixed-matrix membranes based on an adhesive PGMA-co-POEM comb-like copolymer for CO₂ capture. *J. Mater. Chem. A* 7 (24), 14723–14731. doi:10.1039/C9TA02962A.
- Kim, S.M., Armutulu, A., Kierzkowska, A.M., Müller, C.R., 2019. Inverse opal-like, Ca3Al2O6-stabilized, CaO-based CO₂ Sorbent: stabilization of a highly porous structure to improve its cyclic CO₂ uptake. *ACS Appl. Energy Mater.* 2 (9), 6461–6471. doi:10.1021/acs.aem.9b01058.
- RL Kim, E.S., Jiang, H.Z.H., Forse, A.C., 2020. Cooperative carbon capture and steam regeneration with tetraamine-appended metal-organic frameworks. *Science* 369 (6502), 392–396. doi:10.1126/science.abb3976.
- Kim, N.U., Park, B.J., Guiver, M.D., Kim, J.H., 2020. Use of non-selective, high-molecular-weight poly (ethylene oxide) membrane for CO₂ separation by incorporation of comb copolymer. *J. Membr. Sci.* 605, 118092. doi:10.1016/j.memsci.2020.118092.
- Kim, Y., Lim, H.S., Kim, H.S., Lee, M., Lee, J.W., Kang, D., 2022. Carbon dioxide splitting and hydrogen production using a chemical looping concept: A review. *J. CO₂ Util.* 63, 102139. doi:10.1016/j.jcou.2022.102139.
- Kinik, F.P., Altintas, C., Balci, V., Koyuturk, B., Uzun, A., Keskin, S., 2016. [BMIM][PF6] Incorporation doubles CO₂ selectivity of ZIF-8: elucidation of interactions and their consequences on performance. *ACS Appl. Mater. Interfaces* 8 (45), 30992–31005. doi:10.1021/acsami.6b11087.
- Kishor, R., Ghoshal, A.K., 2016. Polyethyleneimine functionalized As-synthesized KIT-6 adsorbent for highly CO₂/N₂ selective separation. *Energy Fuels* 30 (11), 9635–9644. doi:10.1021/acs.energyfuels.6b02082.
- Kiss, A.A., 2014. Distillation technology - still young and full of breakthrough opportunities. *J. Chem. Technol. Biotechnol.* 89 (4), 479–498. doi:10.1002/jctb.4262.
- Kizzie, A.C., Wong-Foy, A.G., Matzger, A.J., 2011. Effect of humidity on the performance of microporous coordination polymers as adsorbents for CO₂ capture. *Langmuir* 27 (10), 6368–6373.
- Klemm, A., Lee, Y.-Y., Mao, H., Gurkan, B., 2020. Facilitated Transport Membranes With Ionic Liquids for CO₂ Separations. 8. <https://doi.org/10.3389/fchem.2020.00637>.
- Klinthong, W., Huang, C.-H., Tan, C.-S., 2016. One-Pot synthesis and pelletizing of polyethyleneimine-containing mesoporous silica powders for CO₂ capture. *Ind. Eng. Chem. Res.* 55 (22), 6481–6491. doi:10.1021/acs.iecr.6b00644.
- Knapik, E., Kosowski, P., Stopa, J., 2018. Cryogenic liquefaction and separation of CO₂ using nitrogen removal unit cold energy. *Chem. Eng. Res. Des.* 131, 66–79. doi:10.1016/j.cherd.2017.12.027.
- Knebel, A., Bavykina, A., Datta, S.J., Sundermann, L., Garzon-Tovar, L., Lebedev, Y., Durini, S., Ahmad, R., Kozlov, S.M., Shterk, G., 2020. Solution processable metal-organic frameworks for mixed matrix membranes using porous liquids. *Nat. Mater.* 19 (12), 1346–1353. doi:10.1038/s41563-020-0764-y.
- Knowles, G.P., Chaffee, A.L., 2016. Aminopropyl-functionalized silica CO₂ adsorbents via sonochemical methods. *J. Chem. 2016*, 1–10. doi:10.1155/2016/1070838.
- Ko, Y.G., Lee, H.J., Oh, H.C., Choi, U.S., 2013. Amines immobilized double-walled silica nanotubes for CO₂ capture. *J. Hazard Mater.* 250–251, 53–60. doi:10.1016/j.jhazmat.2013.01.035.
- Kołodziej, A., Łojewska, J., 2009. Experimental and modelling study on flow resistance of wire gauzes. *Chem. Eng. Process.: Process Intensif.* 48 (3), 816–822. doi:10.1016/j.ccep.2008.10.009.
- Kolle, J.M., Fayaz, M., Sayari, A., 2021. Understanding the effect of water on CO₂ adsorption. *Chem. Rev.* 121 (3), 7280–7345. doi:10.1021/acs.chemrev.0c00762.
- Kong, Y., Shen, X.D., Cui, S., Fan, M.H., 2015. Development of monolithic adsorbent by polymeric sol-gel process for low-concentration CO₂ capture. *Appl. Energy* 147, 308–317. doi:10.1016/j.apenergy.2015.03.011.
- Kong, Y., Shen, X., Fan, M., Yang, M., Cui, S., 2016. Dynamic capture of low-concentration CO₂ on amine hybrid silsesquioxane aerogel. *Chem. Eng. J.* 283, 1059–1068. doi:10.1016/j.ccej.2015.08.034.
- Kong, Y., Zhang, J.Y., Shen, X.D., 2017. One-pot sol-gel synthesis of amine hybrid titania/silsesquioxane composite aerogel for CO₂ capture. *J. Sol-Gel Sci. Technol.* 84 (3), 422–431. doi:10.1007/s10971-017-4516-7.
- Kong, Y.K., Ruan, S., Kurumisawa, K., 2022. Recycling of calcined carbonated cement pastes as cementitious materials: Proposed CCUS technology for calcium looping. *J. Environ. Chem. Eng.* 10 (5), 11. doi:10.1016/j.jece.2022.108247.
- Koronaki, I.P., Prentza, L., Papaefthimiou, V., 2015. Modeling of CO₂ capture via chemical absorption processes - An extensive literature review. *Renew. Sustain. Energy Rev.* 50, 547–566. doi:10.1016/j.rser.2015.04.124.
- Koros, W.J., Zhang, C., 2017. Materials for next-generation molecularly selective synthetic membranes. *Nat. Mater.* 16 (3), 289–297. doi:10.1038/nmat4805.
- Kou, S.G., Peters, L.M., Mucalo, M.R., 2021. Chitosan: A review of sources and preparation methods. *Int. J. Biol. Macromol.* 169, 85–94. doi:10.1016/j.jbiomac.2020.12.005.
- Krödel, M., Landuyt, A., Abdala, P.M., Müller, C.R.J.C., 2020. Mechanistic understanding of CaO-based sorbents for high-temperature CO₂ capture: advanced characterization and prospects. *13* (23), 6259–6272.
- Krödel, M., Oing, A., Negele, J., Landuyt, A., Kierzkowska, A., Bork, A.H., Donat, F., Müller, C.R., 2022. Yolk-shell-type CaO-based sorbents for CO₂ capture: assessing the role of nanostructuring for the stabilization of the cyclic CO₂ uptake. *Nanoscale* 14 (45), 16816–16828. doi:10.1039/D2NR04492G.
- Krekel, D., Samsun, R.C., Peters, R., Stolten, D., 2018. The separation of CO₂ from ambient air – A techno-economic assessment. *Appl. Energy* 218, 361–381. doi:10.1016/j.apenergy.2018.02.144.
- Krishna, R., van Baten, J.M., 2010. In silico screening of zeolite membranes for CO₂ capture. *J. Membr. Sci.* 360 (1–2), 323–333.
- Krishnamurthy, S., Haghpanah, R., Rajendran, A., Farooq, S., 2014a. Simulation and optimization of a dual-Adsorbent, two-bed vacuum swing adsorption process for CO₂ capture from wet flue gas. *Ind. Eng. Chem. Res.* 53 (37), 14462–14473. doi:10.1021/ie5024723.
- Krishnamurthy, S., Rao, V.R., Guntuka, S., Sharratt, P., Haghpanah, R., Rajendran, A., Amanullah, M., Karimi, A., Farooq, S., 2014b. CO₂ capture from dry flue gas by vacuum swing adsorption: A pilot plant study. *AIChE J.* 60 (5), 1830–1842. doi:10.1002/aic.14435.
- Kuhn, P., Antonietti, M., Thomas, A., 2008. Porous, covalent triazine-based frameworks prepared by ionothermal synthesis. *Angew. Chem. Int. Ed.* 47 (18), 3450–3453.
- Kumakiri, X.H.A.I., 2020. Carbon membrane technology: fundamentals and applications.
- Kumar, S., Prasad, K., Gil, J.M., Sobral, A.J.F.N., Koh, J., 2018. Mesoporous zeolite-chitosan composite for enhanced capture and catalytic activity in chemical fixation of CO₂. *Carbohydr. Polym.* 198, 401–406. doi:10.1016/j.carbpol.2018.06.100.
- Kumar, A., Singh, E., Mishra, R., Lo, S.L., Kumar, S., 2022. A green approach towards sorption of CO₂ on waste derived biochar. *Environ. Res.* 214. doi:10.1016/j.envres.2022.113954.
- Kunalan, S., Palanivelu, K., 2022. Polymeric composite membranes in carbon dioxide capture process: a review. *Environ. Sci. Pollut. Res. Int.* 29 (26), 38735–38767. doi:10.1007/s11356-022-19519-x.
- Kundu, P.K., Chakma, A., Feng, X., 2014. Effectiveness of membranes and hybrid membrane processes in comparison with absorption using amines for post-combustion CO₂ capture. *Int. J. Greenh. Gas Control* 28, 248–256. doi:10.1016/j.ijggc.2014.06.031.
- Kung, H.H., Ko, E.I., 1996. Preparation of oxide catalysts and catalyst supports — a review of recent advances. *Chem. Eng. J. Biochem. Eng. J.* 64 (2), 203–214. doi:10.1016/S0923-0467(96)03139-9.
- Kurlov, A., Broda, M., Hosseini, D., Mitchell, S.J., Pérez-Ramírez, J., Müller, C.R., 2016. Mechanochemically activated, calcium oxide-based, magnesium oxide-stabilized carbon dioxide sorbents. *ChemSusChem* 9 (17), 2380–2390. doi:10.1002/cssc.201600510.
- Kurlov, A., Armutulu, A., Donat, F., Studart, A.R., Müller, C.R., 2020a. CaO-Based CO₂ sorbents with a hierarchical porous structure made via microfluidic droplet templating. *Ind. Eng. Chem. Res.* 59 (15), 7182–7188. doi:10.1021/acs.iecr.9b05996.
- Kurlov, A., Kierzkowska, A.M., Huthwelker, T., Abdala, P.M., Müller, C.R.J.P.C.C.P., 2020b. Na 2 CO 3-modified CaO-based CO 2 sorbents: the effects of structure and morphology on CO 2 uptake. *22* (42), 24697–24703.
- Kvamsdal, H.M., Jakobsen, J.P., Hoff, K.A., 2009. Dynamic modeling and simulation of a CO₂ absorber column for post-combustion CO₂ capture. *Chem. Eng. Process.: Process Intensif.* 48 (1), 135–144. doi:10.1016/j.ccep.2008.03.002.
- Kwon, G., Cho, D.-W., Hyun Moon, D., Kwon, E.E., Song, H., 2019. Beneficial use of CO₂ in pyrolysis of chicken manure to fabricate a sorptive material for CO₂. *Appl. Therm. Eng.* 154, 469–475. doi:10.1016/j.applthermaleng.2019.03.110.
- Kwon, G., Cho, D.W., Moon, D.H., Kwon, E.E., Song, H., 2019. Beneficial use of CO₂ in pyrolysis of chicken manure to fabricate a sorptive material for CO₂. *Appl. Therm. Eng.* 154, 469–475. doi:10.1016/j.applthermaleng.2019.03.110.
- Kwon, D.-I., Kim, J.-C., Lee, H., Lee, W., Jo, C., 2022. Engineering micropore walls of beta zeolites by post-functionalization for CO₂ adsorption performance screening under humid conditions. *Chem. Eng. J.* 427. doi:10.1016/j.ccej.2021.131461.
- López, T., Bosch, P., Tzompantzi, F., Gómez, R., Navarrete, J., López-Salinas, E., Llanos, M.E., 2000. Effect of sulfation methods on TiO₂-SiO₂ sol-gel catalyst acidity. *Appl. Catal. A* 197, 107–117.
- López, R., Fernández, C., Martínez, O., Sánchez, M.E., 2016. Techno-economic analysis of a 15MW corn-rape oxy-combustion power plant. *Fuel Process. Technol.* 142, 296–304. doi:10.1016/j.fuproc.2015.10.020.
- Z.X. Lü, B. Li, X. et al., 2021. Mechanism of CO₂ capture into amino-azolylic dual-functionalized ionic liquid biphasic solvent. *Sci. China: Chem.* 51 (12), 1660–1670. doi:10.1360/SSC-2021-0026.
- Laassiri, S., Zeinalipour-Yazdi, C.D., Catlow, C.R.A., Hargreaves, J.S., 2018. The potential of manganese nitride based materials as nitrogen transfer reagents for nitrogen chemical looping. *Appl. Catal. B: Environ.* 223, 60–66.
- Labreche, Y., Fan, Y., Lively, R.P., Jones, C.W., Koros, W.J., 2015. Direct dual layer spinning of aminosilica/T orlon® hollow fiber sorbents with a lumen layer for CO₂ separation by rapid temperature swing adsorption. *J. Appl. Polym. Sci.* 132 (17).
- Lackner, K., Ziock, H.-J., Grimes, P., 1999. Carbon Dioxide Extraction from Air: Is It An Option? United States.
- Lackner, K.S., Brennan, S., Matter, J.M., Park, A.H.A., Wright, A., van der Zwaan, B., 2012. The urgency of the development of CO₂ capture from ambient air. *P Natl. Acad. Sci. USA* 109 (33), 13156–13162. doi:10.1073/pnas.1108765109.
- Lackner, K.S., 2003. A guide to CO₂ sequestration. *Science* 300 (5626), 1677–1678.
- Lahijani, P., Mohammadi, M., Mohamed, A.R., 2018. Metal incorporated biochar as a potential adsorbent for high capacity CO₂ capture at ambient condition. *J. CO₂ Util.* 26, 281–293. doi:10.1016/j.jcou.2018.05.018.
- Lai, J.Y., Ngu, L.H., Hashim, S.S., 2021. A review of CO₂ adsorbents performance for different carbon capture technology processes conditions. *Greenh. Gases* 11 (5), 1076–1117. doi:10.1002/ghg.2112.
- Lail, M., Tanthana, J., Coleman, L., 2014. Non-aqueous solvent (NAS) CO₂ capture process. *Energy Proc.* 63, 580–594. doi:10.1016/j.egypro.2014.11.063.
- Lam, S.S., Liew, R.K., Cheng, C.K., Rasit, N., Ooi, C.K., Ma, N.L., Ng, J.-H., Lam, W.H., Chong, C.T., Chase, H.A., 2018. Pyrolysis production of fruit peel biochar for potential use in treatment of palm oil mill effluent. *J. Environ. Manage.* 213, 400–408. doi:10.1016/j.jenvman.2018.02.092.
- Landelle, A., Tauveron, N., Haberschill, P., Revellin, R., Colasson, S., 2017. Organic Rankine cycle design and performance comparison based on experimental database. *Appl. Energy* 204, 1172–1187. doi:10.1016/j.apenergy.2017.04.012.
- Landuyt, A., Kumar, P., Yuwono, J., Bork, A.H., Abdala, P., Müller, C., 2022. Uncovering the CO₂ capture mechanism of alkali metal nitrate promoted MgO by 18O isotope labeling. [Manuscript submitted for publication.]

- Lappalainen, K., Manninen, M., Alopaeus, V., 2009. CFD modeling of radial spreading of flow in trickle-bed reactors due to mechanical and capillary dispersion. *Chem. Eng. Sci.* 64 (2), 207–218. doi:10.1016/j.ces.2008.10.009.
- Lappalainen, K., Gorskova, E., Manninen, M., Alopaeus, V., 2011. Characteristics of liquid and tracer dispersion in trickle-bed reactors: effect on CFD modeling and experimental analyses. *Comput. Chem. Eng.* 35 (1), 41–49. doi:10.1016/j.compchemeng.2010.06.006.
- Lara-García, H.A., Ovalles-Encinia, O., Ortiz-Landeros, J., Lima, E., Pfeiffer, H., 2019. Synthesis of $\text{Li}^+ \text{xSi}_1 - \text{xFe}_2\text{O}_3$ solid solution by dry ball milling and its highly efficient CO_2 chemisorption in a wide temperature range and low CO_2 concentrations. *J. Mater. Chem. A* 7 (8), 4153–4164. doi:10.1039/C8TA12359D.
- Lasek, J.A., Janusz, M., Zuzala, J., Ghó, K., Iluk, A., 2013. Oxy-fuel combustion of selected solid fuels under atmospheric and elevated pressures. *Energy* 62, 105–112. doi:10.1016/j.energy.2013.04.079.
- Lawal, A., Wang, M., Stephenson, P., Yeung, H., 2009. Dynamic modelling of CO_2 absorption for post combustion capture in coal-fired power plants. *Fuel* 88 (12), 2455–2462. doi:10.1016/j.fuel.2008.11.009.
- Lawal, A., Wang, M., Stephenson, P., Koumpouras, G., Yeung, H., 2010. Dynamic modelling and analysis of post-combustion CO_2 chemical absorption process for coal-fired power plants. *Fuel* 89 (10), 2791–2801. doi:10.1016/j.fuel.2010.05.030.
- Lawal, A., Wang, M., Stephenson, P., Obi, O., 2012. Demonstrating full-scale post-combustion CO_2 capture for coal-fired power plants through dynamic modelling and simulation. *Fuel* 101, 115–128. doi:10.1016/j.fuel.2010.10.056.
- Lawson, S., Rownaghi, A.A., Rezaei, F., 2018. Carbon hollow fiber-supported metal-organic framework composites for gas adsorption. *Energy Technol.* 6 (4), 694–701. doi:10.1002/ente.201700657.
- Laycock, D.E., Collocott, R.J., Alan Skelton, D., Tchir, M.F., 1991. Stereospecific polymerization of propylene oxide on thermally activated synthetic hydroxalcite. *J. Catal.* 130 (2), 354–358. doi:10.1016/0021-9517(91)90119-0.
- León, M., Díaz, E., Bennici, S., Vega, A., Ordóñez, S., Auroux, A., 2010. Adsorption of CO_2 on hydroxalcite-derived mixed oxides: sorption mechanisms and consequences for adsorption irreversibility. *Ind. Eng. Chem. Res.* 49 (8), 3663–3671. doi:10.1021/ie902072a.
- C.B. Leal, O., Ovalles, C., García, J.J., Espidel, Y., 1995. Reversible adsorption of carbon dioxide on amine surface-bonded silica gel. *Inorg. Chim. Acta* 240, 183–189.
- Leavitt, F., 1992. Duplex adsorption process. US Patent 5,085,674.
- Lee, Y., Gurkan, B., 2021. Graphene oxide reinforced facilitated transport membranes with poly (ionic liquid) and ionic liquid carriers for CO_2/N_2 separation. *J. Membr. Sci.* 638, 119652. doi:10.1016/j.memsci.2021.119652.
- Lee, A., Miller, D.C., 2013. A one-dimensional (1-D) three-region model for a bubbling fluidized-bed adsorber. *Ind. Eng. Chem. Res.* 52 (11), 469–484. doi:10.1021/ie300840q.
- Lee, J.H., Park, S.J., 2020. Recent advances in preparations and applications of carbon aerogels: A review. *Carbon* 163, 1–18. doi:10.1016/j.carbon.2020.02.073.
- Lee, S.W., Kim, H.J., Lee, Y.K., Park, K., Son, J.-H., Kwon, Y.-U., 2003. Triply interpenetrating coordination polymers based on paddle-wheel type secondary-building units of $\text{M}_2(\text{CO}_2\text{R})_4$: $[\text{Ni}_3(2,6\text{-NDC})(3\text{ bipy})_1.5]$, $[\text{Co}_3(2,6\text{-NDC})(3\text{ bipy})_1.5]$, and $[\text{Co}(1,3\text{-BDC})(\text{bipyen})]$ (2, 6-NDC= 2, 6-naphthalenedicarboxylate; 1, 3-BDC= 1, 3-benzenedicarboxylate; bipy= 4, 4'-bipyridine; bipyen= trans-1, 2-bis (4-pyridyl) ethylene). *Inorg. Chim. Acta* 353, 151–158.
- Lee, K.B., Verdooren, A., Caram, H.S., Sircar, S., 2007. Chemisorption of carbon dioxide on potassium-carbonate-promoted hydroxalcite. *J. Colloid. Interface Sci.* 308 (1), 30–39. doi:10.1016/j.jcis.2006.11.011.
- Lee, S.C., Chae, H.J., Lee, S.J., Choi, B.Y., Yi, C.K., Lee, J.B., Ryu, C.K., Kim, J.C., 2008. Development of regenerable MgO-based sorbent promoted with K_2CO_3 for CO_2 capture at low temperatures. *Environ. Sci. Technol.* 42 (8), 2736–2741. doi:10.1021/es702693c.
- Lee, J.M., Min, Y.J., Lee, K.B., Jeon, S.G., Na, J.G., Ryu, H.J., 2010. Enhancement of CO_2 sorption uptake on hydroxalcite by impregnation with K_2CO_3 . *Langmuir* 26 (24), 18788–18797. doi:10.1021/la102974s.
- Lee, D., Jin, Y., Jung, N., Lee, J., Lee, J., Jeong, Y.S., Jeon, S., 2011. Gravimetric analysis of the adsorption and desorption of CO_2 on amine-functionalized mesoporous silica mounted on a microcantilever array. *Environ. Sci. Technol.* 45 (13), 5704–5709. doi:10.1021/es200680v.
- Lee, C.S., Ong, Y.L., Aroua, M.K., Daud, W.M.A.W., 2013. Impregnation of palm shell-based activated carbon with sterically hindered amines for CO_2 adsorption. *Chem. Eng. J.* 219, 558–564. doi:10.1016/j.cej.2012.10.064.
- Lee, S.C., Kwon, Y.M., Chae, H.J., Jung, S.Y., Lee, J.B., Ryu, C.K., Yi, C.K., Kim, J.C., 2013. Improving regeneration properties of potassium-based alumina sorbents for carbon dioxide capture from flue gas. *Fuel* 104, 882–885. doi:10.1016/j.fuel.2012.05.037.
- Lee, S.C., Cho, M.S., Jung, S.Y., Ryu, C.K., Kim, J.C., 2014. Effects of alumina phases on CO_2 sorption and regeneration properties of potassium-based alumina sorbents. *Adsorption* 20 (2), 331–339. doi:10.1007/s10450-013-9596-2.
- Lee, W.R., Hwang, S.Y., Ryu, D.W., Lim, K.S., Han, S.S., Moon, D., Choi, J., Hong, C.S., 2014. Diamine-functionalized metal-organic framework: exceptionally high CO_2 capacities from ambient air and flue gas, ultrafast CO_2 uptake rate, and adsorption mechanism. *Energy Environ. Sci.* 7 (2), 744–751. doi:10.1039/c3ee42328j.
- Lee, M.-S., Lee, S.-Y., Park, S.-J., 2015. Preparation and characterization of multi-walled carbon nanotubes impregnated with polyethyleneimine for carbon dioxide capture. *Int. J. Hydrogen Energy* 40 (8), 3415–3421. doi:10.1016/j.ijhydene.2014.12.104.
- Lee, W.R., Jo, H., Yang, L.-M., Lee, H., Ryu, D.W., Lim, K.S., Song, J.H., Min, D.Y., Han, S.S., Seo, J.G., Park, Y.K., Moon, D., Hong, C.S., 2015. Exceptional CO_2 working capacity in a heterodiamine-grafted metal-organic framework. *Chem. Sci.* 6 (7), 3697–3705. doi:10.1039/c5sc01191d.
- Lee, A., Elam, J.W., Darling, S.B., 2016. Membrane materials for water purification: design, development, and application. *Environ. Sci.: Water Res. Technol.* 2 (1), 17–42.
- Lee, J.H., Lee, J., Jo, H.J., Seong, J.G., Kim, J.S., Lee, W.H., Moon, J., Lee, D., Oh, W.J., Yeo, J.-g.J.o.M.S., 2017. Wet CO_2/N_2 permeation through a crosslinked thermally rearranged poly (benzoxazole-co-imide) (XTR-PBOI) hollow fiber membrane module for CO_2 capture. *539*, 412–420.
- Lee, C.H., Choi, S.W., Yoon, H.J., Kwon, H.J., Lee, H.C., Jeon, S.G., Lee, K.B.J.C.E.J., 2018. Na_2CO_3 -doped CaO-based high-temperature CO_2 sorbent and its sorption kinetics. *352*, 103–109.
- Lee, E.J., Bae, J., Choi, K.M., Jeong, N.C., 2019. Exploiting microwave chemistry for activation of metal-organic frameworks. *ACS Appl. Mater. Interfaces* 11, 35155–35161. doi:10.1021/acsmi.9b12201.
- Lee, J., Kim, J.S., Kim, J.F., Jo, H.J., Park, H., Seong, J.G., Lee, Y.M.J.o.M.S., 2019. Densification-induced hollow fiber membranes using crosslinked thermally rearranged (XTR) polymer for CO_2 capture. *573*, 393–402.
- Lee, J., Satheeshkumar, C., Yu, H.J., Kim, S., Lee, J.S., Seo, M., Kim, M., 2020. Pore engineering of covalently connected metal-organic framework nanoparticle-mixed-matrix membrane composites for molecular separation. *ACS Appl. Nano Mater.* doi:10.1021/acsnam.0c01982.
- Lee, Y.-Y., Edgehouse, K., Klemm, A., Mao, H., Pentzer, E., Gurkan, B., 2020. Capsules of reactive ionic liquids for selective capture of carbon dioxide at low concentrations. *ACS Appl. Mater. Interfaces* 12 (16), 19184–19193. doi:10.1021/acsmi.0c01622.
- Lee, J., Kim, J.S., Moon, S.-y., Park, C.Y., Kim, J.F., Lee, Y.M.J.o.M.S., 2020. Dimensionally-controlled densification in crosslinked thermally rearranged (XTR) hollow fiber membranes for CO_2 capture. *595*, 117535.
- Lee, T.H., Ozcan, A., Park, I., Fan, D., Jang, J.K., Mileo, P.G., Yoo, S.Y., Roh, J.S., Kang, J.H., Lee, B.K., 2021a. Disclosing the Role of defect-engineered metal-organic frameworks in mixed matrix membranes for efficient CO_2 separation: a joint experimental-computational exploration. *Adv. Funct. Mater.* 31 (38), 2103973. doi:10.1002/adfm.202103973.
- Lee, T.H., Ozcan, A., Park, I., Fan, D., Jang, J.K., Mileo, P.G., Yoo, S.Y., Roh, J.S., Kang, J.H., Lee, B.K., 2021b. Disclosing the role of defect-engineered metal-organic frameworks in mixed matrix membranes for efficient CO_2 separation: a joint experimental-computational exploration. *Adv. Funct. Mater.* 31 (38), 2103973.
- Lee, C.S., Kang, M., Kim, K.C., Kim, J.H., 2022. In-situ formation of asymmetric thin-film, mixed-matrix membranes with ZIF-8 in dual-functional imidazole-based comb copolymer for high-performance CO_2 capture. *J. Membr. Sci.* 642, 119913. doi:10.1016/j.memsci.2021.119913.
- Lee, W.M., 1980. Selection of barrier materials from molecular structure. *20* (1), 65–69. https://doi.org/10.1002/pen.760200111.
- Lei, L., Bai, L., Lindbräthen, A., Pan, F., Zhang, X., He, X., 2020. Carbon membranes for CO_2 removal: Status and perspectives from materials to processes. *Chem. Eng. J.* 401. doi:10.1016/j.cej.2020.126084.
- Lei, L., Pan, F., Lindbräthen, A., Zhang, X., Hillestad, M., Nie, Y., Bai, L., He, X., Guiver, M.D., 2021. Carbon hollow fiber membranes for a molecular sieve with precise-cutoff ultramicropores for superior hydrogen separation. *Nat. Commun.* 12 (1), 268. doi:10.1038/s41467-020-20628-9.
- Leites, I.L., 1998. Thermodynamics of CO_2 solubility in mixtures monoethanolamine with organic solvents and water and commercial experience of energy saving gas purification technology. *Energy Convers. Manage.* 39 (16–18), 1665–1674. doi:10.1016/S0196-8904(98)00076-4.
- Leng, L., Xiong, Q., Yang, L., Li, H., Zhou, Y., Zhang, W., Jiang, S., Li, H., Huang, H., 2021. An overview on engineering the surface area and porosity of biochar. *Sci. Total Environ.* 763, 144204. doi:10.1016/j.scitotenv.2020.144204.
- Lenzi, D., 2018. The ethics of negative emissions. *Glob. Sustain.* 1, e7. doi:10.1017/sus.2018.5.
- Lepéri, K.T., Snurr, R.Q., You, F., 2016. Optimization of Two-Stage Pressure/Vacuum Swing Adsorption with Variable Dehydration Level for Postcombustion Carbon Capture. *Ind. Eng. Chem. Res.* 55 (12), 3338–3350.
- Lepéri, K.T., Chung, Y.G., You, F., Snurr, R.Q., 2019. Development of a general evaluation metric for rapid screening of adsorbent materials for postcombustion CO_2 capture. *ACS Sustain. Chem. Eng.* 7 (13), 11529–11539. doi:10.1021/acssuschemeng.9b01418.
- Leppänen, P., Inha, T., Pentti, M., 2014. An experimental study on the effect of design flue gas temperature on the fire safety of chimneys. *Fire Technol.* 51 (4), 847–866. doi:10.1007/s10694-014-0415-4.
- Leukel, S., Panthöfer, M., Mondeshki, M., Kieslich, G., Wu, Y., Krautwurst, N., Tremel, W., 2018. Mechanochemical access to defect-stabilized amorphous calcium carbonate. *Chem. Mater.* 30 (17), 6040–6052.
- Leung, D.Y.C., Caramanna, G., Maroto-Valer, M.M., 2014. An overview of current status of carbon dioxide capture and storage technologies. *Renew. Sustain. Energy Rev.* 39, 426–443. doi:10.1016/j.rser.2014.07.093.
- Lewis, W.K., Gilliland, E.R., 1954. Production of pure carbon dioxide. Google Patents.
- Lewis, T., Nielsen, L., 1970. Dynamic mechanical properties of particulate-filled composites. *J. Appl. Polym. Sci.* 14 (6), 1449–1471.
- Li, G., Bai, P., 2012a. New operation strategy for separation of ethanol–water by extractive distillation. *Ind. Eng. Chem. Res.* 51 (6), 2723–2729. doi:10.1021/IE2026579.
- Li, G., Bai, P., 2012b. New operation strategy for separation of ethanol–water by extractive distillation. *Ind. Eng. Chem. Res.* 51 (6), 2723–2729. doi:10.1021/ie2026579.
- Li, H., Hill, M.R., 2017. Low-energy CO_2 release from metal-organic frameworks triggered by external stimuli. *Acc. Chem. Res.* 50 (4), 778–786. doi:10.1021/acs.accounts.6b00591.
- Li, H., Hill, M.R., 2017. Low-energy CO_2 release from metal-organic frameworks triggered by external stimuli. *Accounts Chem. Res.* 50 (4), 778–786.
- Li, G., Pidko, E.A., 2019. The nature and catalytic function of cation sites in zeolites: a computational perspective. *ChemCatChem* 11 (1), 134–156.

- Li, Y., Yang, R.T., 2007. Gas adsorption and storage in metal-organic framework MOF-177. *Langmuir* 23 (26), 12937–12944.
- Li, H.L., Eddaoudi, M., Groy, T.L., Yaghi, O.M., 1998. Establishing microporosity in open metal-organic frameworks. gas sorption isotherms for Zn (BDC)₂ (BDC) 1,4-benzenedicarboxylate). *J. Am. Chem. Soc.* 120 (33), 8571–8572.
- Li, Z.-s., Cai, N.-s., Huang, Y.-y., 2006. Effect of preparation temperature on cyclic CO₂ capture and multiple carbonation–calcination cycles for a new Ca-based CO₂ sorbent. *Ind. Eng. Chem. Res.* 45 (6), 1911–1917. doi:10.1021/ie0512111.
- Li, F., Li, Y., Chung, T.-S., Kawi, S., 2010. Facilitated transport by hybrid POSS@Matrimid@-Zn2+ nanocomposite membranes for the separation of natural gas. *J. Membr. Sci.* 356 (1), 14–21. doi:10.1016/j.memsci.2010.03.021.
- Li, L., Li, Y., Wen, X., Wang, F., Zhao, N., Xiao, F., Wei, W., Sun, Y., 2011. CO₂ capture over K₂CO₃/MgO/Al₂O₃ dry sorbent in a fluidized bed. *Energy Fuels* 25 (8), 3835–3842. doi:10.1021/e1200499b.
- Li, Z.-s., Fang, F., Tang, X.-y., Cai, N.-s., 2012. Effect of temperature on the carbonation reaction of CaO with CO₂. *Energy Fuels* 26 (4), 2473–2482. doi:10.1021/ef201543n.
- Li, J., You, C., Chen, L., Ye, Y., Qi, Z., Sundmacher, K., 2012. Dynamics of CO₂ absorption and desorption processes in alkanolamine with cosolvent polyethylene glycol. *Ind. Eng. Chem. Res.* 51 (37), 12081–12088.
- Li, H., Moullec, Y.L., Lu, J., Chen, J., Marcos, J.C.V., Chen, G., 2014. Solubility and energy analysis for CO₂ absorption in piperazine derivatives and their mixtures. *Int. J. Greenh. Gas Control* 31, 25–32. doi:10.1016/j.jggc.2014.09.012.
- Li, L.-J., Liao, P.-Q., He, C.-T., Wei, Y.-S., Zhou, H.-L., Lin, J.-M., Li, X.-Y., Zhang, J.-P., 2015. Grafting alkylamine in UiO-66 by charge-assisted coordination bonds for carbon dioxide capture from high-humidity flue gas. *J. Mater. Chem. A* 3 (43), 21849–21855. doi:10.1039/c5ta05997f.
- Li, X., Cheng, Y., Zhang, H., Wang, S., Jiang, Z., Guo, R., Wu, H., 2015. Efficient CO₂ capture by functionalized graphene oxide nanosheets as fillers to fabricate multi-permeable mixed matrix membranes. *ACS Appl. Mater. Interfaces* 7 (9), 5528–5537. doi:10.1021/acami.5b00106.
- Li, Y., Wang, S., He, G., Wu, H., Pan, F., Jiang, Z., 2015. Facilitated transport of small molecules and ions for energy-efficient membranes. *Chem. Soc. Rev.* 44 (1), 103–118. doi:10.1039/C4CS00215F.
- Li, Q., Wang, T., Dai, C., Lei, Z., 2016. Hydrodynamics of novel structured packings: an experimental and multi-scale CFD study. *Chem. Eng. Sci.* 143, 23–35. doi:10.1016/j.ces.2015.12.014.
- Li, D., Zhou, Y., Shen, Y., Sun, W., Fu, Q., Yan, H., Zhang, D., 2016. Experiment and simulation for separating CO₂/N₂ by dual-reflux pressure swing adsorption process. *Chem. Eng. J.* 297, 315–324. doi:10.1016/j.cej.2016.03.075.
- Li, H., Hill, M.R., Doblin, C., Lim, S., Hill, A.J., Falcaro, P., 2016. Visible light triggered CO₂ liberation from silver nanocrystals incorporated metal-organic frameworks. *Adv. Funct. Mater.* 26 (27), 4815–4821. doi:10.1002/adfm.201600827.
- Li, K., Jiang, J., Chen, X., Gao, Y., Yan, F., Tian, S., 2016. Research on urea linkages formation of amine functional adsorbents during CO₂ capture process: two key factors analysis, temperature and moisture. *J. Phys. Chem. C* 120 (45), 25892–25902. doi:10.1021/acs.jpcc.6b08788.
- Li, S., Ding, J., Zhang, X., Cheng, D., Hu, X., Li, X., 2016. A feasible energy-saving analysis of a new system for CO₂ cryogenic capture. *Int. J. Low-Carbon Technol.* 11 (2), 235–239. doi:10.1093/ijlct/ct065.
- Li, Z.-H., Wang, Y., Xu, K., Yang, J.-Z., Niu, S.-B., Yao, H., 2016. Effect of steam on CaO regeneration, carbonation and hydration reactions for CO₂ capture. *Fuel Process. Technol.* 151, 101–106. doi:10.1016/j.fuproc.2016.05.019.
- Li, H., Sadiq, M.M., Suzuki, K., Riccio, R., Doblin, C., Hill, A.J., Lim, S., Falcaro, P., Hill, M.R., 2016a. Magnetic metal-organic frameworks for efficient carbon dioxide capture and remote trigger release. *Adv. Mater.* 28 (9), 1839–1844. doi:10.1002/adma.201505320.
- Li, H., Wang, K., Feng, D., Chen, Y.P., Verdegala, W., Zhou, H.C., 2016b. Incorporation of alkylamine into metal-organic frameworks through a bronsted acid-base reaction for CO₂ capture. *ChemSusChem* 9 (19), 2832–2840. doi:10.1002/cssc.201600768.
- Li, P., Liu, W., Dennis, J.S., Zeng, H.C., 2017. Synthetic architecture of MgO/C nanocomposite from hierarchical-structured coordination polymer toward enhanced CO₂ capture. *ACS Appl. Mater. Interfaces* 9 (11), 9592–9602.
- Li, Y., Li, L., Yu, J., 2017. Applications of zeolites in sustainable chemistry. *Chem* 3 (6), 928–949.
- Li, C., Chew, J.J., Mahmoud, A., Liu, S., Sunarso, J., 2018. Modelling of oxygen transport through mixed ionic-electronic conducting (MIEC) ceramic-based membranes: An overview. *J. Membr. Sci.* 567, 228–260. doi:10.1016/j.memsci.2018.09.016.
- Li, H., Li, H., Dai, Q., Li, H., Brédas, J.L., 2018. Hydrolytic stability of boronate ester-linked covalent organic frameworks. *Adv. Theor. Simul.* 1 (2), 1700015.
- Li, M., Tang, Y., Ren, N., Zhang, Z., Cao, Y., 2018. Effect of mineral constituents on temperature-dependent structural characterization of carbon fractions in sewage sludge-derived biochar. *J. Clean. Prod.* 172, 3342–3350. doi:10.1016/j.jclepro.2017.11.090.
- Li, S., Jiang, X., Sun, H., He, S., Zhang, L., Shao, L., 2019. Mesoporous dendritic fibrous nanosilica (DFNS) stimulating mix matrix membranes towards superior CO₂ capture. *J. Membr. Sci.* 586, 185–191. doi:10.1016/j.memsci.2019.05.069.
- Li, H., Wang, K., Hu, Z., Chen, Y.-P., Verdegala, W., Zhao, D., Zhou, H.-C., 2019. Harnessing solvent effects to integrate alkylamine into metal-organic frameworks for exceptionally high CO₂ uptake. *J. Mater. Chem. A* 7 (13), 7867–7874. doi:10.1039/c8ta1300a.
- Li, H., Zhao, Z., Xiouras, C., Stefanidis, G.D., Li, X., Gao, X., 2019. Fundamentals and applications of microwave heating to chemicals separation processes. *Renew. Sustain. Energy Rev.* 114, 109316. doi:10.1016/j.rser.2019.109316.
- Li, H.M., Li, J.H., Thomas, A., Liao, Y.Z., 2019. Ultra-high surface area nitrogen-doped carbon aerogels derived from a Schiff-base porous organic polymer aerogel for CO₂ storage and supercapacitors. *Adv. Funct. Mater.* 29 (40). doi:10.1002/adfm.201904785.
- Li, N., Chang, Z., Huang, H., Feng, R., He, W.W., Zhong, M., Madden, D.G., Zatorokto, M.J., Bu, X.H., 2019. Specific K (+) binding sites as CO₂ traps in a porous MOF for enhanced CO₂ selective sorption. *Small* 15 (22), e1900426. doi:10.1002/smll.201900426.
- Li, S., Prasetya, N., Ladewig, B.P., 2019. Investigation of Azo-COP-2 as a photoresponsive low-energy CO₂ adsorbent and porous filler in mixed matrix membranes for CO₂/N₂ separation. *Ind. Eng. Chem. Res.* 58 (23), 9959–9969. doi:10.1021/acs.iecr.9b00762.
- Li, W., Goh, K., Chuah, C.Y., Bae, T.-H., 2019. Mixed-matrix carbon molecular sieve membranes using hierarchical zeolite: A simple approach towards high CO₂ permeability enhancements. *J. Membr. Sci.* 588. doi:10.1016/j.memsci.2019.117220.
- Li, Z., Shan, X.W., Yang, P.P., Gao, Z.Z., Fang, Q.R., Xue, M., Qiu, S.L., 2019. Preparation, characterization and gas adsorption properties of metal-organic aerogels. *Chem. J. Chin. U* 40 (6), 1116–1120. doi:10.7503/cjcu20190102.
- Li, H., Liu, B., Yang, M., Zhu, D., Huang, Z., Chen, W., Yang, L., Chen, G., 2020. CO₂ separation performance of zeolitic imidazolate framework-8 porous slurry in a pilot-scale packed tower. *Ind. Eng. Chem. Res.* 59 (13), 6154–6163. doi:10.1021/acs.iecr.9b06897.
- Li, Y.W., Jia, P.P., Xu, J., Wu, Y., Jiang, H., Li, Z., 2020. The aminosilane functionalization of cellulose nanofibrils and the mechanical and CO₂ adsorption characteristics of their aerogel. *Ind. Eng. Chem. Res.* 59 (7), 2874–2882. doi:10.1021/acs.iecr.9b04253.
- Li, X., Ding, S., Zhang, J., Wei, Z.J.L.J.o.G.G.C., 2020. Optimizing microstructure of polymer composite membranes by tailoring different ionic liquids to accelerate CO₂ transport. 101, 103136.
- Li, B., Wang, S.-s., Qiao, J., Wang, B., Song, L., 2021. Thermodynamic analysis and optimization of a dual-pressure Allam cycle integrated with the regasification of liquefied natural gas. *Energy Convers. Manage.* 246, 114660.
- Li, D., Motz, A.R., Bae, C., Fujimoto, C., Yang, G., Zhang, F.-Y., Ayers, K.E., Kim, Y.S., 2021. Durability of anion exchange membrane water electrolyzers. *Energy Environ. Sci.* 14 (6), 3393–3419. doi:10.1039/d0ee04086j.
- Li, X., Zhou, X., Wei, J., Fan, Y., Liao, L., Wang, H., 2021. Reducing the energy penalty and corrosion of carbon dioxide capture using a novel nonaqueous monoethanolamine-based biphasic solvent. *Sep. Purif. Technol.* 265. doi:10.1016/j.seppur.2021.118481.
- Li, B., Mbeugang, C.F.M., Huang, Y., Liu, D.J., Wang, Q., Zhang, S., 2022. A review of CaO based catalysts for tar removal during biomass gasification. *Energy* 244, 12. doi:10.1016/j.energy.2022.123172.
- Li, J., Bao, A., Chen, J., Bao, Y., 2022. A green route to CO₂ adsorption on biomass chitosan derived nitrogen-doped micropore-dominated carbon nanosheets by different activators. *J. Environ. Chem. Eng.* 10 (1), 107021. doi:10.1016/j.jece.2021.107021.
- Li, K., Xu, R., Sun, J., Cui, Y., Liu, J., Yang, S., Wang, R., Zhou, Z., Nie, X., 2022. Comparative investigation on thermochemical energy storage stability of Zr/Al-supported dark CaO-based composites under harsh energy storage mode. *Carbon Cap. Sci. Technol.* 5, 100076. doi:10.1016/j.cscst.2022.100076.
- Li, R., Lian, S., Zhang, Z., Song, C., Han, R., Liu, Q., 2022. Techno-economic evaluation of a novel membrane-cryogenic hybrid process for carbon capture. *Appl. Therm. Eng.* 200, 117688. doi:10.1016/j.applthermeng.2021.117688.
- Li, S., Chang, S.-M., Yin, M.-J., Zhang, W.-H., Sun, W.-S., Shiu, A., An, Q.-F., 2022. Build up 'highway' in membrane via solvothermal annealing for high-efficient CO₂ capture. *J. Membr. Sci.* 652, 120444. doi:10.1016/j.memsci.2022.120444.
- Li, T., Yang, C., Tantikhajongosol, P., Sema, T., Tontiwachwuthikul, P., 2022. Studies on advanced configurations of post-combustion CO₂ capture process applied to cement plant flue gases. *Carbon Cap. Sci. Technol.* 4, 100064. doi:10.1016/j.CCST.2022.100064.
- Li, W.L., Liang, H.W., Wang, J.H., Shao, L., Chu, G.W., Xiang, Y., 2022. CFD modeling on the chemical absorption of CO₂ in a microporous tube-in-tube microchannel reactor. *Fuel* 327. doi:10.1016/j.fuel.2022.125064, 125064–125064.
- Li, Y.B., Wen, Z.N., Sun, B.C., Luo, Y., Gao, K.J., Chu, G.W., 2022. Flow patterns, liquid holdup, and wetting behavior of viscous liquids in a disk-distributor rotating packed bed. *Chem. Eng. Sci.* 252. doi:10.1016/j.ces.2021.117256, 117256–117256.
- Lian, G., Zhong, W., 2022. CFD-DEM modeling of oxy-char combustion in a fluidized bed. *Powder Technol.* 407. doi:10.1016/j.powtec.2022.117698, 117698–117698.
- Lian, S., Song, C., Liu, Q., Duan, E., Ren, H., Kitamura, Y., 2021. Recent advances in ionic liquids-based hybrid processes for CO₂ capture and utilization. *J. Environ. Sci.* 99, 281–295. doi:10.1016/j.jes.2020.06.034.
- Liang, Z., Fu, K., Idem, R., Tontiwachwuthikul, P., 2016a. Review on current advances, future challenges and consideration issues for post-combustion CO₂ capture using amine-based absorbents. *Chin. J. Chem. Eng.* 24 (2), 278–288.
- Liang, Z., Idem, R., Tontiwachwuthikul, P., Yu, F., Liu, H., Rongwong, W., 2016b. Experimental study on the solvent regeneration of a CO₂-loaded MEA solution using single and hybrid solid acid catalysts. *AIChE J.* 62 (3), 753–765. doi:10.1002/aic.15073.
- Liang, J., Liang, Z., Zou, R., Zhao, Y., 2017. Heterogeneous catalysis in zeolites, mesoporous silica, and metal-organic frameworks. *Adv. Mater.* 29 (30). doi:10.1002/adma.201701139.
- Liang, W., Huang, J., Xiao, P., Singh, R., Guo, J., Dehdari, L., Li, G.K., 2022. Amine-immobilized HY zeolite for CO₂ capture from hot flue gas. *Chin. J. Chem. Eng.* 43, 335–342. doi:10.1016/j.cjche.2022.02.004.
- Liao, J., Wang, Z., Gao, C., Li, S., Qiao, Z., Wang, M., Zhao, S., Xie, X., Wang, J., Wang, S., 2014. Fabrication of high-performance facilitated transport membranes for CO₂ separation. *Chem. Sci.* 5 (7), 2843–2849. doi:10.1039/C3SC53334D.
- Liao, H., Gao, H., Xu, B., Liang, Z., 2017. Mass transfer performance studies of aqueous blended DEEA-MEA solution using orthogonal array design in a packed column. *Sep. Purif. Technol.* 183, 117–126. doi:10.1016/j.seppur.2017.03.064.
- Liao, Z., Hu, Y., Wang, J., Yang, Y., You, F., 2019. Systematic design and optimization of a membrane-cryogenic hybrid system for CO₂ capture. *ACS Sustain. Chem. Eng.* 7 (20), 17186–17197. doi:10.1021/acssuschemeng.9b03727.

- Liao, P., Li, Y., Wu, X., Wang, M., Oko, E., 2020. Flexible operation of large-scale coal-fired power plant integrated with solvent-based post-combustion CO₂ capture based on neural network inverse control. *Int. J. Greenh. Gas Control* 95. doi:10.1016/j.ijggc.2020.102985.
- Liew, R.K., Azwar, E., Yek, P.N.Y., Lim, X.Y., Cheng, C.K., Ng, J.H., Jusoh, A., Lam, W.H., Ibrahim, M.D., Ma, N.L., Lam, S.S., 2018. Microwave pyrolysis with KOH/NaOH mixture activation: A new approach to produce micro-mesoporous activated carbon for textile dye adsorption. *Bioresour. Technol.* 266, 1–10. doi:10.1016/j.biortech.2018.06.051.
- Liew, R.K., Chai, G., Yek, P.N.Y., Phang, X.Y., Chong, M.Y., Nam, W.L., Su, M.H., Lam, W.H., Ma, N.L., Lam, S.S., 2019. Innovative production of highly porous carbon for industrial effluent remediation via microwave vacuum pyrolysis plus sodium-potassium hydroxide mixture activation. *J. Clean. Prod.* 208, 1436–1445. doi:10.1016/j.jclepro.2018.10.214.
- Lillia, S., Bonalumi, D., Grande, C., Manzolini, G., 2018. A comprehensive modeling of the hybrid temperature electric swing adsorption process for CO₂ capture. *Int. J. Greenh. Gas Control* 74, 155–173. doi:10.1016/j.ijggc.2018.04.012.
- Lillia, S., Bonalumi, D., Fosbol, P.L., Thomsen, K., Jayaweera, I., Valenti, G., 2019. Thermodynamic and kinetic properties of NH₃-K₂CO₃-CO₂-H₂O system for carbon capture applications. *Int. J. Greenh. Gas Control* 85, 121–131. doi:10.1016/j.ijggc.2019.03.019.
- Lim, G., Lee, K.B., Ham, H.C., 2016. Effect of N-containing functional groups on CO₂ adsorption of carbaceous materials: a density functional theory approach. *J. Phys. Chem. C* 120 (15), 8087–8095. doi:10.1021/acs.jpcc.5b12090.
- Lin, H., Wagner, E.V., Swinnea, J.S., Freeman, B.D., Pas, S.J., Hill, A.J., Kalakkunnath, S., Kalika, D.S., 2006. Transport and structural characteristics of crosslinked poly (ethylene oxide) rubbers. *J. Membr. Sci.* 276 (1), 145–161. doi:10.1016/j.memsci.2005.09.040.
- Lin, Y., Yan, Q., Kong, C., Chen, L., 2013. Polyethyleneimine incorporated metal-organic frameworks adsorbent for highly selective CO₂ capture. *Sci. Rep.* 3, 1859. doi:10.1038/srep01859.
- Lin, Y.F., Chen, C.H., Tung, K.L., Wei, T.Y., Lu, S.Y., Chang, K.S., 2013. Mesoporous fluorocarbon-modified silica aerogel membranes enabling long-term continuous CO₂ capture with large absorption flux enhancements. *ChemSuschem* 6 (3), 437–442. doi:10.1002/cssc.201200837.
- Lin, R., Hernandez, B.V., Ge, L., Zhu, Z., 2018. Metal organic framework based mixed matrix membranes: An overview on filler/polymer interfaces. *J. Mater. Chem. A* 6 (2), 293–312.
- Lin, J.-B., Nguyen, T.T.T., Vaidyanathan, R., Burner, J., Taylor, J.M., Durekova, H., Akhtar, F., Mah, R.K., Ghaffari-Nik, O., Marx, S., Fylstra, N., Iremonger, S.S., Dawson, K.W., Sarkar, P., Hovington, P., Rajendran, A., Woo, T.K., Shimizu, G.K.H., 2021. A scalable metal-organic framework as a durable physisorbent for carbon dioxide capture. *Science* 374, 1464–1469.
- Lin, Q., Liao, Z., Hu, Y., Sun, J., Jiang, B., Wang, J., Yang, Y., 2021. Optimal design of a subambient membrane separation system with work and heat integration for CO₂ capture. *Ind. Eng. Chem. Res.* 60 (42), 15194–15207. doi:10.1021/acs.iecr.1c02303.
- Lindqvist, K., Jordal, K., Haugen, G., Hoff, K.A., Anantharaman, R., 2014. Integration aspects of reactive absorption for post-combustion CO₂ capture from NGCC (natural gas combined cycle) power plants. *Energy* 78, 758–767. doi:10.1016/j.energy.2014.10.070.
- Linneen, N.N., Pfeffer, R., Lin, Y.S., 2014. CO₂ adsorption performance for amine grafted particulate silica aerogels. *Chem. Eng. J.* 254, 190–197. doi:10.1016/j.cej.2014.05.087.
- Littel, R.J., Versteeg, G.F., Van Swaaij, W.P.M., 1992. Kinetics of CO₂ with primary and secondary amines in aqueous solutions-I. Zwitterion deprotonation kinetics for DEA and DIPA in aqueous blends of alkanolamines. *Chem. Eng. Sci.* 47 (8), 2027–2035. doi:10.1016/0009-2509(92)80319-8.
- Liu, S.-H., Huang, Y.-Y., 2018. Valorization of coffee grounds to biochar-derived adsorbents for CO₂ adsorption. *J. Clean. Prod.* 175, 354–360. doi:10.1016/j.jclepro.2017.12.076.
- Liu, S.H., Huang, Y.Y., 2018. Valorization of coffee grounds to biochar-derived adsorbents for CO₂ adsorption. *J. Clean. Prod.* 175, 354–360. doi:10.1016/j.jclepro.2017.12.076.
- Liu, B., Smit, B., 2010. Molecular simulation studies of separation of CO₂/N₂, CO₂/CH₄, and CH₄/N₂ by ZIFs. *J. Phys. Chem. C* 114 (18), 8515–8522.
- Liu, Y., Wilcox, J., 2012. Effects of surface heterogeneity on the adsorption of CO₂ in microporous carbons. *Environ. Sci. Technol.* 46 (3), 1940–1947. doi:10.1021/es204071g.
- Liu, S., Zhang, X., Li, J., Zhao, N., Wei, W., Sun, Y., 2008. Preparation and application of stabilized mesoporous MgO-ZrO₂ solid base. *Catal. Commun.* 9 (7), 1527–1532. doi:10.1016/j.catcom.2007.12.007.
- Liu, W., Feng, B., Wu, Y., Wang, G., Barry, J., Diniz da Costa, J., 2010. Synthesis of sintering-resistant sorbents for CO₂ capture. *Environ. Sci. Technol.* 44 (8), 3093–3097.
- Liu, J., Wang, Y., Benin, A.I., Jakubczak, P., Willis, R.R., LeVan, M.D., 2010. CO₂/H₂O adsorption equilibrium and rates on metal-organic frameworks: HKUST-1 and Ni₃DOBDC. *Langmuir* 26 (17), 14301–14307.
- Liu, J., Benin, A.I., Furtado, A.M., Jakubczak, P., Willis, R.R., LeVan, M.D., 2011. Stability effects on CO₂ adsorption for the DOBDC series of metal-organic frameworks. *Langmuir* 27 (18), 11451–11456.
- Liu, W.-J., Jiang, H., Tian, K., Ding, Y.-W., Yu, H.-Q., 2013. Mesoporous carbon stabilized MgO nanoparticles synthesized by pyrolysis of MgCl₂ preloaded waste biomass for highly efficient CO₂ capture. *Environ. Sci. Technol.* 47 (16), 9397–9403.
- Liu, C., Xing, W., Zhou, J., Zhou, S.-p., 2013. N-containing activated carbons for CO₂ capture. *Int. J. Smart Nano Mater.* 4 (1), 55–61. doi:10.1080/19475411.2012.668861.
- Liu, H., Dai, S., Jiang, D., 2013. Insights into CO₂/N₂ separation through nanoporous graphene from molecular dynamics. *Nanoscale* 5 (20), 9984–9987. doi:10.1039/C3NR02852F.
- Liu, Y., Yu, S., Wu, H., Li, Y., Wang, S., Tian, Z., Jiang, Z., 2014. High permeability hydrogels of chitosan/poly ether-block-amide blends for CO₂ separation. *J. Membr. Sci.* 469, 199–208. doi:10.1016/j.memsci.2014.06.050.
- Liu, L., Qiu, W., Sanders, E.S., Ma, C., Koros, W.J., 2016. Post-combustion carbon dioxide capture via 6FDA/BDPA-DAM hollow fiber membranes at sub-ambient temperatures. *J. Membr. Sci.* 510, 447–454. doi:10.1016/j.memsci.2016.03.027.
- Liu, X., Gao, F., Xu, J., Zhou, L., Liu, H., Hu, J., 2016. Zeolite@Mesoporous silica-supported-amine hybrids for the capture of CO₂ in the presence of water. *Microporous Mesoporous Mater.* 222, 113–119. doi:10.1016/j.micromeso.2015.10.006.
- Liu, Y., Luo, Y., Chu, G.W., Luo, J.Z., Arowo, M., Chen, J.F., 2017. 3D numerical simulation of a rotating packed bed with structured stainless steel wire mesh packing. *Chem. Eng. Sci.* 170, 365–377. doi:10.1016/j.ces.2017.01.033.
- Liu, X., Wang, X., Bavykina, A., Chu, L., Shan, M., Sabetghadam, A., Miro, H., Kaptejin, F., Gascon, J., 2018. Molecular-scale hybrid membranes derived from metal-organic polyhedra for gas separation. *ACS Appl. Mater. Interfaces* 10, 21381–21389. doi:10.1021/acsami.8b07045.
- Liu, J., Wang, Z., Wang, Z., Song, J., Li, G., Xu, Q., You, J., Cheng, H., Lu, X., 2019. Alkali carbonates promote CO₂ capture by sodium orthoformate. *Phys. Chem. Chem. Phys.* 21 (24), 13135–13143. doi:10.1039/C9CP01306G.
- Liu, F., Fang, M., Yi, N., Wang, T., 2019a. Research on alkanolamine-based physical-chemical solutions as biphasic solvents for CO₂ capture. *Energy Fuels* 33 (11), 11389–11398. doi:10.1021/acs.energyfuels.9b02392.
- Liu, F., Fang, M., Yi, N., Wang, T., Wang, Q., 2019b. Biphasic behaviors and regeneration energy of a 2- (diethylamino)-ethanol and 2- (2-aminoethyl)amino ethanol blend for CO₂ capture. *Sustain. Energy Fuels* 3 (12), 3594–3602. doi:10.1039/c9se00821g.
- Liu, M., Nothing, M.D., Webley, P.A., Jin, J., Fu, Q., Qiao, G.G., 2020. High-throughput CO₂ capture using PIM-1@MOF based thin film composite membranes. *Chem. Eng. J.* 396, 125328. doi:10.1016/j.cej.2020.125328.
- Liu, L., Jin, S., Ko, K., Kim, H., Ahn, I.-S., Lee, C.-H., 2020. Alkyl-functionalization of (3-Aminopropyl)triethoxysilane-grafted zeolite beta for carbon dioxide capture in temperature swing adsorption. *Chem. Eng. J.* 382, doi:10.1016/j.cej.2019.122834.
- Liu, B., Yang, X., Chiang, P.-C., Wang, T., 2020. Energy consumption analysis of cryogenic-membrane hybrid process for CO₂ capture from CO₂-EOR extraction gas. *Aerosol. Air Qual. Res.* 20 (4), 820–832. doi:10.4209/aaqr.2020.02.0047.
- Liu, F., Shen, Y., Shen, L., Sun, C., Chen, L., Wang, Q., Li, S., Li, W., 2020. Novel amino-functionalized ionic liquid/organic solvent with low viscosity for CO₂ capture. *Environ. Sci. Technol.* 54 (6), 3520–3529. doi:10.1021/acs.est.9b06717.
- Liu, J., Fulong, C.R.P., Hu, L., Huang, L., Zhang, G., Cook, T.R., Lin, H., 2020. Interpenetrating networks of mixed matrix materials comprising metal-organic polyhedra for membrane CO₂ capture. *J. Membr. Sci.* 606, 118122. doi:10.1016/j.memsci.2020.118122.
- Liu, Y., Wu, H., Wu, S., Song, S., Guo, Z., Ren, Y., Zhao, R., Yang, L., Wu, Y., Jiang, Z., 2021. Multifunctional covalent organic framework (COF)-Based mixed matrix membranes for enhanced CO₂ separation. *J. Membr. Sci.* 618, 118693. doi:10.1016/j.memsci.2020.118693.
- Liu, Z.Y., Ma, R., Du, W.J., Wang, G., Chen, T., 2021. Radiation-initiated high strength chitosan/lithium sulfonate double network hydrogel/aerogel with porosity and stability for efficient CO₂ capture. *RSC Adv.* 11 (33), 20486–20497. doi:10.1039/d1ra03041h.
- Liu, B., Li, Z., Li, D., Sun, H., Yao, J., 2021. Poly(zwitterion-grafted UiO-66-PEI) incorporating polyimide membrane for high efficiency CO₂/CH₄ separation. *Sep. Purif. Technol.* 267, 118617. doi:10.1016/j.seppur.2021.118617.
- Liu, K., Li, H., Zhao, Z.-y., Wang, X.-j., Li, X.-g., Gao, X., 2021. Microwave-induced spray evaporation process for separation intensification of azeotropic system. *Sep. Purif. Technol.* 279, doi:10.1016/j.seppur.2021.119702.
- Liu, M., Nothing, M.D., Zhang, S., Fu, Q., Qiao, G.G., 2022. Thin film composite membranes for postcombustion carbon capture: Polymers and beyond. *Progress Polym. Sci.* 126, doi:10.1016/j.progpolymsci.2022.101504.
- Liu, N., Cheng, J., Hu, L., Hou, W., Yang, X., Luo, M., Zhang, H., Ye, B., Zhou, J., 2022. Boosting CO₂ transport of poly (ethylene oxide) membranes by hollow Rubik-like “expressway” channels with anion pillared hybrid ultramicroporous materials. *Chem. Eng. J.* 427, 130845. doi:10.1016/j.cej.2021.130845.
- Liu, Q., Zhong, W., Yu, A., Wang, C.-H., 2022. Co-firing of coal and biomass under pressurized oxy-fuel combustion mode: Experimental test in a 10 kWth fluidized bed. *Chem. Eng. J.* 431, 133457. doi:10.1016/j.cej.2021.133457.
- Liu, F., Huang, K., Yoo, C.-J., Okonkwo, C., Tao, D.-J., Jones, C.W., Dai, S., 2017. Facilely synthesized meso-macroporous polymer as support of poly (ethyleneimine) for highly efficient and selective capture of CO₂. *Chem. Eng. J.* 314, 466–476. doi:10.1016/j.cej.2016.12.004.
- Liu, H., Zhang, X., Gao, H., Liang, Z., Idem, R., Tontiwachwuthikul, P., 2017. Investigation of CO₂ regeneration in single and blended amine solvents with and without catalyst. *Ind. Eng. Chem. Res.* 56 (27), 7656–7664. doi:10.1021/acs.iecr.7b00778.
- Liu, S.H., 2019. Waste-Derived Biochar for CO₂ Sequestration. *Biochar Biomass Waste: Fundament. Appl.* 295–304. doi:10.1016/b978-0-12-811729-3.00016-9.
- Lively, R.P., Chance, R.R., Kelley, B.T., Deckman, H.W., Drese, J.H., Jones, C.W., Koros, W.J., 2009. Hollow fiber adsorbents for CO₂ removal from flue gas. *Ind. Eng. Chem. Res.* 48, 7314–7324.
- Lively, R.P., Chance, R.R., Koros, W.J., 2010. Enabling low-cost CO₂ capture via heat integration. *Ind. Eng. Chem. Res.* 49, 7550–7562.
- Lively, R.P., Chance, R.R., Mysona, J.A., Sabu, V.P., Deckman, H.W., Leta, D.P., Thomann, H., Koros, W.J., 2012. CO₂ sorption and desorption performance of thermally cycled hollow fiber sorbents. *Int. J. Greenh. Gas Control* 10, 285–294. doi:10.1016/j.ijggc.2012.06.019.
- Llewellyn, P.L., Bourrelly, S., Serre, C., Vimont, A., Daturi, M., Hamon, L., Weirald, G.D., Chang, J.S., Hong, D.Y., Hwang, Y.K., Jung, S.H., Fe'reyre, G., 2008. High Uptakes of CO₂ and CH₄ in Mesoporous MetalOrganic Frameworks MIL-100 and MIL-101. *Langmuir* 24 (14), 7245–7250.

- Loganathan, S., Ghoshal, A.K., 2017. Amine tethered pore-expanded MCM-41: A promising adsorbent for CO₂ capture. *Chem. Eng. J.* 308, 827–839. doi:10.1016/j.cej.2016.09.103.
- Lu, H., Kim, J.P., Son, S.H., Park, J.H., 2011. Novel SrCo_{1-2x}(Fe,Nb)xO_{3-δ} (x=0.05, 0.10) oxides targeting CO₂ capture and O₂ enrichment: structural stability and oxygen sorption properties. *Mater. Lett.* 65 (19), 2858–2860. doi:10.1016/j.matlet.2011.06.062.
- Lu, W., Sculley, J.P., Yuan, D., Krishna, R., Wei, Z., Zhou, H.C., 2012. Polyamine-tethered porous polymer networks for carbon dioxide capture from flue gas. *Angew. Chem. Int. Ed. Engl.* 51 (30), 7480–7484. doi:10.1002/anie.201202176.
- Lu, X., Forrest, B., Martin, S., Fetvedt, J., McGroddy, M., Freed, D., 2016. Integration and optimization of coal gasification systems with a near-zero emissions supercritical carbon dioxide power cycle. In: *Turbo Expo: Power for Land, Sea, and Air*. American Society of Mechanical Engineers V009T036A019.
- Lu, X., Xie, P., Ingham, D.B., Ma, L., Pourkashanian, M., 2019. Modelling of CO₂ absorption in a rotating packed bed using an Eulerian porous media approach. *Chem. Eng. Sci.* 199, 302–318. doi:10.1016/j.ces.2019.01.029.
- Lu, J., Zhang, X., Xu, L., Zhang, G., Zheng, J., Tong, Z., Shen, C., Meng, Q., 2021. Preparation of amino-functional UIO-66/PMS mixed matrix membranes with [bmim][Tf₂N] as regulator for enhanced gas separation. *Membranes* 11 (1), 35. doi:10.3390/membranes11010035.
- Lu, W., Shi, X., Zhou, H., Luo, W., Wang, L., He, H., 2022. Tailoring and properties of a novel solar energy-triggered regenerative bionic fiber adsorbent for CO₂ capture. *Chem. Eng. J.* 449. doi:10.1016/j.cej.2022.137885.
- Luberti, M., Oreggioni, G.D., Ahn, H., 2017. Design of a rapid vacuum pressure swing adsorption (RVPSA) process for post-combustion CO₂ capture from a biomass-fueled CHP plant. *J. Environ. Chem. Eng.* 5 (4), 3973–3982. doi:10.1016/j.jece.2017.07.029.
- Luca, A.V., Petrescu, L., 2021. Membrane technology applied to steel production: investigation based on process modelling and environmental tools. *J. Clean. Prod.* 294. doi:10.1016/j.jclepro.2021.126256.
- Lukin, I., Pietzka, L., Groß, K., Görak, A., Schembecker, G., 2020. Economic evaluation of rotating packed bed use for aroma absorption from bioreactor off-gas. *Chem. Eng. Process. - Process Intensif.* 154 (December 2019). doi:10.1016/j.cep.2020.108011, 108011–108011.
- Lunn, J.D., Shantz, D.F., 2009. Peptide brush—Ordered mesoporous silica nanocomposite materials. *Chem. Mater.* 21 (15), 3638–3648. doi:10.1021/cm901025n.
- Luo, H., Kanoh, H., 2017. Fundamentals in CO₂ capture of Na₂CO₃ under a moist condition. *J. Energy Chem.* 26 (5), 972–983. doi:10.1016/j.jechem.2017.08.005.
- Luo, Q., Pentzer, E., 2020. Encapsulation of Ionic Liquids for Tailored Applications. *ACS Appl. Mater. Interfaces* 12 (5), 5169–5176. doi:10.1021/acsami.9b16546.
- Luo, F., Fan, C.B., Luo, M.B., Wu, X.L., Zhu, Y., Pu, S.Z., Xu, W.Y., Guo, G.C., 2014. Photoswitching CO₂ (2) capture and release in a photochromic diarylethene metal-organic framework. *Angew. Chem. Int. Ed. Engl.* 53 (35), 9298–9301. doi:10.1002/anie.201311124.
- Luo, S., Bayham, S., Zeng, L., McGiveron, O., Chung, E., Majumder, A., Fan, L.-S., 2014. Conversion of metallurgical coke and coal using a coal direct chemical looping (CDCL) moving bed reactor. *Appl. Energy* 118, 300–308. doi:10.1016/j.apenergy.2013.11.068.
- Luo, S., Stevens, K.A., Park, J.S., Moon, J.D., Liu, Q., Freeman, B.D., Guo, R., 2016. Highly CO₂-selective gas separation membranes based on segmented copolymers of poly (Ethylene oxide) reinforced with pentiptycene-containing polyimide hard segments. *ACS Appl. Mater. Interfaces* 8 (3), 2306–2317. doi:10.1021/acsami.5b11355.
- Luo, W., Guo, D., Zheng, J., Gao, S., Chen, J., 2016. CO₂ absorption using biphasic solvent: Blends of diethylenetriamine, sulfonate, and water. *Int. J. Greenh. Gas Control* 53, 141–148. doi:10.1016/j.jggc.2016.07.036.
- Luo, X., Liu, S., Gao, H., Liao, H., Tontiwachwuthikul, P., Liang, Z., 2016. An improved fast screening method for single and blended amine-based solvents for post-combustion CO₂ capture. *Sep. Purif. Technol.* 169, 279–288. doi:10.1016/j.seppur.2016.06.018.
- Luo, X.Y., Fan, X., Shi, G.L., Li, H.R., Wang, C.M., 2016. Decreasing the viscosity in CO₂ capture by amino-functionalized ionic liquids through the formation of intramolecular hydrogen bond. *J. Phys. Chem. B* 120 (10), 2807–2813. doi:10.1021/acs.jpcc.5b10553.
- Luo, M., Yi, Y., Wang, S., Wang, Z., Du, M., Pan, J., Wang, Q., 2018. Review of hydrogen production using chemical-looping technology. *Renew. Sustain. Energy Rev.* 81, 3186–3214. doi:10.1016/j.rser.2017.07.007.
- Luo, J., Emelogu, O., Morosuk, T., Tsatsaronis, G., 2021. Exergy-based investigation of a coal-fired allam cycle. *Energy* 218, 119471.
- Luo, X., Wang, M., Lee, J., Hendry, J., 2021. Dynamic modelling based on surface renewal theory, model validation and process analysis of rotating packed bed absorber for carbon capture. *Appl. Energy* 301 (March). doi:10.1016/j.apenergy.2021.117462, 117462–117462.
- Luo, H., Wang, X., Liu, X., Wu, X., Shi, X., Xiong, Q., 2022. A review on CFD simulation of biomass pyrolysis in fluidized bed reactors with emphasis on particle-scale models. *J. Anal. Appl. Pyroly.* 162. doi:10.1016/j.jaap.2022.105433, 105433–105433.
- Lv, B., Jing, G., Qian, Y., Zhou, Z., 2016a. An efficient adsorbent of amine-based amino acid-functionalized ionic liquids for CO₂ capture: High capacity and regeneration ability. *Chem. Eng. J.* 289, 212–218. doi:10.1016/j.cej.2015.12.096.
- Lv, B., Jing, G., Qian, Y., Zhou, Z., 2016b. An efficient adsorbent of amine-based amino acid-functionalized ionic liquids for CO₂ capture: High capacity and regeneration ability. *Chem. Eng. J.* 289, 212–218. doi:10.1016/j.cej.2015.12.096.
- Lv, B., Zhou, X., Zhou, Z., Jing, G., 2019. Kinetics and thermodynamics of CO₂ absorption into a novel DETA-AMP-PMDETA biphasic solvent. *ACS Sustain. Chem. Eng.* 7 (15), 13400–13410. doi:10.1021/acssuschemeng.9b02700.
- Lv, B.H., Huang, Q.S., Zhou, Z.M., Jing, G.H., 2020. Novel biphasic amino-functionalized ionic liquid solvent for CO₂ capture: kinetics and regeneration heat duty. *Environ. Sci. Pollut. Res.* 27 (21), 26965–26973. doi:10.1007/s11356-020-09039-x.
- Lyndon, R., Konstas, K., Ladewig, B.P., Southon, P.D., Kepert, P.C., Hill, M.R., 2013. Dynamic photo-switching in metal-organic frameworks as a route to low-energy carbon dioxide capture and release. *Angew. Chem. Int. Ed. Engl.* 52 (13), 3695–3698. doi:10.1002/anie.201206359.
- Lyndon, R., Konstas, K., Evans, R.A., Keddie, D.J., Hill, M.R., Ladewig, B.P., 2015a. Tunable photodynamic switching of DARE@PAF-1 for carbon capture. *Adv. Funct. Mater.* 25 (28), 4405–4411. doi:10.1002/adfm.201502069.
- Lyndon, R., Konstas, K., Thornton, A.W., Seeber, A.J., Ladewig, B.P., Hill, M.R., 2015b. Visible light-triggered capture and release of CO₂ from stable metal organic frameworks. *Chem. Mater.* 27 (23), 7882–7888. doi:10.1021/acs.chemmater.5b02211.
- Lyngfelt, A., Leckner, B., Mattisson, T., 2001. A fluidized-bed combustion process with inherent CO₂ separation; application of chemical-looping combustion. *Chem. Eng. Sci.* 56 (10), 3101–3113.
- Lyngfelt, A., Brink, A., Langørgen, Ø., Mattisson, T., Rydén, M., Linderholm, C., 2019. 11,000 h of chemical-looping combustion operation—Where are we and where do we want to go? *Int. J. Greenh. Gas Control* 88, 38–56. doi:10.1016/j.jggc.2019.05.023.
- Ma, S., Chen, G., Zhu, S., Wen, J., Gao, R., Ma, L., Chai, J., 2016. Experimental study of mixed additive of Ni (II) and piperazine on ammonia escape in CO₂ capture using ammonia solution. *Appl. Energy* 169, 597–606.
- Ma, C., Liu, C., Lu, X., Ji, X., 2018. Techno-economic analysis and performance comparison of aqueous deep eutectic solvent and other physical adsorbents for biogas upgrading. *Appl. Energy* 225, 437–447. doi:10.1016/j.apenergy.2018.04.112.
- Ma, L., Svec, F., Lv, Y., Tan, T., 2019. In situ bottom-up growth of metal-organic frameworks in a crosslinked poly (ethylene oxide) layer with ultrahigh loading and superior uniform distribution. *J. Mater. Chem. A* 7 (35), 20293–20301. doi:10.1039/C9TA05401D.
- Ma, X., Wu, X., Caro, J., Huang, A., 2019. Polymer composite membrane with penetrating ZIF-7 sheets displays high hydrogen permselectivity. *Angew. Chem. Int. Ed.* 58 (45), 16156–16160. doi:10.1002/anie.201911226.
- Ma, Y., Jue, M.L., Zhang, F., Mathias, R., Jang, H.Y., Lively, R.P., 2019. Creation of well-defined “Mid-Sized” micropores in carbon molecular sieve membranes. *Angew. Chem. Int. Ed. Engl.* 58 (38), 13259–13265. doi:10.1002/anie.201903105.
- Ma, J., Wang, Y.T., Yang, X.Q., Zhu, M.X., Wang, B.H., 2021. DFT study on the chemical absorption mechanism of CO₂ in diamine protic ionic liquids. *J. Phys. Chem. B* 125 (5), 1416–1428. doi:10.1021/acs.jpcc.0c08500.
- Ma, Q.X., Chen, W.H., Jin, Z.H., Chen, L., Zhou, Q.Y., Jiang, X., 2021. One-step synthesis of microporous nitrogen-doped biochar for efficient removal of CO₂ and H₂S. *Fuel* 289. doi:10.1016/j.fuel.2020.119932.
- Ma, X., Li, Y., Huang, X., Feng, T., Mu, M., 2021. Sorption-enhanced reaction process using advanced Ca-based sorbents for low-carbon hydrogen production. *Process. Saf. Environ. Prot.* 155, 325–342. doi:10.1016/j.psep.2021.09.009.
- Mac Dowell, N., Llovel, F., Adjiman, C.S., Jackson, G., Galindo, A., 2010. Modeling the fluid phase behavior of carbon dioxide in aqueous solutions of monoethanolamine using transferable parameters with the SAFT-VR approach. *Ind. Eng. Chem. Res.* 49 (4), 1883–1899. doi:10.1021/ie901014t.
- Machida, M., Kawada, T., Fujii, H., Hinokuma, S., 2015. The role of CeO₂ as a gateway for oxygen storage over CeO₂-grafted Fe₂O₃ composite materials. *J. Phys. Chem. C* 119 (44), 24932–24941. doi:10.1021/acs.jpcc.5b09876.
- Macneil, S., Basu, P., 1998. Effect of pressure on char combustion in a pressurized circulating fluidized bed boiler. *Fuel* 77 (4), 269–275.
- Madejski, P., Chmiel, K., Subramanian, N., Kus, T., 2022. Methods and techniques for CO₂ capture: review of potential solutions and applications in modern energy technologies. *Energies* 15 (3), 21. doi:10.3390/en15030887.
- Mazdaki, H., KarimGhani, W., Rebitanian, N., Alias, A., 2016. Carbon dioxide adsorption on sawdust biochar. In: *Proceeding of 4th International Conference on Process Engineering and Adv. Mater.* (Icpeam 2016), 148, pp. 718–725. doi:10.1016/j.proeng.2016.06.591.
- Mahdipoor, H.R., Halladj, R., Ganji Babakhani, E., Amjad-Iranagh, S., Sadeghzadeh Ahari, J., 2021. Synthesis, characterization, and CO₂ adsorption properties of metal organic framework Fe-BDC, RSC Adv. 11 (9), 5192–5203. doi:10.1039/d0ra09292d.
- Mahr, B., Mewes, D., 2008. Two-phase flow in structured packings: Modeling and calculation on a macroscopic scale. *AIChE J.* 54 (3), 614–626. doi:10.1002/aic.11400.
- Maina, J.W., Pringle, J.M., Raza, J.M., Nunes, S., Vega, L., Gallucci, F., Dumee, L.F., 2021. Strategies for integrated capture and conversion of CO₂ from dilute flue gases and the atmosphere. *ChemSusChem* 14 (8), 1805–1820. doi:10.1002/cssc.202100010.
- Maity, R., Singh, H.D., Yadav, A.K., Chakraborty, D., Vaidyanathan, R., 2019. Water-stable adenine-based MOFs with polar pores for selective CO₂ capture. *Chem. Asian J.* 14 (20), 3736–3741. doi:10.1002/asia.201901020.
- Majchrzak-Kuceba, I., Soltysik, M., 2020. The potential of biocarbon as CO₂ adsorbent in VPSA unit. *J. Therm. Anal. Calorim.* 142 (1), 267–273. doi:10.1007/s10973-020-09858-7.
- Maleki, H., 2016. Recent advances in aerogels for environmental remediation applications: a review. *Chem. Eng. J.* 300, 98–118. doi:10.1016/j.cej.2016.04.098.
- Malhi, G.S., Kaur, M., Kaushik, B., 2021. Impact of climate change on agriculture and its mitigation strategies: a review. *Sustainability* 13 (3). doi:10.3390/su13031318.
- Mangun, C.L., Benak, K.R., Economy, J., Foster, K.L., 2001. Surface chemistry, pore sizes and adsorption properties of activated carbon fibers and precursors treated with ammonia. *Carbon* 39 (12), 1809–1820. doi:10.1016/S0008-6223(00)00319-5.
- Mannan, H.A., Mukhtar, H., Shahrin, M.S., Bustam, M.A., Man, Z., Bakar, M.Z.A., 2016. Effect of [EMIM][Tf₂N] Ionic Liquid on Ionic Liquid-polymeric Membrane (ILPM) for CO₂/CH₄ Separation. *Proc. Eng.* 148, 25–29. doi:10.1016/j.proeng.2016.06.477.
- Manuel Vicent-Luna, J., Jose Gutierrez-Sevillano, J., Antonio Anta, J., Calero, S., 2013. Effect of room-temperature ionic liquids on CO₂ separation by a Cu-BTC metal-organic framework. *J. Phys. Chem. C* 117 (40), 20762–20768. doi:10.1021/jp407176j.
- Manya, J.J., González, B., Azuara, M., Arner, G., 2018. Ultra-microporous adsorbents prepared from vine shoots-derived biochar with high CO₂ uptake and CO₂/N₂ selectivity. *Chem. Eng. J.* 345, 631–639. doi:10.1016/j.cej.2018.01.092.

- Manya, J.J., Gonzalez, B., Azuara, M., Arner, G., 2018. Ultra-microporous adsorbents prepared from vine shoots-derived biochar with high CO₂ uptake and CO₂/N₂ selectivity. *Chem. Eng. J.* 345, 631–639. doi:10.1016/j.cej.2018.01.092.
- Manya, J.J., Garcia-Morcate, D., Gonzalez, B., 2020. Adsorption performance of physically activated biochars for postcombustion CO₂ capture from dry and humid flue gas. *Appl. Sci.-Basel* 10 (1). doi:10.3390/app10010376.
- Manzolini, G., Giuffrida, A., Cobden, P.D., van Dijk, H.A.J., Ruggeri, F., Consonni, F., 2020. Techno-economic assessment of SEWGS technology when applied to integrated steel-plant for CO₂ emission mitigation. *Int. J. Greenh. Gas Control* 94, 102935. doi:10.1016/j.jggcc.2019.102935.
- Maqsood, K., Ali, A., Shariff, A.B.M., Ganguly, S., 2014a. Synthesis of conventional and hybrid cryogenic distillation sequence for purification of natural gas. *J. Appl. Sci.* 14 (21), 2722–2729. doi:10.3923/jas.2014.2722.2729.
- Maqsood, K., Mullaik, A., Ali, A., Kargupta, K., Ganguly, S., 2014b. Cryogenic carbon dioxide separation from natural gas: a review based on conventional and novel emerging technologies. *Rev. Chem. Eng.* 30 (5). doi:10.1515/revce-2014-0009.
- Maqsood, K., Pal, J., Turunawarasu, D., Pal, A.J., Ganguly, S., 2014c. Performance enhancement and energy reduction using hybrid cryogenic distillation networks for purification of natural gas with high CO₂ content. *Korean J. Chem. Eng.* 31 (7), 1120–1135. doi:10.1007/s11814-014-0038-y.
- Maqsood, K., Ali, A., Shariff, A.B.M., Ganguly, S., 2017. Process intensification using mixed sequential and integrated hybrid cryogenic distillation network for purification of high CO₂ natural gas. *Chem. Eng. Res. Des.* 117, 414–438. doi:10.1016/j.cherd.2016.10.011.
- Marin, O., et al., 2003. National Energy Technology Laboratory. Cost and performance for low-rank pulverized. In: *Proc. 28th Intern. Tech. Conf. Coal Util. Fuel Systems, CI March*.
- Maring, B.J., Webley, P.A., 2013a. A new simplified pressure/vacuum swing adsorption model for rapid adsorbent screening for CO₂ capture applications. *Int. J. Greenh. Gas Control* 15, 16–31. doi:10.1016/j.jggcc.2013.01.009.
- Maring, B.J., Webley, P.A., 2013b. A new simplified pressure/vacuum swing adsorption model for rapid adsorbent screening for CO₂ capture applications. *Int. J. Greenh. Gas Control* 15, 16–31. doi:10.1016/j.jggcc.2013.01.009.
- Markewitz, P., Marx, J., Schreiber, A., Zapp, P., 2013. Ecological evaluation of coal-fired oxyfuel power plants – cryogenic versus membrane-based air separation. *Energy Proc.* 37, 2864–2876. doi:10.1016/j.egypro.2013.06.172.
- Marono, M., Torreiro, Y., Cillero, D., Maria Sanchez, J., 2015. Experimental studies of CO₂ capture by a hybrid catalyst/adsorbent system applicable to IGCC processes. *Appl. Therm. Eng.* 74, 28–35. doi:10.1016/j.applthermaleng.2014.02.068.
- Marques, L.M., Carrott, P.J.M., Carrott, M.M.L.R., 2013. Amine-modified Carbon Aerogels for CO₂ capture. *Adsorpt. Sci. Technol.* 31 (2–3), 223–232. doi:10.1260/0263-6174.31.2-3.223.
- Martínez, F., Sanz, R., Orcajo, G., Briones, D., Yáñez, V., 2016. Amino-impregnated MOF materials for CO₂ capture at post-combustion conditions. *Chem. Eng. Sci.* 142, 55–61. doi:10.1016/j.ces.2015.11.033.
- Martínez-Cruz, M.A., Yañez-Aulestia, A., Ramos-Sánchez, G., Oliver-Tolentino, M., Vera, M., Pfeiffer, H., Ramírez-Rosales, D., González, I., 2020. Unraveling the effects on lithium-ion cathode performance by cation doping M-Li₂CuO₂ solid solution samples (M=Mn, Fe and Ni). *Dalton Trans.* 49 (14), 4549–4558. doi:10.1039/D0DT00273A.
- Martínez-dlCruz, L., Pfeiffer, H., 2012. Microstructural thermal evolution of the Na₂CO₃ phase produced during a Na₂ZrO₃-CO₂ chemisorption process. *J. Phys. Chem. C* 116 (17), 9675–9680. doi:10.1021/jp301917a.
- Mashhadikhan, S., Moghadasi, A., Ebadi Amooghini, A., Sanaeepour, H., 2020. Interlocking a synthesized polymer and bifunctional fiber containing the same polymer's monomer for conformable hybrid membrane systems. *J. Mater. Chem. A* 8 (7), 3942–3955. doi:10.1039/c9ta13375e.
- Mason, J.A., Sumida, K., Herm, Z.R., Krishna, R., Long, J.R., 2011. Evaluating metal-organic frameworks for post-combustion carbon dioxide capture via temperature swing adsorption. *Energy Environ. Sci.* 4 (8). doi:10.1039/c1ee01720a.
- Mason, J.A., McDonald, T.M., Bae, T.-H., Bachman, J.E., Sumida, K., Dutton, J.J., Kaye, S.S., Long, J.R., 2015. Application of a high-throughput analyzer in evaluating solid adsorbents for post-combustion carbon capture via multicomponent adsorption of CO₂, N₂, and H₂O. *J. Am. Chem. Soc.* 137 (14), 4787–4803.
- Masoud, N., Bordanaba-Florit, G., van Haasterecht, T., Bitter, J.H., 2021. Effect of support surface properties on CO₂ capture from air by carbon-supported potassium carbonate. *Ind. Eng. Chem. Res.* 60 (38), 13749–13755. doi:10.1021/acs.iecr.1c01229.
- Masoudi Soltani, S., Lahiri, A., Bahad, H., Clough, P., Gorbounov, M., Yan, Y., 2021. Sorption-enhanced steam methane reforming for combined CO₂ capture and hydrogen production: a state-of-the-art review. *Carbon Cap. Sci. Technol.* 1, 100003. doi:10.1016/j.ccsst.2021.100003.
- Masuda, S., Osaka, Y., Tsujiguchi, T., Kodama, A., 2021. CO₂ capture from a simulated dry exhaust gas by internally heated and cooled temperature swing adsorption. *J. Chem. Eng. Jpn.* 54 (5), 248–254. doi:10.1252/cejce.20w112.
- Masuda, S., Osaka, Y., Tsujiguchi, T., Kodama, A., 2022. Carbon dioxide recovery from a simulated dry exhaust gas by an internally heated and cooled temperature swing adsorption packed with a typical hydrophobic adsorbent. *Sep. Purif. Technol.* 284. doi:10.1016/j.seppur.2021.120249.
- Matsumoto, K., Endo, T., 2008. Confinement of ionic liquid by networked polymers based on multifunctional epoxy resins. *Macromolecules* 41 (19), 6981–6986. doi:10.1021/ma801293j.
- Matteucci, S., Raharjo, R.D., Kusuma, V.A., Swinnea, S., Freeman, B.D., 2008. Gas permeability, solubility, and diffusion coefficients in 1, 2-polybutadiene containing magnesium oxide. *Macromolecules* 41 (6), 2144–2156. doi:10.1021/ma702459k.
- Mathews, L., Lipiński, W., 2012. Thermodynamic analysis of solar thermochemical CO₂ capture via carbonation/calination cycle with heat recovery. *Energy* 45 (1), 900–907. doi:10.1016/j.energy.2012.06.072.
- Mattisson, T., Lyngfelt, A., Leion, H., 2009. Chemical-looping with oxygen uncoupling for combustion of solid fuels. *Int. J. Greenh. Gas Control* 3 (1), 11–19.
- Mattisson, T., Keller, M., Linderholm, C., Moldenhauer, P., Rydén, M., Leion, H., Lyngfelt, A., 2018. Chemical-looping technologies using circulating fluidized bed systems: Status of development. *Fuel Process. Technol.* 172, 1–12. doi:10.1016/j.fuproc.2017.11.016.
- Mattisson, T., 2013. Materials for Chemical-Looping with Oxygen Uncoupling. *ISRN Chem. Eng.* 2013, 1–19. doi:10.1155/2013/526375.
- Maurin, G., Llewellyn, P., Bell, R., 2005. Adsorption mechanism of carbon dioxide in faujasites: grand canonical Monte Carlo simulations and microcalorimetry measurements. *J. Phys. Chem. B* 109 (33), 16084–16091.
- Maurya, M., Singh, J.K., 2019. Effect of ionic liquid impregnation in highly water-stable metal-organic frameworks, covalent organic frameworks, and carbon-based adsorbents for post-combustion flue gas treatment. *Energy Fuels* 33 (4), 3421–3428. doi:10.1021/acs.energyfuels.9b00179.
- May, E.F., Zhang, Y., Saleman, T.L.H., Xiao, G., Li, G., Young, B.R., 2017. Demonstration and optimization of the four dual-reflux pressure swing adsorption configurations. *Sep. Purif. Technol.* 177, 161–175. doi:10.1016/j.seppur.2016.12.007.
- Mazzotti, M., Bacciochi, R., Desmond, M.J., Socolow, R.H., 2013. Direct air capture of CO₂ with chemicals: optimization of a two-loop hydroxide carbonate system using a countercurrent air-liquid contactor. *Chem. Change* 118 (1), 119–135. doi:10.1007/s10584-012-0679-y.
- McBain, J.W., 2002. The sorption of gases and vapours by solids. *J. Phys. Chem.* 37 (1), 149–150.
- McCarthy, M.C., Varela-Guerrero, V., Barnett, G.V., Jeong, H.-K., 2010. Synthesis of zeolitic imidazolate framework films and membranes with controlled microstructures. *Langmuir* 26 (18), 14636–14641.
- McCollom, T., 2011. Carbon Dioxide. In: Gargaud, M., Amils, R., Quintanilla, J.C., Cleaves, H.J., Irvine, W.M., Pinti, D.L., Woese, M. (Eds.), *Encyclopedia of Astrobiology*. Springer Berlin Heidelberg, Berlin, Heidelberg, pp. 239–240. doi:10.1007/978-3-642-11274-4_1737.
- McDonald, T.M., Lee, W.R., Mason, J.A., Wiers, B.M., Hong, C.S., Long, J.R., 2012. Capture of carbon dioxide from air and flue gas in the alkylamine-appended metal-organic framework mmen-Mg₂(dobpc). *J. Am. Chem. Soc.* 134 (16), 7056–7065.
- McDonald, T.M., Mason, J.A., Kong, X., Bloch, E.D., Gygi, D., Dani, A., Crocella, V., Giordano, F., Odoh, S.O., Drisdell, W.S., Vlaisavljevich, B., Dzubak, A.L., Poloni, R., Schnell, S.K., Planas, N., Lee, K., Pascal, T., Wan, L.F., Prendergast, D., Neaton, J.B., Smit, B., Kortricht, J.B., Gagliardi, L., Bordiga, S., Reimer, J.A., Long, J.R., 2015. Cooperative insertion of CO₂ in diamine-appended metal-organic frameworks. *Nature* 519 (7543), 303–308. doi:10.1038/nature14327.
- McDonald, T., 2011. D. Alessandro, DM; Krishna, R. Long, JR. *Chem. Sci.* 2 (10), 2022–2028.
- McEwen, J., Hayman, J.-D., Ozgur Yazaydin, A., 2013. A comparative study of CO₂, CH₄ and N₂ adsorption in ZIF-8, Zeolite-13X and BPL activated carbon. *Chem. Phys.* 412, 72–76. doi:10.1016/j.chemphys.2012.12.012.
- McKeown, N., 2012. Polymers of intrinsic microporosity. *ISRN Mater. Sci.* 2012. doi:10.5402/2012/513986.
- Medina-Carrasco, S., Valverde, J.M., 2022. The Calcium Looping process for energy storage: Insights from in situ XRD analysis. *Chem. Eng. J.* 429, 132244.
- Mehrpooiya, M., Ghorbani, B., Manizadeh, A., 2020. Cryogenic biogas upgrading process using solar energy (process integration, development, and energy analysis). *Energy* 203, 117834. doi:10.1016/j.energy.2020.117834.
- Mei, X., Yang, S., Lu, P., Zhang, Y., Zhang, J., 2020. Improving the selectivity of ZIF-8/Polysulfone-mixed matrix membranes by polydopamine modification for H₂/CO₂ separation. *Front. Chem.* 8. doi:10.3389/fchem.2020.00528.
- Meis, D., Neumann, S., Filiz, V., 2022. Thermal rearrangement in thermal cascade reaction polymers via ortho-carbonate ester functionalization of polyimides and their gas separation performance. *J. Membr. Sci.* 655, 120586.
- Meixia Shan, X.L., Wang, X., Yarulina, I., Seoane, B., Freek Kapteijn, J.G., 2018. Facile manufacture of porous organic framework membranes for precombustion CO₂ capture. *Sci. Adv.* 4.
- Meldon, J.H., Stroeve, P., Grégoire, C.E., 1982. Facilitated transport of carbon dioxide: a review. *Chem. Eng. Commun.* 16, 263–300.
- Mendes, D.N.D.L., Gaspar, A., Ferreira, I., Mota, J.P.B., Ribeiro, R.P.P.L., 2021. 3D-printed hybrid zeolitic/carbonaceous electrically conductive adsorbent structures. *Chem. Eng. Res. Des.* 174, 442–453. doi:10.1016/j.cherd.2021.08.020.
- Meng, Y., Ju, T., Meng, F., Han, S., Song, M., Jiang, J., 2021. Insights into the critical role of abundant-porosity supports in polyethyleneimine functionalization as efficient and stable CO₂ adsorbents. *ACS Appl. Mater. Interfaces* 13 (45), 54018–54031. doi:10.1021/acami.1c17132.
- Merkel, T.C., Freeman, B.D., Spontak, R.J., He, Z., Pinnau, I., Meakin, P., Hill, A.J., 2002. Ultra-permeable, reverse-selective nanocomposite membranes. *Science* 296, 519–522. doi:10.1126/science.1069580.
- Merkel, T.C., Pinnau, I., Prabhakar, R., Freeman, B.D., 2006. <https://doi.org/10.1002/047002903X.ch9>.
- Merkel, T.C., Lin, H., Wei, X., Baker, R., 2010. Power plant post-combustion carbon dioxide capture: An opportunity for membranes. *J. Membr. Sci.* 359 (1–2), 126–139. doi:10.1016/j.memsci.2009.10.041.
- Merkel, T.C., Lin, H., Wei, X., Baker, R., 2010. Power plant post-combustion carbon dioxide capture: An opportunity for membranes. *J. Membr. Sci.* 359 (1–2), 126–139.
- Merrick, M.M., Sujanani, R., Freeman, B.D., 2020. Glassy polymers: Historical findings, membrane applications, and unresolved questions regarding physical aging. *Polymer* 211, 123176. doi:10.1016/j.polymer.2020.123176.
- Miccio, F., Murri, A.N., Landi, E., 2016. High-temperature capture of CO₂ by strontium oxide sorbents. *Ind. Eng. Chem. Res.* 55 (23), 6696–6707. doi:10.1021/acs.iecr.6b00184.

- Michael E Parker, P.E., Northrop, S., Valencia, J.A., Foglesong, R.E., Duncan, W.T., 2011. CO₂ management at ExxonMobil's LaBarge field, Wyoming, USA. *Energy Procedia* 4, 5455–5470. doi:10.1016/j.egypro.2011.02.531.
- Mikkelsen, M., Jørgensen, M., Krebs, F.C., 2010. The teraton challenge. A review of fixation and transformation of carbon dioxide. *Energy Environ. Sci.* 3 (1), 43–81.
- Mikulčić, H., Ridjan Skov, I., Dominković, D.F., Wan Alwi, S.R., Manan, Z.A., Tan, R., Duić, N., Hidayat Mohamad, S.N., Wang, X., 2019. Flexible carbon capture and utilization technologies in future energy systems and the utilization pathways of captured CO₂. *Renew. Sustain. Energy Rev.* 114, 109338. doi:10.1016/j.rser.2019.109338.
- Millward, A.R., Yaghi, O.M., 2005. Metal-organic frameworks with exceptionally high capacity for storage of carbon dioxide at room temperature. *J. Am. Chem. Soc.* 127 (51), 17998–17999.
- Milner, P.J., Siegelman, R.L., Forse, A.C., Gonzalez, M.I., Runcevski, T., Martell, J.D., Reimer, J.A., Long, J.R., 2017. A diaminopropane-appended metal-organic framework enabling efficient CO₂ capture from coal flue gas via a mixed adsorption mechanism. *J. Am. Chem. Soc.* 139 (38), 13541–13553. doi:10.1021/jacs.7b07612.
- Min, K., Choi, W., Kim, C., Choi, M., 2018. Oxidation-stable amine-containing adsorbents for carbon dioxide capture. *Nat. Commun.* 9 (1), 726. doi:10.1038/s41467-018-03123-0.
- Min, H.J., Kang, M., Lee, C.S., Kim, J.H., 2021. Dual-functional interconnected pebble-like structures in highly crystalline poly (ethylene oxide) membranes for CO₂ separation. *Sep. Purif. Technol.* 263, 118363. doi:10.1016/j.seppur.2021.118363.
- Miricioiu, M.G., Zahariou, A., Oancea, S., Bucura, F., Raboaca, M.S., Filote, C., Ionete, R.E., Niculescu, V.C., Constantinescu, M., 2021. Sewage sludge derived materials for CO₂ adsorption. *Appl. Sci.* 11 (15), 7139. doi:10.3390/app11157139.
- Mirzaie, M., Talebizadeh, A.R., Hashempour, H., 2020. CFD simulation of benzene adsorption on pistachio activated carbon porous media. *Frontiers in Heat and Mass Transfer* 14, 1–7.
- Miyamoto, M., Fujioka, Y., Yogo, K., 2012. Pure silica CHA type zeolite for CO₂ separation using pressure swing adsorption at high pressure. *J. Mater. Chem.* 22 (38), 20186–20189.
- Mletzko, J., Ehlers, S., Kather, A., 2016. Comparison of natural gas combined cycle power plants with post combustion and oxyfuel technology at different CO₂ capture rates. *Energy Procedia* 86, 2–11. doi:10.1016/j.egypro.2016.01.001.
- Moško, J., Pohořelý, M., Skoblija, S., Fajgar, R., Straka, P., Soukup, K., Beňo, Z., Farták, J., Bičáková, O., Jeremiáš, M., Šyc, M., Meers, E., 2021. Structural and chemical changes of sludge derived pyrolysis char prepared under different process temperatures. *J. Anal. Appl. Pyroly.* 156, 105085. doi:10.1016/j.jaap.2021.105085.
- Modak, A., Jana, S., 2019. Advancement in porous adsorbents for post-combustion CO₂ capture. *Microporous Mesoporous Mater.* 276, 107–132.
- Moghadam, F., Kamio, E., Matsuyama, H., 2017. High CO₂ separation performance of amino acid ionic liquid-based double network ion gel membranes in low CO₂ concentration gas mixtures under humid conditions. *J. Membr. Sci.* 525, 290–297.
- Mohamed, A.M.O., Moncho, S., Krokidas, P., Kakosimos, K., Brothers, E.N., Economou, I.G., 2019. Computational investigation of the performance of ZIF-8 with encapsulated ionic liquids towards CO₂ capture. *Mol. Phys.* 117 (23–24), 3791–3805. doi:10.1080/00268976.2019.1666170.
- Mohamedali, M., Ibrahim, H., Henni, A., 2018. Incorporation of acetate-based ionic liquids into a zeolitic imidazolate framework (ZIF-8) as efficient sorbents for carbon dioxide capture. *Chem. Eng. J.* 334, 817–828. doi:10.1016/j.cej.2017.10.104.
- Monsalve-Bravo, G.M., Bhatia, S.K., 2018. Modeling permeation through mixed-matrix membranes: A review. *Processes* 6 (9), 172. doi:10.3390/pr6090172.
- Moon, H.R., Kobayashi, N., Suh, M.P., 2006. Porous metal-organic framework with coordinatively unsaturated MnII sites: sorption properties for various gases. *Inorg. Chem.* 45 (21), 8672–8676.
- Moore, C.C.S., Autunes, C.H., Kulay, L., 2022. Economic, environmental and energy analysis of carbon capture systems coupled in coal power plants for the reduction of CO₂ emissions in Brazil. *Int. J. Greenh. Gas Control* 114, 11. doi:10.1016/j.ijggc.2022.103606.
- Moors, J.H.J., 1999. Pulverised char combustion and gasification at high temperatures and pressures. Technische Universiteit Eindhoven.
- Moreira, R.F.P.M., Soares, J.L., Casarin, G.L., Rodrigues, A.E., 2006. Adsorption of CO₂ on hydroxalcalite-like compounds in a fixed bed. *Sep. Sci. Technol.* 41 (2), 341–357. doi:10.1080/01496390500496827.
- Mori, G., Cocco, S., Castello, R., Scartezzini, J.-L., 2019. Geospatial analysis and optimization of the incoming and stored CO₂ emissions within the EPFL campus. *J. Phys.: Conf. Ser.* 1343 (1), 012118. doi:10.1088/1742-6596/1343/1/012118.
- Mostafavi, E., Ashrafi, O., Navarri, P., 2021. Assessment of process modifications for amine-based post-combustion carbon capture processes. *Clean Eng. Technol.* 4. doi:10.1016/j.clet.2021.100249.100249.
- Motahari, F., Raisi, A., 2020. UV irradiation-assisted cross-linking of high molecular weight poly (ethylene oxide) with poly (ethylene glycol) diacrylate to prepare CO₂ selective membranes. *Polymer* 205, 122821. doi:10.1016/j.polymer.2020.122821.
- Mubashir, M., Yeong, Y.F., Lau, K.K., Chew, T.L., Norwahyu, J., 2018. Efficient CO₂/N₂ and CO₂/CH₄ separation using NH₂-MIL-53 (Al)/cellulose acetate (CA) mixed matrix membranes. *Sep. Purif. Technol.* 199, 140–151. doi:10.1016/j.seppur.2018.01.038.
- Muchan, P., Saiwan, C., Narku-Tetteh, J., Idem, R., Supap, T., Tontiwachwuthikul, P., 2017. Screening tests of aqueous alkanolamine solutions based on primary, secondary, and tertiary structure for blended aqueous amine solution selection in post combustion CO₂ capture. *Chem. Eng. Sci.* 170, 574–582. doi:10.1016/j.ces.2017.02.031.
- Mukherjee, S., Kumar, P., Yang, A., Fennell, P., 2015. Energy and exergy analysis of chemical looping combustion technology and comparison with pre-combustion and oxy-fuel combustion technologies for CO₂ capture. *J. Environ. Chem. Eng.* 3 (3), 2104–2114.
- Mukherjee, S., Sikdar, N., O'Nolan, D., Franz, D.M., Gascón, V., Kumar, A., Kumar, N., Scott, H.S., Madden, D.G., Kruger, P.E., Space, B., Zaworotko, M.J., 2019. Trace CO₂ capture by an ultramicroporous physisorbent with low water affinity. *Sci. Adv.* 5 (11), eaax9171. doi:10.1126/sciadv.aax9171.
- Mukherjee, A., Borugadda, V.B., Dynes, J.J., Niu, C., Dalai, A.K., 2021. Carbon dioxide capture from flue gas in biochar produced from spent coffee grounds: Effect of surface chemistry and porous structure. *J. Environ. Chem. Eng.* 9 (5). doi:10.1016/j.jece.2021.106049.
- Mukhopadhyay, R.D., Praveen, V.K., Ajayaghosh, A., 2014. Photoresponsive metal-organic materials: exploiting the azobenzene switch. *Mater. Horiz.* 1 (6), 572–576. doi:10.1039/c4mh00122b.
- Mukhtar, A., Saqib, S., Mellon, N.B., Babar, M., Rafiq, S., Ullah, S., Bustam, M.A., Al-Sehemi, A.G., Muhammad, N., Chawla, M., 2020. CO₂ capturing, thermochemical principles, synthesis and amine functionalization of covalent organic polymers for CO₂ separation from natural gas: A review. *J. Nat. Gas Sci. Eng.* 77. doi:10.1016/j.jngse.2020.103203.
- Mulgundmath, V.P., Jones, R.A., Tezel, F.H., Thibault, J., 2012. Fixed bed adsorption for the removal of carbon dioxide from nitrogen: Breakthrough behaviour and modelling for heat and mass transfer. *Sep. Purif. Technol.* 85, 17–27. doi:10.1016/j.seppur.2011.07.038.
- Mungse, P., Saravanan, G., Rayalu, S., Labhsetwar, N., 2015. Mixed oxides of iron and manganese as potential low-cost oxygen carriers for chemical looping combustion. *Energy Technol.* 3 (8), 856–865. doi:10.1002/ente.201500035.
- Munro, S., Åhlén, M., Cheung, O., Sanna, A., 2020. Tuning Na₂ZrO₃ for fast and stable CO₂ adsorption by solid state synthesis. *Chem. Eng. J.* 388, 124284. doi:10.1016/j.cej.2020.124284.
- Murali, B.S., Sankarshana, T., Sridhar, S., 2013. Air separation by polymer-based membrane technology. *Sep. Purif. Technol.* 9, 130–186. doi:10.1080/15422119.2012.686000.
- Murge, P., Dinda, S., Roy, S., 2019. Zeolite-based sorbent for CO₂ capture: preparation and performance evaluation. *Langmuir* 35 (46), 14751–14760. doi:10.1021/acs.langmuir.9b02259.
- Muriithi, G.N., Petrik, L.F., Gitari, W.M., Doucet, F.J., 2017. Synthesis and characterization of hydrotalcite from South African Coal fly ash. *Powder Technol.* 312, 299–309. doi:10.1016/j.powtec.2017.02.018.
- Murugiah, P.S., Oh, P.C., Lau, K.K., 2018. Facilitated transport graphene oxide based PPOdm mixed matrix membrane for CO₂ separation. *Mater. Today: Proc.* 5 (10, Part 2), 21818–21824. doi:10.1016/j.matpr.2018.07.037.
- Muschli, M., Devautour-Vinot, S., Aureau, D., Heymans, N., Sene, S., Emmerich, R., Ploumstos, A., Geneste, A., Steunou, N., Patriarche, G., De Weireld, G., Serre, C., 2021. Metal-organic framework/graphene oxide composites for CO₂ capture by microwave swing adsorption. *J. Mater. Chem. A* 9 (22), 13135–13142. doi:10.1039/d0ta12215g.
- Mutyalu, S., Jonnalagadda, M., Mitta, H., Gundeboyina, R., 2019a. CO₂ capture and adsorption kinetic study of amine-modified MIL-101 (Cr). *Chem. Eng. Res. Des.* 143, 241–248. doi:10.1016/j.cherd.2019.01.020.
- Mutyalu, S., Yakout, S.M., Ibrahim, S.S., Jonnalagadda, M., Mitta, H., 2019b. Enhancement of CO₂ capture and separation of CO₂/N₂ using post-synthetic modified MIL-100 (Fe). *N. J. Chem.* 43 (24), 9725–9731. doi:10.1039/c9nj02258a.
- Nabipour, N., Qasem, S.N., Salwana, E., Baghan, A., 2020. Evaluating LSSVM and ELM models to predict solubility of non-hydrocarbon gases in aqueous electrolyte systems. *Measurement: J. Int. Measur. Confed.* 164. doi:10.1016/j.measurement.2020.107999.107999-107999.
- Nadeali, A., Zamani Pedram, M., Omidkhal, M., Yarmohammadi, M., 2019. Promising performance for efficient CO₂ separation with the p-tert-Butylcalix [4] arene/Pebax-1657 mixed matrix membrane. *ACS Sustain. Chem. Eng.* 7 (23), 19015–19026. doi:10.1021/acssuschemeng.9b04641.
- Naem, M.A., Armutulu, A., Intiaz, Q., Müller, C.R., 2017. CaO-based CO₂ sorbents effectively stabilized by metal oxides. *ChemPhysChem* 18 (22), 3280–3285.
- Naem, M.A., Armutulu, A., Intiaz, Q., Donat, F., Schäublin, R., Kierzkowska, A., Müller, C.R., 2018. Optimization of the structural characteristics of CaO and its effective stabilization yield high-capacity CO₂ sorbents. *Nat. Commun.* 9 (1), 2408. doi:10.1038/s41467-018-04794-5.
- Nagarajan, S., Killen, N.C., Irvine, J.T.S., Lawton, L.A., Robertson, P.K.J., 2017. Cellulose II as bioethanol feedstock and its advantages over native cellulose. *Renew. Sustain. Energy Rev.* 77, 182–192. doi:10.1016/j.rser.2017.03.118.
- Nahak, B.K., Preetam, S., Sharma, D., Shukla, S.K., Syvajarvi, M., Tuncu, D.C., Tiwari, A., 2022. Advancements in net-zero pertinency of lignocellulosic biomass for climate neutral energy production. *Renew. Sustain. Energy Rev.* 161. doi:10.1016/j.rser.2022.112393.
- Naquash, A., Qyyum, M.A., Haider, J., Bokhari, A., Lim, H., Lee, M., 2022. State-of-the-art assessment of cryogenic technologies for biogas upgrading: Energy, economic, and environmental perspectives. *Renew. Sustain. Energy Rev.* 154. doi:10.1016/j.rser.2021.118126.
- Narku-Tetteh, J., Muchan, P., Saiwan, C., Supap, T., Idem, R., 2017. Selection of components for formulation of amine blends for post combustion CO₂ capture based on the side chain structure of primary, secondary and tertiary amines. *Chem. Eng. Sci.* 170, 542–560. doi:10.1016/j.ces.2017.02.036.
- Narku-Tetteh, J., Afari, D.B., Coker, J., Idem, R., 2018. Evaluation of the Roles of Absorber and Desorber Catalysts in the Heat Duty and Heat of CO₂ Desorption from Butylethanolamine–2-Amino-2-methyl-1-propanol and Monoethanolamine–Methyldiethanolamine Solvent Blends in a Bench-Scale CO₂ Capture Pilot Plant. *Energy Fuels* 32 (9), 9711–9726. doi:10.1021/acs.energyfuels.8b02205.

- Natewong, P., Prasongthum, N., Reubroycharoen, P., Idem, R., 2019. Evaluating the CO₂ capture performance using a BEA-AMP blend amine solvent with novel high-performing absorber and desorber catalysts in a bench-scale CO₂ capture pilot plant. *Energy Fuels* 33 (4), 3390–3402. doi:10.1021/acs.energyfuels.8b04466.
- Naueis, N., Herzog, S., Modigell, M., Broeckmann, C., 2019. Membrane module for pilot scale oxygen production. *J. Membr. Sci.* 574, 252–261. doi:10.1016/j.memsci.2018.12.061.
- Neal, L., Shafieefarhood, A., Li, F., 2015. Effect of core and shell compositions on MeOx@LaySr1–yFeO3 core-shell redox catalysts for chemical looping reforming of methane. *Appl. Energy* 157, 391–398. doi:10.1016/j.apenergy.2015.06.028.
- Neumann, K., Gladyszewski, K., Groß, K., Qammar, H., Wenzel, D., Górac, A., Skibrowski, M., 2018. A guide on the industrial application of rotating packed beds. *Chem. Eng. Res. Des.* 134, 443–462. doi:10.1016/j.cherd.2018.04.024.
- Ngamou, P.H.T., Ivanova, M.E., Guillon, O., Meulenberg, W.A., 2019. High-performance carbon molecular sieve membranes for hydrogen purification and pervaporation dehydration of organic solvents. *J. Mater. Chem. A* 7 (12), 7082–7091. doi:10.1039/c8ta09504c.
- Nguyen, M.V., Lee, B.K., 2016. A novel removal of CO₂ using nitrogen doped biochar beads as a green adsorbent. *Process. Saf. Environ. Prot.* 104, 490–498. doi:10.1016/j.psep.2016.04.007.
- Nguyen, N.T., Furukawa, H., Gándara, F., Nguyen, H.T., Cordova, K.E., Yaghi, O.M., 2014. Selective capture of carbon dioxide under humid conditions by hydrophobic chabazite-type zeolitic imidazolate frameworks. *Angew. Chem. Int. Ed.* 53 (40), 10645–10648.
- Nicolas, C.H., Pera-Titus, M., 2012. Nanocomposite MFI-alumina hollow fiber membranes: influence of NO_x and propane on CO₂/N₂ separation properties. *Ind. Eng. Chem. Res.* 51 (31), 10451–10461.
- Nie, H., Jiang, H., Chong, D., Wu, Q., Xu, C., Zhou, H., 2013. Comparison of water scrubbing and propylene carbonate absorption for biogas upgrading process. *Energy Fuels* 27 (6), 3239–3245. doi:10.1021/ef400233w.
- Nigar, H., García-Bañós, B., Peñaranda-Fox, F.L., Catalá-Civera, J.M., Mallada, R., Santamaría, J., 2016. Amine-functionalized mesoporous silica: A material capable of CO₂ adsorption and fast regeneration by microwave heating. *AIChE J.* 62 (2), 547–555. doi:10.1002/aic.15118.
- Nik, O.G., Nohair, B., Kaliaguine, S., 2011. Aminosilanes grafting on FAU/EMT zeolite: Effect on CO₂ adsorptive properties. *Microporous Mesoporous Mater.* 143 (1), 221–229. doi:10.1016/j.micromeso.2011.03.002.
- Nikam, S., Mandal, D., Dabhade, P., 2022. LDF based parametric optimization to model fluidized bed adsorption of trichloroethylene on activated carbon particles. *Particuology* 65, 72–92.
- Nikolaidis, G.N., Kikkiniades, E.S., Georgiadis, M.C., 2018. A model-based approach for the evaluation of new zeolite 13X-based adsorbents for the efficient post-combustion CO₂ capture using P/VSA processes. *Chem. Eng. Res. Des.* 131, 362–374. doi:10.1016/j.cherd.2017.06.016.
- Nithin Mithra, S., Ahankari, S.S., 2022. Nanocellulose-based membranes for CO₂ separation from biogas through the facilitated transport mechanism: a review. *Mater. Today Sustain.*, 100191 doi:10.1016/j.mtsust.2022.100191.
- Nittaya, T., Douglas, P.L., Croiset, E., Ricardez-Sandoval, L.A., 2014. Dynamic modelling and controllability studies of a commercial-scale MEA absorption processes for CO₂ capture from coal-fired power plants. *Energy Procedia* 63, 1595–1600. doi:10.1016/j.egypro.2014.11.169.
- Niu, H., Pan, L., Su, H., Wang, S., 2009. Effects of design and operating parameters on CO₂ absorption in microchannel contacts. *Ind. Eng. Chem. Res.* 48 (18), 8629–8634. doi:10.1021/ie8018966.
- Niu, M., Yang, H., Zhang, X., Wang, Y., Tang, A., 2016. Amine-impregnated mesoporous silica nanotube as an emerging nanocomposite for CO₂ capture. *ACS Appl. Mater. Interfaces* 8 (27), 17312–17320. doi:10.1021/acsami.6b05044.
- NOAA, 2022. Carbon dioxide peaks near 420 parts per million at Muana Loa observatory. *Noble, R.D.J.*, 1990. Analysis of facilitated transport with fixed site carrier membranes. *J. Membr. Sci.* 50 (2), 207–214.
- Nomura, K., Ujihira, Y., Hayakawa, T., Takehira, K., 1996. CO₂ absorption properties and characterization of perovskite oxides, (Ba,Ca) (Co,Fe) O_{3-δ}. *Appl. Catal. A* 137 (1), 25–36. doi:10.1016/0926-860X(95)00317-7.
- Norouzbahari, S., Shahhosseini, S., Ghaemi, A., 2015. Modeling of CO₂ loading in aqueous solutions of piperazine: Application of an enhanced artificial neural network algorithm. *J. Nat. Gas Sci. Eng.* 24, 18–25. doi:10.1016/j.jngse.2015.03.011.
- Notz, R.J., Tönies, I., McCann, N., Scheffknecht, G., Hasse, H., 2011. CO₂ capture for fossil fuel-fired power plants. *Chem. Eng. Technol.* 34 (2), 163–172. doi:10.1002/ceat.201000491.
- Ntiamoah, A., Ling, J., Xiao, P., Webley, P.A., Zhai, Y., 2015. CO₂ capture by vacuum swing adsorption: role of multiple pressure equalization steps. *Adsorption* 21 (6–7), 509–522. doi:10.1007/s10450-015-9690-8.
- Ntiamoah, A., Ling, J., Xiao, P., Webley, P.A., Zhai, Y., 2016. CO₂ capture by temperature swing adsorption: Use of hot CO₂-rich gas for regeneration. *Ind. Eng. Chem. Res.* 55 (3), 703–713. doi:10.1021/acs.iecr.5b01384.
- Nwaoha, C., Saiwan, C., Supap, T., Idem, R., Tontiwachwuthikul, P., Rongwong, W., Al-Marri, M.J., Benamor, A., 2016a. Carbon dioxide (CO₂) capture performance of aqueous tri-solvent blends containing 2-amino-2-methyl-1-propanol (AMP) and methyldiethanolamine (MDEA) promoted by diethylenetriamine (DETA). *Int. J. Greenh. Gas Control* 53, 292–304. doi:10.1016/j.jggc.2016.08.012.
- Nwaoha, C., Saiwan, C., Tontiwachwuthikul, P., Supap, T., Rongwong, W., Idem, R., Al-Marri, M.J., Benamor, A., 2016b. Carbon dioxide (CO₂) capture: Absorption-desorption capabilities of 2-amino-2-methyl-1-propanol (AMP), piperazine (PZ) and monoethanolamine (MEA) tri-solvent blends. *J. Nat. Gas Sci. Eng.* 33, 742–750. doi:10.1016/j.jngse.2016.06.002.
- Nwaoha, C., Idem, R., Supap, T., Saiwan, C., Tontiwachwuthikul, P., Rongwong, W., Al-Marri, M.J., Benamor, A., 2017. Heat duty, heat of absorption, sensible heat and heat of vaporization of 2-Amino-2-Methyl-1-Propanol (AMP), Piperazine (PZ) and Monoethanolamine (MEA) tri-solvent blend for carbon dioxide (CO₂) capture. *Chem. Eng. Sci.* 170, 26–35. doi:10.1016/j.ces.2017.03.025.
- Obergassel, W., Arens, C., Hermwille, L., Kreibich, N., Mersmann, F., Ott, H.E., Wang-Helmreich, H., 2016. Phoenix from the ashes: an analysis of the Paris Agreement to the United Nations framework convention on climate change. *Wuppertal Institut für Klima, Umwelt, Energie*.
- Oexmann, J., Kather, A., 2010. Minimising the regeneration heat duty of post-combustion CO₂ capture by wet chemical absorption: The misguided focus on low heat of absorption solvents. *Int. J. Greenh. Gas Control* 4 (1), 36–43.
- Oexmann, J., Hensel, C., Kather, A., 2008. Post-combustion CO₂-capture from coal-fired power plants: Preliminary evaluation of an integrated chemical absorption process with piperazine-promoted potassium carbonate. *Int. J. Greenh. Gas Control* 2 (4), 539–552. doi:10.1016/j.jggc.2008.04.002.
- Ogieglo, W., Furchner, A., Ma, X., Hazazi, K., Alhazmi, A.T., Pinnau, I., 2019. Thin composite carbon molecular sieve membranes from a polymer of intrinsic microporosity precursor. *ACS Appl. Mater. Interfaces* 11 (20), 18770–18781. doi:10.1021/acsami.9b04602.
- Oh, H.T., Ju, Y., Chung, K., Lee, C.H., 2020. Techno-economic analysis of advanced stripper configurations for post-combustion CO₂ capture amine processes. *Energy* 206. doi:10.1016/j.energy.2020.118164, 118164–118164.
- Okon, E., Wang, M., Joel, A.S., 2017. Current status and future development of solvent-based carbon capture. *Int. J. Coal Sci. Technol.* 4 (1), 5–14. doi:10.1007/s40789-017-0159-0.
- Okon, E., Ramshaw, C., Wang, M., 2018. Study of intercooling for rotating packed bed absorbers in intensified solvent-based CO₂ capture process. *Appl. Energy* 223, 302–316.
- Olabi, A.G., Obaideen, K., Elsaid, K., Wilberforce, T., Sayed, E.T., Maghrabi, H.M., Abdelkarem, M.A., 2022. Assessment of the pre-combustion carbon capture contribution into sustainable development goals SDGs using novel indicators. *Renew. Sustain. Energy Rev.* 153, 111710. doi:10.1016/j.rser.2021.111710.
- Olajire, A.A., 2017. Recent advances in the synthesis of covalent organic frameworks for CO₂ capture. *J. CO₂ Util.* 17, 137–161.
- Olaleye, A.K., Okon, E., Wang, M., Kelsall, G., 2016. Dynamic modelling and analysis of supercritical coal-fired power plant integrated with post-combustion CO₂ capture. In: *Clean Coal Technology and Sustainable Development - Proceedings of the 8th International Symposium on Coal Combustion*, 2015. Springer, pp. 359–363.
- Oliveira, E.L.G., Grande, C.A., Rodrigues, A.E., 2008. CO₂ sorption on hydrocalcite and alkali-modified (K and Cs) hydrocalcites at high temperatures. *Sep. Purif. Technol.* 62 (1), 137–147. doi:10.1016/j.seppur.2008.01.011.
- Omodolor, I.S., Otor, H.O., Andonegui, J.A., Allen, B.J., Alba-Rubio, A.C., 2020. Dual-function materials for CO₂ capture and conversion: a review. *Ind. Eng. Chem. Res.* 59 (40), 17612–17631. doi:10.1021/acs.iecr.0c02218.
- Onda, K., Takeuchi, H., Okumoto, Y., 1968. Mass transfer coefficients between gas and liquid phases in packed columns. *Journal of Chemical Engineering of Japan* 1 (1), 56–62.
- Oreggioni, G.D., Brandani, S., Luberti, M., Baykan, Y., Friedrich, D., Ahn, H., 2015. CO₂ capture from syngas by an absorption process at a biomass gasification CHP plant: Its comparison with amine-based CO₂ capture. *Int. J. Greenh. Gas Control* 35, 71–81. doi:10.1016/j.jggc.2015.01.008.
- Orthman, J., Zhu, H., Lu, G., 2003. Use of anion clay hydrocalcite to remove coloured organics from aqueous solutions. *Sep. Purif. Technol.* 31 (1), 53–59.
- Ortiz, C., Valverde, J.M., Chacartegui, R., Perez-Maqueda, L.A., Gimenez, P., 2019. The Calcium-Looping (CaCO₃/CaO) process for thermochemical energy storage in Concentrating Solar Power plants. *Renew. Sustain. Energy Rev.* 113, 18. doi:10.1016/j.rser.2019.109252.
- Osman, A.I., Hefny, M., Abdel Maksoud, M.I.A., Elgarayh, A.M., Rooney, D.W., 2021. Recent advances in carbon capture storage and utilisation technologies: a review. *Environ. Chem. Lett.* 19 (2), 797–849. doi:10.1007/s10311-020-01133-3.
- Othman, M.R., Helwani, Z., Martunus, Fernando, W.J.N., 2009. Synthetic hydrocalcites from different routes and their application as catalysts and gas adsorbents: a review. *Appl. Organ. Chem.* 23 (9), 335–346. doi:10.1002/aoc.1517.
- Otitoju, O., Oko, E., Wang, M., 2021. Technical and economic performance assessment of post-combustion carbon capture using piperazine for large scale natural gas combined cycle power plants through process simulation. *Appl. Energy* 292. doi:10.1016/j.apenergy.2021.116893, 116893–116893.
- Otitoju, O., Oko, E., Wang, M., 2023. Modelling, scale-up and techno-economic assessment of rotating packed bed absorber for CO₂ capture from a 250 MWe combined cycle gas turbine power plant. *Applied Energy* 335, 120747–120747.
- Otitoju, O.S., 2022. Modelling, Simulation and Performance Evaluation of Post-Combustion Carbon Capture based on Chemical Absorption. The University of Sheffield, United Kingdom.
- Ozkan, M., Nayak, S.P., Ruiz, A.D., Jiang, W., 2022. Current status and pillars of direct air capture technologies. *iScience* 25 (4), 103990. doi:10.1016/j.isci.2022.103990.
- Pérez-Francisco, J.M., Santiago-García, J.L., Loria-Bastarrachea, M.I., Paul, D.R., Freeman, B.D., Aguilar-Vega, M., 2020. CMS membranes from PBI/PI blends: Temperature effect on gas transport and separation performance. *J. Membr. Sci.* 597. doi:10.1016/j.memsci.2019.117703.
- Pachauri, R., Meyer, L., 2014. Climate change 2014: Synthesis report. In: *Contribution of Working Groups I, II and III to the Fifth Assessment Report of the Intergovernmental Panel on Climate Change*.
- Pachitsas, S., Bonalumi, D., 2022. Parametric investigation of CO₂ capture from industrial flue gases using aqueous mixtures of ammonia (NH₃) and potassium carbonate (K₂CO₃). *Int. J. Greenh. Gas Control* 114, 103567. doi:10.1016/j.jggc.2021.103567.

- Pai, K.N., Prasad, V., Rajendran, A., 2021. Practically achievable process performance limits for pressure-vacuum swing adsorption-based postcombustion CO₂ capture. *ACS Sustain. Chem. Eng.* 9 (10), 3838–3849. doi:10.1021/acssuschemeng.0c08933.
- Pakizeh, M., Moradi, A., Ghassemi, T., 2021. Chemical extraction and modification of chitin and chitosan from shrimp shells. *Eur. Polym. J.* 159. doi:10.1016/j.eurpolymj.2021.110709.
- Pal, A., Chand, S., Das, M.C., 2017. A water-stable twofold interpenetrating microporous MOF for selective CO₂ adsorption and separation. *Inorg. Chem.* 56 (22), 13991–13997. doi:10.1021/acs.inorgchem.7b02136.
- Pallarés, J., González-Cencerrado, A., Arauzo, I., 2018. Production and characterization of activated carbon from barley straw by physical activation with carbon dioxide and steam. *Biomass Bioenergy* 115, 64–73. doi:10.1016/j.biombioe.2018.04.015.
- Palomino, M., Corma, A., Rey, F., Valencia, S., 2010. New insights on CO₂-Methane separation using LTA zeolites with different Si/Al ratios and a first comparison with MOFs. *Langmuir* 26 (3), 1910–1917.
- Pan, X., Clodic, D., Toubassy, J., 2013. CO₂ capture by antisublimation process and its technical economic analysis. *Greenh. Gas Sci. Technol.* 3 (1), 8–20. doi:10.1002/ghg.1313.
- Pan, W., Galvin, J., Huang, W.L., Xu, Z., Sun, X., Fan, Z., Liu, K., 2018. Device-scale CFD modeling of gas-liquid multiphase flow and amine absorption for CO₂ capture. *Greenh. Gases: Sci. Technol.* 8 (3), 603–620. doi:10.1002/ghg.1770.
- Panda, D., Kumar, E.A., Singh, S.K., 2019. Amine modification of binder-containing zeolite 4A bodies for post-combustion CO₂ capture. *Ind. Eng. Chem. Res.* 58 (13), 5301–5313. doi:10.1021/acs.iecr.8b03958.
- Pang, Z.-F., Xu, S.-Q., Zhou, T.-Y., Liang, R.-R., Zhan, T.-G., Zhao, X., 2016. Construction of covalent organic frameworks bearing three different kinds of pores through the heterostructural mixed linker strategy. *J. Am. Chem. Soc.* 138 (14), 4710–4713.
- Pang, S.H., Lively, R.P., Jones, C.W., 2018. Oxidatively-stable linear poly (propylenimine)-containing adsorbents for CO₂ capture from ultraldrift streams. *ChemSusChem* 11 (15), 2628–2637. doi:10.1002/cssc.201800438.
- Papalats, T., Polychronidis, I., Antzaras, A.N., Lemonidou, A.A., 2021. Enhancing the intermediate-temperature CO₂ capture efficiency of mineral MgO via molten alkali nitrates and CaCO₃: Characterization and sorption mechanism. *J. CO₂ Util.* 50, 101605. doi:10.1016/j.jcou.2021.101605.
- Park, H.J., Suh, M.P., 2013. Enhanced isosteric heat, selectivity, and uptake capacity of CO₂ adsorption in a metal-organic framework by impregnated metal ions. *Chem. Sci.* 4 (2), 685–690.
- Park, S.W., Lee, J.W., Choi, B.S., Lee, J.W., 2005. Reaction kinetics of carbon dioxide with diethanolamine in polar organic solvents. *Sep. Sci. Technol.* 40 (9), 1885–1898.
- Park, S.-W., Choi, B.-S., Lee, J.-W., 2006. Chemical absorption of carbon dioxide with triethanolamine in non-aqueous solutions. *Korean J. Chem. Eng.* 23 (1), 138–143.
- Park, S.W., Lee, J.W., Choi, B.S., Lee, J.W., 2006. Absorption of carbon dioxide into non-aqueous solutions of N-methyl-diethanolamine. *Korean J. Chem. Eng.* 23 (5), 806–811. doi:10.1007/bf02705932.
- Park, H.B., Jung, C.H., Lee, Y.M., Hill, A.J., Pas, S.J., Mudie, S.T., Van Wagner, E., Freeman, B.D., Cookson, D.J., 2007. Polymers with cavities tuned for fast selective transport of small molecules and ions. *Science (New York, N.Y.)* 318 (5848), 254–258. doi:10.1126/science.1146744.
- Park, Y.-I., Kim, B.-S., Byun, Y.-H., Lee, S.-H., Lee, E.-W., Lee, J.-M.J.D., 2009. Preparation of supported ionic liquid membranes (SILMs) for the removal of acidic gases from crude natural gas. *Desalination* 236 (1–3), 342–348.
- Park, J., Yuan, D., Pham, K.T., Li, J.R., Yakovenko, A., Zhou, H.C., 2012. Reversible alteration of CO₂ adsorption upon photochemical or thermal treatment in a metal-organic framework. *J. Am. Chem. Soc.* 134 (1), 99–102. doi:10.1021/ja209197f.
- Park, S.H., Lee, S.J., Lee, J.W., Chun, S.N., Lee, J.B., 2015. The quantitative evaluation of two-stage pre-combustion CO₂ capture processes using the physical solvents with various design parameters. *Energy* 81, 47–55. doi:10.1016/j.energy.2014.10.055.
- Park, J.H., Celedonio, J.M., Seo, H., Park, Y.K., Ko, Y.S., 2016. A study on the effect of the amine structure in CO₂ dry sorbents on CO₂ capture. *Catal. Today* 265, 68–76. doi:10.1016/j.cattod.2015.10.015.
- Park, S., Cho, K., Jeong, H.-K., 2020. Polyimide/ZIF-7 mixed-matrix membranes: understanding the in situ confined formation of the ZIF-7 phases inside a polymer and their effects on gas separations. *J. Mater. Chem. A* 8 (22), 11210–11217. doi:10.1039/D0TA02761H.
- Pate, S.G., Xu, H., O'Brien, C.P., 2022. Operando observation of CO₂ transport intermediates in polyvinylamine facilitated transport membranes, and the role of water in the formation of intermediates, using transmission FTIR spectroscopy. *J. Mater. Chem. A* 10 (8), 4418–4427. doi:10.1039/D1TA10015G.
- Patel, H.A., Je, S.H., Park, J., Chen, D.P., Jung, Y., Yavuz, C.T., Coskun, A., 2013. Unprecedented high-temperature CO₂ selectivity in N₂-phobic nanoporous covalent organic polymers. *Nat. Commun.* 4 (1), 1–8. doi:10.1038/ncomms2359.
- Patil, T., Dharaskar, S., Sinha, M., Jampa, S.S., 2022. Effectiveness of ionic liquid-supported membranes for carbon dioxide capture: a review. *Environ. Sci. Pollut. Res. Int.* 29 (24), 35723–35745. doi:10.1007/s11356-022-19586-0.
- Paul, D., Kemp, D., 1973. The diffusion time lag in polymer membranes containing adsorptive fillers. *J. Polym. Sci.: Polym. Symp.* 79–93 Wiley Online Library.
- Peh, S.B., Farooq, S., Zhao, D., 2022. A metal-organic framework (MOF)-based temperature swing adsorption cycle for postcombustion CO₂ capture from wet flue gas. *Chem. Eng. Sci.* 250. doi:10.1016/j.ces.2021.117399.
- Peht, M., Henkel, J., 2009. Life cycle assessment of carbon dioxide capture and storage from lignite power plants. *Int. J. Greenh. Gas Control* 3 (1), 49–66. doi:10.1016/j.ijggc.2008.07.001.
- Pellegrini, G., Strube, R., Manfrida, G., 2010. Comparative study of chemical absorbents in postcombustion CO₂ capture. *Energy* 35 (2), 851–857.
- Pellegrini, L.A., De Guido, G., Langé, S., 2018. Biogas to liquefied biomethane via cryogenic upgrading technologies. *Renew. Energy* 124, 75–83. doi:10.1016/j.renene.2017.08.007.
- Peltola, P., Ritvanen, J., Tuynjälä, T., Pröhl, T., Hyppänen, T., 2013. One-dimensional modelling of chemical looping combustion in dual fluidized bed reactor system. *Int. J. Greenh. Gas Control* 16, 72–82.
- Peltzer, D., Múnera, J., Cornaglia, L., Strumendo, M., 2018. Characterization of potassium doped Li₂ZrO₂ based CO₂ sorbents: Stability properties and CO₂ desorption kinetics. *Chem. Eng. J.* 336, 1–11. doi:10.1016/j.cej.2017.10.177.
- Peltzer, D., Múnera, J., Cornaglia, L., 2019. The effect of the Li:Na molar ratio on the structural and sorption properties of mixed zirconates for CO₂ capture at high temperature. *J. Environ. Chem. Eng.* 7 (2), 102927. doi:10.1016/j.jece.2019.102927.
- Peng, X., Ye, L.L., Wang, C.H., Zhou, H., Sun, B., 2011. Temperature- and duration-dependent rice straw-derived biochar: Characteristics and its effects on soil properties of an Ultisol in southern China. *Soil and Tillage Res.* 112 (2), 159–166. doi:10.1016/j.still.2011.01.002.
- Peng, D., Wang, S., Tian, Z., Wu, X., Wu, Y., Wu, H., Xin, Q., Chen, J., Cao, X., Jiang, Z., 2017. Facilitated transport membranes by incorporating graphene nanosheets with high zinc ion loading for enhanced CO₂ separation. *J. Membr. Sci.* 522, 351–362. doi:10.1016/j.memsci.2016.09.040.
- Peng, H.-L., Zhang, J.-B., Zhang, J.-Y., Zhong, F.-Y., Wu, P.-K., Huang, K., Fan, J.-P., Liu, F., 2019. Chitosan-derived mesoporous carbon with ultrahigh pore volume for amine impregnation and highly efficient CO₂ capture. *Chem. Eng. J.* 359, 1159–1165. doi:10.1016/j.cej.2018.11.064.
- Peng, L., Shi, M., Zhang, X., Xiong, W., Hu, X., Tu, Z., Wu, Y., 2022. Facilitated transport separation of CO₂ and H₂S by supported liquid membrane based on task-specific protic ionic liquids. *Green Chem.* 3 (3), 259–266. doi:10.1016/j.gce.2021.12.005.
- Pera-Titus, M., 2014. Porous inorganic membranes for CO₂ capture: present and prospects. *Chem. Rev.* 114 (2), 1413–1492.
- Pereira, A., Ferreira, A.F.P., Rodrigues, A., Ribeiro, A.M., Refuge, M.J., 2022. Evaluation of the potential of a 3D-printed hybrid zeolite 13X/activated carbon material for CO₂/N₂ separation using electric swing adsorption. *Chem. Eng. J.* 450. doi:10.1016/j.cej.2022.138197.
- Perejón, A., Romeo, L.M., Lara, Y., Lisbona, P., Martínez, A., Valverde, J.M.J.A.E., 2016. The Calcium-Looping technology for CO₂ capture: On the important roles of energy integration and sorbent behavior. *Appl. Energy* 162, 787–807.
- Perejón, A., Romeo, L.M., Lara, Y., Lisbona, P., Martínez, A., Valverde, J.M., 2016. The calcium-looping technology for CO₂ capture: On the important roles of energy integration and sorbent behavior. *Appl. Energy* 162, 787–807. doi:10.1016/j.apenergy.2015.10.121.
- Peres, C.B., Rosa, A.H., de Moraes, L.C., 2022. CO₂ adsorption of bagasse waste feedstock using thermogravimetric analyses. *J. Therm. Anal. Calorim.* 147 (10), 5973–5984. doi:10.1007/s10973-021-10949-2.
- Perinu, C., Bernhardt, I.M., Svendsen, H.F., Jens, K.-J., 2017. CO₂ Capture by Aqueous 3-(Methylamino)propylamine in Blend with Tertiary Amines: An NMR Analysis. *Energy Proc.* 114, 1949–1955. doi:10.1016/j.egypro.2017.03.1326.
- Perot, G., Guisnet, M., 1990. Advantages and disadvantages of zeolites as catalysts in organic chemistry. *J. Mol. Catal.* 61 (2), 173–196. doi:10.1016/0304-5102(90)85154-A.
- Perskin, J.B., Traum, M.J., von Hippel, T., Boetcher, S.K.S., 2022. On the feasibility of pre-compression for direct atmospheric cryogenic carbon capture. *Carbon Cap. Sci. Technol.* 4, 100063. doi:10.1016/j.cjcs.2022.100063.
- Peters, A., 2022. A startup in Hawaii just launched the world's first ocean-assisted carbon removal plant. <https://www.fastcompany.com/90750797/a-startup-in-hawaii-just-launched-the-worlds-first-ocean-assisted-carbon-removal-plant>. (Accessed 2022.05.22).
- Petre, C.F., Larachi, F., Illiuta, I., Grandjean, B.P.A., 2003. Pressure drop through structured packings: Breakdown into the contributing mechanisms by CFD modeling. *Chem. Eng. Sci.* 58 (1), 163–177. doi:10.1016/S0009-2509(02)00473-6.
- Petrescu, L., Cormos, C.-C., 2017. Environmental assessment of IGCC power plants with pre-combustion CO₂ capture by chemical & calcium looping methods. *J. Clean. Prod.* 158, 233–244. doi:10.1016/j.jclepro.2017.05.011.
- Petrescu, L., Bonalumi, D., Valenti, G., Cormos, A.-M., Cormos, C.-C., 2017. Life Cycle Assessment for supercritical pulverized coal power plants with post-combustion carbon capture and storage. *J. Clean. Prod.* 157, 10–21. doi:10.1016/j.jclepro.2017.03.225.
- Pfaff, I., Kather, A., 2009. Comparative thermodynamic analysis and integration issues of CCS steam power plants based on oxy-combustion with cryogenic or membrane based air separation. *Energy Procedia* 1 (1), 495–502. doi:10.1016/j.egypro.2009.01.066.
- Pham, D.A., Lim, Y.I., Jee, H., Ahn, E., Jung, Y., 2015. Effect of ship tilting and motion on amine absorber with structured-packing for CO₂ removal from natural gas. *AIChE J.* 61 (12), 4412–4425. doi:10.1002/aic.14962.
- Pham, D.A., Lim, Y.I., Jee, H., Ahn, E., Jung, Y., 2015. Porous media Eulerian computational fluid dynamics (CFD) model of amine absorber with structured-packing for CO₂ removal. *Chem. Eng. Sci.* 132, 259–270. doi:10.1016/j.ces.2015.04.009.
- Pi, S., Zhang, Z., He, D., Qin, C., Ran, J.J.E., 2019. Novel binders-promoted extrusion-spherulized CaO-based pellets for high-temperature CO₂ capture. *Fuels* 33 (3), 2381–2389.
- Pinto, D.D.D., Knuutila, H., Fytianos, G., Haugen, G., Mejdell, T., Svendsen, H.F., 2014a. CO₂ post combustion capture with a phase change solvent. Pilot plant campaign. *Int. J. Greenh. Gas Control* 31, 153–164. doi:10.1016/j.ijggc.2014.10.007.
- Pinto, D.D.D., Zaidy, S.A.H., Hartono, A., Svendsen, H.F., 2014b. Evaluation of a phase change solvent for CO₂ capture: Absorption and desorption tests. *Int. J. Greenh. Gas Control* 28, 318–327. doi:10.1016/j.ijggc.2014.07.002.

- Pirngruber, G.D., Guillou, F., Gomez, A., Clausse, M., 2013. A theoretical analysis of the energy consumption of post-combustion CO₂ capture processes by temperature swing adsorption using solid sorbents. *Int. J. Greenh. Gas Control* 14, 74–83. doi:10.1016/j.ijggc.2013.01.010.
- Plant, D., Maurin, G., Deroche, I., Gaborova, L., Llewellyn, P.L., 2006. CO₂ adsorption in alkali cation exchanged Y faujasites: a quantum chemical study compared to experiments. *Chem. Phys. Lett.* 426 (4–6), 387–392.
- Plaza, M.G., Rubiera, F., 2019. Evaluation of a novel multibed heat-integrated vacuum and temperature swing adsorption post-combustion CO₂ capture process. *Appl. Energy* 250, 916–925. doi:10.1016/j.apenergy.2019.05.079.
- Plaza, M.G., Pevida, C., Arias, B., Fermoso, J., Casal, M.D., Martín, C.F., Rubiera, F., Pis, J.J., 2009. Development of low-cost biomass-based adsorbents for post-combustion CO₂ capture. *Fuel* 88 (12), 2442–2447. doi:10.1016/j.fuel.2009.02.025.
- Plaza, M.G., Pevida, C., Martín, C.F., Fermoso, J., Pis, J.J., Rubiera, F., 2010. Developing almond shell-derived activated carbons as CO₂ adsorbents. *Sep. Purif. Technol.* 71 (1), 102–106. doi:10.1016/j.seppur.2009.11.008.
- Plaza, M.G., García, S., Rubiera, F., Pis, J.J., Pevida, C., 2011. Evaluation of ammonia modified and conventionally activated biomass based carbons as CO₂ adsorbents in post-combustion conditions. *Sep. Purif. Technol.* 80 (1), 96–104. doi:10.1016/j.seppur.2011.04.015.
- Plaza, M.G., Martínez, S., Rubiera, F., 2020. CO₂ capture, use, and storage in the cement industry: state of the art and expectations. *Energies* 13 (21), 28. doi:10.3390/en13215692.
- Plazaola, A.A., Labella, A.C., Liu, Y., Porras, N.B., Tanaka, D.A.P., Annaland, M.V.S., Gallucci, F., 2019. Mixed ionic-electronic conducting membranes (MIEC) for their application in membrane reactors: a review. *Processes* 7, 128. doi:10.3390/PR7030128, 2019, Vol. 7, Page 128.
- Pohako-Esko, K., Bahlmann, M., Schulz, P.S., Wasserscheid, P., 2016. Chitosan containing supported ionic liquid phase materials for CO₂ absorption. *Ind. Eng. Chem. Res.* 55 (25), 7052–7059. doi:10.1021/acs.iecr.6b00862.
- Pokhrel, J., Bhorla, N., Anastasiou, S., Tsoufis, T., Gournis, D., Romanos, G., Karanikolos, G.N., 2018. CO₂ adsorption behavior of amine-functionalized ZIF-8, graphene oxide, and ZIF-8/graphene oxide composites under dry and wet conditions. *Microporous Mesoporous Mater.* 267, 53–67. doi:10.1016/j.micromeso.2018.03.012.
- Policicchio, A., Zhao, Y., Zhong, Q., Agostino, R.G., Bandosz, T.J., 2014. Cu-BTC/aminated graphite oxide composites as high-efficiency CO₂ capture media. *ACS Appl. Mater. Interfaces* 6 (1), 101–108. doi:10.1021/am404952z.
- Portillo, E., Alonso-Fariñas, B., Vega, F., Cano, M., Navarrete, B., 2019. Alternatives for oxygen-selective membrane systems and their integration into the oxy-fuel combustion process: A review. *Sep. Purif. Technol.* 229. doi:10.1016/j.seppur.2019.115708, 115708–115708.
- Prabhakar, R., Freeman, B., 2002. Application of hydrocarbon–fluorocarbon interactions in membrane-based gas separations. *Desalination* 144 (1), 79–83. doi:10.1016/S0011-9164(02)00292-8.
- Prashar, A.K., Seo, H., Choi, W.C., Kang, N.Y., Park, S., Kim, K., Min, D.Y., Kim, H.M., Park, Y.K., 2016. Factors affecting the rate of CO₂ absorption after partial desorption in NaNO₃-promoted MgO. *Energy Fuels* 30 (4), 3298–3305.
- Prasanthum, N., Natewong, P., Reubroycharoen, P., Idem, R., 2019. Solvent regeneration of a CO₂-Loaded BEA-AMP Bi-blend amine solvent with the aid of a solid Brønsted Ce (SO₄)₂/ZrO₂ superacid catalyst. *Energy Fuels* 33 (2), 1334–1343. doi:10.1021/acs.energyfuels.8b03580.
- Pratono, W., Zhang, J., Cui, J., Wang, Y., Zhang, L., 2015. Clarifying the influence of moisture on the ignition and combustion of wet Victorian brown coal in air-firing and oxy-fuel modes: Part 2: Contribution of gasification reaction to char oxidation rate. *Fuel Process. Technol.* 138, 680–686.
- Presser, V., McDonough, J., Yeon, S.-H., Gogotsi, Y., 2011. Effect of pore size on carbon dioxide sorption by carbide derived carbon. *Energy Environ. Sci.* 4 (8), 3059–3066. doi:10.1039/C1EE01176F.
- Preston, C.K., Bruce, C., Monea, M.J., 2018. An update on the integrated CCS project at Saskpower's boundary dam power station.
- Preston, C., 2015. IEA GHG Report #2015-06 "Integrated carbon capture and storage project at saskpower's boundary dam power station". IEA GHG report #2015-06 "integrated carbon capture and storage project at saskpower's boundary dam power station".
- Primo, A., Forneli, A., Corma, A., García, H., 2012. From biomass wastes to highly efficient CO₂ adsorbents: Graphitisation of chitosan and alginate biopolymers. *ChemSusChem* 5 (11), 2207–2214. doi:10.1002/cssc.201200366.
- Prosser, N.M., Shah, M.M., 2011. *Current and Future Oxygen (O₂) Supply Technologies for Oxy-Fuel Combustion*. Elsevier, pp. 195–227.
- Pruna, A., Carcel, A., Benedito, A., Gimenez, E., 2021. Hydrothermal-freeze-casting of poly (amidoamine)-modified graphene aerogels towards CO₂ adsorption. *Int. J. Mol. Sci.* 22 (17). doi:10.3390/ijms22179333.
- Przepełniński, J., Skrodziewicz, M., Morawski, A.W., 2004. High temperature ammonia treatment of activated carbon for enhancement of CO₂ adsorption. *Appl. Surf. Sci.* 225 (1), 235–242. doi:10.1016/j.apsusc.2003.10.006.
- Pu, Y., Yang, Z., Wee, V., Wu, Z., Jiang, Z., Zhao, D., 2022. Amino-functionalized NUS-8 nanosheets as fillers in PIM-1 mixed matrix membranes for CO₂ separations. *J. Membr. Sci.* 641, 119912. doi:10.1016/j.memsci.2021.119912.
- Qasem, N.A.A., Qadir, N.U., Ben-Mansour, R., Said, S.A.M., 2017. Synthesis, characterization, and CO₂ breakthrough adsorption of a novel MWNT/MIL-101 (Cr) composite. *J. CO₂ Util.* 22, 238–249. doi:10.1016/j.jcou.2017.10.015.
- Qasem, N.A.A., Ben-Mansour, R., Habib, M.A., 2018. An efficient CO₂ adsorptive storage using MOF-5 and MOF-177. *Appl. Energy* 210, 317–326. doi:10.1016/j.apenergy.2017.11.011.
- Qi, T., Yang, Y., Wu, Y., Wang, J., Li, P., Yu, J., 2018. Sorption-enhanced methanol steam reforming for hydrogen production by combined copper-based catalysts with hydrotalcites. *Chem. Eng. Process. - Process Intensif.* 127, 72–82. doi:10.1016/j.cep.2018.03.022.
- Qiao, Z., Zhao, S., Wang, J., Wang, S., Wang, Z., Guiver, M.D., 2016. A highly permeable aligned montmorillonite mixed-matrix membrane for CO₂ separation. *Angew. Chem. Int. Ed.* 128 (32), 9467–9471. doi:10.1002/anie.201603211.
- Qiao, Y.Q., Wang, J.Y., Zhang, Y., Gao, W.L., Harada, T., Huang, L., Hatton, T.A., Wang, Q., 2017. Alkali nitrates molten salt modified commercial MgO for intermediate-temperature CO₂ capture: optimization of the Li/Na/K ratio. *Ind. Eng. Chem. Res.* 56 (6), 1509–1517. doi:10.1021/acs.iecr.6b04793.
- Qiao, Y.T., Zhang, S.M., Quan, C., Gao, N.B., Josnston, C., Wu, C.F., 2020. One-pot synthesis of digestate-derived biochar for carbon dioxide capture. *Fuel* 279. doi:10.1016/j.fuel.2020.118525.
- Qiao, Y., Bailey, J.J., Huang, Q., Ke, X., Wu, C., 2022. Potential photo-switching sorbents for CO₂ capture – A review. *Renew. Sustain. Energy Rev.* 158. doi:10.1016/j.rser.2022.112079.
- Qin, C., Yin, J., Ran, J., Zhang, L., Feng, B., 2014. Effect of support material on the performance of K₂CO₃-based pellets for cyclic CO₂ capture. *Appl. Energy* 136, 280–288. doi:10.1016/j.apenergy.2014.09.043.
- Qin, Q., Liu, H., Zhang, R., Ling, L., Fan, M., Wang, B., 2018. Application of density functional theory in studying CO₂ capture with TiO₂-supported K₂CO₃ being an example. *Appl. Energy* 231, 167–178. doi:10.1016/j.apenergy.2018.09.114.
- Qiu, W., Vaughn, J., Liu, G., Xu, L., Brayden, M., Martinez, M., Fitzgibbons, T., Wenz, G., Koros, W.J., 2019. Hyperagating tuning of a carbon molecular-sieve hollow fiber membrane with extraordinary gas-separation performance and stability. *Angew. Chem. Int. Ed. Engl.* 58 (34), 11700–11703. doi:10.1002/anie.201904913.
- Qiu, H., Liu, H., Liu, X., Yao, H., 2022. Synthesis of Novel Al₂O₃ nanoparticle organic hybrid Materials for enhancing the CO₂-separation performance of prepared Al₂O₃-NOHMs/Pebax mixed matrix membrane. *Mater. Lett.*, 132854. doi:10.1016/j.matlet.2022.132854.
- Qiu, Y., Lamers, P., Daigloglu, V., McQueen, N., de Boer, H.-S., Harmsen, M., Wilcox, J., Bardow, A., Suh, S., 2022. Environmental trade-offs of direct air capture technologies in climate change mitigation toward 2100. *Nat. Commun.* 13 (1), 3635. doi:10.1038/s41467-022-31146-1.
- Qu, Z., Zhao, R., Wu, H., Ren, Y., Liu, Y., Guo, Z., Wu, Y., Yang, L., Liang, X., Jiang, Z., 2020. Polyelectrolyte membranes with tunable hollow CO₂-philic clusters via sacrificial template for biogas upgrading. *J. Membr. Sci.* 612, 118445. doi:10.1016/j.memsci.2020.118445.
- Quan, C., Su, R., Gao, N., 2020. Preparation of activated biomass carbon from pine sawdust for supercapacitor and CO₂ capture. *Int. J. Energy Res.* 44 (6), 4335–4351. doi:10.1002/er.5206.
- Qiang, D.V., Dindi, A., Abu-Zahra, M.R.M., 2017. One-step process using CO₂ for the preparation of amino-functionalized mesoporous silica for CO₂ absorption. *ACS Sustain. Chem. Eng.* 5 (4), 3170–3178. doi:10.1021/acsuschemeng.6b02961.
- Que, H., Chen, C.-C., 2011. Thermodynamic modeling of the NH₃-CO₂-H₂O system with electrolyte NRTL model. *Ind. Eng. Chem. Res.* 50 (19), 11406–11421.
- Radfarnia, H.R., Iluta, M.C., 2013. Metal oxide-stabilized calcium oxide CO₂ sorbent for multicycle operation. *Chem. Eng. J.* 232, 280–289. doi:10.1016/j.cej.2013.07.049.
- Rafiq, S., Deng, L., Hägg, M.-B., 2016. Role of facilitated transport membranes and composite membranes for efficient CO₂ capture – a review. *ChemBioEng. Rev.* 3 (2), 68–85. doi:10.1002/cben.201500013.
- Rafizah, W., Ismail, A., 2008. Effect of carbon molecular sieve sizing with poly (vinyl pyrrolidone) K-15 on carbon molecular sieve–polysulfone mixed matrix membrane. *J. Membr. Sci.* 307 (1), 53–61.
- Raganati, F., Chirone, R., Ammendola, P., 2020. CO₂ capture by temperature swing adsorption: Working capacity as affected by temperature and CO₂ partial pressure. *Ind. Eng. Chem. Res.* 59 (8), 3593–3605. doi:10.1021/acs.iecr.9b04901.
- Raganati, F., Miccio, F., Ammendola, P., 2021. Adsorption of carbon dioxide for post-combustion capture: a review. *Energy Fuels* 35 (16), 12845–12868. doi:10.1021/acs.energyfuels.1c01618.
- Rahimi, M., Moosavi, S.M., Smit, B., Hatton, T.A., 2021. Toward smart carbon capture with machine learning. *Cell Rep. Phys. Sci.* 2 (4). doi:10.1016/j.xcrp.2021.100396, 100396–100396.
- Rahimpour, M.R., Kaskhooli, A.Z., 2004. Enhanced carbon dioxide removal by promoted hot potassium carbonate in a split-flow absorber. *Chem. Eng. Process: Process Intensif.* 43 (7), 857–865. doi:10.1016/S0255-2701(03)00106-5.
- Rahman, F.A., Aziz, M.M.A., Saidur, R., Bakar, W.A.W.A., Hainin, M.R., Putrajaya, R., Hassan, N.A., 2017. Pollution to solution: Capture and sequestration of carbon dioxide (CO₂) and its utilization as a renewable energy source for a sustainable future. *Renew. Sustain. Energy Rev.* 71, 112–126. doi:10.1016/j.rser.2017.01.011.
- Rahman, M.M., Abet, C., Shishatskiy, S., Martin, J., Müller, A.J., Abet, V., 2018. CO₂ selective PolyActive membrane: thermal transitions and gas permeance as a function of thickness. *ACS Appl. Mater. Interfaces* 10 (31), 26733–26744. doi:10.1021/acsami.8b09259.
- Rajagopalan, A.K., Avila, A.M., Rajendran, A., 2016. Do adsorbent screening metrics predict process performance? A process optimisation based study for post-combustion capture of CO₂. *Int. J. Greenh. Gas Control* 46, 76–85. doi:10.1016/j.ijggc.2015.12.033.
- Ram Reddy, M.K., Xu, Z.P., Lu, G.Q., Diniz da Costa, J.C., 2006. Layered double hydroxides for CO₂ capture: structure evolution and regeneration. *Ind. Eng. Chem. Res.* 45 (22), 7504–7509. doi:10.1021/ie060757k.
- Ram Reddy, M.K., Xu, Z.P., Diniz da Costa, J.C., 2008. Influence of water on high-temperature CO₂ capture using layered double hydroxide derivatives. *Ind. Eng. Chem. Res.* 47 (8), 2630–2635. doi:10.1021/ie0716060.
- Ramasubramanian, K., Zhao, Y., Winston Ho, W.S., 2013. CO₂ capture and H₂ purification: Prospects for CO₂-selective membrane processes. *Chem. Eng. Pract.* 59 (4), 1033–1045. doi:10.1002/aic.14078.

- Raphael Idem, M.W., Paitoon Tontiwachwuthikul, A.C., Amornvanee Veawab, A.A., Gelowitz, A.D., 2006. Pilot plant studies of the CO₂ capture performance of aqueous MEA and mixed MEA/MDEA solvents at the university of regina CO₂ capture technology development plant and the boundary dam CO₂ capture demonstration plant. *Ind. Eng. Chem. Res.* 45, 2414–2420.
- Rastogi, N.K., Nayak, C.A., 2011. Membranes for Forward Osmosis in Industrial Applications. Elsevier, pp. 680–717.
- Ray, B., Churipard, S.R., Peter, S.C., 2021. An overview of the materials and methodologies for CO₂ capture under humid conditions. *J. Mater. Chem. A* 9 (47), 26498–26527. doi:10.1039/d1ta08862a.
- Raynal, L., Boyer, C., Ballaguet, J.P., 2004. Liquid holdup and pressure drop determination in structured packing with CFD simulations. *Can. J. Chem. Eng.* 82 (5), 871–879. doi:10.1002/cjce.5450820502.
- Raynal, L., Bouillon, P.-A., Gomez, A., Broutin, P., 2011. From MEA to demixing solvents and future steps, a roadmap for lowering the cost of post-combustion carbon capture. *Chem. Eng. J.* 171 (3), 742–752. doi:10.1016/j.cej.2011.01.008.
- Razi, N., Svendsen, H.F., Bolland, O., 2013. Validation of mass transfer correlations for CO₂ absorption with MEA using pilot data. *Int. J. Greenh. Gas Control* 19, 478–491. doi:10.1016/j.ijggc.2013.10.006.
- Realmonde, G., Drouet, L., Gambhir, A., Glynn, J., Hawkes, A., Köberle, A.C., Tavoni, M., 2019. An inter-model assessment of the role of direct air capture in deep mitigation pathways. *Nat. Commun.* 10 (1), 3277. doi:10.1038/s41467-019-10842-5.
- Regmi, C., Ashtiani, S., Průša, F., Friess, K., 2022. Synergistic effect of hybridized TNT@GO fillers in CTA-based mixed matrix membranes for selective CO₂/CH₄ separation. *Sep. Purif. Technol.* 282, 120128. doi:10.1016/j.seppur.2021.120128.
- Reichle, W.T., 1985. Catalytic reactions by thermally activated, synthetic, anionic clay minerals. *J. Catal.* 94 (2), 547–557. doi:10.1016/0021-9157(85)90219-2.
- Reijers, H.T.J., Valster-Schiermeier, S.E.A., Cobden, P.D., van den Brink, R.W., 2006. Hydrocalcite as CO₂ sorbent for sorption-enhanced steam reforming of methane. *Ind. Eng. Chem. Res.* 45 (8), 2522–2530. doi:10.1021/ie050563p.
- Rekhtina, M., Dal Pozzo, A., Stoian, D., Armutulu, A., Donat, F., Blanco, M.V., Wang, Z.J., Willinger, M.G., Fedorov, A., Abdala, P.M., Muller, C.R., 2020. Effect of molten sodium nitrate on the decomposition pathways of hydrated magnesium hydroxycarbonate to magnesium oxide probed by *in situ* total scattering. *Nanoscale* 12 (31), 16462–16473. doi:10.1039/d0nr01760d.
- Ren, S., Boidys, M.J., Dawson, R., Laybourn, A., Khimyak, Y.Z., Adams, D.J., Cooper, A.I., 2012. Porous, fluorescent, covalent triazine-based frameworks via room-temperature and microwave-assisted synthesis. *Adv. Mater.* 24 (17), 2357–2361.
- Ren, J., Li, Z., Chen, Y., Yang, Z., Lu, X., 2018. Supported ionic liquid sorbents for CO₂ capture from simulated flue-gas. *Chin. J. Chem. Eng.* 26 (11), 2377–2384. doi:10.1016/j.cjche.2018.04.025.
- Ren, X., Kanezashi, M., Nagasawa, H., Xu, R., Zhong, J., Tsuru, T., 2019. Ceramic-supported polyhedral oligomeric silsesquioxane-organosilica nanocomposite membrane for efficient gas separation. *Ind. Eng. Chem. Res.* 58 (47), 21708–21716. doi:10.1021/acs.iecr.9b05251.
- Ren, W., Wei, Z.Z., Xia, X.X., Hong, Z.W., Li, S., 2020. CO₂ adsorption performance of CuBTC/graphene aerogel composites. *J. Nanopart. Res.* 22 (7). doi:10.1007/s11051-020-04933-4.
- Research, G.S., 2019. Carbonomics: the future of energy in the age of climate change.
- Rezaei, N., Mohebbi, V., Feyzi, V., 2022. Hybrid hydrate processes for CO₂/H₂ mixture purification: A techno-economic analysis. *Int. J. Hydrog. Energy* 47 (18), 10137–10155. doi:10.1016/j.ijhydene.2022.01.102.
- Rezazakami, M., Mohammadi, T., 2013. Gas sorption in H₂-selective mixed matrix membranes: experimental and neural network modeling. *Int. J. Hydrog. Energy* 38 (32), 14035–14041. doi:10.1016/j.ijhydene.2013.08.062.
- Rhodes, C.J., 2016. The 2015 Paris climate change conference: COP21. *Sci. Prog.* 99 (1), 97–104.
- Rindfleisch, F., DiNoia, T.P., McHugh, M.A., 1996. Solubility of polymers and copolymers in supercritical CO₂. *J. Phys. Chem.* 100 (38), 15581–15587. doi:10.1021/jp9615823.
- Robertson, C., Mokaya, R., 2013. Microporous activated carbon aerogels via a simple subcritical drying route for CO₂ capture and hydrogen storage. *Microporous Mesoporous Mater.* 179, 151–156. doi:10.1016/j.micromeso.2013.05.025.
- Robeson, L.M., Freeman, B.D., Paul, D.R., Rowe, B.W., 2009. An empirical correlation of gas permeability and permselectivity in polymers and its theoretical basis. *J. Membr. Sci.* 341 (1), 178–185. doi:10.1016/j.memsci.2009.06.005.
- Robeson, L.M., Liu, Q., Freeman, B.D., Paul, D.R., 2015. Comparison of transport properties of rubbery and glassy polymers and the relevance to the upper bound relationship. *J. Membr. Sci.* 476, 421–431. doi:10.1016/j.memsci.2014.11.058.
- Robeson, L.M., 1991. Correlation of separation factor versus permeability for polymeric membranes. *J. Membr. Sci.* 62 (2), 165–185. doi:10.1016/0376-7388(91)80060-J.
- Robeson, L.M., 2008. The upper bound revisited. *J. Membr. Sci.* 320 (1–2), 390–400.
- Robeson, L.M., 2008. The upper bound revisited. *J. Membr. Sci.* 320 (1), 390–400. doi:10.1016/j.memsci.2008.04.030.
- Rocco, M.V., Lange, S., Pigoli, L., Colombo, E., Pellegrini, L.A., 2019. Assessing the energy intensity of alternative chemical and cryogenic natural gas purification processes in LNG production. *J. Clean. Prod.* 208, 827–840. doi:10.1016/j.jclepro.2018.10.108.
- Rochelle, G.T., 2009. Amine Scrubbing for CO₂ Capture. *Science* 325 (5948), 1652–1654. doi:10.1126/science.1176731.
- Rodríguez-Mosqueda, R., Bramer, E.A., Brem, G., 2018. CO₂ capture from ambient air using hydrated Na₂CO₃ supported on activated carbon honeycombs with application to CO₂ enrichment in greenhouses. *Chem. Eng. Sci.* 189, 114–122. doi:10.1016/j.ces.2018.05.043.
- Rodríguez Hervás, G., Petrakopoulou, F., 2019. Exergoeconomic analysis of the allam cycle. *Energy Fuels* 33 (8), 7561–7568.
- Rodríguez, S.C., Andrade, M., Moffat, J., Magalhães, F.D., Mendes, A., 2019. Preparation of carbon molecular sieve membranes from an optimized ionic liquid-regenerated cellulose precursor. *J. Membr. Sci.* 572, 390–400. doi:10.1016/j.memsci.2018.11.027.
- Rogelj, J., den Elzen, M., Höhne, N., Fransen, T., Fekete, H., Winkler, H., Schaeffer, R., Sha, F., Riahi, K., Meinshausen, M., 2016. Paris Agreement climate proposals need a boost to keep warming well below 2°C. *Nature* 534, 631. doi:10.1038/nature18307. <https://www.nature.com/articles/nature18307#supplementary-information>.
- Roongrat, Sakwattanaopong, Adisorn, Aroonwilas, Veawab, A., 2005. Behavior of reboiler heat duty for CO₂ capture plants using regenerable single and blended alkanolamines. *Ind. Eng. Chem. Res.* 44, 4465–4473.
- Rose, I., Bezzu, C.G., Carta, M., Comesaña-Gándara, B., Lasseguette, E., Ferrari, M.C., Bernardo, P., Clarizia, G., Fuoco, A., Jansen, J.C., Hart, Kyle E., Liyana-Arachchi, T.P., Colina, C.M., McKeown, N.B., 2017. Polymer ultrapermeability from the inefficient packing of 2D chains. *Nat. Mater.* 16 (9), 932–937. doi:10.1038/nmat4939.
- Rossi, E., Storti, G., Rota, R., 2020. Influence of the main operating parameters on the DRPSA process design based on the equilibrium theory. *Adsorption* 27 (1), 27–39. doi:10.1007/s10450-020-00274-9.
- Rostamizadeh, M., Rezakazemi, M., Shahidi, K., Mohammadi, T., 2013. Gas permeation through H₂-selective mixed matrix membranes: experimental and neural network modeling. *Int. J. Hydrog. Energy* 38 (2), 1128–1135. doi:10.1016/j.ijhydene.2012.10.069.
- Roussanaly, S., Anantharaman, R., Lindqvist, K., Zhai, H., Rubin, E., 2016. Membrane properties required for post-combustion CO₂ capture at coal-fired power plants. *J. Membr. Sci.* 511, 250–264. doi:10.1016/j.memsci.2016.03.035.
- Ruan, X., He, G., Li, B., Yan, X., Dai, Y., 2014. Chemical potential analysis for directing the optimal design of gas membrane separation frameworks. *Chem. Eng. Sci.* 107, 245–255. doi:10.1016/j.ces.2013.11.046.
- Rubin, E.S., Mantripragada, H., Marks, A., Versteeg, P., Kitchin, J., 2012. The outlook for improved carbon capture technology. *Prog. Energy Combust. Sci.* 38 (5), 630–671. doi:10.1016/j.peccs.2012.03.003.
- Rufford, T.E., Smart, S., Watson, G.C.Y., Graham, B.F., Boxall, J., Diniz da Costa, J.C., May, E.F., 2012. The removal of CO₂ and N₂ from natural gas: A review of conventional and emerging process technologies. *J. Petrol. Sci. Eng.* 94–95, 123–154. doi:10.1016/j.petrol.2012.06.016.
- Ruminski, A.M., Jeon, K.-J., Urban, J.J., 2011. Size-dependent CO₂ capture in chemically synthesized magnesium oxide nanocrystals. *J. Mater. Chem.* 21 (31), 11486–11491.
- Rungta, M., Wenz, G.B., Zhang, C., Xu, L., Qiu, W., Adams, J.S., Koros, W.J., 2017. Carbon molecular sieve structure development and membrane performance relationships. *Carbon* 115, 237–248. doi:10.1016/j.carbon.2017.01.015.
- Ruthven, D.M., Farooq, S., 1990. Air separation by pressure swing adsorption. *Gas Sep. Purif.* 4 (3), 141–148. doi:10.1016/0950-4214(90)80016-E.
- Ruuskanen, V., Givirovskiy, G., Elfving, J., Kokkonen, P., Karvinen, A., Järvinen, L., Sillman, V., Vainikka, M., Ahola, J., 2021. Neo-carbon food concept: A pilot-scale hybrid biological–inorganic system with direct air capture of carbon dioxide. *J. Clean. Prod.* 278, 123423. doi:10.1016/j.jclepro.2020.123423.
- Ryden, M., Cleverstam, E., Johansson, M., Lyngfelt, A., Mattisson, T., 2010. Fe₂O₃ on Ce-, Ca-, or Mg-stabilized ZrO₂ as oxygen carrier for chemical-looping combustion using NiO as additive. *AIChE J.* 56 (8), 2211–2220. doi:10.1002/aic.12143.
- Ryden, M., Jing, D., Källén, M., Leion, H., Lyngfelt, A., Mattisson, T., 2014. CuO-Based oxygen-carrier particles for chemical-looping with oxygen uncoupling – experiments in batch reactor and in continuous operation. *Ind. Eng. Chem. Res.* 53 (15), 6255–6267. doi:10.1021/ie4039983.
- Ryder, M.R., Civalieri, B., Bennett, T.D., Henke, S., Rudic, S., Cinque, G., Fernandez-Alonso, F., Tan, J.-C., 2014. Identifying the role of terahertz vibrations in metal-organic frameworks: from gate-opening phenomenon to shear-driven structural destabilization. *Phys. Rev. Lett.* 113 (21), 215502. doi:10.1103/PhysRevLett.113.215502.
- Sánchez-Lainez, J., Zornoza, B., Téllez, C., Coronas, J., 2018. Asymmetric polybenzimidazole membranes with thin selective skin layer containing ZIF-8 for H₂/CO₂ separation at pre-combustion capture conditions. *J. Membr. Sci.* 563, 427–432.
- Sönnechsen, N., 2022. Production of biogas worldwide from 2000 to 2020.
- Sabathghadam, A., Liu, X., Gottmer, S., Chu, L., Gascon, J., Kaptejin, F., 2019. Thin mixed matrix and dual layer membranes containing metal-organic framework nanosheets and Polyactive™ for CO₂ capture. *J. Membr. Sci.* 570, 226–235. doi:10.1016/j.memsci.2018.10.047.
- Sada, E., Kumazawa, H., Han, Z.Q., Matsuyama, H., 1985. Chemical kinetics of the reaction of carbon dioxide with ethanalamines in nonaqueous solvents. *AIChE J.* 31 (8), 1297–1303. doi:10.1002/aic.690310808.
- Sadiq, M.M., Li, H., Hill, A.J., Falcaro, P., Hill, M.R., Suzuki, K., 2016. Magnetic induction swing adsorption: An energy efficient route to porous adsorbent regeneration. *Chem. Mater.* 28 (17), 6219–6226. doi:10.1021/acs.chemmater.6b02409.
- Sadiq, M.M., Batten, M.P., Mulet, X., Freeman, C., Konstas, K., Mardel, J.I., Tanner, J., Ng, D., Wang, X., Howard, S., Hill, M.R., Thornton, A.W., 2020. A pilot-scale demonstration of mobile direct air capture using metal-organic frameworks. *Adv. Sustain. Syst.* 4 (12), 2000101. doi:10.1002/adu.202000101.
- Saeed, M., Rafiq, S., Bergersen, L.H., Deng, L., 2017. Tailoring of water swollen PVA membrane for hosting carriers in CO₂ facilitated transport membranes. *Sep. Purif. Technol.* 179, 550–560. doi:10.1016/j.seppur.2017.02.022.
- Safaei, S., Zeynali, R., Safaei, B., 2021. Modeling study of propane/propylene membrane separation using CFD method. *Macromol. Theory Simul.* 30 (2), 2000092. doi:10.1002/mats.202000092.
- Safdarnejad, S.M., Hedengren, J.D., Baxter, L.L., 2015. Plant-level dynamic optimization of Cryogenic Carbon Capture with conventional and renewable power sources. *Appl. Energy* 149, 354–366. doi:10.1016/j.apenergy.2015.03.100.
- Said Al Hoqani, H.A., Al-Shaqsi, N., Hossain, M.A., Al Sibani, M.A., 2020. Isolation and optimization of the method for industrial production of chitin and chitosan from Omani shrimp shell. *Carbohydr. Res.* 492. doi:10.1016/j.carres.2020.108001.

- Said, W., Nemer, M., Clodic, D., 2011. Modeling of dry pressure drop for fully developed gas flow in structured packing using CFD simulations. *Chem. Eng. Sci.* 66 (10), 2107–2117.
- Said, R.B., Kollé, J.M., Essalah, K., Tangour, B., Sayari, A., 2020. A Unified approach to CO₂-amine reaction mechanisms. *ACS Omega* 5 (40), 26125–26133. doi:10.1021/acsomega.0c03727.
- Sajjadi, B., Chen, W.-Y., Egiebor, N.O., 2019a. A comprehensive review on physical activation of biochar for energy and environmental applications. *Rev. Chem. Eng.* 35 (6), 735–776. doi:10.1515/revce-2017-0113.
- Sajjadi, B., Zubatnik, T., Leszczynska, D., Leszczynski, J., Chen, W.Y., 2019b. Chemical activation of biochar for energy and environmental applications: a comprehensive review. *Rev. Chem. Eng.* 35 (7), 777–815.
- Sakhiya, A.K., Baghel, P., Anand, A., Vijay, V.K., Kaushal, P., 2021. A comparative study of physical and chemical activation of rice straw derived biochar to enhance Zn-2 adsorption. *Bioresour. Technol.* 15, 100774. doi:10.1016/j.biortech.2021.100774.
- Salam, M., Hossain, T., Papri, N., Ahmed, K., Habib, M., Uddin, M., Wilckens, R., 2020. Hydrogen production performances via steam reforming over hydrotalcite derived catalyst: a sustainable energy production review. *Adv. Chem. Eng. Sci.* 10 (4), 259–296.
- Salaudeen, S.A., Acharya, B., Dutta, A., 2018. CaO-based CO₂ sorbents: A review on screening, enhancement, cyclic stability, regeneration and kinetics modelling. *J. CO₂ Util.* 23, 179–199. doi:10.1016/j.jcou.2017.11.012.
- Salvador, C., 2007. Modeling design and pilot-scale experiments of CANMET'S advanced oxy-fuel/steam burner. In: *International oxy-combustion research 2nd workshop, USA*, p. 26.
- Samanta, A., et al., 2011. Post-combustion CO₂ capture using solid sorbents: a review. *Ind. Eng. Chem. Res.* 51 (4), 1438–1463.
- Samanta, A., Zhao, A., Shimizu, G.K.H., Sarkar, P., Gupta, R., 2012. Post-combustion CO₂ capture using solid sorbents: a review. *Ind. Eng. Chem. Res.* 51 (4), 1438–1463. doi:10.1021/ie200686q.
- Sanaeepur, H., Ahmadi, R., Amoooghini, A.E., Ghanbari, D., 2019. A novel ternary mixed matrix membrane containing glycerol-modified poly (ether-block-amide) (Pebax 1657)/copper nanoparticles for CO₂ separation. *J. Membr. Sci.* 573, 234–246. doi:10.1016/j.memsci.2018.12.012.
- Sanchez-Jimenez, P.E., Perez-Maqueada, L.A., Valverde, J.M., 2014. Nanosilica supported CaO: A regenerable and mechanically hard CO₂ sorbent at Ca-looping conditions. *Appl. Energy* 118, 92–99. doi:10.1016/j.apenergy.2013.12.024.
- Sanders, D.F., Smith, Z.P., Guo, R., Robeson, L.M., McGrath, J.E., Paul, D.R., Freeman, B.D., 2013. Energy-efficient polymeric gas separation membranes for a sustainable future: A review. *Polymer* 54 (18), 4729–4761.
- Sangon, S., Hunt, A.J., Attard, T.M., Mengchang, P., Ngernyen, Y., Supanchaiyamat, N., 2018. Valorisation of waste rice straw for the production of highly effective carbon based adsorbents for dyes removal. *J. Clean. Prod.* 172, 1128–1139. doi:10.1016/j.jclepro.2017.10.210.
- Sangroniz, L., Wang, B., Su, Y., Liu, G., Cavallo, D., Wang, D., Müller, A.J., 2021. Fractionated crystallization in semicrystalline polymers. *Prog. Polym. Sci.* 115, 101376. doi:10.1016/j.progpolymsci.2021.101376.
- Sanpasertparnith, T., Idem, R., Bolea, I., deMontigny, D., Tontiwachwuthikul, P., 2010. Integration of post-combustion capture and storage into a pulverized coal-fired power plant. *Int. J. Greenh. Gas Control* 4 (3), 499–510. doi:10.1016/j.jggc.2009.12.005.
- Santiago, R., Lemus, J., Moreno, D., Moya, C., Larriba, M., Alonso-Morales, N., Gilarranz, M.A., Rodríguez, J.J., Palomar, J., 2018. From kinetics to equilibrium control in CO₂ capture columns using Encapsulated Ionic Liquids (ENILs). *Chem. Eng. J.* 348, 661–668. doi:10.1016/j.cej.2018.05.029.
- Santos, M.P.S., Hanak, D.P., 2022. Carbon capture for decarbonisation of energy-intensive industries: a comparative review of techno-economic feasibility of solid looping cycles. *Front. Chem. Sci.* 16 (9), 1291–1317. doi:10.1007/s11705-022-2151-5.
- Sanz-Pérez, E.S., Murdock, C.R., Didas, S.A., Jones, C.W., 2016. Direct capture of CO₂ from ambient air. *Chem. Rev.* 116 (19), 11840–11876. doi:10.1021/acs.chemrev.6b00173.
- Sanz-Pérez, E.S., Murdock, C.R., Didas, S.A., Jones, C.W., 2016a. Direct capture of CO₂ from ambient air. *Chem. Rev.* 116 (19), 11840–11876. doi:10.1021/acs.chemrev.6b00173.
- Sanz-Pérez, E.S., Murdock, C.R., Didas, S.A., Jones, C.W., 2016b. Direct capture of CO₂ from ambient air. *Chem. Rev.* 116 (19), 11840–11876. doi:10.1021/acs.chemrev.6b00173.
- Saravanan, A., Kumar, P.S., Jeevanantham, S., Karishma, S., Vo, D.V.N., 2022. Recent advances and sustainable development of biofuels production from lignocellulosic biomass. *Bioresour. Technol.* 344. doi:10.1016/j.biortech.2021.126203.
- Sartori, G., Savage, D.W.J.L., Fundamentals, E.C., 1983. Sterically hindered amines for carbon dioxide removal from gases. *22*, 239–249.
- Sasikumar, B., Bisht, S., Arthanareeswaran, G., Ismail, A.F., Othman, M.H.D., 2021. Performance of polysulfone hollow fiber membranes encompassing ZIF-8, SiO₂/ZIF-8, and amine-modified SiO₂/ZIF-8 nanofillers for CO₂/CH₄ and CO₂/N₂ gas separation. *Sep. Purif. Technol.* 264, 118471. doi:10.1016/j.seppur.2021.118471.
- Sateesh, C., Nandakishora, Y., Sahoo, R.K., Murugan, S., 2021. Study of cryogenic CO₂ capture with solar-assisted VAR system. *Clean. Eng. Technol.* 5, 100351. doi:10.1016/j.clet.2021.100351.
- T Satyapal, S.F., Trela, J., Strange, J., 2001. Performance and properties of a solid amine sorbent for carbon dioxide removal in space life support applications. *Energy Fuels* 15 (2), 250–255. doi:10.1021/ef0002391.
- Saunier, F., Fradette, S., Clerveaux, F., Lefebvre, S., Madore, É., Veilleux, G., Bulle, C., Surprenant, R., 2019. Comparison of life-cycle assessment between bio-catalyzed and promoted potassium carbonate processes and amine-based carbon capture technologies. *Int. J. Greenh. Gas Control* 88, 134–155. doi:10.1016/j.jggc.2019.05.009.
- Sayari, A., Heydari-Gorji, A., Yang, Y., 2012. CO₂-induced degradation of amine-containing adsorbents: reaction products and pathways. *J. Am. Chem. Soc.* 134 (33), 13834–13842. doi:10.1021/ja304888a.
- Sayari, N., Sila, A., Abdelmalek, B.E., Abdallah, R.B., Ellouz-Chaabouni, S., Bougatef, A., Balti, R., 2016. Chitin and chitosan from the Norway lobster by-products: Antimicrobial and anti-proliferative activities. *Int. J. Biol. Macromol.* 87, 163–171. doi:10.1016/j.ijbiomac.2016.02.057.
- Sayari, P.J.E.H.A.A., 2006. Applications of pore-expanded mesoporous silicas. 3. triamine silane grafting for enhanced CO₂ adsorption. *Ind. Eng. Chem. Res.* 45 (9), 3248–3255.
- Sazali, N., Wan Salleh, W.N., Ismail, A.F., Ismail, N.H., Kadrigama, K., 2021. A brief review on carbon selective membranes from polymer blends for gas separation performance. *Rev. Chem. Eng.* 37 (3), 339–362. doi:10.1515/revce-2018-0086.
- Scaccabarozzi, R., Gatti, M., Martelli, E., 2016. Thermodynamic analysis and numerical optimization of the NET Power oxy-combustion cycle. *Appl. Energy* 178, 505–526.
- Schach, M.-O., Oyarzún, B., Schramm, H., Schneider, R., Repke, J.-U., 2011. Feasibility study of CO₂ capture by anti-sublimation. *Energy Procedia* 4, 1403–1410. doi:10.1016/j.egypro.2011.02.005.
- Schakel, W., Meerman, H., Talaei, A., Ramírez, A., Faaij, A., 2014. Comparative life cycle assessment of biomass co-firing plants with carbon capture and storage. *Appl. Energy* 131, 441–467. doi:10.1016/j.apenergy.2014.06.045.
- Scheffknecht, G., Al-Makhadmeh, L., Schnell, U., Maier, J., 2011. Oxy-fuel coal combustion—A review of the current state-of-the-art. *Int. J. Greenh. Gas Control* 5, S16–S35. doi:10.1016/j.jggc.2011.05.020.
- Scheidema, M.N., Taskinen, P., 2011. Decomposition thermodynamics of magnesium sulfate. *Ind. Eng. Chem. Res.* 50 (16), 9550–9556. doi:10.1021/ie102554f.
- Scholes, C.A., Bacus, J., Chen, G.Q., Tao, W.X., Li, G., Qader, A., Stevens, G.W., Kentish, S.E., 2012. Pilot plant performance of rubbery polymeric membranes for carbon dioxide separation from syngas. *J. Membr. Sci.* 389, 470–477.
- Scholes, C.A., Ho, M.T., Wiley, D.E., Stevens, G.W., Kentish, S.E., 2013. Cost competitive membrane-cryogenic post-combustion carbon capture. *Int. J. Greenh. Gas Control* 17, 341–348. doi:10.1016/j.jggc.2013.05.017.
- Scholes, C.A., Stevens, G.W., Kentish, S.E., 2016. Impact of heavy hydrocarbons on natural gas sweetening using perfluorinated polymeric membranes. *Ind. Eng. Chem. Res.* 55 (28), 7696–7703. doi:10.1021/acs.iecr.6b01823.
- Scholz, M., Frank, B., Stockmeier, F., Fallß, S., Wessling, M., 2013. Techno-economic analysis of hybrid processes for biogas upgrading. *Ind. Eng. Chem. Res.* 52 (47), 16929–16938. doi:10.1021/ie402660s.
- Schröck, K., Schröder, F., Heyden, M., Fischer, R., Havenith, M., 2008. Characterization of interfacial water in H₂O (Zn 4 (O) (BDC) 3)—a combined spectroscopic and theoretical study. *Phys. Chem. Chem. Phys.* 10 (32), 4732–4739.
- Schreiber, A., Marx, J., Zapp, P., 2013. Environmental assessment of a membrane-based air separation for a coal-fired oxyfuel power plant. *J. Membr. Sci.* 440, 122–133. doi:10.1016/j.memsci.2013.03.026.
- Schultz, J.S., Goddard, J.D., Suedho, S.R.J.A.J., 1974. Facilitated transport via carrier-mediated diffusion in membranes: Part I. Mechanistic aspects, experimental systems and characteristic regimes. *20* (3), 417–445.
- Scofield, J.M.P., Gurr, P.A., Kim, J., Fu, Q., Kentish, S.E., Qiao, G.G., 2016a. Blends of fluorinated additives with highly selective thin-film composite membranes to increase CO₂ permeability for CO₂/N₂ gas separation applications. *Ind. Eng. Chem. Res.* 55 (30), 8364–8372. doi:10.1021/acs.iecr.6b02167.
- Scofield, J.M.P., Gurr, P.A., Kim, J., Fu, Q., Kentish, S.E., Qiao, G.G., 2016b. Development of novel fluorinated additives for high performance CO₂ separation thin-film composite membranes. *J. Membr. Sci.* 499, 191–200. doi:10.1016/j.memsci.2015.10.035.
- Sebastiani, F., James, J., van Dijk, H., Pieterse, J.A., Boon, J., Cobden, P., 2021. Modelling of CO₂ and H₂O interaction during adsorption cycles on hydrotalcite for SEWGS applications. In: *Proceedings of the 15th Greenhouse Gas Control Technologies Conference*, pp. 15–18.
- Seema, H., Kemp, K.C., Le, N.H., Park, S.-W., Chandra, V., Lee, J.W., Kim, K.S., 2014. Highly selective CO₂ capture by S-doped microporous carbon materials. *Carbon* 66, 320–326. doi:10.1016/j.carbon.2013.09.006.
- Seepana, S., Jayanti, S., 2010. Steam-moderated oxy-fuel combustion. *Energy Convers. Manage.* 51 (10), 1981–1988. doi:10.1016/j.enconman.2010.02.031.
- Seggiani, M., Stefanelli, E., Puccini, M., Vitolo, S., 2018. CO₂ sorption/desorption performance study on K₂CO₃-doped Li₄SiO₄-based pellets. *Chem. Eng. J.* 339, 51–60. doi:10.1016/j.cej.2018.01.117.
- Seiki, S., Kobayashi, T., Kobayashi, Y., Takei, K., Miyashiro, H., Hayamizu, K., Tsubuki, S., Mitsugi, T., Umebayashi, Y., 2010. Effects of cation and anion on physical properties of room-temperature ionic liquids. *J. Mol. Liq.* 152 (1–3), 9–13. doi:10.1016/j.molliq.2009.10.008.
- Sema, T., Naami, A., Fu, K., Edali, M., Liu, H., Shi, H., Liang, Z., Idem, R., Tontiwachwuthikul, P., 2012. Comprehensive mass transfer and reaction kinetics studies of CO₂ absorption into aqueous solutions of blended MDEA–MEA. *Chem. Eng. J.* 209, 501–512. doi:10.1016/j.cej.2012.08.016.
- Sengupta, S., Amte, V., Dongara, R., Das, A.K., Bhunia, H., Bajpai, P.K., 2015. Effects of the adsorbent preparation method for CO₂ capture from flue gas using K₂CO₃/Al₂O₃ adsorbents. *Energy Fuels* 29 (1), 287–297. doi:10.1021/ef501792c.
- Seo, H., Rahimi, M., Hattori, T.A., 2022. Electrochemical carbon dioxide capture and release with a redox-active amine. *J. Am. Chem. Soc.* 144 (5), 2164–2170. doi:10.1021/jacs.1c10656.
- Serafin, J., Narkiewicz, U., Morawski, A.W., Wróbel, R.J., Michalkiewicz, B., 2017. Highly microporous activated carbons from biomass for CO₂ capture and effective micropores at different conditions. *J. CO₂ Util.* 18, 73–79. doi:10.1016/j.jcou.2017.01.006.
- E Serna-Guerrero, R.D.N., Sayari, A., 2008. New insights into the interactions of CO₂ with amine-functionalized silica. *Ind. Eng. Chem. Res.* 47 (23), 9406–9412. doi:10.1021/ie801186g.
- Serna-Guerrero, R., Belmabkhout, Y., Sayari, A., 2010. Modeling CO₂ adsorption on amine-functionalized mesoporous silica: I. A semi-empirical equi-

- librium model. *Chem. Eng. J.* 161 (1-2), 173–181. doi:10.1016/j.cej.2010.04.024.
- Service, R.F., 2017. *Fossil Power, Guilt Free*. American Association for the Advancement of Science.
- Shafawi, A.N., Mohamed, A.R., Lahijani, P., Mohammadi, M., 2021. Recent advances in developing engineered biochar for CO₂ capture: An insight into the biochar modification approaches. *J. Environ. Chem. Eng.* 9 (6). doi:10.1016/j.jece.2021.106869.
- Shafeeyan, M.S., Daud, W.M.A.W., Houshmand, A., Shamiri, A., 2010. A review on surface modification of activated carbon for carbon dioxide adsorption. *J. Anal. Appl. Pyrol.* 89 (2), 143–151. doi:10.1016/j.jaap.2010.07.006.
- Shafeeyan, M.S., Wan Daud, W.M.A., Houshmand, A., Arami-Niya, A., 2012. The application of response surface methodology to optimize the amination of activated carbon for the preparation of carbon dioxide adsorbents. *Fuel* 94, 465–472. doi:10.1016/j.fuel.2011.11.035.
- Shafeeyan, M.S., Wan Daud, W.M.A., Shamiri, A., 2014. A review of mathematical modeling of fixed-bed columns for carbon dioxide adsorption. *Chem. Eng. Res. Des.* 92 (5), 961–988. doi:10.1016/j.cherd.2013.08.018.
- Shah, K., Moghtaderi, B., Zanganeh, J., Wall, T., 2013. Integration options for novel chemical looping air separation (CLAS) process for oxygen production in oxy-fuel coal fired power plants. *Fuel* 107, 356–370. doi:10.1016/j.fuel.2013.01.007.
- Shah, K., Zhou, C., Song, H., Doroodchi, E., Moghtaderi, B., 2015. A novel hybrid chemical-looping oxy combustor process for the combustion of solid and gaseous fuels: thermodynamic analysis. *Energy Fuels* 29 (2), 602–617. doi:10.1021/EF502389T.
- Shah, S., Shah, M., Shah, A., Shah, M., 2020. Evolution in the membrane-based materials and comprehensive review on carbon capture and storage in industries. *Emergent Mater.* 3 (1), 33–44. doi:10.1007/s42247-020-00069-2.
- Shah, G., Ahmad, E., Pant, K.K., Vijay, V.K., 2021. Comprehending the contemporary state of art in biogas enrichment and CO₂ capture technologies via swing adsorption. *Int. J. Hydrog. Energy* 46 (9), 6588–6612. doi:10.1016/j.ijhydene.2020.11.116.
- Shahkarami, S., Azargohar, R., Dalai, A.K., Soltan, J., 2015. Breakthrough CO₂ adsorption in bio-based activated carbons. *J. Environ. Sci.* 34, 68–76. doi:10.1016/j.jes.2015.03.008.
- Shahkaramipour, N., Adibi, M., Seifkordi, A., Fazli, Y.J.o.m.s., 2014. Separation of CO₂/CH₄ through alumina-supported geminal ionic liquid membranes. 455, 229–235.
- Shalaby, A., Elkamel, A., Douglas, P.L., Zhu, Q., Zheng, Q.P., 2021. A machine learning approach for modeling and optimization of a CO₂ post-combustion capture unit. *Energy* 215. doi:10.1016/j.energy.2020.119113, 119113–119113.
- Shamair, Z., Habib, N., Gilani, M.A., Khan, A.L., 2020. Theoretical and experimental investigation of CO₂ separation from CH₄ and N₂ through supported ionic liquid membranes. *Appl. Energy* 268, 115016. doi:10.1016/j.applenergy.2020.115016.
- Shamsabadi, A.A., Seidi, F., Salehi, E., Nozari, M., Rahimpour, A., Sorush, M., 2017. Efficient CO₂-removal using novel mixed-matrix membranes with modified TiO₂ nanoparticles. *J. Mater. Chem. A* 5 (8), 4011–4025. doi:10.1039/C6TA09990D.
- Shamsabadi, A.A., Isfahani, A.P., Salestan, S.K., Rahimpour, A., Ghalei, B., Sivaniah, E., Sorush, M., 2019. Pushing rubbery polymer membranes to be economic for CO₂ separation: embedment with Ti₃C₂T_x MXene nanosheets. *ACS Appl. Mater. Interfaces* 12 (3), 3984–3992. doi:10.1021/acsami.9b19960.
- Shang, J., Li, G., Singh, R., Gu, Q., Nairn, K.M., Bastow, T.J., Medhekar, N., Doherty, C.M., Hill, A.J., Liu, J.Z., 2012. Discriminative separation of gases by a “molecular trapdoor” mechanism in chabazite zeolites. *J. Am. Chem. Soc.* 134 (46), 19246–19253.
- Shang, J., Li, G., Singh, R., Xiao, P., Liu, J.Z., Webley, P.A., 2013. Determination of composition range for “molecular trapdoor” effect in chabazite zeolite. *J. Phys. Chem. C* 117 (24), 12841–12847.
- Shao, N., Gavrilidis, A., Angeli, P., 2010. Mass transfer during Taylor flow in microchannels with and without chemical reaction. *Chem. Eng. J.* 160 (3), 873–881. doi:10.1016/j.cej.2010.02.049.
- Shao, Z.D., Cheng, X., Zheng, Y.M., 2018. Facile co-precursor sol-gel synthesis of a novel amine-modified silica aerogel for high efficiency carbon dioxide capture. *J. Colloid. Interface Sci.* 530, 412–423. doi:10.1016/j.jcis.2018.06.094.
- Sharma, I., Hoaldley, A.F.A., Mahajani, S.M., Ganesh, A., 2016. Multi-objective optimization of a Rectisol (TM) process for carbon capture. *J. Clean. Prod.* 119, 196–206. doi:10.1016/j.jclepro.2016.01.078.
- Shash, M.M., 2011. Capturing CO₂ from Oxy-Fuel Combustion Flue Gas. In: *International Oxy-Combustion Research Network for CO₂ Capture Report on Inaugural (1st) Workshop*. Cottbus, Germany.
- Shaw, R., Mukherjee, S., 2022. The development of carbon capture and storage (CCS) in India: A critical review. *Carbon Cap. Sci. Technol.* 2, 100036. doi:10.1016/J.CCST.2022.100036.
- Shayegh, S., Bosetti, V., Tavoni, M., 2021. Future prospects of direct air capture technologies: insights from an expert elicitation survey. *Front. Clim.* 3.
- Shen, W., Fan, W., 2013. Nitrogen-containing porous carbons: synthesis and application. *J. Mater. Chem. A* 1 (4), 999–1013.
- Shen, C., Grande, C.A., Li, P., Yu, J., Rodrigues, A.E., 2010. Adsorption equilibria and kinetics of CO₂ and N₂ on activated carbon beads. *Chem. Eng. J.* 160 (2), 398–407. doi:10.1016/j.cej.2009.12.005.
- Shen, C., Liu, Z., Li, P., Yu, J., 2012. Two-stage VPSA process for CO₂ capture from flue gas using activated carbon beads. *Ind. Eng. Chem. Res.* 51 (13), 5011–5021. doi:10.1021/ie202097y.
- Shen, Y., Linville, J.L., Ignacio-de Leon, P.A.A., Schoene, R.P., Urgan-Demirtas, M., 2016. Towards a sustainable paradigm of waste-to-energy process: Enhanced anaerobic digestion of sludge with woody biochar. *J. Clean. Prod.* 135, 1054–1064. doi:10.1016/j.jclepro.2016.06.144.
- Shen, Y., Zhou, Y., Li, D., Fu, Q., Zhang, D., Na, P., 2017. Dual-reflux pressure swing adsorption process for carbon dioxide capture from dry flue gas. *Int. J. Greenh. Gas Control* 65, 55–64. doi:10.1016/j.jggc.2017.08.020.
- Shen, Y., Shi, W., Zhang, D., Na, P., Fu, B., 2018. The removal and capture of CO₂ from biogas by vacuum pressure swing process using silica gel. *J. CO₂ Util.* 27, 259–271. doi:10.1016/j.jcou.2018.08.001.
- Shen, Q., Cong, S., He, R., Wang, Z., Jin, Y., Li, H., Cao, X., Wang, J., Van der Bruggen, B., Zhang, Y., 2019. SIFSIX-3-Zn/PIM-1 mixed matrix membranes with enhanced permeability for propylene/propane separation. *J. Membr. Sci.* 588, 117201. doi:10.1016/j.memsci.2019.117201.
- Shen, R.X., Lu, J.W., Yao, Z.L., Zhao, L.X., Wu, Y.L., 2021. The hydrochar activation and biocure upgrading from hydrothermal treatment of lignocellulosic biomass. *Bioreour. Technol.* 342. doi:10.1016/j.biortech.2021.125914.
- Shen, M.H., Tong, L.G., Yin, S.W., Liu, C.P., Wang, L., Feng, W.J., Ding, Y.L., 2022. Cryogenic technology progress for CO₂ capture under carbon neutrality goals: A review. *Sep. Purif. Technol.* 299. doi:10.1016/j.seppur.2022.121734.
- Shen, X., Li, H., Zhao, Z., Li, X., Liu, K., Gao, X., 2022. Imaging of liquid temperature distribution during microwave heating via thermochromic metal organic frameworks. *Int. J. Heat Mass Transf.* 189. doi:10.1016/j.ijheatmasstransfer.2022.122667.
- Shi, X., Xiang, Y., Wen, L.X., Chen, J.F., 2013. CFD analysis of liquid phase flow in a rotating packed bed reactor. *Chem. Eng. J.* 228, 1040–1049. doi:10.1016/j.cej.2013.05.081.
- Shi, H., Idem, R., Naami, A., Gelowitz, D., Tontiwachwuthikul, P., 2014a. Catalytic solvent regeneration using hot water during amine based CO₂ capture process. *Energy Procedia* 63, 266–272. doi:10.1016/j.egypro.2014.11.028.
- Shi, H., Naami, A., Idem, R., Tontiwachwuthikul, P., 2014b. Catalytic and non catalytic solvent regeneration during absorption-based CO₂ capture with single and blended reactive amine solvents. *Int. J. Greenh. Gas Control* 26, 39–50. doi:10.1016/j.jggc.2014.04.007.
- Shi, H., Zheng, L., Huang, M., Zuo, Y., Li, M., Jiang, L., Idem, R., Tontiwachwuthikul, P., 2018. CO₂ desorption tests of blended monoethanolamine-diethanolamine solutions to discover novel energy efficient solvents. *Asia-Pac. J. Chem. Eng.* 13 (3). doi:10.1002/apj.2186.
- Shi, Y., Zhong, W., Shao, Y., Liu, X., 2019. Energy efficiency analysis of pressurized oxy-coal combustion system utilizing circulating fluidized bed. *Appl. Therm. Eng.* 150, 1104–1115. doi:10.1016/j.applthermaleng.2019.01.085.
- Shi, H., Fu, J., Wu, Q., Huang, M., Jiang, L., Cui, M., Idem, R., Tontiwachwuthikul, P., 2020. Studies of the coordination effect of DEA-MEA blended amines (within 1 + 4 to 2 + 3 M) under heterogeneous catalysis by means of absorption and desorption parameters. *Sep. Purif. Technol.* 236. doi:10.1016/j.seppur.2019.116179.
- Shi, Y., Liang, B., Lin, R.-B., Zhang, C., Chen, B., 2020. Gas separation via hybrid metal-organic framework/polymer membranes. *Trends Chem.* 2 (3), 254–269.
- Shi, F., Sun, J., Wang, J., Liu, M., Yan, Z., Zhu, B., Li, Y., Cao, X., 2021. MXene versus graphene oxide: Investigation on the effects of 2D nanosheets in mixed matrix membranes for CO₂ separation. *J. Membr. Sci.* 620, 118850. doi:10.1016/j.memsci.2020.118850.
- Shi, H., Cheng, X., Peng, J., Feng, H., Tontiwachwuthikul, P., Hu, J., 2022. The CO₂ absorption and desorption analysis of tri-solvent MEA + EAE + AMP compared with MEA + BEA + AMP along with “coordination effects” evaluation. *Environ. Sci. Pollut. Res. Int.* 29 (27), 40686–40700. doi:10.1007/s11356-022-18792-0.
- Shi, H., Peng, J., Cheng, X., Yang, X., Jin, J., Hu, J., 2022. The CO₂ desorption analysis of tri-solvent MEA+BEA+DEEA with several commercial solid acid catalysts. *Int. J. Greenh. Gas Control* 116. doi:10.1016/j.jggc.2022.103647.
- Shin, D., Kang, S., 2018. Numerical analysis of an ion transport membrane system for oxy-fuel combustion. *Appl. Energy* 230, 875–888. doi:10.1016/J.APENERGY.2018.09.016.
- Shin, D.W., Hyun, S.H., Cho, C.H., Han, M.H., 2005. Synthesis and CO₂/N₂ gas permeation characteristics of ZSM-5 zeolite membranes. *Microporous Mesoporous Mater.* 85 (3), 313–323.
- Shin, J.E., Lee, S.K., Cho, Y.H., Park, H.B., 2019. Effect of PEG-MEA and graphene oxide additives on the performance of Pebax® 1657 mixed matrix membranes for CO₂ separation. *J. Membr. Sci.* 572, 300–308. doi:10.1016/j.memsci.2018.11.025.
- Shulman, A., Cleverstam, E., Mattisson, T., Lyngfelt, A., 2009. Manganese/Iron, Manganese/Nickel, and Manganese/Silicon oxides used in chemical-looping with oxygen uncoupling (clou) for combustion of methane. *Energy Fuels* 23 (10), 5269–5275. doi:10.1021/ef9005466.
- Shulman, A., Cleverstam, E., Mattisson, T., Lyngfelt, A., 2011. Chemical – Looping with oxygen uncoupling using Mn/Mg-based oxygen carriers – Oxygen release and reactivity with methane. *Fuel* 90 (3), 941–950. doi:10.1016/j.fuel.2010.11.044.
- Shuyi, H., Ke, W., Yong, H., Yaling, Q., Ling, H., Shenghua, J., 2014. Research progress of natural gas decarbonization and desulfurization based on alkanolamine. *Nat. Gas and Oil* 32 (03), 19–22. doi:10.3969/j.issn.1006-5539.2014.03.006, +8.
- Siahoosh, M., Fatemi, S., Vatani, A., 2009. Mathematical modeling of single and multi-component adsorption fixed beds to rigorously predict the mass transfer zone and breakthrough curves. *Iran. J. Chem. Chem. Eng.* 28 (3), 25–44.
- Sidhikku Kandath Valappil, R., Ghasem, N., Al-Marzouqi, M., 2021. Current and future trends in polymer membrane-based gas separation technology: A comprehensive review. *J. Ind. Eng. Chem.* 98, 103–129. doi:10.1016/j.jiec.2021.03.030.
- Siefert, N.S., Agarwal, S., Shi, F., Shi, W., Roth, E.A., Hopkinson, D., Kusuma, V.A., Thompson, R.L., Luebke, D.R., Nulwala, H.B., 2016. Hydrophobic physical solvents for pre-combustion CO₂ capture: Experiments, computational simulations, and techno-economic analysis. *Int. J. Greenh. Gas Control* 49, 364–371. doi:10.1016/j.jggc.2016.03.014.
- Siegelman, R.L., McDonald, T.M., Gonzalez, M.I., Martell, J.D., Milner, P.J., Mason, J.A., Berger, A.H., Bhowan, A.S., Long, J.R., 2017. Controlling cooperative CO₂ adsorption in diamine-appended Mg₂ (dobcd) metal-organic frameworks. *J. Am. Chem. Soc.* 139 (30), 10526–10538. doi:10.1021/jacs.7b05858.
- Siegelman, R.L., Kim, E.J., Long, J.R., 2021. Porous materials for carbon dioxide separations. *Nat. Mater.* 20 (8), 1060–1072. doi:10.1038/s41563-021-01054-8.

- Sikarwar, V.S., Pfeifer, C., Ronsse, F., Pohořelý, M., Meers, E., Kaviti, A.K., Jeremiáš, M., 2022. Progress in in-situ CO₂-sorption for enhanced hydrogen production. *Prog. Energy Combust. Sci.* 91, 101008. doi:10.1016/j.peccs.2022.101008.
- Silva, F.W.M.d., Magalhães, G.M., Jardim, E.O., Silvestre-Albergo, J., Sepúlveda-Escribano, A., de Azevedo, D.C.S., de Lucena, S.M.P., 2015. CO₂ adsorption on ionic liquid—modified Cu-BTC: experimental and simulation study. *Adsorpt. Sci. Technol.* 33 (2), 223–242. doi:10.1260/0263-6174.33.2.223.
- Silva, L.P., Moya, C., Sousa, M., Santiago, R., Sintra, T.E., Carreira, A.R.F., Palomar, J., Coutinho, J.A.P., Carvalho, P.J., 2020. Encapsulated amino-acid-based ionic liquids for CO₂ capture. *Eur. J. Inorg. Chem.* 2020 (33), 3158–3166. doi:10.1002/ejic.202000364.
- Simo, M., Brown, C.J., Hlavacek, V., 2008. Simulation of pressure swing adsorption in fuel ethanol production process. *Comput. Chem. Eng.* 32 (7), 1635–1649. doi:10.1016/j.compchemeng.2007.07.011.
- Singh, R., Ram Reddy, M.K., Wilson, S., Joshi, K., Diniz da Costa, J.C., Webley, P., 2009. High temperature materials for CO₂ capture. *Energy Procedia* 1 (1), 623–630. doi:10.1016/j.egypro.2009.01.082.
- Singh, G., Lakhi, K.S., Sil, S., Bhosale, S.V., Kim, I., Albahily, K., Vinu, A., 2019. Biomass derived porous carbon for CO₂ capture. *Carbon* 148, 164–186. doi:10.1016/j.carbon.2019.03.050.
- Singh, S., Kumar, V., Dhanjal, D.S., Datta, S., Bhatia, D., Dhiman, J., Samuel, J., Prasad, R., Singh, J., 2020. A sustainable paradigm of sewage sludge biochar: Valorization, opportunities, challenges and future prospects. *J. Clean. Prod.* 269, 122259. doi:10.1016/j.jclepro.2020.122259.
- Singh, E., Mishra, R., Kumar, A., Shukla, S.K., Lo, S.-L., Kumar, S., 2022. Circular economy-based environmental management using biochar: Driving towards sustainability. *Process. Saf. Environ. Prot.* 163, 585–600. doi:10.1016/j.psep.2022.05.056.
- Singto, S., Supap, T., Idem, R., Tontiwachwuthikul, P., Tantayanon, S., Al-Marri, M.J., Benamor, A., 2016. Synthesis of new amines for enhanced carbon dioxide (CO₂) capture performance: The effect of chemical structure on equilibrium solubility, cyclic capacity, kinetics of absorption and regeneration, and heats of absorption and regeneration. *Sep. Purif. Technol.* 167, 97–107. doi:10.1016/j.seppur.2016.05.002.
- Sinha, A., Realf, M.J., 2019. A parametric study of the techno-economics of direct CO₂ air capture systems using solid adsorbents. *AIChE J.* 65 (7), e16607. doi:10.1002/aic.16607.
- Sinha, A., Darunte, L.A., Jones, C.W., Realf, M.J., Kawajiri, Y., 2017. Systems design and economic analysis of direct air capture of CO₂ through temperature vacuum swing adsorption using MIL-101 (Cr)-PEI-800 and mmen-Mg2 (dobpdc) MOF adsorbents. *Ind. Eng. Chem. Res.* 56 (3), 750–764. doi:10.1021/acs.iecr.6b03887.
- Sinha, A., Darunte, L.A., Jones, C.W., Realf, M.J., Kawajiri, Y., 2020. Correction to “systems design and economic analysis of direct air capture of CO₂ through temperature vacuum swing adsorption using MIL-101 (Cr)-PEI-800 and mmen-Mg2 (dobpdc) MOF adsorbents”. *Ind. Eng. Chem. Res.* 59 (1), 503–505. doi:10.1021/acs.iecr.9b06779.
- Sipöcz, N., Tobiesen, F.A., Assadi, M., 2011. The use of Artificial Neural Network models for CO₂ capture plants. *Applied Energy* 88 (7), 2368–2376.
- Sircar, S., Kratz, W., 1988. Simultaneous production of hydrogen and carbon dioxide from steam reformer off-gas by pressure swing adsorption. *Sep. Sci. Technol.* 23 (14), 2397–2415.
- Siriwardane, R.V., Shen, M.-S., Fisher, E.P., Poston, J.A., 2001. Adsorption of CO₂ on molecular sieves and activated carbon. *Energy Fuels* 15 (2), 279–284. doi:10.1021/e000241s.
- Siriwardane, R.V., Shen, M.S., Fisher, E.P., Losch, J., 2005. Adsorption of CO₂ on zeolites at moderate temperatures. *Energy Fuels* 19, 1153–1159.
- Skarstrom, C.W., Attorney, O.-O.I., 1958. Method and apparatus for fractionating gaseous mixtures by absorption. *US Pat.*
- Skarstrom, C.W., 1960. Method and Apparatus for Fractionating Gaseous Mixtures by Adsorption, in: *US (Ed.) ExxonMobil Research and Engineering Co., US.*
- Skorek-Osikowska, A., Bartela, L., Kotowicz, J., 2015. A comparative thermodynamic, economic and risk analysis concerning implementation of oxy-combustion power plants integrated with cryogenic and hybrid air separation units. *Energy Convers. Manage.* 92, 421–430. doi:10.1016/j.enconman.2014.12.079.
- Skulimowska, A., Di Felice, L., Kamińska-Pietrzak, N., Celińska, A., Pławicka, M., Hercog, J., Krauz, M., Aranda, A., 2017. Chemical looping with oxygen uncoupling (CLOU) and chemical looping combustion (CLC) using copper-enriched oxygen carriers supported on fly ash. *Fuel Process. Technol.* 168, 123–130. doi:10.1016/j.fuproc.2017.08.035.
- Slater, A.G., Cooper, A.I., 2015. Porous materials. Function-led design of new porous materials. *Science* 348 (6238), aaa8075. doi:10.1126/science.aaa8075.
- Smith, A.R., Klosek, J., 2001. A review of air separation technologies and their integration with energy conversion processes. *Fuel Process. Technol.* 70 (2), 115–134. doi:10.1016/S0378-3820(01)00131-X.
- Smith, K., Lee, A., Mumford, K., Li, S., Indrawan, Thanumrthy, N., Temple, N., Anderson, C., Hooper, B., Kentish, S., Stevens, G., 2015. Pilot plant results for a precipitating potassium carbonate solvent absorption process promoted with glycine for enhanced CO₂ capture. *Fuel Process. Technol.* 135, 60–65. doi:10.1016/j.fuproc.2014.10.013.
- Smith, S.J., Hou, R., Lau, C.H., Konstas, K., Kitchin, M., Dong, G., Lee, J., Lee, W.H., Seong, J.G., Lee, Y.M., 2019. Highly permeable thermally rearranged mixed matrix membranes (TR-MMM). *J. Membr. Sci.* 585, 260–270. doi:10.1016/j.memsci.2019.05.046.
- Smith, S.J., Hou, R., Konstas, K., Akram, A., Lau, C.H., Hill, M.R., 2020. Control of physical aging in super-glassy polymer mixed matrix membranes. *Acc. Chem. Res.* 53 (7), 1381–1388. doi:10.1021/acs.accounts.0c00256.
- Smith, K.H., Ashkanani, H.E., Morsi, B.I., Siefert, N.S., 2022. Physical solvents and techno-economic analysis for pre-combustion CO₂ capture: A review. *Int. J. Greenh. Gas Control* 118, 103694. doi:10.1016/j.jggcc.2022.103694.
- Sneha, B.R., Thangadurai, V., 2007. Synthesis of nano-sized crystalline oxide ion conducting fluorite-type Y₂O₃-doped CeO₂ using perovskite-like BaCe_{0.9}Y_{0.1}O_{2.95} (BCY) and study of CO₂ capture properties of BCY. *J. Solid State Chem.* 180 (10), 2661–2669. doi:10.1016/j.jssc.2007.07.016.
- Soares, J.L., Moreira, R.F.P.M., José, H.J., Grande, C.A., Rodrigues, A.E., 2005. Hydrotalcite materials for carbon dioxide adsorption at high temperatures: characterization and diffusivity measurements. *Sep. Sci. Technol.* 39 (9), 1989–2010. doi:10.1081/SS-120039307.
- Socolow, R., Desmond, M., Aines, R., Blackstock, J., Bolland, O., Kaarsberg, T., Lewis, N., Mazzotti, M., Pfeffer, A., Sawyer, K., Siirola, J., Smit, B., Wilcox, J., 2011. *Direct Air Capture of CO₂ with Chemicals: A Technology Assessment for the APS Panel on Public Affairs.* American Physical Society.
- Socolow, R., Desmond, M., Aines, R., Blackstock, J., Bolland, O., Kaarsberg, T., Newis, N., Mazzotti, M., Pfeffer, A., Sawyer, K., Siirola, J., Smit, B., Wilcox, J., 2011. Direct air capture of CO₂ with chemicals: a technology assessment for the APS panel on public affairs, in: *Society, A.P. (Ed.)*
- Soetemans, L., Uytendaele, M., Bastiaens, L., 2020. Characteristics of chitin extracted from black soldier fly in different life stages. *Int. J. Biol. Macromol.* 165, 3206–3214. doi:10.1016/j.jbiomac.2020.11.041.
- Sohail, M., An, H., Choi, W., Singh, J., Yim, K., Kim, B.H., Park, Y.C., Lee, J.S., Kim, H., 2021. Sorption-enhanced thin film composites with metal-organic polyhedral nanocages for CO₂ separation. *J. Membr. Sci.* 620, 118826. doi:10.1016/j.memsci.2020.118826.
- Solomenko, Z., Haroun, Y., Fourati, M., Larachi, F., Boyer, C., Augier, F., 2015. Liquid spreading in trickle-bed reactors: Experiments and numerical simulations using Eulerian-Eulerian two-fluid approach. *Chem. Eng. Sci.* 126, 698–710. doi:10.1016/j.ces.2015.01.013.
- Son, W.-J., Choi, J.-S., Ahn, W.-S., 2008. Adsorptive removal of carbon dioxide using polyethyleneimine-loaded mesoporous silica materials. *Microporous Mesoporous Mater.* 113 (1–3), 31–40. doi:10.1016/j.micromeso.2007.10.049.
- Song, C.F., Kitamura, Y., Li, S.H., 2012a. Evaluation of Stirling cooler system for cryogenic CO₂ capture. *Appl. Energy* 98, 491–501. doi:10.1016/j.apenergy.2012.04.013.
- Song, C.F., Kitamura, Y., Li, S.H., Jiang, W.Z., 2012b. Parametric analysis of a novel cryogenic CO₂ capture system based on Stirling coolers. *Environ. Sci. Technol.* 46 (22), 12735–12741. doi:10.1021/es3025947.
- Song, C.F., Kitamura, Y., Li, S.H., Ogasawara, K., 2012c. Design of a cryogenic CO₂ capture system based on Stirling coolers. *Int. J. Greenh. Gas Control* 7, 107–114. doi:10.1016/j.jggcc.2012.01.004.
- Song, C., Kitamura, Y., Li, S., 2014. Energy analysis of the cryogenic CO₂ capture process based on Stirling coolers. *Energy* 65, 580–589. doi:10.1016/j.energy.2013.10.087.
- Song, C., Kansha, Y., Fu, Q., Ishizuka, M., Tsutsumi, A., 2016. Reducing energy consumption of advanced PTA CO₂ capture process—Experimental and numerical study. *J. Taiwan Instit. Chem. Eng.* 64, 69–78. doi:10.1016/j.jtice.2015.12.006.
- Song, C., Liu, Q., Ji, N., Deng, S., Zhao, J., Li, Y., Kitamura, Y., 2017. Reducing the energy consumption of membrane-cryogenic hybrid CO₂ capture by process optimization. *Energy* 124, 29–39. doi:10.1016/j.energy.2017.02.054.
- Song, C.F., Liu, Q.L., Ji, N., Deng, S., Zhao, J., Kitamura, Y., 2017. Advanced cryogenic CO₂ capture process based on Stirling coolers by heat integration. *Appl. Therm. Eng.* 114, 887–895. doi:10.1016/j.applthermaleng.2016.12.049.
- Song, C., Fan, Z., Li, R., Liu, Q., Kitamura, Y., 2018a. Efficient biogas upgrading by a novel membrane-cryogenic hybrid process: Experiment and simulation study. *J. Membr. Sci.* 565, 194–202. doi:10.1016/j.memsci.2018.08.027.
- Song, C., Liu, Q., Ji, N., Deng, S., Zhao, J., Li, Y., Song, Y., Li, H., 2018b. Alternative pathways for efficient CO₂ capture by hybrid processes—A review. *Renew. Sustain. Energy Rev.* 82, 215–231. doi:10.1016/j.rser.2017.09.040.
- Song, C., Liu, J., Xie, M., Qiu, Y., Chen, G., Qi, Y., Kitamura, Y., 2019a. Intensification of a novel absorption-microalgae hybrid CO₂ utilization process via fed-batch mode optimization. *Int. J. Greenh. Gas Control* 82, 1–7. doi:10.1016/j.jggcc.2019.01.001.
- Song, C., Liu, Q., Deng, S., Li, H., Kitamura, Y., 2019b. Cryogenic-based CO₂ capture technologies: State-of-the-art developments and current challenges. *Renew. Sustain. Energy Rev.* 101, 265–278. doi:10.1016/j.rser.2018.11.018.
- Song, C., Xie, M., Qiu, Y., Liu, Q., Sun, L., Wang, K., Kansha, Y., 2019c. Integration of CO₂ absorption with biological transformation via using rich ammonia solution as a nutrient source for microalgae cultivation. *Energy* 179, 618–627. doi:10.1016/j.energy.2019.05.039.
- Soubeyrand-Lenoir, E., Vagner, C., Yoon, J.W., Bazin, P., Ragon, F., Hwang, Y.K., Serre, C., Chang, J.S., Llewellyn, P.L., 2012. How water fosters a remarkable 5-fold increase in low-pressure CO₂ uptake within mesoporous MIL-100 (Fe). *J. Am. Chem. Soc.* 134 (24), 10174–10181. doi:10.1021/ja302787x.
- Soundararajan, R., Gundersen, T., 2013. Coal based power plants using oxy-combustion for CO₂ capture: Pressurized coal combustion to reduce capture penalty. *Appl. Therm. Eng.* 61 (1), 115–122. doi:10.1016/j.applthermaleng.2013.04.010.
- Spiegel, N., Long, X., Berruoco, C., Paterson, M., Millan, M., 2021. Oxy-fuel co-gasification of coal and biomass for negative CO₂ emissions. *Fuel* 306, 121671. doi:10.1016/j.fuel.2021.121671.
- Spitler, E.L., Giovino, M.R., White, S.L., Dichtel, W.R., 2011. A mechanistic study of Lewis acid-catalyzed covalent organic framework formation. *Chem. Sci.* 2 (8), 1588–1593.
- Spitoni, M., Pierantozzi, M., Comodi, G., Polonara, F., Artecconi, A., 2019. Theoretical evaluation and optimization of a cryogenic technology for carbon dioxide separation and methane liquefaction from biogas. *J. Nat. Gas Sci. Eng.* 62, 132–143. doi:10.1016/j.jngse.2018.12.007.
- Sreedhar, I., Nahar, T., Venugopal, A., Srinivas, B., 2017. Carbon capture by absorption – Path covered and ahead. *Renew. Sustain. Energy Rev.* 76, 1080–1107. doi:10.1016/j.rser.2017.03.109.

- Srisang, W., Pouryousefi, F., Osei, P.A., Decardi-Nelson, B., Akachuku, A., Tontiwachuthikul, P., Idem, R., 2017. Evaluation of the heat duty of catalyst-aided amine-based post combustion CO₂ capture. *Chem. Eng. Sci.* 170, 48–57. doi:10.1016/j.ces.2017.01.049.
- Srisang, W., Pouryousefi, F., Osei, P.A., Decardi-Nelson, B., Akachuku, A., Tontiwachuthikul, P., Idem, R., 2018. CO₂ capture efficiency and heat duty of solid acid catalyst-aided CO₂ desorption using blends of primary-tertiary amines. *Int. J. Greenh. Gas Control* 69, 52–59. doi:10.1016/j.jggcc.2017.12.010.
- Stöhr, B., Boehm, H.P., Schlögl, R., 1991. Enhancement of the catalytic activity of activated carbons in oxidation reactions by thermal treatment with ammonia or hydrogen cyanide and observation of a superoxide species as a possible intermediate. *Carbon* 29 (6), 707–720. doi:10.1016/0008-6223(91)90006-5.
- Stadler, H., Beggel, F., Habermehl, M., Persigehl, B., Kneer, R., Modigell, M., Jeschke, P., 2011. Oxidative coal combustion by efficient integration of oxygen transport membranes. *Int. J. Greenh. Gas Control* 5 (1), 7–15. doi:10.1016/j.jggcc.2010.03.004.
- Stanger, R., Wall, T., Spörl, R., Paneru, M., Grathwohl, S., Weidmann, M., Scheffknecht, G., McDonald, D., Myöhänen, K., Ritvanen, J., Rahiala, S., Hyppänen, T., Mletzko, J., Kather, A., Santos, S., 2015. Oxidative combustion for CO₂ capture in power plants. *Int. J. Greenh. Gas Control* 40, 55–125. doi:10.1016/j.jggcc.2015.06.010.
- Stanovsky, P., Zitkova, A., Karaszova, M., Šyc, M., Jansen, J.C., Comesaña Gándara, B., McKeown, N., Izak, P., 2020. Flue gas purification with membranes based on the polymer of intrinsic microporosity PIM-TMN-Trip. *Sep. Purif. Technol.* 242, 116814. doi:10.1016/j.seppur.2020.116814.
- Starr, K., Gabarrell, X., Villalba, G., Talens, L., Lombardi, L., 2012. Life cycle assessment of biogas upgrading technologies. *Waste Manage.* 32 (5), 991–999. doi:10.1016/j.wasman.2011.12.016.
- Steinberg, M., Dang, V.-D., 1977. Production of synthetic methanol from air and water using controlled thermionic reactor power—I. technology and energy requirement. *Energy Convers.* 17 (2), 97–112. doi:10.1016/0013-7480(77)90080-8.
- Stephene, K., 2015. Start-Up of World's first commercial post-combustion coal fired CCS Project: Contribution of shell cansolv to SaskPower boundary dam ICCS project. In: *International Conference on Greenhouse Gas Control Technologies*.
- Stiernet, P., Mazaj, M., Kovačić, S., Debuigne, A., 2022. Bifunctional imidazolium/amine polymer foams: One-pot synthesis and synergistic promotion of CO₂ sorption. *Chem. Eng. J.* 446. doi:10.1016/j.cej.2022.137012.
- Stolaroff, J.K., Keith, D.W., Lowry, G.V., 2008. Carbon dioxide capture from atmospheric air using sodium hydroxide spray. *Environ. Sci. Technol.* 42 (8), 2728–2735. doi:10.1021/es702607w.
- Ströhle, J., Lasheras, A., Galloy, A., Eppe, B., 2009. Simulation of the carbonate looping process for post-combustion CO₂ capture from a coal-fired power plant. *Chem. Eng. Technol.* 32 (3), 435–442. doi:10.1002/CEAT.200800569.
- Ströhle, J., Hilz, J., Eppe, B., 2020. Performance of the carbonator and calciner during long-term carbonate looping tests in a 1 MWh pilot plant. *J. Environ. Chem. Eng.* 8 (1), 103578. doi:10.1016/j.jece.2019.103578.
- Stylianou, M., Christou, A., Dalias, P., Polycarpo, P., Michael, C., Agapiou, A., Papanastasiou, P., Fatta-Kassinos, D., 2020. Physicochemical and structural characterization of biochar derived from the pyrolysis of biosolids, cattle manure and spent coffee grounds. *J. Environ. Syst.* 93 (5), 2063–2073. doi:10.1016/j.joei.2020.05.002.
- Su, F., Lu, C., 2012. CO₂ capture from gas stream by zeolite 13X using a dual-column temperature/vacuum swing adsorption. *Energy Environ. Sci.* 5 (10), doi:10.1039/c2ee22647b.
- Su, F., Lu, C., Chen, W., Bai, H., Hwang, J.F., 2009. Capture of CO₂ from flue gas via multiwalled carbon nanotubes. *Sci. Total Environ.* 407 (8), 3017–3023. doi:10.1016/j.scitotenv.2009.01.007.
- Su, F., Lu, C., Kuo, S.-C., Zeng, W., 2010. Adsorption of CO₂ on amine-functionalized Y-type zeolites. *Energy Fuels* 24 (2), 1441–1448. doi:10.1021/ef901077k.
- Su, F., Lu, C., Chen, H.S., 2011. Adsorption, desorption, and thermodynamic studies of CO₂ with high-amine-loaded multiwalled carbon nanotubes. *Langmuir* 27 (13), 8090–8098. doi:10.1021/la201745y.
- Su, X., Bromberg, L., Martis, V., Simeon, F., Huq, A., Hatton, T.A., 2017. Postsynthetic functionalization of Mg-MOF-74 with tetraethylenepentamine: structural characterization and enhanced CO₂ adsorption. *ACS Appl. Mater. Interfaces* 9 (12), 11299–11306. doi:10.1021/acsmi.7b02471.
- Sublet, J., Pera-Titus, M., Guilhaume, N., Farrusseng, D., Schrive, L., Chanaud, P., Siret, B., Duréu, S., 2012. Technico-economic assessment of MFI-type zeolite membranes for CO₂ capture from postcombustion flue gases. *AIChE J.* 58 (10), 3183–3194.
- Subramanian Balashankar, V., Rajendran, A., 2019. Process optimization-based screening of zeolites for post-combustion CO₂ capture by vacuum swing adsorption. *ACS Sustain. Chem. Eng.* 7 (21), 17747–17755. doi:10.1021/acssuschemeng.9b04124.
- Subramanian Balashankar, V., Rajagopalan, A.K., de Pauw, R., Avila, A.M., Rajendran, A., 2019. Analysis of a batch adsorbent analogue for rapid screening of adsorbents for postcombustion CO₂ capture. *Ind. Eng. Chem. Res.* 58 (8), 3314–3328. doi:10.1021/acs.iecr.8b05420.
- Subraveti, S.G., Li, Z., Prasad, V., Rajendran, A., 2019a. Machine learning-based multi-objective optimization of pressure swing adsorption. *Ind. Eng. Chem. Res.* 58 (44), 20412–20422. doi:10.1021/acs.iecr.9b04173.
- Subraveti, S.G., Pai, K.N., Rajagopalan, A.K., Wilkins, N.S., Rajendran, A., Jayaraman, A., Alptekin, G., 2019b. Cycle design and optimization of pressure swing adsorption cycles for pre-combustion CO₂ capture. *Appl. Energy* 254, 113624. doi:10.1016/j.apenergy.2019.113624.
- Subraveti, S.G., Roussanly, S., Anantharaman, R., Riboldi, L., Rajendran, A., 2021. Techno-economic assessment of optimised vacuum swing adsorption for post-combustion CO₂ capture from steam-methane reformer flue gas. *Sep. Purif. Technol.* 256. doi:10.1016/j.seppur.2020.117832, 117832–117832.
- Subraveti, S.G., Roussanly, S., Anantharaman, R., Riboldi, L., Rajendran, A., 2022. How much can novel solid sorbents reduce the cost of post-combustion CO₂ capture? A techno-economic investigation on the cost limits of pressure–vacuum swing adsorption. *Appl. Energy* 306. doi:10.1016/j.apenergy.2021.117955, 11795–11795.
- Subrenat, A.S., Le Cloirec, P.A., 2006. Volatile organic compound (Voc) removal by adsorption onto activated carbon fiber cloth and electrothermal desorption: An industrial application. *Chem. Eng. Commun.* 193 (4), 478–486. doi:10.1080/00986440500191768.
- Sudhoff, D., Leimbrink, M., Schleinitz, M., Górák, A., Lütze, P., 2015. Modelling, design and flexibility analysis of rotating packed beds for distillation. *Chem. Eng. Res. Des.* 94, 72–89. doi:10.1016/j.cherd.2014.11.015.
- Suhas, Gupta, V.K., Carrott, P.J.M., Singh, R., Chaudhary, M., Kushwaha, S., 2016. Cellulose: A review as natural, modified and activated carbon adsorbent. *Bioresour. Technol.* 216, 1066–1076. doi:10.1016/j.biortech.2016.05.106.
- Sujan, A.R., Koh, D.-Y., Zhu, G., Babu, V.P., Stephenson, N., Rosinski, A., Du, H., Luo, Y., Koros, W.J., Lively, R.P., 2018. High-temperature activation of zeolite-loaded fiber sorbents. *Ind. Eng. Chem. Res.* 57 (34), 11757–11766. doi:10.1021/acs.iecr.8b02210.
- Sun, P., Grace, J.R., Lim, C.J., Anthony, E.J., 2007. The effect of CaO sintering on cyclic CO₂ capture in energy systems. *AIChE J.* 53 (9), 2432–2442. doi:10.1002/aic.11251.
- Sun, Y., Cui, F., Shi, K., Wang, J., Niu, M., Ma, R., 2009. The effect of chitosan molecular weight on the characteristics of spray-dried methotrexate-loaded chitosan microspheres for nasal administration. *Drug Dev. Ind. Pharm.* 35 (3), 379–386. doi:10.1080/03639040802395185.
- Sun, X.F., Liu, S.Y., Khan, A., Zhao, C., Yan, C.Y., Mu, T.C., 2014. Ionicity of acetate-based protic ionic liquids: evidence for both liquid and gaseous phases. *New J. Chem.* 38 (8), 3449–3456. doi:10.1039/c4nj00384e.
- Sun, J., Liu, W., Hu, Y., Li, M., Yang, X., Zhang, Y., Xu, M., 2015. Structurally improved, core-in-shell, CaO-based sorbent pellets for CO₂ capture. *Energy Fuels* 29 (10), 6636–6644. doi:10.1021/acs.energyfuels.5b01419.
- Sun, J., Liang, C., Tong, X., Guo, Y., Li, W., Zhao, C., Zhang, J., Lu, P., 2019. Evaluation of high-temperature CO₂ capture performance of cellulose-templated CaO-based pellets. *Fuel* 239, 1046–1054. doi:10.1016/j.fuel.2018.11.123.
- Sun, H., Wang, J., Liu, X., Shen, B., Parlett, Christopher, M.A., Adwek, G.O., John Anthony, E., Williams, P.T., Wu, C., 2019. Fundamental studies of carbon capture using CaO-based materials. *J. Mater. Chem. A* 7 (16), 9977–9987. doi:10.1039/C8TA10472G.
- Sun, M., Gu, Q., Hanif, A., Wang, T., Shang, J., 2019. Transition metal cation-exchanged SSZ-13 zeolites for CO₂ capture and separation from N₂. *Chem. Eng. J.* 370, 1450–1458.
- Sun, B., Bhatelia, T., Utikar, R.P., Evans, G.M., Pareek, V.K., 2021. Study on hydrodynamic performance of structured packings for gas-liquid flow: Effects of geometry parameters. *Chem. Eng. Res. Des.* 167, 6–9. doi:10.1016/j.cherd.2021.01.003.
- Sun, Q., Mao, Y., Gao, H., Sema, T., Liang, Z., 2021. Efficient nickel-based catalysts for amine regeneration of CO₂ capture: From experimental to calculations verifications. *Sunaro, J., Baumann, S., Serra, J.M., Meulenber, W.A., Liu, S., Lin, Y.S., Diniz da Costa, J.C., 2008. Mixed ionic–electronic conducting (MIEC) ceramic-based membranes for oxygen separation. J. Membr. Sci.* 320, 13–41. doi:10.1016/j.memsci.2008.03.074.
- Suroutseua, D., Amin, R., Barifanji, A., 2011. Design and operation of pilot plant for CO₂ capture from IGCC flue gases by combined cryogenic and hydrate method. *Chem. Eng. Res. Des.* 89 (9), 1752–1757. doi:10.1016/j.cherd.2010.08.016.
- Sutrisna, P.D., Hou, J., Li, H., Zhang, Y., Chen, V., 2017. Improved operational stability of Pebax-based gas separation membranes with ZIF-8: A comparative study of flat sheet and composite hollow fibre membranes. *J. Membr. Sci.* 524, 266–279. doi:10.1016/j.memsci.2016.11.048.
- Sutrisna, P.D., Hou, J., Zulkifli, M.Y., Li, H., Zhang, Y., Liang, W., D'Alessandro, D.M., Chen, V., 2018. Surface functionalized UiO-66/Pebax-based ultrathin composite hollow fiber gas separation membranes. *J. Mater. Chem. A* 6 (3), 918–931. doi:10.1039/C7TA07512J.
- Suzuki, T.J.P., 2021. Gas transport properties of thermally rearranged (TR) polybenzoxazole–silica hybrid membranes. 214, 123274.
- Swati, I.K., Sohaib, Q., Cao, S., Younas, M., Liu, D., Gui, J., Rezakazemi, M., 2021. Protic/aprotic ionic liquids for effective CO₂ separation using supported ionic liquid membrane. *Chemosphere* 267, 128894. doi:10.1016/j.chemosphere.2020.128894.
- Syeda Saba Fatima, A.B., Ayoub, M., Abd Ghani, N., 2021. Development and progress of functionalized silica-based adsorbents for CO₂ capture. *J. Mol. Liq.* 338, 116913. doi:10.1016/j.molliq.2021.116913.
- Taylor, R., Sayari, A., 2016. Grafted propyldiethanolamine for selective removal of SO₂ in the presence of CO₂. *Chem. Eng. J.* 289, 142–149. doi:10.1016/j.cej.2015.12.084.
- Tajima, H., Yamasaki, A., Kiyono, F., 2004. Energy consumption estimation for greenhouse gas separation processes by clathrate hydrate formation. *Energy* 29 (11), 1713–1729. doi:10.1016/j.energy.2004.03.003.
- Takuo, N., Hitoshi, K., Shinzo, Y., Shinzo, K., 1979. The polymerization of β-propiolactone by chelated synthetic hydroxalcalite. 52 (8), 2449–2450. https://doi.org/10.1246/bcsj.52.2449.
- Tan, X., Wang, Z., Meng, B., Meng, X., Li, K., 2010. Pilot-scale production of oxygen from air using perovskite hollow fibre membranes. *J. Membr. Sci.* 352, 189–196. doi:10.1016/j.memsci.2010.02.015.
- Tan, J., Shao, H., Xu, J., Du, L., Luo, G., 2011. Mixture absorption system of monoethanolamine–triethylene glycol for CO₂ capture. *Ind. Eng. Chem. Res.* 50 (7), 3966–3976. doi:10.1021/ie101810a.
- Tan, Y., Nookuea, W., Li, H., Thorin, E., Yan, J., 2017. Cryogenic technology for biogas upgrading combined with carbon capture - a review of systems and property impacts. *Energy Procedia* 142, 3741–3746. doi:10.1016/j.egypro.2017.12.270.
- Tan, H., Wen, N., Ding, Z., 2021. Computational fluid dynamics simulation of multi-phase flow characteristics in an industrial-scale randomly packed tower. *Asia-Pac. J. Chem. Eng.* 16 (6). doi:10.1002/apj.2708, e2708–e2708.

- Tanaka, K., Kita, H., Okano, M., Okamoto, K.-i., 1992. Permeability and permselectivity of gases in fluorinated and non-fluorinated polyimides. *Polymer* 33 (3), 585–592. doi:10.1016/0032-3861(92)90736-6.
- Tang, Z., Han, Z., Yang, G., Yang, J., 2013. Polyethyleneimine loaded nanoporous carbon with ultra-large pore volume for CO₂ capture. *Appl. Surf. Sci.* 277, 47–52. doi:10.1016/j.apsusc.2013.03.142.
- Tang, B., White, S.P., Frisbie, C.D., Lodge, T.P., 2015. Synergistic increase in ionic conductivity and modulus of triblock copolymer ion gels. *Macromolecules* 48 (14), 4942–4950. doi:10.1021/acs.macromol.5b00882.
- Tao, M., Gao, J., Zhang, W., Li, Y., He, Y., Shi, Y., 2018. A novel phase-changing nonaqueous solution for CO₂ capture with high capacity, thermostability, and regeneration efficiency. *Ind. Eng. Chem. Res.* 57 (28), 9305–9312. doi:10.1021/acs.iecr.8b01775.
- Tawalbeh, M., Al-Ismaïl, M., Kruczek, B., Tezel, F.H., 2021. Modeling the transport of CO₂, N₂, and their binary mixtures through highly permeable silicalite-1 membranes using Maxwell–Stefan equations. *Chemosphere* 263, 127935.
- Teixeira, P., Bacariza, C., Correia, P., Pinheiro, C.I.C., Cabrita, I., 2022. Hydrogen production with in situ CO₂ capture at high and medium temperatures using solid sorbents. *Energies* 15 (11), 44. doi:10.3390/en15114039.
- Tepe, J., Dodge, B., 1943. Absorption of carbon dioxide by sodium hydroxide solutions in a packed column. *Trans. Am. Inst. Chem. Eng.* 39, 255–276.
- Teramoto, M., Nakai, K., Ohnishi, N., Huang, Q., Watari, T., Matsuyama, H., 1996. Facilitated transport of carbon dioxide through supported liquid membranes of aqueous amine solutions. *Ind. Eng. Chem. Res.* 35 (2), 538–545. doi:10.1021/ie950112c.
- Teramoto, M., Huang, Q., Watari, T., Tokunaga, Y., Nakatani, R., Maeda, T., Matsuyama, H., 1997. Facilitated transport of CO₂ through supported liquid membranes of various amine solutions—Effects of rate and equilibrium of reaction between CO₂ and Amine—*J. Chem. Eng. Jpn.* 30 (2), 328–335. doi:10.1252/cej.30.328.
- Thakkar, H., Issa, A., Rowanghi, A.A., Rezaei, F., 2017. CO₂ capture from air using amine-functionalized kaolin-based zeolites. *Chem. Eng. Technol.* 40 (11), 1999–2007. doi:10.1002/ceat.201700188.
- Thankamony, R.L., Li, X., Das, S.K., Ostwal, M.M., Lai, Z., 2019. Porous covalent triazine piperazine polymer (CTPP)/PEBAX mixed matrix membranes for CO₂/N₂ and CO₂/CH₄ separations. *J. Membr. Sci.* 591, 117348. doi:10.1016/j.memsci.2019.117348.
- Thiels, M., et al., 2016. Modelling and Design of Carbon Dioxide Absorption in Rotating Packed Bed and Packed Column. *IFAC-PapersOnLine* 49 (7), 895–900.
- Thompson, J.A., Brunelli, N.A., Lively, R.P., Johnson, J.R., Jones, C.W., Nair, S., 2013. Tunable CO₂ adsorbents by mixed-linker synthesis and postsynthetic modification of zeolitic imidazolate frameworks. *J. Phys. Chem. C* 117 (16), 8198–8207. doi:10.1021/jp312590r.
- Thomsen, K., Rasmussen, P., 1999. Modeling of vapour–liquid–solid equilibrium in gas–aqueous electrolyte systems. *Chem. Eng. Sci.* 54 (12), 1787–1802.
- Tian, H., Guo, Q., Chang, J., 2008. Investigation into decomposition behavior of CaSO₄ in chemical-looping combustion. *Energy Fuels* 22 (6), 3915–3921. doi:10.1021/ef800580w.
- Tian, H., Simonyi, T., Poston, J., Sriwardane, R., 2009. Effect of hydrogen sulfide on chemical looping combustion of coal-derived synthesis gas over bentonite-supported metal–oxide oxygen carriers. *Ind. Eng. Chem. Res.* 48 (18), 8418–8430. doi:10.1021/ie900638p.
- Tian, X., Wei, Y., Zhao, H., 2017. Evaluation of a hierarchically-structured CuO/TiO₂-Al₂O₃ oxygen carrier for chemical looping with oxygen uncoupling. *Fuel* 209, 402–410. doi:10.1016/j.fuel.2017.08.022.
- Tian, L., Liang, F., Dong, L.H., Li, J.Y., Jia, Q.L., Zhang, H.J., Yan, S., Zhang, S.W., 2021. Preparation and enhanced adsorption properties for CO (2) and dyes of amino-decorated hierarchical porous BCN aerogels. *J. Am. Ceram. Soc.* 104 (2), 1110–1119. doi:10.1111/jace.17501.
- Tian, M., Wang, C., Han, Y., Wang, X., 2021. Recent advances of oxygen carriers for chemical looping reforming of methane. *ChemCatChem* 13 (7), 1615–1637. doi:10.1002/cctc.202001481.
- Tian, J., Shen, Y., Zhang, D., Tang, Z., 2021. CO₂ capture by vacuum pressure swing adsorption from flue gas with a structured composite adsorption medium. *J. Environ. Chem. Eng.* 9 (5), 106037. doi:10.1016/j.jece.2021.106037.
- Tian, H., Wei, Y., Cheng, S., Huang, Z., Qing, M., Chen, Y., Yang, H., Yang, Y., 2022. Optimizing the gasification reactivity of biochar: The composition, structure and kinetics of biochar derived from biomass lignocellulosic components and their interactions during gasification process. *Fuel* 324, 124709. doi:10.1016/j.fuel.2022.124709.
- Tilford, R.W., Gemmill, W.R., zur Loye, H.-C., Lavigne, J.J., 2006. Facile synthesis of a highly crystalline, covalently linked porous boronate network. *Chem. Mater.* 18 (22), 5296–5301.
- Tinnirello, M., Papurello, D., Santarelli, M., Fiorilli, S., 2020. Thermal activation of digested sewage sludges for carbon dioxide removal from biogas. *Fuels* 1 (1), 30–46. doi:10.3390/fuels1010004.
- Titirici, M.M., Antonietti, M., 2010. Chemistry and materials options of sustainable carbon materials made by hydrothermal carbonization. *Chem. Soc. Rev.* 39 (1), 103–116. doi:10.1039/B819318P.
- Tiwari, S.C., Pant, K.K., Upadhyayula, S., 2021. Efficient CO₂ absorption in aqueous dual functionalized cyclic ionic liquids. *J. Co2 Util.* 45. doi:10.1016/j.jcou.2020.101416.
- Toftgaard, M.B., Brix, J., Jensen, P.A., Glarborg, P., Jensen, A.D., 2010. Oxidative combustion of solid fuels. *Prog. Energy Combust. Sci.* 36 (5), 581–625. doi:10.1016/j.pecs.2010.02.001.
- Togashi, N., Okumura, T., Oh-Ishi, K., 2007. Synthesis and CO₂ absorption property of Li₄TiO₄ as a novel CO₂ absorbent. *J. Ceram. Soc. Jpn.* 115, 324–328. doi:10.2109/jcersj.115.324.
- Tomé, L.C., Marrucho, I., 2016. Ionic liquid-based materials: A platform to design engineered CO₂ separation membranes. *Chem. Soc. Rev.* 45. doi:10.1039/C5CS00510H.
- Tomé, L.C., Marrucho, I.M., 2016. Ionic liquid-based materials: a platform to design engineered CO₂ separation membranes. *Chem. Soc. Rev.* 45 (10), 2785–2824. doi:10.1039/c5cs00510h.
- Tong, Z., Ho, W.S.W., 2017. Facilitated transport membranes for CO₂ separation and capture. *Sep. Sci. Technol.* 52 (2), 156–167.
- Tong, Z., Ho, W.S.W., 2017a. Facilitated transport membranes for CO₂ separation and capture. *Sep. Sci. Technol.* 52 (2), 156–167. doi:10.1080/01496395.2016.1217885.
- Tong, Z., Ho, W.S.W., 2017b. New sterically hindered polyvinylamine membranes for CO₂ separation and capture. *J. Membr. Sci.* 543, 202–211. doi:10.1016/j.memsci.2017.08.057.
- Tong, S., Zhang, S., Yin, H., Wang, J., Chen, M., 2021. Study on co-hydrothermal treatment combined with pyrolysis of rice straw/sewage sludge: Biochar properties and heavy metals behavior. *J. Analyt. Appl. Pyrol.* 155, 105074. doi:10.1016/j.jaap.2021.105074.
- Tranier, J.-P., Dubettier, R., Darde, A., Perrin, N., 2011. Air separation, flue gas compression and purification units for oxy-coal combustion systems. *Energy Procedia* 4, 966–971. doi:10.1016/j.egypro.2011.01.143.
- Trapp, C., Thomaser, T., van Dijk, H.A.J., Colonna, P., 2015. Design optimization of a pre-combustion CO₂ capture plant embedding experimental knowledge. *Fuel* 157, 126–139. doi:10.1016/j.fuel.2015.04.007.
- Tregambi, C., Troiano, M., Montagnaro, F., Solimene, R., Salatino, P., 2021. Fluidized beds for concentrated solar thermal technologies-a review. *Front. Energy Res.* 9, 26. doi:10.3389/fenrg.2021.618421.
- Trivedi, T.J., Bhattacharjya, D., Yu, J.-S., Kumar, A., 2015. Functionalized agarose self-healing ionogels suitable for supercapacitors. *ChemSusChem* 8 (19), 3294–3303. doi:10.1002/cssc.201500648.
- Troy, S., Schreiber, A., Zapp, P., 2016. Life cycle assessment of membrane-based carbon capture and storage. *Clean Technol. Environ. Policy* 18 (6), 1641–1654. doi:10.1007/s10098-016-1208-x.
- Trzpit, M., Soular, M., Patarin, J., Desbiens, N., Cailliez, F., Boutin, A., Demachy, I., Fuchs, A., 2007. The effect of local defects on water adsorption in silicalite-1 zeolite: A joint experimental and molecular simulation study. *Langmuir* 23 (20), 10131–10139.
- Tseng, H.-H., Itta, A.K., 2012. Modification of carbon molecular sieve membrane structure by self-assisted deposition carbon segment for gas separation. *J. Membr. Sci.* 389, 223–233. doi:10.1016/j.memsci.2011.10.031.
- Tseng, H.-H., Wang, C.-T., Zhuang, G.-L., Uchytel, P., Reznickova, J., Setnickova, K., 2016. Enhanced H₂/CH₄ and H₂/CO₂ separation by carbon molecular sieve membrane coated on titania modified alumina support: Effects of TiO₂ intermediate layer preparation variables on interfacial adhesion. *J. Membr. Sci.* 510, 391–404. doi:10.1016/j.memsci.2016.02.036.
- Tu, Z., Liu, P., Zhang, X., Shi, M., Zhang, Z., Luo, S., Zhang, L., Wu, Y., Hu, X.J.S., Technology, P., 2021a. Highly-selective separation of CO₂ from N₂ or CH₄ in task-specific ionic liquid membranes: Facilitated transport and salting-out effect. *254*, 117621.
- Tu, Z., Shi, M., Zhang, X., Liu, P., Wu, Y., Hu, X., 2021b. Selective membrane separation of CO₂ using novel epichlorohydrin-amine-based crosslinked protic ionic liquids: Crosslinking mechanism and enhanced salting-out effect. *J. CO₂ Util.* 46, 101473. doi:10.1016/j.jcou.2021.101473.
- Tuinier, M.J., van Sint Annaland, M., 2012. Biogas purification using cryogenic packed-bed technology. *Ind. Eng. Chem. Res.* 51 (15), 5552–5558. doi:10.1021/ie202606g.
- Tuinier, M.J., van Sint Annaland, M., Kramer, G.J., Kuipers, J.A.M., 2010. Cryogenic CO₂ capture using dynamically operated packed beds. *Chem. Eng. Sci.* 65 (1), 114–119. doi:10.1016/j.ces.2009.01.055.
- Tuinier, M.J., Hamers, H.P., van Sint Annaland, M., 2011a. Techno-economic evaluation of cryogenic CO₂ capture—A comparison with absorption and membrane technology. *Int. J. Greenh. Gas Control* 5 (6), 1559–1565. doi:10.1016/j.ijggc.2011.08.013.
- Tuinier, M.J., van Sint Annaland, M., Kuipers, J.A.M., 2011b. A novel process for cryogenic CO₂ capture using dynamically operated packed beds—An experimental and numerical study. *Int. J. Greenh. Gas Control* 5 (4), 694–701. doi:10.1016/j.ijggc.2010.11.011.
- Tung, H.H., Mah, R.S.H., 1985. Modeling liquid mass transfer in hige separation process. *Chemical Engineering Communications* 39 (1-6), 147–153.
- Turnbull, E., Kossakowski, E.R., Davidson, J.F., Hopes, R.B., Blackshaw, H.W., Goodyer, P.T.Y., 1984. Effect of pressure on combustion of char in fluidised beds. *Chem. Eng. Res. Des.* 62 (4), 223–234.
- Uehara, Y., Karami, D., Mahinpey, N., 2018. Roles of cation and anion of amino acid anion-functionalized ionic liquids immobilized into a porous support for CO₂ capture. *Energy Fuels* 32 (4), 5345–5354. doi:10.1021/acs.energyfuels.8b00190.
- Ullah, A., Saleem, M.W., Kim, W.-S., 2017. Performance and energy cost evaluation of an integrated NH₃-based CO₂ capture-capacitive deionization process. *Int. J. Greenh. Gas Control* 66, 85–96. doi:10.1016/j.ijggc.2017.09.013.
- Ullah Khan, I., Hafiz Dzarfan Othman, M., Hashim, H., Matsuura, T., Ismail, A.F., Rezaei-DashArzhandi, M., Wan Azelee, L., 2017. Biogas as a renewable energy fuel – A review of biogas upgrading, utilisation and storage. *Energy Convers. Manage.* 150, 277–294. doi:10.1016/j.enconman.2017.08.035.
- Uribe-Romo, F.J., Hunt, J.R., Furukawa, H., Klöck, C., O’Keeffe, M., Yaghi, O.M., 2009. A crystalline imine-linked 3-D porous covalent organic framework. *J. Am. Chem. Soc.* 131 (13), 4570–4571.
- Uribe-Romo, F.J., Doonan, C.J., Furukawa, H., Oisaki, K., Yaghi, O.M., 2011. Crystalline covalent organic frameworks with hydrazone linkages. *J. Am. Chem. Soc.* 133 (30), 11478–11481.
- Uwitonze, H., Lee, I., Suh, S.B., Lee, I., 2021. CFD study of oscillatory motion effect on liquid flow distribution into structured packed divided wall column. *Chem. Eng. Process. - Process Intensif.* 165. doi:10.1016/j.cep.2021.108429, 108429–108429.
- Vaccari, A., 1998. Preparation and catalytic properties of cationic and anionic clays. *Catal. Today* 41 (1), 53–71. doi:10.1016/S0920-5861(98)00038-8.

- Valenciano, R., Aylón, E., Izquierdo, M.T., 2015. A critical short review of equilibrium and kinetic adsorption models for vocs breakthrough curves modelling. *Adsorpt. Sci. Technol.* 33 (10), 851–870. doi:10.1260/0263-6174.33.10.851.
- Valverde, J.M., Sanchez-Jimenez, P.E., Perez-Maqueda, L.A., 2015. Ca-looping for post-combustion CO₂ capture: a comparative analysis on the performances of dolomite and limestone. *Appl. Energy* 138, 202–215.
- Valverde, J.M., 2018. The Ca-looping process for CO₂ capture and energy storage: role of nanoparticle technology. *J. Nanopart. Res.* 20 (2), 16. doi:10.1007/s11051-017-4092-3.
- Van Den Bergh, J., Mittelmeijer-Hazeleger, M., Kapteijn, F., 2010. Modeling permeation of CO₂/CH₄, N₂/CH₄, and CO₂/air mixtures across a DD3R zeolite membrane. *J. Phys. Chem. C* 114 (20), 9379–9389.
- Van Der Jagt, R., Vasileiadis, A., Veldhuizen, H., Shao, P., Feng, X., Ganapathy, S., Habisreutinger, N.C., van der Ven, M.A., Wang, C., Wagemaker, M., 2021. Synthesis and structure–property relationships of polyimide covalent organic frameworks for carbon dioxide capture and (aqueous) sodium-ion batteries. *Chem. Mater.* 33 (3), 818–833.
- van Dijk, H.A.J., Walspurger, S., Cobden, P.D., van den Brink, R.W., de Vos, F.G., 2011. Testing of hydrothermalite-based sorbents for CO₂ and H₂S capture for use in sorption enhanced water gas shift. *Int. J. Greenh. Gas Control* 5 (3), 505–511. doi:10.1016/j.jggc.2010.04.011.
- Van Gerwen, T., Stankiewicz, A., 2009. Structure, energy, synergy, time—the fundamentals of process intensification. *Ind. Eng. Chem. Res.* 48 (5), 2465–2474. doi:10.1021/ie801501y.
- Veerabhadrapa, M.G., Maroto-Valer, M.M., Chen, Y., Garcia, S., 2021. Layered double hydroxides-based mixed metal oxides: development of novel structured sorbents for CO₂ capture applications. *ACS Appl. Mater. Interfaces* 13 (10), 11805–11813. doi:10.1021/acami.0c20457.
- Vega, F., Baena-Moreno, F.M., Gallego Fernández, L.M., Portillo, E., Navarrete, B., Zhang, Z., 2020. Current status of CO₂ chemical absorption research applied to CCS: Towards full deployment at industrial scale. *Appl. Energy* 260. doi:10.1016/j.apenergy.2019.114313.
- Veneman, R., Frigka, N., Zhao, W., Li, Z., Kersten, S., Brilman, W., 2015. Adsorption of H₂O and CO₂ on supported amine sorbents. *Int. J. Greenh. Gas Control* 41, 268–275. doi:10.1016/j.jggc.2015.07.014.
- Vera, E., García, S., Maroto-Valer, M.M., Pfeiffer, H., 2019. CO₂-CO capture and kinetic analyses of sodium cobaltate under various partial pressures. *Adsorption* doi:10.1007/s10450-019-0167-6.
- Verdoliva, V., Saviano, M., De Luca, S., 2019. Zeolites as acid/basic solid catalysts: recent synthetic developments. *Catalysts* 9 (3), 248.
- Verma, P., Kuwahara, Y., Mori, K., Raja, R., Yamashita, H., 2020. Functionalized mesoporous SBA-15 silica: recent trends and catalytic applications. *Nanoscale* 12 (21), 11333–11363. doi:10.1039/d0nr00732c.
- Verougstraete, B., Martín-Calvo, A., Van der Perre, S., Baron, G., Finsy, V., Denayer, J.F.M., 2020. A new honeycomb carbon monolith for CO₂ capture by rapid temperature swing adsorption using steam regeneration. *Chem. Eng. J.* 383. doi:10.1016/j.cej.2019.123075.
- Verougstraete, B., Schoukens, M., Suten, B., Vanden Haute, N., De Vos, Y., Rombouts, M., Denayer, J.F.M., 2022. Electrical swing adsorption on 3D-printed activated carbon monoliths for CO₂ capture from biogas. *Sep. Purif. Technol.* 299. doi:10.1016/j.seppur.2022.121660.
- Versteeg, P., Rubin, E.S., 2011. A technical and economic assessment of ammonia-based post-combustion CO₂ capture at coal-fired power plants. *Int. J. Greenh. Gas Control* 5 (6), 1596–1605. doi:10.1016/j.jggc.2011.09.006.
- Versteeg, G., van Swaaij, W.B., 1988. On the kinetics between CO₂ and alkanolamines both in aqueous and non-aqueous solutions—II. Tertiary amines. *Chem. Eng. Sci.* 43 (3), 587–591.
- Veselovskaya, J.V., Derevschikov, V.S., Kardash, T.Y., Stonkus, O.A., Trubitsina, T.A., Okunev, A.G., 2013. Direct CO₂ capture from ambient air using K₂CO₃/Al₂O₃ composite sorbent. *Int. J. Greenh. Gas Control* 17, 332–340. doi:10.1016/j.jggc.2013.05.006.
- Vicent-Luna, J.M., Gutiérrez-Sevillano, J.J., Hamad, S., Anta, J., Calero, S., 2018. Role of ionic liquid [EMIM][SCN] in the adsorption and diffusion of gases in metal–organic frameworks. *ACS Appl. Mater. Interfaces* 10 (35), 29694–29704. doi:10.1021/acami.8b11842.
- Vinayakumar, K., Palliyarayil, A., Kumar, N.S., Sil, S., 2022a. Processing of aerogels and their applications toward CO₂ adsorption and electrochemical reduction: a review. *Environ. Sci. Pollut. Res.* doi:10.1007/s11356-022-20355-2.
- Vinayakumar, K., Palliyarayil, A., Kumar, N.S., Sil, S., 2022b. Processing of aerogels and their applications toward CO₂ adsorption and electrochemical reduction: a review. *Environ. Sci. Pollut. Res.* 29 (32), 47942–47968. doi:10.1007/s11356-022-20355-2.
- Vlahostergios, Z., Misirlis, D., Papadopoulos, A.I., Seferlis, P., 2020. Investigation of the flow field development inside a rotating packed bed with the use of CFD. *Chem. Eng. Trans.* 81, 883–888. doi:10.3303/CET2081148.
- Volkart, K., Bauer, C., Boulet, C., 2013. Life cycle assessment of carbon capture and storage in power generation and industry in Europe. *Int. J. Greenh. Gas Control* 16, 91–106. doi:10.1016/j.jggc.2013.03.003.
- von Hippel, T., 2018. Thermal removal of carbon dioxide from the atmosphere: energy requirements and scaling issues. *Clim. Change* 148 (4), 491–501. doi:10.1007/s10584-018-2208-0.
- Voon, B.K., Shen Lau, H., Liang, C.Z., Yong, W.F., 2022. Functionalized two-dimensional g-C₃N₄ nanosheets in PIM-1 mixed matrix membranes for gas separation. *Sep. Purif. Technol.* 296. doi:10.1016/j.seppur.2022.121354.
- Vu, A.-T., Ho, K., Jin, S., Lee, C.-H., 2016. Double sodium salt-promoted mesoporous MgO sorbent with high CO₂ sorption capacity at intermediate temperatures under dry and wet conditions. *Chem. Eng. J.* 291, 161–173.
- Wahono, S.K., Dwiatmoko, A.A., Cavallaro, A., Indirathankam, S.C., Addai-Mensah, J., Skinner, W., Vinu, A., Vasilev, K., 2021. Amine-functionalized natural zeolites prepared through plasma polymerization for enhanced carbon dioxide adsorption. *Plasma Processes Polym.* 18 (8). doi:10.1002/ppap.202100028.
- Wai, S.K., Nwaoha, C., Saiwan, C., Idem, R., Supap, T., 2018. Absorption heat, solubility, absorption and desorption rates, cyclic capacity, heat duty, and absorption kinetic modeling of AMP–DETA blend for post-combustion CO₂ capture. *Sep. Purif. Technol.* 194, 89–95. doi:10.1016/j.seppur.2017.11.024.
- Wall, T., Liu, Y., Spero, C., Elliott, L., Khare, S., Rathnam, R., Zeenathal, F., Moghtaderi, B., Buhre, B., Sheng, C., 2009a. An overview on oxyfuel coal combustion—State of the art research and technology development. *Chem. Eng. Res. Des.* 87 (8), 1003–1016.
- Wall, T., Liu, Y., Spero, C., Elliott, L., Khare, S., Rathnam, R., Zeenathal, F., Moghtaderi, B., Buhre, B., Sheng, C., 2009b. An overview on oxyfuel coal combustion—State of the art research and technology development. *Chem. Eng. Res. Des.* 87 (8), 1003–1016.
- Walters, M.S., Edgar, T.F., Rochelle, G.T., 2016. Dynamic modeling and control of an intercooled absorber for post-combustion CO₂ capture. *Chem. Eng. Process.: Process Intensif.* 107, 1–10. doi:10.1016/j.ccep.2016.05.012.
- Walton, K.S., Abney, M.B., LeVan, M.D., 2006. CO₂ adsorption in Y and X zeolites modified by alkali metal cation exchange. *Microporous Mesoporous Mater.* 91 (1–3), 78–84.
- Wan, S., Guo, J., Kim, J., Ihee, H., Jiang, D., 2008. A belt-shaped, blue luminescent, and semiconducting covalent organic framework. *Angew. Chem. Int. Ed.* 47 (46), 8826–8830.
- Wang, Z., Cohen, S.M., 2007. Postsynthetic covalent modification of a neutral metal–organic framework. *J. Am. Chem. Soc.* 129 (41), 12368–12369.
- Wang, B., Gan, Z.H., 2014. Feasibility analysis of cryocooler based small scale CO₂ cryogenic capture. Comment on “Energy analysis of the cryogenic CO₂ process based on Stirling coolers” Song CF, Kitamura Y, Li SH [Energy 2014; 65: 580–591]. *Energy* 68, 1000–1003. doi:10.1016/j.energy.2014.02.032.
- Wang, X., Song, C., 2020a. Carbon capture from flue gas and the atmosphere: a perspective. *Front. Energy Res.* 8. doi:10.3389/fenrg.2020.560849.
- Wang, X., Song, C., 2020b. Carbon capture from flue gas and the atmosphere: A perspective. *Front. Energy Res.* 8, 560849.
- Wang, S., Yan, S., Ma, X., Gong, J., 2011. Recent advances in capture of carbon dioxide using alkali-metal-based oxides. *Energy Environ. Sci.* 4 (10), 3805–3819.
- Wang, M., Lawal, A., Stephenson, P., Sidders, J., Ramshaw, C., 2011. Post-combustion CO₂ capture with chemical absorption: A state-of-the-art review. *Chem. Eng. Res. Des.* 89 (9), 1609–1624. doi:10.1016/j.cherd.2010.11.005.
- Wang, Q., Luo, J., Zhong, Z., Borgna, A., 2011. CO₂ capture by solid adsorbents and their applications: current status and new trends. *Energy Environ. Sci.* 4 (1), 42–55. doi:10.1039/C0EE00064G.
- Wang, L., Liu, Z., Li, P., Yu, J., Rodrigues, A.E., 2012. Experimental and modeling investigation on post-combustion carbon dioxide capture using zeolite 13X-APG by hybrid VTSA process. *Chem. Eng. J.* 197, 151–161. doi:10.1016/j.cej.2012.05.017.
- Wang, X., Li, H., Hou, X.-J., 2012. Amine-functionalized metal organic framework as a highly selective adsorbent for CO₂ over CO. *J. Phys. Chem. C* 116 (37), 19814–19821. doi:10.1021/jp3052938.
- Wang, J., Wang, M., Zhao, B., Qiao, W., Long, D., Ling, L., 2013. Mesoporous carbon-supported solid amine sorbents for low-temperature carbon dioxide capture. *Ind. Eng. Chem. Res.* 52 (15), 5437–5444. doi:10.1021/ie303388h.
- Wang, X., Akhmedov, N.G., Duan, Y., Luebke, D., Li, B., 2013. Immobilization of amino acid ionic liquids into nanoporous microspheres as robust sorbents for CO₂ capture. *J. Mater. Chem. A* 1 (9), 2978–2982. doi:10.1039/C3TA00768E.
- Wang, Y., Chen, J., Larachi, F., 2013. Modelling and simulation of trickle-bed reactors using computational fluid dynamics: A state-of-the-art review. *Canadian Journal of Chemical Engineering* 91 (1), 136–180.
- Wang, L., Yang, Y., Shen, W., Kong, X., Li, P., Yu, J., Rodrigues, A.E., 2013a. CO₂ capture from flue gas in an existing coal-fired power plant by two successive pilot-scale VPSA units. *Ind. Eng. Chem. Res.* 52 (23), 7947–7955. doi:10.1021/ie4009716.
- Wang, L., Yang, Y., Shen, W., Kong, X., Li, P., Yu, J., Rodrigues, A.E., 2013b. Experimental evaluation of adsorption technology for CO₂ capture from flue gas in an existing coal-fired power plant. *Chem. Eng. Sci.* 101, 615–619. doi:10.1016/j.ces.2013.07.028.
- Wang, C., Zhou, X., Jia, L., Tan, Y., 2014. Sintering of limestone in calcination/carbonation cycles. *Ind. Eng. Chem. Res.* 53 (42), 16235–16244. doi:10.1021/ie502069d.
- Wang, T., Huang, J., He, X., Wu, J., Fang, M., Cheng, J., 2014. CO₂ fertilization system integrated with a low-cost direct air capture technology. *Energy Procedia* 63, 6842–6851. doi:10.1016/j.egypro.2014.11.718.
- Wang, X., Song, C., Gaffney, A.M., Song, R., 2014. New molecular basket sorbents for CO₂ capture based on mesoporous sponge-like TUD-1. *Catal. Today* 238, 95–102. doi:10.1016/j.cattod.2014.02.022.
- Wang, J.Y., Huang, L., Yang, R.Y., Zhang, Z., Wu, J.W., Gao, Y.S., Wang, Q., O'Hare, D., Zhong, Z.Y., 2014. Recent advances in solid sorbents for CO₂ capture and new development trends. *Energy Environ. Sci.* 7 (11), 3478–3518. doi:10.1039/c4ee01647e.
- Wang, J., Huang, H., Wang, M., Yao, L., Qiao, W., Long, D., Ling, L., 2015. Direct capture of low-concentration CO₂ on mesoporous carbon-supported solid amine adsorbents at ambient temperature. *Ind. Eng. Chem. Res.* 54 (19), 5319–5327. doi:10.1021/acs.iecr.5b01060.
- Wang, M., Joel, A.S., Ramshaw, C., Eimer, D., Musa, N.M., 2015. Process intensification for post-combustion CO₂ capture with chemical absorption: A critical review. *Appl. Energy* 158, 275–291. doi:10.1016/j.apenergy.2015.08.083.
- Wang, S., Li, X., Wu, H., Tian, Z., Xin, Q., He, G., Peng, D., Chen, S., Yin, Y., Jiang, Z., Guiver, M.D., 2016. Advances in high permeability polymer-based membrane materials for CO₂ separations. *Energy Environ. Sci.* 9 (6), 1863–1890. doi:10.1039/C6EE00811A.

- Wang, T., Yu, W., Liu, F., Fang, M., Farooq, M., Luo, Z., 2016. Enhanced CO₂ absorption and desorption by monoethanolamine (MEA)-based nanoparticle suspensions. *Ind. Eng. Chem. Res.* 55 (28), 7830–7838. doi:10.1021/acs.iecr.6b00358.
- Wang, J., Zhao, J., Wang, Y., Deng, S., Sun, T., Li, K., 2017. Application potential of solar-assisted post-combustion carbon capture and storage (CCS) in China: A life cycle approach. *J. Clean. Prod.* 154, 541–552. doi:10.1016/j.jclepro.2017.04.021.
- Wang, L., Zhou, Z.M., Hu, Y.W., Cheng, Z.M., Fang, X.C., 2017. Nanosheet MgO-Based CO₂ sorbent promoted by mixed-alkali-metal nitrate and carbonate: performance and mechanism. *Ind. Eng. Chem. Res.* 56 (20), 5802–5812. doi:10.1021/acs.iecr.7b00483.
- Wang, S., Guo, W., Gao, F., Yang, R., 2017. Characterization and Pb (II) removal potential of corn straw- and municipal sludge-derived biochars. *R. Soc. Open Sci.* 4 (9), 170402. doi:10.1098/rsos.170402.
- Wang, Z., Ren, H., Zhang, S., Zhang, F., Jin, J.J., 2017. Polymers of intrinsic microporosity/metal-organic framework hybrid membranes with improved interfacial interaction for high-performance CO₂ separation. *Chem. Eng. J.* 324, 10968–10977.
- Wang, F., Zhao, J., Miao, H., Zhao, J., Zhang, H., Yuan, J., Yan, J., 2018. Current status and challenges of the ammonia escape inhibition technologies in ammonia-based CO₂ capture process. *Appl. Energy* 230, 734–749.
- Wang, H., He, S., Qin, X., Li, C., Li, T., 2018. Interfacial engineering in metal-organic framework-based mixed matrix membranes using covalently grafted polyimide brushes. *J. Am. Chem. Soc.* 140 (49), 17203–17210. doi:10.1021/jacs.8b10138.
- Wang, H., Zhang, J., Wang, G., Wang, Q., Song, T., 2018. High-temperature capture of CO₂ by Li₂SiO₄ prepared with blast furnace slag and kinetic analysis. *J. Therm. Anal. Calorim.* 133 (2), 981–989. doi:10.1007/s10973-018-7167-1.
- Wang, C., Cao, F., Ruan, Y., Jia, X., Zhen, W., Jiang, X., 2019. Specific generation of singlet oxygen through the russell mechanism in hypoxic tumors and GSH depletion by Cu-TCP nanosheets for cancer therapy. *Angew. Chem. Int. Ed.* 131 (29), 9951–9955. doi:10.1002/anie.201903981.
- Wang, P., Sun, J., Guo, Y., Zhao, C., Li, W., Wang, G., Lei, S., Lu, P., 2019. Structurally improved, urea-templated, K₂CO₃-based sorbent pellets for CO₂ capture. *Chem. Eng. J.* 374, 20–28. doi:10.1016/j.cej.2019.05.091.
- Wang, R., Liu, S., Wang, L., Li, Q., Zhang, S., Chen, B., Jiang, L., Zhang, Y., 2019. Superior energy-saving splitter in monoethanolamine-based biphasic solvents for CO₂ capture from coal-fired flue gas. *Appl. Energy* 242, 302–310. doi:10.1016/j.apenergy.2019.03.138.
- Wang, S., Bai, P., Sun, M., Liu, W., Li, D., Wu, W., Yan, W., Shang, J., Yu, J., 2019. Fabricating mechanically robust binder-free structured zeolites by 3d printing coupled with zeolite sintering: a superior configuration for CO₂ capture. *Adv. Sci.* 6 (17), 1901317.
- Wang, X., Shan, M., Liu, X., Wang, M., Doherty, C.M., Osadchii, D., Kapteijn, F., 2019. High-performance polybenzimidazole membranes for helium extraction from natural gas. *ACS Appl. Mater. Interfaces* 11 (22), 20098–20103. doi:10.1021/acsami.9b05548.
- Wang, X., Shang, D., Zeng, S., Wang, Y., Zhang, X., Zhang, X., Liu, J., 2019. Enhanced CO₂ capture by binary systems of pyridinium-based ionic liquids and porous ZIF-8 particles. *J. Chem. Thermodyn.* 128, 415–423. doi:10.1016/j.jct.2018.08.038.
- Wang, K., Hong, J., Zhou, Z., Lin, Z., Zhao, P., 2019. Development of alkali nitrate-containing Li₂SiO₄ for high-temperature CO₂ capture. *Energy Technol.* 7 (2), 325–332. doi:10.1002/ente.201800229.
- Wang, W.J., Chen, M., Huang, D.L., Zeng, G.M., Zhang, C., Lai, C., Zhou, C.Y., Yang, Y., Cheng, M., Hu, L., Xiong, W.P., Li, Z.H., Wang, Z.W., 2019a. An overview on nitride and nitrogen-doped photocatalysts for energy and environmental applications. *Compos. Part B-Eng.* 172, 704–723. doi:10.1016/j.compositesb.2019.05.097.
- Wang, W.J., Motuzas, J., Zhao, X.S., da Costa, J.C.D., 2019b. 2D/3D amine functionalised sorbents containing graphene silica aerogel and mesoporous silica with improved CO₂ sorption. *Sep. Purif. Technol.* 222, 381–389. doi:10.1016/j.seppur.2019.04.050.
- Wang, B., Qiao, Z., Xu, J., Wang, J., Liu, X., Zhao, S., Wang, Z., Guiver, M.D., 2020. Unobstructed ultrathin gas transport channels in composite membranes by interfacial self-assembly. *Adv. Mater.* 32 (22), 1907701. doi:10.1002/adma.201907701.
- Wang, C., Guo, F., Li, H., Xu, J., Hu, J., Liu, H., Wang, M., 2020. A porous ionic polymer bionic carrier in a mixed matrix membrane for facilitating selective CO₂ permeability. *J. Membr. Sci.* 598, 117677. doi:10.1016/j.memsci.2019.117677.
- Wang, T., Wang, X., Hou, C., Liu, J., 2020. Quaternary functionalized mesoporous adsorbents for ultra-high kinetics of CO₂ capture from air. *Sci. Rep.* 10 (1), 21429. doi:10.1038/s41598-020-77477-1.
- Wang, Y.L., Guo, B.H., Guo, J.N., Zhang, M., Yang, H.R., Jin, Y., 2020. K₂CO₃-impregnated Al/Si aerogel prepared by ambient pressure drying for CO₂ capture: synthesis, characterization and adsorption characteristics. *Materials* 13 (17). doi:10.3390/ma13173741.
- Wang, Z., Shen, Q., Liang, J., Zhang, Y., Jin, J., 2020. Adamantane-grafted polymer of intrinsic microporosity with finely tuned interchain spacing for improved CO₂ separation performance. *Sep. Purif. Technol.* 233, 116008.
- Wang, H., Wang, H., Liu, G., Yan, Q., 2021. In-situ pyrolysis of Taihu blue algae biomass as appealing porous carbon adsorbent for CO₂ capture: Role of the intrinsic N. *Sci. Total Environ.* 771, 145424. doi:10.1016/j.scitotenv.2021.145424.
- Wang, J., Fu, J., Zeng, X., 2021. Research on dynamic modelling of amine-based carbon capture pilot plant based on gCCS. *Proc. CSEE* 41 (18), 6340–6350. doi:10.13334/j.0258-8013.psee.201642.
- Wang, J., Guo, Z., Deng, S., Zhao, R., Chen, L., Xue, J., 2021. A rapid multi-objective optimization of pressure and temperature swing adsorption for CO₂ capture based on simplified equilibrium model. *Sep. Purif. Technol.* 279. doi:10.1016/j.seppur.2021.119663.
- Wang, Y., Zhang, N., Wu, H., Ren, Y., Yang, L., Wang, X., Wu, Y., Liu, Y., Zhao, R., Jiang, Z., 2021. Exfoliation-free layered double hydroxides laminates intercalated with amino acids for enhanced CO₂ separation of mixed matrix membrane. *J. Membr. Sci.* 618, 118691. doi:10.1016/j.memsci.2020.118691.
- Wang, J., Chen, S., Xu, J.-y., Liu, L.-c., Zhou, J.-c., Cai, J.-j., 2021. High-surface-area porous carbons produced by the mild KOH activation of a chitosan hydrochar and their CO₂ capture. *New Carbon Mater.* 36 (6), 1081–1090. doi:10.1016/j.nccm.2021.06.0074.
- Wang, S., Wu, J., Ma, N., Chen, S., 2021. High molecular weight polyethyleneimine encapsulated into a porous polymer monolithic by one-step polymerization for CO₂ capture. *New J. Chem.* 45 (28), 12538–12548. doi:10.1039/d1nj01288f.
- Wang, Y., Pan, Z., Zhang, W., Borhani, T.N., Li, R., Zhang, Z., 2022. Life cycle assessment of combustion-based electricity generation technologies integrated with carbon capture and storage: A review. *Environ. Res.* 207, 112219. doi:10.1016/j.envres.2021.112219.
- Wang, S., Qiu, X., Chen, Y., Chen, S., 2022. Preparation and structure tuning of CO₂ adsorbent based on in-situ amine-functionalized hierarchical porous polymer. *Microporous Mesoporous Mater.* 330. doi:10.1016/j.micromeso.2021.111585.
- Ward, J., Habgood, H., 1966. The infrared spectra of carbon dioxide adsorbed on zeolite X. *J. Phys. Chem.* 70 (4), 1178–1182.
- Wawrzynczak, D., Majchrzak-Kuceba, I., Srokosz, K., Kozak, M., Nowak, W., Zdeb, J., Smółka, W., Zajchowski, A., 2019. The pilot dual-reflux vacuum pressure swing adsorption unit for CO₂ capture from flue gas. *Sep. Purif. Technol.* 209, 560–570. doi:10.1016/j.seppur.2018.07.079.
- Wesley, P.A., 2014. Adsorption technology for CO₂ separation and capture: a perspective. *Adsorption* 20 (2–3), 225–231. doi:10.1007/s10450-014-9603-2.
- Wei, J., Shi, J., Pan, H., Zhao, W., Ye, Q., Shi, Y., 2008. Adsorption of carbon dioxide on organically functionalized SBA-16. *Microporous Mesoporous Mater.* 116 (1–3), 394–399. doi:10.1016/j.micromeso.2008.04.028.
- Wei, L., Guo, R.F., Tang, Y.Q., Zhu, J.M., Liu, M.Y., Chen, J.Q., Xu, Y., 2020. Properties of aqueous amine based protic ionic liquids and its application for CO₂ quick capture. *Sep. Purif. Technol.* 239. doi:10.1016/j.seppur.2020.116531.
- Weidong, Z., Dong, Z., Kezhong, T., 2009. Carbon capture and sequestration technology. *Sino-Glob. Energy* 14 (11), 7–14.
- Wen, X., et al., 2007. CFD modeling of columns equipped with structured packings: I. Approach based on detailed packing geometry. *Asia-Pacific Journal of Chemical Engineering* 2 (4), 336–344.
- Wen, J.J., Gu, F.N., Wei, F., Zhou, Y., Lin, W.G., Yang, J., Yang, J.Y., Wang, Y., Zou, Z.G., Zhu, J.H., 2010. One-pot synthesis of the amine-modified meso-structured monolith CO₂ adsorbent. *J. Mater. Chem.* 20 (14). doi:10.1039/b920027d.
- White, J.C., Dutta, P.K., Shiq, K., Verweij, H., 2010. Synthesis of ultrathin zeolite Y membranes and their application for separation of carbon dioxide and nitrogen gases. *Langmuir* 26 (12), 10287–10293.
- Widenmeyer, M., Wieggers, K.S., Chen, G., Yoon, S., Feldhoff, A., Weidenkaff, A., 2020. Engineering of oxygen pathways for better oxygen permeability in Cr-substituted Ba₂In₂O₅ membranes. *J. Membr. Sci.* 595, 117558. doi:10.1016/j.memsci.2019.117558.
- Wijmans, J.G., Baker, R.W., 1995. The solution-diffusion model: a review. *J. Membr. Sci.* 107 (1–2), 1–21. doi:10.1016/0376-7388(95)00102-1.
- Wilcox, J., Haghpanah, R., Rupp, E.C., He, J., Lee, K., 2014. Advancing adsorption and membrane separation processes for the gigaton carbon capture challenge. *Annu. Rev. Chem. Biomol. Eng.* 5, 479–505. doi:10.1146/annurev-chembioeng-060713-040100.
- Williams, R., Burt, L.A., Esposito, E., Jansen, J.C., Tocci, E., Rizzuto, C., Lanč, M., Carta, M., McKeown, N.B.J.J.o.M.C.A., 2018. A highly rigid and gas selective methanopentacene-based polymer of intrinsic microporosity derived from Tröger's base polymerization. *Chem. Commun.* 6 (14), 5661–5667.
- Wilm, L.F.B., Das, M., Janssen-Muller, D., Muck-Lichtenfeld, C., Glorius, F., Dielmann, F., 2022. Photoswitchable nitrogen superbases: using light for reversible carbon dioxide capture. *Angew. Chem. Int. Ed. Engl.* 61 (3), e202112344. doi:10.1002/anie.202112344.
- Wirawan, S.K., Creaser, D., 2006a. CO₂ adsorption on silicalite-1 and cation exchanged ZSM-5 zeolites using a step change response method. *Microporous Mesoporous Mater.* 91 (1–3), 196–205.
- Wirawan, S.K., Creaser, D., 2006b. Multicomponent H₂/CO/CO₂ adsorption on BaZSM-5 zeolite. *Sep. Purif. Technol.* 52 (2), 224–231.
- Wirawan, S.K., Creaser, D., Lindmark, J., Hedlund, J., Bendiyasa, I.M., Sediawan, W.B., 2011. H₂/CO₂ permeation through a silicalite-1 composite membrane. *J. Membr. Sci.* 375 (1–2), 313–322.
- Woo, K.T., Dong, G., Lee, J., Kim, J.S., Do, Y.S., Lee, W.H., Lee, H.S., Lee, Y.M., 2016a. Ternary mixed-gas separation for flue gas CO₂ capture using high performance thermally rearranged (TR) hollow fiber membranes. *J. Membr. Sci.* 510, 472–480.
- Woo, K.T., Lee, J., Dong, G., Kim, J.S., Do, Y.S., Ho, J.H., Lee, Y.M., 2016b. Thermally rearranged poly (benzoxazole-co-imide) hollow fiber membranes for CO₂ capture. *J. Membr. Sci.* 498, 125–134.
- Wormeyer, K., Smirnova, I., 2013. Adsorption of CO₂, moisture and ethanol at low partial pressure using aminofunctionalised silica aerogels. *Chem. Eng. J.* 225, 350–357. doi:10.1016/j.cej.2013.02.022.
- Wormeyer, K., Alnaief, M., Smirnova, I., 2012. Amino functionalised Silica-Aerogels for CO₂-adsorption at low partial pressure. *Adsorpt.-J. Int. Adsorpt. Soc.* 18 (3–4), 163–171. doi:10.1007/s10450-012-9390-6.
- Wu, Y., Wang, C., Tan, Y., Jia, L., Anthony, E.J., 2011. Characterization of ashes from a 100kWh pilot-scale circulating fluidized bed with oxy-fuel combustion. *Appl. Energy* 88 (9), 2940–2948. doi:10.1016/j.apenergy.2011.03.007.
- Wu, H., Chua, Y.S., Krunglevičiute, V., Yagi, M., Chen, P., Yildirim, T., Zhou, W., 2013. Unusual and highly tunable missing-linker defects in zirconium metal-organic framework UiO-66 and their important effects on gas adsorption. *J. Am. Chem. Soc.* 135 (28), 10525–10532. doi:10.1021/ja404514f.

- Wu, H., Li, X., Li, Y., Wang, S., Guo, R., Jiang, Z., Wu, C., Xin, Q., Lu, X., 2014. Facilitated transport mixed matrix membranes incorporated with amine functionalized MCM-41 for enhanced gas separation properties. *J. Membr. Sci.* 465, 78–90. doi:10.1016/j.memsci.2014.04.023.
- Wu, X., Tian, Z., Wang, S., Peng, D., Yang, L., Wu, Y., Xin, Q., Wu, H., Jiang, Z., 2017. Mixed matrix membranes comprising polymers of intrinsic microporosity and covalent organic framework for gas separation. *J. Membr. Sci.* 528, 273–283. doi:10.1016/j.memsci.2017.01.042.
- Wu, F., Argyle, M.D., Dellenback, P.A., Fan, M., 2018. Progress in O₂ separation for oxy-fuel combustion—A promising way for cost-effective CO₂ capture: A review. *Prog. Energy Combust. Sci.* 67, 188–205. doi:10.1016/j.pecs.2018.01.004.
- Wu, Q., Gao, M., Zhang, G., Zhang, Y., Liu, S., Xie, C., Yu, H., Liu, Y., Huang, L., Yu, S., 2019. Preparation and application performance study of biomass-based carbon materials with various morphologies by a hydrothermal/soft template method. *Nanotechnology* 30 (18). doi:10.1088/1361-6528/ab0042.
- Wu, J., Lv, B., Wu, X., Zhou, Z., Jing, G., 2019. Aprotic heterocyclic anion-based dual-functionalized ionic liquid solutions for efficient CO₂ uptake: quantum chemistry calculation and experimental research. *ACS Sustain. Chem. Eng.* 7 (7), 7312–7323. doi:10.1021/acssuschemeng.9b00420.
- Wu, X., Wang, M., Liao, P., Shen, J., Li, Y., 2020. Solvent-based post-combustion CO₂ capture for power plants: A critical review and perspective on dynamic modelling, system identification, process control and flexible operation. *Appl. Energy* 257. doi:10.1016/j.apenergy.2019.113941.
- Wu, Y., Chen, X., Ma, J., Wu, Y., Liu, D., Xie, W., 2020. System integration optimization for coal-fired power plant with CO₂ capture by Na₂CO₃ dry sorbents. *Energy* 211, 118554. doi:10.1016/j.energy.2020.118554.
- Wu, J.J., Qiu, X.Y., Chen, S.X., 2022. Preparation and characterization of an amine-modified graphene aerogel for enhanced carbon dioxide adsorption. *J. Mater. Sci.* 57 (3), 1727–1737. doi:10.1007/s10853-021-06768-3.
- Wurzbacher, J.A., Gebald, C., Steinfeld, A., 2011. Separation of CO₂ from air by temperature-vacuum swing adsorption using diamine-functionalized silica gel. *Energy Environ. Sci.* 4 (9). doi:10.1039/c1ee01681d.
- Wurzbacher, J.A., Gebald, C., Piatkowski, N., Steinfeld, A., 2012. Concurrent separation of CO₂ and H₂O from air by a temperature-vacuum swing adsorption/desorption cycle. *Environ. Sci. Technol.* 46 (16), 9191–9198. doi:10.1021/es301953k.
- Wurzbacher, J.A., Gebald, C., Brunner, S., Steinfeld, A., 2016. Heat and mass transfer of temperature-vacuum swing desorption for CO₂ capture from air. *Chem. Eng. J.* 283, 1329–1338. doi:10.1016/j.cej.2015.08.035.
- Xi, L., Guo, R., Wang, Z., Zhang, J., 2019. Constructing unique cross-sectional structured mixed matrix membranes by incorporating ultrathin microporous nanosheets for efficient CO₂ separation. *ACS Appl. Mater. Interfaces* 11 (27), 24618–24626. doi:10.1021/acami.9b07815.
- Xia, Y., Zhu, Y., Tang, Y., 2012. Preparation of sulfur-doped microporous carbons for the storage of hydrogen and carbon dioxide. *Carbon* 50 (15), 5543–5553. doi:10.1016/j.carbon.2012.07.044.
- Xian, S., Wu, Y., Wu, J., Wang, X., Qiao, J., 2015a. Enhanced dynamic CO₂ adsorption capacity and CO₂/CH₄ selectivity on polyethyleneimine-impregnated UiO-66. *Ind. Eng. Chem. Res.* 54 (44), 11151–11158. doi:10.1021/acs.iecr.5b03517.
- Xian, S., Xu, F., Ma, C., Wu, Y., Xia, Q., Wang, H., Li, Z., 2015b. Vapor-enhanced CO₂ adsorption mechanism of composite PEI@ZIF-8 modified by polyethyleneimine for CO₂/N₂ separation. *Chem. Eng. J.* 280, 363–369. doi:10.1016/j.cej.2015.06.042.
- Xiao, M., Liu, H., Idem, R., Tontiwachuthikul, P., Liang, Z., 2016. A study of structure-activity relationships of commercial tertiary amines for post-combustion CO₂ capture. *Appl. Energy* 184, 219–229. doi:10.1016/j.apenergy.2016.10.006.
- Xiao, J., Wang, Y., Zhang, T.C., Ouyang, L., Yuan, S., 2022. Phytic acid-induced self-assembled chitosan gel-derived N, P-co-doped porous carbon for high-performance CO₂ capture and supercapacitor. *J. Power Sources* 517, 230727. doi:10.1016/j.jpowsour.2021.230727.
- Xiao, Y., Raheem, A., Ding, L., Chen, W.-H., Chen, X., Wang, F., Lin, S.-L., 2022. Pretreatment, modification and applications of sewage sludge-derived biochar for resource recovery—A review. *Chemosphere* 287, 131969. doi:10.1016/j.chemosphere.2021.131969.
- Xie, Y., Zhang, Y., Lu, X., Ji, X., 2014. Energy consumption analysis for CO₂ separation using imidazolium-based ionic liquids. *Appl. Energy* 136, 325–335. doi:10.1016/j.apenergy.2014.09.046.
- Xie, W.J., Yu, M.Q., Wang, R., 2017. CO₂ capture behaviors of amine-modified resorcinol-based carbon aerogels adsorbents. *Aerosol. Air Qual. Res.* 17 (11), 2715–2725. doi:10.4209/aaqr.2016.12.0597.
- Xie, K., Fu, Q., Webley, P.A., Qiao, G.G., 2018. MOF scaffold for a high-performance mixed-matrix membrane. *Angew. Chem. Int. Ed.* 130 (28), 8733–8738. doi:10.1002/anie.201804162.
- Xie, P., et al., 2019. A mesoscale 3D CFD analysis of the liquid flow in a rotating packed bed. *Chemical Engineering Science* 199, 528–545.
- Xie, Y.Q., Wang, L., Li, H.L., Westholm, L.J., Carvalho, L., Thorin, E., Yu, Z.X., Yu, X.H., Kreiberg, O., 2022. A critical review on production, modification and utilization of biochar. *J. Anal. Appl. Pyrol.* 161. doi:10.1016/j.jaap.2021.105405.
- Xing, L., Wei, K., Li, Y., Fang, Z., Li, Q., Qi, T., An, S., Zhang, S., Wang, L., 2021. TiO₂ coating strategy for robust catalysis of the metal-organic framework toward energy-efficient CO₂ capture. *Environ. Sci. Technol.* 55 (16), 11216–11224. doi:10.1021/acs.est.1c02452.
- Xiong, J., Zhao, H., Zheng, C., 2011. Exergy analysis of a 600 MWe oxy-combustion pulverized-coal-fired power plant. *Energy Fuels* 25 (8), 3854–3864. doi:10.1021/EF200702K.
- Xiong, J., Zhao, H., Zheng, C., 2012. Thermoeconomic cost analysis of a 600 MWe oxy-combustion pulverized-coal-fired power plant. *Int. J. Greenh. Gas Control* 9, 469–483. doi:10.1016/j.IJGGC.2012.05.012.
- Xiong, Z., Shihong, Z., Haiping, Y., Tao, S., Yingqian, C., Hanping, C., 2013. Influence of NH₃/CO₂ modification on the characteristic of biochar and the CO₂ capture. *Bioenerg. Res.* 6 (4), 1147–1153. doi:10.1007/s12155-013-9304-9.
- Xiong, Q., Wu, X., Lv, H., Liu, S., Hou, H., Wu, X., 2021. Influence of rice husk addition on phosphorus fractions and heavy metals risk of biochar derived from sewage sludge. *Chemosphere* 280, 130566. doi:10.1016/j.chemosphere.2021.130566.
- C Xu, X.S., Andresen, J.M., Miller, B.G., Scaroni, A.W., 2002. Novel polyethyleneimine-modified mesoporous molecular sieve of MCM-41 type as high-capacity adsorbent for CO₂ capture. *Energy Fuels* 16, 1463–1469.
- S.C. Xu, X., Miller, B.G., Scaroni, A.W., 2005. Influence of Moisture on CO₂ Separation from Gas Mixture by a Nanoporous Adsorbent Based on Polyethyleneimine-Modified Molecular Sieve MCM-41. *Ind. Eng. Chem. Res.* 44 (21), 8113–8119.
- Xu, L., Rungta, M., Hessler, J., Qiu, W., Brayden, M., Martinez, M., Barbay, G., Koros, W.J., 2014. Physical aging in carbon molecular sieve membranes. *Carbon* 80, 155–166. doi:10.1016/j.carbon.2014.08.051.
- Xu, X.Y., Kan, Y., Zhao, L., Cao, X.D., 2016. Chemical transformation of CO₂ during its capture by waste biomass derived biochars. *Environ. Pollut.* 213, 533–540. doi:10.1016/j.envpol.2016.03.013.
- Xu, Y., Luo, C., Zheng, Y., Ding, H., Zhou, D., Zhang, L., 2017. Natural calcium-based sorbents doped with sea salt for cyclic CO₂ capture. *J. Chem. Eng.* 40 (3), 522–528.
- Xu, Y., Ding, H., Luo, C., Zheng, Y., Zhang, Q., Li, X., Sun, J., Zhang, L., 2018. Potential synergy of chlorine and potassium and sodium elements in carbonation enhancement of CaO-based sorbents. *ACS Sustain. Chem. Eng.* 6 (9), 11677–11684. doi:10.1021/acssuschemeng.8b01941.
- Xu, Y., He, Q., Chen, Y.G., 2018. A rational design of microporous aerogel for excellent CO₂ capture and selectivities via Co-synergistic effects of electrostatic in-plane and pi-pi stacking interactions (1, 2). *Polym. Sci. Ser. B+ 60 (3)*, 317–323. doi:10.1134/S1560090418030193.
- Xu, J., Wang, Z., Qiao, Z., Wu, H., Dong, S., Zhao, S., Wang, J., 2019. Post-combustion CO₂ capture with membrane process: Practical membrane performance and appropriate pressure. *J. Membr. Sci.* 581, 195–213. doi:10.1016/j.memsci.2019.03.052.
- Xu, Y., Cui, D., Zhang, S., Xu, G., Su, Z., 2019. Facile synthesis of conjugated microporous polymer-based porphyrin units for adsorption of CO₂ and organic vapours. *Polym. Chem.* 10 (7), 819–822. doi:10.1039/C8PY01476K.
- Xu, Y., Jin, B., Chen, X., Zhao, Y., 2019. Performance of CO₂ absorption in a spray tower using blended ammonia and piperazine solution: Experimental studies and comparisons. *Int. J. Greenh. Gas Control* 82, 152–161. doi:10.1016/j.ijggc.2019.01.008.
- Xu, Y.C., Li, Y.B., Liu, Y.Z., Luo, Y., Chu, G.W., Zhang, L.L., Chen, J.F., 2019. Liquid jet impaction on the single-layer stainless steel wire mesh in a rotating packed bed reactor. *AIChE J.* 65 (6). doi:10.1002/aic.16597, e16597-e16597.
- Xu, M., Wang, S., Xu, L., 2019. Screening of physical-chemical biphasic solvents for CO₂ absorption. *Int. J. Greenh. Gas Control* 85, 199–205. doi:10.1016/j.ijggc.2019.03.015.
- Xu, X., Myers, M.B., Versteeg, F.G., Pejic, B., Heath, C., Wood, C.D., 2020. Direct air capture (DAC) of CO₂ using polyethyleneimine (PEI) “snow”: a scalable strategy. *Chem. Commun.* 56 (52), 7151–7154. doi:10.1039/D0CC02572K.
- Xu, X.Y., Xu, Z.B., Gao, B., Zhao, L., Zheng, Y.L., Huang, J.S., Tsang, D.C.W., Ok, Y.S., Cao, X.D., 2020. New insights into CO₂ sorption on biochar/Fe oxyhydroxide composites: kinetics, mechanisms, and in situ characterization. *Chem. Eng. J.* 384. doi:10.1016/j.cej.2019.123289.
- Xu, Y., Jin, B., Jiang, H., Li, L., Wei, J., 2020. Investigation of the regeneration of a CO₂-loaded ammonia solution with solid acid catalysts: A promising alternative for reducing regeneration energy. *Fuel Process. Technol.* 205, 106452.
- Xu, Y., Yang, Z., Zhang, G., Zhao, P., 2020. Excellent CO₂ adsorption performance of nitrogen-doped waste biochar prepared with different activators. *J. Clean. Prod.* 264, 121645. doi:10.1016/j.jclepro.2020.121645.
- Xu, J., Jia, P.P., Wang, X.J., Xie, Z.Y., Chen, Z.Y., Jiang, H., 2021. The aminosilane functionalization of cellulose nanocrystal aerogel via vapour-phase reaction and its CO₂ adsorption characteristics. *J. Appl. Polym. Sci.* 138 (35). doi:10.1002/app.50891.
- Xu, Y., Shen, C., Lu, B., Luo, C., Wu, F., Li, X., Zhang, L., 2021. Study on the effect of NaBr modification on CaO-based sorbent for CO₂ capture and SO₂ capture. *Carbon Cap. Sci. Technol.* 1, 100105. doi:10.1016/j.cst.2021.100105.
- Xu, Y., Donat, F., Luo, C., Chen, J., Kierzkowska, A., Awais Naem, M., Zhang, L., Müller, C.R., 2023. Investigation of K₂CO₃-modified CaO sorbents for CO₂ capture using in-situ X-ray diffraction. *Chem. Eng. J.* 453, 139913. doi:10.1016/j.cej.2022.139913.
- Xuan, Y., Yu, Q., Qin, Q., Wang, K., Duan, W., Liu, K., Zhang, P., 2018. Selection of desulfurizer and control of reaction products on flue-gas desulfurization using chemical-looping technology. *Energy Fuels* 32 (1), 889–900.
- Xue, J., Liao, Q., Chen, W., Bouwmeester, H.J.M., Wang, H., Feldhoff, A., 2015. A new CO₂-resistant Ruddlesden-Popper oxide with superior oxygen transport: A-site deficient (Pr_{0.9}La_{0.1})₂ (Ni_{0.74}Cu_{0.21}Ga_{0.05})O_{4+δ}. *J. Mater. Chem. A* 3, 19107–19114. doi:10.1039/C5TA02514A.
- Xuepeng, B., 2014. CO₂ capture technologies and application. *Clean Coal Technol.* 20 (05) 9-13+19.
- Yañez-Aulestia, A., Wang, Q., Pfeiffer, H., 2020. Enhancing CO₂ chemisorption on lithium cuprate (Li₂CuO₂) at moderate temperatures and different pressures by alkaline nitrate addition. *Phys. Chem. Chem. Phys.* 22 (5), 2803–2813. doi:10.1039/C9CP05512F.
- Yadav, S., Mondal, S.S., 2022. A review on the progress and prospects of oxy-fuel carbon capture and sequestration (CCS) technology. *Fuel* 308. doi:10.1016/J.FUEL.2021.122057, 122057-122057.
- Yamazaki, T., Katoh, M., Ozawa, S., Ogino, Y., 1993. Adsorption of CO₂ over univalent cation-exchanged ZSM-5 zeolites. *Mol. Phys.* 80 (2), 313–324.
- Yan, X., Zhang, L., Zhang, Y., Qiao, K., Yan, Z., Komarneni, S., 2011a. Amine-modified mesocellular silica foams for CO₂ capture. *Chem. Eng. J.* 168 (2), 918–924. doi:10.1016/j.cej.2011.01.066.

- Yan, X., Zhang, L., Zhang, Y., Yang, G., Yan, Z., 2011b. Amine-modified SBA-15: effect of pore structure on the performance for CO₂ capture. *Ind. Eng. Chem. Res.* 50 (6), 3220–3226. doi:10.1021/ie101240d.
- Yan, Q., Lin, Y., Kong, C., Chen, L., 2013. Remarkable CO₂/CH₄ selectivity and CO₂ adsorption capacity exhibited by polyamine-decorated metal-organic framework adsorbents. *Chem. Commun. (Camb.)* 49 (61), 6873–6875. doi:10.1039/c3cc43352h.
- Yan, X., Komarneni, S., Yan, Z., 2013. CO₂ adsorption on santa barbara amorphous-15 (SBA-15) and amine-modified santa barbara amorphous-15 (SBA-15) with and without controlled microporosity. *J. Colloid. Interface Sci.* 390 (1), 217–224. doi:10.1016/j.jcis.2012.09.038.
- Yan, X., Komarneni, S., Zhang, Z., Yan, Z., 2014. Extremely enhanced CO₂ uptake by HKUST-1 metal-organic framework via a simple chemical treatment. *Microporous Mesoporous Mater.* 183, 69–73. doi:10.1016/j.micromeso.2013.09.009.
- Yan, H., Fu, Q., Zhou, Y., Li, D., Zhang, D., 2016. CO₂ capture from dry flue gas by pressure vacuum swing adsorption: A systematic simulation and optimization. *Int. J. Greenh. Gas Control* 51, 1–10. doi:10.1016/j.jggc.2016.04.005.
- Yan, S., Zhu, D., Zhang, Z., Li, H., Chen, G., Liu, B., 2019. A pilot-scale experimental study on CO₂ capture using zeolitic imidazolate framework-8 slurry under normal pressure. *Appl. Energy* 248, 104–114. doi:10.1016/j.apenergy.2019.04.097.
- Yan, Y., Borhani, T.N., Subraveti, S.G., Pai, K.N., Prasad, V., Rajendran, A., Nkuliyyinka, P., Ashbor, J.O., Zhang, Z., Shao, D., Wang, L., Zhang, W., Yan, Y., Ampomah, W., You, J., Wang, M., Anthony, E.J., Manovic, V., Clough, P.T., 2021. Harnessing the power of machine learning for carbon capture, utilisation, and storage (CCUS) a state-of-the-art review. *Energy Environ. Sci.* 14 (12), 6122–6157. doi:10.1039/d1ee02395k.
- Yan, Y.-T., Wu, G., Chen, S.-C., Wang, Y.-Z., 2022. Controlled synthesis and closed-loop chemical recycling of biodegradable copolymers with composition-dependent properties. *Sci. China Chem.* 65 (5), 943–953. doi:10.1007/s11426-021-1196-7.
- Yang, J.-I., Kim, J.-N., 2006. Hydrothermalities for adsorption of CO₂ at high temperature. *Korean J. Chem. Eng.* 23 (1), 77–80. doi:10.1007/BF02705695.
- Yang, Q., Lin, Y.S., 2006. Kinetics of carbon dioxide sorption on perovskite-type metal oxides. *Ind. Eng. Chem. Res.* 45 (18), 6302–6310. doi:10.1021/ie060264f.
- Yang, Z., Lin, Y.S., Zeng, Y., 2002. High-temperature sorption process for air separation and oxygen removal. *Ind. Eng. Chem. Res.* 41 (11), 2775–2784. doi:10.1021/IE017366k.
- Yang, D., Wang, Z., Wang, J., Wang, S., 2009. Potential of two-stage membrane system with recycle stream for CO₂ capture from postcombustion gas†. *Energy Fuels* 23 (10), 4755–4762. doi:10.1021/ef801109p.
- Yang, Q., Wiersum, A.D., Llewellyn, P.L., Guiller, V., Serre, C., Maurin, G., 2011. Functionalizing porous zirconium terephthalate UiO-66 (Zr) for natural gas upgrading: a computational exploration. *Chem. Commun. (Camb.)* 47 (34), 9603–9605. doi:10.1039/c1cc13543k.
- Yang, S.-T., Kim, J.-Y., Kim, J., Ahn, W.-S., 2012. CO₂ capture over amine-functionalized MCM-22, MCM-36 and ITQ-2. *Fuel* 97, 435–442. doi:10.1016/j.fuel.2012.03.034.
- Yang, D., Hou, M., Ning, H., Zhang, J., Ma, J., Han, B., 2013. Efficient SO₂ capture by amine functionalized PEG. *Phys. Chem. Chem. Phys.* 15 (41), 18111–18118. doi:10.1039/c3cp52911h.
- Yang, M., Song, Y., Jiang, L., Liu, Y., Li, Y., 2014. CO₂ hydrate formation characteristics in a water/brine-saturated silica gel. *Ind. Eng. Chem. Res.* 53 (26), 10753–10761. doi:10.1021/ie5012728.
- Yang, N., Yu, H., Xu, D.Y., Conway, W., Maeder, M., Feron, P., 2014. Amino acids/NH₃ mixtures for CO₂ capture: Effect of neutralization methods on CO₂ mass transfer and NH₃ vapour loss. *Energy Procedia* 63, 773–780.
- Yang, J., Pruvost, S., Livi, S., Duchet-Rumeau, J., 2015. Understanding of versatile and tunable nanostructure of ionic liquids on fluorinated copolymer. *Macromolecules* 48 (13), 4581–4590. doi:10.1021/acs.macromol.5b00931.
- Yang, Y., Xiang, Y., Li, Y., Chu, G., Zou, H., Arowo, M., Chen, J., 2015. 3D CFD modelling and optimization of single-phase flow in rotating packed beds. *Can. J. Chem. Eng.* 93 (6), 1138–1148. doi:10.1002/cjce.21183.
- Yang, X., Zhao, L., Liu, Y., Sun, Z., Xiao, Y., 2016. Carbonation performance of NaNO₃ modified MgO sorbents. *Ind. Eng. Chem. Res.* 55 (1), 342–350.
- Yang, X., Liu, W., Sun, J., Hu, Y., Wang, W., Chen, H., Zhang, Y., Li, X., Xu, M., 2016a. Alkali-doped lithium orthosilicate sorbents for carbon dioxide capture. *ChemSusChem* 9 (17), 2480–2487. doi:10.1002/cssc.201600737.
- Yang, X., Liu, W., Sun, J., Hu, Y., Wang, W., Chen, H., Zhang, Y., Li, X., Xu, M., 2016b. Preparation of novel Li₂SiO₄ sorbents with superior performance at low CO₂ concentration. *ChemSusChem* 9 (13), 1607–1613. doi:10.1002/cssc.201501699.
- Yang, L., Tian, Z., Zhang, X., Wu, X., Wu, Y., Wang, Y., Peng, D., Wang, S., Wu, H., Jiang, Z., 2017. Enhanced CO₂ selectivities by incorporating CO₂-philic PEG-POSS into polymers of intrinsic microporosity membrane. *J. Membr. Sci.* 543, 69–78. doi:10.1016/j.memsci.2017.08.050.
- Yang, Z., Yi, H., Tang, X., Zhao, S., Yu, Q., Gao, F., Zhou, Y., Wang, J., Huang, Y., Yang, K., Shi, Y., 2017. Potential demonstrations of “hot spots” presence by adsorption-desorption of toluene vapour onto granular activated carbon under microwave radiation. *Chem. Eng. J.* 319, 191–199. doi:10.1016/j.cej.2017.02.157.
- Yang, Y., Lin, X., Chen, X., Guo, W., Wang, Y., Zhang, J., Kawa, O., 2018. Investigation on the effects of different forms of sodium, chlorine and sulphur and various pretreatment methods on the deposition characteristics of Na species during pyrolysis of a Na-rich coal. *Fuel* 234, 872–885. doi:10.1016/j.fuel.2018.07.130.
- Yang, Y., Chuah, C.Y., Bae, T.-H., 2019. Polyamine-appended porous organic polymers for efficient post-combustion CO₂ capture. *Chem. Eng. J.* 358, 1227–1234. doi:10.1016/j.cej.2018.10.122.
- Yang, H., Yang, L., Wang, H., Xu, Z., Zhao, Y., Luo, Y., Nasir, N., Song, Y., Wu, H., Pan, F., 2019. Covalent organic framework membranes through a mixed-dimensional assembly for molecular separations. *Nat. Commun.* 10 (1), 1–10. doi:10.1038/s41467-019-10157-5.
- Yang, Z., Zhang, G., Xu, Y., Zhao, P., 2019. One step N-doping and activation of biomass carbon at low temperature through NaNH₂: An effective approach to CO₂ adsorbents. *J. CO₂ Util.* 33, 320–329. doi:10.1016/j.jcou.2019.06.021.
- Yang, Z., Guo, W., Mahurin, S.M., Wang, S., Chen, H., Cheng, L., Jie, K., Meyer, H.M., Jiang, D.-e., Liu, G., Jin, W., Popovs, I., Dai, S., 2020. Surpassing robeson upper limit for CO₂/N₂ separation with fluorinated carbon molecular sieve membranes. *Chem* 6 (3), 631–645. doi:10.1016/j.chempr.2019.12.006.
- Yang, C., Zhang, B., Zhang, S., Wu, Y., Wang, T., Qiu, J., 2021. Highly permeable and selective sepiolite hybrid mixed matrix carbon membranes supported on plate carbon substrates for gas separation. *Chem. Eng. Res. Des.* 174, 319–330. doi:10.1016/j.cherd.2021.08.012.
- Yang, Y., Li, Y.J., Yan, X.Y., Zhao, J.L., Zhang, C.X., 2021. Development of thermochemical heat storage based on CaO/CaCO₃ cycles: a review. *Energies* 14 (20), 26. doi:10.3390/en14206847.
- Yang, Z., Khatri, D., Verma, P., Li, T., Adeosun, A., Kumfer, B.M., Axelbaum, R.L., 2021. Experimental study and demonstration of pilot-scale, dry feed, oxy-coal combustion under pressure. *Appl. Energy* 285, 116367. doi:10.1016/j.apenergy.2020.116367.
- Yang, C., Zhao, T., Pan, H., Liu, F., Cao, J., Lin, Q., 2022. Facile preparation of N-doped porous carbon from chitosan and NaNH₂ for CO₂ adsorption and conversion. *Chem. Eng. J.* 432, 134347. doi:10.1016/j.cej.2021.134347.
- Yang, F., Ge, T., Zhu, X., Wu, J., Wang, R., 2022. Study on CO₂ capture in humid flue gas using amine-modified ZIF-8. *Sep. Purif. Technol.* 287. doi:10.1016/j.seppur.2022.120535.
- Yang, Z., Ying, Y., Pu, Y., Wang, D., Yang, H., Zhao, D., 2022. Poly (ionic liquid)-functionalized UiO-66-(OH)₂: Improved interfacial compatibility and separation ability in mixed matrix membranes for CO₂ separation. *Ind. Eng. Chem. Res.* 61 (22), 7626–7633. doi:10.1021/acs.iecr.1c04648.
- Yanuka-Golub, K., Baransi-Karkaby, K., Szczupak, A., Reshef, L., Rishpon, J., Shechter, R., Gophna, U., Sabbah, I., 2019. An electrode-assisted anaerobic digestion process for the production of high-quality biogas. *Water Sci. Technol.* 79 (11), 2145–2155. doi:10.2166/wst.2019.214.
- Yao, Q., Su, J., Cheung, O., Liu, Q., Hedin, N., Zou, X., 2012. Interpenetrated metal-organic frameworks and their uptake of CO₂ at relatively low pressures. *J. Mater. Chem.* 22 (20), 11933. doi:10.1039/c2jm15933c.
- Yassin, M.M., Anderson, J.A., Dimitrakis, G.A., Martin, C.F., 2021. Effects of the heating source on the regeneration performance of different adsorbents under post-combustion carbon capture cyclic operations. A comparative analysis. *Sep. Purif. Technol.* 276. doi:10.1016/j.seppur.2021.119326.
- Yave, W., Car, A., Funari, S.S., Nunes, S.P., Peinemann, K.-V., 2010. CO₂-philic polymer membrane with extremely high separation performance. *Macromolecules* 43 (1), 326–333. doi:10.1021/ma901950u.
- Yay, B., Gizli, N., 2019. A review on silica aerogels for CO₂ capture applications. *Pamukkale Univ. J. Eng. Sci.-Pamukkale Univ. Muhendislik Bilimleri Dergisi* 25 (7), 907–913. doi:10.5505/pajes.2018.35651.
- Yazaydin, A.O., Benin, A.I., Faheem, S.A., Jakubczak, P., Low, J.J., Willis, R.R., Snurr, R.Q., 2009. Enhanced CO₂ adsorption in metal-organic frameworks via occupation of open-metal sites by coordinated water molecules. *Chem. Mater.* 21, 1425–1430.
- Ye, Q., Wang, X., Lu, Y., 2015. Screening and evaluation of novel biphasic solvents for energy-efficient post-combustion CO₂ capture. *Int. J. Greenh. Gas Control* 39, 205–214. doi:10.1016/j.jggc.2015.05.025.
- Ye, L., Jie, X., Wang, L., Xu, G., Sun, Y., Kang, G., Cao, Y., 2021. Preparation and gas separation performance of thermally rearranged poly (benzoxazole-co-amide) (TR-PBOA) hollow fiber membranes deriving from polyamides. *Sep. Purif. Technol.* 257, 117870.
- Yek, P.N.Y., Peng, W., Wong, C.C., Liew, R.K., Ho, Y.L., Wan Mahari, W.A., Azwar, E., Yuan, T.Q., Tabatabaei, M., Aghbashlo, M., Sonne, C., Lam, S.S., 2020. Engineered biochar via microwave CO₂ and steam pyrolysis to treat carcinogenic Congo red dye. *J. Hazard. Mater.* 395, 122636. doi:10.1016/j.jhazmat.2020.122636.
- Yi, C.-K., Jo, S.-H., Seo, Y., Lee, J.-B., Ryu, C.-K., 2007. Continuous operation of the potassium-based dry sorbent CO₂ capture process with two fluidized-bed reactors. *Int. J. Greenh. Gas. Con. 1* (1), 31–36. doi:10.1016/s1750-5836(07)00014-x.
- Yi, F., Zou, H.K., Chu, G.W., Shao, L., Chen, J.F., 2009. Modeling and experimental studies on absorption of CO₂ by Benfield solution in rotating packed bed. *Chem. Eng. J.* 145 (3), 377–384. doi:10.1016/j.cej.2008.08.004.
- Yi, J., Schroeder, M., Weirich, T., Mayer, J., 2010. Behavior of Ba (Co, Fe, Nb)O_{3-δ} Perovskite in CO₂-containing atmospheres: degradation mechanism and materials design. *Chem. Mater.* 22 (23), 6246–6253. doi:10.1021/cm101665r.
- Yi, J., Weirich, T.E., Schroeder, M., 2013. CO₂ corrosion and recovery of perovskite-type BaCo_{1-x-y}FexNbyO_{3-δ} membranes. *J. Membr. Sci.* 437, 49–56. doi:10.1016/j.memsci.2013.02.049.
- Yin, J.-Z., Zhen, M.-Y., Cai, P., Zhou, D., Li, Z.-J., Zhu, H.-Y., Xu, Q.-Q., 2018. Supercritical CO₂ preparation of SBA-15 supported ionic liquid and its adsorption for CO₂. *Mater. Res. Exp.* 5 (6), 065060. doi:10.1088/2053-1591/aacdb4.
- Yin, X., Xi, M., Li, Y., Kong, F., Jiang, Z., 2021. Improvements in physicochemical and nutrient properties of sewage sludge biochar by the co-pyrolysis with organic additives. *Sci. Total Environ.* 779, 146565. doi:10.1016/j.scitotenv.2021.146565.
- Yin, Y., Chen, W., Wu, C., Zhang, X., Fu, T., Zhu, C., Ma, Y., 2022. Bubble dynamics and mass transfer enhancement in split-and-recombine (SAR) microreactor with rapid chemical reaction. *Sep. Purif. Technol.* 287, 120573. doi:10.1016/j.seppur.2022.120573.
- Ying, Z., Zheng, X., Cui, G., 2016. Pressurized oxy-fuel combustion performance of pulverized coal for CO₂ capture. *Appl. Therm. Eng.* 99, 411–418. doi:10.1016/j.applthermaleng.2016.01.023.
- Ying, W., Cai, J., Zhou, K., Chen, D., Ying, Y., Guo, Y., Kong, X., Xu, Z., Peng, X., 2018. Ionic liquid selectively facilitates CO₂ transport through graphene oxide membrane. *ACS Nano* 12 (6), 5385–5393. doi:10.1021/acsnano.8b00367.

- Yong, Z., Rodrigues, A., 2002. Hydrotalcite-like compounds as adsorbents for carbon dioxide. *Energy Convers. Manage.* 43, 1865–1876. doi:10.1016/S0196-8904(01)00125-X.
- Yong, Z., Mata, Rodrigues, A.E., 2001. Adsorption of carbon dioxide onto hydrotalcite-like compounds (HTCs) at high temperatures. *Ind. Eng. Chem. Res.* 40 (1), 204–209. doi:10.1021/ie000238w.
- Yoo, D.K., Jhung, S.H., 2022. Selective CO₂ adsorption at low pressure with a Zr-based UiO-67 metal-organic framework functionalized with aminosilanes. *J. Mater. Chem. A* 10 (16), 8856–8865. doi:10.1039/d1ta09772e.
- Yoshimura, T., Tamenori, Y., Suzuki, A., Kawahata, H., Iwasaki, N., Hasegawa, H., Nguyen, L.T., Kuroyanagi, A., Yamazaki, T., Kuroda, J., Ohkouchi, N., 2017. Al-ternative substitution of sodium for calcium in biogenic calcite and aragonite. *Geochim. Cosmochim. Acta* 202, 21–38. doi:10.1016/j.gca.2016.12.003.
- Younas, M., Rezakazemi, M., Daud, M., Wazir, M.B., Ahmad, S., Ullah, N., Inamuddin, Ramakrishna, S., 2020. Recent progress and remaining challenges in post-combustion CO₂ capture using metal-organic frameworks (MOFs). *Prog. Energy Combust. Sci.* 80. doi:10.1016/j.peccs.2020.100849.
- Young, B., Krynock, M., Carlson, D., Hawkins, T.R., Marriotti, J., Morelli, B., Jamieson, M., Cooney, G., Skone, T.J., 2019. Comparative environmental life cycle assessment of carbon capture for petroleum refining, ammonia production, and thermo-electric power generation in the United States. *Int. J. Greenh. Gas Control* 91. doi:10.1016/j.jggcc.2019.102821.
- Young, J., Garcia-Diez, E., Garcia, S., van der Spek, M., 2021. The impact of binary water-CO₂ isotherm models on the optimal performance of sorbent-based direct air capture processes. *Energy Environ. Sci.* 14 (10), 5377–5394. doi:10.1039/d1ee01272j.
- Yousef, A.M., El-Maghlany, W.M., Eldrainy, Y.A., Attia, A., 2018a. Low-temperature distillation process for CO₂/CH₄ separation: a study for avoiding CO₂ freeze-out. *J. Heat Transf.* 140 (4), 042001. doi:10.1115/1.4038193.
- Yousef, A.M., El-Maghlany, W.M., Eldrainy, Y.A., Attia, A., 2018b. New approach for biogas purification using cryogenic separation and distillation process for CO₂ capture. *Energy* 156, 328–351. doi:10.1016/j.energy.2018.05.106.
- Yousef, A.M., El-Maghlany, W.M., Eldrainy, Y.A., Attia, A., 2019. Upgrading biogas to biomethane and liquid CO₂: A novel cryogenic process. *Fuel* 251, 611–628. doi:10.1016/j.fuel.2019.03.127.
- Yu, J., Balbuena, P.B., 2013. Water effects on postcombustion CO₂ capture in Mg-MOF-74. *J. Phys. Chem. C* 117 (7), 3383–3388.
- Yu, J., Wang, S., 2015. Modeling analysis of energy requirement in aqueous ammonia based CO₂ capture process. *Int. J. Greenh. Gas Control* 43, 33–45. doi:10.1016/j.jggcc.2015.10.010.
- Yu, K., Curcic, I., Gabriel, J., Tsang, S., 2008. Recent advances in CO₂ capture and utilization. *ChemSusChem* 1 (11), 893–899.
- Yu, X., Wang, Z., Wei, Z., Yuan, S., Zhao, J., Wang, J., Wang, S., 2010. Novel tertiary amino containing thin film composite membranes prepared by interfacial polymerization for CO₂ capture. *J. Membr. Sci.* 362 (1–2), 265–278.
- Yu, M., Funke, H.H., Noble, R.D., Falconer, J.L., 2011. H₂ separation using defect-free, inorganic composite membranes. *J. Am. Chem. Soc.* 133 (6), 1748–1750. doi:10.1021/ja108681n.
- Yu, C.-H., Huang, C.-H., Tan, C.-S., 2012. A review of CO₂ capture by absorption and adsorption. *Aerosol. Air Qual. Res.* 12 (5), 745–769. doi:10.4209/aaqr.2012.05.0132.
- Yu, Y.S., Lu, H.F., Zhang, T.T., Zhang, Z.X., Wang, G.X., Rudolph, V., 2013. Determining the performance of an efficient nonaqueous CO₂ capture process at desorption temperatures below 373 K. *Ind. Eng. Chem. Res.* 52 (35), 12622–12634. doi:10.1021/ie400353f.
- Yu, Y., Mai, J., Wang, L., Li, X., Jiang, Z., Wang, F., 2014. Ship-in-a-bottle synthesis of amine-functionalized ionic liquids in NaY zeolite for CO₂ capture. *Sci. Rep.* 4, 5997. doi:10.1038/srep05997.
- Yu, Y., Mai, J., Huang, L., Wang, L., Li, X., 2014. Ship in a bottle synthesis of ionic liquids in NaY supercages for CO₂ capture. *RSC Adv.* 4 (25), 12756–12762. doi:10.1039/C3RA46971A.
- Yu, G., Zou, X., Sun, L., Liu, B., Wang, Z., Zhang, P., Zhu, G., 2019. Constructing connected paths between UiO-66 and PIM-1 to improve membrane CO₂ separation with crystal-Like gas selectivity. *Adv. Mater.* 31 (15), 1806853. doi:10.1002/adma.201806853.
- Yu, Z., Yang, Y., Yang, S., Zhang, Q., Zhao, J., Fang, Y., Hao, X., Guan, G., 2019. Iron-based oxygen carriers in chemical looping conversions: A review. *Carbon Resour. Convers.* 2 (1), 23–34. doi:10.1016/j.crcon.2018.11.004.
- Yu, Y., Wang, J., Wang, Y., Pan, W., Liu, C., Liu, P., Liang, L., Xu, C., Liu, Y., 2020. Polyethyleneimine-functionalized phenolphthalein-based cardo poly (ether ether ketone) membrane for CO₂ separation. *J. Ind. Eng. Chem.* 83, 20–28. doi:10.1016/j.jiec.2019.10.007.
- Yu, H., Gundersen, T., Gençer, E., 2021. Optimal liquefied natural gas (LNG) cold energy utilization in an Allam cycle power plant with carbon capture and storage. *Energy Convers. Manage.* 228, 113725.
- Yu, H., 2018. Recent developments in aqueous ammonia-based post-combustion CO₂ capture technologies. *Chin. J. Chem. Eng.* 26 (11), 2255–2265.
- Yuan, H., Lu, T., Huang, H., Zhao, D., Kobayashi, N., Chen, Y., 2015. Influence of pyrolysis temperature on physical and chemical properties of biochar made from sewage sludge. *J. Anal. Appl. Pyroly.* 112, 284–289. doi:10.1016/j.jaap.2015.01.010.
- Yuan, J., Zhu, H., Sun, J., Mao, Y., Liu, G., Jin, W., 2017. Novel ZIF-300 mixed-matrix membranes for efficient CO₂ capture. *ACS Appl. Mater. Interfaces* 9 (44), 38575–38583.
- Yuan, Y., Qiao, Z., Xu, J., Wang, J., Zhao, S., Cao, X., Wang, Z., Guiver, M.D.J., M.S., 2021. Mixed matrix membranes for CO₂ separations by incorporating microsporous polymer framework fillers with amine-rich nanochannels. *J. Membr. Sci.* 620, 118923.
- Yue, M.B., Chun, Y., Cao, Y., Dong, X., Zhu, J.H., 2006. CO₂ capture by as-prepared SBA-15 with an occluded organic template. *Adv. Funct. Mater.* 16 (13), 1717–1722. doi:10.1002/adfm.200600427.
- Yue, J., Chen, G., Yuan, Q., Luo, L., Gonthier, Y., 2007. Hydrodynamics and mass transfer characteristics in gas-liquid flow through a rectangular microchannel. *Chem. Eng. Sci.* 62 (7), 2096–2108. doi:10.1016/j.ces.2006.12.057.
- Yue, B., Liu, S., Chai, Y., Wu, G., Guan, N., Li, L., 2022. Zeolites for separation: Fundamental and application. *J. Energy Chem.* 71, 288–303. doi:10.1016/j.jechem.2022.03.035.
- Zafar, Q., Mattisson, T., Gevert, B., 2006. Redox investigation of some oxides of transition-state metals Ni, Cu, Fe, and Mn supported on SiO₂ and MgAl₂O₄. *Energy Fuels* 20 (1), 34–44. doi:10.1021/ef0501389.
- Zahedi, R., Ayazi, M., Aslani, A., 2022. Comparison of amine adsorbents and strong hydroxides soluble for direct air CO₂ capture by life cycle assessment method. *Environ. Technol. Innov.* 28. doi:10.1016/j.eti.2022.102854.
- Zakuciová, K., Štefanica, J., Carvalho, A., Kočí, V., 2020. Environmental assessment of a coal power plant with carbon dioxide capture system based on the activated carbon adsorption process: a case study of the Czech Republic. *Energies* 13 (9). doi:10.3390/en13092251.
- Zalewski, M., Krawczyk, T., Siewniak, A., Sobolewski, A., 2021. Carbon dioxide capture using water-imidazolium ionic liquids-amines ternary systems. *Int. J. Greenh. Gas Control* 105. doi:10.1016/j.jggcc.2020.103210.
- Zan, H., Chen, X., Ma, J., Liu, D., Wu, Y., 2020. Experimental study of NOx formation in a high-steam atmosphere during a pressurized oxygen-fuel combustion process. *ACS Omega* 5 (26), 16037–16044. doi:10.1021/acsomega.0c01480.
- Zanco, S.E., Joss, L., Hefti, M., Gazzani, M., Mazzotti, M., 2017. Addressing the criticalities for the deployment of adsorption-based CO₂ capture processes. *Energy Procedia* 114, 2497–2505. doi:10.1016/j.egypro.2017.03.1407.
- Zapata Ballesteros, A., De Witte, N., Denayer, J.F.M., Van Assche, T.R.C., 2022. Effect of pellet size on PSA performance: monolayer and multilayer bed case study for biogas upgrading. *Adsorption* doi:10.1007/s10450-022-00365-9.
- Zarghami, S., Hassanzadeh, A., Arastoopour, H., Abbasian, J., 2015. Effect of steam on the reactivity of MgO-based sorbents in precombustion CO₂ capture processes. *Ind. Eng. Chem. Res.* 54 (36), 8860–8866. doi:10.1021/acs.iecr.5b01175.
- Zelenak, V., Halamova, D., Gaberova, L., Bloch, E., Llewellyn, P., 2008. Amine-modified SBA-12 mesoporous silica for carbon dioxide capture: Effect of amine basicity on sorption properties. *Microporous Mesoporous Mater.* 116 (1–3), 358–364. doi:10.1016/j.micromeso.2008.04.023.
- Zeman, F., Lackner, K., 2004. Capturing carbon dioxide directly from the atmosphere. *World Resour. Rev.* 16 (2), 157–172.
- Zeman, F., 2007. Energy and material balance of CO₂ capture from ambient air. *Environ. Sci. Technol.* 41 (21), 7558–7563. doi:10.1021/es070874m.
- Zeng, W., Bai, H., 2015. High-performance CO₂ capture on amine-functionalized hierarchically porous silica nanoparticles prepared by a simple template-free method. *Adsorption* 22 (2), 117–127. doi:10.1007/s10450-015-9698-0.
- Zeng, Y., Zou, R., Zhao, Y., 2016. Covalent organic frameworks for CO₂ capture. *Adv. Mater.* 28 (15), 2855–2873.
- Zeng, Y., Li, K., Zhu, Q., Wang, J., Cao, Y., Lu, S., 2018. Capture of CO₂ in carbon nanotube bundles supported with room-temperature ionic liquids: A molecular simulation study. *Chem. Eng. Sci.* 192, 94–102. doi:10.1016/j.ces.2018.07.025.
- Zeng, L., Cheng, Z., Fan, J.A., Fan, L.-S., Gong, J., 2018. Metal oxide redox chemistry for chemical looping processes. *Nat. Rev. Chem.* 2 (11), 349–364. doi:10.1038/s41570-018-0046-2.
- Zeng, P., Zhao, C., Wang, X., Wei, X., Sun, J., Wang, R., Guo, Y., 2022. One-step synthesis of structurally improved, Al₂O₃-supported K₂CO₃ pellets via graphite-casting method for low-temperature CO₂ capture. *Sep. Purif. Technol.* 292, 120929. doi:10.1016/j.seppur.2022.120929.
- Zhai, L., Huang, N., Xu, H., Chen, Q., Jiang, D., 2017. A backbone design principle for covalent organic frameworks: the impact of weakly interacting units on CO₂ adsorption. *Chem. Commun.* 53 (30), 4242–4245.
- Zhan, G., Bai, L., Zeng, S., Bai, Y., Su, H., Wu, B., Cao, F., Shang, D., Li, Z., Zhang, X., Zhang, S., 2020. Dynamic process simulation and assessment of CO₂ removal from confined spaces using pressure swing adsorption. *Ind. Eng. Chem. Res.* 59 (37), 16407–16419. doi:10.1021/acs.iecr.0c2255.
- Zhan, G., Bai, L., Wu, B., Cao, F., Duan, Y., Chang, F., Shang, D., Bai, Y., Li, Z., Zhang, X., Zhang, S., 2021. Dynamic process simulation and optimization of CO₂ removal from confined space with pressure and temperature swing adsorption. *Chem. Eng. J.* 416. doi:10.1016/j.ccej.2021.129104.
- Zhang, C., Bokil, A., 1997. A quasi-three-dimensional approach to simulate the two-phase fluid flow and heat transfer in confusers. *Int. J. Heat Mass Transf.* 40 (15), 3537–3546. doi:10.1016/S0017-9310(97)00014-8.
- Zhang, C., Koros, W.J., 2017. Ultrasensitive carbon molecular sieve membranes with tailored synergistic sorption selective properties. *Adv. Mater.* 29 (33). doi:10.1002/adma.201701631.
- Zhang, H., Liu, Z., 2013. Research progress of CO₂ capture materials for post-combustion. *Modern Chem. Ind.* 33 (05). doi:10.16606/j.cnki.issn0253-4320.2013.05.034, 17-20+22.
- Zhang, W., Xie, P., Li, Y., Zhu, J., 2022. Modeling of gas-liquid flow in a rotating packed bed using an Eulerian multi-fluid approach. *AIChE Journal* 68 (4). doi:10.1002/aic.17561, e17561-e17561.
- Zhang, J., Webley, P.A., Xiao, P., 2008. Effect of process parameters on power requirements of vacuum swing adsorption technology for CO₂ capture from flue gas. *Energy Conversion and Management* 49 (2), 346–356.
- Zhang, Y., Chen, H., Chen, C.C., Plaza, J.M., Dugas, R., Rochelle, G.T., 2009. Rate-based process modeling study of CO₂ Capture with aqueous monoethanolamine solution. *Ind. Eng. Chem. Res.* 48 (20), 9233–9246. doi:10.1021/ie900068k.
- Zhang, X., Zheng, X., Zhang, S., Zhao, B., Wu, W., 2012. AM-TEPA impregnated disordered mesoporous silica as CO₂ capture adsorbent for balanced adsorption-desorption properties. *Ind. Eng. Chem. Res.* 51 (46), 15163–15169. doi:10.1021/ie300180u.

- Zhang, K.L., Li, X.H.S., Duan, Y.H., King, D.L., Singh, P., Li, L.Y., 2013. Roles of double salt formation and NaNO₃ in Na₂CO₃-promoted MgO absorbent for intermediate temperature CO₂ removal. *Int. J. Greenh. Gas Control* 12, 351–358. doi:10.1016/j.jggc.2012.11.013.
- Zhang, Z., Xian, S., Xia, Q., Wang, H., Li, Z., Li, J., 2013. Enhancement of CO₂ adsorption and CO₂/N₂ selectivity on ZIF-8 via postsynthetic modification. *AIChE J.* 59 (6), 2195–2206. doi:10.1002/aic.13970.
- Zhang, B., Dang, X., Wu, Y., Liu, H., Wang, T., Qiu, J., 2014. Structure and gas permeation of nanoporous carbon membranes based on RF resin/F-127 with variable catalysts. *J. Mater. Res.* 29 (23), 2881–2890. doi:10.1557/jmr.2014.327.
- Zhang, K., Li, X.S., Li, W.-Z., Rohatgi, A., Duan, Y., Singh, P., Li, L., King, D.L., 2014. Phase transfer-catalyzed fast CO₂ absorption by MgO-based absorbents with high cycling capacity. *Adv. Mater. Interfaces* 1 (3), 1400030. doi:10.1002/admi.201400030.
- Zhang, X., Singh, B., He, X., Gundersen, T., Deng, L., Zhang, S., 2014. Post-combustion carbon capture technologies: Energetic analysis and life cycle assessment. *Int. J. Greenh. Gas Control* 27, 289–298. doi:10.1016/j.jggc.2014.06.016.
- Zhang, X.P., Singh, B., He, X.Z., Gundersen, T., Deng, L.Y., Zhang, S.J., 2014. Post-combustion carbon capture technologies: energetic analysis and life cycle assessment. *Int. J. Greenh. Gas Control* 27, 289–298. doi:10.1016/j.jggc.2014.06.016.
- Zhang, K., Li, X.S., Chen, H., Singh, P., King, D.L., 2015. Molten salt promoting effect in double salt CO₂ absorbents. *J. Phys. Chem. C* 120 (2), 1089–1096.
- Zhang, R., Liang, Z., Liu, H., Rongwong, W., Luo, X., Idem, R., Yang, Q., 2016. Study of formation of bicarbonate ions in CO₂-loaded aqueous single IDMA2P and MDEA tertiary amines and blended MEA-IDMA2P and MEA-MDEA amines for low heat of regeneration. *Ind. Eng. Chem. Res.* 55 (12), 3710–3717. doi:10.1021/acs.iecr.5b03097.
- Zhang, W., Liu, H., Sun, Y., Cakstins, J., Sun, C., Snape, C.E., 2016. Parametric study on the regeneration heat requirement of an amine-based solid adsorbent process for post-combustion carbon capture. *Appl. Energy* 168, 394–405. doi:10.1016/j.apenergy.2016.01.049.
- Zhang, X., Wu, J., Yang, H., Shao, J., Wang, X., Chen, Y., Zhang, S., Chen, H., 2016. Preparation of nitrogen-doped microporous modified biochar by high temperature CO₂-NH₃ treatment for CO₂ adsorption: effects of temperature. *RSC Adv.* 6 (10), 98157–98166.
- Zhang, Y., Ji, X., Xie, Y., Lu, X., 2016. Screening of conventional ionic liquids for carbon dioxide capture and separation. *Appl. Energy* 162, 1160–1170. doi:10.1016/j.apenergy.2015.03.071.
- Zhang, C., Sunarso, J., Liu, S., 2017. Designing CO₂-resistant oxygen-selective mixed ionic-electronic conducting membranes: Guidelines, recent advances, and forward directions. *Chem. Soc. Rev.* 46, 2941–3005.
- Zhang, J.P., Luo, Y., Chu, G.W., Sang, L., Liu, Y., Zhang, L.L., Chen, J.F., 2017. A hydrophobic wire mesh for better liquid dispersion in air. *Chem. Eng. Sci.* 170, 204–212. doi:10.1016/j.ces.2017.03.058.
- Zhang, M., Li, Y., Li, Y., Han, H., Teng, L., 2017. Numerical simulations on the effect of sloshing on liquid flow maldistribution of randomly packed column. *Appl. Therm. Eng.* 112, 585–594. doi:10.1016/j.applthermaleng.2016.10.049.
- Zhang, S., Zhang, J., Zhang, Y., Deng, Y., 2017. Nanofinanced ionic liquids. *Chem. Rev.* 117 (10), 6755–6833. doi:10.1021/acs.chemrev.6b00509.
- Zhang, W., Chen, J., Luo, X., Wang, M., 2017. Modelling and process analysis of post-combustion carbon capture with the blend of 2-amino-2-methyl-1-propanol and piperazine. *Int. J. Greenh. Gas Control* 63, 37–46. doi:10.1016/j.jggc.2017.04.018.
- Zhang, X., Liu, H., Liang, Z., 2017. CO₂ desorption in single and blended amine solvents with and without catalyst. *Energy Procedia* 114, 1862–1868. doi:10.1016/j.egypro.2017.03.1316.
- Zhang, X.-M., Tu, Z.-H., Li, H., Li, L., Wu, Y.-T., Hu, X.-B., 2017a. Supported protic-ionic-liquid membranes with facilitated transport mechanism for the selective separation of CO₂. *J. Membr. Sci.* 527, 60–67. doi:10.1016/j.memsci.2017.01.006.
- Zhang, X.-M., Tu, Z.-H., Li, H., Li, L., Wu, Y.-T., Hu, X.-B., 2017b. Supported protic-ionic-liquid membranes with facilitated transport mechanism for the selective separation of CO₂. *J. Membr. Sci.* 527, 60–67.
- Zhang, B., Wei, M., Mao, H., Pei, X., Alshmiri, S.A., Reimer, J.A., Yaghi, O.M., 2018. Crystalline dioxin-linked covalent organic frameworks from irreversible reactions. *J. Am. Chem. Soc.* 140 (40), 12715–12719.
- Zhang, H., Tian, H., Zhang, J., Guo, R., Li, X., 2018. Facilitated transport membranes with an amino acid salt for highly efficient CO₂ separation. *Int. J. Greenh. Gas Control* 78, 85–93. doi:10.1016/j.jggc.2018.07.014.
- Zhang, S., Shen, Y., Shao, P., Chen, J., Wang, L., 2018. Kinetics, thermodynamics, and mechanism of a novel biphasic solvent for CO₂ capture from flue gas. *Environ. Sci. Technol.* 52 (6), 3660–3668. doi:10.1021/acs.chem.7b05936.
- Zhang, X., Hong, J., Liu, H., Luo, X., Olson, W., Tontiwachwuthikul, P., Liang, Z., 2018a. SO₄²⁻/ZrO₂ supported on γ -Al₂O₃ as a catalyst for CO₂ desorption from CO₂-loaded monoethanolamine solutions. *AIChE J.* 64 (11), 3988–4001. doi:10.1002/aic.16380.
- Zhang, X., Liu, H., Liang, Z., Idem, R., Tontiwachwuthikul, P., Jaber Al-Marri, M., Benamor, A., 2018b. Reducing energy consumption of CO₂ desorption in CO₂-loaded aqueous amine solution using Al₂O₃/HZSM-5 bifunctional catalysts. *Appl. Energy* 229, 562–576. doi:10.1016/j.apenergy.2018.07.035.
- Zhang, X., Zhang, R., Liu, H., Gao, H., Liang, Z., 2018c. Evaluating CO₂ desorption performance in CO₂-loaded aqueous tri-solvent blend amines with and without solid acid catalysts. *Appl. Energy* 218, 417–429. doi:10.1016/j.apenergy.2018.02.087.
- Zhang, M., Li, J., Wang, Y., Yang, C., 2019. Impacts of different biochar types on the anaerobic digestion of sewage sludge. *RSC Adv.* 9 (72), 42375–42386. doi:10.1039/C9RA08700A.
- Zhang, P., Xu, R., Li, H., Gao, H., Liang, Z., 2019. Mass transfer performance for CO₂ absorption into aqueous blended MDEA/MEA solution with optimized molar ratio in a hollow fiber membrane contactor. *Sep. Purif. Technol.* 211, 628–636. doi:10.1016/j.seppur.2018.10.034.
- Zhang, W., Gao, E., Li, Y., Bernards, M.T., He, Y., Shi, Y., 2019. CO₂ capture with polyamine-based protic ionic liquid functionalized mesoporous silica. *J. CO₂ Util.* 34, 606–615. doi:10.1016/j.jcou.2019.08.012.
- Zhang, X., Xiong, W., Tu, Z., Peng, L., Wu, Y., Hu, X., 2019. Supported ionic liquid membranes with dual-site interaction mechanism for efficient separation of CO₂. *ACS Sustain. Chem. Eng.* 7. doi:10.1021/acsuschemeng.9b01604.
- Zhang, Y., Feng, D., Gao, J., Du, Q., Wu, S., 2019. Thermodynamic properties in ternary system of NH₄HCO₃-H₂O-ethanol based on antisolvent method to strengthen crystallization of carbonized ammonia. *Adsorpt. Sci. Technol.* 37 (1–2), 127–138.
- Zhang, J., Xin, Q., Li, X., Yun, M., Xu, R., Wang, S., Li, Y., Lin, L., Ding, X., Ye, H., 2019a. Mixed matrix membranes comprising aminosilane-functionalized graphene oxide for enhanced CO₂ separation. *J. Membr. Sci.* 570, 343–354. doi:10.1016/j.memsci.2018.10.075.
- Zhang, X., Huang, Y., Gao, H., Luo, X., Liang, Z., Tontiwachwuthikul, P., 2019a. Zeolite catalyst-aided tri-solvent blend amine regeneration: An alternative pathway to reduce the energy consumption in amine-based CO₂ capture process. *Appl. Energy* 240, 827–841. doi:10.1016/j.apenergy.2019.02.089.
- Zhang, X., Huang, Y., Gao, H., Luo, X., Liang, Z., Tontiwachwuthikul, P., 2019a. Zeolite catalyst-aided tri-solvent blend amine regeneration: An alternative pathway to reduce the energy consumption in amine-based CO₂ capture process. *Appl. Energy* 240 (APR.15), 827–841.
- Zhang, X., Zhu, Z., Sun, X., Yang, J., Gao, H., Huang, Y., Luo, X., Liang, Z., Tontiwachwuthikul, P., 2019b. Reducing energy penalty of CO₂ capture using Fe promoted SO₄ (2-)/ZrO₂/MCM-41 catalyst. *Environ. Sci. Technol.* 53 (10), 6094–6102. doi:10.1021/acs.est.9b01901.
- Zhang, X., Zhu, Z., Sun, X., Yang, J., Gao, H., Huang, Y., Luo, X., Liang, Z., Tontiwachwuthikul, P., 2019b. Reducing energy penalty of CO₂ capture using Fe promoted SO₄²⁻/ZrO₂/MCM-41 catalyst. *Environ. Sci. Technol.* 53 (10), 6094–6102. doi:10.1021/acs.est.9b01901.
- Zhang, J., Xin, Q., Li, X., Yun, M., Xu, R., Wang, S., Li, Y., Lin, L., Ding, X., Ye, H., Zhang, Y., 2019b. Mixed matrix membranes comprising aminosilane-functionalized graphene oxide for enhanced CO₂ separation. *J. Membr. Sci.* 570–571, 343–354. doi:10.1016/j.memsci.2018.10.075.
- Zhang, T.M., Zhang, W.W., Zhang, Y., Shen, M.X., Zhang, J.F., 2020. Gas phase synthesis of aminated nanocellulose aerogel for carbon dioxide adsorption. *Cellulose* 27 (6), 2953–2958. doi:10.1007/s10570-020-03035-7.
- Zhang, W., Xie, P., Li, Y., Teng, L., Zhu, J., 2020. CFD analysis of the hydrodynamic characteristics in a rotating packed bed with multi-nozzles. *Chem. Eng. Process. - Process Intensif.* 158. doi:10.1016/j.cep.2020.108107, 108107–108107.
- Zhang, W.D., Sun, S.Z., Zhao, Y.J., Zhao, Z.J., Wang, P.X., Feng, D.D., Li, P.F., 2020. Effects of total pressure and CO₂ partial pressure on the physicochemical properties and reactivity of pressurized coal char produced at rapid heating rate. *Energy* 208. doi:10.1016/j.energy.2020.118297.
- Zhang, W., Li, Y., Li, B.Y., Wang, Y.Z., Qian, Y.Q., Wang, Z.Y., 2020a. Simultaneous NO/CO₂ removal by Cu-modified biochar/CaO in carbonation stage of calcium looping process. *Chem. Eng. J.* 392. doi:10.1016/j.cej.2019.123659.
- Zhang, W., Li, Y.J., Ma, X.T., Qian, Y.Q., Wang, Z.Y., 2020b. Simultaneous NO/CO₂ removal performance of biochar/limestone in calcium looping process. *Fuel* 262. doi:10.1016/j.fuel.2019.116428.
- Zhang, B., Yan, Q., Chen, G., Yi, C., Qi, S., Yang, B., 2021. Fabrication of mixed matrix membranes with zinc ion loaded titanium dioxide for improved CO₂ separation. *Sep. Purif. Technol.* 254, 117472. doi:10.1016/j.seppur.2020.117472.
- Zhang, W., Xie, P., Li, Y., Teng, L., Zhu, J., 2021. 3D CFD simulation of the liquid flow in a rotating packed bed with structured wire packing. *Chem. Eng. J.* 427. doi:10.1016/j.cej.2021.130874, 130874–130874.
- Zhang, Z., Rao, S., Han, Y., Pang, R., Ho, W.S.W., 2021. CO₂-selective membranes containing amino acid salts for CO₂/N₂ separation. *J. Membr. Sci.* 638, 119696. doi:10.1016/j.memsci.2021.119696.
- Zhang, Q., Zhou, M., Liu, X., Zhang, B., 2021a. Pebax/two-dimensional MFI nanosheets mixed-matrix membranes for enhanced CO₂ separation. *J. Membr. Sci.* 636. doi:10.1016/j.memsci.2021.119612.
- Zhang, Q., Zhou, M., Liu, X., Zhang, B., 2021b. Pebax/two-dimensional MFI nanosheets mixed-matrix membranes for enhanced CO₂ separation. *J. Membr. Sci.* 636, 119612.
- Zhang, B., Peng, J., Li, Y., Shi, H., Jin, J., Hu, J., Lu, S., 2022. Evaluating CO₂ desorption activity of tri-solvent MEA + EAE + AMP with various commercial solid acid catalysts. *Catalysts* 12 (7). doi:10.3390/catal12070723.
- Zhang, G., Tran, T.N., Huang, L., Deng, E., Blevins, A., Guo, W., Ding, Y., Lin, H., 2022. Thin-film composite membranes based on hyperbranched poly (ethylene oxide) for CO₂/N₂ separation. *J. Membr. Sci.* 644, 120184. doi:10.1016/j.memsci.2021.120184.
- Zhang, J.J., Huang, D.R., Shao, J.A., Zhang, X., Zhang, S.H., Yang, H.P., Chen, H.P., 2022. A new nitrogen-enriched biochar modified by ZIF-8 grafting and annealing for enhancing CO₂ adsorption. *Fuel Process. Technol.* 231. doi:10.1016/j.fuproc.2022.107250.
- Zhang, P., Xin, Y., He, Y., et al., 2022. Exploring a blue-light-sensing transcription factor to double the peak productivity of oil in nanochloropsis oceanica. *Nat. Commun.* 13 (1664). doi:10.1038/s41467-022-29337-x.
- Zhang, X., Rong, M., Qin, P., Tan, T., 2022. PEO-based CO₂-philic mixed matrix membranes comprising N-rich ultramicroporous polyaminals for superior CO₂ capture. *J. Membr. Sci.* 644, 120111. doi:10.1016/j.memsci.2021.120111.
- Zhang, X., Zhang, F., Song, Z., Lin, L., Zhao, X., Sun, J., Mao, Y., Wang, W., 2022. Review of chemical looping process for carbonaceous feedstock conversion: rational design of oxygen carriers. *Fuel* 325, 124964.
- Zhang, X.Y., Cao, L.Y., Xiang, W., Xu, Y., Gao, B., 2022. Preparation and evaluation of fine-tuned micropore biochar by lignin impregnation for CO₂ and VOCs adsorption. *Sep. Purif. Technol.* 295. doi:10.1016/j.seppur.2022.121295.
- Zhang, Y., Ma, L., Lv, Y., Tan, T., 2022. Facile manufacture of COF-based mixed

- matrix membranes for efficient CO₂ separation. *Chem. Eng. J.* 430, 133001. doi:10.1016/j.cej.2021.133001.
- Zhang, Y., Wang, S.Z., Feng, D.D., Gao, J.M., Dong, L.H., Zhao, Y.J., Sun, S.Z., Huang, Y.D., Qin, Y.K., 2022. Functional biochar synergistic solid/liquid-phase CO₂ capture: a review. *Energy Fuels* 36 (6), 2945–2970. doi:10.1021/acs.energyfuels.1c04372.
- Zhang, Z., Zheng, Y., Qian, L., Luo, D., Dou, H., Wen, G., Yu, A., Chen, Z., 2022. Emerging trends in sustainable CO₂-management materials. *Adv. Mater.* 34 (29), 2201547. doi:10.1002/adma.202201547.
- Zhang, G., Ingham, D., Ma, L., Pourkashanian, M., 2022. Modelling of 3D liquid dispersion in a rotating packed bed using an Eulerian porous medium approach. *Chem. Eng. Sci.* 250. doi:10.1016/j.ces.2021.117393, 117393–117393.
- Zhang, C., Li, Y., Yang, L., Fan, X., Chu, L., 2022. Analysis on H₂ production process integrated CaO/Ca(OH)₂ heat storage and sorption enhanced staged gasification using calcium looping. *Energy Convers. Manage.* 253, 115169.
- Zhang, G., Ma, L., Pourkashanian, M., 2023. A porous medium approach to the 3D modelling of an entire rotating packed bed for post-combustion carbon capture. *Chem. Eng. Sci.* 274. doi:10.1016/j.ces.2023.118687, 118687–118687.
- Zhang, Z., Guo, K., Luo, H., Song, J., Qian, Z., 2014. Characteristics of mass transfer between gas-liquid phases in a hige reactor. *Chemical Industry and Chemical Engineering Quarterly* 20 (4), 523–530. doi:10.2298/CICEQ130729034Z.
- Zhao, Y., Ho, W.W., 2012. Steric hindrance effect on amine demonstrated in solid polymer membranes for CO₂ transport. *J. Membr. Sci.* 415, 132–138.
- Zhao, Y., Winston Ho, W.S., 2012. Steric hindrance effect on amine demonstrated in solid polymer membranes for CO₂ transport. *J. Membr. Sci.* 415–416, 132–138. doi:10.1016/j.memsci.2012.04.044.
- Zhao, J., Wang, Z., Wang, J., Wang, S., 2006. Influence of heat-treatment on CO₂ separation performance of novel fixed carrier composite membranes prepared by interfacial polymerization. *J. Membr. Sci.* 283 (1), 346–356. doi:10.1016/j.memsci.2006.07.004.
- Zhao, T., Ochoa-Fernández, E., Ronning, M., Chen, D., 2007. Preparation and high-temperature CO₂ capture properties of nanocrystalline NaZrO₃. *Chem. Mater.* 19 (13), 3294–3301.
- Zhao, L., Bacsik, Z., Hedin, N., Wei, W., Sun, Y., Antonietti, M., Titirici, M.M., 2010. Carbon dioxide capture on amine-rich carbonaceous materials derived from glucose. *ChemSusChem* 3 (7), 840–845. doi:10.1002/cssc.201000044.
- Zhao, Y., Ding, H., Zhong, Q., 2012. Preparation and characterization of aminated graphite oxide for CO₂ capture. *Appl. Surf. Sci.* 258 (10), 4301–4307. doi:10.1016/j.apsusc.2011.12.085.
- Zhao, Y., Yao, K.X., Teng, B., Zhang, T., Han, Y., 2013. A perfluorinated covalent triazine-based framework for highly selective and water-tolerant CO₂ capture. *Energy Environ. Sci.* 6 (12), 3684–3692.
- Zhao, M., Bilton, M., Brown, A.P., Cunliffe, A.M., Dvinnov, E., Dupont, V., Comyn, T.P., Milne, S.J., 2014. Durability of CaO-CaZrO₃ sorbents for high-temperature CO₂ capture prepared by a wet chemical method. *Energy Fuels* 28 (2), 1275–1283. doi:10.1021/ef4020845.
- Zhao, R., Deng, S., Zhao, L., Liu, Y., Tan, Y., 2015. Energy-saving pathway exploration of CCS integrated with solar energy: Literature research and comparative analysis. *Energy Convers. Manage.* 102, 66–80. doi:10.1016/j.enconman.2015.01.018.
- Zhao, S., Feron, P.M., Deng, L., Favre, E., Chabanon, E., Yan, S., Hou, J., Chen, V., Qi, H., 2016. Status and progress of membrane contactors in post-combustion carbon capture: A state-of-the-art review of new developments. *J. Membr. Sci.* 511, 180–206. doi:10.1016/j.memsci.2016.03.051.
- Zhao, L., Chen, Y., Wang, B., Sun, C., Chakraborty, S., Ramasubramanian, K., Dutta, P.K., Ho, W.W., 2016. Multilayer polymer/zeolite Y composite membrane structure for CO₂ capture from flue gas. *J. Membr. Sci.* 498, 1–13.
- Zhao, B., Liu, F., Cui, Z., Liu, C., Yue, H., Tang, S., Liu, Y., Lu, H., Liang, B., 2017. Enhancing the energetic efficiency of MDEA/PZ-based CO₂ capture technology for a 650 MW power plant: Process improvement. *Appl. Energy* 185, 362–375. doi:10.1016/j.apenergy.2016.11.009.
- Zhao, M., Lu, Q., Ma, Q., Zhang, H., 2017. Two-dimensional metal-organic framework nanosheets. *Small Methods* 1 (1–2), 1600030. doi:10.1039/C8CS00268A.
- Zhao, X., Zhou, H., Sikarwar, V.S., Zhao, M., Park, A.-H.A., Fennell, P.S., Shen, L., Fan, L.-S., 2017. Biomass-based chemical looping technologies: the good, the bad and the future. *Energy Environ. Sci.* 10 (9), 1885–1910. doi:10.1039/C6EE03718F.
- Zhao, Q., Wu, F., He, Y., Xiao, P., Webley, P.A., 2017. Impact of operating parameters on CO₂ capture using carbon monolith by Electrical Swing Adsorption technology (ESA). *Chem. Eng. J.* 327, 441–453. doi:10.1016/j.cej.2017.06.123.
- Zhao, R., Deng, S., Liu, Y., Zhao, Q., He, J., Zhao, L., 2017a. Carbon pump: Fundamental theory and applications. *Energy* 119, 1131–1143. doi:10.1016/j.energy.2016.11.076.
- Zhao, R., Deng, S., Zhao, L., Zhao, Y., Li, S., Zhang, Y., Yu, Z., 2017b. Experimental study and energy-efficiency evaluation of a 4-step pressure-vacuum swing adsorption (PVSA) for CO₂ capture. *Energy Convers. Manage.* 151, 179–189. doi:10.1016/j.enconman.2017.08.057.
- Zhao, R., Zhao, L., Deng, S., Song, C., He, J., Shao, Y., Li, S., 2017c. A comparative study on CO₂ capture performance of vacuum-pressure swing adsorption and pressure-temperature swing adsorption based on carbon pump cycle. *Energy* 137, 495–509. doi:10.1016/j.energy.2017.01.158.
- Zhao, Q., Wu, F., Xie, K., Singh, R., Zhao, J., Xiao, P., Webley, P.A., 2018. Synthesis of a novel hybrid adsorbent which combines activated carbon and zeolite NaUSY for CO₂ capture by electric swing adsorption (ESA). *Chem. Eng. J.* 336, 659–668. doi:10.1016/j.cej.2017.11.167.
- Zhao, T.X., Zhang, X.M., Tu, Z.H., Wu, Y.T., Hu, X.B., 2018. Low-viscous diamino protic ionic liquids with fluorine-substituted phenolic anions for improving CO₂ reversible capture. *J. Mol. Liq.* 268, 617–624. doi:10.1016/j.molliq.2018.07.096.
- Zhao, X., Ji, G.Z., Liu, W., He, X., Anthony, E.J., Zhao, M., 2018. Mesoporous MgO promoted with NaNO₃/NaNO₂ for rapid and high-capacity CO₂ capture at moderate temperatures. *Chem. Eng. J.* 332 (Supplement C), 216–226. doi:10.1016/j.cej.2017.09.068.
- Zhao, Y., Kuang, Y., Liu, M., Wang, J., Pei, R., 2018. Synthesis of metal-organic framework nanosheets with high relaxation rate and singlet oxygen yield. *Chem. Mater.* 30 (21), 7511–7520. doi:10.1021/acs.chemmater.8b02467.
- Zhao, H., Luo, X., Zhang, H., Sun, N., Wei, W., Sun, Y., 2018. Carbon-based adsorbents for post-combustion capture: a review. *Greenh. Gases: Sci. Technol.* 8 (1), 11–36. doi:10.1002/ghg.1758.
- Zhao, J., Xie, K., Liu, L., Liu, M., Qiu, W., Webley, P.A., 2019. Enhancing plasticization-resistance of mixed-matrix membranes with exceptionally high CO₂/CH₄ selectivity through incorporating ZSM-25 zeolite. *J. Membr. Sci.* 583, 23–30. doi:10.1016/j.memsci.2019.03.073.
- Zhao, Q., Wu, F., Men, Y., Fang, X., Zhao, J., Xiao, P., Webley, P.A., Grande, C.A., 2019. CO₂ capture using a novel hybrid monolith (H-ZSM5/activated carbon) as adsorbent by combined vacuum and electric swing adsorption (VESA). *Chem. Eng. J.* 358, 707–717. doi:10.1016/j.cej.2018.09.196.
- Zhao, Y., Feng, D., Li, B., Sun, S., Zhang, S., 2019. Combustion characteristics of char from pyrolysis of Zhundong sub-bituminous coal under O₂/steam atmosphere: Effects of mineral matter. *Int. J. Greenh. Gas Control* 80, 54–60. doi:10.1016/j.ijggc.2018.12.001.
- Zhao, R., Liu, L., Zhao, L., Deng, S., Li, S., Zhang, Y., 2019a. A comprehensive performance evaluation of temperature swing adsorption for post-combustion carbon dioxide capture. *Renew. Sustain. Energy Rev.* 114. doi:10.1016/j.rser.2019.109285, 109285–109285.
- Zhao, R., Liu, L., Zhao, L., Deng, S., Li, S., Zhang, Y., Li, H., 2019b. Thermodynamic exploration of temperature vacuum swing adsorption for direct air capture of carbon dioxide in buildings. *Energy Convers. Manage.* 183, 418–426. doi:10.1016/j.enconman.2019.01.009.
- Zhao, H., Li, H., Li, X., Gao, X., 2021. Process intensification for improving the uniformity and efficiency of microwave heating reactor by bubbles-enhanced flow method. *Appl. Therm. Eng.* 197. doi:10.1016/j.applthermaleng.2021.117346.
- Zhao, Z., Li, H., Zhao, K., Wang, L., Gao, X., 2022a. Microwave-assisted synthesis of MOFs: Rational design via numerical simulation. *Chem. Eng. J.* 428. doi:10.1016/j.cej.2021.131006.
- Zhao, Z., Shen, X., Li, H., Liu, K., Wu, H., Li, X., Gao, X., 2022b. Watching microwave-induced microscopic hot spots via the thermosensitive fluorescence of Europium/Terbium mixed-metal organic complexes. *Angew. Chem.-Int. Ed.* 61 (6). doi:10.1002/anie.2021.14340.
- Zheng, C., Tan, J., Wang, Y., Luo, G., 2012. CO₂ solubility in a mixture absorption system of 2-amino-2-methyl-1-propanol with glycol. *Ind. Eng. Chem. Res.* 51 (34), 11236–11244.
- Zheng, H., Wang, Z., Deng, X., Zhao, J., Luo, Y., Novak, J., Herbert, S., Xing, B., 2013. Characteristics and nutrient values of biochars produced from giant reed at different temperatures. *Bioresour. Technol.* 130, 463–471. doi:10.1016/j.biortech.2012.12.044.
- Zheng, F., Heldebrandt, D.J., Mathias, P.M., Koeh, P., Bhakta, M., Freeman, C.J., Bearden, M.D., Zwoster, A., 2016. Bench-scale testing and process performance projections of CO₂ capture by CO₂-binding organic liquids (CO₂BOLs) with and without polarity-swung-assisted regeneration. *Energy Fuels* doi:10.1021/acs.energyfuels.5b02437.
- Zheng, W.T., Zhang, F., Wu, Y.T., Hu, X.B., 2017. Concentrated aqueous solutions of protic ionic liquids as effective CO₂ adsorbents with high absorption capacities. *J. Mol. Liq.* 243, 169–177. doi:10.1016/j.molliq.2017.08.035.
- Zheng, W.-T., Huang, K., Dai, S., 2019. Solvothermal and template-free synthesis of N-Functionalized mesoporous polymer for amine impregnation and CO₂ adsorption. *Microporous Mesoporous Mater.* 290. doi:10.1016/j.micromeso.2019.109653.
- Zheng, X., Fukuhara, K., Hijikata, Y., Pirillo, J., Sato, H., Takahashi, K., Noro, S., Nakamura, T., 2020. Understanding the interactions between the bis(trifluoromethylsulfon)imide anion and adsorbed CO₂ using X-ray diffraction analysis of a soft crystal surrogate. *Commun. Chem.* 3 (1), doi:10.1038/s42004-020-00390-1.
- Zheng, S., Zeng, S., Li, Y., Bai, L., Bai, Y., Zhang, X., Liang, X., Zhang, S., 2021. State of the art of ionic liquid-modified adsorbents for CO₂ capture and separation. *AIChE J.* 68 (2). doi:10.1002/aic.17500.
- Zheng, W., Liu, Z., Ding, R., Dai, Y., Li, X., Ruan, X., He, G., 2022. Constructing continuous and fast transport pathway by highly permeable polymer electrospon fibers in composite membrane to improve CO₂ capture. *Sep. Purif. Technol.* 285, 120332. doi:10.1016/j.seppur.2021.120332.
- Zheng, Q., Xie, Y., Tan, J., Xu, Z., Luo, P., Wang, T., Liu, Z., Liu, F., Zhang, K., Fang, Z., Zhang, G., Jin, W., 2022. Coupling of dielectric barrier discharge plasma with oxygen permeable membrane for highly efficient low-temperature permeation. *J. Membr. Sci.* 641, 119896. doi:10.1016/j.memsci.2021.119896.
- Zhou, S., Chen, X., Nguyen, T., Voice, A.K., Rochelle, G.T., 2010. Aqueous ethylenediamine for CO₂ capture. *ChemSusChem* 3 (8), 913–918. doi:10.1002/cssc.20090293.
- Zhou, C., Shah, K., Moghtaderi, B., 2015a. Techno-economic assessment of integrated chemical looping air separation for oxy-fuel combustion: An Australian case study. *Energy Fuels* 29 (4), 2074–2088. doi:10.1021/EF5022076/SUPPL_FILE/EF5022076_SI_001.PDF.
- Zhou, C., Shah, K., Song, H., Zanganeh, J., Doroodchi, E., Moghtaderi, B., 2015b. Integration options and economic analysis of an integrated chemical looping air separation process for oxy-fuel combustion. *Energy Fuels* 30 (3), 1741–1755. doi:10.1021/ACS.ENERGYFUELS.5B02209.
- Zhou, C., Shah, K., Song, H., Zanganeh, J., Doroodchi, E., Moghtaderi, B., 2016. Integration options and economic analysis of an integrated chemical looping air separation process for oxy-fuel combustion. *Energy Fuels* 30 (3), 1741–1755. doi:10.1021/ACS.ENERGYFUELS.5B02209/ASSET/IMAGES/LARGE/EF-2015-02209K_0023.JPEG.
- Zhou, Z., Zhou, X., Jing, G., Lv, B., 2016. Evaluation of the multi-amine functionalized

- ionic liquid for efficient postcombustion CO₂ capture. *Energy Fuels* 30 (9), 7489–7495. doi:10.1021/acs.energyfuels.6b00692.
- Zhou, K., Chaemchuen, S., Verpoort, F., 2017. Alternative materials in technologies for biogas upgrading via CO₂ capture. *Renew. Sustain. Energy Rev.* 79, 1414–1441. doi:10.1016/j.rser.2017.05.198.
- Zhou, X., Liu, F., Lv, B., Zhou, Z., Jing, G., 2017. Evaluation of the novel biphasic solvents for CO₂ capture: Performance and mechanism. *Int. J. Greenh. Gas Control* 60, 120–128. doi:10.1016/j.jggc.2017.03.013.
- Zhou, Z., Anderson, C.M., Butler, S.K., Thompson, S.K., Whitty, K.J., Shen, T.C., Stowers, K.J., 2017. Stability and efficiency of CO₂ capture using linear amine polymer modified carbon nanotubes. *J. Mater. Chem. A* 5 (21), 10486–10494. doi:10.1039/c7ta02576a.
- Zhou, Z., Balijepalli, S.K., Nguyen-Sorenson, A.H.T., Anderson, C.M., Park, J.L., Stowers, K.J., 2018. Steam-stable covalently bonded polyethylenimine modified multiwall carbon nanotubes for carbon dioxide capture. *Energy Fuels* 32 (11), 11701–11709. doi:10.1021/acs.energyfuels.8b02864.
- Zhou, H., Zhao, B., Fu, C., Wu, Z., Wang, C., Ding, Y., Han, B.-H., Hu, A., 2019. Synthesis of conjugated microporous polymers through cationic cyclization polymerization. *Macromolecules* 52 (10), 3935–3941. doi:10.1021/acs.macromol.9b00437.
- Zhou, S., Zhao, Y., Zheng, J., Zhang, S., 2019. High-performance functionalized polymer of intrinsic microporosity (PIM) composite membranes with thin and stable interconnected layer for organic solvent nanofiltration. *J. Membr. Sci.* 591, 117347. doi:10.1016/j.memsci.2019.117347.
- Zhou, X., Jing, G., Lv, B., Liu, F., Zhou, Z., 2019. Low-viscosity and efficient regeneration of carbon dioxide capture using a biphasic solvent regulated by 2-amino-2-methyl-1-propanol. *Appl. Energy* 235, 379–390. doi:10.1016/j.apenergy.2018.10.118.
- Zhou, H.C., Xu, X., Chen, X.C., Yu, G.R., 2020. Novel ionic liquids phase change solvents for CO₂ capture. *Int. J. Greenh. Gas Control* 98. doi:10.1016/j.jggc.2020.103068.
- Zhou, X., Li, X., Wei, J., Fan, Y., Liao, L., Wang, H., 2020. Novel nonaqueous liquid-liquid biphasic solvent for energy-efficient carbon dioxide capture with low corrosivity. *Environ. Sci. Technol.* 54 (24), 16138–16146. doi:10.1021/acs.est.0c05774.
- Zhou, S., Sun, Y., Xue, B., Li, S., Zheng, J., Zhang, S., 2020a. Controlled superacid-catalyzed self-cross-linked polymer of intrinsic microporosity for high-performance CO₂ separation. *Macromolecules* 53 (18), 7988–7996.
- Zhou, S., Sun, Y., Xue, B., Li, S., Zheng, J., Zhang, S., 2020b. Controlled superacid-catalyzed self-cross-linked polymer of intrinsic microporosity for high-performance CO₂ separation. *Macromolecules* 53 (18), 7988–7996.
- Zhou, G., Wang, K.L., Liu, R.L., Tian, Y., Kong, B., Qi, G.S., 2021. Synthesis and CO₂ adsorption performance of TEPa-loaded cellulose whisker/silica composite aerogel. *Colloid Surf. A* 631. doi:10.1016/j.colsurfa.2021.127675.
- Zhou, Q., Fu, X., Hui Lim, K., Li, Z., Liao, M., Lu, J., Liu, F., Kawi, S., 2022. Complete confinement of Ce/Ni within SiO₂ nanotube with high oxygen vacancy concentration for CO₂ methane reforming. *Fuel* 325, 124819. doi:10.1016/j.fuel.2022.124819.
- Zhu, L., Fan, Y., 2011. A real options-based CCS investment evaluation model: Case study of China's power generation sector. *Appl. Energy* 88 (12), 4320–4333. doi:10.1016/j.apenergy.2011.04.005.
- Zhu, Y., Zhang, W., 2014. Reversible tuning of pore size and CO₂ adsorption in azobenzene functionalized porous organic polymers. *Chem. Sci.* 5 (12), 4957–4961. doi:10.1039/c4sc02305f.
- Zhu, L., Zhang, Y.-B., 2017. Crystallization of covalent organic frameworks for gas storage applications. *Molecules* 22 (7), 1149.
- Zhu, W., Hrabanek, P., Gora, L., Kapteijn, F., Moulijn, J.A., 2006. Role of adsorption in the permeation of CH₄ and CO₂ through a silicalite-1 membrane. *Ind. Eng. Chem. Res.* 45 (2), 767–776.
- Zhu, Y., Liu, X., Zhou, Z., 2006. Optimization of cryogenic air separation distillation columns. In: *Proceedings of the World Congress on Intelligent Control and Automation (WCICA)*, 2, pp. 7702–7705. doi:10.1109/WCICA.2006.1713466.
- Zhu, X., Tian, C., Chai, S., Nelson, K., Han, K.S., Hagaman, E.W., Veith, G.M., Mahurin, S.M., Liu, H., Dai, S., 2013. New tricks for old molecules: development and application of porous N-doped, carbonaceous membranes for CO₂ separation. *Adv. Mater.* 25 (30), 4152–4158. doi:10.1002/adma.201300793.
- Zhu, L., Swihart, M.T., Lin, H., 2017. Tightening polybenzimidazole (PBI) nanostructure via chemical cross-linking for membrane H₂/CO₂ separation. *J. Mater. Chem. A* 5 (37), 19914–19923.
- Zhu, X., Song, M.L., Xu, Y.J., 2017. DBU-based protic ionic liquids for CO₂ capture. *ACS Sustain. Chem. Eng.* 5 (9), 8192–8198. doi:10.1021/acssuschemeng.7b01839.
- Zhu, J., He, B., Huang, J., Li, C., Ren, T., 2018. Effect of immobilization methods and the pore structure on CO₂ separation performance in silica-supported ionic liquids. *Microporous Mesoporous Mater.* 260, 190–200. doi:10.1016/j.micromeso.2017.10.035.
- Zhu, L., Swihart, M.T., Lin, H., 2018. Unprecedented size-sieving ability in polybenzimidazole doped with polyprotic acids for membrane H₂/CO₂ separation. *Energy Environ. Sci.* 11 (1), 94–100. doi:10.1039/c7ee02865b.
- Zhu, Z., Chen, Y., Wu, J., Zhang, S., Zheng, S., 2019a. A modified Allam cycle without compressors realizing efficient power generation with peak load shifting and CO₂ capture. *Energy* 174, 478–487.
- Zhu, Z., Chen, Y., Wu, J., Zheng, S., Zhao, W., 2019b. Performance study on s-CO₂ power cycle with oxygen fired fuel of s-water gasification of coal. *Energy Convers. Manage.* 199, 112058.
- Zhu, W.K., Yao, Y., Zhang, Y., Jiang, H., Wang, Z., Chen, W., Xue, Y.Y., 2020. Preparation of an amine-modified cellulose nanocrystal aerogel with chemical vapour deposition and its application in CO₂ capture. *Ind. Eng. Chem. Res.* 59 (38), 16660–16668. doi:10.1021/acs.iecr.0c02687.
- Zhu, X., Chen, L., Chen, Y., Cao, Q., Liu, X., Li, D., 2020. Effect of H₂ addition on the microbial community structure of a mesophilic anaerobic digestion system. *Energy* 198, 117368. doi:10.1016/j.energy.2020.117368.
- Zhu, X., Intiaz, Q., Donat, F., Müller, C.R., Li, F., 2020. Chemical looping beyond combustion – a perspective. *Energy Environ. Sci.* 13 (3), 772–804. doi:10.1039/C9EE03793D.
- Zhu, X., Ge, T., Yang, F., Wang, R., 2021. Design of steam-assisted temperature vacuum-swing adsorption processes for efficient CO₂ capture from ambient air. *Renew. Sustain. Energy Rev.* 137, 110651. doi:10.1016/j.rser.2020.110651.
- Zhu, L., Yin, D., Qin, Y., Konda, S., Zhang, S., Zhu, A., Liu, S., Xu, T., Swihart, M.T., Lin, H., 2019. Sorption-enhanced mixed matrix membranes with facilitated hydrogen transport for hydrogen purification and CO₂ capture. *Adv. Funct. Mater.* 29 (36), 1904357.
- Zhuang, Q., Clements, B., 2018. CO₂ capture by biphasic absorbent—adsorption performance and VLE 2 characterisation. *Energy* 147, 169. doi:10.1016/j.energy.2018.07.015.
- Zhuang, Y., Seong, J.G., Lee, W.H., Do, Y.S., Lee, M.J., Wang, G., Guiver, M.D., Lee, Y.M., 2015. Mechanically tough, thermally rearranged (TR) random/block poly (benzoxazole-co-imide) gas separation membranes. *Macromolecules* 48 (15), 5286–5299.
- Zhuo, H., Hu, Y.J., Tong, X., Zhong, L.X., Peng, X.W., Sun, R.C., 2016. Sustainable hierarchical porous carbon aerogel from cellulose for high-performance supercapacitor and CO₂ capture. *Ind. Crops Prod.* 87, 229–235. doi:10.1016/j.indcrop.2016.04.041.
- Ziółkowski, P., Zakrzewski, W., Kaczmarsczyk, O., Badur, J., 2013. Thermodynamic analysis of the double Brayton cycle with the use of oxy combustion and capture of CO₂. *Arch. Thermodyn.* 34 (2), 23–38. doi:10.2478/aoter-2013-0008.
- Ziaï, S., Rochelle, G.T., Edgar, T.F., 2009. Dynamic modeling to minimize energy use for CO₂ capture in power plants by aqueous monoethanolamine. *Ind. Eng. Chem. Res.* 48 (13), 6105–6111. doi:10.1021/ie801385q.
- Zoghalmi, A., Paes, G., 2019. Lignocellulosic biomass: understanding recalcitrance and predicting hydrolysis. *Front. Chem.* 7. doi:10.3389/fchem.2019.00874.
- Zornoza, B., Téllez, C., Coronas, J., Esekile, O., Koros, W.J., 2015. Mixed matrix membranes based on 6FDA polyimide with silica and zeolite microsphere dispersed phases. *AIChE J.* 61 (12), 4481–4490.
- Zou, C., Zhang, L., Cao, S., Zheng, C., 2014a. A study of combustion characteristics of pulverized coal in O₂/H₂O atmosphere. *Fuel* 115, 312–320. doi:10.1016/j.fuel.2013.07.025.
- Zou, C., Zhang, L., Cao, S., Zheng, C., 2014b. A study of combustion characteristics of pulverized coal in O₂/H₂O atmosphere. *Fuel* 115, 312–320.
- Zou, C., Cai, L., Wu, D., Liu, Y., Liu, S., Zheng, C., 2015a. Ignition behaviors of pulverized coal particles in O₂/N₂ and O₂/H₂O mixtures in a drop tube furnace using flame monitoring techniques. *Proc. Combust. Instit.* 35 (3), 3629–3636. doi:10.1016/j.proci.2014.06.067.
- Zou, C., Cai, L., Wu, D., Liu, Y., Liu, S., Zheng, C., 2015b. Ignition behaviors of pulverized coal particles in O₂/N₂ and O₂/H₂O mixtures in a drop tube furnace using flame monitoring techniques. *Proc. Combust. Instit.* 35 (3), 3629–3636.
- Zou, L., Sun, Y., Che, S., Yang, X., Wang, X., Bosch, M., Wang, Q., Li, H., Smith, M., Yuan, S., Perry, Z., Zhou, H.C., 2017. Porous organic polymers for post-combustion carbon capture. *Adv. Mater.* 29 (37). doi:10.1002/adma.201700229.
- Zubbri, N.A., Mohamed, A.R., Kamiuchi, N., Mohammadi, M., 2020. Enhancement of CO₂ adsorption on biochar sorbent modified by metal incorporation. *Environ. Sci. Pollut. Res.* 27 (11), 11809–11829. doi:10.1007/s11356-020-07734-3.
- Zubbri, N.A., Mohamed, A.R., Lahijani, P., Mohammadi, M., 2021. Low temperature CO₂ capture on biomass-derived KOH-activated hydrochar established through hydrothermal carbonization with water-soaking pre-treatment. *J. Environ. Chem. Eng.* 9 (1). doi:10.1016/j.jece.2021.105074.
- Zydney, A.L., 1995. Membrane handbook edited by W. S. Winston Ho, and Kamallesh K. Sirkar, Van Nostrand Reinhold, New York, 1992, 954 pp. \$131.95. 41 (10), 2343–2344. https://doi.org/10.1002/aic.690411024.

Curriculum vitae

Personal data

Name: Mais Hanna Suleiman Baqain
Date of birth: 3rd May 1987
Place of birth: Birmingham, United Kingdom
Citizenship: Jordanian

Contact data

E-mail: mais.baqain@taltech.ee

Education

2020–2024 Tallinn University of Technology, PhD
2016–2018 German Jordanian University, Environmental and renewable energy engineering management, MSC
2005–2010 Mutah University, Chemical Engineering, BSC
2004–2005 Latin Baptic School, High school

Language competence

English Fluent
Arabic Native

Professional employment

2023– R&D Engineer, Industrial decarbonization, SUMITOMO SHI FW, Espoo, Finland
2020–2024 Early-stage researcher, Tallinn University of Technology, Tallinn, Estonia
2019–2020 Senior Lab Engineer, Attarat Mining Co., Jordan
2018–2019 Lab Trainer and consultant, Shell, Jordan
2016–2017 Senior Lab Engineer, Shell, Jordan
2011–2016 Lab Engineer, Shell, Jordan
2010–2011 Tender Engineer, International Technical Construction Co., Jordan

Elulookirjeldus

Isikuandmed

Nimi: Mais Hanna Suleiman Baqain
Sünniaeg: 03.05.1987
Sünnikoht: Birmingham, Ühendkuningriik
Kodakondsus: Jordaania

Kontaktandmed

E-post: mais.baqain@taltech.ee

Hariduskäik

2020–2024 Tallinna Tehnikaülikool, Inseneriteaduskond, Energiatehnoloogia instituut, PhD
2016–2018 German Jordanian University, Keskkonna- ja taastuvenergiajuhtimine, MSC
2005–2010 Mutahi ülikool, keemiatehnika, BSC
2004–2005 Ladina Ristikool, Keskkool

Keelteoskus

Inglise keel Kõrgtase
Araabia keel Emakeel

Teenistuskäik

2023–... Teadus- ja arendusinsener, Tööstuslik dekarboniseerimine, SUMITOMO SHI FW, Soome
2020–2024 Nooremteadur, Energiatehnoloogia instituut, Tallinna Tehnikaülikool, Eesti
2019–2020 Vanemlaboriinsener, Attarat Mining Co., Jordaania
2018–2019 Laborikoolitaja ja konsultant, Shell, Jordaania
2016–2017 Vanemlaboriinsener, Shell, Jordaania
2011–2016 Laboriinsener, Shell, Jordaania
2010–2011 Hankeinsener, International Technical Construction Co., Jordaania

ISSN 2585-6901 (PDF)
ISBN 978-9916-80-149-9 (PDF)